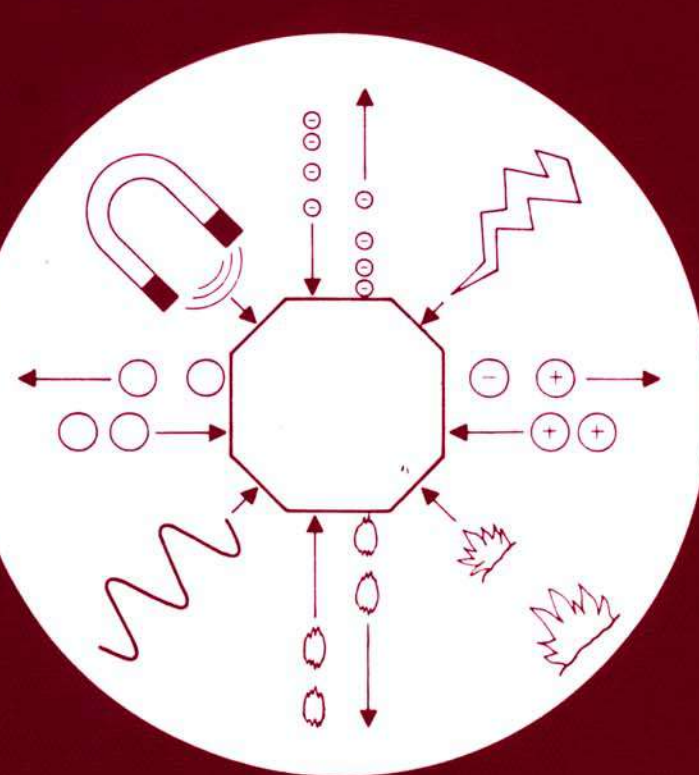


**studies in surface science and catalysis**

**90**



**ACID-BASE  
CATALYSIS II**

**H. Hattori  
M. Misono  
Y. Ono  
(editors)**

**elsevier**

**Studies in Surface Science and Catalysis 90**

**ACID-BASE CATALYSIS II**

**Proceedings of the International Symposium on  
Acid-Base Catalysis II, Sapporo,  
December 2-4, 1993**

This Page Intentionally Left Blank

**Studies in Surface Science and Catalysis**  
**Advisory Editors : B. Delmon and J. T. Yates**  
**Vol. 90**

# **ACID-BASE CATALYSIS II**

**PROCEEDINGS OF THE INTERNATIONAL SYMPOSIUM ON  
ACID-BASE CATALYSIS II, Sapporo,  
DECEMBER 2-4, 1993**

Edited by

Hideshi Hattori      *Hokkaido University*  
Makoto Misono      *The University of Tokyo*  
Yoshio Ono      *Tokyo Institute of Technology*

  
**KODANSHA**  
Tokyo

1994



Amsterdam-London-New York-Tokyo

*Copublished by*

KODANSHA LTD., Tokyo

*and*

ELSEVIER SCIENCE B.V., Amsterdam

*exclusive sales rights Japan*

KODANSHA LTD.

12-21, Otowa 2-chome, Bunkyo-ku, Tokyo 112, Japan

*for the rest of the world*

ELSEVIER SCIENCE B.V.

25 Sara Burgerhartstraat, P.O. Box 211, 1000 AE Amsterdam, The Netherlands

ISBN 0-444-98655-3

ISBN 4-06-207061-8 (Japan)

Copyright © 1994 by Kodansha Ltd.

All rights reserved

No part of this book may be reproduced in any form, by photostat, microfilm, retrieval system, or any other means, without the written permission of Kodansha Ltd. (except in the case of brief quotation for criticism or review)

PRINTED IN JAPAN

## **Organizing Committee**

H. Hattori      Hokkaido University, Japan (Chairman)  
M. Misono      The University of Tokyo, Japan (Vice Chairman)  
Y. Ono      Tokyo Institute of Technology, Japan (Vice Chairman)

## **Scientific Advisory Board**

S. Coluccia	University of Turin, Italy
A. B. Halgeri	Indian Petrochemicals Co. Ltd., India
W. Hölderich	RWTH-Aachen, Germany
Y. Izumi	Nagoya University, Japan
T. Inui	Kyoto University, Japan
M. Iwamoto	Hokkaido University, Japan
H. Kita	Hokkaido University, Japan
E. Kikuchi	Waseda University, Japan
K. J. Klabunde	Kansas State University, U.S.A.
H. Knözinger	University of Munich, Germany
A. Mitsutani	Nippon Chemtec Consulting Inc., Japan
Y. Moro-oka	Tokyo Institute of Technology, Japan
R. Ohnishi	Hokkaido University, Japan
G.K.S. Prakash	University of Southern California, U.S.A.
K. Segawa	Sophia University, Japan
G. Suzukamo	Sumitomo Chemical Co. Ltd., Japan
A. Tada	Kitami Institute of Technology, Japan
N. Takezawa	Hokkaido University, Japan
S. Tsuchiya	Yamaguchi University, Japan
T. Uematsu	Chiba University, Japan
M. Ueshima	Nippon Shokubai Co. Ltd., Japan
J.C. Védrine	CNRS Institute for Catalysis, France
T. Yamaguchi	Ehime University, Japan
T. Yashima	Tokyo Institute of Technology, Japan
S. Yoshida	Kyoto University, Japan

This Page Intentionally Left Blank

## List of Contributors

Numbers in parentheses refer to the pages on which a contributor's paper begins.

- AIKA, K. (195) Department of Environmental Chemistry and Engineering, Interdisciplinary Graduate School of Science and Engineering, Tokyo Institute of Technology, Midori-ku, Yokohama 227, Japan
- AIKAWA, K. (495) Institute of Materials Science, University of Tsukuba, Tsukuba 305, Japan
- ANDO, T. (9) Department of Chemistry, Shiga University of Medical Science, Otsu 520-21, Japan
- ANPO, M. (479) Department of Applied Chemistry, University of Osaka Prefecture, Gakuen-Cho, Sakai 593, Japan
- ARATA, K. (251) Department of Science, Hokkaido University of Education, Hakodate 040, Japan
- AYAME, A. (257) Department of Applied Chemistry, Muroran Institute of Technology, Mizumoto-cho, Muroran 050, Japan
- BABA, T. (117, 135) Department of Chemical Engineering, Tokyo Institute of Technology, Meguro-ku, Tokyo 152, Japan
- BABOU, F. (519) Institut de Recherches sur la Catalyse, UPR 5401 CNRS, 2 avenue A Einstein, F. Villeurbanne 69626, France
- BARTALINI, D. (183) Dipartimento di Chimica Inorganica, Chimica Fisica e Chimica dei Materiali, Università di Torino, via P. Giuria 7, 10125 Torino, Italy
- BIGOT, B. (519) Institut de Recherches sur la Catalyse, UPR 5401 CNRS, 2 avenue A Einstein, F. Villeurbanne 69626, France / Ecole Normale Supérieure de Lyon, 46 allée d'Italie, Lyon 69007, France
- BORELLO, E. (169) Dipartimento di Chimica Inorganica, Chimica Fisica e Chimica dei Materiali, Università di Torino, via P. Giuria 7, 10125 Torino, Italy
- BRADLEY, S. (129) Department of Physical Chemistry, University of New South Wales, Kensington, NSW 2033, Australia
- CAI, B.-X. (451) Institute of Catalysis, Hangzhou University, Hangzhou, 310028, P.R.China
- CAMBELL, S.M. (129) Department of Physical Chemistry, University of New South Wales, Kensington, NSW 2033, Australia
- CHEN, J.-M. (507) Department of Chemistry, Fudan University, Shanghai 200433, P.R.China

viii List of Contributors

- COLUCCIA, S. (169, 183) Dipartimento di Chimica Inorganica, Chimica Fisica e Chimica dei Materiali, Università di Torino, via P. Giuria 7, 10125 Torino, Italy
- CORNAGLIA, L.M. (429) Instituto de Investigaciones en Catálisis y Petroquímica - INCAPe - (FIQ, UNL - CONICET) Santiago del Estero 2829 - 3000 - Santa Fe, Argentina
- COUDURIER, G. (519) Institut de Recherches sur la Catalyse, UPR 5401 CNRS, 2 avenue A Einstein, F. Villeurbanne 69626, France
- DIMITROV, L. (413) Institute of Kinetics and Catalysis, Bulgarian Academy of Sciences, Sofia 1113, Bulgaria
- DISPENZIERE, N. (537) Exxon Chemical Company, Intermediates Technology Division, Clinton Township, Route 22 East, Annandale, N.J. 08801, U.S.A.
- DOMEN, K. (157) Research Laboratory of Resources Utilization, Tokyo Institute of Technology, Midori-ku, Yokohama 227, Japan
- DONG, J. (299, 327) Institute of Special Chemicals, Taiyuan University of Technology, Taiyuan, 030024, Shanxi, P.R.China
- EBITANI, K. (409) Department of Chemical Engineering, Faculty of Engineering, Tokyo Institute of Technology, Meguro-ku, Tokyo 152, Japan
- EI-DUSOUQUI, O.M.E. (141) Institute of Physical Chemistry, Vienna University of Technology, Getreidemarkt 9/156, A-1060 Wien, Austria
- ERNST, H. (105) Fachbereich Physik der Universität Leipzig, Linnéstraße 5, D-04103 Leipzig, Germany
- FEI, J.-H. (451) Institute of Catalysis, Hangzhou University, Hangzhou, 310028, P.R.China
- FIGUERAS, F. (183) Laboratoire de Chimie Organique Physique et Cinétique Chimique Appliquées - U.A. 418 du C.N.R.S., E.N.S.C.M., 8, rue de l'Ecole Normale 34075 Montpellier CEDEX, France
- FREUDE, D. (105) Fachbereich Physik der Universität Leipzig, Linnéstraße 5, D-04103 Leipzig, Germany
- FUJISAWA, H. (263) Department of Chemistry, Faculty of Science, Hokkaido University, Kita-ku, Sapporo 060, Japan
- FUJITA, N. (47) Research Center, Mitsubishi Kasei Corporation, Midori-ku, Yokohama 227, Japan
- FUNABIKI, T. (473, 485) Department of Molecular Engineering, Kyoto University, Sakyo-ku, Kyoto 606-01, Japan
- GAO, Z. (507) Department of Chemistry, Fudan University, Shanghai 200433, P.R.China
- GARRONE, E. (183) Dipartimento di Chimica Inorganica, Chimica Fisica e Chimica dei Materiali, Università di Torino, via P. Giuria 7, 10125 Torino, Italy
- GIAMELLO, E. (169) Dipartimento di Chimica Inorganica, Chimica Fisica e Chimica dei Materiali, Università di Torino, via P. Giuria 7, 10125 Torino, Italy

- GOULDING, P.A. (269) MEL Chemicals, Swinton, Manchester, M27 8LS, U.K.
- GUISET, M. (367) URA CNRS 350, Université de Poitiers, 40 avenue du Recteur Pineau, 86022 Poitiers Cedex, France
- GUO, C. (543) Department of Chemistry, Jilin University, Changchun 130023, P.R.China
- HANAOKA, T. (397) National Institute of Materials and Chemical Research, AIST, Tsukuba 305, Japan
- HASEGAWA, S. (549) Department of Chemistry, Tokyo Gakugei University, Koganei, Tokyo 184, Japan
- HATTORI, H. (349) Graduate School of Environmental Earth Science, Hokkaido University, Sapporo 060, Japan
- HATTORI, T. (229) Department of Applied Chemistry, Nagoya University, Chikusa-ku, Nagoya 464-01, Japan
- HE, H. (279) Department of Chemistry, Jilin University, Changchun 130023, P.R.China
- HIMEI, H. (217) Department of Molecular Chemistry and Engineering, Faculty of Engineering, Tohoku University, Aoba-ku, Sendai 980, Japan
- HIRAO, K. (89) Graduate School of Environmental Earth Science, Hokkaido University, Kita-ku, Sapporo 060, Japan
- HIROSE, C. (157) Research Laboratory of Resources Utilization, Tokyo Institute of Technology, Midori-ku, Yokohama 227, Japan
- HONDA, K. (257) Department of Applied Chemistry, Muroran Institute of Technology, Mizumoto-cho, Muroran 050, Japan
- HOOK, J. (129) Department of Physical Chemistry, University of New South Wales, Kensington, NSW 2033, Australia
- HOWE, R.F. (129) Department of Physical Chemistry, University of New South Wales, Kensington, NSW 2033, Australia
- HUA, W.-M. (507) Department of Chemistry, Fudan University, Shanghai 200433, P.R.China
- HUANG, J. (543) State Key Laboratory of Catalysis, Dalian Institute of Chemical Physics, Chinese Academy of Sciences, Dalian 116023, P.R.China
- ICHIHASHI, H. (67) Organic Synthesis Research Laboratory, Sumitomo Chemical Co., Ltd., Takatsuki 569, Japan
- ICHIKAWA, M. (101, 339) Catalysis Research Center, Hokkaido University, Kita-ku, Sapporo 060, Japan
- IGLESIAS, E. (531) Department of Chemical Engineering, University of California, Berkeley, California 94720, U.S.A.
- IINO, T. (97) Department of Materials Science, Kitami Institute of Technology, Koen-cho, Kitami 090, Japan
- IMAMURA, H. (467) Department of Advanced Materials Science and Engineering, Faculty of Engineering, Yamaguchi University, Tokiwadai, Ube 755, Japan

x List of Contributors

- IMIZU, Y. (97, 311, 317, 321, 339, 457) Department of Materials Science, Kitami Institute of Technology, Koen-cho, Kitami 090, Japan
- INUI, T.(355)Division of Energy and Hydrocarbon Chemistry, Graduate School of Engineering, Kyoto University, Sakyo-ku, Kyoto 606-01, Japan
- ISHIDA, R. (321) Department of Applied and Environmental Chemistry, Kitami Institute of Technology, Koen-cho, Kitami 090, Japan
- ISHIHARA, T.(441)Department of Applied Chemistry, Faculty of Engineering, Oita University, Dannoharu, Oita 870-11, Japan
- ISHIKAWA, K. (467) Department of Advanced Materials Science and Engineering, Faculty of Engineering, Yamaguchi University, Tokiwadai, Ube 755, Japan
- ITOH, H. (97, 311, 317, 321, 339, 457) Department of Materials Science, Kitami Institute of Technology, Koen-cho, Kitami 090, Japan
- ITO, T.(177, 233)School of Social Information Studies, Otsuma Women's University, Karakida, Tama 206, Japan
- ITO, T. (441) Department of Applied Chemistry, Faculty of Engineering, Oita University, Dannoharu, Oita 870-11, Japan
- IWAMATSU, E. (195) Department of Environmental Chemistry and Engineering, Inter-disciplinary Graduate School of Science and Engineering,Tokyo Institute of Technology, Midori-ku, Yokohama 227, Japan
- IWAMOTO, M. (71) Catalysis Research Center, Hokkaido University, Kita -ku, Sapporo 060, Japan
- IWASAKI, K. (35) Department of Environmental Chemistry and Engineering, Tokyo Institute of Technology, Midori-ku, Yokohama 227, Japan
- IZUMI, Y. (1, 85) Department of Applied Chemistry, Faculty of Engineering, Nagoya University, Chikusa-ku, Nagoya 464, Japan
- JACKSON, K. (129) Department of Physical Chemistry, University of New South Wales, Kensington, NSW 2033, Australia
- JIANG, D.(163, 279) Department of Chemistry, Jilin University, Changchun 130023, P.R.China
- JIN, S.-S. (451) Institute of Catalysis, Hangzhou University, Hangzhou 310028, P.R.China
- JOHN,S(141) Institute of Physical Chemistry, Vienna University of Technology, Getreidemarkt 9/156, A-1060 Wien, Austria
- KAKEGAWA, H. (97) Research & Development Center, Osaka Gas Co., Ltd., Konohana-ku, Osaka 554, Japan
- KALVACHEV, Y. (413) Institute of Kinetics and Catalysis, Bulgarian Academy of Sciences, Sofia 1113, Bulgaria
- KANNO, T.(207)Department of Chemical System Engineering, Kitami Institute of Technology, Kohen-cho, Kitami 090, Japan
- KANUKA, N. (349) Graduate School of Environmental Earth Science, Hokkaido University,

- Kita-ku, Sapporo 060, Japan
- KATADA, N.(333) Department of Materials Science, Faculty of Engineering, Tottori University  
Kozan-cho, Tottori 680, Japan
- KATAGIRI, M. (217) Department of Molecular Chemistry and Engineering, Faculty of  
Engineering, Tohoku University, Aoba-ku, Sendai 980, Japan
- KATO, C. (285) Department of Applied Chemistry, Waseda University, Shinjuku-ku, Tokyo  
169, Japan
- KATO, K. (251) Catalysis Research Center, Hokkaido University, Kita-ku, Sapporo 060,  
Japan
- KATOH, M. (263) Department of Chemistry, Faculty of Science, Hokkaido University,  
Kita-ku, Sapporo 060, Japan
- KAWAI, H. (461) Department of Applied Chemistry, Saitama University, Shimo - Okubo,  
Urawa 338, Japan
- KIHARA, N. (303) Department of Chemistry, Sophia University, Chiyoda-ku, Tokyo 102,  
Japan
- KIKUCHI, E. (391) Department of Applied Chemistry, School of Science & Engineering,  
Waseda University, Shinjuku-ku, Tokyo 169, Japan
- KIM, J.-H. (379) Department of Material Science, Tottori, University, Kozan-cho, Tottori  
680, Japan
- KIM, J.-H. (397) National Institute of Materials and Chemical Research, AIST, Tsukuba  
305, Japan
- KITA, H. (349) Graduate School of Environmental Earth Science, Hokkaido University,  
Kita-ku, Sapporo 060, Japan
- KITAMURA, M. (67) Organic Synthesis Research Laboratory, Sumitomo Chemical Co., Ltd.,  
Takatsuki 569, Japan
- KITAYAMA, Y. (245) Department of Chemistry and Chemical Engineering, Faculty of  
Chemical Engineering, Niigata University, Ikarashi, Niigata 950-21, Japan
- KITO, S. (229) Department of Industrial Engineering, Aichi Institute of Technology, Toyota  
470-03, Japan
- KOBAYASHI, H. (177, 233) Department of Applied Chemistry, Kyoto Prefectural University,  
Shimogamo, Kyoto 606, Japan
- KOBAYASHI, M. (207) Department of Chemical System Engineering, Kitami Institute of  
Technology, Kohen-cho, Kitami 090, Japan
- KOGELBAUER, A. (147) Institute for Physical Chemistry and Christian Doppler Laboratory  
for Heterogeneous Catalysis, Technical University of Vienna, Getreidemarkt 9, A-  
1060 Vienna,Austria
- KOMATSU, T. (295, 379) Department of Chemistry, Tokyo Institute of Technology, Meguro-  
ku, Tokyo 152, Japan

xii List of Contributors

- KONDO, J. (157) Research Laboratory of Resources Utilization, Tokyo Institute of Technology, Midori-ku, Yokohama 227, Japan
- KOSTOVA, N. (413) Institute of Kinetics and Catalysis, Bulgarian Academy of Sciences, Sofia 1113, Bulgaria
- KOZHEVNIKOV, I.V. (21) Institute of Catalysis, 630090 Novosibirsk, Russia
- KRAMER, G.M. (531) Exxon Research and Engineering Company, Corporate Research Laboratories, Clinton Township, Route 22, East, Annandale, N.J. 08801, U.S.A.
- KUBO, M. (217) Department of Molecular Chemistry and Engineering, Faculty of Engineering, Tohoku University, Aoba-ku, Sendai 980, Japan
- KUBOTA, Y. (397) National Institute of Materials and Chemical Research, AIST, Tsukuba 305, Japan
- KUDO, M. (549) Department of Chemistry, Tokyo Gakugei University, Koganei 184, Japan
- KURODA, K. (285) Department of Applied Chemistry, Waseda University, Shinjuku -ku, Tokyo 169, Japan
- KUROSAKI, K. (441) Department of Applied Chemistry, Faculty of Engineering, Oita University, Dannoharu, Oita 870-11, Japan
- KUWABARA, T. (35) Research Laboratories of Resources Utilization, Tokyo Institute of Technology, Midori-ku, Yokohama 227, Japan
- LERCHER, J. A. (147) Department of Chemical Technology, University of Twente, Postbus 217, 7500 AE Enschede, The Netherlands / Institute for Physical Chemistry and Christian Doppler Laboratory for Heterogeneous Catalysis, Technical University of Vienna, Getreidemarkt 9, 1-1060 Vienna, Austria
- LI, J. (299, 327) Institute of Special Chemicals, Taiyuan University of Technology, Taiyuan 030024, Shanxi, P.R.China
- LI, W. (501) Department of Chemical Engineering, Tianjin Univ., Tianjin 300072, P.R.China
- LIU, G. (299, 327) Institute of Special Chemicals, Taiyuan University of Technology, Taiyuan 030024, Shanxi, P.R.China
- LIU, S.B. (291) Institute of Atomic and Molecular Sciences, Academia Sinica, Taipei 10764, Taiwan
- LIU, J. (77) East China University of Science and Technology, 130 Meilong Road, Shanghai 200237, P.R.China
- LOMBARDO, E.A. (429) Instituto de Investigaciones en Catálisis y Petroquímica- INCAPE- (FIQ, UNL-CONICET) Santiago del Estero 2829-3000-Santa Fe, Argentina
- LUKYANOV, D. (367) URA CNRS 350, Université de Poitiers, 86022 Poitiers Cedex, France
- MA, J. (163) Department of Chemistry, Jilin University, Changchun 130023, P.R.China
- MAEDA, M. (391) Department of Applied Chemistry, School of Science & Engineering, Waseda University, Shinjuku-ku, Tokyo 169, Japan

- MAKI, T. (47) Research Center, Mitsubishi Kasei Corporation, Midori-ku, Yokohama 227, Japan
- MAO, J.-X. (451) Institute of Catalysis, Hangzhou University, Hangzhou 310028, P.R.China
- MARTRA, G. (169, 183) Dipartimento di Chimica Inorganica, Chimica Fisica e Chimica dei Materiali, Università di Torino, via P. Giuria 7, 10125 Torino, Italy
- MARUYA, E. (217) Department of Molecular Chemistry and Engineering, Faculty of Engineering, Tohoku University, Aoba-ku, Sendai 980, Japan
- MATSUBA, K. (355) Division of Energy and Hydrocarbon Chemistry, Graduate School of Engineering, Kyoto University, Sakyo-ku, Kyoto 606-01, Japan
- MATSUDA, A. (491) Late Emeritus Professor, Hokkaido University, Kita-ku, Sapporo 060, Japan
- MATSUDA, T. (391) Department of Applied Chemistry, School of Science & Engineering, Waseda University, Shinjuku-ku, Tokyo 169, Japan
- MATSUHASHI, H. (251) Department of Science, Hokkaido University of Education, Hachimancho, Hakodate 040, Japan
- MATSUMOTO, M. (397) Research & Development Center, Osaka Gas Co., Ltd., Konohana-ku, Osaka 554, Japan
- MATSUYAMA, S. (317) Department of Applied Chemistry, Kitami Institute of Technology, Koen-cho, Kitami 090, Japan
- MATSUZAKI, T. (397) National Institute of Materials and Chemical Research, AIST, Tsukuba 305, Japan
- MILDNER, T. (105) Fachbereich Physik der Universität Leipzig, Linnéstraße 5, D-04103 Leipzig, Germany
- MIN, E. (163) Research Institute of Petroleum Processing, Beijing 100083, P.R.China
- MIRTH, G. (147) Department of Chemical Technology, University of Twente, Postbus 217, 7500 AE Enschede, The Netherlands
- MISONO, M. (419) Department of Synthetic Chemistry, Faculty of Engineering, The University of Tokyo, Bunkyo-ku, Tokyo 113, Japan
- MIURA, H. (461) Department of Applied Chemistry, Saitama University, Shimo-Okubo, Urawa 338, Japan
- MIYAMOTO, A. (217) Department of Molecular Chemistry and Engineering, Faculty of Engineering, Tohoku University, Aoba-ku, Sendai 980, Japan
- MIZUHARA, Y. (441) Department of Applied Chemistry, Faculty of Engineering, Oita University, Dannoharu, Oita 870-11, Japan
- MIZUNO, N. (71) Catalysis Research Center, Hokkaido University, Kita-ku, Sapporo 060, Japan
- MOLES, P.J. (269) MEL Chemicals, Swinton, Manchester, M27 8LS, U.K.
- MOON, S.-C. (479) Department of Applied Chemistry, University of Osaka Prefecture,

Gakuen-cho, Sakai 593, Japan

MORIKAWA, A. (409) Department of Chemical Engineering, Faculty of Engineering,  
Tokyo Institute of Technology, Meguro-ku, Tokyo 152, Japan

MORIKAWA, Y. (35) Research Laboratories of Resources Utilization, Tokyo Institute of  
Technology, Midori-ku, Yokohama 227, Japan

MURAKAMI, Y. (229, 333) Department of Applied Chemistry, School of Engineering,  
Nagoya University, Chikusa-ku, Nagoya 464-01, Japan

NA, K. (419) Department of Synthetic Chemistry, Faculty of Engineering, The University of  
Tokyo, Bunkyo-ku, Tokyo 113, Japan

NAKADE, M. (285) Department of Applied Chemistry, Waseda University, Shinjuku-ku,  
Tokyo 169, Japan

NAKAMURA, J. (495) Institute of Materials Science, University of Tsukuba, Tsukuba 305,  
Japan

NAKANO, T. (295) Department of Chemistry, Tokyo Institute of Technology, Meguro-ku,  
Tokyo 152, Japan

NAKATA, S. (135, 303) R&D Center, Chiyoda Corporation, Kanagawa-ku, Yokohama 221,  
Japan

NAKATO, T. (285) Department of Chemistry, Faculty of Science, Hokkaido University,  
Kita-ku, Sapporo 060, Japan

NAKATSUKA, K. (473) Department of Molecular Engineering, Kyoto University, Sakyo-ku,  
Kyoto 606-01, Japan

NAMBA, S. (379) Department of Materials, The Nishi-Tokyo University, Kitatsuru - gun,  
Yamanashi 409 - 01, Japan

NARBESCHUBER, T. (147) Department of Chemical Technology, University of Twente,  
Postbus 217, 7500 AE Enschede, The Netherlands / Institute for Physical Chemistry  
and Christian Doppler Laboratory for Heterogeneous Catalysis, Technical University  
of Vienna, Getreidemarkt 9, A-1060 Vienna, Austria

NISHIMURA, T. (419) Department of Synthetic Chemistry, Faculty of Engineering, The  
University of Tokyo, Bunkyo-ku, Tokyo 113, Japan

NIWA, H. (229) Department of Applied Chemistry, Nagoya University, Chikusa-ku, Nagoya  
464-01, Japan

NIWA, M. (333) Department of Materials Science, Faculty of Engineering, Tottori University,  
Kozan-cho, Tottori 680, Japan

NOLEN, E. (85) Department of Chemistry, Colgate University, Hamilton, New York 13346-  
1398, U.S.A.

NOMOTO, Y. (447) Department of Chemical Engineering, Tokyo Institute of Technology,  
Meguro-ku, Tokyo 152, Japan

NOMURA, M. (117) Department of Chemical Engineering, Tokyo Institute of Technology,

- Meguro-ku, Tokyo 152, Japan
- NOMURA, M. (245) Department of Chemistry and Chemical Engineering, Faculty of Chemical Engineering, Niigata University, Ikarashi, Niigata 950-21, Japan
- NORMAN, C. J. (269) Alcan Chemicals Limited, Chalfont Park, Gerrards Cross, Bucks, SL9 0QB, U.K.
- NOTOYA, R. (491) Catalysis Research Center, Hokkaido University, Kita-ku, Sapporo 060, Japan
- ODASHIMA, T. (273) Department of Applied Chemistry, School of Engineering, Chiba University, Inage-ku, Chiba 263, Japan
- OHNISHI, R. (101, 339) Catalysis Research Center, Hokkaido University, Kita-ku, Sapporo 060, Japan
- OHNO, Y. (117) Research & Development Center, Cosmo Research Institute, Satte, Saitama 340-01, JAPAN
- OHOWA, H. (35) Department of Environmental Chemistry and Engineering, Tokyo Institute of Technology, Midori-ku, Yokohama 227, Japan
- OHSHIDA, T. (35) Research Laboratories of Resources Utilization, Tokyo Institute of Technology, Midori-ku, Yokohama 227, Japan
- OHSHIO, N. (409) Department of Chemical Engineering, Faculty of Engineering, Tokyo Institute of Technology, Meguro-ku, Tokyo 152, Japan
- OHTA, H. (379) Department of Material Science, Tottori University, Kozan-cho, Tottori 680, Japan
- OISHI, M. (311) Department of Applied and Environmental Chemistry, Kitami Institute of Technology, Koen-cho, Kitami 090, Japan
- OKAZAKI, N. (97, 311, 317, 321, 339, 457) Department of Applied and Environmental Chemistry, Kitami Institute of Technology, Koen-cho, Kitami 090, Japan
- OKUHARA, T. (419) Department of Synthetic Chemistry, Faculty of Engineering, The University of Tokyo, Bunkyo-ku, Tokyo 113, Japan
- ONAKA, M. (85) Department of Applied Chemistry, Faculty of Engineering, Nagoya University, Chikusa-ku, Nagoya 464, Japan
- ONO, Y. (117, 135, 447) Department of Chemical Engineering, Tokyo Institute of Technology, Meguro-ku, Tokyo 152, Japan
- PFEILER, D. (141) Institute of Physical Chemistry, Vienna University of Technology, Getreidemarkt 9/156, A-1060 Wien, Austria
- PFEIFER, H. (105) Fachbereich Physik der Universität Leipzig, Linnéstraße 5, D-04103 Leipzig, Germany
- PRASAD, S. (291) Institute of Atomic and Molecular Sciences, Academia Sinica, Taipei 10764, Taiwan
- QI, Y. (77) East China University of Science and Technology, Meilong Road, Shanghai

200237, P.R.China

- QIAN, Z. (543) Department of Chemistry, Jilin University, Changchun 130023, P.R.China
- SAITO, N. (59) Central Research Laboratory, Nippon Shokubai Co., Ltd., Nishi Otabi-cho Saita 564, Japan
- SAKATA, Y. (467) Department of Advanced Materials Science and Engineering, Faculty of Engineering, Yamaguchi University, Tokiwadai, Ube 755, Japan
- SALAHUB, D.R. (233) Universite de Montreal, Department de Chimie, Montreal, Quebec, H3C 3J7, Canada
- SALEH, R. (537) Exxon Chemical Company, Intermediates Technology Division, Clinton Township, Route 22 East, Annandale, N.J. 08801, U.S.A.
- SATO, K. (495) Institute of Materials Science, University of Tsukuba, Tsukuba 305, Japan
- SATO, N. (343) Department of Applied Chemistry, Muroran Institute of Technology, Mizumoto-cho, Muroran 050, Japan
- SATSUMA, A. (229) Department of Applied Chemistry, Nagoya University, Chikusa-ku, Nagoya 464-01, Japan
- SAUTET, P. (519) Institut de Recherches sur la Catalyse, UPR 5401 CNRS, 2 avenue A Einstein, F. Villeurbanne 69626, France / Ecole Normale Supérieure de Lyon, 46 allée d'Italie, Lyon 69007, France
- SAWADA, K. (391) Department of Applied Chemistry, School of Science & Engineering, Waseda University, Okubo, Shinjuku-ku, Tokyo 169, Japan
- SEGAWA, K. (303) Department of Chemistry, Sophia University, Chiyoda-ku, Tokyo 102, Japan
- SETOYAMA, T. (47) Research Center, Mitsubishi Kasei Corporation, Midori-ku, Yokohama 227, Japan
- SHEN, J. (163) Department of Chemistry, Jilin University, Changchun 130023, P.R.China
- SHIMAZU, S. (273) Department of Applied Chemistry, School of Engineering, Chiba University, Inage-ku, Chiba 263, Japan
- SHIMIZU, N. (59) Central Research Laboratory, Nippon Shokubai Co., Ltd., Nishi Otabi-cho, Saita 564, Japan
- SHINODA, T. (85) Department of Applied Chemistry, Faculty of Engineering, Nagoya University, Chikusa-ku, Nagoya 464, Japan
- SHOJI, H. (273) Department of Applied Chemistry, School of Engineering, Chiba University, Inage-ku, Chiba 263, Japan
- SIM, R.-B. (177) Department of Chemistry, Faculty of Science, Tokyo Metropolitan University, Minami-Osawa, Hachioji 192-03, Japan
- SOLED, S. L. (531, 537) Exxon Research and Engineering Company, Corporate Research Laboratories, Clinton Township, Route 22 East, Annandale, N.J. 08801, U.S.A.
- SOUAMA, Y. (93) Osaka National Research Institute, AIST, Midorigaoka, Ikeda 563, Japan

- SPOJAKINA, A. (413) Institute of Kinetics and Catalysis, Bulgarian Academy of Sciences, Sofia 1113, Bulgaria
- STOCKENHUBER, M. (147) Institute for Physical Chemistry and Christian Doppler Laboratory for Heterogeneous Catalysis, Technical University of Vienna, Getreidemarkt 9, A-1060 Vienna, Austria
- SU, X. (77) East China University of Science and Technology, Meilong Road, Shanghai 200237, P.R.China
- SUGI, Y. (397) National Institute of Materials and Chemical Research, AIST, Tsukuba 305, Japan
- SUGIOKA, M. (343) Department of Applied Chemistry, Muroran Institute of Technology, Mizumoto-cho, Muroran 050, Japan
- SUN, T. (163) Department of Chemistry, Jilin University, Changchun 130023, P.R.China
- SUZUKI, E. (447) Department of Chemical Engineering, Tokyo Institute of Technology, Meguro-ku, Tokyo 152, Japan
- TABATA, M. (71) Catalysis Research Center, Hokkaido University, Kita-ku, Sapporo 060, Japan
- TADA, A. (97, 311, 317, 321, 339, 457) Department of Applied and Environmental Chemistry, Kitami Institute of Technology, Koen-cho, Kitami 090, Japan
- TAGUCHI, T. (461) Department of Applied Chemistry, Saitama University, Shimo-Okubo, Urawa 338, Japan
- TAKAHARA, K. (339) Department of Materials Science, Kitami Institute of Technology, Koen-cho, Kitami 090, Japan
- TAKAHASHI, H. (89) Graduate School of Environmental Earth Science, Hokkaido University, Kita-ku, Sapporo 060, Japan
- TAKAOKA, K. (201) Department of Physics, Nara University of Education, Takabatake-cho, Nara 630, Japan
- TAKENAKA, S. (485) Department of Molecular Engineering, Kyoto University, Sakyo-ku, Kyoto 606-01, Japan
- TAKITA, Y. (441) Department of Applied Chemistry, Faculty of Engineering, Oita University, Dannoharu, Oita 870-11, Japan
- TAN, S. (213) Research Institute for Chemical Engineering of Coal, Taiyuan University of Technology, Taiyuan, Shanxi, 030024, P.R.China
- TANAKA, M. (93) Osaka National Research Institute, AIST., Midorigaoka, Ikeda 563, Japan
- TANAKA, N. (97) Department of Applied and Environmental Chemistry, Kitami Institute of Technology, Koen-cho, Kitami 090, Japan
- TANAKA, T. (473, 485) Department of Molecular Engineering, Kyoto University, Sakyo-ku, Kyoto 606-01, Japan

xviii List of Contributors

- TANAKA, Y. (135) Chiyoda Corporation, R&D Center, Kanagawa-ku, Yokohama 221, Japan
- TANG, Y. (507) Department of Chemistry, Fudan University, Shanghai 200433, P.R.China
- TASHIRO, T. (177) Department of Chemistry, Faculty of Science, Tokyo Metropolitan University, Minami-Osawa, Hachioji 192-03, Japan
- THOMKE, K. (141) Institute of Physical Chemistry, Vienna University of Technology, Getreidemarkt 9/156, A-1060 Wien, Austria
- TICHIT,D.(183)Laboratoire de Chimie Organique Physique et Cinétique Chimique Appliquées-U.A.418 du C.N.R.S., E.N.S.C.M., 8, rue de l'Ecole Normale 34075 Montpellier CEDEX, France
- TOI, K. (177) Department of Chemistry, Faculty of Science, Tokyo Metropolitan University, Minami-Osawa, Hachioji 192-03, Japan
- TOKUMITSU, K. (97) Research & Development Center, Osaka Gas Co., Ltd., Konohana-ku, Osaka 554, Japan
- TOYOFUKU, M. (457) Department of Material Science, Kitami Institute of Technology, Koen-cho, Kitami 090, Japan
- TSUCHIYA, S. (467) Department of Advanced Materials Science and Engineering, Faculty of Engineering, Yamaguchi University, Tokiwadai, Ube 755, Japan
- TSUJI, H. (349) Graduate School of Environmental Earth Science, Hokkaido University, Kita-ku, Sapporo 060, Japan
- TU, X. (397) Research & Development Center, Osaka Gas Co., Ltd., Konohana-ku, Osaka 554, Japan
- UCHIDA, D. (343) Department of Applied Chemistry, Muroran Institute of Technology, Mizumoto-cho, Muroran 050, Japan
- UCHIJIMA, T. (495) Institute of Materials Science, University of Tsukuba, Tsukuba 305, Japan
- UEDA, W. (35) Department of Environmental Chemistry and Engineering, Tokyo Institute of Technology, Midori-ku, Yokohama 227, Japan
- UEMATSU, T. (71) Catalysis Research Center, Hokkaido University, Kita-ku, Sapporo 060, Japan
- UEMATSU, T. (273) Department of Applied Chemistry, School of Engineering, Chiba University, Inage-ku, Chiba 263, Japan
- UESHIMA, M. (59) Catalyst Research Laboratory, Nippon Shokubai Co., Ltd., Aboshi-ku, Himeji 671-12, Japan
- URABE, K. (1) Department of Applied Chemistry, School of Engineering, Nagoya University, Chikusa-ku, Nagoya 464-01, Japan
- VAN GORKOM, L. (129) Department of Physical Chemistry, University of New South Wales, Kensington, NSW 2033, Australia

- VÉDRINE, J.C. (519) Institut de Recherches sur la Catalyse, UPR 5401 CNRS, 2 avenue A Einstein, F. Villeurbanne 69626, France
- VETRIVEL, R. (217, 291) Department of Molecular Chemistry and Engineering, Faculty of Engineering, Tohoku University, Aoba-ku, Sendai 980, Japan
- WAKABAYASHI, F.(157) Department of Science and Engineering, National Science Museum, Taito-ku, Tokyo 110, Japan
- WANG, H. (213) Research Institute for Chemical Engineering of Coal, Taiyuan University of Technology, Taiyuan, Shanxi 030024, P.R.China
- WANG, W.-L. (101) Catalysis Research Center, Hokkaido University, Sapporo 060, Japan
- WATANABE, H. (419) Department of Synthetic Chemistry, Faculty of Engineering, The University of Tokyo, Bunkyo-ku, Tokyo 113, Japan
- WESTI, Y. (229) Department of Applied Chemistry, Nagoya University, Chikusa-ku, Nagoya 464-01, Japan
- WOLF, I. (105) Fachbereich Physik der Universität Leipzig, Linnéstraße 5, D-04103 Leipzig, Germany
- WU, H. (77) East China University of Science and Technology, Meilong Road, Shanghai 200237, P.R.China
- WU, P. (295) Department of Chemistry, Tokyo Institute of Technology, Meguro-ku, Tokyo 152, Japan
- WU, Y. (279) Changchun Institute of Applied Chemistry, Chinese Academy of Science, Changchun 130022, P.R.China
- XU, Y. (543) State Key Laboratory of Catalysis, Dalian Institute of Chemical Physics, Chinese Academy of Sciences, Dalian 116023, P.R.China
- XU, Z. (163) Department of Chemistry, Jilin University, Changchun 130023, P.R.China
- XU, Z. (279) Changchun Institute of Applied Chemistry, Chinese Academy of Science, Changchun 130022, P.R.China
- YAGI, F. (349) Graduate School of Environmental Earth Science, Hokkaido University, Kita-ku, Sapporo 060, Japan
- YAMABE, S. (201) Department of Chemistry, Nara University of Education, Takabatake-cho, Nara 630, Japan
- YAMAGUCHI, T. (263) Department of Applied Chemistry, Faculty of Engineering, Ehime University, Bunkyo-cho, Matsuyama 790, Japan
- YAMASHITA, H. (479) Department of Applied Chemistry, University of Osaka Prefecture, Gakuen-cho, Sakai 593, Japan
- YANAGISAWA, Y. (201) Department of Physics, Nara University of Education, Takabatake-cho, Nara 630, Japan
- YASHIMA, T.(295, 379) Department of Chemistry, Tokyo Institute of Technology, Ookayama, Meguro-ku, Tokyo 152, Japan

**xx List of Contributors**

- YAMADA, T. (467) Department of Advanced Materials Science and Engineering, Faculty of Engineering, Yamaguchi University, Tokiwadai, Ube 755, Japan
- YOKOYAMA, T. (47) Research Center, Mitsubishi Kasei Corporation, Midori-ku, Yokohama 227, Japan
- YOSHIDA, H. (473) Department of Molecular Engineering, Kyoto University, Sakyo-ku, Kyoto 606-01, Japan
- YOSHIDA, S. (473, 485) Department of Molecular Engineering, Kyoto University, Sakyo-ku, Kyoto 606-01, Japan
- YOSHINAGA, Y(549) Department of Chemistry, Tokyo Gakugei University, Nukuikitamachi, Koganei 184, Japan
- YU, Z. (543) Department of Chemistry, Jilin University, Changchun 130023, P.R.China
- ZHENG, X.-M. (451) Institute of Catalysis, Hangzhou University, Hangzhou 310028, P.R. China
- ZHI, F. (213) Research Institute for Chemical Engineering of Coal, Taiyuan University of Technology, Taiyuan, Shanxi 030024, P.R.China
- ZHONG, S. (501) Department of Chemical Engineering, Tianjin Univ., Tianjin 300072, P.R.China

# Contents

Organizing Committee	v
List of Contributors	vii
Preface	xxvii

## 1. Organic Synthesis

1.1 Acidic Salts of Heteropolyacids as Solid Acid Catalysts for Liquid-phase Organic Reactions.....	1
Y. Izumi and K. Urabe	
1.2 Inorganic Solid Supported Reagents as Acids and Bases.....	9
T. Ando	
1.3 Heteropoly Acids as Catalysts for Organic Reactions.....	21
I.V. Kozhevnikov	
1.4 Methanol-Based Synthetic Reactions over Solid-Base Catalysts .....	35
W. Ueda, H. Ohowa, K. Iwasaki, T. Kuwabara, T. Ohshida and Y. Morikawa	
1.5 Novel Direct Hydrogenation Process of Aromatic Carboxylic Acids to the Corresponding Aldehydes with Zirconia Catalyst .....	47
T. Yokoyama, T. Setoyama, N. Fujita and T. Maki	
1.6 Role of Acid and Base Properties of V <sub>2</sub> O <sub>5</sub> -Base Metal Oxide Catalysts for Partial Oxidation of <i>p</i> -Substituted Toluene .....	59
M. Ueshima, N. Saito and N. Shimizu	
1.7 The Role of Alcohols on Lactam Selectivity in the Vapor-Phase Beckmann Rearrangement Reaction .....	67
M. Kitamura and H. Ichihashi	
1.8 Direct Amination of Lower Alkenes with Ammonia over Zeolite Catalysts .....	71
N. Mizuno, M. Tabata, T. Uematsu and M. Iwamoto	
1.9 Etherification of Diethylene Glycol with Ethanol on Heteropolyacid .....	77
Y. Qi, J. Liu, H. Wu and X. Su	
1.10 Acidic Clay-Directed Polymerization-Cyclization of Aldehydes and Pyrrole to Porphyrins.....	85
M. Onaka, T. Shinoda, Y. Izumi and E. Nolen	
1.11 Acid-catalyzed Rearrangement of Pentacyclic Cage Compound via an Unexpected Route [Part II] : Application of PM3 Calculations to the Reaction Mechanism .....	89
K. Hirao and H. Takahashi	

1.12	Formylation of Aromatic Compounds under Atmospheric CO Pressure	93
	Y. Souma and M. Tanaka	
1.13	Friedel-Crafts Polyalkylation of Mesitylene with Trichlorotoluene — a Synthesis of 1,3-Connected Polyarylmethanes as Precursors for Organic Magnets	97
	Y. Imizu, T. Iino, N. Tanaka, N. Okazaki, H. Itoh, A. Tada, K. Tokumitsu and H. Kakegawa	
1.14	Selective Hydrogenation of CFC-12 to HFC-32 on Zr-Pd/C Catalyst	101
	R. Ohnishi, W.-L. Wang and M. Ichikawa	

## 2. Characterization

2.1	NMR Studies Concerning the Acidity and Catalysis in Zeolites	105
	D. Freude, H. Ernst, T. Mildner, H. Pfeifer and I. Wolf	
2.2	Catalytic Properties and Physicochemical Nature of Highly Active Protons in Partially Reduced $\text{Ag}_3\text{PW}_{12}\text{O}_{40}$	117
	T. Baba, M. Nomura, Y. Ono and Y. Ono	
2.3	Extra-Framework Sites in H-Al MFI and H-GaMFI Zeolite Catalysts	129
	S.M. Bradley, S.M. Cambell, J. Hook, K. Jackson, L. Van Gorkom and R.F. Howe	
2.4	Solid-state $^{109}\text{Ag}$ -MASNMR Spectroscopic Studies of Trisilver Dodecatungstophosphates	135
	S. Nakata, Y. Tanaka, T. Baba and Y. Ono	
2.5	Exchange of Isotopic Hydrogen over Solid Acid/Base Catalysts	141
	D. Pfeiler, S. John, K. Thomke and O.M.E. El-Dusouqui	
2.6	Elementary Steps of Acid-Base Catalyzed Reactions in Molecular Sieves	147
	J.A. Lercher, G. Mirth, M. Stockenhuber, T. Narbeshuber and A. Kogelbauer	
2.7	Infrared Spectroscopic Observation of $\text{N}_2$ Species Adsorbed on Brønsted and Lewis Acid Sites of H-Zeolites at Low Temperatures	157
	F. Wakabayashi, J. Kondo, K. Domen and C. Hirose	
2.8	Studies of Adsorption of Benzene on the Acid and Base Sites of $\text{KH}\beta$ Zeolite by IR <i>in Situ</i>	163
	J. Shen, J. Ma, T. Sun, Z. Xu, D. Jiang and E. Min	
2.9	Interaction of $\text{NH}_3$ with $\text{O}_2$ at the Surface of $\text{MgO}$	169
	G. Martra, E. Borello, E. Giannello and S. Coluccia	
2.10	Behavior of CO Monomers Adsorbed on $\text{MgO}$ Surfaces at Low Temperatures	177
	T. Ito, R.-B. Sim, T. Tashiro, K. Toi and H. Kobayashi	
2.11	UV-Vis Study of the Condensation Reaction of Carbonylic Compounds on $\text{MgO}$ and Hydrotalcites	183
	E. Garrone, D. Bartalini, S. Coluccia, G. Martra, D. Tichit and F. Figueras	

2.12	O <sub>2</sub> -Formation through N <sub>2</sub> O on ZrO <sub>2</sub> Surface .....	195
	K. Aika and E. Iwamatsu	
2.13	Oxygen Isotope Exchange between CO <sub>2</sub> Adsorbate and MgO Surfaces .....	201
	Y. Yanagisawa, K. Takaoka and S. Yamabe	
2.14	Evaluation of Basicity of Alkali Metal-doped MgO in the Scope of Change of Carbonate Species.....	207
	T. Kanno and M. Kobayashi	
2.15	IR Characterization of Base Heterogeneity of Solid Catalysts.....	213
	H. Wang, S. Tan and F. Zhi	
2.16	Structure and Dynamics of Exchanged Cations in Zeolites as Investigated by Molecular Dynamics and Computer Graphics .....	217
	A. Miyamoto, H. Himei, E. Maruya, M. Katagiri, R. Vetrivel and M. Kubo	
2.17	Acid Strength of Binary Mixed Oxide—Estimation by Neural Network and Experimental Verification .....	229
	T. Hattori, S. Kito, H. Niwa, Y. Westi, A. Satsuma and Y. Murakami	
2.18	Quantum Chemical Study on Reactions of Small Molecules on Various MgO Surfaces .....	233
	H. Kobayashi, D.R. Salahub and T. Ito	
2.19	Acidic Properties of Sepiolite.....	245
	Y. Kitayama and M. Nomura	

### **3. Design and Preparation of Catalyst**

3.1	Synthesis of Solid Superacid of Borate Supported on Zirconium Oxides .....	251
	H. Matsuhashi, K. Kato and K. Arata	
3.2	Preparation of Platinum-Supported Alumina Lewis Superacid Catalyst Using a CVD Method.....	257
	A. Ayame and K. Honda	
3.3	Synthesis and Catalytic Properties of Sulfate Ion-Promoted Zr-Pillared Clays .....	263
	M. Katoh, H. Fujisawa and T. Yamaguchi	
3.4	The Role of Sulphate in the Stabilisation of Zirconia .....	269
	C.J. Norman, P.A. Goulding and P.J. Moles	
3.5	Catalytic Properties of Interlayer Acid Sites of Cation-Exchanged Synthetic Taeniolites.....	273
	T. Uematsu, H. Shoji, T. Odashima and S. Shimazu	
3.6	Alkylation of Isobutane with Butene over Layered Double Hydroxide Pillared Heteropolyoxometalate Acid-Base Catalysts.....	279
	Z. Xu, Y. Wu, H. He and D. Jiang	

xxiv Contents

3.7	Intercalation of <i>n</i> -Alkylamines into Perovskite-related Layered Niobic Acid HBiNb <sub>2</sub> O <sub>6</sub> · <i>n</i> H <sub>2</sub> O .....	285
	T. Nakato, M. Nakade, K. Kuroda and C. Kato	
3.8	Controlled Pore Opening of VPI-5 by Partial Removal of Water Molecules .....	291
	S. Prasad, S.B. Liu and R. Vetrivel	
3.9	Incorporation of Aluminum and Antimony into Mordenite Framework by Atom-Planting Method .....	295
	P. Wu, T. Nakano, T. Komatsu and T. Yashima	
3.10	A New Method for Preparing High Silica ZSM-48 Catalysts .....	299
	J.Li G.Liu and J.Dong	
3.11	Preparation and Catalytic Properties of Composite Zirconium Phosphonates.....	303
	K. Segawa, N. Kihara and S. Nakata	
3.12	Grinding of Zirconium Pyrophosphate and its Catalytic Activity for 1-Butene Isomerization.....	311
	A. Tada, M. Oishi, N. Okazaki, H. Itoh and Y. Imizu	
3.13	Preparation of Amorphous Metal-substituted Aluminum Phosphates and Their Acid-Base Properties .....	317
	H. Itoh, S. Matsuyama, N. Okazaki, Y. Imizu and A. Tada	
3.14	Surface Properties and Catalytic Activities of Superconducting Bi-Pb-Sr-Ca-Cu Oxides for 1-Butene Isomerization .....	321
	A. Tada, R. Ishida, N. Okazaki, Y. Imizu and H. Itoh	
3.15	Preparation and Properties of a New Kind of Acid Catalyst of Zeolite Coating on Metal Surface .....	327
	J.Li, J. Dong and G.Liu	
3.16	Acidic Property of Silica Monolayers on Metal Oxides Prepared by CVD Method.....	333
	N. Katada, M. Niwa and Y. Murakami	
3.17	Preparation of Silica-Deposited Alumina Catalyst by Utilizing Organosilicon Complexes as Building Blocks for the Synthesis of Acidic Sites .....	339
	Y. Imizu, K. Takahara, N. Okazaki, H. Itoh, A. Tada, R. Ohnishi and M. Ichikawa	
3.18	Activity Enhancement of Me <sup>++</sup> /SiO <sub>2</sub> Catalysts by Sulfiding with Hydrogen Sulfide for Acid-Catalyzed Reactions .....	343
	M. Sugioka, N. Sato and D. Uchida	
3.19	Preparation of Basic Zeolite .....	349
	F. Yagi, N. Kanuka, H. Tsuji, H. Kita and H. Hattori	

**4. Catalytic Features**

- 4.1 Prominent Change in Reaction Characteristics of High Silica Zeolite Induced by Isomorphous Substitution with Transition Metals ..... 355  
T. Inui and K. Matsuba
- 4.2 Aromatization of Short Chain Alkanes on Ga MFI Catalysts ..... 367  
M. Guisnet and D. Lukyanov
- 4.3 Shape Selective Alkylation of Aromatics on Metallosilicates ..... 379  
T. Yashima, J.-H. Kim, H. Ohta, S. Namba and T. Komatsu
- 4.4 Alkylation of Naphthalene with Propene to 2, 6-Diisopropynaphthalene on Mordenite Catalysts ..... 391  
E. Kikuchi, K. Sawada, M. Maeda and T. Matsuda
- 4.5 Shape-Selective Isopropylation of Naphthalene and Biphenyl over Dealuminated H-Mordenites ..... 397  
Y. Sugi, T. Matsuzaki, T. Hanaoka, Y. Kubota, J.-H. Kim, X. Tu and M. Matsumoto
- 4.6 Promotion Effect of Hydrogen on Catalytic Decomposition of Nitrous Oxide ( $N_2O$ ) by H-ZSM-5 Catalyst ..... 409  
K. Ebitani, N. Ohshio and A. Morikawa
- 4.7 Acid-Base Properties of ALPO-5 Molecular Sieves Modified by Nickel and Molybdenum ..... 413  
Y. Kalvachev, A. Spojakina, N. Kostova and L. Dimitrov
- 4.8 Novel Catalysis of Cesium Salt of Heteropolyacid and its Characterization by Solid-state NMR ..... 419  
T. Okuhara, T. Nishimura, H. Watanabe, K. Na and M. Misono
- 4.9 The Role of Acid-Base and Redox Features in the Catalytic Behavior of Vanadium-Phosphorus-Oxygen Formulations ..... 429  
L.M. Cornaglia and E.A. Lombardo
- 4.10 Role of Acidic Sites on Metal Phosphates in the Catalytic Oxidation of *iso*-Butane ..... 441  
Y. Takita, K. Kurosaki, T. Ito, Y. Mizuhara and T. Ishihara
- 4.11 Production of Silane and Dialkoxy silane by the Disproportionation of Trimethoxy- and Triethoxysilanes over Solid Base Catalysts ..... 447  
Y. Nomoto, E. Suzuki and Y. Ono
- 4.12 Oxidative Dehydrogenation of Ethane over Modified Magnesium Oxides ..... 451  
X.-M. Zheng, J.-X. Mao, B.-X. Cai, J.-H. Fei and S.-S. Jin
- 4.13 Hydrogenation of 1,3-Dienes over Tetramethyltin-Promoted Zinc Oxide Catalyst ..... 457  
Y. Imizu, M. Toyofuku, N. Okazaki, H. Itoh and A. Tada

xxvi Contents

4.14	Dehydrogenation of Ethylbenzene over K <sub>2</sub> FeO <sub>4</sub> – Catalyst Structure and Reaction Intermediate .....	461
	H. Miura, H. Kawai and T. Taguchi	
4.15	Acid-Base Nature of Antimony Oxides .....	467
	S. Tsuchiya, T. Yamada, K. Ishikawa, Y. Sakata and H. Imamura	
4.16	Base Sites of Magnesium Oxide Dispersed on Silica as Active Sites for CO Photooxidation .....	473
	H. Yoshida, T. Tanaka, K. Nakatsuka, T. Funabiki and S. Yoshida	
4.17	Dynamics of the Adsorption and Hydrogenation of CO on Active ZrO <sub>2</sub> Catalyst – <i>In Situ</i> Photoluminescence, FT-IR, and ESR Investigations .....	479
	S.-C. Moon, H. Yamashita and M. Anpo	
4.18	Photocatalytic Oxidation of Ethanol over Tantalum Oxide Supported on Silica .....	485
	T. Tanaka, S. Takenaka, T. Funabiki and S. Yoshida	
4.19	The Relationship between the Absolute Acidities of Monoatomic Cations and their Catalytic Activities in a Few Heterogeneous Systems .....	491
	R. Notoya and A. Matsuda	
4.20	The Role of Support in Methane Reforming with CO <sub>2</sub> over Rhodium Catalysts .....	495
	J. Nakamura, K. Aikawa, K. Sato and T. Uchijima	
4.21	Laser Stimulated CO + H <sub>2</sub> to Form C <sub>2</sub> H <sub>4</sub> on the Surface of Nickel Sulfate .....	501
	W. Li and S. Zhong	
4.22	Characterization of Solid Superacidity by <i>n</i> -Alkane Isomerization Reactions at Low Temperature .....	507
	Z. Gao, J.-M. Chen, W.-M. Hua and Y. Tang	
4.23	Sulfated Zirconia for <i>n</i> -Butane Experimental and Theoretical Approaches .....	519
	F. Babou, B. Bigot, G. Coudurier, P. Sautet and J. C. Védrine	
4.24	Modification of Isomerization Activity and Selectivity over Sulfated Zirconia Catalysts .....	531
	S. L. Soled, E. Iglesia and G. M. Kramer	
4.25	Butene Dimerization over Sulfate and Tungstate Modified Solid Acids .....	537
	S. Soled, N. Dispensiere and R. Saleh	
4.26	Alkylation of Isobutane with Butenes over Silica-supported SO <sub>4</sub> <sup>2-</sup> -ZrO <sub>2</sub> .....	543
	C. Guo, Z. Yu, Z. Qian, J. Huang and Y. Xu	
4.27	Acid Property and Metathesis Activity of WO <sub>3</sub> -ZrO <sub>2</sub> Catalysts .....	549
	M. Kudo, Y. Yoshinaga and S. Hasegawa	

## Preface

Solid acid catalysts are being studied intensively in both academic and applied fields to expand their capabilities in a variety of reactions. They are, of course, already in use in various processes of petroleum refining. At the same time, solid base catalysts have been recognized as potential catalysts for their characteristic features in catalysis. Both acidic and basic catalysts are promising not only in application to acid and base-catalyzed reactions but also in materials sciences, including the production of adsorbents, sensors, ceramics, etc. Fundamental study of acid-base catalysis promotes progress in these areas. Development of the acid-base catalysis may crystallize into, for instance, environmentally friendly catalytic processes by replacing environmentally unsound homogeneous catalysts with heterogeneous ones. The International Symposium on Acid-Base Catalysis II was held to develop the field of acid-base catalysis by exchange of information and ideas among scientists gathered from all over the world.

In the past, two international symposia on acid-base catalysis were held. The first one was held at Villeurbanne, France, in 1984, organized by the Institute of Research on Catalysis-CNRS. In response to the recognition by a number of scientists that the international symposium on acid-base catalysis is important and should be continued, a subsequent international symposium on "Acid-Base Catalysis" was organized by Professor Kozo Tanabe of Hokkaido University at Sapporo in 1988.

In 1990, Professor Kozo Tanabe retired from the University. On this occasion, a foundation was established to honor his achievement in the field of acid-base catalysis. The foundation plans to support activities contributing to the development of the field of acid-base catalysis. The International Symposium on "Acid-Base Catalysis II" was one such activity supported by the foundation, and held December 2-4, 1993 at Sapporo. One hundred thirty-seven participants from 13 countries got together to discuss the presented papers for future development in acid-base catalysis.

The present volume contains the text of 21 invited oral presentations and 58 poster presentations. The contents cover a wide range of aspects on acid-base catalysis, from quantum chemistry to industrialized processes, in four chapters.

The organizing committee is particularly grateful to the participants for their presentations and discussion at the symposium. We also thank the Graduate School of Environmental Earth Science, Hokkaido University, and the Sapporo International Communication Plaza Foundation for their support.

February 15, 1994

Hideshi Hattori  
Makoto Misono  
Yoshio Ono

This Page Intentionally Left Blank

# 1. Organic Synthesis

## 1.1 Acidic Salts of Heteropolyacids as Solid Acid Catalysts for Liquid-phase Organic Reactions

Y. Izumi and K. Urabe

Department of Applied Chemistry, School of Engineering, Nagoya University, Furo-cho, Chikusa-ku, Nagoya 464-01, Japan

### Abstract

Several types of solid acid catalysts which can be applicable to liquid-phase organic reactions in polar reaction media have recently been developed to replace the conventional problematic homogeneous acids such as aluminum chloride and sulfuric acid. The present paper describes acidic salts of heteropolyacid and their modifications with silica as active insoluble solid acid catalysts for liquid-phase Friedel-Crafts reactions and hydrolysis of ethyl acetate. Silica-included heteropolyacid salts newly developed were readily separable from water and polar organic media, although the non-modified heteropolyacid salts formed colloidal solutions with polar solvents.

### 1. INTRODUCTION

Aluminum chloride is widely used as an efficient homogeneous catalyst for the liquid-phase Friedel-Crafts alkylation and acylation using alkyl halides, acyl halides, carboxylic acids and anhydrides. Several insoluble solid acids catalysts relevant to Friedel-Crafts reactions have recently been developed to replace conventional problematic homogeneous catalysts; those include Nafion-H, zeolite [1], clay montmorillonite [2],  $\text{SiO}_2\text{-Al}_2\text{O}_3$ , sulfate-doped metal oxides [3], and heteropolyacids and their salts [4-6]. As for heteropolyacid, we have reported efficient catalysis of silica-supported heteropolyacid [4] and acidic alkali metal salts of heteropolyacid [5] for alkylation and acylation in the liquid phase. Misra and Okuhara have first demonstrated high catalytic activity of insoluble acidic salt of 12-tungstophosphoric acid with a large surface area of  $157 \text{ m}^2 \text{ g}^{-1}$  [7] for alkylation in nonpolar reaction media [6].

Liquid-phase hydrolysis, esterification, and hydration, in which water exists as a reactant or a product, are usually catalyzed by homogeneous acids such as sulfuric acid. However, insoluble solid acid catalysts are preferable to homogeneous acids to facilitate product separation and catalyst recovery. Acidic ion-exchange resins are often employed [8,9], but their use is limited to the reactions at relatively low temperatures of less than 100 °C because of low thermal stability. Carbon-entrapped heteropolyacid previously reported by us is also applicable as a solid acid catalyst to liquid-phase dehydration of alcohol [10], but the heteropolyacid entrapped partly dissolves out when treated with water over 100 °C. Unlike silica-alumina and Y-type zeolite, a high-silica zeolite of H-ZSM-5 keeps its strong acidity in aqueous organic media owing to hydrophobicity. H-ZSM-5 is reported to work as a solid acid catalyst for the hydrolysis of ethyl acetate [11], but its catalytic efficiency is much lower than that of an ion-exchange resin, Amberlyst-15, because of smaller acid amount. Recently, we demonstrated that acidic salts of the Keggin-type heteropolytungstic acids and their new

modifications by encapsulation with silica sol are considerably durable against hydrothermal treatment, so applicable as effective and insoluble solid acid catalysts to hydrolysis and esterification reactions [12]. Particularly the silica-included salts of heteropolytungstic acids have been found to be active and easily separable solid acid catalysts.

In this paper, we discuss catalytic properties of acidic alkali metal salts and their modifications with silica sol as new catalyst materials through their applications to liquid-phase Friedel-Crafts reactions and hydrolysis of ethyl acetate.

## 2. EXPERIMENTAL

### 2.1 Catalyst Preparation

Acidic alkali metal salts and ammonium salts of heteropolyacid were prepared through partial neutralization of aqueous 12-tungstophosphoric and 12-tungstosilicic acids with aqueous alkali metal carbonates or ammonium hydroxide, followed by calcination at 300 °C 3 h under a reduced pressure. The silica-included composites were prepared through hydrolysis of ethyl orthosilicate with its 5 molar equivalents of water at 80 °C in the presence of colloidal salts of heteropolyacid dispersed in ethanol, followed by evaporation, extraction with water at 80 °C, and calcination at 300 °C. The weight ratios of W/M and Si/M (M=alkali metal) of the resultant catalysts and composites observed by XRF analysis agreed with the values calculated from the amounts of orthosilicate and the salts of heteropolyacid initially fed.

### 2.2 Reactions and Product Analysis

Friedel-Crafts alkylation and acylation were performed using a Pyrex flask (30 ml) containing a vigorously stirred suspension of catalyst powder (60 mesh pass) and reactants, if necessary, under a stream of nitrogen gas to remove the HCl liberated in the course of the reaction when alkyl chloride and acyl chloride were used as electrophiles. The products were analyzed by gas chromatography using a Silicone SE-30 column (3 m) and *n*-tridecane or *n*-hexadecane as an internal standard.

The hydrolysis of ethyl acetate and the esterification of acetic acid with ethanol were performed in a Pyrex flask (30 ml) containing a suspension of catalyst powder (60 mesh pass) and reactants with vigorous agitation. The products were analyzed by gas chromatography using a PEG Unisole 30T column (2 m) and *n*-tridecane as an internal standard.

## 3. RESULTS AND DISCUSSION

### 3.1 Friedel-Crafts Reactions

Figure 1 illustrates the change in catalytic activity of cesium salts of 12-tungstophosphoric acid ( $Cs_xH_{x-3}PW_{12}O_{40}$ ) with the content denoted by  $x$  for the benzylation of benzene and benzoylation of *p*-xylene, together with the change in surface area of the salt. Each catalytic activity once decreased with increasing  $x$  between 0 and 2 because of the decrease in acidity, then jumped to attain the maximum at  $x = 2.5$ , which well corresponds to the sharp increase in the surface area at  $x = 2.5$ . Such a characteristic pattern of activity change with the content was first reported by Misono *et al.* concerning the dehydration of 2-propanol and the conversion of dimethyl ether in the vapor phase [7]. The turnover of  $Cs_{2.5}H_{0.5}PW_{12}O_{40}$  in the benzylation is  $188\text{ mol}^{-1}$ , thus the catalytic activity is as high as that of the most active silica-supported heteropolyacid [4]; the selectivity for the major monoalkylated product of diphenylmethane was 63%. As for the benzoylation, the catalytic activity of the most active  $Cs_{2.5}H_{0.5}PW_{12}O_{40}$  is much higher (turnover =  $285\text{ mol}^{-1}$ ) than those of silica-supported heteropolytungstic acids (turnover = ca. 100) [4]. Dissolution of any active catalyst species from  $Cs_{2.5}H_{0.5}PW_{12}O_{40}$  was not observed for both reactions, since the reactions did not proceed if  $Cs_{2.5}H_{0.5}PW_{12}O_{40}$  was removed from the reactor on the way of each reaction. It was confirmed through IR measurements that  $Cs_{2.5}H_{0.5}PW_{12}O_{40}$  was stable during the

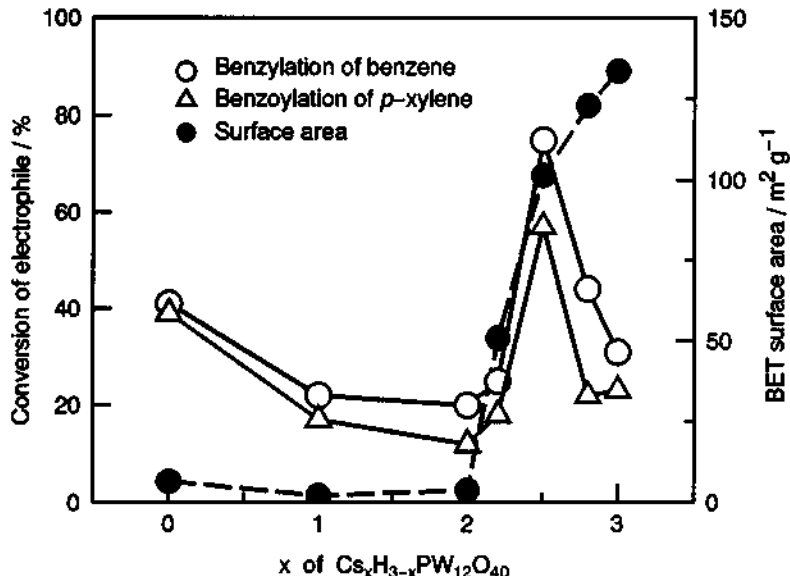


Fig. 1 Benzylation and benzoylation of benzene over  $\text{Cs}_x\text{H}_{3-x}\text{PW}_{12}\text{O}_{40}$ .  
Benzene/ $\text{PhCH}_2\text{Cl}/\text{catalyst} = 100/5/0.02$  mmol, benzene reflux 2 h;  
 $p$ -xylene/ $\text{PhCOCl}/\text{catalyst} = 100/5/0.01$  mmol,  $p$ -xylene reflux 2 h.

reactions retaining its Keggin structure. Y-type zeolite and clay montmorillonite exchanged with metal cations such as  $\text{Al}^{3+}$ ,  $\text{Fe}^{3+}$ , and  $\text{Zn}^{2+}$ , which have been reported as effective catalysts for alkylation and acylation [1,2], were inadequate to the acylation with acyl halide because considerable deactivations occurred due to the dissolution of active metal components. Acidic salts of heteropolytungstic acid having large surface areas such as  $\text{Cs}_{2.5}\text{H}_{0.5}\text{PMo}_{12}\text{O}_{40}$  (surface area =  $146 \text{ m}^2 \text{ g}^{-1}$ ) were ineffectual as acylation catalysts because they readily decomposed during the reaction.

Table 1 summarizes the catalytic efficiency of various active acidic salts of heteropolytungstic acid for the benzylation of benzene and the benzoylation of  $p$ -xylene. Acidic salts of heteropolytungstic acid generally worked as effective solid acid catalysts for alkylation and acylation in the liquid phase holding their Keggin structures, and no dissolution of the active species was observed with all of these salts catalysts. As for the salts of 12-tungstosilicic acid ( $\text{M}_x\text{H}_{4-x}\text{SiW}_{12}\text{O}_{40}$ ), the maximum catalytic activity for the benzylation of benzene was obtained at  $x = 2$  for all of the alkali metal salts and the ammonium salt. It should be noted that the surface area of the active acidic salt increases with the ionic radii of the metal cation.

Other examples of acylation over the  $\text{Cs}_{2.5}\text{H}_{0.5}\text{PW}_{12}\text{O}_{40}$  catalyst were shown in Table 2, comparing with the results obtained for the parent free acid,  $\text{H}_3\text{PW}_{12}\text{O}_{40}$ . The free acid was usually much less effective for the acylation because of the dissolution into organic reaction media in addition to lower surface area.

Reactive aromatic compounds such as anisole and  $p$ -xylene were acylated with benzoic anhydride and acetic anhydride effectively over  $\text{Cs}_{2.5}\text{H}_{0.5}\text{PW}_{12}\text{O}_{40}$  without the dissolution of the catalyst. Carboxylic acids were much less active as acylating agents than the corresponding anhydrides because of the liberation of water, but the acylation became to proceed smoothly when the water produced was continuously removed, for example, by

Table 1. Friedel-Crafts Reactions over Alkali Metal Acidic Salts of Heteropolyacids

Catalyst	Surface area /m <sup>2</sup> g <sup>-1</sup>	Benzylation of benzene <sup>a)</sup> Conversion of PhCH <sub>2</sub> Cl/%	Benzoylation of p-xylene <sup>b)</sup> Conversion of PhCOCl/%
Cs <sub>2.5</sub> H <sub>0.5</sub> PW <sub>12</sub> O <sub>40</sub>	102	75	57
Rb <sub>2.5</sub> H <sub>0.5</sub> PW <sub>12</sub> O <sub>40</sub>	91	49	64
(NH <sub>4</sub> ) <sub>2.5</sub> H <sub>0.5</sub> PW <sub>12</sub> O <sub>40</sub>	90	53	46
K <sub>2.5</sub> H <sub>0.5</sub> PW <sub>12</sub> O <sub>40</sub>	41	75	18
Cs <sub>2</sub> H <sub>2</sub> SiW <sub>12</sub> O <sub>40</sub>	23	99	12
Rb <sub>2</sub> H <sub>2</sub> SiW <sub>12</sub> O <sub>40</sub>	35	43	-
(NH <sub>4</sub> ) <sub>2</sub> H <sub>2</sub> SiW <sub>12</sub> O <sub>40</sub>	52	26	-
K <sub>2</sub> H <sub>2</sub> SiW <sub>12</sub> O <sub>40</sub>	4	72	-

a) Benzene/PhCH<sub>2</sub>Cl/catalyst = 100/5/0.02 mmol, benzene reflux 2 h.

b) p-Xylene/PhCOCl/catalyst = 100/5/0.01 mmol, p-xylene reflux 2 h.

Table 2. Friedel-Crafts Acylation over Cs<sub>2.5</sub>H<sub>0.5</sub>PW<sub>12</sub>O<sub>40</sub><sup>a)</sup>

Acylating agent	Aromatic compound	Product yield/% <sup>b)</sup>	
		Cs <sub>2.5</sub> H <sub>0.5</sub> PW <sub>12</sub> O <sub>40</sub>	H <sub>3</sub> PW <sub>12</sub> O <sub>40</sub>
(PhCO) <sub>2</sub> O	p-xylene	57	3
(PhCO) <sub>2</sub> O	anisole	85	69 <sup>c)</sup>
(PhCO) <sub>2</sub> O	chlorobenzene	0	0
PhCO <sub>2</sub> H	p-xylene	11 <sup>d)</sup>	8 <sup>e)</sup>
PhCO <sub>2</sub> H	anisole	3	4 <sup>f)</sup>
Ac <sub>2</sub> O	anisole	89	50 <sup>f)</sup>
AcOH	anisole	16	15 <sup>f)</sup>
n-C <sub>7</sub> H <sub>15</sub> COCl	mesitylene	80	44 <sup>f)</sup>

a) Yield is based on acylating agent. b) Acylating agent/aromatic compound/catalyst = 5/100/0.01 mmol, reflux 2 h. c) Catalyst was dissolved. d) Acylating agent/aromatic compound/catalyst = 5/100/0.05 mmol. The water liberated was continuously removed by means of Dean-Stark equipment. e) Acylating agent/aromatic compound /catalyst = 5/100/0.10 mmol. f) Catalyst was partly dissolved.

means of Dean-Stark equipment. Metal cation (Zn<sup>2+</sup>, Fe<sup>3+</sup>)-exchanged montmorillonites were ineffectual for catalyzing the acylation of p-xylene with benzoic acid and anhydride [13]. Ce<sup>3+</sup>-exchanged Y-type zeolite was reported to catalyze the acylation with long-chain aliphatic carboxylic acids, but ineffectual for the acylation using acetic acid [1]. Cs<sub>2.5</sub>H<sub>0.5</sub>PW<sub>12</sub>O<sub>40</sub> was also active for the acylation with aliphatic acyl halide such as n-octanoyl chloride. Insoluble acidic salts of heteropolytungstic acid thus behaved as preferable solid acid catalysts for

liquid-phase Friedel-Crafts reactions using polar alkylating and acylating agents.

Table 3 demonstrates significant hydrothermal durability of  $\text{Cs}_{2.5}\text{H}_{0.5}\text{PW}_{12}\text{O}_{40}$ ; its catalytic activity for the benzylation of benzene did not change even after hydrothermal treatment at 120 °C, and the Keggin structure was completely retained.

This result suggests that acidic salts of heteropolyacid may be applicable as effective solid acid catalysts to several types of water-involving organic reaction in the liquid-phase.

**Table 3. Effect of Hydrothermal Treatment on Catalytic Property of  $\text{Cs}_{2.5}\text{H}_{0.5}\text{PW}_{12}\text{O}_{40}$**

Hydrothermal treatment	Catalytic activity for benzylation of benzene <sup>a)</sup>	
	PhCH <sub>2</sub> Cl conversion/%	Ph <sub>2</sub> CH <sub>2</sub> Yield/%
None	90	48
120 °C, 6 days <sup>b)</sup>	100	53

a) Benzene/PhCH<sub>2</sub>Cl/catalyst = 100/5/0.02 mmol, benzene reflux 2 h.

b) Treated in an autoclave, the recovered catalyst was calcined at 300 °C for 3 h prior to reuse for benzylation.

### 3.2 Hydrolysis of Ethyl Acetate

As shown in Table 4, water-insoluble acidic heteropolytungstates,  $\text{Cs}_{2.5}\text{H}_{0.5}\text{PW}_{12}\text{O}_{40}$ , and  $\text{Cs}_{2.5}\text{H}_{1.5}\text{SiW}_{12}\text{O}_{40}$ , exhibited higher catalytic activity than a comparative inorganic solid acid of H-ZSM-5 in terms of specific rate per unit catalyst weight and turnover frequency for the hydrolysis of ethyl acetate and the esterification of acetic acid with ethanol in the liquid phase. These acidic salts were stable and insoluble during the reaction. Amberlyst-15, an organic solid acid, was two or three times more active than the acidic salts of heteropolytungstic acids with respect to the catalytic activity per unit weight, but its turnover frequency that denotes the specific rate per unit acid amount was much lower than those of the salts. Other salts with lower Cs contents, acidic potassium and ammonium salts of heteropolytungstic acids, and acidic salts of heteropolymolybdic acids were all ineffectual, since they partly dissolved into the liquid phase in the course of the reactions.

Table 5 indicates qualitative estimation of acid strength for the solid acids used in the liquid media relevant to the reactions listed in Table 4. Both  $\text{Cs}_{2.5}\text{H}_{0.5}\text{PW}_{12}\text{O}_{40}$  and  $\text{Cs}_{2.5}\text{H}_{1.5}\text{SiW}_{12}\text{O}_{40}$  showed relatively higher acid strengths than H-ZSM-5 in each liquid medium, which corresponds well to their higher turnover frequency than that of H-ZSM-5; in a non-polar solvent  $\text{CsCs}_{2.5}\text{H}_{0.5}\text{PW}_{12}\text{O}_{40}$  shows a higher acid strength of less than -13.16 in terms of  $\text{H}_0$  [14]. Thus these two acidic Cs salts of heteropolytungstic acids may be useful as solid acid catalysts to replace ion-exchange resins for acid-catalyzed water-involving organic reactions which depend on strong acidity or high temperatures.

The crystal sizes of acidic Cs salts of heteropolyacids, however, are very small. For example, the average size of primary crystal particles of  $\text{Cs}_{2.5}\text{H}_{0.5}\text{PW}_{12}\text{O}_{40}$  was about 10 nm. Such heteropolyacid salts easily disperse in water forming colloidal solutions, so become inseparable by filtration.  $\text{Cs}_{2.5}\text{H}_{0.5}\text{PW}_{12}\text{O}_{40}$  could be supported on silica gel, but the salt thus supported was easily removed from silica when put into water or alcohol. We tried to modify the Cs salt not to form colloid, consequently to be readily recoverable from aqueous media, and found a preferable composite in which the Cs salt was tightly bound or encapsulated with silica.

Table 4. Catalytic Activity of Solid Acids in Water-involving Organic Reactions

Solid acid	Surface area /m <sup>2</sup> g <sup>-1</sup>	Acid amount /mequiv. g <sup>-1</sup>	Hydrolysis <sup>a)</sup>		Esterification <sup>b)</sup>	
			Activity <sup>c)</sup>	TF <sup>d)</sup>	Activity <sup>c)</sup>	TF <sup>d)</sup>
Cs <sub>2.5</sub> H <sub>0.5</sub> PW <sub>12</sub> O <sub>40</sub>	102	0.156 <sup>h)</sup>	2.04	13.1	0.52	33.3
Cs <sub>2.5</sub> H <sub>1.5</sub> SiW <sub>12</sub> O <sub>40</sub>	49	0.468 <sup>h)</sup>	4.56	9.7	-	-
Cs <sub>3</sub> HSiW <sub>12</sub> O <sub>40</sub>	83	0.305 <sup>h)</sup>	1.76	5.8	-	-
Amberlyst-15 <sup>e)</sup>	-	4.9 <sup>i)</sup>	7.80	1.6	1.64	3.5
H-ZSM-5 <sup>e,f)</sup>	-	0.234 <sup>h)</sup>	0.43	1.8	0.03	1.3
SiO <sub>2</sub> -Al <sub>2</sub> O <sub>3</sub> <sup>e,g)</sup>	-	-	0	0	-	-

a) Ethyl acetate/water/catalyst = 1080/27.8/0.1 mmol, 60 °C. b) Acetic acid/ethanol/catalyst = 100/100/0.1 mmol, 60 °C. c) Specific rate//10<sup>-3</sup> min<sup>-1</sup> g<sup>-1</sup>. d) Turnover frequency/min<sup>-1</sup>. e) 321 mg. f) Si/Al = 70. g) Si/Al = 6.25. h) Calculated value based on chemical composition. i) Determined by titration.

Table 5. Acid Strength of Solid Acid in Polar Liquid Media<sup>a)</sup>

Solid Acid	Water			Water-AcOEt <sup>b)</sup>			AcOH-EtOH <sup>c)</sup>			
	pK <sub>a</sub> =	+1.5	+0.8	-3.0	+1.5	+0.8	-3.0	+1.5	+0.8	-3.0
Cs <sub>2.5</sub> H <sub>0.5</sub> PW <sub>12</sub> O <sub>40</sub>	+	±	-	+	-	-	+	+	-	-
Cs <sub>2.5</sub> H <sub>1.5</sub> SiW <sub>12</sub> O <sub>40</sub>	+	±	-	-	-	-	+	+	-	-
H-ZSM-5	+	-	-	-	-	-	-	-	-	-

a) Qualitative estimation by Hammett indicators, +: acidic color, -: basic color, ±: border line. b) 95 wt% AcOEt. c) An equimolar mixture of AcOH and EtOH.

Figure 2 shows the change in BET surface area of silica-included Cs<sub>2.5</sub>H<sub>0.5</sub>PW<sub>12</sub>O<sub>40</sub> with silica content. The surface area increased with silica content up to a value of 1.2 in terms of weight ratio of silica to the Cs salt, where adsorption of nitrogen conformed to Langmuir isotherms, but at higher silica contents the adsorption complying with BET isotherms became predominant. Figure 3 depicts pore size distributions of silica-included Cs<sub>2.5</sub>H<sub>0.5</sub>PW<sub>12</sub>O<sub>40</sub> with a silica content of 1.2 and non-modified Cs salt. The former has a microporous structure, whereas the latter mesoporous structure.

Table 6 denotes the catalytic efficiency of the silica-included Cs<sub>2.5</sub>H<sub>0.5</sub>PW<sub>12</sub>O<sub>40</sub> for the hydrolysis of ethyl acetate with excess water, comparing with the results by Amberlyst-15 and H-ZSM-5. Silica itself was inactive for the hydrolysis, but the silica-included Cs<sub>2.5</sub>H<sub>0.5</sub>PW<sub>12</sub>O<sub>40</sub> catalysts were active and thermally stable up to 450 °C. They are catalytically more efficient than Amberlyst-15 and H-ZSM-5 with respect to turnover frequency based on the unit acid site. No migration of colloidal Cs<sub>2.5</sub>H<sub>0.5</sub>PW<sub>12</sub>O<sub>40</sub> was observed during the reaction provided the weight ratio of silica matrix exceeded 0.8. Such favorable catalytic behavior of silica-included Cs<sub>2.5</sub>H<sub>0.5</sub>PW<sub>12</sub>O<sub>40</sub> was never obtained

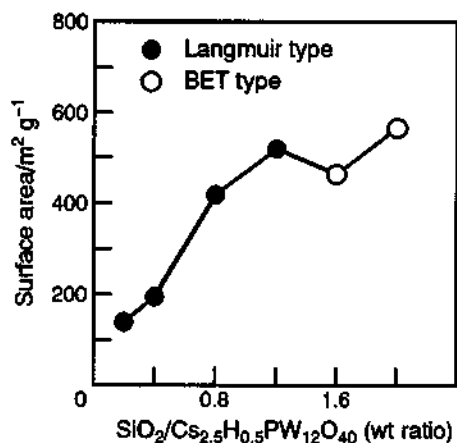


Fig. 2 Surface area of silica-bound  $\text{Cs}_{2.5}\text{H}_{0.5}\text{PW}_{12}\text{O}_{40}$

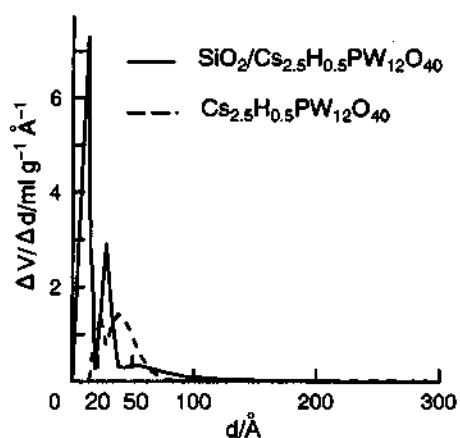


Fig. 3 Pore size distribution

Table 6. Hydrolysis of Ethyl Acetate Catalyzed by Silica-included  $\text{Cs}_{2.5}\text{H}_{0.5}\text{PW}_{12}\text{O}_{40}$ <sup>a)</sup>

Weight ratio of $\text{SiO}_2$ to $\text{Cs}_{2.5}\text{H}_{0.5}\text{PW}_{12}\text{O}_{40}$	Surface area / $\text{m}^2\text{ g}^{-1}$	Catalytic activity		
		$k_1$ <sup>b)</sup> $\times 10^3$	$k_2$ <sup>c)</sup> $\times 10^3$	TF <sup>d)</sup>
0.0	102	2.04	2.04	13.1
0.2	139	1.87	2.25	14.4
0.4	194	1.98	2.76	17.7
0.8	418	1.67	3.06	19.6
1.2	520	1.38	3.10	19.9
1.6 <sup>e)</sup>	714	0.66	1.75	11.2
$\text{SiO}_2$ <sup>e,f,g)</sup>	-	0.0	-	0.0
Amberlyst-15 <sup>e,h)</sup>	-	19.13	-	3.9
H-ZSM-5 <sup>e,f)</sup>	-	1.90	-	8.1

a) Water/Ethyl acetate/ $\text{Cs}_{2.5}\text{H}_{0.5}\text{PW}_{12}\text{O}_{40}$  = 9500/500/353 mg, 60 °C. b) Specific rate/min⁻¹ g-cat⁻¹. c) Specific rate per unit weight of  $\text{Cs}_{2.5}\text{H}_{0.5}\text{PW}_{12}\text{O}_{40}$  included/min⁻¹ g⁻¹. d) Turnover frequency/min⁻¹. e) Catalyst 160 mg. f) Calcined at 300 °C. g) Prepared by hydrolysis of ethyl orthosilicate. h) Dried at 100 °C.

for the other composites prepared from alumina sol, titania sol, and zirconia sol as matrix materials.

The silica-encapsulated  $\text{Cs}_{2.5}\text{H}_{0.5}\text{PW}_{12}\text{O}_{40}$  found through the present study may be preferable as an insoluble solid acid catalyst particularly to the reactions conducted at relatively higher temperatures in highly polar liquid media such as esterification, hydrolysis, and hydration reactions.

## REFERENCES

1. B. Chiche, A. Finiels, C. Gauthier, and P. Geneste, *J. Org. Chem.*, **51**, 2128 (1986).
2. a) P. Laszlo and A. Mathy, *Helv. Chim. Acta*, **70**, 577 (1987); b) B. Chiche, A. Finiels, C. Gauthier, P. Geneste, J. Graille, and D. Pioch, *J. Mol. Catal.*, **42**, 229 (1987);  
c) J. H. Clark, A. P. Kybett, D. J. Macquarrie, S. J. Barlow, and P. Landon, *J. Chem. Soc., Chem. Commun.*, **1989**, 1353; d) A. Cornelis, A. Gerstmans, P. Laszlo, A. Mathy, and I. Zieba, *Catal. Lett.*, **6**, 103 (1990).
3. M. Hino and K. Arata, *Chem. Lett.*, **1981**, 1671.
4. Y. Izumi, N. Natsume, H. Takamine, I. Tamaoki, and K. Urabe, *Bull. Chem. Soc. Jpn.*, **62**, 2159 (1989).
5. Y. Izumi, M. Ogawa, W. Nohara, and K. Urabe, *Chem. Lett.*, **1992**, 1987.
6. a) T. Nishimura, T. Okuhara, and M. Misono, *Chem. Lett.*, **1991**, 1695;  
b) T. Nishimura, T. Okuhara, and M. Misono, *Appl. Catal.*, **73**, L7 (1991).
7. a) S. Tatematsu, T. Hibi, T. Okuhara, and M. Misono, *Chem. Lett.*, **1984**, 865;  
b) T. Hibi, K. Takahashi, T. Okuhara, and M. Misono, *Appl. Catal.*, **24**, 69 (1986).
8. S. A. Bernard and L. P. Hammett, *J. Am. Chem. Soc.*, **75**, 1798, 5834 (1953).
9. S. Sussman, *Ind. Eng. Chem.*, **38**, 1228 (1946).
10. Y. Izumi, and K. Urabe, *Chem. Lett.*, **1981**, 663.
11. S. Namba, N. Hosonuma, and T. Yashima, *J. Catal.*, **72**, 16 (1981).
12. Y. Izumi, M. Ono, M. Ogawa, and K. Urabe, *Chem. Lett.*, **1993**, 825.
13. M. Hisada, K. Urabe, and Y. Izumi, unpublished results.
14. T. Okuhara, T. Nishimura, H. Watanabe, and M. Misono, *J. Mol. Catal.*, **74**, 247 (1992).

## 1.2 Inorganic Solid Supported Reagents as Acids and Bases

Takashi Ando

Department of Chemistry, Shiga University of Medical Science, Otsu 520-21, Japan

### Abstract

The idea of supported reagents casted a new light on the chemistry of catalysis. Potassium fluoride supported on neutral alumina shows effective basicity and is used for catalytic and non-catalytic reactions in organic solvents. Irradiation of ultrasound controls the acidity of the surface of alumina through the solid-solid interaction with a basic salt. Pulverization of hydrogen halide-treated silica gel activates solid iodosobenzene to undergo the reactions with solid organic substrates. Mechanisms and applications of those examples are discussed.

### 1. INORGANIC SOLID SUPPORTED REAGENTS

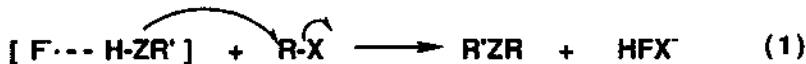
It is not easy to absolutely define the term inorganic solid supported reagent, but it is generally used for a variety of materials including inorganic high surface area supports such as aluminas, clays, silicas, or zeolites. Although these supports have long been used for heterogeneous catalysts, the idea of supported reagents was born not by catalysis chemists but by synthetic organic chemists as a novel methodology in heterogeneous organic synthesis. Thus, reagents supported are usually inorganics, but do not involve heavy metals. Reagents are adsorbed on, dispersed over, or intercalated in those insoluble supports and used generally in organic solvents. Compared with the corresponding homogeneous solution reactions, those using the supported reagents are generally simpler in work up, usually easier in controlling the reactivity, and often more characteristic in selectivity.

A large number of inorganic solid supported reagents have been proposed for almost all the types of organic reactions including oxidation, reduction, aliphatic and aromatic substitution, addition, elimination, and molecular rearrangement [1-3]. Several examples of the reagents used as acids and bases have also been reported. In this paper our studies on the development of those supported reagents and the chemistry of their behavior as solid acids or bases will be summarized and discussed.

### 2. KF-CELITE AND KF-ALUMINA AS SOLID BASES

Fluoride salts are important as fluorination reagents because of the importance of fluorinated organic compounds. Although fluoride salts are neutral in water, it has been known that they behave as basic catalysts in several reactions.

In 1977 Clark and Miller proposed an interesting idea of hydrogen-bond-assisted reactions as shown in Eq. 1 [4].



The idea originates from the strong hydrogen bond between the fluoride anion and a protic compound HZR' as a result of the large electron density of the small fluoride anion. Z stands for an oxygen, nitrogen, sulfur, or carbon. This strong hydrogen bond causes extensive polarization of the Z-H bond in this hydrogen bond complex. The electron density and thus the nucleophilicity of Z is enhanced under still neutral conditions. Various types of nucleophilic substitution reactions can be carried out easily based on this principle.

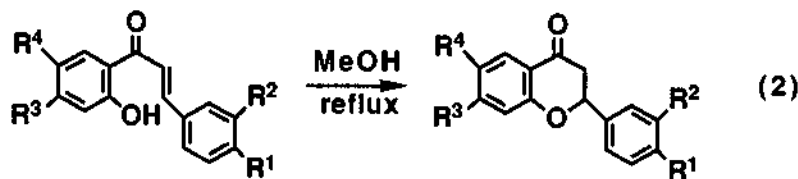
Although the idea of hydrogen-bond assisted reactions had a broad possibility, the poor solubility of fluoride salts in organic solvents hampered its application. Supported reagents of fluoride salts appeared on the scene at that moment. Shortly after tetrabutylammonium fluoride on silica gel was reported by Clark [5], we reported that KF supported on Celite was a mild but efficient reagent for the alkylation of various protic compounds [6]. Typical examples are summarized in Table 1.

**Table 1. Alkylation with KF-Celite in CH<sub>3</sub>CN**

Reactant	Product	T/°C	t/h	Yield/% <sup>a)</sup>
PhOH + MeI + PhCH <sub>2</sub> Cl	PhOMe PhOCH <sub>2</sub> Ph	rt 60	40 17	89 99 (87)
PhSH + MeI + n-BuCl	PhSMe PhSBu-n	rt rt	0.5 20	100 94
PhNH <sub>2</sub> + PhCH <sub>2</sub> Cl	PhNHCH <sub>2</sub> Ph	60	24	- (74)
C <sub>5</sub> H <sub>10</sub> NH + n-BuI	C <sub>5</sub> H <sub>10</sub> NBu-n	rt	2	75
(CH <sub>3</sub> CO) <sub>2</sub> CH <sub>2</sub> + MeI	(CH <sub>3</sub> CO) <sub>2</sub> CHMe	rt	20	100 (75)
(PhCO) <sub>2</sub> CH <sub>2</sub> + MeI	(PhCO) <sub>2</sub> CHMe	rt	48	- (86)

a) Isolated yields are shown in parentheses; others were determined by GLPC

Later, KF-Celite in methanol was found more effective than KOH in ethanol in a catalytic reaction (Eq. 2) [7].

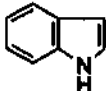
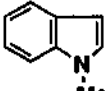
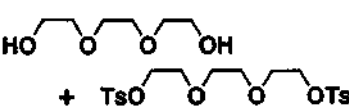


Comparative studies on various fluoride salts, solid supports, and organic solvents showed that KF supported on alumina was the most convenient and efficient reagent for alkylation [8]. KF-alumina was used in promoting alkylation of various types of compounds including alcohols, amides, and lactams and other nitrogen heterocycles involving uracil and xanthine derivatives; crown ethers could also be prepared in good yields (Table 2) [9-11].

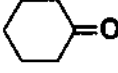
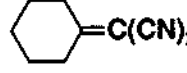
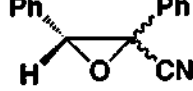
KF-alumina was found also effective in catalyzing a variety of reactions such as the Michael addition, aldol condensation, the Knoevenagel reaction, Darzens condensation, and similar reactions (Table 3). [12].

As this type of carbon-carbon bond formation is important in synthetic organic chemistry, many research groups studied on the application of KF-alumina and

**Table 2. Alkylation with KF-Alumina**

Reactant	Product	T/°C	t/h	Yield/%
$(\text{CH}_3\text{CO})_2\text{CH}_2 + \text{MeI}$	$(\text{CH}_3\text{CO})_2\text{CMe}_2$	rt	16	84
 + MeI		rt	3	85
PhOH + MeI	PhOMe	rt	1	96
$\text{CH}_3(\text{CH}_2)_7\text{OH} + \text{MeI}$	$\text{CH}_3(\text{CH}_2)_7\text{OMe}$	rt	40	90
 + TsO 		rt	72	78

**Table 3. Addition and Condensation with KF-Alumina at Room Temperature**

Reactant	Product	Solvent	t/h	Yield/% <sup>a)</sup>
PhCH=CHCOPh + $\text{CH}_3\text{NO}_2$	$\text{PhCH}(\text{CH}_2\text{COPh})\text{CH}_2\text{NO}_2$	CH <sub>3</sub> CN	3.5	74
PhCHO + $\text{CH}_2(\text{CN})_2$	PhCH=C(CN) <sub>2</sub>	CH <sub>3</sub> CN	3	86
PhCHO + PhCH <sub>2</sub> CN	PhCH=C(CN)Ph	DME	21	82
 + $\text{CH}_2(\text{CN})_2$		DME	15	55
PhCHO + PhCHClCN		Benzene	21	82 <sup>b)</sup>

a) Isolated yields after purification. b) Yield determined by <sup>1</sup>H-NMR.

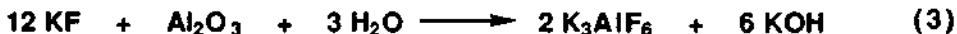
usually obtained better yields under milder conditions than with the conventional base catalysts. Some of the reactions including the Knoevenagel, Darzens, and Wittig-Horner reactions were carried out by the flow method using a column packed with KF-alumina [13]. Products were isolated by simple elution of starting materials in dichloromethane.

All the examples described above are reactions promoted with bases as catalysts or reagents. More clearly, it was found that KF-alumina was effective in promoting  $\alpha$ - and  $\beta$ -elimination reactions giving alkenes, alkynes, or cyclopropanes [12]. Thus, although the idea of hydrogen bond-assisted reactions assume that the fluoride anion operates under neutral conditions, KF-alumina apparently behaves as an effective solid base. It is completely opposite to the fact that fluorinated alumina is known as a solid acid in catalysis chemistry. KF-alumina is now a commercially available common reagent in daily use for organic chemists.

### 3. MECHANISMS OF THE BASICITY OF KF-ALUMINA

Why the efficiency of the hydrogen bond-assisted reactions is increased when KF is supported on alumina? What are the mechanisms of the appearance of the practical and efficient basicity of KF-alumina? These are important and interesting questions for which much effort has been devoted [14-15]. Dispersion of inorganic salt reagents over the high surface area of solid supports is generally regarded as the main reason of the efficiency of solid supported reagents and must also operate in the case of KF-alumina. Insufficient coordination only with surface hydroxyl groups may result in the production of the so-called 'half-naked' and thus active fluoride anion. This possibility was supported by solid state  $^{19}\text{F}$  MAS NMR [14,16-17].

On the other hand, fluoride anion is known to react with alumina to produce strong basic species (Eq. 3 and 4).



As the powder X-ray analysis of KF-alumina showed the presence of  $\text{K}_3\text{AlF}_6$  other than KF and  $\text{Al}_2\text{O}_3$ , the formation of such basic substances on the surface of KF-alumina could reasonably be assumed [14]. Based on similar observations, Weinstock and his coworkers proposed that the enhanced reactivity of KF-alumina was a consequence of the production of hydroxide and/or aluminate [18]. In order to clarify the question, the reactivities of supported and unsupported KF, NaF, KOH, and NaOH were compared in catalytic and non-catalytic reactions [15]. Part of the results are summarized in Table 4.

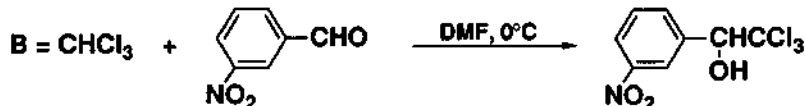
It is known that KF is much more reactive than NaF in hydrogen bond-assisted reactions when unsupported while KOH and NaOH have similar reactivity as a base catalyst. The results shown in Table 4 indicate that NaF-alumina was reactive only in a limited case and usually much less reactive than KF-alumina. Thus, the relative reactivities of the supported reagents generally resemble those of the unsupported fluoride salts, but not those of the hydroxide bases.

As summarized in Table 5, titration study showed that the amounts of water-soluble strong base on the surface of NaF- and KF-alumina were much less than that on the surface of KOH-alumina.

**Table 4. Reactivities of NaF- and KF-Alumina**

reaction <sup>a)</sup>	MF-alumina mmol/g	time	conversion % M = Na ( M = K )
A	0.6	150s ; 210s ; 270s	38 (40) ; 47 (62) ; 56 (69)
	2.0		25 ; 32 (60) ; 39 (70)
	5.0		9 (43) ; 13 (62) ; 15 (77)
B	0.6	3.0h	9
	5.0		3 (64)
C	0.6	1.5h	1 (7)
	5.0	1.5h ; 5.0h	4 (90); 8 (100)

a)

**Table 5. Titration of NaF, KF, and KOH/Al<sub>2</sub>O<sub>3</sub> Basicity**( 2 mmol MF or 1 mmol KOH on 1g Al<sub>2</sub>O<sub>3</sub>, dried at 90°C/20 mmHg )

aqueous wash → water-soluble base

NaF	KF	KOH
0.13	0.21	0.68

(mmol base/mmol MF or KOH)

aq. acid wash → total base

NaF	KF	KOH <sup>a)</sup>
0.86	0.81	(0.79)

(mmol base/mmol MF or KOH)

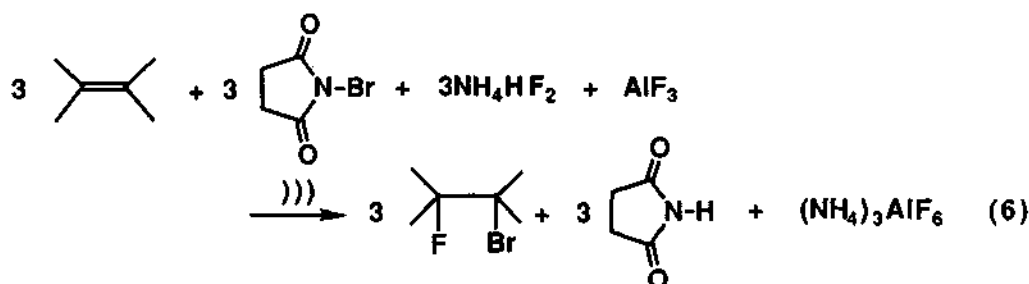
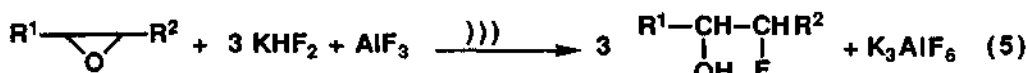
a) dried at 200°C/0.1 mmHg

On the contrary, the amounts of the total base washed out with aqueous acid from the three supported reagents were almost the same and more than that expected from the equation of the reaction between fluoride and alumina (Eq. 3).

Recently, Winfield and his coworkers claimed from their study using radio isotopes that there is no evidence of free hydroxide anions on the surface of the calcined KF-alumina [19]. From those described above and other pieces of evidence including FTIR, thermogravimetry, and SEM, we concluded that there are three basic species or the mechanisms of the appearance of the basicity on the surface of KF-alumina: (i) the well-dispersed and incompletely coordinated thus reactive fluoride anion, (ii) [Al-O<sup>-</sup>] ion which generates OH<sup>-</sup> when water is present, (iii) the cooperation of F<sup>-</sup> and [Al-OH] which can behave as an *in situ*-generated base during the course of the reaction [15].

#### 4. POSSIBILITY OF *IN SITU*-GENERATED SOLID ACID

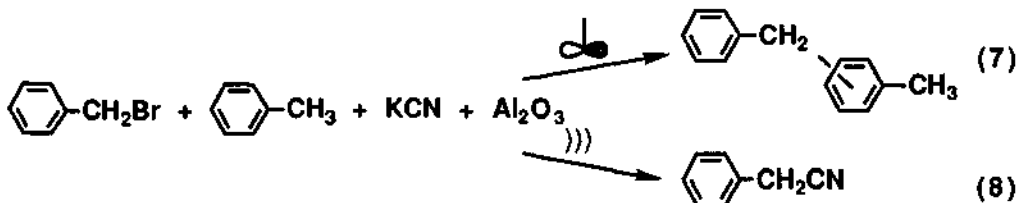
From the thermodynamic point of view, the basicity of KF-alumina can be regarded as the result of an unusually large bond dissociation energy of the bond between aluminium and fluorine ( $671 \text{ kJ mol}^{-1}$ ) in comparison with those between aluminium and oxygen ( $492 \text{ kJ mol}^{-1}$ ) or between fluorine and other metals (e.g.  $581 \text{ kJ mol}^{-1}$  for Ba-F). Reactive basic species can be generated easily during the course of the reaction by taking advantage of this energy difference. If this trick can be applied to other combinations of bonds, *in situ*-generated acid could also be expected. This was realized by Ichihara and her coworkers in the following examples (Eq. 5 and 6) [20-21].



*In situ*-generated hydrogen fluoride is used for fluorohydrin formation from epoxides and bromosfluorination of alkenes. In both reactions the formation of the thermodynamically stable fluoroaluminates is the driving force of the reactions. Unfortunately, no example of the use of the *in situ*-generated hydrogen fluoride for catalytic reactions has been reported.

#### 5. ULTRASOUND AS A CATALYST FOR HETEROGENEOUS REACTIONS

Unusual catalytic acidity was observed for neutral  $\gamma$ -alumina in use for column chromatography in the case of attempted aliphatic nucleophilic substitution of benzyl bromide with cyanide anion (Eq. 8). When the reaction was carried out in toluene as a solvent, aromatic electrophilic substitution or the Friedel-Crafts alkylation was the observed actual pathway (Eq. 7) [22].



In the reaction, the supported reagent, KCN-alumina, was not prepared beforehand, but KCN, alumina, and then benzyl bromide were added separately into toluene and the mixture was agitated mechanically. Alumina played the role

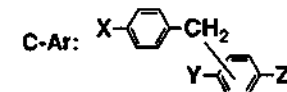
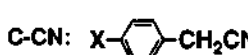
of a Lewis acid under these conditions. It is unusual that neutral alumina without any special activation process behaves as a Lewis acid in catalyzing aromatic electrophilic substitution. The reason of this unusual acidity can be attributed to the cooperation of alumina and hydrogen bromide, the latter of which is evolved from benzyl bromide. As benzyl bromide is very reactive, the active sites on the surface of alumina must catalyze its ionization to initiate the aromatic electrophilic substitution in a small amount. If the aromatic substitution once proceeds even a minute amount, then hydrogen bromide is a product of the reaction and the reaction mixture becomes more acidic to further accelerate the reaction. Thus, it is another example of an *in situ*-generated acid catalyst.

Interestingly, irradiation of ultrasound can switch the course of the reaction from the aromatic electrophilic substitution to the first expected aliphatic nucleophilic substitution (Eq. 8) [22]. Thus, the acidity of alumina was somehow controlled by ultrasound. The chemistry under irradiation of ultrasound became topical quite recently by the name of sonochemistry. Sonochemical switching from Eq. 7 to Eq. 8 was the first clear-cut example in heterogeneous sonochemistry [23].

**Table 6. Sonochemical Switching**

X-  -CH <sub>2</sub> Br	Conditions	GLPC Yield / %							
		Benzene		Toluene		p-Xylene		Anisole	
		C-CN	C-Ar	C-CN	C-Ar	C-CN	C-Ar	C-CN	C-Ar
X=H	M	0	9	0	83	0	76	0	61
	U	70	1	72	1	0	76	50	14
	U*-U					(76	(6)	(73	(3)
Br	M	0	22	0	87	0	83		
	U	67	1	69	10	40	52		
	U*-U					(70	(8)		
Me	M	0	75	0	80	0	83		
	U	77	1	0	84	0	86		
	U*-U				(9	(77)			

M: Mechanical Agitation U: Ultrasound U\*: Ultrasonic Pretreatment



This sonochemical switching was rather general for the combination of substituted benzyl bromides and aromatic solvents (Table 6) [22]. When a benzyl bromide and/or aromatic solvent was too reactive, aromatic substitution proceeded even under ultrasonic irradiation. However, when alumina and KCN in an aromatic solvent was sonicated before a benzyl bromide was added (ultrasonic pretreatment) and then the mixture was sonicated, the sonochemical switching was observed in several additional cases (Table 6).

Luche attributed this sonochemical switching to the acceleration of single electron transfer under sonication which results in the acceleration of aliphatic nucleophilic substitution via the radical chain mechanism [24].

**Table 7. Effect of Ultrasonic Pretreatment on Sonochemical Switching**

System	Reaction Conditions	Time	C-Br	C-CN	C-Ar
A	{PhCH <sub>2</sub> Br, KCN} {toluene, Al <sub>2</sub> O <sub>3</sub> }	U	24h	0%	71%
		M	3h	0	83
B	{KCN, Al <sub>2</sub> O <sub>3</sub> } {toluene}	U*	1h-M	24h	48
		U*	3h-M	24h	86
		U*24h-M	24h	61	7
		U*	3h-U	24h	0
C	{PhCH <sub>2</sub> Br, toluene, Al <sub>2</sub> O <sub>3</sub> }	U	3h	0	--
		M	3h	0	--

As shown in Table 7, however, we observed that the aliphatic substitution under sonication was slower than the aromatic substitution under mechanical agitation (Table 7, system A) [23]. Furthermore, alumina as a Lewis acid was deactivated depending on the length of time of ultrasonic pretreatment (Table 7, system B). Thus, although ultrasound is necessary for the aliphatic nucleophilic

**Table 8. Solid-state Pulverization Reactions of Di-Substituted Alkenes and a Alkyne with HX-Silica Gel and PhIO**

Entry	Substrate <sup>a)</sup>	Products, Yield(%) <sup>b)</sup>		
		HCl-Silica gel	HBr-Silica gel	HI-Silica gel
1		 65	 39	 5<
2		 58	 58	 36, no adducts
3		 74	 51	 trace(6>)
4		 80	 27	 41

a) substrate: 100mg, PhIO: 2.2eq(ca.150mg-720mg) for each alkenyl bond, HX-silica gel: 20g.

b) isolated yield.

substitution (system B), it is not so accelerated that it becomes a faster step than the aromatic substitution, but the switching is the enforced results of the retardation or inhibition of aromatic substitution. Ultrasound must accelerate the interaction of the active acidic sites on the alumina surface with the basic salt KCN to result in their deactivation. The solid-solid interaction, which is intrinsically most disadvantageous under the conventional conditions, can be most accelerated under sonication. Thus, we conclude that ultrasound can be used to control the acidity of solid supports by the interaction across the phase boundary.

## 6. PULVERIZATION AS AN ACTIVATION DEVICE FOR SOLID REACTIONS

Recently, we have been interested in the pulverization activation of all solid reactions involving solid organic substrates, solid reagents, and acidic solid supports in the absence of solvents. This reaction system is interesting because of the possibility of the intervention of mechanochemistry or tribochemistry.

**Table 9. Solid-state Pulverization Reactions of Aromatic Compounds with HCl-Silica Gel and PhIO**

Entry	Substrate <sup>a)</sup>	Product	Yield(%) <sup>b)</sup>
1			31 <sup>c)</sup>
2			32
3			31
4			79
5			42 / 52
6			46

a) Substrate: 50 mg, PhIO: 4.4 eq. to the substrate, HCl-silica gel: 10 g.

b) Isolated yields. c) Determined by GLC.

We used iodosobenzene as a solid reagent which is actually an insoluble polymer and can be activated with a Brønsted acid. As a solid support, silica gel treated with the vapor of hydrogen halide by keeping it over concentrated hydrogen halide acid for one or two weeks. A mixture of these two with a solid organic substrate was crushed and ground in a mortar for just 5 minutes and worked up. By these simple procedures, alkenes and an alkyne of high- and low-melting-point solids gave halogenation and oxidation products depending on the substrates and hydrogen halides used (Table 8) [25]. Steric hindrance in the structure of the substrates and the acidity of the hydrogen halides are apparently the factors determining the course of the reaction. Solid aromatic compounds were also chlorinated or oxidized under the same reaction conditions using hydrogen chloride-treated silica gel (Table 9) [26].

**Table 10. One-Step Synthesis of Sulfonyl Chlorides from Sulfides with HCl-Silica Gel and PhIO in Solid-state**

Entry	Substrate <sup>a)</sup>	Product	Yield(%) <sup>b)</sup>
1	Ph $\swarrow$ S $\searrow$ Ph	Ph $\swarrow$ SO <sub>2</sub> Cl	98
2	Ph-S $\swarrow$ Ph	Ph-SO <sub>2</sub> Cl	96
3	Ph $\swarrow$ S $\searrow$ Ph	Ph $\swarrow$ SO <sub>2</sub> Cl	89
4	CH <sub>3</sub> -S $\swarrow$ Ph	CH <sub>3</sub> -SO <sub>2</sub> Cl	91 <sup>c)</sup>
5	CH <sub>3</sub> (CH <sub>2</sub> ) <sub>3</sub> -S $\swarrow$ Ph	CH <sub>3</sub> (CH <sub>2</sub> ) <sub>3</sub> -SO <sub>2</sub> Cl	90
6	CH <sub>3</sub> (CH <sub>2</sub> ) <sub>5</sub> -S $\swarrow$ Ph	CH <sub>3</sub> (CH <sub>2</sub> ) <sub>5</sub> -SO <sub>2</sub> Cl	93
7	CH <sub>3</sub> (CH <sub>2</sub> ) <sub>7</sub> -S $\swarrow$ Ph	CH <sub>3</sub> (CH <sub>2</sub> ) <sub>7</sub> -SO <sub>2</sub> Cl	92
8	Ph <sub>3</sub> C-S $\swarrow$ Ph	Ph <sub>3</sub> C-SO <sub>2</sub> Cl / Ph $\swarrow$ SO <sub>2</sub> Cl	57 / 43
9	Ph $\swarrow$ S-C(=NH)-NH <sub>2</sub> Cl	Ph $\swarrow$ SO <sub>2</sub> Cl	65

a) Substrate: 50 mg, PhIO: 4.4 eq. to the substrate, HCl-silica gel: 10 g. b) Isolated yields otherwise noted. c) Determined by GLC.

The same experimental procedures of 5 minutes pulverization with organic sulfides as substrates gave sulfonyl chlorides in one step in excellent yields (Table 10) [27]. Half of the starting sulfides used are solid materials. Sulfonyl chlorides are an important class of compounds which can be prepared from various types of organic sulfur compounds with chlorine gas. Compared with those conventional procedures, the present method is easy and efficient without the use of troublesome chlorine gas. It is especially recommendable for a small scale preparation.

In this reaction pulverization is essential to exert the effect of the solid acid on the solid reagent.

## 7. CONCLUSION

In this paper characteristic behavior of solid supported reagents as acids or bases has been reviewed. Some of the characteristics, e.g. *in situ*-generation of acids or bases by consuming solid supports, control of acidity by accelerating solid-solid interaction by ultrasonic irradiation or pulverization, or appearance of the maximum reactivity by the addition of a trace amount water [23] or other additives which is not reviewed in the present paper, are apparently novel ideas in the chemistry of catalysis. Interaction of the two fields of chemistry must be stimulative and profitable for both fields.

## REFERENCES

1. P. Laszlo (ed), "Preparative Chemistry Using Supported Reagents", Academic, San Diego (1987).
2. K. Smith (ed), "Solid Supports and Catalysts in Organic Synthesis", Ellis Horwood, Chichester (1992).
3. J. H. Clark, A. P. Kybett, and D. J. Macquarrie, "Supported Reagents: Preparation, Analysis, and Applications", VCH, New York (1992).
4. J. H. Clark and J. M. Miller, *J. Am. Chem. Soc.*, **1977**, 99, 498.
5. J. H. Clark, *J. Chem. Soc., Chem. Commun.*, **1978**, 789.
6. T. Ando and J. Yamawaki, *Chem. Lett.*, **1979**, 45.
7. L. M. Harwood, G. C. Loftus, A. Oxford, and C. Thomson, *Synth. Commun.*, **1990**, 20, 649.
8. J. Yamawaki and T. Ando, *Chem. Lett.*, **1979**, 755.
9. J. Yamawaki and T. Ando, *Chem. Lett.*, **1980**, 533.
10. J. Yamawaki, T. Ando, and T. Hanafusa, *Chem. Lett.*, **1981**, 1143.
11. T. Ando, J. Yamawaki, T. Kawate, S. Sumi, and T. Hanafusa, *Bull. Chem. Soc. Jpn.*, **1982**, 55, 2504.
12. J. Yamawaki, T. Kawate, T. Ando, and T. Hanafusa, *Bull. chem. Soc. Jpn.*, **1983**, 56, 1885.
13. D. Villemin, *Chem. Ind. (London)*, **1985**, 166.
14. T. Ando, S. J. Brown, J. H. Clark, D. G. Clark, T. Hanafusa, J. Ichihara, J. M. Miller, and M. S. Robertson, *J. Chem. Soc., Perkin Trans. 2*, **1986**, 1133.
15. T. Ando, J. H. Clark, D. G. Cork, T. Hanafusa, J. Ichihara, and T. Kimura, *Tetrahedron Lett.*, **1987**, 28, 1421.
16. J. H. Clark, E. M. Goodman, D. K. Smith, S. J. Brown, and J. M. Miller, *J. Chem. Soc., Chem. Commun.*, **1986**, 657.
17. C. V. A. Duke, J. M. Miller, J. H. Clark, and A. P. Kybett, *J. Mol. Catal.*, **1990**, 62, 233.
18. L. M. Weinstock, J. M. Stevenson, S. A. Tomellini, S.-H. Pan, T. Utne, R. B. Jobson, and D. F. Reinhold, *Tetrahedron Lett.*, **1986**, 27, 3845.
19. T. Baird, A. Bendada, G. Webb., and J. M. Winfield, *J. Mater. Chem.*, **1991**, 1, 1071.
20. J. Ichihara and T. Hanafusa, *J. Chem. Soc., Chem. Commun.*, **1989**, 1848.
21. J. Ichihara, K. Funabiki, and T. Hanafusa, *Tetrahedron Lett.*, **1990**, 31, 3167.
22. T. Ando, S. Sumi, T. Kawate, J. Ichihara (nee Yamawaki), and T. Hanafusa, *J. Chem. Soc., Chem. Commun.*, **1984**, 439.

23. T. Ando and T. Kimura, *Adv. Sonochem.*, **1991**, *2*, 211.
24. J. L. Luche, *Ultrasonics*, **1992**, *30*, 156.
25. H. Sohmiya, T. Kimura, P. Bauchat, M. Fujita, and T. Ando, *Chem. Lett.*, **1991**, 1391.
26. H. Sohmiya, unpublished results.
27. H. Sohmiya, T. Kimura, M. Fujita, and T. Ando, *Chem. Lett.*, **1992**, 891.

# 1.3 Heteropoly Acids as Catalysts for Organic Reactions

Ivan V. Kozhevnikov

Institute of Catalysis, 630090 Novosibirsk, Russia

## ABSTRACT

Catalysis with heteropoly acids (HPA) is a field of growing importance. A brief discussion of structure and properties of HPA relevant to the topic is given. The use of HPA as acid catalysts for fine chemical synthesis is reviewed. A wide variety of syntheses of antioxidants, medicines, vitamins and other fine chemicals based on HPA catalysis in homogeneous and heterogeneous liquid-phase systems is discussed.

## 1. INTRODUCTION

During the past two decades much attention has been paid to the catalysis by heteropoly acids (HPA) [1-7]. HPA have a unique set of physicochemical properties that are of great value for catalysis. Among them most important are: well defined structure, strong Bronsted acidity, ability to reversible redox reactions, high solubility in water and polar solvents, as well as fairly high stability in the solid state, etc. By virtue of these properties HPA are used both as acid and oxidative catalysts either in homogeneous or heterogeneous (bulk and supported) systems. Bulk HPA exhibit not only usual surface-type catalytic properties, but also, like concentrated acid solutions, a bulk-type catalytic behaviour ("pseudoliquid phase"), due to the lability of their crystal structure and high proton mobility [6].

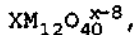
In the past years, our knowledge of mechanisms of HPA catalysis at molecular level has greatly extended [1-6]. Also, new catalytic technologies based on the HPA catalysis for large-scale industrial processes have been developed and commercialized. Examples are hydration of olefins, polymerization of tetrahydrofuran and oxidation of methacrolein to methacrylic acid [7].

A new promising field for the use of HPA catalysis is the fine chemical synthesis [8]. By now, many works on the HPA catalysis in syntheses of antioxidants, medicines, vitamins, etc., have been done. In this review the use of HPA as acid catalysts for fine chemical synthesis in homogeneous and heterogeneous liquid-phase systems is discussed. Relevant examples are mainly taken from author's studies. A short outline of HPA properties is also given.

## 2. GENERAL FEATURES OF HPA

### 2.1. Structure

Among a wide variety of HPA, those belonging to the saturated 12th series are most important for catalysis. They include the heteropoly anions (HPAN)



where X is the central atom ( $\text{Si}^{4+}$ ,  $\text{P}^{5+}$ , etc.), x is the degree of its oxidation, and M is the metal ion ( $\text{Mo}^{6+}$ ,  $\text{W}^{6+}$ ,  $\text{V}^{5+}$ , etc.). These HPAN have a well known Keggin structure [9]. They are most stable and studied in a more detail.

### 2.2. Acid properties of HPA

HPA are strong Bronsted acids [1-7], while HPAN are "soft" weakly solvated bases [10].

The proton structure of HPA has been discussed elsewhere [4]. According to  $^{17}\text{O}$  NMR data [11], the protons in the free HPA molecules (e.g., in solution) are assumed to be localized predominantly at the oxygen atoms of the angular bridges M—O—M. In the bulk HPA hydrates, the bulk proton sites are represented as dioxonium ions  $\text{H}_2\text{O} \dots \text{H}^+ \dots \text{OH}_2$ , each of which links four neighbouring HPAN by forming hydrogen bonds between the protons of water molecules and the terminal oxygen atoms of the M = O group [12]. There are no exact data on proton positions in the dehydrated acids, but, by analogy with hydrates, the non-hydrated protons are likely the bridges between the terminal O atoms of the M = O group belonging to the neighbouring HPAN [4].

HPA in solution are much stronger than the usual mineral acids such as  $\text{H}_2\text{SO}_4$ ,  $\text{HCl}$ ,  $\text{HBr}$ ,  $\text{HNO}_3$ , etc. The strength of the Keggin HPA depends weakly on their composition. However, W-HPA are markedly stronger than Mo-HPA. The strongest and most stable acid among the acids of the 12th series is  $\text{H}_3\text{PW}_{12}\text{O}_{40}$  [4]. The dissociation constants of HPA were measured in such solvents as  $\text{H}_2\text{O}$  [13],  $\text{Me}_2\text{CO}$ ,  $\text{EtOH}$ ,  $\text{AcOH}$  [14], the Hammett acidity function in  $\text{H}_2\text{O}$  and  $\text{H}_2\text{O}-\text{AcOH}$ ,  $\text{H}_2\text{O}$ -dioxane,  $\text{H}_2\text{O}-\text{EtOH}$  and  $\text{H}_2\text{O}-\text{Me}_2\text{CO}$  mixtures [15].

Solid HPA possess purely Bronsted acidity and are stronger than such conventional acid catalysts as  $\text{SiO}_2-\text{Al}_2\text{O}_3$ ,  $\text{H}_3\text{PO}_4/\text{SiO}_2$ , HX and HY zeolites [16]. The acidity of bulk and supported HPA has been studied by a variety of methods, e.g. chemical titration with indicators [17], diffusion [18], conductivity [19], ion exchange [20], thermal desorption of bases [16], IR spectroscopy [16, 21, 22], NMR  $^1\text{H}$  [23], NMR  $^1\text{H}$  (MAS) [24, 25], ESCA [26], etc.

Proton sites in the bulk dehydrated  $\text{H}_3\text{PW}_{12}\text{O}_{40}$  are essentially uniform. They are characterized by the heat of  $\text{NH}_3$  adsorption of  $140-165 \text{ kJ mol}^{-1}$ , that is almost the same as the heat of  $\text{NH}_3$  adsorption on H-mordenite [27]. There is also a small amount (<3%) of stronger sites with the heat of  $\text{NH}_3$  adsorption of  $>170 \text{ kJ mol}^{-1}$ . These are probably surface proton sites localized on the bridging oxygen atoms M—O—M. When loading HPA on  $\text{SiO}_2$ , the proton sites become weaker and less uniform, the heat of  $\text{NH}_3$  adsorption approaching that for acid sites of HX and HY zeolites [27]. According to the  $\text{NH}_3$  thermal desorption data [27], the acid strength of supported  $\text{H}_3\text{PW}_{12}\text{O}_{40}$  decreases in the series of carriers:  $\text{SiO}_2 > \text{Al}_2\text{O}_3 >$  activated charcoal (Sibunit).

Magic angle spinning (MAS)  $^1\text{H}$  NMR spectra of dehydrated bulk  $\text{H}_3\text{PW}_{12}\text{O}_{40}$ ,  $\text{H}_4\text{SiW}_{12}\text{O}_{40}$ ,  $\text{H}_3\text{PMo}_{12}\text{O}_{40}$  and  $\text{H}_4\text{SiMo}_{12}\text{O}_{40}$  consist of one single line with isotropic chemical shift of 9.3, 9.7, 8.5 and 7.4 ppm, respectively [24, 25]. This may also confirm the uniformity of HPA protons. As expected, W-HPA, being stronger acids, have larger chemical shifts than Mo-HPA. In the spectrum of the  $\text{SiO}_2$ -supported  $\text{H}_3\text{PW}_{12}\text{O}_{40}$ , no line with  $\delta = 9.3$  ppm, typical for crystalline  $\text{H}_3\text{PW}_{12}\text{O}_{40}$ , can be seen up to 50 wt % content of HPA. However, at  $\geq 20$  % HPA content a line with  $\delta = 5$  ppm appears in the spectra, indicating the interaction of HPA with  $\text{SiO}_2$  and the formation of a new type of proton sites on the  $\text{SiO}_2$  surface [25].

$^{31}\text{P}$  MAS NMR spectra of bulk and  $\text{SiO}_2$ -supported  $\text{H}_3\text{PW}_{12}\text{O}_{40}$  also indicate the significant interaction of HPA with  $\text{SiO}_2$  regardless of the extent of HPA hydration [25].

The strength and number of acid sites of HPA catalysts can be regulated by varying the chemical composition of HPA, the type of a carrier, the conditions of pre-treatment, etc. [4].

### 2.3 Preparation of catalysts

Such HPA as  $\text{H}_3\text{PW}_{12}\text{O}_{40}$ ,  $\text{H}_4\text{SiW}_{12}\text{O}_{40}$  and  $\text{H}_3\text{PMo}_{12}\text{O}_{40}$  are commercially available as crystalline hydrates. HPA are usually obtained by acidifying an aqueous solution containing the salt of the heteroelement and the alkali metal molybdate or tungstate with subsequent isolation of the HPA by extracting with ether or by ion exchange [9].

Electrodialysis provides new opportunities for the synthesis of HPA [28, 29]. This method allows to obtain many HPA in a high yield. Efficient electromembrane method has been developed to prepare  $\text{H}_3\text{PW}_{12}\text{O}_{40}$  by interacting  $\text{Na}_2\text{WO}_4$  with  $\text{H}_3\text{PO}_4$  in aqueous solution, a selective cation-exchange membrane being used to remove  $\text{Na}^+$  ions [28]. The anion  $\text{PW}_{12}\text{O}_{40}^{3-}$  is formed in the anode compartment of dialyzer from  $\text{WO}_4^{2-}$  and  $\text{PO}_4^{3-}$  taken in an almost stoichiometric ratio. Acidification needed for that is provided by electrolysis of water.  $\text{Na}^+$  ions are transferred by electric potential from anodic to cathodic compartment through a cation-exchange membrane. As a result,  $\text{H}_3\text{PW}_{12}\text{O}_{40}$  aqueous solution at the anode and  $\text{NaOH}$  at the cathode are formed. The HPA is isolated by crystallization. The alkali obtained can be used to prepare  $\text{Na}_2\text{WO}_4$  from  $\text{WO}_3$  or  $\text{H}_2\text{WO}_4$ . Thus this method is practically wasteless. The yield of HPA based on W is  $\sim 100\%$ . The  $\text{Na}^+$  content in the final product  $\leq 0.01$  wt %. Other HPA, such as  $\text{H}_4\text{SiW}_{12}\text{O}_{40}$ ,  $\text{H}_5\text{PW}_{11}\text{TiO}_{40}$ ,  $\text{H}_5\text{PW}_{11}\text{ZrO}_{40}$ ,  $\text{H}_6\text{PW}_{11}\text{BiO}_{40}$ ,  $\text{H}_5\text{PW}_{11}\text{CeO}_{40}$ ,  $\text{H}_6\text{P}_2\text{W}_{21}\text{O}_{71}$ , etc., can be prepared in a similar manner [28, 29].

Usually, tungstic HPA are the preferred acid catalysts in the series of HPA. This is due to their stronger acidity, higher hydrolytic and thermal stability, and lower oxidation potentials compared to the Mo and V acids [4].

Bulk HPA have a low specific surface ( $1-5 \text{ m}^2\text{g}^{-1}$ ) [4, 30], but it can be increased by loading HPA on a carrier, preferably  $\text{SiO}_2$ . When loading HPA on  $\text{SiO}_2$ , the Keggin structure is retained [21]. According to XRD data [21, 32], crystal HPA phase on  $\text{SiO}_2$  is developed at HPA loading above 20 wt %. Various HPA forms have been observed on the  $\text{SiO}_2$  surface by TEM: discrete molecules, clusters 50 Å in size, and large crystallites of 500 Å [32]. Their relative amounts depend on the HPA loading.

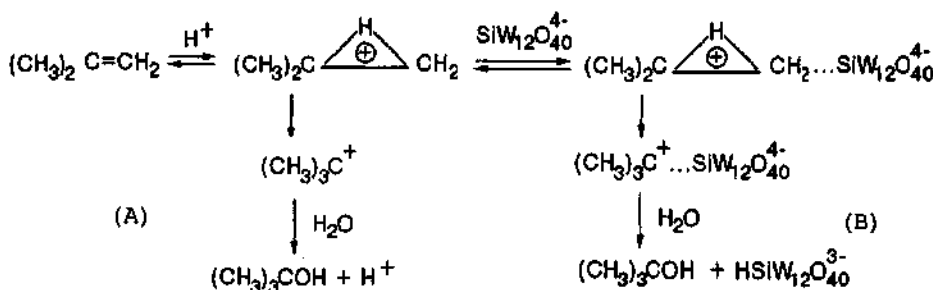
### 3. MECHANISMS OF ACID CATALYSIS BY HPA

#### 3.1. Homogeneous catalysis

In principle, mechanisms of homogeneous catalysis by HPA and by ordinary mineral acids are of the same origin. Reactions catalyzed either by HPA or by mineral acids usually follow the same rules: both show correlations between the catalytic activity and acid strength (the Bronsted rule) in diluted acid solutions [2, 4], and relationships between the rate constants and Hammett acidity function  $H_o$  in concentrated acid solutions [15, 33].

However, there are some peculiarities of the HPA catalysis in solution associated with a high degree of HPA dissociation and a high charge of HPAN in solution as well as with the ability of "soft" HPAN to a specific coordination of organic molecules [6, 7].

Urabe et al. [34], first to study the mechanism of the HPA catalyzed hydration of isobutene, have found that the reaction order with respect to HPA is dependent on [HPA]: ~1 in diluted HPA solution and ~2 in concentrated (~0.5 mol l<sup>-1</sup>) solution. By contrast, the reaction with mineral acids is first order in the catalyst. A two-path mechanism has been suggested:



Path A is a commonly accepted mechanism, including the fast formation of a  $\pi$ -complex between olefin and  $H^+$  followed by its slow conversion to carbenium ion. Path B includes the formation of a complex of HPAN with olefin, in which the olefin is supposedly activated by its coordination to HPAN. It is the path B that is assumed to be responsible for the increasing order with respect to HPA [34].

As found later, the rate constants of isobutene hydration catalyzed by  $H_3PW_{12}O_{40}$  or  $H_4SiW_{12}O_{40}$  obey the equation (in  $H_2O$ , 25°C) [33]:

$$\log k = -1.04H_o - 3.46$$

This equation is also valid for  $H_2SO_4$ ,  $HCl$ ,  $HNO_3$  and  $HClO_4$ . This indicates the reaction to proceed via the commonly accepted mechanism (path A). The increase of the order with respect to HPA with raising [HPA] is assumed to be caused by the salt effect [33].

Salt effects on the rate constant of a reaction between a non-electrolyte and an ionic reactant can be assessed with an empirical Setschenow equation. For a bimolecular reaction:

$$\log k = \log k_0 + (B - B^\#)[H^+],$$

where  $k$  is the second order rate constant at a given  $[H^+]$ ,  $k_0 = k$  at  $[H^+] = 0$ ,  $B$  and  $B'$  are the Setschenow salt effect parameters for the reaction ground and transition states, respectively [33]. This equation is well obeyed for the hydration of isobutene catalyzed by HPA as well as by mineral acids. This supports that the true order with respect to HPA is unity, as with mineral acids, and its rise with  $[HPA]$  increase is caused by the salt effect.

In fact, these two mechanisms of this industrially important reaction appear to be the same and differ only when the medium effect is interpreted. The latter is considered either traditionally by viewing the salt effects on the activity coefficients of the reaction ground and transition states or at molecular level by assuming the formation of weak complexes between HPAN and the substrate. It would be of interest to obtain more evidence in favour of the formation of such complexes.

### 3.2. Heterogeneous catalysis

In heterogeneous as well as in homogeneous systems, HPA are generally more efficient catalysts than conventional ones, such as  $Al_2O_3$ ,  $Al_2O_3-SiO_2$ ,  $HX$  and  $HY$  zeolites, etc., that is in full agreement with relative acid strengths [2, 4, 6]. Note that HPA have purely Bronsted acidity while conventional metal-oxide systems have both Bronsted and Lewis acid sites.

HPA have been found, similarly to other strong solid acids, to be capable of generating carbonium ions from adsorbed arenes and olefins such as styrene, naphthalene, anthracene, etc. under mild conditions. The carbonium ions are likely to be generated in the adsorption of  $\alpha$ -xylene,  $m$ -xylene, pseudocumene, and durene on HPA [35].

In many respects, crystalline HPA behave like solutions, that allows to expect the similarity of mechanisms of homogeneous and heteroheneous reactions catalyzed by HPA. First of all, this is associated with the fact that HPA in solution and in the solid state have the same molecular (Keggin) structure. Also of importance are such properties of solid HPA as high proton conductivity and ability to form crystalline solvates with the molecules of polar substances.

By virtue of the easy absorption of polar molecules, their catalytic reactions can occur not only on the surface but also in the bulk of crystalline HPA. Towards polar substances, solid HPA behave as highly concentrated solutions, i.e. all HPA protons, not only the surface proton sites, participate in the catalytic reaction. This phenomenon, unusual for heterogeneous acid catalysis, is described by the term "pseudoliquid phase" [2, 6]. Unlike polar molecules, non-polar reactants are incapable of being absorbed in the HPA bulk; they interact only with the surface of the catalyst. This is described in detail in Ref. [2, 4, 6,].

## IV. HETEROPOLY ACIDS AND FINE CHEMICAL SYNTHESIS

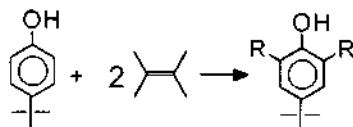
In general, reactions of fine chemical synthesis occur in liquid phase under rather mild conditions. The advantages of HPA over conventional acid catalysts in fine chemical synthesis are as follows [8]:

- a) due to their stronger acidity, HPA have a significantly higher catalytic activity in homogeneous and heterogeneous systems compared to  $H_2SO_4$ ,  $Al_2O_3-SiO_2$ , resinsulfonic acids, etc.;
- b) efficient operating under mild conditions;
- c) in homogeneous systems less alkali is needed to work up the reaction mixture and less wastes is formed thereupon;
- d) the lack of side reactions such as sulfonation, chlorination, etc., which easily proceed with conventional liquid acids.

#### 4.1. Alkylation, dealkylation, and transalkylation of phenols

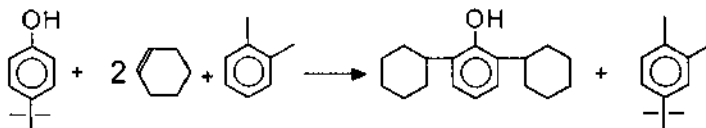
These reactions are widely used for the preparation of antioxidants, thermal and light protectors, bioactive substances, etc.

HPA are highly efficient in the alkylation of benzene and alkylbenzenes with olefins [21, 36, 37]. Phenol is readily alkylated, too, but not selectively [38, 39]. More selective is the alkylation of p-t-butylphenol (TBP). The reaction of TBP with cyclohexene, 1-hexene, styrene, as well as with benzyl chloride in the presence of bulk and  $SiO_2$ -supported  $H_3PW_{12}O_{40}$  or  $H_4SiW_{12}O_{40}$  (1 wt % based on TBP) at 100–150°C gives 2,6-dialkyl-4-t-butylphenols in a 63–90 % yield [38].



Most selective is the reaction with styrene: the yield reaches 90% at a 100% conversion of TBP (100–110°C, 1 h). With α-methylstyrene, the monoalkylation dominates yielding 70% of 2-cumyl-4-t-butylphenol.

HPA catalyzed alkylation of TBP in the presence of o-xylene, which is an acceptor of t-butyl group, allows to prepare 2,6-dialkylphenols in one step; no isolation of intermediate 2,6-dialkyl-4-t-butylphenol is needed. For example, 2,6-dicyclohexylphenol is obtained in a 77% yield [38].

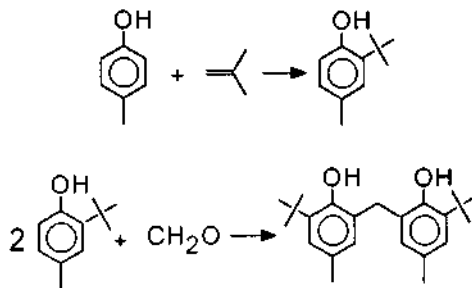


t-Butylxylene formed in this reaction as a side product can be used in the synthesis of pigments. Since HPA are insoluble in the reaction mixture, they are easily separated and can be re-used.

Alkylation of TBP with olefins appears to proceed via a mechanism including the formation of ethers as primary products, followed by their subsequent rearrangement to C-alkylated products. This mechanism is supported by detecting the ethers in the initial stage of the reaction [38].

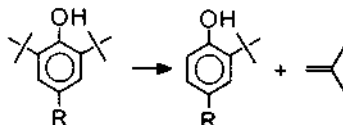
The acid-catalyzed alkylation of p-cresol with isobutene is an industrial process to synthesize phenolic antioxidants. This reaction proceeds easily with HPA as a heterogeneous catalyst. The activity of  $H_3PW_{12}O_{40}$  based on the amount of accessible surface protons is a factor of  $10^4$  higher than that of  $H_2SO_4$  [38].

A commercial alkylation of p-cresol with isobutene with the use of  $H_3PW_{12}O_{40}$  as an alternative to  $H_2SO_4$  has been developed in Russia and applied since 1986. It is the first step in the synthesis of an antioxidant 2,2-methylene-bis-(6-t-butyl-4-methyl-phenol), which is widely used for stabilizing polymers.



The second step, the reaction of 2-t-butyl-4-methylphenol with formaldehyde, is carried out via conventional method, using HCl as a catalyst. The use of HPA provides the gain in selectivity and almost complete elimination of water pollution in the first step of the process.

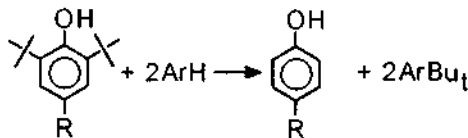
#### Dealkylation of 2,6-di-t-butylphenol derivatives to 2-t-butylphenols



is also widely used for the synthesis of antioxidants. Here  $H_3PW_{12}O_{40}$  and  $H_4SiW_{12}O_{40}$  are efficient homogeneous and heterogeneous catalysts ( $R = H, Me, Et, CH_3CH_2COOMe$ ) [40, 41]. The heterogeneous process proceeds at 130–150°C in the presence of HPA (<1 wt %) in the melted substrate. Mo-HPA are rapidly deactivated due to their reduction by the reaction medium. HPA are tens of times more active than such catalysts as ion-exchange resins,  $Al_2O_3-SiO_2$ , aluminium sulfate, etc. The homogeneous process is even more effective. In AcOH, dealkylation takes place already at 80°C. The catalytic activity of HPA correlates with their acid strength and exceeds by a factor of >100 the activity of  $H_2SO_4$  [41].

Trans-de-alkylation of 2,6-di-tert-butyl-phenols in the presence of HPA has been studied in detail [42, 43]. This reaction is widely used in synthetic organic chemistry as a method providing positional protection in the regioselective functionalization of phenols.

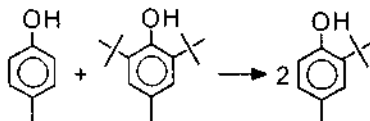
Bulk and  $SiO_2$ -supported tungstic HPA (0.5–7 wt %) are versatile catalysts for the complete trans-de-t-butylation of phenols:



where R = H, Me, Et,  $\text{CH}_3\text{CH}_2\text{COMe}$ ,  $\text{CH}_3\text{CH}_2\text{COOMe}$ ,  $\text{CH}_3\text{CH}_2\text{CH}_2\text{OCOMe}$ ,  $\text{CH}_3\text{CH}_2\text{CH}_2\text{Cl}$ ,  $\text{CH}_3\text{CH}_2\text{CH}_2\text{OCOC}_{17}\text{H}_{35}$  [42]. The reaction occurs at 100–140°C and the mole ratio ArH/phenol of 17–34 with a 92–98% yield. Toluene and o-xylene are the best acceptors of t-butyl group. The catalyst can be easily separated without neutralization and re-used. HPA show a higher activity compared to other acid catalysts. Even Nafion-H, a polymeric perfluororesinsulfonic acid comparable in its strength to 100%  $\text{H}_2\text{SO}_4$ , is appreciably less active than HPA [42, 45].

Trans-de-t-butylation of 2,6-di-t-butylphenols is first order with respect to both phenol and HPA. The rate is dependent on the nature of ArH; the dependence is typical of electrophilic aromatic substitution [43]. With  $\text{SiO}_2$ -supported catalysts the rate depends dramatically on HPA loading. The rate of de-t-butylation of 2,6-di-t-butyl-4-methylphenol over  $\text{H}_3\text{PW}_{12}\text{O}_{40}/\text{SiO}_2$ , based on the total amount of HPA protons in the catalyst, increases with increasing HPA loading, reaching a maximum for 30 wt % HPA/ $\text{SiO}_2$ , then tends to decrease. Assuming a surface-type catalysis, such behaviour can be explained by simultaneous influence of enhancing the strength and reducing the number of the surface proton sites with increasing the loading of HPA. Analogous dependence was recently observed for the vapor-phase dehydration of t-butanol over  $\text{H}_3\text{PW}_{12}\text{O}_{40}$  and  $\text{H}_3\text{PMo}_{12}\text{O}_{40}$  [46]. By contrast, the rate based on the amount of the surface protons of HPA increases monotonically as acid strength increases with HPA loading, showing a fair correlation between the catalytic activity and catalyst acid strength [43].

HPA catalyze efficiently the reaction:

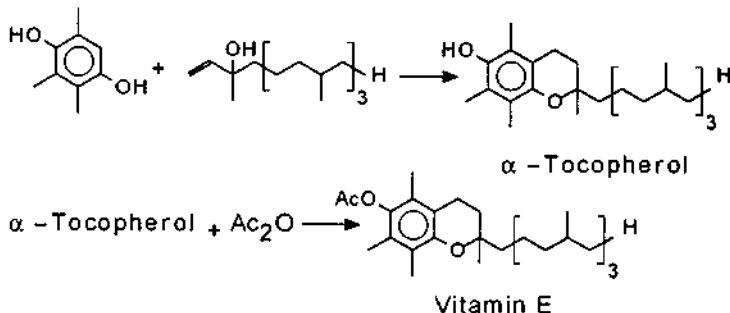


which is also of practical value to produce phenolic antioxidants. Again the catalytic activity of HPA based on the amount of accessible protons is a factor of  $10^4$  higher than that of  $\text{H}_2\text{SO}_4$  [42]. This process has been commercialized in Russia since 1991. It has the same advantages over the  $\text{H}_2\text{SO}_4$  catalyzed conventional process as the above mentioned alkylation of p-cresol with isobutene.

#### 4.2. Condensation

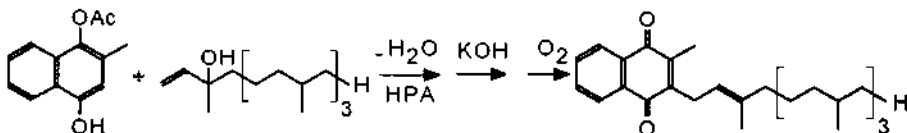
HPA catalyzed condensation of ketones and phenols has long been known [47, 48]. Recently, HPA have been found to catalyze condensations in the synthesis of vitamins E, K<sub>1</sub>, and C [49, 50].

$\text{H}_3\text{PW}_{12}\text{O}_{40}$  and  $\text{H}_4\text{SiW}_{12}\text{O}_{40}$  catalyze the condensation of isophytol with 2,3,5-trimethylhydroquinone (TMHQ), yielding  $\alpha$ -tocopherol, as well as the conversion of  $\alpha$ -tocopherol to  $\alpha$ -tocopherol acetate (vitamin E) [49].

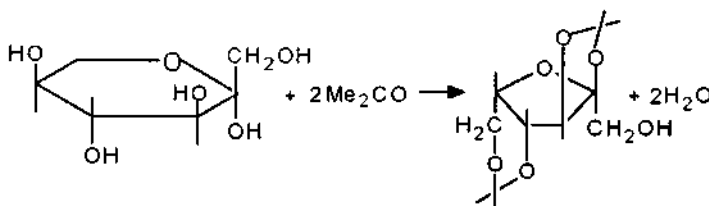


The condensation proceeds in homogeneous (in  $\text{AcOH}$  or  $\text{BuOH}$ ) or heterogeneous (in toluene or  $\text{o-xylene}$ ) systems in the presence of 1 wt % HPA (based on TMHQ). The yield of vitamin E attains 91–92%, its content in the obtained product being 95%. Commercial synthesis of  $\alpha$ -tocopherol is carried out with the use of  $\text{H}_2\text{SO}_4$  or  $\text{ZnCl}_2$  as catalysts [51]. With  $\text{ZnCl}_2$ , a high-quality product containing  $\geq 95\%$  vitamin E is obtained; its yield amounts to 80%. An essential drawback to this process is the high consumption of the catalyst ( $\sim 1$  mole  $\text{ZnCl}_2$  per 1 mole TMHQ) and the large amount of waste products. With  $\text{H}_2\text{SO}_4$ , the product obtained contains 10–20% of admixtures which are difficult to be separated from vitamin E. With HPA, the yield of vitamin E is 10% higher and the quality of the product prepared is not lower than that in the case of  $\text{ZnCl}_2$ . HPA can easily be separated from the reaction mixture and re-used.

HPA are also active in the similar reaction of isophytol condensation with 1-acetoxy-4-hydroxy-2-methylnaphthalene, which is the key step in the synthesis of vitamin K<sub>1</sub> [49]. The reaction gives pure product in a high yield. HPA are  $\sim 50$  times as active as  $\text{ZnCl}_2$  and  $\text{Al}_2\text{O}_3\text{-SiO}_2$ .



Acetonation of L-sorbose, a step in the synthesis of ascorbic acid (vitamine C), proceeds smoothly in acetone solution in the presence of 0.1–0.35 wt %  $\text{H}_3\text{PW}_{12}\text{O}_{40}$  or  $\text{H}_4\text{SiW}_{12}\text{O}_{40}$  as homogeneous catalyst, yielding 85% diacetone-L-sorbose (DAS) [50].

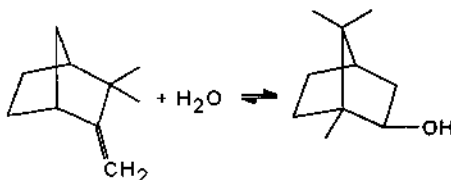


Water formed is absorbed by NaA zeolite or distilled. In industry, this reaction is carried out in the presence of oleum to afford DAS in a 80% yield [51]. Since oleum is both a catalyst and a desiccant, it is added in large excess ( 5% based on acetone). The disadvantage of this method is a large quantity of waste  $\text{Na}_2\text{SO}_4$  obtained after oleum neutralization. Thus the application of HPA in this reaction can increase the yield of DAS and eliminate waste products.

#### 4.3. Hydration and dehydration

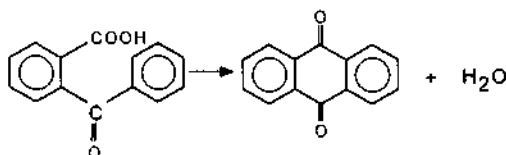
HPA catalyzed hydration of  $\text{C}_2\text{-C}_4$  olefins has been studied both in liquid phase and vapor phase [4]. As mentioned, hydration of propene and butenes is used in industry to produce the corresponding alcohols [7].

$\text{H}_3\text{PW}_{12}\text{O}_{40}$  and  $\text{H}_4\text{SiW}_{12}\text{O}_{40}$  are excellent catalysts for the homogeneous hydration of camphene to isoborneol ( $50^\circ\text{C}$ ,  $0.05 \text{ mol l}^{-1}$  HPA in  $\text{Me}_2\text{CO}-\text{H}_2\text{O}$ ) [52].



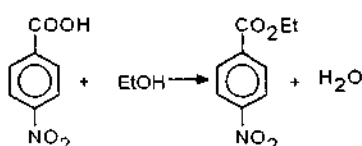
Isoborneol is formed almost exclusively. The conversion of camphene is up to 35%. Under comparable conditions, the reaction rate with  $\text{H}_2\text{SO}_4$  is far lower and the conversion of camphene does not exceed 3%. The stronger acid,  $\text{H}_3\text{PW}_{12}\text{O}_{40}$  has a slightly higher activity than  $\text{H}_4\text{SiW}_{12}\text{O}_{40}$ . Isoborneol is used as an intermediate in the synthesis of camphor. The direct one-step hydration of camphene to isoborneol is of practical interest because the current procedure is a two-step process via an intermediate product, bornyl acetate.

$\text{H}_3\text{PW}_{12}\text{O}_{40}$  can be used instead of sulfuric acid as a catalyst of dehydration of o-benzoylebenzoic acid to anthraquinone (53).



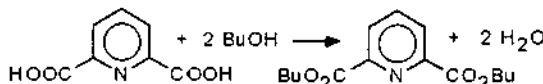
#### 4.4. Esterification and etherification

Ethyl p-nitrobenzoate (ENB), an intermediate product in the synthesis of anesthetics, is obtained in > 99% yield by esterification of p-nitrobenzoic acid (NBA) with ethanol in the presence of  $\text{H}_3\text{PW}_{12}\text{O}_{40}$  (3-7 wt %) at  $75^\circ\text{C}$  [54].



Water formed in the reaction course is separated by azeotroping with toluene. Being initially homogeneous, the reaction mixture turns to a two-phase system in the end of the reaction. The upper phase contains ENB, toluene, and ethanol. The lower phase is a concentrated solution of HPA in ethanol. So the catalyst is easily separated and can be re-used. In conventional process, when sulfuric acid is the catalyst, the yield of ENB is ca. 95%, large amount of waste products being formed.

Esterification of dipicolinic acid (DA) with butanol is a step of the synthesis of pharmaceuticals.



This is an example of organonitrogen compound conversion catalyzed by HPA [55]. Usually, HPA, being easily deactivated by N-bases, e.g. amines or pyridines, have failed to catalyze such reactions. But DA can be subjected to HPA catalysis, since its N-basisity is substantially reduced by two neighbouring carboxyl groups.

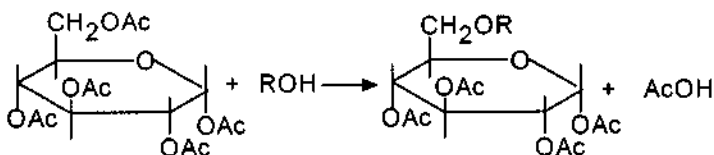
$\text{H}_3\text{PW}_{12}\text{O}_{40}$  (1 wt %) as a homogeneous catalyst is almost as efficient as sulfuric acid (per unit catalyst weight), yielding 100% of DA dibutyl ester ( $118^\circ$ , 3 h).  $\text{CePW}_{12}\text{O}_{40}$ , insoluble in butanol, has been found to be fairly active as a heterogeneous catalyst to give a 100% yield of diester (5.4 wt %,  $118^\circ$ , 4 h). Although less active than homogeneous  $\text{H}_3\text{PW}_{12}\text{O}_{40}$ , it can be easily separated and re-used. So far, only  $\text{Cs}_{2.5}\text{H}_{0.5}\text{PW}_{12}\text{O}_{40}$  (water-insoluble) has been used as heterogeneous acid catalyst for liquid-phase reactions [56]. It is noteworthy that  $\text{CePW}_{12}\text{O}_{40}$  is far more active than  $\text{Cs}_{2.5}\text{H}_{0.5}\text{PW}_{12}\text{O}_{40}$  in DA esterification. The mechanism of  $\text{CePW}_{12}\text{O}_{40}$  catalysis is as yet unknown. In this case both Bronsted and Lewis acid sites may be important.

HPA, both bulk and supported on  $\text{SiO}_2$ ,  $\text{Al}_2\text{O}_3$  or  $\text{TiO}_2$ , catalyze the preparation of hydroquinone (HQ) monoethers, which are used in the synthesis of medicines, perfumes, stabilizers, inhibitors, etc.

For example, the reaction with 1-hexanol in the presence of  $\text{H}_3\text{PMo}_{12}\text{O}_{40}$  (3%) gives monoether with a 99% selectivity and 83% HQ conversion ( $105^\circ\text{C}$ , 5 h) [57].

Dialkyl phthalates widely used as plasticizers are obtained by esterification of phthalic anhydride with  $\text{C}_8\text{-C}_{10}$  alcohols at  $100\text{-}120^\circ\text{C}$  in the presence of  $\text{H}_3\text{PW}_{12}\text{O}_{40}$  (1-2%) as homogeneous or heterogeneous catalyst [58]. In the latter case activated charcoal is used as a carrier. The catalytic activity of HPA is significantly higher than that of  $\text{H}_2\text{SO}_4$  and p-toluenesulfonic acid. HPA/C is less active than the homogeneous catalyst, but it can be easily separated from reaction mixture.

Synthesis of glycosides catalyzed by HPA is of industrial importance [7]. Many patents cover this reaction. Thus monosaccharides interact readily with alcohols in the presence of HPA ( $85^\circ\text{C}$ , 4h) yielding 47-83% of glycosides. For example, octyl tetraacetyl glycoside is obtained from glucose pentaacetate and 1-octanol with  $\text{H}_3\text{Mo}_{12}\text{O}_{40}$  (3%) in a 70% yield [59]. Glycosides are used in the production of medicines.



Esterification and acetalization of steroids (e.g. testosterone, 17 $\alpha$ -hydroxyprogesterone, etc.) catalyzed by  $H_3PW_{12}O_{40}$  or 25%  $H_3PW_{12}O_{40}/SiO_2$  (1.5-9%) occur with a quantitative yield at 40-82°C [60]. HPA show almost the same activity as  $HClO_4$ . These reactions are used for preparation of modified hormones.

## 5. CONCLUSION

The selected examples reviewed here show that the application of HPA as catalysts in a wide variety of processes of fine chemical synthesis is promising. In many cases HPA provide the gain in activity and/or selectivity as compared to conventional catalysts. Some of this reactions have already been brought to practice, e.g. alkylation and transalkylation of phenols and preparation of glycosides. In the future the number of such processes will undoubtedly increase.

## REFERENCES

1. M.Misono, K.Sakata, Y.Yoneda and W.Y.Lee, VII Int. Congress on Catalysis. Preprints. Tokyo, 1980, B. 27.
2. Y.Ono, Perspectives in Catalysis/Ed. J.M.Thomas and K.I.Zamaraev, Oxford: Backwell Scientific Publication, 1992, 431.
3. I.V.Kozhevnikov and K.I.Matveev, Usp. Khim., 1982, 52, 1433.
4. I.V.Kozhevnikov, Ibid., 1987, 56, 1417.
5. J.B.Moffat, Rev. Chem. Intermediates., 1987, 8, 1
6. M.Misono, Catal. Rev. Sci. Eng., 1987, 29, 269
7. M.Misono and N.Nojiri, Applied Catal., 1990, 64, 1
8. I.V.Kozhevnikov, Usp. Khim., 1993, 62, 510
9. M.T.Pope, Heteropoly and Isopoly Oxometalates. Berlin: Springer - Verlag, 1983
10. Y.Izumi, K.Matsuo and K.Urabe, J. Mol. Catal., 1983, 18, 299
11. W.G.Klemperer and W.Shum, J. Amer. Chem. Soc., 1977, 99, 3544
12. G.M.Brown, M.R.Noe-Spirlet, W.R.Busing and H.A.Levy, Acta Crystallogr., 1977, 33, 1038
13. A.A.Ivakin, L.D.Kurbatova and L.A.Kapustina, Zhur. Neorg. Khim., 1978, 23, 2545
14. S.M.Kulikov and I.V.Kozhevnikov, Izv. Akad. Nauk. SSSR, Ser. Khim., 1981, 498
15. I.V.Kozhevnikov, S.T.Khankhasaeva and S.M.Kulikov, Kinetika i Kataliz, 1988, 29, 76
16. M.Misono, N.Mizuno, K.Katamura, A.Kasai, Y.Konishi, K.Sakata, T.Okuhara and Y.Yoneda, Bull. Chem. Soc. Japan, 1982, 55, 400

17. A.K.Ghosh and J.B.Moffat, *J. Catal.*, **1986**, *101*, 238
18. T.Utada, N.Sugiura, R.Nakamura and H.Niiyama, *J. Chem. Eng. Japan*, **1991**, *24*, 417
19. V.F.Chuvaev, A.B.Yaroslavtsev, E.M.Yaroslavtseva and E.S.Oniani, *Zhur. Neorg. Khim.*, **1991**, *36*, 2101
20. G.B.McGarvey and J.B.Moffat, *J. Catal.*, **1991**, *128*, 69
21. Y.Izumi, R.Hasebe and K.Urabe, *J. Catal.*, **1983**, *84*, 402
22. E.A.Paukshtis, O.I.Goncharova, T.M.Yurieva and E.N.Yurchenko, *Kinetika i Kataliz*, **1986**, *27*, 463
23. V.F.Chuvaev, K.I.Popov and V.I.Spitsyn, *Dokl. Akad. Nauk SSSR*, **1980**, *255*, 892
24. Y.Kanda, K.Y.Lee, S.Nakata, S.Asaka and M.Misono, *Chem. Letters*, **1988**, 139
25. V.M.Mastikhin, S.M.Kulikov, A.V.Nosov, I.V.Kozhevnikov, I.L.Mudrakovskiy and M.N.Timofeeva, *J. Mol. Catal.*, **1990**, *60*, 65
26. B.Wiswanathan, M.J.Omana and T.K.Varadarajan *Chem. Letters*, **1989**, *3*, 217
27. G.I.Kapustin, T.R.Brueva, A.L.Klyachko, M.N.Timofeeva, S.M.Kulikov and I.V.Kozhevnikov, *Kinetika i Kataliz*, **1990**, *31*, 1017
28. O.M.Kulikova, R.I.Maksimovskaya, S.M.Kulikov and I.V.Kozhevnikov, *Izv. Akad. Nauk SSSR, Ser. Khim.*, **1990**, 1944; **1991**, 1726; **1992**, 494
29. G.M.Maksimov, R.I.Maksimovskaya and I.V.Kozhevnikov, *Zhur. Neorg. Khim.*, **1992**, *37*, 2279
30. T.Okuhara, A.Kasai, N.Hayakawa, Y.Yoneda and M.Misono, *J. Catal.*, **1983**, *83*, 121
31. S.Tatematsu, T.Hibi, T.Okuhara and M.Misono, *Chem. Letters*, **1984**, 865
32. S.M.Kulikov, M.N.Timofeeva, I.V.Kozhevnikov, V.I.Zaikovsky, L.M.Plyasova and I.A.Ovsyanikova, *Izv. Akad. Nauk SSSR, Ser. Khim.*, **1989**, 763
33. I.V.Kozhevnikov, S.T.Khankhasaeva and S.M.Kulikov, *Kinetika i Kataliz*, **1989**, *30*, 50
34. K.Urabe, K.Futsita and Y.Izumi, *Shokubai*, **1980**, *22*, 223
35. M.N.Timofeeva, A.V.Demidov, A.A.Davydov and I.V.Kozhevnikov, *J. Mol. Catal.*, **1993**, *79*, 21
36. T.Okuhara, T.Nishimura, H.Watanabe and M.Misono, *J. Mol.Catal.*, **1992**, *74*, 247
37. Y.Izumi, N.Natsume, H.Takamine, I.Tamaoki and K.Urabe, *Bull. Chem. Soc. Japan*, **1989**, *62*, 2159
38. I.V.Kozhevnikov, A.I.Tsyganok, M.N.Timofeeva, S.M.Kulikov and V.N.Sidelnikov, *React. Kinet. Catal. Letters*, **1992**, *46*, 17
39. T.Nishimura, H.Watanabe, T.Okuhara and M.Misono, *Shokubai*, **1991**, *33*, 420
40. S.M.Kulikov, I.V.Kozhevnikov, M.N.Fomina and A.P.Krysin, *Kinetika i Kataliz*, **1986**, *27*, 750
41. S.M.Kulikov, I.V.Kozhevnikov, M.N.Fomina and A.P.Krysin, *Izv. Akad. Nauk SSSR, Ser. Khim.*, **1987**, 752
42. I.V.Kozhevnikov, S.M.Kulikov, M.N.Timofeeva, A.P.Krysin and T.F.Titova, *React. Kinet. Catal. Letters*, **1991**, *45*, 257
43. I.V.Kozhevnikov and M.N.Timofeeva, *J. Mol. Catal.*, **1992**, *75*, 179

44. G.Olah, G.K.S.Prakash and J.Sommer, Superacids. New York: Wiley, Interscience, 1985
45. G.Olah, G.K.S.Prakash, P.S.Iyer, M.Tashiro and T.Yamato, J. Org. Chem., 1987, 52, 1881
46. R.Ohtsuka, Y.Morioka and J.Kobayashi, Bull. Chem. Soc. Japan, 1989, 62, 3195
47. S.T.Khankhasaeva, S.M.Kulikov and I.V.Kozhevnikov, Kinetika i Kataliz, 1990, 31, 216
48. S.Yamamatsu, Y.Ishibashi and Y.Susuki, Pat. Japan 2-454397; C. A. 1990, 113, 24665
49. I.V.Kozhevnikov, S.M.Kulikov, N.G.Chukaeva, A.T.Kirisanov, A.B.Letunova and V.I.Blinova, React. Kinet. Catal. Letters, 1992, 47, 59
50. I.V.Kozhevnikov, I.B.Vasilieva and V.V.Zarutsky, Ibid., 83
51. L.O.Shnaidman, Proizvodstvo vitaminov, Moscow: Pischevaya Promyshlennost, 1973
52. M.A.Schwegler and H. van Bekkum, Bull. Soc. Chim. Belg., 1990, 99, 113
53. W.C.Hsin, C.C.Lai, M.H.Chou, Y.T.Chen and C.T.Su, Shih Yu (Taipei), 1988, 24, 193; C. A. 1990, 113, 134556
54. S.M.Kulikov, S.T.Khankhasaeva and I.V.Kozhevnikov, II Vsesoyuzn. Konf. "Kataliz i Kataliticheskie Protsesy Khimfarmproizvodstv", Part I, Moscow, 1989, 119
55. M.N.Timofeeva and I.V.Kozhevnikov, To be published
56. T.Okuhara, T.Nishimura, H.Watanabe and M.Misono, J. Mol. Catal., 1992, 74, 247
57. K.Taniguti, Pat. Japan 60-215643
58. M.A.Schwegler, H. van Bekkum and N.A. de Munk, Applied Catal., 1991, 74, 191
59. R.Kiromura, S.Kitazawa, Y.Takata and T.Sakakibara, Pat. USA 4,874,852
60. M.N.Timofeeva, V.S.Grosheva, B.I.Demchenko and I.V.Kozhevnikov React. Kinet. Catal. Letters., 1991, 45, 215

## 1.4 Methanol-Based Synthetic Reactions over Solid-Base Catalysts

W. UEDA<sup>a</sup>, H. Ohowa<sup>a</sup>, K. Iwasaki<sup>a</sup>, T. Kuwabara<sup>b</sup>, T. Ohshida<sup>b</sup>, and Y. Morikawa<sup>b</sup>

<sup>a</sup>Department of Environmental Chemistry and Engineering, Tokyo Institute of Technology, Yokohama 227, Japan

<sup>b</sup>Research Laboratories of Resources Utilization, Tokyo Institute of Technology, Yokohama 227, Japan

### Abstract

Novel methods for catalytically synthesizing  $\alpha,\beta$ -unsaturated compounds and higher alcohols were developed, where methanol was used as a key reagent for C-C bond formation. Reactants were saturated ketones, esters, nitriles, or alcohols besides methanol, and  $\text{CH}_2=$  or  $\text{CH}_3-$  group is introduced into their methyl or methylene carbons by the addition of methanol. For the catalytic synthesis of  $\alpha,\beta$ -unsaturated compounds, magnesium oxide activated by manganese ion or chromium ion has been found to give the most effective catalytic performance. The most promising application of this synthetic method is demonstrated by the selective synthesis of acrylonitrile from acetonitrile and methanol over Mn-MgO catalyst. The selectivity to acrylonitrile was more than 95% and no deactivation of the catalyst was observed. The method was also applied to the conversion of acetone to methyl vinyl ketone and methyl propionate to methyl methacrylate. Condensations of various primary alcohols( $\text{C}_2\text{-C}_5$ ) with methanol were carried out at atmospheric pressure over various metal oxides having a solid-base property. The reactions gave one or two carbon higher alcohol than the reacted primary alcohol. MgO catalyst was most active for the reaction and yielded the alcohol products in high selectivity(>80%). Based on the kinetic measurements, reaction mechanisms for both reactions are discussed.

### 1. INTRODUCTION

Methanol has become one of the major raw chemicals produced presently in chemical industries, ranking third in volume behind ammonia and ethylene. World production of methanol is currently about 20 million tons per year. More production of methanol is now expected since it is assumed that methanol will be utilized more in the future not only as chemical raw material but also as an energy carrier for the various types of engines and for fuel cell[1]. Recently, the utilization of methanol for MTBE is increasing, currently above 23 % of the total production of methanol.

Developments of the methods of transforming methanol to industrial chemicals have a long history over several decades[2~4]. The development has progressed markedly since methanol was manufactured via the hydrogenation of carbon monoxide over solid catalysts at elevated temperature and pressure. The stimulated industrial and research trend to utilize methanol for chemicals synthesis resulted in many new process developments. Some of methanol-based processes have been industrialized instead of traditional synthetic routes based on olefins. Some of others seem to be technologically ready for commercialization[5].

The object of this paper is to deal with solid base-catalyzed synthetic reactions of  $\alpha,\beta$ -unsaturated compounds[6] and higher alcohols with methanol[7], which are very important and basic among the

various methanol-based synthetic reactions. On the basis of the results of catalytic performance tests and kinetic measurements, both methanol-based synthetic reactions over magnesium oxide catalyst having solid-base are compared in terms of reaction mechanism.

## 2. EXPERIMENTAL METHODS

### 2.1 Catalyst Preparation

The metal ion-containing catalysts(3 wt%) was prepared by the following impregnation method. Commercial MgO(Soekawa Rika, 99.92%, surface area 11 m<sup>2</sup>.g<sup>-1</sup>) is impregnated with an aqueous solution of the corresponding metal nitrate with stirring for 12 hrs at an ambient temperature. Water is then evaporated by heating, followed by drying in air at 110°C for 24 hrs. Heat treatment in a nitrogen stream at about 600°C is necessary in order to decompose the impregnated metal nitrate and to desorb water and CO<sub>2</sub>. Unless otherwise noted, the prepared MgO was used.

### 2.2 Catalytic Reaction

The reactions to produce α,β-unsaturated compounds were carried out at atmospheric pressure using a continuous flow reaction system with a quartz fixed-bed reactor. The reaction was run at 623 K with 1.3 kPa of substrate in N<sub>2</sub> carrier. The molar ratio of methanol/substrate was 10 in all cases and the space velocity (methanol + substrate + N<sub>2</sub>) was 80 ml.min<sup>-1</sup>.g-cat<sup>-1</sup>. The reactions of primary alcohols(C<sub>n</sub>H<sub>2n+1</sub>OH, n=2-5) with methanol were also carried out at atmospheric pressure using the same continuous flow reaction system with a quartz fixed-bed reactor. The following standard reaction conditions were used; feed gas composition, N<sub>2</sub>: methanol : C<sub>n</sub>H<sub>2n+1</sub>OH = 10 : 3 : 0.15, total flow rate, 66 ml.min<sup>-1</sup>, catalyst weight, 1 g, and reaction temperature range, 573~673 K.

## 3. RESULTS AND DISCUSSION

### 3.1 Synthesis of α, β-Unsaturated Compounds

α,β-Unsaturated compounds are very important chemicals in the chemical industries, in particular for polymers. The production of these compounds has been accomplished through the catalytic processes based on olefins. For example, acrylonitrile is manufactured by ammonoxidation of propene over multicomponent bismuth molybdate catalysts[8]. In recent years, however, other synthetic methods based on the utilization of C<sub>1</sub> chemicals such as CO, methanol, and methane instead of olefins have been developed markedly.

An interesting example is the acrylonitrile synthesis by the oxidative methylenation of acetonitrile with methane over metal oxide catalysts[9]. Since acetonitrile can be synthesized from CO, H<sub>2</sub>, and NH<sub>3</sub> catalytically[10], the process may provide a promising route for acrylonitrile synthesis from C<sub>1</sub> chemicals only. Many similar approaches have recently been undertaken extensively[11]. Other examples are the classical processes where base- or acid-catalyzed condensation reactions with formaldehyde are utilized[12]. The well-known examples are the condensation of acetaldehyde, where acrolein can be normally obtained because the initially formed aldol condensation product undergoes dehydration simultaneously over the catalysts. In principle, this reaction can be used for the synthesis of other unsaturated compounds. Alternatively, it is possible to carry out this type of reaction with *in situ* generation of formaldehyde from methanol by oxidative dehydrogenation[13,14].

We have recently developed the reaction for the synthesis of various α,β-unsaturated compounds using methanol as a reagent for C=C bond formation over solid-base catalysts promoted by transition metal ions[5,6,15~20]. General reaction scheme is described in Figure 1. This process is a base-catalyzed reaction, where methyl or methylene group activated by inductive electron withdrawal by the unsaturated substituent such as carbonyl, cyano or phenyl group, is converted into vinyl group by the addition of methanol.

The most promising application of this method is demonstrated by the selective formation of acrylonitrile from acetonitrile and methanol[16]. The conversion of acetonitrile proceeds catalytically at an elevated temperature(>300°C) and yields acrylonitrile(AN) selectively through dehydrogenation,

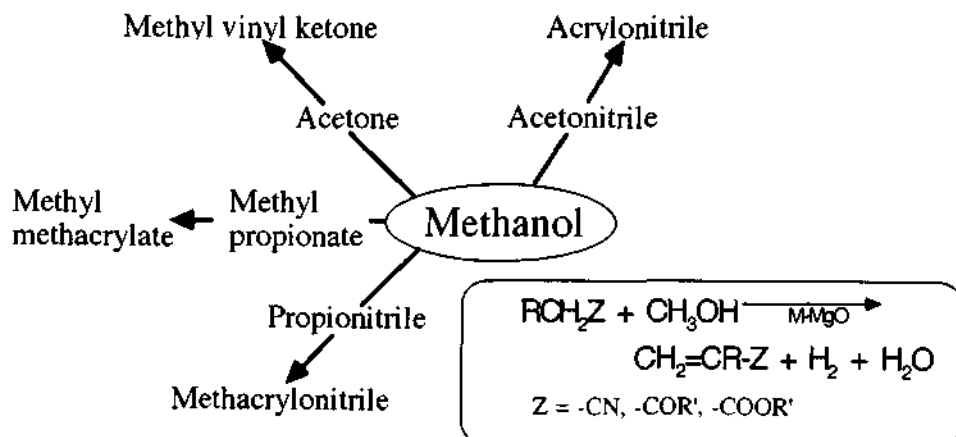
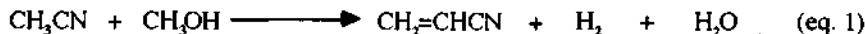


Figure 1 Catalytic syntheses of  $\alpha,\beta$ -unsaturated compounds with methanol over solid-base.

cross-condensation, and dehydration(eq. 1).



Catalysts are based on metal oxides which are well-known as solid-base materials, such as MgO, CaO, La<sub>2</sub>O<sub>3</sub>, and so forth. These metal oxides themselves are, however, virtually inactive for this reaction, so that the catalytic properties of these basic oxides must be improved by the addition of small amounts of transition metal cations. Table I shows examples for the magnesium-based oxide catalysts. Obviously, a synergism or bifunctional feature of the promoted M-MgO catalysts, depending on the kind of added element, is significant for the catalytic activity and selectivity for the reaction. The addition of manganese, chromium, or iron has a pronounced effect on the course of the reaction; overall catalytic activity based on acetonitrile conversion increased by a factor of 100. The reaction is really selective and by-products are small amounts of propionitrile(PN) and methacrylonitrile(MAN) which are formed by the consecutive reactions of the main product, AN. At the present best conditions, one pass conversion of acetonitrile reaches more than 30% keeping the higher selectivity(>90%) to AN over these catalysts. Stability of these catalysts is extremely good. A prolonged reaction, however, revealed that the activity decreased very slowly but in an appreciable level. Selectivity was almost unchanged during the slow decay of the activity. Slow coke formation

Table 1 Synthesis of  $\alpha,\beta$ -unsaturated nitriles over metal ion-containing MgO catalysts at 623K

Catalyst M <sup>n+</sup> -MgO	$\text{CH}_3\text{CN}$ Conv.(%) <sup>1)</sup>	Selectivity (%)			$\text{CH}_3\text{CH}_2\text{CN}$ Conv.(%) <sup>2)</sup>	Selectivity (%)		
		AN	PN	MAN		MAN	IBN	CTN
MgO	0.1	tr	tr	-	0.9	65.9	20.9	13.2
Fe <sup>3+</sup> -MgO	11.2	73.2	11.6	tr	5.0	94.6	4.6	0.8
Cr <sup>3+</sup> -MgO	9.6	94.2	5.4	tr	11.0	88.6	6.8	2.3
Mn <sup>2+</sup> -MgO	9.1	96.4	2.7	0.9	11.4	97.1	2.2	0.7
Ni <sup>2+</sup> -MgO	5.5	2.8	33.5	tr	-	-	-	-
Cu <sup>2+</sup> -MgO	2.2	91.0	9.0	-	2.3	87.5	9.4	3.1

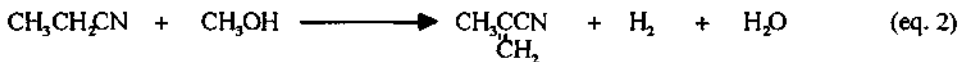
1) W/F = 38 g.hr.mol<sup>-1</sup>, 2) W/F = 145 g.hr.mol<sup>-1</sup>.

on the surface, in particular on the surface basic site, seems to be responsible for the slow deactivation because the catalyst was slightly darken. Almost the same activity as of the fresh catalyst can be recovered by calcination of the used catalyst in an air stream at an elevated temperature, followed by the activation process of the catalyst.

Looking at the other promoted catalysts, less active catalysts were obtained by the addition of nickel or copper because of remarkable decay of activity in a short reaction time. Characteristically, magnesium oxide containing nickel was extremely inactive for the formation of AN but gave propionitrile in relatively higher yield than the others. Some of the produced AN oligomerized over nickel site to form higher molecular weight compound. It seems that the added nickel ion on the surface of magnesium oxide can catalyze hydrogenation of AN to propionitrile much effectively. The addition of aluminium did not result in appreciable effects on both activity and selectivity.

Effect of metal ion content in magnesium oxide on the catalytic property is significant. The formation of AN increases with the Cr content and then decreases after passing through a maximum at 3 wt%. Excess addition causes a decrease in activity and induces the decomposition of methanol and ultimately pure metal oxide used for dopant predominantly catalyzes the decomposition of methanol, so that about 3wt% loading of metal ion is preferable for attaining effective catalytic property for the over-all reaction. The selectivity to AN on the basis of acetonitrile conversion was scarcely affected by the content of metal ion. This activity change is not attributed to surface area change because every catalysts have nearly the same surface area(ca. 100m<sup>2</sup>.g<sup>-1</sup>). Therefore, the drastic increase in activity implies that the reaction needs both functions of added metal ion and surface base site. The activity decreases by the excess addition is thought likely due to the decrease of the surface base site.

The above nitrile synthetic process can be applied for the methacrylonitrile synthesis from propionitrile(eq. 2).

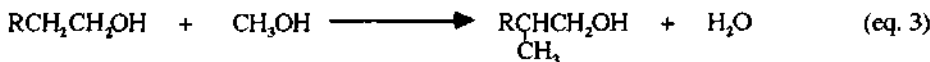


Almost the same trend in catalytic performance is observed for MAN synthesis as that for AN synthesis(Table 1). Hence the improved catalytic property of magnesium oxide is obtainable by the specific promotion effect of Mn, Cr, and Fe ions. By using these three catalysts, 95% selectivity to MAN is achieved at about 30% conversion of propionitrile under the optimized conditions. By-products are isobutyronitrile(IBN) and crotononitrile(CTN).

### 3.2 Condensation of Alcohol to Form Higher Alcohols

Numerous attempts have been made in the past to develop synthetic methods for higher alcohols, particularly from C<sub>1</sub> chemicals such as CO and methanol, and many processes have already been established.[21] One of the important industrial processes is the so-called oxo reaction or hydroformylation of alkenes where CO is a key reactant. Other reported methods include homologation of lower alcohols to higher ones using carbon monoxide and hydrogen,[22] and metal- or metal oxide-catalyzed direct synthesis of alcohols from syn gas.[23] In addition, Guerbet reaction, where a primary or secondary alcohol reacts with itself or another alcohol to produce a higher alcohol, is also an important reaction as higher alcohol synthesis. This reaction has been much developed and various types of heterogeneous catalyst have been reported in patents.[24~26]

In an extension of our studies on catalysis by solid-base catalysts,[5] we recently developed a new catalytic reaction process for producing higher alcohols using methanol as a main building block(eq. 3). In this reaction, methanol is condensed with other primary or secondary alcohol



[R = H, Alkyl]

having a methyl or methylene group at the  $\alpha$ -position over metal oxide catalyst having a solid-base property, and then higher alcohols are formed in high selectivities.

### 3.2.1 Catalytic performance of MgO and metal ion-containing MgO catalysts

Table 2 lists the catalytic performance of MgO, CaO, ZnO, and ZrO<sub>2</sub> in the condensation reaction of ethanol with methanol at 633 K. MgO, a well known solid-base, showed the best catalytic performance in the reactions, yielding higher alcohols selectively in every case. When ethanol was allowed to react with methanol over MgO catalyst, ethanol was readily converted into 1-propanol and 2-methyl propanol. Total selectivity to both products was about 80%. Minor products were C<sub>2</sub>-, C<sub>3</sub>- and C<sub>4</sub>-saturated carbonyl compounds and thereby small amount of hydrogen was also formed. Very small amounts of methane and CO were also formed, indicating a few side reactions of methanol took place under the conditions. However, the extents of such reactions were low and thus the excess methanol was most recovered. Other solid-base metal oxide, CaO, was surprisingly inactive. ZnO catalyst was active for the conversion of ethanol but non-selective, mainly catalyzing the dehydrogenation of alcohols to aldehydes. ZrO<sub>2</sub> catalyst showed acidic character in the present reaction conditions, promoting the formation of various ethers from alcohols. As a result, MgO catalyst was found uniquely active for the condensation of alcohol to produce higher alcohols.

The addition effect of metal ions in the MgO catalyst was tested in similar to the catalytic syntheses of  $\alpha,\beta$ -unsaturated compounds with methanol and the results are shown in Table 3. Unfortunately, the addition effect was negative in all cases; the MgO catalysts containing metal ion were either less active or less selective. The manganese-containing MgO catalyst, which was most active in the synthesis of  $\alpha,\beta$ -unsaturated compounds with methanol, was poorly selective for the

Table 2 Condensation of ethanol with methanol over various metal oxide catalysts at 633 K

Catalyst	Surface area (m <sup>2</sup> .g <sup>-1</sup> )	Conversion of ethanol (%)	Selectivity(%)				
			1-Propanol	2-Methyl propanol	1-Butanol	Acet- aldehyde	2-Methyl propanal
MgO	137	29.6	50.7	27.6	0.7	12.4	1.9
CaO	65	0.8	34.6	0	0	65.4	0
ZnO	-	74.5	tr	tr	0	84.5	0.5
ZrO <sub>2</sub> <sup>1)</sup>	-	66.9	0	0	0	0	0

1) Main products were dimethyl ether and methyl ethyl ether.

Table 3 Condensation of ethanol with methanol over various metal ion-doped MgO catalysts(633 K)

Catalyst M-MgO (3wt%)	Surface area (m <sup>2</sup> .g <sup>-1</sup> )	Conversion of ethanol (%)	Selectivity(%)				
			1-Propanol	2-Methyl propanol	1-Butanol	Acet- aldehyde	2-Methyl propanal
MgO	137	29.6	50.7	27.6	0.7	12.4	1.9
Mn	168	32.9	24.3	9.9	tr	31.9	3.7
Cr	105	35.1	16.0	7.3	tr	36.4	5.2
Al	106	24.6 <sup>1)</sup>	4.6	0	0	4.6	0
Na	-	0.8	33.3	0	0	66.7	0
Cs	-	0	0	0	0	0	0

1) Various ethers were formed.

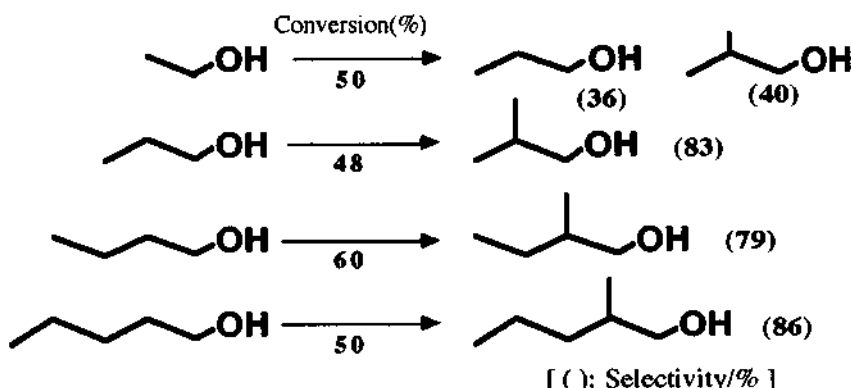


Figure 2 Condensation of various alcohols with methanol over MgO catalyst at 653 K.

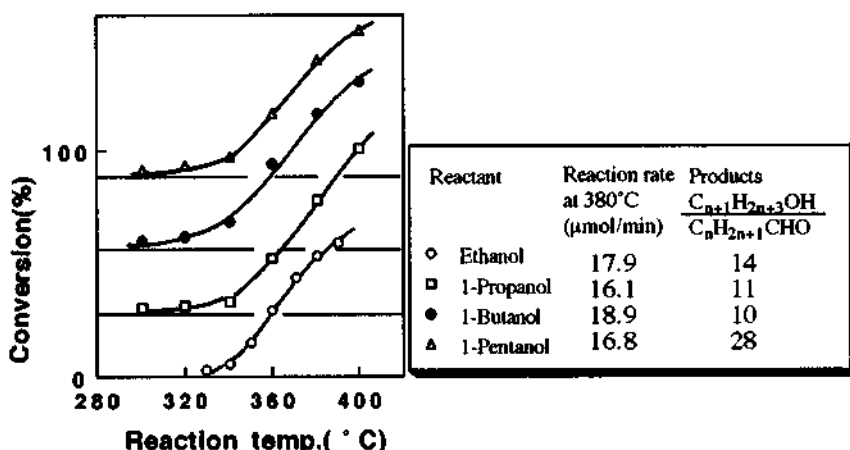


Figure 3 Comparison of the condensation rates of various alcohols with methanol over MgO.

formation of saturated alcohols like 1-propanol and 2-methyl propanol, mainly catalyzing the formation of unsaturated compounds like acrolein, allyl alcohol, and aldehydes in accordance to its catalytic performance in the reaction of nitriles with methanol, although the catalyst showed a slightly improved activity for the methanol conversion in the reaction of ethanol and methanol. More characteristically, the addition of sodium cation into MgO catalyst resulted in the complete disappearance of the activity, although the sodium ion-containing catalyst would be stronger base than original MgO catalyst. By taking account that the CaO catalyst is also completely inactive for the reaction, it seems that catalysts having much stronger basicity are not suitable for the reaction.

Figures 2 and 3 summarize the results of the condensation reaction of various alcohols with methanol over MgO catalyst at the temperature range of 573~673 K. When the other primary alcohol was allowed to react with methanol, the reaction features were almost the same as described above for the ethanol conversion; that is, the reactions readily took place and formed the 2-methyl form of

the higher alcohol mainly with small amount of aldehydes produced by the dehydrogenation of the reactant and product alcohols. The only difference between the ethanol reaction and the other reaction is two alcohol products in the ethanol reaction but one higher alcohol product in the other. This is because the propanol produced in the ethanol conversion can subsequently react with methanol to form 2-methyl propanol.

Two points emerge from the figures. First, the conversions obtained in each reaction under the standard conditions were essentially the same (50-60%) and the temperature dependency of each reaction was also similar as shown in Figure 3. This strongly implies the rate independency of the reactant. Secondly, the product selectivity is little influenced by the reactant; the alcohol selectivity is around 80% in every case and the high molar ratio of alcohol to corresponding aldehyde is also similar in every reaction.

### 3.2.2 Catalytic performance of MgO catalysts containing oxo anion

As the MgO catalyst was found most active for the condensation reactions of alcohols with methanol, we have tested the catalytic performance of MgO prepared by various methods. The MgO catalyst designated by MgO-(OH) was prepared by the method described in the experimental section. The MgO catalyst designated by MgO-(FD) was prepared by freeze-dry method. In this method a slurry in a boiling water was freeze-dried instead of the evaporation of water and drying at 383 K in the preparation of the MgO-(OH) catalyst. The MgO catalysts designated by MgO-(NO) and MgO-(SO) were prepared by precipitation method from aqueous solution of magnesium nitrate and magnesium sulfate, respectively. Solidification procedure is the same as for the preparation of the MgO-(OH) catalyst. The MgO catalyst designated by MgO-(CO) was from a commercial basic magnesium carbonate which was directly used for the reaction without any treatments except the standard heat-treatment. The MgO catalyst designated by MgO-(ME) was prepared by the use of methanol instead of water as a media. All the other procedures were the same as the MgO-(OH) preparation.

The catalytic activities of these prepared catalysts in the condensation of 1-propanol with methanol at 633 K are illustrated in Figure 4. Figure 4 also shows surface area of each catalyst and molar ratio of produced 2-methyl propanol to produced 2-methyl propanal. It can be seen that the catalytic activity of MgO changed significantly by the preparation method. The MgO-(FD) catalyst had the highest surface area among the catalysts prepared here. The crystallinity of MgO-(ME) catalyst particles were very high and thus its surface area was lowest. This catalyst, however, showed the highest specific activity for the formation of 2-methyl propanol in the reaction.

Although it is very hard to see any relations among the preparation method, surface area, activity, and selectivity, it appears that such changes are mainly caused by small amount of anion species

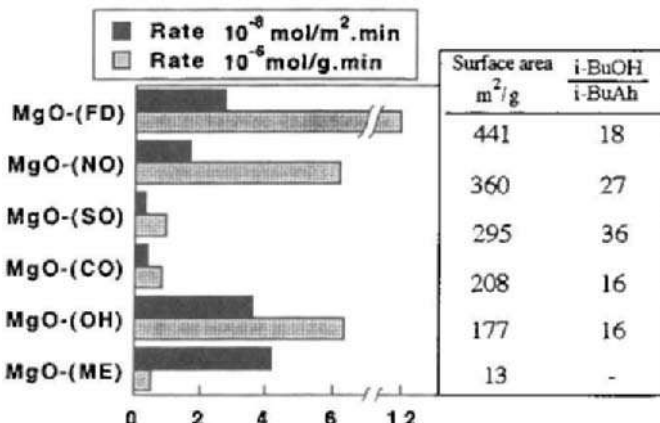


Figure 4 Catalytic performance of MgO prepared by various methods.

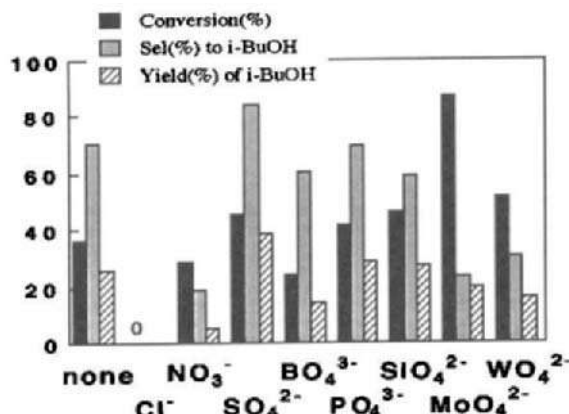


Figure 5 Addition effects of halide anion or oxo anions on the catalytic performance of MgO.

remained on the MgO surface; these anions may strongly influence the catalytic performance of MgO, since it is very difficult to remove the anions of starting materials completely by repeated washing and since these anion largely change the surface structure of MgO and have electronic effects. We, therefore, conducted experiments to test the addition effect of anions to MgO surface.

Various anion-doped MgO catalysts were prepared and tested for the reaction of 1-propanol with methanol. Eight kinds of anion, chloride anion and oxo anions, were doped into MgO catalyst as shown in Figure 5. Preparation procedure of these catalysts is the same as for the preparation of metal ion-containing MgO catalyst. Either acidic form of anion or ammonium salt was used in the preparation.

Chloride anion-doped MgO catalyst was virtually inactive for the condensation of 1-propanol with methanol, simply because its surface area was low; it was found that chloride anion effectively promoted crystallization of MgO during the heat-treatment. Nitrate anion was ineffective. This might be due to that nitrate anion easily decomposes during the heat-treatment even in the MgO lattice. However, there must be another reason for that the nitrate anion-doped MgO catalyst was

Table 4 Condensation of 1-propanol with methanol over various sulfate anion-containing MgO catalysts at 633K

Catalyst Added compound (3 wt%)	Conversion/%		Selectivity/%		
	1-Propanol	Methanol			
none	47.4	8.9	63.5	tr	7.7
$(\text{NH}_4)_2\text{SO}_4$	72.8	19.7	70.4	12.0	4.5
$\text{MgSO}_4$	78.7	11.9	70.0	2.5	2.0
$\text{MgSO}_4 \cdot (\text{NH}_4)_2\text{SO}_4$	74.1	15.6	64.9	8.5	7.5
$\text{CH}_3\text{SO}_3\text{H}$	59.4	15.5	62.9	1.3	3.3
$(\text{CH}_3\text{SO}_3)_2\text{Mg}$	58.7	4.1	57.8	tr	2.7

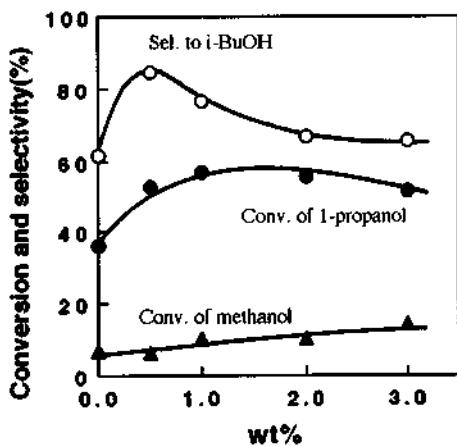


Figure 6 Effect of sulfate anion loading on the activity of MgO catalyst in the condensation of 1-propanol with methanol.

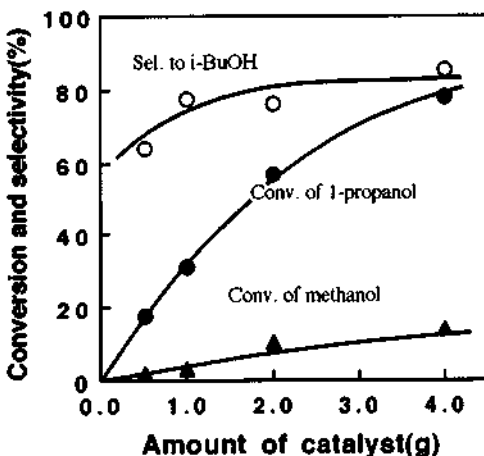


Figure 7 Condensation of 1-propanol with methanol over 1 wt% sulfate anion-doped MgO catalyst at 633 K.

less active than the pure MgO catalyst. The addition of borate anion resulted in no change in the catalytic performance of MgO. Apparent improvement in the yield of 2-methyl propanol was observed by the additions of sulfate and phosphate anions. Particularly, the addition of sulfate anion improved both activity and selectivity. The catalysts modified with silicate, molybdate, and tungstate anions were less selective although the conversion of 1-propanol was higher.

Various sulfate anion-doped MgO catalysts were prepared by the use of various sulfate precursor and tested for the reaction of 1-propanol with methanol because the sulfate-doped MgO catalyst showed the highest activity for 2-methyl propanol formation. The results are shown in Table 4. Three kinds of inorganic sulfate precursor and two kinds of organic sulfate precursor were added into MgO catalyst as shown in the table. Apparently every inorganic sulfate dopants were found to be effective to improve the catalytic performance of MgO. The organic sulfate dopants were less effective. It was observed from TPD spectra of CO<sub>2</sub> and XRD analysis that the surface basicity and the crystallinity of MgO particle did not change by the addition of sulfate anion. Therefore, it seems that the improvement of the catalytic performance by the addition of sulfate anion is attributable to the increase of surface area and the generation of sites which are much highly active for the reaction.

Figure 6 shows the effect of loading amount of sulfate anion on the catalytic performance of MgO catalyst in the condensation of 1-propanol with methanol at 633 K. The conversions of 1-propanol and methanol increased with increasing the loading amount of sulfate anion. The selectivity to 2-methyl propanol also increased but further addition caused the decrease in the selectivity after a maximum at about 1 wt %. As a result, the addition of sulfate anion in 1 wt % to MgO catalyst is suitable to achieve the highest catalytic performance in the reaction. By the use of 4 g of 1wt% sulfate anion-doped MgO catalyst, 60 % yield of 2-methyl propanol was attained in the condensation of 1-propanol with methanol at 633 K(Figure 7).

### 3.3 Aspect for Reaction Mechanism

Reaction mechanisms for the synthetic reactions of  $\alpha,\beta$ -unsaturated compounds and for the condensation reaction of alcohols with methanol are discussed here on the basis of the following summarized observations. For the synthetic reactions of  $\alpha,\beta$ -unsaturated compounds:

1. MgO catalyst without any additives is virtually inactive.

2. MgO catalysts containing metal cation, such as  $\text{Fe}^{3+}$ ,  $\text{Cr}^{3+}$ , and  $\text{Mn}^{2+}$ , which provide Lewis acid site in the MgO lattice, are active and selective.
3. The rate of product formation is not proportional to the total amount of surface base site.
4. A correlation between the rates of reaction and the pKa values of the substrates is observed; the reaction rate is higher for the substrate with a lower pKa value[27].
5. The kinetic isotope effect on the reaction rate of acetonitrile with methanol was clearly observed only when the methanol deuterated at the methyl group was allowed to react at 603 K, giving  $k(\text{CH}_3\text{OH})/k(\text{CD}_3\text{OD}) = 2.2$ . No kinetic isotope effects were caused by deuterium substitution at hydroxyl hydrogen of methanol and acetonitrile[18].
6. The exchange reaction between hydroxyl hydrogen of methanol and hydrogen of acetonitrile takes place readily both over Mn-MgO and over MgO[28].
7. Methanol is easily decomposed to CO by passing over the metal ion-containing catalyst, while MgO is inactive for methanol decomposition. However, the rate of methanol decomposition is seriously depressed by the existence of substrates[6].
8. When  $\text{CO}_2$  is co-fed in the reaction acetonitrile with methanol, the reaction readily takes place even over the pure MgO catalyst.

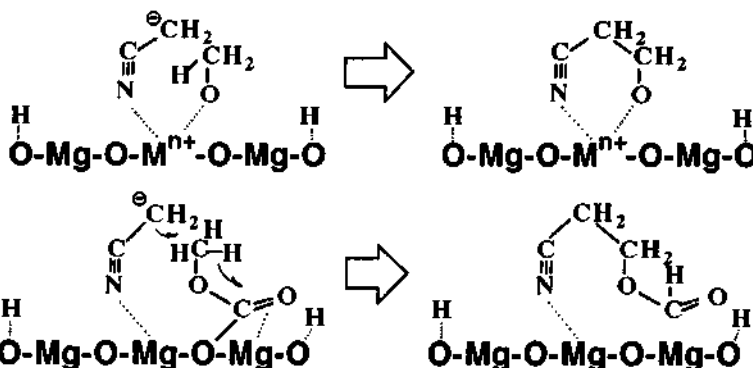
For the alcohol condensation with methanol:

1. Pure MgO catalyst is active, while CaO, which is also solid-base catalyst, is inactive. The addition of sodium cation to MgO catalyst completely depresses the catalytic activity of MgO.
2. The addition of  $\text{CO}_2$  in the feed greatly enhances the rate of alcohol condensation.
3. Sulfate anion-doped MgO catalyst shows much higher activity than MgO catalyst.
4. Reaction rate is almost independent of primary alcohols used for the reaction as substrates.
5. No 2-methyl propanal was detected at a very short contact time, indicating that 2-methyl propanal is a primary product and 2-methyl propanal is subsequently formed by the dehydrogenation of produced 2-methyl propanol over MgO catalyst.
6. Both MgO and CaO are active for the reaction of propanal with methanol. However, main product is not 2-methyl propanol but 2-methyl propenal and 2-methyl propenol at a short contact time.
7. Very small kinetic isotope effect on the reaction rate of 1-propanol with methanol was observed only when the methanol deuterated at the methyl group was allowed to react at 633 K, giving  $k(\text{CH}_3\text{OH})/k(\text{CD}_3\text{OD}) = 1.3$ .

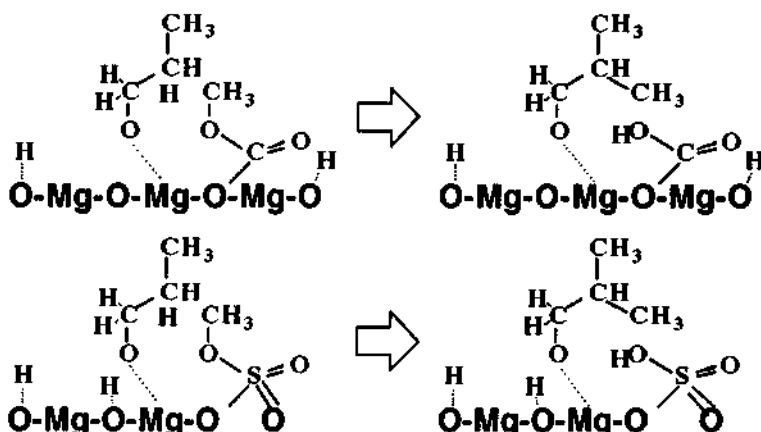
A possible reaction scheme for the catalytic synthesis of  $\alpha,\beta$ -unsaturated compounds is depicted in Figure 8. The following discussion is made for the reaction of acetonitrile with methanol as a representative. Methoxy anion is first formed from adsorbed methanol by O-H dissociation on the surface base site. This species may be adsorbed on the added metal ion site because the metal ion is a stronger Lewis acid than magnesium ion. Similarly an intermediate methylene anion formed by  $\alpha$ -hydrogen abstraction by the surface base site from adsorbed acetonitrile may also be adsorbed on the added metal ion site. Then, the C-H bond fission of the adsorbed methoxy anion takes place and formed hydride is accepted by the added metal cation. This step seems to be the rate determining one. Once this step occurs on the surface, subsequent attack of the adsorbed methylene anion readily takes place, followed by dehydration and desorption to form products.

Methoxy anion is normally a much weaker base than intermediate carbon anion; the intermediate methylene anions may be adsorbed more strongly on the added metal ion site than methoxy anion. The intermediate anion formed from the substrate with higher pKa value can be adsorbed more stably to the metal ion site because of the stronger basic character. Therefore, the hydride accepting ability of metal ions from adsorbed methoxy anions may be affected by the adsorption of intermediate methylene anions, depending strongly on the kind of substrate used. Since the hydride accepting ability of the metal ion is directly related to the rate determining step, the reaction rate must decrease with the increasing pKa value of the substrate.

A possible reaction scheme for the catalytic condensation of alcohols with methanol is also depicted in Figure 8. The reaction scheme for the alcohol condensation is essentially the same as that for the synthesis of  $\alpha,\beta$ -unsaturated compounds. However, in order to rationally explain the high ability of MgO catalyst for the alcohol condensation, we tentatively propose a  $\text{CO}_2$  assisted mechanism



(a) Scheme for the reaction of acetonitrile with methanol to form acrylonitrile



(b) Scheme for the alcohol condensation with methanol

Figure 8 Reaction mechanism.

as shown in Figure 8, since  $\text{CO}_2$  can be easily formed from higher alcohols and clear enhancement effect of  $\text{CO}_2$  was observed in the condensation reaction. The formed  $\text{CO}_2$  may react with methanol over  $\text{MgO}$  surface to produce methyl carbonate-like species,  $-\text{Mg-O-CO-OCH}_3$ . This species then reacts with an adsorbed alkoxy anion to form corresponding higher alcohols. The role of sulfate anion doped on the  $\text{MgO}$  surface is interpreted in a similar manner. The surface sulfate anion reacts with methanol to form methyl ester-like species on the surface and this species then reacts with the adsorbed alkoxy anion. The addition effect of  $\text{CO}_2$  on the reaction of acetonitrile with methanol over pure  $\text{MgO}$  catalyst is also interpreted similarly. When an adsorbed  $\text{CO}_2$  is present on pure  $\text{MgO}$  surface, this species may assist the activation of methanol by reacting with methoxy anion and accepting hydride from methyl group as shown in Figure 8, resulting in the higher yield of acrylonitrile.

## References

- [1] Tsuneshige, T., *PETROTECH*, 1993, 16, 208.
- [2] Kein, W., "Catalysis in  $\text{C}_1$  Chemistry," D. Reidel Publishing Company, Dordrecht, 1983, p.89.

- [3] Wender, I., *Catal. Rev.-Sci. Eng.*, **1984**, *26*, 303.
- [4] Calkins, W.H., *Catal. Rev.-Sci. Eng.*, **1984**, *26*, 347.
- [5] W. Ueda, *J. Japan Petrol. Inst.*, **1993**, *36*, 421.
- [6] Ueda, W., Yokoyama, T., Kurokawa, H., Moro-oka, Y., and Ikawa, T., *J. Japan Petrol. Inst.*, **1986**, *29*, 72.
- [7] Ueda, W., Ohshida, T., Kuwabara, T., and Morikawa, Y., *Catal. Lett.*, **1992**, *12*, 97.
- [8] Grasselli, R.K., Burrington, J.D., and Brazdil, J.F., *Faraday Discuss. Chem. Soc.*, **1982**, *72*, 203.
- [9] Khcheyan, Kh.E., Revenko, O.M., Shatalova, A.N., Gel'perina, E.G., Klebanova, F.D., and Arunskaya, L.I., *Neftekhimiya*, **1979**, *17*, 586.
- [10] Monsanto, U.S. Patent 4 179 462, **1979**.
- [11] Firuzi, P.G., *Petrol. Chem. U.S.S.R.*, **24**, 80 **1984**.
- [12] Vitcha, J.F., and Sims, V.A., *Ind. Eng. Chem. Prod. Res. Dev.*, **1966**, *5*, 50.
- [13] Albanesi, G., and Moggi, P., *Appl. Catal.*, **1984**, *6*, 293.
- [14] Ai, M., *J. Catal.*, **1988**, *112*, 194.
- [15] Ueda, W., Yokoyama, T., Moro-oka, Y., and Ikawa, T., *J. Chem. Soc., Chem. Commun.*, **1984**, 39.
- [16] Ueda, W., Yokoyama, T., Moro-oka, Y., and Ikawa, T., *Ind. Eng. Chem. Prod. Dev.*, **1985**, *24*, 340.
- [17] Kurokawa, H., Kato, T., Ueda, W., Morikawa, Y., Moro-oka, Y., and Ikawa, T., *J. Catal.*, **1990**, *126*, 199.
- [18] Kurokawa, H., Kato, T., Kuwabara, T., Ueda, W., Morikawa, Y., Moro-oka, Y., and Ikawa, *J. Catal.*, **1990**, *126*, 208.
- [19] Ueda, W., Kurokawa, H., Moro-oka, Y., and Ikawa, T., *Chem. Lett.*, **1985**, 819.
- [20] Kurokawa, H., Ueda, W., Morikawa, Y., Moro-oka, Y., and Ikawa, T., *MRS Int. Mtg. on Adv. Mats.* **1989**, Vol.2, p309.
- [21] Sheldon, R.A., "Chemicals from Synthesis Gas," D. Reidel Publishing Company, Dordrecht, **1983**, p.127.
- [22] M. Ichikawa, *J. Catal.*, **1979**, *56*, 127.
- [23] T. Mizorogi and M. Nakayama, *Bull. Chem. Soc. Jpn.*, **1964**, *39*, 236.
- [24] M.W. Farrar (Monsanto Chemical Co.), US Pat. 2 971 033 **1961**.
- [25] G. Pregalia, G. Gregorio and F. Conti (Montecatini Edison S.p.A), French Pat. 1 531 2612 **1968**.
- [26] R.T. Clark (Celanese Corporation), US Pat. 3 972 952 **1976**.
- [27] Ueda, W., Yokoyama, Y., Moro-oka, Y., and Ikawa, T., *Chem. Lett.*, **1985**, 1059.
- [28] Ueda, W., Kuwabara, T., Kurokawa, H., and Morikawa, Y., *Chem. Lett.*, **1990**, 265.

# 1.5 Novel Direct Hydrogenation Process of Aromatic Carboxylic Acids to the Corresponding Aldehydes with Zirconia Catalyst

T. YOKOYAMA, T. SETOYAMA, N. FUJITA and T. MAKI

Research Center, Mitsubishi Kasei Corporation, 1000 Kamoshida-cho, Midori-ku, Yokohama 227, Japan

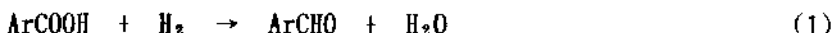
## ABSTRACT

A novel process for producing aromatic aldehydes by a direct hydrogenation reaction of the corresponding carboxylic acids was established. The catalyst, modified zirconia, showed excellent performance for commercial production. The catalyst screening, application to various carboxylic acid hydrogenation, and reaction mechanism are reported.

## 1. INTRODUCTION

Aromatic aldehydes are important intermediates for the production of organic fine chemicals such as pharmaceuticals, agrochemicals and perfumes. The conventional methods for the production of these aldehydes are composed of several stoichiometric reactions. For example, the halogenation of methyl substituted aromatics followed by hydrolysis or oxidation is known as a commercial process. However, this process includes several disadvantages such as environmental pollution, production cost and product quality.

Direct hydrogenation of aromatic carboxylic acid [eqn. (1)]



is considered to be one of the most efficient methods to solve these problems. However the catalytic performance of some oxide catalysts, such

as  $\gamma$ -alumina [1] or yttrium oxide [2] was not sufficient to apply a commercial production. Another excellent catalyst has been sought after.

Based on a preliminary survey, zirconium oxide,  $ZrO_2$ , was found to be a potential catalyst because of its high selectivity to aldehyde and acid-tolerant character. Although  $ZrO_2$  itself has been known as a catalyst carrier or ceramic component, its own catalytic activity has been scarcely reported except acid-base function.

By modifying  $ZrO_2$  with metal ions such as  $Pb^{2+}$ ,  $In^{3+}$ , and  $Cr^{3+}$ , the activity of  $ZrO_2$  was remarkably enhanced and its catalytic stability was improved to establish a multi-purpose catalyst for the hydrogenation of a wide range of carboxylic acids [3].

In this paper, the roles of acid-base function of  $ZrO_2$  surface and of metal ion promotor upon the activity are discussed. The reaction mechanism are also proposed.

## 2. EXPERIMENTAL

### 2.1. Catalyst Preparation

$ZrO_2$  used in this study was prepared by calcining zirconyl hydroxide, which was synthesized by a precipitation method from  $ZrO(NO_3)_2$  or  $ZrOCl_2$  with aqueous ammonium hydroxide in conventional way. Commercial  $ZrO_2$  was also used.

Modification of  $ZrO_2$  was carried out by an impregnation of corresponding metal salt. The atomic ratio of each promotor metal to zirconium was chosen as 0.05. All catalysts were calcined in an air stream at 600 °C for 3h.

### 2.2. Hydrogenation Reaction

The hydrogenation reactions of carboxylic acids were carried out under atmospheric pressure by using fixed bed reactor ( $\phi$  19 mm) and the charged amount of catalyst was 10 ml. The reactant concentration was adjusted to 2 volume %. The reaction products were analyzed by GLC and the amount of unreacted carboxylic acids was determined by titration.

### 2.3. Determination of acid-base properties of $ZrO_2$

The acid-base strength of  $ZrO_2$  was determined by the Hammett indicator method [4]. The acid and base quantities of  $ZrO_2$  were determined by

temperature programmed desorption (TPD) of adsorbed NH<sub>3</sub> and CO<sub>2</sub> as follows. The adsorption of NH<sub>3</sub> and CO<sub>2</sub> was carried out at 100 °C in ahead, and the desorption of NH<sub>3</sub> and CO<sub>2</sub> was started at 100 °C to 550 °C with temperature increasing rate of 10 °C/min. Desorbed NH<sub>3</sub> and CO<sub>2</sub> were determined by GLC.

#### 2.4. IR Study of Adsorbed Species

FT-IR diffuse reflectance spectra of adsorbed species on the catalysts were studied. The catalyst was pre-treated with hydrogen stream at 350 °C for 2 h. Then the hydrogenation reaction was carried out for 5 h. The catalyst was subsequently flushed with nitrogen gas at the same temperature before cooling. The sample was placed into an in-situ cell equipped with Zn-Sn windows and a heating unit under nitrogen or hydrogen conditions. The spectra were recorded on Spectratec Model 0030-102.

### 3. RESULTS AND DISCUSSION

#### 3.1. Hydrogenation Reaction over Various Metal Oxides

The hydrogenation of benzoic acid to benzaldehyde was carried out as a screening reaction to survey the catalytic performance of various metal oxides. The results are shown in Table 1. Among them, ZrO<sub>2</sub> showed the best selectivity to benzaldehyde, but its activity was low.

Table 1. Hydrogenation of benzoic acid over various metal oxide catalysts.

Catalyst	Temperature / (°C)	Conversion of benzoic acid/ (%)	Selectivity to benzaldehyde/ (%)
20% Y <sub>2</sub> O <sub>3</sub> / $\alpha$ -Al <sub>2</sub> O <sub>3</sub>	440	100	87
$\gamma$ -Al <sub>2</sub> O <sub>3</sub>	440	20	53
MgO	440	62	4
TiO <sub>2</sub>	440	15	10
ZrO <sub>2</sub>	400	53	97
ZnO	400	55	54

Reaction conditions: H<sub>2</sub>, GHSV=625 h<sup>-1</sup>, benzoic acid/H<sub>2</sub>=2/98 vol.-%, under atmospheric pressure.

20wt%  $\text{Y}_2\text{O}_3/\alpha\text{-Al}_2\text{O}_3$  showed relatively low selectivity compared to  $\text{ZrO}_2$ . It was also accompanied by decarboxylation reaction of benzoic acid. Basic  $\text{MgO}$  showed low selectivity. It was broken down into powder probably by benzoate salt formation.

From these results,  $\text{ZrO}_2$  was chosen as active component of the catalyst because of its high selectivity and its-acid tolerant character.

### 3. 2. Correlation between acid-base properties and activities of $\text{ZrO}_2$

A number of commercially available  $\text{ZrO}_2$  samples were tested. Catalytic activity varied drastically by changing samples, suggesting that the surface characters of  $\text{ZrO}_2$  to be an important factor for this reaction.

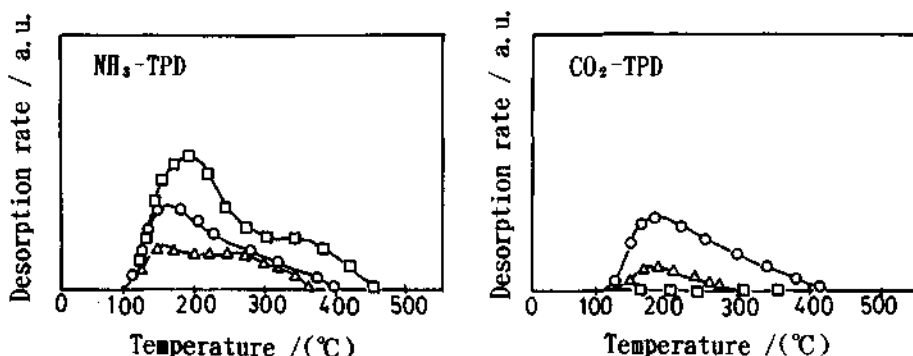
Correlation between acid-base strength of  $\text{ZrO}_2$  and the activity expressed by the formation rate of benzaldehyde, is given in Table 2. Non-acidic  $\text{ZrO}_2$  having  $H_\alpha$  in the range from +6.8 to +7.2 ( $\text{ZrO}_2\text{-A,B}$ ) showed high activity. The activity was also enhanced by increasing surface area. On the other hand, acidic  $\text{ZrO}_2$  ( $\text{ZrO}_2\text{-C,D}$ ) showed low activity and selectivity, accompanied by an undesirable decarboxylation of carboxylic acid.

The  $\text{NH}_3$ - and  $\text{CO}_2$ -TPD profiles of  $\text{ZrO}_2$  are shown in Fig. 1. For non-acidic  $\text{ZrO}_2$ , the maximum desorption temperatures of  $\text{NH}_3$  and  $\text{CO}_2$  were 160 °C and 150°C, respectively. The peak profiles were considered to be due to the presence of a weak acid or base sites on the  $\text{ZrO}_2$  surface. The amount of desorbed  $\text{NH}_3$  was nearly the same as that of  $\text{CO}_2$ .

Table 2. Correlation between acid-base properties of various  $\text{ZrO}_2$  and their catalytic activities.

Catalyst	Strength		Surface area ( $\text{m}^2/\text{g}$ )	Formation rate of benzaldehyde ( $\text{mol}/\text{kg}\cdot\text{cat.h}$ )
	Acid[ $H_\alpha$ ]	Base[ $H_-$ ]		
$\text{ZrO}_2\text{-A}$	+6.8<	<+ 7.2	31	0.19
$\text{ZrO}_2\text{-B}$	+6.8<	<+ 7.2	38	0.28
$\text{ZrO}_2\text{-C}$	+3.3<	<+ 7.2	29	0.09
$\text{ZrO}_2\text{-D}$	-5.6<	<+ 7.2	86	0
$\text{MgO}$	-	$\leq +15.0$	-	0.02

Reaction conditions:  $\text{H}_2$  GHSV=625  $\text{h}^{-1}$ , benzoic acid/ $\text{H}_2$ =2/98 vol.-%, 350 °C, under atmospheric pressure; calcination temperature:  $\text{ZrO}_2$ =600 °C,  $\text{MgO}$ =900 °C.



symbol	Catalyst	Amount of desorbed <sup>a</sup>		Activity <sup>b</sup>
		NH <sub>3</sub>	CO <sub>2</sub>	
○	ZrO <sub>2</sub> -A	0.15	0.130	0.172
△	ZrO <sub>2</sub> -C	0.09	0.022	0.050
□	ZrO <sub>2</sub> -D	0.31	0	0.002

<sup>a</sup>mmol/g. <sup>b</sup> Formation rate of benzaldehyde at 350 °C, mol/kg-cat. h.

Fig. 1. TPD profiles of adsorbed ammonia and carbon dioxide from ZrO<sub>2</sub>.

For acidic ZrO<sub>2</sub>-C, the profile of NH<sub>3</sub> desorption was the same as ZrO<sub>2</sub>-A, only the desorption amount was small. For ZrO<sub>2</sub>-D having H<sub>e</sub> ≥ -5.6, a new peak due to strong acid sites appeared at 350 °C, and the total amount of desorbed NH<sub>3</sub> increased. On the contrary, the amount of desorbed CO<sub>2</sub> of ZrO<sub>2</sub> decreased with increasing surface acidity, and became almost nil with ZrO<sub>2</sub>-D.

It is known that a decarboxylation of aromatic carboxylic acid proceeds over an acidic catalyst [5]. It is considered that the strong acidic sites on the ZrO<sub>2</sub> have a role to polarize the adsorbed carboxyl group, resulting in the decarboxylation. On the other hand, strong basic sites on MgO reacts with the acid to form salt, and further reaction does not occur under hydrogenation condition.

It is known that ZrO<sub>2</sub> having moderate acid-base strength shows the significant catalytic activity in H-D exchange reactions between methyl group of deuterated isopropyl alcohol and surface OH group [6]. It is also known that non-acidic ZrO<sub>2</sub> shows specific catalytic activity for hydrogenation of 1,3-butadiene [7]. The surface of ZrO<sub>2</sub> is considered to play as acid-base bifunctional catalysis. The mechanism of this

hydrogenation reaction has closely related to these phenomena, because non-acidic  $ZrO_2$  shows better catalytic performance.

### 3.3. Modification of the $ZrO_2$ with Metal Ions

The activity of simple  $ZrO_2$  was considered to be insufficient for a practical application. Some kind of modification was necessary to increase the activity and it has been known that there is a good relation between the activity and the surface area. Thus the modification by adding metal ions were tried in order to increase the surface area. Results are given in Table 3. By adding  $Pb^{2+}$ ,  $In^{3+}$ , or  $Cr^{3+}$ , activity of the  $ZrO_2$  was remarkably enhanced [8]. The addition of  $Ca^{2+}$  did not show any effect.

Table 3. Hydrogenation of benzoic acid with modified  $ZrO_2$  catalyst.

Additives	Temperature /( $^{\circ}C$ )	Conversion of benzoic acid/(\%)	Selectivity to benzaldehyde/(\%)
None	350	51	97
Pb	310	89	96
In	330	100	91
Cr	350	98	96
Mn	350	70	97
Ca	350	50	98

Reaction conditions:  $H_2$  GHSV=625  $h^{-1}$ , benzoic acid/ $H_2$ =2/98 vol.-%, under atmospheric pressure.

The roles of added metal ions can be discussed as follows. It is known that the amorphous  $ZrO_2$  crystallizes at about 460°C and drastic decrease of surface area takes place by this crystallization. Added metal ions are considered to suppress the crystallization of  $ZrO_2$ . For example, by modifying  $ZrO_2$  with  $Cr^{3+}$ , the surface area increased from 31  $m^2/g$  to 88  $m^2/g$  and the formation rate of benzaldehyde (mol/kg-cat.h) at 350 °C increased from 0.28 to 0.61. The effect of  $Cr^{3+}$  on the acid-base properties of  $ZrO_2$  were also studied by TPD. The  $NH_3$ - and  $CO_2$ -TPD profiles of modified  $ZrO_2$  were similar to those of unmodified  $ZrO_2$ . The amounts of desorbed  $NH_3$  and  $CO_2$  per surface area did not show any significant change. Thus the enhancement of the catalytic activity is considered to be

mainly due to the increase of surface area of the catalyst.

The stability of catalytic performance was checked by a long-term hydrogenation reaction. The results are given in Fig. 3. Unmodified  $ZrO_2$  deactivated quickly by coke formation. On the contrary, it was confirmed that its catalytic stability was improved significantly by adding  $Cr^{3+}$ . Furthermore, modified  $ZrO_2$  retained its high surface area after the reaction so that the adding  $Cr^{3+}$  has also an important role to suppress the coke formation.

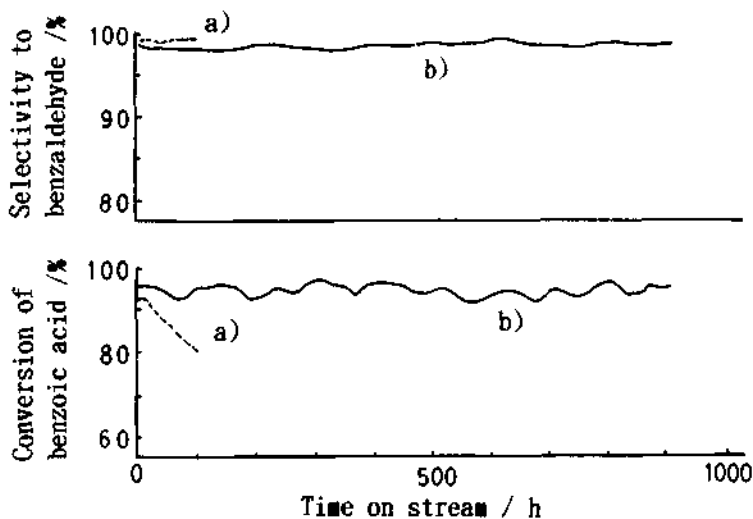


Fig. 2. Deterioration of catalytic activity.  
a)  $ZrO_2$ , b)  $Cr^{3+}$ -modified  $ZrO_2$ .

### 3.4. Hydrogenation of Various Carboxylic Acids

$Cr^{3+}$ -modified  $ZrO_2$  was used for the hydrogenation of various carboxylic acids or esters, and the results are given in Table 4. Alkyl and phenoxy substituted benzoic acids were converted to the corresponding aldehydes with high selectivity. Terephthalaldehyde and 4-carbomethoxybenzaldehyde were obtained by the hydrogenation of dimethyl terephthalate [9]. Aliphatic or alicyclic aldehyde, such as trimethylacetaldehyde and cyclohexanecarboxaldehyde, were also obtained selectively. However, in the case of primary aliphatic carboxylic acid, the selectivity was low, accompanied by the ketone formation by the condensation of two carboxylic acid molecules [eqn. (2)]. The ketonization activity of the  $ZrO_2$  was,

however, suppressed to some degree.



Heterocyclic carboxylic acids having nitrogen or sulfur atom could also be hydrogenated to the corresponding aldehydes.

These results indicate that the modified  $\text{ZrO}_2$  catalyst is useful to apply the hydrogenation of a wide range of carboxylic acids as well as benzoic acid.

Table 4. Hydrogenation of various carboxylic acids or esters with  $\text{Cr}^{3+}$  - modified  $\text{ZrO}_2$  catalyst.

Carboxylic acids or esters	Conversion of acid or ester /(%)	Selectivity to aldehyde /(%)
Benzoic acid	98	96
<i>o</i> -Methylbenzoic acid	98	97
<i>m</i> -Phenoxybenzoic acid	97	96
Dimethyl terephthalate	64	73
<i>m</i> -Chlorobenzoic acid	82	77
Trimethylacetic acid	97	99
Methyl <i>n</i> -hexanoate	50	70
cyclohexanecarboxylic acid	95	98
Methyl nicotinate	86	83
4-Methyl-5-carmomethoxythiazole	74	80
3-Furoic acid	62	52

### 3.5. Mechanistic Consideration

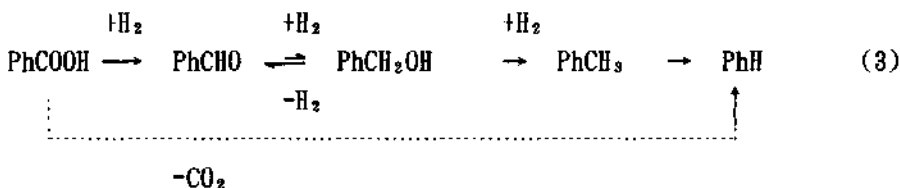
The main by-products of the hydrogenation reaction of benzoic acid to benzaldehyde were benzyl alcohol, toluene and benzene. Their amounts increased along with increasing of conversion or reaction temperature. To study the reaction pathway, benzaldehyde and other by-products were introduced over the catalyst under the same hydrogenation conditions. The results are shown in Table 5.

Benzaldehyde was hydrogenated to benzyl alcohol with the formation of

high boiling products. However, the formation rate of benzyl alcohol was low compared to that of aldehyde from carboxylic acid. It was found that the hydrogenation of benzoic acid have a faster reaction rate than that of benzaldehyde. Benzyl alcohol was converted to toluene by hydrogenolysis and to benzaldehyde by dehydrogenation. Under the hydrogenation conditions, dehydrogenation was more rapid than hydrogenolysis. Benzene was formed by the hydrogenolysis of toluene and decarboxylation of benzoic acid.

It was found that benzoic acid is more easily reduced than aldehyde. The reason why aldehyde is produced in good yield, is considered as follows. Reaction equilibrium between aldehyde and alcohol is favored for aldehyde, and strong interaction of carboxylic acid with the catalyst surface inhibits consecutive reactions of aldehyde by removing it immediately as formed from the catalyst surface.

We propose the following reaction pathway for the hydrogenation of benzoic acid in Eq. (3).



The rate of aldehyde formation is expressed as

$$r = \frac{k_1 [P_{\text{H}_2}]^a [P_{\text{CA}}]^b}{(1 + \sqrt{k_2 [P_{\text{H}_2}]})^c} \quad (4)$$

where  $r$  is the rate of aldehyde formation,  $k_1$ ,  $k_2$  are reaction constants,  $P_{\text{H}_2}$ ,  $P_{\text{CA}}$  are partial pressures of hydrogen and carboxylic acid, and  $a$ ,  $b$ , and  $c$ , are reaction orders. Equation (4) suggests that hydrogen molecules are activated via dissociative adsorption which is considered to be the rate determining step, because  $b$  is negligibly small and  $a$  and  $c$  equals nearly 1 and 2, respectively [10].

Onishi et al have also suggested that the molecular hydrogen is activated on  $\text{ZrO}_2$  by dissociative adsorption [11]. Thus it is reasonable to consider that the dissociative adsorption step plays an important role

for this reaction.

Table 5. Reactivity of benzaldehyde and benzyl alcohol over the modified  $\text{ZrO}_2$  catalyst.

Substrates	Formation rate(mol/kg-cat. h)			
	PhCHO	PhCH <sub>2</sub> OH	PhCH <sub>3</sub>	High boilers
PhCHO	-	0.08	0.01	0.12
PhCH <sub>2</sub> OH	0.28	-	0.09	0.19
PhCOOH	0.54	Trace	Trace	Trace

Reaction conditions:  $\text{H}_2$  GHSV=625  $\text{h}^{-1}$ , LHSV=0.07 kg/l-cat. h, 330 °C.

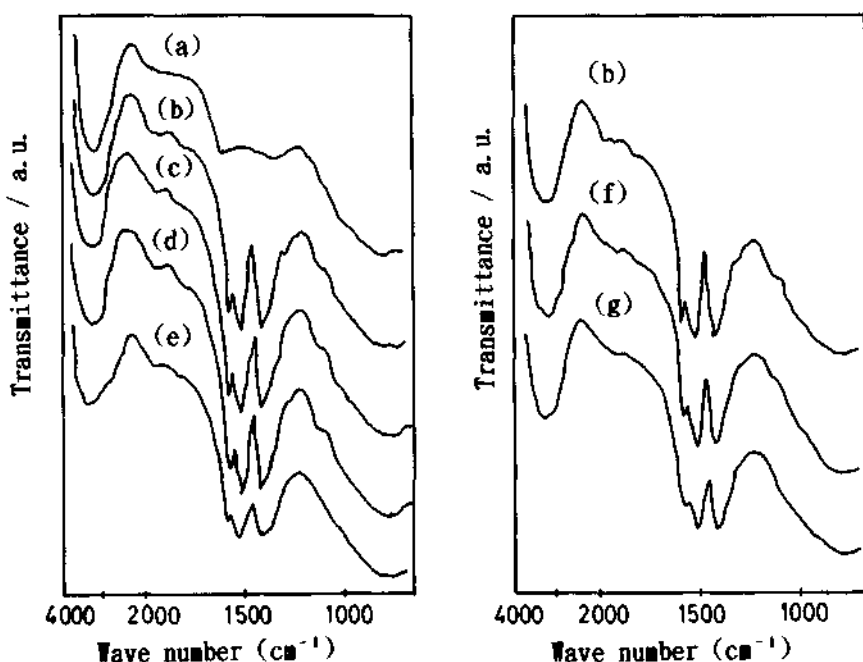


Fig. 3. FT-IR spectra of adsorbed species on the  $\text{ZrO}_2$ . Behavior of carboxylate species by thermal treatment in  $\text{N}_2$  or  $\text{H}_2$  stream.  
 (a) The  $\text{ZrO}_2$  catalyst after  $\text{H}_2$  reduction at 350 °C for 2h,  
 (b) adsorbed benzoic acid after hydrogenation at 350 °C;  
 (c)  $\text{N}_2$  treatment of (b) at 350 °C for 1h, (d) at 400 °C  
 for 1h, (e) 450 °C for 1h; (f)  $\text{H}_2$  treatment of (b) at 350 °C  
 for 1h, (g) at 350 °C for 2h.

Table 6. Products desorbed from the surface benzoate species by treatment with H<sub>2</sub> or N<sub>2</sub>.

Treatment condition	Desorbed products( μmol/ml-cat.)			
	PhCHO	PhCH <sub>2</sub> OH	PhH	PhCOOH
N <sub>2</sub> , 350 °C, 1 h	1.0	Trace	Trace	6.0
N <sub>2</sub> , 400 °C, 1 h	1.6	Trace	Trace	4.4
N <sub>2</sub> , 450 °C, 1 h	1.2	Trace	60.7	Trace
H <sub>2</sub> , 350 °C, 1 h	19.9	1.1	1.3	2.3
H <sub>2</sub> , 350 °C, 2 h	1.2	0.2	Trace	Trace

Conditions: GHSV=625 h<sup>-1</sup>.

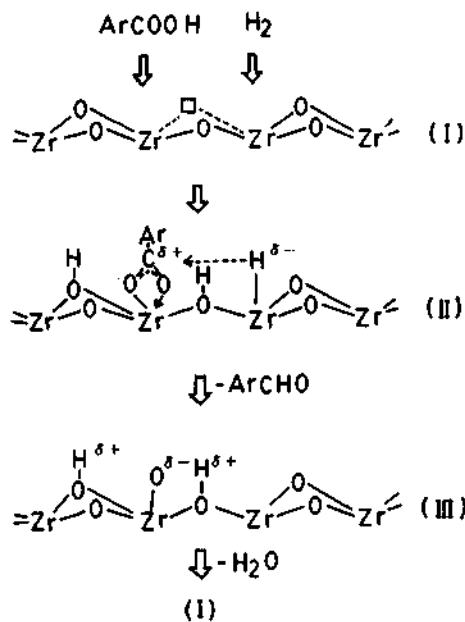


Fig. 4. Proposed reaction mechanism.

The adsorbed surface species of benzoic acid was studied by FT-IR spectroscopy. The results are shown in Fig. 3. After hydrogenation of benzoic acid, bidentate carboxylate (1540, 1440 cm<sup>-1</sup>) was detected on ZrO<sub>2</sub>. Its desorption behavior under nitrogen or hydrogen stream was also studied. The results are shown in Table 6. This surface carboxylate

species was stable up to 400 °C under nitrogen but decomposed to benzene above 450 °C. On the other hand, it reacted under a hydrogen stream at 350 °C and benzaldehyde was detected as the main desorbed product in the effluent. The surface carboxylate will probably be an intermediate of the hydrogenation.

Thus aldehyde is considered to be formed by reaction of the surface carboxylate and dissociated hydrogen atoms as shown in Fig. 4. However, dissociated hydrogen species could not be recognized at elevated temperature. Further study on the reaction mechanism is undergoing.

#### 4. CONCLUSIONS

Modified ZrO<sub>2</sub> catalyst showed high selectivity for the hydrogenation of aromatic carboxylic acids to the corresponding aldehydes. This catalyst has good performance to apply to the commercial operation. There is a good relation between catalytic activity and surface character. The surface carboxylate is considered as an intermediate for the reaction.

#### ACKNOWLEDGEMENT

The authors express their thanks to Professor Kozo Tanabe, Professor Hideshi Hattori, and Dr. Tsutomu Yamaguchi of Hokkaido University for their helpful advice.

#### REFERENCES

- 1 A. Feinstein and E. K. Field, U.S. Patent, 3,935,265 (1976).
- 2 E. J. Strojny, U.S. Patent 4,328,373 (1982).
- 3 T. Yokoyama, T. Setoyama, N. Fujita, M. Nakajima, T. Maki and K. Fujii, Appl. Catal., 1993, 88, 149.
- 4 K. Tanabe, "Solid Acids and Bases", Kodansha, Tokyo, 1970, p. 6.
- 5 G. A. Olah, K. Laali, and A. K. Mehrotra, J. Org. Chem., 1983, 48, 3360.
- 6 T. Yamaguchi, Y. Nakano, T. Iizuka, and K. Tanabe, Chem. Lett., 1970, 677.
- 7 Y. Nakano, T. Yamaguchi, and K. Tanabe, J. of Cat., 1983, 90, 307
- 8 T. Maki and T. Yokoyama, Japan Kokai Patent, 85-126242 (1985).
- 9 T. Maki and T. Yokoyama, U.S. Patent, 4,613,700 (1986).
- 10 J. J. Carberry, "Chemical and Catalytic Reaction Engineering", McGraw-Hill, New York, 1976, p. 387.
- 11 T. Onishi, H. Abe, K. Maruya, and K. Domen, J. Chem. Soc., Commun., 1985, 617.

# 1.6 Role of Acid and Base Properties of V<sub>2</sub>O<sub>5</sub>-Base Metal Oxide Catalysts for Partial Oxidation of *p*-Substituted Toluene

Michio Ueshima <sup>a</sup>, Noboru Saito <sup>b</sup> and Noboru Shimizu <sup>b</sup>

<sup>a</sup> Catalyst Research Laboratory, Nippon Shokubai Co., Ltd. 992-1 Aza Nishioki  
Okihama Aboshi-ku Himeji, Hyogo, 671-12, Japan

<sup>b</sup> Central Research Laboratory, Nippon Shokubai Co., Ltd. 5-8 Nishi Otabi-cho  
Suita, Osaka 564, Japan

## ABSTRACT

The partial oxidation of *p*-methoxy toluene (PMT) to *p*-methoxy benzaldehyde (PMBA) in the vapor phase was effectively carried out over V<sub>2</sub>O<sub>5</sub>-base metal oxide (such as Ti<sub>2</sub>O or Cs<sub>2</sub>O), in which the catalytic activity and the selectivity are related to acid and base properties of the catalyst respectively. Furthermore, in selective oxidation reactions of various *p*-substituted toluene to corresponding benzaldehyde over V<sub>2</sub>O<sub>5</sub>-Ti<sub>2</sub>O, high selectivities were obtained. Reactivity of *p*-substituted toluene over this catalyst depended on the electron donating ability of the *p*-position substituted group. It was found that this catalyst was in molten state at reaction temperature.

## 1. INTRODUCTION

*p*-Substituted benzaldehyde are the important chemicals in the chemical industry. It is known that the partial oxidation of *p*-substituted toluene to corresponding benzaldehyde in the liquid phase are carried out in the presence of Co salts in acetic acid with oxygen [1-2] or by the anodic oxidation [3]. However, efficiencies of these reactions are not so high. On the other hand, the vapor phase catalytic oxidation of *p*-substituted toluene to *p*-substituted benzaldehyde has not been reported except the oxidation of *p*-methoxy toluene to *p*-methoxy benzaldehyde using V<sub>2</sub>O<sub>5</sub>-P<sub>2</sub>O<sub>5</sub> - K<sub>2</sub>SO<sub>4</sub> system catalyst [4]. A partial oxidation is a reaction to get an intermediate selectively on the way of complete oxidation, and it is generally said that it is difficult to control the consecutive reaction of an intermediate such as substituted benzaldehyde in the vapor phase over the strong acidic metal oxides such as V<sub>2</sub>O<sub>5</sub>, Cr<sub>2</sub>O<sub>3</sub> and MnO<sub>2</sub> or their mixed oxides which have been used as the vapor phase oxidation catalysts.

In present paper, the reactivities of various V<sub>2</sub>O<sub>5</sub>-M<sub>m</sub>O<sub>n</sub> (M<sub>m</sub>O<sub>n</sub>: an acidic or basic metal oxide) binary oxides catalysts in the vapor phase oxidation of *p*-methoxy toluene (PMT) to *p*-methoxy benzaldehyde (PMBA) were studied. Addition of Ti<sub>2</sub>O or Cs<sub>2</sub>O to V<sub>2</sub>O<sub>5</sub> enhanced the selectivity to PMBA, and it was found that the catalytic activity and selectivity in this oxidation reaction were depended on the acidity and the basicity of catalysts. Furthermore, the partial

oxidation reactions of *p*-substituted toluene(*p*-methyl, -isopropyl, -tertiary butyl and -methoxy) to the corresponding benzaldehyde in the vapor phase were studied over V<sub>2</sub>O<sub>5</sub>-Tl<sub>2</sub>O ( Tl/V=0.4, atomic ratio). The high activity and the selectivity were obtained in these partial oxidations over this catalyst [5-6]. The correlation between the reactivity of reactants and the substituted groups were discussed. From the results of DTA and XRD analyses, this catalyst was in molten state in reaction temperature.

## 2. EXPERIMENTAL

### 2.1. Catalyst Preparation

All catalysts were used in this study were prepared as follows. Ammonium metavanadate (17.55 g) and oxalic acid (3.3 g) were dissolved in 200 ml deionized hot water. To this solution, optimum amount of the aqueous solution containing a nitrate of M elements (M = Li, Na, K, Rb, Cs, Mg, Ba, Tl, Cu, Ag), ammonium molybdate or H<sub>3</sub>PO<sub>4</sub> was added respectively, with stirring. And then diatomaceous earth (13.6 g) was added and heated to evaporate water under vigorous stirring. The resulting clay-like mass was dried at 120 °C, calcined at 600 °C for 6 hours in air, and pulverized to a size of 9 - 20 mesh to prepared a catalyst.

### 2.2. Oxidation Reaction

The vapor phase oxidation reactions of *p*-substituted toluene were carried out using the conventional fixed bed flow system at atmospheric pressure. Five ml of a catalyst was filled up in a stainless steel reaction tube having an inside diameter of 10mm, and the reaction tube was heated. The reaction gas mixture containing 1.0 mol % *p*-substituted toluene in air was passed through the reaction tube at a flow rate of 500ml/min(STP). All the products were analyzed by gas chromatography in one hour after beginning of reaction.

### 2.3. Measurement of Acidity and Basicity of Catalyst

The acidity and the basicity of the catalyst were measured by the technique of the dehydration and dehydrogenation reaction of iso-propyl alcohol (IPA)[7]. The gas mixture containing 2 mol% IPA in air was introduced to the reaction tube packed by 2g of the catalyst at a flow rate of 360ml/min (STP). Acetone and propylene formed were analyzed by gas chromatography. The acidity was determined by the rate of propylene formation (rp), and the basicity was decided by calculation of the rate of acetone formation being divided by the rate of propylene formation : (ra/rp).

### 2.4. XRD Analysis

XRD spectra were measured by X-ray diffractometer with high temperature attachment (Rigaku Geiger Flex RAD-RC, Cu-K $\alpha$  radiation).

## 3. RESULTS AND DISCUSSION

### 3.1. Oxidation of *p*-Methoxy Toluene

The reactivities in the vapor phase oxidation of *p*-methoxy toluene (PMT) to *p*-methoxy benzaldehyde (PMBA) over various V<sub>2</sub>O<sub>5</sub>-M<sub>m</sub>On [M<sub>m</sub>On: an acidic metal oxide (M=Mo,P) or basic metal oxide (M= alkali metal, alkaline earth metal, Ag, Cu and Tl)] binary oxides catalysts were studied, in which the atomic ratio M to V was fixed 0.4.

The correlation between the selectivity to PMBA and the reaction temperature when the PMT conversion is 50 mol % on each catalyst are shown in Figure 1. It is observed that higher active catalysts ( $M_mO_n = MgO, BaO, CuO, Li_2O, Na_2O, P_2O_5$  and  $MoO_3$ ) which show a low reaction temperature give lower selectivity to PMBA.

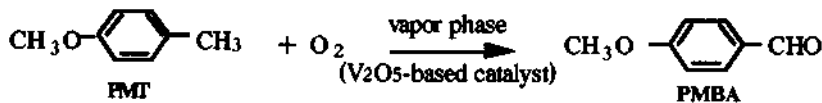
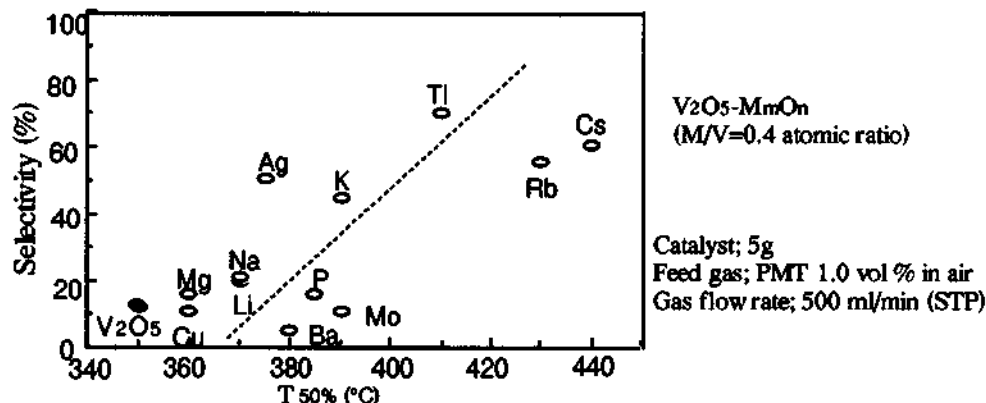


Fig.1 Selectivity to PMBA and Reaction Temperature when PMT Conversion is 50 mol % (T 50%) over V<sub>2</sub>O<sub>5</sub>-M<sub>m</sub>O<sub>n</sub> Catalysts



On the other hand, lower active catalysts, such as  $K_2O$ ,  $Rb_2O$ ,  $Cs_2O$ ,  $Tl_2O$  and  $AgO$  composite catalysts which have relatively strong base properties, show higher selectivity. Particularly,  $Tl$  composite catalyst showed the highest selectivity and moderate activity.

### 3.2. Acid and Base Properties of Catalysts

A correlation between acid-base properties and catalytic performances was examined. The acid-base properties of these catalysts were measured by the dehydration and dehydrogenation reaction of IPA.

In the  $V_2O_5-Tl_2O$  binary system, the correlation between the acidity ( $r_p$ ) and the catalytic activity (reaction temperature;  $T_{50\%}$ , PMT conversion = 50 mol %) is plotted against  $Tl_2O$  content in Figure 2. There is a good correlation between an activity and an acidity of the catalyst. The activity decreases with increase in  $Tl_2O$  content and at the same time the acidity decreases. Furthermore the basicity ( $r_a / r_p$ ) and the PMBA selectivity are plotted against  $Tl_2O$  content in Figure 3. The selectivity related on behavior of the basicity. It is suggested that this oxidation is effectively carried out by the acid and base cooperative mechanism.

In the  $V_2O_5-Cs_2O$  binary system, the same tendency with  $V_2O_5-Tl_2O$  was also observed as shown in Figures 4 and 5.

The vapor phase oxidation reaction of PMT to PMBA was effectively performed over  $V_2O_5-Tl_2O$  ( $Cs_2O$ ) binary catalyst when the atomic ratio,  $Tl(Cs) / V$ , was 0.4. However, in other various  $V_2O_5-M_mO_n$  binary catalysts except Cs

Fig. 2 The Relation between Activity (T50%) and Acidity ( $r_p$ ) against Ti/V Atomic Ratio

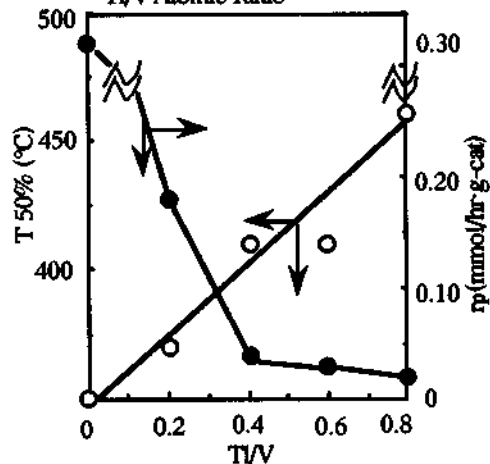
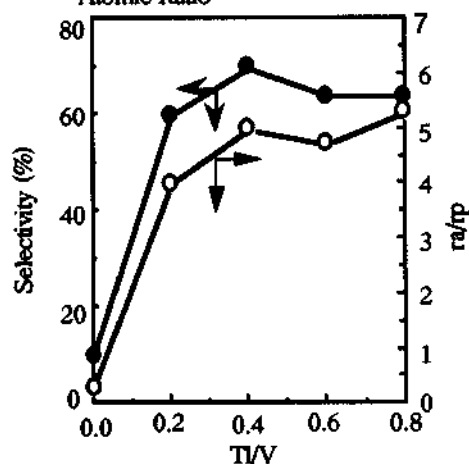


Fig. 3 The Relation between Selectivity and Basicity ( $r_a/r_p$ ) against Ti/V Atomic Ratio



and Ti composed catalysts, any good correlations were not observed as mentioned above. It suggests that other factors such as the acid and base strengths of the catalysts except acidity and basicity (acid amount and base amount) may affect the reaction behavior. The acid and base strengths of them were not measured here, because there is no useful method of a measurement the determination for acid and base strengths of such colored oxides catalysts.

Fig. 4 The Relation between Activity (T50%) and Acidity ( $r_p$ ) against Cs / V Atomic Ratio

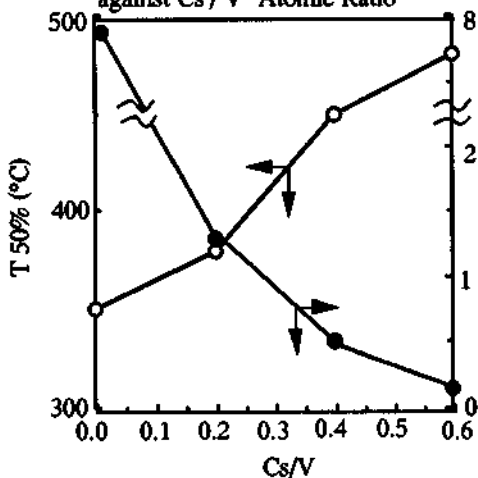
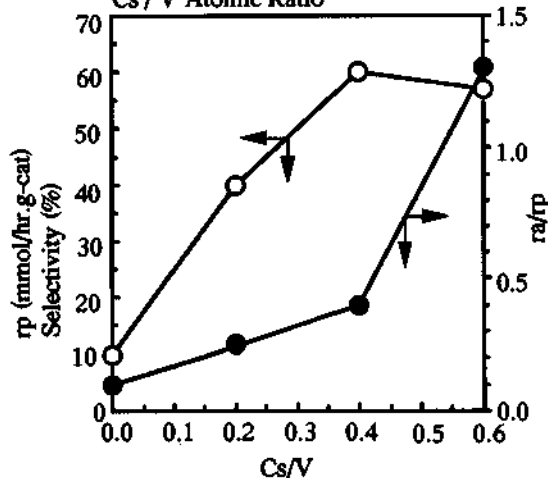


Fig. 5 The Relation between Selectivity and Basicity ( $r_a / r_p$ ) against Cs / V Atomic Ratio



### 3.3. Partial Oxidation of *p*-Substituted Toluene over V<sub>2</sub>O<sub>5</sub>-Tl<sub>2</sub>O

The vapor phase selective oxidation of various *p*-substituted toluenes(1) to the corresponding benzaldehydes over V<sub>2</sub>O<sub>5</sub>-Tl<sub>2</sub>O(Tl/V = 0.4 atomic ratio) were studied. In these reactions, *p*-methyl, *p*-isopropyl, *p*-*t*-butyl and *p*-methoxy substituted toluene were used as a reactant as shown in Table1. It was observed that these partial oxidations could be effectively performed with high activity and the selectivity. The products were corresponding benzaldehyde (2), benzoic acid (3), substituted benzene (4), CO, CO<sub>2</sub> (CO / CO<sub>2</sub> = 1 / 4 ~ 1 / 6 ; mole ratio ) and unknown products ( polymer and tar ). The para substituted methyl, isopropyl, *t*-butyl and methoxy groups activate aromatic methyl group of 1. The isopropyl group by itself is not so stable as other *p*-substituted groups. In the case of methoxy group which has a stronger electron donating ability than other substituted groups, the highest activity and the selectivity to *p*-methoxy benzaldehyde were observed. It is likely that the acidity and basicity of the catalyst promote the activation of aromatic methyl group of reactant and the desorption of a product from the surface of catalyst.

Table 1 Partial Oxidation Reactions of *p*-Substituted Toluene

Reactant R	Conversion /mol 1	Selectivity/mol% CO <sub>2</sub> +CO					Ionization potential/eV	
		2	3	4	CO <sub>2</sub>	Unknown	1	2
H	4.0	44.2	21.4	0.4	30.3	3.7	9.34	10.02
CH <sub>3</sub>	44.3	57.0	14.3	0.6	23.6	4.5	9.06	9.72
i-Pr	49.5	38.2	11.0	1.0	33.3	2.0	9.11	9.80
t-Bu	48.7	61.4	4.4	1.5	27.4	(14.5 <sup>a</sup> ) 5.3	9.09	9.80
OCH <sub>3</sub>	83.1	75.5	2.0	1.0	18.6	2.9	8.86	9.37

a) Toluic acid

Reaction conditions: Reaction temperature 430°C. Catalyst 5g.

Feed gas, 1.0vol% of reactant in air. Gas flow rate, 500ml/min(STP).

The values of the ionization potential (Ip) of *p*-substituted toluene (1) and *p*-substituted benzaldehyde calculated by Semi-Empirical Molecular Orbital Method, MOPAC , Ver. 6. ( PM 3 ), are shown in Table 1. The order of Ip value in *p*-substituted toluene (1) is as follows; R = OCH<sub>3</sub> < CH<sub>3</sub>, i-Pr, t-Bu < H. This means the electron donating ability of methoxy group is stronger than that of other substituted groups, namely *p*-methoxy toluene is easily activated on the catalyst by donating its electron to active sites on the catalyst which are supposed to be Lewis acid.

There is a good relationship between the Ip value of reactant and the activity in these reactions. On the other hand, the selectivity to *p*-substituted benzaldehyde

(2) was enhanced with decreasing its Ip value such as PMBA. This suggests that the elimination of 2 from the surface of catalyst is promoted with decreasing its Ip value. These results coincided well with the correlation observed between the Ip value of reactant and the reactivity in the vapor phase oxidation of hydrocarbons by Dadyburjor et al[8]. According to their report, the vapor phase selective oxidation of hydrocarbons over the acidic metal oxides catalysts is a type of reaction of [Base reactant] to [Acid product]. In the present work, the Ip values of main product 2 are larger than that of the reactants 1 as shown in Table 1. The present reactions are also the same type. From these results, it is supposed that the step of electron transfer from reactant to Lewis acidic site of the catalyst is a rate determining step in this partial oxidation reaction.

*p*-Substituted toluene changes cation radical form by the electron transfer to the catalyst, then V<sub>2</sub>O<sub>5</sub> is reduced to V<sub>2</sub>O<sub>4</sub>. On the other hand, V<sub>2</sub>O<sub>4</sub> is oxidized to V<sub>2</sub>O<sub>5</sub> again by molecular oxygen in air with the formation of O<sub>2</sub><sup>-</sup>. *p*-Substituted toluene cation radical is transformed to benzyl radical form through the attraction of proton from aromatic methyl group by O<sub>2</sub><sup>-</sup>. *p*-Substituted benzyl radical is oxidized to the corresponding aldehyde by the molecular oxygen.

The Tl element of catalyst controls the acidity and the basicity of catalyst active sites and promotes adsorption of reactant to the catalyst surface and elimination of the product from the surface of catalyst. The V<sub>2</sub>O<sub>5</sub>-Tl<sub>2</sub>O combination catalyst has proper acid and base properties for these *p*-substituted toluene partial oxidations.

### 3.4. Physical Properties of Catalysts

The V<sub>2</sub>O<sub>5</sub> based catalysts composed of an univalent element with large ionic radius such as Cs and Rb showed relatively higher selectivity to PMBA. However, Tl composed catalyst had also higher selectivity in spite of being bivalence states of Tl atom, Tl<sup>+</sup> and Tl<sup>3+</sup>. The valence state of Tl in V<sub>2</sub>O<sub>5</sub>-Tl<sub>2</sub>O (Tl/V = 0.4 atomic ratio) catalyst was measured by XRD analysis (Table 2). The XRD pattern of this catalyst showed the crystal structure of Tl<sub>3</sub>V<sub>5</sub>O<sub>14</sub> and TlV<sub>3</sub>O<sub>8</sub>, it was clear that the valence state of Tl atom in this catalyst was univalent. The crystal structures of other catalysts were shown in Table 2. The crystal structures of Ag and Cu composed catalyst were univalent and divalent, respectively. This means that V<sub>2</sub>O<sub>5</sub> based catalyst composing an univalent basic metal element shows relatively high selectivity to PMBA.

Table 2 Structure and melting point in V<sub>2</sub>O<sub>5</sub>-M<sub>m</sub>O<sub>n</sub> binary catalysts (M/V = 0.4, atomic ratio)

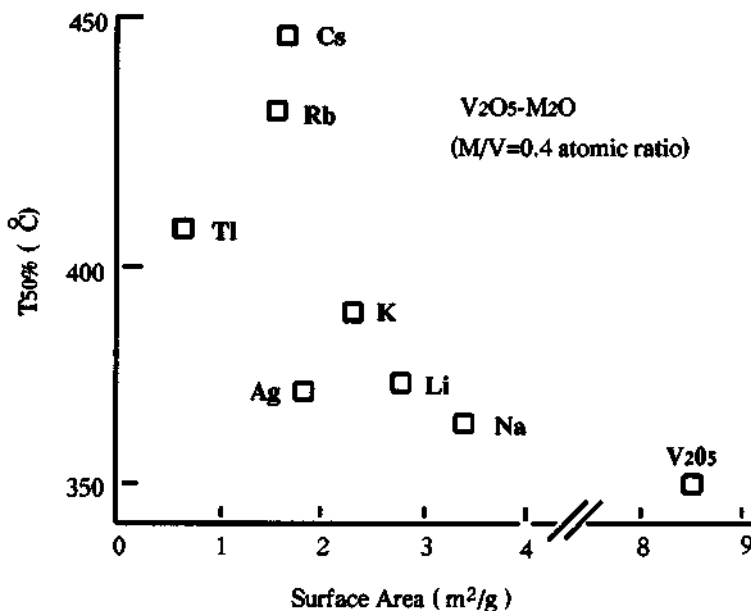
M	XRD pattern	m.p (°C)
Li	LiV <sub>3</sub> O <sub>8</sub>	575
Na	Na <sub>5</sub> V <sub>12</sub> O <sub>32</sub>	565
K	K <sub>2</sub> V <sub>8</sub> O <sub>21</sub>	470
Rb	Rb <sub>2</sub> V <sub>8</sub> O <sub>21</sub>	515
Cs	CsV <sub>3</sub> O <sub>8</sub>	470
Tl	Tl <sub>3</sub> V <sub>5</sub> O <sub>14</sub> , TlV <sub>3</sub> O <sub>8</sub>	400
Ag	(Ag <sub>2</sub> V <sub>4</sub> O <sub>11</sub> )	520
Cu	CuV <sub>2</sub> O <sub>6</sub>	670

It is generally said that V<sub>2</sub>O<sub>5</sub>-alkali metal oxide is in molten state at relatively lower temperature comparing with other mixed metal oxides (as shown in Table 2).

The XRD patterns of the V<sub>2</sub>O<sub>5</sub>-Tl<sub>2</sub>O ( Tl/V=0.4, atomic ratio) catalyst changed with elevating temperature, and crystal structure was transformed to the amorphous state at higher temperature. From results of XRD and DTA analysis, the surface of this catalyst was in molten and amorphous state at about 400 °C. The surface area is an important factor to improve an catalytic activity in the heterogeneous catalysis. The relationships between catalytic activity and surface area of V<sub>2</sub>O<sub>5</sub>-univalent metal oxide catalysts in this PMT oxidation were studied.

Figure 6 shows the relations of the reaction temperature in 50 % conversion of PMT against surface area of alkali metal, Tl and Ag composite catalysts. The lower reaction temperature means high activity. K<sub>2</sub>O, Rb<sub>2</sub>O, Cs<sub>2</sub>O, Ag<sub>2</sub>O and Tl<sub>2</sub>O composite catalysts which showed the higher selectivity to PMBA in Figure 1 had the small surface area ( 0.5 to 2.3 m<sup>2</sup> / g ) . It is very interesting that V<sub>2</sub>O<sub>5</sub>-Tl<sub>2</sub>O catalyst shows the higher activity and selectivity than V<sub>2</sub>O<sub>5</sub>-Rb<sub>2</sub>O and V<sub>2</sub>O<sub>5</sub>-Cs<sub>2</sub>O, in spite of its smallest surface area.

Fig. 6 Relation between Reaction Temperature and Surface Area of V<sub>2</sub>O<sub>5</sub>-M<sub>2</sub>O



This suggests that the effectiveness factor of V<sub>2</sub>O<sub>5</sub>-Tl<sub>2</sub>O catalyst appears in the molten state at higher reaction temperature, and furthermore the redox ability of this catalyst is enhanced. It was reported that the V<sub>2</sub>O<sub>5</sub>-K<sub>2</sub>SO<sub>4</sub> catalyst effectively worked under molten state in the vapor phase oxidation of naphthalene to phthalic anhydride[9]. In the not only PMT oxidation but also other *p*-substituted toluene, it seems that the molten state of catalyst surface through the reaction and harmonization between the acidity and the basicity are important factors to enhance the activity and the selectivity of the catalyst.

#### 4. CONCLUSIONS

The partial oxidation of *p*-substituted toluenes to *p*-substituted benzaldehydes can be effectively performed by use of V<sub>2</sub>O<sub>5</sub>-Tl<sub>2</sub>O (or Cs<sub>2</sub>O) binary oxide catalyst with the high activity and selectivity comparing with conventional oxidation catalysts such as V<sub>2</sub>O<sub>5</sub>, Cr<sub>2</sub>O<sub>3</sub> and MnO<sub>2</sub> or their mixed oxides.

The selectivity to *p*-substituted benzaldehyde relates to the basicity of catalyst and the activity depends on the acidity. These partial oxidation reaction are selectively carried out by harmonization of acid and base properties of a catalyst and, furthermore, under molten state of the catalyst surface through the reaction.

The elucidation of reaction behavior between the reactivity and the acid-base properties(amount and strength) of the catalyst under molten state of the active compositions of the catalyst at high reaction temperture is essential.

#### 5. REFERENCES

- 1) K. Shimizu, K. Kizawa, T. Yoshimoto, and J. Imamura, *J. Jpn. Petrol. Inst.*, 1982, 25, 7.
- 2) Y. Kamiya, *J. Catal.*, 1974, 33, 480.
- 3) I. Nishiguchi, and T. Hirashima, *J. Org. Chem.*, 1985, 50, 539.
- 4) H. Seko, Y. Tokuda, and M. Matsuoka, *Nippon Kagaku Kaishi*, 1975, 558.
- 5) N. Shimizu, N. Saito, and M. Ueshima, "Successful Design of Catalysis" Elsevir, 1988, 44, 131.
- 6) M. Ueshima, and N. Saito, *Chem. Lett.*, 1992, 7, 1341.
- 7) M. Ai, *Shokubai*, 1976, 18, 2, 17.
- 8) D. B. Dadyburjor, S. Jewur, and E. Ruckenstein, *Catal. Rev. Sci. Eng.*, 1979, 19, 293.
- 9) H. Kakinoki, N. Sahara, I. Kamata, and Y. Aigami, *Shokubai*, 1962, 4, 113.

## 1.7 The Role of Alcohols on Lactam Selectivity in the Vapor-Phase Beckmann Rearrangement Reaction

M. Kitamura and H. Ichihashi

Organic Synthesis Research Laboratory, Sumitomo Chemical Co., Ltd.  
Takatsuki-City, Osaka 569, Japan

### Abstract

For the vapor-phase Beckmann rearrangement reaction of cyclohexanone oxime over high-silicious pentasil zeolites, the selectivity to  $\epsilon$ -caprolactam increased when methanol was supplied with cyclohexanone oxime into the reaction system. FT-IR measurements showed that the neutral silanol groups of the zeolite were methylated by the alcohol. This indicates that the neutral silanol is not the active site for producing  $\epsilon$ -caprolactam.

### 1. INTRODUCTION

$\epsilon$ -caprolactam is an important starting material for the production of nylon-6 polymers. It is commercially synthesized by the Beckmann rearrangement reaction of cyclohexanone oxime using fuming sulfuric acid in the liquid phase. The reaction in this system proceeds with a high selectivity to  $\epsilon$ -caprolactam. The process is considered to be disadvantageous, however, because it produces a large amount of ammonium sulfate as a by-product. Recently Sato et al. reported that a highly silicious pentasil zeolite treated with trimethylchlorosilane had the effect of greatly increasing the selectivity to lactam. [1-2]

### 2. EXPERIMENTAL METHOD

#### 2.1. Preparation of Catalysts

Tetraethylorthosilicate, 10% aqueous tetra-n-propylammonium hydroxide solution, and water were charged in an autoclave. A hydrothermal reaction was conducted at 105°C for 96 hours. White solids were filtered out, washed, and dried. The crystals were then calcined at 530°C. The ion-exchange treatment by 5% aqueous ammonium chloride solution was carried out at 60°C for 1 hour. This treatment was repeated four times.

#### 2.2. Reaction Procedure

The reaction was carried out using a fixed-bed type reactor at atmospheric pressure. The reaction temperature was 350°C. Cyclohexanone oxime was fed as a benzene solution. The reaction products were analyzed by G.C.

### 2.3. FT-IR Measurement

A diffuse reflection type FT-IR was used. The catalyst was pretreated at 350°C for 1 hour in a helium atmosphere. The spectra were measured at 350°C in an atmosphere of helium gas containing methanol vapor.

## 3. RESULTS AND DISCUSSION

### 3.1. Effects of Additives

Table 1 shows the effects of additives on catalytic performance. When oxime was fed with methanol, the selectivity to lactam increased to more than 90%. The same effect was observed when oxime was fed with other alcohols. The longer the length of the alkyl chain, however, the larger the decline of catalytic activity. The other solvents, for example, phenol, acetaldehyde, and acetic acid, did not increase the selectivity to lactam.

In addition, another interesting point was discovered. The methanol used as an additive was recovered quantitatively. Generally speaking, methanol converts to hydrocarbons on a ZSM-5 type zeolite, but in this case, this reaction did not occur.

As shown in Table 2, when some kinds of other catalysts were used instead of highly silicious pentasil zeolite, the effect of methanol to increase the selectivity to lactam was not observed. When borontrioxide was used as a catalyst, the reaction could not be continued, because the boron is lost from the catalyst as a methyl ester.

Table 1. Effect of Additives (1)

additives	conv. (%)	sel (%)
Benzene	100 → 98.6	78
CH <sub>3</sub> OH	100 → 99.6	92
C <sub>2</sub> H <sub>5</sub> OH	99.0 → 97.0	92
n-C <sub>3</sub> H <sub>7</sub> OH	96.6 → 92.6	91
iso-C <sub>3</sub> H <sub>7</sub> OH	99.8 → 94.3	91
C <sub>6</sub> H <sub>5</sub> OH	40.5 → 21.4	79
CH <sub>3</sub> CHO	99.6 → 94.2	79
CH <sub>3</sub> COOH	100 → 85.2	73 → 63

Table 2. Effect of additives (2)

catalyst	Lactam sel. (%)	Benzene	Methanol
Pentasil zeolite (Si/Al=147000)	78	92	
Silica-Alumina (Al <sub>2</sub> O <sub>3</sub> 13wt%)	66	58	
Silica-Alumina (Al <sub>2</sub> O <sub>3</sub> 28wt%)	52	60	
Silica	29	30	
Boron trioxide	90	—	

\*Catalyst: Pentasil zeolite  
(Si/Al=147000)

\*Oxime/Solvent=3.5~4.0  
(mol ratio)

\*W/F=41~43  
(g-cat/mol-oxime/hr)

\*1) 1st hour \*2) 6th hour

\*Oxime/Solvent=3.5~4.0 (mol ratio)

\*W/F=41~43 (g-cat/mol-oxime/hr)

In order to identify precisely the role of alcohols on lactam selectivity, we studied the effect between the selectivity and the methanol/oxime weight ratio. The results are shown in Fig. 1. Up to a methanol/oxime weight ratio of one, the selectivity to lactam increases gradually. And over the methanol/oxime weight ratio of one, the selectivity to lactam reaches a constant value of over 90%, but the conversion of oxime decreases.

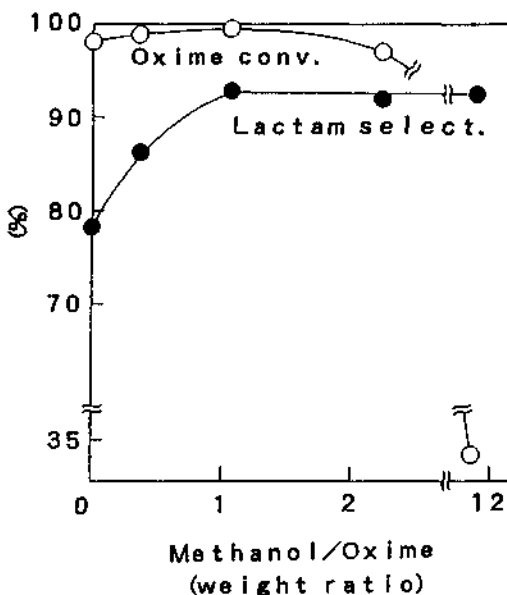


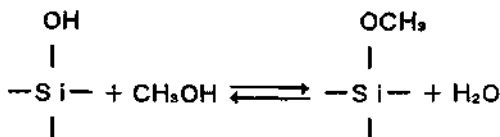
Fig. 1. Effect of Methanol/Oxime Ratio

This result indicates that the interaction between methanol and the catalyst is very important. In the range of the lower methanol/oxime weight ratio, the stronger the interaction between methanol and the zeolite, the greater the selectivity to lactam. On the other hand, in the range of the higher methanol/oxime weight ratio, strong adsorption of methanol on the catalyst surface occurs, decreasing the conversion.

### 3.2. Modification of the Catalyst Surface by Alcohols

To completely understand the interaction between methanol and catalyst, the FT-IR spectra of catalysts treated with methanol were measured by a diffuse reflection type FT-IR. Fig. 2 shows the FT-IR spectra of the catalyst: one is treated with methanol and the other is not. The non-treated catalyst has a sharp IR absorption at  $3740\text{ cm}^{-1}$ , which is attributed to the neutral silanol. In the case of the catalyst treated with methanol, however, this peak decreases notably and a new peak at  $2970\text{ cm}^{-1}$  is clearly observed. This is attributed to the C-H stretching of the methyl group. These data indicate that the neutral silanol is methylated by methanol, and we believe this phenomenon to be the main reason enhancing the selectivity to lactam (Scheme 1).

(Scheme 1)



This result shows that the neutral silanol groups on the zeolite are not the active sites for converting oxime to lactam; on the contrary, it disturbs the smooth rearrangement reaction. The loss of catalytic activity is quick when the alcohols with a long alkyl chain are fed into the reaction system. It is suggested that the long alkyl chains, which modify the neutral silanol of the catalyst, cover the active sites and block the smooth rearrangement reaction.

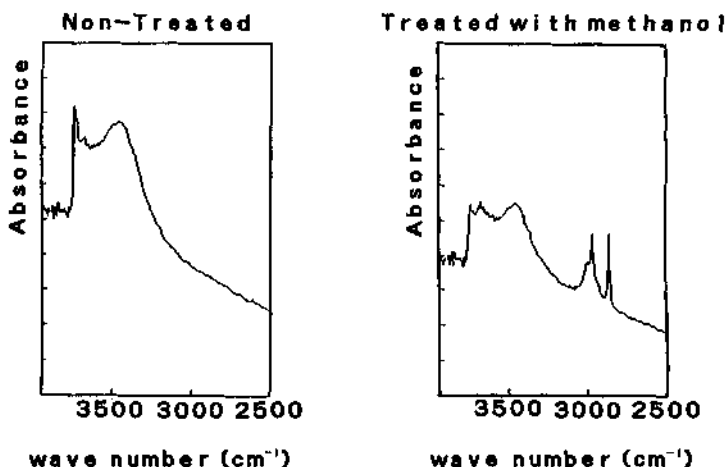


Fig. 2. FT-IR Spectra of Zeolite

#### REFERENCES

1. H. Sato, N. Ishii, K. Hirose, and S. Nakamura, Proc. 7th Int. Zeolite Conference, 1986, 755
2. H. Sato, K. Hirose, M. Kitamura, and Y. Nakamura, Proc. 8th Int. Zeolite Conference, 1989, 1213

## 1.8 Direct Amination of Lower Alkenes with Ammonia over Zeolite Catalysts

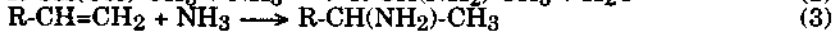
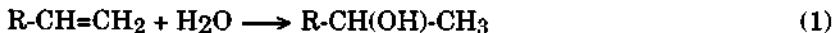
Noritaka Mizuno, Masahiro Tabata, Takeshi Uematsu, and Masakazu Iwamoto  
Catalysis Research Center, Hokkaido University, Sapporo 060, Japan

### Abstract

The reaction between ethene or 2-methylpropene and ammonia in the presence or absence of water vapor was studied over various zeolite catalysts, solid acid catalysts, and solid base MgO. The proton-exchanged zeolites were effective for the amination. The addition of water vapor increased the activity of H-MFI-41 for the amination of ethene while the activity for the amination of 2-methylpropene was hardly changed. It was clarified that amounts and strength of Brønsted acid sites are factors controlling the direct amination of 2-methylpropene and that due to the proper possession of above two factors proton-exchanged ZSM-5 zeolite with silica/alumina ratio of 81 was the most active among the catalysts tested.

### 1. INTRODUCTION

Zeolites can catalyze a wide variety of reactions and have practically been of importance in the catalytic cracking and residual hydrocracking because of their acidic properties and microporous structures [1]. We also reported that the hydration (Eq. (1)) [2-4] and ketonization [5-7] of lower alkenes were efficiently catalyzed by proton-exchanged zeolites.



Aliphatic amines are commercially important and have been industrially made by the reaction between the corresponding alcohols and ammonia (Eq. (2)) [8]. Recently, selective synthesis of dimethylamine from methanol and ammonia on small pore zeolites has also been reported [9]. Since the alcohols are usually obtained through the direct or indirect hydration of the alkene with the same carbon number (Eq. (1)), it would be more desirable to avoid the alcohol and synthesize the amine by a direct reaction between alkene and ammonia (Eq. (3)) [10]. Direct amination of ethene to ethylamine has been achieved using alkali metal catalysts in homogeneous system [11]. However, these system provide low yields of higher alkylamines.

As for the direct amination of alkenes with the carbon number more than two, Deeba et al. reported that the amination of 2-methylpropene was promoted by Y-type and mordenite zeolites in heterogeneous system [12,13]. Recently, we reported that the direct amination of 2-methylpropene was most efficiently catalyzed by proton-exchanged ZSM-5 zeolite with silica/alumina ratio of 50 among various oxide catalysts [14]. In the present paper the amination of ethene and 2-methylpropene over zeolite catalysts, solid acid catalysts, and solid base MgO has been studied.

## 2. EXPERIMENTAL

### 2.1. Catalysts

Parent zeolites, ZSM-5 (denoted as MFI) with silica/alumina ratio of 23, 40, and 50, ferrierite (FER), L-type (LTL), offretite/erionite (OFF/ERI), mordenite (MOR), and Y-type (FAU) zeolites were supplied by Tosoh Corporation. ZSM-5 zeolites with silica/alumina ratio of 93 and 1340 were supplied by Catalysis Society of Japan. The other ZSM-5 zeolites were prepared by hydrothermal crystallization of alkaline reaction mixtures in a similar method to that described in Mobil's patent [15]. Ultrastable Y-type zeolites were prepared by steaming.  $Cs_xH_{3-x}PW_{12}O_{40}$  ( $x = 2.5 - 3.15$ ) catalysts were prepared according to ref. [16]. The other catalysts were commercially obtained.

Each proton-exchanged zeolite was prepared according to the literatures [2-4]. The amounts of Al, Si, and Na or K in each zeolite were determined by atomic absorption spectroscopy after the zeolite samples were dissolved in hydrogen fluoride solution and silica/alumina ratios in the zeolite framework were determined by  $^{29}Si$  MASNMR as described previously [6,7]. The catalysts were abbreviated as H-MFI-81 (cation-zeolite structure-silica/alumina ratio). The exchange level of proton in each zeolite was approximately 100% except for H-FAU-6 (72%).

The  $SiO_2/Al_2O_3$  ratios obtained by atomic absorption spectroscopy well agreed with those obtained by  $^{29}Si$  MASNMR in the case of H-MFI, H-MOR, and H-LTL zeolites, showing that there is no extraframework aluminum ion on these zeolites and that little dealumination was occurred during the preparation. Therefore, the later discussion would not be affected by the extraframework aluminum ion. The  $SiO_2/Al_2O_3$  ratios of two kinds of ultrastable Y-type zeolites (H-FAU) were 5.9 and 14 by atomic absorption spectroscopy and 12 and 40 by  $^{29}Si$  MASNMR. Clearly, the difference is due to dealumination and therefore the latter values were used hereafter for the abbreviation. The  $SiO_2/Al_2O_3$  ratios of zeolite numbers 1 - 19 correspond to 1340, 129, 113, 93, 81, 50, 40, 23, 23 (Na form), 19, 15, 15 (Na form), 40, 12, 5.6, 5.6 (Na form), 17, 8.0, and 6.0, respectively. Sample numbers 20 - 22 correspond to  $Cs_{2.5}H_{0.5}PW_{12}O_{40}$ ,  $Cs_{2.85}H_{0.15}PW_{12}O_{40}$ , and  $Cs_{3.15}PW_{12}O_{40}$ , respectively.

The total amount of acidic sites on zeolites were obtained from the profiles of temperature programmed desorption of ammonia as has been described previously [2].

### 2.2. Infrared Spectra

All self-supporting disks of H-MFI-40 (7 - 20 mg, 2 cm in diameter) were prepared by pressing powder under a pressure of  $300 \text{ kg}\cdot\text{cm}^{-2}$  for 30 min and the IR spectra were recorded at 298 K with an IR-810 spectrometer (Japan Spectroscopic Co., Ltd.).

The ratio of the amount of Brønsted acid sites to that of Lewis acid sites on H-MFI-40 was studied by the pyridine adsorption method. After a H-MFI-40 disk was evacuated in an in situ IR cell at 423 - 973 K for 1 h, it was exposed to pyridine vapor (ca. 10 mmHg) at 423 K for 2 h and evacuated at the same temperature for 1 h. The IR spectra were recorded at 298 K. In a similar way, the acidic properties of H-MFI-93, -81, and -23, H-MOR-15 and -19,  $Cs_{2.85}H_{0.15}PW_{12}O_{40}$  and  $SiO_2-Al_2O_3$  were measured. The IR bands at  $1545$  and  $1455 \text{ cm}^{-1}$  assigned to pyridinium ion and coordinatively bound pyridine, respectively, were used to determine the relative concentrations of Brønsted and Lewis acid sites. Due to the difficulty in measuring the weak IR absorption bands of pyridine adsorbed on high-silica zeolites, this method could be applied to the zeolites with the  $SiO_2/Al_2O_3$  ratios of 93 or less.

### 2.3. Reaction

The reaction of ethene and 2-methylpropene with ammonia was carried out in a conventional flow reactor at 473 K at an atmospheric pressure using 0.5 - 1.0 g

catalysts. Before the experimental run the catalysts were treated in a  $N_2$  stream ( $20 \text{ cm}^3 \cdot \text{min}^{-1}$ ) at 573 - 973 K for 1 h except for  $Cs_xH_{3-x}PW_{12}O_{40}$  ( $x = 2.5 - 3.15$ ) samples, which were used without the treatment due to the thermal instability. The standard treatment temperature in  $N_2$ , flow rates of alkene and ammonia, and catalyst weight were 773 K,  $4.0 \text{ cm}^3 \cdot \text{min}^{-1}$ ,  $16.0 \text{ cm}^3 \cdot \text{min}^{-1}$ , and 1.0 g, respectively, unless otherwise stated. The reactants and products were analyzed by gas chromatography.

### 3. RESULTS AND DISCUSSION

#### 3.1. Reaction

Figure 1 shows the time course of the conversion into t-butylamine from 2-methylpropene and ammonia on H-MFI-40 at 473 K. The conversion into t-butylamine increased with time and an approximately steady formation of t-butylamine was attained after 2 h. The same product distribution and similar increases of the conversion with time to those on H-MFI-40 were observed for the other catalysts. Little oligomerization and isomerization products were observed and the selectivity was less than 1%. The number of t-butylamine formed per number of Al content or Brønsted acid site after a 30 h reaction on H-MFI-40 was greater than 2, showing that the reaction is catalytic. The initial small value (0.14%) of the conversion into t-butylamine at 0.67 h is probably due to the adsorption of the basic t-butylamine on the acidic sites of the catalysts. A similar increase in the conversion into ethylamine was observed for the amination of ethene. The low conversion of 2-methylpropene to t-butylamine is probably due to the equilibrium limitation between starting materials (2-methylpropene and ammonia) and the product (t-butylamine).

The activities of various catalysts at 473 K are summarized in Table 1. H-MFI-81 showed the highest activity among the zeolite catalysts, solid acid catalysts ( $Cs_xH_{3-x}PW_{12}O_{40}$  ( $x = 2.5 - 3.15$ ),  $SiO_2-Al_2O_3$ ,  $SiO_2-TiO_2$ ), and solid base  $MgO$ . It is noted that the selectivity to t-butylamine is more than 95% for each zeolite.

When the water vapor was added to the reactant gases of 2-methylpropene and ammonia, the activity of each zeolite little changed and the selectivity to t-butylamine slightly decreased to 87 - 97% from 95 - 100% due to the formation of 2-methyl-2-propanol. Thus, the addition of water vapor did not improve the catalytic properties.

On the other hand, the addition of water vapor increased the activity of H-MFI-40 for the reaction of ethene with ammonia by a factor of about two. Table 2 summarizes the catalytic properties of various oxide catalysts in the presence of water vapor. The activities decreased in the order of proton-exchanged zeolites > mixed metal oxides  $\geq$  metal ion-exchanged zeolites except for H-FAU-12 and -40. H-MOR-15 was the most active among the catalysts tested. The selectivity to ethylamine was 33 - 77% upon proton-exchanged zeolites and the major by-product was ethyl alcohol.

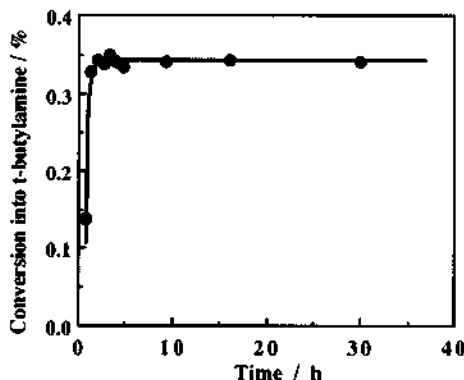


Fig. 1. Time course of the conversion into t-butylamine from 2-methylpropene and ammonia on H-MFI-40 at 473 K. Catalyst weight, 0.5 g. 2-Methylpropene,  $4.0 \text{ cm}^3 \cdot \text{min}^{-1}$ ; ammonia,  $16.0 \text{ cm}^3 \cdot \text{min}^{-1}$ .

Table 1. Catalytic activities of various catalysts for the amination of 2-methylpropene into t-butylamine at 473 K<sup>a)</sup>

Catalyst	Conv. <sup>b)</sup> %	Select. <sup>c)</sup> %
H-MFI-81	1.73	99
H-MFI-93	1.18	99
H-MFI-113	0.90	98
H-MFI-50	0.85	99
H-MFI-129	0.80	99
H-MFI-40	0.68	99
H-MFI-23	0.62	99
H-MOR-19	0.53	99
H-MOR-15	0.42	99
H-FAU-40	0.22	95
H-LTL-6	0.11	99
H-FAU-12	0.06	99
H-OFF/ERI-8	0.05	98
H-MFI-1340	0.04	99
H-FAU-6	0.04	99
H-FER-17	0.02	99
Na-MFI-40	0.01	99
Na-FAU-6	0.01	99
Na-MOR-15	0	-
Cs <sub>2.5</sub> H <sub>0.5</sub> PW <sub>12</sub> O <sub>40</sub>	0.17	89
Cs <sub>2.85</sub> H <sub>0.15</sub> PW <sub>12</sub> O <sub>40</sub>	0.15	84
SiO <sub>2</sub> -Al <sub>2</sub> O <sub>3</sub>	0.08	98
SiO <sub>2</sub> -TiO <sub>2</sub>	0.03	100
Al <sub>2</sub> O <sub>3</sub>	0.01	99
Cs <sub>3.15</sub> PW <sub>12</sub> O <sub>40</sub>	0	-
MgO	0	-

a) 2-Methylpropene, 4.0 cm<sup>3</sup>·min<sup>-1</sup>; ammonia, 16.0 cm<sup>3</sup>·min<sup>-1</sup>; catalyst weight, 1.0 g. b) Mol t-butylamine formed/mol 2-methylpropene introduced. c) Mol t-butylamine formed/total mol of products.

Table 2. Catalytic properties of various catalysts for the amination of ethene into ethylamine at 623 K<sup>a)</sup>

Catalyst	Conv. <sup>b)</sup> %	Select. <sup>c)</sup> %
H-MOR-15	0.19	77
H-FER-17	0.17	72
H-MFI-50	0.14	87
H-MFI-40	0.14	60
H-MOR-11	0.14	48
H-MFI-23	0.11	48
H-FAU-40	0.04	38
H-FAU-12	0.01	33
Cu-MOR-11	0.07	57
Mg-MOR-15	0.03	73
Ni-MOR-15	0.03	6
Co-MOR-15	0.02	4
Zn-MOR-15	Trace	2
Na-MOR-15	Trace	16
SiO <sub>2</sub> -Al <sub>2</sub> O <sub>3</sub>	0.11	79
TiO <sub>2</sub> -ZrO <sub>2</sub>	0.07	72
SiO <sub>2</sub> -TiO <sub>2</sub>	0.06	94
SiO <sub>2</sub> -ZrO <sub>2</sub>	0.05	80

a) Ethene, 7.5 cm<sup>3</sup>·min<sup>-1</sup>; ammonia, 7.5 cm<sup>3</sup>·min<sup>-1</sup>; water vapor, 0.68cm<sup>3</sup>·min<sup>-1</sup>; catalyst weight, 1.0 g. b) Mol ethylamine formed/mol ethene introduced. c) Mol ethylamine formed/total mol of products.

### 3.2. Factors Controlling Catalytic Activity of Direct Amination of 2-Methylpropene

The conversions into t-butylamine were much decreased from 0.68 to 0.01% by the Na<sup>+</sup> substitution for H<sup>+</sup> in H-MFI-40, the preadsorption of diisopropylamine greatly decreased the initial rate of t-butylamine formation on H-MFI-40, and MgO showed little activity, suggesting that the amination of 2-methylpropene is catalyzed by the acidic sites.

Next, we investigated how the catalytic activities can be recognized by Brønsted or Lewis acidity. Figure 2 shows the changes in the catalytic activity and the number of Brønsted acid sites of H-MFI-40 with the pretreatment (evacuation) temperature. The conversion (○) was constant in the range of 473 - 773 K and then a little decreased above 773 K. The number of Brønsted acid sites (●) similarly changed with the evacuation temperature, but that of Lewis acid sites

changed in a different way. The parallel change of the catalytic activity of H-MFI-40 with the amount of Brønsted acid site at elevated temperatures supports that the direct amination of 2-methylpropene is catalyzed by the Brønsted acidity. The fact that  $Cs_xH_{3-x}PW_{12}O_{40}$  ( $x = 2.5, 2.85$ ) heteropoly compounds having only Brønsted acid sites showed the activity for the amination while  $Al_2O_3$  having only Lewis acid sites showed little activity also supports the above idea.

Figure 3 shows the correlation between the activity of the various catalysts and the amounts of Brønsted acid sites. The conversions increased with the amounts of Brønsted acid sites, reached the maximum at H-MFI-81, and then decreased. The increase was consistent with the idea that Brønsted acid sites are the active centers. The decrease shows that the amination is not a simple function of the amount of Brønsted acid sites and is probably due to the lower acid strength as investigated in the later part.

Figure 4 shows the correlation between the turnover frequencies per Brønsted acid site and the  $SiO_2/Al_2O_3$  ratios of zeolites. The turnover frequencies can be expressed by one line and increased with the increment of the  $SiO_2/Al_2O_3$  ratios up to 93. Therefore, the decrease of the conversion above the amount of Brønsted acid site of  $0.09 \text{ mmol}\cdot\text{g}^{-1}$  in Fig. 3 is probably due to the change of the turnover frequencies. On the basis of the report that the acid strength increases with increasing the  $SiO_2/Al_2O_3$  ratios [18], the increase of the turnover frequencies in Fig. 4 is probably due to the increment of the acid strength. Thus, not only the amounts of Brønsted acid sites but also the acid strength is an important factor for the present reaction as has been usually interpreted in the cracking of alkanes [19]. Due to the proper possession of the above two factors, H-MFI-81 is the most active for the reaction to form directly t-butylamine among the catalysts tested.

Consequently, the above consideration made clearer the proposal by Deeba et al. that the formation of t-butylamine would involve a cationic intermediate on the zeolite surface [13]. By analogy with the observation of t-butyl and isopropyl cation on H-FAU zeolite [20] and the reaction mechanism for the hydration of ethene [21], the cationic intermediate is probably the t-butyl cation. t-Butyl cation may be formed through the protonation of 2-methylpropene by a surface

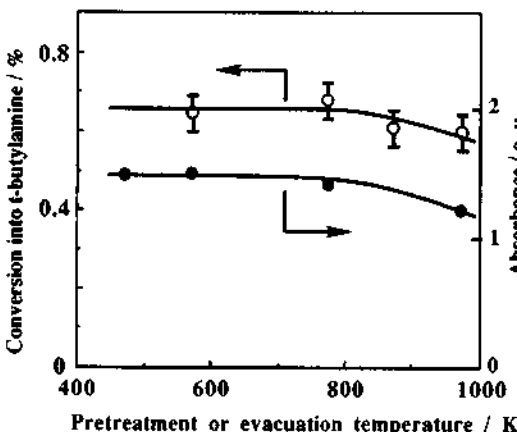


Fig. 2. Change in the conversion into t-butylamine and the amount of Brønsted acid sites with the pretreatment temperature. Sample, H-MFI-40. ○, the conversion into t-butylamine; ●, the relative integrated intensities of the  $1545\text{-cm}^{-1}$  band of pyridine.

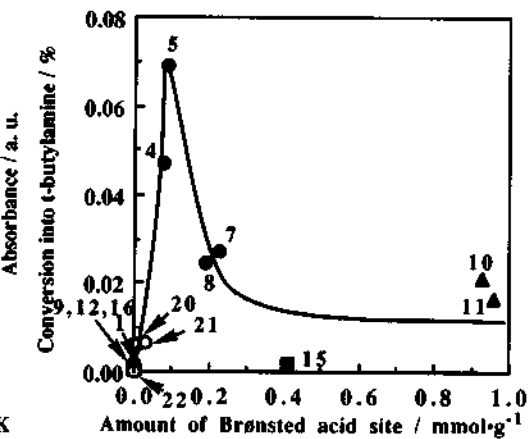


Fig. 3. Correlation between the conversions into t-butylamine and the amounts of Brønsted acid sites. ●, MFI; ▲, MOR; ■, FAU; ○,  $Cs_xH_{3-x}PW_{12}O_{40}$ .

Brønsted acid site or ammonia. Subsequently the Brønsted acid site is regenerated by the desorption of t-butylamine.

#### 4. ACKNOWLEDGMENTS

We thank Prof. T. Yashima (Tokyo Institute of Technology) for helping to synthesize ZSM-5 zeolite catalysts. This work was supported by a Grant-in-Aid for Scientific Research from the Ministry of Education, Science and Culture of Japan.

#### 5. REFERENCES

- 1) Y. Ono, *Catal. Rev.-Sci. Eng.*, 1992, 34, 179; J. A. Rabo and G. J. Gajda, *Catal. Rev.-Sci. Eng.*, 1989-90, 31, 385.
- 2) M. Iwamoto, M. Tajima, and S. Kagawa, *J. Catal.*, 1986, 101, 195.
- 3) M. Iwamoto, H. Yahiro, H. Mori, and I. Takasu, in "Catalytic Science and Technology", (S. Yoshida, N. Takezawa, and T. Ono, Eds.), Vol. 1, p. 415. Kodansha, Tokyo, 1991.
- 4) H. Mori, N. Mizuno, T. Shirouzu, S. Kagawa, and M. Iwamoto, *Bull. Chem. Soc. Jpn.*, 1991, 64, 2681.
- 5) H. Mori, H. Ueno, N. Mizuno, H. Yahiro, and M. Iwamoto, *Chem. Lett.*, 1990, 2289.
- 6) H. Mori, N. Mizuno, M. Tajima, S. Kagawa, and M. Iwamoto, *Catal. Lett.*, 1991, 10, 35.
- 7) N. Mizuno, H. Mori, M. Tajima, S. Kagawa, H. Ueno, H. Yahiro, and M. Iwamoto, *J. Mol. Catal.*, 1993, 80, 229.
- 8) A. E. Schweizer, R. L. Fowlkes, J. H. McMakin, and T. E. Whyte, in "Encyclopedia of Chemical and Technology", (H. F. Mark, D. F. Othmer, C. G. Overberger, and G. T. Seaborg, Eds.), Vol. 2, p. 272. John Wiley, New York, 1978.
- 9) K. Segawa and H. Tachibana, *J. Catal.*, 1991, 131, 482.
- 10) J. F. Roth, *Stud. Surf. Sci. Catal.*, 1990, 54, 3.
- 11) M. R. Gagné, C. L. Stern, and T. J. Marks, *J. Am. Chem. Soc.*, 1992, 114, 275.
- 12) M. Deeba, M. E. Ford, and T. A. Johnson, in "Catalysis", (J. W. Ward, Ed.), p. 221. Elsevier Science Publishers B. V., Amsterdam 1987.
- 13) M. Deeba and M. E. Ford, *J. Org. Chem.*, 1988, 53, 4594.
- 14) M. Tabata, N. Mizuno, and M. Iwamoto, *Chem. Lett.*, 1991, 1027; N. Mizuno, M. Tabata, T. Uematsu, and M. Iwamoto, *J. Chem. Soc., Faraday Trans.*, 1993, 89, 3513; idem., *J. Catal.*, in press.
- 15) British Patent 1972, 1,402,981.
- 16) S. Tatematsu, T. Hibi, T. Okuhara, and M. Misono, *Chem. Lett.*, 1984, 865.
- 17) S. Namba, N. Hosonuma, and T. Yashima, *J. Catal.*, 1981, 72, 16.
- 18) P. A. Jacobs, W. J. Mortier, and J. B. Uytterhoeven, *J. Inorg. Nucl. Chem.*, 1978, 40, 1919; W. J. Mortier and P. Geerlings, *J. Phys. Chem.*, 1980, 84, 1982.
- 19) I. Wang, T. J. Chen, K. J. Chao, and T. C. Tsai, *J. Catal.*, 1979, 60, 140.
- 20) N. D. Lazo, B. R. Richardson, P. D. Schettler, J. L. White, E. J. Munson, and J. F. Haw, *J. Phys. Chem.*, 1991, 95, 9420.
- 21) K. Tanabe, M. Misono, Y. Ono, and H. Hattori, "New Solid Acids and Bases", p. 252. Kodansha-Elsevier, Tokyo-Amsterdam, 1989.

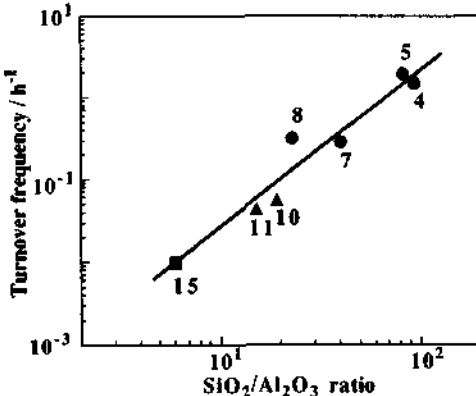


Fig. 4. Correlations between the  $\text{SiO}_2/\text{Al}_2\text{O}_3$  ratios the turnover frequencies.<sup>a</sup> a Turnover frequencies, amounts of t-butylamine formed per 1 h / amounts of Brønsted acid sites. ●, H-MFI; ▲, H-MOR; ■, H-FAU.

## 1.9 Etherification of Diethylene Glycol with Ethanol on Heteropolyacid

Qi Yunshi, Liu Jingfun, Wu Haixia and Su Xiaoli  
East China University of Science and Technology  
130 Meilong Road, Shanghai 200237, China

### Abstract

In the paper, catalytic performance of HPA (heteropolyacid) and the effects of thermal treatment on heteropolyacids such as  $H_3PMo_{12}O_{40}$ ( $PMo_{12}$ ),  $H_3PW_{12}O_{40}$ ( $PW_{12}$ ) and  $H_4SiW_{12}O_{40}$ ( $SiW_{12}$ ) have been studied by the etherification of diethylene glycol with ethanol. It has been shown that  $PW_{12}$  and  $SiW_{12}$  have high activities for the etherification, the conversion being 97.5 and 93.8 percent respectively. Also, the activity of  $PMo_{12}$  is lower and its conversion is only 45.3 percent. After treatment at 350 °–500°C for 3hr, the activity and selectivity of ether for three heteropolyacids decrease with the increase in treatment temperature. By IR, XRD, TG and n-butylamine titrimetry, the effect of thermal treatment has been studied and the order of thermal stability for three heteropolyacids is shown to be as follows:



### 1. INTRODUCTION

There are three kinds of methods by which diethylene glycol ether can be prepared with diethylene glycol: (1) diethylene glycol reaction with haloalkane over NaOH catalyst, (2) diethylene glycol reaction with ethylene oxide over NaOH catalyst, (3) diethylene glycol reaction with ethanol by catalysis of sulfuric acid. The cost of the first and second is high and their yield of ether is low. The final one is unfavorable to industrial production due to the corrosion of sulfuric acid.

Heteropolyacids possess the properties of acidity and redox [1–3]. It has been shown that the main catalysis of HPA occurs through B acid [4]. It has been reported [5] that the rates of dehydration and etherification are directly proportional to the total acidity of heteropolyacids. For etherification HPA shows excellent catalytic activity [6]. So, in the paper, using HPA as catalysts for the reaction of diethylene glycol and ethanol, catalytic performance, thermal stability, and the effect of thermal treatment on the catalytic performance are examined by many methods such as IR, XRD and TG.

### 2. EXPERIMENT

#### 2.1 Experimental Apparatus and Reaction Method

Etherification proceeds in a 400ml autoclave, with electromagnetic stirring and electric furnace heating through a temperature controller. Also, there is a sampling tube connected to the autoclave. The autoclave and sampling tube are made of stainless steel.

**Reaction method:** 100g diethylene glycol, 86g ethanol (molar ratio 2 : 1) and 0.5 wt% catalyst are placed into an autoclave. First, put in nitrogen to 17 kgf / cm<sup>2</sup>, then raise temperature up to 200°C, the pressure is up to 50 kgf / cm<sup>2</sup>. The reaction then occurs under stirring and after 2hrs, it is sampled and analyzed.

## 2.2 Analysis Method

The products are quantitatively analyzed with internal standard by thermal conduct detector of 102 G-type gas chromatograph made by the Shanghai Analysis Instrument Factory.

## 2.3 Catalyst

The catalysts H<sub>3</sub>PW<sub>12</sub>O<sub>40</sub> • 29H<sub>2</sub>O, H<sub>4</sub>SiW<sub>12</sub>O<sub>40</sub> • 26H<sub>2</sub>O and H<sub>3</sub>PMo<sub>12</sub>O<sub>40</sub> • 28H<sub>2</sub>O, all of grade AR, were calcined at 350 °, 400 °, 450 °, and 500°C in air.

## 2.4 Catalyst Characterization

Surface acidity is measured by n-butylamine titrimetry.

IR spectrum: measuring by 5 SXC-type instrument made in Nicolet, America, with KBr tablet.

XRD: measuring by XD-3A type made in Japan with Cu K<sub>α</sub> radiation and Ni filter.

TG: measuring by DT-2B type instrument made in Japan. Condition: the rate of raising temperature is 3°C / min, paper rate 0.35cm / min.

## 3. RESULTS AND DISCUSSION

### 3.1 Study on the Reaction Condition over SiW<sub>12</sub>

#### (1) The effect of reaction temperature

The reaction conditions are as follow:

Pressure 50 kgf / cm<sup>2</sup>, feed: the ratio of diethylene glycol to ethanol, 1 : 2 (molar ratio); the catalyst concentration 0.5 wt%; reaction time, 2hr.

Under the above reaction conditions, reaction temperature varies from 140 ° to 220°C. The results are shown in Fig.1.

Figure 1 shows that the relation of the conversion to the reaction temperature is linear and that conversion increases with rising temperature. The selectivity for DME will decrease with rising temperature. However, the selectivity for DDE will change slightly under the same condition. At the same time, the selectivity for DOX increases with the reaction temperature. It shows that the effects of the reaction temperature mainly reflects the competition in the formation of DME and DOX. The rising temperature will cause intramolecular dehydration of diethylene glycol to increase. If the reaction temperature is too high, e.g. 220°C, the conversion reaches 96 percent, but side reactions occur so that the yield of DME decreases. However, if the reaction temperature is too low, the conversion is very low. Generally, the range of the reaction temperature is 200 °–210°C.

#### (2) The effect of reaction pressure

Apart from the same other conditions as shown in Fig.1, the reaction temperature is maintained at 200°C and the pressure change in the range of 30–60 kgf / cm<sup>2</sup>. The result is shown in Fig.2.

Figure 2 shows that the conversion clearly increases when the reaction pressure increases from 30 kgf / cm<sup>2</sup> to 40 kgf / cm<sup>2</sup>. However, when the pressure continues to increase, the conversion does not change essentially. The selectivity for DME remains unchange with the reaction pressure and the selectivity for DDE and DOX change slightly. Under conditions such as 200°C and pressure less than 36 kgf / cm<sup>2</sup>, DME yield is lower because ethanol partially vaporizes due to too low pressure. At 200°C, the saturated vapor pressure of ethanol is 36 kgf / cm<sup>2</sup>, so the reaction pressure must be in the range of 40 to 50 kgf / cm<sup>2</sup>.

### (3) The effect of the amount of catalyst

Under the same conditions as above, variation in the amount of catalyst in the range 0.2–1.5 wt% and results are shown in Fig.3

Figure 3 shows that when the amount of catalyst increases from 0.2 to 0.5 wt%, the conversion and selectivity change greatly. In particular there is a point in the conversion and selectivity curves at which conversion and selectivity increase greatly. However, when the amount of catalyst resides in the range 0.7 to 1.5 wt%, conversion will increase slightly. When the amount of catalyst increases to more than 1.0 wt%, the selectivity for DME and DDE decreases and that for DOX increases. So the amount of catalyst must be in the range of 0.5–1.0 wt%.

### 3.2 The Effect of Calcining Temperature on Conversion and Selectivity

Three heteropolyacids  $\text{PW}_{12}$ ,  $\text{SiW}_{12}$  and  $\text{PMo}_{12}$  are placed in the air at  $350^\circ - 500^\circ\text{C}$  for 3hr and their activity and selectivity are measured under the following conditions: reaction temperature  $200^\circ\text{C}$ ; pressure,  $50 \text{ kgf/cm}^2$ ; reaction time, 2hr; and the ratio of diethylene glycol and ethanol, 1 : 2 (mole). The results are shown in Table 1.

Table 1 shows that the activities of three kinds of untreated HPA are 97.5% for  $\text{PW}_{12}$ , 93.8% for  $\text{SiW}_{12}$  and 45.3% for  $\text{PMo}_{12}$ . Through calcining at  $350^\circ\text{C}$ , their conversion is lowered about 11 percent. After calcining at  $400^\circ\text{C}$ , the activity of  $\text{PW}_{12}$  is lowered 16 percent and  $\text{SiW}_{12}$ , 3.3 percent. Clearly, the thermal stability of  $\text{SiW}_{12}$  is better than  $\text{PW}_{12}$  and the activity of  $\text{PMo}_{12}$  is lower. According to catalytic activity, the order of thermal stability is  $\text{SiW}_{12} > \text{PW}_{12} > \text{PMo}_{12}$ . Comparing selectivity, it decreases with increase of calcining temperature, but the selectivity for dioxane increases, that is, calcined HPA has very high selectivity in intramolecular dehydration. It is possible that intramolecular dehydration needs lower surface acidity.

### 3.3 The Effect of Calcining Temperature on the Surface Acidity

The surface acidity and acid quantity of the calcined HPA have been examined by n-butylamine titration and the results shown in Table 2.

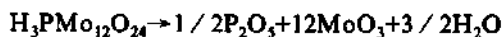
In Table 2, methyl red ( $\text{PK}_a +4.8$ ), dimethyl yellow ( $\text{PK}_a +3.3$ ), bromocresol green ( $\text{PK}_a -3.7$ ) and anthraquinone ( $\text{PK}_a -8.2$ ) are used as Hammett indicators. Table 2 shows that the acidity distribution of three kinds of HPA changes slightly. After calcination at  $350^\circ\text{C}$ , the acidity in range of  $-8.2 \leq \text{Ho} \leq -3.7$  decreases, but the acidity in the range  $+3.3 \leq \text{Ho} \leq +4.8$  of  $\text{PW}_{12}$  and  $\text{SiW}_{12}$  remains unchanged and  $\text{PMo}_{12}$  decreases 50 percent.

Comparing the changes in acidity, the order of thermal stability is  $\text{PW}_{12} \sim \text{SiW}_{12} > \text{PMo}_{12}$ .

### 3.4 The Effect of Calcining Condition on IR Spectrum

IR study on  $\text{PMo}_{12}$  before and after calcining is shown in Fig.4.

Figure 4 shows that, in the IR spectra, two bands in the  $1600-1700 \text{ cm}^{-1}$  region have been assigned to the bending modes of  $\text{H}_2\text{O}$  ( $1630 \text{ cm}^{-1}$ ) and  $\text{H}^+(\text{H}_2\text{O})$  ( $1720 \text{ cm}^{-1}$ ) [7]. It is notable that the bands at  $600-1100 \text{ cm}^{-1}$  are characteristic of the Keggin structure. Absorbing peaks of bonds P–O and Mo–O–Mo of  $\text{PMo}_{12}$  at  $350^\circ\text{C}$  become narrow. This shows that part of  $\text{PMo}_{12}$  proceeded pyrogenic decomposition. The peak strength and peak broadness changed, due to hydrogen-bond disappearance. The absorbing peaks of bonds P–O and Mo–O–Mo of  $\text{PMo}_{12}$  at  $400^\circ\text{C}$  disappear, which shows that most  $\text{PMo}_{12}$  decomposed; the reaction is as follows:



The disappearance of bond P–O results from the loss of  $\text{P}_2\text{O}_5$  produced in decomposition due to the sublimation of  $\text{P}_2\text{O}_5$  (the sublimation temperature for  $\text{P}_2\text{O}_5$  is  $359^\circ\text{C}$ ). At the same time, two new absorbing peaks of bonds Mo–O and Mo–O–Mo of produced  $\text{MoO}_3$  appear, which shows that most  $\text{PMo}_{12}$  decomposed at  $400^\circ\text{C}$ .

### 3.5 XRD Study

XRD of  $\text{PMo}_{12}$  has been studied under different calcining conditions and the results are shown in Fig.5.

Figure 5 shows characteristic diffraction peaks of  $\text{MoO}_3$  and  $\text{P}_2\text{O}_5$  begin appearing at 350°C and at 400°C approach the peak patterns of  $\text{MoO}_3$ , which shows that  $\text{PMo}_{12}$  begins decomposition at 350°C with most of it decomposed at 400°C.

In the IR study on  $\text{PMo}_{12}$ , bands at 600–1100  $\text{cm}^{-1}$  are characteristic of the Keggin structure and bands of first-order anion structure. XRD study has characterized the second-order crystal structure of  $\text{PMo}_{12}$ . When  $\text{PMo}_{12}$  is calcined at 350°C, the IR spectra change slightly. However, in contrast with the XRD result of  $\text{PMo}_{12}$ , their XRD patterns (due to the loss of crystal water at 350°C) change markedly.

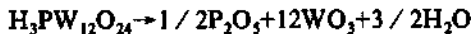
The destruction of the primary structure and the secondary structure will result in decrease of  $\text{PMo}_{12}$  acidity and followed by marked changes in catalytic activity and selectivity.

In contrast to  $\text{PMo}_{12}$ , the thermal stabilities of  $\text{PW}_{12}$  and  $\text{SiW}_{12}$  are higher. From XRD result,  $\text{PW}_{12}$  calcined at 350°C does not produce the characteristic diffraction peaks of  $\text{WO}_3$  and  $\text{P}_2\text{O}_5$ . When calcined at 500°C, the majority of them decompose.

### 3.6 TG Study

In the TG study shown in Fig.6, there are two stages on the  $\text{PMo}_{12}$  curve, the first stage resulting from the loss of water, adsorbent water and crystal water. There is a large amount of crystal water within heteropolyacids, which is emitted at 100°C. The second stage occurs at 350°–400°C due to the decomposition of  $\text{PMo}_{12}$  which results from the sublimation of  $\text{P}_2\text{O}_5$  produced by the decomposition of  $\text{PMo}_{12}$  and the loss of water.

On the curve of  $\text{PW}_{12}$  in Fig.5, the first stage at 100°C results from the loss of water, adsorbent water and 24 parts crystal water of 29  $\text{H}_2\text{O}$  within  $\text{H}_3\text{PW}_{12} \cdot 29\text{H}_2\text{O}$ . The second stage at 200°C is due to the loss of 5 parts of remaining crystal water and the third stage at 500°C is due to the decomposition of  $\text{PW}_{12}$ :



with the loss of  $\text{P}_2\text{O}_5$  and water.

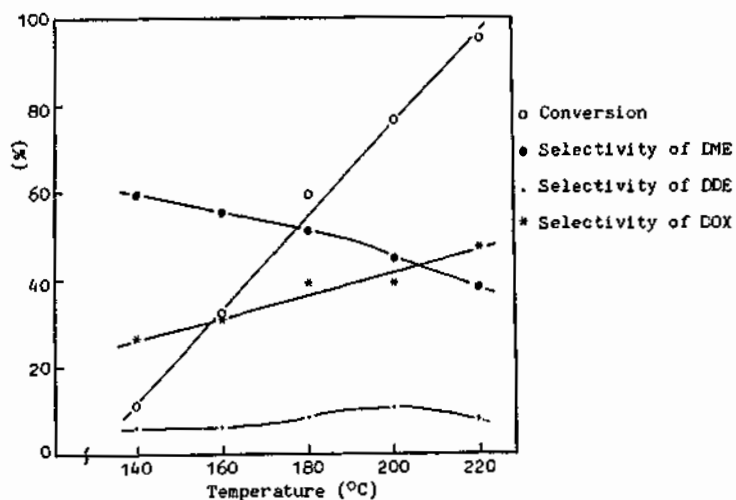
According to the above results the thermal stability order is:



Correlating the acidity study in Table 2 with the IR, XRD, TG study on calcined samples, it is shown that the acid quantities in the acidity range of  $+3.3 \leq \text{Ho} \leq +4.8$  of  $\text{SiW}_{12}$  and  $\text{PW}_{12}$  calcined at 350°C remain unchanged. Thus, the acidity range of  $+3.3 \leq \text{Ho} \leq +4.8$  may be related essentially to the primary Keggin structure and the acidity range of  $-8.2 \leq \text{Ho} \leq -3.7$  to the secondary structure. Study of the catalytic reaction has shown that the effects of two kinds of acidity on the activity and selectivity for HPA correspond with each other.

## REFERENCES

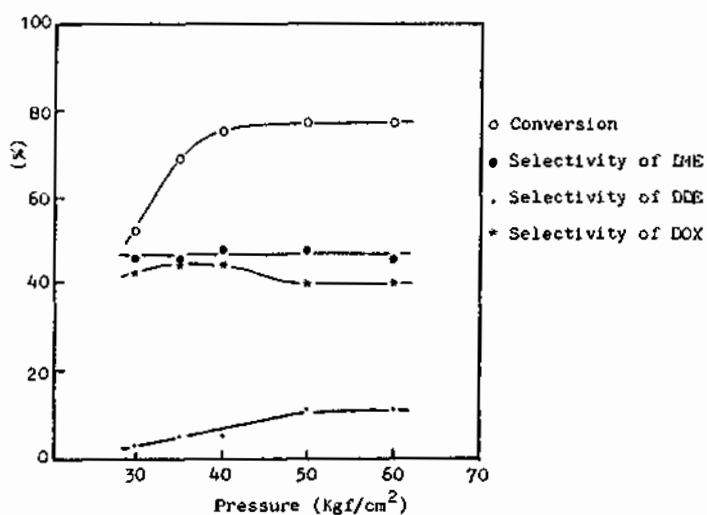
- [1] C.Sanchez, J.Livage, J.P.Launay, M.Fournier, Y.Jeannin, J. A. C. S., 1982, 104, 3192
- [2] Mamoru Ai, J. Catal., 1981, 71, 88
- [3] H.Tsuneki, H.Niiyama, E.Echigoya, Chem. Letter, 1978, 645
- [4] J.G.Highfield, J.B.Moffat, J. Catal., 1986, 98, 245
- [5] T.Bara, Y.Ono, T.Ishimoto, S.Moritaka, S.Tanooka, Bull.Chem.Soc.Japan, 1985, 58, 2155
- [6] M.Misono, Catal. Rev. Sci. Eng., 1987, 29(2&3), 269–321
- [7] M.Misono, N.Mizuno, K.Katamura, A.Kasai, Y.Konishi, Bull. Chem. Soc. Japan, 1982, 55, 400

Fig.1 Effect of reaction temperature on performance of  $\text{SiW}_{12}$ 

DME: Diethylene glycol monoethyl ether

DDE: Diethylene glycol diethyl ether

DOX: Dioxane

Fig.2 Effect of pressure on performance of  $\text{SiW}_{12}$

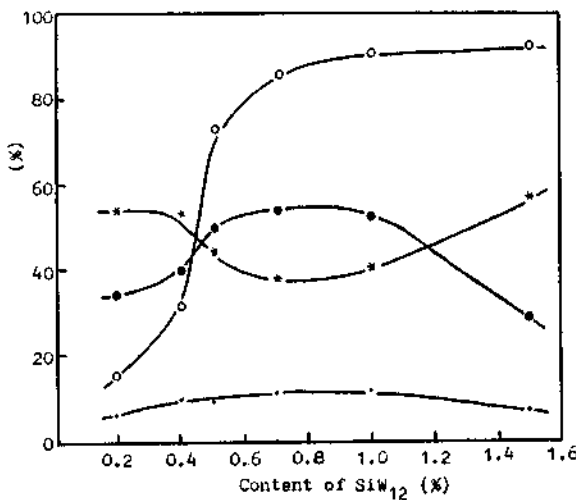


Fig.3 Effect of  $\text{SiW}_{12}$  content on performance of catalysis  
( For Key to ○,●,·,\* see Fig.2)

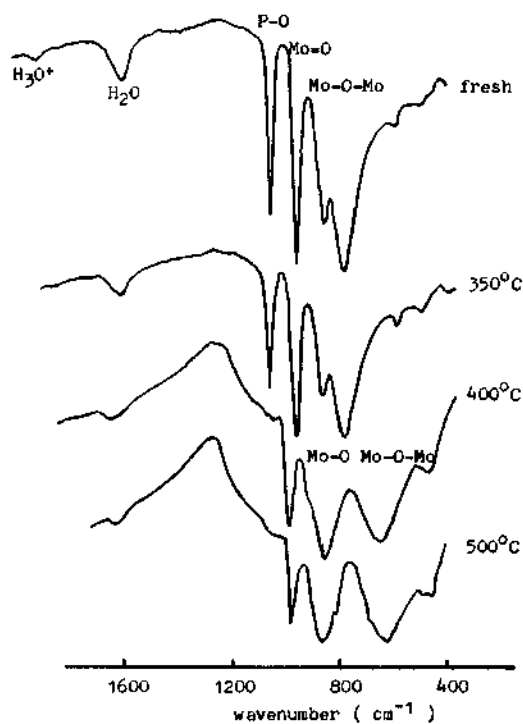


Fig.4 IR spectrum of  $\text{PMo}_{12}$  after calcination

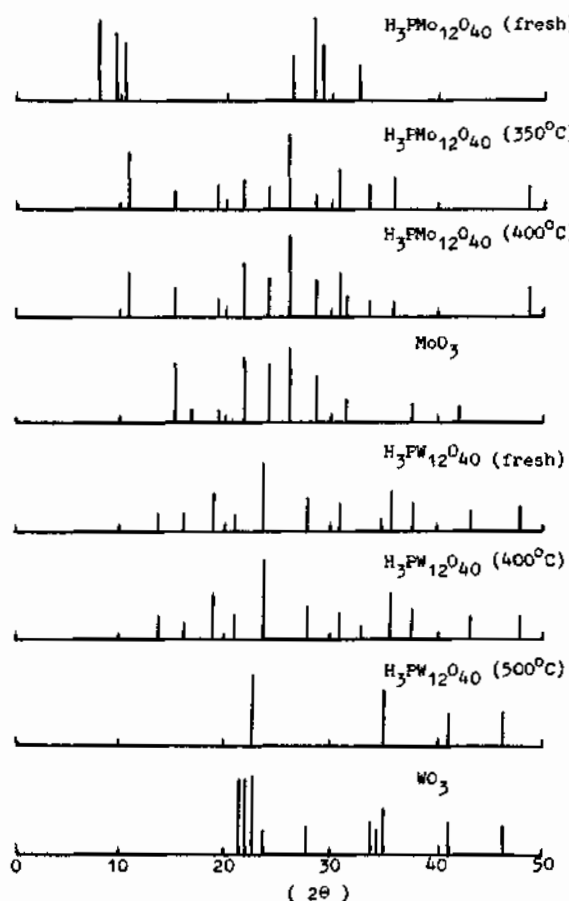


Fig. 5 XRD pattern of  $\text{PMo}_{12}$  and  $\text{PW}_{12}$  after calcining for 3 h.

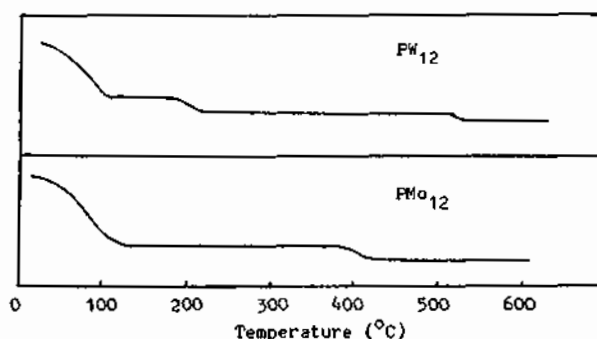


Fig. 6 TG curve of  $\text{PW}_{12}$  and  $\text{PMo}_{12}$

Table 1. Effect of calcining temperature on activity and selectivity  
 (Temperature: 200°C, pressure: 50 kgf/cm<sup>2</sup>, reaction time: 2 h,  
 DEG/EOL=1:2 (mole), calcined condition: air, 3 h.)

Catalysts	PW <sub>12</sub>			SiW <sub>12</sub>			PMo <sub>12</sub>					
	Calcined temperature (°C)	Conversion (%)	Selectivity (%)		Conversion (%)	Selectivity (%)		Conversion (%)	Selectivity (%)			
			DME	DDE		DME	DDE		DME	DDE	DOX	
fresh	97.5	35.4	6.62	55.2	93.8	35.8	6.91	53.0	45.3	72.4	11.3	11.5
350	86.5	35.9	8.34	54.6	82.1	39.6	9.50	49.7	33.0	38.8	6.21	52.1
400	70.5	28.8	6.60	62.8	79.4	24.7	7.62	65.0	27.0	23.3	0	72.6
450	52.3	19.5	3.56	74.0	49.5	20.2	6.08	71.5	25.3	20.9	0	73.9
500	25.2	20.1	0	75.0	26.3	15.2	0	77.2	24.8	10.7	0	71.0

Abbr.-- diethylene glycol: DEG, ethanol: EOL, diethylene glycol monoethyl ether:  
 DME, diethylene glycol diethyl ether: DDE, dioxane: DOX.

Table 2. Effect of calcining temperature on acidity of HPA\*

Acidity of HPA Temperature (°C) \ PK <sub>a</sub>	PW <sub>12</sub> (meq/g)			SiW <sub>12</sub> (meq/g)			PMo <sub>12</sub> (meq/g)		
	A	B	Sum	A	B	Sum	A	B	Sum
Fresh	0.80	0.20	1.0	0.70	0.20	0.90	0.70	0.20	0.90
350	0.60	0.20	0.80	0.55	0.20	0.75	0.30	0.10	0.40
400	0.40	0.15	0.55	0.40	0.15	0.55	0.15	0.05	0.20
450	0.25	0.10	0.35	0.20	0.10	0.30	0.05	0.02	0.07
500	0.10	0.05	0.15	0.05	0.04	0.09	0.03	0.01	0.04

\* A: -8.2 ≤ Ho ≤ -3.7, B: +3.3 ≤ Ho ≤ +4.8

## 1.10 Acidic Clay-Directed Polymerization-Cyclization of Aldehydes and Pyrrole to Porphyrins

Makoto ONAKA,<sup>a</sup> Tomotaka SHINODA,<sup>a</sup> Yusuke IZUMI,<sup>a</sup> and Ernest NOLEN<sup>b</sup>

<sup>a</sup> Department of Applied Chemistry, Faculty of Engineering, Nagoya University, Chikusa, Nagoya 464, Japan;

<sup>b</sup> Department of Chemistry, Colgate University, Hamilton, New York 13346-1398, U. S. A.

### Abstract

Intrinsic nanospaces of acidic clay **K10** were found to serve as micro reactors directing polymerization-cyclization of aldehydes and pyrrole to porphyrins efficiently.

### 1. INTRODUCTION

It has been focused on porphyrin chemistry from a variety of interests concerning organic chemistry, inorganic chemistry, physical chemistry, analytical chemistry, biochemistry, and so on. From a standpoint of synthetic organic chemistry, it is very significant to develop efficient methodologies for creating porphyrin compounds which can provide us useful functions.

It has been suggested that minerals serve as possible catalysts for porphyrin abiogenesis from pyrroles and aldehydes in the prebiotic era. By analogy, mineral clays are expected to be promising candidates for promoting artificial porphyrin formation *in vitro*.

Symmetrical *meso*-tetrasubstituted porphyrins are synthesized directly from their components, pyrroles and aldehydes, as shown in Scheme 1: pyrroles and aldehydes alternately oligomerize to form  $O_8$  as an intermediate. An *intramolecular* cyclization of  $O_8$  leads to porphyrinogen, a precursor to porphyrin, otherwise linear copolymers are produced from  $O_8$ . The *intramolecular* cyclization to porphyrinogen is normally not a predominant process in the copolymerization of pyrroles and aldehydes.

We supposed that if the porphyrinogen formation was carried out in a restricted nano-size space, the *intramolecular* cyclization would be more dominant than the cyclization conducted in a homogeneous solution, and the longer copolymer formation from  $O_8$  would be suppressed. Based on this idea, we applied different acidic clays as reaction media (**micro reactors**) to *meso*-tetrasubstituted porphyrin synthesis from pyrrole and aldehydes, and we discovered [1] that montmorillonite **K10** [2] is the best clay for producing the porphyrins in much higher yields, compared with the conventional methodologies which have been developed so far [3].

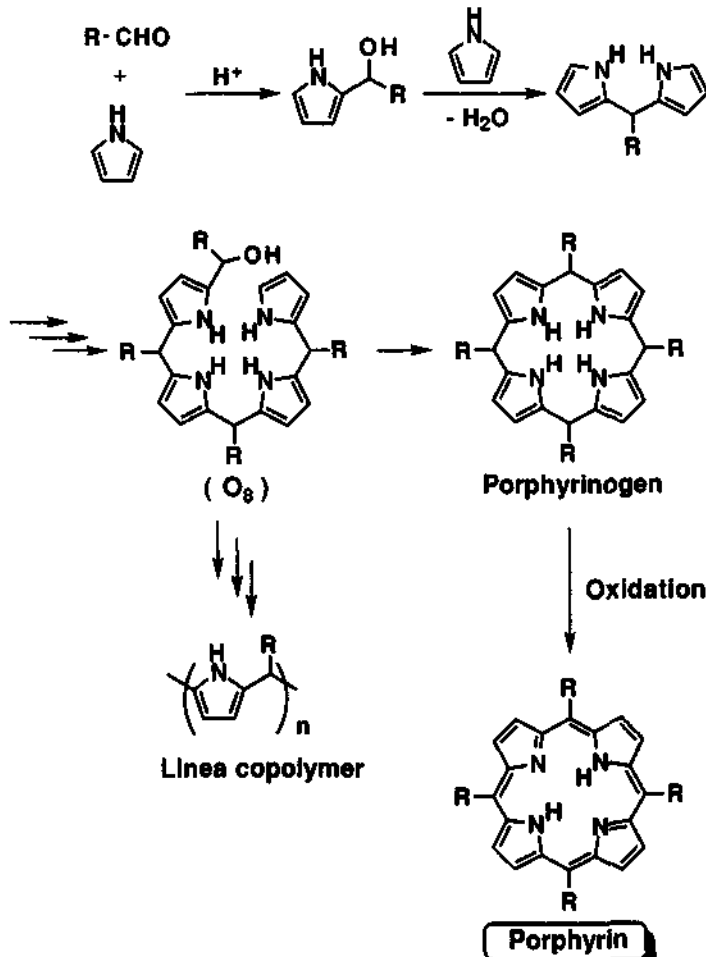
### 2. EXPERIMENTAL METHODS

#### 2.1. Materials.

Montmorillonite **K10** was purchased from Aldrich and used. Fe-Mont (iron ion-exchanged montmorillonite) was prepared by cation exchange from sodium ion-exchanged montmorillonite "Kunipia F" supplied by Kunimine Industries Co. Japan.  $SiO_2-Al_2O_3$  was JRC-SAL-2 from the

Catalysis Society of Japan.

Aldehydes, pyrrole,  $\text{BF}_3 \cdot \text{OEt}_2$ , and  $\text{CF}_3\text{CO}_2\text{H}$  were distilled before use.  $\text{CH}_2\text{Cl}_2$  was dried on molecular sieves 4A.



Scheme 1. Porphyrin formation from aldehyde and pyrrole.

## 2.2. Reaction procedure.

We conducted two synthetic steps in one pot: polymerization-cyclization to porphyrinogen from aldehyde and pyrrole, followed by oxidation with *p*-chloranil to porphyrin.

A clay (1 g) was activated at 120 °C and below 0.5 Torr for 3 h in a 200-ml flask, and then  $\text{N}_2$  was introduced. The flask was shielded from light with foil. To the flask were added dry  $\text{CH}_2\text{Cl}_2$  (95 ml) and then a  $\text{CH}_2\text{Cl}_2$  (5 ml) solution of aldehyde (1 mmol). To the well-stirred mixture was introduced dropwise neat pyrrole (1 mmol) at room temperature, and the stirring was continued for 1 h. Solid *p*-chloranil (0.75 mmol) was added and the mixture was gently refluxed at 45 °C for 1 h. Solid materials were removed through a Celite pad and washed with  $\text{AcOEt}$  or  $\text{CH}_2\text{Cl}_2$  (60 ml). The combined filtrate contained free base porphyrin, and was condensed and adsorbed on Florisil (2 g).

The adsorbate was placed on the top of an  $\text{Al}_2\text{O}_3$  (Merck Aluminum Oxide 90, Activity II-III, 100 g) column and developed with hexane- $\text{AcOEt}$  or hexane- $\text{CH}_2\text{Cl}_2$ . The porphyrin fraction was collected, condensed, charged on an alumina (100 g) column, and purified again. The purified porphyrin was dried at 80 °C and below 0.5 Torr for 6 h.

### 3. RESULTS AND DISCUSSION

It was found that the montmorillonite **K10**-mediated porphyrin formation is especially outstanding in the *meso*-tetraalkylporphyrin synthesis from *aliphatic* aldehydes and pyrrole, because conventional methods under the influence of homogeneous acids only afforded the porphyrins in poor yields. Table 1 shows the comparison between the present **K10** method and the conventional methods using homogeneous acids ( $\text{BF}_3 \cdot \text{OEt}_2$  and  $\text{CF}_3\text{CO}_2\text{H}$ ) for the syntheses of typical *meso*-tetraalkylporphyrins.

Table 1. Syntheses of *meso*-tetraalkylporphyrins.<sup>a)</sup>

R	<b>K10</b>	Yields / %	
		$\text{BF}_3 \cdot \text{OEt}_2$	$\text{CF}_3\text{CO}_2\text{H}$
$-(\text{CH}_2)_4\text{CH}_3$	46	20	15
$-(\text{CH}_2)_9\text{CH}_3$	39	20	16
$-(\text{CH}_2)_5\text{Cl}$	40	21	13
$-(\text{CH}_2)_3\text{CH}=\text{CH}_2$	24	21	11
Cyclohexyl	35	14	0

a) Aldehyde, Pyrrole (1 mmol,  $10^{-2}$  M), **K10** (1 g),  $\text{BF}_3 \cdot \text{OEt}_2$  (0.1 mmol,  $10^{-3}$  M),  $\text{CF}_3\text{CO}_2\text{H}$  (0.5 mmol,  $5 \times 10^{-3}$  M), in  $\text{CH}_2\text{Cl}_2$ .

As shown in Table 2, **K10** was found to give a remarkably high yield of *meso*-tetrapentylporphyrin among solid strong acids of montmorillonites (**K10** and Fe-Mont [4]) as well as amorphous silica-alumina.

In order to clarify the origin of the difference in porphyrin synthesis between **K10** and another montmorillonite Fe-Mont, the morphology of **K10** and Fe-Mont was examined in terms of specific surface area and powder X-ray diffractometry. Fe-Mont has a surface area of  $26 \text{ m}^2/\text{g}$  and a peak at  $2\theta = 5.6^\circ$  in X-ray diffraction, while **K10** has  $223 \text{ m}^2/\text{g}$  and no diffraction peaks. Consequently it can be deduced that Fe-Mont has a typical laminated structure (Fig. 1a) with a basal spacing of 1.58 nm, whereas **K10** is delaminated or a card-house structure, as shown in Fig. 1b. Recently

Pinnavaia reported that the pore structure of **K10** is mainly composed of mesopores ranging between 3 and 5 nm [5]. The molecular size of *meso*-tetrapentylporphyrin is estimated to be 1.8 nm from a molecular model. Therefore, the three-dimensional mesopores in **K10** serve as suitable reaction media (templates) for formation of bulky porphyrinogens and porphyrins.

Table 2. Formation of *meso*-tetrapentylporphyrin.

Solid acid	Yield / %
<b>K10</b>	46
Fe-Mont	4
$\text{SiO}_2\text{-Al}_2\text{O}_3$	trace

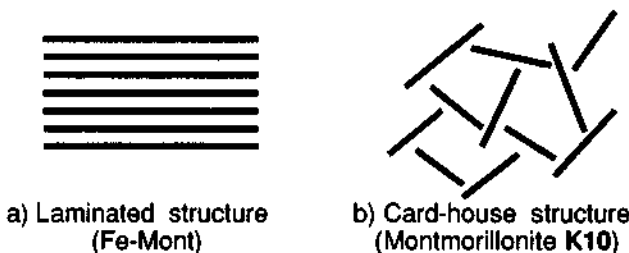


Fig. 1. Morphology of montmorillonites.

In addition, *meso*-tetraarylporphyrins were successfully synthesized from *aromatic* aldehydes and pyrrole by using **K10** clay. Interestingly, the yields of *meso*-tetraarylporphyrins varied depending on the substituents and their substitution patterns under both heterogeneous and homogeneous conditions.

Table 3. *meso*-Tetraarylporphyrin Syntheses.<sup>a)</sup>

R	<b>K10</b>	Yields (%)	
		$\text{BF}_3 \cdot \text{OEt}_2$	$\text{CF}_3\text{CO}_2\text{H}$
Ph	30	42	36
<i>o</i> -MeC <sub>6</sub> H <sub>4</sub>	21	45 <sup>b)</sup>	31
<i>p</i> -MeC <sub>6</sub> H <sub>4</sub>	20	28	29
<i>o</i> -MeOC <sub>6</sub> H <sub>4</sub>	30	20 <sup>b)</sup>	trace
<i>p</i> -MeOC <sub>6</sub> H <sub>4</sub>	trace	trace	trace
<i>o</i> -ClC <sub>6</sub> H <sub>4</sub>	3	28 <sup>b)</sup>	9
<i>p</i> -ClC <sub>6</sub> H <sub>4</sub>	9	trace	17

a) Aldehyde (1 mmol,  $10^{-2}$  M), Pyrrol (1 mmol,  $10^{-2}$  M), **K10** (1 g),  $\text{BF}_3 \cdot \text{OEt}_2$  (0.1 mmol,  $10^{-3}$  M), TFA (0.5 mmol,  $5 \times 10^{-3}$  M), in  $\text{CH}_2\text{Cl}_2$ .

b) Data were quoted from Ref. 3.

#### 4. REFERENCES AND NOTES.

- [1] M. Onaka, T. Shinoda, Y. Izumi, E. Nolen, *Chem. Lett.*, **1993**, 117; *Tetrahedron Lett.*, **1993**, 34, 2625.
- [2] **K10** is a sulfuric acid-leached montmorillonite.
- [3] a) J. S. Lindsey, I. C. Schreiman, H. C. Hsu, P. C. Kearney, A. M. Marguerettaz, *J. Org. Chem.*, **1987**, 52, 827; J. S. Lindsey, R. W. Wagner, *ibid.*, **1989**, 54, 828.
- [4] **K10** and Fe-Mont were found to have almost the same acid strength: M. Onaka, Y. Hosokawa, K. Higuchi, Y. Izumi, *Tetrahedron Lett.*, **1993**, 34, 1171.
- [5] J.-R. Butruille, T. J. Pinnavaia, *Catal. Today*, **1992**, 14, 141.

Finally, it should be noted that the present **K10** method has another synthetic advantage: porphyrin products can easily be separated and isolated from by-product polymers, which tend to be selectively adsorbed on **K10** and separated from a solution phase in the filtration procedure.

*meso*-Tetraalkylporphyrins have not been studied intensively concerning their physical and chemical properties and applications to catalysis from lack of their efficient syntheses. Uncovering the new chemical characteristics of *meso*-tetraalkylporphyrins is in progress.

## 1.11 Acid-catalyzed Rearrangement of Pentacyclic Cage Compound *via* an Unexpected Route [Part II]: Application of PM3 Calculations to the Reaction Mechanism

K. Hirao and H. Takahashi

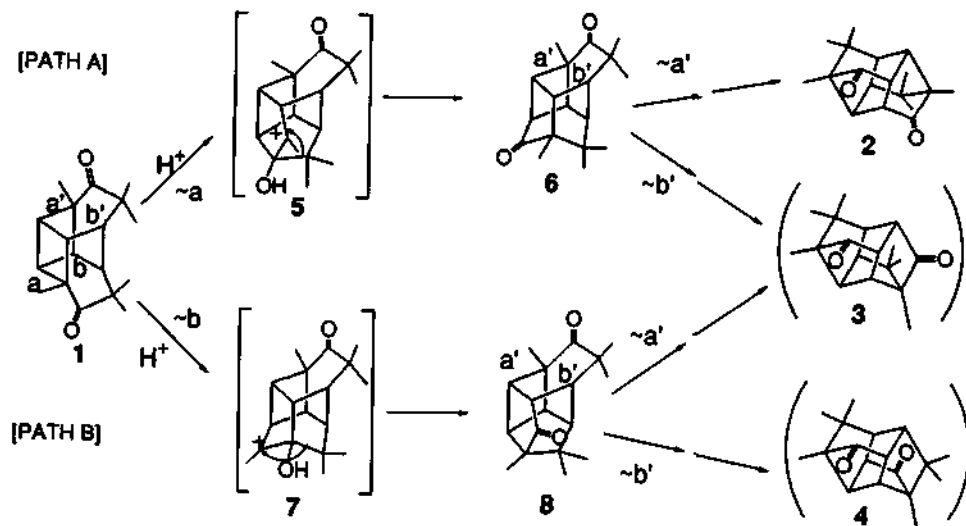
Graduate School of Environmental Earth Science, Hokkaido University, Sapporo 060, Japan

### Abstract

Contrary to expectation, pentacyclic mesylketone (9) rearranges to dienediones (11) and (12) on treatment with  $\text{BF}_3$  in benzene. The structure of the intermediate (13) indicates that these dienediones are formed *via* a novel route including (13)  $\rightarrow$  (14)  $\rightarrow$  (15). The molecular orbital calculations by the PM3 method are applied to justify the validity of the mechanism.

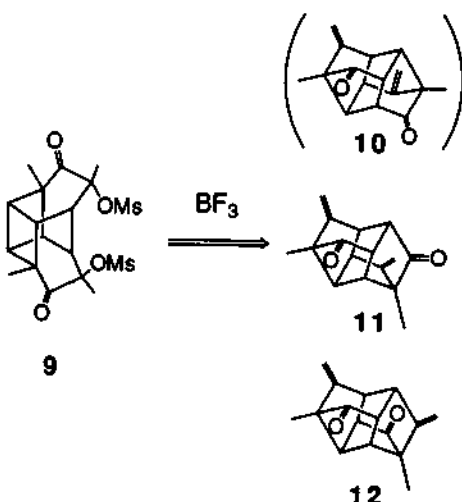
### 1. INTRODUCTION

By using a Brønsted acid the pentacyclic cage compound (1) was found to rearrange quantitatively into (2). [1] The complete regiospecificity of the reaction was attributable to the preferable formation of the cationic intermediate (5), which readily isomerizes to (6) and to another set of analogous two-fold rearrangements involving bond a' giving (2). [PATH A]



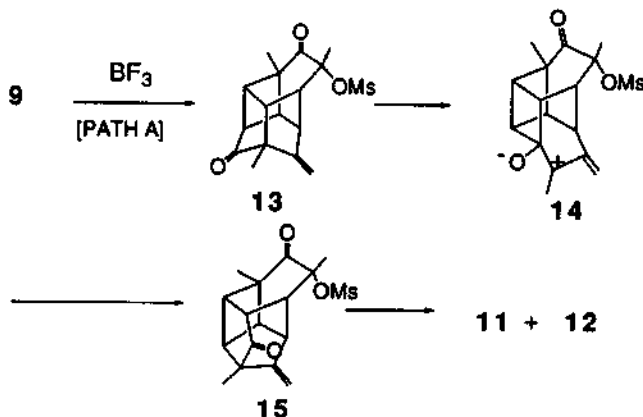
These were supported by convincing explanation by the use of empirical force field calculations. [2]

In contrast with the compound (1), the mesylketone (9) was found to give two rearranged dienediones (11) and (12), whose skeletons are comparable to those of (3) and (4), in 49 and 10% isolated yields, respectively, when treated with  $\text{BF}_3$  in benzene at room temperature. If the reaction proceeded following the same mechanism as in the formation of (2), another symmetrical dienedione (10) having the same frame work as that of (2) should be the only product. However, (10) was completely missing in the reaction mixtures. [3]



## 2. RESULTS AND DISCUSSION

Among the reaction products other than (11) and (12), a set of two isomeric mesylenones (13) and (15) have been obtained in 13 and 0.4% yields, respectively. Contrary to our expectation, the structure of the major mesylenone has been revealed not to be (15)



but (13) by X-ray analysis. [4] Under the same conditions of the acid-catalyzed reaction of (9), this mesylenone (13) was transformed into (11) and (12). Therefore, (13) should be an intermediate from (9) to (11) and (12). Thus, the formation route of (11) and (12) should involve an unexpected type path to (15) through (13). A straightforward and simple interpretation may be obtained if we assume the intervention of a novel cation (14) between (13) and (15).

In order to confirm this idea, a computational analysis of the validity of this route by the use of the molecular orbital calculations by the PM3 method with MOPAC Ver. 6 was performed [5]. Results of the calculated heats of formation for the hexamethylpentacyclo-dodecane-diones (1), (6), and (8) as substitutes for the transition state species (14) and the intermediates (13) and (15), respectively are given in Table 1. Such a rearrangement

Table 1 Calculated heats of formation for pentacyclic cage compounds

Compounds <sup>a</sup>	$\Delta H_f/\text{kcal mol}^{-1}$ b
5,7,7,10,10,12-[6.4.0.02.5.03.12.04.9]-6,11 (1)	- 65.11 <sup>c</sup>
6,7,7,10,10,12-[6.4.0.02.6.03.10.04.9]-5,11 (6)	- 62.16 <sup>c</sup>
5,7,7,11,12,12-[6.4.0.02.5.03.11.04.9]-6,10 (8)	- 81.32 <sup>c</sup>

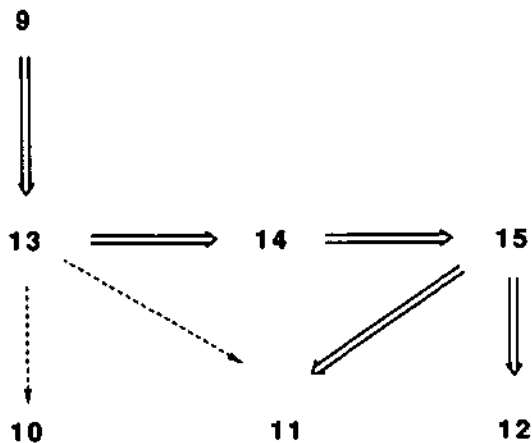
<sup>a</sup>Full IUPAC names are abbreviated. For example, (1) is 5,7,7,10,10,12-hexamethylpentacyclo[6.4.0.02.5.03.12.04.9]dodecane-6,11-dione. <sup>b</sup>1 cal = 4.184 J. <sup>c</sup>MOPAC Ver.6, J. J. Stewart, QCPE Bull., 1989, 9, 10; Revised as Ver. 6.01 by T. Hirano, University of Tokyo, for HITAC and UNIX machines, JCPE Newsletter, 1989, 1, 10.

which proceeds by a multi-step carbocation mechanism generally progresses in the direction of the more stable form. The calculated  $\Delta\Delta H_f$  value of (8) is ca 20 kcal mol<sup>-1</sup> lower than that of (6), and thus this value must exert the influence on the course of the reaction. In addition, the change in enthalpies between (6) and (1) is small enough for a progress of the reaction. Although the skeleton (ii), the parent hydrocarbon of (3) and (4), is calculated to be 8 kcal mol<sup>-1</sup> more stable than the isomeric structure (i), the parent skeleton of (2) [2], acid-catalyzed reaction of (1) gives (2) exclusively. [1] This has been attributable to the absence of a mechanistically acceptable path. [2] In the present case the intermediate (13) opens up a road to the stabilomer (ii), i.e. (11) and (12).



### 3. CONCLUSIONS

The present study gives an explanation of formation of (11) and (12) from (9) via the unexpected route as shown in the following scheme. However, it is still vague why the rearrangement of a' bond of (6) occurs preferentially, whereas the intermediate (13) proceeds toward (14).



### 4. REFERENCES

- 1) K. Hirao, M. Taniguchi, O. Yonemitsu, J. L. Flippen, and B. Witkop, *J. Am. Chem. Soc.*, 1979, 101, 408.
- 2) E. Osawa, K. Aigami, and Y. Inamoto, *J. C. S. Perkin II*, 1979, 181.
- 3) K. Hirao, H. Takahashi, Y. Ohuchi, and O. Yonemitsu, *J. Chem. Research (S)*, 1992, 2601.
- 4) K. Hirao, H. Takahashi, and K. Kobayashi, presented at the NINTH FRENCH-JAPANESE SYMPOSIUM on MEDICINAL and FINE CHEMISTRY, Sapporo, 1992.
- 5) MOPAC Ver.6, J. J. Stewart, *JCPE Bull.*, 1989, 9, 10; Revised as Ver. 6.01 by T. Hirano, University of Tokyo, for HITAC and UNIX machines, *JCPE Newsletter*, 1989, 1, 10.

## 1.12 Formylation of Aromatic Compounds under Atmospheric CO Pressure

Y. Souma and M. Tanaka  
Osaka National Research Institute, AIST,  
Midorigaoka-1, Ikeda, Osaka, 563, Japan

### Abstract

Formylation of aromatic compounds such as toluene, xylene, mesitylene, and halogenatedbenzene was carried out in  $\text{HSO}_3\text{F-SbF}_5$  under atmospheric CO pressure at 0°C. In  $\text{HSO}_3\text{F-SbF}_5$ , both formylation and sulfonylation took place to give formyl and sulfonyl compounds depending on the acidity of the solution. Diformylation of polynuclear aromatic compounds such as naphthalene, diphenyl, diphenylmethane and dibenzyl was carried out in  $\text{HF-SbF}_5$  system by a one-pot reaction.

### 1. INTRODUCTION

The formylation of aromatic compounds by super strong acid is known as the Gattermann-Koch reaction.[1-2] Several super acid systems such as  $\text{HCl-AlCl}_3$ ,  $\text{HF-BF}_3$ ,  $\text{HF-CF}_3\text{SO}_3\text{H-BF}_3$ , were used for the formylation under CO pressure.[3-4]

In this paper, we wish to report on the formylation of aromatic compounds in  $\text{HSO}_3\text{F-SbF}_5$  under atmospheric CO pressure, and also the diformylation of polynuclear aromatic compounds in  $\text{HF-SbF}_5$  by one-pot reaction.

### 2. EXPERIMENTAL METHODS

The typical formylation was carried out using 20mmol substrate, 174mmol of  $\text{HSO}_3\text{F}$  and 69 to 138mmol of  $\text{SbF}_5$  under atmospheric CO pressure at 0°C in a 300ml three-necked flask equipped with a CO gas buret. The aromatics were added slowly into a  $\text{HSO}_3\text{F-SbF}_5$  mixture with vigorous stirring. The diformylation of polynuclear compounds in  $\text{HF-SbF}_5$  was carried out using 10mmol of substrate, 25mmol of  $\text{SbF}_5$ , and 500mmol of HF under 20atm of CO pressure in hasteroi autoclave at 0°C for 3h. The reaction mixture was poured on ice-water, and products were extracted by benzene, and then analyzed by GC, IR, GC-MS and NMR.

### 3. RESULTS AND DISCUSSION

When aromatic compounds were added into a mixture of  $\text{HSO}_3\text{F}$  and  $\text{SbF}_5$  under atmospheric CO pressure at 0°C, both formylation and sulfonation took place to give four products, and a new compound 2 was obtained by a one-pot reaction.[5-6] Electrophilic attack of formyl or fluorosulfonyl group took place to the para position of alkyl group. The influence of acid strength on the composition of products was studied, and the results are shown in Table 2. When the amount of  $\text{SbF}_5$  was small, the sulfonation was the main reaction. However, the formylation became predominant with

the increase of  $\text{SbF}_5$ . The formylation products of various aromatic compounds were shown in Table 1.

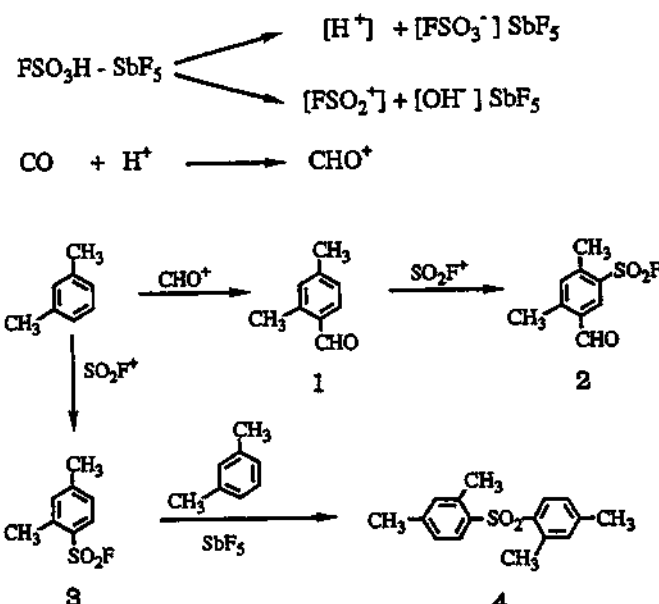


Table 1. Formylation of Aromatic Compounds

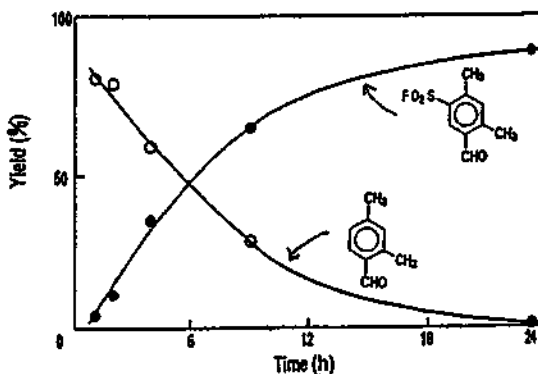
substrate	reaction time(h)	$\text{SbF}_5$ (mmol)		product, yield(%)
toluene	168	138	 2	 90 (76:24)
<i>m</i> -xylene	24	69	 0	 93
mesitylene	48	69	 48 (60:40)	 34
tetralin	24	138	 2	 21 (90:10)

In order to clarify the reaction path of compound 2, the time dependence of product composition of 1 and 2 was studied. As shown in Fig. 1, compound 1 was formed first, and it decreased with time, while the yield of 2 increased gradually.

Table 2. Relation between the selectivity of products and acidity

$\text{SbF}_5$ (nmol)	acidity -H <sub>0</sub>	product yield (%)			
		1	2	3	4
0	15.1	0	0	50 (83:17)	48 (78:22)
19.8	18.3	17 (100:0)	0	41 (80:20)	38 (79:21)
69.0	22.4	83 (100:0)	4	6 (100:0)	2 (100:0)
138	22.7	79 (100:0)	15	0	0

Fig. 1. Time dependence of formylation and sulfonylation



Diformylation of polynuclear aromatic compounds such as naphthalene, diphenyl, diphenylmethane and dibenzyl was also accomplished in HF-SbF<sub>5</sub> system by a one-pot reaction.[7] Monoaldehyde was obtained, when the ratio of SbF<sub>5</sub>/substrate was smaller than 1, and dialdehyde was obtained when the ratio of SbF<sub>5</sub>/substrate was greater than 1. The results were shown in Table 3 and Fig. 2.

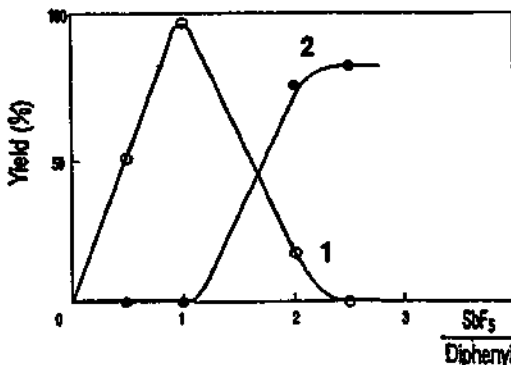
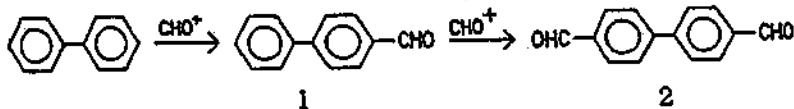
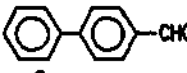
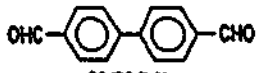
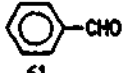
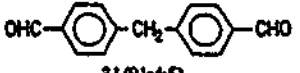
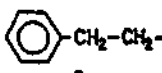
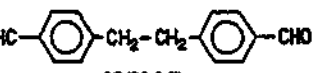
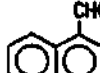
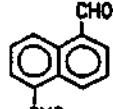


Fig. 2. Formation of monoaldehyde and dialdehyde in the formylation of diphenyl

Table 3. Diformylation of Aromatic Compounds

substrate	time(h)		product, yield(%)
diphenyl	3		OHC-  81(93:7:0)
diphenylmethane	2		OHC-  31(91:4:5)
dibenzyl	2		OHC-  98(90:3:7)
naphthalene	3		 39(71:18:11:0)

substrate 10mmol, HF 500mmol, CO 20atm, temp. 0°C

**Reference**

1. L. Gattermann and J. A. Koch, Chem. Ber., 1987, 30, 1622.
2. G. A. Olah, Friedel-Crafts and Related Reaction, Wiley-Interscience, New York, 1964, vol. III, 1153.
3. Y. Takezaki, N. Sugita, H. Kubo, K. Kudo, T. Yasutomi, Sekiyugakkaishi, 1964, 7, 564.
4. G. A. Olah, K. Laali, O. Farooq, J. Org. Chem., 1985, 50, 1483.
5. M. Tanaka, J. Iyoda and Y. Souma, J. Org. Chem., 1992, 57, 2677.
6. M. Tanaka and Y. Souma, J. Org. Chem., 1992, 57, 3738.
7. M. Tanaka and Y. Souma, J. Chem. Soc., Chem. Commun., 1991, 1551.

## 1.13 Friedel-Crafts Polyalkylation of Mesitylene with Trichlorotoluene : A Synthesis of 1,3-Connected Polyarylmethanes as Precursors for Organic Magnets

Y. Imizu,<sup>\*a</sup> T. Iino,<sup>a</sup> N. Tanaka,<sup>b</sup> N. Okazaki,<sup>b</sup> H. Itoh,<sup>a</sup> A. Tada,<sup>b</sup> K. Tokumitsu,<sup>c</sup> and H. Kakegawa<sup>\*c</sup>

<sup>a</sup>Department of Materials Science, Kitami Institute of Technology, Kitami, Hokkaido, 090 Japan

<sup>b</sup>Department of Applied and Environmental Chemistry, Kitami Institute of Technology, Kitami, Hokkaido, 090 Japan

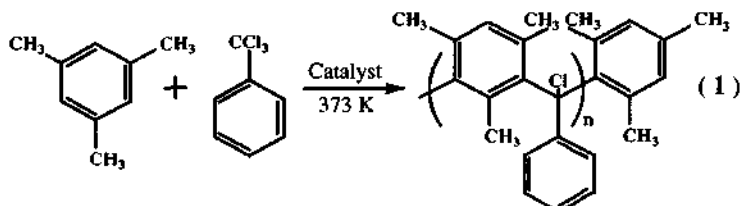
<sup>c</sup>Research & Development Center, Osaka Gas Co., Ltd. Konohana-ku, Osaka 554, Japan

### Abstract

Friedel-Crafts polyalkylation of mesitylene with trichlorotoluene was carried out to synthesize precursors of organic magnets without metal. More than twenty kinds of solid acid and base catalysts and inorganic salts are examined for this reaction. Among these, Zn(II)(OTf)<sub>2</sub> and Cu(II)(OTf)<sub>2</sub> were observed to be the excellent catalysts showing the highest catalytic performance in yield and efficiency. Also zinc(II) chloride displayed good catalytic performance showing the highest molecular weight from the economical point of view. Weak Lewis acid having high solubility properties in the organic media is concluded to be the best catalyst for this reaction. The reaction encountered significant extent of methyl dealkylation requiring further work in order to solve this structural deficiencies.

### 1. INTRODUCTION

Organic magnet may provide a novel insight into the nature of magnetism, leading to materials with unusual optical, electronic, and magnetic properties. One of the general approaches to ferromagnetism in purely organic molecules is based on  $\pi$ -conjugated polyyradicals with a high-spin ground state, where the electron spins of a pair of radical centers can be aligned in parallel when these centers are connected through an appropriate ferromagnetic molecular unit.[1] Recently, many molecular ferromagnets have been synthesized by using m-phenylene fragment as a coupling unit,[2-4] however, largely because the intricate multistep synthetic pathways for carbon-carbon bond formation, they are based on relatively small molecules in which the radical centers are aligned with less than 10 units. To synthesize the precursors for the polyyradicals with up to 10 unpaired electrons in one-pot catalytic reaction, we employed Friedel-Crafts polyalkylation of mesitylene with



trichlorotoluene. The goal of our synthesis are 1, 3-connected polyarylmethanes precursors **1** which undergo dechlorination to produce polyradicals. In this paper, we investigate the scope of this Friedel-Crafts polyalkylation.

## 2. EXPERIMENTAL METHODS

### 2.1. Reaction Procedures

Friedel-Crafts polyalkylation was carried out in a 200mL-tree neck flask under a Ar atmosphere. Trichlorotoluene (11.7g, 60 mmol) was added dropwisely and with stirring to a catalyst (3-120mol)-dispersed mesitylene (7.2g, 60 mmol) in a nitrobenzene solvent (40mL) at 373 K for 1-2 h. After 1-2h the reaction was completed by addition of mesitylene (1.4g, 10 mmol), then the solution was cooled to room temperature. The resulting crude products were washed with water, extracted with  $\text{CH}_2\text{Cl}_2$ . In order to remove any remaining unreacted material, solid material was suspended in hexane (3L, 30 min with stirring). Finally the product was isolated by filtration followed by drying overnight.

### 2.2. Product Analyses

The molecular weight measurement was performed by a conventional GPC method (Tosoh TSK Gels column connected to a guard column), employing THF as a carrier. NMR spectra were recorded on a JEOL FX-200 ( $^1\text{H}$ , 200MHz). Conformational analysis was carried out with MM2 program packed in Personal CAChe program (CAChe Scientific, Inc.) on a Macintosh IIvx.

## 3. RESULTS AND DISCUSSION

### 3.1. Catalytic Activity of Solid Catalyst

Table I summarizes the results of titled reaction over various solid catalysts. Although the number of mesitylene-arylmethane units were observed to be 5-6, all solid catalysts did not give any solid products. These result indicates that solid catalysts are not effective to connect more longer mesitylene-arylmethane units which are insoluble in  $\text{CH}_2\text{Cl}_2$  and hexane, suggesting that the adsorbed product polymers can not migrate on and desorb from the catalyst surface. In addition, solid bases such as  $\text{MgO}$  and  $\text{La}_2\text{O}_3$  as well as solid acids such as K10 montmorillonite and silica-alumina displayed the similar catalytic performance, suggesting that the carbocations are easily formed from trichlorotoluene (TCT) in the reaction condition and strong acidic sites are not necessary to perform the titled Friedel-Crafts reaction.

### 3.2. Catalytic Activity of Lewis Acid Catalyst

Catalysts such as aluminum(III), iron(III), or zinc(II) chlorides have been used widely for side-chain alkylation of aromatics. These inorganic chlorides gave solid products as shown in Table II. Among these,  $\text{ZnCl}_2$ , which is weak Lewis acid, showed high catalytic performance in both yield and catalytic efficiency, where efficiency was defined as the percent of yield per amounts of employed catalyst. Poor catalytic efficiency observed on  $\text{AlCl}_3$  is probably due to side reactions which occurred to significant extent, suggesting again that the strong Lewis acid catalyst is rather detrimental. The elemental analysis of the polymers prepared with  $\text{ZnCl}_2$  shows a 7% Cl content as well as a 3% O content. The Zn impurities were shown to be less than 3ppm levels, indicating that the nearly Zn-free materials can be obtained by simply washing the products with water. Clearly metal-free materials are favorable in order to prepare the precursor of organic magnets.

From above results, we focused attention to zinc compounds and examined their catalytic activities (Table III). First, we examined several zinc halides. It was found that fluoride, bromide, iodide except chloride gave no solid product. Then, we examined zinc oxide and metallic zinc. Zinc oxide showed fairly good catalytic performance, however, Zn did not, suggesting that zinc cation were more readily dissolved from oxide surface into the reaction media comparing with metallic Zn. To obtain the optimum conditions to perform high catalytic efficiency, the ratio of catalyst to TCT were varied from 2 to 0.5. With  $\text{ZnO}$  (ratio of 0.2), the efficiency was observed to be 46%, however, the

**Table I.** Friedel-Crafts Reaction of Mesitylene with Trichlorotoluene on Various Solid catalysts

Catalyst	Yield (%)	MN <sup>a)</sup>	n <sup>b)</sup>
Montmorillonite K10	-c)	1513	6
TiO <sub>2</sub>	-c)	1488	6
SiO <sub>2</sub> -Al <sub>2</sub> O <sub>3</sub>	-c)	1478	6
SiO <sub>2</sub>	-c)	1422	5
Al <sub>2</sub> O <sub>3</sub>	-c)	1390	5
MgO	-c)	1362	5
HY zeolite	-c)	1346	5
La <sub>2</sub> O <sub>3</sub>	-c)	1319	5

a) Number of average molecular weight.

b) Number of mesitylene-arylmethane unit.

c) No solid product was obtained.

**Table II.** Friedel-Crafts Reaction of Mesitylene with Trichlorotoluene on Various Inorganic Chlorides

Catalyst	Mole ratio of catalyst / TCT	Yield	Efficiency (%) <sup>a)</sup>	MN <sup>b)</sup>	n <sup>c)</sup>
AlCl <sub>3</sub>	2 / 1	0.47g 2%	1	2163	8
FeCl <sub>3</sub>	2 / 1	2.59g 14%	7	3006	12
ZnCl <sub>2</sub>	2 / 1	3.92g 21%	10	3833	15

a) Percent of yield per catalyst used.

b) Number of average molecular weight.

c) Number of unit.

percent yield was decreased. These results indicate that the solubility of catalyst is essential to perform this reaction.

Finally, we examine zinc trifluoromethanesulfonate (Zn(II)(OTf)<sub>2</sub>) which was expected to be easily dissolved into the reaction media. The trifluoromethanesulfonate (triflate) is known as one of the best leaving groups in organic chemistry and the triflate anion is an extremely weak base. Using this catalyst, 148% efficiency and 15% yield were achieved. This efficiency which exceeds over 100% indicates that the catalyst cycle completed more than one time at single Zn sites. Moreover, we examined Cu(II)(OTf)<sub>2</sub> (Table IV). In sharp contrast to Cu(II) halides, it was surprising that Cu(II)(OTf)<sub>2</sub> displayed excellent catalytic performance. The catalytic efficiency was observed to be 256%. From these results, it was concluded that weak Lewis acid having high solubility properties in the organic media is the best catalyst for the titled reaction.

### 3.3. NMR and Conformational analyses of 1, 3-Connected Polyarylmethanes

To examine the structure of polymers, we undertook <sup>1</sup>H NMR analyses. The <sup>1</sup>H NMR spectrum shows aliphatic dealkylation (demonstrated by lowered aliphatic integration) and only a slight indication of methylene formation (very weak signal at  $\delta = 4$ ). To judge the extent of methyl dealkylation, aromatic vs. aliphatic integration ratios were calculated and summarized in Table V. Methyl dealkylation were observed to occur significantly, about two methyl groups were lost from one mesitylene-arylmethane unit which contains (3+3/n) methyl groups. These structural deficiencies might disrupt trityl radical coupling in the final dechlorinated polyradicals. Although, in the present study, several attempt including lowering the reaction temperature failed to eliminate the methyl dealkylation, it could be possible to find out suitable catalysts for this purpose since Cu(II)(OTf)<sub>2</sub>, FeCl<sub>3</sub>, and ZnO showed slightly low extent of the methyl dealkylation.

Conformational analysis of tetramer was carried out with MM2 program. Nearly straight chain structure was calculated as a one of the most stable structures. This calculation suggest that these polymers could be easily processed on the substrate in the form of thin film.

**Table III.** Friedel-Crafts Reaction of Mesitylene with Trichlorotoluene on Zn compounds

Catalyst	Mole ratio of catalyst / TCT	Yield	Efficiency (%) <sup>a)</sup>	MN <sup>b)</sup>	n <sup>c)</sup>
ZnF <sub>2</sub>	2 / 1	.d)	.d)	1325	5
ZnCl <sub>2</sub>	2 / 1	3.92g 21%	10	3833	15
ZnBr <sub>2</sub>	2 / 1	.d)	.d)	2129	8
ZnI <sub>2</sub>	2 / 1	.d)	.d)	1357	5
ZnCl <sub>2</sub>	2 / 1	3.92g 21%	10	3833	15
	1 / 2	3.34g 18%	35	3272	13
	1 / 10	0.35g 2%	18	2170	8
ZnO	1 / 1	0.40g 2%	2	2248	9
	1 / 2	2.25g 12%	24	2507	10
	1 / 5	1.75g 9%	46	3533	14
Zn(OTf) <sub>2</sub>	1 / 10	2.81g 15%	148	2797	11
Zn	1 / 1	0.44g 2%	2	1600	6

<sup>a)</sup> Percent of yield per catalyst used.<sup>b)</sup> Number of average molecular weight.<sup>c)</sup> Number of unit.<sup>d)</sup> No solid product was obtained.**Table IV.** Friedel-Crafts Reaction of Mesitylene with Toriflate on Cu(II) Salts

Catalyst	Mole ratio of catalyst / TCT	Yield	Efficiency (%) <sup>a)</sup>	MN <sup>b)</sup>	n <sup>c)</sup>
Zn(OTf) <sub>2</sub>	1 / 10	2.81g 15%	148	2797	11
Cu(OTf) <sub>2</sub>	1 / 20	2.42g 13%	256	3012	12
Cu(II)F <sub>2</sub>	2 / 1	.d)	.d)	1298	5
Cu(II)Cl <sub>2</sub>	2 / 1	.d)	.d)	1375	5

<sup>a)</sup> Percent of yield per catalyst used.<sup>b)</sup> Number of average molecular weight.<sup>c)</sup> Number of unit.<sup>d)</sup> No solid product was obtained.**Table V.** Extent of Dealkylation during Friedel-Crafts Polyalkylation

Catalyst	Ratio of aliphatic H to aromatic H		Number of methyl group lost per unit
	Calculation <sup>b)</sup>	Observed	
ZnCl <sub>2</sub>	1.55	0.35	2.2
Zn(OTf) <sub>2</sub>	1.57	0.49	1.9
Cu(II)(OTf) <sub>2</sub>	1.56	0.60	1.7
FeCl <sub>3</sub>	1.56	0.63	1.6
ZnO	1.58	0.59	1.7
Zn	1.61	0.33	2.5

<sup>a)</sup> Per mesitylene-aryl methane unit which contains (3+3/n) methyl groups.<sup>b)</sup> Ideal Ratios when no dealkylation occur.

#### 4. REFERENCES

1. N. Mataga, *Theor. Chim. Acta*, **1968**, 10, 372.
2. I. Fujita, Y. Teki, T. Takui, T. Kinoshita, K. Itoh, F. Miko, Y. Sawaki, H. Iwamura, A. Izuoka, T. Sugawara, *J. Am. Chem. Soc.*, **1990**, 112, 4074.
3. J. Veciana, C. Rovira, N. Ventosa, M. I. Crespo, and F. Palacio, *J. Am. Chem. Soc.*, **1993**, 115, 57.
4. A. Rajca, S. Utamapanya, and S. Thayumanavan, *J. Am. Chem. Soc.*, **1992**, 114, 1884.

## 1.14 Selective Hydrogenation of CFC-12 to HFC-32 on Zr-Pd/C Catalyst

R. Ohnishi, W.-L. Wang and M. Ichikawa  
Catalysis Research Center, Hokkaido University, Sapporo 060 JAPAN

### Abstract

Reaction of dichlorodifluoromethane(CFC-12) and chlorodifluoromethane(HCFC-22) with  $H_2$  was carried out on modified Pd catalysts. On 5wt% Pd/C, hydrogenation of CFC-12 gave mainly difluoromethane(HFC-32) at 200°C and methane at 350°C, respectively. Zr and V modifiers promoted to increase in activity with no change in selectivity and, thus, to enhance the yield of HFC-32. From temperature programmed reduction (TPR) measurements, formation of Pd-Zr hydride, which desorbed hydrogen at ca. 200°C, was observed. This hydride may play a role to supply active hydrogen in the reaction at the reaction temperature.

### 1. INTRODUCTION

Usage of chlorofluorocarbons (CFCs) has to be discontinued by the year of 1996 because of the global environmental problems, e.g. destructive effect on the stratospheric ozone layer promoted by chlorine atom dissociated from CFCs. Therefore, it is promising that CFCs recovered is effectively converted to some unharful compounds, preferably to useful chemicals, by using the catalytic reaction [1]. Dichlorodifluoromethane (CFC-12), one of the CFCs and a coolant for use in refrigerator and air-conditioner, may be converted to difluoromethane (HFC-32) via hydrodechlorination without loss of fluorine atoms in the molecule. HFC-32, which has no destructive power to ozone, may be used as a CFC substitute. It was reported in the reaction of CFC-12 with  $H_2$  that the chlorodifluoromethane (HCFC-22) was produced with 85% selectivity on a Ni/Al<sub>2</sub>O<sub>3</sub> catalyst at 550°C but no HFC-32 was observed [2]. We will report here that Pd catalysts modified by selected metal additives provide with both high activity and selectivity in hydrodechlorination of CFC-12 to HFC-32 at a low temperature between 200 and 300°C. Reaction of HCFC-22 with  $H_2$  was also conducted. XRD and TPR measurements have been carried out for catalyst characterization.

### 2. EXPERIMENTAL

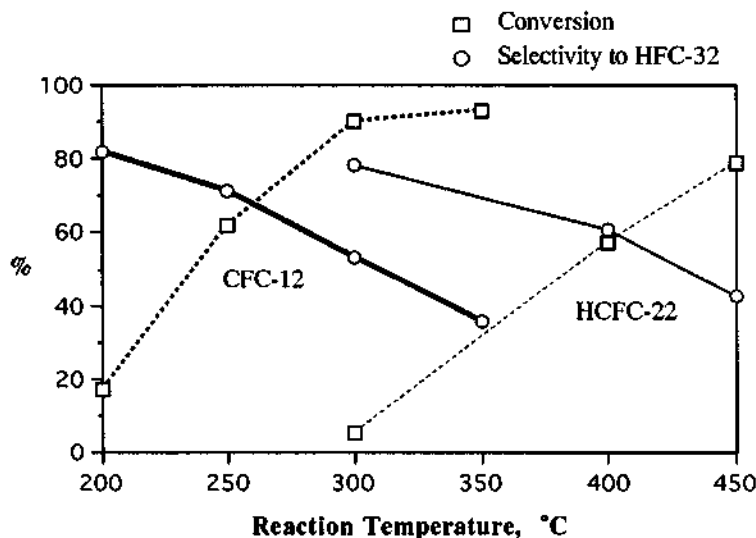
Five wt%Pd/C was purchased from N.E.Chemcat. Some seleceted metal salt modifiers were subsequently impregnated with the Pd catalyst and dried at 100°C for overnight. Before use, all the catalysts were reduced in a  $H_2$  stream at 400°C in a reactor. The reaction of CFC-12 or HCFC-22 with  $H_2$  was carried out by using a continuous flow system with a fixed-bed reactor made from stainless steel or Cu tube ( $\phi$ 10 mm × 200 mm). The flow rates of CFC-12 or HCFC-22 and  $H_2$  were 10 and 20 ml/min, respectively. The gas effluent from the reactor washed with water and a 20 wt% KOH aqueous solution to remove HCl and HF, was analyzed by using a GC with a 2m Porapak Q column.

Temperature programmed reduction (TPR) was performed by use of Altamila AMI1. Before TPR measurement, the catalysts were calcined at 400°C for 2h in a TPR reactor, cooled down to -50°C in Ar flow and a mixture gas ( $H_2$  : Ar = 9.8 : 91.2) was passed through on the catalyst. Then, TPR was started. The experimental parameters used were flow rate of the mixture gas ; 20ml/min, heating rate ; 5°C/min, weight of catalyst ; 50-100mg, temperature span ; 30-600°C, respectively. The XRD was carried out by using a MXP-3 (Mac Sci. Co.) diffractometer with CuK $\alpha$  radiation at 45KV, 30mA with scanning rate of 1 deg/min (2θ).

### 3. RESULTS AND DISCUSSION

Reactivity in the reaction of CFC-12 with H<sub>2</sub> was compared with one of HCFC-22. The results were shown in Figure 1. Both of reactants gave HCF-32 and methane as main products. HCFC-22 reacted with H<sub>2</sub> at much slower rate than CFC-12, in which there is 150°C temperature difference to have the same activity. This is reasonable because bond dissociation energy of C-Cl of CFC-12 (76kcal/mole) is larger than that of HCFC-22 (88kcal/mole). Thus, HCFC-22 is not an intermediate in the reaction of CFC-12 to HFC-32. Another finding from the Figure is that the selectivity to HFC-32 falls down as the reaction temperature rose.

Figure 1 Conversion and selectivity in the reaction of CFC-12 and HCFC-22 with H<sub>2</sub>



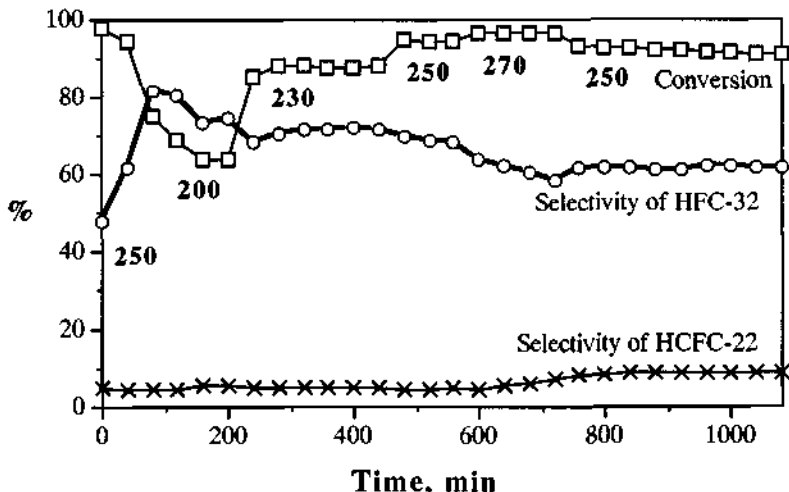
Attempts was made to find a preferable modifier. Results are given in Table 1. Tl was selected because Tl found to decrease the hydrogenation activity of Pd catalyst[4], but Tl modified Pd catalyst gave low reactivity and HCFC-22 as a main product, which would not react further under the reaction conditions. Many modifiers to Pd catalyst were tested to get high selectivity and conversion. As will be

Table 1 Catalytic performances on modified Pd catalysts

Metal	M/Pd	Temp. °C	Conv. %	methane	Selectivity HFC-32	% HCFC-22
-	0	200	17-16	10	80-83	10- 7
		250	60-64	24-19	63-74	8- 6
Tl	0.7	250	25-20	9- 7	33-40	50-44
		200	39-22	8- 9	86	5
V	0.2	250	72-74	16-15	79-81	5- 4
		200	50-34	15-11	79-86	6- 4
Zr	0.5	250	84-91	19-14	68-81	4- 3
		200	50-34	15-11	79-86	6- 4
		1	57-62	26-20	59-67	6
	2	250	44-48	20-16	69-75	6- 5

seen in Table 1, Zr and V modified Pd catalysts gave higher activity than parent Pd catalyst and the similar selectivity. In particular, Zr modified 5wt%Pd/C with Zr/Pd=0.5 in atomic ratio brought about 65% yield (95% conversion and 70% selectivity). Time course on the catalyst was shown in Figure 2. The selectivity of HFC-32 stays over 60% for 10h at 200 - 250°C.

Figure 2 Time course of the reaction on 0.5Zr-5wt%Pd/C catalyst



The XRD spectra of  $x$ Zr-5wt%Pd/C ( $x=0, 0.2, 0.5, 1, 2$ ) reduced with  $H_2$  at 400°C for 2h were presented in Figure 3. Only broad peaks due to small crystal size of Pd were observed. At least three peaks are identified in the region at around  $2\theta = 40, 46.5, 68$ , assigned to (1,1,1), (2,0,0), (2,2,0), respectively, in (h,k,l). Addition of Zr to Pd merely causes any change in the spectra, showing only Pd crystal.

Figure 3 XRD of Zr modified 5wt%/Pd reduced at 400°C for 2h

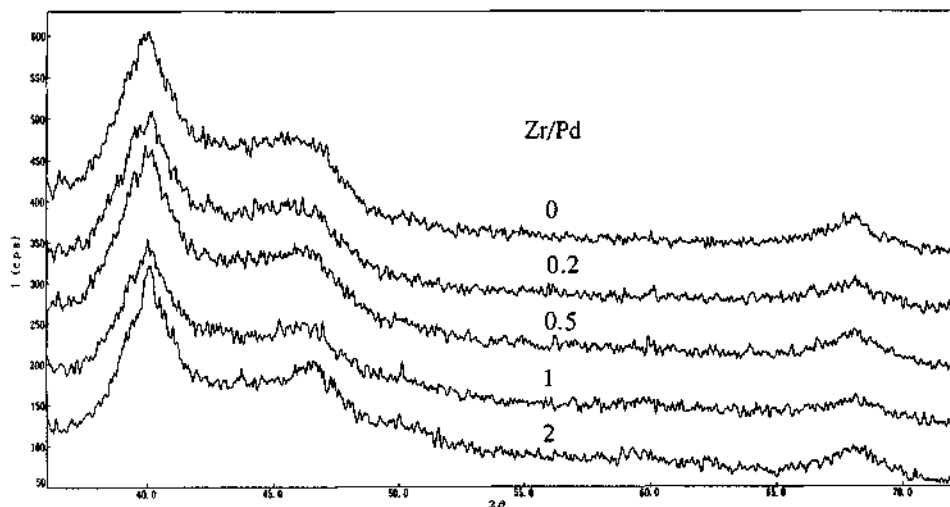
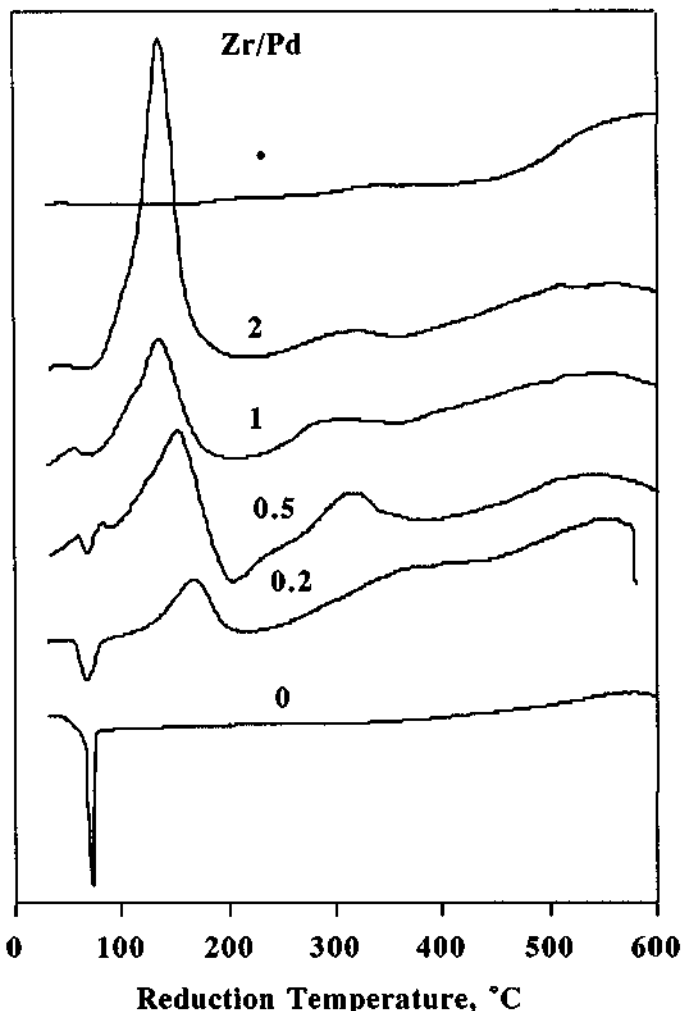


Figure 4 TPR spectra of Zr modified 5wt%Pd/C



The TPR spectra of  $x\text{Zr-Swt\%Pd/C}$  ( $x=0, 0.2, 0.5, 1, 2, \infty$ , which depict Zr/Pd in atomic ratio) catalyst calcined at  $400^\circ\text{C}$  for 1 h were shown in Figure 4. Every catalyst except for  $\text{Zr/C}$  and  $2\text{Zr-Swt\%Pd/C}$ , gave a negative peak at ca.  $70^\circ\text{C}$ , indicative of formation of big Pd cluster. A broad peak at ca.  $500^\circ\text{C}$  may come from oxygenated species on C support since it did not observed on the samples calcined at  $100^\circ\text{C}$ . A positive peak between  $30-200^\circ\text{C}$  will be due to Zr-Pd alloy or intermetallic compound because no peak was observed in this region on  $\text{Pd/C}$  and  $\text{Zr/C}$ . A prominent negative peak was observed at  $200^\circ\text{C}$  on  $0.5\text{Zr-Swt\%Pd/C}$ , which suggests hydride formation. It is noteworthy that the catalyst which forms the hydride, gave the highest yield of HFC-32 in the reaction of CFC-12 with  $\text{H}_2$ .

It was found in these experiments that 1) CFC-12 reacts with  $\text{H}_2$  faster than HCFC-22 on 5wt%Pd/C catalyst, 2) a preferable product, HFC-32, produces less as reaction temperature rises in the reaction, 3) Ti modified Pd catalyst, which is less active in hydrogenation than parent Pd

catalyst, gives HCFC-22 as a main product in the reaction of CFC-12, 4) Zr and V modified Pd catalysts give higher conversions and similar selectivities in the reaction, 5) TPR experiment suggests the formation of Pd-Zr alloy or intermetallic compound, 6) Pd-Zr hydride is observed, 7) XRD experiment shows no appreciable change in addition of Zr to Pd/C catalyst. It is noteworthy that the catalyst which forms the hydride, gave the highest yield of HFC-32 in the reaction of CFC-12 with  $\text{H}_2$ .

#### 4 REFERENCES

- 1 a) R. Ohnishi, Shokubai (Catalysis), **1992**, *34*, 471.  
b) L.E. Manzer and V.N.M. Rao, **1993**, *39*, 329.
- 2 Y. Takita, K. Yamada, T. Ishihara and Y. Mizuno, Nihon Kagaku Kaishi, **1991**, 584.
- 3 R. Ohnishi, W.-L. Wang and M. Ichikawa, submitted to Appl. Catal.
- 4 R. Ohnishi, H. Suzuki and M. Ichikawa, in preparation.

## 2. Characterization

### 2.1 NMR Studies Concerning the Acidity and Catalysis in Zeolites

D. Freude, H. Ernst, T. Mildner, H. Pfeifer and I. Wolf

Fachbereich Physik der Universität Leipzig, Linnéstraße 5, D-04103 Leipzig, Germany

#### Abstract

Two NMR techniques, namely  $^2\text{H}$  MAS NMR and echo Fourier  $^{27}\text{Al}$  NMR have been applied for the first time to study Brönsted acidity of dehydrated zeolites. The  $^{27}\text{Al}$  signal of Si-OH-Al sites, which was NMR-invisible until now, yield a quadrupole coupling constant  $C_{qcc} = 16$  MHz for zeolite H-ZSM-5. The values of  $C_{qcc}$  determined from the  $^2\text{H}$  MAS NMR spectra of Si-OH-Al sites increase with the framework aluminium content of the zeolites from 208 kHz (H-ZSM-5) to 236 kHz (H-X and H-Y) due to the decreased acid strength of the bridging OH groups. The state of art of the two techniques,  $^2\text{H}$  MAS NMR and  $^1\text{H}$  MAS NMR, applied to study Brönsted acidity of dehydrated zeolites is compared.

Concerning the methanol to hydrocarbons conversion (MTG process) in the zeolite H-ZSM-5 we observed the time dependence of the first step of the reaction at 200 °C using a MAS (magic-angle spinning) probe with laser heating system and found that the concentration of protons in the species with stronger polarized O-H bonds increases during the reaction up to 60% at equilibrium.

#### 1. INTRODUCTION

Surface sites capable of donating protons or accepting electrons from adsorbed molecules are essential for the phenomenon of heterogeneous catalysis. The strong acidity of zeolites is generated by bridging hydroxyl groups. Their strength of acidity depends on the electronic charge of the hydrogen atom which can be measured by means of  $^1\text{H}$  or  $^2\text{H}$  MAS NMR spectroscopy of dehydrated samples. The nature of non-framework aluminium compounds plays an important role for the Lewis acidity of partly dealuminated zeolites and can be studied by  $^{27}\text{Al}$  NMR. The NMR investigations of the adsorption and reaction of probe molecules in zeolites can elucidate the acidic properties but also the nature of the catalytic activity of the zeolites. The field of solid-state NMR has developed very rapidly during the last years. The number of published NMR studies of zeolites amounts now to 200 per year and a significant portion of those papers is devoted to the acidity and basicity of zeolites, cf. [1].

The Brönsted sites in zeolites are bridging hydroxyl groups of type Si-OH-Al of the aluminosilicate framework. They can be characterized by various NMR parameters: chemical shift, intensity, dipole broadening, and quadrupole parameters (spin > 1/2). The bare sites can be studied by  $^1\text{H}$ ,  $^2\text{H}$  (after H-D exchange),  $^{17}\text{O}$  (cf.[2]),  $^{29}\text{Si}$  (cf.[3]), or  $^{27}\text{Al}$  NMR measurements of the dehydrated (also denoted as activated or calcined) samples.

Numerous  $^1\text{H}$  NMR studies concerning the acidity of zeolites can be found in the literature and are reviewed by Pfeifer and Ernst [1] and Freude [4]. However, studies concerning the geometry of Brönsted sites are rare [3-7]. Vega et al. have measured the  $^2\text{H}$  NMR powder pattern of the zeolite RHO exchanged with  $\text{ND}_4^+$  ions [8]. On heating the samples above 400 °C without evacuation

results in a spectrum with a spin = 1 quadrupole powder pattern which is due to rigidly bound hydroxyl groups and can be described by a quadrupole coupling constant  $C_{qcc} = 251$  kHz and an asymmetry parameter of the electric field gradient (EFG) tensor  $\eta = 0$ . Gluszak et al. [9] have discussed the two components of the  $^2\text{H}$  NMR signal of a deuterium exchanged and partly dealuminated zeolite  $\text{NH}_4\text{-Y}$  which was evacuated under vacuum to  $450^\circ\text{C}$ . They ascribe the quadrupole powder pattern to hydroxyl deuterons with  $C_{qcc} = 234$  kHz and  $\eta = 0.03$  and a Gaussian shaped signal with a FWHM(full width at half maximum)of 63.1 kHz to silanol groups.

$^{27}\text{Al}$  NMR (as well as  $^{29}\text{Si}$  NMR) experiments were mainly carried out on hydrated samples. From the strongly broadened signal of the  $^{27}\text{Al}$  nuclei in a dehydrated zeolite Na-Y the following quadrupole parameters could be determined [6]:  $C_{qcc} = 6.8$  MHz and  $\eta \approx 0.5$ . The signal of the  $^{27}\text{Al}$  nuclei being constituents of the Si-OH-Al sites in the dehydrated of zeolites was "NMR-invisible" until now.

In the present paper it is shown that the  $^{27}\text{Al}$  NMR signal of the bridging Brönsted sites becomes visible at 11.744 T using an echo Fourier technique. The MAS technique cannot improve the resolution of the second-order powder pattern of the  $^{27}\text{Al}$  signal. But for the first-order quadrupole broadened  $^2\text{H}$  NMR signal of the deuterated zeolites by means of the MAS technique a two-dimensional spectrum can be obtained giving information about the chemical shift and the first-order quadrupole shift as well.

The gradual transition of heterogeneous systems contained in sealed samples from the initial to the final state, i.e. the catalytic reaction itself, can be studied either by a cyclic heating of the sample to increasing temperatures and measurement of the NMR spectra at a low temperature, mostly room temperature, where the reaction is frozen (method A) or by *in situ* variable temperature measurements (method B) [1]. The introduction of the magic-angle spinning (MAS) technique to  $^{13}\text{C}$  NMR spectroscopy of heterogeneous catalytic reactions has led to two important improvements: (i) The resolution of the spectra and hence the sensitivity to ascertain reaction products could be enhanced significantly, and (ii) it has become possible to observe also the carbon-13 signals of strongly bound reaction products including coke. Among the MAS NMR studies the catalytic conversion of methanol to hydrocarbons (MTG process) using zeolite ZSM-5 has attracted a great deal of attention because this process is used on an industrial scale. *In situ* NMR investigations of this process were performed by Anderson and Klinowski (cf. [10],[11]) and Haw et al. (cf. [12]). In our report we present  $^1\text{H}$  and  $^{13}\text{C}$  MAS NMR results of the time dependence of the conversion of methanol in the zeolite H-ZSM-5. Compared with the previous NMR *in situ* techniques (A) and (B), the temperature switching behaviour in the laser heated sample is closer to that in a gaseous flow reactor.

## 2. EXPERIMENTAL

The zeolite H-Y 92 containing 8%  $\text{Na}^+$  of the original content of cations, was prepared by a repeated exchange of a sample of Na-Y ( $\text{Si}/\text{Al} = 2.6$ ) in an aqueous solution of  $\text{NH}_4\text{NO}_3$ , followed by calcination. The samples H-Y 85 were prepared from a 85%  $\text{NH}_4^+$  and 15%  $\text{Na}^+$  containing zeolite Y ( $\text{Si}/\text{Al} = 2.4$ ). The zeolite H-X 50 ( $\text{Si}/\text{Al} = 1.4$ ) contains 50% of the original content of sodium ions. Zeolites Na-ZSM-5 and H-ZSM-5 with  $\text{Si}/\text{Al} = 22$  were synthesized using mono-n-butylamine as template, and then exchanged with 0.5 N HCl. A template-free synthesized zeolite H-ZSM-5 ( $\text{Si}/\text{Al} = 15$ ) was used for the methanol conversion.

Samples for  $^1\text{H}$  and  $^2\text{H}$  MAS NMR were prepared by heating 8 mm deep layers of zeolite in glass tubes 4 mm or 5 mm diameter. The temperature was increased at a rate of  $10\text{ K h}^{-1}$  under vacuum. After maintaining the samples at  $400^\circ\text{C}$  and at a pressure less than  $10^{-2}$  Pa for 24 h, several samples were partially deuterated by contact with 2 kPa  $\text{D}_2\text{O}$  at  $400^\circ\text{C}$  or  $230^\circ\text{C}$  for 30 minutes, followed by evacuation. This procedure was repeated 8 times followed by a final evacuation at  $300^\circ\text{C}$  for 12 h. The samples were then loaded under a pressure of 13 kPa of  $\text{O}_2$  and sealed off.

The adsorption of O<sub>2</sub> shortens the spin-lattice relaxation time T<sub>1</sub> for the <sup>1</sup>H and <sup>2</sup>H nuclei, so that the MAS NMR spectra could be acquired with 1 s repetition time. Without oxygen, the proton longitudinal relaxation times T<sub>1</sub> of the OH groups have been found to be ca. 10 s, while an average value of 26 s has been determined for the corresponding deuteron T<sub>1</sub> [9].

The same exchange treatment at 230 °C, except for the use of H<sub>2</sub>O instead of D<sub>2</sub>O, has been carried out on zeolite H-Y 85. By comparing the <sup>1</sup>H MAS NMR spectrum of this sample with the spectrum of the sample which had not treated at 230 °C, it could be shown that the deuteration did not change the concentration of hydroxyl groups in the zeolite.

In order to obtain a signal of residual water molecules and residual ammonium ions, the zeolite H-Y 92 was evacuated at a maximum temperature of only 230 °C and denoted as H-Y 92/230.

For <sup>27</sup>Al and <sup>29</sup>Si NMR measurements on dehydrated samples, the zeolites were treated as described above using a final evacuation at 400 °C, then loaded with ca. 300 mg n-octane per gram zeolite under vacuum and sealed off. After the homogenisation of the sample at 100 °C the zeolite was fully immersed in octane. Before the measurements the glass tubes (10 mm diameter) were opened and the samples were transferred into the MAS sample container under air.

The NMR measurements at room temperature were carried out using a Bruker MSL 500 spectrometer. The <sup>27</sup>Al pulse length was 0.5 μs, which corresponded to a π/6 pulse for non-selective excitation (π/2 pulse for selective excitation of the central transition, cf.[13]). The rf power used corresponds to a (non-selective) nutation frequency of ν<sub>rf</sub> = 167 kHz, so that for all samples ν<sub>rf</sub> exceeds the spectral width of the central transition. If the latter value exceeded 50 kHz, a phase cycled selective echo sequence [14] (π/2<sub>0.5μs</sub>, delay<sub>20 μs</sub>, π<sub>1μs</sub>) was used, starting the acquisition 20 μs after the second pulse. For <sup>1</sup>H MAS NMR (ν<sub>rot</sub> = 12.5 kHz) and <sup>2</sup>H MAS NMR (ν<sub>rot</sub> = 5 kHz), the acquisition was initiated one rotation period after the single pulse. The number of scans varied from 1000 for <sup>1</sup>H to 100 000 for <sup>2</sup>H MAS NMR.

For the *in situ* methanol conversion the zeolite H-ZSM-5 was loaded with 8 methanol molecules (99% enriched in <sup>13</sup>C) per unit cell corresponding to two molecules per channel intersection. Fused quartz ampoules were used for the temperature dependent experiments and the <sup>1</sup>H and <sup>13</sup>C MAS NMR measurements (partially with decoupling) were performed at spinning rates of about 1 kHz using a Bruker MAS NMR probe with a CO<sub>2</sub> laser heating system together with the MSL 300.

### 3. RESULTS

Some of the <sup>1</sup>H MAS NMR spectra of the dehydrated zeolites are given in Fig. 1. The different proton signals are denoted by (a) - (e), cf. Refs [1,4]: Line (a) at 1.9 ppm is due to non-acidic hydroxyl groups at framework defects and in the amorphous part of the sample. Line (b) at 3.7 ppm for H-X 50, 3.9 ppm for H-Y 85, 4.0 ppm for H-Y 92, and 4.3 ppm for H-ZSM-5 is due to bridging OH groups pointing into the large zeolite cages or into the intersections, respectively. Line (c) at 4.8 - 4.9 ppm in the spectra of zeolites H-Y is caused by bridging OH groups pointing into the sodalite cage. Line (d) at 7 ppm is assigned to residual ammonium cations. Line (e) at ca. 2.7 ppm represents hydroxyl groups associated with non-framework aluminium species and bonded to framework oxygen atoms. The spinning sidebands not shown in Fig. 1, contain less than 10% of the total intensity of the spectra. By a comparison of the signal intensities of deuterated and non-deuterated samples an exchange degree of 75% - 95% of the hydrogen species has been found.

Fig. 2A shows the <sup>2</sup>H MAS NMR sideband pattern of sample H-Y 92/230. In this presentation the structure of the spinning sidebands is lost. Fig. 2B presents the same spectrum in a two-dimensional stack-plot. The 2D plot was created using the Bruker WINNMR software by dividing the sideband spectrum (32768 points) into single sideband files. The shape of the sidebands is plotted in the second dimension, representing the chemical shift, whereas the first (horizontal) dimension represents the first-order quadrupole broadened (static) linewidth of species having the corresponding value of the chemical shift. This type of representation of a sideband spectrum by a

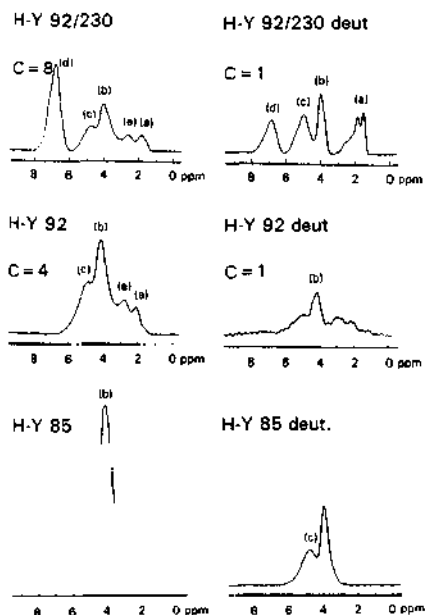


**Figure 1.**  $^1\text{H}$  MAS NMR spectra of some samples. The two observable spinning sidebands in the distance of 12.5 kHz (ca. 30 ppm and -20 ppm) contain less than 10% of the total intensity of the spectra. Concentrations of species can be determined from the spectra after multiplication of their intensities with the factor C given for each of them in the Figure.

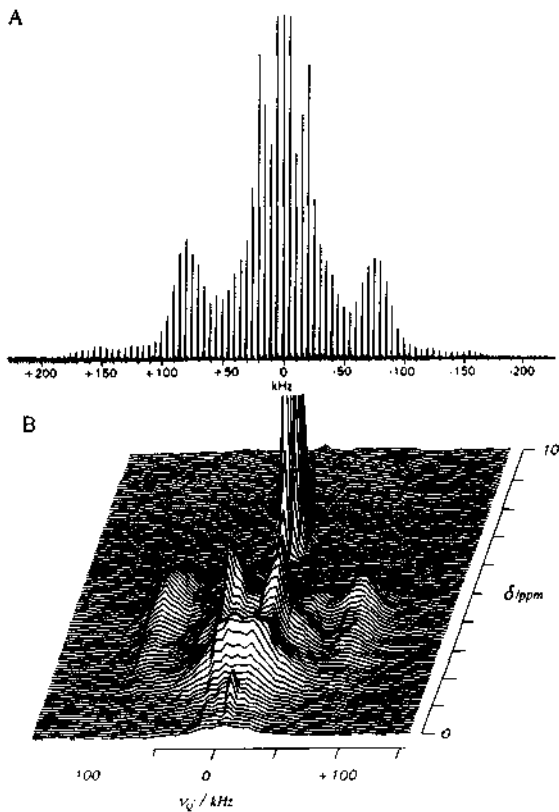


**Figure 2.** A shows the  $^2\text{H}$  MAS sideband pattern of sample H-Y 92/230. B presents the same spectrum in a two-dimensional stack-plot. The 2D plot was created using the Bruker WINNMR software by dividing the sideband spectrum (32768 points) into single sideband files. The shape of the sidebands is plotted in the second dimension, representing the chemical shift, whereas the first (horizontal) dimension represents the first-order quadrupole broadened linewidth of species having the corresponding value of the chemical shift.  $v_Q'$  represents the angular dependent first-order quadrupole shift for the both transitions -1,0 and 0,+1.

two dimensional spectrum was used for the first time by Blümich et al. [15].  $\nu_Q'$  represents the angular dependent first-order quadrupole shift for the transitions -1,0 and 0,+1:

$$\nu_Q' = \pm (3/8) C_{qcc} (3 \cos^2\beta - 1 + \eta \sin^2\beta \cos 2\alpha).$$

$C_{qcc}$  =  $e^2 Q/h$  denotes the quadrupole coupling constant with  $eQ$  as the electric quadrupole moment and  $eQ = V_{zz}$ .  $\eta = (V_{xx} - V_{yy})/V_{zz}$  with  $|V_{zz}| \geq |V_{yy}| \geq |V_{xx}|$  define the components of the traceless EFG tensor.  $\alpha$  and  $\beta$  are the Euler angles for the rotation of the principal axes system with respect to the laboratory system. The distance between the two singularities in a theoretical powder spectrum, which are due to both transitions in the case of  $\beta = \pi/2$  and  $\eta = 0$ , corresponds to the quadrupole frequency  $\nu_Q$ . For spin=1 nuclei  $\nu_Q$  is equal to  $(3/4) C_{qcc}$ . Figure 3 shows contour plots of the  $^2\text{H}$  MAS NMR spectra. Although from these figures the values of  $C_{qcc}$  can be estimated only roughly, a MAS sideband simulation of Fenzke et al. [7] allows the exact determination of the quadrupole parameters, which are presented in table 1 for the bridging hydroxyl groups. Four different species can be distinguished due to different quadrupole coupling parameters: bridging hydroxyl groups ( $C_{qcc} = 208 - 236$  kHz,  $\eta \approx 0.10 \pm 0.05$ ), AlOH groups ( $C_{qcc} = 67$  kHz,  $\eta = 0.2$ ), silanol groups (quadrupole broadened structureless signal with FWHM = 65 kHz), and residual ammonium ions (weak quadrupole broadening, FWHM < 5 kHz).

**Table 1.** NMR parameters describing the hydrogen forms of the zeolites. Si/Al denote the framework Si/Al ratio determined by  $^{29}\text{Si}$  MAS NMR. NFAI refer to non-framework aluminium giving rise to the lines at ca. 0 ppm and ca. 30 ppm in the  $^{27}\text{Al}$  MAS NMR spectra of the hydrated samples.  $^1\text{H}$  c.s. [int.] denote the values of the isotropic chemical shift (accuracy  $\pm 1$  ppm) determined from the MAS spectrum measured at  $\nu_{rot} = 12.5$  kHz for lines (a), (b), (c), (e), the values in brackets give the concentration of the corresponding number of species per unit cell.  $C_{qcc}(^2\text{H})$  and  $\eta$  denote the quadrupole coupling constant of the signal of the bridging hydroxyl groups and the corresponding asymmetry parameter, respectively.  $C_{qcc}(^{27}\text{Al})$  and  $\eta$  give the values for the aluminium nuclei in the SiOHAi sites.

Samples	H-X 50	H-Y 85	H-Y 92	H-ZSM-5
Si/Al	1.4 $\pm$ 0.1	2.4 $\pm$ 0.1	3.1 $\pm$ 0.1	22 $\pm$ 1
NFAI	< 2%	< 2%	20 $\pm$ 4%	5 $\pm$ 2%
$^1\text{H}$ c.s. [int.]				
line (a)				
line (b)	3.7 ppm [40 $\pm$ 4]	3.9 ppm [23 $\pm$ 2]	2.0 ppm [4.3 $\pm$ 0.5]	2.0 ppm [0.5 $\pm$ 0.1]
line (c)		4.8 ppm [25 $\pm$ 2]	4.1 ppm [21 $\pm$ 2]	4.3 ppm [4 $\pm$ 0.4]
line (e)	3.0 ppm [10 $\pm$ 3]		4.9 ppm [22 $\pm$ 2]	
			2.8 ppm [12 $\pm$ 1]	
$C_{qcc}(^2\text{H})$	236 $\pm$ 10 kHz	236 $\pm$ 10 kHz	224 $\pm$ 10 kHz	208 $\pm$ 10 kHz
$\eta$	0.10 $\pm$ 0.05	0.06 $\pm$ 0.05	0.13 $\pm$ 0.05	0.15 $\pm$ 0.05
$C_{qcc}(^{27}\text{Al})$	10.8 $\pm$ 1.0 MHz	12.7 $\pm$ 1.0 MHz	12.7 $\pm$ 1.0 MHz	16.0 $\pm$ 1.0 MHz
$\eta$	0.9 $\pm$ 0.1	0.7 $\pm$ 0.1	0.7 $\pm$ 0.1	0.1 $\pm$ 0.1

The  $^{27}\text{Al}$  MAS NMR spectra of the hydrated samples, which are not shown here, consist of three signals: Framework aluminium gives rise to a narrow line at ca. 60 ppm, whereas the narrow line at ca. 0 ppm and the broad line at ca. 30 ppm must be attributed to non-framework aluminium. The relative amounts of non-framework aluminium atoms, obtained from the relative intensities of the lines at ca. 0 ppm and at ca. 30 ppm in the spectra of the hydrated samples, are presented in table 1.

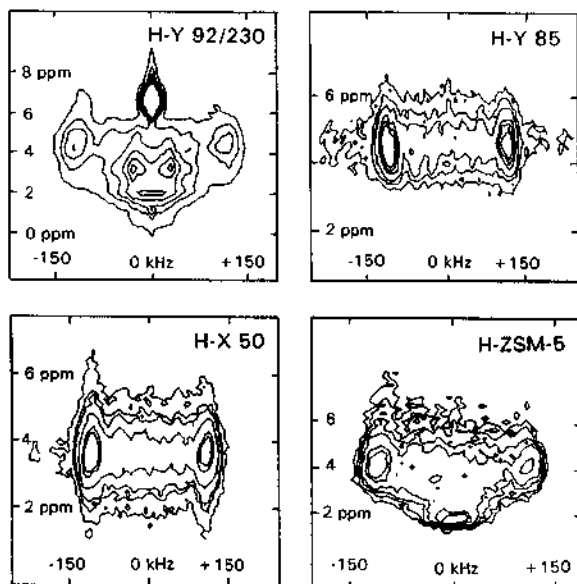


**Figure 3.** Contour plots of the  $^2\text{H}$  MAS spectra. An sideband simulation allows the exact determination of the quadrupole parameters. Four different species can be distinguished due to different quadrupole coupling parameters: bridging hydroxyl groups ( $C_{qcc} = 208\text{--}236 \text{ kHz}$ ,  $\eta = 0.10 \pm 0.05$ , see table 1), defect AlOH groups ( $C_{qcc} = 67 \text{ kHz}$ ,  $\eta = 0.2$ ), defect silanol groups (quadrupole broadened structureless signal with  $\text{FWHM} = 65 \text{ kHz}$ ), and residual ammonium ions (weak quadrupole broadening,  $\text{FWHM} < 5 \text{ kHz}$ ).

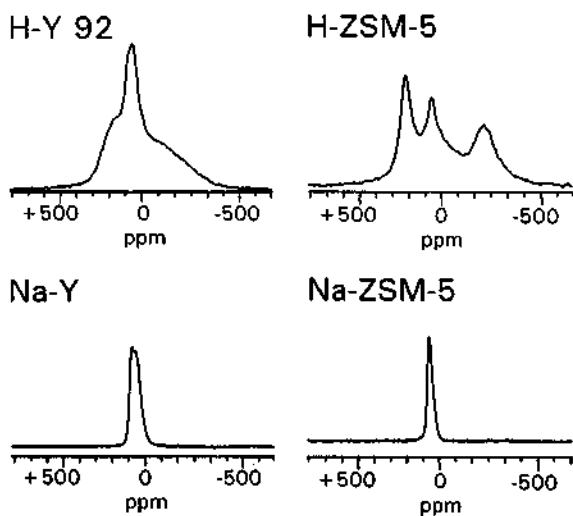


**Figure 4.**  $^{27}\text{Al}$  NMR spectra of the dehydrated zeolites. Aluminium atoms in negatively charged oxygen tetrahedra, compensated by sodium cations, give rise to the spectra of the sodium zeolites and to the narrow component in the spectra of the hydrogen zeolites. Therefore, the spectra of the hydrogen forms must be split into two components. The lineshape simulation for the broad components gives the values:  
 $C_{qcc} = 12.7 \text{ MHz}$ ,  $\eta = 0.7$  for H-Y 92,  
 $C_{qcc} = 16 \text{ MHz}$ ,  $\eta = 0.1$  for H-ZSM-5,  
 $C_{qcc} = 5.5 \text{ MHz}$ ,  $\eta = 0.3$  for Na-Y,  
 $C_{qcc} = 4.7 \text{ MHz}$ ,  $\eta = 0.5$  for Na-ZSM-5.

$^{27}\text{Al}$  NMR spectra of the dehydrated zeolites are shown in Fig. 4. The full width of the spectra varies from 24 kHz (Na-ZSM-5) to 100 kHz (H-ZSM-5). This means that the available maximum value of the MAS frequency  $\nu_{\text{rot}} = 15$  kHz does not exceed the second-order broadening of the central transition and thus the application of MAS is pointless. Aluminium atoms in negatively charged oxygen tetrahedra, compensated by sodium cations, give rise to the spectra of the sodium zeolites and to the "narrow" component in the spectra of the hydrogen zeolites. Therefore, the spectra of the hydrogen forms must be split into at least two components. Moreover, different crystallographic positions of the aluminium atoms in the sodium form, and, in addition, different distances to the hydroxyl protons in zeolites H-Y, should give rise to a distribution of the quadrupole parameters. The values of  $C_{\text{qc}}$ , see Fig. 4, were determined by means of a lineshape simulation with the programme WINFIT (Bruker) assuming only one or two sets of parameters for the sodium and hydrogen form of the zeolites, respectively. A comparison of the FWHM of the dehydrated zeolite H-ZSM-5 with the rehydrated one (not shown here) yields a factor of about 100. Therefore, the absence of a component narrowed by water in the spectrum of a sample measured one month after the filling of the MAS rotor proves that the octane loading prevented the sample from rehydration while exposed to air.

The resonance position of the  $^{27}\text{Al}$  NMR (central transition) signal of the dehydrated samples is given by the centre of gravity of the line. The second moment of the line with respect to this centre of gravity gives a value for the (high field) second-order quadrupole shift of the centre of gravity, cf. Freude and Haase [13] p. 30. Finally, the chemical shift  $\delta$  with respect to the reference  $\text{Al}(\text{H}_2\text{O})_6^{3+}$  in aqueous solution is obtained by the addition of the resonance position of the centre of gravity and the magnitude of the quadrupole shift, giving  $\delta = 105 \pm 20$  ppm for the dehydrated zeolites H-Y and  $\delta = 82 \pm 20$  ppm for the zeolite H-ZSM-5.

Figure 5 shows the  $^{27}\text{Al}$  NMR spectra of dehydrated samples H-ZSM-5 before (Fig. 5A) and after a mild hydrothermal treatment at a water vapour pressure of 7 kPa, 13 kPa, and 93 kPa. The steaming procedure is described in Ref. [16]. All spectra must be split into at least two components. One component of the signals must be due to the framework aluminium atoms ( $\eta = 0.1$ , see Fig. 4), the other component, which seems to be caused by an asymmetric EFG tensor, must be explained by extra-framework aluminium atoms. The total intensities of all signals are about equal.

Some proton decoupled  $^{13}\text{C}$  MAS NMR spectra of the methanol conversion at 200 °C are given in Fig. 6. Relevant resonance positions are: methanol 50.5 ppm, dimethylether 60.5 ppm, CO 183.3 ppm,  $\text{CO}_2$  124.2 ppm, and methane -10.7 ppm. The time dependent molar concentrations of the species collected from a series of samples are presented in Fig. 7. The water content (dashed line) was calculated from the concentration of other reactants. Fig. 8 shows some corresponding proton spectra, which are well-resolved at the reaction temperature compared with the results of the room temperature measurements. Relevant resonance positions are:  $\text{CH}_3\text{OH}$  adsorbed in H-ZSM-5 ca. 9.1 - 10.5 ppm [10], water 4.78 ppm, hydroxonium ion ca. 10 ppm (cf.[17]), and bridging OH groups 4.3 ppm. The methane doublet at 0.23 ppm arises from the  $^1\text{H}-^{13}\text{C}$  coupling.

## 4. DISCUSSION

### 4.1. Acid Sites

The characterization of solid acids by  $^1\text{H}$  MAS NMR is now well-established. In order to interpret the spectra of Brönsted acid catalysts it is normally accepted that the strength of acidity increases with decreasing electronic charge of the hydrogen atom, which corresponds to a larger value of the chemical shift of the proton magnetic resonance. Since the NMR intensity of a resolved line in the high speed MAS spectrum is directly proportional to the concentration of its Brönsted acid sites, the spectrum may be interpreted as a distribution function of acidity. This approach allows an interpretation of lines (a) and (b) in the spectra. For example, when one considers the acidic hydroxyl groups, the values of the chemical shift of line (b) increases from 3.7 ppm for zeolite H-X

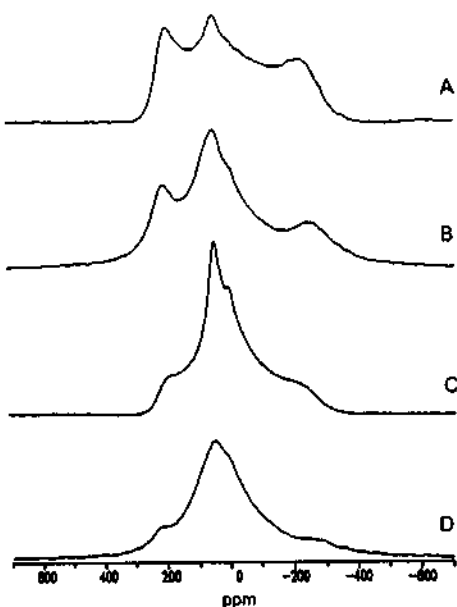


Figure 5.  $^{27}\text{Al}$  NMR spectra of dehydrates samples H-ZSM-5 before A, and after mild hydrothermal steaming at a water vapour pressure of 7 kPa B, 13 kPa C, and 93 kPa D.

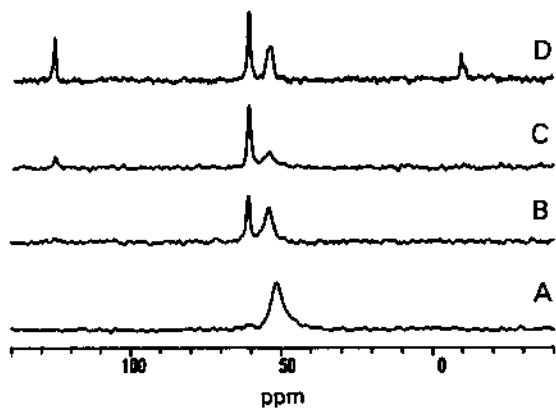


Figure 6. Proton decoupled  $^{13}\text{C}$  MAS NMR spectra of the methanol conversion. The zeolite H-ZSM-5 was loaded with 8 methanol molecules per unit cell. Spectrum A is measured at room temperature. *In situ* measurements started immediately after heating the sample up to 200 °C (spectrum B), after 10 minutes (spectrum C), and after 40 minutes (spectrum D). The measuring time was 3 minutes for each of the spectra. Therefore, e.g. the spectrum B starting at 0 minutes represents the mean value between 0 and 3 minutes.

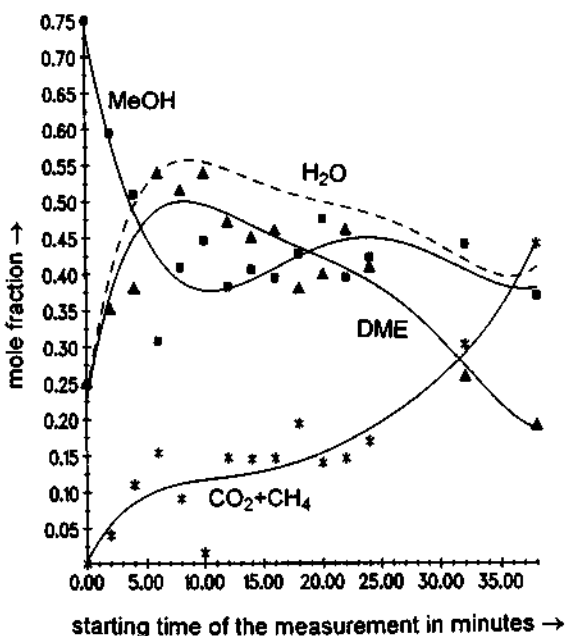


Figure 7. Time dependent molar concentrations of the  $^{13}\text{C}$  species for the conversion at 200 °C. The zeolite H-ZSM-5 was loaded with 8 methanol molecules per unit cell at room temperature. The water content (dashed line) was calculated from the concentration of the other reactants.

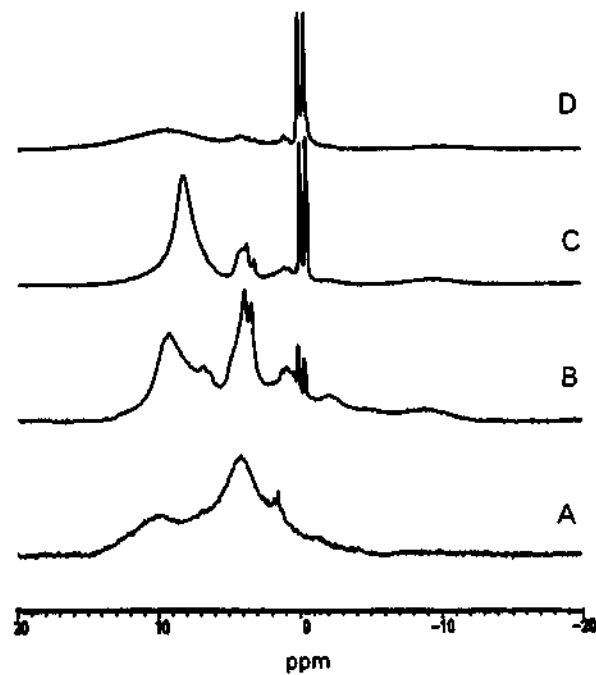


Figure 8.  $^1\text{H}$  MAS NMR spectra of the methanol conversion. The zeolite H-ZSM-5 was loaded with 8 methanol molecules per unit cell. Spectrum A is measured at room temperature. *In situ* measurements were performed 25 minutes (spectrum B) and 40 minutes (spectrum C) after heating the sample up to 200 °C. Spectrum D was measured at room temperature after cooling down the sample after the conversion.

through 3.9 - 4.0 ppm for zeolite H-Y to 4.3 ppm for zeolite H-ZSM-5 corresponding to the increasing acid strength, whereas the concentration of hydroxyl groups giving rise to line (b), decreases on going from faujasites to H-ZSM-5 (see table 1). With respect to the non-acidic hydroxyl groups, the intensity of line (a) at ca. 2 ppm is a measure of the concentration of defect silanol groups. However, the spectra in Fig. 1 show two more hydroxyl group signals, i.e. (c) and (e), for which the value of the chemical shift cannot be explained by the simple model above: The corresponding hydroxyl groups experience an additional electrostatic interaction with other oxygen atoms in the neighbourhood. This increases the value of the chemical shift but not the acid strength. These hydroxyl protons point to other framework oxygen atoms which reduces the accessibility of the hydroxyl protons to adsorbed molecules and therefore, their ability to act as acid sites.

In the present paper the  $^1\text{H}$  MAS NMR investigations were carried out in order to demonstrate the deuteration of the hydroxyl groups and to compare the  $^2\text{H}$  spectra with those of the  $^1\text{H}$  MAS NMR. The spectrum of zeolite H-92/230, Fig. 1A, consists of five signals including the line (d) due to the incomplete deammonisation (8.5 residual ammonium ions per unit cell) at the maximum treatment temperature of 230 °C. The quantitative comparison of spectra A, C, E, with B, D, F in Fig. 1 verifies the decrease (75% - 95%) of the lines (a) - (d) upon deuteration. In Fig. 1C the line (e) due to AlOH groups is best resolved. The concentration of 12 AlOH groups and 4.3 silanol groups per unit cell in sample H-Y 92 is caused by the calcination of the ammonium form under air during the modification from Na-Y to H-Y. In contrast, the spectrum of the zeolite H-Y 85 shows neither line (e) nor line (a). This characterizes the zeolite H-Y 85 as defect-free.

From the  $^2\text{H}$  MAS NMR spectra of the deuterated zeolites values for the chemical shift can be determined, which should be the same as from the  $^1\text{H}$  MAS NMR spectra. However, the separation of the two types of bridging OH groups giving rise to lines (b) and (c) with a separation of ca. 1 ppm in the  $^1\text{H}$  MAS NMR spectrum is not yet possible. The residual MAS linewidth (FWHM) due to second-order quadrupole broadening, cf. [13], is  $\delta_{\text{2nd-order}} = (C_{\text{qcc}}/8\nu_L)^2$  for  $I \approx 1$  and  $\eta = 0$  yielding 0.1 ppm for  $C_{\text{qcc}} = 220$  kHz and  $\nu_L = 76.775$  MHz. The residual linewidth (FWHM for  $I = 1$ ,  $\eta = 0$ ) caused by a deviation from the magic angle between the rotation axis and the external magnetic field is more significant:  $\delta_{\text{MAS}} = (3/8) C_{\text{qcc}} (3 \cos^2\theta - 1)/\nu_L$ . It yields 1 ppm in our case for a deviation of 0.02° from the magic angle. Thus an instability of the rotor axis or a static deviation from the magic angle can limit the resolution in the  $^2\text{H}$  MAS NMR spectra. Another explanation of the decreased resolution compared with the  $^1\text{H}$  MAS NMR spectra may be the mobility of the OH groups. The mean residence time of a hydrogen atom on one oxygen site must be much greater than the reciprocal frequency difference between the two lines (b) and (c). The latter value increases by a factor of 6.6 going from  $^1\text{H}$  to  $^2\text{H}$  NMR. The ability to resolve lines (b) and (c) and relatively short acquisition times are still the advantage of the  $^1\text{H}$  MAS NMR.

The  $^2\text{H}$  MAS NMR technique reveals a new dimension for the study of surface hydroxyl groups, which can be used in two ways: Firstly, it is evident from Fig. 2B that the quadrupole dimension increases the resolution of signals having similar positions in the  $\delta$ -scale but different values in the  $\nu_Q$ -scale. Signals of residual ammonium ions or of residual adsorbed molecules (not shown here) appear predominantly close to  $\nu_Q = 0$  kHz. Secondly, in addition to the values of chemical shifts, the quadrupole coupling constants  $C_{\text{qcc}}$  can be studied in order to characterize the hydroxyl groups. The values of  $C_{\text{qcc}}$  of the bridging hydroxyl groups (see table 1) increase with the framework aluminium content of the zeolite from 208 kHz (H-ZSM-5) to 235 kHz (H-X 50 and H-Y 85) due to the decreased acid strength of the bridging OH groups. Relations between the proton chemical shift and the corresponding deuterium quadrupole coupling constant can be found in literature: Rosenberger et al. [18] derived the equation  $\delta/\text{ppm} = c_1 - c_2 \times C_{\text{qcc}}/\text{kHz}$  with the constants  $c_1 = 18.88$  and  $c_2 = 0.05$  for polycrystalline trihydrogen selenites. Sternberg and Brunner [19] have predicted for hydroxyl groups in solids values of 26 and 0.095 for the constants  $c_1$  and  $c_2$ , respectively. Using this correlation, it follows from our values of  $C_{\text{qcc}} = 208$  kHz and 235 kHz that the values of  $\delta$  should be 6.24 ppm and 3.68 ppm, respectively. The absolute value is well predicted

for the  $^1\text{H}$  MAS NMR signal of zeolite H-X. But the average chemical shift of bridging hydroxyl groups in the zeolites H-Y (lines (b) and (c)) is very close to the value of 4.3 ppm measured for the zeolite H-ZSM-5, whereas from the theoretical prediction [19] a difference of 2.56 ppm should follow from our experimental values of  $C_{qcc}$ .

The quadrupole dimension of the signals of defect hydroxyl groups shows signals reduced in the FWHM in comparison with those of the bridging hydroxyl groups. For the Al hydroxyl groups the signal shows two singularities; the fitting procedure yields  $C_{qcc} = 67 \text{ kHz}$ ,  $\eta = 0.2$ . The signal of the silanol groups has only one maximum, the FWHM is 65 kHz and the fit yields  $C_{qcc} = 75 \text{ kHz}$  and  $\eta = 0.6$ . The simple explanation of the quadrupole coupling constant predicts a decrease of  $C_{qcc}$  for the weakening of the oxygen-hydrogen bond. But bond weakening of the defect hydroxyl groups in comparison to bridging hydroxyl groups is in disagreement with the explanation of the corresponding values of the chemical shift. A motional narrowing of the spectral width due to fast jumps between oxygen atoms can also be excluded. If the spinning sideband pattern exists, the jump frequency must be small in comparison with the rotation frequency, which is small in comparison with the spectral width. But a fast rotational diffusion of the hydrogen around the Si-O or Al-O axis reduces the static linewidth by a factor of  $(1/2)(3 \cos^2\theta - 1)$ . Ernst [20] has determined an angle of  $\theta = 40^\circ \pm 5^\circ$  between the Si-O and O-H axes of silanol groups. The fast rotation around the Si-O (Al-O) axis with an Si-O-H angle in the corresponding range reduces the static linewidth by a factor of 0.25 - 0.5. This effect and a distribution of an additional electrostatic interaction between defect hydroxyl groups and framework oxygen atoms can explain the quadrupole lineshape of the  $^2\text{H}$  MAS NMR spectra of defect hydroxyl groups.

Whereas a detailed discussion exists about the correlation between proton chemical shift values (cf. [1, 4]) or deuteron quadrupole coupling constants (cf. [18, 19]) with the weakening of the oxygen-hydrogen bond, which describes the property of the Brønsted site, the correlation between the aluminium quadrupole coupling constant of the Brønsted site with its acidic properties is unknown until now. In the present study first experimental values are given for  $C_{qcc}$  of the aluminium atom in a SiOHAl site. Experiments with hydrated zeolite samples could not give information about this site, because the hydroxyl proton is involved in the formation of hydroxonium ions [17]. The values of  $C_{qcc}$  in Fig. 4 demonstrate that the electric field gradient at the position of the aluminium atom increases by a factor of 2.3 or 3.4 for the zeolites Y or ZSM-5, respectively, going from the dehydrated sodium form to the dehydrated hydrogen form of the zeolite. This proves the influence of the acidic proton upon the EFG tensor at the position of the framework aluminium atoms. A comparison between the samples under study yields the higher value of  $C_{qcc}$  for the Brønsted site in the zeolite H-ZSM-5, which is supposed to have the strongest polarized O-H bond. The higher rotational symmetry of the EFG tensor for zeolite H-ZSM-5 can be explained by an isolated Brønsted site, whereas in zeolites of faujasite type the Brønsted sites in the neighbourhood of aluminium cations can destroy the symmetry of the tensor. Further experiments and also calculations of the EFG tensor are necessary in order to correlate the field gradient tensor at the site of the  $^{27}\text{Al}$  nucleus in the SiOHAl group with the properties of the Brønsted site.

Values of the  $^{27}\text{Al}$  NMR chemical shift can be determined with a high accuracy for the hydrated zeolites. The value for the 4-coordinated framework aluminium is ca. 60 ppm for the hydrogen and sodium forms of the zeolites Y and ZSM-5, whereas a narrow signal of 6-coordinated extra-framework aluminium appears at ca. 0 ppm. In the case of dehydrated hydrogen zeolites one Al-O bond in the bridging groups ( $=\text{Si}-\text{OH}-\text{Al}=$ ) is weakened or broken, commonly denoted by a dotted line instead of a solid line in the picture of the structure. This can be understood as an intermediate case between 4- and 3-coordination. Consequently the chemical shift values of these nuclei should be expected to be higher than those in hydrated samples. The values of  $\delta = 105 \pm 20 \text{ ppm}$  for the dehydrated zeolites H-Y and  $\delta = 82 \pm 20 \text{ ppm}$  for the zeolite H-ZSM-5 obtained for the first time in this study support this suggestion.

Figure 5 shows that also the extra-framework aluminium in the dehydrated sample can be observed now. The signal assigned to extra-framework aluminium is narrower compared with that of the bridging SiOHAl positions. Therefore, the quadrupole broadening of the extra-framework aluminium species is smaller corresponding to a higher symmetry of these positions.

#### 4.2. Methanol Conversion

The results presented in Figs. 6 and 7 show that the methanol conversion starts immediately after the reaction temperature was switched from room temperature to 200 °C by the laser beam. The concentration of methanol and dimethylether goes through a minimum and maximum, respectively, until chemical equilibrium is approached after 40 minutes. This equilibrium corresponds to values measured with method (B) and is different from that at room temperature [method (A)], as was shown by a room temperature measurement after the conversion at 200 °C. It is important to note that CO<sub>2</sub> is observed as a reaction product in our experiment.

The *in situ* <sup>1</sup>H MAS spectra (cf. Fig. 8) show broad lines, with peaks at 9 ppm and 8 ppm after a reaction time of 25 minutes and 40 minutes, respectively. Anderson et al. observed at room temperature the signal of the methanol hydroxyl at 9.1–10.5 ppm, the latter value for a methanol loading similar to that used in our study. They explain the strong low field shift by hydrogen bonding or protonation of the methanol molecules in the zeolite H-ZSM-5. The chemical shift of water is 4.78 ppm, that of the bridging hydroxyl group is 4.3 ppm, and a signal of a hydroxonium ion is supposed to have a chemical shift of ca. 10 ppm (cf. [17]). A fast chemical exchange of the <sup>1</sup>H nuclei between these species gives a mean value of the chemical shift, which increases with mean degree of polarization of the O-H bond. From the intensity of the line at 8–9 ppm it can be concluded that the concentration of protons in the species with stronger polarized O-H bonds increases during the reaction up to 60% at equilibrium. The nature of the species is not yet clear and further time-resolved *in situ* MAS NMR experiments could be helpful to solve this question.

#### Literature

- [1] H. Pfeifer and H. Ernst, Ann. Reports NMR Spectr. 1993, 28, in press.
- [2] H.K.C. Timken, G.L. Turner, J.-G. Gilson, L.B. Welsh and E. Oldfield, J. Am. Chem. Soc. 1986, 108, 7231.
- [3] M. Hunger, M.W. Anderson, A. Ojo and H. Pfeifer, Microporous Materials 1993, 1, 17.
- [4] D. Freude, Stud. Surf. Sci. Catal. 1989, 52, 169.
- [5] R.L. Stevenson, J. Catal. 1971, 21, 113.
- [6] D. Freude, J. Klinowski and H. Hamdan, Chem. Phys. Lett. 1988, 149, 355.
- [7] D. Fenzke, M. Hunger and H. Pfeifer, J. Magn. Reson. 1991, 95, 477.
- [8] A.J. Vega and Z. Luz, J. Phys. Chem. 1987, 1, 365.
- [9] T.J. Gluszak, D.T. Chen, S.B. Sharma, J.A. Dumesik and T.W. Root, Chem. Phys. Lett. 1992, 190, 36.
- [10] M. W. Anderson, P.J. Barrie and J. Klinowski, J. Phys. Chem. 1991, 95, 235
- [11] J. Klinowski, Chem. Rev. 1991, 91, 1459
- [12] E.J. Munson, A.A. Kheir, N.D. Lazo and J.F. Haw, J. Am. Chem. Soc. 1992, 96, 7740
- [13] D. Freude and J. Haase, NMR, Basic Principles and Progress 1993, 29, 1.
- [14] A.C. Kunwar, G.L. Turner and E. Oldfield, J. Magn. Reson. 1986, 69, 124.
- [15] B. Blümich, P. Blümler and J. Jansen, Solid State NMR 1992, 1, 111.
- [16] E. Brunner, H. Ernst, D. Freude, T. Fröhlich, M. Hunger, H. Pfeifer, J. Catal. 1991, 127, 34.
- [17] P. Batamak, C. Dorémieux-Morin, J. Fraissard and D. Freude, J. Phys. Chem. 1991, 95, 979.
- [18] H. Rosenberger, G. Scheeler and Yu.N. Moskovich, Magn. Reson. Chem. 1989, 27, 50.
- [19] U. Sternberg and E. Brunner, J. Magn. Reson., in press.
- [20] H. Ernst, Z. Phys. Chem. (Leipzig), 1987, 268, 405.

## 2.2 Catalytic Properties and Physicochemical Nature of Highly Active Protons in Partially Reduced $\text{Ag}_3\text{PW}_{12}\text{O}_{40}$

Toshihide Baba, Mamoru Nomura and Yoshio Ono

Department of Chemical Engineering, Tokyo Institute of Technology, Ookayama, Meguro-ku, Tokyo 152, Japan.

Yo-ichi Ohno

Research & Development Center, Cosmo Research Institute, Gongendō, Saitama 340-01, Japan.

### Abstract

The catalytic properties and the physicochemical nature of protons generated by the partial reduction of  $\text{Ag}^+$  cations in  $\text{Ag}_3\text{PW}_{12}\text{O}_{40}$  with hydrogen was investigated by examining the catalytic activities for isomerizations of 1-butene and hexane and by  $^1\text{H}$  MAS NMR spectroscopy.

The catalytic activity of partially reduced  $\text{Ag}_3\text{PW}_{12}\text{O}_{40}$  reversibly changes with hydrogen pressure, indicating that on  $\text{Ag}_3\text{PW}_{12}\text{O}_{40}$  hydrogen molecules are reversibly transformed into protons which are active for the isomerizations of 1-butene and hexane.

When  $\text{Ag}_3\text{PW}_{12}\text{O}_{40}$  was partially reduced with hydrogen, the  $^1\text{H}$  MAS NMR spectrum demonstrated the generation of two kinds of acidic protons, which are observed at 6.4 and 9.3 ppm. The protons at 6.4 ppm exist only in the presence of hydrogen in the gas phase. The amount of these protons reversibly changes with the hydrogen pressure. In contrast, the amount of protons at 9.3 ppm is independent of the hydrogen pressure.

The protons at 9.3 and 6.4 ppm catalyze the isomerization of 1-butene. Only the protons at 6.4 ppm are active for hexane isomerization, though the protons at 9.3 ppm are inactive. In both reactions, the reversible change of the activities with hydrogen pressure is caused by the reversible change in the number of the protons at 6.4 ppm.

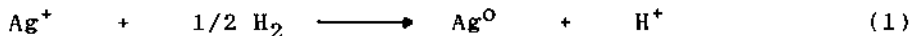
### Introduction

Heteropoly acids with Keggin structure like  $\text{H}_3\text{PW}_{12}\text{O}_{40}$  (HTP) are highly active for various acid-catalyzed reactions [1,2] such as the conversion of methanol into hydrocarbons.[3] We have also found that the activities of silver salts of heteropoly acids

such as  $\text{Ag}_3\text{PW}_{12}\text{O}_{40}$  (AgTP) as a solid-acid are greatly enhanced by the presence of hydrogen in the gas phase in several systems.[4] The catalytic activities of silver salts are much higher than those of proton type heteropoly acids.

The catalytic activities of not only silver salts, but also  $\text{Ag}^+$ -exchanged zeolites such as Ag-Y zeolite are also greatly enhanced by the presence of hydrogen.[4,5]

In these systems, Bronsted acid sites are generated by the reduction of  $\text{Ag}^+$  cations with hydrogen to  $\text{Ag}^0$  metals.[6,7]



However, the higher catalytic activities of silver salts and  $\text{Ag}^+$ -exchanged zeolites can not be ascribed solely to the number of protons, since the amount of protons in silver salts and  $\text{Ag}^+$ -exchanged zeolites can not be given more than the stoichiometric amount of protons in parent heteropoly acids and in proton-exchanged zeolites, respectively by the reduction of silver cations with hydrogen.[7]

The enhancing effect of hydrogen on the activity of solid-acid has never been reported. The purpose of the present review is to describe "the hydrogen effect" in  $\text{Ag}_3\text{PW}_{12}\text{O}_{40}$  (denoted hereinafter AgTP) as a solid-acid catalyst. Special emphasis will be placed the origin of the enhancing effect of hydrogen on the catalytic activity of AgTP, and the characterization of protons in AgTP partially reduced with hydrogen.  $^1\text{H}$  MAS NMR, IR and XRD were applied.

### 1) Enhancing effect of hydrogen on the catalytic activity of AgTP in the isomerization of hexane

Isomerization of hexane is a reaction catalyzed by Bronsted acid. The reaction was carried out at 488 K in the absence or presence of hydrogen. AgTP (30 wt%) was supported on silica ( $\text{AgTP/SiO}_2$ ). AgTP/ $\text{SiO}_2$  as prepared had no catalytic activity for hexane isomerization at 488 K; the catalytic activity developed only when AgTP had been reduced by hydrogen.

The effect of the partial pressure of hydrogen on the initial rate of isomerization of hexane was examined 488 K. After AgTP/ $\text{SiO}_2$  was reduced with hydrogen (40.0 kPa) at 488 K for 1 h (denoted as R-AgTP/ $\text{SiO}_2$ ), the reaction was carried out under 16.5 kPa of hexane in the presence of hydrogen. As shown in Fig. 1, the rate of isomerization increased with increasing hydrogen pressure. The rate at the pressure zero was measured after evacuating the system at 488 K for 1 h.

The catalytic activity of the parent acid, HTP was not affected by hydrogen pretreatment and no enhancing effect of hydrogen on the catalytic activity was observed either.

To examine the reversibility of the enhancement with hydrogen, the following experiments were carried out. R-AgTP/ $\text{SiO}_2$  was evacuated for 1 h at 488 K. The R-AgTP/ $\text{SiO}_2$  has no catalytic activity for the isomerization of hexane. Thus, R-AgTP has no catalytic activity in the absence of hydrogen. When 40 kPa

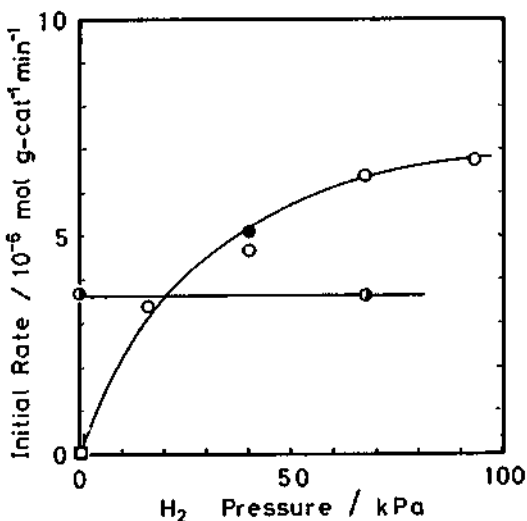


Fig.1 Reversible enhancement of the catalytic activity of R-AgTP (30 wt%)/ $\text{SiO}_2$  for the isomerization of hexane. Reaction temperature: 488 K, (○): AgTP/ $\text{SiO}_2$ , (●): HTP/ $\text{SiO}_2$ .

Hexane 16.5 kPa. AgTP/ $\text{SiO}_2$  reduced with hydrogen (40 kPa) at 488 K for 1 h. (●) R-AgTP/ $\text{SiO}_2$  evacuated at 488 K for 1 h and then reexposed to hydrogen (40 kPa) at 488 K for 1 h.

of hydrogen was reintroduced into the system at the reaction temperature, the catalytic activity almost recovered to the initial value as shown in Fig. 1. This result clearly shows that the enhancing effect of hydrogen on the catalytic activity is reversible.

As mentioned before, the catalytic activity disappeared by evacuating hydrogen from the system (Fig. 1), and hydrogen effect was reversible. These results indicate that the protons which exist only in the presence of hydrogen, catalyze the isomerization of hexane.

## 2) Isomerization of 1-butene

Not only in the isomerization of hexane, but also in that of 1-butene to 2-butenes, the reversible enhancing effect of hydrogen was also observed at 304 K.[4]

The effect of the partial pressure of hydrogen on the rate of isomerization was examined at 304 K.[4] AgTP was reduced with hydrogen at 488 K for 1 h, giving degree of  $\text{Ag}^+$  reduction of 32 %, which was estimated from the consumption of hydrogen. The AgTP thus reduced is denoted hereinafter as R-AgTP. The rate of isomerization ( $R$ ) could be expressed by eq. (2)

$$R = R_0(1 + k P_{\text{H}_2}) \quad (2)$$

Here,  $R_0$ ,  $P_{H_2}$  and  $k$  are the rate of isomerization in the absence of hydrogen, the hydrogen pressure and a constant, respectively. The catalytic activity of R-AgTP in the presence of 16.5 kPa of hydrogen is about 2.5 times higher than that in the absence of hydrogen and about 20 times higher than that of HTP.

On the basis of eq. (2) and the reversible enhancing effect of hydrogen, we presume that two kinds of protons (Bronsted acid sites) are generated by reducing the  $Ag^+$  cations with hydrogen; the protons which only exist in the presence of hydrogen in the gas phase and the protons which are irrespective of the presence of gaseous hydrogen.

It is well-known that the isomerization of hexane requires protons with acid strength higher than that of 1-butene. On the basis of this fact, the protons which exist only in the presence of hydrogen, have high acid strength. The other protons do not have enough acid strength to catalyze hexane isomerization, though two kinds of protons can catalyze 1-butene isomerization.

The reversible enhancing effect of hydrogen on the catalytic activity was also observed in the disproportionation of ethylbenzene over the reduced form of silver exchanged Y-zeolite [5]. The turnover frequency of  $Ag^+$  exchanged Y-zeolite for the disproportionation of ethylbenzene in the presence of hydrogen, was about 500 times as high as that of H-Y zeolite.[5] This indicates that the nature of protons in Ag-Y, which are responsible for the higher activity under hydrogen, should be different from that of protons in H-Y.

### 3) Characteristics of silver salts of heteropoly acids and $Ag^+$ -exchanged zeolites in the presence of hydrogen

The characteristics of the catalysis can be summarized as follows;

- (1) The enhancing effect of hydrogen is a phenomenon common to many acid-catalyzed reactions over silver salt of heteropoly acids and  $Ag^+$ -exchanged zeolites.
- (2) The enhancing effect of hydrogen is reversible. Thus, the effect vanishes if hydrogen is eliminated from the system, and the catalytic activity returns to the original level by reintroducing hydrogen into the system.
- (3) The catalytic activities of silver salts of heteropoly acids or  $Ag^+$ -exchanged zeolites in the presence of hydrogen are higher than those of the parent acids or proton-type zeolites.

The facts (1) and (2) indicate that the Bronsted acid sites (protons) are reversibly generated by chemisorption of hydrogen, and hydrogen molecules in the gas phase are reversibly transformed into protons. The fact (3) indicates that highly active protons exist only in the presence of hydrogen. Since  $Ag^0$  metal does not chemisorb hydrogen molecules [8], the cationic species must be the chemisorption center for hydrogen molecules.

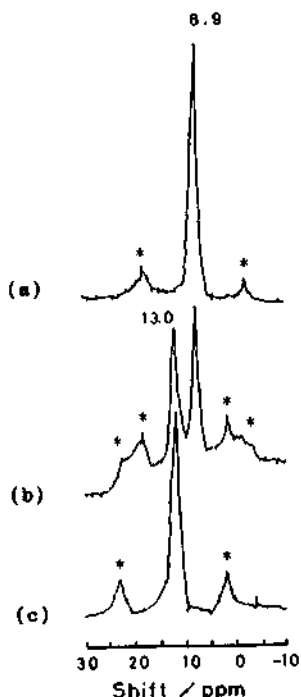


Fig. 2

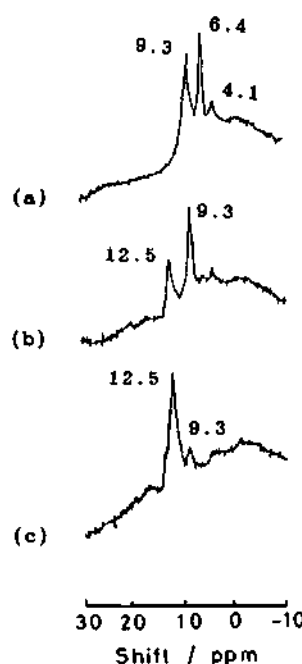


Fig. 3

Fig. 2  $^1\text{H}$  MAS NMR spectra of HTP

(\*) shows the spinning sidebands. (a): HTP evacuated at 523 K for 2 h. (b): (a) exposed to D-Py (1.4 kPa) at 303 K for 0.5 h and then evacuated at 303 K for 1.5 h. (c): (a) exposed to D-Py (1.4 kPa) at 373 K for 0.5 h and then evacuated at 303 K for 0.5 h.

Fig. 3  $^1\text{H}$  MAS NMR spectra of AgTP

(a): AgTP reduced with 40 kPa of hydrogen at 488 K for 1 h and recorded in the presence of 40 kPa of hydrogen.

(b): (a) exposed to D-PY (1.4 kPa) at 303 K for 0.5 h and then evacuated at 303 K for 0.5 h. (c): (a) exposed to D-PY (1.4 kPa) at 303 K for 1 h and then evacuated at 303 K for 0.5 h.

#### 4) $^1\text{H}$ MAS NMR studies on the highly active protons in partially reduced $\text{Ag}_3\text{PW}_{12}\text{O}_{40}$

To further investigate the chemical nature of protons in HTP and that of protons in reduced AgTP with hydrogen, solid-state  $^1\text{H}$  MAS NMR was applied.

##### a) Acidic protons of HTP

$^1\text{H}$  MAS NMR spectrum of HTP evacuated at 523 K for 2 h showed a single peak at 8.9 ppm (Fig. 2 a).

To confirm that the protons observed at 8.9 ppm are acidic, deuterated pyridine ( $C_5D_5N$ , D-Py) was adsorbed on HTP: HTP, evacuated at 523 K for 2 h, was exposed to 1.3 kPa of D-Py at 303 K for 0.5 h and then evacuated at the same temperature for 0.5 h. As shown in Fig. 2 b, the intensity of the peak at 8.9 ppm decreased to about half times of that of the original HTP and a new peak due to the deuterated pyridinium ion ( $C_5D_5NH^+$ ) [10,11] was observed at 13.0 ppm. When D-Py was adsorbed on HTP at 373 K for 0.5 h, the peak at 8.9 ppm disappeared completely (Fig. 2 c). These results indicate that the protons at 8.9 ppm in HTP are acidic. The acidic protons in HTP may be directly bonded to oxygen anions of the Keggin anions. Kozhevnikov et al. reported that chemical shift of protons in HTP heated under vacuum at 473 K was  $9.2 \pm 0.3$  ppm.[12]

#### b) Generation of Acidic Protons in AgTP

AgTP, which was heated under vacuum at 523 K for 1 h, gave no signal. This result indicates that protons (Bronsted acid sites) do not exist in the prepared AgTP.

The  $^1H$  MAS NMR spectrum of R-AgTP was recorded in the presence of hydrogen. Three NMR peaks were observed at 9.3, 6.4 and 4.1 ppm as shown in Fig. 3 a. The peak at 4.1 ppm is ascribed to  $H_2O$  molecules formed during the hydrogen treatment, since the peak at 4.1 ppm was observed also from  $Ag_3^{PW_{12}O_{40}}4H_2O$ , which was prepared by exposing  $H_2O$  vapor to evacuated AgTP at 523 K.

To confirm that the protons observed at 9.3 and 6.4 ppm are acidic, D-Py was adsorbed on R-AgTP at 303 K in the presence of hydrogen. After adsorption of D-Py (1.4 kPa) for 0.5 h, the system was evacuated for 0.5 h at 303 K. The NMR peak at 6.4 ppm almost exclusively disappeared, and concomitantly the formation of pyridinium ion ( $C_5D_5NH^+$ ) was observed at 12.5 ppm (Fig. 3 b). On the other hand, the intensity of the peak at 9.3 ppm remained almost unchanged.

When R-AgTP was exposed to D-Py at 303 K for 1 h instead of 0.5 h, the intensity of the peak at 9.3 ppm considerably diminished as shown in Fig. 3 c. The reactivity of protons at 6.4 ppm toward pyridine is much higher than that of protons at 9.3 ppm. This result suggests that the acid strength of protons at 6.4 ppm higher than that of protons at 9.3 ppm.

As shown in Fig. 3 c, when D-Py was adsorbed on R-AgTP at 303 K for 1 h, two kinds of acidic protons mostly changed to pyridinium ions. While, the protons in HTP reacted with pyridine to form pyridinium ions at 373 K for 1 h, indicating that the reactivity of protons in R-AgTP to pyridine is higher than that of protons in HTP.

#### c) Effect of evacuation temperature on the amount of protons in R-AgTP and reversibility

The thermal stability of the two types of acidic protons in R-AgTP was examined by evacuating the system at prescribed temperatures, after reducing AgTP with hydrogen at 488 K (R-AgTP).

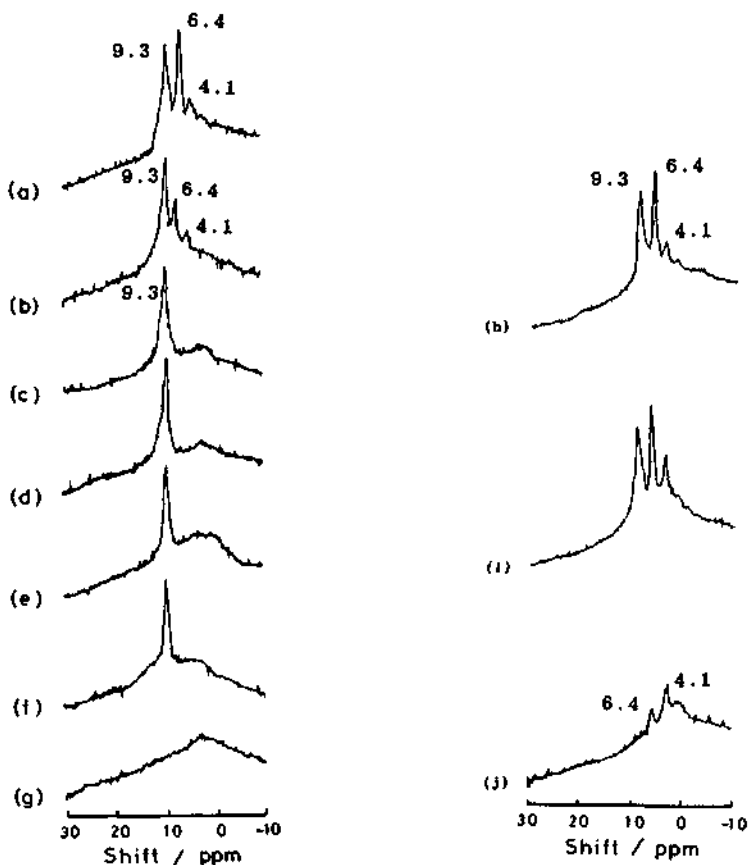


Fig. 4 Effect of the evacuation temperature on the  $^1\text{H}$  NMR spectrum of partially reduced AgTP and reversibility.

(a): AgTP reduced with 40 kPa of hydrogen at 488 K for 1 h and recorded in the presence of 40 kPa of hydrogen. (b)-(g): recorded after evacuating hydrogen for 1 h at 77 K (b), 303 K (c), 333 K (d), 488 K (e), 523 K (f), 623 K (g).  
 (h): the sample of (c) reexposed to hydrogen at 303 K for 1 h.  
 (i): the sample (e) reexposed to hydrogen (40 kPa) at 488 K for 1 h.  
 (j): the sample (g) reexposed to hydrogen (40 kPa) at 333 K for 1 h.

The evacuation of hydrogen at 77 K, sharply decreased the intensity of the peak at 6.4 ppm (Fig. 4 b), compared with that in R-AgTP in the presence of hydrogen (Fig. 4 a). In contrast, the intensity of the peak at 9.3 ppm did not change at all. Upon raising the evacuation temperature from 77 K to 303 K, the peak at 6.4 ppm completely vanished, as shown in Fig. 4 c. This result clearly indicates that the protons at 6.4 ppm exist only

in the presence of hydrogen in the gas phase. In contrast, the intensity of the peak at 9.3 ppm remained almost unaltered upon eliminating hydrogen at 303 K.

The protons at 9.3 ppm were stable up to 523 K (Fig. 4 d-f). At higher temperature, 623 K, the peak disappeared (Fig. 4 g). IR measurement of R-AgTP confirmed that the Keggin structure of R-AgTP was maintained even after heating R-AgTP under vacuum at 623 K.

After evacuating R-AgTP between 303 and 523 K, the R-AgTP was reexposed to hydrogen (40 kPa) at the same temperature as the hydrogen evacuation temperature. As shown in Fig. 4 h-j, the intensity of the peak at 6.4 ppm completely recovered to that of the peak of R-AgTP in the presence of 40 kPa of hydrogen (Fig. 4 a). Thus, the amount of protons observed at 6.4 ppm reversibly varies by introducing and withdrawing hydrogen.

In a partially reduced AgTP whose degree of reduction of silver cations is 32 %, the XRD of silver metal particles and the IR measurements of chemisorbed CO on  $\text{Ag}^+$  cations gave the evidence that the reversible interconversion between  $\text{Ag}^+$  cations and silver metal particles occurred concomitantly with the reversible interconversion of protons and hydrogen molecules.<sup>[9]</sup>

As shown in Fig. 4 g, peaks at 9.3 and 6.4 ppm disappeared, when R-AgTP was evacuated at 623 K. This sample was reexposed to hydrogen at 333 K. As shown in Fig. 4 j, the peak at 6.4 ppm reappeared, though the peak was about 1/5 times that of R-AgTP (Fig. 4 a), while the peak at 9.3 ppm did not appear at all by reintroducing hydrogen. The intensity of the peak at 4.1 ppm slightly increased upon evacuating and reintroducing hydrogen.

#### d) Effect of the Hydrogen Pressure on the Amount of Protons

$^1\text{H}$  MAS NMR spectra of R-AgTP were recorded under different pressures of hydrogen. The pressure of hydrogen was adjusted to 0, 16, 40 and 66 kPa at 303 K, after AgTP was reduced with 40 kPa of hydrogen at 488 K for 1 h. The sample under 0 kPa of hydrogen refers to a R-AgTP sample evacuated at 303 K for 1 h.

In Fig. 5, the relative areas of the NMR peaks at 9.3, 6.4, and 4.1 ppm are plotted against the hydrogen pressure. In the absence of hydrogen, protons at 6.4 ppm dose not exist at all. The protons exist only in the presence of hydrogen. The amount of protons at 6.4 ppm in R-AgTP increases with increasing hydrogen pressure, whereas that of protons at 9.3 ppm is independent of hydrogen pressure. The amount of water formed increased with hydrogen partial pressure.

On the basis of the effect of hydrogen pressure on the initial rate of isomerization of 1-butene over R-AgTP, it is concluded that the protons at both 9.3 and 6.4 ppm catalyze this reaction and that the reversible change of the activity with hydrogen pressure is caused by the reversible change in the number of the protons at 6.4 ppm.

In contrast to 1-butene isomerization, the catalytic activity of R-AgTP/SiO<sub>2</sub> for the isomerization of hexane, completely disappeared when R-AgTP/SiO<sub>2</sub> was evacuated at 488 K for 1 h.

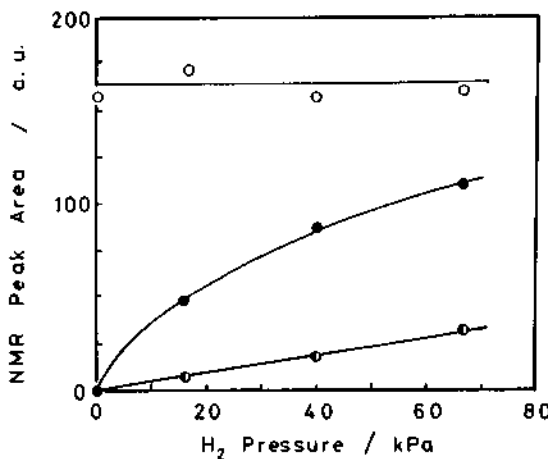


Fig. 5 Influence of hydrogen pressure on the intensities of protons observed at 9.3, 6.4 and 4.1 ppm. (○): 9.3 ppm, (●): 6.4 ppm, (◐): 4.1 ppm.

Moreover, the catalytic activity returned to the initial level when R-AgTP/SiO<sub>2</sub> evacuated at 488 K was reexposed to hydrogen at 488 K. These results suggest that only the protons observed at 6.4 ppm are active for hexane isomerization but that the protons at 9.3 ppm are totally inactive for hexane isomerization.

The hexane isomerization requires protons with higher acid strength than the isomerization of 1-butene. The reactivity of the protons at 6.4 ppm to pyridine is higher than that of protons at 9.3 ppm. These facts suggest that protons at 9.3 ppm do not have enough acid strength to catalyze hexane isomerization, though they can catalyze 1-butene isomerization.

#### e) Evidence of delocalized protons in R-AgTP

The reactions catalyzed by heteropoly acids and their salts are often carried out at elevated temperature as in the case of isomerization of hexane. It is often presumed that acidic OH groups in proton-exchanged zeolites are dissociated under the reaction and that the protons migrate in the zeolite cavities.[13]

To further investigate the physicochemical properties of acidic protons at elevated temperature, NMR spectra were measured at several temperatures between 298 and 373 K. Spectra of R-AgTP were recorded by raising the sample temperature stepwise from 298 to 373 K.

As shown in Fig. 6 a-e, the line widths and chemical shifts depended on the temperature.[14] When the temperature was

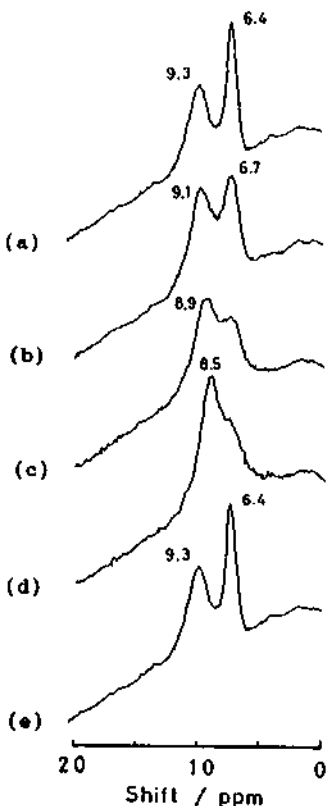


Fig. 6 Effect of the temperature on  $^1\text{H}$  MAS NMR spectrum in  $\text{Ag}_3\text{PW}_{12}\text{O}_{40}$ .

The recording temperature; (a) 298 K, (b) 333 K, (c) 353 K, and (d) 373 K. Each spectrum was recorded by heating the sample (a) stepwise from 298 K to 373 K. The spectrum (e) was recorded at 298 K after the sample (d) was cooled down to 298 K.

raised from 298 to 333 K, mainly the line width of protons at 6.4 ppm broadened (Fig. 6 b). The line broadening of the peak strongly indicates that proton, bonded to oxygen anion in Keggin anion, are reversibly broken and reformed. Thus, protons at 6.4 ppm are mobile and migrate in R-AgTP at temperature as low as 333 K.

The line width of the peak at 9.3 ppm was also influenced (fig. 6 b). However, the line width of these protons was not so pronounced in contrast to that of protons at 6.4 ppm. This result indicates that protons at 6.4 ppm are more mobile than those at 9.3 ppm. These mobile protons at 6.4 ppm presumably are more active in catalysis than those at 9.3 ppm.

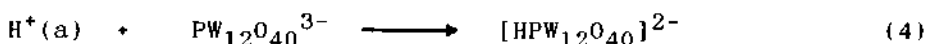
Not only the line broadening of two kinds of protons, but also the chemical shifts of these protons changed obviously by raising temperature. When the temperature was raised stepwise from 333 K to 353 and 373 K, two peaks observed at 9.3 and 6.4 ppm at 298 K, approached each other and broadened. These peaks could not be completely distinguished at 373 K, and the chemical shift of the main peak was observed at 8.5 ppm (Fig. 6 d). This phenomenon shows that chemical exchange between protons at 6.4 ppm and those at 9.3 ppm proceeds.

When the sample (d) was cooled down to 298 K, the peaks at 9.3 and 6.4 ppm reappeared with the same intensity and line width as the original sample. This result indicates that the identity of these protons is exact at 298 K, and it is not exact at higher temperature.

In contrast to R-AgTP, the line width of HTP was hardly influenced at least at 373 K, the half line width being 498 Hz. This result seems that the higher catalytic activity of silver salt than that of proton type heteropoly acid is caused by the mobile protons.

##### 5) Highly active protons in R-AgTP in the presence of hydrogen

As mentioned above, there are two types of acidic protons in R-AgTP in the presence of hydrogen, and they have different mobility. We considered the mechanism of the generation of protons to differentiate two kinds of protons in R-AgTP in the presence of hydrogen as follows;



In eq. (3), protons ( $\text{H}^*(\text{a})$ ), which are less stabilized by weakly interacting with Keggin anions ( $\text{PW}_{12}\text{O}_{40}^{3-}$ ), are reversibly generated by the reduction of  $\text{Ag}^+$  cations with hydrogen. The amount of these protons depends on the hydrogen pressure. The reversibility of eq.(3) has been also confirmed for  $\text{Ag}^+$  and  $\text{Ag}^\circ$  [13]. Moreover, desorption of hydrogen molecules from R-AgTP was observed when the hydrogen pressure decreased after preparing R-AgTP in which the degree of reduction of  $\text{Ag}^+$  cations was 32%; the 0.12 mol of hydrogen per mole of AgTP was regenerated by decreasing hydrogen pressure from 40 to 11 kPa at 303 K. In contrast with protons ( $\text{H}^*(\text{a})$ ) in eq. (3), the part of the protons are stabilized by strongly interacting with Keggin anions ( $\text{PW}_{12}\text{O}_{40}^{3-}$ ) (eq.(4)). The remaining protons ( $\text{H}^*(\text{a})$ ) are less stabilized, and more reactive. These two types of protons may be related to protons observed at 9.3 and 6.4 ppm, respectively. The chemical exchange between the protons at 6.4 ppm and those at 9.3 ppm proceeds and the identity of these protons is not exact at higher temperature than 373 K.

### Conclusions

The chemical nature of protons in AgTP partially reduced with hydrogen was examined by  $^1\text{H}$  MAS NMR spectroscopy and the catalytic activity of R-AgTP was discussed with relevance to the NMR results. The main results are summarized as follows.

- (1) the reversibility in the catalytic activity is caused by the generation of acid sites with concomitant reduction of silver cations to silver metal particles.
- (2) The  $^1\text{H}$  MAS NMR spectrum gives direct evidence of the existence of two kinds of acidic protons in R-AgTP. One is observed at 6.4 ppm, while the other is observed at 9.3 ppm.
- (3) The protons at 6.4 ppm exist only in the presence of hydrogen in the gas phase, and the amount of these protons reversibly varies with hydrogen pressure. In contrast, the amount of protons observed at 9.3 ppm is independent of hydrogen pressure.
- (4) The high catalytic activity of R-AgTP in the presence of hydrogen is caused by the existence of highly acidic protons which are observed at 6.4 ppm.
- (5) The protons at 6.4 ppm is more mobile than protons at 9.3 ppm.
- (6) The chemical exchange between the protons at 6.4 ppm and those at 9.3 ppm proceeds and the identity of these protons is not exact at higher temperature than 373 K.

### References

- [1] M. Misono, Catal. Rev. 1987, 29, 269.
- [2] Y. Ono, "Prospective in Catalysis", ed by J. A. Thomas and I. Zamaraev, Blackwell Scientific Publications, 1992, p. 431.
- [3] T. Baba, J. Sakai, H. Watanabe and Y. Ono, Bull. Chem. Soc. Jpn., 1982, 55, 2555.
- [4] T. Baba and Y. Ono, Appl. Catal., 1989, 55, 301.
- [5] T. Baba and Y. Ono, Zeolites, 1987, 7, 292.
- [6] T. Baba, H. Watanabe and Y. Ono, J. Phys. Chem., 1983, 87, 2406.
- [7] H. Beyer, P. A. Jacobs and J. B. Uytterhoeven, J. Chem. Soc. Faraday 1, 1976, 72, 674.
- [8] Z. Knol, "Catalysis", ed. by J. R. Anderson, M. Boudart, Springer-Verlag, Berlin, Vol. III, p.231 (1982).
- [9] T. Baba, M. Nomura, Y. Kansaki and Y. Ono, J. Chem. Soc. Faraday 1, 1992, 88, 71.
- [10] I. W. Shuppert and C. A. Angell, J. Chem. Phys., 1977, 67, 3050.
- [11] D. Freude, M. Hunger and H. Pfeifer, Chem. Phys. Lett., 1986, 128, 62.
- [12] I. V. Kozhevnikov, I. L. Mudrakovskiy and M. N. Timefeeva, J. Mol. Catal., 1990, 60, 65.
- [13] T. Baba, Y. Inoue, H. Shoji, T. Uematsu, and Y. Ono, J. Chem. Soc., Chem. Commun., submitted.
- [14] T. Baba and Y. Ono, to be published.

## 2.3 Extra-Framework Sites in H-Al MFI and H-GaMFI Zeolite Catalysts

Susan M. Bradley, Sharelle M. Campbell, Jim Hook, Ken Jackson, Leon Van Gorkom and Russell F. Howe\*  
Department of Physical Chemistry, University of New South Wales, Box 1, Kensington, NSW 2033, Australia.

### Abstract

This paper presents results of  $^{29}\text{Si}$ ,  $^{27}\text{Al}$ ,  $^{71}\text{Ga}$  and  $^{129}\text{Xe}$  NMR experiments aimed at characterizing extra framework sites in aluminosilicate and gallosilicate MFI zeolites. It is shown that the presence of extra-framework aluminium or gallium species inferred from solid state NMR measurements is confirmed by  $^{129}\text{Xe}$  NMR measurements of physisorbed xenon.  $^{129}\text{Xe}$  NMR also indicates changes in the nature of the extra-framework sites on the steam treatment.

### 1. INTRODUCTION

The acidity of zeolites is associated with the substitution of aluminium or other trivalent elements for silicon in the zeolite lattice. There is growing evidence that acidity of aluminosilicate zeolites can be modified either deliberately or inadvertently by steam treatment [1]. Hydrolysis of the zeolite lattice will reduce the concentrations of Bronsted acid sites associated with framework substituted aluminium, producing extra-framework aluminium species which may or may not be acidic. In the case of gallosilicate zeolites, both framework and extra-framework gallium appear to be necessary for catalysis of the aromatization of propane, which requires both acidic and dehydrogenation functions [2].

The balance between framework and extra-framework species, the nature of the extra-framework species, and the way in which they are influenced by preparation and pretreatment conditions, are important issues in catalysis over acid zeolites. This paper explores the extent to which solid state and  $^{129}\text{Xe}$  NMR spectroscopy can address these issues in MFI zeolites.

### 2. EXPERIMENTAL METHODS

AlMFI and GaMFI zeolites containing varying Si:Al and Si:Ga ratios were obtained commercially (Conteka, PQ Corporation) or synthesized using established procedures [3]. Zeolites were exhaustively ammonium ion exchanged and subsequently calcined in air at 550°C to convert to the hydrogen form. Powder x-ray diffraction confirmed that all samples were well crystalline MFI zeolites. Bulk compositions were determined by x-ray fluorescence. Solid state  $^{27}\text{Al}$ ,  $^{29}\text{Si}$  and  $^{71}\text{Ga}$  NMR spectra were recorded on a Bruker MSL300 instrument of samples packed in boron nitride MAS rotors; details of the NMR measurements are presented elsewhere [3].  $^{129}\text{Xe}$  NMR spectra were measured from known amounts of xenon added to zeolite samples in 10 mm NMR tubes fitted with high vacuum stopcocks, using a Bruker AC300P instrument at 83.019 MHz. Chemical shifts were referenced to that of xenon gas extrapolated to zero pressure. Steam treatments involved exposing zeolite samples to a saturated water vapour pressure at various temperatures for varying lengths of time.

### 3. RESULTS AND DISCUSSION

#### 3.1. H-Al MFI Zeolites

The  $^{129}\text{Xe}$  chemical shift of physically adsorbed xenon is a commonly used probe of the environment within zeolite pores [4]. We have previously showed that for a series of well characterized H-Al MFI zeolites of varying aluminium content in which no spectroscopic evidence could be found for extra-framework aluminium species, the  $^{129}\text{Xe}$  chemical shift was a linear function of the amount of xenon added to the zeolite (adsorbed plus gas phase) [5]. This can be understood in terms of the model proposed by Ito and Fraissard [6] for xenon in zeolite pores, in which a linear variation of chemical shift with effective density of xenon in the zeolite is due to xenon-xenon interactions.

We further found that the xenon chemical shift extrapolated to zero coverage of adsorbed xenon was sensitive to the amount of aluminium in the zeolite. This is likewise consistent with the Ito-Fraissard model; the chemical shift at zero coverage is due to xenon-zeolite interactions which depend on the total negative charge on the zeolite framework.

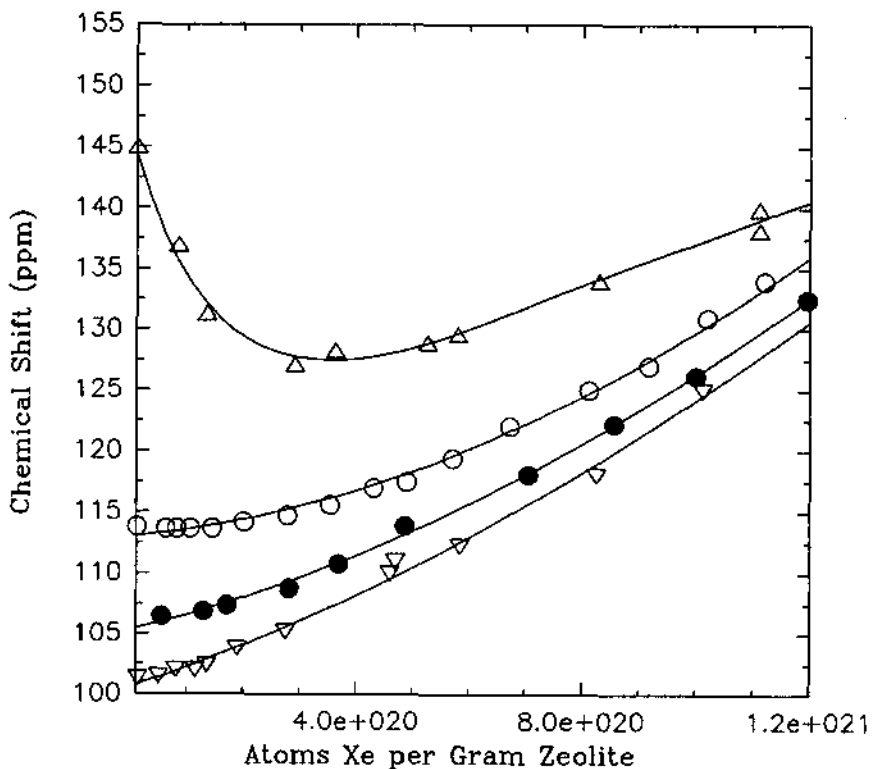


Figure 1.  $\text{Xe-129}$  chemical shifts for xenon adsorbed in H-AlMFI zeolites with Si:Al ratios of  $\Delta$  18,  $\circ$  70,  $\bullet$  160,  $\nabla$  1000

We have subsequently found that the xenon chemical shift variation may be quite different in zeolites containing extra-framework aluminium. This is illustrated in Figure 1, which shows  $^{129}\text{Xe}$  chemical shifts as a function of xenon content for several different commercial H-Al MFI zeolites, plus a locally synthesized silicalite. At high xenon coverages, the chemical shift plots for all samples tend to linearity with a similar gradient, and for a given xenon coverage the chemical shift depends on the aluminium content of the zeolite, consistent with the earlier report [5]. The sample having a bulk Si:Al ratio of 18 shows a marked deviation from linearity however at lower xenon coverages, and the chemical shift increases again as the coverage decreases. Some much lesser indications of upwards deviations from linearity can be seen in the data for the other zeolite samples.

Similar upward curvature in xenon chemical shift plots has been reported by Bonardet et al [7] for xenon adsorbed in steam treated ultrastable  $\text{NH}_4\text{Y}$  zeolites, and attributed by these authors to specific interaction of Xe with extra-framework aluminium species. Likewise, Chen et al [8] observed highly curved chemical shift versus coverage plots for xenon in 3 H-Al MFI zeolites prepared in nonalkaline fluoride media, and proposed the existence of a heterogeneous distribution of highly charged extra-framework aluminium species in these particular zeolites.

$^{27}\text{Al}$  MAS NMR spectra of the zeolites in Figure 1 showed (with the exception of the silicalite, for which no  $^{27}\text{Al}$  signal was detected) a single resonance at about 54 ppm characteristic of tetrahedral Al. The  $^{29}\text{Si}$  MAS NMR spectrum of the Si:Al=18 sample showed clearly however that as much as half of the aluminium in this sample was not present in the zeolite framework. This conclusion is based on the relative intensities of the  $^{29}\text{Si}$  signals at ca. -112 ppm ( $\text{Si}(0\text{Al})$ ) and -104 ppm ( $\text{Si}(1\text{Al})$ ). The extra-framework aluminium is thus present not as octahedral  $\text{Al}^{3+}$ , but as some partially polymerized species which is still sufficiently highly charged to have a specific interaction with adsorbed xenon at low coverages.

Steam treatment of zeolite Y is known to produce high concentrations of highly charged extra-framework aluminium species [7]. This does not appear to be the case for MFI zeolites however. Steam treatment of the MFI zeolites described in [5] caused substantial dealumination of the framework, as revealed by loss of the tetrahedral  $^{27}\text{Al}$  NMR signal, loss of Bronsted v(OH) infrared band, and shifts in the framework infrared frequencies for example [9]. Figure 2 shows schematically how the relative concentrations of framework aluminium vary with extent of steam treatment for zeolites containing different initial concentrations of framework aluminium. The terminology used for sample treatment is: H, ammonium form heated in dry nitrogen to 673K; HD, heated in dry nitrogen to 998K; LS, heated in water vapour to 873K for 1.5 hours; HS, heated in water vapour to 1023K for 7 hours. Figure 2 reveals that the extent of framework aluminium loss depends on the severity of the treatment, but also on the initial framework aluminium concentration. In particular, samples containing a Si:Al ratio of 70 or higher are much more resistant to framework aluminium loss than the high aluminium content samples. Steam treatment did not however produce an upward curvature in the xenon chemical shift versus coverage plots for adsorbed xenon; on the contrary, the approximately linear plots were displaced to lower chemical shift with increasingly severe steam treatment, consistent with loss of aluminium from the framework.

The conclusions drawn from the studies of H-AlMFI zeolites are that the  $^{129}\text{Xe}$  chemical shifts are extremely sensitive to the presence of any highly charged extra-framework aluminium species which may be generated during zeolite synthesis.

Steam treatment however does not produce such highly charged species; initial hydrolysis of the framework to release aluminium must be followed by hydrolysis and polymerization to produce relatively uncharged species which do not interact strongly with xenon.

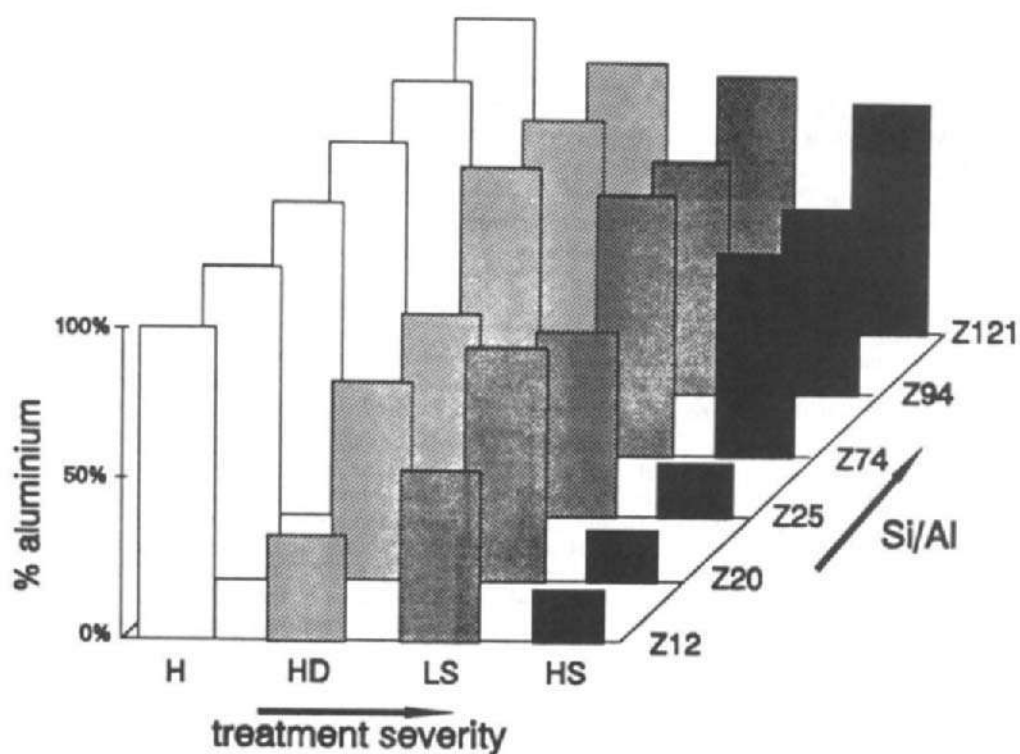


Figure 2. Extent of framework aluminium loss as a function of treatment severity and Si:Al ratio (see text for explanation of nomenclature).

### 3.2. H-Ga MFI Zeolites

Figure 3 shows  $^{129}\text{Xe}$  chemical shifts versus coverage plots for xenon adsorbed in several H-Ga MFI zeolites of varying Si:Ga ratio. The samples with higher gallium content show a marked upturn in chemical shift at low xenon coverage. The  $^{71}\text{Ga}$  MAS NMR spectrum of the highest Ga content sample showed, in addition to the tetrahedral Ga signal at ca. 120 ppm (relative to  $\text{Ga}(\text{H}_2\text{O})_6^{3+}$ ), a broad asymmetric peak at about 10 ppm which must be attributed to octahedrally coordinated extra-framework gallium [10]. The relative amounts of framework and extra-framework gallium cannot be quantified from the  $^{71}\text{Ga}$  NMR spectra, but the framework composition can be estimated from the  $^{29}\text{Si}$  NMR spectra, as for Al MFI zeolites. For the samples showing upward curvature in the xenon chemical shift plots, 30-50% of the gallium content is estimated to be extra-framework. For lower gallium contents, the  $^{29}\text{Si}$  NMR spectra cannot be used reliably to estimate framework gallium content, but the absence of curvature in the xenon chemical shift plots indicates the absence of highly charged extra-framework gallium at least.

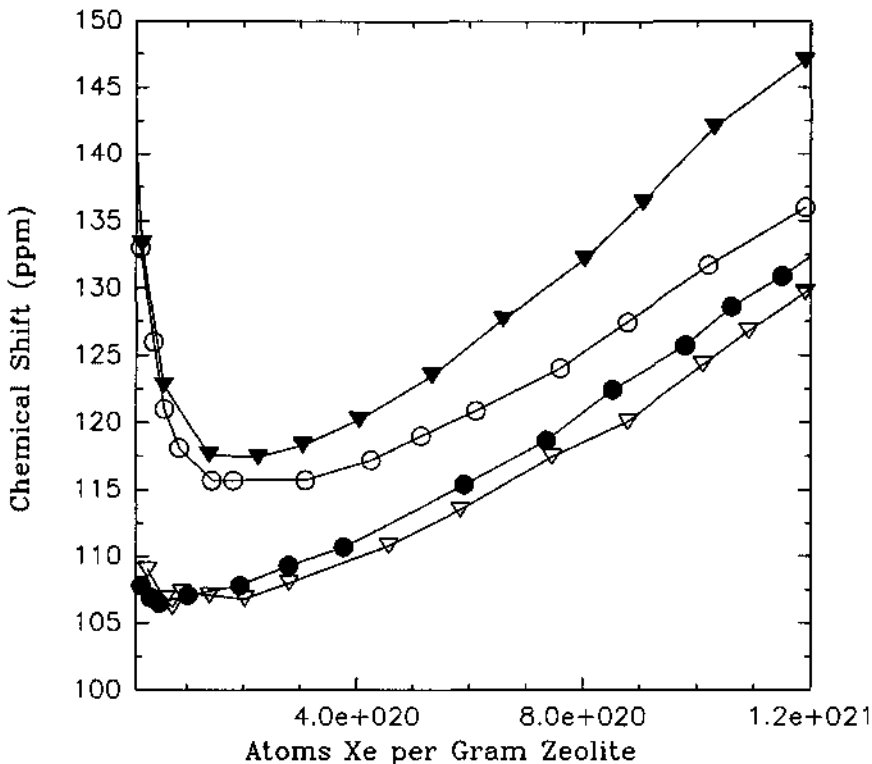


Figure 3. Xenon-129 chemical shifts for xenon adsorbed in H-GaMFI zeolites with Si:Ga ratios of  $\blacktriangledown$  11,  $\circ$  27,  $\bullet$  93,  $\nabla$  210

The H-Ga MFI sample with bulk Si:Ga=11 was subjected to steam treatment for increasing lengths of time at 650°C. Brief (30 minutes) steam treatment caused removal of the upward curvature in the xenon chemical shift versus coverage plot upon subsequent xenon adsorption. Steam treatment for longer periods displaced the chemical shift plots to lower chemical shift, consistent with loss of gallium from the framework seen in  $^{29}\text{Si}$  NMR spectra of steamed samples. No  $^{71}\text{Ga}$  NMR signals could be measured from steamed H-Ga MFI samples, indicating that any gallium remaining in the lattice had become distorted, and that extra-framework gallium in steamed samples likewise has low symmetry.

Conclusions drawn concerning H-Ga MFI zeolites are that high gallium content zeolites, as synthesized, contain high concentrations of highly charged extra-framework gallium species, possibly  $\text{Ga}^{3+}$ , which interact strongly with adsorbed xenon. We note that the requirement for overall charge balance means that such samples may contain very few if any Bronsted acid sites. Steam treatment, as in the case of Al MFI zeolites, causes both degalliation of the framework and extensive hydrolysis of the extra-framework gallium species. We note also that gallium (III) is more readily hydrolyzed than aluminium (III) [11]; the resulting gallium hydroxide or oxy-hydroxide species may partially block the zeolite pores and modify diffusion rates.

Finally, it is evident that aluminium and/or gallium species present in an acid MFI zeolite catalyst depend critically on total aluminium or gallium content, method of zeolite synthesis and the extent of any hydrolysis during catalyst pretreatment.

#### Acknowledgements

This work was supported by the Australian Research Council. SMB acknowledges award of an NSERC (Canada) Postdoctoral Fellowship.

#### References

- [1] See for example, R M Lago *et al*, in Y Murakami, A Iijima and J M Ward, eds, Proc 7th International Zeolite Conference, Kodansha, Tokyo, 1986, p 677
- [2] D J Simmons, R Szostak, P K Agrawal and T L Thomas, *J Catal* 106, 287 (1987)
- [3] A fuller account of this work will be published elsewhere
- [4] P J Barrie and J Klinowski, *Prog. in NMR Spectroscopy* 24, 91 (1992)
- [5] S M Alexander, J M Coddington and R F Howe, *Zeolites* 11, 368 (1991)
- [6] J Fraissard and T Ito, *Zeolites* 8, 350 (1988)
- [7] J L Bonardet, M C Barrage and J P Fraissard, in R von Ballmoos *et al*, eds, Proc. 9th International Zeolite Conference, Butterworth-Heinemann, 1992, p 475
- [8] Q J Chen, J L Guth, A Seive, P Caullet and J Fraissard, *Zeolites* 11, 798, (1991)
- [9] S.M.Cambell, D M Bibby, J M Coddington, R F Howe and R H Meinhold, submitted for publication in *J Catalysis*
- [10] S M Bradley, R F Howe and R A Kydd, *Magnetic Resonance in Chemistry*, 31, 883, (1993)
- [11] S M Bradley, R A Kydd and R Yamdagni, *J Chem Soc Dalton Trans*, 2653 (1990)

## 2.4 Solid-state $^{109}\text{Ag}$ -MASNMR Spectroscopic Studies of Trisilver Dodecatungstophosphates

Shin-ichi Nakata, Yoshinori Tanaka, Toshihide Baba\* and Yoshiro Ono\*

Chiyoda Corporation, R&D Center, 3-13 Moriya-cho, Kanagawa-ku, Yokohama 221 Japan

\*Department of Chemical Engineering, Tokyo Institute of Technology, 2-12-1 Ookayama, Meguro-ku, Tokyo 152 Japan

### *Abstract*

A high-resolution solid-state  $^{109}\text{Ag}$ -MASNMR spectroscopy has been used to characterize the microenvironments on silver atoms of trisilver dodecatungstophosphates, silver-substituted heteropolyacids. The spectra we obtained in this work are the first examples on solid acid catalysts such as heteropolyacid.

Heteropolyacid (HPA) compounds (Fig. 1) are widely used as acid as well as oxidation catalysts [1]. Dodecatungstophosphoric acid ( $\text{H}_3\text{PW}_{12}\text{O}_{40}$ ; HTP), one of the representative HPA catalysts, have higher catalytic activities for the conversion of methanol into hydrocarbons [2-4]. Besides the acids themselves, the metal salts of HPA such as silver and copper (II) salts, are also active for methanol conversion [5-7]. Especially trisilver dodecatungstophosphate ( $\text{Ag}_3\text{PW}_{12}\text{O}_{40}$  : AgTP) under hydrogen shows higher activities than the parent HTP. Baba and Ono et al. have reported the generation [8] and the unique reversible enhancing effect of hydrogen in connection with Bronsted acid sites on the catalytic activity of AgTP in relation to the isomerization of 1-butene [9].

The characteristics of protons on AgTP, which had been partially reduced with hydrogen, have been reported by means of  $^1\text{H-NMR}$ , indicating the reversible transformation between cationic and metallic silver as a function of the hydrogen pressure in the gas phase [10]. Furthermore the distinctive signals ascribed to two acidic protons on AgTP have been attractively observed by high-resolution solid-state  $^1\text{H-NMR}$  with magic angle spinning (MAS) [11].

This paper is aimed to highlight the microenvironmental features on silver atoms of AgTP by utilizing high-resolution solid-state  $^{109}\text{Ag}$ -MASNMR. The spectra of  $^{109}\text{Ag}$ -MASNMR we obtained in this work are the first examples on solid acid catalysts such as heteropolyacid. In addition, microenvironments on phosphorus atoms of AgTP have been characterized by  $^{31}\text{P}$ -MASNMR.

Spectroscopic data of silver isotope  $^{109}\text{Ag}$ , one of the "Cinderella nuclei"[12], on high-resolution solid-state NMR found in the literature are sparse, since these isotopes are difficult to observe experimentally [12,13]. The isotope has spin 1/2, thus nuclear relaxation is dominated only by magnetic interactions which are relatively inefficient due to the small magnetic moments ( $-0.2251 \mu_N$ ). Therefore the spin-lattice relaxation time  $T_1$  of this isotope of solid compounds, even if they include high concentration of diamagnetic silver species, are extremely long. Moreover this isotope has lower resonance frequency (23.27MHz in the case of 500MHz for  $^1\text{H}$ ) and lower relative receptivity ( $1.01 \times 10^{-4}$  against  $^1\text{H}$ ). These characteristic NMR parameters make observation of the silver nuclei difficult. The problems associated with silver nuclei,  $^{107}\text{Ag}$  and  $^{109}\text{Ag}$ , are apparent from Table 1 [12].  $^{109}\text{Ag}$  nucleus is usually used because of its higher receptivity than that of  $^{107}\text{Ag}$ .

Table 1 NMR parameters of the nuclei  $^{107}\text{Ag}$  and  $^{109}\text{Ag}$  [12].

Parameter \ Isotope	$^{107}\text{Ag}$	$^{109}\text{Ag}$
Natural abundance / N(%)	51.82	48.18
Magnetic moment / $\mu$ ( $\mu_N$ )	-0.1957	-0.2251
Magnetogyric ratio / $\gamma$ ( $10^7 \text{ rad T}^{-1}\text{s}^{-1}$ )	-1.0828	-1.2449
NMR frequency / $\Theta$ (MHz)	4.047649	4.653623
Relative receptivity / $D^P$	$3.44 \times 10^{-5}$	$4.86 \times 10^{-5}$
/ $D^C$	0.195	0.276

Some data of high-resolution solid-state  $^{109}\text{Ag}$ -NMR with MAS dealing with solid compounds have been very recently reported. Plischke et al. have reported the spectra of silver dispersed on oxide supports [14]. Villa et al. have reported on silver borate glasses [15]. By using cross polarization (CP) together with MAS, the spectra of silver complexes coordinated with organic functional groups including protons have been reported by Merwin et al. [16] and Kitagawa et al. [17]. For the

compounds connected with protons, CP makes <sup>109</sup>Ag resonance line more detectable. The Knight shift and relaxation times on <sup>109</sup>Ag of silver particles supported on metal oxides have been investigated by Mastikhin et al. [18] and Bercier et al. [19].

AgTP for the <sup>109</sup>Ag-NMR measurements in the present work was obtained as a precipitate by adding a stoichiometric amount of powdered silver carbonate to an aqueous solution of HTP. The detailed properties of AgTP were described in the previous papers [10,11]. From the result of the determination of the Miller index and the distance between the faces by powder XRD analysis, it has been considered that the crystal structure of AgTP is not different from the parent HTP. This AgTP contained 6H<sub>2</sub>O and has a cubic structure with a lattice constant of 1.199nm. From the XRD analysis, schematic model of a part of secondary structure could be illustrated in Fig.1(b). Two pyridine(Py)- adsorbed AgTP samples, Py-AgTP-I (Ag<sup>+</sup>/Py=3/1) and Py-AgTP-II (Ag<sup>+</sup>/Py=3/2), were also prepared for NMR measurement.

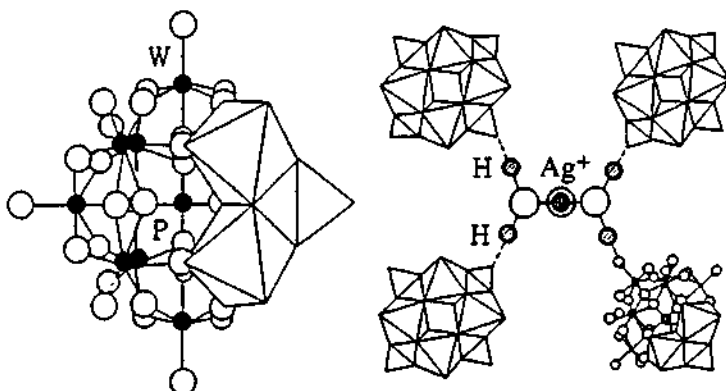


Fig. 1 A schematic (a) primary structure (Keggin structure; PW<sub>12</sub>O<sub>40</sub><sup>-3</sup>) [20] and (b) secondary structure (a part) of Ag<sub>3</sub>PW<sub>12</sub>O<sub>40</sub> · 6H<sub>2</sub>O from the XRD analysis in this work. The model of (b) is arranged from the literature [21].

The <sup>109</sup>Ag-NMR spectra of AgTP were obtained using a JEOL JNM-GSX-500WB spectrometer at 23.27MHz for <sup>109</sup>Ag nucleus. Single-pulse was used with MAS and without both CP and <sup>1</sup>H-decoupling. The pulse width for <sup>109</sup>Ag was 2.5 μ s(26°). The spinning speed of samples was 7KHz to accumulate, for 12500~15000 acquisitions, with 60 sec. of repetition time. AgNO<sub>3</sub> crystal in solid was used as the second reference of <sup>109</sup>Ag chemical shift, assigned to -87ppm against the single peak of 0ppm for an aqueous solution of [9.08M-AgNO<sub>3</sub>+0.24M-Fe(NO<sub>3</sub>)<sub>3</sub>][14].

The  $^{109}\text{Ag}$ -NMR spectra for AgTP, Py-AgTP-I and Py-AgTP-II are given in Fig. 2. For AgTP, a single peak with a chemical shift of 31 ppm and with a half-line width ( $\Delta \nu_{1/2}$ ) of 70 Hz was resolved, indicating homogeneous microenvironment of  $\text{Ag}^+$  ions, coordinated with  $6\text{H}_2\text{O}$ , with good symmetry. After pyridine-adsorbing substituted for  $\text{H}_2\text{O}$ , the peaks obtained for Py-AgTP-I and Py-AgTP-II became broader (Py-AgTP-I :  $\Delta \nu_{1/2} = 240\text{Hz}$ , Py-AgTP-II :  $\Delta \nu_{1/2} = 280\text{Hz}$ ) than that of AgTP. This result suggests that the surroundings on electronic state of silver atoms of Py-AgTP become more heterogeneous by partly pyridine-adsorption. There is no appreciable changes in chemical shift position.

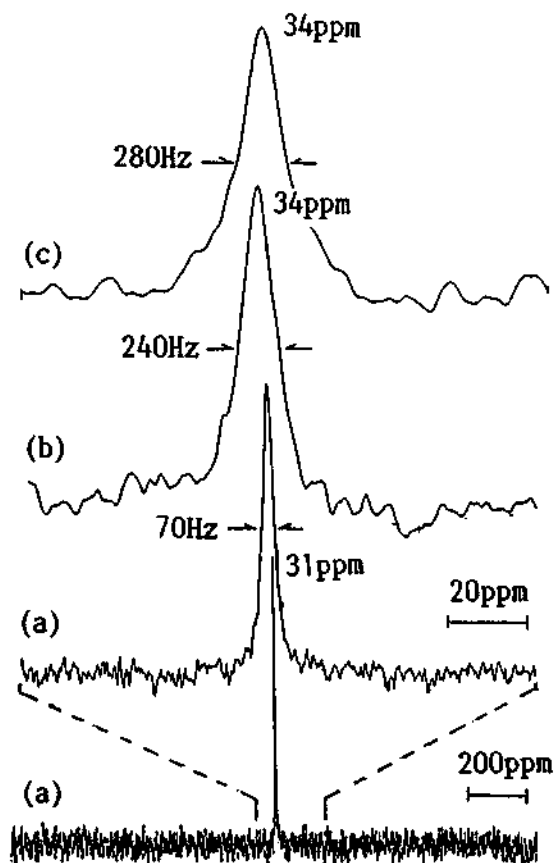


Fig. 2  $^{109}\text{Ag}$ -MASNMR spectra of trisilver dodecatungstophosphates (AgTP).  
The first direct observation for heteropolyacids in solid.  
(a) AgTP, (b) Py-AgTP-I (Pyridine-adsorbed AgTP; Ag/Py=3/1),  
(c) Py-AgTP-II (Ag/Py=3/2)

In addition to the <sup>109</sup>Ag-NMR spectra, <sup>31</sup>P-NMR with (CP)MAS were investigated to characterize the microenvironmental feature of phosphorus atoms. The <sup>31</sup>P-NMR spectra for AgTP and pyridine-adsorbed AgTP are shown in Fig. 3, indicating that more than two chemical environments exist on phosphorus atoms in the case of pyridine-adsorbed AgTP. In Fig. 3 <sup>31</sup>P-NMR spectra of HTP are also shown for reference.

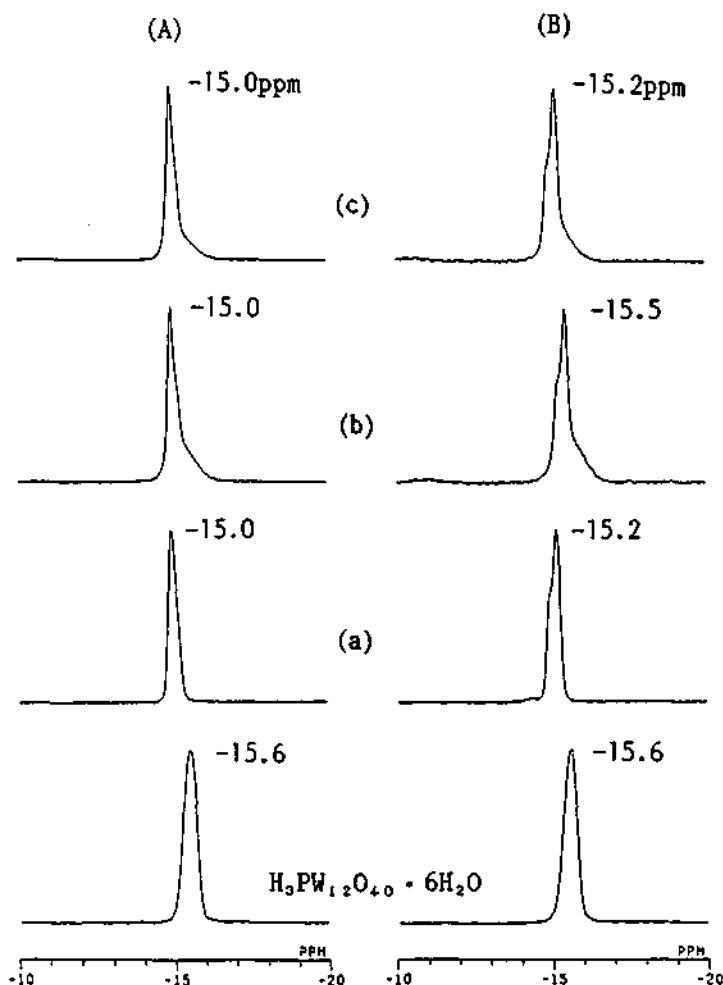


Fig. 3 <sup>31</sup>P-MASNMR spectra of AgTP (A) with and (B) without CP.  
(contact time = 3msec.) (a) AgTP, (b) Py-AgTP-I, (c) Py-AgTP-II.

## References

- [1] Misono, M., Stud. Surf. Sci. Catal., 1993, 75, 69; Catal. Rev. -Sci. Eng., 1987, 29, 269;  
*ibid.*, 1988, 30, 339.
- [2] Ono, Y., Mori, T. and Keii, T., in "Proceedings, 7th International Congress on Catalysis, Tokyo, 1980", 1981, Kodansha-Elsevier, 1414.
- [3] Ono, Y. and Mori, T., J.Chem. Soc. Faraday, Trans. 1, 1981, 77, 2209.
- [4] Baba, T., Sakai, J., Watanabe, H. and Ono, Y., Bull. Chem. Soc. Jpn., 1982, 55, 2555.
- [5] Ono, Y., Baba, T., Sakai, J. and Keii, T., J. Chem. Soc., Chem. Commun., 1981, 400.
- [6] Baba, T., Sakai, J. and Ono, Y., Bull. Chem. Chem. Soc. Jpn., 1982, 55, 2635.
- [7] Ono, Y., Kogai, M. and Baba, T., in "Proceedings of Pan-Pacific Synfuels Conference", Japan Petroleum Institute, Tokyo, 1982, I, 115.
- [8] Baba, T., Watanabe, H. and Ono, Y., J.Phys. Chem., 1983, 87, 2406
- [9] Baba, T. and Ono , Y., Appl. Catal., 1989, 55, 301.
- [10] Baba ,T., Nomura, M., Ono, Y. and Kansaki, Y., J.Chem., Soc.Faraday Trans., 1992, 88,71.
- [11] Baba, T., Nomura, M., Ono, Y.and Ohno, Y., J. Phys. Chem., in press.
- [12] Mann, B.E., Annual Reports on NMR Spectroscopy, 1991, 23, 141.
- [13] Looser, H. and Brinkmann, D., J. Magn. Reson., 1985, 64, 76.
- [14] Plischke, J.K., Benesi, A.J. and Vannice, M.A., J. Phys. Chem., 1992, 96, 3799.
- [15] Villa, M. and Licheri, G., J. Chem. Phys., 1986, 85, 2392.
- [16] Merwin , L.H. and Sebald, A., J. Magn. Reson., 1992, 97, 628.
- [17] Sugino, H., Kawata, S., Kitagawa, S., Maekawa, M. and Munakata, M., 65th Annual Meeting(Spring), Chem. Soc. Jpn., Tokyo, March 28-31, 1993, Prepr.I, 1E112, p.366; Maekawa, M., Honda, K., Kitagawa, S., Kawata, S. and Kondo, M., 32nd NMR Confer. Jpn., Tokyo, Nov. 4-6, 1993, Prepr., p61.
- [18] Mastikhin, V.M., Mudrakovskiy, I.L., Goncharova, S.N., Balzhinimaev, B.S., Noskova, S.P. and Zaikovsky, V.I., React. Kinet. Catal. Lett., 1992, 2, 425.
- [19] Bercier, J.J.,van der Klink, J.J., Jirousek, M. and Gratzel, 11th Specialized Colloque AMPERE on Magnetic Resonance in Homogeneous and Heterogeneous Catalysis, Menton, France, Spet. 6-10, 1993
- [20] Dekker, M., Catal. Rev., 1987, 29, 271.
- [21] Okuhara, T., Hyomen (Surface), 1989, 27, 629

## 2.5 Exchange of Isotopic Hydrogen over Solid Acid/Base Catalysts

D. Pfeiler, S. John, K. Thomke and O. M. E. El-Dusouqui

Institute of Physical Chemistry, Vienna University of Technology, Getreidemarkt 9/156,  
A-1060 Wien, Austria

### Abstract

Heterogeneously catalysed gas-phase H/D exchange reactions of a number of susceptible organic substrates using various solid acids and bases as catalytic agents are reported. The reactions were carried out under continuous flow conditions using helium as carrier gas for the premixed vapours of substrate and D<sub>2</sub>O as deuterium source. Additionally, the catalysts were characterized using various adsorption and appropriate spectroscopic techniques.

### 1. INTRODUCTION

Deuterium labeling of oxo, nitro and cyano carbogens using deuterium oxide and suitable acid and base catalysts have been well documented for solution reactions. Substrates susceptible to E1cB pathways such as the systems under study allow exchange of isotopic hydrogen between the substrate and the reaction medium [1]. The presence of an effective EPD site in the reaction environment and an acidic β-hydrogen and a poor nucleofuge in the substrate help to initiate and promote the reaction. We now report part of the results obtained in a study of parallel gas-phase deutero-de-protiations of these systems with solid acids and solid bases ranging from the weak to the strong as catalytic agents [2].

### 2. EXPERIMENTAL

In all, four solid bases (CaO, MgO, La<sub>2</sub>O<sub>3</sub>, Sm<sub>2</sub>O<sub>3</sub>), five solid acids ( $\gamma$ -Al<sub>2</sub>O<sub>3</sub>, AlPO<sub>4</sub>, Fe<sub>2</sub>O<sub>3</sub>, Cr<sub>2</sub>O<sub>3</sub>, H-ZSM5), ZnO, ZrO<sub>2</sub> and the mixed oxide TiO<sub>2</sub>/WO<sub>3</sub>/V<sub>2</sub>O<sub>5</sub> have been examined for their catalytic efficacy. All reactions were gas-phase processes in which D<sub>2</sub>O vapour provided the deuterium isotope required for exchange. Using helium as a carrier gas, premixed vapours of D<sub>2</sub>O and the substrate were passed in continuous flow over the catalyst bed at set temperature. The investigation involved nine substrates: three ketones, two nitriles, two alcohols, and two nitroalkanes.

The continuous-flow reactor in which both the acid-catalyzed and base-catalyzed exchange reactions were performed is shown in the diagram below. The reactions were

investigated over the temperature range of 30-500°C. The diagram also shows the satellite set-up for the TPD experiments undertaken. Product analyses were made using a Balzers QMG 420 mass-spectrometer. The characterization of the catalysts and surface complexes involved, where appropriate, TPD experiments with the substrates and with H<sub>2</sub>O, D<sub>2</sub>O and pyridine. The adsorption profiles of H<sub>2</sub>O and D<sub>2</sub>O on the basic oxides were probed in an IR-continuous-flow reactor and in IR-vacuum

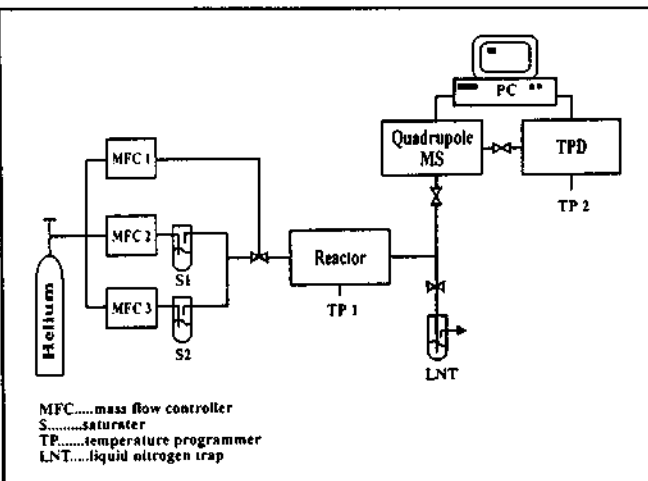


Fig. 1 experimental setup for reaction and TPD

cells. Desorption activation energies have been calculated. Further, XPS measurements were made on these oxides in an attempt to establish the nature of the surface oxide and hydroxide centers. Beside TPD analysis, the nature and strength of acid and basic sites are also the domain of investigations using Hammett indicators.

### 3. RESULTS AND DISCUSSION

Table 1 shows the observed H/D exchange degrees for the base catalyzed reactions carried out in the experimental setup described compared with the results previously obtained in a micropulse reactor [3]. Superior deuteration degrees and exhaustive deuteration are realized under continuous flow conditions. The deuteration degrees and the deuterated isomer ratios for selected substrates and basic or acidic catalysts, respectively, are summarized in tables 2 and 3. Overall, deuteration degrees were enhanced with increased reactant-catalyst contact time, and with increased temperature but at the expense of some substrate decomposition.

In alcohols, exchange of hydroxyl hydrogen is also conceivable. However, the deuterium exchanged is lost equally easily to the ubiquitous water vapour [4]. Because of keto-enol and nitro-acid form tautomerism, ketones and nitroalkanes would also be expected to undergo acid-catalyzed hydrogen-exchange reactions conditioned by the nature and strength of EPA sites available for catalysis. Both reactions initiated and promoted by basic EPA sites and acidic EPA sites are likely to benefit from the presence of complementary acid/base moieties in a bifunctional-like mode of acid/base catalysis as shown in figure 2.

Typically, CH<sub>3</sub>NO<sub>2</sub> has undergone 75% deuteration over Sm<sub>2</sub>O<sub>3</sub> at 70°C with negligible substrate decomposition. At 70°C, exhaustive deuteration amounted to 43% of the reaction product. Both the degree (%) of composite deuteration and the degree

of exhaustive deuteration seem to correlate qualitatively (Fig. 3) with relative base strength and relative acid strength of, respectively, the solid bases (e.g. at 70°C and for both categories of deuteration degrees:  $\text{CaO} > \text{MgO} > \text{La}_2\text{O}_3$ ) and solid acids (e.g. at 100°C :  $\text{Cr}_2\text{O}_3 > \text{AlPO}_4 > \gamma\text{-Al}_2\text{O}_3$ ). However, a more elaborate analysis of the findings is needed to accommodate apparent exceptions, such as the higher deuteration degrees exhibited by  $\text{Sm}_2\text{O}_3$ .

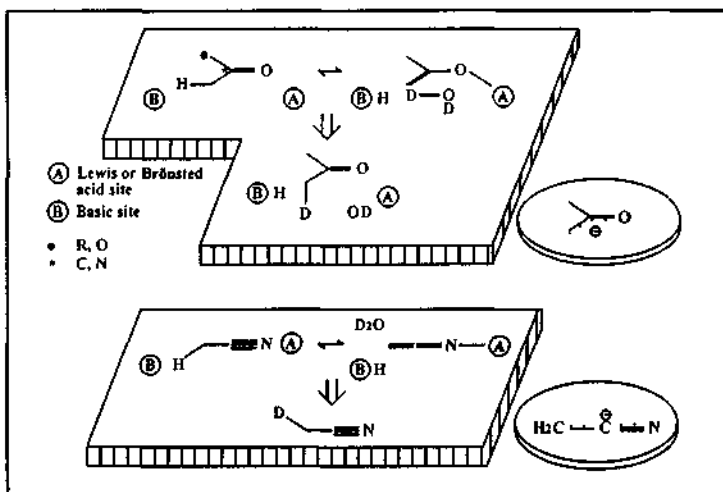


Fig. 2 plausible bifunctional reaction pathway

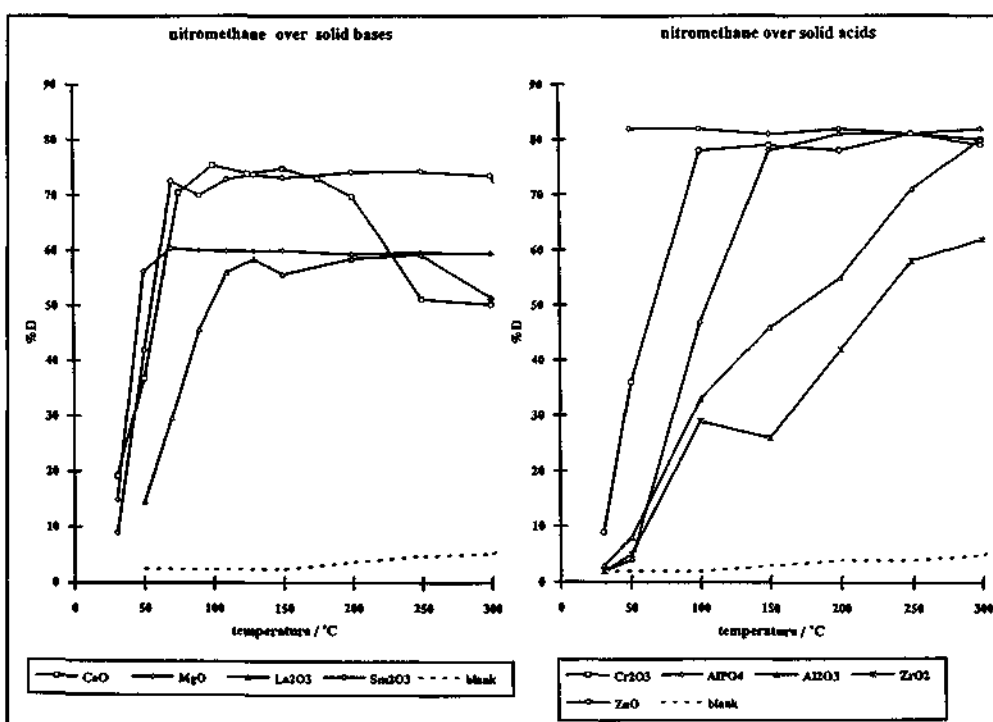


Fig. 3 % composite deuteration of  $\text{CH}_3\text{NO}_2$  over solid base and acid catalysts

The solid base catalysts were characterized using TPD, IR, XRD and XPS experiments. For CaO, MgO and  $\text{La}_2\text{O}_3$  hydroxide species were found to predominate the catalyst bulk and surface. The  $\text{Sm}_2\text{O}_3$  catalyst exhibited both oxide and hydroxide sites. The results of the H/D exchange reactions under continuous flow conditions seem to reflect the behaviour of solvent-influenced reaction pathways. To illustrate, the TPD and XPS of CaO and  $\text{Sm}_2\text{O}_3$  are given in figure 4.

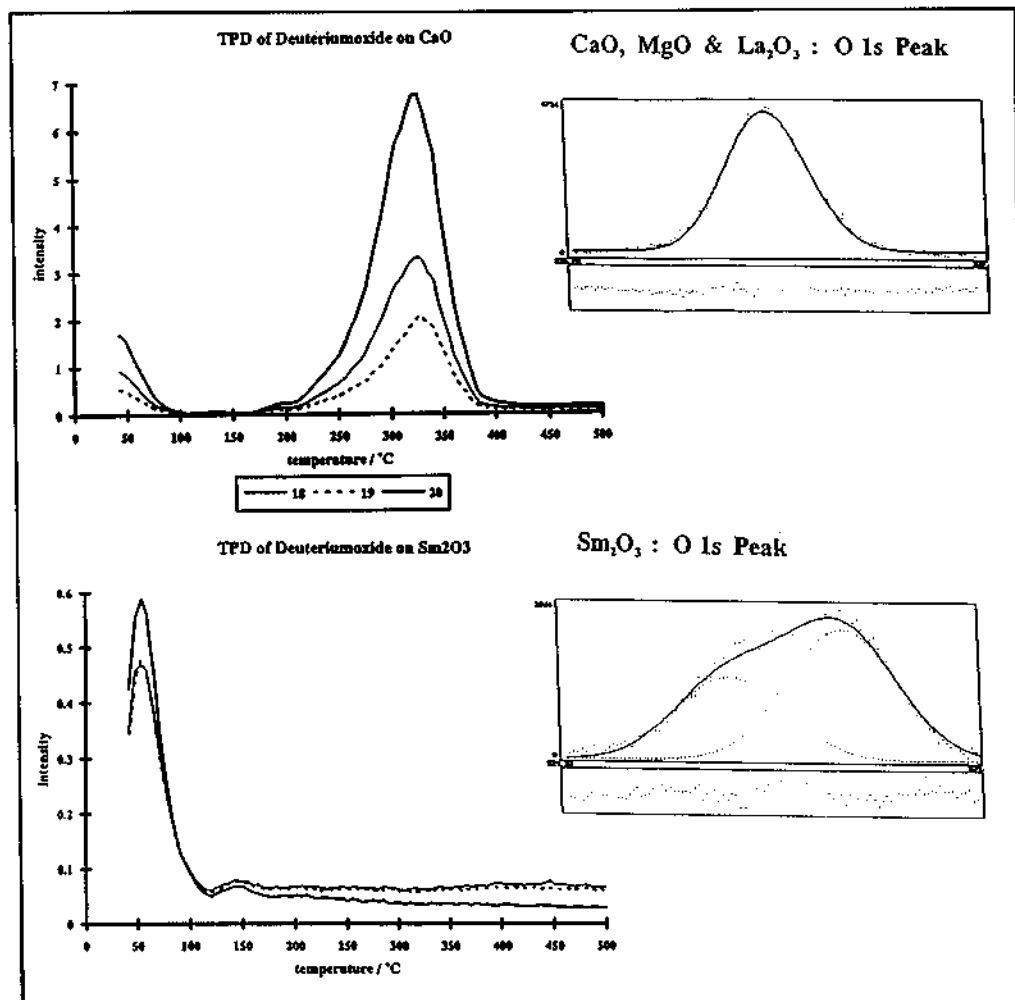


Fig. 4 TPD and XPS (O1s Peak) of CaO and  $\text{Sm}_2\text{O}_3$

Table 1 Comparative deuteration degree &amp; exchange temperature

substrate	pulsreactor	flowreactor
acetone	15 - 40% ( 50 - 120°C)	30 - 65% ( 50 - 100°C)
cyclopentanone	5 - 25% ( 50 - 140°C)	30 - 70% ( 50 - 100°C)
methanol	5 - 35% ( 50 - 250°C)	30 - 35% ( 50 - 100°C)
nitromethane	5 - 20% ( 60 - 150°C)	30 - 75% ( 70 - 100°C)
acetonitrile	5 - 20% (110 - 200°C)	65 - 85% (100 - 150°C)
propionitrile	-	70 - 95% (100 - 150°C)

Table 2 Deuteration degree &amp; deuterated isomer ratio for selected substrates and bases

substrates	catalyst	T/°C	%D	%d <sub>0</sub>	%d <sub>1</sub>	%d <sub>2</sub>	%d <sub>3</sub>	%d <sub>4</sub>	%d <sub>5</sub>	%d <sub>6</sub>
acetone	La <sub>2</sub> O <sub>3</sub>	75	65	2	3	10	21	30	24	10
cyclopentanone	La <sub>2</sub> O <sub>3</sub>	100	70	4	8	25	35	28		
methanol	Sm <sub>2</sub> O <sub>3</sub>	100	35	65	35					
nitromethane	Sm <sub>2</sub> O <sub>3</sub>	70	75	5	16	36	43			
acetonitrile	CaO	150	85	0	6	34	60			
propionitrile	CaO	150	95	7	0	93				

Table 3 Deuteration degree &amp; deuterated isomer ratio for selected substrates and acids

substrates	catalyst	T/°C	%D	%d <sub>0</sub>	%d <sub>1</sub>	%d <sub>2</sub>	%d <sub>3</sub>	%d <sub>4</sub>	%d <sub>5</sub>	%d <sub>6</sub>
acetone	HZSM5	200	70	2	5	6	14	26	30	17
cyclopentanone	mix-ox.	100	70	0	2	31	47	20		
methanol	Al <sub>2</sub> O <sub>3</sub>	300	10	65	35					
nitromethane	ZnO	50	80	2	9	30	59			
acetonitrile	ZnO	350	55	16	31	26	27			

#### 4. CONCLUSIONS

Both solid acids and solid bases initiate and promote deuterium exchange in oxo, nitro, cyano and hydroxy compounds. Fine tuning of catalytic efficacy and reaction temperature is conceivable. Superior deuteration degrees at lower threshold reaction temperatures are obtained under continuous-flow conditions compared with micropulse techniques. Labeling of ketones is less sensitive to acidity and basicity, whereas nitro compounds respond differentially more to acid strength than to basic strength. Cyano organics deuterate better over solid bases, and deuteration improves with relative base strength.

The investigations concluded and the results obtained provide an adequate basis for an understanding of the mechanisms of the exchange reactions, the role of catalytically active sites and surface complexes, and the structural features of a substrate which might selectively promote an acid, a base or a bifunctional catalytic pathway for the exchange reaction. The results also seem to present an attractive route to the preparation of valuable deuterated carbogens.

#### 5. ACKNOWLEDGEMENTS

The financial support of the Fonds zur Förderung der Wissenschaftlichen Forschung through Project P7753 is gratefully acknowledged.

#### 6. REFERENCES

- [1] J. March: Advanced Organic Chemistry - Reactions, Mechanisms, and Structure, Wiley-Interscience, New York, 1992, 991.
- [2] K. Tanabe in Catalysis by Acids and Bases, eds. B. Imelik et al, Elsevier Science Publishers, Amsterdam 1985, 1.
- [3] W. Baumann, S. Lippert and K. Thomke, *J. Mol. Catal.*, 1991, 68, 33; 69, 117.
- [4] A. F. Thomas, Deuterium Labeling in Organic Chemistry, Appleton-Century-Crofts, New York 1991.

## 2.6 Elementary Steps of Acid-Base Catalyzed Reactions in Molecular Sieves

### ELEMENTARY STEPS OF ACID-BASE CATALYZED REACTIONS IN MOLECULAR SIEVES

Johannes A. Lercher<sup>a,b</sup>, Gabriele Mirth<sup>a</sup>, Michael Stockenhuber<sup>b</sup>, Thomas Narbeshuber<sup>a,b</sup> and Andreas Kogelbauer<sup>b</sup>

<sup>a</sup>Department of Chemical Technology, University of Twente, Postbus 217, 7500 AE Enschede, The Netherlands

<sup>b</sup>Institute for Physical Chemistry and Christian Doppler Laboratory for Heterogeneous Catalysis, Technical University of Vienna, Getreidemarkt 9, A-1060 Vienna, Austria.

#### Abstract

The role of Brønsted acid (and basic) sites of molecular sieves is compared for four different acid-base catalyzed reactions, i.e., n-alkane conversion, isomerization of xylene, reaction of methanol to dimethylether and alkylation of toluene. The coverage at the catalytically active sites and the surface chemistry during the reaction is followed by *in situ* i.r. spectroscopy using CSTR with i.r. light transparent windows. This allows to directly compare the surface chemistry with the catalytic activities and selectivities. Conventional isotope labelling and steady state isotope transient experiments are used to further support the mechanistic models of the acid-base catalyzed reactions outlined above.

#### 1. INTRODUCTION

Heterogeneously catalyzed reactions consist of a series of elementary steps that each may control or influence the overall reaction rate. These steps include transport of the reactant to the catalyst, adsorption on the surface, surface diffusion and reaction, desorption and transport of the products from the catalyst. At steady state, all these reactions proceed at the same rate. The simplifying assumption that only one reaction step controls the overall reaction rate suggests that all reaction steps except one are in microscopic thermodynamic equilibrium and are only differentially disturbed as the reaction proceeds. The rate determining step is the only one having a negative Gibbs free energy [1].

In order to formulate a microscopic kinetic model of a catalyzed reaction, the knowledge of the equilibrium constants of all steps involved in the reaction prior to this rate determining step is required. In the most simple case, i.e., if only transport and adsorption precede the rate determining surface reaction, the concentration of the adsorbed reactant at the catalytically active sites will determine the overall rate of reaction. Hence, the rate of reaction will be controlled by the concentration of the active sites at the surface, their Gibbs energy of interaction with the adsorbed molecules and the partial pressures of the reactants and products.

For better understanding the elementary steps of acid-base catalyzed reactions, the use of well defined molecular sieves as catalysts poses an unique opportunity and a challenge at the

same time. Unlike with single or mixed oxides, the catalytically active sites in zeolites are geometrically well defined and might have a very narrow distribution of acid strength, which can be fine tuned to specific needs by modification of the chemical environment [2,3]. Our understanding of the nature and strength of these sites has advanced considerably by recent results of theoretical calculations [4,5,6]. One has to consider, however, that the pore diameters of molecular sieves are close to the size of the reacting molecules and that this may induce perturbations which are absent on the surfaces of macroporous materials [7,8].

This communication will give specific examples for the role of the active sites in acid-base catalyzed reactions. Direct i.r. spectroscopic probing of the surface concentrations of reactants, intermediates and products will be used together with isotope labelling experiments and steady state and non-steady state kinetic methods to develop a microscopic understanding of the acid-base catalyzed reactions in molecular sieves.

## 2. EXPERIMENTAL METHODS

For most reactions described below, zeolite HZSM5 which was provided in the ammonium exchanged form (by Mobil) and activated either in vacuum or He flow (with an increment of 10 K/min up to 870 K) was used. The Si/Al ratio of the sample was 35, the diameter of the crystals was approximately 1  $\mu\text{m}$ .

*In situ* studies during the catalyzed reaction were performed in a CSTR reactor with i.r. transparent windows. The reactor was placed in the focus of the i.r. beam to monitor the catalyst during all treatments by time resolved transmission absorption spectroscopy. The reactants and products in the effluent gas stream were analyzed by gas chromatography or alternatively by mass spectroscopy. In order to decouple the sampling of the gas stream at the reactor outlet from the time needed for gas chromatographic analysis, the effluent gas stream was stored in a multiport valve with 16 sample loops (for details see ref. [9]).

For the kinetic isotope and pressure transient measurements, a tubular reactor operated in plug flow mode was used. The volume of the system was minimized to obtain a well defined transient function. The effluent gas stream was analyzed by means of a Hewlett Packard GC-MS system equipped with a sampling system that allowed to store gas samples in 24 loops. This allowed to keep the time resolution of the sampling very low (typically in the range of 10 sec.). The FID signal was used to obtain the quantitative information of the product molecules, the isotopic selectivity of labelled molecules was calculated from the mass spectra.

## 3. RESULTS AND DISCUSSION

Since it is not possible to describe and explain all experimental observations of the reactions discussed in this contribution, we will focus on the role of the acidic and the corresponding basic sites in catalyzing these reactions. Reference to the more extensive description of these reactions is given. In the following, the reactions are arranged according to increasing stability of the complex of the reactant with the acid site involving carbonium-, arenium-, oxonium and carbonium ions. The zeolites used had a very narrow distribution of the strength of the acid sites, which is characterized by 150 kJ/mol for the heat of adsorption of ammonia [10].

### 3.1. n-Alkane conversion

The monomolecular reactions of light n-alkanes (H/D exchange, dehydrogenation and cracking) are used as examples in which the concentration and strength of the Brönsted acid sites control the adsorption constants of the hydrocarbons as well as the catalytic activity of the

catalyst. The transport of the reactants and products into and out of the pores of the molecular sieve have hardly any effect upon the rate of the reaction [11]. Because the catalytic activity for n-hexane conversion over HZSM5 was found to be directly proportional to the concentration of the Brönsted acid sites of this material [12], we used this type of zeolite as the model catalyst for our investigations.

The sorption of n-alkanes was found to be very fast and completely reversible at 300 K. I.r. studies of the adsorption under non-reactive conditions indicated the formation of weak hydrogen bonds between the Brönsted acid sites of HZSM5 and the hydrocarbon molecules. The strength of hydrogen bonding was deduced from the downward shift of the i.r. band of the acidic hydroxyl groups ( $\text{SiOHAl}$  groups) after the alkane adsorption [13]. A direct correlation between the heat of adsorption as derived from the adsorption isosters and the wavenumber difference between the perturbed and unperturbed OH group was observed (see Fig. 1). This indicates a similar nature of interaction of all investigated n-alkanes. The strength of interaction, however, increased with the chain length of the hydrocarbon. Indirectly, the results also confirm the relatively narrow distribution of the acid sites strength in the material used.

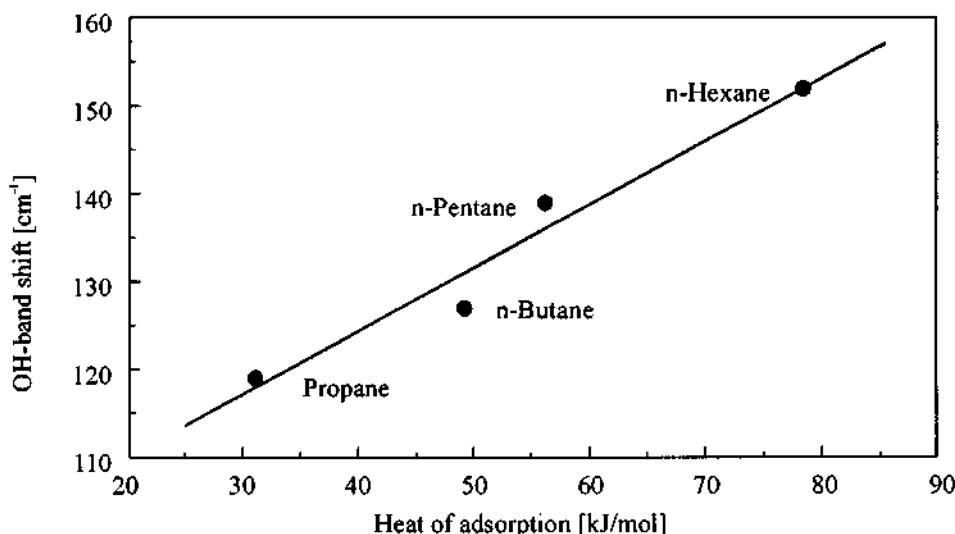


Figure 1: Correlation between enthalpy of adsorption and the wavenumber difference between the free and perturbed OH band of HZSM5 after adsorption of n-alkanes

In parallel to the increase in the strength of interaction between the sorbed reactant molecule and the Brönsted acidic  $\text{SiOHAl}$  group of HZSM5, the logarithm of the turnover frequency (TOF) for hydrocarbon cracking increased (see Fig. 2). The direct linear correlation between these two parameters suggests that the adsorption/desorption equilibrium (for a given zeolite it is determined by the chain length of the n-alkane) plays a major role for the cracking rate. On the other hand, the chemistry of the carbon-carbon bond cleavage is very similar for all alkanes from propane to n-hexane. These results are indirectly supported by two other observations: (i) The apparent energy of activation for cracking is independent from the position of the carbon-carbon bond to be broken. (ii) The sum of the apparent energy of activation and the negative heat of adsorption is constant for all hydrocarbons.

I.r. spectroscopy indicated that the acidic hydroxyl groups of the zeolite were exchanged for

deuteroxyl groups upon contact with deuterated butane. The rate of H/D exchange exceeded the rates of dehydrogenation and cracking by at least one order of magnitude. The apparent energies of activation for these reactions decreased in the order of 140, 105 and 85 kJ.mol<sup>-1</sup> for cracking, dehydrogenation and H/D exchange, respectively. As the reactant molecule (and therefore the heat of adsorption) is the same for all three reactions and the catalyst (HZSM5) has a uniform site distribution, the difference in the activation energies requires to propose three different transition states. This indicates either that the protonated and hydrogen bonded n-butane are in equilibrium and protonation, thus, does not limit the rates of the monomolecular reactions or that the H/D exchange represents a reaction channel different from that of dehydrogenation and cracking. Recent theoretical calculations support the later proposal [4] indicating that the carbonium might only exist in a transition state.

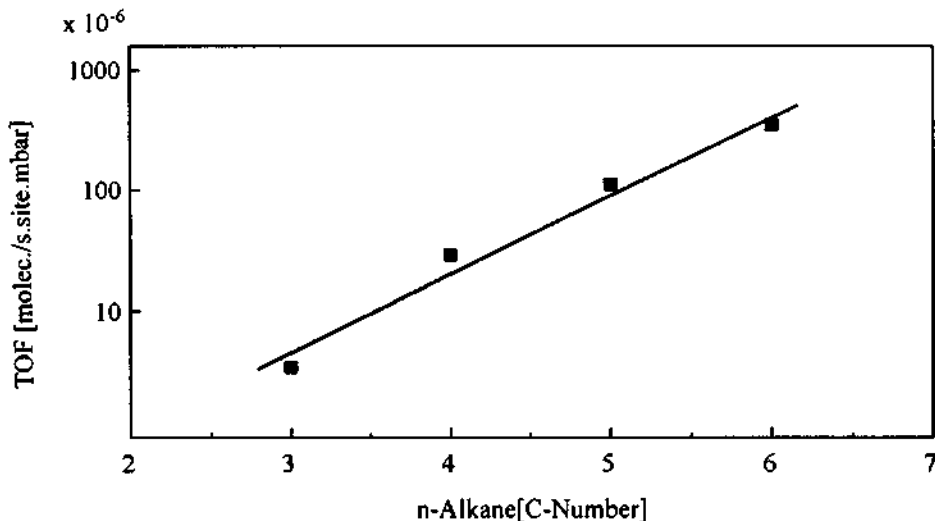


Figure 2: Turnover frequencies of n-alkanes over HZSM5 at 773 K

Even under these conditions steady state isotope transient experiments using <sup>13</sup>C and deuterium labelled n-butane indicate that the residence time of the alkenes formed exceed by far the residence times of the alkanes. These carbonium ions undergo secondary reactions and - as their concentration in the pores increases - bimolecular reactions that result in multiple carbon-carbon bond formation and carbon-carbon bond cleaving reactions [14].

### 3.2. Isomerization of Xylenes

The acid catalyzed isomerization of xylenes over HZSM5 zeolites is taken as an example where arenium ions act as intermediates [15]. The transport, adsorption and reaction properties of the xylene isomers on the pentasil zeolite HZSM5 have been studied by *in situ* i.r. spectroscopy combined with a kinetic analysis of the gas phase (a detailed description is given in ref. [16]). The rates of transport of the p:-o:-m-xylene isomers in zeolite HZSM5 (as determined from the adsorption kinetics) showed a ratio of 1000:10:1, respectively. It is important to note that the minimum kinetic diameter and the apparent energy of activation of the diffusion (~30 kJ/mol) were approximately equal for o- and m-xylene. Thus, the differences in the apparent diffusion constants have to be caused by differences in the activation entropy of the transport

in the pores.

Because the rates of isomerization for all three xylene isomers were found to be equal at low reaction temperatures (473 K), while the rate of diffusion differed by orders of magnitude, we concluded that the catalyzed reactions were not influenced by reactant diffusion. The rate of isomerization at steady state was  $0.0012 (+/- 0.0001)$  molecules $*[H^+]*sec^{-1}$ . At higher reaction temperatures (573 K), the rates of isomerization were 0.0088, 0.0067 and 0.0054 molecules $*[H^+]*sec^{-1}$  for p-, o-, and m-xylene, respectively. The normalization to the concentration of the adsorbed xylene molecules at steady state leads, however, to equal rate constants for the three isomers (see Table 1). This shows clearly that the slower rate of transport of o- and m-xylene decrease the concentration of adsorbed reactants on the acid sites thereby decreasing the rate of reaction. Thus, only a fraction of the available catalytically active sites takes part in the reaction resulting in a lower catalyst efficiency.

Table 1: Reactant coverage, turn over frequencies [molecules $*[H^+]*sec^{-1}$ ] and rate constants  $k$ , of xylene isomerization over HZSMS

Reaction temp.	473 K			573 K		
	$\Theta_{reactant}$	TOF	$k$	$\Theta_{reactant}$	TOF	$k$
m-xylene	0.55	0.0013	0.0024	0.05	0.0054	0.108
o-xylene	0.55	0.0011	0.0020	0.06	0.0067	0.112
p-xylene	0.60	0.0012	0.0020	0.08	0.0088	0.110

Measurements under steady state conditions allowed, thus, to directly determine the rate constants, the catalyst efficiency and the role of reactant diffusion plays for the overall reaction. In order to assess the influence of product diffusion on the catalytic activity and selectivity, additional experiments under non steady state conditions were needed. In the presented work this is done by a stepwise increase of the reactant pressure and parallel monitoring of the reaction rates and the surface concentrations during relaxation into the new steady state.

For m-xylene isomerization, the i.r. spectra recorded during the stepwise increase of the partial pressure suggest that only m-xylene is adsorbed in detectable quantities. I.r. bands attributed to isomerization products (i.e., o- and p-xylene) were not detected. Therefore we conclude that the transport of the products out of the zeolite pores is faster than isomerization under all reaction conditions. After changing the reactant pressure, the variation in the reaction rate was directly proportional to the concentration of m-xylene adsorbed on the SiOHAl sites of the zeolite (see Fig. 3). This suggests that all acid sites which adsorb m-xylene have the same catalytic activity, i.e., the reaction is of strict first order with respect to the xylene surface concentration. At all reaction temperatures under investigation (473 - 573 K), the ratio of p- to o-xylene was 2. Thus, the reaction pathways to o- and p-xylene have an identical apparent energy of activation indicating that the preferential formation of p-xylene is due to differences in the transition entropies (transition state selectivity) and not due to a lower energy of activation of one of the routes.

In contrast, for o-xylene isomerization the rate increased slowly at low coverages (i.e.,

shortly after the pressure step up) and then increased steeply (see Fig. 3). The i.r. analysis of the adsorbed phase shows that the low rates at the beginning are due to the accumulation of the primary product, m-xylene, in the pores. As this surface concentration increased, the secondary isomerization of m-xylene to p- and o-xylene (isomer ratio 2:1) increased. This leads finally to the same overall rate constant as when o-xylene was used as reactant. Thus, the experiments clearly show that the diffusion limitation of the primary product, m-xylene, causes the enhanced selectivity to p-xylene. It should be again emphasized that intrinsically the turnovers of all xylene molecules at the acid sites proceed with the same rate and that the differences in the reaction rates are only due to the differences in the surface concentrations of reactants and intermediates in the zeolite pores.

TOF (molecules/site.s)

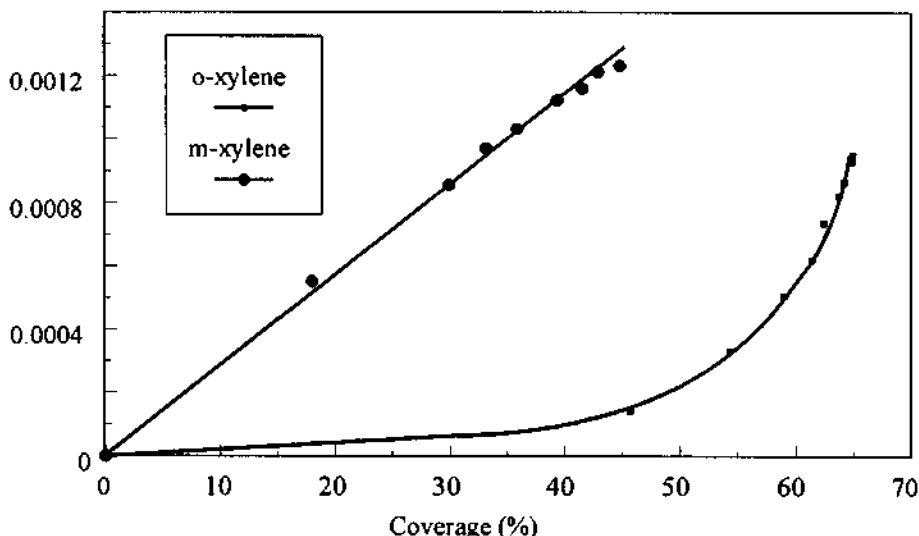


Figure 3: Correlation of the coverage and the TOF in the isomerization of m- and o-xylene over HZSM5 at 473 K

### 3.3. Reaction of methanol to dimethylether

The acid catalyzed formation of methoxy groups and dimethylether from methanol is used to discuss the reactions of polar compounds *via* oxonium and carbenium ion intermediates. The sorption and reaction of methanol on HZSM5 was studied by means of i.r. spectroscopy and mass spectroscopy. Details can be found in refs. [17,18]. Temperature programmed desorption / reaction (t.p.d. / t.p.r.) was used to asses the role and stability of the different surface species.

At ambient temperature, the i.r. spectra of the zeolite with one methanol adsorbed per Brönsted acid site suggest that the largest fraction of the molecules was protonated and formed a methoxonium ion. In HZSM5, the methoxonium ions are bound in two orientations to the negatively charged zeolite lattice [17,18]. It should be noted, however, that recent theoretical calculations propose that the potential well between the protonated and non protonated structure of methanol is very broad and the energy difference between the two forms is rather small [19]. Fast H/D exchange between the hydroxyl groups of the zeolite and the OD- group of deuterated methanol ( $\text{CH}_3\text{OD}$ ) was found at ambient temperature. In contrast, H/D exchange between

deuterium in the methyl group ( $\text{CD}_3\text{OH}$ ) and the proton of the  $\text{SiOHAI}$  group of HZSM5 did not occur. Despite the strong bonding of methanol to the Brønsted acid site of the zeolite, surface reactions were not observed at ambient temperature.

During t.p.d. / t.p.r. (one methanol molecule adsorbed per acid site) the largest fraction of methanol desorbed unreacted up to 500 K (see Fig. 4). Water was released from the surface in two steps: the first maximum of the rate of desorption occurred at 370 K, the second at 520 K (see Fig. 5). I.r. spectra recorded during that procedure indicate that the release of water is paralleled by the formation of methoxy groups at the acid sites ( $\text{Si-OCH}_3\text{-Al}$ ) and the silanol groups ( $\text{Si-OCH}_3$ ) of the catalyst. This reaction represents the formation of the smallest carbonium ion. MAS-NMR spectroscopy suggests, that the methoxy group resembles rather a covalently bonded methyl group in a methyl silyl ether than a free methyl carbonium ion [20]. Note that both types of methoxy groups can only desorb via reaction with another methanol molecule and are, thus, relatively stable surface species. If ethanol was used as reactant, monomolecular decomposition of the ethylcarbenium ion to ethene and the free acid site becomes the primary reaction channel.

#### M.S. Response (Arb.U.)

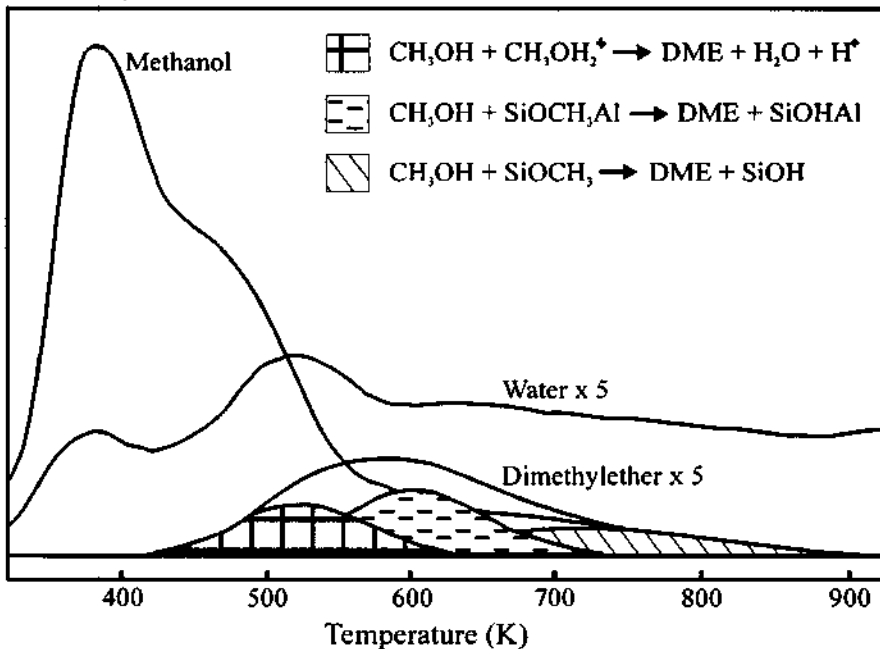


Figure 4: Temperature programmed desorption/reaction of methanol on HZSM5

The formation of dimethylether is possible via three different reaction routes as indicated by the t.p.d. curves given in Fig.5. At low temperatures (around 520 K), mobile methanol reacts with chemisorbed methanol (methoxonium ions) to yield dimethylether and water (second maximum of water production at 520 K). Between 550 and 650 K, the  $\text{Si-OCH}_3\text{-Al}$  (methoxy) groups are the most abundant reactive intermediate at the surface. Desorbing methanol is suggested to react with the methoxy groups by producing dimethylether. Some residual water is also speculated to rehydrolyze methoxy groups to methanol and a  $\text{SiOHAI}$  group. At high

temperatures (above 650 K), also  $\text{SiOCH}_3$  groups begin to react with desorbing methanol to yield dimethylether. This clearly shows that the reactivity of chemisorbed methanol decreases once the carbon-oxygen bond of the alcohol is cleaved ( $\text{CH}_3\text{OH}_2^+ > \text{Si-OCH}_3\text{-Al} > \text{Si-OCH}_3$ ). The strong and covalent bond between the lattice oxygen and the carbon atom of the adsorbed methoxy group reduces the reactivity of the methyl group. Because there is no way for the methoxy groups to react via an intramolecular reaction channel, the  $-\text{CH}_3$  group is retained at the surface allowing energetically more demanding reaction to occur. The contribution of each reaction path to the overall rate of dimethylether formation depends on the reaction conditions applied.

### 3.4. Acid catalyzed methylation of toluene

The reaction of methxonium ions with toluene will serve as example for the bimolecular reaction of oxonium and carbenium ions with aromatic molecules leading to the formation of a carbon-carbon bond. Over large pore zeolites preferential formation of the carbon-carbon bond at the para- and ortho- relative to the meta- position was observed at low conversions, while an equilibrium mixture of the xylene isomers was found at high conversions [21,22]. Over medium pore zeolites like HZSM5, on the other hand, preferential formation of p-xylene was observed over wide range of conversions. The contribution of the type and strength of the acid sites and the contribution of the steric constraints to direct the product selectivity in toluene alkylation were extensively studied [e.g.23,24]. Kinetic and spectroscopic evidence will be given here that the rate of alkylation is determined by the concentration of the coadsorption complex between the methxonium ions and/or methoxy groups and toluene. The selectivity can be explained in terms of parallel and consecutive reactions that are limited more by the constraints in the environment than by the chemical nature of the catalytically active sites [25, 26]).

I.r.spectroscopic studies showed that a 1:1 coadsorption complex of one chemisorbed methanol molecule (methxonium ion) and one toluene molecule is formed at each Brönsted acid site of zeolite HZSM5 [27]. The moiety is stable up to approximately 500 K and decreases then sharply in concentration with time on stream or with increasing temperature. Because the rate of alkylation varied in parallel to the surface concentration of the complex, we conclude it to be a direct precursor to the active intermediate in the rate determining step. It should be emphasized that the concentration of the complex depends primarily upon the concentration of the chemisorbed methanol (methxonium ions). As the temperature increases above 500 K, the methxonium ions are converted to methoxy groups which act then as reactive intermediate in the bimolecular reaction.

Not only the reaction mechanism but also the selectivity differed significantly between the experiments at low (473 K) and high (573 K) reaction temperature. At 473 K, the analysis of the effluent gas stream showed, that all three xylene isomers were observed immediately after the onset of the reaction. Initially, the selectivity to p- and o-xylene was high but shifted with increasing time on stream to lower values. This shift was paralleled with a decrease in the surface concentration of the reactive coadsorption complex and an increase in the concentration of formed products (mainly m-xylene) in the pores. The accumulation of the bulkier products is a direct result of the large differences in the rates of diffusion of the three primary products, p-, o- and m-xylene. As all acid sites of the zeolite were interacting with reactant or product molecules at any time on stream, the increase in the concentration of adsorbed reaction products decreased the surface concentration of chemisorbed methanol. It should be noted, however, that it had hardly any effect on the coverage with toluene. The rate of isomerization of the xylenes (formed as primary products in the alkylation) was too low to affect the product distribution under these experimental conditions (473 K).

At higher reaction temperatures (573 K and above), enhanced selectivity to p-xylene and

constant catalytic activity were observed. Again, the accumulation of the bulkier products in the pores was found resulting in a high coverage ( $Q_{xyl}$ ) of m- and o- xylene. But in contrast to the low temperature regime, the rate of isomerization ( $r_{iso} = k \cdot Q_{xyl}$ ) of the adsorbed xylenes exceeded the rate of alkylation. The high rate of isomerization of the bulky isomers to the fast diffusing p-xylene increased the p-selectivity in the gas phase and allowed a constant activity of the catalyst as sufficient acid sites were available for alkylation. These experiments demonstrate unequivocally that the rapid secondary isomerization of the primary formed xylene molecules is indispensable for shape selective alkylation.

#### 4. CONCLUSIONS

The examples discussed above show that Brönsted acid-base catalyzed reactions in zeolites can be completely described in terms of elementary reaction steps. The use of *in situ* spectroscopic techniques allows to estimate the concentrations of the reactants and intermediates under reaction conditions. This permits to directly establish reaction sequences and to derive and test microscopic models. Examples for carbonium-, arenium-, oxonium and carbenium ion intermediates were given. The methyl carbenium ion was found to be the thermally most stable species among these intermediates.

For the acidic conversion of n-alkanes, the reaction rate over a given catalyst is directly proportional ( $r = k \cdot Q_{reactant}$ ) to the concentration of the reactants adsorbed at the acid sites. As the reaction rate equals the rate constants times the concentration of adsorbed reactant molecules, it can be clearly seen that the adsorption constant of the reactant determines the overall reaction rate,  $r$ .

Using isomerization of m-xylene over HZSM5 as example, it could be shown that the true rate constants,  $k$ , of diffusion disguised reactions can be derived from the direct measurement of the surface coverage of the reactant and the reaction rate. Intracrystalline reactant diffusion limitation leads to a lower concentration of the reactant under reaction conditions than expected from adsorption studies under non reactive conditions. Although the decreased reactant coverage caused a lower reaction rate, the rate constants,  $k$ , were not effected (see Table 1).

Taking the methylation of toluene as example, it was shown that if the desorption and/or transport of the products are the rate determining step of a reaction, high fugacities of the product build up in the pores. This high surface concentration impedes the reaction until the intrinsic rate of formation of the product equals its rate of transport out of the zeolite pores. This is well demonstrated by the decrease in catalytic activity of toluene methylation at 473 K. At 573 K, the rapid isomerization of the adsorbed m- and o-xylene molecules to the faster desorbing p-xylene was the reason that the surface reaction and not the desorption or transport of the products determined the overall reaction rate.

#### 5. ACKNOWLEDGEMENTS

This work was supported by the "Fonds zur Förderung der Wissenschaftlichen Forschung" under project CHE-P7312 and by the Christian Doppler Laboratory. We are grateful to Mobil Research for providing the HZSM5 samples.

## 5. REFERENCES

1. M. Boudart and G. Djega-Mariadassou, "Kinetics of Heterogeneous Catalytic Reaction", Princeton University Press, Princeton, 1984.
2. D. Bartomeuf, E.G. Derouane and W. Hölderich, "Guidelines for Mastering the Properties of Molecular Sieves", Plenum Press, 1990.
3. H.van Bekkum, E.M. Flanigen and J.C. Jansen, Eds., "Introduction to Zeolite Science and Practice", Stud.Surf. Sci.Catal. **1991**, 58.
4. J.A. Lercher, R.A. van Santen and H.Vinek, Catal. Lett., submitted for publication **1993**.
5. K.P. Schröder, J.Sauer, M. Leslie and C.R.A. Catlow, Zeolites **1992**, 12,20.
6. J.D. Gale, C.R. Catlow and A.K. Cheetham, J.Chem.Soc., Chem.Commun. **1991**, 178.
7. S.M. Csicsery, Zeolites **1984**, 4,202.
8. P.B. Weisz, Pure & Appl. Chem. **1980**, 52, 2091.
9. G. Mirth, F.Eder and J.A. Lercher, Appl. Spectroscopy, submitted for publication **1993**
10. M.Stockenhuber, unpublished results.
11. W.O. Haag, R.M. Lago and P.P. Weisz, Farad.Disc.Chem.Soc. **1981**, 72, 317.
12. W.O.Haag, R.M. Lago and P.B. Weisz, Nature **1984**, 309, 14.
13. M.L. Hair and W. Hertl, J.Phys.Chem. **1970**, 74, 91.
14. W.O.Haag, M.Dessau and R.M. Lago, Stud.Surf.Sci.Catal. **1991**, 60, 255.
15. D.H. Olson and W.O. Haag, Am.Chem.Soc.Symp.Ser. **1984**, 248, 275.
16. G. Mirth, J. Cejka and J.A. Lercher, J.Catal. **1993**, 139, 24.
17. G. Mirth and J.A. Lercher, Stud. Surf.Sci.Catal. **1991**, 437.
18. G. Mirth, J.A. Lercher, M.W. Anderson and J. Klinowski, J.Chem.Soc.Farad.Trans **1990**, 86, 3039.
19. F. Haase and J. Sauer, private communication **1993**.
20. M.T. Aronson, R.J. Gorte, W.E. Farneth and D. White, Langmuir **1988**, 4, 702.
21. R.H. Allen and L.D. Yats, J.Amer.Chem.Soc. **1961**, 83, 2799.
22. T.Yashima, H.Almad, K.Yamazaki, M.Katsura and N.Hara, J.Catal. **1970**, 16, 273.
23. N.Y. Chen, Kaeding W.W. and Dwyer T., J.Am.Chem.Soc. **1979**, 101, 6783.
24. W.W.Kaeding, C. Chu, L.B. Young and L.B. Butter, J.Catal. **1981**, 67, 159.
25. G. Mirth and J.A. Lercher, J.Catal. **1991**, 132, 244.
26. G. Mirth and J.A. Lercher, J.Catal. **1993**, accepted for publication.
27. G. Mirth and J.A. Lercher, J.Phys.Chem. **1991**, 95, 3736.

## 2.7 Infrared Spectroscopic Observation of N<sub>2</sub> Species Adsorbed on Brønsted and Lewis Acid Sites of H-Zeolites at Low Temperatures

Fumitaka Wakabayashi,<sup>a</sup> Junko Kondo,<sup>b</sup> Kazunari Domen,<sup>b</sup> and Chiaki Hirose<sup>b</sup>

<sup>a</sup> Department of Science and Engineering, National Science Museum, Tokyo 110, Japan

<sup>b</sup> Research Laboratory of Resources Utilization, Tokyo Institute of Technology, Yokohama 227, Japan

### Abstract

Nitrogen adsorption on H-mordenite, H-Y and H-ZSM-5 at low temperatures was studied by *in-situ* FT-IR. For each zeolites pretreated at higher temperatures (typically above 773 K), two absorption bands were observed at around 2334 and 2352 cm<sup>-1</sup> in the  $\nu(\text{NN})$  region. By examining the effects of water-vapor treatment and the pretreatment temperature, these bands were assigned to the  $\nu(\text{NN})$  bands of the dinitrogen species adsorbed on Brønsted and Lewis acid sites of the zeolites, respectively. For highly siliceous ZSM-5 (without acidity), the  $\nu(\text{NN})$  band was not observed. Therefore, N<sub>2</sub> species can be used as a probe of acid sites of zeolites. Advantages of N<sub>2</sub> species as a probe are discussed.

### 1. INTRODUCTION

The acid sites of zeolites play an important role in the catalytic process over zeolites. Their properties have been extensively studied using various techniques [1–2]. Pyridine and ammonia act as useful probes of acid sites and are routinely used nowadays in IR, TPD, and NMR studies [1–2]. They are, however, so strong bases compared with the reactants which participate in the practical catalytic reactions that interact even with weak acid sites which are not responsible for the reactions [3]. It is favorable to use weaker bases to identify the actually active acid sites. We have studied N<sub>2</sub> adsorption on H-zeolites at low temperatures using FT-IR spectroscopy, and have experimentally proved that there are two kinds of infrared-active N<sub>2</sub> species adsorbed on Brønsted acid sites (BAS) and Lewis acid sites (LAS)[4–5]. N<sub>2</sub> has lower proton affinity (494.5 kJ/mol) compared with pyridine (924 kJ/mol) and ammonia (853.5 kJ/mol) and is regarded as very weak base [6]. Further, it is smaller than pyridine in molecular diameter to make it an excellent candidate as a probe of acid sites in zeolite cages where the steric hindrance is effective. We report here the IR observation of above-mentioned N<sub>2</sub> species and discuss the advantages of N<sub>2</sub> as a probe of acid sites.

## 2. EXPERIMENTAL

The zeolites used in this study were H-mordenite *JRC-Z-HM20* ( $\text{Si}/\text{Al}=10$ ) and H-Y zeolite *JRC-Z-HY5.6* ( $\text{Si}/\text{Al}=2.8$ ) provided by the Catalysis Society of Japan, and H-ZSM-5 ( $\text{Si}/\text{Al}=48$ ) provided by Professors Tatsuaki Yashima of Tokyo Institute of Technology and Seitaro Namba of the Nishi Tokyo University. Highly siliceous ZSM-5 ( $\text{Si}/\text{Al} \geq 30,000$ ) was synthesized according to a patent [7]. The self-supporting disks (density: 6–10  $\text{mg}/\text{cm}^2$ ) of the zeolites were placed in a quartz cell which in turn was attached to a closed circulation system. The IR cell allows us *in-situ* sample treatment and IR measurement in the temperature range between 95 and 1000 K [8]. The samples were pretreated with oxygen at 773 K followed by the evacuation at the same temperature.

Nitrogen gas (99.9 %) was purified by passing it slowly through a cold trap at liquid-nitrogen temperature to remove residual water and other impurities.  $\text{D}_2\text{O}$  with a purity of 99.9 atom% in D content was used after degassing in vacuum.

IR measurements were performed using a Jasco FT/IR-7000 spectrometer equipped with a MCT detector at a resolution of  $2 \text{ cm}^{-1}$ .

## 3. RESULTS AND DISCUSSION

### 3.1. $\text{N}_2$ adsorption on H-mordenite

Nitrogen adsorption on H-mordenite at 135 K gave two bands at  $2352 \text{ cm}^{-1}$  and  $2335 \text{ cm}^{-1}$  in the  $\nu(\text{NN})$  region as shown in Fig. 1a. These bands showed exact isotope shift when  $^{15}\text{N}_2$  was used as adsorbate (Table 1 as well as Raman data of free  $\text{N}_2$  [9]). Therefore, they were assigned to the  $\nu(\text{NN})$  bands of  $\text{N}_2$  species adsorbed on H-mordenite. They exhibited distinct dependence on the  $\text{N}_2$  pressure and the substrate temperature, suggesting that the  $2352\text{-cm}^{-1}$  species is more stable than  $2335\text{-cm}^{-1}$  species and that they originated

Table 1 IR bands observed for  $\text{N}_2$  adsorption on H-mordenite at 135 K ( $\text{cm}^{-1}$ ).

	$\nu(^{14}\text{N}_2)$	$\nu(^{15}\text{N}_2)$	ratio <sup>a</sup>	site
Gas Phase (Raman) <sup>b</sup>	2330	2252	1.035	
Adsorbed species	2352	2272	1.035	LAS
	2335	2256	1.035	BAS

<sup>a</sup> Theoretical value is 1.035.

<sup>b</sup> ref. 9.

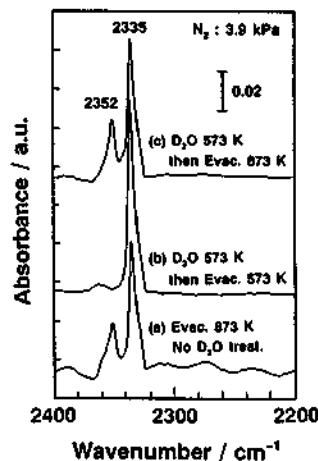


Fig. 1 FT-IR spectra of  $\text{N}_2$  species adsorbed on H-mordenite at 135 K and the effect of  $\text{D}_2\text{O}$  vapor treatment and evacuation temperature.

from the N<sub>2</sub> species on the different sites.

Fig. 1b shows the effect of D<sub>2</sub>O pretreatment on the  $\nu(\text{NN})$  bands. The pretreatment with D<sub>2</sub>O vapor at 573 K for 30 min followed by the evacuation at 573 K for 30 min enhanced the 2335- $\text{cm}^{-1}$  band while suppressed completely the 2352- $\text{cm}^{-1}$  band. As seen from Fig. 1c, the pretreatment of thus treated disk with evacuation at 873 K for 30 min restored the  $\nu(\text{NN})$  bands to the one observed before the D<sub>2</sub>O treatment. It is well known that LAS of H-zeolite are generated on the expense of BAS during the dehydroxylation of zeolites at elevated temperature and BAS are regenerated on the rehydration of LAS [10–13]. Thus we attributed the  $\nu(\text{NN})$  band at 2352  $\text{cm}^{-1}$  to the N<sub>2</sub> species adsorbed on LAS.

The  $\nu(\text{OH})$  bands of H-mordenite exhibited significant change with the increase of N<sub>2</sub> pressure as shown in Fig. 2: on increasing N<sub>2</sub> pressure, the intensity of the  $\nu(\text{OH})$  band at 3616  $\text{cm}^{-1}$  which originates from the bridging OH groups decreased and a new broad band, which is characteristic to the hydrogen-bonded OH groups [14], grew at 3510  $\text{cm}^{-1}$ . This fact suggests that hydrogen bonding between the bridging OH groups and the adsorbed N<sub>2</sub> species were formed. However, the  $\nu(\text{OH})$  band at 3752  $\text{cm}^{-1}$ , which originates from the terminal silanol groups, was virtually independent of N<sub>2</sub> adsorption, consistent with the low acidity of the silanol groups.

The perturbation of the  $\nu(\text{OH})$  bands was observed in regardless of the appearance of the 2352- $\text{cm}^{-1}$  band, indicating that the perturbation is caused by the 2335- $\text{cm}^{-1}$  species. Spectral features between 3300 and 3700  $\text{cm}^{-1}$  in Fig. 2 were deconvoluted into three component bands at 3510, 3590 and 3616  $\text{cm}^{-1}$  [4]. Integrated absorbance of these bands are plotted against that of the  $\nu(\text{NN})$  band at 2335  $\text{cm}^{-1}$ . As seen from Fig. 3, the increment of the 2335- $\text{cm}^{-1}$  band linearly coincides with both the decrement of the 3616- $\text{cm}^{-1}$  band and the increment of the 3510- $\text{cm}^{-1}$  band. Therefore, we conclude that the 2335- $\text{cm}^{-1}$  band is due to the N<sub>2</sub> species adsorbed on BAS through hydrogen bonding.

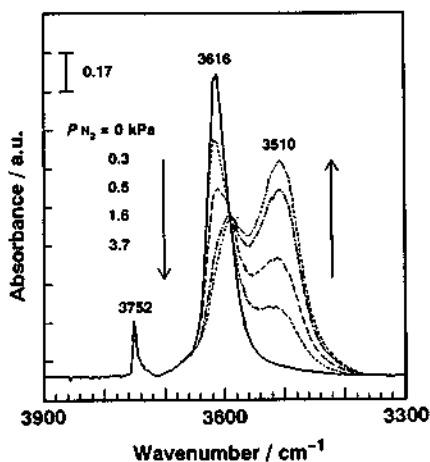


Fig. 2 Spectral change of the  $\nu(\text{OH})$  bands of H-mordenite with the increase of N<sub>2</sub> pressure at 135 K.

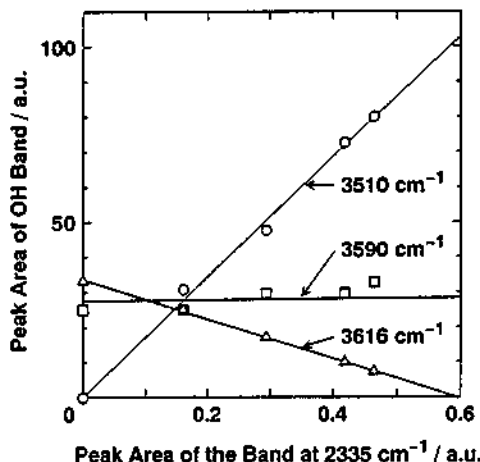


Fig. 3 Correlation of the peak area of the  $\nu(\text{NN})$  band at 2335  $\text{cm}^{-1}$  with those of the  $\nu(\text{OH})$  bands.

### 3.2. N<sub>2</sub> adsorption on H-Y

Similar behavior of the  $\nu(\text{NN})$  and  $\nu(\text{OH})$  bands were observed for the N<sub>2</sub> adsorption on H-Y zeolite at 150 K as shown in Figs. 4 and 5. Two  $\nu(\text{NN})$  bands were observed at 2353 and 2338 cm<sup>-1</sup> for H-Y pretreated at 773 K (Fig. 4a). After the pretreatment of the disk with D<sub>2</sub>O vapor at 573 K followed by the evacuation at 573 K, the former band was not observed while the latter band was observed (Fig. 4b). The pretreatment with evacuation at higher temperature (above 673 K) restored the 2353-cm<sup>-1</sup> band (Fig. 4c).

The  $\nu(\text{OH})$  bands due to bridging OH groups were observed at 3648 and 3555 cm<sup>-1</sup>. Solely the 3648-cm<sup>-1</sup> band suffered the perturbation from the N<sub>2</sub> species while the 3555-cm<sup>-1</sup> band was almost independent (Fig. 5). This fact supports the well-known assignment, that is, the  $\nu(\text{OH})$  band at 3648 cm<sup>-1</sup> is due to the bridging OH groups located in the supercages of Y-zeolite, and the  $\nu(\text{OH})$  band at 3555 cm<sup>-1</sup> to those in the small cavities to where nitrogen molecule is hard to access [15].

### 3.3. N<sub>2</sub> adsorption on H-ZSM-5

In contrast to the case of H-mordenite and H-Y, the H-ZSM-5 disk pretreated below 773 K gave only the  $\nu(\text{NN})$  band at 2334 cm<sup>-1</sup> when N<sub>2</sub> was dosed at 98 K (Fig. 6a). Thus treated disk was evacuated at 908 K and then gave the additional  $\nu(\text{NN})$  band at 2352 cm<sup>-1</sup> when N<sub>2</sub> was adsorbed at 98 K (Fig. 6b). This result shows that more severe condition of pretreatment is needed to produce significant amount of LAS in H-ZSM-5 than in H-mordenite and H-Y. The  $\nu(\text{OH})$  bands of H-ZSM-5 were more drastically perturbed by the N<sub>2</sub> adsorption than those of H-mordenite and H-Y, as shown in Fig. 7. On increasing the N<sub>2</sub> pressure, the  $\nu(\text{OH})$  band at 3619 cm<sup>-1</sup> which is due to the bridging OH groups decreased and a new broad  $\nu(\text{OH})$  band grew at 3499 cm<sup>-1</sup>. The 3619-cm<sup>-1</sup> band diminished almost completely at the N<sub>2</sub> pressure of 0.13 kPa where the  $\nu(\text{NN})$  band at 2335 cm<sup>-1</sup> was almost saturated.

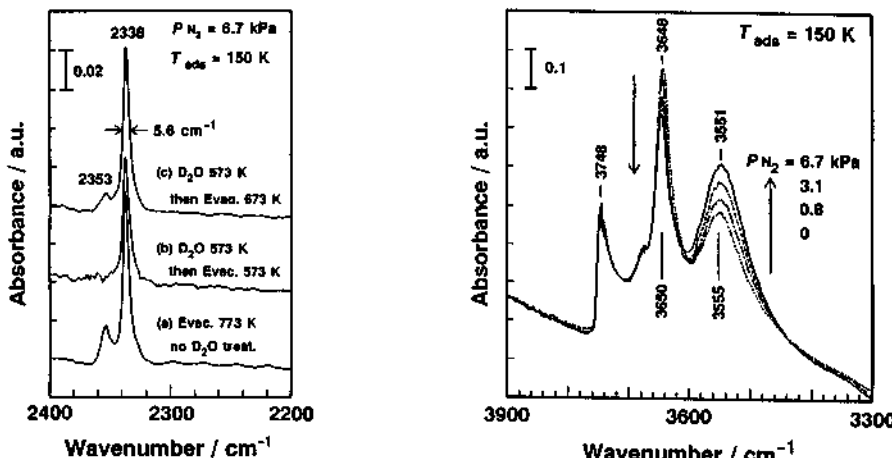


Fig. 4 FT-IR spectra of N<sub>2</sub> species adsorbed on H-Y at 150 K and the effect of D<sub>2</sub>O vapor treatment and evacuation temperature.

Fig. 5 Spectral change of the  $\nu(\text{OH})$  bands of H-Y with the increase of N<sub>2</sub> Pressure at 150 K.

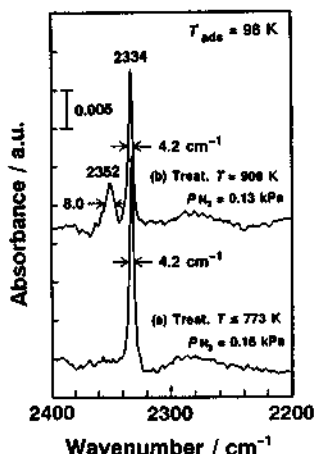


Fig. 6 Effect of the pretreatment temperature on the  $\nu(\text{NN})$  bands observed for N<sub>2</sub> adsorption on H-ZSM-5 at 98 K.

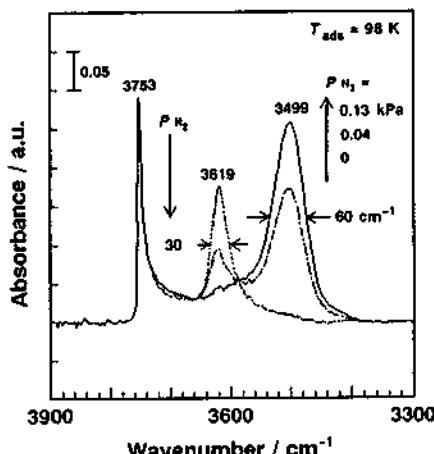


Fig. 7 Spectral change of the  $\nu(\text{OH})$  bands of H-ZSM-5 with the increase of N<sub>2</sub> pressure at 98 K.

### 3.4. N<sub>2</sub> adsorption on highly siliceous ZSM-5

N<sub>2</sub> adsorption on highly siliceous ZSM-5 that has no acidity [7] was examined. As seen from Fig. 8, no absorption band was observed in the  $\nu(\text{NN})$  region at 108 K. This result confirms that the  $\nu(\text{NN})$  band is not observed if distinguished adsorption site, such as acid site, is not available for N<sub>2</sub> molecule.

### 3.5. Perturbation degrees of the ν(OH) band of acidic OH groups

The frequency shifts of the  $\nu(\text{OH})$  bands upon N<sub>2</sub> adsorption are summarized in Table 2. The degree of the shift is usually regarded as a measure of the acid strength of the OH groups [16]. The table shows that the acid strength of the bridging OH groups in the zeolites is in the order of H-ZSM-5 > H-mordenite > H-Y.

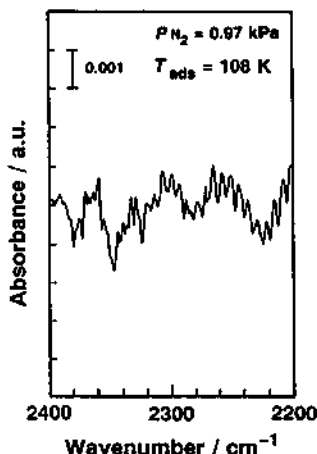


Fig. 8 FT-IR spectrum in the  $\nu(\text{NN})$  region observed for the N<sub>2</sub> adsorption on highly siliceous ZSM-5 at 108 K.

Table 2 Frequency shifts of the  $\nu(\text{OH})$  bands of the bridging OH groups upon N<sub>2</sub> adsorption at low temperatures (cm<sup>-1</sup>).

Zeolites	Free OH	Perturbated OH	$\Delta\nu$
H-Y	3648	3551	97
H-MOR	3616	3510	106
H-ZSM-5	3619	3499	120

### 3.6. Advantages of N<sub>2</sub> as a probe of acid sites

We have revealed that N<sub>2</sub> molecule gives characteristic IR bands when it specifically interacts with BAS or LAS of zeolites at low temperature regardless of zeolite structures. This fact implies that the adsorbed N<sub>2</sub> species serve as a versatile probe of acid sites. Seen as a probe of acid sites, N<sub>2</sub> has several advantages compared with the conventionally used probes such as pyridine and ammonia as follows:

- I. N<sub>2</sub> can be regarded as very weak base so that N<sub>2</sub> interacts and thus probes only the strong acid sites.
- II. N<sub>2</sub> is smaller than pyridine in molecular diameter so that N<sub>2</sub> has better access to narrower space. N<sub>2</sub> will serve in discriminating the steric or size effect.
- III. There is no interference from the gas-phase absorption band because the  $\nu(\text{NN})$  band is forbidden to free N<sub>2</sub> molecule.
- IV. Rather weak interaction of N<sub>2</sub> with zeolites enables us the removal of the adsorbed N<sub>2</sub> by simply evacuating at low temperature. This means that the contamination of sample and apparatus can be made minimal.
- V. N<sub>2</sub> is chemically much inert compared with pyridine or ammonia and the catalytic function of zeolites are least affected in the course of their characterization.

### Acknowledgements

The authors thank Professors T. Yashima and S. Namba for providing H-ZSM-5 sample. This work was partly supported by the Grant-in-Aid for Scientific Research (Nos. 02740414 and 0370247) from the Ministry of Education, Science and Culture, Japan.

### References

- [1] J. A. Rabo, G. J. Gajda, *Catal. Rev.-Sci. Eng.*, 1989-90, 31, 355, and references therein.
- [2] H. G. Karge, *Stud. Surf. Sci. Catal.*, 1991, 65, 133, and references therein.
- [3] H. Knözinger, *Adv. Catal.*, 1976, 25, 184.
- [4] F. Wakabayashi, J. Kondo, A. Wada, K. Domen, C. Hirose, *J. Phys. Chem.*, 1993, 97, 10761.
- [5] F. Wakabayashi, J. Kondo, K. Domen, C. Hirose, *Catal. Lett.*, 1993, 21, 257.
- [6] S. G. Lias, J. F. Liebman, R. D. Levin, *J. Phys. Chem. Ref. Data*, 1984, 13, 695.
- [7] Du Pont, Japan Patent 59-164617, 1984.
- [8] M. Furuki, J. Kondo, Y. Goto, F. Wakabayashi, J. Kondo, A. Wada, K. Domen, C. Hirose, *J. Electron Spectrosc. Relat. Phenom.*, in press.
- [9] J. Bendtsen, *J. Raman Spectrosc.*, 1974, 2, 133.
- [10] J. B. Uytterhoeven, L. G. Christner, W. K. Hall, *J. Phys. Chem.*, 1965, 69, 2117.
- [11] T. R. Hughes, H. M. White, *J. Phys. Chem.*, 1967, 71, 2192.
- [12] F. R. Canning, *J. Phys. Chem.*, 1968, 72, 4691.
- [13] M. Lefrancois, G. Malbois, *J. Catal.*, 1971, 20, 350.
- [14] G. C. Pimentel, A. L. McClellan, "The Hydrogen Bond", W. H. Freeman and Company, San Francisco, 1960.
- [15] P. A. Jacobs, J. B. Uytterhoeven, *J. Chem. Soc. Faraday Trans. 1*, 1973, 69, 359.
- [16] J. C. Védrine, *Stud. Surf. Sci. Catal.*, 1991, 69, 25.

## 2.8 Studies of Adsorption of Benzene on the Acid and Base Sites of KH $\beta$ Zeolite by IR *in Situ*

Jian-ping Shen<sup>a</sup> Jun Ma<sup>a</sup> Tie Sun<sup>a</sup> Zheng Xu<sup>a</sup>

Da-zhen Jiang<sup>a</sup> and En-ze Min<sup>b</sup>

<sup>a</sup>Department of Chemistry, Jilin University, Changchun, 130023, China

<sup>b</sup>Research Institute of Petroleum Processing, Beijing, 100083, China

### Abstract

The IR studies *in situ* of adsorbed benzene on several KH  $\beta$  zeolites, where the extent of potassium exchange varied from 0 to 88.32 were investigated under different conditions. The bands of adsorbed benzene on KH  $\beta$  zeolites in the range 2050-1750cm<sup>-1</sup> were assigned. The KH  $\beta$  zeolite shows basicity only when the % (K/Al) of KH  $\beta$  is up to 88.32, its basicity is stronger and its acidity is weaker. The order of stability of the various adsorbed benzene species on the samples is as follows: O<sup>-</sup>benzene > H<sup>+</sup>benzene > K<sup>+</sup>benzene > benzene.

Key words: KH  $\beta$ , IR *in situ*, benzene adsorption, acid-base site.

### 1. INTRODUCTION

Beta has been demonstrated to be useful as an acid-catalyzed reaction in several hydroisomerization and hydrocracking and as a sorbent in the separation of aromatics since it was first synthesized by Mobil in 1967. Its structure has been published and shows the existence of channels with a three-dimensional 12-membered ring. However, the acid-base properties of beta and its catalytic conversions have been received little attention. In our previous work we reported<sup>[1]</sup> the effects of exchanged conditions on the exchange degree of H  $\beta$  zeolite and the isomerization reactions of  $\alpha$  ( $\beta$ )-methylnaphthalene over a series of KH  $\beta$  zeolite. The IR spectra of adsorbed benzene on some zeolites are already known. The understanding of the adsorption mode of hydrocarbons is of interest since it may explain the behaviour and reactivity of the molecules in the pores. In this paper adsorption of benzene on the acid and base sites of KH  $\beta$  zeolites was studied by IR *in situ* on the basis of previous work.

## 2.EXPERIMENTAL

The starting material is a beta zeolite of which the composition for 64 T atoms per unit cell is  $H_{0.50}Na_{0.01}Al_{2.51}Si_{60.48}O_{128}$ . The preparation of different exchange degrees of KH $\beta$  was conducted as in ref.[1], the chemical composition of four samples is given in Table 1.

Table 1. The chemical composition of the samples

Sample	Chemical composition	%(K/Al)*
H $\beta$	$H_{0.50}Na_{0.01}Al_{2.51}Si_{60.48}O_{128}$	0
KH $\beta$ -1	$H_{1.48}K_{1.48}Na_{0.01}Al_{2.48}Si_{60.48}O_{128}$	53.40
KH $\beta$ -2	$H_{1.08}K_{2.48}Al_{2.48}Si_{60.48}O_{128}$	69.60
KH $\beta$ -3	$H_{0.41}K_{8.10}Al_{2.61}Si_{60.48}O_{128}$	88.32

\*:molar ratio

The IR studies *in situ* were carried out on self-supported wafers. The wafers placed in an IR cell were evacuated at 673K and 0.2Pa for 40 minutes, then cooled and admitted benzene vapour at room temperature. IR spectra were recorded with Nicolet FTIR-5DX at different time, vacuum and temperature. The spectrum of the adsorbed phase was obtained after subtraction of the zeolite contribution.

## 3.RESULTS

The main observation is that the frequencies( $2050\text{--}1700\text{cm}^{-1}$ ) of overtone and combination tone of C-H out of plane bands are shifted to higher wavenumbers in regard to the ones of liquid benzene.

Figure 1 shows the IR spectra in the  $2050\text{--}1700\text{cm}^{-1}$  region of adsorbed benzene on KH $\beta$ -3 zeolite at different adsorption time. Compared to the pure liquid the C-H out of plane vibrations of benzene on the sample are disturbed by the adsorption time. The bands at  $1756$ ,  $1816$ ,  $1840$  and  $1960\text{cm}^{-1}$  are observed just when adsorption time is one minute. With further increasing time the intensities of  $1816$  and  $1960\text{cm}^{-1}$  decrease rapidly and simultaneously shoulders are observed at wavenumbers  $1840$  and  $1973\text{ cm}^{-1}$ . In comparison with Fig.1(f) the adsorption equilibrium is allowed to reach after one hour; the spectrum of adsorption equilibrium (1h) compared to that of initial adsorption is quite different: the intensities of the bands at  $1960$  and  $1816\text{cm}^{-1}$  decrease; the band at

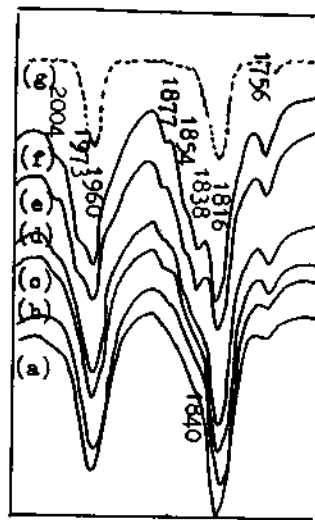


Fig.1 IR spectra of adsorbed benzene on KH $\beta$ -3 zeolite at 300K;(a) 1min; (b) 5min;(c) 15min;(d) 30min;(e) 1h; (f) 12h;(g) liquid.

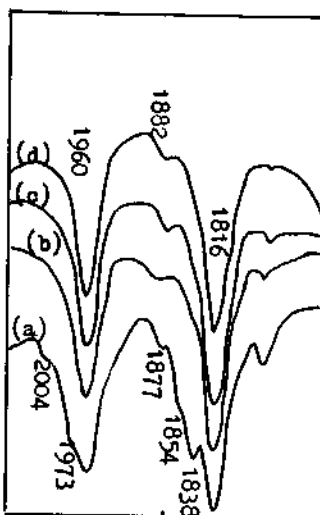


Fig. 2 IR spectra of benzene adsorption equilibrium of the samples at 300K;(a) KH $\beta$ -3;(b) KH $\beta$ -2;(c) KH $\beta$ -1;(d) H $\beta$ .

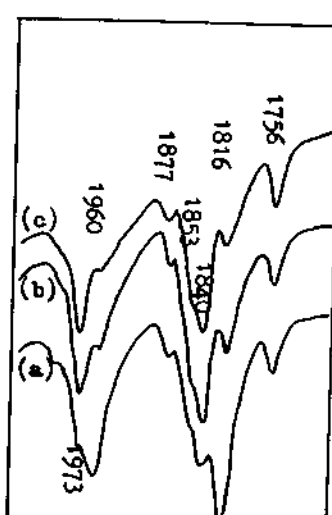


Fig.3 IR spectra of adsorption benzene on KH $\beta$ -3 zeolite at 300K under different vacuum;(a)  $1.0 \times 10^4$ Pa;(b) 13.3Pa; (c) 3.2Pa.

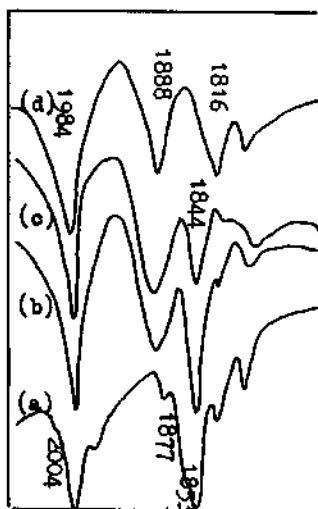


Fig.4 IR spectra of adsorbed benzene on the samples under 3.2Pa and 300K;(a)KH $\beta$ -3;(b) KH $\beta$ -2;(c) KH $\beta$ -1;(d)H $\beta$ .

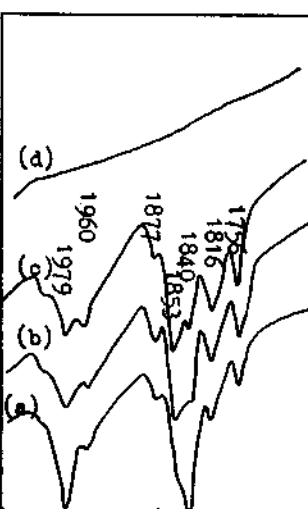


Fig.5 IR spectra of adsorbed benzene on KH $\beta$ -3 zeolite at different temperature;(a)300K (b) 323K;(c) 423K;(d) 483K.



Fig.6 IR spectra of adsorbed benzene on the samples under 223K and 3.2Pa ; (a) KH $\beta$ -3; (b) KH $\beta$ -2;(c)KH $\beta$ -1;(d)H $\beta$

$1840\text{cm}^{-1}$  is shifted to low values ( $1838\text{cm}^{-1}$ ) and become sharper; four new bands at 1854, 1876, 1973 and  $2004\text{cm}^{-1}$  are formed.

The equilibrium of adsorbed benzene on  $\text{KH}\beta$  zeolites is reached after one hour. From Fig.2 it can be seen that all the samples have bands at  $1960$  and  $1816\text{cm}^{-1}$  observed in the IR spectrum of liquid benzene. Similar IR spectra are obtained when the  $\%(\text{K}/\text{Al})$  of  $\text{KH}\beta$  zeolite is less than 88.32 except for a small band shift at  $1838\text{cm}^{-1}$ . With decreasing the  $\%(\text{K}/\text{Al})$  of  $\text{KH}\beta$  zeolite the intensity of the band at  $1877\text{cm}^{-1}$  increases and its wavenumbers are shifted to high values.

The IR spectra of adsorbed benzene on  $\text{KH}\beta$ -3 zeolite under different vacuum are shown in Fig.3. With increasing vacuum the intensities of the bands at  $1960$  and  $1816\text{cm}^{-1}$  decrease rapidly and the peaks of  $1960$ ,  $1877$ ,  $1853$  and  $1840\text{cm}^{-1}$  become sharper. Comparing (a) with (c) the preferential adsorption of benzene from  $\text{KH}\beta$  zeolite is seen. The IR spectra of the different  $\%(\text{K}/\text{Al})$  samples under the same vacuum are seen in Fig.4. The intensity of the band at  $1877\text{cm}^{-1}$  increases with decreasing potassium content of  $\text{KH}\beta$  zeolite and it is shifted to high frequencies. The band at  $1853\text{cm}^{-1}$ , however, disappears under a  $\%(\text{K}/\text{Al})$  of 88.32. The band at  $1840\text{cm}^{-1}$ , not observed in the spectrum of adsorbed benzene on  $\text{H}\beta$  zeolite, grows with the amount of potassium and shifts to low wavenumbers. Simultaneously, the band at  $1984\text{cm}^{-1}$  also shifts to low values.

Figure 5 shows for  $\text{KH}\beta$ -3 the progressive changes in spectra as the desorption temperature increases. The intensities of all bands except  $1853\text{cm}^{-1}$  decrease with increasing temperature. The adsorbed benzene is completely desorbed at  $453\text{K}$  from the sample. Under  $323\text{K}$  and  $3.20\text{Pa}$  the behaviour of adsorbed benzene is reported in Fig.6. The bands at  $2004$  and  $1853\text{cm}^{-1}$  are only observed for  $\text{KH}\beta$ -3 zeolite. The band at  $1840\text{cm}^{-1}$  totally disappears on  $\text{H}\beta$ . On the other hand, the band at  $1877\text{cm}^{-1}$  increases with decreasing potassium content. The maximum intensity of this band is observed on  $\text{H}\beta$  zeolite.

#### 4. DISCUSSION

In liquid benzene bands have been assigned to stretching C-H and combination of bending C-C in the range  $3050$ - $3000\text{cm}^{-1}$ , to overtone and combination tone of C-H out-of-plane deformation vibration at  $1960$  and  $1816\text{cm}^{-1}$  and to ring deformation at  $1479\text{cm}^{-1}$ , the  $1960$  and  $1816\text{cm}^{-1}$  bands are assigned to the  $V_5+V_{17}$  and  $V_{10}+V_{17}$ , respectively. Upon adsorption of benzene on  $\text{KH}\beta$  zeolite, a shift in frequencies and a splitting this pair of bands occur. These trends in the IR spectra parallel those found by previous workers who studied the adsorption of benzene on  $\text{Na,CaY}$  and  $\text{Na,Ca}\beta$ <sup>(2-8)</sup> and

lend further credence to an adsorption mechanism which perturbs the  $\pi$ -electron bonds of the aromatic ring while simultaneously locking the ring into a fixed configuration which does not favour out-of-plane vibrations. The bands resulting from the split of the starting pair are assigned to as the low-frequency (LF) and high-frequency (HF) pair. The LF pair of bands can be referred to benzene interaction with cations through the  $\pi$  electron cloud and the HF pair of bands would result from interaction with the framework oxygen. It was also indicated that the extent of each type of interaction depends on the acidity of cations and on the oxygen basicity.

Figure 1~6 show some similarities in the behaviour of adsorbed benzene on KH  $\beta$  zeolites. The LF and HF consist of the bands at 1840~1973 and 1853~2004  $\text{cm}^{-1}$ , respectively. These trends are similarly observed in the adsorption of benzene on alkali Na  $\beta$  and Cs  $\beta$  zeolites [3]. The frequencies of these bands are affected by the microenvironment, e.g. cations and framework oxygen. The intensity of the LF at 1840  $\text{cm}^{-1}$  is positively changed with the content of potassium and this band totally disappears on H  $\beta$  zeolite; thus it can be assigned to interaction with potassium cations through the  $\pi$  cloud. The intensity of the other LF at 1980  $\text{cm}^{-1}$ , which reflects the effects of alkali metal on benzene, does not change obviously when the % (K/Al) of KH  $\beta$  zeolite is less than 88.32. Its intensity, however, decreases rapidly over the sample of % (K/Al) of 88.32. This may result from benzene interaction with K $^+$  and H $^+$  cations. It is proposed that the HF pair of bands (2004 and 1853  $\text{cm}^{-1}$ ) results from interaction between the framework oxygen of the 12-membered ring and benzene on KH  $\beta$ -3 zeolite, this pair of bands, on the other hand, can not be observed when the ratio of % (K/Al) is less than 88.32. The basicity of conjugate acid-base pairs in zeolites suggests that it would be associated with framework oxygen<sup>[4]</sup>. In other words, the KH  $\beta$  shows certain basicity to some extent just when the % (K/Al) reaches 88.32.

A further point of interest is that in our experiments a new band at 1877  $\text{cm}^{-1}$ , which is higher than 1840  $\text{cm}^{-1}$ , is observed in a series of KH  $\beta$  zeolites, and with increasing proton content its intensity increases and its frequency is shifted to high values. We suggest that the band at 1877  $\text{cm}^{-1}$  should be referred to benzene interaction with proton through the  $\pi$  electron cloud. The reasons are as follows: First, in comparison with K $^+$  the electrostatic field of H $^+$  is very strong and consequently the interaction of H $^+$  with benzene is stronger than that of K $^+$ . Second, with increasing proton content of zeolite the strength of acid sites on zeolite surface increases, and the interaction of H $^+$  with benzene becomes strong. The assignment of these bands is given in Table 2.

Table 3 shows the relative ratio of integrated absorbance of the

that the basicity of  $\text{KH}\beta-3$  is stronger and its acidity is weaker. This result is in good agreement with that of  $\text{NH}_3(\text{CO}_2)_x$ -TPD<sup>[4]</sup>. The ratio of  $\text{H}^+/\text{K}^+$  increases with increasing desorption.

Table 2. The assignment of bands at 2050-1700cm<sup>-1</sup>

Liquid	Assignment	Species of interaction	Wavenumber(cm <sup>-1</sup> )	Assignment
1816 γ(C-H)	$\text{V}_{16}+\text{V}_{17}$	$\text{K}^+/\text{b}$	1840	$\text{V}_{16}+\text{V}_{17}$
		$\text{O}^-/\text{b}$	1853	$\text{V}_{16}+\text{V}_{17}$
		$\text{H}^+/\text{b}$	1877	$\text{V}_{16}+\text{V}_{17}$
1960	$\text{V}_8+\text{V}_{17}$	$(\text{K}^+,\text{H}^+)/\text{b}$	1980	$\text{V}_8+\text{V}_{17}$
		$\text{O}^-/\text{b}$	2004	$\text{V}_8+\text{V}_{17}$

b: benzene

Table 3. The relative ratio of integrated absorbance of four samples

$\text{KH}\beta-3$			$\text{KH}\beta-2$			$\text{KH}\beta-1$			$\text{H}\beta$
$\text{O}^-/\text{b}/\text{H}^+/\text{b}$	$\text{H}^+/\text{b}/\text{K}^+/\text{b}$	$\text{b}/\text{K}^+/\text{b}$	$\text{O}^-/\text{b}/\text{H}^+/\text{b}$	$\text{H}^+/\text{b}/\text{K}^+/\text{b}$	$\text{b}/\text{K}^+/\text{b}$	$\text{O}^-/\text{b}/\text{H}^+/\text{b}$	$\text{H}^+/\text{b}/\text{K}^+/\text{b}$	$\text{b}/\text{K}^+/\text{b}$	$\text{O}^-/\text{b}/\text{H}^+/\text{b}$
—	0.80	1.76	—	1.08	0.73	0	2.47	0.10	0 <sup>*</sup>
0.72	1.22	0.17	—	1.41	0.06	0	4.16	0.04	0 <sup>**</sup>
3.59	1.57	0.10	—	8.22	0	0	12.81	0	0 <sup>***</sup>

\*:300K,1.0×10<sup>6</sup>Pa    \*\*:300K,13.8Pa    \*\*\*:323K,3.20Pa

temperature, vacuum and also with  $\text{H}^+$  content. It is proposed that the species of benzene interaction with potassium is preferentially desorbed, which may result from the fact that the electrostatic field intensity of  $\text{H}^+$  is stronger than that of  $\text{K}^+$ . An increase of the  $\text{b}/\text{K}^+/\text{b}$  is observed under higher vacuum and lower temperature. This shows that the liquid benzene is desorbed first from the zeolite. The order of stability of the adsorbed benzene species is as follows:

$\text{O}^-/\text{benzene} > \text{H}^+/\text{benzene} > \text{K}^+/\text{benzene} > \text{benzene}$ .

#### REFERENCES

- 1.Jian-ping Shen,Tie Sun,Jun Ma,Da-zhen and En-ze Min., 34th IUPAC Congress,Session 5,Beijing(China),1993
- 2.Coughlan,B.,Carroll,W.M,O'Malley,P.and Nunan, J. , J.Chem. Soc., Faraday Trans.,1981,77,303
- 3.Dzwigaj,S.,Mallmann,A.D. and Barthomeuf,D., J.Chem. Soc. Faraday Trans.,1990,86(2),481
- 4.Wilson,E.B, Phys.Rev.1934,45,706

## 2.9 Interaction of NH<sub>3</sub> with O<sub>2</sub> at the Surface of MgO

G. Martra, E. Borello, E. Giannello and S. Coluccia

Dipartimento di Chimica Inorganica, Chimica Fisica e Chimica dei Materiali dell'Università di Torino, via P. Giuria 7, 10125 Torino Italy

### Abstract

The adsorption of NH<sub>3</sub> and its interaction with O<sub>2</sub> at the surface of highly dispersed MgO has been studied by Infrared Spectroscopy. NH<sub>3</sub> is predominantly adsorbed in molecular forms, but a small fraction undergoes heterolytic dissociation. The NH<sub>2</sub><sup>-</sup> fragments react with oxygen to produce a number of oxidized species, the relative population depending strongly on the coverage and the treatment temperature. N<sub>2</sub><sup>-</sup>, N<sub>3</sub><sup>-</sup>, NO<sup>-</sup>, NO<sub>2</sub><sup>-</sup> and NO<sub>3</sub><sup>-</sup> species are identified.

### 1. INTRODUCTION

NH<sub>3</sub> has been widely used as a probe molecule for oxide surfaces [1-3]. Acting as a base through the electron lone pair on the nitrogen atom it is able to reveal acid sites such as metal cations and hydroxyls, whereas acting as an acid through the hydrogen atoms it reveals basic sites such as oxygen anions. As the vibrational modes of adsorbed NH<sub>3</sub> molecules are very sensitive to the strength of the interactions, ammonia is able to evidence surface sites heterogeneity, which is typical of highly dispersed systems.

In most cases the same NH<sub>3</sub> molecule interacts with an anion-cation couple and this produces a polarization of the N-H bond. The sites with the strongest acid-base character may break this bond to produce NH<sub>2</sub><sup>-</sup> and H<sup>+</sup> fragments. All such phenomena occur on the surface of MgO, where NH<sub>3</sub> is mostly adsorbed in molecular forms and a small fraction undergoes heterolytical dissociation [2-3].

The reactivity of the anionic NH<sub>2</sub><sup>-</sup> fragments is of interest to enrich the information on the very peculiar surface activity of MgO [4-6], and, possibly, to contribute to the general understanding of the role of NH<sub>3</sub> in a number of reactions which might be also important in environmental control.

Following the analysis of the reaction of NH<sub>3</sub> with N<sub>2</sub>O [7], the results of the interaction of ammonia with molecular oxygen are described in this report.

### 2. EXPERIMENTAL METHODS

Mg(OH)<sub>2</sub> in the form of self supporting pellets suitable for IR spectra was carefully decomposed by thermal treatment at 500 K and then outgassed at gradually increasing temperature up to 1173 K.

No infrared bands of residual OH groups on the surface of the MgO sample were observable after such pretreatment. Specific surface area was 200 m<sup>2</sup>g<sup>-1</sup>.

All spectra were obtained at beam temperature by a Perkin-Elmer 580 B spectrometer. High purity gases (Matheson) were allowed onto the catalyst, and ammonia underwent further purification by several freezing - evacuation - distillation cycles.

The infrared spectra are shown in Absorbance scale after subtracting the background of the clean MgO pellet. When observable, the contribution from gas phase NH<sub>3</sub> was subtracted as well.

### 3. RESULTS AND DISCUSSION

#### 3.1. Molecular and Dissociative Adsorption of Ammonia.

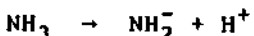
The interaction of ammonia with hydroxylated and fully dehydroxylated MgO surfaces was studied by IR spectroscopy showing that molecular NH<sub>3</sub> species are mostly produced [2-3]. A number of different adsorbed structures can be recognized, summarized in Table 1 together with the relevant infrared absorptions:

NH <sub>3</sub> Molecule		NH <sub>3</sub> Adsorbed Species					
I.R. mode	Liq cm <sup>-1</sup>	Sol. cm <sup>-1</sup>					
v <sub>2</sub>	1050	1060	1024	1050 1080	1080 1065	1113 1042	
v <sub>4</sub>	1648	1646	1620	1630 1600	1600	1625	
v <sub>1</sub>	3220	3223	3200	3360 - 3270	3370 - 3300	3390 - 3300	
v <sub>4</sub>	3385	3378					

Table 1

The relative populations of the various molecular adsorbates depend on the hydroxylation degree of the MgO surface.

A small fraction of NH<sub>3</sub> undergoes heterolytic dissociation, monitored by weak bands at 1600-1555 cm<sup>-1</sup> due to the bending modes of ammide species [2-3]:



NH<sub>2</sub><sup>-</sup> fragments are stabilized by Mg<sub>LC</sub><sup>2+</sup> cations, whereas the protons interact with the O<sub>LC</sub><sup>2-</sup> anions to give surface hydroxyl groups

which produce bands at high frequency ( $3400 \sim 3800 \text{ cm}^{-1}$ ).

All above species are observed at various steps of the experiments described here and will not be discussed further.

### 3.2. Ammonia - Oxygen Interaction at Room Temperature.

In contrast with molecular species, the latter NH<sub>2</sub><sup>-</sup> entities are not desorbed at room temperature.

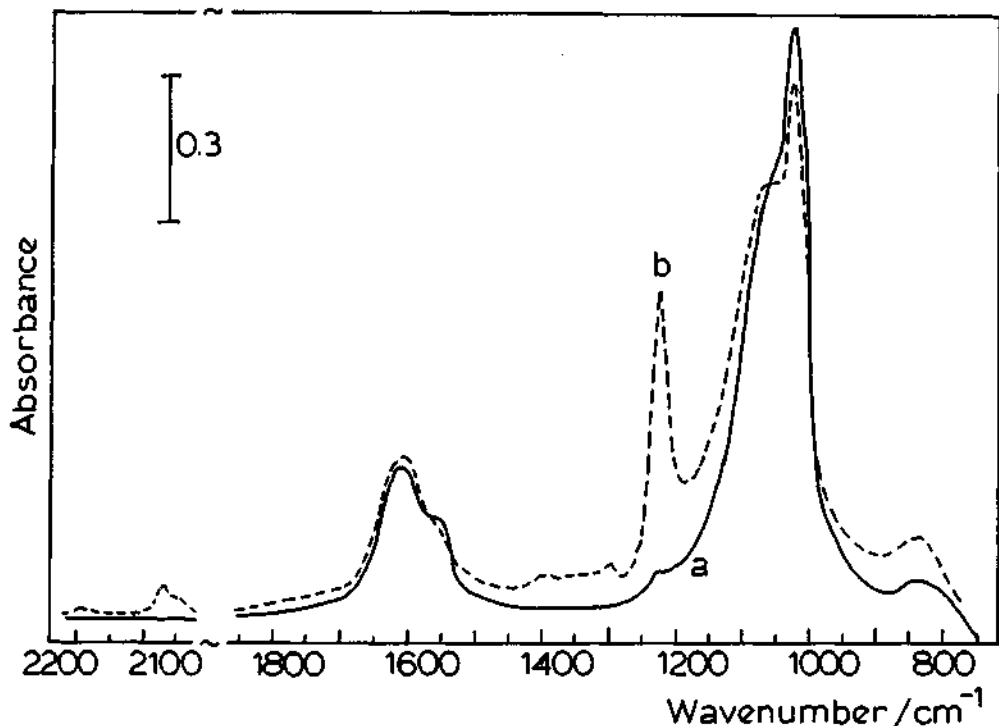


Figure 1. Ammonia-oxygen interaction at R.T. on MgO preoutgassed at 1173 K. Infrared spectra in the presence of 110 Torr NH<sub>3</sub>/O<sub>2</sub> (10:1): a) immediately after admission, b) after 16 hours contact at R.T..

They diminish by subsequent admission of O<sub>2</sub>, but very weak new bands show up under these conditions. All phenomena are enhanced in the presence of excess NH<sub>3</sub>/O<sub>2</sub> mixture (110 Torr) and upon prolonged contact, as illustrated in Fig. 1. Immediately after the admission, the spectrum is identical to that observed when NH<sub>3</sub> alone is sent onto the pellet [2-3]. The strong bands at 900-1100 cm<sup>-1</sup> and 1620 cm<sup>-1</sup> in spectrum a are due to molecular ammonia while the weak component at  $\approx 1550 \text{ cm}^{-1}$  is due to NH<sub>2</sub><sup>-</sup> species.

After 16 hours contact at R.T. the amide band disappears and a new strong and sharp peak develops at 1228 cm<sup>-1</sup>. Neither in this experiment nor in others (some are shown in the following), this band appears to be related to any other component and, consequently, it should be associated with a diatomic entity. This band shows isotopic shift with both <sup>15</sup>NH<sub>3</sub> and <sup>18</sup>O<sub>2</sub> and may be ascribed

to nitric oxide species.

However, the NO molecule absorbs at much higher frequency (1876 cm<sup>-1</sup> in the gas phase) [8] and interaction with surface sites might move it downward by some 200 cm<sup>-1</sup>. A shift of  $\approx$  650 cm<sup>-1</sup> down to 1228 cm<sup>-1</sup> as observed in Fig. 1 can only be justified by the presence of an extra-electron to give NO<sup>-</sup> species which do indeed absorb in such region [8].

Very weak bands showing up with time at 1250 - 1500 cm<sup>-1</sup> (Fig. 1,b) are due to nitrite and nitrate groups produced in small amounts under these mild conditions (300 K). Other components appear also after long time of contact at high frequency (2000 - 2100 cm<sup>-1</sup>). Though weak, these bands monitor peculiar aspect of the oxidation reactions of NH<sub>3</sub> and will be considered in more details in the next sections.

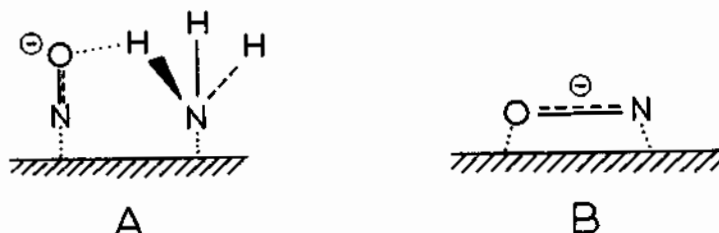
Comparison of spectra a and b shows that the intensity of NH<sub>2</sub><sup>-</sup> band (1555 cm<sup>-1</sup>) decreases in presence of oxygen, indicating that these surface species undergo oxidation. Apparently, also the bands due to adsorbed NH<sub>3</sub> slightly decrease, suggesting that molecular species progressively dissociate, producing intermediates (NH<sub>2</sub> fragments) which are then subjected to further oxidation.

New hydroxyl groups are also produced as the NH<sub>3</sub>/O<sub>2</sub> reactions proceed, causing a significant increase of the intensity of the OH stretching bands at 3500 - 3700 cm<sup>-1</sup>. These effects do not add relevant information and will not be discussed further in this work.

### 3.3. Structure of Adsorbed NO<sup>-</sup> Species and Solvation Effects.

Fig. 2 shows that dramatic changes occur in the spectra upon pumping off the excess NH<sub>3</sub>/O<sub>2</sub> mixture at room temperature: a) molecularly adsorbed NH<sub>3</sub> species are almost completely eliminated; b) the original NO<sup>-</sup> band at 1228 cm<sup>-1</sup> fades away; c) the weak bands due to nitrites and nitrates at 1250 - 1500 cm<sup>-1</sup> and those at 2000 - 2100 cm<sup>-1</sup> are somewhat shifted. A detailed description of these effects and of the spectrum of the species present after outgassing (Fig. 2,b) will be given elsewhere. It is relevant to stress here that when NH<sub>3</sub> alone is admitted (with no oxygen!) into the cell spectrum a and in particular the band of NO<sup>-</sup> species are fully recovered. This suggests that NO<sup>-</sup> species are not eliminated upon outgassing and stay on the surface though with a different structure and, consequently, different vibrational behaviour. Re-adsorption of NH<sub>3</sub> restores the original structure.

The following schemes may account for these effects:



In structure A, the end-on position of NO<sup>-</sup> might be stabilized by coadsorbed NH<sub>3</sub> molecules. When these are eliminated, the NO<sup>-</sup> species might lie flat on the surface, as reported for O<sub>2</sub><sup>-</sup> species

described by Garrone et al. [9]. Notice that the more symmetric structure of scheme B might justify a lower extinction coefficient and, consequently, the intensity variations observed in Fig. 2. Readmission of ammonia would restore structure A, and the cycle may be repeated indefinitely.

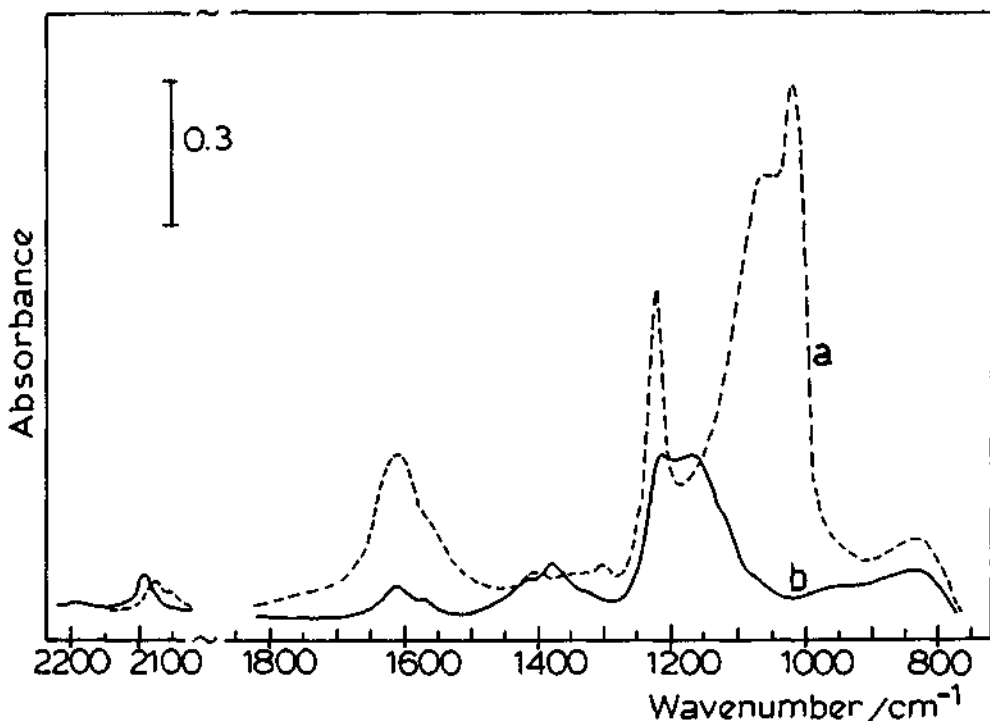


Fig. 2. Ammonia-oxygen interaction at R.T. on MgO. Solvation effects. Infrared spectra: a) in the presence of 110 Torr NH<sub>3</sub>/O<sub>2</sub> (10:1) after 16 hours at 300 K (the same as b in Fig. 1); b) after pumping off the excess NH<sub>3</sub>/O<sub>2</sub> for 60 min. at 300 K. Admission of NH<sub>3</sub> (100 Torr) after b restores spectrum a.

### 3.4. Ammonia - Oxygen Interaction at High Temperature. N<sub>2</sub><sup>-</sup> and N<sub>3</sub><sup>-</sup> Species.

Complex modifications of the IR spectra occur upon heating the catalyst in the presence of the NH<sub>3</sub>/O<sub>2</sub> mixture at gradually increasing temperature.

Fig. 3 shows that: a) all bands due to the molecular NH<sub>3</sub> species are progressively depleted; b) the band of NO<sup>-</sup> (1228 cm<sup>-1</sup>) increases first (curves a-b) and then decreases (curves c-e); c) the bands due to nitrites, nitrates and other NO<sub>x</sub> species (1250 - 1600 cm<sup>-1</sup>) increase continuously with changes in shape at the various steps (curves a-e); d) the weak bands at 2000 - 2100 cm<sup>-1</sup> disappear and are replaced by much more intense bands at 2197 cm<sup>-1</sup> and 2173 cm<sup>-1</sup>, which sharply disappear at 623 K.

Details are outside the scope of this presentation, and will be given elsewhere together with other spectroscopic evidences and isotopic effects [10]. Only the last mentioned bands at high frequency will be commented on.

As no isotopic effect is observed with  $\text{ND}_3$  and  $^{18}\text{O}_2$ , whereas shifts occur with  $^{15}\text{NH}_3$ , it may be concluded that the species absorbing above  $2000 \text{ cm}^{-1}$  contain only nitrogen. On the basis of the data on nitrogen complex of magnesium [11], nitrogen species on K-promoted oxides [12-13] and on  $\text{MgO}$  [7], it may be proposed that

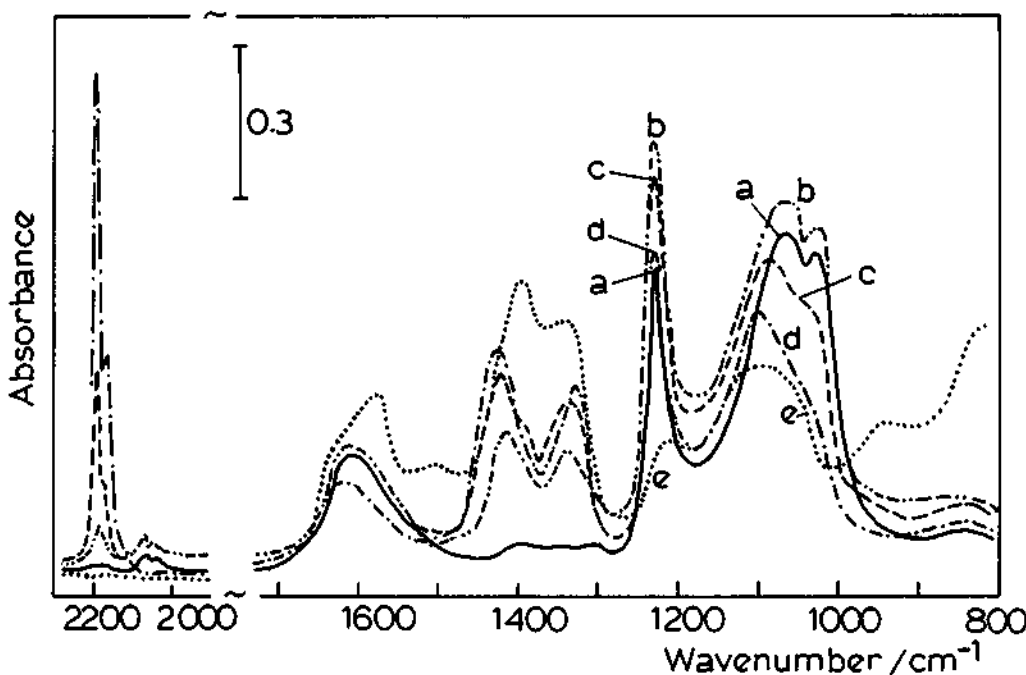


Fig. 3. Ammonia-oxygen interaction on  $\text{MgO}$  at progressively increasing temperature. Infrared spectra: a) in the presence of 110 Torr  $\text{NH}_3/\text{O}_2$  (10:1) after 16 hours at 300 K, and then after heating at b) 423 K for 60 min.; c) 523 K for 15 min.; d) 593 K for 15 min.; e) at 623 K for 15 min.

the weak bands at  $2000 - 2100 \text{ cm}^{-1}$  are due to azide species, while those, more intense, at  $2197 \text{ cm}^{-1}$  and  $2173 \text{ cm}^{-1}$  are due to dinitrogen species. It was reported that in molecular complexes trinitrogen species ( $\text{N}_3^-$ ) absorb at lower frequency than dinitrogen species ( $\text{N}_2^-$ ). Significantly, azide species, relatively unstable, decompose at lower temperature than the dinitrogen ones.

**AKNOWLEDGEMENTS**

Financial support by CNR and ASP is gratefully acknowledged.

**4. REFERENCES**

- 1) T. J. Dines, C. H. Rochester and A. M. Ward, *J. Chem. Soc. Faraday Trans.*, **1991**, *87*, 643.
- 2) S. Coluccia, E. Garrone and E. Borello, *J. Chem. Soc. Faraday Trans.* **1**, **1983**, *79*, 607.
- 3) S. Coluccia, S. Lavagnino and L. Marchese, *J. Chem. Soc. Faraday Trans.* **1**, **1987**, *83*, 477.
- 4) H. Tsuji, F. Yagi, H. Hattori and H. Kita, in "New Frontiers in Catalysis, Proceedings of the 10<sup>th</sup> International Congress on Catalysis", L. Gucci, F. Solymosi and P. Tétényi eds., Akadémiai Kiadó, Budapest, 1993, p. 1171.
- 5) S. Coluccia and L. Marchese, in "Acid-Base Catalysis", K. Tanabe, H. Hattori, Y. Yamaguchi and T. Tanabe eds., Kodasha Ltd. Sapporo, 1989, p.207.
- 6) E. Garrone, G. Martra, D. Bartalini, D. Tichit and F. Figueras, in "Acid-Base Catalysis II", H. Hattori ed., Kodasha Ltd., Sapporo, 1994.
- 7) E. Garrone, S. Coluccia and E. Giannello, *Spectrochim. Acta*, **1987**, *43A*, 1567.
- 8) J. Laane and J. R. Ohlsen, *Prog. Inorg. Chem.*, **1980**, *27*, 465.
- 9) E. Giannello, E. Garrone, P. Ugliengo, M. Che and A. J. Tench, *J. Chem. Soc. Faraday Trans.* **1**, **1989**, *85*, 3987.
- 10) S. Coluccia and G. Martra, in preparation.
- 11) K. C. Petil, C. Nasomani and V. R. Paiverneker, *Polyhedron*, **1982**, *1*, 421.
- 12) K. Aika, H. Midorikawa and A. Ozaki, *J. Phys. Chem.*, **1982**, *86*, 9263.
- 13) K. Aika, A. Ohya, A. Ozaki, Y. Iwao and I. Yasumori, *J. Catal.*, **1985**, *92*, 305.

This Page Intentionally Left Blank

## 2.10 Behavior of CO Monomers Adsorbed on MgO Surfaces at Low Temperatures

T. Ito,<sup>a</sup> R.-B. Sim,<sup>b</sup> T. Tashiro,<sup>b</sup> K. Toi,<sup>b</sup> and H. Kobayashi<sup>c</sup>

<sup>a</sup>Department of Environmental Science, School of Social Information Studies, Otsuma Women's University, Karakida, Tama, Tokyo 206, Japan

<sup>b</sup>Department of Chemistry, Faculty of Science, Tokyo Metropolitan University, Minami-Osawa, Hachioji, Tokyo 192-03, Japan

<sup>c</sup>Department of Applied Chemistry, Kyoto Prefectural University, Shimogamo, Kyoto 606, Japan

### Abstract

CO monomers adsorbed on well-degassed MgO surfaces were investigated below room temperature. Linear-type monomers on  $Mg_{LC}^{2+}$  ( $K_0$  species) are stable irrespective of their coordination number. On the other hand a linear-type monomer on  $O_{LC}^{2-}$  ( $CO_2^{2-}$ -species designated  $K_1'$ ) is very unstable and can be observed only when it makes a pair with  $K_0$  in the presence of CO gas phase. A chained-type monomer on  $O_{LC}^{2-}$  ( $CO_2^{2-}$ -species designated  $K_1$ ) is most stable among three types of monomers observed.  $K_1$  is reversibly transformed into  $K_1'$ , with coproduction of  $K_0$ , at lower temperatures in the presence of CO. Adsorbed molecules are movable on the surface at low temperatures and can exchange their O atoms with surface  $O^{2-}$ . All the monomers observable on  $O_{LC}^{2-}$  (namely  $K_1$  and  $K_1'$  species) *cannot* take part in the formation of CO oligomers.

### 1. INTRODUCTION

Adsorption of CO on MgO, a typical base catalyst, has been investigated by many groups using mainly IR spectroscopy [1,2]. This adsorption system has been known to be complex and to produce several kinds of oligomers of CO molecules (e.g., trimer and hexamer). Mechanism for the formation of these oligomers has been gradually becoming clearer [2,3]. CO monomers, the simplest adsorbed species, are also produced on surface  $O_{LC}^{2-}$  and  $Mg_{LC}^{2+}$  ions, respectively. However, behavior and structures of these monomers are not necessarily obvious. In this study we have investigated CO monomers produced on MgO below room temperature using both TPD and IR spectroscopies.

### 2. EXPERIMENTAL METHODS

A JRC-MgO-3 powder sample was pressed into disks and pretreated at 1123 K in vacuum. The same sample disks were repeatedly used in a series of runs. Adsorption of CO was carried out in a closed and static system. FTIR measurements at low temperatures were carried out by introducing a He gas at 266 Pa into a sample cell to get better thermal contact.

### 3. RESULTS AND DISCUSSION

In Table 1 CO monomers observed in this study are summarized. Three kinds of monomers are detected below room temperature and each type is discussed separately.

Table 1 List of CO monomers observed at low temperature

Symbol	Type	Structure	Desorption Temp.	IR Band
$K_0$	Linear CO on $Mg^{2+}$		ca. 240 K <sup>a</sup>	2200 cm <sup>-1</sup> a
$K_1$	Chained CO on $O^{2-}$		ca. 250 K	1315 cm <sup>-1</sup> 1280 cm <sup>-1</sup>
$K_1'$	Linear CO on $O^{2-}$		ca. 200 K (in CO)	1475 cm <sup>-1</sup>

<sup>a</sup>  $K_0$  on  $Mg_{3C}^{2+}$

#### 3.1. Linear-type Monomer on $Mg_{LC}^{2+}$ ( $K_0$ Species)

A linear type monomer on  $Mg_{LC}^{2+}$ , designated  $K_0$  species, has only one absorption band at 2200 cm<sup>-1</sup> (on a 3-coordinated ion,  $Mg_{3C}^{2+}$ ). More unstable  $K_0$  species adsorbed on  $Mg_{4C}^{2+}$  and  $Mg_{5C}^{2+}$  appeared at lower frequency region of 2185-2145 cm<sup>-1</sup>.  $K_0$  species on  $Mg_{3C}^{2+}$  was desorbed around 240 K. However, this species was able to migrate on the surface at temperatures much below 240 K and able to exchange its O atom with a surface  $O^{2-}$  before desorption.

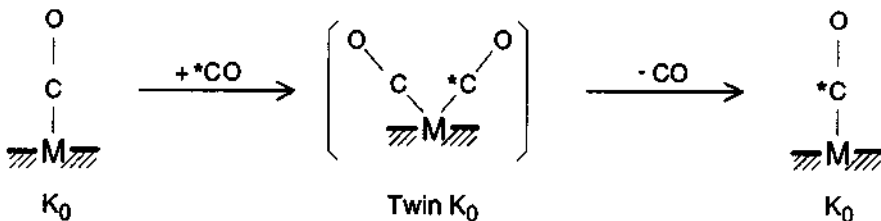


Fig. 1 Mechanism of CO substitution between  $K_0$  species and a CO molecule

One more thing to be stressed is that substitution between CO adsorbed as  $K_0$  and gaseous CO can easily occur at temperatures much below its desorption temperature: for example,  $^{12}CO$  as adsorbed on  $Mg_{3C}^{2+}$  is replaced by corresponding  $^{13}CO$  species upon the introduction of  $^{13}CO$  at 130 K. This substitution is believed to proceed via twin-type  $K_0$  as shown in Fig. 1. The presence of such a twin-type  $K_0$  species is strongly

suggested by the diminution in intensity of  $K_0$  on  $Mg_{3C}^{2+}$  with the increase in CO pressure at low temperature.

### 3.2. Chained-type Monomer on $O_{LC}^{2-}$ ( $K_1$ Species)

CO adsorption below room temperature also gave a pair of absorption bands at 1315 (main) and 1280  $\text{cm}^{-1}$  besides  $K_0$  species.  $^{13}\text{CO}$  gave corresponding bands at 1282 and 1252  $\text{cm}^{-1}$ . This species designated  $K_1$  has been proved to contain only one C atom since a mixture of both the gases gave only absorption bands consisting of those of each component gas.  $K_1$  species produced from a mixture of  $C^{16}\text{O}$  and  $C^{18}\text{O}$  gave three pairs of absorption bands as shown in Table 2. These facts indicate that  $K_1$  species has the form of  $\text{CO}_2^{2-}$ , where two O atoms are nearly equivalent; one of O comes from CO and the other from a surface oxygen. Hence  $K_1$  is a monomer adsorbed on  $O_{LC}^{2-}$  and seems to have a chained-type structure; the two end O atoms of  $K_1$  species are linked to two  $\text{Mg}^{2+}$ , respectively (cf. Table 1). Therefore the adsorption site,  $O_{LC}^{2-}$ , for  $K_1$  adsorption is considered to have specific configuration with a low surface concentration.

Table 2 IR bands of  $K_1$  species containing O isotopes

$^{12}\text{C}^{16}\text{O}^{16}\text{O}^{2-}$	$^{12}\text{C}^{16}\text{O}^{18}\text{O}^{2-}$	$^{12}\text{C}^{18}\text{O}^{18}\text{O}^{2-}$
1315 $\text{cm}^{-1}$	1308 $\text{cm}^{-1}$	1292 $\text{cm}^{-1}$
1280 $\text{cm}^{-1}$	1259 $\text{cm}^{-1}$	1246 $\text{cm}^{-1}$

$K_1$  species is desorbed as CO above 250 K, leaving  $\text{O}^{2-}$  on the surface. Since two O atoms in  $K_1$  species are equivalent,  $K_1$  sites are active for O atom exchange between CO and surface  $\text{O}^{2-}$  via its adsorption-desorption cycle. Three kinds of  $K_1$  species observed have the O-isotope composition shown in Table 2.  $K_1$  species play no roles for the oligomer formation.

### 3.3. Linear-type Monomer on $O_{LC}^{2-}$ ( $K_1'$ Species)

$K_1$  species is stable below room temperature in the presence of a CO gas. However this species gradually disappeared as the temperature was cooled down below 200 K as shown in Fig. 2, resulting in the formation of a new species  $K_1'$  which has only one absorption band at 1475  $\text{cm}^{-1}$ . This transformation of  $K_1$  to  $K_1'$  was possible only when gaseous CO was present, and reverse transformation of  $K_1'$  to  $K_1$  easily occurred when the temperature was raised above 200 K or the gas phase was evacuated. This  $K_1$  to  $K_1'$  (or  $K_1'$  to  $K_1$ ) transformation was always accompanied by the formation (or disappearance) of  $K_0$  species on  $Mg_{LC}^{2+}$ , and hence  $K_1'$  species can be stably observable only when  $K_0$  species is present as a neighbor. No  $K_1'$  species without neighboring  $K_0$  species was found under the experimental conditions used.  $K_1'$  species is considered to be a linear-type monomer on  $O_{LC}^{2-}$ , namely  $\text{CO}_2^{2-}$ , judging from its IR band [4] and behavior as shown in Fig. 3.

The  $K_1$  to  $K_1'$  transformation was further studied using  $^{13}\text{CO}$  as shown in Fig. 4.  $K_1$  species formed from  $^{12}\text{CO}$  (1315 and 1280  $\text{cm}^{-1}$ ) at 150 K (then evacuated at 180 K) gave  $K_1'$  species containing only  $^{12}\text{C}$  (1475  $\text{cm}^{-1}$ ) upon subsequent introduction of  $^{13}\text{CO}$ . At the same time  $K_0$  species with  $^{13}\text{CO}$  appeared at the frequency range of 2150-2100  $\text{cm}^{-1}$ . This formation of  $^{12}\text{C}$ -containing  $K_1'$ , but not  $^{13}\text{C}$ -containing one, indicates that  $K_1'$  is not an addition product of CO toward  $K_1$  species;  $K_1'$  is produced by structural change

of  $K_1$  itself. Evacuation of excess  $^{13}\text{CO}$  gas at 220 K again reproduced  $K_1$  species. Most of  $K_0$  species were also desorbed. Surprisingly, this reproduced  $K_1$  species contained only  $^{13}\text{C}$  (1282 and 1252  $\text{cm}^{-1}$ ).

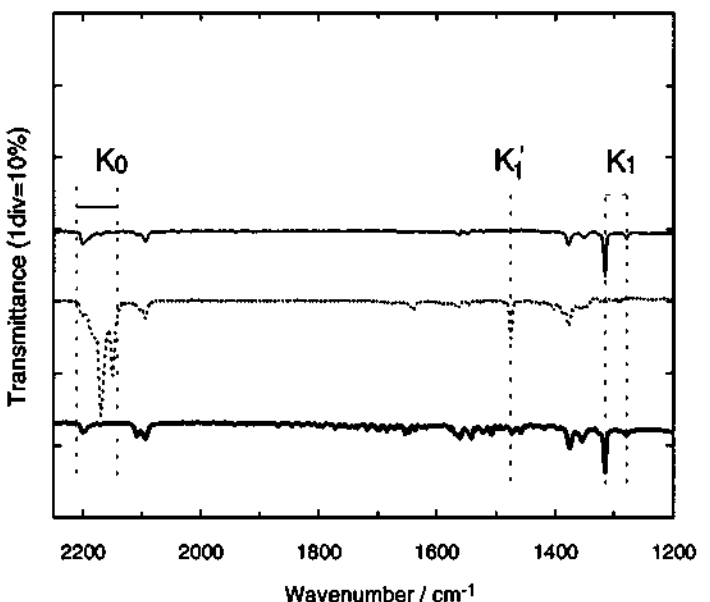


Fig. 2 Reversible transformation between  $K_1$  and  $K_1'$  species. a: 13Pa CO ads. at 210K, then b: temp. down to 170K, then c: temp. up to 210K. All spectra were measured in CO.

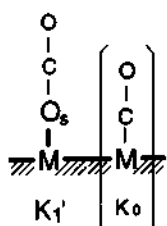


Fig. 3 Model of  $K_1'$  species. This species is stable only when  $K_0$  species is present as a neighbor.

The observed transformation cycle of  $K_1 \rightarrow K_1' \rightarrow K_1$  is explained by the model shown in Fig. 5. Either  $Mg_{LC}^{2+}$  linked to O of chained-type monomer  $K_1$  can transiently adsorb  $^{13}\text{CO}$ , resulting in the rupture of the Mg-O bond of  $K_1$  species. Thus  $K_1'$  and  $^{13}\text{CO}$ -containing  $K_0$  are produced. Desorption of CO is easier from  $K_1'$  species than  $K_0$  when the temperature is raised since the former is more unstable species. However  $K_0$  species ( $^{13}\text{CO}$ ) remaining on the surface is easily reconstructed to again form chained-type  $K_1$  species ( $^{13}\text{CO}$ ) since the latter is more stable species.

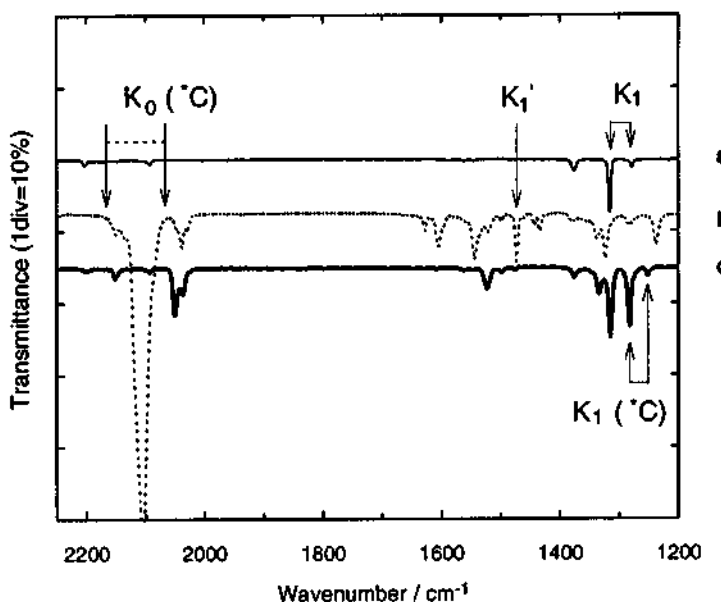


Fig. 4 Reversible transformation between  $^{13}\text{CO}$ -containing  $\text{K}_1$  and  $\text{K}_1'$  species.  
a: 7Pa  $^{12}\text{CO}$  ads. at 150K followed by evac. at 180K, then b: 67Pa  $^{13}\text{CO}$  ads. at 150K, then c: evac. at 220K.

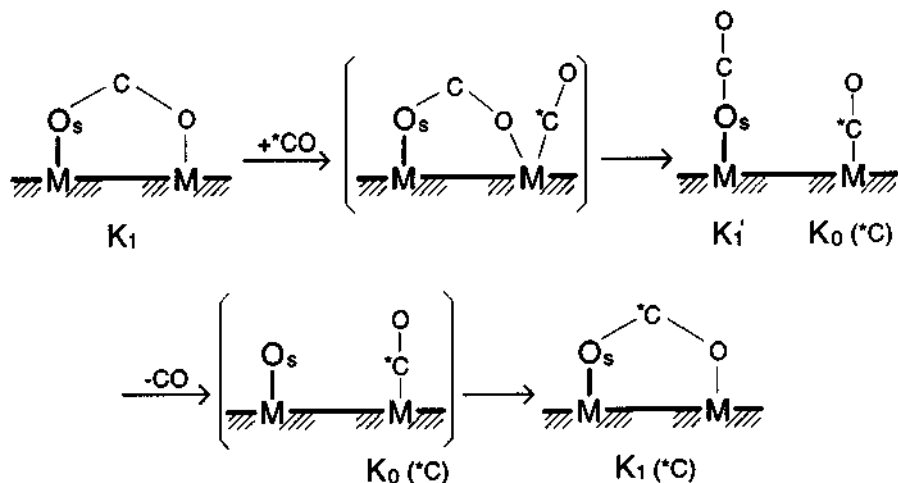


Fig. 5 Transformation mechanism between  $\text{K}_1$  and  $\text{K}_1'$  species

In general  $O_{LC}^{2-}$  is known to play more important roles than  $Mg_{LC}^{2+}$  on typical base MgO catalysts. However, opposite nature has been observed as to the formation of the linear-type CO monomer though  $O_{LC}^{2-}$  easily reacts with CO to produce  $C_nO_{n+1}^{2-}$  oligomers [2].

#### 4. REFERENCES

1. R.St.C.Smart, T.L.Slager, L.H.Little, and R.G.Greenler, *J.Phys.Chem.*, 1973, 77, 1019.
2. A.Zecchina, S.Coluccia, G.Spoto, D.Scarano, and L.Marchese, *J.Chem.Soc.,Faraday Trans.*, 1990, 86, 703.
3. Unpublised data.
4. E.Garrone and A.Zecchina, *J.Chem.Soc.,Faraday Trans.1*, 1988, 84, 2843.

## 2.11 UV-Vis Study of the Condensation Reaction of Carbonylic Compounds on MgO and Hydrotalcites

E. Garrone<sup>a</sup>, D. Bartalini<sup>a</sup>, S. Coluccia<sup>a</sup>, G. Martra<sup>a</sup>, D. Tichi<sup>b</sup> and F. Figueras<sup>b</sup>

<sup>a</sup>Dipartimento di Chimica Inorganica, Chimica Fisica e Chimica dei Materiali, Università di Torino, via P. Giuria 7, 10125 Torino Italy

<sup>b</sup>Laboratoire de Chimie organique physique et cinétique chimique appliquées - U.A. 418 du C.N.R.S., E.N.S.C.M., 8, rue de l'Ecole Normale 34075 Montpellier CEDEX, France

### Abstract

UV-Vis diffuse-reflectance spectroscopy has been employed to study the reaction of acetone and acetaldehyde alone on three basic substances, MgO and two hydrotalcite samples with different  $\text{CO}_3^{2-}/\text{Cl}^-$  ratio. Aldolic condensation followed by dehydration takes place, leading to carbonylic polyenic species, with electronic transitions in the UV-Vis. So far, formation of mesityl oxide and phorone from acetone had been documented. The spectroscopic technique affords evidence about the presence on the surface of species involving up to five acetone units and probably more than eight in the case of acetaldehyde. The order of activity is:  $\text{Cl}^-$ -rich hydrotalcite <  $\text{Cl}^-$ -poor hydrotalcite < MgO: the effect of thermal pretreatment has also been studied. On MgO dehydrated only at 270°C, a second reaction takes place with acetaldehyde, possibly consisting in a Cannizzaro disproportionation. The frequency of the  $\pi \rightarrow \pi^*$  transitions in the reaction products is observed to differ somewhat from solid to solid, and from the values in solution, because of a "solvent" effect exerted by the solids.

### 1. INTRODUCTION

Basic solids such as alkaline earth oxides (or hydroxides), lanthanum oxide and hydrotalcites notoriously catalyze condensation reactions of carbonylic compounds (Knoevenagel reaction, Michael addition, Claisen and aldolic condensation), or disproportionation (Cannizzaro reaction), all involving carbanionic intermediates [1, 2]. The same reactions are also catalyzed by solid acids through carbocationic intermediates: in recent years, the activity of zeolites for such reactions has been investigated to a rather large detail, by means of catalytic tests and IR spectroscopy [3-5]. In contrast, spectroscopic studies on basic solids have been carried out to a much less extent, and in practice only on magnesium oxide: Busca et al. have studied the Cannizzaro disproportionation of formaldehyde [6], and Lercher and coworkers the adsorption of acetone [7]. One reason for the paucity of IR studies is that, though the temperatures of pretreatment necessary for the basic substances to be catalytically active are some 450°C [1, 2], water is a product of reaction, so that the population of OH species increases in the course of the experiment and the samples turn to be not really suitable for IR studies.

The characterization of largely hydrated MgO samples has been carried out, both

through IR and luminescence studies, though it is more difficult than that of fully dehydrated ones [8]. In contrast, some of us have recently shown for hydrotalcites [9] that IR measurements are not particularly meaningful (because intrinsic absorptions due to OH and CO<sub>3</sub> species dominate the spectra), and do not rival other sources of information like the catalytic tests and isotopic exchange measurements [10-12].

The main features of the reactivity of carbonylic compounds on basic substances are well understood, and do not differ much from the standard reactivity of such organics in basic liquid media [1, 2, 6]. In the present paper, results concerning the reaction of acetone and acetaldehyde alone on MgO and two types of hydrotalcites are reported, obtained by means of a spectroscopic technique (diffuse UV-Vis reflectance) not yet employed for such systems. The two hydrotalcite samples contain chloride anions to a different extent, which modulate their basic properties in that the higher the carbonate content, the more basic is the sample: indeed, the fully carbonated sample is known to be the most basic [13].

## 2. EXPERIMENTAL METHODS

Magnesium oxides samples were prepared in powdered form by slowly decomposing the parent hydroxide at a temperature about 250°C, according to a well established procedure, assuring a high specific surface area [14]. The samples then underwent thermal pretreatment at the desired temperature.

Proper hydrotalcite is the double-layered hydroxycarbonate Mg<sub>6</sub>Al<sub>2</sub>(OH)<sub>16</sub>CO<sub>3</sub>-4H<sub>2</sub>O. Here we consider two hydrotalcite samples which differ from the ideal formula in the first instance because the Mg/Al ratio is 2.45 instead of 3. Moreover, the carbonate anion has been partially substituted for the chloride anion: sample HT-A has a carbonate/chloride ratio equal to 0.7; sample HT-B has a ratio 3.1. Structural formulae are Mg<sub>0.71</sub>Al<sub>0.29</sub>(OH)<sub>1.86</sub>(CO<sub>3</sub>)<sub>0.10</sub>Cl<sub>0.14</sub> for sample HT-A and Mg<sub>0.71</sub>Al<sub>0.29</sub>(OH)<sub>2.03</sub>(CO<sub>3</sub>)<sub>0.19</sub>Cl<sub>0.06</sub> for sample HT-B, respectively. Details about the preparation and characterization of the two samples are given in reference [9], where they are referred to as HT(2.5)-Cl-CO<sub>3</sub> and HT(2.5)-CO<sub>3</sub>-B, respectively.

Spectra were taken in an all-quartz cell allowing thermal treatments in situ by means of a Cary 5 spectrophotometer; they are reported as Schuster-Kubelka-Munk function of the reflectance against wavenumbers. For simplicity, the notation 1000 cm<sup>-1</sup> = 1 kK is adopted.

## 3. RESULTS AND DISCUSSION

### 3.1. Adsorption of Acetone

Figure 1 reports the spectra obtained by contacting sample HT-A with few torrs acetone. The solid curve is the background spectrum before reaction, which only shows sizable absorption above 44 kK. This, as well the similar spectrum in Figure 2 referring to HT-B, is basically due to minute amounts of impurities, mainly Cu<sup>2+</sup> and Fe<sup>3+</sup>, documented by ESR spectra [15], which have intense charge-transfer bands at high frequencies, and relatively weak d-d transition.

Dosing acetone causes the appearance of an isolated band at 39.5 kK, and the marked increase of absorption above 44 kK. Heating of the sample decreases the absorption above 44 kK, causes a marked increase of the 39.5 kK band, and brings about the appearance of a weak shoulder at about 33 kK.

Dosing acetone onto HT-B (Figure 2) causes the immediate appearance of two bands at 41.8 and 32.8 kK, the latter with a shoulder at about 27.5 kK. With time, the band at 32.8 kK grows at the expenses of that initially at 41.8 kK: a clear shoulder at 22.8 kK becomes

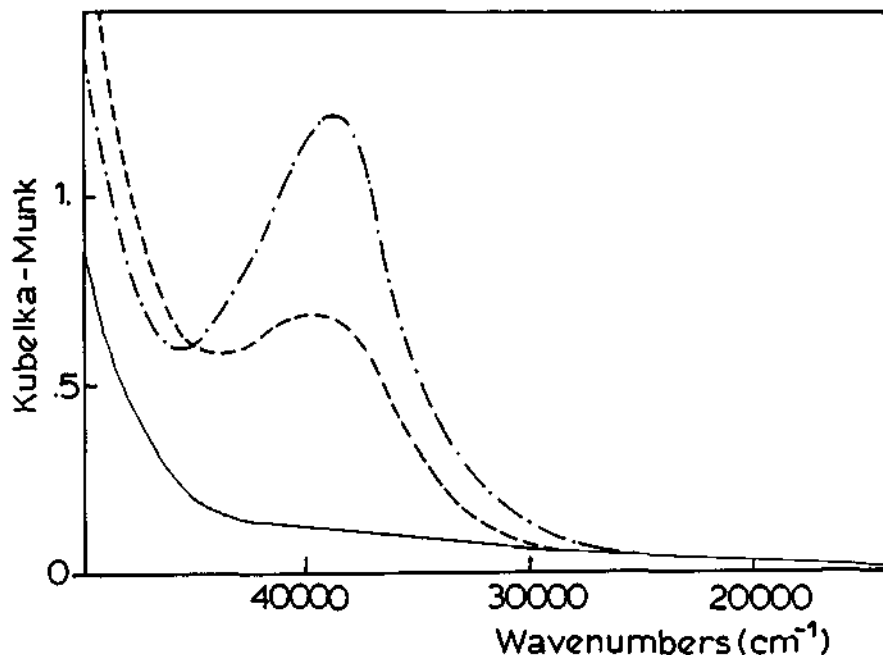


Figure 1. Acetone on HT-A outgassed at 400°C. Solid curve: back ground; broken curve: immediately after contact of 58 torr acetone; dot-dash curve: after one hour at 100°C.

visible. Evolution with time also causes a slight shift to lower frequencies of the two main bands to 39.5 and 32.0 kK, respectively.

Previous work [13, 16-18] has shown that main products of the self-reaction of acetone on hydrotalcites are the dimeric species mesityl oxide ( $\text{CH}_3)_2\text{C}=\text{CH}-\text{C}(\text{O})-\text{CH}_3$ , and the trimeric species phorone ( $\text{CH}_3)_2\text{C}=\text{CH}-\text{C}(\text{O})-\text{CH}=\text{C}(\text{CH}_3)_2$ ; in the presence of transition metal cations, isomerization and dehydrogenation reactions take place, leading to isophorone and mesitylene.

Carbonylic compounds are characterized in the UV region by three transitions:  $n \rightarrow \pi^*$ , usually at low frequencies, intrinsically weak because symmetry-forbidden;  $n \rightarrow \sigma^*$  and  $\pi \rightarrow \pi^*$ , the relative position of which depends on the compound, but in any case falling at higher frequency and being more intense than the band  $n \rightarrow \pi^*$ . The  $\pi \rightarrow \pi^*$  transition is by far the most intense, and therefore such type of band is to be considered in the interpretation of the present spectra, with the exception of acetone, for which the  $\pi \rightarrow \pi^*$  band is at 60.8 kK [19]. The  $n \rightarrow \sigma^*$  of acetone is at 51.2 kK, i.e. falls just outside the spectral range: the tail of this absorption is consequently responsible for some changes in absorbance above 44 kK. The band at 39.5 kK is to be related to mesityl oxide, which has a  $\pi \rightarrow \pi^*$  transition at 43.3 in apolar compounds. It is well known, however, that such transitions are red-shifted in polar media by few kK, because the excited state of the molecule is stabilized [19].

We propose that the occurrence of the  $\pi \rightarrow \pi^*$  band of mesityl oxide on hydrotalcites at frequencies lower than in apolar compounds is amenable to the polar nature of the solid: in this respect, the solid may be regarded as exerting a "solvating" action on the mesityl oxide molecule at the surface. The shift in the band frequency observed in Figure 2 is due

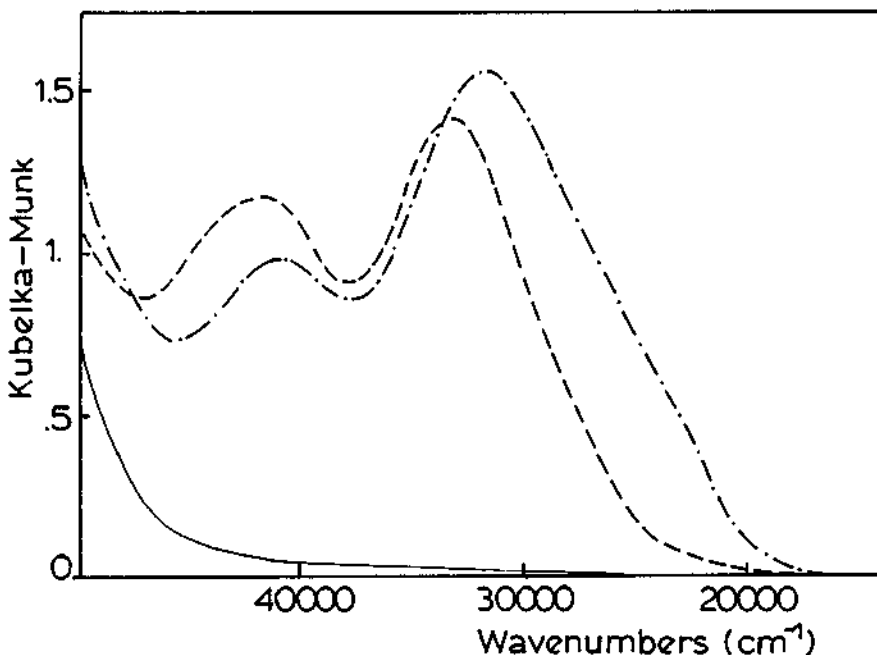


Figure 2. Acetone on HT-B outgassed at room temperature. Solid curve: background; broken curve: immediately after contact of 47 torr acetone; dot-dash curve: after one hour and a half.

to a similar cause: a lower frequency is observed when excess acetone is present (intense absorption above 44 kK), because liquid-like acetone act as a polar solvent, adding its effect to that of the surface.

The band at 32.8 kK has to be assigned, on a similar ground, to phorone, and the shoulder components to higher polymeric species, e.g. of the type:  $(CH_3)_2C=CH-C(O)-CH=C(CH_3)-CH=C(CH_3)_2$ . It is interesting to note that spectroscopic evidence indicates that on the surface condensation may proceed beyond the trimeric species.

Figures 3 and 4 describe the reaction on MgO. The former reports the course of the reaction on the sample outgassed at a low temperature ( $270^\circ C$ ), the latter compares the spectra taken immediately after contact for three pretreatment temperatures. The overall picture is rather similar to that observed with hydrotalcites. The band due to mesityl oxide appears at 42.1 kK, and decreases with time in favour of the band of phorone at 34.2 kK: a definite shoulder at 27.9 kK is also seen. The most active sample appears to be that outgassed at  $800^\circ C$ , both as far as the overall intensity of the spectrum and the number of components are concerned (further shoulder at 22.2 kK). This is in contrast with the usually accepted picture that hydroxyl species are the active sites for catalysis: we are far, however, in the present circumstances of room temperature reaction, from catalytic conditions, both for the absence of a reactor where fresh reactant is fed, and the temperature of reaction (e.g.  $210^\circ C$  in ref. [16]).

### 3.2. Adsorption of Acetaldehyde

Acetaldehyde is expected to give rise, by condensation and successive dehydration, to polyenic carbonylic species of the type  $CH_3-(CH=CH)_n-CHO$ , the shortest of which is

crotonaldehyde. Points of interest are what is the extent of condensation (i.e., how large n may be), and whether this is the only process taking place.

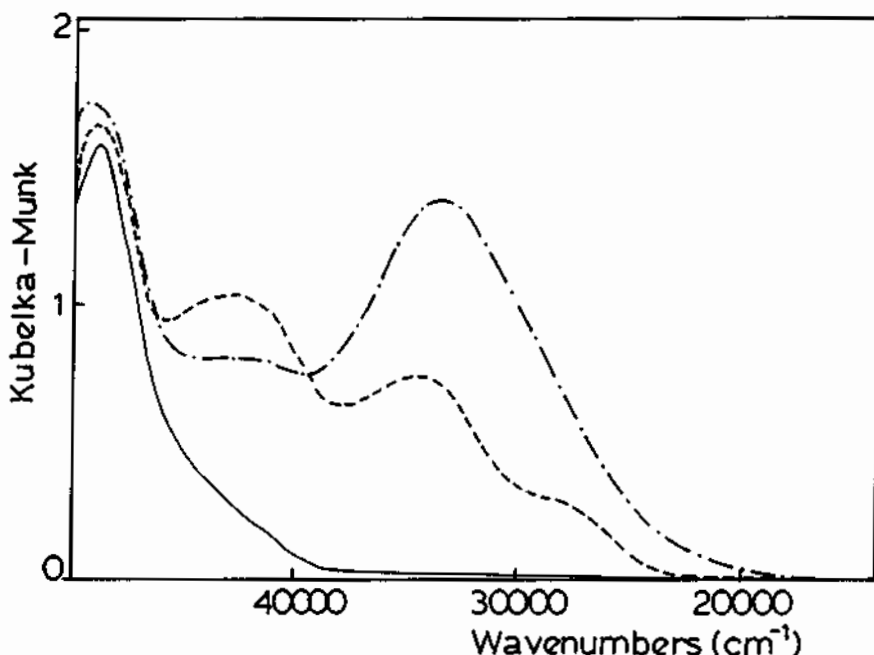


Figure 3. Acetone on MgO outgassed at 270°C. Solid curve: background; broken curve: immediately after contact of 27 torr acetone; dot-dash curve: after one hour at 100°C.

As far as hydrotalcite samples are concerned, only the HT-B type has been considered, though at two different pretreatment temperatures. Figure 5 illustrates the room temperature reaction of acetaldehyde with HT-B outgassed at room temperature, i.e. in the mildest conditions possible. The spectrum taken immediately after contact (Figure 5a) shows several bands, at 45, 36.5, 31.7 kK and a shoulder at about 26 kK. The absorbance has also increased in the region above 47 kK. With time, all bands increase: after one day, however, the component at 31.7 kK is decreased in favour of the band at 25.7 kK and a new one at about 20 kK. A mild heating at 150°C (Figure 5b) accelerates the conversion of bands lying at high frequency into components at lower frequency: the band at 45 kK is no longer present; the prominent band is that at 25.7 kK; the shoulder around 20 kK is now clearly seen at 19.7 kK and other components extending down to 6 kK are present. Adsorption on the sample outgassed at 400°C follows the same patterns: such sample is, however, definitely more active than that outgassed at room temperature.

As to the spectroscopic nature of the observed bands, considerations hold very similar to those made for acetone and its condensation products. Acetaldehyde has: a very weak  $n \rightarrow \pi^*$  transition at 34.6 kK; a more intense band at 55 kK, of the type  $n \rightarrow \sigma^*$ , and finally a very intense  $\pi \rightarrow \pi^*$  at 66 kK. The first may be discarded here because of its weakness, as well as the last, falling well above the 50 kK instrumental limit. A tail of the  $n \rightarrow \sigma^*$  transition is observed, when the monomer is substantially present, in the region just below 50 kK. With crotonaldehyde and higher homologues, the  $n \rightarrow \sigma^*$  band remains at

high frequency, whereas the  $\pi \rightarrow \pi^*$  transition is lowered (the more so the larger the  $\pi$  system), as also is the  $n \rightarrow \pi^*$ , which still has negligible intensity. The  $\pi \rightarrow \pi^*$  transition of crotonaldehyde in apolar solvents is at 49.2 kK, which corresponds to the band observed at 45 kK on HT-B, if account is taken of the polar nature of the solid. The other bands correspond to higher polyenic species.

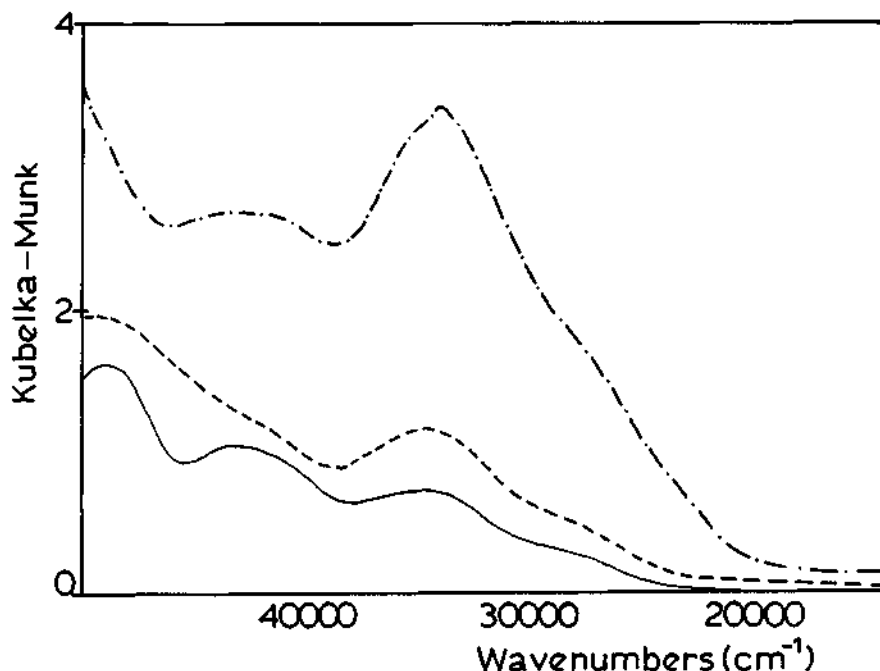


Figure 4. Effect of pretreatment temperature on the reactivity of acetone on MgO. Solid curve: sample outgassed at 270°C; broken curve: sample outgassed at 400°C; dot-dash curve: sample outgassed at 800°C.

Adsorption of acetaldehyde on MgO has been followed after thermal pretreatment at three different temperatures, i.e. 270, 400 and 800°C. Spectra concerning the sample outgassed at 270°C are reported in Figure 6. Figure 7 compares the final situation on the three samples pretreated at different temperatures. The spectra not reported are, however, of help in locating the various components. Immediately after contact with acetaldehyde, several bands are visible at 34, 29.8, 25.4 and 19.5 kK. After heating, a new component is present at 16.0 kK, and an overall increase in absorption is observed. Note the absence of the band related to crotonaldehyde: all bands are due to polyenic carbonylic species with  $n = 2$  and more.

A puzzling feature of the spectrum is the increase in the region around 40 kK, which is as a consequence rather flat: this is in contrast with what observed in all previous cases, where heating causes the conversion of high-lying bands into low-lying bands. Such feature is unique to MgO outgassed at 270°C: indeed, Figure 7 shows that the spectra of the other two MgO samples have, after completion of the experiment, the expected upward concavity. In order to investigate the nature of the absorption around 40 kK, the sample in Figure 6 was contacted with oxygen at 250°C: whereas all bands below 40 kK are eroded because the related species are oxidized, the absorption around 40 kK is unaffected. This

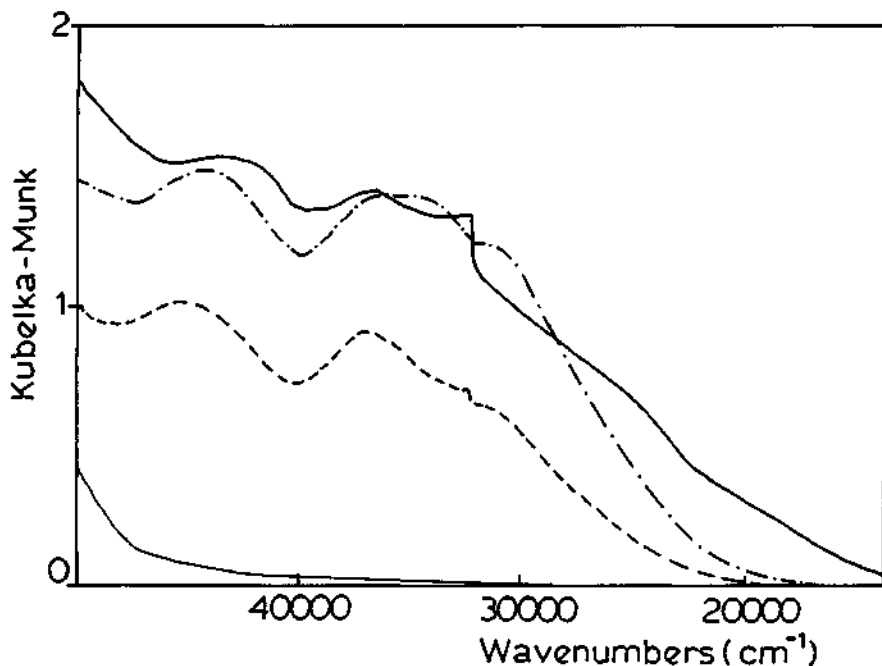


Figure 5a. Acetaldehyde on HT-B outgassed at room temperature. Thin solid curve: background; broken curve: immediately after contact of 41 torr acetaldehyde; dot-dash curve: after one hour and a half; bold solid curve: after one day (jumps in the spectra are due to instrumental faults).

is evidence that, whereas polyenic carbonylic species are unstable in oxygen, the species responsible for the absorption centred about 40 KK are saturated. Possible candidates are carboxylic acids, which usually have  $\pi \rightarrow \pi^*$  transitions around 47 KK, probably red-shifted again because of the surface fields. A scheme for the formation of carboxylate species from acetaldehyde, in the absence of molecular oxygen, is provided by the Cannizzaro reaction, by which disproportionation takes place to acetic acid and ethanol. Such a reaction does not occur in organic chemistry, because the aldolic condensation takes place instead. In the present case, one may admit that, once the more strongly basic have reacted to give aldolic condensation, less basic OH species may promote the less demanding Cannizzaro disproportionation: such moderately basic hydroxyl species are likely to be present on the sample poorly outgassed at room temperature, and not on the more severely outgassed sample.

Figure 7 shows that the most active sample is that outgassed at 800°C: keeping in mind that practically no hydroxyl species is left on such sample, one is compelled to admit that surface oxygen anions act as basic centres, even more efficient than surface hydroxyls.

### 3.3. Extent of Condensation

Frequencies of the bands clearly identified in the spectra are gathered in Table 1 (acetone) and 2 (acetaldehyde), listed according to  $n$ , the assumed number of C=C double bonds. Considering Table 1, it appears that the transition of the same molecule on HT-B and MgO are practically the same, whereas the band due to mesityl oxide ( $n = 1$ ) on HT-A

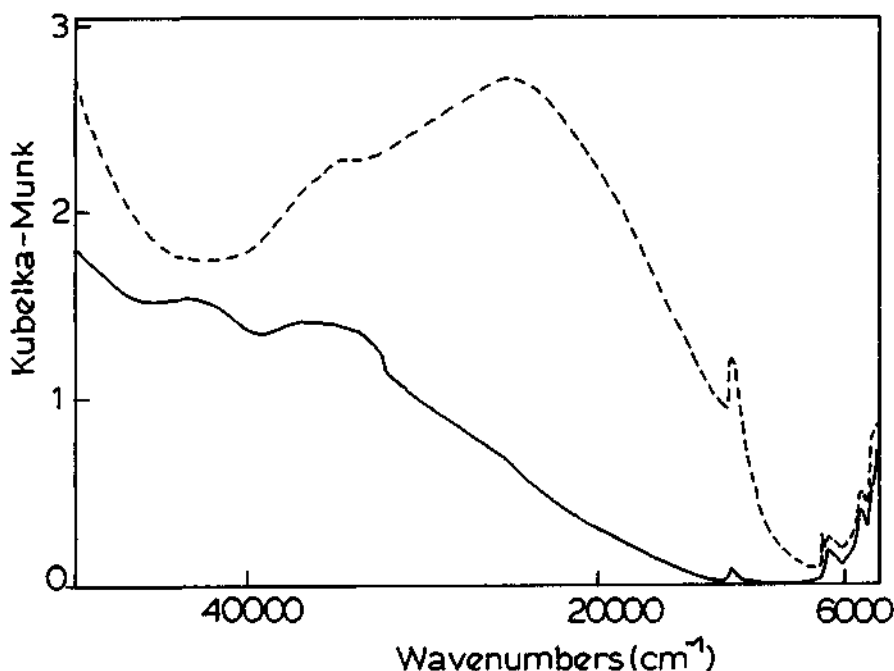


Figure 5b. Continuation of the experiment. Solid curve: after one day (same spectrum as the last in Figure 5a); broken curve: after one hour at 150°C.

is at somewhat different frequency. Whereas acetone ( $n = 0$ ), mesityl oxide ( $n = 1$ ) and phorone ( $n = 2$ ) cannot, from a spectroscopic point of view, be considered as omologues in a series, because the growth of the polyenic system does not occur on the same side of the molecule, this happens with the molecules corresponding to  $n = 2, 3, 4$ . The frequencies of the  $\pi \rightarrow \pi^*$  transitions of such molecules are expected to be a smooth function of  $n$  [19]: indeed, linear dependence on  $n$  of the wavelength (or its square) has been found for several families of polyenic compounds. In the present case, with only three values, it is unfeasible to draw any such correlation: we note, anyway, that the three frequencies are regularly spaced.

As to the condensation products of acetaldehyde (Table 2), all species observed constitute a set, and their frequencies may be usefully compared with the values for the same substances in apolar solutions (first row in Table 2). For the latter, a linear dependence of  $\lambda^2$  on  $n$  may be drawn from the data in Table 2. Crotonic aldehyde is not observed on MgO. As already noted, the value on HT-B is in very good agreement with the value in solution. As to the next omologue ( $n = 2$ ), the frequency of the species observed on MgO is slightly lower than that on HT-B, which is in turn only marginally smaller than the values observed in apolar solutions. The same holds for the species  $n = 3$ . As to the band at 25.7 kK on HT-B and 25.4 kK on MgO, reference to the value in solution suggest that the assignent to  $n = 4$  is unsatisfactory, and the assumption  $n = 5$  appears more likely. The other transitions at 19.5 and 16.0 kK do not correspond to any polyenic species in solution, and probably are due to rather high values of  $n$  (e.g.  $n > 8$ ). Assignment at this stage becomes uncertain: it may happen that the "solvent" effect of MgO, which is already sizable, becomes exceptionally strong when long-chain polyenes are concerned; other

components may be hidden in the broad band envelopes.

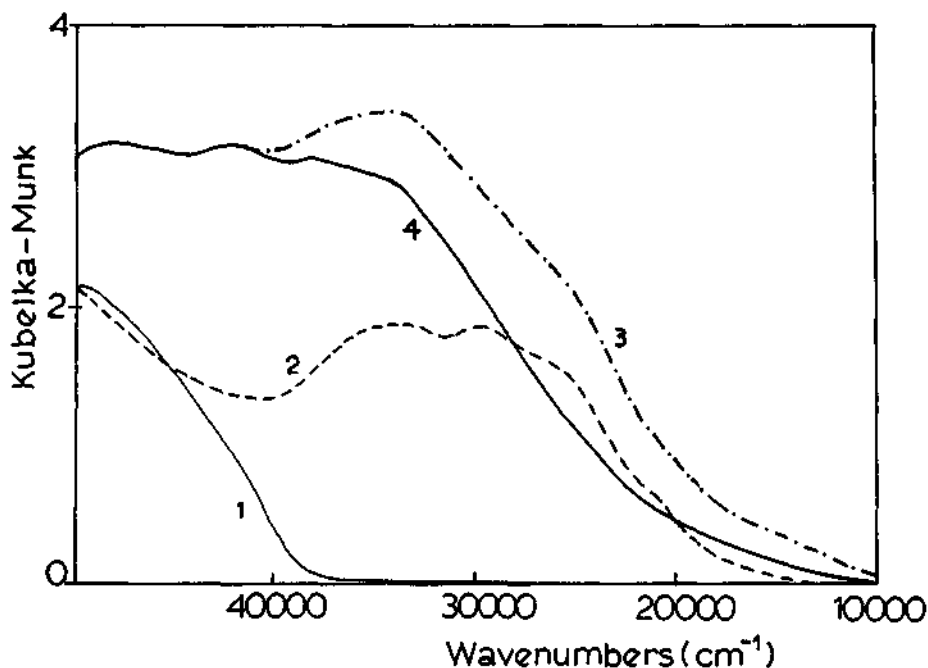


Figure 6. Acetaldehyde on MgO outgassed at 270°C: 1) thin solid curve: background; 2) broken curve: immediately after contact of 13 torr acetaldehyde; 3) dot-dash curve: after 3/4 hour at 200°C; 4) bold solid curve: after contact of 40 torr O<sub>2</sub> at 250°C.

#### 4. CONCLUSIONS

UV-Vis results afford evidence on processes not readily studied with other spectroscopic techniques. Some information is as expected on the basis of the knowledge about the reactivity of acetone and acetaldehyde in basic media: aldol condensation and dehydration occur, giving rise to well known species like mesityl oxide, phorone and crotonaldehyde. Being under circumstances far from those of catalysis, higher homologues in the series of condensation products are obtained ( $n = 4$  for acetone and  $n > 8$  for acetaldehyde).

The chemical composition and the dehydration temperature determine the overall reactivity (as judged from the overall intensity of the spectrum and the development of low-lying components). HT-A, because of its higher chloride content, is less active than HT-B, in that condensation of acetone is limited to mesityl oxide. HT-B outgassed at 400°C is more active than that outgassed at room temperature, in agreement with literature [16, 17]. The most active sample towards acetone is MgO outgassed at 800°C, though it has no hydroxyls, which are usually assumed to be the active centres. The same happens with acetaldehyde, where activity seems to depend inversely from the pretreatment temperature (degree of hydroxylation).

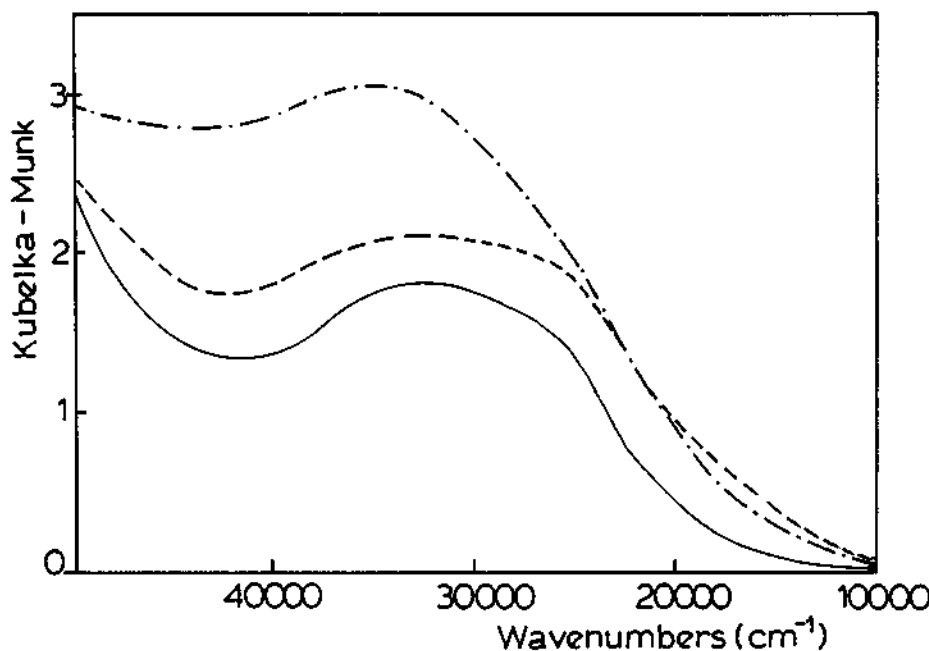


Figure 7. Effect of pretreatment temperature on the reactivity of acetaldehyde on MgO. Solid curve: sample outgassed at 270°C; broken curve: sample outgassed at 400°C; dot-dash curve: sample outgassed at 800°C.

Table 1 Bands observed for the reaction products from acetone (in kK; numbers refer to the proposed number of C=C bonds).

Sample	1	2	3	4
HT-A	39.5			
HT-B	41.8 (39.5)	32.8 (32.0)	27.5	22.8
MgO	42.1	34.2	27.9	22.2

Table 2 Bands observed for reaction products from acetaldehyde (in kK; numbers refer to the proposed number of C=C double bonds).

Sample	1	2	3	4	5	6	7	?
Polyenes in solution	45.5	37.0	32.0	29.1	27.0	25.4	24.1	
HT-B	45.0	36.5	31.7	/	25.7	/	/	19.7
MgO	/	34.0	29.8	/	25.4	/	/	19.5, 16.0

## 5. BIBLIOGRAPHY

- 1) K. Tanabe, M. Misono, Y. Ono and H. Hattori, "New solid acids and bases", Elsevier-Kodansha **1989**.
- 2) H. Hattori, Mat. Chem. Phys., **1988**, 18, 533.
- 3) L. Kubelkova, J. Cejka and J. Novakova, Zeolites, **1991**, 11, 48.
- 4) Z. Dolejsek, J. Novakova, V. Bosacek and L. Kubelkova, Zeolites, **1991**, 11, 244.
- 5) C.D. Chavez Diaz, S. Locatelli and E. E. Gonzo, Zeolites, **1992**, 12, 851.
- 6) G. Busca, J. Lamotte, J-C. Lavalle and V. Lorenzelli, J. Am. Chem. Soc., **1987**, 109, 5197.
- 7) J.A. Lercher, H. Noller and G. Ritter, J. Chem. Soc. Faraday I, **1981**, 77, 621.
- 8) S. Coluccia and L. Marchese, "Acid-Base Catalysis", Proc. Int. Symp. Sapporo **1988**, p. 207.
- 9) D. Tichit, M.H. Lhouty, A. Guida, C. Bich Huong, F. Figueras, A. Auroux, D. Bartalini and E. Garrone, submitted to J. Catal.
- 10) S. Miyata, T. Kumura, H. Hattori and K. Tanabe, Nippon Kagakukaishi, **1971**, 92, 514.
- 11) G. Zhang, H. Hattori and K. Tanabe, Appl. Catal., **1988**, 36, 189.
- 12) G. Zhang, H. Hattori and K. Tanabe, Appl. Catal., **1988**, 40, 183.
- 13) E. Suzuki and Y. Ono, Bull. Chem. Soc. Japan, **1988**, 61, 1008.
- 14) E. Guglielminotti, S. Coluccia, E. Garrone, L. Cerruti and A. Zecchina, J. C. S. Faraday I, **1979**, 75, 96.
- 15) E. Garrone and D. Bartalini, unpublished.
- 16) W.T Reichle, J. Catal. **1985**, 94, 547.
- 17) W.T Reichle, S.Y. Kang and D.S. Everhardt, J. Catal. **1986**, 101, 352.
- 18) A. Corma, V. Fornés, R.M. Martin-Aranda and F. Rey, J. Catal., **1992**, 134, 58.
- 19) G. Herzberg, "Electronic spectra of polyatomic molecules", Van Nostrand, N. York, **1966**.

This Page Intentionally Left Blank

## 2.12 O<sub>2</sub><sup>-</sup> Formation through N<sub>2</sub>O on ZrO<sub>2</sub> Surface

### O<sub>2</sub><sup>-</sup> Formation through N<sub>2</sub>O on ZrO<sub>2</sub> Surface

Ken-ichi Aika and Eiji Iwamatsu

Department of Environmental Chemistry and Engineering  
Interdisciplinary Graduate School of Science and Engineering, Tokyo Institute of  
Technology, 4259 Nagatsuta, Midori-ku, Yokohama 227, Japan

#### ABSTRACT

The authors intended to form O<sup>-</sup> on ZrO<sub>2</sub> through the interaction of N<sub>2</sub>O which was a well-known precursor molecule of O<sup>-</sup> on MgO or V<sub>2</sub>O<sub>5</sub>/SiO<sub>2</sub>. However, EPR spectra of O<sup>-</sup> were not obtained, but the spectra of O<sub>2</sub><sup>-</sup> were observed. Other spectra which were identified to be O<sub>3</sub><sup>-</sup> were also observed when N<sub>2</sub>O was interacted with ZrO<sub>2</sub> at 183 to 303 K. O<sub>2</sub><sup>-</sup> was the most stable species, the half life time of which was 5 days at room temperature, and O<sub>3</sub><sup>-</sup> was less stable on ZrO<sub>2</sub>. O<sup>-</sup> was considered to be a precursor of O<sub>2</sub><sup>-</sup>; however, the half life time of O<sup>-</sup> must be quite short. Those species are discussed as possible intermediates of N<sub>2</sub>O decomposition.

#### 1. INTRODUCTION

Surface anion radicals such as O<sup>-</sup>, O<sub>2</sub><sup>-</sup>, or O<sub>3</sub><sup>-</sup> can be detected by EPR and are sometimes important model intermediates of the oxidation reactions [1,2]. N<sub>2</sub>O has been used as O<sup>-</sup> sources on MgO [3,4]. ZrO<sub>2</sub> has been studied well by spectroscopic methods such as EPR[5] or IR[6] and it is also known to be a selective catalyst for CO hydrogenation [7]. Although O<sub>2</sub> has been known to give O<sub>2</sub><sup>-</sup> on ZrO<sub>2</sub> [5], formation of O<sup>-</sup> has not been reported on this surface. The authors tried to yield O<sup>-</sup> through N<sub>2</sub>O on ZrO<sub>2</sub>, however, observed O<sub>2</sub><sup>-</sup> and O<sub>3</sub><sup>-</sup> by EPR. We studied the reactivity of these surface radicals.

#### 2. EXPERIMENTAL METHODS

ZrO<sub>2</sub> was prepared by the hydration of zirconium oxynitrate [7]. It was calcined at 773 K for 3 h, and evacuated at 973 K for 3 h. The adsorption and the decomposition reaction were carried out in a conventional closed circulation system. Two sample holders, a U-tube reactor with an EPR tube and an EPR tube itself, were used. The former contains 2g of ZrO<sub>2</sub> and the latter contains 0.2g of it. Gases were analyzed by a gaschromatography and the surface anion radicals were detected by a JEOL JES-FE-1X spectrometer (X-band) at 77 K. FTIR spectra were measured by a JEOL JIR-100 at room temperature.

#### 3. RESULTS AND DISCUSSION

## 2.1 Formation of $O_2^-$

When  $N_2O$  was introduced on  $ZrO_2$  at room temperature (298 K and cooled to 77 K), EPR spectra ( $g_1=2.031$ ,  $g_2=2.008$ ,  $g_3=2.001$ ) were observed as are shown in Fig. 1-a. The spectra completely disappeared after evacuating at 973 K for 3 h (Fig. 1-c). When  $O_2$  was introduced on the  $ZrO_2$  at 298 K, the same spectra were observed (Fig. 1-d). We assigned this to  $O_2^-$  on  $ZrO_2$  surface, the spectroscopic data of which was almost identical to those reported earlier on  $ZrO_2$  ( $g_1=2.027$ ,  $g_2=2.008$ ,  $g_3=2.003$ )[5], and those on Sc-Y Zeolite ( $g_1=2.030$ ,  $g_2=2.009$ ,  $g_3=2.002$ )[8]. We expected the spectra of  $O^-$  on  $ZrO_2$  because  $N_2O$  is a well-known reagent to give  $O^-$  on the surface. The g-values and the shape of the spectra were different from  $O^-$  on  $SnO_2$  ( $g_1=2.030$ ,  $g_2=2.028$ ,  $g_3=2.002$ )[9] or  $MgO$  ( $g_1=2.0385$ ,  $g_2=2.0385$ ,  $g_3=2.0032$ )[3].

The peak height of the spectra was decreased to 50% after standing for 5 days at 298 K (Fig. 1-a to b). The half life of  $O_2^-$  on  $ZrO_2$  was thus 5 days at room temperature. The reason of the decaying must be either the further reaction of  $O_2^-$  or the decaying the surface structure to keep the radical ions. The evacuation at the temperature below 773 K did not give the spectra through  $N_2O$  contact. In order to build the active sites (defects) on  $ZrO_2$ , the evacuation at higher temperature than 773 K was necessary.

The evacuation (973 K, 3 h; Fig. 1-c, e and g) and  $N_2O$  introduction (Fig. 1-a, f, and h) were repeated more than three times. After every evacuation, the spectra seem to become greater. The longer evacuation at high temperature seems to build the active sites, probably defect sites or less-coordinated sites. In some cases, a singal which might come from electron ( $g=2.000$ ) appears (Fig. 1-g). This state may be ready to give electrons to surface oxygen species. Another interesting thing is that  $O_2$  and  $N_2O$  give almost the same spectra, however,  $O_2$  gives just a greater peak. See Fig. 1-d ( $O_2$ ) vs. Fig. 1-a, f ( $N_2O$ ), and Fig. 4-c ( $O_2$ ) vs. Fig. 4-a, b ( $N_2O$ ).

Fig. 2 shows the reactivity of  $N_2O$  to give  $O_2^-$  at two temperatures.  $N_2O$  can

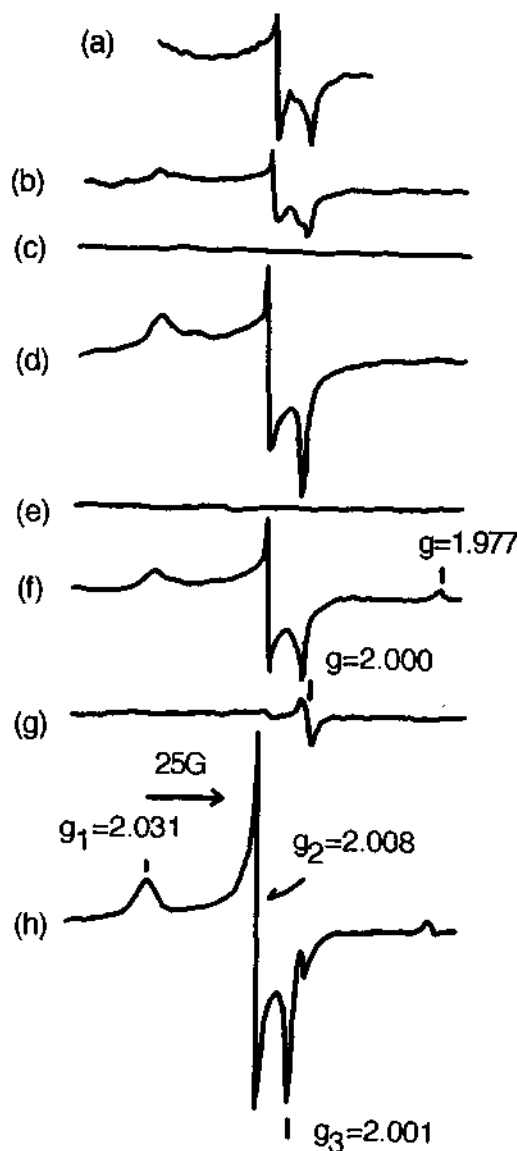


Fig. 1 EPR spectra of surface species on  $ZrO_2$  measured at 77 K. The conditions are changed as follows;

- $N_2O$  introduction at 298 K onto  $ZrO_2$  evacuated at 973 K for 3 h: (b)
- standing for 5 days at 298 K: (c)
- Evacuation at 973 K for 3 h: (d)
- $O_2$  introduction at 298 K: (e)
- Evacuation at 973 K for 3 h: (f)
- $N_2O$  introduction at 298 K: (g)
- Evacuation at 973 K for 3 h: (h)
- $N_2O$  introduction at 298 K:

decompose even at 195 K and yield O<sub>2</sub><sup>-</sup>, however, the peak was not great (Fig. 2-b). It gives a greater peak at 298 K (Fig. 2-c).

### 3.2 Adsorbed State of N<sub>2</sub>O

When N<sub>2</sub>O was introduced N<sub>2</sub>O pressure was decreased by the adsorption, while neither N<sub>2</sub> or O<sub>2</sub> was detected in a gas phase gaschromatographically. Amount of N<sub>2</sub>O adsorption was about 0.07 mmol/g. FTIR spectra of this sample were measured. As is shown in Fig. 3, it gave strong peaks at 2243 ( $\nu_1$ ) and 1240cm<sup>-1</sup> ( $\nu_3$ ) which were similar to the data of gas phase molecule (2224, 1285cm<sup>-1</sup>). Most of the N<sub>2</sub>O must be adsorbed as a molecule, while a small amount of N<sub>2</sub>O may be decomposed and finally to give O<sub>2</sub><sup>-</sup>. EPR spectrum of N<sub>2</sub>O<sup>-</sup>, which has been observed on TiO<sub>2</sub>/SiO<sub>2</sub> ( $g_s=2.003$ )[10], was not observed.

### 3.3 Formation of O<sub>3</sub><sup>-</sup>

Fig. 4-a shows O<sub>3</sub><sup>-</sup> spectra which are formed at 298 K through N<sub>2</sub>O and are measured at 77 K. The spectroscopic data are summarized in Table 1 including the reported results. In order to investigate the stability or reactivity of this species, the sample was warmed up first to 183 K once, then to 303 K with a 10 degree interval. The sample was cooled to 77 K for every 12 measurements. A new peak appeared at  $g=2.010$  during these 12 measurements with the maximum at the temperature of 243 to 253 K (Fig. 4-b). The authors tentatively assigned this to O<sub>3</sub><sup>-</sup> because the g-value ( $g_s=2.010$ ) is close to that on TiO<sub>2</sub> ( $g_1=2.014$ ,  $g_2=2.009$ ,  $g_3=2.006$ )[11]. The ratio of peak height of O<sub>3</sub><sup>-</sup> against that of O<sub>2</sub><sup>-</sup> is shown as a function of temperature in Fig. 5.

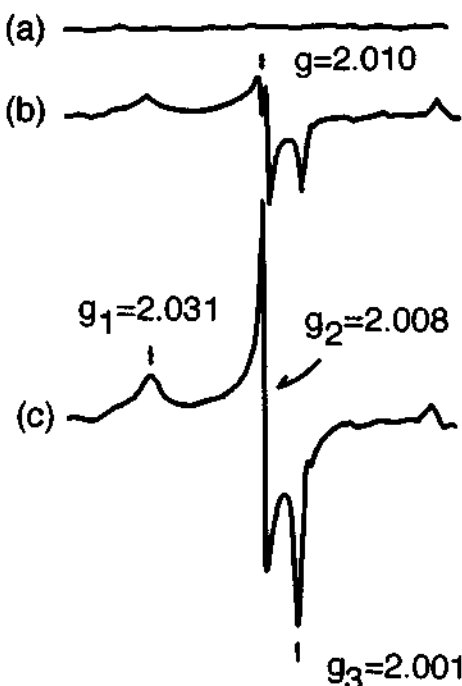


Fig. 2 Relative concentration of O<sub>2</sub><sup>-</sup> as a function of the temperature of N<sub>2</sub>O introduction; Spectra (a) after evacuation at 973 K for 3 h; (b) N<sub>2</sub>O introduction at 195 K; (c) N<sub>2</sub>O introduction at 298 K.

Table 1 Spectroscopic data of oxygen radicals

Radicals	Oxides	$g_1$	$g_2$	$g_3$	ref.
O <sup>-</sup>	SnO <sub>2</sub>	2.030	2.028	2.002	[9]
O <sup>-</sup>	MgO	2.0385	2.0385	2.0032	[3]
O <sub>2</sub> <sup>-</sup>	Sc-Y Zeolite	2.030	2.009	2.002	[8]
O <sub>2</sub> <sup>-</sup>	ZrO <sub>2</sub>	2.027	2.008	2.003	[5]
O <sub>2</sub> <sup>-</sup>	ZrO <sub>2</sub>	2.031	2.008	2.001	This work
O <sub>3</sub> <sup>-</sup>	ZrO <sub>2</sub>	2.010	-	-	This work
O <sub>3</sub> <sup>-</sup>	TiO <sub>2</sub>	2.014	2.009	2.006	[11]
N <sub>2</sub> O <sup>-</sup>	TiO <sub>2</sub> /SiO <sub>2</sub>	2.003	-	-	[10]

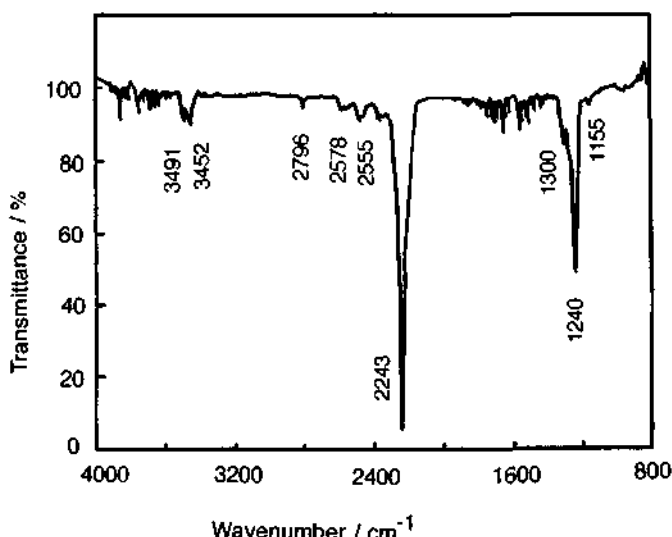
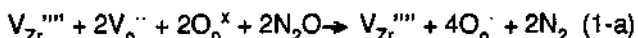


Fig. 3 FTIR spectra of adsorbed  $\text{N}_2\text{O}$  on  $\text{ZrO}_2$  at 298 K.

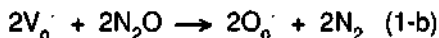
This species finally disappeared at room temperature. In order to examine whether this species come from  $\text{N}_2\text{O}$  or  $\text{O}_2^-$ , the sample was contacted with  $\text{O}_2$  at 253 K instead of  $\text{N}_2\text{O}$ . However, this species was not observed, but only  $\text{O}_2^-$  was observed as is shown in Fig. 4-c. Thus, this species is only formed above 183 K through  $\text{N}_2\text{O}$  with an activation energy of about 19 kJ/mol, however, it is further converted to other species such as  $\text{O}_2^-$  above 253 K.

### 3.4 Mechanism of Oxygen Anion Radical Formation on $\text{ZrO}_2$ Surface

Through the evacuation at 973 K, the surface of  $\text{ZrO}_2$  loses the adsorbed species such as hydroxyl and carbonate groups leading the surface state which only contains  $\text{Zr}^{4+}$  cations and  $\text{O}_2^-$  anions. Such a surface state is considered to be full of defects ( $\text{V}_{\text{Zr}}^{'''}$  +  $2\text{V}_o^{..}$ ) or unsaturated states, however, electronically neutral. Most of the  $\text{N}_2\text{O}$  is strongly adsorbed as a molecule as is observed by FTIR spectra (Fig. 3). Electron is not transferred to  $\text{N}_2\text{O}$  as is discussed in 3.2 and shown in Table 1. A part of  $\text{N}_2\text{O}$  must be decomposed on some active sites forming atomic O and  $\text{N}_2$ . The atomic O must be immediately turned to  $\text{O}^-$  through Reaction (1-a).

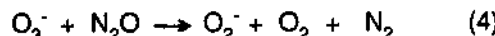
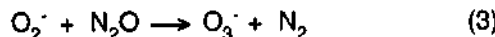
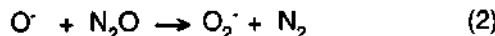
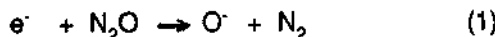


where O atom sits on a defect site and an electron comes from lattice oxygen ( $\text{O}_o^{\times}$ ). Because oxygen in the defect is surrounded by cations and tend to accept electrons. Another possibility is that the lattice oxygen is partly released leaving two electrons at the oxygen defect (reduction through the evacuation). The spectra of Fig. 1-g may correspond to it ( $\text{V}_o^-$ ), which reacts with  $\text{N}_2\text{O}$  as follows



where  $O_0^-$  means  $O^-$ .

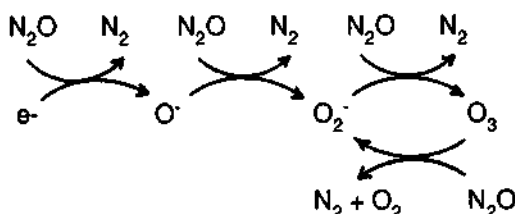
Reaction (1-a) or (1-b) is simply expressed as Reaction (1), and the subsequent reactions are also written like that.



Since we did not observe  $O^-$  but  $O_2^-$ , the  $O^-$  further reacts with  $N_2O$  or  $O$  atom which is the decomposed product of  $N_2O$ . Thus, the reaction (2) occurs. Probably Reaction (2) is faster than Reaction (1) so that  $O^-$  is not observed.  $O_2^-$  is considered to be the most stable anion radicals among  $O^-$ ,  $O_2^-$ , and  $O_3^-$  under the existence of  $N_2O$ .

$O_3^-$  was discussed to be formed through the reaction of  $O_2^-$  and  $N_2O$  in 3.3, thus, Reaction (3) and (4) is considered to occur. The Arrhenius plot of Fig.5 gives the straight line below 253 K. So, Reactions (3) has an activation energy of 19 kJ/mol. On the other hand, the activation energy of Reaction (4) might be higher than this, because Reaction (4) is prevailing at higher temperature. The produced  $N_2$  and  $O_2$  may be so little to be detected gaschromatographically.

At the high temperature such as 573 K,  $N_2O$  decomposition reaction may occur catalytically. Under these conditions, the concentration of such radical species must be quite low because of the short life time. However, these radicals can be the intermediate of the catalysis as follows:



Active site formation

Catalysis

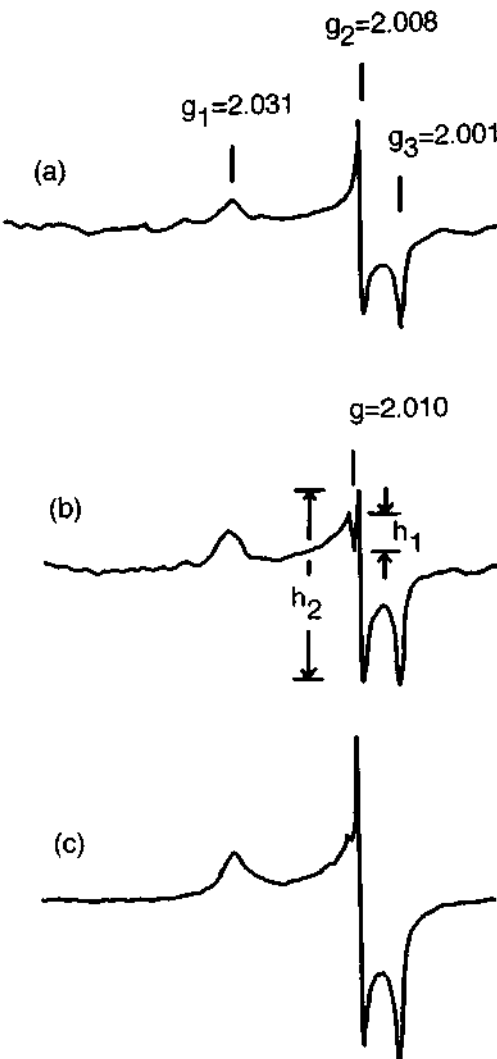


Fig. 4 EPR spectra of surface oxygen species on  $ZrO_2$  at 77 K. a) Sample contacted with  $N_2O$  at 298 K. b) Sample warmed up to 253 K under  $N_2O$ . c) Sample contacted with  $O_2$  at 253 K.

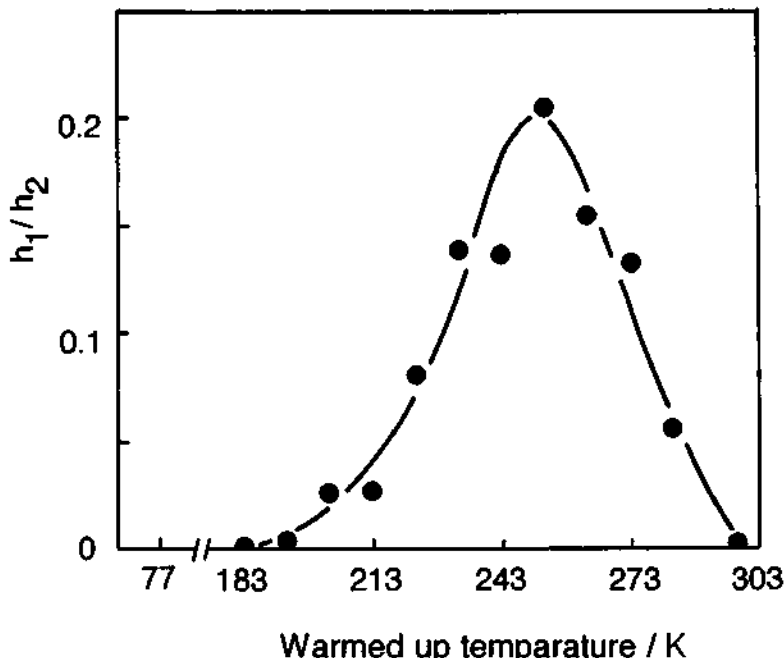


Fig. 5 Relative peak height ratio of  $O_3(h_1)$  vs.  $O_2(h_2)$  as a function of temperature. The spectra were taken after  $N_2O$  introduction on  $ZrO_2$ .  $h_1$  and  $h_2$  are shown in Fig. 4-b.

These findings must contribute to the study of catalytic decomposition of  $N_2O$  and catalytic oxidation reactions at the high temperature. Of course a further study is necessary as is shown in the other system[12].

#### References

1. M. Che and A. J. Tench, *Adv. Catal.*, 1982, **31**, 77.
2. M. Che and A. J. Tench, *Adv. Catal.*, 1983, **32**, 1.
3. N. B. Wong and J. H. Lunsford, *J. Chem. Phys.*, 1971, **55**, 3007.
4. K. Aika and J. H. Lunsford, *J. Phys. Chem.*, 1977, **81**, 1393.
5. M. Setaka and T. Kwan, *Bull. Chem. Soc. Jpn.*, 1970, **43**, 2727.
6. J. Kondo, Y. Sakata, K. Domenn, K. Maruya, and T. Onishi, *J. Chem. Soc., Faraday Trans.*, 1990, **86**, 397.
7. T. Maehashi, K. Maruya, K. Domen, K. Aika, and T. Onishi, *Chem. Lett.*, 1984, 747.
8. K. M. Wang and J. H. Lunsford, *J. Phys. Chem.*, 1971, **75**, 1165.
9. Y. Mizokawa, S. Nakamura, *Ohyobutsuri*, 1977, **46**, 580.
10. M. Anpo, N. Aikawa, and Y. Kubokawa, *J. Chem. Soc., Chem. Commun.*, 1984, 644.
11. P. Meriaudeau, and J. C. Vedrine, *J. Chem. Soc., Faraday Trans. II*, 1976, **72**, 472.
12. K. Aika, M. Isobe, M. Tajima, and T. Onishi, *Proc. 8th. Intern. Congr. Catal.*, Dechema ed. Verlag Chemie., Weinheim, 1984, vol. 3, 335.

## 2.13 Oxygen Isotope Exchange between CO<sub>2</sub> Adsorbate and MgO Surfaces

Y. Yanagisawa,<sup>a</sup> K. Takaoka,<sup>a</sup> and S. Yamabe<sup>b</sup>

<sup>a</sup>Department of Physics, <sup>b</sup>Department of Chemistry, Nara University of Education, Takabatake-cho, Nara 630, Japan

### Abstract

Thermal desorption (TD) of C<sup>18</sup>O<sup>16</sup>O and C<sup>16</sup>O<sub>2</sub> gases after C<sup>18</sup>O<sub>2</sub> adsorption on MgO powders was observed in the temperature range 350-1000 K, suggesting that single and double oxygen exchanges occur on the surfaces. To elucidate the exchange mechanism, an *ab initio* molecular orbital (MO) calculation was performed using a cluster model of defect sites of MgO surfaces. The single exchange is found to take place via a bidentate CO<sub>3</sub> intermediate, and the double exchange may proceed by surface migration through a CO<sub>3</sub> intermediate.

### 1. INTRODUCTION

MgO is widely known to be a catalyst for hydrogenation and oxidation of CO and for H-D exchanges between CH<sub>4</sub> and D<sub>2</sub>. These reactions are explained in terms of basic properties of the surfaces[1]. Recently, CO<sub>2</sub> adsorption on an MgO(100) surface was precisely investigated below room temperature (RT) under ultra-high vacuum, where only weakly physisorbed CO<sub>2</sub> was observed[2]. More recently, we have reported preliminarily the observation of oxygen isotope exchange between C<sup>18</sup>O<sub>2</sub> and defective MgO surfaces[3]. In this work, we report the TD of C<sup>18</sup>O<sub>2</sub>, C<sup>16</sup>O<sup>18</sup>O and C<sup>16</sup>O<sub>2</sub> from C<sup>18</sup>O<sub>2</sub> adsorbed MgO powders and a plausible oxygen exchange mechanism based on CO<sub>3</sub>-type intermediate species. This is the first MO calculation dealing with the oxygen bond interchange between CO<sub>2</sub> and oxide surfaces.

### 2. EXPERIMENTAL

Two kinds of MgO samples, "Specpure" grade powders from Johnson-Matthey Chem. Ltd. (MgO-JM) and grinding single crystals from Tateho Co. (MgO-T), were preheated at 1150 K in a quartz tube attached to a vacuum system. The base pressure was about 1×10<sup>-8</sup> Torr. After being cooled down to

RT, the sample was exposed to  $\text{C}^{18}\text{O}_2$  gas (99% purity, ICON) with the exposure range of  $10^2$  to  $10^5$  L ( $1 \text{ L} = 10^{-6}$  Torr·s) in the dark. Temperature programmed desorption (TPD) measurements were carried out up to 1150 K with a heating rate of 0.5 K/s by using a quadrupole mass spectrometer (ULVAC, MSQ-400). The mass peaks from 28 to 36 and from 44 to 48 were repetitively scanned.

### 3. EXPERIMENTAL RESULTS

After several cycles of exposure and TPD, reproducible TD curves of  $\text{C}^{16}\text{O}_2$ ,  $\text{C}^{16}\text{O}^{18}\text{O}$  and  $\text{C}^{18}\text{O}_2$  gases were obtained for both MgO powders. The TPD profiles of  $\text{CO}_2$  and CO from MgO-JM and MgO-T powders are observed after 2000 L  $\text{C}^{18}\text{O}_2$  exposure at RT as shown in Fig. 1 (a) and (b), respectively.

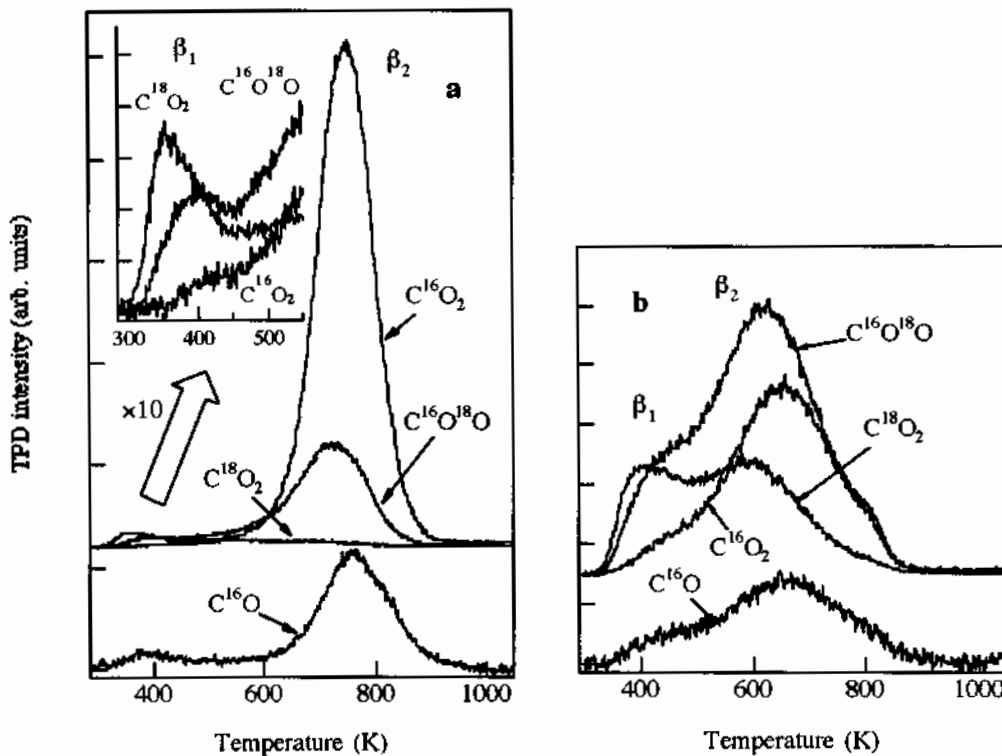


Fig. 1. TD curves after  $\text{C}^{18}\text{O}_2$  exposure at RT from (a) MgO-JM and (b) MgO-T powders.

For (a) MgO-JM, TD's of  $\text{C}^{18}\text{O}_2$  and  $\text{C}^{16}\text{O}^{18}\text{O}$  have weak peaks ( $\beta_1$ ) at 350 and 400 K, respectively, while almost negligible desorption amount of  $\text{C}^{18}\text{O}_2$  is observed more than 600 K. Peak  $\beta_2$  at about 720–750 K consists mainly of  $\text{C}^{16}\text{O}_2$  with a small amount of  $\text{C}^{16}\text{O}^{18}\text{O}$ . For (b) MgO-T, main TD peaks ( $\beta_2$ ) of  $\text{C}^{18}\text{O}_2$ ,  $\text{C}^{16}\text{O}^{18}\text{O}$  and  $\text{C}^{16}\text{O}_2$  are observed at 600, 620 and 650 K, respectively.

TD of C<sup>18</sup>O<sub>2</sub> has a peak ( $\beta_1$ ) at 400 K with a nearly equal amount of C<sup>16</sup>O<sup>18</sup>O. Thus, a thermal oxygen exchange between adsorbed CO<sub>2</sub> molecules and lattice oxygens takes place on both MgO surfaces. The TD of C<sup>16</sup>O is observed in the same temperature range as that of C<sup>16</sup>O<sub>2</sub>. This carbon monoxide seems to be a fragment product of desorbed C<sup>16</sup>O<sub>2</sub>, while the relative intensity of the CO TD is slightly larger than that of ordinary fragment component of CO<sub>2</sub>. No TD's of oxygen molecules were observed with or without C<sup>18</sup>O<sub>2</sub> exposure. The TD amounts of C<sup>16</sup>O<sub>2</sub>, C<sup>16</sup>O<sup>18</sup>O and C<sup>18</sup>O<sub>2</sub>, which correspond to the areas under the respective TD peaks, increased linearly up to 4000 L and are almost saturated at more than 10<sup>4</sup> L. The total TD amounts of MgO-JM are five times as large as those of MgO-T for the same sample weight. The ratios (R's) of total TD amounts among C<sup>18</sup>O<sub>2</sub>, C<sup>16</sup>O<sup>18</sup>O and C<sup>16</sup>O<sub>2</sub> for MgO-JM and MgO-T are about 0.1:0.2:0.7 and 0.3:0.5:0.2, respectively. The difference of the total TD amounts and R's between two MgO samples may be due to the different distributions of reactive adsorption sites. By the initial rise method based on the Arrhenius plot of the C<sup>16</sup>O<sub>2</sub> TD intensity for the peak  $\beta_2$ , the activation energies for desorption (E<sub>d</sub>'s) are roughly estimated to be ~1.2 and 1.0 eV for MgO-JM and MgO-T, respectively. These large E<sub>d</sub>'s suggest that bond interchange for the exchange may occur via the chemisorption, leading to the C<sup>16</sup>O<sub>2</sub> and C<sup>16</sup>O<sup>18</sup>O TD peaks.

#### 4. DISCUSSION ON THE OXYGEN EXCHANGE MECHANISM

O<sub>2</sub> molecules are adsorbed on metal oxides as monodentate or bidentate carbonate species based on infrared spectroscopy[4,5]. On magnetite (Fe<sub>3</sub>O<sub>4</sub>) surfaces, oxygen exchange between CO<sub>2</sub> and the surfaces was examined with TPD measurements after C<sup>18</sup>O<sub>2</sub> exposure, and C<sup>16</sup>O<sup>18</sup>O TD was observed in the temperature range from 200 to 500 K[6]. This indicated that single oxygen exchange occurred through bidentate CO<sub>3</sub> intermediates including a surface oxygen atom (16O<sub>S</sub>). To study the oxygen bond interchanges on MgO surfaces, a preliminary cluster-model geometry optimization with the *ab initio* MO is performed. Recently, Pacchioni investigated the interaction of CO<sub>2</sub> with regular and defect sites on the MgO(100) surface by means of *ab initio* cluster model SCF calculation, and indicated the formation of monodentate carbonates at a low-coordinated oxygen (OLC) site such as a step on the (100) surface (O<sub>4C</sub>)[7]. At first, we examine the CO<sub>2</sub> adsorption at three types of low-coordinated oxygen atoms (O<sub>5C</sub>, O<sub>4C</sub> and O<sub>3C</sub>) in order to compare the stability of adsorbed species and the formation of monodentate and/or bidentate carbonates. Since we prefer to use a cluster as large as possible, the RHF/STO-3G method implemented in the GAUSSIAN 92 program (G92)[8] was used without the Madelung potential. All the calculations were carried out,

using G92 installed at the CONVEX computer at the Information Processing Center of Nara University of Education.

The surface cluster models optimized partially are shown in Fig. 2. As pointed out by Pacchioni[7], a monodentate carbonate is obtained at the O<sub>4C</sub> site (b), while a weak adsorption state is obtained at O<sub>5C</sub> site (a) in the present calculation. The equilibrium distances ( $r_e$ 's) of C-O<sub>LC</sub> (LC=4C and 5C) are 1.33 and 1.44 Å, respectively, and the bending of adsorbed CO<sub>2</sub> molecule occurs (bending angle=140°). The STO-3G stabilization energies (E<sub>s</sub>'s), which are obtained by the difference of the STO-3G total energies, are -7.83 and -1.36 eV, for O<sub>4C</sub> and O<sub>5C</sub>, respectively. These values appear to be overestimated by the small basis set. A bidentate-like carbonate is formed at a corner site (O<sub>3C</sub>) (in Fig. 2 (c)). E<sub>s</sub> is -6.59 eV,  $r_e$  is 1.41 Å, the C=O distance is 1.23 Å with a small bond elongation (1.19 Å for free CO<sub>2</sub>), and a newly formed Mg-O bond is of 1.82 Å.

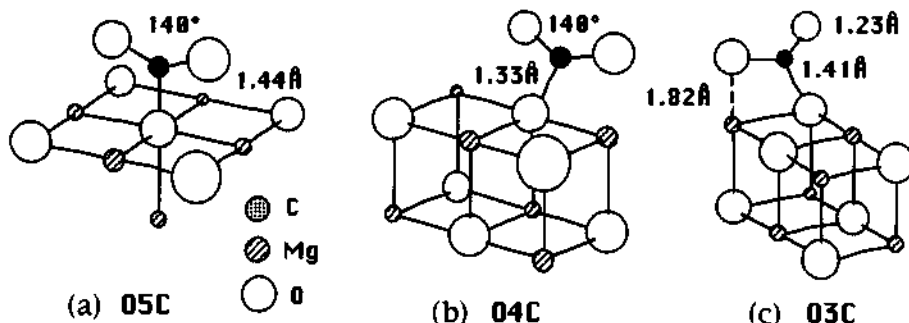


Fig. 2. Surface cluster models of CO<sub>2</sub> adsorption at low-coordinative oxygen ions (OLC). All surface atoms are located at lattice points, and the position of CO<sub>2</sub> molecule is optimized partially with RHF/STO-3G. (a) Mg<sub>5</sub>O<sub>5</sub>/CO<sub>2</sub> for O<sub>5C</sub>, (b) Mg<sub>6</sub>O<sub>6</sub>/CO<sub>2</sub> for O<sub>4C</sub>, and (c) Mg<sub>6</sub>O<sub>6</sub>/CO<sub>2</sub> for O<sub>3C</sub> sites. The Mg-O distance is taken to be 2.1065 Å, the bulk value.

The optimized geometries in Fig. 2 have shown that step sites on a (100) surface do not provide a reaction site for the exchange and that an O<sub>3C</sub> site

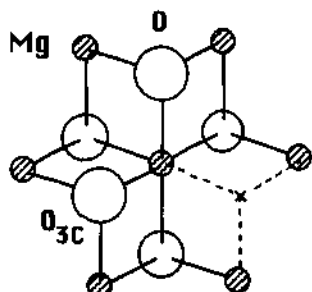


Fig. 3. The surface model of a step site on a (111) micro-surface as an Mg<sub>7</sub>O<sub>5</sub> cluster. The point x stands for an oxygen vacancy. O<sub>3C</sub> learned from Fig. 2(c) and prepared for formation of a bidentate-like carbonate.

is necessary to form bidentate carbonates. Hence, as shown in Fig. 3, we select a Mg<sub>7</sub>O<sub>5</sub> cluster for the O<sub>3C</sub> site with a nearby oxygen vacancy (x) on a (111) micro-surface, as in the case of CaO/O<sub>2</sub>[9]. The vacancy x would allow more

$^{18}\text{O}\cdot\text{Mg}$  contact and the subsequent transformation of the adsorbate oxygen to the lattice one.

The single exchange is examined in the surface model of Fig. 3. When a  $\text{C}^{18}\text{O}_2$  approaches the undistorted  $\text{MgO}$  surface, it is trapped as a bidentate-like carbonate (state B) in Fig. 4. It is noteworthy that the one oxygen atom O(3) is captured near the oxygen vacancy site (point  $\times$ ). In state B, the C(2)-O(3) bond length is 1.38 Å, and C(2)-O(1) and C(2)=O(4) distances are 1.40 and 1.23 Å, respectively. Thus,  $\text{CO}_2$  is bound tightly to the surface to form the asymmetric bidentate  $\text{CO}_3$  via chemisorption. Next, the  $C_s$ -symmetry structure is obtained for independent determination of locations of four atoms O(1), C(2), O(3) and O(4) (state C). This bridged and symmetric bidentate geometry is the turning point of the single oxygen exchange. That is, if the C(2)-O(3) bond is cleaved in the state C, the  $\text{C}(2)\text{O}(1)\text{O}(4)$  molecule is formed, and it is possible for the half-exchanged  $\text{CO}_2$  molecule (i.e.,  $\text{C}^{16}\text{O}^{18}\text{O}$ ) to desorb thermally ( $\text{C}\rightarrow\text{D}\rightarrow\text{E}$ ). Thus, the state C is the key intermediate for the single exchange. The  $E_s$  at route  $\text{A}\rightarrow\text{B}$  is -6.59 eV and that at  $\text{B}\rightarrow\text{C}$  is -0.51 eV. It is interesting that the former  $E_s$  (-6.59 eV) is the same as that in Fig. 2(c) in spite of the difference of  $^{18}\text{O}\cdot\text{Mg}$  linkages. This accidental coincidence suggests that not  $\text{Mg}\cdots\text{O}$  but  $\text{C}\cdots\text{O}$  bond formation and cleavage are the driving force of the reaction.

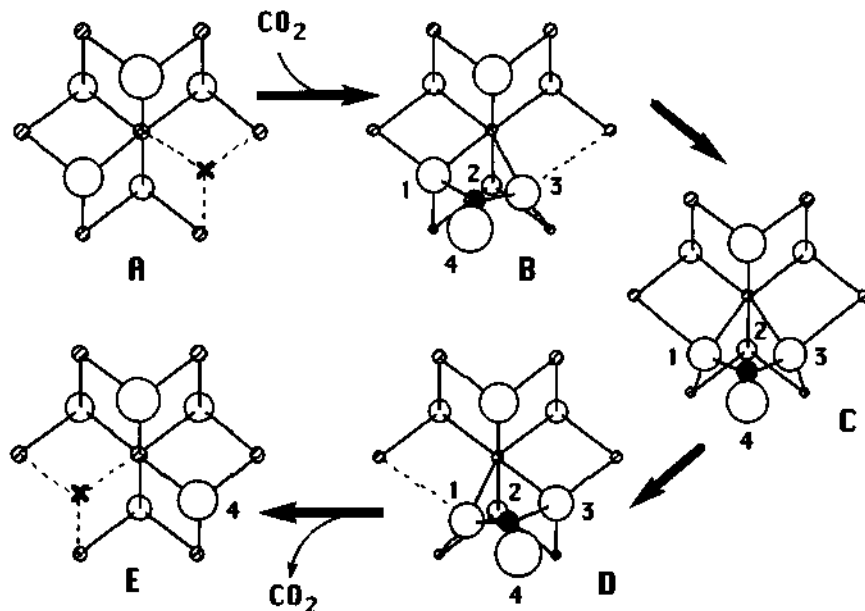


Fig. 4. Schematic representation of geometric changes of the single oxygen exchange reaction optimized partially with RHF/STO-3G. In state B, positions of C(2), O(3), and O(4) are optimized. In state C, positions of O(1), C(2), O(3), and O(4) are optimized. States B, C and D are of  $\text{Mg}_7\text{O}_5\text{-CO}_2$ .

A simple bidentate carbonate, however, may not be compatible with the large amount of the TD peak  $\beta_2$  of double exchanged  $\text{CO}_2$  species in Fig. 1. Thus, the process described above may be operative for  $\text{C}^{16}\text{O}^{18}\text{O}$  TD (peak  $\beta_1$ ), or may correspond to a precursor state for the double exchange process. One probable double oxygen exchange process between adsorbed  $\text{C}^{18}\text{O}_2$  molecules and  $^{16}\text{O}_8$  atoms is as follows.  $\text{CO}_2$  may be trapped at  $\text{O}_3\text{C}$  site with a nearby oxygen vacancy, and oxygen exchange may take place through bidentate  $\text{CO}_3$  formation (Fig. 4) on the first step. As the next step, the double bond,  $\text{C}(2)=\text{O}(4)$ , in the bidentate  $\text{CO}_3$  may be broken when this oxygen atom is trapped at another nearby oxygen vacancy to elongate the C-O distance. Adsorbed  $\text{CO}_2$  may migrate across the surface before desorption, and oxygen exchange may take place successively through bidentate  $\text{CO}_3$  formation. A long  $\text{CO}_2$  residence time on surfaces may yield a substantial exchange because of a high excess of the lattice oxygen. The  $\text{MgO-JM}$  powder would have a larger population of neighboring oxygen vacancies available for the  $\text{CO}_2$  migration than the  $\text{MgO-T}$  powder, which results in the difference of the yield R. However, an actual double exchange mechanism is not yet obvious, and an MO calculation with new cluster models is now in progress.

Another possibility for  $\text{C}^{16}\text{O}_2$  TD may be the formation of surface peroxy-type ions,  $(^{16}\text{O}_8)_2^{2-}$ , before  $\text{CO}_2$  exposure, and adsorbed  $\text{C}^{18}\text{O}_2$  may interact with the peroxy ions to form temporary intermediate rolling carbonate ions during the exposure or TD run[3]. However, we have no evidence of the presence of surface peroxy ions.

## References

- [1] H.Hattori, in *Adsorption and Catalysis on Oxide Surfaces*, ed. M.Che and G.C.Bond (Elsevier, Amsterdam, 1985), pp. 319-330.
- [2] D.L.Meixner, D.A.Arthur and S.M.George, *Surf. Sci.*, 1992, 261, 141.
- [3] Y.Yanagisawa, Y.Shimotama and A.Ito, *J. Chem. Soc. Chem. Commun.* 1993, 610.
- [4] J.Kondo, H.Abe, Y.Sakata, K.Maruya, K.Domen and T.Onishi, *J. Chem. Soc. Faraday Trans. I*, 1988, 84, 511.
- [5] R.Philipp and K. Fujimoto, *J. Phys. Chem.*, 1992, 96, 9035.
- [6] T.J.Udovic and J.A.Dumesic, *J. Catal.*, 1984, 89, 314.
- [7] G.Pacchioni, *Surf. Sci.*, 1993, 281, 207.
- [8] GAUSSIAN 90, revision F, M.J.Frisch, M.Head-Gordon, G.W.Trucks, J.B.Foresman, H.B.Schlegel, K.Raghavachari, M.A.Robb, J.S.Binkley, C.Gonzalez, D.J.DeFrees, D.J.Fox, R.A.Whiteside, R.Seeger, C.F.Melius, J.Baker, R.L.Martin, L.R.Kahn, J.J.P.Stewart, S.Topiol and J.A.Pople, Gaussian, Inc., Pittsburgh, PA, 1990.
- [9] Y.Yanagisawa, S.Yamabe, K.Matsumura and R.Huzimura, *Phys. Rev.*, 1993, B48, 4925.

## 2.14 Evaluation of Basicity of Alkali Metal-doped MgO in the Scope of Change of Carbonate Species

Tohru Kanno and Masayoshi Kobayashi

Department of Chemical System Engineering, Kitami Institute of Technology,  
165 Kohen-cho, Kitami 090, Japan

### Abstract

Four kinds of alkali metals were used as the modifier of the surface of MgO in order to evaluate basicity qualitatively and quantitatively. Doses of them changed the composition of CO<sub>2</sub>-derived species drastically: increased the intensity of IR absorption of unideterminate carbonate and decreased the intensities of bidentate carbonate and linear CO<sub>2</sub>. This result was associated with the change of acid/base properties of the surface.

More quantitative parameters were derived from the IR frequency of unideterminate carbonate and the TPD profile, and these two parameters showed a linear correlation. This correlation seemed to make it possible to characterize basicity comparably with two techniques.

### 1. INTRODUCTION

Much works have been devoted to solid acid catalysts so far. The numbers of the results concerning basic materials, on the other hand, seem to be much few; one of the reason may rise in the fact that they are poisoned by water and CO<sub>2</sub> more easily, which causes the steep decrease of catalytic activity and makes it difficult to characterize the surface. Nevertheless, investigating the properties of basic solids especially in terms of proper evaluation of basicity would be desirable from the viewpoint of catalyst design.

Alkali metal is used as one of the typical modifiers of many kinds of metal and metal oxide catalysts [1]. As is well-known, one of their distinct functions is electron-donating ability leading to the enhancement of basicity of metal oxides. What we would like to make an attempt in this paper is qualitative and quantitative evaluation of basicity of alkali metal-doped MgO by correlating two results: IR (infrared) spectra with TPD (temperature programmed desorption) profiles after CO<sub>2</sub> admission, focusing on the changes of composition of CO<sub>2</sub>-derived species and their IR frequencies, and also the dependency of alkali metals on this change.

### 2. EXPERIMENTAL

#### (1) Preparation of the Sample

10 g of MgO powder (Merck Corp.) was suspended in 100ml-redistilled water on a hot plate. The obtained Mg(OH)<sub>2</sub>-slurry was evaporated under agitation for several hours, dried in an oven at 363 K overnight and then crushed to be under 400 meshed powder. The alkali metal-doped samples were prepared by adding aqueous alkali metal

hydroxide (Wako Pharmaceutical Corp., Special Grade) solutions into the  $Mg(OH)_2$ -slurry and the amount added was ranging from 0.46 to 10 wt%-metal to  $MgO$ . The other procedure was same as in the case of non-doped  $MgO$ .

### (2)IR Measurement

50 mg of the powder mentioned above was compressed to be a disk of 2 cm in diameter and was put in the IR cell made of quartz glass. Prior to exposure of gases, the disk was heated gradually and kept at 1073 K for 3 hrs *in vacuo*. IR measurement, using Shimadzu FT-IR 8000, was made at beam temperature through KBr windows. The resolution and scanning times were  $4\text{ cm}^{-1}$  and 100, respectively.

### (3)TPD Measurement

1 g of the powder was packed in the tubular flow reactor, which was made of quartz glass (I.D. 8 mm), and was pretreated at 1073 K in an helium stream. TPD spectra were obtained in an helium stream of 100 ml/min(STP) after the samples were exposed to  $CO_2$  gas-flow at 573 K for 3 hrs, followed by cooling down to room temperature. The heating rate was 3 K/min. The composition of the gas evolved at the outlet of the reactor was analyzed by a gas chromatograph with a thermal conductivity detector.

## 3.RESULTS AND DISCUSSION.

### 3-1.Presentation of a TPD Parameter for Evaluating Basicity

Figure 1 shows TPD profiles of  $CO_2$  on  $MgO$  and alkali metal-modified  $MgO$ , where the parenthesized numbers mean the wt. % of the doped-alkali metal to  $MgO$ . Peaks at higher temperature were observed on the alkali metal-doped samples. A dose of 1 wt.-%-Li, in particular, gave rise to two clear peaks at higher temperature than 673 K: at around 680 and 820 K, which did not appear on non-doped  $MgO$ . The other samples also showed the similar tendency although it was less clearer. As the decomposition temperatures of alkali metal carbonates are 891, 1125 and 1164 K for Li, Na and K, respectively, these peaks mentioned above were ascribed to the species not on alkali metals but on  $MgO$ , and therefore to its acid/base properties. There was no effect of doses of Cs as far as the TPD profiles are concerned, which were not shown in the figure.

The distribution of basic sites reflects upon that of the temperatures at which  $CO_2$  desorbs; the higher is the temperature, the stronger is the basicity [2-3]. From the graphical integrations of the TPD profile of  $CO_2$  for each sample, we employed the ratio of the amount desorbed at higher temperature than 673 K, shown in the shaded area in Fig.1, to the total amount:  $\frac{\text{higher temp}}{\text{total}} (= R)$

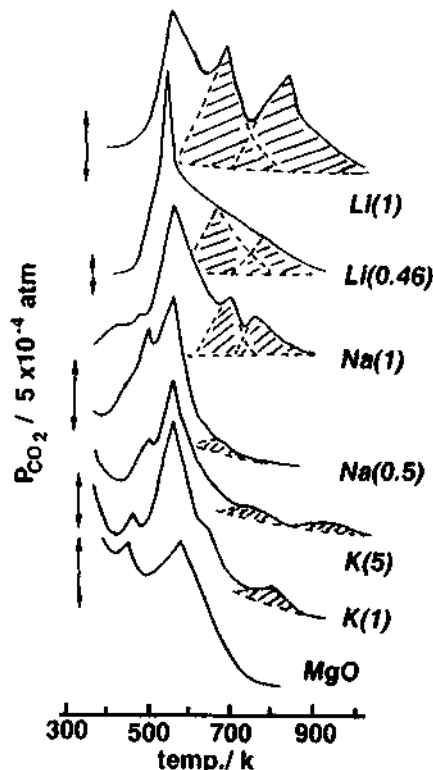


Fig.1. TPD profiles in an He stream after exposure of a  $CO_2$ -flow at 573 K.

as a parameter for evaluating basicity, which we call *TPD parameter*. As is easily seen from the original data (Fig.1), Li(1) showed much the highest value of R of all the samples.

### 3-2. Characterization of IR Spectra.

IR spectra on MgO and alkali metal-doped MgO after exposure of CO<sub>2</sub> are shown by Fig.2. On MgO, bidentate carbonate at 1660-1620, 1330-1270 cm<sup>-1</sup>, (designated as bi.c.) and linear CO<sub>2</sub> at around 2350 cm<sup>-1</sup> were mainly observed. On the alkali metal-doped samples, the intensities of bi.c. and/or linear CO<sub>2</sub> decreased, while the intensity of unidentate carbonate at 1570-1530, 1410-1360 cm<sup>-1</sup> (designated as uni.c.) increased. This tendency became much more prominent on Li(1) as in the case of our TPD profiles in which Li showed the highest modification effect on MgO.

It is widely accepted that acidic sites are responsible for linear CO<sub>2</sub> and both acidic and basic sites are for carbonates [4]. Furthermore, it would be reasonable that surface lattice oxygen contributes to producing uni.c. more than bi.c. taking into account the difference of structures between two carbonate species; bi.c. has the direct ligand to Mg<sup>2+</sup>(acidic site) as well as O<sup>2-</sup>(basic one) on MgO for its formation, while uni.c. needs the only one ligand to O<sup>2-</sup>. So the alkali metal-enhanced basicity are favorable to uni.c. due to the strengthened bond of C

and lattice O. Bi.c., on the other hand, would tend to be unstable, because the bond of Mg and O of bi.c. is weakened by less acidity, which was clarified by the decreased intensities of linear CO<sub>2</sub>. This idea was illustrated by Fig.3. Conclusively higher basicity by doses of alkali metals leads to change in the make-up of CO<sub>2</sub>-derived species due to the modification of the surface anion and cation properties.

### 3-3. Presentation of an IR Parameter

From the IR results obtained and the consideration above, doses of alkali metals were found to cause the change of the composition of carbonates. But this change is rather qualitative than quantitative for evaluating basicity because of ambiguous separation of the IR peaks.

As the numerical parameter, we should focus on the frequencies of IR absorptions. Tanabe et al.[5] reported that the partial charge of oxygen on metal

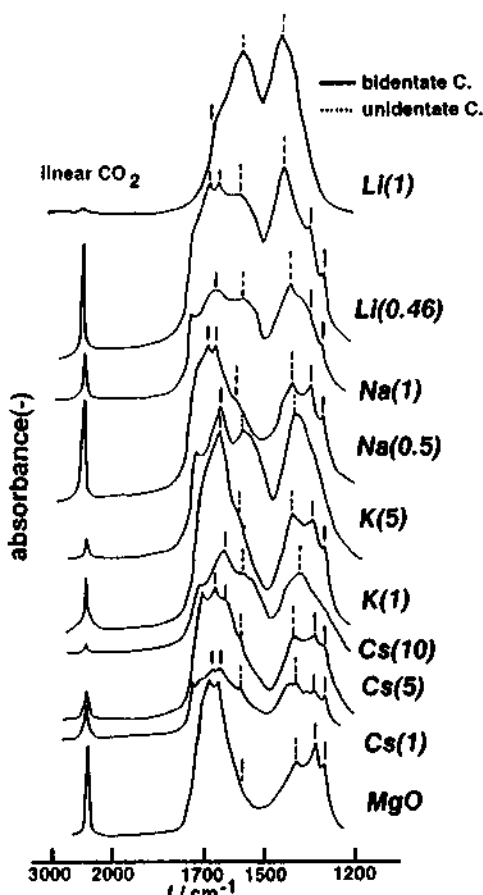


Fig.2. IR spectra of CO<sub>2</sub>-derived species after exposure of 5 torr at r.t., followed by 573 K.

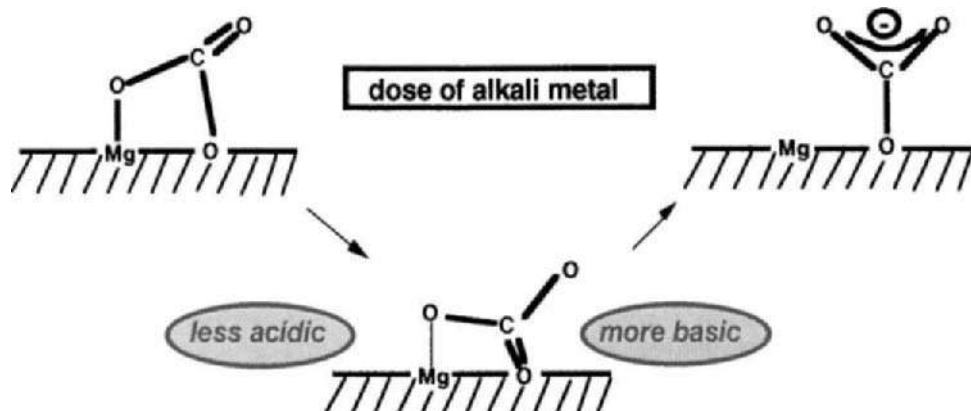


Fig.3. A scheme of change of the carbonate by a dose of alkali metal.

oxides:  $\delta_{\text{O}}$  correlated with  $\Delta\nu$ : the difference of the IR frequencies between asymmetric and symmetric stretching vibration of OCO of unidentate carbonate; the decrease of  $\Delta\nu$  was accompanied by the increase of  $\delta_{\text{O}}$ , leading to the enhancement of basicity. On  $\text{MgO}/\text{Al}_2\text{O}_3$  [6] and  $\text{MgO}/\text{CaO}$  [7-8] mixed oxides, furthermore,  $\Delta\nu$  was found to depend on the make-up of each sample and these diversified  $\Delta\nu$  were ascribed to changes in the surface basicity. In the former case, the mixture of basic and non-basic metal oxides, reciprocal  $\Delta\nu$  increased linearly with the increase of the content of  $\text{MgO}$  and was, therefore, confirmed to be a proper index of basicity. So we employed this parameter for alkali metal-

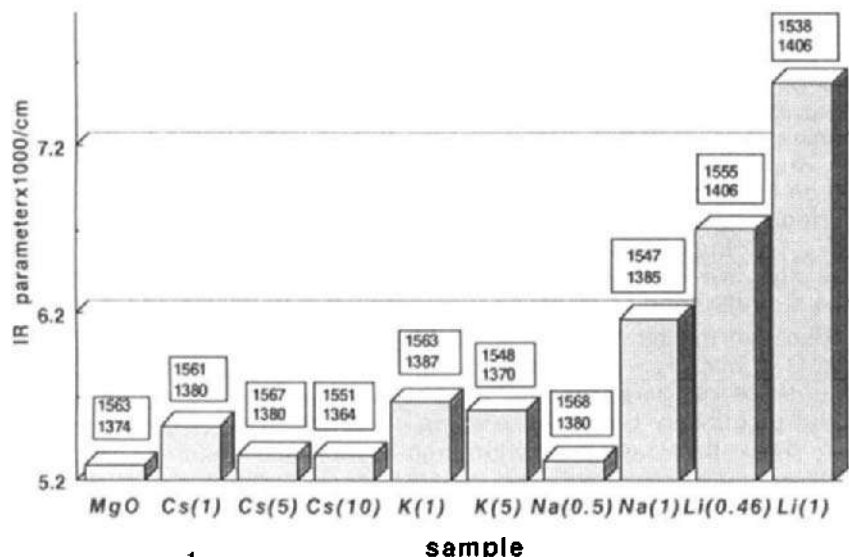


Fig.4.  $(\Delta\nu)^{-1}$  of alkali metal-doped  $\text{MgO}$ .

$\Delta\nu$ : wavenumber difference of asym. and sym.str.vib.of OCO of unidentate carbonate; observed wavenumbers are shown over each bar by upper and lower parts, respectively.

doped MgO, where we designate  $(\Delta \nu)^{-1}$  as IR parameter. The estimated  $(\Delta \nu)^{-1}$  and the observed IR frequencies were compared for the alkali metal-doped samples in Fig.4. Li(1) showed the largest value in the order of Li- > Na- > K- > Cs- > non-doped MgO.

### 3-4.A New Correlation of the IR parameter with the TPD parameter.

As is  $\Delta \nu$  so, R is considered to be a parameter for evaluating the relatively averaged strength of base on each sample, because it is not the quantity of  $\text{CO}_2$  but the ratio of the two quantities. It is, therefore, interesting to look at how the two parameters [R and  $(\Delta \nu)^{-1}$ ] correlate and the result was plotted in Fig.5. They showed a linear correlation. This correlation made us expect the feasibility of comparable evaluation of basicity with employing two techniques, that is to say, evaluation of the distribution of the basic sites of various strength. Nevertheless, the detailed correlation of each species obtained from the IR spectra and the TPD profiles remained questionable.

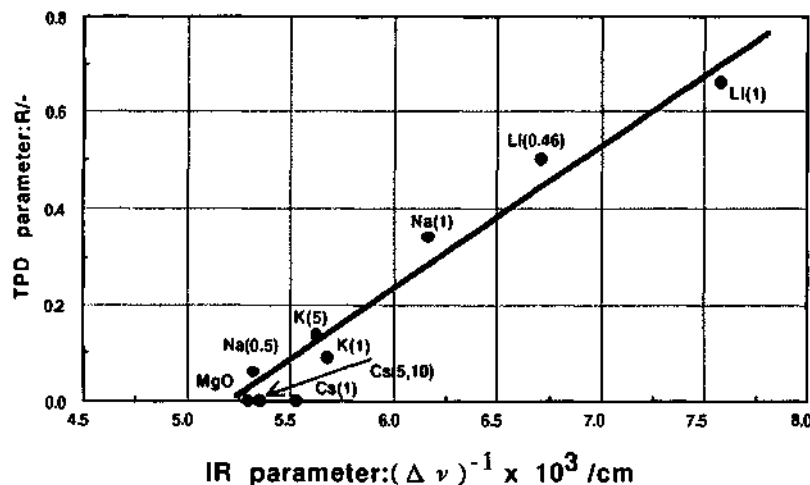


Fig.5. Correlation of the basicity evaluated by the two parameters.

R:  $q_{\text{higher temp.}}/q_{\text{total}}$

$\Delta \nu$ : wavenumber difference of asym. and sym.str.vib.of OCO of unidentate carbonate

In this figure,  $(\Delta \nu)^{-1}$  resulted in ranging from  $5.29 \sim 7.58 \times 10^{-3}$  under the change in R of 0.66. This estimation corresponds to the change of  $6.93 \times 10^{-6}$  mol- $\text{CO}_2/\text{m}^2$  desorbed at higher temp., and to the increase of about 37 % of stronger basic sites in the total number of the surface lattice oxygens:  $18.7 \times 10^{-6}$  based on (001) face. That may lead to the idea that  $(\Delta \nu)^{-1}$  also has a quantitative aspect to evaluate basicity. In other words, the IR spectroscopy may be one method to reconfirm the quantity of the stronger basic sites. Still more profound discussion would be necessary in terms of physical and chemical significance of the correlation of the two parameters.

The modification effect of alkali metals on MgO obtained from both IR and TPD spectroscopies consistently resulted in the order of ionization potential of Li > Na >

K > Cs: the reverse order of electron donating ability. The reason of lithium's commonly much high values of two parameters has not been clarified at present. But if ionization potential had been a primary factor of modification, lithium would have shown the least effect because of its lowest electron donating ability. The other factor such as ion size, therefore, must exist in the case of MgO because the sizes of Mg and Li ions are very close: 0.066 and 0.068 nm, respectively. One of our speculation is that such a Li-substituted Mg site as suggested by Itoh, Lunsford et al. [9] and Wang and Lunsford [10] can be a more effective electron donor, and consequentially induces the stronger basic sites than any other alkali metal.

## REFERENCES

- [1] W.D.Mross, *Catal.Rev.-Sci.Eng.*, **1983**, 25(4), 591.
- [2] G.Zhang, H.Hattori and K.Tanabe, *Appl.Catal.*, **1988**, 36, 189.
- [3] V.R.Choudhary and V.H.Rane, *Catal.Lett.*, **1990**, 4, 101.
- [4] C.Morterra, G.Ghiotti, F.Bocuzzi and S.Coluccia, *J.Catal.*, **1978**, 51, 299 .
- [5] Y.Fukuda and K.Tanabe, *Bull.Chem.Soc.Jpn.*, **1973**, 46, 1616.
- [6] A.Lercher, C.Colombier and H.Noller, *J.Chem.Soc., Faraday Trans.1*, **1984**, 8, 949.
- [7] R.Philipp and K.Fujimoto, *J.Phys.Chem.*, **1992**, 96, 9035.
- [8] R.Philipp, K.Omata, A.Aoki and K.Fujimoto, *J.Catal.*, **1992**, 134, 422.
- [9] T.Itoh, J.Wang, C.Lin and J.H.Lunsford, *J.Am.Chem.Soc.*, **1985**, 107, 5062.
- [10] J.Wang and J.H.Lunsford, *J.Phys.Chem.*, **1986**, 90, 5883.

## 2.15 IR Characterization of Base Heterogeneity of Solid Catalysts

Hui Wang, Shishao Tan and Fu Zhi

Research Institute for Chemical Engineering of Coal, Taiyuan University of Technology,  
Taiyuan, Shanxi, 030024, China

### Abstract

When a pyrrole molecule interacts with some Lewis bases, its NH stretching band in the infrared spectrum shifts to the lower frequency in varying degrees. The amount of the shift depends on the base strength of those bases with which the pyrrole interacts. Similarly, when pyrrole is adsorbed on basic sites with different basicities on a solid catalyst, separate shifts of the NH stretching band to lower wavenumbers are observed. The amount of these shifts is related to the basicity of the sites as well. Hence, an infrared method to characterize the base heterogeneity of solid catalysts has been developed using pyrrole as the probe molecule.

### 1. INTRODUCTION

IR characterization of acidity of solid catalysts has been practical for almost 30 years<sup>[1]</sup>. On the other hand, IR characterization of basicity of solid catalysts needs to be perfected because, so far, it provides no more information than the apparent basicity<sup>[2]</sup>. The aim of this work is to seek an IR method to characterize the base heterogeneity of solid catalysts.

### 2. BASIC THEORETICAL CONSIDERATIONS

Nozari and Drago<sup>[3]</sup> have found that, when a pyrrole molecule interacts with some Lewis bases, its NH stretching band in the infrared spectrum shifts to the lower frequency in varying degrees and that the amount of the shift depends on the base strength of those bases with which the pyrrole interacts. Seokart and Rouxhet<sup>[2]</sup> also observed the shift of the NH stretching band of pyrroles to lower wavenumbers when they are adsorbed on the basic sites of a solid catalyst. It was found that the amount of the shift from  $3410\text{cm}^{-1}$ , the band of NH stretching of liquid pyrrole,  $\Delta\nu_{\text{NH}}$ , is related to the

basic strength of the adsorbed sites. Therefore, it is believed that, when pyrrole molecules are adsorbed on an adsorbent, the basic sites of which are of different strength, different amounts of shift will be observed. The stronger the basic sites, the more the  $\Delta\upsilon_{NH}$  of pyrrole molecules adsorbed on them. And the area of a certain band is proportional to the number of the corresponding sites with certain basic strength.

### 3. EXPERIMENTATION

#### 3. 1 Adsorbents and Adsorbate Preparation

The adsorbents or samples are pure  $\gamma$ - $Al_2O_3$  and  $\gamma$ - $Al_2O_3$  with different amounts of deposited  $K_2O$  and  $Na_2O$  (0—8%wt) made by depositing different concentrations of potassium acetate or sodium nitrate solutions on small  $\gamma$ - $Al_2O_3$  posts and burning them at 450°C for several hours.

Pyrrole was distilled under vacuum into a storing cell, which was kept away from light and connected to the adsorption system. The pyrrole cell was removed from the system as soon as the yellow coloration appeared again.

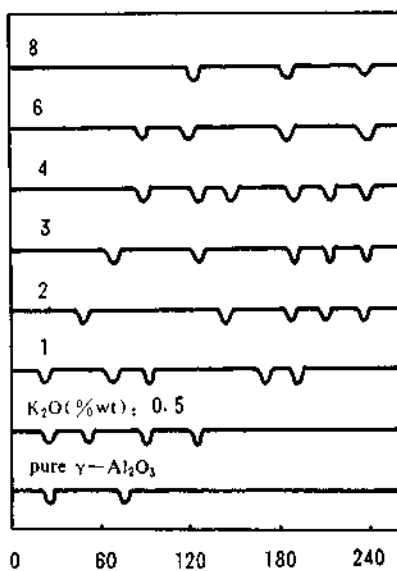


Fig. 1 IR Band positions of NH stretching of pyrrole adsorbed on samples of pure  $\gamma$ - $Al_2O_3$  and  $\gamma$ - $Al_2O_3$  deposited with different amounts of  $K_2O$

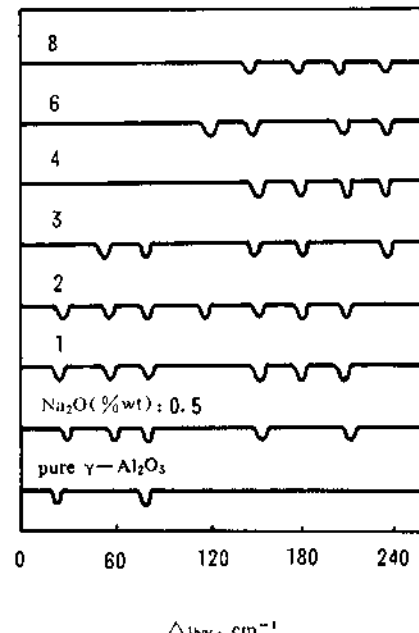


Fig. 2 IR Band positions of NH stretching of pyrrole adsorbed on samples of pure  $\gamma$ - $Al_2O_3$  and  $\gamma$ - $Al_2O_3$  deposited with different amounts of  $Na_2O$

### 3. 2 Experimental Procedures

The samples were made into self-supporting films with effective thickness of 20–30mg/cm<sup>2</sup> obtained by pressing the powder under about 600kg/cm<sup>2</sup>. The films were evacuated in the cell with CaF<sub>2</sub> windows at 500°C for 4 hours until the vacuum reached below  $5.0 \times 10^{-3}$ Pa. Pyrrole was adsorbed at its vapor pressure at 30°C for 10 minutes and then evacuated at the same temperature for 30 minutes. The spectra were recorded using the FTIR—8101 spectrophotometer made by Shimadzu Corporation, Japan.

### 4. RESULTS AND DISCUSSION

According to Scokart and Rouxhet<sup>[2]</sup>, the shift from a limit reference value of 3410cm<sup>-1</sup> of the NH stretching band of adsorbed pyrrole to low wavenumbers ( $\Delta\nu_{\text{NH}}$ ) is related to an increase in the basic strength of the adsorbed sites. Several NH stretching bands in the range of 3410–3050cm<sup>-1</sup> for each sample were observed instead of one as reported in ref. 2. Figures 1 and 2 show all the band positions of those two series of samples, respectively. They show that the band positions are not disorderly. Instead, most of them appear at certain wavenumbers for one series of samples. This makes it reasonable to believe that one band position represents one kind of basic sites with a certain base strength on the surface of adsorbents. Pyrrole molecules adsorb on basic sites of different strength on the surface of one adsorbent, resulting in different shifts of their NH stretching band. Conversely, the different shifts in NH stretching bands of pyrrole adsorbed on a solid catalyst can be used to characterize its base heterogeneity. Plotting the area of each band against its shift value ( $\Delta\nu_{\text{NH}}$ ) we obtain the base distribution for one sample.

On the basis of this it can be deduced that there are two kinds of basic sites on the surface of  $\gamma$ -Al<sub>2</sub>O<sub>3</sub>, since there are two different shifts of NH stretching band of pyrrole adsorbed on it. Compared with the result of Nozari and Drago<sup>[3]</sup> for some liquid Lewis bases, the base strength of these two kinds of sites is equivalent to that of benzene ( $\Delta\nu_{\text{NH}}=30\text{cm}^{-1}$ ) and acetonitrile ( $\Delta\nu_{\text{NH}}=77\text{cm}^{-1}$ ), respectively. Those two kinds of basic sites probably correspond to the structures of basic sites on  $\gamma$ -Al<sub>2</sub>O<sub>3</sub> described in Tanabe's work<sup>[4]</sup>:



Other samples that were deposited with different amounts of K<sub>2</sub>O and Na<sub>2</sub>O have more than two kinds of basic sites. Most of them are stronger than those in  $\gamma$ -Al<sub>2</sub>O<sub>3</sub>. Although the structures of these newly formed sites after depositing cannot be known from the information obtained by this method, the result shows the number of kinds of basic sites

and the relative strength of each kind of site of these deposited samples.

In order to obtain the apparent base strength of a sample,  $B_{ap}$ , we use the equation

$$B_{ap} = \frac{\sum \frac{S_i}{S} \Delta v_{NH,i}}{\sum \frac{S_i}{S}}, \text{ cm}^{-1}$$

where  $\sum$  means summation,  $S_i$  and  $\Delta v_{NH,i}$  represent the area and the shift value ( $\text{cm}^{-1}$ ) of each NH stretching band, respectively and  $S$  represents the area of all NH stretching bands for one sample. The equation can be simplified as follows

$$B_{ap} = \frac{\sum S_i \Delta v_{NH,i}}{S}, \text{ cm}^{-1}$$

In this case, the area of every shifted NH stretching band is almost the same for one sample. Hence, the results of the apparent base strength for these two series of samples, calculated according to the above equation, are shown in Figure 3. The distribution of the base sites with the strength for every sample is a simple straight line.

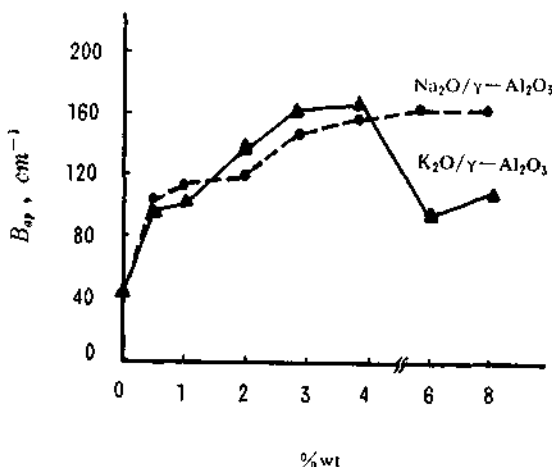


Fig. 3 Apparent base strength,  $B_{ap}$ , of the two series of samples.

#### References

1. Parry, E. P., J. catal., 1963, 2, 371.
2. Seokart, P. O., Rouxhet, P. G., J. C. S. Faraday Trans. I, 1980, 76, 1476.
3. Nozari, M. S., Drago, R. G., J. Amer. Chem. Soc., 1970, 92, 7086.
4. Tanabe, K., "Solid Acids and Bases", Academic Press; New York, 1970.

## 2.16 Structure and Dynamics of Exchanged Cations in Zeolites as Investigated by Molecular Dynamics and Computer Graphics

A. Miyamoto, H. Himei, E. Maruya, M. Katagiri, R. Vetrivel and M. Kubo  
Department of Molecular Chemistry and Engineering, Faculty of Engineering,  
Tohoku University, Aoba-ku, Sendai 980, Japan

### Abstract

The application of molecular dynamics and computer graphics techniques to understand the structure and the dynamics of different exchanged metal cations in zeolite-A, ZSM-5 and mordenite is described. The specific information derived from the above investigations include the distribution of the exchanged cations as well as the aluminum ions in the zeolite frameworks. The relevance of this information to their adsorption and catalytic properties, in many industrially important processes are studied. The illustrative examples include the molecular sieving effect of zeolite-A for the separation of O<sub>2</sub> and N<sub>2</sub>, the role of multivalent cations in ZSM-5 for the deNO<sub>x</sub> process and the distribution of aluminum in mordenite.

### 1. INTRODUCTION

Theoretical approaches to the atomistic scale understanding of the acidic and basic centers are becoming active areas of investigation, because the fundamental study of acid-base centers is important to understand many novel reactions such as the oxidation, hydrogenation and hydrocracking reactions, in addition to the conventional acid-base catalyzed reactions. Additionally, such studies will have strong impact on the progress in various other functional materials including for example, adsorbents, sensors, ceramics, cosmetics, etc. and bioscience or biotechnology by enzymes. The above vision expressed by Professor Kozo Tanabe in the previous international symposium on 'Acid-Base Catalysis', held at Sapporo in 1988 have exactly come true[1]. The importance of the location and orientation of acidic and basic sites in relation to the size and shape of the reacting molecule was precisely discussed by Tanabe[2] and the guidelines to design and develop efficient heterogeneous acid-base bifunctional catalysts were also provided.

Earlier, the role of cooperative acid-base catalysis in the side chain alkylation of toluene on various metal exchanged zeolites has been brought out by us using a theoretical approach combined with computer graphics technique[3]. As mentioned above, the structure and dynamics of the exchanged metal cations are very important and the theoretical approach is ideally suited to probe this problem. From our earlier experience of applying the molecular dynamics(MD) and computer graphics(CG) techniques to derive valuable insight on the structural aspects of various materials such

---

<sup>1</sup>on leave from: National Chemical Laboratory, Pune - 411008, India.

as supported metal catalysts[4], superconducting materials[5], epitaxial heterojunctions[6], etc., we extended those techniques to study metal exchanged cations and the results are reviewed here.

## 2. METHODS

The MD calculation was made with the MXDORTO program developed by Kawamura[7]. The Verlet algorithm was used for the calculation of atomic motions, while the Ewald method was applied for the calculation of electrostatic interactions. Temperature and pressure were controlled by means of scaling of atom velocities and unit cell parameters under 3-dimensional periodic boundary condition. The two body central force interaction potential, given below in Eq. 1 was used for all the calculations.

$$u(r_{ij}) = Z_i Z_j e^2 / r_{ij} + f_0 (b_i + b_j) \exp[(a_i + a_j - r_{ij}) / (b_i + b_j)] + D_{ij} [\exp[-2b_{ij}(r_{ij} - r^*_{ij})] - 2\exp[-b_{ij}(r_{ij} - r^*_{ij})]] \quad (1)$$

First, second, and third terms in the above equation refer to Coulomb potential, exchange repulsion interaction potential, and Morse potential, respectively.  $Z_i$  is an atomic charge,  $e$  is an elementary electric charge,  $r_{ij}$  is an interatomic distance, and  $f_0$  is a constant. The parameters  $a$  and  $b$  in Eq. 1 represent the size and stiffness of the atoms, respectively, in the exchange repulsion interaction potential. The calculations were made for 1,000-10,000 steps with the time step of  $0.2-2.5 \times 10^{-15}$  seconds. The visualization was made with INSIGHT II code supplied by BIOSYM Technol. Inc. in SiliconGraphics IRIS4D-TG/25 engineering workstation, while the dynamic visualization was made with MOMOVIE code developed in our laboratory on OMRON LUNA88K engineering workstation.

## 3. RESULTS AND DISCUSSION

### 3.1 Metal Exchanged Zeolite-A

Before applying the MD method to unknown structural details of zeolites, the simple diatomic potential given as in Eq. 1 was demonstrated to be effective for reproducing the

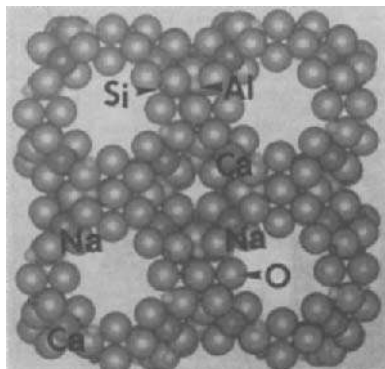


Fig.1 The CG picture of CaNaA, showing an open 8-member window for the free diffusion of O<sub>2</sub> and N<sub>2</sub>.

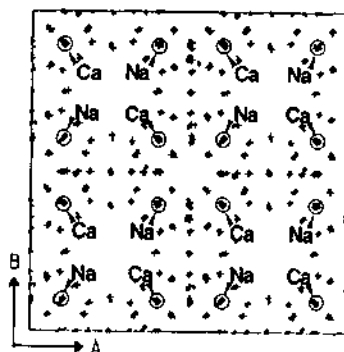


Fig.2 The trajectory of atoms in CaNaA at 600K.

lattice structure of zeolites as reported by X-ray crystallographic study. As an example, the results of the MD calculations carried out for CaNaA are shown in Fig.1. Fig.1 shows the CG picture of different atoms in the CaNaA at 600K, while Fig. 2 shows the trajectory of motion of atoms. It can be observed that the MD positions shown by the trajectory are very close to the equilibrium positions (indicated as '+') determined by X-ray studies. Similarly, the lattice structure of NaA zeolite was also simulated by MD method and the CG picture of NaA at 600K is shown in Fig.3.

For NaA zeolite, the extra framework  $\text{Na}^+$  cations are occupying the site I (at the window of the 8-member ring) and the site II (at the double-4 rings connecting the supercages)[8]. However for CaNaA zeolite, there were less number of extra framework cations due to the 2+ charge on Ca and all the extra framework cations are occupying site II, thus leading to an open 8-member ring[8].

*The molecular sieving mechanism:* The mechanism of diffusion and separation processes of  $\text{O}_2$  and  $\text{N}_2$  in NaA and CaNaA were studied by MD method. The dynamic behavior of  $\text{O}_2$  and  $\text{N}_2$  molecules in the micropores of CaNaA was simulated by MD method. A free diffusion of  $\text{O}_2$  and  $\text{N}_2$  through the open 8-member window was observed even at low temperatures such as 50K. Hence, both  $\text{O}_2$  and  $\text{N}_2$  could freely diffuse from one super cage to the other. However, when the dynamic behavior of  $\text{O}_2$  and  $\text{N}_2$  in the micropore of NaA was simulated, it was found that the dynamic behavior of  $\text{O}_2$  and  $\text{N}_2$  were different from that of CaNaA. Their dynamics were mostly restricted to a single super cage at lower temperatures. The dynamics was also influenced by the temperature, unlike in the case of CaNaA. At temperatures such as 262K, the trajectories of  $\text{O}_2$  and  $\text{N}_2$  molecules in NaA are shown in Figs. 4 and 5, respectively. It was observed that the  $\text{O}_2$  molecule is able to migrate through the 8-member window, in spite of the presence of  $\text{Na}^+$  ion at the site I, whereas the  $\text{N}_2$  molecule is repelled by  $\text{Na}^+$  and hence its mobility and diffusion are restricted to a single super cage. Thus the molecular sieving effect dependence on the location of exchanged cation is brought out. At higher temperatures such as 300K, both  $\text{O}_2$  and  $\text{N}_2$  molecules could diffuse through the 8-member window (Figs. 6 and 7) into the adjacent super cage. As described

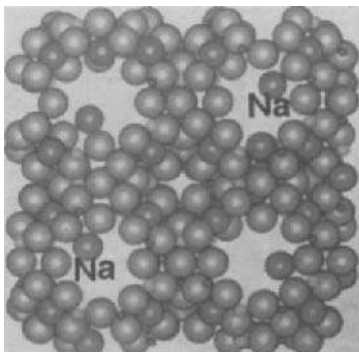


Fig.3 The CG picture of NaA, showing the presence of extra framework  $\text{Na}^+$  cation in the 8-member window.

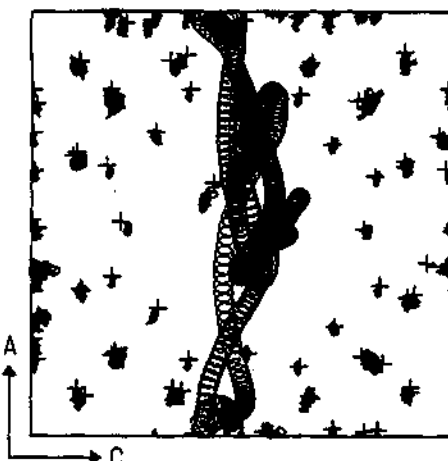


Fig.4 The trajectory of the oxygen molecule in NaA zeolite at 262K. The molecule can diffuse between the supercages.

below, the increase in the mobility of  $\text{Na}^+$  at site I, at higher temperatures provides reason for the observed behavior.

A detailed analysis of the motion of  $\text{Na}^+$  at site I, showed that its mean square displacement (MSD) from the equilibrium position was much larger compared to the  $\text{Na}^+$  at site II or the other framework atoms, as given in Fig.8. It was also observed that the MSD of  $\text{Na}^+$  increased with the temperature. Thus the results provide a quantitative understanding of the effect of the location of cations and the temperature on the molecular sieving effect.

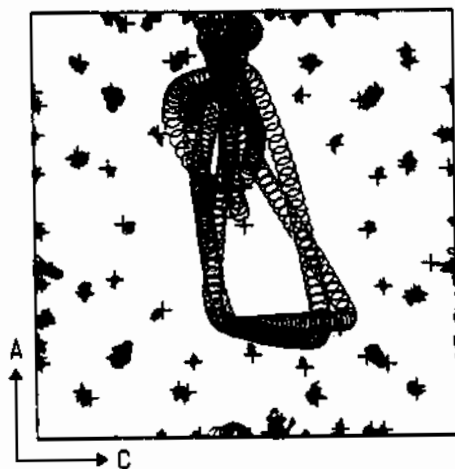


Fig.5 The trajectory of the nitrogen molecule in NaA zeolite at 262K. The molecule resides in the same super cage for most of the time.

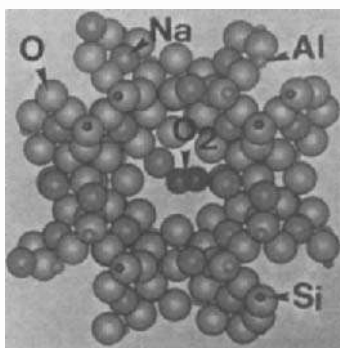


Fig.6 The CG picture, showing the diffusion of  $\text{O}_2$  through the 8-member window of NaA.

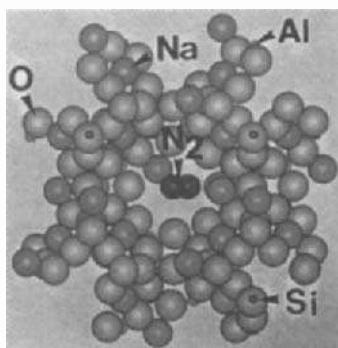


Fig.7 The CG picture, showing the diffusion of  $\text{N}_2$  through the 8-member window of NaA.

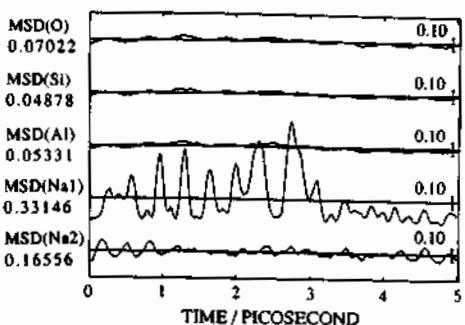


Fig.8 The changes in MSD values of various atoms in NaA at 300K.

### 3.2 Metal Exchanged ZSM-5

#### a. Alkali metal exchanged ZSM-5

The location of extra framework metal exchanged cations in ZSM-5 has not been reported in the literature based on X-ray crystallographic studies due to their low concentration. However, two possible extra framework sites had been proposed[8] for ZSM-5. Schroder *et al*[9] have performed energy minimization calculation and shown that a random Al substitution is possible since the substitution energy for different sites fall in close range of energy values. Quantum chemical calculations by Fripiat *et al*[10,11] indicate that the T12 and T2 sites are the preferred sites of Al substitution. In this background, we have considered all silicon lattice and substituted a part of the eight T12 sites by aluminum, corresponding to Si/Al ratio of 95, 47 and 31, charge compensated the anionic framework with different metal cations and simulated their structure. Exchange of protons in HZSM-5 with different alkali cations allows one to modulate and fine tune its acid-base properties. MD simulation of various cations such as  $H^+$ ,  $Li^+$ ,  $Na^+$ ,  $K^+$  and  $Cs^+$  were simulated and the results are discussed in detail elsewhere[12]. Here we report the salient findings from these calculations. All the cations migrated to the vicinity of T12 site, where Al is substituted for the Si. When the initial position was close to the T12 site, the ions readily migrated towards Al, even at low temperatures such as 300K. But, if the initial positions are far from the ion-exchange site, higher temperature, such as 600K was needed for the migration of the cation to the vicinity of Al(Fig.9), while at 300K,  $Na^+$  can not migrate to the vicinity of Al(Fig. 10). The final position and orientation of the cations are also leading to a predicted adsorption pattern for  $O_2$  and  $N_2$ , which are consistent with the experimental reports of Yamazaki *et al*[13].

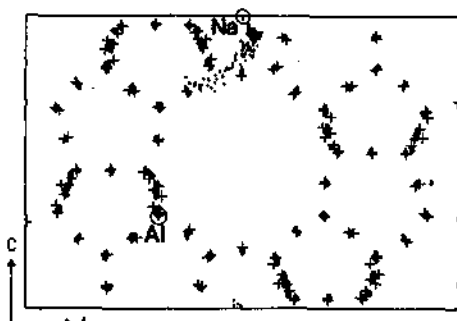


Fig.9 The trajectory of atoms in NaZSM-5 at 600K.



Fig.10 The trajectory of atoms in NaZSM-5 at 300K.

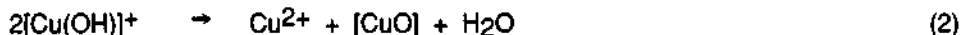
#### b. Multi-valent cation exchanged ZSM-5

Multi-valent cation exchanged zeolites have catalytic efficiency to selectively reduce NO, which is a potential pollutant. The pioneering work of Iwamoto *et al*[14] brought out the application of metal exchanged ZSM-5, mainly CuZSM-5 for the NO removal reaction. Later, it was shown that GaZSM-5[15] and CeZSM-5[16] had additional advantages in terms of activity and life-time, for the NO removal reaction. Hence, we studied the dynamics of copper, gallium and cerium in various oxidation states and coordinations. The salient results are discussed in the following section.

*Cu exchanged ZSM-5:* Initially, we considered  $Cu^+$  to be the charge compensation cation and different sites in the channel of ZSM-5 were considered to be the starting position of  $Cu^+$ . It was found that  $Cu^+$  always migrated towards the neighborhood of

T12 site where Al is substituted with the progress of dynamic simulation. The CG picture of the final equilibrium position of Cu<sup>+</sup> at 600K is shown in Fig. 11. The trajectory of the atoms in CuZSM-5 with two Cu<sup>+</sup> ions in the unit cell of ZSM-5 containing two aluminum ions at 600K is shown in Fig. 12. Thus, it is observed that under the NO decomposition reaction conditions (~773K), the ion-exchange site is in the vicinity of [AlO<sub>4</sub>]<sup>-</sup> tetrahedron.

A redox mechanism has been proposed for the direct decomposition of NO over CuZSM-5, as shown in Fig. 13. Copper is known to be reversibly changing its oxidation state between +2 and +1 during the reaction[17]. Therefore, the structure and dynamics of Cu<sup>2+</sup> ion in ZSM-5 was also studied. At lower temperatures, Cu<sup>2+</sup> ion in CuZSM-5 is considered to be in a hydrated state as [Cu(OH)]<sup>+</sup>. However, at an elevated temperature dehydration occurs as follows:



Under the reaction conditions, the copper is expected to be in dehydrated state and hence, we have simulated both Cu<sup>2+</sup> and [CuO] inside ZSM-5 channels. It was observed that both these species also prefer a location closer to [AlO<sub>4</sub>]<sup>-</sup> tetrahedron. When two silicon atoms in an unit cell were substituted by aluminum atoms at the T12 sites, the trajectories of atoms in CuZSM-5 with Cu<sup>2+</sup> and [CuO] at 600K are shown in Fig. 14. As can be seen from Fig. 14, the cation exchange sites are far apart and the exchange of O<sup>2-</sup> ion between the two Cu<sup>2+</sup> ions is not proceeding.

*Role of ZSM-5 framework in stabilizing Cu<sup>+</sup> and Cu<sup>2+</sup>* : [CuO] formed according to Eq. 2 cannot neutralize the anionic framework, even when it is present near the vicinity of [AlO<sub>4</sub>]<sup>-</sup>. Cu<sup>2+</sup> present in the vicinity of [AlO<sub>4</sub>]<sup>-</sup>, however possess an extra positive charge after compensating the anionic framework. Two nearby Al sites are needed for Cu<sup>2+</sup> to act as charge compensator simultaneously, which is unlikely in ZSM-5, which is a high-silica zeolite. It was observed[18] that the Coulomb energy is

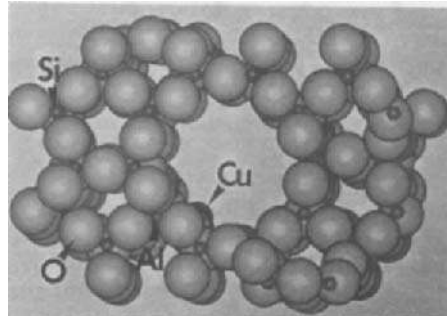


Fig. 11 The CG picture of the final position of Cu<sup>+</sup> ion in ZSM-5 lattice where one aluminum ion is present at the T12 site after 5000 steps at 600K.

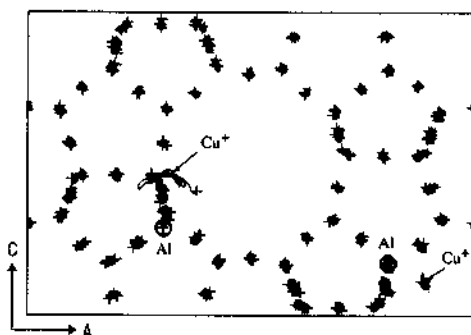


Fig. 12 The trajectory of the atoms in CuZSM-5 at 600K. There are two aluminum ions at the T12 sites of the unit cell and the anionic charges are compensated by two Cu<sup>+</sup> ions.

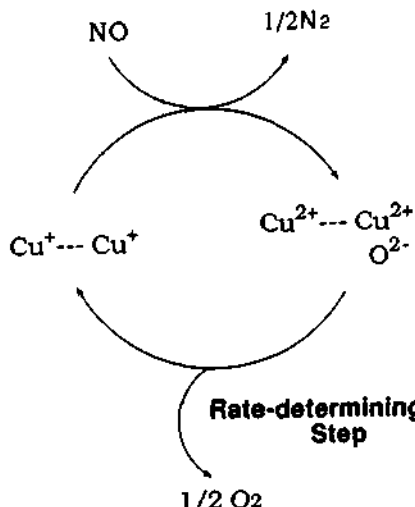


Fig. 13 The redox cycle of NO decomposition over CuZSM-5.

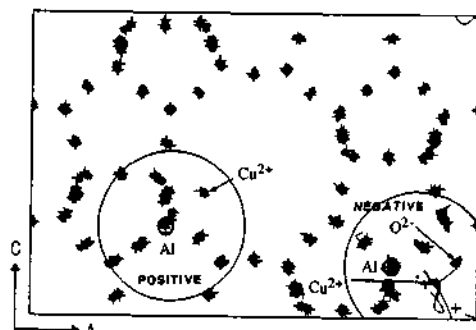


Fig. 14 The trajectory of the atoms in CuZSM-5 at 600K. There are two aluminum ions in the unit cell at the T12 sites and the anionic charges are compensated by Cu<sup>2+</sup> ion and [CuO].

less favorable, when two aluminum atoms are present at a distance of ~11 Å (at two T12 sites) with a Cu<sup>2+</sup> ion. Thus, Cu<sup>2+</sup> is not stable and it prefers to be as Cu<sup>+</sup> even under the reaction conditions. The possibility of oxidation of Cu<sup>+</sup> to Cu<sup>2+</sup> in the oxidation atmosphere always exists. Thus an equilibrium between Cu<sup>+</sup> and Cu<sup>2+</sup>, which is conducive for NO decomposition, is established in the ZSM-5 framework.

*Effect of Si/Al ratio :* The Si/Al ratio could be directly related to the distance between the exchanged cations. When the Al content is low, the copper ions are expected to be farther from each other, leading to unfavorable Coulombic energy and unstable Cu<sup>2+</sup>. When a situation corresponding to the presence of more number of aluminum in an unit cell was simulated, it was observed that the Cu<sup>2+</sup> behaves in the similar way as Cu<sup>+</sup>, in migrating towards Al site. The decomposition of NO is expected to leave adsorbed O<sub>2</sub> on Cu<sup>2+</sup>, according to the mechanism proposed by Li and Hall[17]. The desorption of O<sub>2</sub> from Cu<sup>2+</sup> to form Cu<sup>+</sup> is the key step in the reaction. Our results show that when the Al content is low, Cu<sup>2+</sup> is unstable and hence the desorption of O<sub>2</sub> is facilitated.

*Ga exchanged ZSM-5 :* GaZSM-5 is efficient in selective catalytic reduction of NO in the presence of hydrocarbons. The way in which the gallium ion is dispersed in GaZSM-5 is expected to be the cause for the catalytic activity. These materials are simulated to understand the salient features of this catalyst which imparts high activity to this catalyst. Various gallium species such as Ga<sup>3+</sup>, [GaO]<sup>+</sup>, [Ga(OH)]<sup>2+</sup> and [Ga(OH)<sub>2</sub>]<sup>+</sup> were simulated inside ZSM-5. Gallium also behaves similar to copper in migrating towards T12 site, where Al is substituted. There is low coordination for gallium in GaZSM-5 for various species. There is a maximum coordination of 3 for [Ga(OH)<sub>2</sub>]<sup>+</sup>, when Ga is close to the framework oxygen bridging the silicon and aluminum. The dehydration of gallium hydroxide at 600K to form gallium oxide is expected to happen as follows:



It was observed that the  $[GaO]^+$  cation is more dynamic than the hydroxylated gallium ions and the structure is shown in Fig.15.  $[GaO]^+$  is in a position bridging the two oxygen atoms of  $[AlO_4]^-$  group. Preliminary studies on the behavior of water molecules showed that water undergoes preferential adsorption on  $[GaO]^+$  ion causing the reversible reaction shown in Eq. 3 to occur, leading to the formation of  $[Ga(OH)_2]^+$ . The hydroxylation also increases the coordination of Ga ion, thus making the adsorption of NO more difficult. In spite of the dynamic behavior of the gallium ions, it was found that the atomic positions of ZSM-5 framework remain stationary as can be seen from Fig. 16, where the trajectories of atoms in ZSM-5, with  $[GaO]^+$  are shown. It was also found that the oxygen attached to  $Ga^{3+}$  has more mobility indicating the easy approachability and less steric hindrance for NO or hydrocarbons to gallium. Our preliminary results from *ab initio* quantum chemical calculations indicate that the  $O^{2-}$  attached to Ga is very different from the framework oxygens, in terms of the charge density and molecular electrostatic potential. These results bring out the effect of electronic and steric factors on the catalytic activity of  $Ga^{3+}$ .

*Ce exchanged ZSM-5:* We carried out molecular dynamic simulation of CeZSM-5 and found many similarities to the results obtained for GaZSM-5.  $Ce^{3+}$ , its oxide and hydroxides were similar to their Ga counter-part in their dynamic behavior inside ZSM-5. Cerium ions in ZSM-5 also had low coordination compared to its oxide lattice. It also shows greater affinity towards water molecule. However, a subtle difference was also noted, namely  $Ce^{3+}$  is larger than  $Ga^{3+}$  and hence, its position is farther from the zeolite framework. This means that the coordination unsaturation in Ce is still higher than Ga. Fig. 17 shows the computer graphic picture of  $[CeO]^+$  ion in ZSM-5 lattice after 5000 steps at 600K. The electronic structure of Ce is expected to be very different from Ga, with its diffused 4f orbitals.

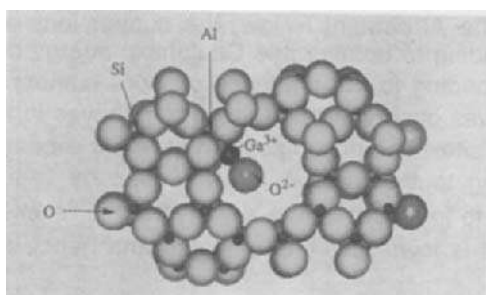


Fig. 15 The CG picture showing the position of  $[GaO]^+$  ion in GaZSM-5 when one aluminum ion is present at the T12 site, at 300K after 5000 steps.

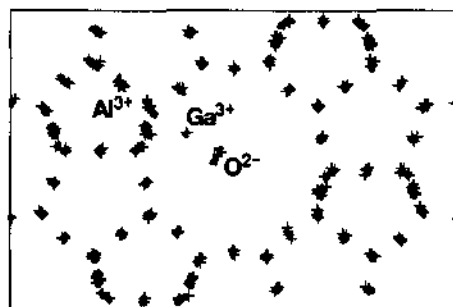


Fig. 16 The trajectory of the atoms in GaZSM-5 at 600K. There is one aluminum ion in the unit cell at the T12 site and the anionic charge is compensated by  $[GaO]^+$ .

### 3.3 Metal Exchanged Mordenite

The crystal structure of sodium exchanged mordenite (NaM) has been reported by Meier[19]. The location of the framework atoms are well established, while there is still ambiguity in the non-framework atoms. The  $Na^+$  ions in NaM are classified into two types; the first type denoted by Na(1) is located at the 8-member channel of the

mordenite structure, while the exact location of the other type denoted by Na(2) is not established. As such, there are four possible extra framework cation locations in the 12-member channel[8]. It has been reported from the adsorption experiments that the Na(2) ions are located in the 12-member channel, because they are capable of adsorbing large molecules such as benzene[20].

The distribution of Al atoms in the 8-member channel was determined by MD simulation. The position of Al in the framework was located by trial calculations to reproduce the known positions of Na(1). The trajectories of various atoms in NaM, obtained by the MD calculation for a system containing Al atoms at inappropriate locations are shown in Fig. 18. The '+' represent the equilibrium atomic positions as determined by X-ray structural studies, the solid lines refer to the calculated trajectories. Since, the assumed position of Al is not appropriate, the calculated position of Na(1) does not agree with the experimentally reported positions. Similar simulations were made for various distributions of Al in the 8-member channel, till the appropriate locations are identified. Fig. 19 shows the trajectory of various atoms in NaM, where the calculated trajectory of Na(1) is located near the experimental position. These results emphasize the point that the position of  $\text{Na}^+$  ions is a sensitive function of the position of Al in the framework. Hence, these results indicate that the distribution of Al can be determined, if the positions of exchanged cations are known.

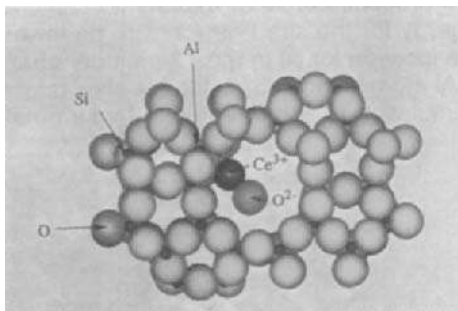


Fig. 17 The CG picture showing the position of  $[\text{CeO}_4]^{4-}$  in CeZSM-5 with one aluminum ion present at the T12 site, at 600K after 5000 steps.

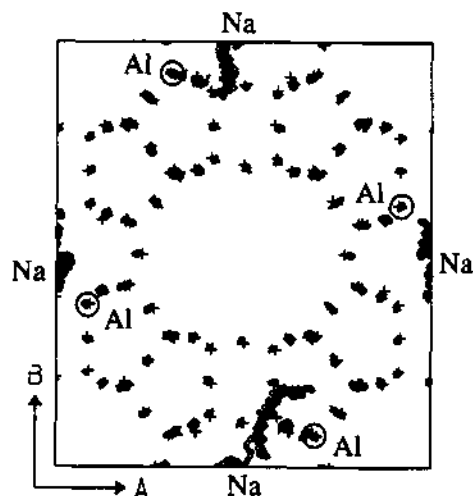


Fig.18 The trajectory of atoms in NaM with inappropriate Al distribution in 8-member ring.

The determination of the distribution of Al atoms in the 12-member channel was also attempted in a similar way. However, the exchanged cation positions in 12-member channel are not known and hence many MD calculations with different distribution of Al in the framework of 12-member ring were required. Still, the intensity of computation was reduced by taking into account of the symmetry of crystal. Five different sites denoted as I, II, III,  $I^*$ , and  $III^*$  are defined as shown in Fig.20. The aluminum was distributed in all these sites and the calculations were performed. In Fig. 21, the results of calculated energy values for different Al distribution are shown. The presence of Al in sites  $I^*$  and  $III^*$  lead to two Al in adjacent positions, which violates the empirical Lowenstein's rule.

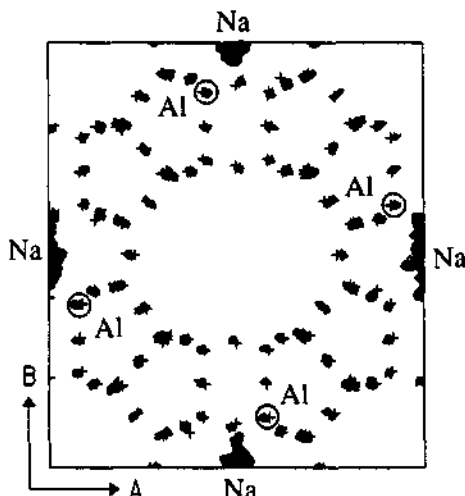


Fig.19 The trajectory of atoms in NaM with appropriate Al distribution in 8-member ring.

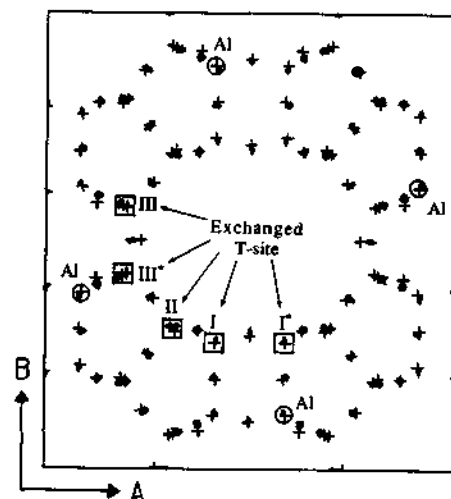


Fig.20 Different location for siting of Al in 12-member ring of the mordenite.

Our calculations predict higher energy for the presence of Al at these sites, reiterating the validity of Lowenstein's rule. The total energy for the site I happens to be lowest of all, suggesting that site I is the most favorable location for Al in the 12-member channel. In Fig. 22, the CG picture of NaM, where the Al atom is located at site I is shown. It was observed that the picture derived from the simulation is consistent with those obtained by Itabashi *et al.*[20].

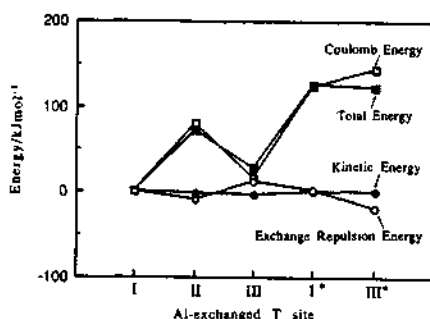


Fig.21 The calculated energy values for different Al distribution in the 12-member ring of mordenite.

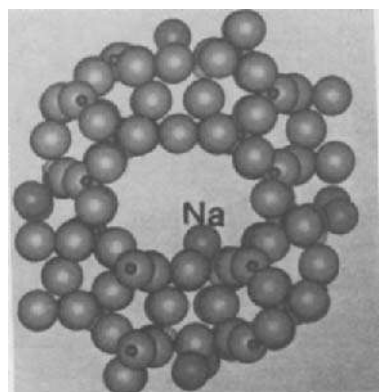


Fig.22 The CG picture of NaM with Al at site I.

#### 4. SUMMARY

The valuable information that could be derived on the structure and dynamics of metal exchanged zeolites by MD and CG studies are highlighted. Such information is relevant to understand many important adsorption and diffusion processes related to

adsorption and catalytic properties . The causes of difference in the molecular sieving effects of CaNaA and NaA as well as the effect of temperature on the separation of O<sub>2</sub> and N<sub>2</sub> are revealed. The distribution and location of framework aluminum and the extra framework cations could be predicted in mordenite and ZSM-5. The role of multivalent cations of ZSM-5 in the NO removal reaction is also brought out from our calculations.

## References

- 1 K. Tanabe, in: "Proc. Int. Symp. on Acid-Base Catalysis", Eds. K. Tanabe *et al*, Kodansha-VCH, Tokyo, (1989), p.XIX.
- 2 K. Tanabe, in: "Proc. Int. Symp. on Acid-Base Catalysis", Eds. K. Tanabe *et al*, Kodansha-VCH, Tokyo, (1989), p.513.
- 3 A. Miyamoto, S. Iwamoto, K. Agusa and T. Inui, in: "Proc. Int. Symp. on Acid-Base Catalysis", Eds. K. Tanabe *et al*, Kodansha-VCH, Tokyo, (1989), p.497.
- 4 A. Miyamoto, T. Hattori and T. Inui, Appl. Surf. Sci., 60 (1992) 660.
- 5 A. Miyamoto, T. Hattori and T. Inui, Physica C,190 (1991) 93.
- 6 A. Miyamoto, K. Takeichi, T. Hattori, M. Kubo and T. Inui, Jpn. J. Appl. Phys., 31 (1992) 4463.
- 7 K. Kawamura, in: "Introduction to molecular simulations", Eds. I. Okada and E. Osawa, Kaibun-do, Tokyo, (1989 ), Chap. 6 and 7.
- 8 W.J. Mortier, "Compilation of extra framework sites in zeolites", Butterworth Scientific Limited, Surrey, (1982).
- 9 K.P. Schroder, J. Sauer, M. Leslie and C.R.A. Catlow, Zeolites, 12 (1992) 20.
- 10 J.G. Fripiat, F. Berger-Andre, J. Andre and E.G. Derouane, Zeolites, 3 (1983) 306.
- 11 E.G. Derouane and J.G. Fripiat, Zeolites, 5 (1985) 165.
- 12 A. Miyamoto, K. Matsuba, M. Kubo, K. Kawamura and T. Inui, Chemistry Lett., (1991) 2055.
- 13 T. Yamazaki, I. Watanuki, S. Ozawa and Y. Ogino, Langmuir, 4 (1988) 433.
- 14 M. Iwamoto, H. Furukawa, Y. Mine, F. Uemura, S. Mikuriya and S. Kagawa, J. Chem. Soc. , Chem. Comm., 1272 (1986).
- 15 K. Yogo, S. Tanaka, M. Ihara, T. Hishiki and E. Kikuchi, Chem. Lett., (1992) 1025.
- 16 M. Misono and K. Kondo, Chem. Lett., (1991) 1001.
- 17 Y. Li and W.K. Hall, J. Phys. Chem., 94 (1990) 6145.
- 18 A. Miyamoto, M. Kubo, K. Matsuba and T. Inui, in: "Computer aided innovation of new materials II", Eds. M. Doyama *et al*, Elsevier Science Publishers, Amsterdam (1993) 1025.
- 19 W.M. Meier, Zeit. Krist., 115 (1961) 439.
- 20 K. Itabashi, T. Okada and K.Igawa, in: "Proc. 7th Int. Conf. Zeolites", Eds. Y. Murakami *et al*, Kodansha, Tokyo, 1986, p.369.

This Page Intentionally Left Blank

## 2.17 Acid Strength of Binary Mixed Oxides —Estimation by Neural Network and Experimental Verification

T. Hattori,<sup>a</sup> S. Kito,<sup>b</sup> H. Niwa,<sup>a</sup> Yenni Westi,<sup>a</sup> A. Satsuma,<sup>a</sup> and Y. Murakami<sup>a</sup>

<sup>a</sup> Department of Applied Chemistry, Nagoya University, Chikusa, Nagoya 464-01, JAPAN.

<sup>b</sup> Department of Industrial Engineering, Aichi Institute of Technology, Toyota 470-03, JAPAN.

### Abstract

In order to demonstrate the feasibility of neural network system for the estimation of acid strength of mixed oxide, two series of mixed oxides were prepared and their acid strengths were compared with those predicted by the neural network. It was revealed that the acid strength of mixed oxide can be estimated by the system within a reasonable error.

### INTRODUCTION

We have developed a prototype expert system, INCAP (INtegration of Catalyst Activity Pattern) for the selection of catalyst component(s) [1], and demonstrated the feasibility of INCAP through the experimental verification by taking the selection of promoter oxide to be added to SnO<sub>2</sub> catalyst for the oxidative dehydrogenation of ethylbenzene as an example [2]. After these results, we are planning to develop an advanced system, ARCADE (ARTificial Intelligence System for CAtalyst DEsign) [3]. For this purpose, two advanced modules are to be developed for the creation of reaction mechanism [4] and for the estimation of synergistic effect.

The solid acidity of mixed oxide is one of the most typical examples of the synergistic effect, and several models have been proposed to predict the acidic properties of mixed oxide [5-8]. However, we experienced in the development of INCAP that the proposed correlations for the acid strength can not be applied to some mixed oxides. Recently, we developed a noble estimation method of acid strength of mixed oxide by applying an artificial neural network, which is a simplified model of human brain [9].

In this study, two series of mixed oxides were prepared and their acid strengths were compared with those predicted by the neural network in order to demonstrate the feasibility of the estimation of acid strength by the neural network system.

### ORGANIZATION OF NEURAL NETWORK

In the proposed correlations [6,7], the acid strength is represented as a function of the following parameters: valence (Z), coordination number (CN), ionic radius (r), and electro-negativity of metal ion (X), and partial charge of oxygen ion ( $\delta_o$ ) of constituent oxides. Thus,

$$\text{Acid strength} = f(Z_i, CN_i, r_i, X_i, \delta_o, Z_j, CN_j, r_j, X_j, \delta_o)$$

where sub i and j stand for constituent oxides, respectively.

In the present study, the 'form of function' is estimated by using an artificial neural network. The neural network as a function approximator can learn the 'function' as a network pattern, if one gives a training set of known pairs of input data (parameters representing the factors controlling acid strength) and output data (acid strength). Then, unknown output data can be calculated by substituting corresponding input data into the 'function'.

A simulator of back propagation neural network was developed by using C language, and its organization is shown in Fig. 1. The network consists of input layer corresponding to the factors, output layer representing the acid strength, and a hidden layer including ten units each of which, roughly speaking, corresponds to a medium parameter.

The training set includes the acid strengths of 21 mixed oxides shown in Table 1, most of which are taken from a literature [6], and parameters representing the properties of 8 constituent oxides. The acid strength of mixed oxide is represented by a color change pattern of Hammett indicators with various pKa's. For example, in the case of  $\text{SiO}_2\text{-ZnO}$ , indicators with  $\text{pKa} = +6.8, +4.8, +4.0, +3.3, +1.5$  and  $-3.0$  changed their colors upon adsorption, but those with  $\text{pKa} = -5.6$  and  $-8.2$  not. This pattern was represented as '1 1 1 1 1 1 0 0'. The input data include not only the above-mentioned five parameters but also the heat of formation of oxide per oxygen atom ( $\Delta H_f^\circ$ ) [9b].

#### LEAVE-ONE-OUT TEST

The possibility of estimating the acid strength of unknown mixed oxide was examined by a leave-one-out test. The neural network was trained by excluding one mixed oxide from the training set, and the color change pattern of the mixed oxide excluded was calculated and compared with the observed value. The calculated acid strength in all cases agreed with the observed value within a reasonable experimental error, as shown in Table 1. This result indicates the possibility of extrapolation of the 'function' to the outside of the training set. It should be added that the results calculated by the network including one hidden layer in the present study agree well with those calculated with two hidden layers [9].

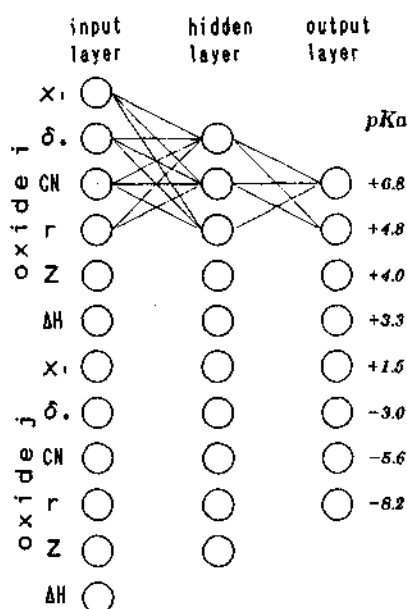


Fig. 1 Construction of neural network used in the present study.

Table 1 Calculated Acid Strength<sup>a</sup> in Comparison with Observed Value

	MgO	$\text{Al}_2\text{O}_3$	$\text{SiO}_2$	$\text{TiO}_2$	ZnO	$\text{ZrO}_2$	$\text{SnO}_2$	$\text{Bi}_2\text{O}_3$
MgO	obs <sup>b</sup> cal <sup>c</sup>	- +4.8	+4.8 -5.6	-5.6 +1.5	+3.3 +4.8	+4.8 -5.6	- -5.6	- +1.5
$\text{Al}_2\text{O}_3$	obs <sup>b</sup> cal <sup>c</sup>	+4.8 +4.8	- -5.6	-8.2 -5.6	-5.6 -8.2	+1.5 +3.3	-5.6 -5.6	+1.5 +1.5
$\text{SiO}_2$	obs <sup>b</sup> cal <sup>c</sup>	-5.6 -5.6	-8.2 -5.6	- -8.2	-8.2 -5.6	-3.0 -8.2	-5.6 -3.0	- -
$\text{TiO}_2$	obs <sup>b</sup> cal <sup>c</sup>	+3.3 +1.5	-5.6 -8.2	-8.2 -8.2	- -	-3.0 +1.5	-8.2 -5.6	+1.5 -3.0
ZnO	obs <sup>b</sup> cal <sup>c</sup>	+4.8 +3.3	+1.5 +3.3	-3.0 -5.6	-3.0 +1.5	- +	+1.5 +1.5	+3.3 +1.5
$\text{ZrO}_2$	obs <sup>b</sup> cal <sup>c</sup>	- -	-5.6 -5.6	-8.2 -8.2	-8.2 -5.6	+1.5 +3.3	-5.6 -3.0	- -
$\text{SnO}_2$	obs <sup>b</sup> cal <sup>c</sup>	- -	- -	-5.6 -3.0	-3.0 -5.6	+1.5 +1.5	-5.6 -5.6	- -
$\text{Bi}_2\text{O}_3$	obs <sup>b</sup> cal <sup>c</sup>	- -	+1.5 +1.5	- -	+1.5 -3.0	+3.3 +1.5	- -	- -

<sup>a</sup>  $\text{pKa(max)}$ , <sup>b</sup> observed, <sup>c</sup> calculated by leave-one-out test.

## PREDICTION BY NEURAL NETWORK

The neural network was applied to the prediction of acid strengths of unknown samples by taking two series of mixed oxides as examples: the mixed oxides whose acid strengths are not given in Table 1 and promoted  $\text{SnO}_2$  catalysts. The acid strengths were predicted in the following way. First, the neural network was trained by using the acid strengths of mixed oxides given in Table 1 as output data and above-mentioned parameters of oxides of Mg, Al, Si, Ti, Zn, Zr, Sn and Bi as input data. Then, the color change pattern of indicators was calculated by substituting input data (parameters) of components of target mixed oxides into thus trained network.

The results of prediction were given in Tables 2 and 3 for the first and the second series, respectively, in terms of  $p\text{K}_a(\text{max})$ , i.e., the lowest  $p\text{K}_a$  among the indicators which changed their colors upon adsorption on mixed oxide.

## PREPARATION AND ACID STRENGTH OF MIXED OXIDES

Two series of mixed oxides mentioned above were actually prepared to compare their acid strengths with those thus predicted. In the first series, the mixed oxides were prepared by a co-precipitation method or a sol-gel method by using precursors shown in Table 2. In the former method, excess ammonium hydroxide was added to a hydrochloric acid solution or an ethanol solution containing precursors, and the precipitates were dried and calcined at 773 K. In the sol-gel method, water was slowly added to ethanol solution of precursors, followed by drying and calcination at 773 K. Molar ratio of oxides was 1/1. In the second series, the promoted  $\text{SnO}_2$  were prepared by a gel mixing method or a co-precipitation method by using precursors shown in Table 3. The promoter content was 10 atom%. Preparation methods have been described elsewhere [2b].

Acid strength of mixed oxide thus obtained was measured from the color change pattern of Hammett indicators adsorbed on the sample precalcined at 773K.

## COMPARISON OF OBSERVED ACID STRENGTH WITH PREDICTED VALUE

Table 2 summarizes the observed acid strengths of the first series of mixed oxides. As shown, the observed acid strengths agree well with the predicted acid strength except for  $\text{MgO-ZrO}_2$ . In this case, the neural network was trained by using physical/chemical properties of oxides including the components of target mixed oxides whose acid strengths were to be estimated. The training set also included the acid strengths of mixed oxides containing either of the constituent oxides. In other words, the neural network 'learned' the strength of acid sites generated when each constituent oxide was mixed with the others excluding the partner of target mixed oxides.

In the second series, a severer test was applied to the neural network by taking, as an example, a series of  $\text{SnO}_2$  containing promoter oxides which are not included in Table 1. Thus, the neural network 'learned' the properties of  $\text{SnO}_2$  and the acid strengths of several  $\text{SnO}_2$ -containing mixed oxides shown in Table 1. However, the neural network did not 'learn' anything about the properties of promoter-oxides and the acid strength of mixed oxides containing promoter-oxides. Then, the properties of  $\text{SnO}_2$  and promoter-oxides were substituted into the trained network to calculate the acid strength of promoted  $\text{SnO}_2$ .

Table 2 Preparation method and acid strength of the first series of mixed oxides

Mixed Oxide	Precursors	Preparation Method	$p\text{K}_a(\text{max})$	
			observed	predicted
$\text{MgO-ZrO}_2$	$\text{Mg}(\text{CH}_3\text{COO})_2$	$\text{ZrO}(\text{CH}_3\text{COO})_2$	sol-gel	+1.5 +4.8
$\text{MgO-SnO}_2$	$\text{Mg}(\text{CH}_3\text{COO})_2$	$\text{SnCl}_2(\text{acac})_2$	sol-gel	-3.0 -3.0
$\text{MgO-Bi}_2\text{O}_3$	$\text{Mg}(\text{CH}_3\text{COO})_2$	$\text{BiCl}_3$	co-prec.(HCl)	+1.5 +3.3
$\text{Al}_2\text{O}_3-\text{SnO}_2$	$\text{Al}[\text{OCH}_3(\text{CH}_3)_2]_3$	$\text{SnCl}_2(\text{acac})_2$	sol-gel	-8.2 -5.6
$\text{SiO}_2-\text{Bi}_2\text{O}_3$	$\text{Si}(\text{OC}_2\text{H}_5)_4$	$\text{BiO}(\text{CH}_3\text{COO})$	co-prec.(EtOH)	+1.5 +1.5
$\text{ZrO}_2-\text{Bi}_2\text{O}_3$	$\text{ZrO}(\text{CH}_3\text{COO})_2$	$\text{BiCl}_3$	co-prec.(HCl)	+1.5 +1.5
$\text{SnO}_2-\text{Bi}_2\text{O}_3$	$\text{SnCl}_2(\text{acac})$	$\text{BiO}(\text{CH}_3\text{COO})$	co-prec.(EtOH)	+1.5 +1.5

Table 3 Preparation method and acid strength of promoted SnO<sub>2</sub> catalysts

Promoter		Preparation Method	pKa(max) observed	pKa(max) predicted		
Element	Source			this study	ref [6b]	ref [7]
B	H <sub>3</sub> BO <sub>3</sub>	gel-mixing	-3.0	-3.0	<-5.6	<-5.6
P	H <sub>3</sub> PO <sub>4</sub>	gel-mixing	-3.0	-5.6	N/A*	N/A*
Cu	Cu(NO <sub>3</sub> ) <sub>2</sub>	gel-mixing	+3.3	+1.5	-5.6 to +1.5	-3.0 to +3.3
Ge	GeCl <sub>4</sub>	co-precipitn	-3.0	-3.0	N/A*	-8.2 to -3.0
Nb	NbCl <sub>5</sub>	co-precipitn	-5.6	-3.0	N/A*	<-5.6
Mo	(NH <sub>4</sub> ) <sub>6</sub> Mo <sub>7</sub> O <sub>24</sub>	gel-mixing	-3.0	-3.0	N/A*	N/A*
Sb	SbCl <sub>3</sub>	co-precipitn	+1.5	+1.5	<-5.6	-3.0 to +3.3
Ce	CeCl <sub>3</sub>	co-precipitn	-3.0	-3.0	-8.2 to -3.0	-3.0 to +3.3
W	WCl <sub>6</sub>	co-precipitn	-3.0	-3.0	N/A*	N/A*

\* correlation is not applicable to this mixed oxide.

The observed acid strengths are shown in Table 3 together with the acid strengths predicted as mentioned above. As shown, the observed results agree well with predicted results. The error remains within the interval between adjacent pKa values of Hammett indicators. The experimentally observed acid strength also should contain some error which is expected to be at best within the adjacent pKa values. Thus, the results shown in Table 3 indicate that the neural network estimates the acid strength of mixed oxide with the accuracy similar to that in the experimental measurement.

Table 3 also compares the acid strength estimated by neural network with those by semi-empirical correlations proposed by Tanabe et al [6b] and Aso et al [7]. As can be seen from the table, the neural network gave much better estimates than both of correlations, though the comparison was made only for promoted SnO<sub>2</sub>.

Thus, it may be concluded that the neural network is a powerful tool to estimate the acid strength of mixed oxides.

## REFERENCES

1. (a) T. Hattori, S. Kito and Y. Murakami, Chem. Lett., 1988, 1269; (b) S. Kito, T. Hattori and Y. Murakami, Appl. Catal., 1989, 48, 107; (c) Chem. Eng. Sci., 1990, 45, 2661; (d) Proc. 3rd Intern. Symp. IEA/AIE, 1990, 2, 610; (e) "Catalytic Science and Technology", Kodansha, Tokyo, 1991, 285.
2. (a) T. Hattori, H. Niwa, A. Satsuma, S. Kito and Y. Murakami, Appl. Catal., 1989, 50, L11; (b) Proc. 10th Intern. Cong. Catal., 1993, 489.
3. (a) T. Hattori and S. Kito, Shokubai, 1989, 31, 9; (c) Catal. Today, 1991, 10, 165.
4. Z.-Y. Teng, S. Kito, T. Hattori, Y. Murakami, and Y. Yoneda, "Computer Aided Innovation of New Materials II", Elsevier, Amsterdam, 1993, 1095.
5. C.L. Thomas, Ind. Eng. Chem., 1949, 41, 2564.
6. (a) K. Shibata, T. Kiyoura, J. Kitagawa, T. Sumiyoshi, K. Tanabe, Bull. Chem. Soc. Jpn., 1973, 46, 2985; (b) K. Tanabe, T. Sumiyoshi, K. Shibata, ibid., 1974, 47, 1064.
7. I. Aso, N. Yamazoe, T. Seiyama, Preprints of 39th Annual Meeting of Catalysis Society of Japan, 1976, 10.
8. H. Kung, J. Solid State Chem., 1984, 52, 191.
9. (a) S. Kito, T. Hattori and Y. Murakami, Anal. Sci., 1991, 7(supplement), 761; (b) IEC. Res., 1992, 31, 979; (c) "Computer Aided Innovation of New Materials II", Elsevier, Amsterdam, 1993, 901.

## 2.18 Quantum Chemical Study on Reactions of Small Molecules on Various MgO Surfaces

Hisayoshi Kobayashi<sup>a</sup>, Dennis R. Salahub<sup>b</sup> and Tomoyasu Ito<sup>c</sup>

<sup>a</sup>Department of Applied Chemistry, Kyoto Prefectural University, Shimogamo, Kyoto, 606 Japan

<sup>b</sup>Universite de Montreal, Departement de chimie, Montreal, Quebec, H3C 3J7 Canada

<sup>c</sup>Shool of Social Information Studies, Otsuma Women's University, Kami-oyamada-cho, Tama, Tokyo, 206 Japan

### Abstract

The density functional (DF) method is applied to chemisorption of hydrogen, methane and carbon monoxide molecules onto the MgO surfaces including the atoms with different coordination numbers. Hydrogen is easily adsorbed dissociatively at the three-coordination (3c-3c) site, whereas the dissociation products are unstable for the four- (4c-4c) and five-coordination (5c-5c) sites. The mixed coordination sites, the Mg(3c)-O(4c) and Mg(4c)-O(3c) sites weakly bind hydrogen and the binding in the latter is still weaker. For the adsorption of methane, the product forming the Mg-CH<sub>3</sub> and O-H bonds is stable whereas that forming the O-CH<sub>3</sub> and Mg-H bonds is hardly bound. To the adjacent site of the Mg-CH<sub>3</sub> and O-H bonds, the second methane molecule can be adsorbed in the both types of bond formation since the site is activated by the first methane just as the case of hydrogen adsorption. Based on the calculated results, the mechanism of oxidative coupling is suggested.

CO is adsorbed to the Mg atom by either the C or O end, but not to the surface O atom. Only when the adjacent Mg site is occupied by CO, the second CO is adsorbed to the O atom. Compared to the H<sub>2</sub> and CH<sub>4</sub> molecules, the CO adsorption is less sensitive to the coordination number of surface atoms, and the second CO gains smaller adsorption energy than the first CO.

### 1. INTRODUCTION

MgO catalyzes various reactions such as oxidative coupling of methane[1] and polymerization of adsorbed CO molecules[2]. MgO is thought to be a very promising material in the industrial and also in the environmental chemistry. Especially many experimental works have been continuously reported for systems consisting of hydrogen containing molecules, e.g., dissociative adsorption of hydrogen[3,4] and methane,[5] hydrogen isotope exchange reactions between two hydrogen molecules[6,7] and between hydrogen and olefin molecules,[8,9] hydrogenation of olefins,[8,9] and isomerization of olefins.[8] In these many reactions the surface atoms (especially oxygen atoms) with very low coordination number seem to play important roles.

Based on their spectroscopic observations, Coluccia et al.[3] and Garrone et al.[4] have shown that the dissociation of hydrogen molecule occurs heterolytically. Ito and co-workers have also suggested using the TPD and other experimental technique that the heterolytic adsorption

mechanism is operative on MgO surfaces.[10] A pair of three-coordinated Mg and O atoms on the surfaces are the most probable active sites for the heterolytic dissociation.[3a,4b,10] Four-coordinated surface atoms may also participate in this adsorption,[4c,10] but with lower interaction energy. The presence of such lowly-coordinated surface atoms has been evidenced spectroscopically.[11-13]

From theoretical side, Fujioka et al. proposed a mechanism of hydrogen atom migration at the step site.[14] Kobayashi and Ito examined the mechanism of dissociative adsorption of hydrogen and methane as well as hydrogen atom migration and second hydrogen adsorption using the  $Mg_4O_4$  cluster model,[15] and later their works were extended by Sawabe et al. using the larger clusters.[16] Recently Knozinger et al.[17] and Shluget et al.[18] also studied the dissociative adsorption of hydrogen. H abstraction from  $CH_4$  is investigated by Mehandru et al.[19] and by Aray et al.[20] The former referred to the effects of Li-doping using the ASE MO theory, and the latter examined the charge topology of the MgO molecule employing the MCSCF method.

As for the adsorption of CO, Matsumura, Huzimura and co-workers have reported the oxidation and oxygen-isotope exchange reaction of adsorbed CO.[21] Recently Pacchioni et al. investigated the interactions of CO and MgO atoms with different coordination numbers.[22]

At present the following facts are obtained from experimental and theoretical works and accepted as common sense: (1) The surface atoms or adsorption sites are classified by their coordination number to the nearest neighbors. (2) The atoms at lower coordination numbers are more active in the interactions with adsorbates, and the three-coordination site is the most active one. (3) The sites are activated if their adjacent sites are occupied by the dissociated atoms or fragments. However the explanation of these facts in terms of more basic concepts is left as future works. In this work we have investigated the interactions of  $H_2$ ,  $CH_4$ , and CO molecules with the MgO surfaces modeled by various clusters and slabs. For adsorption of  $H_2$ , the differences due to the coordination number of surface atoms are extensively examined. The obtained results are explained in terms of more basic concept, which we call "the local enhancement of covalence." The  $CH_4$  adsorption is also calculated using small models. Assuming some resemblance between  $H_2$  and  $CH_4$ , which was obtained in our previous work[15(b)], a mechanism for the oxidative coupling is proposed. Different from  $H_2$  and  $CH_4$ , CO is adsorbed associatively. The calculated results are utilized to explain the CO exchange reaction on the surface.

## 2. MODELS AND METHOD OF CALCULATION

Fig.1 shows shapes of cluster and slab models with the configuration of adsorbed hydrogen atoms discussed in this work. We specify the individual adsorption site uniquely by the atomic component of cluster and the coordination number of surface atoms to which the H atoms are bonded. There is only one type site, i.e., the three-coordination (3c) site for the  $Mg_4O_4$  cluster, which is represented as  $Mg_4O_4(3c-3c)$ . A similar naming rule is adopted also for  $CH_4$  adsorption. For CO, terms such as "linear", "bridged", "chain", and "twin" are used to specify the adsorbed configuration.

The calculations are processed in the following way. (1) The energy profile of hydrogen molecule dissociation is first investigated for the  $Mg_4O_4$  cluster.(Fig.1(a)) (2) Using the reference Mg-H and O-H bond lengths taken from the  $Mg_4O_4$  cluster calculation, the single point calculations are carried out for the other models. (3) For the cluster models with positive adsorption energies (stabilization), the geometry of H atoms is optimized. (4) The energy is recalculated by a higher-quality single point calculation including the non-local correction.

The linear combination of Gaussian type orbital (LCGTO) DF method program developed at University of Montreal, "deMon"[23] and its extended version to periodic systems called "Bloch deMon"[24] were employed for the cluster and slab calculations, respectively. The basis sets used for Mg, O, C, and H atoms are (6321/411), (5211/411), (5211/411/1), and (31/1), respectively.[25] The quality is equal to or better than the split valence bases. A diffuse function is put on the O and C atoms, and a polarization function on the C and H atoms. The polarization function for H is dropped in case of the slab calculation and for the unreactive H atoms in CH<sub>3</sub>. The uncontracted auxiliary fitting functions of the types, (8/3/3), (7/2/2), (7/2/2), and (6/1/1) are used for Mg, O, C, and H atoms, respectively.[25] The Vosko, Wilk, and Nusair local potential[26] and the non-local potential proposed by Perdew and Yue, and Perdew[27] are employed.

### 3. RESULTS AND DISCUSSION

#### 3.1. Adsorption Energy of Hydrogen

The change of energy along dissociative adsorption is examined using the Mg<sub>4</sub>O<sub>4</sub> cluster. The monotonous decrease in the energy is obtained, as shown in Fig.2. This result indicates the absence of reaction barrier, and is consistent with the our previous result[15(a)] and other workers result.[16] The adsorption energy at the optimized structure is calculated to be 31.9 and 24.5 kcal/mol, respectively at the level of calculations with the local and non-local potentials. Inclusion of the non-local correction decreases the adsorption energy by compensating the overestimated binding. Table 1 summarizes the adsorption energies as well as the charge of atoms estimated by Mulliken population. The tabulated values are those for the optimized configuration in case of the bound systems or for the reference configuration in case of the unbound systems. The adsorption also occurs stably for the Mg<sub>6</sub>O<sub>6</sub>(3c-3c) model.(Fig.1(b)) The calculated adsorption energies, 33.1 and 23.5 kcal/mol with the local and non-local potentials are close to those obtained for the Mg<sub>4</sub>O<sub>4</sub>(3c-3c) model. This means that the cluster size does not effect the results significantly for the present problem.

Table 1 Energy for hydrogen molecule adsorption and charges  
of Mg and O atoms before adsorption

model	energy(kcal/mol)		Mulliken charge	
	local	non-local	Mg-(H) <sup>a</sup>	O-(H) <sup>a</sup>
Mg <sub>4</sub> O <sub>4</sub> (3c-3c)	31.9	24.5	+1.105	-1.105
Mg <sub>6</sub> O <sub>6</sub> (3c-3c)	33.1	23.5	+1.064	-1.087
Mg <sub>6</sub> O <sub>6</sub> (4c-4c)	-28.7 <sup>b</sup>		+1.204	-1.158
Mg <sub>4</sub> O <sub>4</sub> (100)(5c-5c)	-45.2 <sup>b</sup>		+1.461	-1.461
Mg <sub>3</sub> O <sub>3</sub> (110)(4c-4c)	6.9	5.0	+1.083	-0.936
			(+1.219	-1.513) <sup>c</sup>
Mg <sub>6</sub> O <sub>6</sub> (3c-4c)	13.3	10.5	+1.064	-1.158
Mg <sub>6</sub> O <sub>6</sub> (4c-3c)	12.9	4.3	+1.204	-1.087
Mg <sub>6</sub> O <sub>6</sub> H <sub>2</sub> (4c-4c)	11.9	12.5	+1.226	-1.094

<sup>a</sup>The charge of atoms to which H atom is bonded.

<sup>b</sup>The single point calculation with the reference configuration.

<sup>c</sup>Charge of second (valley) layer atoms with the six coordination number.

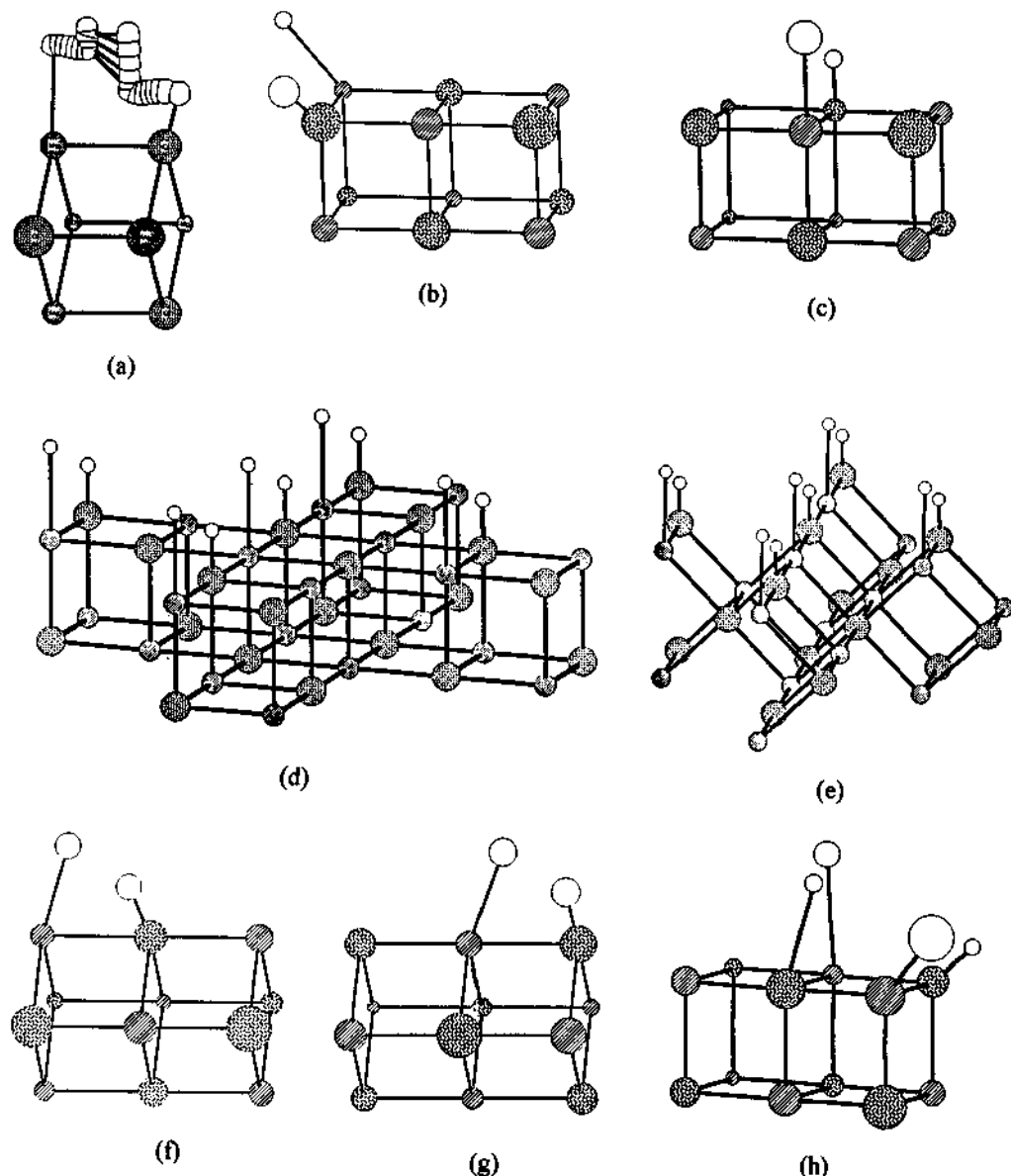


Fig.1. Models used in the calculations. (a)  $\text{Mg}_4\text{O}_4$ (3c-3c) cluster, (b)  $\text{Mg}_6\text{O}_6$ (3c-3c) cluster, (c)  $\text{Mg}_6\text{O}_6$ (4c-4c) cluster, (d)  $\text{Mg}_4\text{O}_4$ (100)(5c-5c) slab, (e)  $\text{Mg}_3\text{O}_3$ (110)(4c-4c) slab, (f)  $\text{Mg}_6\text{O}_6$ (3c-4c) cluster, (g)  $\text{Mg}_6\text{O}_6$ (4c-3c) cluster, (h)  $\text{Mg}_6\text{O}_6\text{H}_2$ (4c-4c) cluster.

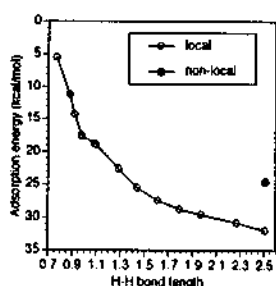


Fig.2. Change of adsorption energy along the approximate reaction path for the  $\text{Mg}_4\text{O}_4$ (3c-3c) model.

Adsorption is not stable for the  $Mg_6O_6(4c\text{-}4c)$  cluster model simulating the edge sites. The geometry optimization leads to the free cluster and free H<sub>2</sub>. The interaction is again repulsive for the sites on the (100) surface modeled by the  $Mg_4O_4(100)(5c\text{-}5c)$  slab. The  $Mg_3O_3(110)(4c\text{-}4c)$  model gives a small stabilization. However it is ascribed to the co-adsorption effects by formation of the H atom rows, and an artifact due to smallness of the unit cell. Thus the obtained results indicate that the H atoms are not bound at the (4c-4c) nor (5c-5c) sites. There are two configurations for the (3c-4c) mixed sites. The calculations show that the adsorption occurs stably although the adsorption energies are much smaller than that for the (3c-3c) site. Hydrogen is still weakly bound for the  $Mg_6O_6(4c\text{-}3c)$  site rather than the  $Mg_6O_6(3c\text{-}4c)$  site. The difference becomes more distinct with the non-local level calculation. Sawabe et al. have reported that stable adsorption occurs only at the  $Mg_6O_6(3c\text{-}4c)$  site.[16] We think that our result is qualitatively consistent with theirs.

Theoretically obtained results on the adsorption energy described above agree with experimental results already reported.[10,28] Using TPD, IR and other techniques, Ito has classified adsorbed species of hydrogen on MgO into several group, all of which seem to consist of heterolytically dissociated species.[10,28] A main species, designated W5, observable above room temperatures is desorbed at 300 K. This adsorption seems to have very low (nearly zero) activation energy since W5 species is easily formed even at 77 K and at low hydrogen pressure of, e.g., 6.7 Pa. The experimental fact coincides with the absence of reaction barrier already mentioned. Ito has also estimated from rates of the adsorption and desorption that the adsorption energy of W5 species to be about 24 kcal/mol.[28] This value agrees very nicely with the calculated adsorption energy for the (3c-3c) site, i.e., 24.5 and 23.5 kcal/mol for the  $Mg_4O_4$  and  $Mg_6O_6$  clusters at the non-local level. Table 1 also indicates that an Mg-O ion pair site in any models, which contains no three-coordinated ions, cannot adsorb hydrogen. This result is completely accordance with experimental ones since all the adsorbed species observable in TPD spectra have been proved to be present on a surface ion pair which contains at least one three-coordinated ion.[10(b)]

### 3.2 Local Density of States for MgO/H systems

To investigate the differences in adsorption among the sites, the local density of states (LDOS) are evaluated for some models. Fig.3(a) and (b) shows the LDOS for the  $Mg_4O_4(100)(5c\text{-}5c)$  and  $Mg_4O_4(3c\text{-}3c)$  models before adsorption. In the  $Mg_4O_4(100)(5c\text{-}5c)$  model, the band gap as the difference between the HOMO (-5.2 eV) and LUMO (-1.9 eV) is calculated to be 3.3 eV. This band gap is reduced to 1.2 eV for the  $Mg_4O_4(3c\text{-}3c)$  model. This is a consequence of the HOMO's shifting to higher energy region and the LUMO's shifting to lower energy region. The energy levels for the hydrogen 1 $\sigma$  and 1 $\sigma^*$  MO's are calculated to be -10.12 and +1.23 eV. The charge transfer occurs from the 1 $\sigma$  MO to the surface unoccupied MO's (donation) and from the surface occupied MO's to the 1 $\sigma^*$  MO (back-donation) in the course of the H-H bond fission and the Mg-H and O-H bond formation. The narrow gap is clearly favorable for the dissociative adsorption including the bond alternation process. Figs.3(a) and (b) show another common feature. Almost all the valence and conduction bands consist of the oxygen and magnesium orbitals, respectively, which is a typical feature of the metal oxide semiconductors. (In Fig.3(a), main peaks of the conduction band are not seen since they locate much higher energy region.) Figs.3(c) and (d) represent the LDOS calculated at the (4c-4c) and (3c-3c) sites for the  $Mg_6O_6$  cluster. The MO's in the top of valence band and in the bottom of conduction band are mainly localized to the atoms at the (3c) site. Thus, the characteristic difference between the (4c-4c) and (3c-3c) sites is similar to the difference between

the  $\text{Mg}_4\text{O}_4(100)(5c\text{-}5c)$  and  $\text{Mg}_4\text{O}_4(3c\text{-}3c)$  models, and it suggests again that the interaction with  $\text{H}_2$  is favorable for the (3c) sites but not for the (4c) and (5c) sites. In more detail, the lowering of LUMO levels is more remarkable than the rising of HOMO levels.

Band gap energies for surface ions on MgO have been experimentally obtained by using UV diffuse reflectance[11-13] and photoluminescence[3a,13] spectroscopies. These observations indicate that the band gap energy decreases with reduction in the coordination number of the surface ions. For example, UV diffuse reflectance spectra have revealed that surface band gap energies for five-, four-, and three-coordinated ions are 6.6, 5.8, and 4.6 eV, respectively.[11-13] Although the absolute value of band gap is calculated much narrower than the experimental values due to a well known demerit of the DF method at least for the present stage, the trend in the change is in accord with the experiments.

The difference between the  $\text{Mg}_6\text{O}_6(4c\text{-}3c)$  and (3c-4c) sites is explained from the relative magnitude in the shifting of the surface HOMO and LUMO levels. Comparing the LDOS of the (3c-3c) and (4c-4c) site for the  $\text{Mg}_6\text{O}_6$  cluster, we can see that the energy lowering of the LUMO levels is more remarkable. The LUMO's are almost all localized on the Mg atoms, and the reaction proceeds more easily in the configuration with the Mg(3c) atom rather than that with the O(3c) atom. The adsorbed hydrogen molecule becomes charged positive as a whole, and the net charge transfer is from  $\text{H}_2$  to the surface, which is also consistent with superior importance of the surface LUMO's.

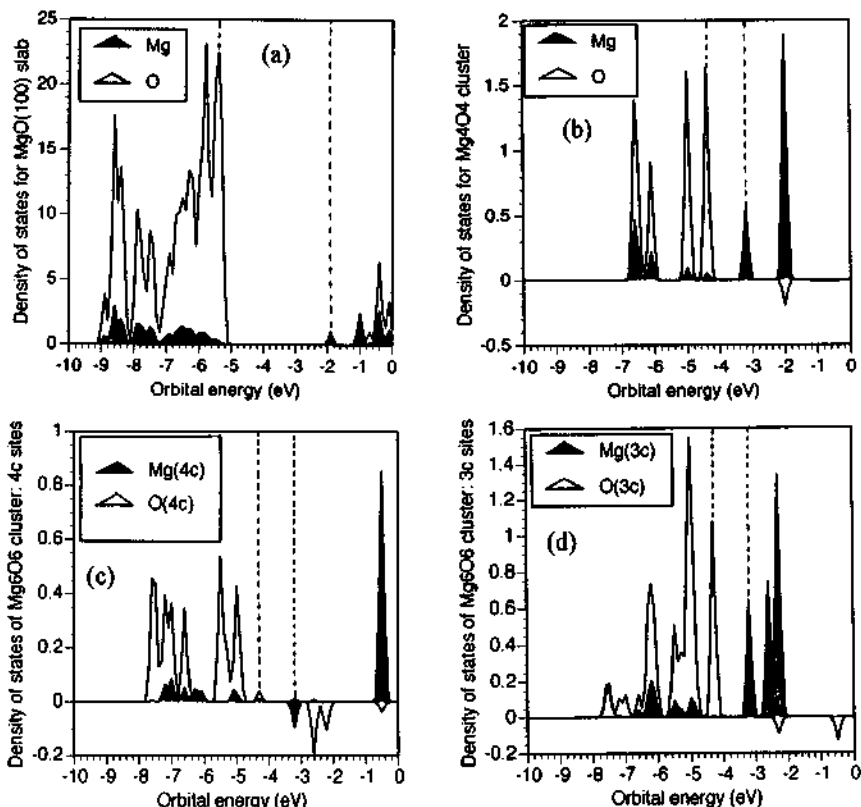


Fig.3. Local density of states for Mg and O atoms. (a)  $\text{Mg}_4\text{O}_4(100)(5c\text{-}5c)$  slab, (b)  $\text{Mg}_4\text{O}_4(3c\text{-}3c)$  cluster, (c) (4c-4c) sites of  $\text{Mg}_6\text{O}_6$  cluster, (d) (3c-3c) sites of  $\text{Mg}_6\text{O}_6$  cluster.

### 3.3 Adsorption of Methane

The interactions of one and two methane molecules with the surface are investigated using the  $Mg_4O_4$  cluster. The structures optimized for the  $CH_4$  moiety are illustrated in Fig.4, and their adsorption energies are shown in Table 2. At the non-local level of calculations, the formation of  $Mg-CH_3$  and  $O-H$  bonds leads to the stabilization of 26 kcal/mol, whereas almost no stabilization for the  $O-CH_3$  and  $Mg-H$  bond formation. This result is consistent with our previous work.[15(b)] Once the  $Mg-CH_3$  and  $O-H$  bonds are formed, the adjacent sites are activated similar to the case of hydrogen adsorption. Adsorption of the second molecule leads to stabilization for either type of

Table 2 Adsorption energies for  $Mg_4O_4-CH_4$  system<sup>a</sup>

	Neutral	Anion
$Mg-CH_3+O-H$	25.5	
$Mg-H+O-CH_3$	0.1	
$(Mg-CH_3+O-H)_2$	57.5	57.4
$Mg-CH_3+O-H+Mg-H+O-CH_3$	32.8	32.3
$Mg-H+O-H + C_2H_6$	10.1	
$H_2+C_2H_6$	-16.6	

<sup>a</sup>Results of non-local calculation. Unit is kcal/mol. The sum of energies of free cluster and two free  $CH_4$  molecules is taken as the reference energy.

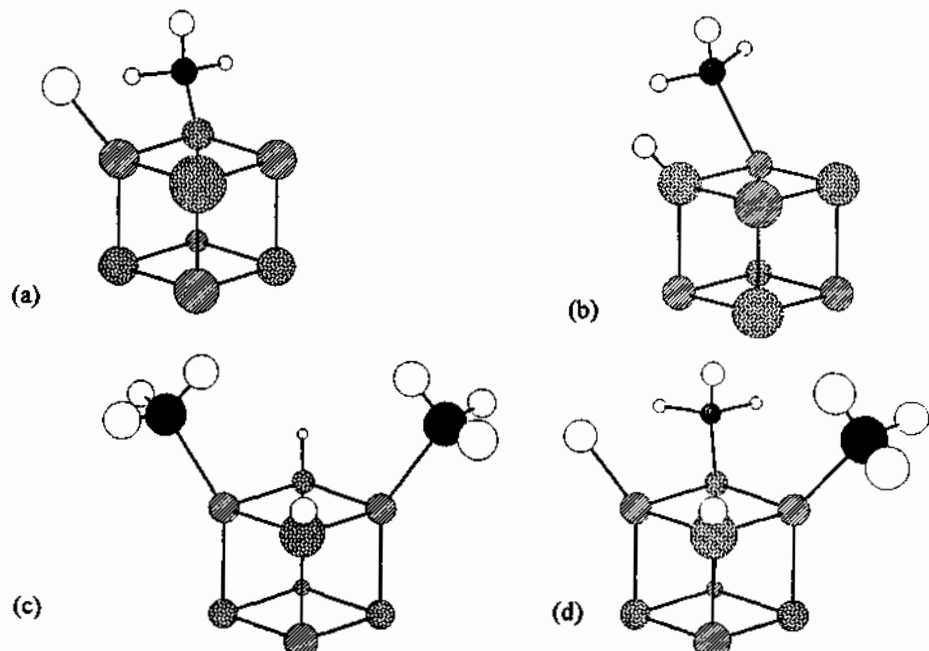


Fig.4. Optimized structures for one and two  $CH_4$  adsorption to  $Mg_4O_4$  cluster. (a)  $Mg-CH_3+O-H$ , (b)  $Mg-H+O-CH_3$ , (c)  $(Mg-CH_3+O-H)_2$ , (d)  $Mg-CH_3+O-H+Mg-H+O-CH_3$

bond formation with the adsorption energies of 58 and 33 kcal/mol, respectively. The difference is still 25 kcal/mol. However if the O-CH<sub>3</sub> and Mg-H bonds are formed on the surface, more than one species are produced by desorption. That is, C<sub>2</sub>H<sub>6</sub> and H<sub>2</sub> as well as CH<sub>4</sub>. The recombination of two CH<sub>3</sub> produces ethane leaving the Mg-H and O-H bonds. This system is still bound with respect to the initial state, i.e., the Mg<sub>4</sub>O<sub>4</sub> cluster and two CH<sub>4</sub> molecules. (The further desorption of H<sub>2</sub> is an endothermic reaction, and these H atoms must be removed by oxygen atom or molecule, although this reaction is not discussed here.) The effects of the Li or other alkaline atoms are estimated roughly by the calculations using the anionic Mg<sub>4</sub>O<sub>4</sub> cluster, but significant difference is not obtained. The adsorption of two methane molecules to this small cluster is an unrealistic model, and very large stabilization energies are calculated. Using much larger clusters including the (3c-4c) site or the (4c-4c) site which is activated by the first molecule, smaller and more reasonable adsorption energy is expected to be obtained along with the case of hydrogen.

### 3.4 Adsorption of Carbon Monoxide

The adsorption of CO is examined using Mg<sub>4</sub>O<sub>4</sub> cluster. Table 3 shows the adsorption energies for the Mg<sub>4</sub>O<sub>4</sub>-CO and Mg<sub>4</sub>O<sub>4</sub>-(CO)<sub>2</sub> systems. The structures of systems are illustrated in Fig.5. For the Mg-CO binding mode, the energy continuously lowers from the linear to bridged configurations, whereas there is a small barrier between the linear and chain configurations for the Mg-OC mode. The adsorption to the surface oxygen atom is found to be unstable in both the O-CO and O-OC modes. When the two molecules are adsorbed, the Mg atom binds two CO. (The twin configuration.) The further optimization leads to the twin-opt configuration, where one CO is adsorbed to the Mg atom and the other is to the O atom. Thus adsorption to the surface oxygen atom occurs only in the co-adsorption to the adjacent Mg atom. Based on the results obtained here, we can propose the mechanism for the CO exchange reaction observed experimentally.

We consider the reaction cycle starting with MgCO(bridged), as shown in the bottom of Fig.5. The second CO molecule can be further adsorbed to the Mg atom, which produces the twin species. The increase in the adsorption energy is 16 kcal/mol. The optimization of the twin form leads to the twin-opt form with a further gain of 1.6 kcal/mol. There are two possibility removing one CO from the twin-opt form. The calculated desorption energies are 18.6 and 18.3 kcal/mol, for the right side and left side CO, and nearly the same energy suggests that either CO may desorb in equal probability. The desorbed complexes are labeled the twin-left and twin-right, and the optimization of either complex reproduces a common species, that is, the bridged configuration. This mechanism is realistic energetically and structurally. So the route through the twin-left complex replaces the first CO with the second CO when the cycle reproduces the bridged configuration.

Table 3 Adsorption energies for Mg<sub>4</sub>O<sub>4</sub>-CO and Mg<sub>4</sub>O<sub>4</sub>-CO<sub>2</sub> systems<sup>a</sup>

	linear	linear'	bridged /chain	twin	twin-opt	twin-left	twin-right
MgCO	19.0	20.6	21.9	38.0	39.6	21.0	21.3
MgOC	12.8	7.3	19.9				

<sup>a</sup>Results of non-local calculation. Unit is kcal/mol.

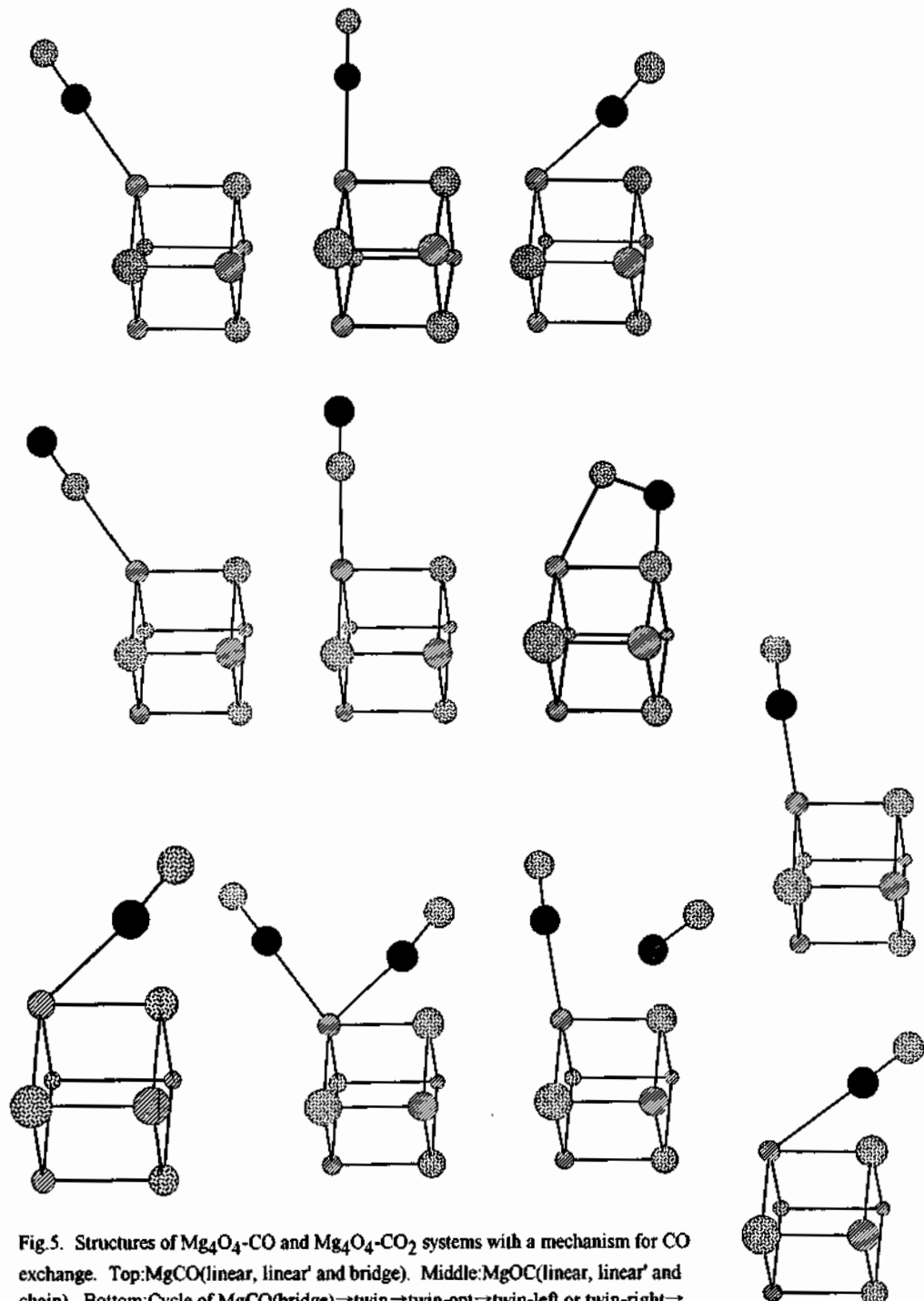


Fig. 5. Structures of  $\text{Mg}_4\text{O}_4$ -CO and  $\text{Mg}_4\text{O}_4$ - $\text{CO}_2$  systems with a mechanism for CO exchange. Top:  $\text{MgCO}$ (linear, linear' and bridge). Middle:  $\text{MgOC}$ (linear, linear' and chain). Bottom: Cycle of  $\text{MgCO}(\text{bridge}) \rightarrow \text{twin} \rightarrow \text{twin-opt} \rightarrow \text{twin-left or twin-right} \rightarrow \text{MgCO}(\text{bridge})$ .

#### 4. Conclusion

In this paper we investigated the interactions between the MgO surface and H<sub>2</sub>, CH<sub>4</sub> and CO molecules employing the DF method and several cluster and slab models. For the dissociative adsorption of H<sub>2</sub> and CH<sub>4</sub>, following consequences are drawn: (1) The surface atoms at the (3c) site are much more reactive to the adsorbing molecule than the atoms at the higher coordination number sites, and it is necessary to include at least one (3c) site for stable adsorption. (2) The adsorbed H atom and CH<sub>3</sub> fragment activate the neighboring sites, which explains the co-adsorption or pre-adsorption effects. On the other hand, CO is adsorbed associatively in the present work. So the effects on the coordination number are expected to be relatively small. (Although we did not discuss the adsorption to larger clusters, a tentative result to the Mg(4c) site shows 17.4 kcal/mol of stabilization energy. The difference between the Mg(4c) and Mg(3c) sites is below 2 kcal/mol.)

Simple discussion based on the qualitative crystal field theory is instructive. With decrease in the number of surrounding opposite ions, the electrostatic field which stabilizes the ionic lattice structures becomes weak. That is, both the attractive field for the O derived orbitals and the repulsive field for the Mg derived orbitals become weak. The system tries to supplement the stability with the covalent nature, and the charge on atoms decreases. The HOMO and LUMO levels shift to the higher and lower energy regions, respectively, and consequently the band gap is reduced. These changes in the electronic structures make the bond alternation process through the charge transfer interactions much more facile. Thus we can understand the enhancement of reactivity at the low coordination number site in terms of the local increase of covalence.

#### Acknowledgment

The major part of this work was supported by a Grant-in-Aid for Scientific Research from the Ministry of Education of Japan.

#### References

- 1.(a)Ito, T.; Lunsford, J.H. *Nature (London)*, 1985, 314, 721. (b)Ito, T.; Wang, J.-X.; Lunsford, J. H. *J.Am.Chem.Soc.*, 1985, 107, 5062.
2. Guglielminotti, E.; Coluccia, S.; Garrone, E.; Cerruti, L.; Zecchina, A. *J.Chem.Soc., Faraday Trans. 1*, 1979, 75, 96.
3. (a) Coluccia, S.; Tench, A. J., *Proc. 7th Int.Congr.Catal.*, 1981, p.1154. (b)Coluccia, S.; Bocuzzi, F; Ghiootti, G.; Mirra, C., *Z.Phys.Chem. (Frankfurt)*, 1980, 121, 141.
4. (a)Garrone, E.; Zecchina, A.; Stone, F. S., *J.Catal.*, 1980, 62, 396. (b)Garrone, E.; Stone, F. S., *Proc.8th Int.Congr.Catal.*, Verlag Chem., Weinheim, 1984, vol.3, p.441. (c)Garrone, E.; Stone, F. S., *J.Chem.Soc., Faraday Trans. 1*, 1987, 83, 1237.
5. Ito, T.; Tashiro, T.; Watanabe, T.; Toi, K.; Kobayashi, H., *J.Phys.Chem.*, 1991, 95, 4476.
6. Boudart, M.; Delbouille, A.; Derouane, E. G.; Indovina, V.; Walters, A.B., *J.Am.Chem.Soc.*, 1972, 94, 6622.
7. Ito, T.; Tominaga, N.; Tashiro, T.; Toi, K.; Ikemoto, I.; Kobayashi, H., *Bull.Chem.Soc.Jpn.*, 1990, 63, 3016.
8. (a)Hattori, H., "Adsorption and Catalysis on Oxide Surfaces", 1985, p.319. (b)Hattori, H.; Satoh, A. *J.Catal.*, 1976, 45, 32.
9. Tanaka, Y.; Imizu, Y.; Hattori, H.; Tanabe, K., *Proc. 7th Int. Congr. Catal.*, 1981, p.1254.

10. (a)Ito, T.; Sekino, T.; Morai, N.; Tokuda, T., J.Chem.Soc. Faraday Trans. 1, 1983, 77, 2181.  
(b)Ito, T.; Kuramoto, M.; Yoshioka, M.; Tokuda, T., J. Phys. Chem. 1983, 87, 4411.
11. Zecchina, A.; Lofthouse, M. G.; Stone, F. S., J. Chem. Soc., Faraday Trans. 1, 1975, 71, 1476.
12. Garrone, E.; Zecchina, A.; Stone, F. S., Phil.Mag., 1980, B42, 683.
13. Che, M.; Tench, A. J., Adv.Catal., 1982, 31, 77.
14. Fujioka, H.; Yamabe, S.; Yanagisawa, Y.; Matsumura, K.; Huzimura, R., Surface Sci., 1985, 149, L53.
15. (a)Kobayashi, H.; Yamaguchi, M.; Ito, T., J.Phys.Chem., 1990, 94,7206. (b) Ito, T.; Tashiro, T.; Kawasaki, M.; Watanabe, T.; Toi, K.; Kobayashi, H., J.Phys.Chem., 1991, 95, 4477.
16. (a)Sawabe, K.; Koga, N.; Morokuma, K., J.Chem.Phys., 1992, 97,6871. (b)Sawabe, K., Ph.D. Thesis, Institute of Molecular Science.
17. Knozinger, E.; Jacob, K.; Singh, S.; Hofmann, P., Surface Sci., 1993, 290, 388.
18. Shluger, A. L.; Gale, J.D.; Catlow, C.R.A., J.Phys.Chem., 1992, 96, 10398.
19. Mehandru, S.P.; Anderson, A.B.; Brazdil, J.F., J.Am.Chem.Soc., 1988, 110, 1715.
20. Aray, Y.; Rodriguez, J.; Murgich, J.; Ruette, F., J.Phys.Chem., 1993, 97, 8393.
21. (a)Matsumura, K.; Yamabe, S.; Fujioka, H.; Yanagisawa, Y.; Huzimura, R., Phys. Rev., 1987, B36, 6145. (b) Huzimura, R.; Yanagisawa, Y.; Matsumura, K.; Yamabe, S., Phys. Rev., 1990, B41, 3786.
22. Pacchioni, G.; Minerva, T.; Bagus, P.S., Surface Sci., 1992, 275, 450.
23. (a)Salahub, D. R.; Fournier, R.; Mlynarski, P.; Papai, I.; St-Amant, A.; Ushio, J., "Density Functional Methods in Chemistry", edited by Labanowski, J. K.; Andzelm J. W., Springer Verlag, 1991, p.77. (b) St-Amant, A., Ph.D. Thesis, Universite de Montreal, 1991.
24. Kobayashi H.; St.-Amant, A.; Salahub, D. R.; Ito, T. Proc. 10th Int.Congr.Catal.1993, p.2527.
25. Godbout, N.; Andzelm, J.; Salahub, D.R.; Wimmer, E., Can. J.Chem., 1992, 70, 560.
26. Vosko, S. J.; Wilk, L.; Nusair, M., Can. J.Phys., 1980, 58, 1200.
27. (a) Perdew, J. P.; Yue, W., Phys. Rev., 1986, B33, 8800. (b) Perdew, J. P., ibid, 1986, B33, 8822; ibid, 1986, B34, 7406.
28. Ito, T.; Murakami, T.; Tokuda, T., J.Chem.Soc., Faraday Trans. 1, 1983, 79, 913.

This Page Intentionally Left Blank

## 2.19 Acidic Properties of Sepiolite

Y. KITAYAMA and M. NOMURA

Department of Chemistry and Chemical Engineering, Faculty of Chemical Engineering, Niigata University, Ikarashi Niigata 950-21 Japan

### Abstract

Surface area, adsorptive capacities for NH<sub>3</sub> and acidity of sepiolite are largely dependent on the H<sub>2</sub>O molecules containing in the tunnels of sepiolite crystals. Ammonia exchanged with the H<sub>2</sub>O coordinated to Mg<sup>2+</sup> along the tunnel wall of sepiolite tetrahydrate. On sepiolite dihydrate, NH<sub>3</sub> coordinated to the Mg<sup>2+</sup> along the tunnel wall and complete octahedral coordination. The Mg<sup>2+</sup> along the tunnel wall acts as Lewis acid. Acidities measured by n-butylamine titration were not consistent with the acid sites measured by ammonia adsorption.

### 1. INTRODUCTION

Sepiolite is a fibrous magnesia-silicate clay mineral and its ideal formula is Mg<sub>6</sub>Si<sub>12</sub>O<sub>30</sub>(OH)<sub>4</sub>·4H<sub>2</sub>O·nH<sub>2</sub>O (4H<sub>2</sub>O and nH<sub>2</sub>O represent respectively the coordinated water and zeolitic water)[1]. Sepiolite is a shape selective catalyst for cyclodehydration of 1,4-butanediol and diethylene glycol [2-3], since it contains uniform-size paralellpiped tunnels along the fiber (c-axis). In general, the dehydration occurred on acid sites of the catalysts. We have reported that the cyclodehydration of the diols occurred on the acid site inside the tunnel of sepiolite.

The structural change occurred by losing coordinated water to magnesium situated along the tunnel wall of sepiolite [4]. The coordination number of the magnesium ion along the tunnel wall changes reversibly by the dehydration of coordinated water molecules and the magnesium ions have a possibility to supply acid sites in the catalytic reactions. Therefore,

sepiolite is a suitable material to obtain structural information concerning with acid sites.

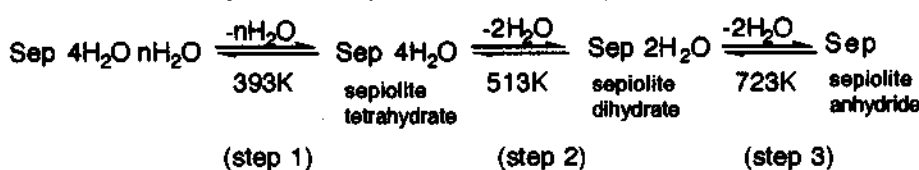
In this paper, acidic property of sepiolite outgassing at various conditions has been studied by butylamine titration using Hammet's indicator, IR spectroscopy of adsorbed basic materials and by adsorption of ammonia. Especially, roles of the acid sites inside the tunnel have been discussed.

## 2. EXPERIMENTAL METHODS

Fibrous sepiolite of Chinese origin was washed in the distilled water to eliminate impurities such as talc, magnesite and dolomite powder. Films were prepared by drying the fiber on teflon plate from suspension. Self supported films of sepiolite was mounted in the vacuum IR cell. Calcination of the samples and gas adsorption were carried out in the vacuum IR cell with cesium iodide window. Surface area and gas adsorption isotherm were measured by BET adsorption apparatus.

## 3. RESULTS and DISCUSSION

The dehydration process of sepiolite exhibits as follows;



The crystal structure is not changed by the dehydration of zeolithic water (step 1), while the crystal folds by the dehydration of a half of the coordinated water molecules (step 2). No structural change occurred in step 3 [4].

### 3.1. Surface Area

The surface area of sepiolite was increased by outgassing at 393K to

Table1 Surface area, acidity and NH<sub>3</sub> adsorption capacity

sample	surface area m <sup>2</sup> /g	Acidity* mmol/g	NH <sub>3</sub> adsorption** ml/g(STP)
Sep4H <sub>2</sub> O/nH <sub>2</sub> O	147	0.6	100
Sep4H <sub>2</sub> O	212	0.9	69
Sep2H <sub>2</sub> O	71	1.6	18
Sep	96	0.6	---

\* The acidity was measured at pKa=6.8

\*\* The values are adsorption capacities at the pressure of 600mmHg and at the temperature of 298K.

remove zeolitic water. The result suggests that the zeolitic water in the tunnel of sepiolite prevents the adsorption of N<sub>2</sub> into the inner surface of the tunnel at 77K. The surface area of sepiolite dihydrate was very small (71m<sup>2</sup>/g) as shown in Table 1. When sepiolite tetrahydrate transforms to dihydrate, the unit cell is folded as shown in Fig.1[4]. The effective cross sectional area of the tunnels decreases from 0.45x1.05nm<sup>2</sup> of tetrahydrate to 0.14x1.05nm<sup>2</sup> of dihydrate. Therefore, the surface area of sepiolite is affected by the fold of the tunnels.

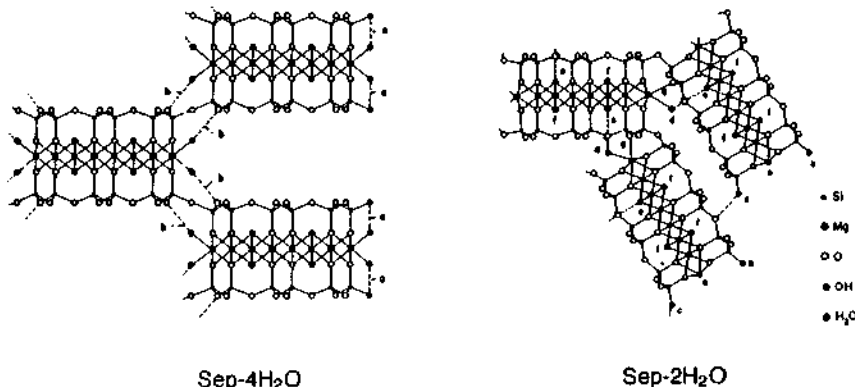
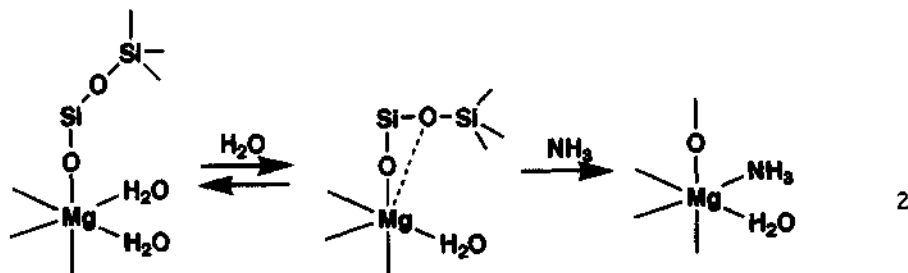
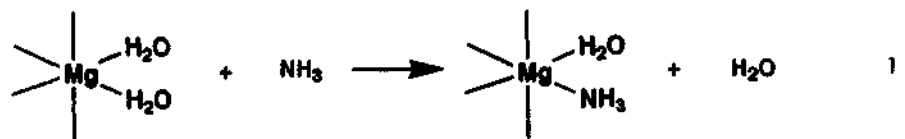


Fig. 1 End view of the right-hand edge of sepiolite tetrahydrate (Sep-4H<sub>2</sub>O) and dihydrate (Sep-2H<sub>2</sub>O).

### 3.2. NH<sub>3</sub> adsorption isotherm

Sepiolite adsorbed a large amount of ammonia. Adsorption capacity of NH<sub>3</sub> is about 15 times larger than that of O<sub>2</sub> and N<sub>2</sub>. Ammonia adsorption isotherms at 293K are presented in Fig.2. As can be seen, the capacity of sepiolite to adsorb NH<sub>3</sub> is decreased by an increase of outgassing temperature to remove the water containing in sepiolite(Sep4H<sub>2</sub>O-nH<sub>2</sub>O > Sep4H<sub>2</sub>O > Sep2H<sub>2</sub>O), although the surface area decreased in the order of Sep4H<sub>2</sub>O > Sep4H<sub>2</sub>O-nH<sub>2</sub>O > Sep2H<sub>2</sub>O. It is expected that the adsorption capacities of NH<sub>3</sub> largely depends on the existence of adsorbed, zeolitic and coordinated water and folding the tunnels in sepiolite crystals. This can be interpreted by a special interaction of NH<sub>3</sub> with the adsorbed and zeolitic water in sepiolite. As discussed in following section, the vibration band due to NH<sub>4</sub><sup>+</sup> was not found in the IR spectrum. The ammonia adsorbs as the form of NH<sub>3</sub> on Sep4H<sub>2</sub>O-nH<sub>2</sub>O and may be dissolved in zeolitic water inside the tunnels of sepiolite. The adsorbed NH<sub>3</sub> have no basicity to dissociate the zeolitic water molecules. The very small adsorption capacity for NH<sub>3</sub> of sepiolite dihydrate(Sep2H<sub>2</sub>O) is attributed to the small cross-sectional area of the tunnel by folding.

After the adsorption isotherm of NH<sub>3</sub> was measured on fresh sepiolite, the sample was outgassed at 293K. Then the subsequent adsorption isotherm have been measured and is shown with the filled symbols in Fig. 2. The subsequent NH<sub>3</sub> adsorption curves (filled symbols) lie well bellow the isotherms for fresh outgassed samples (open symbols). The difference between the fresh and the subsequent isotherms is evidence for the irreversible adsorption. The adsorbed NH<sub>3</sub> molecules on the fresh samples are remaining in sepiolite as shown in the following scheme;



### 3.3. IR spectra

The evidence on the forms of retaining ammonia in the samples evacuated, after the NH<sub>3</sub> adsorption has been carried out, has been examined by measurements of IR spectra. The dry NH<sub>3</sub> gas was introduced to the sepiolite film mounted in vacuum IR cell and evacuated at room temperature. The band at 3374cm<sup>-1</sup> was observed on sepiolite outgassing at room temperature, sepiolite tetrahydrate and dihydrate. No peaks in the region from 1400 to 1500 cm<sup>-1</sup> due to the deformation of NH<sub>4</sub><sup>+</sup> were observed. The results suggest that NH<sub>3</sub> coordinates directly to Mg<sup>2+</sup> along the tunnel wall instead of the coordinated H<sub>2</sub>O because the stretching band due to NH<sub>3</sub> of [Mg(NH<sub>3</sub>)<sub>6</sub>]Cl<sub>2</sub> have been observed at 3353cm<sup>-1</sup> [5]. The

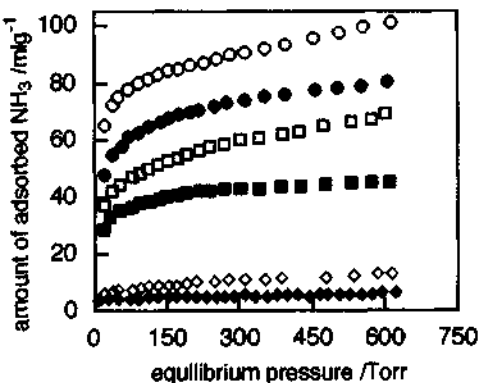


Fig.2 Adsorption isotherms of NH<sub>3</sub> at 293K on sepiolite evacuated at 293K(○,●), 413K (□,■) and 523K(◇,◆). The open and filled marks are the first and second isotherms, respectively.

coordinated  $\text{NH}_3$  could not removed by outgassing the sample at the room temperature, therefore the decrease of the subsequent  $\text{NH}_3$  adsorption was inhibited by the retaining  $\text{NH}_3$  in the sepiolite during the first adsorption. Since the bands due to  $\text{NH}_4^+$  were not observed in our experiments,  $\text{NH}_4^+$  was not produced on sepiolite or was too small quantity to observe by IR as if  $\text{NH}_4^+$  was formed. The intensity of the bending bands of the coordinated water in tetrahydrate ( $1622$  and  $1615\text{ cm}^{-1}$ ) decreased by ammonia adsorption. This supports that ammonia exchange with the coordinated water as shown scheme 1. Dandy *et al* has proposed a similar mechanism with us on sepiolite from Tunzania [6].

On sepiolite dihydrate, the band due to NH stretching of  $\text{Mg}(\text{NH}_3)$  was observed and the bending bands by the coordinated water was not affected by ammonia adsorption. This means that unstable five coordination of magnesium is changed to octahedral coordination by the addition of  $\text{NH}_3$  as shown in scheme 2. Therefore, magnesium located along the tunnel wall in sepiolite acts as Lewis acid.

### 3.4. Acidity

The acidity of sepiolite increased with the loss of zeolitic water and a further increase of acidity was observed by losing of half of coordinated water in sepiolite as shown in table 1. The reagents for the measurement of acdity were thoroughly dried and the measurements were carried out in dried  $\text{N}_2$  gas. Sepiolite anhydride shows a small acidity. On this results, the two  $\text{H}_2\text{O}$  molecules coordinated to the  $\text{Mg}^{2+}$  along the tunnel wall plays an important role for the acidic property of sepiolite. The octahedral  $\text{Mg}^{2+}$  along the tunnel wall is completed by the coordination of two  $\text{H}_2\text{O}$  molecules as shown in Fig.1. The coordination of  $\text{Mg}^{2+}$  along the tunnel wall in sepiolite is changed from six coordination to five coordination by dehydration of a half of coordination water molecules. In the absence of one  $\text{H}_2\text{O}$  of coordination, the unstable coordination site on the magnesium ions located at the tunnel wall can provide acid sites inside the tunnel of sepiolite. Acid strength of sepiolite containing zeolitic water ( $\text{Sep4H}_2\text{O}$   $n\text{H}_2\text{O}$ ) was distributed in the range from  $\text{pKa}=2.0$  to  $6.8$ . The stronger acid sites at  $\text{pKa}=-1.5$  were produced by eliminating zeolitic water ( $\text{Sep4H}_2\text{O}$ ) and half of the coordinated water ( $\text{Sep2H}_2\text{O}$ ) in addition to the acidity in the range of  $\text{pKa}=2.0-6.8$ , while no acidity at  $\text{pKa}=-1.5$  was observed in sepiolite anhydride. These results suggest that the octahedral magnesium located along the tunnel wall play an important role to produce acid site by outgassing at various temperature. Silanol groups on the edge of sepiolite surface may also give acid sites. Acidities measured by n-butylamine titration is not compatible with the amounts of adsorbed  $\text{NH}_3$ . Since the

molecular size of n-butylamine is larger than that of NH<sub>3</sub>, n-butylamine may not be able to enter into the tunnels of sepiolite. Therefore, NH<sub>3</sub> adsorbed on the outside and inside of the tunnels, while n-butylamine adsorbed only on the outside of the tunnels.

#### 4. Conclusions

(1) Adsorption of NH<sub>3</sub>, surface area and acidity of sepiolite were largely depended on the existence of adsorbed, zeolitic and coordinated water molecules and on the crystal structures.

(2)The Mg<sup>2+</sup> located at tunnel wall acts as Lewis acidic sites, since the water coordinated to the Mg<sup>2+</sup> exchanges with NH<sub>3</sub> in sepiolite tetrahydrate and an addition of NH<sub>3</sub> occurs to the unstable Mg<sup>2+</sup> of tunnel wall in sepiolite dihydrate as shown in the scheme. The Mg<sup>2+</sup> of the unstable coordination in sepiolite dihydrate plays an important role as Lewis acidic sites for catalytic dehydration.

(3)There are no relationship between acidity, surface area and NH<sub>3</sub> adsorption on sepiolite calcining at various temperature.

Acidity(pKa=6.8) Sep4H<sub>2</sub>O-nH<sub>2</sub>O < Sep4H<sub>2</sub>O < Sep2H<sub>2</sub>O > Sep

Surface area Sep4H<sub>2</sub>O-nH<sub>2</sub>O < Sep4H<sub>2</sub>O > Sep2H<sub>2</sub>O > Sep

NH<sub>3</sub> adsorption Sep4H<sub>2</sub>O-nH<sub>2</sub>O > Sep4H<sub>2</sub>O > Sep2H<sub>2</sub>O

#### References

- [1] A. Preiginger, "Clays & Clay Minerals" Earth Sci. Ser. vol.12, Pergamon Oxford, 1963, pp365.
- [2] Y. Kitayama and M. Kamimura, Chem. Express, 1990, 5, 554.
- [3] Y. Kitayama and A. Mitishita, J. Chem. Soc. Chem. Comm. 1981, 401.
- [4] H. Nagata, S. Shimoda and T. Sudo, Clays Clay Miner., 1974, 22, 285.
- [5] A. J. Dandy, J. Chem. Soc. (A), 1971, 2383.
- [6] K. Nakamoto, "Infrared and Raman spectra of inorganic and coordination compounds" 3rd ed., John Wiley & Sons, New York, 1978, pp199.

### **3. Design and Preparation of Catalyst**

#### **3.1 Synthesis of Solid Superacid of Borate Supported on Zirconium Oxides**

Hiromi MATSUHASHI<sup>a</sup>, Kazuyoshi KATO<sup>b</sup>, and Kazushi ARATA<sup>a</sup>

<sup>a</sup>Department of Science, Hokkaido University of Education, 1-2 Hachiman-cho, Hakodate 040, Japan

<sup>b</sup>Catalysis Research Center, Hokkaido University, Sapporo 060, Japan

#### **Abstract**

A solid superacid catalyst was synthesized from hydrated zirconium oxide and boric acid, the latter having quite low acidity. The results of ethanol decomposition revealed that  $\text{B}_2\text{O}_3/\text{ZrO}_2$  catalyst, containing 60 mol% B atom and calcined at 673 K, has superacidity. The acid strength was estimated to be closed to  $\text{Ho}=-13$  by TPD experiment. The results of IR and XPS show that three coordinated B atoms pull the electron from oxygen of  $\text{ZrO}_2$  and the negative charge on B atom is diffused into  $\text{B}_2\text{O}_3$  bulk by the resonance which occurs between the lone pair of oxygen and the empty orbital of B. The structure of active site was discussed.

#### **1. INTRODUCTION**

We have previously reported that solid superacid catalysts with an acid strength of up to  $\text{Ho}<-16.04$  were obtained by exposing hydroxides or oxides of Fe, Ti, Zr, Hf, Al, Sn, and Si, prior to the crystallization, to sulfate ion followed by calcination in air.[1] Also, the superacids of  $\text{ZrO}_2$  were synthesized by using tungstate and molybdate ions, called oxo-acids, instead of sulfate ion.[1] The synthesized superacids showed common properties as follows; the acid strength of solid superacids is higher than that of oxo-acids used for the treatment, specific surface area of the treated oxides is much larger, and the degree of crystallization is lower.

In our continuous effort in creating the superacidic surface acidity on metal oxide, the activity enhancement of  $\text{ZrO}_2$  was observed by the impregnation of boric acid which has very low acidity ( $\text{pKa}=5.0$ ); the activity for an acid-catalyzed reaction was higher than that of  $\text{SiO}_2-\text{Al}_2\text{O}_3$  catalyst, whose acid strength was in the range of  $-12.70 < \text{Ho} < 11.35$ .

## 2. EXPERIMENT METHODS

### 2.1. Catalyst Preparation

The catalyst was prepared as follows. Hydrated zirconium oxide ( $\text{ZrO(OH)}_2$ ) was obtained by hydrolyzing  $\text{ZrO}(\text{NO}_3)_2 \cdot 2\text{H}_2\text{O}$  with aqueous ammonia, washing, drying at 373 K, and powdering the precipitate (32-60 mesh). The hydrated oxide was impregnated with aqueous boric acid followed by evaporating water, drying, and calcining in air for 3 h at desired temperature. The concentration was calculated on the basis of mole fraction. The catalyst containing 30 mol% of borate ( $\text{B}/(\text{B}+\text{Zr})=0.3$ ) is denoted as 30 mol%  $\text{B}_2\text{O}_3/\text{ZrO}_2$ .

### 2.2. Reaction Procedure and Spectrum measurement

Decomposition of ethanol was selected as a test reaction to compare the activity of the catalyst with that of  $\text{SiO}_2\text{-Al}_2\text{O}_3$  (Nikki N-631L, 13 wt%  $\text{Al}_2\text{O}_3$  contained, heated at 773 K). The reaction was carried out in a microcatalytic pulse reactor with a fixed-bed catalyst (reaction temperature 523 K; flow rate of He carrier gas 30 mL/min; pulse size 1.0  $\mu\text{L}$ ; catalyst weight 20 mg). The catalysts were again heated at 523 K for 2 h in He flow before reaction. Effluent products were trapped at the end of the reactor by liq.  $\text{N}_2$ , then introduced into gas chromatographic column for analysis (API-201, 2 m).

TG-DTA was employed for pyridine TPD. The catalyst was heated in vacuum at 443 K for 30 min, then suspended in dried pyridine. After that, excess pyridine was removed by evaporation. The sample was heated in a He stream with temperature programmed rate of 10 K/min. The TPD profile was calculated as a differential line from the change of catalyst weight due to pyridine desorption.

XRD spectra of powdered samples were measured to estimate the degree of crystallization and the crystal structure. IR spectra of the catalyst and boron compounds were measured by KBr method.

## 3. RESULTS

### 3.1. Catalytic Activity

The dependency of the catalytic activity for ethanol decomposition on the calcination temperature and the content of  $\text{B}_2\text{O}_3$  is shown in Fig. 1. The products were predominantly ethylene and a small amount of diethyl ether. The catalytic activity increased with increasing the content of  $\text{B}_2\text{O}_3$ , and 60 mol%  $\text{B}_2\text{O}_3/\text{ZrO}_2$  gave the maximum activity. The calcination temperature which gave the maximum activity was dependent on the content of  $\text{B}_2\text{O}_3$ , and that fell with increasing the content.

The activity of 60 mol%  $\text{B}_2\text{O}_3/\text{ZrO}_2$  calcined at 673 K for the decomposition of ethanol at 423 K was compared with that of  $\text{SiO}_2\text{-Al}_2\text{O}_3$ . The activity of  $\text{B}_2\text{O}_3/\text{ZrO}_2$  (7.9 % in conversion) was higher than that of  $\text{SiO}_2\text{-Al}_2\text{O}_3$  (1.6%). The results indicate possibility of holding superacidity on the catalyst surface.

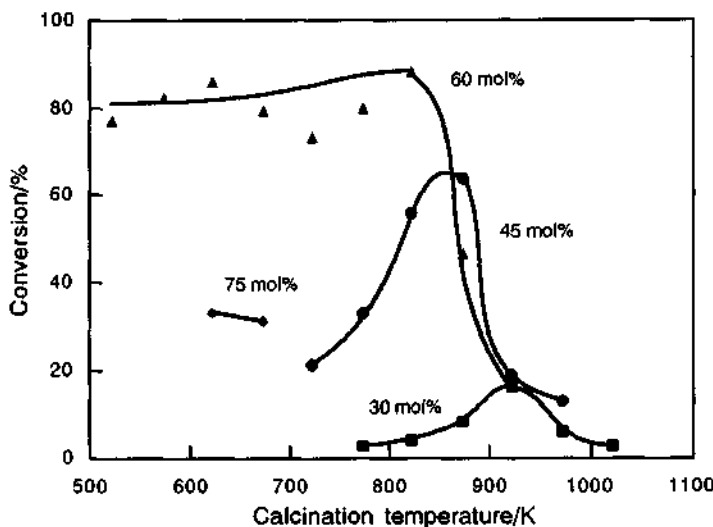


Fig. 1. Effect of calcination temperature and content of  $BO_3^{3-}$  on ethanol decomposition activity of  $B_2O_3/ZrO_2$ .

### 3.2. TPD Experiment

The acid strength of the  $B_2O_3/ZrO_2$  was estimated by temperature-programmed desorption (TPD). As is shown in Fig. 2, linear relationship was found between the maximum acid strength in the Hammett function scale ( $H_o$ ) and the termination temperature of pyridine desorption. The termination was 789 K for 60 mol%  $B_2O_3/ZrO_2$  calcined at 773 K, 701 K for  $SiO_2-Al_2O_3$ , and 921 K for  $SO_4^{2-}/ZrO_2$ , whose surface acidity was reported to be  $H_o < -16.04$ . From the results of TPD experiment, it is clear that the acid strength of 60 mol%  $B_2O_3/ZrO_2$  is higher than that of  $SiO_2-Al_2O_3$ . Also the acid strength of  $B_2O_3/ZrO_2$  was almost estimated to be -13.0 in  $H_o$  scale.

### 3.3. XRD measurement

XRD spectra of the  $B_2O_3/ZrO_2$  calcined at various temperatures were measured (Fig. 3). Any peak could not be found in all catalysts except the catalysts calcined at 923 K or higher, which are a mixture of tetragonal and monoclinic structures of  $ZrO_2$ . These results show that the crystallization of  $ZrO_2$  was retarded by the treatment with  $BO_3^{3-}$ . The analogous phenomena were also observed with the  $ZrO_2$  and  $TiO_2$  catalysts treated with sulfate ions.[1] Amorphous hydrated zirconium oxide crystallizes at 683 K, and the  $ZrO_2$  heated at 773 K consists of a mixture of tetragonal and monoclinic forms; the former converts into the latter form by calcination over 773 K. Also there was no peak assigned to a compound containing boron, though a large amount of  $BO_3^{3-}$  ion was impregnated on the surface.

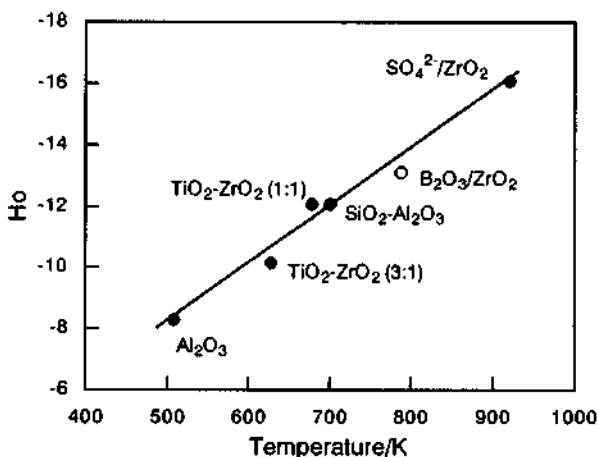


Fig. 2. The relation between acid strength and termination temperature of pyridine desorption.

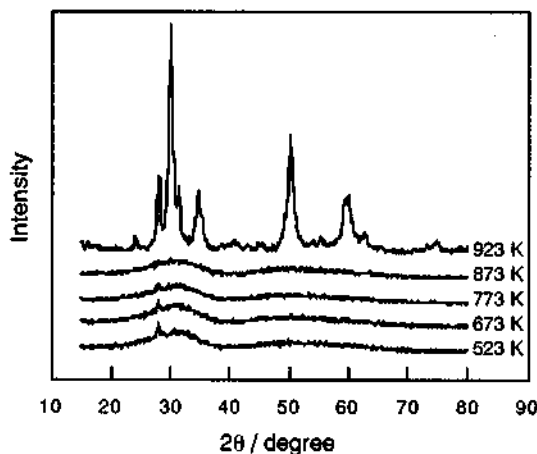


Fig. 3. XRD profiles of  $\text{B}_2\text{O}_3\text{/ZrO}_2$  calcined at various temperature.

### 3.4. IR measurement

IR spectra of  $\text{B}_2\text{O}_3\text{/ZrO}_2$  calcined at various temperatures are shown in Fig. 4 and 5, together with those of boric acid, boron oxide and borates. An absorption band assigned to antisymmetric stretching of B-O bond was appeared around  $1400\text{-}1500\text{ cm}^{-1}$ . This band was moved to high frequency with increasing the calcination temperature. As is shown in Fig. 4, with  $\text{H}_3\text{BO}_3$  and  $\text{B}_2\text{O}_3$ , which have three coordinated boron atom, the absorption band of the antisymmetric stretching was observed at  $1472\text{ cm}^{-1}$ . In the case of  $\text{Na}_2\text{B}_4\text{O}_5(\text{OH})_4\cdot 8\text{H}_2\text{O}$ , which has three and four coordinated boron atoms, this band was

observed at 1420 and 1356  $\text{cm}^{-1}$ . The absorption of B-O bond of  $B_2O_3/ZrO_2$  calcined at 773 K appeared at 1420  $\text{cm}^{-1}$  and this position agrees with that of three coordinated boron atoms in borates. From these results, it is concluded that the coordination number of boron cation in  $B_2O_3/ZrO_2$  was predominantly three.

The peak appeared at 3216  $\text{cm}^{-1}$  in Fig. 4 is quite close to those observed on  $B_2O_3$  and  $H_3BO_3$  at 3212  $\text{cm}^{-1}$ , as shown in Fig. 5. The broad peak at 3400-3500  $\text{cm}^{-1}$  is due to surface OH on  $ZrO_2$ . With the increase of calcination temperature, OH peak disappeared, and the intensity of the peak at 3216  $\text{cm}^{-1}$  increased. This phenomenon means that a new bond is formed between  $H_3BO_3$  and OH of  $ZrO_2$  surface by heat treatment.

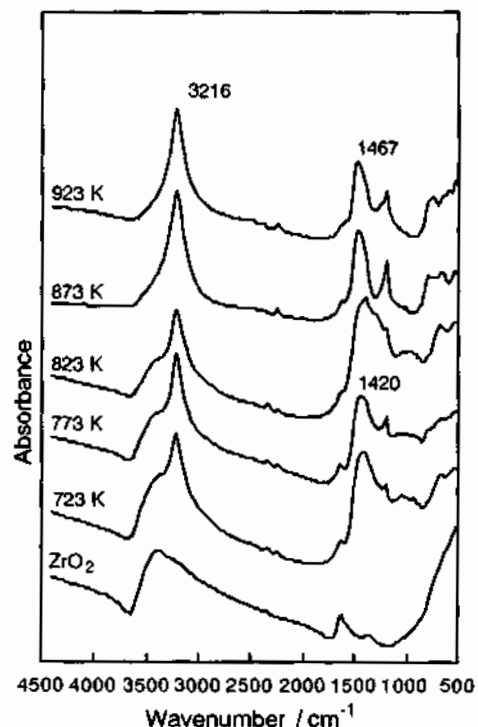


Fig. 4. IR spectra of  $ZrO_2$  and 60 mol%  $B_2O_3/ZrO_2$  calcined at various temperature.

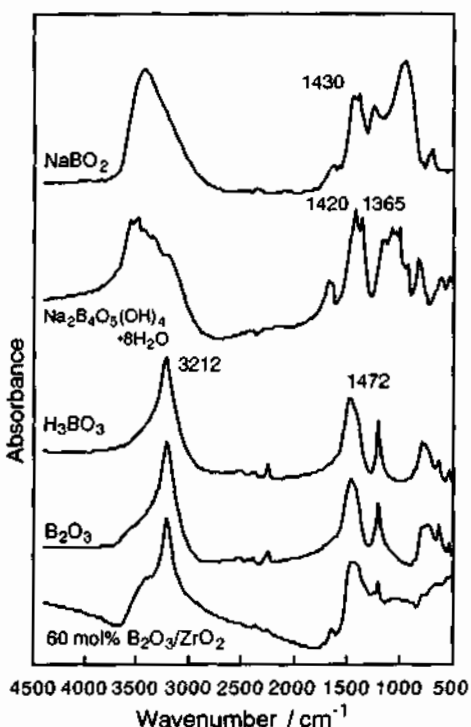


Fig. 5. IR spectra of 60 mol%  $B_2O_3/ZrO_2$  and boron compounds.

### 3.5. XPS measurement

Table 1 shows the results of XPS measurement of  $B_2O_3/ZrO_2$  calcined at 773 K and 923 K. All data of binding energy were corrected using  $C_{1s}$  (284.6 eV). The binding energy of  $B_{1s}$  of  $B_2O_3/ZrO_2$  calcined at 773 K was low compared with that of  $B_2O_3$ , which has three coordinated boron, and close to that of borate which has three and four coordinated

boron. From the point of view of the electron density, it could be concluded that the coordination number of surface boron atom was close to four.

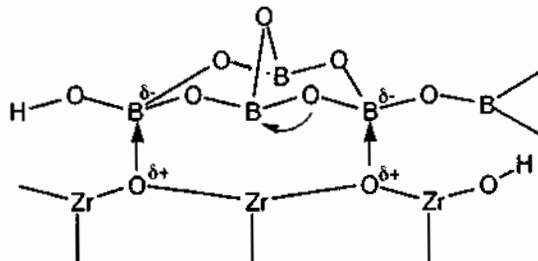
Table 1. Result of XPS measurement.

Sample	Binding energy of B <sub>1s</sub> /eV
60 mol% B <sub>2</sub> O <sub>3</sub> /ZrO <sub>2</sub> , 773 K	192.6
60 mol% B <sub>2</sub> O <sub>3</sub> /ZrO <sub>2</sub> , 973 K	193.2
B <sub>2</sub> O <sub>3</sub>	193.1
B(OH) <sub>3</sub>	192.8
Na <sub>2</sub> B <sub>4</sub> O <sub>5</sub> (OH) <sub>4</sub> ·8H <sub>2</sub> O	192.4

#### 4. DISCUSSION

The acid strength of 60 mol% B<sub>2</sub>O<sub>3</sub>/ZrO<sub>2</sub> calcined at 773 K was almost equal to  $H_o = -13$ . The structure of acid site was studied by XRD, IR, and XPS. From the results of XRD experiment, the degree of crystallization of B<sub>2</sub>O<sub>3</sub> was very low. The results of IR experiment show that OH of the ZrO<sub>2</sub> surface reacted with H<sub>3</sub>BO<sub>3</sub> during calcination, and that the coordination number of boron was three. It was shown by XPS that the electron density of boron atom was higher, and that the coordination number expected was four.

The structure of active site proposed by the experimental results are shown in scheme 1. The acid site is Zr<sup>4+</sup> or H<sup>+</sup> attached to Zr-O<sup>-</sup>. The electron on oxygen of ZrO<sub>2</sub> was pulled by the three coordinated B, which has an empty orbital. The negative charge of B is diffused into B<sub>2</sub>O<sub>3</sub> bulk by the resonance which occurs between the lone pair of oxygen and the empty orbital of B.[2]



Scheme 1. A proposed structure of active site.

#### References:

- [1] K. Arata, *Adv. Catal.*, **1990**, *37*, 165.
- [2] G. E. Jellison, Jr., L. W. Panek, P. J. Bray, and G. B. Pouse, Jr., *J. Chem. Phys.*, **1977**, *66*, 802.

## 3.2 Preparation of Platinum-Supported Alumina Lewis Superacid Catalyst Using a CVD Method

Akimi AYAME and Kazunori HONDA

Department of Applied Chemistry, Muroran Institute of Technology,  
27-1 Mizumoto-cho, Muroran, 050 Japan

### Abstract

An attempt was made to prepare a platinum-supported alumina Lewis superacid, which activates both dehydrogenation of alkanes and alkylation of aromatics. Platinum dichloride was supported on alumina Lewis superacid from amorphous platinum film heated in chlorine gas, and the supported sample was reduced *in vacuo* above 923 K or in hydrogen at 673 K. Platinum-supported alumina catalyst obtained had no hydroxyl groups and indicated such a strong Lewis acidity that coordinated pyridine was not desorbed even at 773 K and that benzene alkylation with propene was promoted at room temperature. Furthermore, the catalyst activated aromatization of cyclohexane at 373 K and benzene alkylation with propane at 573 K.

### 1. INTRODUCTION

The preparation of OH-free alumina Lewis superacid catalysts with  $H_0 < -14.52$  from  $\eta$ - and  $\gamma$ -aluminas by high-temperature chlorination using dry chlorine gas and its high activity to Friedel-Crafts type alkylation of aromatics at 0-303 K have been reported by one of the authors [1-3]. In alkylation of benzene using propene, the catalysts were also active but were deactivated by oligomers of propene formed on the surface of Lewis acid sites within a comparatively short time [4]. In order to avoid the deactivation, the supply of hydrogen atoms to reaction intermediates and protection of Lewis acid sites from the formation of oligomers using metal supporting or other organic compounds as alkylating reagent were required. The fact that  $\gamma$ -alumina is activated by treatments with  $CCl_4$  and HCl have been known since 1965 [5]. Similar activation of  $Pt/Al_2O_3$  with HCl or  $CCl_4$  has been carried out [6]. However, the investigators have adopted lower temperatures than 823 K as the treatment temperature, because  $PtCl_2$  formed by chlorination of Pt sublimes above 833 K. The chlorinated  $Pt/Al_2O_3$  catalysts obtained have both Lewis and Brønsted acid sites, although the acid strength and catalytic activity were promoted. In the present study, an attempt was made to prepare a bifunctional catalyst which activates both dehydrogenation of alkanes and alkylation of aromatics. In other words, supporting of Pt on the alumina Lewis superacid without OH groups and characterization of the supported catalyst obtained were performed.

## 2. EXPERIMENTAL

Principally,  $\gamma$ -alumina prepared from aluminum isopropoxide was used in the form of self-supporting disk (15 mg, 13 mm<sup>2</sup>). Its surface area was ca. 100 m<sup>2</sup>g<sup>-1</sup>. OH-free alumina solid Lewis superacids (AmLSA) were prepared by chlorination of  $\gamma$ -alumina (Am) at 1073 K for 60 min and then outgassing the product and remaining gases in glassware at the same temperature for 10 min [1-3]. PtCl<sub>2</sub> was supported on AmLSA from Pt-wire or amorphous Pt film heated in Cl<sub>2</sub> at 573-873 K for 30 min (PtCl<sub>2</sub>/AmLSA), and the supported sample was reduced in vacuo or in hydrogen above 573 K (Pt/AmLSA). The apparatus used for the catalyst preparation was a cross-shaped glassware comprising of the following parts; a quartz glass tube (QG) for dehydration, chlorination, and reduction at high temperatures, an *in situ* IR cell on the opposite end, an hourglass-shaped pyrex glass tube (PG) for deposition of PtCl<sub>2</sub> on one end of the other arm, and on the opposite side a pyrex glass joint equipped with a stopcock for attachment to the vacuum system. The AmLSA prepared in the QG was transferred to the neck of the PG in order to support PtCl<sub>2</sub>. The PtCl<sub>2</sub>-supported AmLSA obtained was again transferred to the QG for reduction, and the reduced sample was finally moved into the IR cell. Chlorine was distilled three times in a vacuum system and stored in a glass reservoir. Organic compounds distilled were stored in small flasks containing MS-4A. Hydrogen was dehydrated by passing it through a MS-4A column at 77 K to eliminate trace amount of water. Nitrogen was dried using a P<sub>2</sub>O<sub>5</sub> column. As reference catalysts, two samples were used; one was Pt-supported  $\gamma$ -alumina catalyst prepared by impregnation of H<sub>2</sub>PtCl<sub>6</sub> and subsequent hydrogen reduction at 673 K (Pt(1m)/Am), and the other was a Pt catalyst supported on AmEV ( $\gamma$ -alumina dehydrated *in vacuo* at 1073 K) in analogy with Pt/AmLSA (Pt/AmEV).

## 3. RESULTS AND DISCUSSION

### 3.1. Chemical Vapour Deposition

The formation and sublimation rates of PtCl<sub>2</sub> from Pt wire was very slow at 773 K. A suitable sublimation rate was obtained when the amorphous Pt film was chlorinated at 773 K. Above this temperature, the deposition yield of PtCl<sub>2</sub> on AmLSA decreased. From such preexperimental results, the amorphous Pt film (2 mg) was selected, and the adopted Cl<sub>2</sub> pressure, temperature, and operation time were 200 Torr, 773 K, and 30 min, respectively. In the case of AmLSA, PtCl<sub>2</sub> was deposited homogeneously on the front and back surfaces of the disk and diffused on the surface of bulk AmLSA particles. PtCl<sub>2</sub> was deposited on the surface of about two-third of total AmLSA particles. The deposition on AmEV took place only on the front surface of the disk and no diffusion of PtCl<sub>2</sub> on bulk particle surface occurred. The distinctions are caused by difference in the interaction between PtCl<sub>2</sub> and substrates, which is mainly attributable to the surface properties of OH- and O<sup>-</sup>-free AmLSA [1-3].

### 3.2. Reduction of PtCl<sub>2</sub>/AmLSA

Reduction of PtCl<sub>2</sub>/AmLSA and PtCl<sub>2</sub>/AmEV was performed by heating *in vacuo* at 773-1073 K for 30 min and contacting H<sub>2</sub> (400 Torr) at 573-773 K for 60 min. XRD patterns of thermally reduced samples are shown in Fig. 1. Both samples treated at 773 K showed no diffraction patterns of Pt

metal and  $\text{PtCl}_2$ . Complete reduction occurred at above 923 K. Crystallite size of Pt particles after the reduction at 1073 K, which was estimated from the peak at  $2\theta = 39.7^\circ$ , was 8.2 nm for Pt/AmLSA and 5.9 nm for Pt/AmEV. In ESCA measurements of typical samples some important results were obtained (Table 1). Pt/AmLSA showed no  $\text{Pt}4f_{7/2}$  spectrum, while Pt/AmEV indicated the spectrum at 314.1 eV, which agreed with that for Pt metal. The binding energy of  $\text{Cl}2p_{3/2}$  was coincided with that on AmLSA[1], but it was lower than 199.7 eV for  $\text{PtCl}_2$ . These results indicate that Cl atoms of  $\text{PtCl}_2$  supported on AmLSA and also Cl on AmLSA bond to  $\text{Al}^{3+}$  cations.

$\text{Al}2p$  appeared at 74.2, 74.0, 73.8 eV for AmLSA, Pt/AmLSA, and Pt/AmEV, respectively. The binding energy of  $\text{Al}2p$  seems to shift to the lower binding energy side with decrease in the amount of Cl bonded to  $\text{Al}^{3+}$  (AmEV was exposed to  $\text{Cl}_2$  when  $\text{PtCl}_2$  was supported).

Three Pt/AmLSA disks were powdered and the amount of Pt supported on AmLSA was determined by XRF. Pt on Pt/AmLSA sample was 0.0626 mg per disk, that is, 0.42 wt%. The amount corresponded to 31.3 % of that of an amorphous Pt film. The average density of Pt atom on the AmLSA surface was  $1.3 \text{ atm nm}^{-2}$ . As described earlier, since Pt was supported on about two-third of total AmLSA particles, the density on the Pt-deposited surface was estimated to be about  $2 \text{ atom nm}^{-2}$ .

### 3.3. FT-IR Spectra of OH Group and Adsorbed Pyridine

There is the possibility of OH groups forming again on AmLSA after the deposition and hydrogen reduction of  $\text{PtCl}_2$  had been performed. The formation may occur, of course, by water contamination during the complex handling. However, on Pt/AmLSA reduced thermally and by  $\text{H}_2$  at 673 K and  $\text{PtCl}_2/\text{AmLSA}$ , the IR band based on OH-stretching vibration was not detected. Consequently, it was ascertained that OH group and  $\text{O}^-$  species were absent on the samples. In the case of Pt/AmEV, a

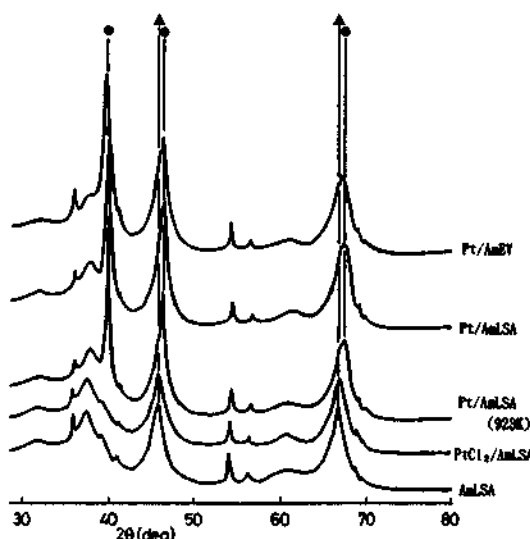


Fig.1. XRD patterns of various samples. Pt/AmLSA(923 K) implies  $\text{PtCl}_2/\text{AmLSA}$  reduced in vacuo at 923 K.  
 ●: Pt metal and ▲:  $\eta$ -alumina.

Table 1. ESCA data for Pt and Cl

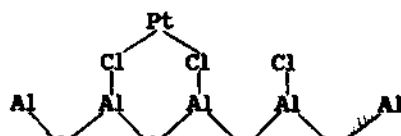
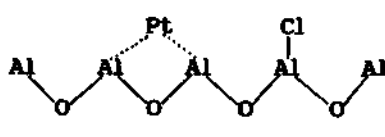
Sample	Temp./K	$\text{Pt}4f_{7/2}$	$\text{Cl}2p_{3/2}$
$\text{PtCl}_2/\text{AmLSA}$	773 <sup>a</sup>	315.5	198.8
Pt/AmLSA	1073	n.d.	198.8
Pt/Am	1073	314.1	198.7
Pt metal	-	314.4	-
$\text{PtCl}_2$	773 <sup>a</sup>	316.5	199.7

<sup>a</sup> Sublimation temperature.  
 n.d. indicates "not detected".

weak spectrum was observed at  $3678\text{ cm}^{-1}$ . Further, for Pt(im)/Am a strong absorption of the light of  $3676\text{ cm}^{-1}$  was observed.

Using two samples of Pt/AmLSA and Pt/AmEV, IR spectra of coordinated pyridine were measured (Fig. 2). All the peaks at  $1456$ ,  $1495$ ,  $1578$ , and  $1627\text{ cm}^{-1}$  observed on Pt/AmLSA were assigned to pyridine coordinated to Lewis acid sites. The peaks at  $1559$  and  $1505\text{ cm}^{-1}$  assigned to pyridine adsorbed on Brønsted acid sites were observed only on the Pt/AmEV.

From the results described above, possible surface structures of the  $\text{PtCl}_2/\text{AmLSA}$  and Pt/AmLSA are represented as follows:

[  $\text{PtCl}_2/\text{AmLSA}$  ]

[ Pt/AmLSA ]

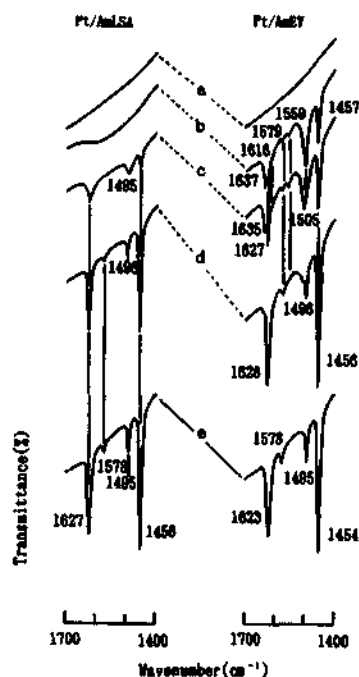


Fig.2. FT-IR spectra of adsorbed pyridine. Evacuation temperature of pyridine: b 873 K, c 773 K, d 583 K, e 493 K. a is background spectra.

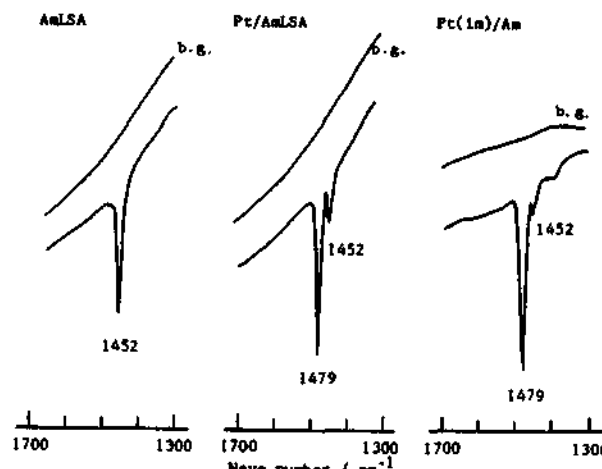
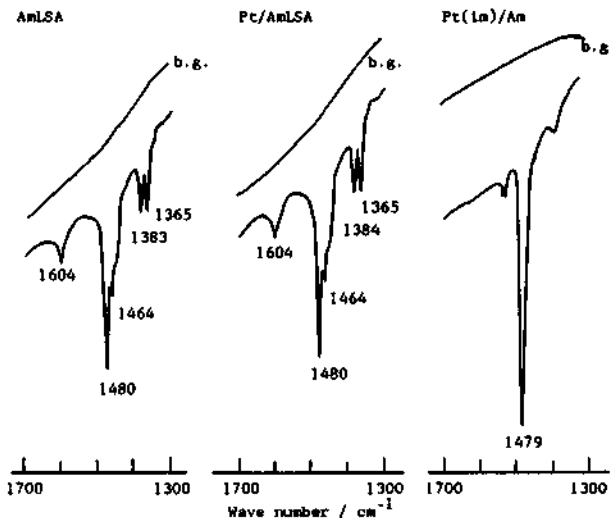
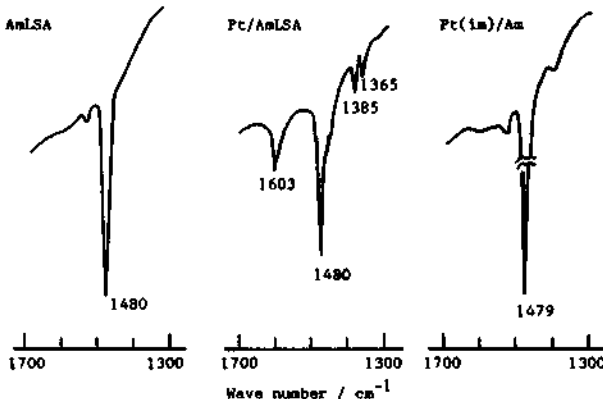


Fig.3. FT-IR spectra of cyclohexane and the product adsorbed when cyclohexane (20 Torr) was contacted to the samples indicated in figure at 573 K for 30 min.



**Fig.4.** FT-IR spectra when an equimolar mixture (60 Torr) of benzene and propene was contacted to the samples indicated in figure at room temperature for 10 min.



**Fig.5.** FT-IR spectra when an equimolar mixture (60 Torr) of benzene and propane was contacted to the samples indicated in figure at 673 K for 30 min.

### 3.4. Catalytic Properties

Catalytic properties of Pt/AmLSA were examined by heating in reactant gas mixtures and measuring IR spectra of products adsorbed on it at room temperature. The results were compared with those over AmLSA and Pt(im)/Am. When cyclohexane was introduced on the samples in the IR cell at room temperature, no IR spectra due to the products were detected. When Pt/AmLSA and Pt(im)/Am were subsequently heated above 373

K, the  $1479\text{ cm}^{-1}$  peak due to planar skeletal vibration of benzene ring was observed (Fig.3). The  $1452\text{ cm}^{-1}$  peak is due to cyclohexane adsorbed. The results imply that Pt/AmLSA possesses catalytic activity to dehydrogenation of alkanes.

Exposure of both AmLSA and Pt/AmLSA to equimolar mixture of benzene and propene at room temperature instantly resulted in quite similar spectra to those of isopropylbenzene, but on Pt(im)/Am such spectra were not detected (Fig.4). The appearance of  $1604\text{ cm}^{-1}$  peak and a twin peak at  $1385$  and  $1365\text{ cm}^{-1}$  indicates unquestionable evidence of the formation of isopropylbenzene. The former is assigned to ring vibration of mono-substituted benzenes and the latter does to the symmetrical deformation vibrations of C-H bond of isopropyl group. The  $1464\text{ cm}^{-1}$  peak is also due to asymmetric deformation vibration of C-H of the group.

In addition, when propane was used as alkylating reagent, clear evidence of the occurrence of benzene alkylation were obtained only on the Pt/AmLSA heated above 473 K for 30 min (Fig.5). The formation of isopropylbenzene (quimene) was confirmed by gas chromatographic analysis of the gases remaining in the catalyst preparation glassware.

From the results mentioned above, it is clear that the Pt/AmLSA is one of the bifunctional catalysts having activities for dehydrogenation of alkanes and alkylation of aromatics. Modification of the activity or acidity of Pt-supported alumina catalysts using impregnation of chloride ion or treating with various chlorine and fluorine compounds have been attempted by many investigators [5,6]. However, these methods are incapable of preparing such OH-free Pt-supported alumina catalysts as Pt/AmLSA in the present work. In the case of chlorine treatment of Pt(im)/Am above 773 K, the desorption or sublimation of Pt from alumina surfaces as  $\text{PtCl}_2$  took place together with elimination of OH group even for shorter time than 60 min. So, the present study proposes a unique preparation method of OH-free metal-supported metal oxide catalysts.

#### References

1. A. Ayame, G. Sawada, H. Sato, G. Zhang, T. Ohta, and T. Izumizawa, *Appl. Catal.*, 1989, 48, 25.
2. A. Ayame, T. Izumizawa, and K. Imanishi, " Acid-Base Catalysis " (Ed. K. Tanabe et al.), Kohdansha (Japan), pp. 371.
3. A. Ayame and T. Izumizawa, *Hyosen*, 1989, 27, 640.
4. A. Ayame and K. Inui, Unpublished data.
5. T. M. Oelderik and J. C. Platteeuw, " Proc. 3rd Intern. Congr. Catal. ", North Holland(Amsterdam), 1965, pp. 736;
- J. Basset, F. Figueras, M. V. Mathieu, and M. Prette, *J. Catal.*, 1970, 16, 53;
- E. Garbowski, J. P. Candy, and M. Primet, *J. Chem. Soc., Faraday Trans. 1*, 1983, 79, 835;
- M. Marczewski, M. Derewinski, and S. Malinowski, *Can. J. Chem. Eng.*, 1983, 60, 93;
- T. Tanaka and S. Ogasawara, *J. Catal.*, 1970, 16, 157; and so on.
6. J. M. Myers, *Ind. Eng. Chem. Prod. Res. Dev.*, 1971, 10, 200 ;
- A. G. Goble and P. A. Lawrence, " Proc. 3rd Intern. Congr. Catal. ", North Holland (Amsterdam), 1965, pp. 320;
- A. Melchor, E. Garbowkii, M. V. Mathieu, and M. Primet, *J. Chem. Soc., Faraday Trans. 1*, 1986, 82, 3667; and so on.

### 3.3 Synthesis and Catalytic Properties of Sulfate Ion-Promoted Zr-Pillared Clays

M. Katoh, H. Fujisawa and T. Yamaguchi<sup>†</sup>

Department of Chemistry, Faculty of Science, Hokkaido University, Sapporo 060, Japan

#### Abstract

Preparation of zirconium polycation-exchanged montmorillonite, which was promoted by sulfate ion, was examined in terms of the ion exchanging process and sulfation process. The acidic properties and the catalytic activities of thus prepared catalyst was examined by the isomerizations of 1-butene and cyclopropane and the disproportionation of alkylsilanes as well as the FT-IR of adsorbed basic molecules. It was found that the aging of the exchanging solution ( $ZrOCl_2$  solution) by reflux has a fatal importance to obtain a high surface area with a large interlayer-spacing pillared clays. A sulfation of thus obtained pillared clays gave a remarkable enhancement in acidic properties.

#### 1. INTRODUCTION

Sulfated metal oxides such as iron oxide, titanium oxide and zirconium oxide are known to show superacidity and they are called solid superacid. We have proposed the structure and the mechanism of the generation of superacidity [1]. We have extended this system to the two-dimensionally dispersed solid superacid which was reconstructed over a silica surface [2]. Generation of superacidity seems to be dependent on the particle (or crystal) size of the base oxide such as zirconium oxide [2]. Layered clay minerals such as montmorillonite can be modified by the polycation exchange to yield pillared clays. The pillar parts may be a highly dispersed metal oxide which are located in a nano-space. It is of our interest whether the acidic properties of such nano-scale metal oxides can be promoted by the sulfation.

In this article, we wish to report an attempt of the synthesis of a nano-scale solid acid constructed between the interlayer of the layered clay minerals such as montmorillonite and their acidic and catalytic properties.

#### 2. EXPERIMENTAL METHODS

##### 2.1. Catalyst Preparation

Four types of zirconium polycation-exchanged montmorillonite (Zr-MONT) were prepared as illustrated in Fig. 1. Zr-MONT(A/1) was prepared by exchanging  $Na^+$ -MONT (Kunipia-G, Kunimine Ind.) with an aqueous solution of 0.1M  $ZrOCl_2$  at room temperature, followed by washing and drying at 110°C. Zr-MONT(R-a), Zr-MONT(R-b), and Zr-MONT(R-C) were prepared by exchanging  $Na^+$ -MONT with an aqueous solution of 0.1M  $ZrOCl_2$  under reflux conditions. In case of R-a reflux was performed after the addition of  $Na^+$ -MONT to the exchanging solution, while the exchanging solution to prepare R-b was refluxed prior to the admission of  $Na^+$ -MONT to the solution, and the

<sup>†</sup>Present address : Department of Applied Chemistry, Faculty of Engineering, Ehime University, Matsuyama 790, Japan

two-step reflux was applied before and after the dispersion of  $\text{Na}^+$ -MONT to prepare R-c.

Zirconium polycation-exchanged saponite (Zr-SAPO) was prepared by following the preparation procedure of Zr-MONT (R-c) by using Sumecon-A (Kunimine Ind.). Aluminum polycation-exchanged saponite (Al-SAPO) was prepared by following the literature [3].

Two types of sulfated Zr-MONT (AS/Zr-MONT\* and AS/Zr-MONT) were prepared from 110°C-dried Zr-MONT directly and from 300°C-calcined Zr-MONT, respectively. The sulfation was performed at room temperature by using the R-c sample as a starting material and a 1N aqueous solution of ammonium sulfate (AS), since the use of sulfuric acid solution resulted in a partial dissolution of the zirconium pillars.

The preparations of sulfated  $\text{ZrO}_2$  (AS/ $\text{ZrO}_2$ ) and Zr-SAPO (AS/Zr-SAPO) are the same as that of AS/Zr-MONT.

## 2.2. Catalytic Reaction

The catalytic performance was evaluated by the isomerizations of 1-butene (1-B) at 0°C and cyclopropane (CP) at 100°C and the disproportionation of diethyldimethylsilane (E2M2) at 300°C. All the reactions were carried out in a closed recirculating reactor.

## 2.3. Physical Properties

Interlayer spacings were measured by XRD. BET surface area was measured by using  $\text{N}_2$  adsorption at liquid nitrogen temperature and by applying the finite BET equation. FT-IR spectra were recorded on a JASCO FT-IR/7000 spectrometer.

## 3. RESULTS AND DISCUSSION

### 3.1. Interlayer Spacing and Surface Area

Zirconium polycation exchanges give rise to an enlargement in both surface areas and interlayer spacings. As is shown in Figure 2, the interlayer spacings and the surface areas of A/1, which was obtained by a simple exchange method without a reflux process, gave an unsatisfactory result : low surface areas, small interlayer spacings and low thermal stability. R-c, which was obtained by a deep exchanging condition with a two-step reflux, exhibited large interlayer spacings and large surface areas regardless the calcination temperatures. Interlayer spacings and surface areas of R-a and R-b samples were slightly lower than those of R-c. Thermal stabilities of R-a, -b, and -c by calcination were also excellent. Refluxing and aging of  $\text{ZrOCl}_2$  solution may result in a growth in the size of polycations by a condensation. Ammonium sulfate treatment did not influence much those properties, however, AS/Zr-MONT\*, which was obtained by the AS treatment for 110°C dried R-c, gave slightly lower surface areas and interlayer spacings than AS/Zr-MONT, which was prepared from 300°C calcined R-c.

### 3.2. Acidic Properties

#### 3.2.1. IR

FT-IR spectra of a 500°C-evacuated AS/Zr-MONT sample (Fig. 3(A)) which was calcined at 600°C prior to the evacuation exhibited a sharp, strong absorption band at  $1373\text{cm}^{-1}$  that has been assigned to the stretching frequency of  $\text{O}=\text{S}=\text{O}$  species [1]. Since this absorption band could not be observed in either sulfated MONT (AS/MONT) or R-c (Fig. 3(B) and (C), respectively), it is clear that sulfate species are not bonded to silicate sheets but bonded to Zr-pillars which are located in interlayer nano-space of montmorillonite.

IR spectra of adsorbed pyridine on AS/Zr-MONT revealed exclusive presence of coordinated pyridine which strongly indicates the acidic sites being Lewis acid. The adsorption of pyridine on AS/Zr-MONT at room temperature resulted in the large shift in  $1373\text{cm}^{-1}$  band to lower frequencies and the evacuation at elevated temperatures removed pyridine and recovered  $1373\text{cm}^{-1}$  band. This clearly indicates that the adsorbed

pyridine locates closely to the O=S=O species which is bonded to a Zr cation. Pyridine also adsorbs on Zr-MONT which suggests the promotion of acidic properties of montmorillonite by the AS treatment.

### 3.3. Catalytic Performances

#### 3.3.1. Isomerization of cyclopropane

Figure 4 summarizes the comparison of the catalytic activities of several catalysts calcined at 500°C including AS/ZrO<sub>2</sub> and AS/Zr-SAPO in the CP isomerization which were evaluated after the 60 min reactions.

MONT, SAPO, Zr-SAPO and AS/SAPO were totally inactive. Zr-MONT and AS/MONT exhibited low activities. The sulfation to Zr-MONT (AS/Zr-MONT and AS/Zr-MONT\*) and Zr-SAPO (AS/Zr-SAPO) exhibited a remarkable activity enhancement.

Thus it can be concluded that the sulfation to polycation-exchanged clays is fatally important to obtain a high activity for the CP isomerization.

The effect of the calcination temperature on the catalytic activity was examined and the results are summarized in Figure 5. It is of interest that the activity maximum was found around 400°C in case of the CP isomerization over AS treated clay minerals, though the activity maximum for the benzoylation of chlorobenzene to yield benzophenone derivatives appeared at 550°C or 600°C by a sulfuric acid treatment or an ammonium sulfate addition, [4].

#### 3.3.2. Isomerization of 1-butene

As is shown in Figure 6, MONT and SAPO were inactive for this reaction, which indicates these two clay minerals has neither acidic nor basic properties. A large activity enhancement was found by the polycation exchange to both clays (Zr-MONT and Zr-SAPO). The sulfation to Zr-MONT (AS/Zr-MONT) enhances further the catalytic activity. It is quite interesting finding that although the sulfation to MONT did not enhances the acidic property, a remarkable enhancement was found for the same procedure on SAPO. The catalytic activity of AS/SAPO for 1-B isomerization was almost comparable to that of AS/Zr-SAPO.

As in the case of the CP isomerization, the sulfation is effective for the activity enhancement in the 1-B isomerization, however, the extent of the enhancement being not so high in case of the 1-B isomerization than in the CP isomerization.

#### 3.3.3. Disproportionation of alkylsilane

Alkylsilanes such as diethylsilane and diethyldimethylsilane (E2M2) disproportionate to yield ethylsilane and triethylsilane, and ethyltrimethylsilane and triethylmethysilane over acidic catalysts [5]. The disproportionation of E2M2 was examined over modified clay minerals and the results are summarized in Figure 7. Zr-polycation modifications resulted in a marked enhancement in the catalytic activity and the sulfation gave further promotion. The promotion effect was similar in the 1-B isomerization and the E2M2 disproportionation, which suggests both reactions take place on relatively weak acid sites. Thus Zr-polycation modifications exhibited to generates only weaker acidic sites, while further sulfate modification generates the stronger acid sites.

#### 3.3.4. Enhancement of acidic properties of clay minerals

The construction of acidic sites in the interlayer of clay minerals was attempted by the polycation exchange and sulfation to MONT and SAPO and the acidic properties of resultant materials were evaluated by means of FT-IR and model reactions. It can be pointed out that the acidic properties of zirconium oxide in the nano-space interlayer of clay minerals can be promoted remarkably by the proper sulfation.

In the isomerization of 1-B and the disproportionation of E2M2, it was found that a cation exchange itself effectively promotes the acidic properties. Further sulfation

enhanced the catalytic activity further but not to a great extent. This may indicate that the polycation exchange resulted in the increase or the generation of weak acid sites which are responsible for both reactions. Increase in the surface area and the interlayer spacing also contribute the activity enhancement and the increase in the number of weakly acidic sites. The disproportionation of E2M2 took place even at 100°C on ZrO<sub>2</sub> treated with sulfuric acid. However, the reaction on AS/Zr-MONT proceeded around 300°C. This indicates the acid strength of AS/Zr-MONT is not so strong.

The sulfated SAPO (AS/SAPO) can catalyze the isomerization of 1-B, while AS/MONT does not. This may be attributed to the difference in the structures, namely layered (MONT) or the card house (SAPO).

In the isomerization of CP, which may require stronger acid sites, a cation exchange itself is not enough to generate proper acidic sites to promote the reaction. The sulfation is necessary to generate the proper acid strength or, in other words, the stronger acid sites are only obtained by the sulfation. Thus, the polycation exchanges gave the weaker acid sites and the further sulfation gave moderately strong acid sites.

Thus, although the reactions which require strong acidity such as superacidity have not been attempted, acid strengths of the sulfated, Zr-polycation-exchanged clay minerals seem lower than that of bulk ZrO<sub>2</sub> treated with sulfuric acid or promoted by ammonium sulfate. Several reasons may be pointed out why extremely strong acid has not been obtained by this method.

1. Amount of sulfate ions were insufficiently introduced because of the use of ammonium sulfate for sulfation. Anions like a sulfate ion adsorb on zirconia surface more at low pH region. An aqueous solution of ammonium sulfate is almost neutral.

2. The particle size of pillar zirconia is so small that the sulfation resulted in the formation of compounds such as zirconium sulfate or zirconium oxysulfate. The chemistry of sulfation may be different from that of bulk zirconia.

3. The crystal size is so small that the mechanism of the generation of acidity is different from that of the sulfated bulk zirconia.

In case of the sulfation of bulk metal oxide, a proper amount of sulfate ions is necessary to generate superacidity; a lower amount of the sulfate ions does not generate superacidity. A quantitative analysis of the ratio of S/Zr is required to examine the consideration of category 1.

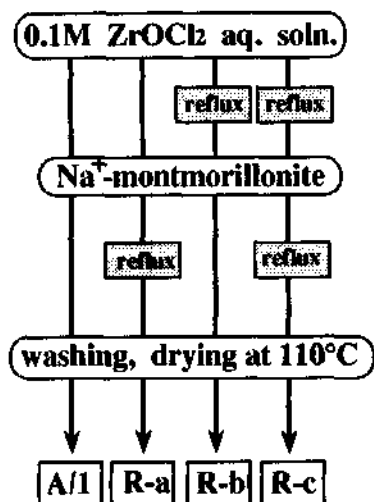
The mechanism of the generation of acidic properties in metal sulfates such as nickel sulfate has been well established [6, 7]. The acidity generation corresponds to the structural change of the monohydrated states to anhydrous state by the removal of coordinated water by calcination and the optimum temperature for the generation of acidic properties is found to be around 350°C to 400°C in case of nickel sulfate. This temperature range is almost the same as that of AS/Zr-MONT. This consideration may support category 2.

A crystal size effect on the appearance of the superacidity has been pointed out for the compound of sulfated ZrO<sub>2</sub> dispersed on SiO<sub>2</sub> [2]. Superacidity can be obtained only when dispersed ZrO<sub>2</sub> starts to crystallize or to form a long-range ordered structure. A consideration on category 3 is still under investigations.

## References

1. T.Jin, T.Yamaguchi, K.Tanabe, *J. Phys. Chem.*, **1986**, 90, 3148.
2. T.Yamaguchi, T.Jin, T.Ishida, K.Tanabe, *Mater. Chem. Phys.*, **1987**, 17, 3.
3. K.Urabe, H.Sakurai, Y.Izumi, *J. C. S. Chem. Comm.*, **1988**, 1520.
4. K.Tanabe, T.Yamaguchi, K.Akiyama, A.Mitoh, K.Iwabuchi, K.Isozaki, *Proc. 8th Intern. Congr. Catal.*, West Berlin, **1984**, V-601.
5. H.Fujisawa, T.Yamaguchi, *Catal. Lett.*, **1993**, 17, 319 ; *Chem. Lett.*, **1993**, 593.
6. T.Takeshita, R.Ohnishi, T.Matsui, K.Tanabe, *J. Phys. Chem.* **1965**, 69, 4077.
7. T.Takeshita, K.Tanabe, *Adv. Catal.*, **1967**, 17, 315.

### Preparation of Zr-MONT



### Preparation of Sulfate Ion-promoted Zr-MONT

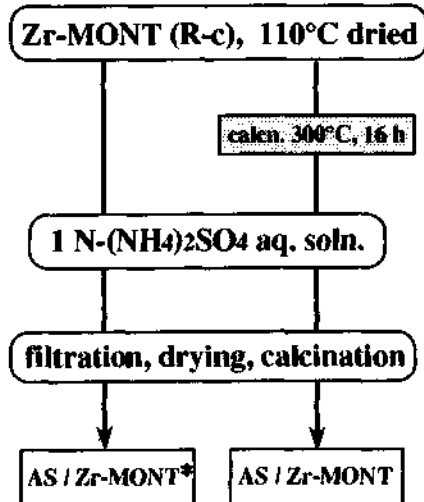


Fig. 1 Preparation of catalyst.

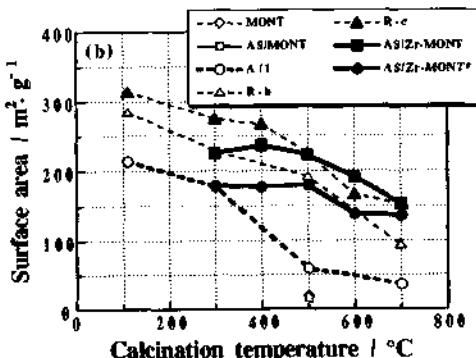
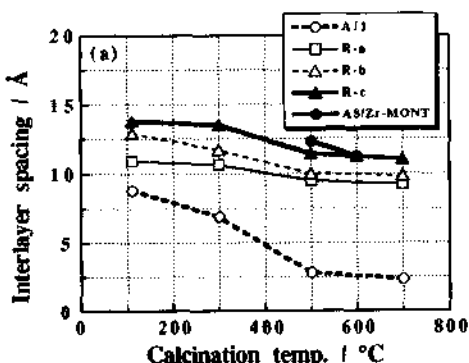


Fig. 2 Interlayer spacing (a) and surface area (b).

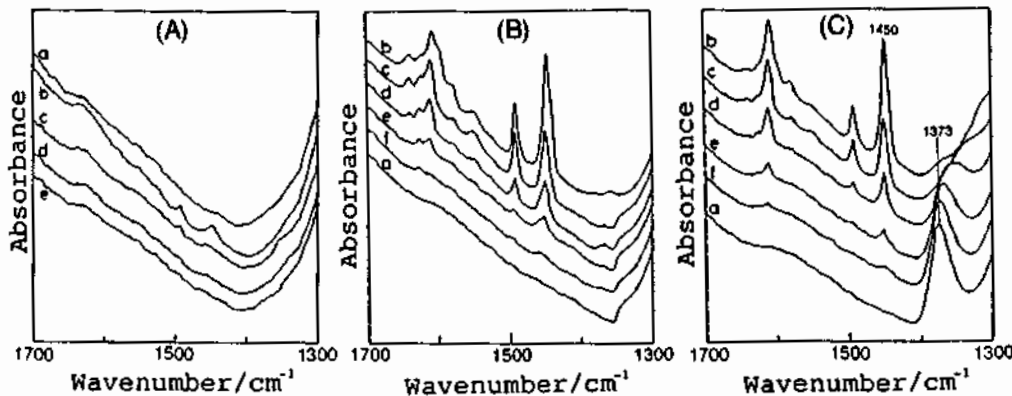


Fig. 3 FT-IR spectra of AS/MONT (A), Zr-MONT (B) and AS/Zr-MONT (C).  
 a. evac. at 500°C, b. adsorption of pyridine followed by evac. at room temperature, c.  
 evac. at 100°C, d. evac. at 200°C, e. evac. at 300°C, and f. evac. at 400°C.

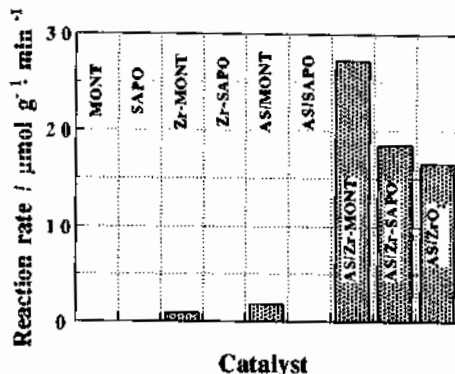


Fig. 4 Catalytic activity in isomerization  
of cyclopropane.

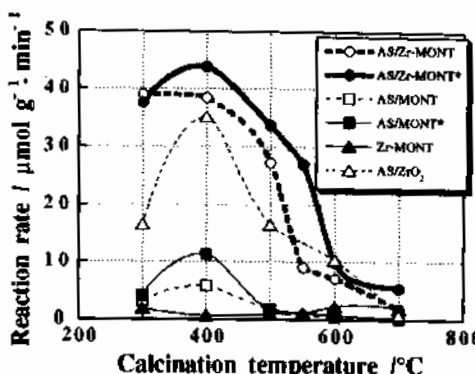


Fig. 5 Calcination temperature dependency  
in CP isomerization.

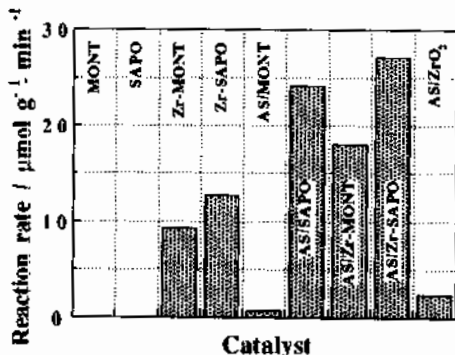


Fig. 6 Catalytic activity in isomerization  
of 1-butene.

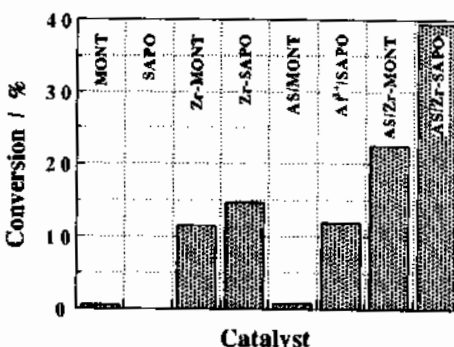


Fig. 7 Catalytic activity in  
disproportionation of E2M2.

### 3.4 The Role of Sulphate in the Stabilisation of Zirconia

C. J. Norman\*, P. A. Goulding, P. J. Moles.

MEL Chemicals, P.O. Box 6, Swinton, Manchester, M27 8LS, UK.

\*Alcan Chemicals Limited, Chalfont Park, Gerrards Cross, Bucks, SL9 0QB, UK.

#### INTRODUCTION

There is now considerable interest in the use of sulphated zirconia as a superacid catalyst<sup>(1-10)</sup>. The nature of the acid sites, whether Bronsted and/or Lewis has been extensively studied<sup>(3,5,6,8,10)</sup> as well as the roles of platinum and hydrogen in the isomerisation reactions of hydrocarbons utilising these materials<sup>(3,5-8,10)</sup>.

It has been observed that the surface area obtained with the sulphated zirconia is higher than the untreated material<sup>(11)</sup>. Furthermore the tetragonal phase of zirconia is also stabilised by sulphate<sup>(11)</sup>, but ideas are limited as to how surface area and phase stabilisation are achieved.

Based on infra-red spectroscopy, both a bidentate chelating<sup>(2)</sup> and a bidentate bridging mode<sup>(12)</sup> of attachment have been ascribed to the sulphate. The work of Squattrito, Rudolf and Clearfield<sup>(13)</sup> presented some rules for rationalising the structures of basic zirconium sulphates which we feel are germane to sulphated zirconia superacids. Application of the rules suggests that any monodentate or non-bridging sulphate ions are unstable and will either bridge or be displaced by a hydroxyl group.

The object of this work was to develop ideas as to the function of sulphate in stabilising surface area and the tetragonal phase of zirconia.

#### EXPERIMENTAL

A zirconium sulphate (MEL Chemicals) was treated with aqueous ammonia to remove sulphate in part or wholly to produce samples A and B respectively. Some of B was dried and sulphated using ammonium sulphate solution (sample C). All the samples were then dried prior to calcination. The heating rate used during calcination was 5°C min<sup>-1</sup> and the samples were held at temperature for 2 hours before cooling naturally to ambient temperature.

Surface area was measured following degassing at 260°C for ½ an hour (Flosorb). Pyridine adsorption was performed at 145°C and 230°C (Perkin Elmer TGS-2 TGA). FTIR was carried out in pressed discs. X-ray diffraction on the powder used operating conditions of 40kV 50mA and steps of 0.005° per 5 seconds (Philips 1710 Diffractometer). Differential Thermal Analysis (PL Thermal Sciences STA 1500) on the dried materials was also performed.

## RESULTS

The chemical analyses and surface area results are shown in Table 1 and Figure 1. The sulphate containing materials had higher surface areas compared to the unsulphated material until 950°C by which temperature the sulphate is lost.

The FTIR spectra of the sulphate containing materials (A, C) showed a number of bands corresponding to  $C_{2v}$  symmetry sulphate anion<sup>(14)</sup> Figure 2; these can be either bridging or chelating. By comparison with zirconium basic sulphates of known structure<sup>(13)</sup>, a bridging assignment was made (Figure 3).

The differential thermal analyses of the three materials were quite different (Figure 4). A sharp "glow" exotherm occurred at 426°C with the sulphate free zirconium hydroxide, sample B. A less pronounced exotherm at 591°C occurred with the sample A whereas the sulphate impregnated material, sample C, did not show the exothermic change. The exotherm is normally associated with the crystallisation of zirconia<sup>(15)</sup>.

The pyridine absorption results are given in Table 2. The sulphate containing materials had more acidic sites which were stronger because of the higher pyridine retention at 230°C.

After calcination at 700°C the phase contents of the three materials were 50, <1 and 97% tetragonal for A, B and C respectively.

TABLE 1  
Results After Calcination of Precursors

Sample	% SO <sub>4</sub> (700°C)	Surface Area/m <sup>2</sup> g <sup>-1</sup>		
		500°C	700°C	950°C
A	2.4	130	70	6
B	<0.05	85	34	13
C	3.4	160	90	6

TABLE 2  
Pyridine Adsorption After Calcination at 450°C

Sample	Pyridine adsorbed (μmol m <sup>-2</sup> )	
	145°C	230°C
A	—	1.25
B	1.05	0.57
C	—	1.22

FIGURE 1  
The Effect of Variation in Calcination Temperature  
on the Resultant Surface Area of the Oxides.

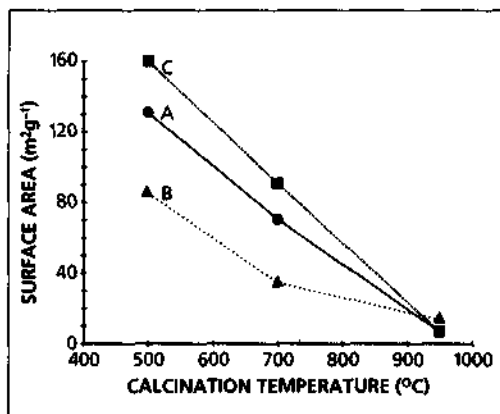
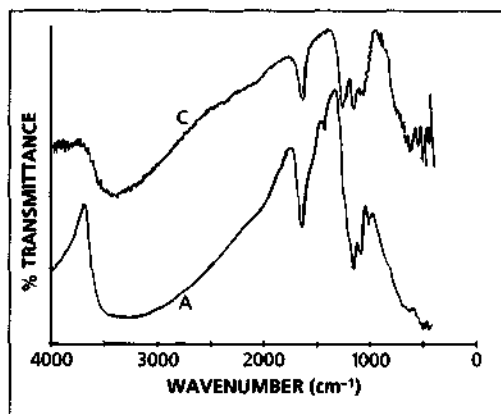
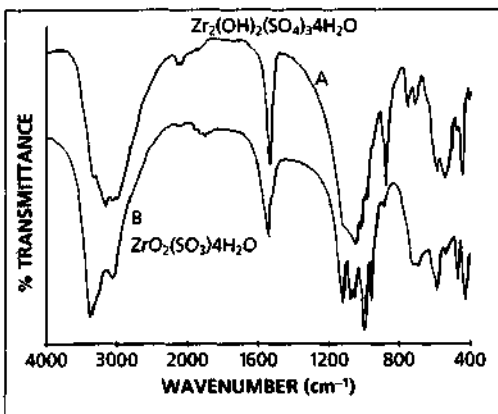


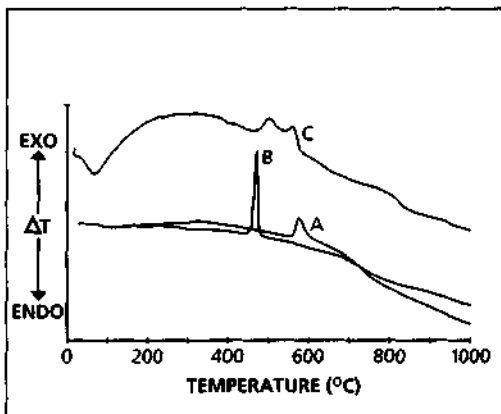
FIGURE 2  
FTIR Spectra of Sulphate Containing  
Hydroxides



**FIGURE 3**  
FTIR Spectra of Basic Zirconium Sulphate



**FIGURE 4**  
Differential Thermal Analyses of Materials A, B and C after Drying at 110°C



## DISCUSSION

In addition to the enhancement of acidity, the presence of sulphate within calcined zirconium hydroxides stabilised both the surface area and the tetragonal phase relative to a sulphate free system. However calcination eventually leads to the loss of surface area and phase stabilisation above about 700°C whereupon the sulphate is lost. The decomposition of zirconium hydroxide to zirconia is considered to proceed via three stages<sup>(15-16)</sup>.

- (1) Loss of loosely bound water.
- (2) Oxidation of hydroxy bridges to form embryonic oxide nuclei.
- (3) Growth of the nuclei to form observable crystallites.

These processes occur concurrently during calcination because no distinct steps can be seen during thermal analysis. The important step is the formation of the oxide nuclei as a result of dehydroxylation of hydroxy bridges<sup>(17)</sup>.

We propose that the presence of bridging sulphate has two effects. The first is the improved thermal stability of sulphate over hydroxy bridges and the second is an increased Zr-Zr separation (from 3.3 - 3.7 Å for the hydroxy bridges<sup>(15)</sup> to 3.5 - 4.3 Å for the sulphate bridges<sup>(13)</sup>). Both of these factors reduce the tendency to form oxide nuclei. We further propose that the underlying reason for stabilisation of surface area and restricted crystallite growth, which in the latter instance stabilises the tetragonal phase of zirconia<sup>(18)</sup>, is impeded diffusional processes due to the rigidity imparted to the structure by bridging sulphate.

Preliminary experiments have shown that the sulphated material (C) can isomerise butane<sup>(19)</sup> and is thus a superacid.

## ACKNOWLEDGEMENTS

Dr. P. D. Mercera and Prof. J. R. H. Ross (University of Twente) carried out much of the characterisation of the materials described here. Dr. S. L. Jones and Dr. C. F. Pygall (Alcan Chemicals Limited) are thanked for their many comments on the nature of sulphate in zirconium compounds.

**REFERENCES**

- (1) K. Tanabe Mater Chem Phys 13 347 (1985).
- (2) T. Yamaguchi K. Tanabe Y. C. Kung Mater Chem Phys 16 67(1986).
- (3) K. Ebitani J. Konishi A. Horie H. Hattori K. Tanabe in Acid Base Catalysis Ed K Tanabe et al 1988 ISBN 3-527-27883-4 P491.
- (4) J. R. Sohn H. W. Kim J. Mol Catal 52 361 (1989).
- (5) K. Ebitani H. Hattori K. Tanabe Langmuir 6 1743 (1990).
- (6) K. Ebitani J. Konishi H. Hattori J. Catal 130 257 (1991).
- (7) F. Garin D. Andriumasinoro A. Abdulsamad J. Sommer J. Catal 131 199 (1991).
- (8) K. Ebitani J. Tsuji H. Hattori H. Kita J. Catal 135 509 (1992).
- (9) S. Soled N. Dispenziere R. Saleh Prog in Catal 73 (1992).
- (10) P. Nescimento C. A. Kratopoulou M. Oszagyne G. Coudurier C. Travers J. F. Joly J. C. Vedrine in L Guczi et al New Frontiers in Catalysis 1993 Elsevier p1186.
- (11) J. M. Parera Cat Today 15 481 (1992).
- (12) H. Arata Adv in Catal 37 165 (1990).
- (13) P. J. Squatrito P. R. Rudolf A. Clearfield Inorg Chem 26 420 (1987)
- (14) K. Nakamoto Infrared Spectra of Inorganic and Co-ordination Compounds J Wiley 1970 ISBN 471-62980-4.
- (15) J. Livage K. Doi C. Mazieres J. Am Ceram Soc 51 349 (1968).
- (16) E. D. Whitney J. Am Ceram Soc 53 697 (1970).
- (17) A. Clearfield. Rev Pure Appl Chem 14 91 (1964).
- (18) R. C. Garvie. J.Phys.Chem 82 218 (1978).
- (19) C. F. Pygall. Unpublished Results

### **3.5 Catalytic Properties of Interlayer Acid Sites of Cation-Exchanged Synthetic Taeniolites**

T. Uematsu, H. Shoji, T. Odashima and S. Shimazu

Department of Applied Chemistry, School of Engineering,  
Chiba University, Chiba 263, Japan

#### **Abstract**

Interlayer acid sites were prepared by cation exchange of lithium cations on synthetic taeniolite. Their acidic properties were characterized by means of TPD, FT-IR, NMR and XRD. Catalytic behavior was studied for the dehydration of alcohols and discussed in terms of characteristics of interlayer acid sites.

#### **1. INTRODUCTION**

Modified interlayers of lamella compounds provide new host spaces for catalytic reactions. We have developed various modification methods to prepare intercalated fine metal particles, metal complexes and multiply modified layer hosts for molecular recognizing catalysis. This paper describes some trials to prepare interlayer acids sites on taeniolite. Catalytic properties were studied for the dehydration of alcohols.

#### **2. EXPERIMENTAL METHODS**

The interlayer  $\text{Li}^+$  of synthetic fluoro lithium hectorite, LTN:  $\text{Li}(\text{Mg}_2\text{Li})\text{Si}_4\text{O}_{10}\text{F}_2$ , was partially exchanged with poloyvalent metal cations M (M = Zr, Ta, Fe, Al, Ga, etc.,) using suitable solutions. The basal spacings ( $d_{001}$ ) of M/LTN were determined by XRD. Acidic properties of Fe/LTN were studied by pyridine-TPD, FT-IR,  $^{15}\text{N}$ -CP/MAS. The catalytic test was carried out by pulse method.

#### **3. RESULTS AND DISCUSSION**

##### **3.1 XRD observation**

The basal spasing of the metal form M/LTN was expanded by cation exchange of

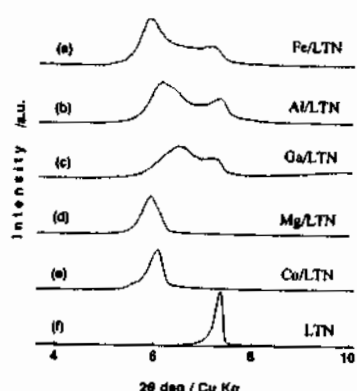


Fig. 1 XRD patterns of M/LTN.

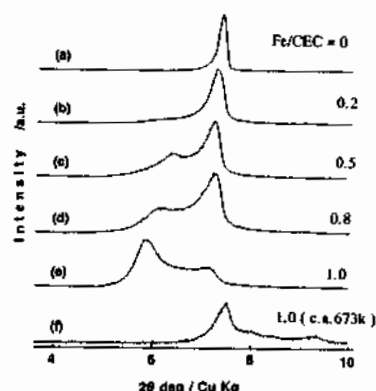


Fig. 2 XRD patterns of Fe/LTN.

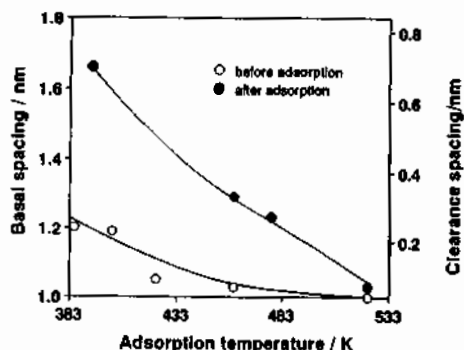


Fig. 3 Basal spacing of Fe/LTN swollen with EtOH.

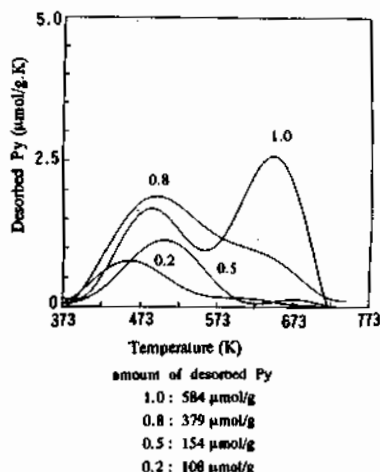


Fig. 4 Py-TPD profiles of Fe/LTN.  
amount of desorbed Py

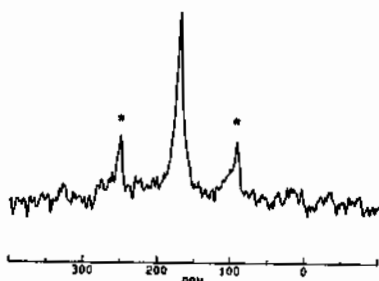


Fig. 5  $^{15}\text{N}$  CP/MAS NMR for Fe/LTN (1.0).

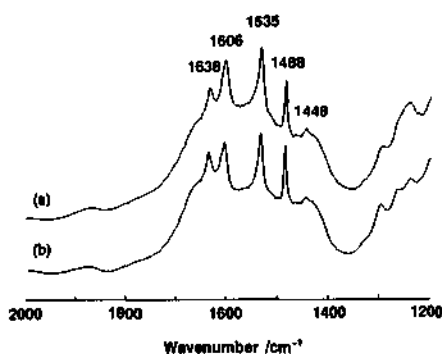


Fig. 6 IR spectrum of Py adsorbed on Fe/LTN .  
(a) 2h evac , 673K (b) 2h evac , R.T.

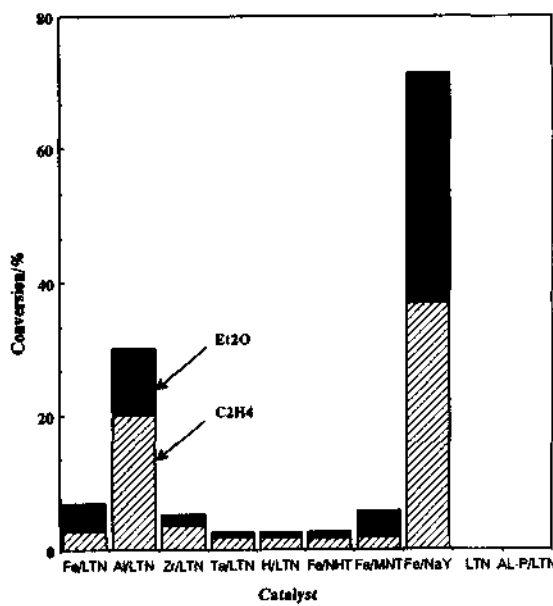


Fig.7 Dehydration of EtOH on various cation-form clays and zeolite.  
Pretreated and reacted at 473K.

interlayer  $\text{Li}^+$ . Divalent cation exchange to form M/LTN (M=Mg, Co) led to the complete shifts of XRD peak from  $d_{001}=1.21\text{nm}$  (the original LTN) to 1.46 - 1.49nm indicating simple transfer to each single phase structure, while the trivalent cation exchange to prepare Fe/LTN, Al/LTN, Ga/LTN ( $d_{001} = 1.52$ , 1.45, 1.52nm, respectively) gave residual LTN structure (Fig.1). Figure 2 shows the effects of  $\text{Fe}^{3+}$  exchange on the XRD profiles of Fe/LTN. The amount of expanded structure of Fe/LTN increased gradually with the  $\text{Fe}^{3+}$  concentration, and finally, predominated by loading  $\text{Fe}^{3+}$  equivalent to the CEC (0.86mmeq/g-Fe/LTN). However, the  $d_{001}$  distance decreased again after calcination at 673K due to the dehydration of interlayer water. Thus, Fe/LTN has no rigid oxide pillar structure like  $\text{Fe}_2\text{O}_3$  which is usually prepared by introducing polycations and calcination at higher temperatures[1].

The intercalation of ethanol was directly confirmed by in-situ measurement of  $d_{001}$  by means of high temperature adsorption XRD (Fig. 3). On introduction of ethanol vapor with  $\text{N}_2$  carrier gas at 383K over  $d_{1/2}$  phase of Fe/LTN, the  $d_{001}$  spacing increased very rapidly upto 1.64nm by the host-guest complexation to form EtOH-Fe/LTN monolayer phase (closed circle). The intercalation of ethanol at higher temperature expanded  $d_{001}$  by 5nm - 2nm. However, once dehydrated irreversibly at above 533K, no stable host-guest complex with ethanol was formed.

### 3.2 Acid properties

Temperature programmed desorption (TPD) of pyridine was studied for Fe/LTNs with different  $\text{Fe}^{3+}$ -concentration. Pyridine was adsorbed at room temperature on Fe/LTN pretreated in a dry  $\text{N}_2$  flow. Typical pyridine -TPD profiles (Fig. 4) show clearly two differnt desorption peaks at around 483K and 653K. The peak intensity for stronger acid sites appears to increase greatly with the increase in  $\text{Fe}^{3+}$  concentration. Thus, the acid sites are probably associated to the interlayer  $\text{Fe}^{3+}$  sites. In order to determine the type of acid sites,  $^{15}\text{N}$ -CP/MAS NMR and IR techniques were applied to adsorbed pyridine. NMR spectrum given in Fig. 5 shows a singlet peak at 171ppm except for two spinning side bands. This can be ascribed to pyridinium cations formed on protonic sites by comparing a similar shift caused by pyridine on H-mordenite [2]. A strong absorption band of FT-IR observed at  $1535\text{ cm}^{-1}$  in Fig. 6 confirms the presence of Bronsted acid sites which appeared over Fe/LTN evacuated at room temperature and remained after evacuation at 673K. However, another absorption band at  $1448\text{ cm}^{-1}$  due to Lewis acid sites became relatively weak. Since no such absorption bands were detected for LTN, these acid sites were induced by  $\text{Fe}^{3+}$  exchange.

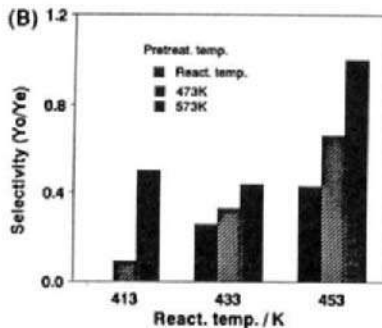
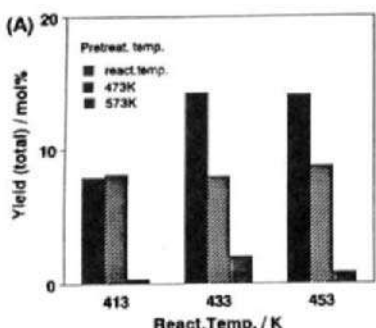


Fig. 8 Effect of pretreatment temperature for dehydration of ethanol with Fe/LTN (CEC<sub>x</sub>1.0)  
(A) Yield ; (B) product selectivity

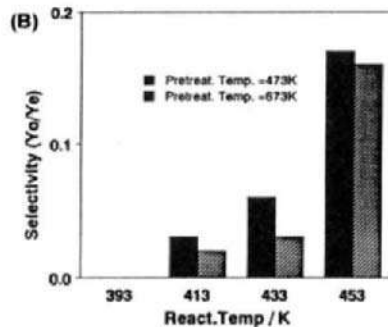
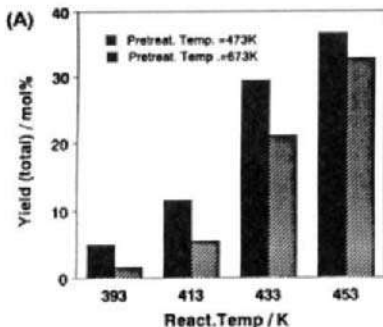


Fig. 9 Effect of prealment temperature for dehydration of ethanol with zeolite .  
(A) Yield ; (B) Product selectivity

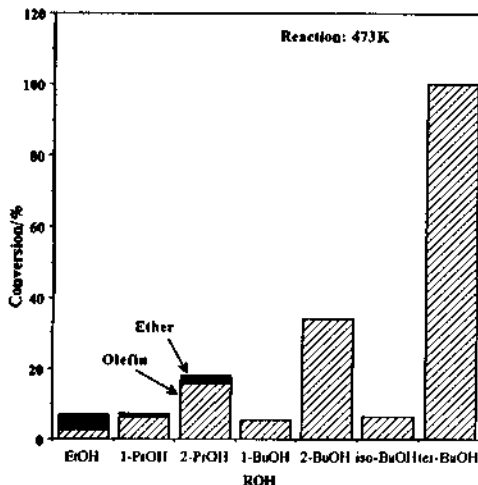


Fig. 10 Dehydration of ROH on Fe/LTN(1.0)  
Pretreated and reacted at 473K.

### 3.3 Catalytic behavior

Catalytic activity of variously cation exchanged LTN, hectorite (NHT), montmorillonite (MNT) and zeolite (NaY) are compared in Fig 7. The original LTN has no activity, while H-form and M-LTN (M= Fe, Al, Zr, Ta) developed considerable activity for the dehydration of EtOH at 473K. The selectivities defined by the ratio, C<sub>2</sub>H<sub>4</sub>/Et<sub>2</sub>O, were mostly more than unity, except Fe/LTN and Fe/MNT. These facts indicate that the monomolecular dehydration of ethanol is predominating over bimolecular dehydration over these catalysts at 473K. Al/LTN was most active among M/LTN; however, Al-pillared LTN showed no activity. This suggests that the active sites are associated to the interlayer metal cations but not to rigid oxide Al<sub>2</sub>O<sub>3</sub> pillar. Fe/NaY (cage host) was two times more active than Fe/LTN (layer host).

The effects of pretreatment temperatures were compared between Fe/LTN and Fe/NaY in Fig. 8 and 9. In both cases, higher temperature treatments in a He flow decreased catalytic activities. Especially, Fe/LTN lost almost activity by heating at 573K. The major reaction was diethylether formation on both catalysts. However, a marked contrast was obtained for the selectivity; the selectivity for olefin formation was much lower on Fe/NaY than Fe/LTN; in contrast to Fe/NaY, high temperature pretreatments of Fe/LTN retarded diethylether formation and thus increased the selectivity.

Shape selective catalysis by interlayer active sites were reported previously for the hydrogenation of olefins by Ru metal-pillared LTN[3] and aldehydes by Pd complex intercalated in LHT[4]. As a primitive trial, shape selective catalysis by interlayer acid sites was studied; catalytic behavior of Fe/LTN(1.0) for the dehydration reaction of various alcohols were compared in Fig. 10. The total conversion of primary alcohols, EtOH, 1-PrOH, 1-BuOH took place at similar rates showing little recognition of the chain length. While, secondary alcohols were decomposed more rapidly than primary alcohols.

Further, the rates for C<sub>4</sub>-alcohols were in the following order: 2-methyl-2-propanol > 2-butanol > 1-butanol > 2-methyl-1-propanol. This might suggest that "shape selective effects" play a role by flexible host of LTN. The monomolecular dehydration of alcohols predominated over bimolecular dehydration for alcohols with longer carbon chains (>C<sub>4</sub>).

## 4. REFERENCES

1. S. Yamanaka, T. Doi, S. Sako and M. Hattori, Mater. Res. Bull. (1984) 161.
2. J. A. Ripmeester, J. Am. Chem. Soc., (1983) 105, 2925.
3. S. Shimazu, T. Hirano and T. Uematsu, Appl. Catal. (1987) 34, 255.
4. S. Shimazu, T. Ishida and T. Uematsu, Proc. Int. Congr. Catal. (1988) 4, 1913.

### 3.6 Alkylation of Isobutane with Butene over Layered Double Hydroxide Pillared Heteropolyoxometalate Acid-Base Catalysts

Xu Zheng\* and Wu Yue

Changchun Institute of Applied Chemistry, Chinese Academy of Science, Changchun, China, 130022

He Heming and Jiang Dazhen

Department of Chemistry, Jilin University, Changchun, China, 130023

#### Abstract

[Si(W<sub>2</sub>O<sub>7</sub>)<sub>6</sub>]<sup>2-</sup>-pillared LDH structure hydroxides were synthesized by the method of restructuring of the thermally decomposed hydrotalcite-like compounds for Zn-Al and Mg-Al oxide systems. [P(W<sub>2</sub>O<sub>7</sub>)<sub>6</sub>]<sup>2-</sup>-pillared Ni-Al LDH structure hydroxide was synthesized by a new method developed in our laboratory, through direct anion exchange under microwave field. The pillared structure compounds were first used in alkylation of isobutane with butene. The reaction results indicated that this kind of catalysts possess good activity and selectivity towards this reaction.

#### 1. INTRODUCTION

Layered double hydroxides (LDHs, or so called anionic clays) are an important class of materials currently receiving considerable attention<sup>[1,2,3]</sup>. The LDHs consist of positively charged metal oxide/hydroxide sheets with intercalated anions, such as organic and inorganic<sup>[4]</sup>, isopolymetalate<sup>[5]</sup> and heteropolyoxometalate (HPOM) anions<sup>[1,5]</sup>, and water molecules. Narita<sup>[6]</sup> et al. used the method that an amorphous zinc-aluminium oxide solid solution Zn<sub>0.67</sub>Al<sub>0.33</sub>O<sub>1.17</sub>, prepared by the thermal decomposition of the layered double hydroxide (LDH) [Zn<sub>0.67</sub>·Al<sub>0.33</sub>(OH)<sub>2</sub>](CO<sub>3</sub>)<sub>0.17</sub>·0.33H<sub>2</sub>O is reacted with Keggin-like heteropolyoxometalate anions α-[Si·W<sub>11</sub>O<sub>39</sub>]<sup>2-</sup> and α-1,2,3-[SiV<sub>6</sub>W<sub>6</sub>O<sub>40</sub>]<sup>7-</sup> in acid solution to form pillared LDH structures. As a basic catalyst in the first open literature referring to precursors of LDH, hydrotalcite-like compounds were reported in 1971<sup>[7]</sup> and used in hydrogenation reaction by Brocher and Kaempfer<sup>[8]</sup>. Up to the present, only a few papers deal with the catalytic properties of heteropolyoxometalate pillared

layered double hydroxide.

In this paper, we synthesized  $[Si(W_2O_7)_6]^{2-}$ -pillared LDH structure hydroxides by the method described in literature through restructuring of the thermally decomposed hydrotalcite-like compounds for Zn-Al and Mg-Al oxide systems and also by a new method developed in our laboratory, through direct anion exchange under microwave field for Ni-Al LDH. The  $[Si(W_2O_7)_6]^{2-}$  pillared structure compounds were firstly used as the catalysts in alkylation of isobutane with butene. The reaction results indicated that this kind of catalysts possess good activity and selectivity towards this reaction.

## 2. EXPERIMENTAL METHOD

### 2.1. Restructuring of Mixed Oxides to Heteropolyoxometalate (HPOM) Pillared LDHs

The synthesis of LDHs was carried out by the Cavani's method<sup>[10]</sup> for  $Zn_6Al_2(OH)_{16}CO_3 \cdot 4H_2O$ ,  $Ni_6Al_2(OH)_{16}CO_3 \cdot nH_2O$  and Reichle et al.'s method for  $Mg_6Al_{2.26}(OH)_{16.26}(CO_3)_{1.14} \cdot 6H_2O$ <sup>[11]</sup>. The synthesized hydrotalcite-like compounds of  $Zn_6Al_2(OH)_{16}CO_3 \cdot 4H_2O$ ,  $Mg_6Al_{2.26}(OH)_{16.26}(CO_3)_{1.14} \cdot 6H_2O$  and  $Ni_6Al_2(OH)_{16} \cdot CO_3 \cdot nH_2O$  were then calcined in air at 500°C for 3h to form mixed oxides.

Restructuring of the mixed oxides into HPOM pillared LDH derivatives was accomplished by adding the calcined product mentioned above in small portions to a boiling solution containing 10mmol dm<sup>-3</sup> HPOM with vigorous stirring, keeping the mole ratio of HPOM/Al equal to 1.0 and 2.0. A solution containing of 0.2 mol dm<sup>-3</sup> HNO<sub>3</sub> was dropwise added to maintain the pH at desired values and prevent HPOM hydrolysis. Upon the addition of oxide, the mixture was allowed to stir for 0.5 h. All procedures were carried out under nitrogen atmosphere to avoid possible reaction of the calcined LDHs with atmospheric CO<sub>2</sub>. The final products were washed with water and dried in air at 90°C.

### 2.2. Synthesis of HPOM pillared LDH with Direct Anion Exchange under Microwave Field

The pillarating of Ni<sub>2</sub>Al-LDH was achieved by diret anion exchange of the corresponding intercalated NO<sub>3</sub><sup>-</sup> with H<sub>7</sub>[P(W<sub>2</sub>O<sub>7</sub>)<sub>6</sub>] · nH<sub>2</sub>O Keggin anion.

The precursor Ni<sub>2</sub>Al(OH)<sub>6</sub>NO<sub>3</sub> · nH<sub>2</sub>O was synthesized as follows: Ni(NO<sub>3</sub>)<sub>2</sub> and Al(NO<sub>3</sub>)<sub>3</sub> (mole ratio=2/1), and a suitable amount of NaOH dissolved in water with different vessels. Then, the two solutions were added to one vessel to maintain pH=8. Upon the addition, the mixture was allowed to stir for 14h at 70°C. All the procedures were carried out under nitrogen. Washed at room temp., Ni<sub>2</sub>Al(OH)<sub>6</sub>NO<sub>3</sub> · nH<sub>2</sub>O was formed. The prepared Ni<sub>2</sub>Al(OH)<sub>6</sub>NO<sub>3</sub> · nH<sub>2</sub>O was first dispersed into water and then HNO<sub>3</sub> solution was

added dropwise to maintain pH=4. For adjusting pH to 4, the solutions  $H_7[Si(W_2O_7)_6] \cdot nH_2O$  and NaHCO<sub>3</sub> were added alternatively into the solution. The precipitate was stirred for 10 min under microwave field, then washed with water and dried in air at 90°C.

### 2.3. Alkylation Reaction Procedures:

The reaction of isobutane with butene was carried out in a flow reactor. A mixture containing isobutane and butene in a constant mole ratio of 11:1 was fed through a constant volume of catalyst (2.0cm<sup>3</sup>) at a total pressure of 20 atm. The products were analyzed by gas chromatography(SHIMADUZU GC-9A) with an OV-101 column.

### 2.4. XRD Measurement:

The x-ray powder diffraction patterns were recorded by using a RIGAKU D/MAX III-A X-ray diffractometer with Cu K $\alpha$  (0.15418nm) radiation. Samples were mounted on glass slides by using double-seal type and inserted into sample holders.

### 2.5. IR Measurement:

The infrared spectra of hydrotalcite - like compounds and HPOM-pillared LDHs were recorded with a NICOLET 5DX FT-IR spectrometer.

## 3. RESULTS AND DISCUSSION

### 3.1. XRD Analysis

According to TG-DTA analysis of the parent LDHs, weight loss occurs in two stages. The loss below 220°C corresponds to the loss of 0.33H<sub>2</sub>O per metal ion. The loss between 220-500°C corresponds to concomitant decomposition of carbonate and partial dehydroxylation. Narita<sup>[4]</sup> reported that the diffuse of XRD pattern corresponding to a zinc-aluminium solid solution was observed when parent [Zn<sub>0.7</sub>Al<sub>0.33</sub>(OH)<sub>2</sub>](CO<sub>3</sub>)<sub>0.17</sub> · H<sub>2</sub>O was calcined at 500°C. So, the mixed oxides prepared by calcining each parent hydrotalcite-like compounds at 500°C were confirmed to form zinc-aluminium, magnesium-aluminium and nickel-aluminium solid solutions. Fig.1 shows the XRD patterns of the restructuring  $H_7[Si(W_2O_7)_6] \cdot nH_2O$  intercalated LDHs. Fig.1A shows that the XRD patterns of [Zn<sub>0.7</sub>Al]-[Si(W<sub>2</sub>O<sub>7</sub>)<sub>6</sub>]<sup>6-</sup> containing several 001 harmonics are almost the same as that reported by Narita<sup>[4]</sup>. The XRD pattern of [Mg<sub>0.7</sub>Al]-[Si(W<sub>2</sub>O<sub>7</sub>)<sub>6</sub>]<sup>6-</sup> is shown in Fig. 1B, which also contains several 001 harmonics. These results indicate that heteropolyoxometalate derivatives of LDHs can be conveniently prepared by reconstruction of the corresponding mixed metal oxide solid solution in the presence of the POM anion. However, the restructuring of [Ni<sub>0.7</sub>Al]-[Si(W<sub>2</sub>O<sub>7</sub>)<sub>6</sub>]<sup>6-</sup> from metal oxide solution

needs a higher reaction pressure. Fig. 2 shows the XRD patterns of  $[P(W_2O_7)_6]^{7-}$ -pillared LDH prepared by anion exchange method under microwave field and its parent LDH  $Ni_2Al(OH)_6NO_3 \cdot nH_2O$ . The results illustrate that the heteropolyoxometalate derivatives of LDHs also can be prepared by direct anion exchange under microwave field within a significant short time of 10 min.

The 14.6, 16.8 and 19.6 Å basal spacing given in Figs. 1 and 2 shows the HPOM pillared LDHs structures with gallery height of 9.9, 12.1 and 14.9 Å, as the thickness of the LDH layer is taken to be 4.7 Å<sup>[11]</sup>.

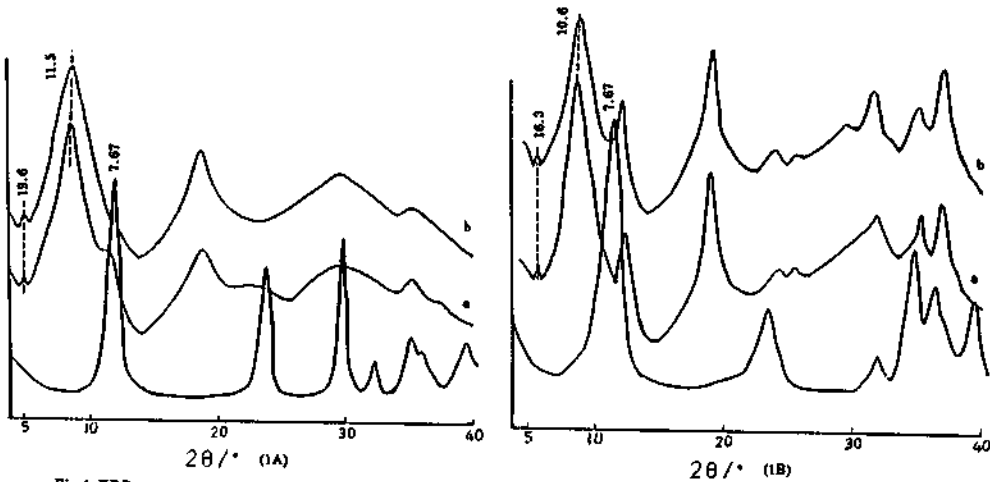


Fig. 1 XRD patterns for HPOM pillared LDHs formed by calcined LDHs  
 IA for  $[Zn_2Al_2(OH)_4CO_3] \cdot 4H_2O$ (bottom),  $[2nAl]-[Si(W_2O_7)_6]^{7-}$  (a)(POM/Al-1/1) and (b)(POM/Al-2/1)  
 IB for  $[Mg_2Al_2(OH)_4CO_3] \cdot 6H_2O$ (bottom),  $[Mg_2Al]-[Si(W_2O_7)_6]^{7-}$  (a)(POM/Al-1/1) and (b)(POM/Al-2/1)

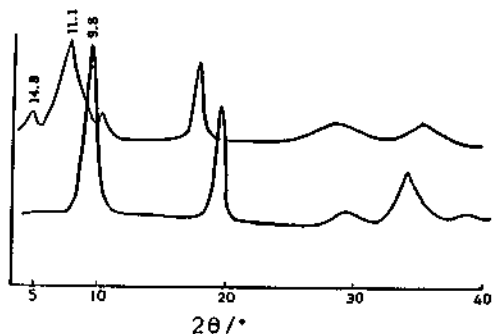


Fig. 2 XRD patterns for  $[Ni_2Al(OH)_6NO_3]$ -LDH(bottom) and for  $[Ni_2Al]-[P(W_2O_7)_6]^{7-}$  product formed by anion exchange in microwave field

### 3.2. IR Measurement:

IR spectra provide further evidence for the retention of the HPOM structure in the intercalated state. Fig. 3 shows the IR spectra of restructuring  $H_2[Si(W_2O_7)_6] \cdot nH_2O$  intercalated LDHs, their parent LDH  $[Zn_2Al]$ -LDH,  $[Mg_2Al]$ -LDH, and  $H_2[Si(W_2O_7)_6] \cdot nH_2O$ . Fig. 4 shows the IR spectra of HPOM pillared  $[Ni_2Al]-[P(W_2O_7)_6]^{7-}$ , parent LDH and HPOM. The IR spectra of HPOM pillared LDHs, formed with restructuring from metal oxide solid solution and anion exchange

under microwave field, illustrate that the intratriad group frequencies for  $[\text{Si}(\text{W}_2\text{O}_7)_6]^{4-}$  and  $[\text{P}(\text{W}_2\text{O}_7)_6]^{7-}$  were almost unchanged and kept the Keggin structure, but slightly different from that in HPOM, and similar to those observed for an authentic salt of ions<sup>[4]</sup>.

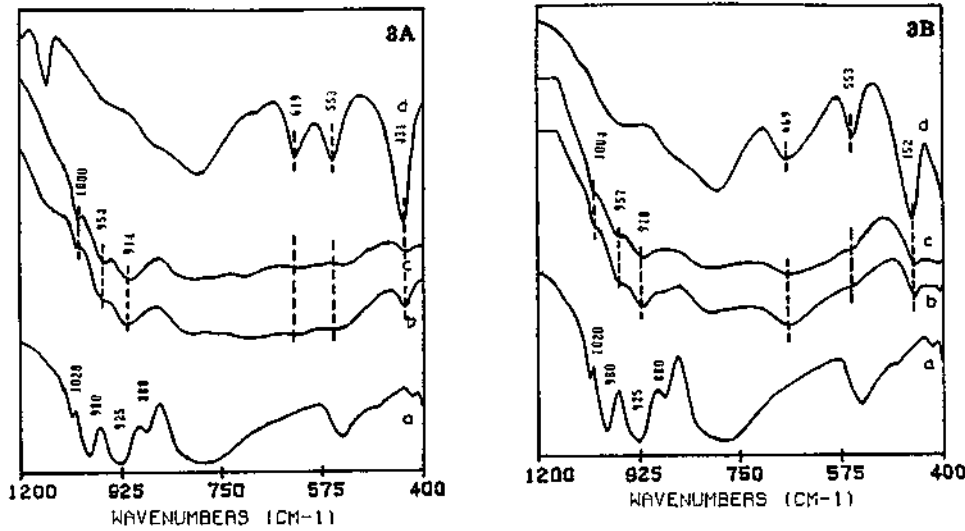
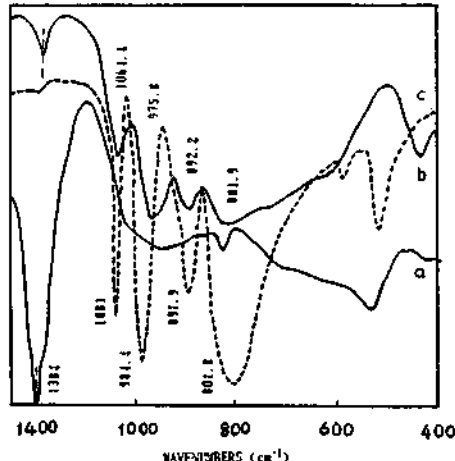


Fig.3 Infrared spectra showing the intratriad group frequencies  
3A of  $[\text{Si}(\text{W}_2\text{O}_7)_6]^{4-}$ -(b)(POM/Al-2/1) and (c)(POM/Al-1/1)  
intercalated in  $\text{Zn}_2\text{Al}$ -LDH,  $\text{H}_2[\text{Si}(\text{W}_2\text{O}_7)_6]$ -HPOM(a) and  
 $\text{Zn}_2\text{Al}$ -LDH(d)  
3B of  $[\text{Si}(\text{W}_2\text{O}_7)_6]^{4-}$ -(b)(POM/Al-2/1) and (c)(POM/Al-1/1)  
intercalated in  $\text{Mg}_2\text{Al}$ -LDH,  $\text{H}_2[\text{Si}(\text{W}_2\text{O}_7)_6]$ -HPOM(a) and  
 $\text{Mg}_2\text{Al}$ -LDH(d)

Fig.4 Infrared spectra showing the intratriad group frequencies  
of  $[\text{P}(\text{W}_2\text{O}_7)_6]^{7-}$ -(b) intercalated in a  $\text{Ni}_2\text{Al}$ -LDH,  
 $\text{H}_2[\text{P}(\text{W}_2\text{O}_7)_6]$ -HPOM(c) and  $\text{Ni}_2\text{Al}$ -LDH(a)



### 3.3. Alkylation Reactivity

As catalysts, both LDHs and HPOM pillared LDHs showed obvious activity toward the alkylation of isobutane with butene. Table 1 summarizes the alkylation activity of LDHs and HPOM pillared LDHs.

For LDHs,  $\text{Ni}_2\text{Al}_2(\text{OH})_{16}\text{CO}_3 \cdot n\text{H}_2\text{O}$  shows higher alkylation activity than  $\text{Zn}_2\text{Al}_2(\text{OH})_{16}\text{CO}_3 \cdot 4\text{H}_2\text{O}$  and  $\text{Mg}_2\text{Al}_{2.22}(\text{OH})_{15.55} \cdot (\text{CO}_3)_{1.14} \cdot 6\text{H}_2\text{O}$ . The restructuring intercalate  $\text{H}_2[\text{Si}(\text{W}_2\text{O}_7)_6] \cdot n\text{H}_2\text{O}$  LDHs shows almost the same butene conversion toward the alkylation of isobutane with butene, but kept a stable conversion, compared with their parent  $\text{ZnAl}_2(\text{OH})_{16}\text{CO}_3 \cdot 4\text{H}_2\text{O}$  and

**Table 1 Alkylation Activity of Isobutane with Butene<sup>a)</sup>**

Catalysts	Butene Conv. (%)	Products Distribution (%) <sup>b)</sup>				
		<C <sub>7</sub>	C <sub>8</sub>	C <sub>9-11</sub>	C <sub>12</sub>	C <sub>16</sub>
Zn <sub>2</sub> Al <sub>2</sub> (OH) <sub>10</sub> CO <sub>3</sub> · 4H <sub>2</sub> O	17.2	27.9	66.5	5.0	0.6	0
Mg <sub>2</sub> Al <sub>2.22</sub> (OH) <sub>10.88</sub> (CO <sub>3</sub> ) <sub>1.14</sub> · 6H <sub>2</sub> O	13.4	35.8	60.0	3.8	0.6	0
Ni <sub>2</sub> Al <sub>2</sub> (OH) <sub>10</sub> CO <sub>3</sub> · nH <sub>2</sub> O	35.6	24.2	68.8	3.8	3.4	0
[Zn <sub>2</sub> Al] <sub>2</sub> -[Si(W <sub>2</sub> O <sub>7</sub> ) <sub>6</sub> ] <sup>2-</sup>	17.5	29.6	65.7	3.8	1.1	0
[Mg <sub>2</sub> Al] <sub>2.22</sub> -[Si(W <sub>2</sub> O <sub>7</sub> ) <sub>6</sub> ] <sup>2-</sup>	18.4	39.1	57.2	3.1	0.6	0
[Ni <sub>2</sub> Al] <sub>2</sub> -[P(W <sub>2</sub> O <sub>7</sub> ) <sub>6</sub> ] <sup>2-</sup>	6.6					
[Ni <sub>2</sub> Al] <sub>2</sub> -[P(W <sub>2</sub> O <sub>7</sub> ) <sub>6</sub> ] <sup>2-</sup> (300°C)	65.8	1.6	46.8	6.2	37.9	7.7

Reaction conditions: Reac. Temp: 100 Isobutane/Butene = 11/1(mole)  
 Reac. Pressure: 2.0MPa Input rate: 5ml/min  
 Reac. Time: 4h Catalyst volume = 2.0cm<sup>3</sup>

a) Catalysts in reactor were pretreated in N<sub>2</sub> at 100°C.

for [Ni<sub>2</sub>Al]<sub>2</sub>-[P(W<sub>2</sub>O<sub>7</sub>)<sub>6</sub>]<sup>2-</sup>(300°C), 300°C, before the reaction

b) C<sub>7</sub>, C<sub>8-11</sub>, C<sub>12</sub> and C<sub>16</sub>: Products C number <7, =8-11, =12 and =16

c) CP content in C<sub>8</sub> were about 40%—50% over all catalysts

Mg<sub>2</sub>Al<sub>2.22</sub>(OH)<sub>10.88</sub>(CO<sub>3</sub>)<sub>1.14</sub>H<sub>2</sub>O LDHs. It should be mentioned that [Ni<sub>2</sub>Al]<sub>2</sub>-[P(W<sub>2</sub>O<sub>7</sub>)<sub>6</sub>]<sup>2-</sup>(300°C) shows a much higher butene conversion than [Ni<sub>2</sub>Al]<sub>2</sub>-[P(W<sub>2</sub>O<sub>7</sub>)<sub>6</sub>]<sup>2-</sup>, and a higher content of C<sub>12</sub> and C<sub>16</sub> in products, respectively. These can be considered due to the loss of H<sub>2</sub>O interlayer<sup>[12]</sup> exhibiting more heteropolyoxometalate site. The increase of C<sub>12</sub> and C<sub>16</sub> product contents can be attributed to the polymerization of butene over heteropolyoxometalate H<sub>7</sub>[P(W<sub>2</sub>O<sub>7</sub>)<sub>6</sub>] acidic sites. Considering the butene conversion referring to all the catalysts, alkylation could occur on both LDHs basic sites and heteropolyoxometalate acidic sites. Thus, heteropolyoxometalate pillared LDHs seems to be a kind of acid-base bifunctional catalysts.

#### References:

- [1] T.Kwon, G.A.Tsigdinos, and T.J.Pinnavaia, J.Am.Chem.Soc., 1988,110,3653
- [2] W.T.Reichle, J.Catal., 1985,94,547
- [3] M.A.Dredson, Inorg. Chem., 1988,27,4628
- [4] K.Chibwe and W.Jones, J.Chem.Soc., Chem.Commun., 1989,926
- [5] E.D.Dimotakis, T.J.Pinnavaia, Inorg.Chem., 1990,29,2393
- [6] E.Narita, P.Kaviratna and J.Pinnavaia, Chem. Lett., 1991, 805
- [7] S.Miyata, T.Kumura, H.Hattori and K.Tanabe, Nippon Kagaku Zasshi, 1971,92, 514
- [8] F.J.Brocker and K.Kaempfer, Chemie Ing. Techn., 1975,47,513
- [9] F.Cavani, F.Trifiro and V.Vaccari, Catalysis Today, 1991,11,204
- [10] W.T.Reichle, S.Y.Kang, and D.S.Everhardt, J.Catal., 1986,101,352
- [11] T.Kwon and T.J.Pinnavaia, Chem. of Miner., 1989, Vol.1, No.4, 381
- [12] J.Twu and P.K.Dutta, J.Phys. Chem., 1989,93,7863

\* Having finished postdoctoral work in Changchun Institute of Applied Chemistry, and now working in Chemistry Department of Jilin University.

### 3.7 Intercalation of *n*-Alkylamines into Perovskite-related Layered Niobic Acid $\text{HBiNb}_2\text{O}_7 \cdot n\text{H}_2\text{O}$

Teruyuki Nakato,<sup>a</sup> Masato Nakade,<sup>b</sup> Kazuyuki Kuroda,<sup>b</sup> and Chuzo Kato<sup>b</sup>

<sup>a</sup>Department of Chemistry, Faculty of Science, Hokkaido University, Sapporo 060, Japan

<sup>b</sup>Department of Applied Chemistry, Waseda University, Ohkubo-3, Shinjuku-ku, Tokyo 169, Japan

#### Abstract

*n*-Alkylammonium- $\text{H}_x\text{BiNb}_2\text{O}_7$  intercalation compounds were synthesized by the reaction of perovskite-related layered oxide  $\text{HBiNb}_2\text{O}_7 \cdot n\text{H}_2\text{O}$  with *n*-alkylamines.  $\text{HBiNb}_2\text{O}_7 \cdot n\text{H}_2\text{O}$  was not completely converted to the intercalation compounds except for the methylammonium-intercalate. The intercalating capability of  $\text{HBiNb}_2\text{O}_7 \cdot n\text{H}_2\text{O}$  was much lower than those of other previously reported perovskite-related layered niobates such as  $\text{HCa}_2\text{Nb}_3\text{O}_{10}$ . The poor reactivity was assumed to be related to unusual irreversible dehydrating behavior of  $\text{HBiNb}_2\text{O}_7 \cdot n\text{H}_2\text{O}$ . On the other hand, the interlayer structure was similar to that of the *n*-alkylammonium- $\text{H}_x\text{Ca}_2\text{Nb}_3\text{O}_{10}$  intercalates in contrast to the difference in the reactivity.

#### 1. INTRODUCTION

"Intercalation" has been paid considerable attention as a method of preparing structurally defined advanced catalysts. Layered niobates and titanates are valuable host materials of intercalation compounds because of their photocatalytic activities [1-3]. There is a family of layered niobates and titanates which are characterized by perovskite-related structures [4]. The general formula is expressed as  $\text{M}[\text{A}_{n-1}\text{B}_n\text{O}_{3n+1}]$  or  $\text{M}_2[\text{A}_{n-1}\text{B}_n\text{O}_{3n+1}]$  where M is exchangeable interlayer cation, A is 12-coordinated metal ion located in the holes provided by  $\text{BO}_6$  metal-oxygen octahedra linked by corner-sharing, and B is 6-coordinated metal ion, i.e.  $\text{Nb}^{5+}$  and/or  $\text{Ti}^{4+}$ , consisting the octahedra. Several perovskite-related ion-exchangeable layered niobates and titanates have been studied as host of intercalation compounds. When the interlayer cations  $\text{M}^+$  are  $\text{H}^+$  ions, the layered perovskites act as Brønsted acid which may intercalate organic bases such as *n*-alkylamines [5-11]. Jacobson et al. investigated intercalation chemistry of  $\text{HCa}_2\text{Nb}_3\text{O}_{10}$  with organic amines in detail, and clarified that the perovskite-related niobate has high intercalating ability to intercalate weak bases such as pyridine [5]. Likewise,  $\text{HLaNb}_2\text{O}_7$  has been characterized by such high intercalating capability [6].  $\text{H}[\text{Ca}_2\text{Na}_{n-3}\text{Nb}_n\text{O}_{3n+1}]$  ( $n=3-7$ ) [7,8],  $\text{HNdNb}_2\text{O}_7$  [8],  $\text{H}[\text{Ca}_2(\text{Ca},\text{Sr})_{n-3}\text{Ti}_{n-3}\text{Nb}_3\text{O}_{3n+1}]$  ( $n=4,5$ ) [9], and  $\text{H}_{1-x}[\text{La}_x\text{Ca}_{2-x}\text{Nb}_3\text{O}_{10}]$  [10] have also been reported to intercalate *n*-alkylamines.

Recently, Gopalakrishnan et al. have studied intercalation chemistry of layered perovskites  $\text{H}[\text{Ca}_{2-x}\text{La}_x\text{Ti}_x\text{Nb}_{3-x}\text{O}_{10}]$  ( $x=0-2$ ) [11]. The materials have  $\text{Ca}^{2+}$  and  $\text{La}^{3+}$  as A ion, and  $\text{Nb}^{5+}$  and  $\text{Ti}^{4+}$  as B ion. They have found that intercalating capability of the materials decreases with increase in the x value, i.e. increasing Ti content of the B site. This fact means that intercalating reactivity of the perovskite-related layered niobates and titanates can be changed by B ions. On the other hand, Domen et al. have reported photocatalysis of various perovskite-related layered niobates with different A ions for water splitting [12]. They observed that the photocatalytic activity varied with A ion. We have also found recently that the difference in A ion of  $\text{HA}_2\text{Nb}_3\text{O}_{10}$  (A= Ca, Sr) causes discrepancy in photochemical behavior of their intercalation compounds [13]. We therefore considered that intercalating properties of the layered perovskites may be changed by A ions.

In the present study, we investigated intercalation of *n*-alkylamines into perovskite-related ion-exchangeable layered niobate  $\text{HBiNb}_2\text{O}_7 \cdot n\text{H}_2\text{O}$  (Fig.1) [14]. We have found that the intercalating reactivity of  $\text{HBiNb}_2\text{O}_7 \cdot n\text{H}_2\text{O}$  is poor in contrast to  $\text{HLaNb}_2\text{O}_7$  and  $\text{HCa}_2\text{Nb}_3\text{O}_{10}$ , although the perovskite host lattice arranges the guest molecules in a manner similar to that in the  $\text{HCa}_2\text{Nb}_3\text{O}_{10}$  system.

## 2. EXPERIMENTAL

$\text{HBiNb}_2\text{O}_7 \cdot n\text{H}_2\text{O}$  was prepared by acid treatment of  $\text{CsBiNb}_2\text{O}_7$  [14].  $\text{CsBiNb}_2\text{O}_7$  was obtained by heating a stoichiometric mixture of  $\text{Cs}_2\text{CO}_3$ ,  $\text{Bi}_2\text{O}_3$ , and  $\text{Nb}_2\text{O}_5$  at 1000 °C for 24 h. The powder X-ray diffraction (XRD) pattern of the product was indexed as an orthorhombic cell except a few small peaks due to  $\text{CsBi}_2\text{Nb}_5\text{O}_{16}$  (Fig.2a). The composition of the product was determined by inductively-coupled plasma emission and flame emission spectroscopies as follows: Found: Cs, 22.1; Bi, 33.0; Nb, 29.7 wt% (Cs/Bi/Nb = 1.0/1.0/2.0) Calcd. for  $\text{CsBiNb}_2\text{O}_7$ : Cs, 20.8; Bi, 32.7; Nb, 29.1. Consequently,  $\text{CsBiNb}_2\text{O}_7$  was synthesized nearly as a single phase. The obtained  $\text{CsBiNb}_2\text{O}_7$  was treated with 12 mol  $\text{dm}^{-3}$   $\text{HNO}_3$  at room temperature for 3 d. The acid treatment removed 96 % of  $\text{Cs}^+$  ions in  $\text{CsBiNb}_2\text{O}_7$ . The sample was indexed as an orthorhombic cell (Fig.2b). The obtained  $\text{HBiNb}_2\text{O}_7 \cdot n\text{H}_2\text{O}$  was kept in water at room temperature.

$\text{HBiNb}_2\text{O}_7 \cdot n\text{H}_2\text{O}$  was then allowed to react with an excess amount of  $\text{C}_1\text{-C}_6$ ,  $\text{C}_8$ ,  $\text{C}_{10}$ , and  $\text{C}_{12}$  amines ( $\text{C}_n$  means that *n* carbon atoms are present in the *n*-alkyl chain). The reactions were carried out in glass ampules at 80 °C for 1 week.  $\text{C}_1\text{-C}_4$  amines were allowed to react as an aqueous solution (amine/water = 1/3 in volume). Other amines were used without dissolution in solvents. The reaction with pyridine was also carried out under the same condition. All the products were washed with acetone and dried at ambient conditions.

## 3. RESULTS

### 3.1. Dehydration of $\text{HBiNb}_2\text{O}_7 \cdot n\text{H}_2\text{O}$

$\text{HBiNb}_2\text{O}_7 \cdot n\text{H}_2\text{O}$  showed a monotonous weight loss from about 30 °C to 500 °C on its thermogravimetric curve. This weight loss is attributable to elimination of interlayer water molecules and  $\text{H}^+$  ions as  $\text{H}_2\text{O}$  from  $\text{HBiNb}_2\text{O}_7 \cdot n\text{H}_2\text{O}$ , and the amount of the interlayer water molecule is determined to be ca. 0.7 mol /  $\text{HBiNb}_2\text{O}_7$ . The basal spacing ( $d_{002}$  value) of  $\text{HBiNb}_2\text{O}_7 \cdot n\text{H}_2\text{O}$  continuously decreased by the heat treatment. For example, it was 1.16 nm after heating at 100 °C, 1.10 nm at 200 °C, whereas wet  $\text{HBiNb}_2\text{O}_7 \cdot n\text{H}_2\text{O}$  had the basal spacing of 1.19 nm. The heat-treated samples did not rehydrate, and the decreased basal spacing did not increase again even by stirring the samples in water. The XRD patterns of the heat-treated products were similar to that of  $\text{HBiNb}_2\text{O}_7 \cdot n\text{H}_2\text{O}$ , while intensities of the (00*l*) diffraction peaks of  $\text{HBiNb}_2\text{O}_7 \cdot n\text{H}_2\text{O}$  decreased with the heating temperature. The sample heated at 600 °C also showed appreciable resemblance of the XRD pattern to  $\text{HBiNb}_2\text{O}_7 \cdot n\text{H}_2\text{O}$ . We assume that  $\text{HBiNb}_2\text{O}_7 \cdot n\text{H}_2\text{O}$  gradually decomposes with retaining the perovskite-related structure by heat treatment at least up to 500 °C.

The above results indicate that the dehydration of  $\text{HBiNb}_2\text{O}_7 \cdot n\text{H}_2\text{O}$  is irreversible. Taking the irreversibility into account, we used wet  $\text{HBiNb}_2\text{O}_7 \cdot n\text{H}_2\text{O}$  as the starting material for intercalation experiments in order to obtain reproducible results.

### 3.2. Reaction of $\text{HBiNb}_2\text{O}_7 \cdot n\text{H}_2\text{O}$ with *n*-alkylamines

Figs.2c-e show the XRD patterns of some reaction products of  $\text{HBiNb}_2\text{O}_7 \cdot n\text{H}_2\text{O}$  with *n*-alkylamines. All the products had the basal spacing which is larger than that of  $\text{HBiNb}_2\text{O}_7 \cdot n\text{H}_2\text{O}$ . The (040) diffraction peaks of the products appeared at almost the same 2θ angle as that of  $\text{HBiNb}_2\text{O}_7 \cdot n\text{H}_2\text{O}$ , indicating the retention of the layered structure. The infrared spectra of the products had several absorption bands due to *n*-alkylammonium ions (not *n*-alkylamines) despite

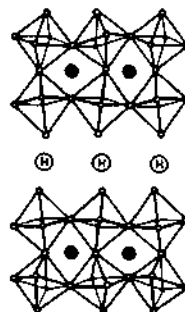


Fig.1 Schematic description of the structure of  $\text{HBiNb}_2\text{O}_7 \cdot n\text{H}_2\text{O}$  [14].

of washing. *n*-Alkylamines must have been protonated by the interlayer H<sup>+</sup> ions. Therefore, the formation of the *n*-alkylammonium-H<sub>x</sub>BiNb<sub>2</sub>O<sub>7</sub> intercalation compounds was confirmed. However, unreacted HBiNb<sub>2</sub>O<sub>7</sub>·*n*H<sub>2</sub>O was observed on the XRD patterns of the reaction products except the sample with C<sub>1</sub> amine. Although we carried out the reactions with different reaction times in the C<sub>3</sub> amine system, the unreacted phase was still clearly observed even by extending the reaction time to 3 weeks and the organic content little increased with the reaction time. The organic contents, which were determined by C,H,N analysis, of the intercalation compounds decreased with increase in the chain length of amines; RNH<sub>3</sub>/[BiNb<sub>2</sub>O<sub>7</sub>]<sup>+</sup> = 0.73 (R= C<sub>1</sub>), 0.68 (C<sub>2</sub>), 0.50 (C<sub>3</sub>). This result shows that longer-chain *n*-alkylamines are intercalated to lower degrees.

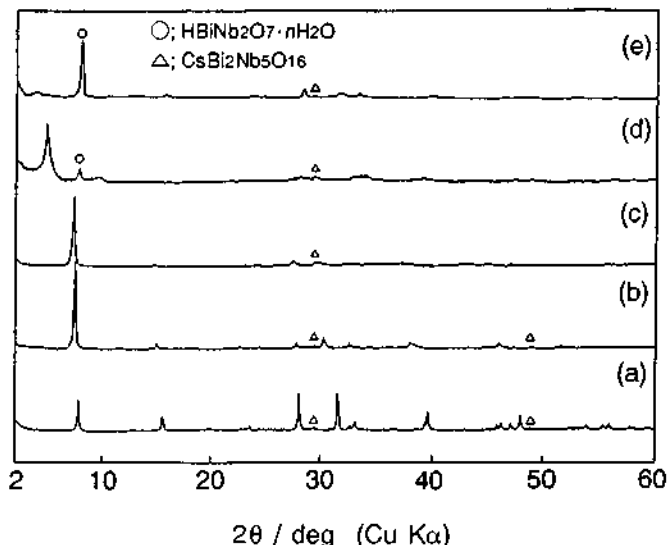


Fig.2 XRD patterns of (a) CsBiNb<sub>2</sub>O<sub>7</sub>, (b) wet HBiNb<sub>2</sub>O<sub>7</sub>·*n*H<sub>2</sub>O, and (c)–(e) reaction products of HBiNb<sub>2</sub>O<sub>7</sub>·*n*H<sub>2</sub>O with *n*-alkylamines (with (c) C<sub>1</sub> amine, (d) C<sub>3</sub> amine, and (e) C<sub>6</sub> amine).

The intercalating property of HBiNb<sub>2</sub>O<sub>7</sub>·*n*H<sub>2</sub>O irreversibly changed by heat treatment in accord with the irreversible dehydration. HBiNb<sub>2</sub>O<sub>7</sub>·*n*H<sub>2</sub>O heated at 300 °C did not intercalate *n*-alkylamines, indicating that HBiNb<sub>2</sub>O<sub>7</sub>·*n*H<sub>2</sub>O loses its intercalating capability by heat-treatment. Although the starting materials heated at around 100 °C still maintained the intercalating ability, products from the heated materials did not have reproducibility of the basal spacing and the amount of the incorporated guest (but smaller than those in the samples from wet HBiNb<sub>2</sub>O<sub>7</sub>·*n*H<sub>2</sub>O). Such gradual loss of intercalating capability is in agreement with the gradual dehydrating behavior of HBiNb<sub>2</sub>O<sub>7</sub>·*n*H<sub>2</sub>O.

The reactivity of HBiNb<sub>2</sub>O<sub>7</sub>·*n*H<sub>2</sub>O with *n*-alkylamines largely differs from that of HCa<sub>2</sub>Nb<sub>2</sub>O<sub>10</sub>·*n*H<sub>2</sub>O [5] and HLaNb<sub>2</sub>O<sub>7</sub>·*n*H<sub>2</sub>O [6]. They reversibly form anhydrous compounds (HCa<sub>2</sub>Nb<sub>2</sub>O<sub>10</sub> and HLaNb<sub>2</sub>O<sub>7</sub>), and are fully converted into *n*-alkylammonium-intercalates. Moreover, they have capabilities of intercalating pyridine. Although we also carried out a reaction of HBiNb<sub>2</sub>O<sub>7</sub>·*n*H<sub>2</sub>O with pyridine, intercalation did not occur. These results clarify that the intercalating capability of HBiNb<sub>2</sub>O<sub>7</sub>·*n*H<sub>2</sub>O is rather low.

### 3.3. Increase in the basal spacing with the intercalation

The increment of the basal spacing of HBiNb<sub>2</sub>O<sub>7</sub>·*n*H<sub>2</sub>O on intercalation became large with the increase in the chain length of *n*-alkylamines (Fig.3). The data in Fig.3 can be divided into three divisions (C<sub>1</sub>, C<sub>2</sub>–C<sub>5</sub>, and C<sub>6</sub>–C<sub>12</sub>), indicating that the arrangement of the interlayer *n*-

alkylammonium ions differs with the chain length. In the range of  $C_2$ - $C_5$  amines, a linear relationship exists between the number of carbon atoms in the alkyl chain and the basal spacing with a gradient of 0.18. Since the length of alkyl chain increases by 0.127 nm per addition of one carbon, the gradient of 0.18 indicates an inclined bilayer arrangement of *n*-alkylammonium. The tilt angle of the alkyl chains to the layer surface is calculated as  $\sin^{-1}(0.18/0.254) = 45^\circ$ . Likewise, the plot of the basal spacing against the carbon number shows linear relationship with a slope of 0.09 in the range of  $C_6$ - $C_{12}$  amines. Although the gradient of 0.09 does not reject monolayer arrangements, the absolute values of the basal spacing indicate a bilayer arrangement. The tilt angle is calculated as  $21^\circ$ . Further, the basal spacing of the  $C_1$  amine-intercalate is smaller than the expected value from the relationship. The small increment suggests that  $C_1$  ammonium ions are "keyed" into depressions of  $[BiNb_2O_7]^-$  layers.

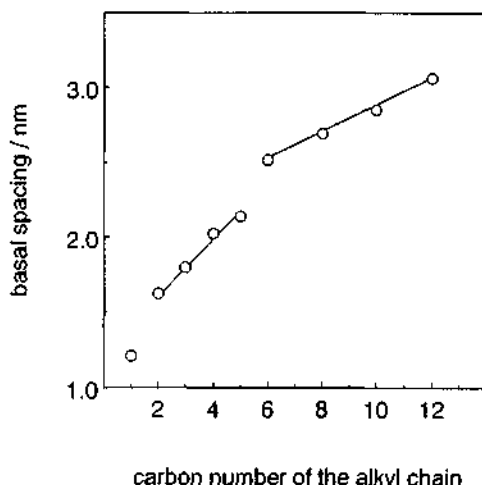


Fig.3 Relationship between the basal spacing of the *n*-alkylammonium- $H_xBiNb_2O_7\cdot nH_2O$  intercalation compounds and carbon number of the alkyl chain.

#### 4. DISCUSSION

The above results clearly show the peculiar property of the interlayer  $H^+$  ions of  $HBiNb_2O_7\cdot nH_2O$ . The irreversible and gradual dehydration of  $HBiNb_2O_7\cdot nH_2O$  is not common to many other layered niobates and titanates, such as  $HCa_2Nb_3O_8\cdot 1.5H_2O$  (perovskite) [15] and  $HNb_3O_8\cdot H_2O$  [16] (not perovskite), which undergo reversible dehydration at around  $100^\circ C$  to form anhydrous layered oxides. However, the dehydrating behavior is similar to  $HLa_2Ti_2NbO_{10}\cdot nH_2O$  (perovskite) [11],  $H_2Ti_4O_9\cdot nH_2O$  [16] and  $HK_2Ti_5NbO_{14}\cdot nH_2O$  (not perovskite) [18] to some extent. These layered oxides show monotonous weight loss from around room temperature to  $600^\circ C$ , and do not form stable unhydrated materials (thus the dehydration should be irreversible). The unusual dehydration of these layered oxides including  $HBiNb_2O_7\cdot nH_2O$  indicates a peculiar interaction between oxide layers and interlayer  $H^+$  ions. It is noteworthy that the above three layered oxides which undergo the irreversible dehydration have been characterized by low intercalating capability. For example,  $HLa_2Ti_2NbO_{10}\cdot nH_2O$  do not intercalate *n*-alkylamines [11]. We therefore suppose that the intercalating reactivity of  $HBiNb_2O_7\cdot nH_2O$  is correlated to the characteristic thermal behavior.

The loss of the intercalating capability with heating accompanied by irreversible dehydration has also been observed for  $H_2Ti_4O_9\cdot nH_2O$  [17]. It has been reported that the heat treatment endows  $H_2Ti_4O_9\cdot nH_2O$  with three-dimensional nature by a strong bonding between  $[Ti_4O_9]^{2-}$

layers through interlayer H<sup>+</sup> ions, and that H<sub>2</sub>Ti<sub>4</sub>O<sub>9</sub>·*n*H<sub>2</sub>O with small *n* value (e.g. anhydrous H<sub>2</sub>Ti<sub>4</sub>O<sub>9</sub>) obtained by heat treatment can not intercalate *n*-alkylamines. As to HBiNb<sub>2</sub>O<sub>7</sub>·*n*H<sub>2</sub>O, its protonic conductivity has been reported to drastically decrease at above 50 °C, indicating little mobility of the unhydrated interlayer H<sup>+</sup> ions [14]. The interlayer H<sup>+</sup> ions of HBiNb<sub>2</sub>O<sub>7</sub>·*n*H<sub>2</sub>O would be strongly held by the perovskite layers so that their reactivity becomes poor. We infer that HBiNb<sub>2</sub>O<sub>7</sub>·*n*H<sub>2</sub>O loses its intercalating capability with elimination of interlayer water molecules. In other words, the intercalating capability would be originated from H<sub>3</sub>O<sup>+</sup> ions, but the dehydrated interlayer H<sup>+</sup> ions are not reactive.

The poor intercalating reactivity of HBiNb<sub>2</sub>O<sub>7</sub>·*n*H<sub>2</sub>O contrasts with the intercalating property of previously studied other perovskite-related layered oxides having Nb<sup>5+</sup> as B ion, HLaNb<sub>2</sub>O<sub>7</sub> [6] and HCa<sub>2</sub>Nb<sub>3</sub>O<sub>10</sub> [5], which are strong solid acids being capable of intercalating pyridine. This fact manifests that the intercalating reactivity of perovskite-related ion-exchangeable layered oxides H[A<sub>*n*-1</sub>B<sub>*n*</sub>O<sub>*3n*+1</sub>] is changed by A ion. Since B ion of the layered perovskites also largely affects their intercalating reactivity as mentioned in the Introduction section, we conclude that the layered perovskites are peculiar host materials which can vary their intercalating properties with the combination of A and B ions although they are structurally similar to one another.

Nevertheless, it seems difficult to rationalize the reason for the differences in intercalating properties. Layered niobates and titanates having H<sup>+</sup> ions as their interlayer cations (thus they are considered as layered niobic and titanic acids) are regarded as solid Brønsted acids, which intercalate *n*-alkylamines through acid-base reactions with interlayer protons (or oxonium ions) [19]. Thus, poor intercalating reactivity with *n*-alkylamines indicates low acidity. In general, acidity of oxide materials are related to the electronegativity of metal ions ( $\chi_i$ ), and metal ions with large  $\chi_i$  lead to high acidity [20]. For the case of H[Ca<sub>2-x</sub>La<sub>x</sub>Ti<sub>x</sub>Nb<sub>3-x</sub>O<sub>10</sub>] studied by Gopalakrishnan et al. [11], the difference in  $\chi_i$  between Nb<sup>5+</sup> ( $\chi_i = 17.6$ ) and Ti<sup>4+</sup> ( $\chi_i = 13.5$ ) indicates weak acidity of the perovskites with large Ti content [21], and this explains the low intercalating reactivity of the Ti-containing niobates for amines. However,  $\chi_i$  of Bi<sup>3+</sup> (13.3), La<sup>3+</sup> (7.7), and Ca<sup>2+</sup> (5.0) suggests that the acidity, so that the intercalating capability, of HBiNb<sub>2</sub>O<sub>7</sub> is higher than that of HLaNb<sub>2</sub>O<sub>7</sub> and HCa<sub>2</sub>Nb<sub>3</sub>O<sub>10</sub>, and this expectation completely disagrees with the present results. Hence, there should be other reasons, which is related to interactions between the perovskite lattices and the interlayer H<sup>+</sup> ions suggested by the thermal analysis, for the difference in the intercalating reactivity. Gopalakrishnan et al. have very recently reported intercalation chemistry of H<sub>2-x</sub>[La<sub>2</sub>Ti<sub>3-x</sub>Nb<sub>x</sub>O<sub>10</sub>] ( $x = 0-1$ ), and mentioned relationship between their Brønsted acidity and structure [22]. They have found that H<sub>2</sub>La<sub>2</sub>Ti<sub>3</sub>O<sub>10</sub> has no acidity whereas HLa<sub>2</sub>Ti<sub>3</sub>NbO<sub>10</sub> is a very weak solid acid. The structure of H<sub>2</sub>La<sub>2</sub>Ti<sub>3</sub>O<sub>10</sub> is characterized by displacement of adjacent perovskite layers. They have explained that the interlayer spacing of the layered perovskites becomes small to lose the acidity by the displacement which facilitates close packing of the adjacent layers. The structure of HBiNb<sub>2</sub>O<sub>7</sub>·*n*H<sub>2</sub>O also involves the displacement [14]. Thus, the structural feature is a possible reason for the low acidity of this material. However, we mention that the layer charge density of H<sub>2</sub>La<sub>2</sub>Ti<sub>3</sub>O<sub>10</sub> is twice as high as that of HBiNb<sub>2</sub>O<sub>7</sub>·*n*H<sub>2</sub>O, HLa<sub>2</sub>Ti<sub>3</sub>NbO<sub>10</sub>, or HCa<sub>2</sub>Nb<sub>3</sub>O<sub>10</sub>, and that the absence of the acidity in H<sub>2</sub>La<sub>2</sub>Ti<sub>3</sub>O<sub>10</sub> can also be explained by the high layer charge density leading to strong electrostatic interactions, which may inhibit the interlayer H<sup>+</sup> ions from reactions, between the perovskite sheets and H<sup>+</sup> ions. It should be necessary to investigate many other layered perovskites.

Contrary to the intercalating reactivity, the relationship between the basal spacing and the chain length is similar to that in the *n*-alkylammonium-HCa<sub>2</sub>Nb<sub>3</sub>O<sub>10</sub> system [5]. In that system, the results were implied by contribution of two different mechanisms to the arrangements of alkyl chains; the arrangement of short-chain *n*-alkylammonium ions are mainly determined by hydrogen bonding interactions between the -NH<sub>3</sub><sup>+</sup> group of *n*-alkylammonium ions and oxygen atoms on the [Ca<sub>2</sub>Nb<sub>3</sub>O<sub>10</sub>]<sup>-</sup> layer surface whereas van der Waals interactions between alkyl chains dominantly affect the conformation of long-chain alkylammonium ions. The result in Fig.3 indicates that the interlayer structure of the *n*-alkylammonium-HBiNb<sub>2</sub>O<sub>7</sub> system is basically similar to those of the *n*-alkylammonium-HCa<sub>2</sub>Nb<sub>3</sub>O<sub>10</sub> system. This is reasonable because both the perovskite materials have almost the same layer structure and layer charge density. Thus, we deduce that the orientation of the guest ions are structurally defined by the perovskite lattices regardless of the reactivity of the hosts.

However, the tilt angles of the alkyl chains in HBiNb<sub>2</sub>O<sub>7</sub> are smaller than those in HCa<sub>2</sub>Nb<sub>3</sub>O<sub>10</sub>. Although the interlayer density of *n*-alkylammonium ions can not be determined because the products contain unreacted HBiNb<sub>2</sub>O<sub>7</sub>·*n*H<sub>2</sub>O, this fact indicates that *n*-

alkylammonium ions are not so closely packed in  $\text{HBiNb}_2\text{O}_7 \cdot n\text{H}_2\text{O}$ , as in  $\text{HCa}_2\text{Nb}_3\text{O}_{10}$ . This would be related to the intercalating reactivity. In particular, the small tilt angle of long-chain ( $C_6-C_{12}$ ) alkylammonium ions to the layer surface ( $21^\circ$ ) suggests smaller amounts of the intercalated guest species. In this case, it is possible that the alkyl chains are not arranged in a linear chain but have kink-blocks and/or gauche-blocks [23] which are also mentioned in the  $\text{HCa}_2\text{Nb}_3\text{O}_{10}$  system [5].

## 5. CONCLUSION

Intercalation compounds of layered perovskite  $\text{HBiNb}_2\text{O}_7 \cdot n\text{H}_2\text{O}$  with  $n$ -alkylammonium ions were synthesized.  $\text{HBiNb}_2\text{O}_7 \cdot n\text{H}_2\text{O}$  is characterized by poor intercalating reactivity, which differs from other layered niobates, such as  $\text{HCa}_2\text{Nb}_3\text{O}_{10}$ , having perovskite-related structures with different A ions. The results demonstrate that intercalating properties of layered perovskites are altered by A ion. Since a previous study has already shown the effect of B ion on the intercalating properties, intercalating behavior of the perovskite-related ion-exchangeable layered oxides can be modified by both A and B ions consisting the perovskite layers. In addition, other properties, such as photochemical ones, of the layered perovskites can also be changed by A ion. On the other hand, the structural similarity of the present system to the  $n$ -alkylammonium- $\text{HCa}_2\text{Nb}_3\text{O}_{10}$  system reveals that the perovskite host lattices arrange the intercalated  $n$ -alkylammonium ions in the same manner regardless of the reactivity of the hosts. Because property and structure work together to materialize novel functions of intercalation compounds, the perovskite-related layered oxides form a unique family as host of intercalation compounds. We may obtain perovskite materials optimized for various applications by choosing appropriate combinations of A and B ions.

## References

- 1 B.Raveau, *Rev. Inorg. Chem.*, **1987**, 9, 38.
- 2 A.Kudo, K.Sayama, A.Tanaka, K.Asakura, K.Domen, K.Maruya and T.Onishi, *J. Catal.*, **1987**, 120, 337.
- 3 T.Nakato, K.Kuroda and C.Kato, *Chem. Mater.*, **1992**, 4, 128.
- 4 J.Gopalakrishnan, *Rev. Solid State Sci.*, **1987**, 1, 515.
- 5 A.J.Jacobson, J.W.Johnson and J.T.Lewandowski, *Mater. Res. Bull.*, **1987**, 22, 45.
- 6 J.Gopalakrishnan, V.Bhat and B.Raveau, *Mater. Res. Bull.*, **1987**, 22, 413.
- 7 A.J.Jacobson, J.W.Johnson and J.T.Lewandowski, *Inorg. Chem.*, **1984**, 24, 3729.
- 8 M.Dion, M.Ganne and M.Tournoux, *Rev. Chim. Miner.*, **1986**, 23, 61.
- 9 R.A.Mohan Ram and A.Clearfield, *J. Solid State Chem.*, **1991**, 94, 45.
- 10 S.Uma and J.Gopalakrishnan, *J. Solid State Chem.*, **1993**, 102, 332.
- 11 J.Gopalakrishnan, S.Uma and V.Bhat, *Chem. Mater.*, **1993**, 5, 132.
- 12 K.Domen, Y.Yoshimura, T.Sekine, A.Tanaka and T.Onishi, *Catal. Lett.*, **1990**, 4, 339.
- 13 T.Nakato, K.Ito, K.Kuroda and C.Kato, *Microporous Mater.*, **1993**, 1, 283.
- 14 M.A.Subramanian, J.Gopalakrishnan and A.W.Sleight, *Mater. Res. Bull.*, **1988**, 23, 837.
- 15 A.J.Jacobson, T.Lewandowski and J.W.Johnson, *J. Less-Common Metals*, **1986**, 116, 137.
- 16 R.Nedjar, M.M.Borel and B.Raveau, *Mater. Res. Bull.*, **1985**, 20, 1291.
- 17 R.Marchand, L.Brohan, R.M'Bedi and M.Tournoux, *Rev. Chim. Miner.*, **1984**, 21, 476.
- 18 A.Grandin, M.M.Borel, M.Hervieu and B.Raveau, *J. Solid State Chem.*, **1987**, 68, 369.
- 19 S.Kikkawa and M.Koizumi, *Mater. Res. Bull.*, **1980**, 15, 533.
- 20 T.Seiyama, "Kinzoku Sankabutsu To Sono Shokubai Sayou (Metal Oxides and Their Catalysis, in Japanese)", Kodansha, 1978.
- 21 Electronegativity of metal ions,  $\chi_i$ , is calculated from that of the corresponding metals,  $\chi_0$ , by the relation of  $\chi_i = (1+2\alpha)\chi_0$  where  $\alpha$  is the valence of the ions [19]. We used Pauling's  $\chi_0$  values for the calculation of  $\chi_i$ .
- 22 S.Uma, A.R.Raju, and J.Gopalakrishnan, *J. Mater. Chem.*, **1993**, 3, 709.
- 23 G.Lagaly, *Angew. Chem. Int. Ed. Engl.*, **1976**, 15, 575.

### 3.8 Controlled Pore Opening of VPI-5 by Partial Removal of Water Molecules

S. Prasad<sup>a</sup>, Shang-Bin Liu<sup>a</sup> and R. Vetrivel<sup>b</sup>

<sup>a</sup>Institute of Atomic and Molecular Sciences, Academia Sinica, P.O. Box 23-166, Taipei, Taiwan 10764, ROC

<sup>b</sup>Department of Molecular Chemistry and Engineering, Faculty of Engineering, Tohoku University, Aoba-ku, Sendai 980, Japan

#### Abstract

A careful TGA experiment shows that the water molecules are desorbed from the molecular sieve VPI-5 in a step-wise fashion. The pore size altered in a controlled manner by partial dehydration has been probed by xenon adsorption.

#### INTRODUCTION

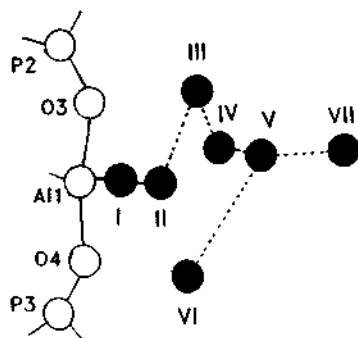


Figure 1. Al(I)-site and the seven associated water molecules. The numbers assigned to the water molecules are in accordance to the nomenclature followed in ref. 2.

The presence of large one dimensional channels in the molecular sieve VPI-5 shows potential in the separation of large molecules, catalytic cracking, and, more recently in the self assembly of molecules on a quantum scale [1]. Recent structure refinement of VPI-5 [2] revealed the possible role for water molecules to act as 'template' forming a triple helix inside the void. One third of the Al-sites [Al(I)-site at the junction of the fused 4-membered rings] are coordinately bonded to two water molecules [ $\text{H}_2\text{O}(\text{I})$  and  $\text{H}_2\text{O}(\text{II})$ ]. The rest of five water molecules form a hydrogen bonded structure. On the otherhand, the different helices are linked by  $\text{H}_2\text{O}$  (VII) (Figure 1). The

use of the VPI-5 as a molecular sieve and as a catalyst primarily depend on the removal of this helical arrangement of water molecules in absence of structural breakdown. In the present study, we distinguish the 7 different water molecules in the VPI-5 lattice.

## EXPERIMENTAL

TGA experiments were performed in a ULVAC Sinku-Riko Differential Thermogravimetric Analyser TGD 7000. Typically, 10 mg of the sample was used each time under the following conditions: reference, alumina; atmosphere, nitrogen; temperature range, 30–600°C; range of scan rate, 0.5–10°C min<sup>-1</sup>. Partially dehydrated VPI-5 samples were prepared by vacuum treating 0.5 g of the samples at room temperature. By this procedure, samples with 2.2%, 4.5% and 9.5% weight losses could be obtained. A fully dehydrated sample, corresponding to 23.2% weight loss and designated as VPI-5 (23.2), was prepared by slow programmed heating of the fully hydrated sample upto a final temperature of 300 °C after evacuating at room temperature for 24 hrs. Xenon adsorption experiments were carried out in a vacuum manifold.

## RESULTS AND DISCUSSION

We have varied the heating rates in a systematic thermogravimetric study. Table I shows the data derived from an experiment where a heating rate of 0.5 °C min<sup>-1</sup> was used. The weight loss in each step corresponds to ~3.3%. We attribute these weight losses to the seven different water molecules present in the structure of VPI-5. The most loosely bound water molecule, H<sub>2</sub>O (VII), is removed first; the water molecules H<sub>2</sub>O(V), H<sub>2</sub>O(IV), H<sub>2</sub>O(VI), and H<sub>2</sub>O(III) are removed during the next 4 successive steps, respectively. The weight losses in the final steps attributed to H<sub>2</sub>O(II), and H<sub>2</sub>O(I) almost merge. This is due to the fact that water molecules I and II are strongly bonded directly to the framework in an identical fashion. We used MNDO (modified neglect of differential overlap) calculations on cluster models to study the energetics of adsorption of water molecules over various sites in VPI-5. The results indicate that the Al(I)-site is the energetically preferred site for the adsorbed water [3].

Table 1 The variation of void space with water content in VPI-5.

Temperature (°C)	Cumulative Wt. Loss (%)	Diameter of Void (Å)*	Water being removed
---	---	0.3	None
35.0	2.7	4.1	VII
39.0	6.2	5.8	V
42.0	8.5	7.4	IV
45.0	11.2		
51.0	14.7	8.0	III & VI
54.0	19.3	10.0	II**
60.0	23.2	12.5	I**

\* see Figure 3.

\*\* The weight losses attributed to these water molecules are less pronounced.

Though as-synthesized VPI-5 does not adsorb any xenon (Figure 2), a simple vacuum dehydration with 2.2 % weight loss results in the uptake of xenon. This adsorption can only be attributed to the partial breakdown of the water structure. A mild weight loss resulted in sufficiently large void space to accommodate a xenon atom (diameter ca. 4.4 Å) to diffuse into the channels (*vide supra*, Table 1). On progressive dehydration, though the xenon adsorption increases, but not markedly, even for the completely dehydrated sample (VPI-5 (23.2)). It should be pointed out that, due to the electric neutrality of the VPI-5 framework, the adsorption potential for xenon is low unlike the observations in zeolites.

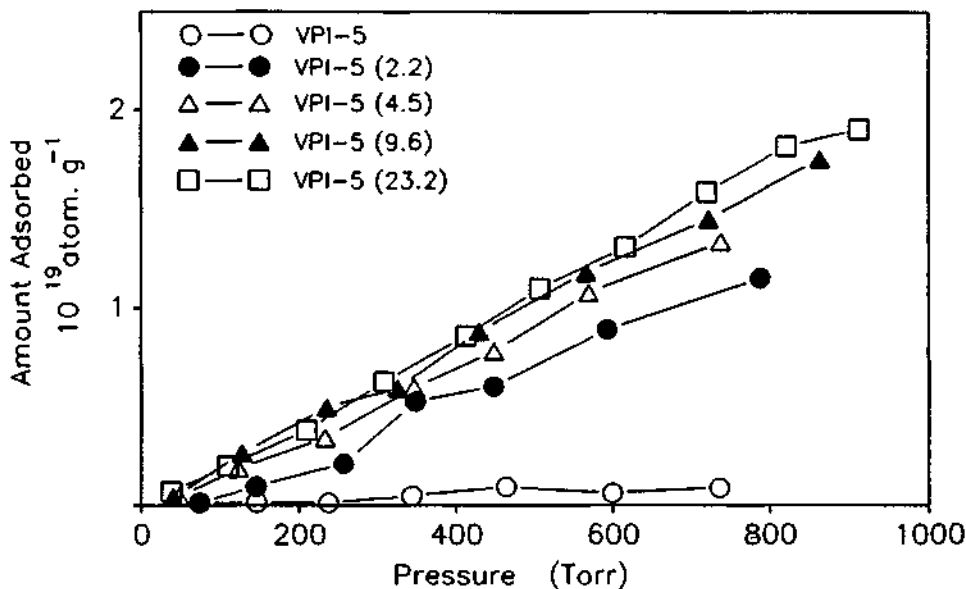


Figure 2. The adsorption of xenon over VPI-5 samples at different levels of dehydration. VPI-5 stands for a fully hydrated sample and the numbers in parentheses represent percentage wt. loss.

Figure 3 shows that the water molecules form a network inside the large pore of VPI-5. For fully hydrated VPI-5, there are six sets of water molecules per unit cell, each set comprising of seven water molecules H<sub>2</sub>O (I) to H<sub>2</sub>O (VII) and hence there is practically no void space for xenon adsorption. Because of the hexagonal symmetry, the top layer containing three sets of water molecules repeat themselves in the second layer but with a 60° rotation along the axis passing through the pore-center of the 18-member ring. The TGA weight loss corresponding to step one is 2.7 %. The bonds connecting the helices are ruptured hence creating a void space. After the step 1 weight loss, the diameter of the void formed for VPI-5 (2.2) hence corresponds to 4.1 Å (Figure 3 and Table 1), and thus a xenon atom is able to diffuse into the channel. The above studies therefore show that the effective pore diameter of VPI-5 could be altered by carefully adjusting the hydration level.

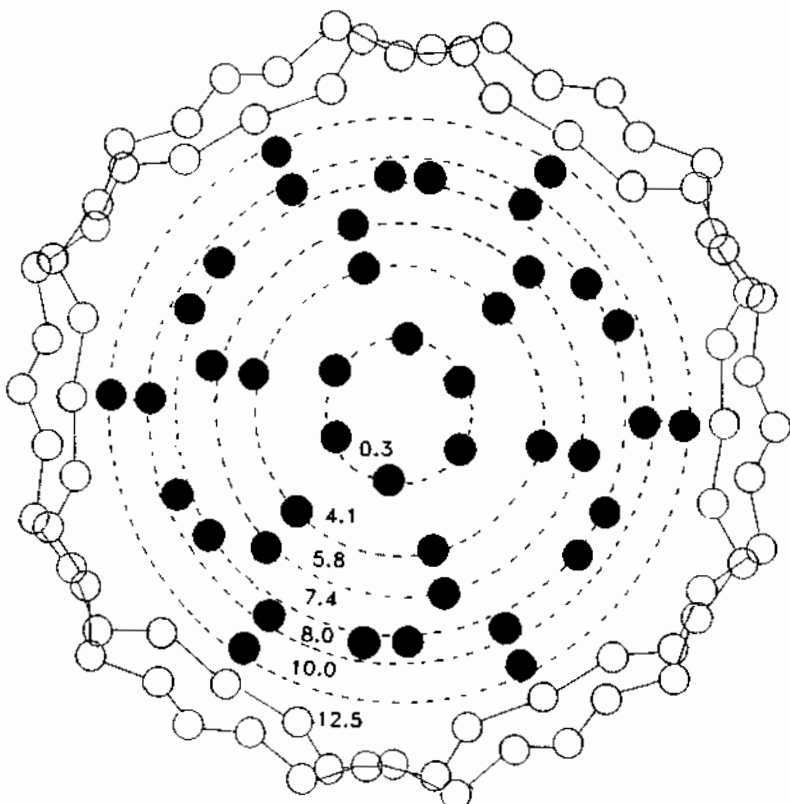


Figure 3. The void space reduction in the 18-member pore due to the presence of 7 different water molecules in the form of a triple helix. The connected open circles illustrate the framework T-sites (Al-O-P), while filled circles represent the arrangement of water molecules.

## CONCLUSIONS

A distinction has been made among the seven different types of water molecules in the molecular sieve VPI-5. The creation of a void space ca  $4.1 \text{ \AA}^{\circ}$  by the removal of the most loosely bound water,  $\text{H}_2\text{O}$  (VII), accommodates a xenon atom into the structure. Careful dehydration / thermal treatment is thus the key to modulate the pore size in VPI-5.

## REFERENCES

1. M.W. Anderson, J. Shi, D.A. Leigh, A.E. Moody, F.A. Wade, B. Hamilton and S.W. Carr, *J. Chem. Soc. Chem. Comm.*, 1993, p. 533.
2. L.B. McCusker, Ch. Baerlocher, E. Jahn and M. Bülow, *Zeolites*, 1991, 11, 308.
3. S. Prasad and R. Vetrivel, *J. Phys. Chem.*, submitted for publication.

## 3.9 Incorporation of Aluminum and Antimony into Mordenite Framework by Atom-planting Method

P. WU, T. NAKANO, T. KOMATSU and T. YASHIMA

Department of Chemistry, Tokyo Institute of Technology, Ookayama, Meguro-ku, Tokyo 152, Japan

### Abstract

By using an atom-planting method, the alumination and antimonation of dealuminated mordenite zeolites with  $\text{AlCl}_3$  and  $\text{SbCl}_3$  at elevated temperatures were carried out.  $^{29}\text{Si}$ -MAS NMR shows that introduction of 4-coordinated aluminum atoms into the zeolite framework occurred during the alumination. The generation of both Brønsted and Lewis acid sites by the alumination are demonstrated by IR spectroscopy of adsorbed pyridine. An acidic hydroxyl band at  $3663 \text{ cm}^{-1}$  in the IR spectrum of OH stretching vibration region was developed by the antimonation, and was assigned to a  $\text{Sb(OH)Si}$  hydroxyl in the zeolite framework.

### 1. INTRODUCTION

Aluminum atoms could be introduced into the framework of highly siliceous MFI-type zeolites by a treatment with  $\text{AlCl}_3$  vapor at elevated temperatures [1-5]. By such an alumination, not only Brønsted acid sites but also Lewis acid sites were generated [1]. Aluminum atoms have been suggested to be introduced into the zeolite framework mainly through the reaction of  $\text{AlCl}_3$  with the defect sites [3]. This method, namely, by the treatment of the silicate with metal chloride vapor at the elevated temperatures, has also been demonstrated to be adoptable to prepare metallosilicates with MFI structure, and is named as atom-planting method [6].

For metallosilicates with mordenite structure, few work has been reported. In this study, with the purpose to clarify the applicability of the atom-planting method to mordenite, mordenite was dealuminated to create defect sites, and then the alumination and antimonation were carried out using aluminum and antimony as seed atoms. The incorporation of aluminum and antimony was examined by MAS NMR and IR.

### 2. EXPERIMENTAL METHODS

Dealuminated mordenite M1 (Tosoh, bulk Si/Al atomic ratio of 56) was a commercial sample. Atom-planting was similar to the method described in refs. 1 and 2. M1 was treated with  $\text{AlCl}_3$  or  $\text{SbCl}_3$  at 873 K for 1 h and 4 h, respectively. Then the sample was washed with a large amount of water, exchanged with 0.1 N  $\text{NH}_4\text{NO}_3$  at

343 K for 48 h, and dried in air for 24 h.

The bulk aluminum content and framework Si/Al ratios of the samples were determined by atomic adsorption spectrophotometry and  $^{29}\text{Si}$  MAS NMR spectroscopy, respectively.  $^{29}\text{Si}$  MAS NMR measurements were carried out on a JEOL GX-270 Fourier Transform Spectrometer equipped with a magic-angle probe. Infrared spectra were recorded on a FTIR-8000 (SHIMADZU) spectrometer. The procedure has been described in ref. 1. All IR spectra were recorded at room temperature.

### 3. RESULTS AND DISCUSSION

#### 3.1 MAS NMR Studies

All samples before and after atom-planting treatments were checked with X-ray diffraction to have a mordenite structure and high crystallinity.

Fig. 1 shows the  $^{29}\text{Si}$  MAS NMR spectra of M1 and [Al]-M1 prepared from the alumination of M1 with  $\text{AlCl}_3$  by atom-planting. M1 (Fig. 1, a) consists of two sharp peaks at -115 and -113 ppm and a broad peak between -107 and -102 ppm. The -115 and -113 ppm signals are responsible for the splitting of Si(0Al) peak with relative intensities of 1:1. Since the mordenite is known to contain four crystallographically nonequivalent tetrahedral sites in the population ratio 2:1:1:2 [7], each of these two peaks must be a composite of two sites. The broad and weak signal between -107 and -102 ppm is due to the overlap of Si(0Al) and  $(\text{SiO})_3\text{SiOH}$  groups which are probably related to the Al-defect sites generated by the dealumination. The presence of such SiOH groups in dealuminated mordenites have been evidenced with  $^{29}\text{Si}$  CP NMR techniques [7]. After alumination with  $\text{AlCl}_3$ , in the spectrum of [Al]-M1 (Fig. 1b), there was no significant change in the signals due to Si(0Al) sites. However, with the disappearance of the weak signal around -102 ppm, a single but stronger -107 ppm signal due to Si(1Al) sites was observed clearly. These facts indicate that 4-coordinated aluminum atoms have been introduced into the zeolite framework by the alumination with  $\text{AlCl}_3$ . The  $^{29}\text{Si}$  MAS NMR spectra of M1 and [Al]-M1 were computer-simulated, and from the deconvoluted areas of the signals at -115, -113 and -107 ppm, the framework Si/Al ratios was calculated. The framework Si/Al ratios were 71 and 30 for M1 and [Al]-M1, respectively (Table I). Both bulk and framework Si/Al ratio were increased by the alumination.

#### 3.2 IR Studies

Several hydroxyl absorptions were observed in the hydroxyl stretching region of IR spectra as shown in Fig. 2. Before the pyridine adsorption (solid lines), three hydroxyl bands at 3745, 3610 and 3500  $\text{cm}^{-1}$  were observed in the dealuminated mordenite M1 (Fig. 2, a). The 3745  $\text{cm}^{-1}$  band is assigned to the terminal,

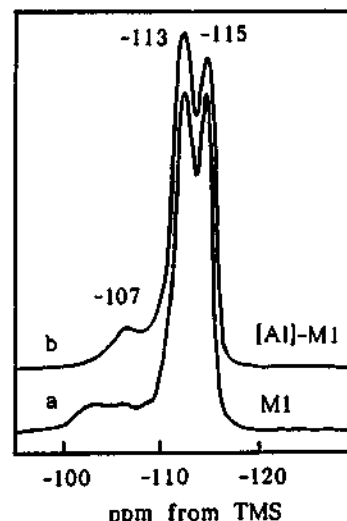


Fig. 1.  $^{29}\text{Si}$  MAS NMR spectra.

Table 1 Characterization of M1 and [Al]-M1

Sample	Bulk Al content <sup>a</sup> (mmol g <sup>-1</sup> )	Framework Si/Al <sup>b</sup>	Acidity (Abs. g <sup>-1</sup> ) <sup>c</sup>	
			Brønsted	Lewis
M1	0.23	71	3.3	1.7
[Al]-M1	0.86	30	5.8	9.9

a. Determined by atomic adsorption spectrophotometry.

b. Determined by <sup>29</sup>Si MAS NMR spectroscopy.

c. Determined by IR after adsorbed pyridine was desorbed at 523 K.

nonacidic silanol. The 3610 cm<sup>-1</sup> band decreased by the pyridine adsorption (dotted lines). This band is due to the framework Al(OH)Si, the Brønsted acid site. The broad band around 3500 cm<sup>-1</sup> which generally is not present in the synthesized mordenite was generated by the dealumination. This band is also nonacidic and usually identified as SiOH groups at the Al-defect sites [3]. For [Al]-M1 (Fig. 2, b), only two bands at 3745 and 3610 cm<sup>-1</sup> were present, while the broad 3500 cm<sup>-1</sup> band was no longer observed. Comparing Fig. 2, b with Fig. 2, a, it is found that the alumination made the 3610 cm<sup>-1</sup> band more intense, while the intensity of 3745 cm<sup>-1</sup> band has been decreased. The IR spectra of adsorbed pyridine show that [Al]-M1 has more acid sites of both Brønsted acid (1545 cm<sup>-1</sup> band) and Lewis acid (1450 cm<sup>-1</sup> band) than M1 (Fig. 2a' and 2b'). The relative amounts of Brønsted and Lewis acid sites in both M1 and [Al]-M1 which were measured after removing physically adsorbed pyridine at 523 K are listed in Table 1. The IR results demonstrate that aluminum atoms have been put into the silanol (Al-defect) sites in the dealuminated mordenite by the alumination and that these planted aluminum atoms can be framework atoms to contribute to the Brønsted acid. A large amount of Lewis acid sites also have been generated by the alumination. The part of aluminum introduced into the nonframework sites may be responsible for the Lewis sites. The nonframework aluminum species probably results from the reaction of terminal SiOH with AlCl<sub>3</sub> as suggested in ref. 1. It is supported by the fact that the band at 3745 cm<sup>-1</sup> was dramatically decreased by the aluminati-

The IR spectra of antimonated sample, [Sb]-M1, are shown in Fig. 2, c and c'. Compared with the spectra of M1 and [Al]-M1, a new hydroxyl band at 3663 cm<sup>-1</sup> arose in [Sb]-M1. This is an acidic band which disappeared completely with the pyridine adsorption even after evacuation at 423 K. However, it was partially recovered by the evacuation at 523 K as shown by Fig. 2, c', while the Al(OH)Si band at 3610 cm<sup>-1</sup> was still not recovered. These results indicate that the incorporated antimony generates acidic hydroxyl weaker than Al(OH)Si. In [Sb]-ZSM-5 prepared by the atom-planting method, a band at 3665 cm<sup>-1</sup> has been assigned to the Sb(OH)Si hydroxyl in the framework [6]. In [Sb]-M1, therefore, the new band at 3663 cm<sup>-1</sup> should be assigned to the structural Sb(OH)Si group. We conclude that by using the atom-planting method antimony can be incorporated into mordenite framework to obtain successfully the antimonosilicate with mordenite structure.

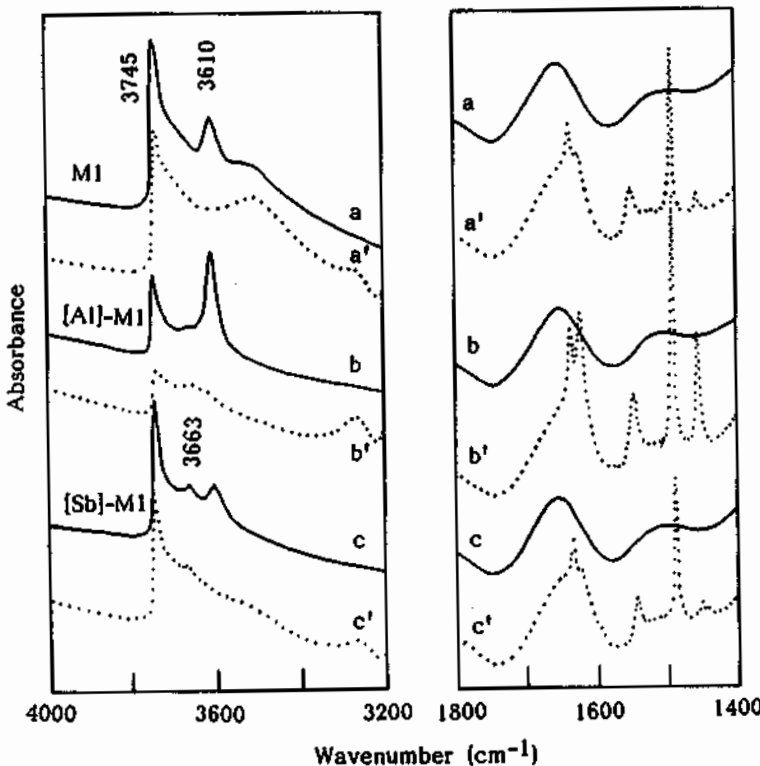


Fig. 2 IR spectra of M1 before and after alumination and antimonation.

In conclusion, aluminum and antimony atoms can be incorporated into the mordenite framework with atom-planting method. Both Brønsted and Lewis acid sites are generated with the alumination. The antimony atoms introduced into the mordenite framework give an acidic hydroxyl band at  $3663\text{ cm}^{-1}$ .

#### ACKNOWLEDGMENT

Special thanks are due to Dr. S. Nakata who performed the MAS NMR measurements.

#### REFERENCES

1. K. Yamagishi, S. Namba, and T. Yashima, *J. Catal.*, **1990**, *121*, 47.
2. K. Yamagishi, S. Namba, and T. Yashima, *Stu. Surf. Sci. Catal.*, **1989**, *49*, 459.
3. K. Yamagishi, S. Namba, and T. Yashima, *J. Phys. Chem.*, **1991**, *95*, 872.
4. C. D. Chang, C. T.-W. Chu, J. N. Miale, R. F. Bridger, and R. B. Calvert, *J. Amer. Chem. Soc.*, **1984**, *106*, 8143.
5. R. M. Desso, and G. T. Kerr, *Zeolites*, **1984**, *4*, 315.
6. T. Yashima, K. Yamagishi, and S. Namba, *Stu. Surf. Sci. Catal.*, **1991**, *60*, 171.
7. J. T. Miller, P. D. Hopkins, B. L. Meyers, G. J. Ray, R. T. Roginski, G. W. Zajac, and N. H. Rosenbaum, *J. Catal.*, **1992**, *138*, 115.

### 3.10 A New Method for Preparing High Silica ZSM-48 Catalysts

Li Jianquan, Liu Guanghuan and Dong Jinxiang

Institute of Special Chemicals, Taiyuan University of Technology, Taiyuan, 030024, Shanxi, P.R.China

#### Abstract

Zeolite ZSM-48 was prepared by the kneading method for the first time. The reactant mixture contains a little 1,6-hexanediamine and much solid material. The weight ratio of aluminosilicate gels to C<sub>6</sub>DN is 3.4. Due to adding much less liquid material, the autoclave is used more efficiently and the yield of per volume of autoclave increases by a large margin. A separation procedure is not needed after crystallization. This method shows a bright future in the zeolite industry.

#### 1. INTRODUCTION

The formation of natural zeolites with volcanic glass and saline water as reactants occurs in a temperature range from 300 to 328K and requires crystallization time as long as 50,000 years. Barrer's gel method was proposed as early as 1940 as a means of duplicating these natural conditions. The primary variables of this method are synthesis temperature, reactivity of silica source, silica-to-alumina ratio in the synthesis mixture and nature of the alkali. Such a system is always supersaturated with respect to the constituents. Under hydrothermal conditions (373-473K), this supersaturation is then removed through nucleation of metastable zeolite phases. Later, the method was slightly modified, an organic quaternary cation was added. ZSM series of high silica were prepared in a system containing a lot of water and amine[1]. Zeolite ZSM-48 with high-silica was first synthesized by the hydrothermal method[2]. Later, KZSM-48 was also synthesized in the nonaqueous system[3]. ZSM-48 is of higher selectivity for p-xylene in the alkylation of toluene and higher catalytic behavior of CO+H<sub>2</sub> reaction[4]. On the other hand, there is much liquid medium in the ZSM-48 synthesis system whether hydrothermal[1,2] or nonaqueous [3].

Due to the addition of much liquid material into the hydrothermal system, there is much silicate and aluminum lifted into the mother-liquor which is drained away after crystallization, increasing cost and environmental pollution. Recently, a new, kneading method to synthesize zeolite ZSM-35 was reported, which has better catalytic behavior for o-xylene isomerization than ZSM-35 prepared by the nonaqueous method[5,6].

Here we report the synthesis of ZSM-48 by the kneading method. Zeolite ZSM-48 was first prepared from reaction mixtures that contain little 1,6-hexanediamine but no water ( $H_2O/SiO_2$  ratio is 0). The weight ratio of aluminosilicate gel to  $C_6DN$  is 3.4. Since much less liquid material is added, the autoclave is used more efficiently greatly increasing the yield per volume of autoclave increased.

## 2. EXPERIMENTAL

The aluminosilicate gel was prepared according to Ref. [4]. ZSM-48 samples were synthesized by mixing an appropriate amount of the aluminosilicate gel, sodium hydroxide and 1,6-hexanediamine( $C_6DN$ ). The  $R/SiO_2$  ratio is 0.16 and  $H_2O/SiO_2$  is 0. The reactant mixture was vigorously stirred and poured into the autoclaves. The crystallization of ZSM-48 was carried out in the temperature range 423--473K have needed to be separated as usual because there is almost no liquid material seen before and after the crystallization. The XRD pattern were recorded on a Rigaku 2034 diffractometer using CuKa radiation.

## 3. RESULTS AND DISCUSSION

### 3.1 XRD Analysis

The phase purity of the crystalline ZSM-48 and compounds was examined by XRD. The XRD patterns of ZSM-48 synthesized by the kneading method and those of ZSM-48 synthesized by the hydrothermal method are illustrated in Fig. 1. It is clear that the XRD pattern of the product synthesized by the kneading method resemble those synthesized by the hydrothermal method with respect to the position and intensity of reflexes. No other crystalline byproducts could be detected.

Traditionally, zeolites are synthesized in a system containing a large amount of water. The following proprietary zeolites, denoted ZSM-48, Eu-2, Eu-11 and ZBM-30, have comparable XRD patterns. Comparing XRD patterns of Eu-11, ZSM-48 and ZBM-30 zeolites, Araya and Lowe concluded that these materials have essentially the same XRD pattern and aluminosilicate structure[6]. The preferred

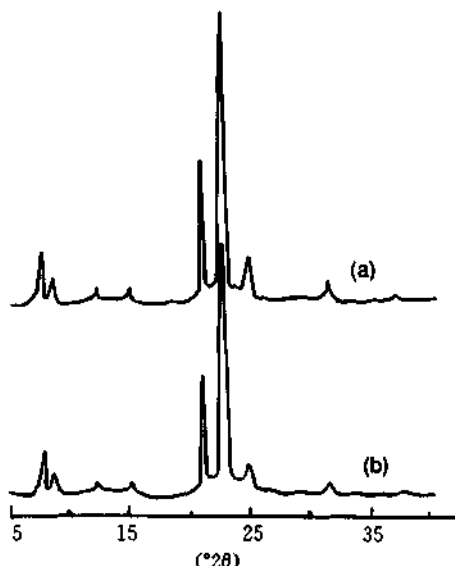


Fig.1 The XRD pattern of ZSM-48 synthesized by: (a) the kneading method and (b) the hydrothermal method.

conditions for the synthesis of ZSM-48, related zeolites[1] and our sample are shown in Table 1.

It is indicated that all the samples in the previous works were synthesized from the system containing a large amount of water. On the other hand, there is a little amine but no water in our reactant system of ZSM-48. It is the first time that ZSM-48 has been formed in such an extremely dense system. Due to the addition of very little of amine, this method greatly increases productivity and has a bright future in the zeolite industry.

Table 1 The reactant composition of the different samples

	ZSM-48*	ZSM-48*	ZSM-48*	Eu-2*	Eu-2*	Eu-2*	Eu-11*	ZSM-48
H <sub>2</sub> O/SiO <sub>2</sub>	20-100	10-100	20-71	1-100	50	50	50	0
R/SiO <sub>2</sub>	0.1-0.5	0.05-1	0.05-1		0.08	0.08	0.33	0.15
R	alkylamine +trialkylamine	CnDN	diquaternary ammonium	diquaternary ammonium	diquat-3	diquat-3	C <sub>6</sub> DN	C <sub>6</sub> DN

\*Ref. [1]

### 3.2 Effect of the Reactant Composition

Table 2 shows the effect of the reactant composition on the crystalline product. It can be seen that the amount of Na<sub>2</sub>O plays an important role in the formation of ZSM-48. When the Na<sub>2</sub>O/SiO<sub>2</sub> was 0.09, pure ZSM-48 was formed. The amount of Na<sub>2</sub>O determines the amount of impurities.

Table 2 Variation of the product with the reactant composition

Sample	Na <sub>2</sub> O/SiO <sub>2</sub>	C <sub>6</sub> DN/SiO <sub>2</sub>	Temperature (K)	Time (h)	Products
5311	0.11	0.13	453	63	α-SiO <sub>2</sub> +T
5312	0.11	0.16	453	63	ZSM-48+T
5313	0.06	0.16	453	60	α-SiO <sub>2</sub> +T
5314	0.09	0.16	453	60	ZSM-48
5315	0.13	0.16	453	60	ZSM-48+ α-SiO <sub>2</sub> +T
5316	0.16	0.16	453	60	T+α-SiO <sub>2</sub>

In short, we report a new method for the synthesis of zeolite ZSM-48. The marked reduction in the amount of amine and water leads to lower cost and pollution, and increases productivity.

#### 4. ACKNOWLEDGMENT

We thank the National Nature Science Foundation of China for financial support.

#### 5. REFERENCES

- [1] P. A. Jacobs and J. A. Martens, Stud. in Surf. Sci. and Catal., 1987, 33, 275 .
- [2] P. Chu, U. S. P, 4, 337, 287 (1981).
- [3] X. Wenyang, L. Jianquan and L. Guanghuan, Zeolites, 1990, 10, 755 .
- [4] L. Jianquan, L. Guanghuan and X. Wenyang, Ran Liao Hua Xue Xue Bao, 1991, 19, 27.
- [5] L. Jianquan, D. Jinxiang, L. Guanghuan, G. Shunquan and W. Feng, J. Chem. Soc. Chem. Comm., 1993, 659.
- [6] L. Jianquan, W. Feng, D. Jinxiang and L. Guanghuan, China Pat. 92, 109, 402 (1992).
- [7] A. Araya and B. M. Lowe, J.Chem. Res. , 1985, 192.

### 3.11 Preparation and Catalytic Properties of Composite Zirconium Phosphonates

K. Segawa<sup>a</sup> N. Kihara<sup>a</sup>, and S. Nakata<sup>b</sup>

<sup>a</sup> Department of Chemistry, Sophia University, Tokyo 102, Japan

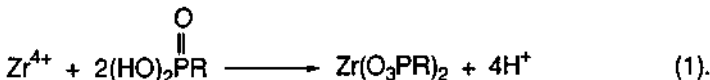
<sup>b</sup> R & D Center, Chiyoda Corp., Yokohama 221, Japan

#### Abstract

Composite zirconium phosphonates (pendant and pillared) in single crystal phase have been investigated and characterized by XRD,  $^{13}\text{C}$ -, and  $^{31}\text{P}$ -MASNMR. These compounds are lamellar structures comprising zirconium phosphates or organophosphonates. Each layer consists of planes of zirconium bridged through phosphonate groups that alternate above and below the Zr atom planes, oriented away from the basal surfaces in a bilayered fashion in the interlayer region. The catalytic performance over zirconium phosphonates is evaluated by esterification of acetic acid. When the composite zirconium phosphonate is composed with an acidic function and with a hydrophobic function in single crystal phase, the catalytic activity showed a higher activity without swelling of the catalyst in the reaction media. The composite materials become accessible to any reactant molecule and improve hydrophobicity.

#### 1. INTRODUCTION

Recently, several kinds of layered compounds have been proposed for use as catalysts, including silicates, graphite, and acid salts of tetravalent metals. Acid salts of tetravalent metals are usually prepared as amorphous precipitates. Zirconium phosphonates are solid materials typically synthesized in amorphous forms under aqueous conditions by the reaction of a soluble salt of a tetravalent metal and a phosphonic acid or an organophosphoric acid:



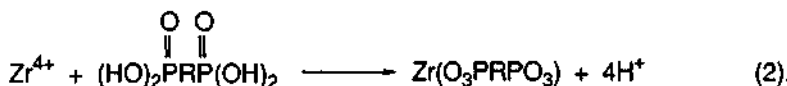
However, it is possible to synthesize many of them as crystalline compounds. The potential applications of crystalline zirconium phosphonates have significant recent interest. Depending on the R group, different applications for these materials in the field of chromatographic separation, photochemistry, fuel cell, and catalysis are expected. In the case of zirconium phosphates (one kind of zirconium phosphonate), with the general formula  $\text{Zr}(\text{O}_3\text{POH})_2 \cdot n\text{H}_2\text{O}$ , the most extensively investigated crystalline zirconium phosphate is an  $\alpha$ -layered acid salt [1].  $\alpha\text{-Zr}(\text{O}_3\text{POH})_2 \cdot \text{H}_2\text{O}$  crystallizes in the monoclinic system, as assigned by Troup and Clearfield from their single crystal work [2]. For the zirconium phosphonates, however, the two-dimensional tetravalent metal plane has a structure essentially similar to the zirconium phosphate structure; substituted for hydroxyl groups are the desired organic functional groups, oriented away from the basal surfaces in a bilayered fashion in the interlayer region [3]. Therefore, zirconium phosphonate materials can act as a series of modified surfaces, and become accessible for reactant molecules of catalysis. We have reported that the preparation and characterization of two-dimensional single component zirconium phosphonates [4]. The acidic function of single zirconium phosphonate showed rather poor catalytic activities for esterification of acetic acid and hydrolysis of ethyl acetate except over  $\text{Zr}(\text{O}_3\text{PCH}_2\text{SO}_3\text{H})_2$ .

In addition, over  $Zr(O_3PCH_2SO_3H)_2$  catalyst, the reaction proceeds as a homogeneous reaction, even though the catalytic activity is higher than those of other acidic zirconium phosphonates. In this study, to overcome the problem of water solubility, and/or to improve hydrophobic properties, a second function was introduced to achieve a catalytic advantage in certain applications. The objective of this study is to explore the role of a second phosphonate function in single crystal phase on the catalytic performance of acidic function and hydrophobic function of zirconium phosphonates, and to learn how to exploit this second function to achieve a catalytic advantage in certain applications.

## 2. EXPERIMENTAL METHODS

### 2.1. Preparation of zirconium phosphonates

Addition of a water-soluble Zr(IV) salt to organo-phosphoric acid results in the precipitation of a gelatinous amorphous precipitate. Several types of zirconium phosphonates,  $Zr(O_3PR)_2$ , either in single component, such as one kind of R, or in composite zirconium phosphonates, such as two different R's, were prepared (pendant type); here R could be -OH, -CH<sub>3</sub>, -C<sub>6</sub>H<sub>13</sub>, -C<sub>12</sub>H<sub>25</sub>, -C<sub>22</sub>H<sub>45</sub>, -CH<sub>2</sub>COOH, and -CH<sub>2</sub>SO<sub>3</sub>H. Most of the zirconium phosphonate derivatives were obtained by the addition of aqueous solution of  $ZrOCl_2 \cdot 8H_2O$  (1.17 M) to the (organo) phosphonate reagent,  $(HO)_2P(O)R$ , (0.75 M, [R]/[Zr]=2-10) to yield small particle, amorphous zirconium phosphonates (see eq. 1). When organo-diphosphonic acid was reacted with Zr<sup>4+</sup> instead of organophosphoric acid, the pillared type of zirconium phosphonates,  $Zr(O_3PRPO_3)$ , can be obtained. Here R could be -C<sub>6</sub>H<sub>12</sub>-, -C<sub>10</sub>H<sub>20</sub>-, -C<sub>12</sub>H<sub>24</sub>-, -C<sub>6</sub>H<sub>4</sub>C<sub>6</sub>H<sub>4</sub>-:



For the crystallization process, the amorphous zirconium phosphonate was treated with HF solution. The use of HF as a complexing reagent to inhibit release of free Zr<sup>4+</sup> had a considerable effect on increasing crystallinity and particle size. The zirconium fluoro-complexes were decomposed slowly by removing the hydrofluoric acid in the presence of phosphonic acid. The crystallinity of composite zirconium phosphonates increased with increasing concentrations of HF. However, some phase segregation of each function was observed when HF concentrations, [F]/[Zr], exceeded 9. Usually for the crystallization, amorphous zirconium phosphonates were treated with HF solution ([F]/[Zr] = 6 or 8) at 333K [5].

### 2.2. Characterization of zirconium phosphonates

The experimental procedures of TGA, XRD, and measurement of ion-exchange capacity have been described in detail elsewhere [6]. The interlayer d-spacing from XRD pattern was determined by the angle of (001) reflection.

*<sup>31</sup>P- and <sup>13</sup>C-MASNMR spectroscopy:* High-resolution solid-state MASNMR spectra were obtained on a Fourier Transform pulsed NMR spectrometer (JEOL, JNM-GX270) equipped with a CP/MAS unit (JEOL, NM-GSH27MU). All <sup>31</sup>P-NMR spectra combined with cross polarization (CP) and/or with magic angle spinning (MAS) at 109.38 MHz were measured with high-power proton decoupling during data acquisition [7]. The <sup>13</sup>C-MASNMR spectra were obtained at 67.94 MHz with CP and proton decoupling. Sample spinning speeds, determined from the side-band spacing in spinning spectra, were 3.6 to 4.0 kHz. <sup>31</sup>P and <sup>13</sup>C chemical shifts were determined by phosphoric acid and TMS, respectively, and observing its resonance frequency in the absence of spinning.

*Catalytic reactions:* The catalytic activities of esterification of acetic acid with ethanol at 343 K were measured. 250 mg of catalyst was suspended in ethanol solution of acetic acid or aqueous solution of ethyl acetate, and the reaction rates were measured by GC (PORA Pak Q, 2-m).

*Adsorption measurements:* Adsorption measurements of base molecules were performed under vacuum conditions. A McBain-type of quartz spiral spring was hung down to the sample basket. The catalyst was evacuated at 373 K for 2 h. After evacuation, 0.7 kPa of base molecules ( $CH_3NH_2$ ,  $(CH_3)_3N$ , n-C<sub>4</sub>H<sub>9</sub>NH<sub>2</sub>, t-C<sub>4</sub>H<sub>9</sub>NH<sub>2</sub>, NH<sub>3</sub>) were admitted at 373 K for several hours

until adsorption had equilibrated. The amount of chemisorption of base molecules was determined by the change in length of the spring, which was equipped with a displacement meter (Type 2U, Shinko Electronic).

### 3. RESULTS AND DISCUSSION

#### 3.1. Preparation and structure of zirconium phosphonates

The structure of a zirconium phosphonate,  $\text{Zr}(\text{O}_3\text{PR})_2$  or  $\text{Zr}(\text{O}_3\text{PRPO}_3)$ , comprises a metal phosphate core layer with pendant or pillared organic groups attached to this core and normal to the plane of the layer. Compounds of the type  $\text{Zr}(\text{O}_3\text{PR})_2$  and  $\text{Zr}(\text{O}_3\text{PRPO}_3)$  (R: organic group) with lamellar  $\alpha$ -type structures are prepared by simply replacing phosphoric acid with phosphonic acid or organo-phosphonic acid [6]. Elemental analysis results were in fairly good agreement with values calculated from the theoretical chemical formulae.

The Zr atoms in zirconium phosphonates lie very nearly in a plane and are bridged by phosphorus tetrahedra. These tetrahedra are situated alternately above and below the Zr atom plane. Thus, each phosphonate R group in  $\text{Zr}(\text{O}_3\text{PR})_2$  (pendant) or in  $\text{Zr}(\text{O}_3\text{PRPO}_3)$  (pillared) is directed into the interlayer space. In intercalated zirconium phosphates and phosphonates, guest molecules are accommodated in the interlayer region, and such materials do not usually have any porosity. For this reason, it is of interest to study the possibility of obtaining three-dimensional zirconium phosphate derivatives by pillaring. In these pillared compounds, the interlayer d-spacing should be independent of the size of the counterions and intercalated species. The use of solid state, magic-angle spinning NMR is a recent development for characterizing layered compounds [7]. In particular,  $^{13}\text{C}$  and  $^{31}\text{P}$ -MASNMR spectra are very informative characterizing the micro environments of phosphonates, which cannot be proved by XRD.

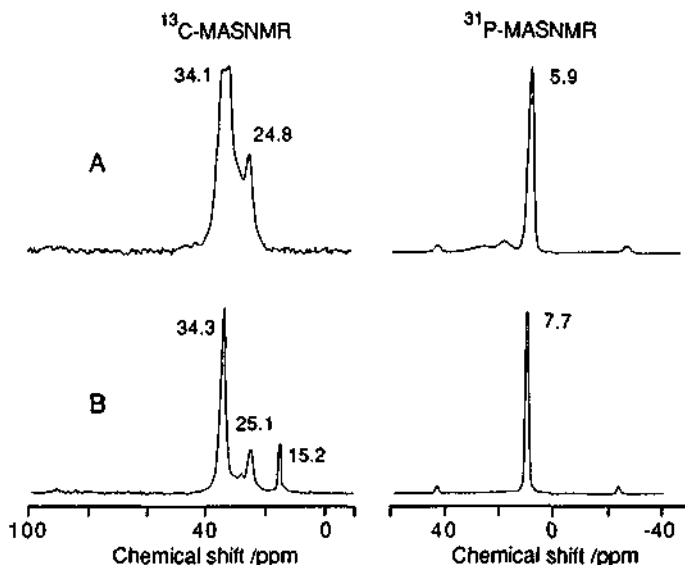


Fig. 1  $^{13}\text{C}$ - and  $^{31}\text{P}$ -MASNMR spectra of pillared (A) and pendant (B) type of n-alkyl zirconium phosphonates: (A)  $\text{Zr}(\text{O}_3\text{PC}_{10}\text{H}_{20}\text{PO}_3)_2$ , (B)  $\text{Zr}(\text{O}_3\text{PC}_{12}\text{H}_{25})_2$ .

The MASNMR spectra of pendant and pillared alkyl zirconium phosphonates are shown in Fig. 1. In the case of  $^{31}\text{P}$ -MASNMR spectra of pillared or pendant zirconium phosphonate, the chemical shifts represent a single resonance;  $\text{Zr}(\text{O}_3\text{PC}_{10}\text{H}_{20}\text{PO}_3)_2$  at 5.9 ppm, and  $\text{Zr}(\text{O}_3\text{PC}_{12}\text{H}_{25})_2$  at 7.7 ppm. This indicates the presence of only one kind of phosphorus environment between each

pair of layers.  $^{13}\text{C}$ -CP/MASNMR spectrum of pillared zirconium phosphonate compounds (Fig.1A) shows the two resonance lines. The major resonance line, which is attributed to the methylene carbons is observed at 34.1 ppm from TMS (tetramethylsilane). The other line of  $\text{Zr}(\text{O}_3\text{PC}_{12}\text{H}_{25})_2$  in  $^{13}\text{C}$ -CP/MASNMR spectrum is attributed to the carbon of P-CH<sub>2</sub>- (24.8 ppm). On the other hand,  $^{13}\text{C}$ -CP/MASNMR spectrum of pendant zirconium phosphonate compounds (Fig.1B) shows the three resonance lines. The major resonance line of  $\text{Zr}(\text{O}_3\text{PC}_{12}\text{H}_{25})_2$  is also attributed to the methylene carbon. The other two lines in  $^{13}\text{C}$ -CP/MASNMR spectrum are attributed to the carbon of P-CH<sub>2</sub>- at 25.1 ppm and to the terminal methyl carbon at 15.2 ppm [8]. The absence of methyl carbon in  $^{13}\text{C}$ -CP/MASNMR spectrum of pillared zirconium phosphonate is different from that of pendant zirconium phosphonate.

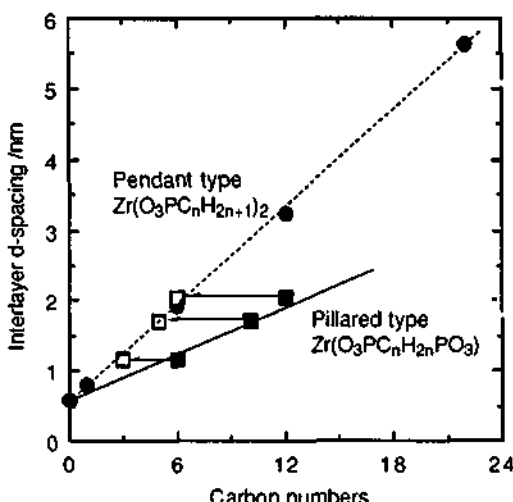


Fig. 2 Interlayer d-spacing of pendant and pillared alkyl zirconium phosphonates as a function of carbon numbers.

The layer separation (interlayer d-spacing) of each crystalline zirconium phosphonate was determined from the first reflection line of the XRD pattern. Diffraction data confirmed from the expected correlation of interlayer spacing with the size of the pendant or pillared organic group. Solid products consisting of layered sheets with ordered arrays of the pendant and pillared organic groups on both sides of the layer were obtained with most phosphonic acids [6]. As shown in Fig. 2, the interlayer d-spacing of n-alkyl zirconium phosphonates both in pendant type and in pillared type is increasing linearly with increasing carbon numbers. The results suggest that n-alkyl groups are distributed uniformly between each pair of Zr atom planes and that the interlayer d-spacing obeyed the bulkiness of n-alkyl groups.

In addition to single component zirconium phosphonate derivatives, layered structures with multiple functionality can be prepared by incorporating more than one phosphonic acid during the preparation. The synthesis of derivatives of  $\alpha$ -zirconium phosphate with the general formula,  $\text{Zr}[(\text{O}_3\text{POH})_x(\text{O}_3\text{PR})_{1-x}]_2$  (pendant) or  $\text{Zr}[(\text{O}_3\text{POH})_x(\text{O}_3\text{PRPO}_3)_{1-x/2}]_2$  (pillared), is effected by precipitating a mixture of two phosphonic acids with a zirconium salt in the presence of HF. Many other zirconium phosphonate derivatives may be prepared easily by using other mixtures of phosphonic acids. Because of the large variety of possible compositions of the two functional groups, the composite compounds should exhibit a broad range of applications in ion-exchange, adsorption, intercalation, and catalysis.

### 3.2. Adsorption and catalytic activity over composite zirconium phosphonates

The crystal structure of  $\alpha$ -zirconium phosphate,  $\alpha\text{-Zr}(\text{O}_3\text{POH})_2\cdot\text{H}_2\text{O}$ , was first determined to possess a unique structure [2]. The phosphate-bridged Zr atoms lie very nearly in a plane, in a pseudo hexagonal arrangement. The  $\text{PO}_4$  tetrahedra are alternately above and below the plane of Zr atoms. Three oxygen atoms of each phosphate group are bonded to three different Zr atoms to form a distorted equilateral triangle. Thus, each layer may be considered a planar macro anion with a formula  $[\text{Zr}_n(\text{PO}_4)_{2n}]^{2n^-}$ . The negatively charged oxygen of the macro anion is balanced by an equal number of protons. Adsorption uptake of  $\text{NH}_3$  on  $\alpha$ -zirconium phosphate or pillared zirconium phosphate has been measured by using the vacuum balance. Figure 3 shows the sorption uptake of  $\text{NH}_3$  on  $\alpha\text{-Zr}(\text{O}_3\text{POH})_2\cdot\text{H}_2\text{O}$  and pillared  $\text{Zr}[(\text{O}_3\text{POH})_{0.7}(\text{O}_3\text{PC}_{10}\text{H}_{20}\text{PO}_3)_{0.15}]_2$ . Adsorption of  $\text{NH}_3$  on  $\alpha$ -zirconium phosphate (Fig. 3A) requires a longer time to be saturated. While on pillared-zirconium phosphate (Fig. 3B),  $\text{NH}_3$  is quickly saturated. The results suggest that the composite zirconium phosphonates have much higher interlayer d-spacing than that of  $\alpha$ -zirconium phosphate, because of the presence of pillared diphosphonic alkyl groups, and become accessible to base molecules such as  $\text{NH}_3$ .

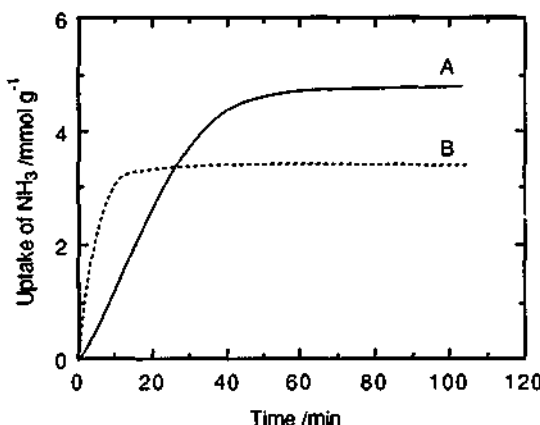


Fig. 3 Adsorption of  $\text{NH}_3$  (1.3 kPa) over zirconium phosphate and pillared zirconium phosphate at 373 K: (A)  $\alpha\text{-Zr}(\text{O}_3\text{POH})_2\cdot\text{H}_2\text{O}$  (d-spacing; 0.76 nm), (B)  $\text{Zr}[(\text{O}_3\text{POH})_{0.7}(\text{O}_3\text{PC}_{10}\text{H}_{20}\text{PO}_3)_{0.15}]_2$  (d-spacing; 1.62 nm).

Table 1 Chemisorption uptake of amines over several zirconium phosphates at 373 K.

	I.D.*	H <sup>++</sup>	Adsorption uptake*** /mmol/H <sup>+</sup>				
	/nm	/meq g <sup>-1</sup>	NH <sub>3</sub>	MMA	TMA	n-BA	t-BA
Kinetic diameter /nm			0.34	0.40	0.61	0.40	0.64
Amberlyst 15	—	5.69	0.61	0.62	0.52	0.70	0.53
$\alpha\text{-Zr}(\text{O}_3\text{POH})_2\cdot\text{H}_2\text{O}$	0.76	6.17	0.55	0.13	0.09	0.23	0.02
$\gamma\text{-Zr}(\text{O}_3\text{POH})_2\cdot2\text{H}_2\text{O}$	1.26	6.27	0.48	0.30	0.05		
$\text{Zr}[(\text{O}_3\text{POH})_{0.5}(\text{O}_3\text{PC}_{10}\text{H}_{20}\text{PO}_3)_{0.25}]_2$	1.62	2.90				0.35	0.02
$\text{Zr}[(\text{O}_3\text{POH})_{0.65}(\text{O}_3\text{PC}_{10}\text{H}_{20}\text{PO}_3)_{0.075}]_2$	1.62	5.46				0.44	0.02

\* Interlayer d-spacing determined by XRD

\*\* Number of protons determined by potentiometric titration

\*\*\* MMA; monomethylamine, TMA; trimethylamine, n-BA; n-butylamine, t-BA; *tert*-butylamine

Table 1 shows the amount of chemisorption of various base molecules on zirconium phosphates or pillared zirconium phosphonates. After becoming equilibrated with 1.3 kPa of base molecules, the sample was evacuated at the same temperature of adsorption for 2 h. Adsorption of base molecules on Amberlyst 15 (cross linked ion-exchange resin) shows no shape-selective adsorption, regardless of bulkiness of molecules. On the other hand, not only on  $\alpha$ - or  $\gamma$ -zirconium phosphate but also on the composite pillared zirconium phosphates, adsorption of base molecules shows somewhat shape-selective. Adsorption of the bulkier base molecules, such as TMA (0.61 nm) and *t*-BA (0.64 nm) are extremely retarded than that of the smaller base molecules, such as ammonia (0.34 nm), MMA (0.40 nm), and *n*-BA (0.40).

In  $\alpha$ - or  $\gamma$ -zirconium phosphate, the protons of the phosphate group can be adsorbed by base molecules without any significant change in the structure of the layer itself. Adjacent layers are stacked such that the phosphate groups in the lower layer are directly below the zirconium atoms in the adjacent layer. The distinct feature of this, and other zirconium phosphonate compounds, are that the forces holding the layers together are van der Waals and electrostatic interactions. However, when base molecules adsorbed on phosphate protons, the predominant forces are probably ionic attractions between interposed counterions and adjacent macro anions. Between layers are cavities a well-defined size [2]. In case of  $\alpha$ -zirconium phosphate, these cavities are filled with water of crystallization [9]. The structure is stabilized by hydrogen bonding between these waters and phosphate groups in adjacent planes. The interlayer distance of the  $\alpha$ -layered acid salt is 0.76 nm. The cavities are interconnected by openings with a maximum diameter of 0.27 nm [2]. The single-crystal structure of  $\gamma$ -zirconium phosphate has not been determined, because crystals sufficiently large for single crystal XRD are not available. Nevertheless, Yamanaka and Tanaka determined the crystal lattice parameters and density from powder samples [10]. The lattice parameters of  $\gamma$ -form are different from that of  $\alpha$ -form, however, the cell dimension in  $\alpha$ -form is associated with that in the  $\gamma$ -form.

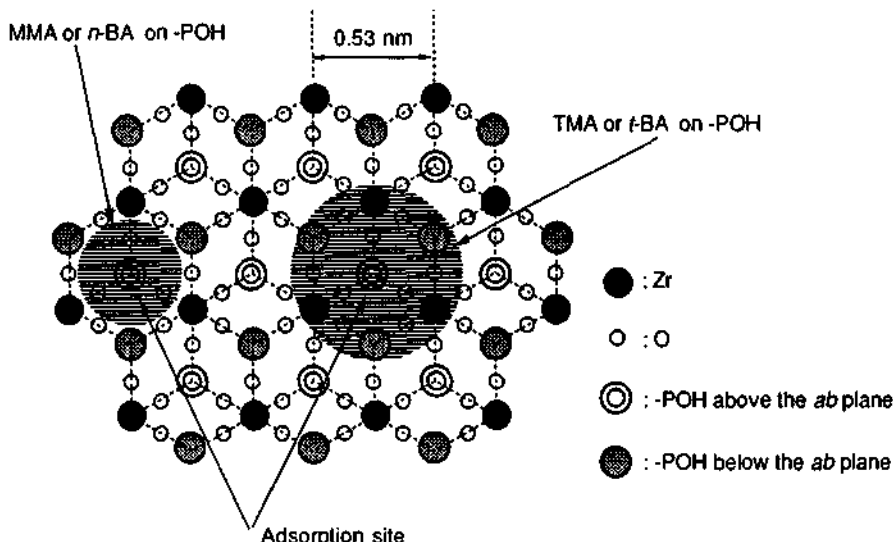


Fig. 4 Shape selective adsorption of base molecules over the *ab* plane of zirconium phosphate: MMA; monomethylamine, *n*-BA; *n*-butylamine, TMA; trimethylamine, *t*-BA; *tert*-butylamine.

Structural models for  $\alpha$ - and  $\gamma$ -zirconium phosphate explain the planar construction. Although the interlayer atomic arrangements are considerably different for the two structures, the atomic stacking within the layer appears very similar in the projection along the direction normal to the layer plane. Figure 4 shows idealized structure of  $\alpha$ -zirconium phosphate showing the relationship of the pseudo hexagonal unit cell to the monoclinic unit cell [2]. When the bulkier base molecules

adsorbed on one phosphate proton, the adjacent six protons may not participate for adsorption. However, the smaller base molecules will not interfere the adsorption on adjacent six phosphate protons.

For catalytic esterification of acetic acid in ethanol medium over zirconium phosphonates, the composite materials showed higher catalytic activities than single phosphate as shown in Table 2. It is quite interesting that no matter how small the proton concentration became in comparison with a-form, the reaction rate for esterification was enhanced. After introduction of hydrophobic functions (pendant:  $-C_6H_5$ ,  $-C_{12}H_{25}$ , pillared:  $-C_{10}H_{20}^-$ ) to zirconium phosphonate ( $-OH$ ,  $-CH_2COOH$ ,  $-CH_2SO_3H$ ), composite materials became accessible to any reactant molecule, since the interlayer d-spacing were increased, and improved in hydrophobicity. Thus, the functional groups for catalysis are incorporated in one crystal phase. The findings suggest that the composite compounds may be variety of reactions in aqueous or polar organic solvents. Some of these compounds, such as pendant  $Zr[(O_3PCH_2SO_3H)_{0.5}(O_3PC_{12}H_{25})_{0.5}]_2$  or pillared  $Zr[(O_3PCH_2SO_3H)_{0.5}(O_3PC_{10}H_{20}PO_3)_{0.25}]_2$  showed much higher catalytic activities for the esterification of acetic acid than the hydrogen type of Nafion.

Table 2 Catalytic activity for the esterification of acetic acid over composite zirconium phosphonates at 343 K.

	d-spacing /nm	Catalytic activity $/10^{-7} \text{ mol g}^{-1} \text{ s}^{-1}$
H-Nafion		21.8
$\alpha\text{-Zr(O}_3\text{POH)}_2\text{H}_2\text{O}$	0.76	0.80
$Zr[(O_3POH)_{0.5}(O_3PC_6H_5)_{0.5}]_2$	1.55	1.28
$Zr[(O_3PCH_2COOH)_{0.5}(O_3PC_6H_5)_{0.5}]_2$	1.55	12.8
$Zr[(O_3PCH_2SO_3H)_{0.5}(O_3PC_6H_5)_{0.5}]_2$	1.55	18.7
$Zr[(O_3PCH_2SO_3H)_{0.5}(O_3PC_{10}H_{20}PO_3)_{0.25}]_2$	1.63	66.2
$Zr[(O_3PCH(C_6H_5)_3)COOH]_2$	1.83	10.7
$Zr[(O_3POH)_{0.5}(O_3PC_{12}H_{25})_{0.5}]_2$	3.24	5.47
$Zr[(O_3PCH_2SO_3H)_{0.5}(O_3PC_{12}H_{25})_{0.5}]_2$	3.24	42.3

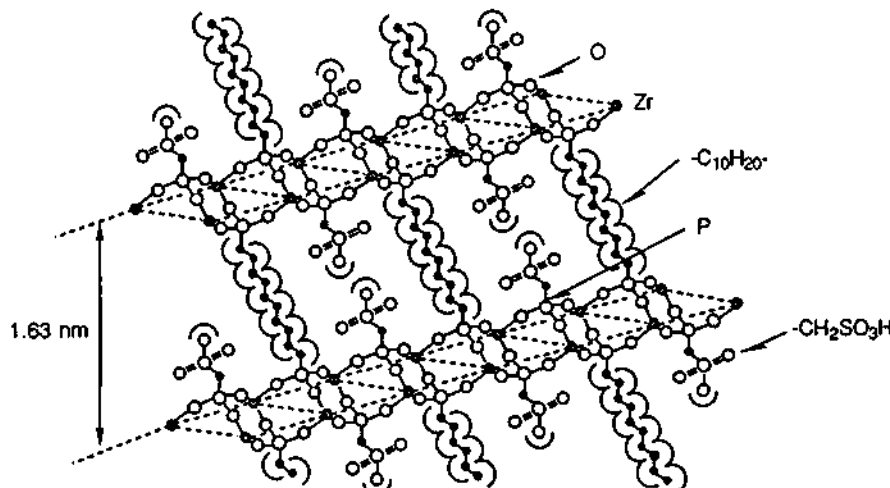


Fig. 5 Idealized structure of pillared  $Zr[(O_3PCH_2SO_3H)_{0.5}(O_3PC_{10}H_{20}PO_3)_{0.25}]_2$ .

#### 4. Conclusions

The idealized structure of pillared  $\text{Zr}[(\text{O}_3\text{PCH}_2\text{SO}_3\text{H})_{0.5}(\text{O}_3\text{PC}_{10}\text{H}_{20}\text{PO}_3)_{0.25}]_2$  is illustrated in Fig. 5. In such compounds, which show the similar  $\alpha$ -layered structure as zirconium phosphate, two different tetrahedral phosphates are bonded to the plane of zirconium atoms. Thus it is of great interest to examine the possibility of obtaining various organic derivatives of zirconium phosphonate in which two or more different functional groups are present in the same compounds. No single crystals for XRD structural determination has yet been obtained. Only speculations on the structure of the composite compounds may be made on the basis of their MASNMR spectra and XRD powder patterns, their chemical behavior, and existing knowledge of the structure of  $\alpha$ -zirconium phosphate and its organic derivatives. Diffraction data confirm the expected correlation of interlayer spacing with the size of pendant or pillared organic group. Solid products consisting of layered sheets with ordered arrays of the pendant/pillared organic groups on both sides of the layer are obtained with most phosphonic acids.

Because of their layered structure, zirconium phosphonate materials can act as a series of modified surfaces, accessible by introducing pendant or pillared functional groups.

- The structure of zirconium phosphonates is similar to the zirconium phosphate core layer with pendant organic groups attached to this core and extending perpendicular to the plane of the layer.
- The pendant and polar groups of zirconium phosphonates are distributed uniformly between each pair of Zr atom planes and the interlayer d-spacing obeyed the bulkiness of alkyl groups.
- The composite zirconium phosphonates show higher catalytic activities for acid catalyzed reactions than that of the corresponding single zirconium phosphonate.
- After introduction of hydrophobic functions (alkyl groups), the composite zirconium phosphonates become accessible to any reactant molecules and improve hydrophobic properties.

#### REFERENCES

1. Whittingham, M. S. and Jacobson, A. J., *Intercalation Chemistry* (Materials Science Series) Academic Press, New York, 1982
2. Troup, J.M. and Clearfield, A., *Inorg. Chem.*, 1977, 16, 3311
3. Alberti, G., Costantino, U., Allulli, S., and Tomassini, N., *J. Inorg. Nucl. Chem.*, 1978, 40, 1113
4. Segawa, K., Kihara, N., Yamamoto, H., and Nakata, S., in "Proceedings of the 9th International Zeilite Conference" (R. von Ballmoos et al., Eds.), p. 255, Butterworth-Heinemann, Boston, 1993
5. Dines, M. B. and DiGiacomo, P. M., *Inorg. Chem.*, 1981, 20, 92
6. Segawa, K., Sugiyama, A., and Kurusu, Y., *Studies in Surface Sci. and Catal.*, 1991, 60, 73
7. Segawa, K., Nakajima, Y., Nakata, S., and Asaoka, S., *J. Catal.*, 1986, 101, 81
8. Segawa, K., Kihara, N., and Yamamoto, H., *J. Molec. Catal.*, 1992, 74, 213.
9. Segawa, K., Kurusu, Y., Nakajima, Y., and Kinoshita, M., *J. Catal.*, 1985, 94, 491
10. Yamanaka, S. and Tanaka, M., *J. Inorg. Nucl. Chem.*, 1979, 41, 45

## 3.12 Grinding of Zirconium Pyrophosphate and its Catalytic Activity for 1-Butene Isomerization

Akio Tada<sup>a</sup>, Mitsuru Oishi<sup>a</sup>, Noriyasu Okazaki<sup>a</sup>, Hidenobu Itoh<sup>b</sup>, and Yuzo Imizu<sup>b</sup>

<sup>a</sup>Department of Applied and Environmental Chemistry, Kitami Institute of Technology, Kitami 090, Japan

<sup>b</sup>Department of Materials Science, Kitami Institute of Technology, Kitami 090, Japan

### Abstract

Grinding zirconium pyrophosphate catalysts resulted in enhanced catalytic activities (weight basis), which were strongly influenced by their calcination temperatures before grinding as well as by evacuation temperatures prior to use for the titled reaction. The grinding effect on activity was also investigated.

### 1. INTRODUCTION

The crystalline bis-(monohydrogenorthophosphate) of zirconium, with general formula of  $Zr(HPO_4)_2 \cdot nH_2O$  (abbreviated as ZrP), has been extensively investigated as a material of solid acid catalysts, especially from the view point of the correlation between its structure and the catalytic properties after heat treatment.[1-2] It should be emphasized that the presence of P-O-P bonds in a ZrP-derived catalyst is closely related with the generation of its high activity, regardless of the original ZrP.[3] Recently, zirconium pyrophosphate (abbreviated as ZrPP), which was synthesized by heating zirconium phosphate gel (abbreviated as ZrP-gel) in phosphoric acid solution, has been reported to show much higher activity for the isomerization of n-butene than ZrP-gel,  $\alpha$ -Zr( $HPO_4$ )<sub>2</sub> $\cdot H_2O$  (abbreviated as  $\alpha$ -ZrP), and  $\epsilon$ -Zr( $HPO_4$ )<sub>2</sub> (abbreviated as  $\epsilon$ -ZrP), although the synthesized ZrPP had exactly the same X-ray diffraction pattern of cubic ZrPP which is catalytically inactive.[4] These results suggest that the formation of a precursor of cubic ZrPP is critical to the generation of the catalytic activity of a ZrPP catalyst. However, most studies have been concentrated on ZrP-derived catalysts, and accordingly a little study has been made on a nominal ZrPP which is characterized by infrared bands due to P-O-P bond and/or X-ray diffraction (abbreviated as XRD) pattern of cubic ZrPP.

Very recently, we found that grinding and successive heating of such a nominal ZrPP results in enhancement of its catalytic activity for the isomerization of 1-butene. Our finding will give a clue for understanding of the catalytically active precursor suggested above. The present paper describes the grinding effect of two kinds of nominal ZrPP samples prepared in two different ways.

### 2. EXPERIMENTAL

One type of nominal ZrPP was prepared by calcining  $\alpha$ -ZrP at 800 °C or above for 3 h (referred as  $\alpha$ -ZrPP).  $\alpha$ -ZrP was prepared by refluxing a mixture of zirconia and 85% phosphoric acid (molar ratio  $P_2O_5/ZrO_2 = 2$ ) at 150 °C for 48 h, followed by washing with distilled water, filtrating, and drying at 90 °C for 20 h. The other type of nominal ZrPP was directly prepared by refluxing a mixture

of 15 g of amorphous zirconium phosphate and 235 g of 85% phosphoric acid solution at 160 °C for 48 h, followed by the same treatment as mentioned above (referred as syn-ZrPP). Amorphous zirconium phosphate was prepared by adding slowly 0.5 M ZrOCl<sub>2</sub> solution into 3 M phosphoric acid solution. The resulting slurry was washed with distilled water, followed by filtrating and drying at 110 °C for 45 h. Both ZrPP samples were pressed into disks, crushed, and sieved (16-30 mesh). Grinding of catalyst samples was performed by using an agate mortar and a pestle.

The crystalline phases in samples were identified from XRD patterns, which were measured on an X-ray diffractometer using CuK $\alpha$  radiation. The microstructures of samples were characterized by scanning electron microscopy (SEM).

The isomerization of 1-butene (50 Torr) was carried out at 25 or 50 °C using a closed circulation system (ca. 430 ml) over 0.2 g of catalyst. Prior to use, all catalyst samples were evacuated in a reactor at a specified temperature for 2 h. The reaction products were analyzed by using a gaschromatograph equipped with a 2 m column of propylene carbonate maintained at 20 °C.

### 3. RESULTS AND DISCUSSION

#### 3.1. syn-ZrPP

Figure 1 shows the XRD patterns of various syn-ZrPP samples. The peaks assigned to  $\alpha$ -ZrP disappear on evacuation at 500 °C (Figs. 1a and 1b), and the peaks due to cubic ZrPP are growing with increasing evacuation temperature (Figs. 1b and 1c). It is noted that the XRD pattern of the syn-ZrPP evacuated at 500 °C is closely similar in terms of diffraction line position to that of the syn-ZrPP evacuated at 1100 °C, although the activities of those two catalysts were very different as shown in Fig. 3. Grinding as-prepared syn-ZrPP brought about the disappearance of the XRD lines of  $\alpha$ -ZrP

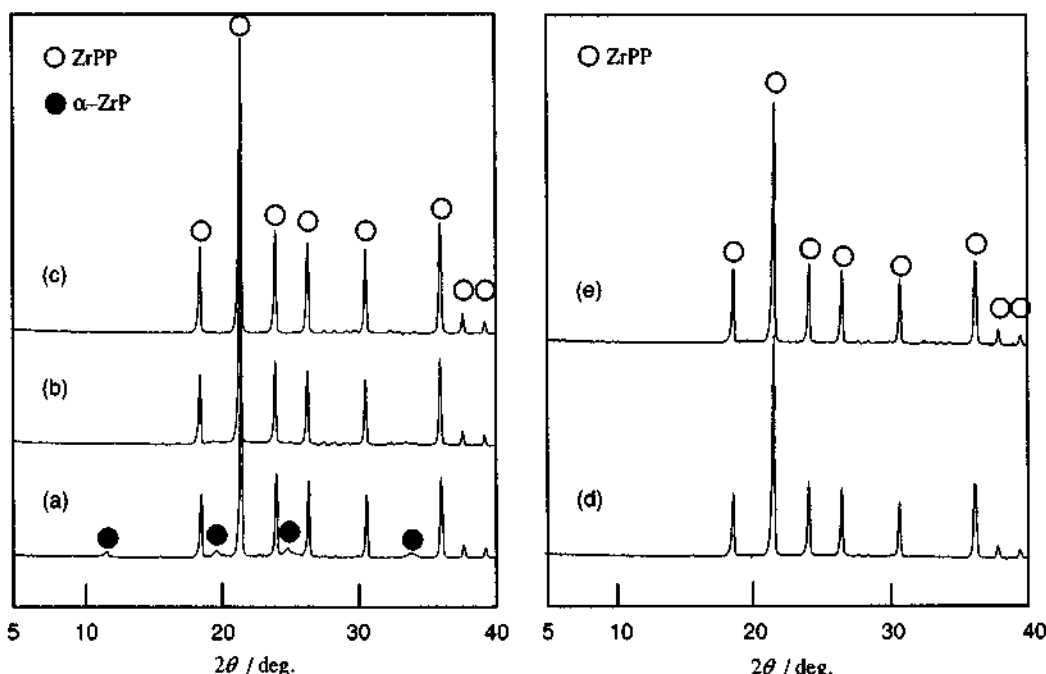


Fig. 1. X-ray diffraction patterns of various syn-ZrPP powdered samples: (a) as-prepared, (b) after evacuation (500 °C, 1 h), (c) after evacuation (1100 °C, 1 h), (d) after grinding (1 h), (e) after grinding (1 h), pressing, sieving, and evacuating (500 °C, 1 h).

suggesting that  $\alpha$ -ZrP was transformed into amorphous (Figs. 1a and 1d). No differences in XRD pattern and intensity were observed before and after grinding of syn-ZrPP, when evacuated at 500 °C; the XRD pattern of cubic ZrPP alone was observed (Fig. 1b and 1e).

The microstructures of syn-ZrPP samples are shown in Fig. 2. The SEM micrograph of as-prepared syn-ZrPP (Fig. 2a) features fine crystallites with almost uniform size (4 - 8  $\mu\text{m}$ ). Grinding the above sample for 1 h results in the formation of fine grains (Fig. 2b). When 1 h-ground syn-ZrPP was pressed into disks, crushed, sieved, and evacuated at 500 °C for 1 h (Fig. 2c), the fine grains

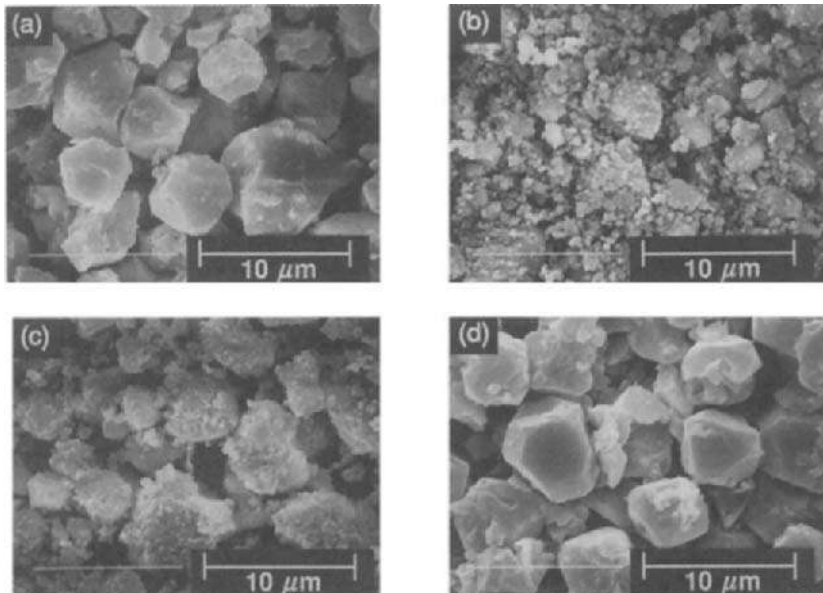


Fig. 2. SEM micrographs of various syn-ZrPP powdered samples: (a) as-prepared, (b) after grinding (1 h), (c) after grinding (1 h), pressing, sieving, and evacuating (500 °C, 1 h), (d) after evacuation (500 °C, 1 h).

change to large crystallites, which are nearly similar in size to those of as-prepared syn-ZrPP as well as those of unground syn-ZrPP evacuated at 500 °C (Fig. 2d). When evacuated at 1100 °C, the SEM micrograph similar to that shown in Fig. 2d was observed. It should be noted here that a lot of very fine particles are attached to the large crystallites shown in Fig. 2c.

Figure 3a shows the catalytic activity of syn-ZrPP as a function of evacuation temperature. The activity remarkably changes from below to above evacuation at 500 °C. Figure 3b clearly shows the activity of syn-ZrPP which was ground in the atmosphere for 1 h, followed by evacuating at various temperatures, increases remarkably. As seen in Table 1, under a given evacuation

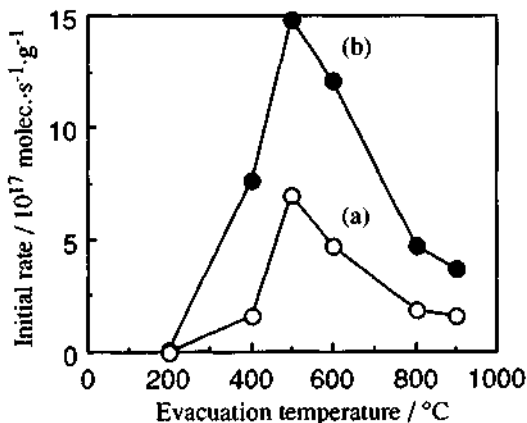


Fig. 3. Catalytic activities of syn-ZrPP for the isomerization of 1-butene at 25 °C as a function of evacuation temperature.  
(a) ○, original syn-ZrPP (b) ●, ground syn-ZrPP

Table 1. Catalytic activities and selectivities of syn-ZrPP catalysts for the isomerization of 1-butene at 25 °C.

Calcin. temp. / °C	Grinding time / h	Evac. temp. / °C	Rate / $10^{16}$ molec. ·s <sup>-1</sup> ·m <sup>-2</sup>	cis / trans	Surface area / m <sup>2</sup> ·g <sup>-1</sup>
—	0	200	0.050	—	6.02
—	0	400	2.46	2.0	6.56
—	0	500	9.82	2.0	7.11
—	0	600	7.19	2.1	6.51
—	0	800	2.94	1.9	6.22
—	0	900	3.16	2.0	5.10
—	1	200	0.086	—	14.0
—	1	400	5.38	1.7	14.2
—	1	500	9.93	1.7	14.9
—	1	600	8.34	1.8	14.5
—	1	800	3.54	1.8	13.2
—	1	900	3.22	1.8	11.6
1100	0	500	0.909	—	3.52
1100	1	500	0.950	—	4.01
1100	3	500	0.902	2.0	21.6

temperature, grinding of syn-ZrPP which underwent no calcination causes an increase in surface area but a little change in activity based on a unit surface area. This means that the increase in the activity of each catalyst by grinding as shown in Fig. 3 is nearly attributed to the respective increased surface area. More noticeable is the marked dependence of the activity of ground syn-ZrPP on evacuation temperature. Therefore the similarities of both the evacuation-temperature dependence of the activity and the selectivity value of the ground syn-ZrPP to those of the original syn-ZrPP imply that the active sites of the former are almost identical with those of the latter.

When syn-ZrPP was calcined at 1100 °C, followed by evacuating at 500 °C, the activity based on a unit surface area decreased to about one tenth. This result can be accounted for by the transformation of catalytically active precursor to inactive cubic ZrPP upon calcination at 1100 °C, since the intensities of XRD lines due to cubic ZrPP increased appreciably (not shown). In the case of syn-ZrPP calcined at 1100 °C, the surface area change was not very sharp upon grinding for 1 h; it was not until 3 h after grinding that the change became appreciable. Interestingly the activity based on a unit surface area is virtually independent of the grinding time, indicating that the activity (surface area basis) is essentially determined by the calcination temperature.

The syn-ZrPP calcined at 1100 °C that have proved difficult to be ground may consist of well-sintered cubic ZrPP, while a syn-ZrPP sample which can easily be ground will have grain boundaries at which cubic ZrPP grains are connected weakly one another probably through the precursor of cubic ZrPP. Such a precursor existed in the bulk will be allowed to adsorb water molecules and to become partly rehydroxylated state rapidly upon exposure to moisture during grinding. The successive dehydration could generate active sites during evacuation at elevated temperatures. The extent of the dehydration is thought to be crucial to the formation of active sites, since syn-ZrPP calcined at 1100 °C, followed by grinding and evacuating at temperatures below 200 °C showed no catalytic activity. The precursor phase should be amorphous, since no crystalline phase except for cubic ZrPP was observed in syn-ZrPP evacuated at 1100 °C (Fig. 1c). For  $\alpha$ -ZrP, amorphous layered zirconium pyrophosphate, which is a precursor of cubic ZrPP, has been reported to be an active phase.[1-2] Therefore, it is quite reasonable to assume that the same phase will exist on the surface of ground syn-ZrPP as its precursor.

### 3.2. $\alpha$ -ZrPP

A series of structural change of  $M(HPO_4)_2 \cdot nH_2O$  has been summarized as follows: hydrated layered hydrogenorthophosphate  $\rightarrow$  anhydrous layered hydrogenorthophosphate  $\rightarrow$  layered pyrophosphate  $\rightarrow$  cubic pyrophosphate.[2] Figure 4 shows the XRD patterns of  $\alpha$ -ZrP evacuated at various temperatures. Clearly,  $\alpha$ -ZrP turned into almost amorphous at 500 °C, began to change into cubic ZrPP at 600 °C, and thereafter the crystallite of cubic ZrPP continued growing up to 1000 °C. The transformation of  $\alpha$ -ZrP to amorphous material can be explained by assuming the random condensation of interlayered phosphate groups.[3]

Figure 5 shows the SEM micrographs of  $\alpha$ -ZrP samples. The crystallites of as-prepared  $\alpha$ -ZrP exhibit hexagonal plate-like morphology. The crystallites of  $\alpha$ -ZrPP evacuated at 1000 °C (Fig. 5b) look thinner than those of syn-ZrPP evacuated at 500 °C (Fig. 2d). This will be caused by the difficulty of the structural change from  $\alpha$ -ZrP to cubic ZrPP in  $\alpha$ -ZrPP preparation.

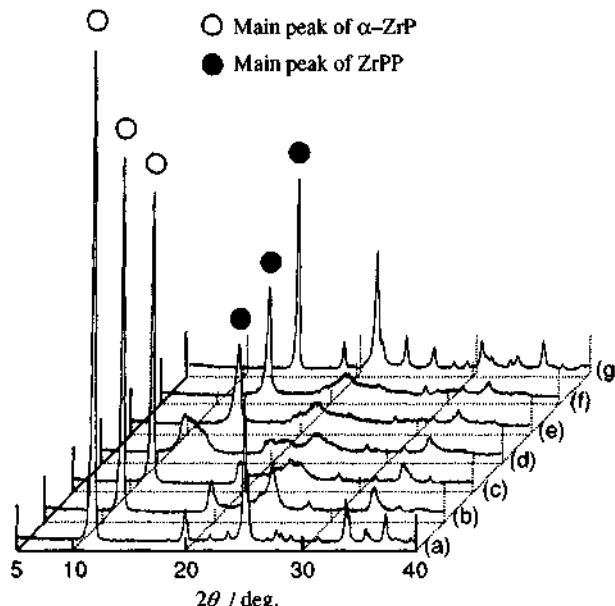


Fig. 4. X-ray diffraction patterns of  $\alpha$ -ZrP evacuated at ; (a) -; (b) 200 °C; (c) 400 °C; (d) 500 °C; (e) 600 °C; (f) 700 °C; (g) 1000 °C.

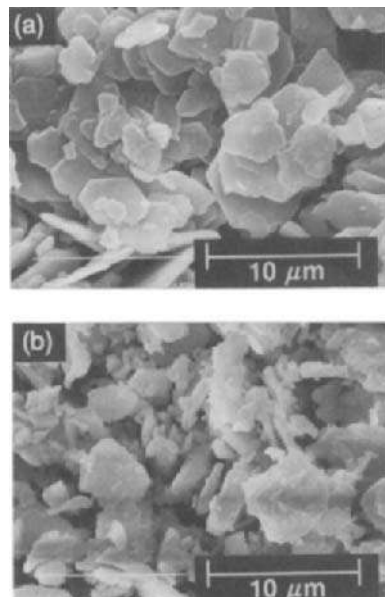


Fig. 5. SEM micrographs of various  $\alpha$ -ZrP samples: (a) as-prepared, (b) after evacuation (1000 °C, 1 h).

In Table 2 the catalytic activities of  $\alpha$ -ZrPP catalysts are listed. Their selectivities (*cis* / *trans*) were ca. 1.5 (not shown), regardless of the temperature of evacuation or calcination and of whether the catalysts are ground or not. It is clear by comparing Table 2 (react. temp., 50 °C) with Table 1 (react. temp., 25 °C) that the activity of unground  $\alpha$ -ZrPP evacuated at 1000 °C is much lower than that of the unground syn-ZrPP evacuated at 1100 °C. The difference in activity may be due to that in the morphology of the crystallites seen in Figs. 5b and 2d.

It is very interesting that the activity of  $\alpha$ -ZrPP calcined at 800 °C, followed by grinding was greatly affected by evacuation temperature and reached a maximum on evacuation at 700 °C, which was higher by 200 °C than the temperature at which the activity of syn-ZrPP reached a maximum. Under specified temperatures of calcination and evacuation, the catalytic activity of  $\alpha$ -ZrPP based on a unit weight increased after grinding. The enhancement in activity (weight basis) will be due to

Table 2. Catalytic activities of  $\alpha$ -ZrPP catalysts for the isomerization of 1-butene at 50 °C.

Calcination temp. / °C	Grinding time/h	Evac. temp. / °C	Rate/		Surface area/ m <sup>2</sup> . g <sup>-1</sup>
			$10^{16}$ molec. s <sup>-1</sup> .g <sup>-1</sup>	$10^{16}$ molec. s <sup>-1</sup> .m <sup>-2</sup>	
800	0	700	14.0	1.41	9.93
800	1	200	0.46	0.038	12.0
800	1	500	13.42	1.07	12.5
800	1	700	22.2	1.73	12.8
800	1	800	17.4	1.55	11.2
1000	0	700	1.7	0.22	7.9
1000	1	700	4.2	0.25	16.9
1200	0	700	0.61	0.17	3.5
1200	1	700	0.70	0.17	4.1
1200	3	700	1.4	0.11	13.2

mainly the increase in surface area, because no change in XRD patterns upon grinding was observed like in the situation of syn-ZrPP (not shown). The catalytic activity of  $\alpha$ -ZrPP decreased sharply with an increase in calcination temperature from 800 °C to 1200 °C. Similar correlation is seen for ground  $\alpha$ -ZrPP. These results indicate that the activities of both original and ground  $\alpha$ -ZrPP are determined predominantly by calcination temperature. The negligibly low activities of original and ground  $\alpha$ -ZrPP calcined at 1000 and 1200 °C are consistent with the fact that  $\alpha$ -ZrP is transformed completely to cubic ZrPP on calcining above 1300 K and became catalytically inactive.[1] The interpretation for the grinding effect of syn-ZrPP on the activity can be applied for that of  $\alpha$ -ZrPP. The reason the activity of syn-ZrPP is higher than that of  $\alpha$ -ZrPP is interpreted as follows; the structural orderliness of syn-ZrPP is superior to that of  $\alpha$ -ZrPP (as was stated above,  $\alpha$ -ZrPP passes amorphous state prior to changing into ZrPP) and so syn-ZrPP is supposed to involve larger amount of the precursor phase than  $\alpha$ -ZrPP.

#### 4. CONCLUSIONS

Based on the present work, the following conclusions may be drawn. (1) Grinding ZrPP samples results in enhancement of the activities (weight basis), suggesting the existence of a precursor in the bulk of the corresponding unground ZrPP. (2) The activity of ground ZrPP depends strongly on the calcination temperature; the activity decreases with increase in the calcination temperature (800 - 1200 °C). (3) The activity of ground ZrPP depends strongly on the evacuation temperature and the dependence is similar to that of the corresponding unground ZrPP.

#### 5. ACKNOWLEDGEMENT

The authors wish to thank Mr. Nobuaki Muramami of Kitami Institute of Technology for his help in sample preparation.

#### REFERENCES

1. K. Segawa, S. Nakata, and S. Asaoka, *Materials Chem. Phys.*, **1987**, 17, 181.
2. A. La Ginestra and P. Patrono, *ibid.*, **1987**, 17, 161.
3. K. Segawa, Y. Kurusu, Y. Nakajima, and M. Kinoshita, *J. Catal.*, **1985**, 94, 491.
4. K. Segawa, Y. Nakajima, S. Nakata, S. Asaoka, and H. Takahashi, *ibid.*, **1986**, 101, 81.

### 3.13 Preparation of Amorphous Metal-substituted Aluminum Phosphates and Their Acid-Base Properties

H. Itoh<sup>a</sup>, S. Matsuyama<sup>b</sup>, N. Okazaki<sup>b</sup>, Y. Imizu<sup>a</sup>, and A. Tada<sup>b</sup>

<sup>a</sup>Department of Materials Science, Kitami Institute of Technology,  
165 koen-cho, kitami, Hokkaido 090, Japan

<sup>b</sup>Department of Applied Chemistry, Kitami Institute of Technology,  
165 Koen-cho, Kitami, Hokkaido 090, Japan

#### Abstract

Metal(Ti, Fe, Zn, K) substituted aluminum phosphates (Me-Al-P-O, (Al+Me)/P=1) were prepared by a sol-gel method. As compared with the acid-base properties of AlPO<sub>4</sub>, the amounts of basic sites on Me-Al-P-O were significantly increased, while the amounts of acid sites slightly changed. For 1-butene isomerization, Me-Al-P-O showed higher activities than AlPO<sub>4</sub>. It was suggested that basic sites generated by metal substitution enhanced the activities of Me-Al-P-O.

#### 1. INTRODUCTION

Many studies have been focused on the catalytic properties of metal phosphates [1]. Especially amorphous aluminum phosphate(Al/P=1) has been studied in more depth due to its structural similarity to SiO<sub>2</sub>, large surface area, and high surface acidity. And it has been revealed that pure aluminum phosphate has little basic sites which behave as active sites in cooperation with acidic sites. Therefore, the catalytic activity of pure aluminum phosphate for hydrocarbon conversion is relatively low[2]. On the other hand, the family of alumino-phosphate molecular sieves(ALPO-n, MeAPO) have recently been developed by Union Carbide[3]. However, in general, these zeolite-like materials have low acidity and show poor catalytic activities. In this report, we studied the surface acid-base and catalytic properties of metal substituted aluminum phosphates.

#### 2. EXPERIMENTAL METHODS

Various metal(K, Zn, Fe, Ti) substituted aluminum phosphates were prepared as follows[4]. Aluminum chloride(AlCl<sub>3</sub>·6H<sub>2</sub>O, 27.2g), 85% orthophosphoric acid(14.4g), and a specified amount of metal chloride were dissolved in water(44.7ml)(Me:Al:P=0.1:0.9:1.0). The

solution was kept at ca. 0°C, followed by addition of propylene oxide(32.7g) with agitation. After standing for 15h at room temperature, the resulting gel was ground and washed with ethanol thoroughly. Then it was dried under vacuum at 60°C for 15-20h and heated at 550°C for 20h in air.

### 3. RESULTS AND DISCUSSION

#### 3.1 Chemical identification and structure

The addition of propylene oxide forced the gelatination reaction to completion within few minutes. This exothermic reaction proceeded with violence. Therefore, the gels were opaque because of the presence of gas bubbles. The results of surface composition analysis using SEM-EDS are shown in Table 1. When no metal cation which should be substituted for Al<sup>3+</sup> is coexisted in the starting solution, amorphous aluminum phosphate(Al/P=1) was obtained [4]. The ratios Me/(Me+Al) are not far from those in starting solutions. Metal chloride which did not react with phosphoric acid

**Table 1 Results of SEM-EDS analysis**

Sample	(Raw material)	Me/(Me+Al)×100	Chlorine (wt%)
AlPO <sub>4</sub>	(AlCl <sub>3</sub> ·6H <sub>2</sub> O)	-	0
Ti-Al-P-O	(TiCl <sub>4</sub> +AlCl <sub>3</sub> ·6H <sub>2</sub> O)	8.4	0
Fe-Al-P-O	(FeCl <sub>3</sub> +AlCl <sub>3</sub> ·6H <sub>2</sub> O)	8.3	0
Zn-Al-P-O	(ZnCl <sub>2</sub> +AlCl <sub>3</sub> ·6H <sub>2</sub> O)	8.5	0
K-Al-P-O	(KCl +AlCl <sub>3</sub> ·6H <sub>2</sub> O)	9.2	0

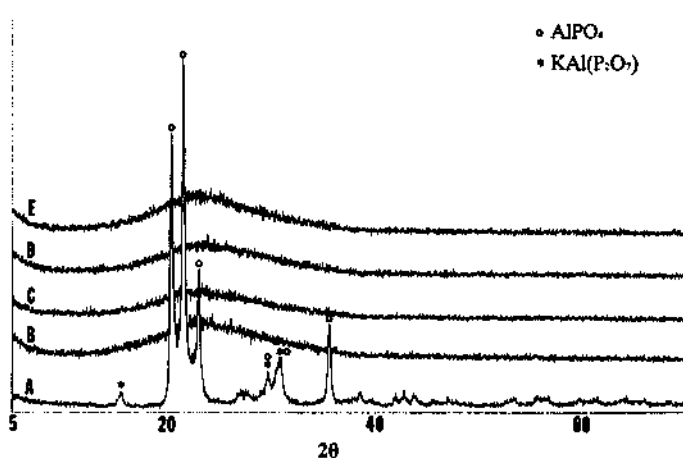


**Fig.1 XRD patterns of Me-Al-P-O(A-D) and AlPO<sub>4</sub> (E)**

pretreated at 550 °C.

Me: K(A), Zn(B), Fe<sup>III</sup>(C), Ti<sup>IV</sup>(D)

might have been washed out by ethanol. Figure 1 shows XRD patterns of the gel heated at 550°C. The samples except K-Al-P-O are amorphous. For K-Al-P-O the diffraction peaks due to AlPO<sub>4</sub> (mainly tridymite form) [5] and KAl(P<sub>2</sub>O<sub>7</sub>) [6] appeared. The formation of KAl(P<sub>2</sub>O<sub>7</sub>) was supported by IR spectrum (Fig. 2), in which characteristic absorption bands due to pyrophosphate (P-O-P, 943cm<sup>-1</sup> and 733cm<sup>-1</sup>) appeared. IR spectra of the other samples are almost same as that of AlPO<sub>4</sub>.

### 3.2 surface acid-base properties

Table 2 shows the acid-base properties of the Me-Al-P-O pretreated at 550°C. The maximum acid strength is varied by metal substitution, but does not exceed that of AlPO<sub>4</sub>. It seems that the order follows to the valence of metal ion substituted. On the other hand, there is no big difference in acid amount per unit surface area. The number of basic sites, however, increased extremely on the Me-Al-P-O catalysts. It has been considered that the inactivity of AlPO<sub>4</sub> probably reflects the inadequacy of basic sites [2]. Therefore the finding that the metal substitution

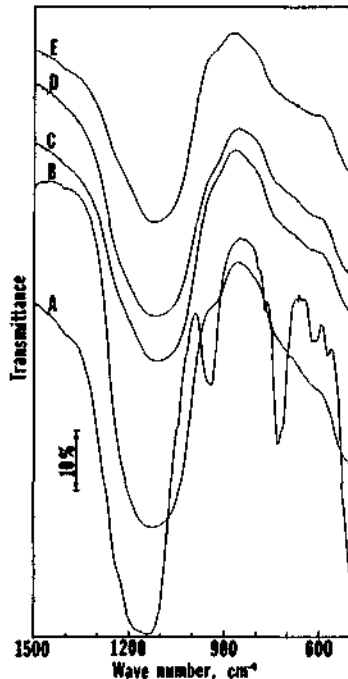


Fig. 2 IR spectra of Me-Al-P-O(A-D) and AlPO<sub>4</sub> (E) pretreated at 550 °C.  
Me: K(A), Zn(B), Fe<sup>III</sup>(C), Ti<sup>IV</sup>(D)

Table 2 Acid base properties of the Me-Al-P-O pretreated at 550°C

Sample	Maximum acid strength, H <sub>0</sub>	Acid amount <sup>a)</sup> , mol/m <sup>2</sup>	Base amount <sup>b)</sup> , mol/m <sup>2</sup>	Surface area, m <sup>2</sup> /g
AlPO <sub>4</sub>	-5.6	1.6x10 <sup>-6</sup>	8.9x10 <sup>-10</sup>	310
Ti-Al-P-O	-5.6	1.4x10 <sup>-6</sup>	1.4x10 <sup>-8</sup>	350
Fe-Al-P-O	-5.6	2.6x10 <sup>-6</sup>	3.0x10 <sup>-8</sup>	110
Zn-Al-P-O	-3.0	2.0x10 <sup>-6</sup>		200
K-Al-P-O	+1.5			27

a) measured by adsorption of pyridine at 90°C

b) measured by adsorption of carbon dioxide(30mmHg) at 25°C

**Table 3 Catalytic activities and selectivities of Me-Al-P-O samples for 1-butene isomerization**

Sample	Activity <sup>a)</sup> min <sup>-1</sup> g <sup>-1</sup>	Selectivity cis/trans
AlPO <sub>4</sub>	1.4x10 <sup>-3*</sup> (9.9x10 <sup>-3</sup> ) **	0.5* (0.4) **
Ti-Al-P-O	3.6x10 <sup>-2</sup> (1.3x10 <sup>-1</sup> )	2.8 (2.2)
Fe-Al-P-O	9.7x10 <sup>-3</sup> (1.3x10 <sup>-2</sup> )	1.0 (1.2)
Zn-Al-P-O	1.9x10 <sup>-2</sup> (8.9x10 <sup>-4</sup> )	1.1 (0.9)

\*pretreated at 400°C in vacuo

\*\*pretreated at 750°C in vacuo

a)k in  $\ln[Xe/(Xe-X)] = kt$

Reaction temperature: 100°C

technique resulted in the increase of basic sites is very important.

### 3.3 1-Butene isomerization

The catalytic activity and selectivity of the Me-Al-P-O system for 1-butene isomerization are summarized in Table 3. The samples evacuated at 400°C show remarkably high activities compared with AlPO<sub>4</sub>. The selectivities(cis-2-butene/trans-2-butene) did not change with pretreatment temperatures, and are higher than that of AlPO<sub>4</sub>. The low value in the selectivity for AlPO<sub>4</sub> is considered to reflect its extremely high activity for cis-trans rotation(CTR), in which the activity reached to a maximum on evacuation at 750°C(cis/trans ratio at equilibrium state is 0.431) [7]. These facts suggest that the contribution of CTR to the isomerization may be smaller in Me-Al-P-O system. In general, it has been considered that the value of cis/trans increases with increasing contribution of basic site to the reaction. Perhaps, basic sites on Me-Al-P-O catalysts will behave as active sites in cooperation with acid sites. In conclusion the catalytic properties of aluminum phosphate can be improved by modification using the above metal substitution technique.

### References

1. J.B.Moffat, Catal. Rev.-Sci. Eng., 1978, 18, 199.
2. J.B.Peri, Discuss. Faraday Soc., 1971, 52, 55.
3. E.M.Flanigen, B.M.Lok, R.L.Patton, and S.T.Wilson, Proc. 7th Zeolite Conf., Kodansha-Elsevier, Tokyo-Amsterdam, 1986, 103.
4. J.M.Campelo, J.M.Marinas, S.Mendioroz, and J.A.Pajares, J. Catal., 1986, 101, 484.
5. JCPDS File, 20-45.
6. JCPDS File, 34-1370.
7. H.Itoh, A.Tada, and K.Tanabe, Chem. Lett., 1981, 1567.

### 3.14 Surface Properties and Catalytic Activities of Superconducting Bi-Pb-Sr-Ca-Cu Oxides for 1-Butene Isomerization

Akio Tada<sup>a</sup>, Ryouichi Ishida<sup>a</sup>, Noriyasu Okazaki<sup>a</sup>, Yuzo Imizu<sup>b</sup>, and Hidenobu Itoh<sup>b</sup>

<sup>a</sup>Department of Applied and Environmental Chemistry, Kitami Institute of Technology, Kitami 090

<sup>b</sup>Department of Materials Science, Kitami Institute of Technology, Kitami 090

#### Abstract

The isomerization of 1-butene was carried out in order to detect trace amounts of acidic and/or basic impurities which are supposed to localize on the surfaces of the titled superconducting oxides. It was found that the superconducting oxides containing almost only a high critical-temperature phase ( $T_c = 110$  K) showed no catalytic activity, whereas precursor compounds of the high  $T_c$  phase showed considerable activities as well as the selectivity featured by the base-catalyzed reaction. On the basis of the catalytic properties and other data of XRD, SEM, and  $T_c$ -measurement, we have concluded that CaO as an impurity remains on the surface of imperfect Bi-based superconducting oxides.

#### 1. INTRODUCTION

Since the discovery of the two distinct phases with superconducting transition temperatures of 85 and 110 K in the Bi-Sr-Ca-Cu-O system by Maeda *et al.*[1], many studies have been made in order to increase the fraction of the 110 K phase. Takano *et al.*[2] found that a proper addition of PbO enhanced the transformation of 85 K phase which has a nominal stoichiometry of  $\text{Bi}_2\text{Sr}_2\text{CaCu}_2\text{O}_{8+y}$  (abbreviated as the 2212 phase) into 110 K phase with that of  $\text{Bi}_2\text{Sr}_2\text{Ca}_2\text{Cu}_3\text{O}_{10+y}$  (abbreviated as the 2223 phase). In addition, it is also known that  $\text{Ca}_2\text{PbO}_4$  is formed in the Bi-Pb-Sr-Ca-Cu-O system and its amount decreases with the growth in 2223 phase after sintering.[3]

Recently a reaction mechanism for producing 2223 phase by a powder mixing method has been proposed :  $\text{Ca}_2\text{PbO}_4$  decomposes to a mixture of a liquid phase and CaO, followed by the reaction among CuO, CaO, and the liquid phase.[4] In this scheme CaO plays an important role. However, the existence of CaO has never been proved so far.

We have incidentally found that the isomerization of 1-butene takes place over several Bi-based superconducting oxides evacuated at 500°C and the feature of their catalytic selectivities suggests the existence of basic sites on the surface. This finding may be very useful for understanding of the behavior of  $\text{Ca}_2\text{PbO}_4$  and accordingly of the mechanism of the solid-state reactions to give a high- $T_c$  Bi-based superconductor. The present paper describes the surface basic properties and the superconducting properties of the selected samples of the Bi-Pb-Sr-Ca-Cu-O system.

#### 2. EXPERIMENTAL

##### 2.1 Preparation and Analysis of Bi-based Superconducting Oxides.

A superconducting oxide having a nominal composition of  $\text{Bi}_{1.6}\text{Pb}_{0.4}\text{Sr}_2\text{Ca}_2\text{Cu}_3\text{O}_y$  was prepared fundamentally as described previously.[5] High-purity nitrate and acetate salts,

$\text{Bi}(\text{NO}_3)_3 \cdot 5\text{H}_2\text{O}$ ,  $\text{Sr}(\text{CH}_3\text{COO})_2 \cdot 1/2\text{H}_2\text{O}$ ,  $\text{Ca}(\text{CH}_3\text{COO})_2 \cdot \text{H}_2\text{O}$ ,  $\text{Cu}(\text{CH}_3\text{COO})_2 \cdot \text{H}_2\text{O}$ , and  $\text{Pb}(\text{CH}_3\text{COO})_2 \cdot 3\text{H}_2\text{O}$  were dissolved in 250 ml of 1.75 M acetic acid solution in this order so as to reach the molar ratio of  $\text{Bi}:\text{Sr}:\text{Ca}:\text{Cu}:\text{Pb} = 0.016:0.020:0.020:0.030:0.004$  (solution A). Simultaneously, 17.5 g of dimethyl oxalate was also dissolved in 200 ml of distilled water (solution B). After adding the solution B to the solution A, the resulting solution was stirred for 2 weeks at room temperature until a complete precipitation was attained. Then this solution was filtered after stirring for a few minute, washed with distilled water, and dried at room temperature under vacuum. The precursor thus obtained was subsequently calcined at 500°C for 5 h. The calcined aggregates were ground, pressed into a disk (13 mm in diameter and ca. 1 mm thick), and sintered at 835 or 850°C in static air for 24 h. Structural characterization of a sample was carried out by X-ray diffraction (XRD) and scanning electron microscopy (SEM) studies. The electrical resistance of sintered compacts was measured as a function of temperature by the four-probe method using silver paste as contacts.

## 2.2 Catalytic Reaction.

The isomerization of 1-butene (50 Torr) was carried out at 26 or 100°C using a closed circulation system (ca. 430 ml) over 0.1 g of catalyst. Prior to use, all catalyst samples were evacuated in the reactor at 500°C for 2 h. The reaction products were analyzed by using a gaschromatograph equipped with a 2 m column of propylene carbonate maintained at 26°C.

## 3. RESULTS AND DISCUSSION

Table 1 summarizes the catalytic activities and characteristics of Bi-Pb-Sr-Ca-Cu oxides. The catalytic activity of each sample decreased in the order C800 > C850 > A835 > C700 > C500, A850, B835, B850. The composition of superconducting phases was strongly affected by their processing conditions. C700, which was obtained by heating the as-prepared precursor powder (denoted as C500) at 700°C, remained as non-superconductor. A835 and A850 obtained by grinding and pressing C500 into a disk under a pressure of 2500 kg cm<sup>-2</sup>, followed by heating at 835 and 850°C respectively were found to be a mixture of 2223 phase and 2212 phase. B835 and B850 obtained by a two-stage sintering

Table 1 Catalytic properties and characteristics of Bi-Pb-Sr-Ca-Cu oxides

Sample <sup>a)</sup>	Catalytic properties <sup>b)</sup>		Composition of crystalline substances / % <sup>c)</sup>			Surface area <sup>d)</sup> / m <sup>2</sup> g <sup>-1</sup>	
	code	activity	cis/trans	Total	2223	2212	
C850	70	10		80.4	45.8	34.7	4.2
C800	120	6		65.8	17.9	47.9	9.4
C700	1	10		-	-	-	13.1
C500	0	-		-	-	-	-
A850	0	-		91.7	86.1	5.6	1.9
A835	5	8		86.6	57.1	29.5	4.4
B850	0	-		97.1	94.7	2.4	0
B835	0	-		88.1	85	3.1	4.2

a) Heating time : A and C series, 24 h ; B series, 48 h. The numerals in a sample code show each sintering temperature (°C).

b) Relative activities for 1-butene isomerization at 26°C. C700 :  $8.36 \times 10^{-3} \text{ min}^{-1} \text{ g}^{-1}$ .

c) The composition of 2223 phase, 2212 phase, and  $\text{Ca}_2\text{PbO}_4$  was determined on the basis of the intensities of the peak areas of crystalline substances.

d) Samples were evacuated at 500°C for 2 h.

process were composed of nearly complete 2223 phase. The two-stage sintering process means a series of processing, grinding - pressing - heating - regrinding - repressing - reheating at a specified temperature under different pressures (first, 2500 kg cm<sup>-2</sup>; second, 10000 kg cm<sup>-2</sup>). The order of catalytic activity mentioned above seems to have an inverse correlation with the superconducting feature of each sample. All samples can be classified into three groups. The first group, C800, C850, and A835 were catalytically active and were rich in 2212 phase. The second group, A850, B835, and B850 were catalytically inactive even at the reaction temperature of 100°C, and were all excellent superconductors with very high content of 2223 phase. The third group, C500 and C700 showed no activity or only low activity, and exhibited no superconducting property. The selectivities (defined as initial ratio of *cis*-2-butene/*trans*-2-butene) of the first group of samples were very high, suggesting that the active sites on the samples are basic sites.[6]

Figure 1 shows the X-ray diffraction patterns of B850, A835, C800, C700, and C500. Major diffraction lines were assigned to those of 2223 phase, 2212 phase, and Ca<sub>2</sub>PbO<sub>4</sub>. In addition to these three substances a computer-survey of the XRD data provided the indications of the existence of the following substances ; Bi<sub>2</sub>O<sub>3</sub>, BiO, SrO, CaO, PbO, Pb<sub>2</sub>O<sub>3</sub>, PbO<sub>2</sub>, Cu<sub>2</sub>O, CuO, CaCO<sub>3</sub>, SrCO<sub>3</sub>, Bi<sub>2</sub>Sr<sub>2</sub>CuO<sub>x</sub>, Ca<sub>2</sub>PbO<sub>4</sub>, and CaPbO<sub>3-x</sub>. However, the existences of none of them could be confirmed, since the intensities of their XRD lines were negligibly weak and/or their lines agreed very closely with those of 2212 and 2223 phases. Among them Bi<sub>2</sub>O<sub>3</sub> and PbO are known as solid acid, whereas CaO, SrO, CaCO<sub>3</sub>, and SrCO<sub>3</sub> as solid base.[7] Table 2 summarizes the catalytic activities and selectivities of the above four solid bases as well as Ca<sub>2</sub>PbO<sub>4</sub> whose acid-base properties have not been reported. As expected, the former catalysts evacuated at 500°C showed considerable activities, especially CaO and SrO being remarkably active, while the composite oxide was inactive. From these results, it is readily thought that if a small amount of CaO or SrO presents on the surface of the Bi-Pb-Sr-Ca-Cu oxides given in Table 1, they will exhibit very high activities.

Figure 2 depicts the structures of three Bi-

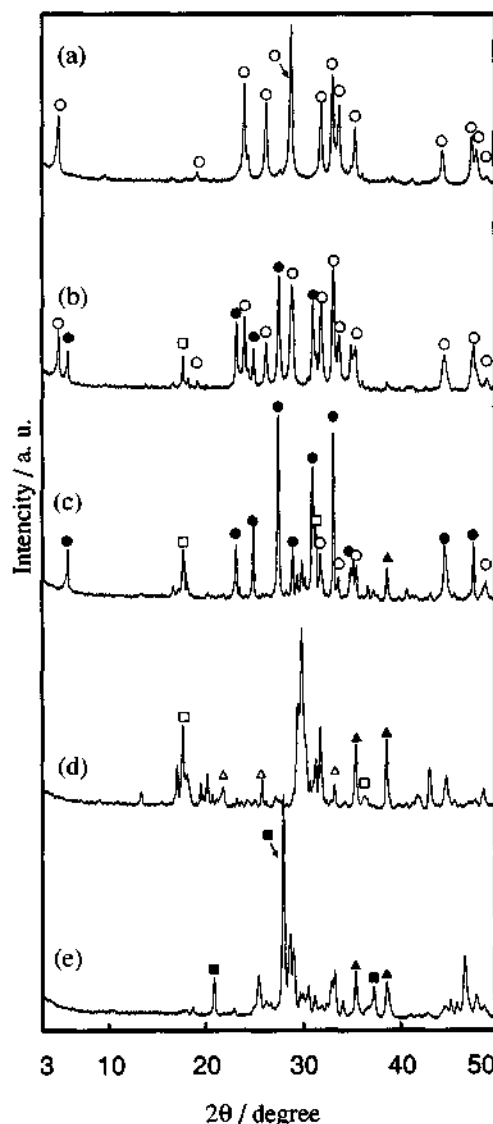


Fig. 1 The X-ray diffraction patterns of (a) B850, (b) A835, (c) C800, (d) C700, and (e) C500 ; (○) 2223 phase, (●) 2212 phase, (□) Ca<sub>2</sub>PbO<sub>4</sub>, (▲) CuO, (■) Cu-Bi-O, (△) Bi-Sr-Cu-O.

Table 2 Catalytic properties of various compounds related to Bi-Pb-Sr-Ca-Cu oxides

Sample <sup>a)</sup>	Catalytic activity at		Selectivity <i>cis/trans</i>
	26°C	100°C	
CaCO <sub>3</sub>	23	-	15
SrCO <sub>3</sub>	4	-	5
CaO	120	-	7
SrO	>400	-	0.5
Ca <sub>2</sub> PbO <sub>4</sub>	0	0	-

a) Evacuated at 500°C for 2 h prior to the reaction.

b) Relative activities for 1-butene isomerization at 26°C.

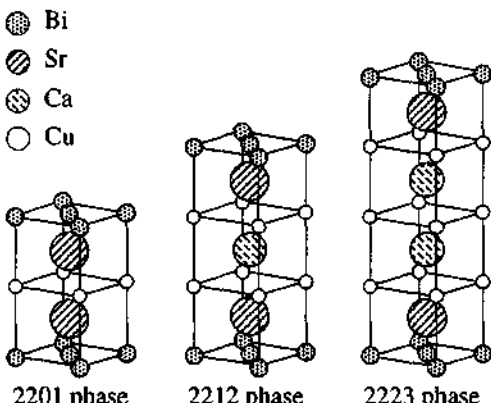
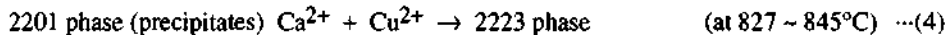
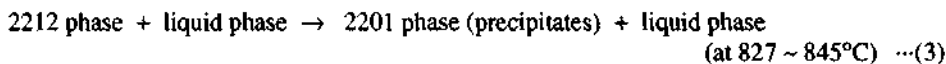
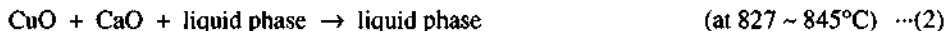


Fig. 2 Structures of Bi-based superconducting phases.

based superconducting phases. The 2201 phase inevitably involves Sr atoms, and the 2212 phase involves more Sr atoms than Ca atoms. In the case of the samples which are composed of at least 2212 phase, Sr atoms that failed to be involved in 2212 phase may be negligibly few. Therefore CaO rather than SrO could exist on the surface of the superconducting samples belonging to the first group.

It is widely accepted that 2223 phase grows at the expense of 2212 phase together with several phases, such as Ca<sub>2</sub>PbO<sub>4</sub>, Ca<sub>2</sub>CuO<sub>3</sub>, and CuO, etc. According to Kijima *et al.*, [8] Ca<sub>2</sub>PbO<sub>4</sub> is formed around 750°C, decomposes into a mixture of CaO and a liquid phase on heating at 822°C, and these two phases may enhance the interaction of CuO and 2212 phase to form 2223 phase. Additionally, the following scheme has recently been proposed.[8]



If this mechanism is true, it is very likely that CaO exists by chance on the surface of several Bi-based superconducting oxides. However, the detection of CaO by X-ray diffraction analysis is very difficult as described above.

Figure 3 shows SEM micrographs of Bi-Pb-Sr-Ca-Cu composite oxide samples. Clearly, their microstructures differ significantly. A C800 sample appears very fine particles with heterogeneity in size, suggesting the formation of porous structure. The microstructure of C850 exhibits a multiphase structure. The microstructure of A835 exhibits plate-like morphology and that of B850 exhibits remarkably developed layered structure. Consistent with the microstructural development, the bulk densities of the samples should differ: the specific surface area of C800 is the largest (Table 1). The reactions shown in the scheme should occur not only within each particle but also between particles. In that case, the cations could transfer more easily in more dense samples such as A835 and B850.

Assuming that CaO exists on the surface of the precursor system of 2223 phase, the results listed

in Table 1 can be explained reasonably as follows.

In the case of C800, which showed the highest activity,  $\text{Ca}_2\text{PbO}_4$  plausibly decomposes in the sintering stage slightly according to the reaction (1), although the sintering temperature is lower than  $822^\circ\text{C}$ . The subsequent reactions (2) to (4) in the scheme is probably very slow, since the reaction (2) is thought to require higher energy and to occur considerably at  $845^\circ\text{C}$ . Therefore, substantial amount of CaO should accumulate in C800 and consequently, C800 is supposed to exhibit the very high activity. In C850, which showed secondly high activity,  $\text{Ca}_2\text{PbO}_4$  can decompose to give a mixture of CaO and liquid phase, and moreover, the subsequent reactions (2) to (4) can proceed easily, since the sintering temperature is over the critical reaction temperature,  $450^\circ\text{C}$ . As a result, the amount of CaO that is available for the isomerization reaction became lower than in C800. In the case of C700 having a very much low activity, a large amount of  $\text{Ca}_2\text{PbO}_4$  was observed (Table 1), namely, a substantial amount of Ca was entrapped in  $\text{Ca}_2\text{PbO}_4$ . The rest of Ca also could have been involved in 2201 phase. It should be noted here that at  $700^\circ\text{C}$ ,  $\text{Ca}_2\text{PbO}_4$  can not undergo the decomposition reaction giving a mixture of CaO and the liquid. In view of these results, the low activity of C700 is quite reasonable. No activity of C500 can be ascribed to the lack of CaO, evidenced by X-ray analysis.

In A835, a series of solid state reactions shown in the scheme can occur more easily than in C800 or C850, since the density of A835 is higher and so the transfer of the reactants is easy. For this reason, the activity of A835 is supposed to be lower than that of C800 or C850. In A850, the reaction (2) will proceed very easily, because of the sintering temperature beyond  $450^\circ\text{C}$ .

In B835 and B850 samples, which were prepared by the two-stage sintering procedure, all of CaO should be involved in the bulk of the superconducting oxides. Therefore no catalytic activity can be expected.

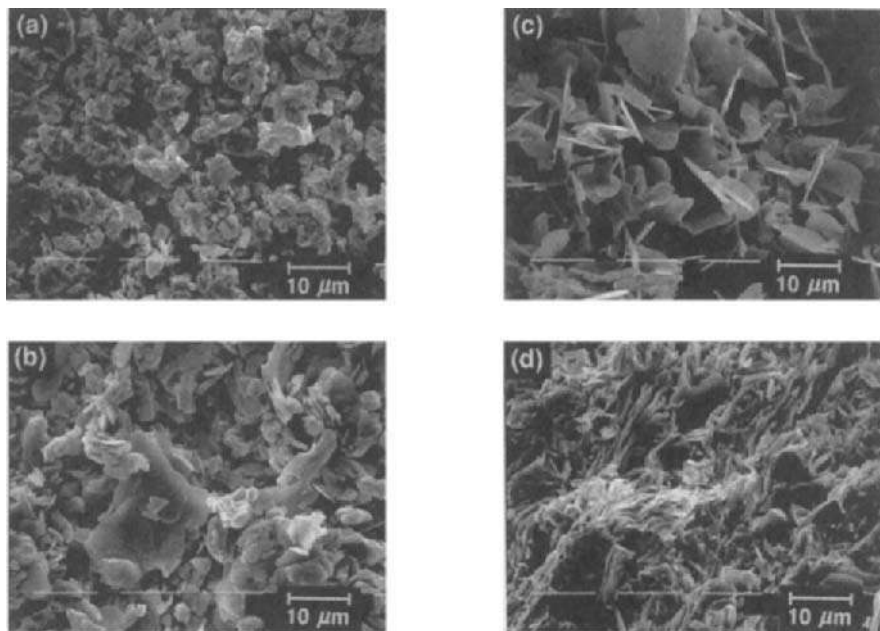


Fig. 3 SEM micrographs of different Bi-Pb-Sr-Ca-Cu oxides : (a) C800, (b) C850, (c) A835, and (d) B850.

In conclusion, the isomerization of 1-butene has been proved useful as a probe reaction for detecting trace amounts of acidic or basic impurities localized on the surface of superconducting Bi-Pb-Sr-Ca-Cu oxides. From the results and discussion described above, we conclude that CaO exists on the surface of Bi-based superconducting oxides which are composed predominantly of 2212 phase.

#### 4. ACKNOWLEDGEMENT

The authors wish to thank Mr. Nobuaki Murakami of Kitami Institute of Technology for assistance with sample characterization.

#### REFERENCES

1. H. Maeda, Y. Tanaka, M. Fukutomi, and T. Asano, *Jpn. J. Appl. Phys.*, **1988**, *27*, L209.
2. M. Takano, J. Takeda, K. Oda, H. Kitaguchi, Y. Miura, Y. Ikeda, Y. Tomii, and H. Mazaki, *ibid.*, **1988**, *27*, L1041.
3. T. Uzumaki, K. Yamanaka, N. Kamehara, and K. Niwa, *ibid.*, **1989**, *28*, L75.
4. Y. L. Chen, R. Stevens, *J. Am. Ceram Soc.*, **1992**, *75*[5], 1150-59.
5. H. Itoh, K. Okada, T. Fujisawa, N. Okazaki, and A. Tada, *Chem. Lett.*, **1990**, 429.
6. K. Tanabe, M. Misono, Y. Ono, and H. Hattori, "NEW SOLID ACIDS AND BASES", **1989**, p.215., Kodansha.
7. K. Tanabe, M. Misono, Y. Ono, and H. Hattori, *ibid.*, **1989**, p.1., Kodansha.
8. N. Kijima, H. Endo, J. Tsuchiya, A. Sumiyama, M. Mizuno, and Y. Oguri, *Jpn. J. Appl. Phys.*, **1988**, *27*, L1852.

### 3.15 Preparation and Properties of a New Kind of Acid Catalyst of Zeolite Coating on Metal Surface

Li Jianquan, Dong Jinxiang and Liu Guanghuan

Institute of Special Chemicals, Taiyuan University of Technology, Taiyuan 030024, Shanxi, P.R.China

#### Abstract

The catalytic material of mordenite coating on metal Cr surface (MOR/Cr) is first synthesized by the vapor phase method and characterized by IR, SEM and microprobe techniques. The experimental results show that the crystals of mordenite grow on metal Cr surface and Cr does not enter the mordenite framework. It seems that Cr does not exert any effect on the position of IR absorption bands of mordenite. In HMOR/Cr sample, there exist Si, Al, Cr and a little Na, and the Cr atom content is 1.02% as determined by the microprobe method. As a catalyst, HMOR/Cr shows good catalytic properties for the reaction of o-xylene isomerization.

#### 1. INTRODUCTION

Recently, Davis et al.[1] reported that the crystals of zeolite Y can be prepared on metal surface by modified hydrothermal alteration procedures. This kind of composite material has a bright future.

The catalytic importance of chromium has prompted numerous attempts to introduce chromium cations into zeolite. Huang and coworkers[2] studied Cr species in the Cr/mordenite system and we investigated the properties of Cr/ZSM-35[3] and Cr/HNAM (HNAM synthesized in the nonaqueous system) [4]. But in these papers, chromium was introduced via an aqueous exchange method.

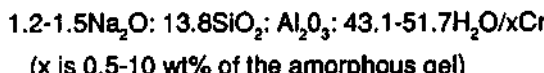
In this article, the material of mordenite coating on metallic Cr (MOR/Cr), which is prepared by a novel vapor phase method of zeolite synthesis reported in 1990[5], is first described. MOR/Cr was formed in the system  $\text{Na}_2\text{O}\text{-Al}_2\text{O}_3\text{-SiO}_2\text{-H}_2\text{O}$  and Cr metal. The results of XRD, IR, and microprobe indicate that mordenite crystals grow on Cr metal. This material is a good catalyst for xylene isomerization.

#### 2. EXPERIMENTAL

##### 2.1 Preparation

For preparation, solutions of aluminum sulfate, sodium silicate and sodium

hydroxide are mixed and stirred for 15 min. This mixture is filtered and washed, to become is the amorphous gel. Then the amorphous gel and Cr metal are put into a container, the bottom of which is a sieve. H<sub>2</sub>O is placed into a special reactant autoclave. Then, the container is placed on the support of the autoclave (the experimental setup is described in Ref.[5]). The autoclave is sealed and the reaction is carried out at 453K for 6-10 days under autogenous pressure. The reactant composition is expressed in mole ratios as follows:



To stop the crystallization process, the autoclave was removed from the air oven and quenched in cold water. The solid products were extracted, washed with distilled water and dried at 393K.

## 2.2 Characterization Method

XRD patterns were taken on powdered samples with a D/max- rA type diffractometer. FT-IR spectra were recorded on a Perkin-Elmer 1730 spectrometer using the KBr wafer technique. The microanalyses were made on a TN-5400 instrument.

Xylene isomerization on MOR/Cr was carried out in a microreactor connected to an automated system with a SP-2305 gas chromatograph.

The sample was shaped into 40-60 mesh particles and 100mg was charged into the reactor.

## 3. RESULTS AND DISCUSSION

### 3.1 XRD Analysis

The ion diameters of Cr<sup>3+</sup> and Al<sup>3+</sup> are 0.63Å and 0.39Å respectively. Because the diameter of Cr<sup>3+</sup> is larger than that of Al<sup>3+</sup>, the unit cell volume increases if the chromium enters the zeolite skeleton. It can be seen from Table 1 that the unit cell volume of MOR/Cr is equal to that of HMOR, which indicates that Cr does not enter the mordenite skeleton and MOR/Cr is formed.

It can also be seen that the unit cell volume decreases when MOR/Cr is exchanged with HCl and calcined at 823K into HMOR/Cr. This phenomenon may result from dealumination.

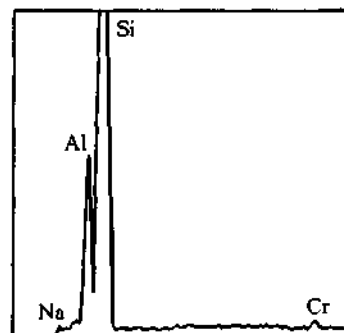


Fig. 1 Microprobe analysis of HMOR/Cr

**Table 1 Unit parameters of the samples**

Sample	a	b	c	Unit cell volume (Å <sup>3</sup> )
HMOR	18.14	20.36	7.49	2766
HMOR/Cr	18.14	20.36	7.49	2766
MOR/Cr	18.07	20.44	7.51	2774

**3.2 Microanalysis**

Based on microprobe analysis, the surface content of HMOR/Cr are shown

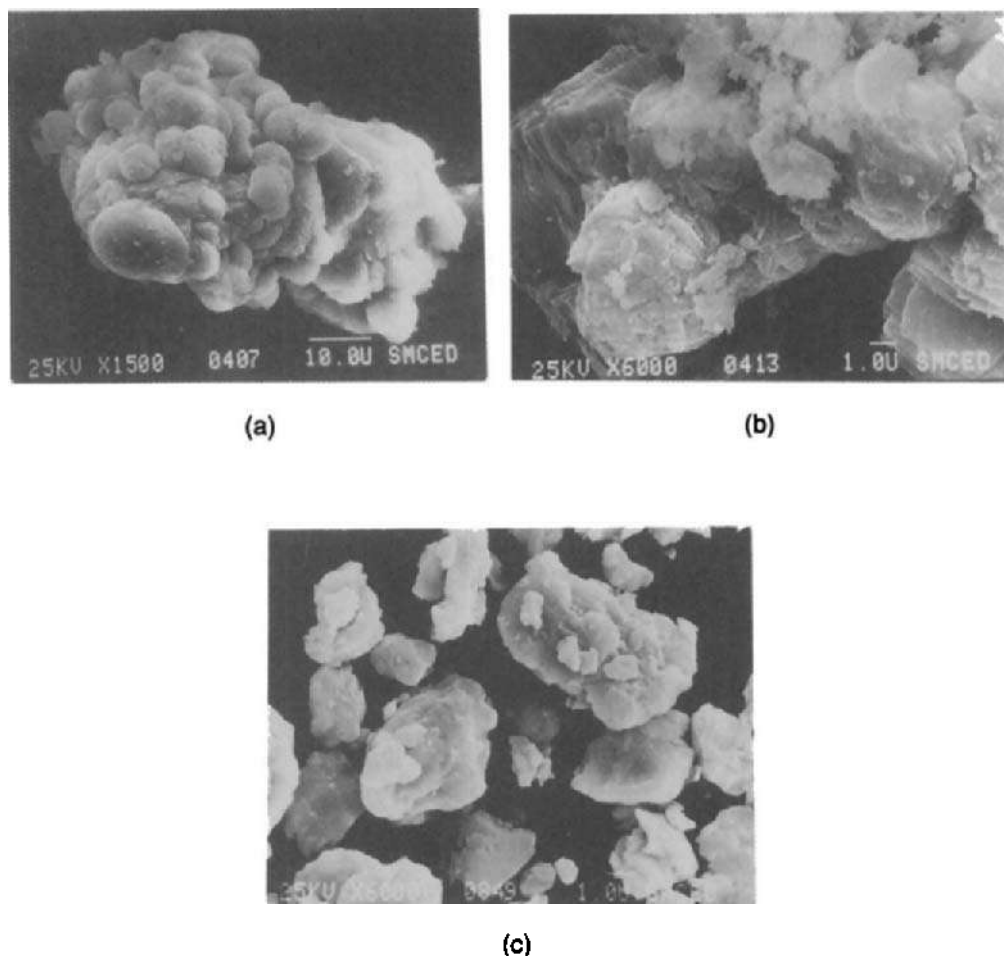


**Fig.2 SEM photographs of the three samples**  
 (a) HMOR/Cr (b) HMOR (c) Cr powder

in Fig.1. It is clear that there exist elements of Si, Al, Cr and a little Na in the HMOR/Cr sample bulk and the Cr atom content is 1.02%. This proves that zeolite coating on the metal surface is formed.

### 3.3 SEM Analysis

Figures 2a, 2b and 2c show SEM photographs of HMOR/Cr, HMOR and Cr respectively. It is clear that the morphology of HMOR/Cr is very different from that of Cr, and the morphologies of HMOR/Cr and HMOR are similar. This experiment indicates that the composite material is formed at a different angle.

### 3.4 IR Analysis

Figure 3 illustrates the IR spectra of HMOR/Cr and HMOR respectively. If chromium enters the zeolitic skeleton, the positions of the absorption bands move lower. It is clear that the positions of the IR bands of HMOR/Cr are the same as those of HMOR, which indicates that Cr does not enter the mordenite skeleton and that a new material is formed.

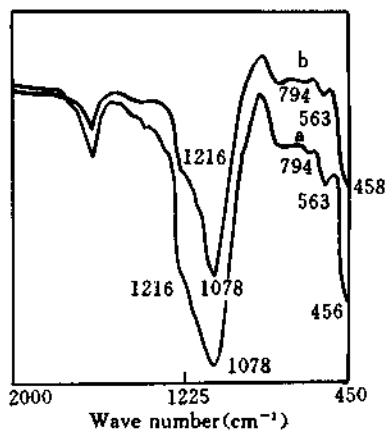


Fig. 3 IR spectra of HMOR (a) and MOR/Cr (b)

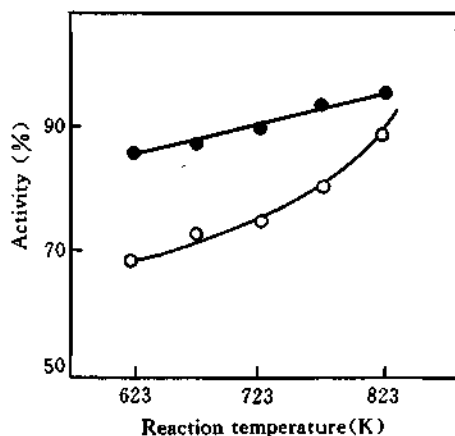


Fig. 4 Activity of HMOR/Cr for xylene isomerization  
 (o) o-xylene (○) m-xylene

### 3.5 Catalytic Properties

Figure 4 shows the activity of HMOR/Cr catalyst for xylene isomerization. It can be seen that HMOR/Cr is a good catalyst for xylene isomerization, especially for m-xylene isomerization.

#### 4. ACKNOWLEDGMENT

We thank the National Natural Science Foundation of China for financial support.

#### 5. REFERENCES

- [1] S. P. Davis, E. V. R. Borgstedt, S. L. Suib, *Chem. Mater.*, **1990**, *2*, 712.
- [2] M. Huang, I. Deng, Q. Wang, *Zeolites*, **1990**, *10*, 272.
- [3] W. Y. Xu, J. H. Cao, D. Tao, J. Q. Li and J. H. Ma, *Shiyou Huagong*, **1988**, *17*, 782 .
- [4] W. Y. Xu, J. Q. Li, G. H. Liu, *Ranliao Huaxue Xuebao*, **1991**, *19*, 82.
- [5] W. Y. Xu, J. X. Dong, J. P. Li, J. Q. Li, *J. Chem. Soc., Chem. Comm.*, **1990**, 755 .

This Page Intentionally Left Blank

### 3.16 Acidic Property of Silica Monolayers on Metal Oxides Prepared by CVD Method

Naonobu Katada<sup>a</sup>, Miki Niwa<sup>a</sup> and Yuichi Murakami<sup>b</sup>

<sup>a</sup>Department of Materials Science, Faculty of Engineering, Tottori University, Tottori 680, Japan

<sup>b</sup>Department of Applied Chemistry, School of Engineering, Nagoya University, Nagoya 464-01, Japan

#### Abstract

Thin silica layers were prepared on several metal oxides by chemical vapor deposition of Si methoxide. Monolayers of silica covered the surfaces almost completely. Generation of the Brønsted acidity was shown by IR measurements and test reactions. The monolayers were active for isomerization of *I*-butene and dehydration of *tert*-butanol, but inactive for cracking of cumene and dehydration of ethanol. Therefore, the acid strength is suggested to be so weak to catalyze only facile reactions. The acid strength of monolayers was ordered as on  $\text{Al}_2\text{O}_3 > \text{TiO}_2 > \text{ZrO}_2$ , based on the activity for isomerization of *I*-butene. The species M-O-SiOH (M = cation of support) is suggested to possess acidity due to interactions between M and Si. The presence of only weak acid sites suggests a fine distribution of acid strength due to a simple structure.

#### 1. INTRODUCTION

Several models of acid sites on mixed solid-acids, e.g. silica-alumina, have been proposed [1-2]. However, origin of the acidity is difficult to be understood by such simple models, because the mixed oxides possess complicated structures of the interface between the two components. In order to overcome the difficulty, a thin oxide-layer on another oxide surface is promising as a model of interface. We have used chemical vapor deposition (CVD) of a Si alkoxide to form thin  $\text{SiO}_2$  layers on zeolites; the layer narrows the pore-opening size [3]. In the present study, we applied CVD as a hopeful method to prepare an ultra thin layer of silica on several metal oxides. Our preliminary studies have been published [4-6]. Silica layers on oxides prepared by similar methods have been investigated [7-10].

#### 2. EXPERIMENTAL METHODS

##### 2.1. Preparation of Catalyst

Alumina was supplied from Catalysis Society of Japan as a reference catalyst, JRC-ALO4 ( $158 \text{ m}^2 \text{ g}^{-1}$ ,  $\gamma$ - $\text{Al}_2\text{O}_3$ ). Titania was supplied by Nippon Aerosil Co. Ltd., P-25 ( $44 \text{ m}^2 \text{ g}^{-1}$ , anatase containing a small amount of rutile). Zirconia ( $66 \text{ m}^2 \text{ g}^{-1}$ , baddeleyite) was prepared as follows; zirconium hydroxide was precipitated from a solution of  $\text{ZrCl}_4\text{O}$  by addition of ammonia; this was calcined at 673 K in air.

The support oxide was set in a micro-balance in order to monitor the weight during the deposition. The sample was evacuated at 673 K until no change of weight was observed. Vapor of  $\text{Si(OCH}_3)_4$  (tetramethoxysilane) was then admitted to the sample at 593 K; cycles of introduction of

vapor and evacuation were repeated in order to allow the fresh vapor to contact with the sample. The vapor pressure was kept at *ca.* 2.5 Torr by chilling the reservoir with an ice bath. The degree of evacuation was *ca.*  $10^{-3}$  Torr (1 Torr = 133.3 Pa). In order to decompose the methoxide,  $\text{H}_2\text{O}$  vapor or  $\text{O}_2$  was introduced after the deposition. Finally, the sample was calcined at 673 K in flowing  $\text{O}_2$  in order to remove the organic residue completely. The surface concentration of Si was calculated from the following equation based on the assumption that  $\text{SiO}_2$  was formed;

$$\text{Si concentration (nm}^{-2}\text{)} = \frac{\text{weight gain by deposition (g / g-support)} \cdot 6.02 \cdot 10^{23}}{\text{formula weight of } \text{SiO}_2 \text{ (60.02)} \cdot \text{BET surface area (m}^2 \text{ g-support}^{-1}\text{)} \cdot 10^{18}}$$

## 2.2. Benzaldehyde-ammonia Titration (BAT)

Benzoate anions are adsorbed on  $\text{Al}_2\text{O}_3$ ,  $\text{TiO}_2$  and  $\text{ZrO}_2$ , but not on  $\text{SiO}_2$ . On the basis of this, the coverage of  $\text{SiO}_2$  was measured by using BAT method [11-12]. Sample was set in a Pyrex tube connected to a GC directly. After drying at 673 K, 1  $\mu\text{l}$  ( $9.8 \cdot 10^{-6}$  mol) of benzaldehyde was injected repeatedly until no adsorption was observed, in order to make the surface saturated with benzoate anions. At 673 K, 10 ml ( $4.2 \cdot 10^{-4}$  mol) of gaseous ammonia was injected repeatedly to be reacted with the adsorbent into benzonitrile. Surface density of benzoate anions was estimated from the amount of desorbed benzonitrile. The coverage was calculated from the following equation;

$$\text{coverage} = \frac{\text{density of benzoate on sample}}{\text{density of benzoate on pure oxide}}$$

## 2.3. Infrared (IR) Measurements

Sample powder was molded into a thin disk; this was placed in a holder hanged in a vacuum line, evacuated at the upper part of the *in-situ* cell, and then exposed to an IR beam at the lower part with windows of  $\text{CaF}_2$ . Spectra of adsorbed ammonia and pyridine were measured after adsorption at 373 K followed by evacuation at 373 and 423 K, respectively, on the sample evacuated at 673 K.

## 2.4. Test Reactions

Isomerization of *l*-butene, cracking of cumene and dehydration of alcohols were performed by pulse method in 40 to 60 ml  $\text{min}^{-1}$  of flowing He on the catalyst pretreated at 673 K. In some experiments, the pretreatment temperature was varied.

## 3. RESULTS

Silica was readily deposited by cycle of introduction of alkoxide vapor and evacuation. Fig. 1 shows that the coverage increased almost linearly against the concentration of Si, and reached close to 100 % at 8, 12 and 13  $\text{Si nm}^{-2}$  on  $\text{ZrO}_2$ ,  $\text{TiO}_2$  and  $\text{Al}_2\text{O}_3$ , respectively. The samples with these concentration of Si will be termed as "monolayer samples" in the following description. Excess of Si kept the coverage above 90 %.

Fig. 2A shows the change of IR spectra of the surface hydroxyl groups by the deposition on  $\text{Al}_2\text{O}_3$ . Absorption of  $\text{AlOH}$  was observed at 3585, 3677, 3730 and  $3763 \text{ cm}^{-1}$  on pure  $\text{Al}_2\text{O}_3$ . A sharp absorption of  $3745 \text{ cm}^{-1}$ , ascribable to an isolated  $\text{SiOH}$ , and a broad one at  $3600 \text{ cm}^{-1}$  appeared with the deposition. As shown in Fig. 2B and C, the isolated  $\text{SiOH}$  appeared also on the monolayer samples prepared on  $\text{TiO}_2$  and  $\text{ZrO}_2$ , in place of the original hydroxyl groups.

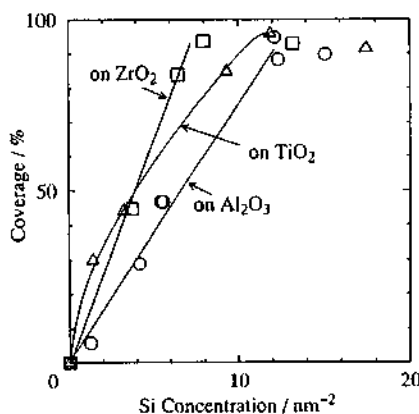


Fig. 1 : Relationship between coverage and surface concentration of Si.

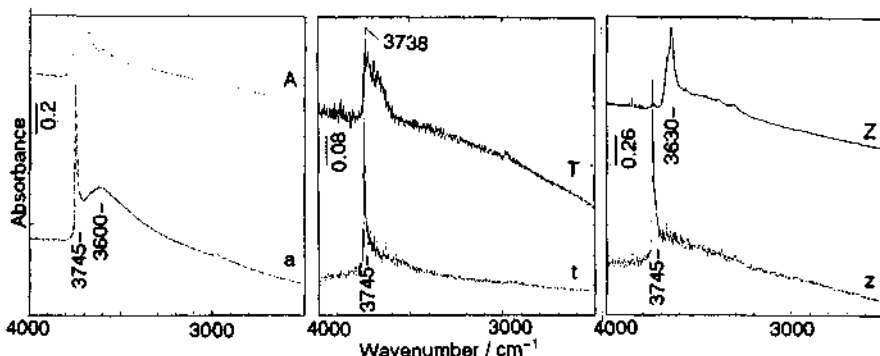


Fig. 2 : IR spectra of  $\text{Al}_2\text{O}_3$  (A),  $\text{TiO}_2$  (T) and  $\text{ZrO}_2$  (Z), and samples with  $15, 12$  and  $8 \text{ nm}^{-2}$  of Si (a, t and z, respectively), evacuated at  $673 \text{ K}$ .

Fig. 3 shows the spectra of adsorbed ammonia. On the monolayer samples, ammonium cation ( $1450 \text{ cm}^{-1}$ ) was observed, while almost no absorption was observed on the unmodified oxides. Ammonia adsorbed on Lewis acid site ( $1620 \text{ cm}^{-1}$ ) was observed on the pure oxides, and diminished by the deposition. As shown in Fig. 4, pyridine adsorbed on Lewis acid sites ( $1455 \text{ cm}^{-1}$ ) was observed on the unmodified oxides, and decreased by the deposition. Small absorptions of pyridinium cation ( $1545 \text{ cm}^{-1}$ ) were observed on the monolayer samples.

Fig. 5 shows the change of activity for the isomerization of 1-butene by the deposition. The activity increased with the deposition and showed the maximum at  $8, 12$  and  $13 \text{ Si nm}^{-2}$  over  $\text{ZrO}_2$ ,  $\text{TiO}_2$  and  $\text{Al}_2\text{O}_3$ , respectively. The enhanced activity decreased with excess of  $\text{SiO}_2$ , and was estimated to almost disappear at  $16, 20$  and  $24 \text{ Si nm}^{-2}$  over  $\text{ZrO}_2$ ,  $\text{TiO}_2$  and  $\text{Al}_2\text{O}_3$ , respectively. Table 1 compares the activity per surface area over the silica layers (at the maximum on each support), silica gel and commercial silica-alumina. The silica layer on  $\text{Al}_2\text{O}_3$  showed ca.  $2/3$  of the activity over silica-alumina. The silica layer on  $\text{Al}_2\text{O}_3$ ,  $\text{TiO}_2$  and  $\text{ZrO}_2$  was ca.  $1000, 100$  and  $10$  times as active as silica gel, respectively. Table 1 also shows that the ratio of *cis*-/*trans*-2-butene was in the range between  $1$  to  $2$  over the monolayer samples. Since the isomerization was carried out under the differential conditions, the initial ratio is estimated to be  $1 - 2$ .

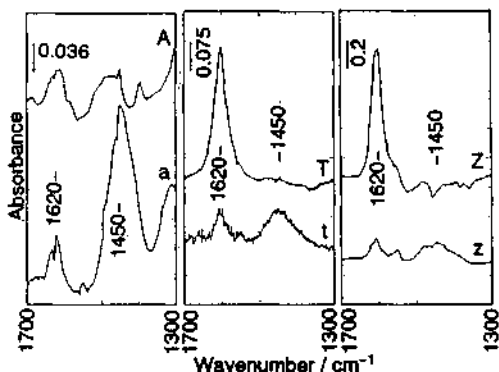


Fig. 3 : IR spectra of ammonia adsorbed on  $\text{Al}_2\text{O}_3$  (A),  $\text{TiO}_2$  (T) and  $\text{ZrO}_2$  (Z), and samples with  $15, 12$  and  $8 \text{ nm}^{-2}$  of Si (a, t and z, respectively), and evacuated at  $373 \text{ K}$ .

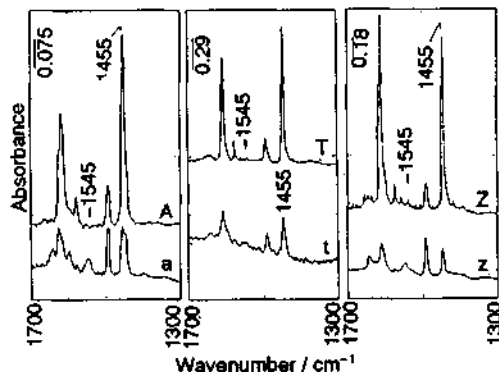
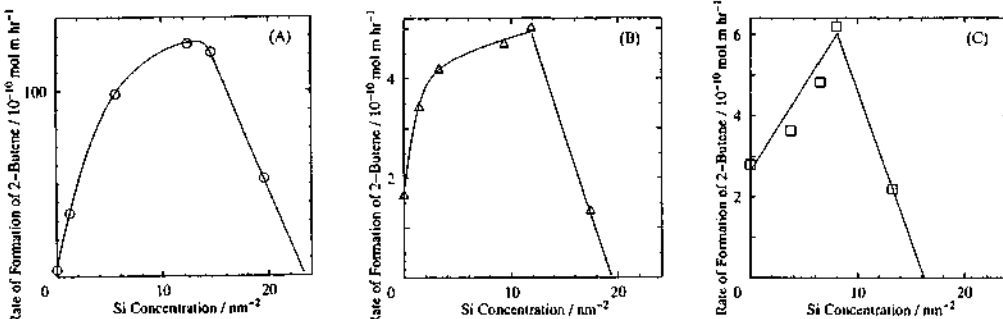


Fig. 4 : IR spectra of adsorbed pyridine on  $\text{Al}_2\text{O}_3$  (A),  $\text{TiO}_2$  (T) and  $\text{ZrO}_2$  (Z), and samples with  $15, 12$  and  $8 \text{ nm}^{-2}$  of Si (a, t and z, respectively) at  $373 \text{ K}$  and evacuated at  $423 \text{ K}$ .



**Fig. 5 : Activity for Isomerization of 1-butene over  $\text{Al}_2\text{O}_3$  (A, 393 K, 4 atm),  $\text{TiO}_2$  (B, 473 K, 1 atm) and  $\text{ZrO}_2$  (C, 503 K, 1 atm) dried at 673 K. Experiments were carried out under the differential conditions.**

**Table 1 : Comparison of activity over silica monolayer, silica gel and silica-alumina under the differential conditions.**

Catalyst	Concentration of Si $/\text{nm}^{-2}$	Rate per Surface Area / $10^{-10} \text{ mol m hr}^{-1}$ for Isomerization of 1-Butene Cracking of Cumene	
		393K (cis/trans)	623K
$\text{SiO}_2/\text{Al}_2\text{O}_3$	12	126 (1.9)	5.5
$\text{SiO}_2/\text{TiO}_2$	12	9.9 (1.2)	0.3
$\text{SiO}_2/\text{ZrO}_2$	8	1.5 (1.3)	0.2
$\text{SiO}_2$ (Silica gel)		0.1#(2.3)	0.1##
Silica-alumina##		183 (1.3)	89

# : N-602A, Nikki Kagaku Co. Ltd. ## : MB-4B, Fuji-Davidson Co. Ltd. ### : N-631L, Nikki Kagaku Co. Ltd.

For cracking of cumene, the activity increased with the deposition and showed the maximum at  $12 \text{ Si nm}^{-2}$  over  $\text{Al}_2\text{O}_3$ . However, Table 1 shows that the activity, even at the maximum, was much smaller than silica-alumina. Silica layers on  $\text{TiO}_2$  and  $\text{ZrO}_2$  showed almost no activity.

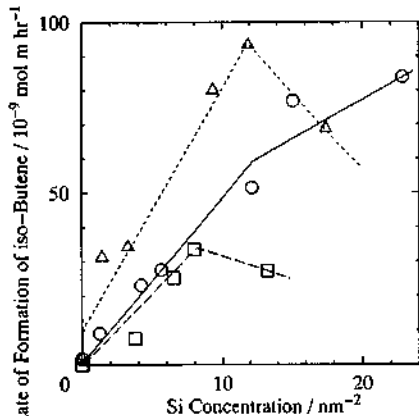
Fig. 6 shows the activity for dehydration of *tert*-butanol. The activity increased with the deposition and showed the maximum at  $8$  and  $12 \text{ Si nm}^{-2}$  over  $\text{ZrO}_2$  and  $\text{TiO}_2$ , respectively. The activity is estimated to completely disappear at the concentration of Si above  $30 \text{ nm}^{-2}$  from relationship between the activity and Si concentration. Over  $\text{Al}_2\text{O}_3$ , the activity continued to increase.

Fig. 7 shows the change of activity for dehydration of ethanol by the deposition. The activity monotonously decreased with the deposition over  $\text{TiO}_2$  and  $\text{ZrO}_2$ . Over  $\text{Al}_2\text{O}_3$ , the activity increased with a small amount of Si, showed the maximum at  $4 \text{ Si nm}^{-2}$  and decreased with further increase of Si over  $\text{Al}_2\text{O}_3$ .

## 4. DISCUSSION

### 4.1. Formation of Silica Monolayer

From the crystal structure, the cation density is estimated to be  $7$  and  $11 - 14 \text{ nm}^{-2}$  on  $\text{ZrO}_2$  and  $\text{TiO}_2$ , respectively. On  $\text{Al}_2\text{O}_3$ , the density of  $\text{Al}^{3+}$  was reported to be in  $9$  to  $14.5 \text{ nm}^{-2}$  [13]. The concentration of Si where the coverage reached at almost 100 %, i.e.  $8$ ,  $12$  and  $13 \text{ nm}^{-2}$  on  $\text{ZrO}_2$ ,



**Fig. 6 : Activity for dehydration of *tert*-butanol at 373 K over  $\text{Al}_2\text{O}_3$  (○),  $\text{TiO}_2$  (△) and  $\text{ZrO}_2$  (□) dried at 673 K. Experiments were carried out at 5 mg of catalyst and 10  $\mu\text{l}$  of *tert*-butanol on  $\text{Al}_2\text{O}_3$  and under the differential conditions on  $\text{TiO}_2$  and  $\text{ZrO}_2$ .**

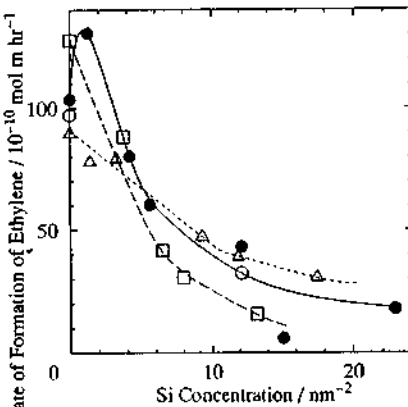


**Fig. 7 : Activity for dehydration of ethanol over  $\text{Al}_2\text{O}_3$  (● and ○, 523 K),  $\text{TiO}_2$  (△, 573 K) and  $\text{ZrO}_2$  (□, 543 K) under the differential conditions. Experiments were carried out after pretreatment at 573 K (●) and 673 K (○, △ and □).**

$\text{TiO}_2$  and  $\text{Al}_2\text{O}_3$ , respectively, corresponded to the cation density on the support oxide. Therefore, it is suggested that the Si atoms were deposited onto the surface like M-O-Si (M = surface cation of support), and the silica monolayer was thus formed. The homogeneous structure is indicated to be formed from the initial stage of deposition until it covers the surface because of the almost linear increase of the coverage against the concentration of Si. Isolated SiOH groups were observed in place of hydroxyl groups of the supports where the monolayer was estimated to cover the surface. From the high density of Si, Si-O-Si bond is presumed to be formed. Therefore, it is concluded that the silica monolayer, constructed by M-O-SiOH and Si-O-Si, covered the surface almost completely at 8, 12 and 13 Si nm<sup>-2</sup> on  $\text{ZrO}_2$ ,  $\text{TiO}_2$  and  $\text{Al}_2\text{O}_3$ , respectively.

#### 4.2. Generation of Weak Brønsted Acid Sites on Monolayer

Evidence for Brønsted acidity over the silica monolayer was shown by IR measurements of adsorbed ammonia, because ammonium cation appeared on the monolayer samples. Moreover, the activity for isomerization of *I*-butene was generated by the deposition. The maximum of the activity was observed at the concentration of Si where the monolayer covered the surface. The isomerization was suggested to proceed over the Brønsted acid sites, because the initial ratio of *cis*- / *trans*-2-butene was in the range between 1 to 2 over the monolayers. On these findings, it is concluded that the Brønsted acid sites are formed on the silica monolayers.

For cracking of cumene, the activity over monolayer prepared on  $\text{Al}_2\text{O}_3$  was much lower than silica-alumina, whereas the activity for the isomerization of *I*-butene over both catalysts was in the same order. The monolayers on other oxides showed almost no activity for the cracking. Because the cracking of cumene requires a strong Brønsted acid site [14], it is suggested that the Brønsted acid sites on the monolayers are so weak and thus active for only facile reactions such as the hydrogen transfer of olefin. The presence of only weak acid sites suggests a fine distribution of acid strength.

The monolayers showed activities also for dehydration of *tert*-butanol, in spite of the inactivity for dehydration of ethanol. The basicity of *tert*-butanol is stronger than ethanol because the substi-

tution of methyl groups in place of protons enhances the basicity [15]. This shows that only strong basic alcohol reacts on the monolayers; this supports that the acid strength of monolayer is low. The IR spectra of adsorbed pyridine showed a very small absorption band due to pyridinium cations on the monolayer samples. It is suggested that pyridine is not adsorbed on the Brønsted acid sites of monolayers because of the low strength.

The original active sites on the support, e.g. Lewis acid sites, are suggested to diminish with the deposition, because the activity for ethanol dehydration decreased. In addition to this, IR measurements showed that ammonia adsorbed on Lewis acid sites decreased with the deposition. IR spectra of adsorbed pyridine showed the disappearance of Lewis acidity also.

As described previously, the monolayers have M-O-SiOH (M = surface cation of the support). Protons of M-O-SiOH are suggested to possess acidity. The monolayer samples prepared on  $\text{Al}_2\text{O}_3$ ,  $\text{TiO}_2$  and  $\text{ZrO}_2$  was ca. 1000, 100 and 10 times more active for the isomerization of *l*-butene than silica gel, respectively. Therefore, the acid strength of M-O-SiOH is estimated as M = Al > Ti > Zr > Si (because  $\text{SiO}_2$  has Si-O-SiOH on the surface). The coordination number of cation is 6, 6, 8 and 4, and the valence is 3, 4, 4 and 4 in  $\text{Al}_2\text{O}_3$ ,  $\text{TiO}_2$ ,  $\text{ZrO}_2$  and  $\text{SiO}_2$ , respectively. These parameters did not affect the acid strength. Therefore, we suppose that the acidity is due to some interactions between M and Si, such as charge transfer or a strained structure of  $\text{SiO}_2$  by support. It is suggested that the monolayers possess a fine distribution of acid strength due to the homogeneous structure of M-O-SiOH.

The activity for isomerization of *l*-butene is estimated to disappear at twice the concentration of Si on the monolayer samples, 16, 20 and 24 Si nm<sup>-2</sup> on  $\text{ZrO}_2$ ,  $\text{TiO}_2$  and  $\text{Al}_2\text{O}_3$ , respectively. This indicates that "second-layer" was formed upon the monolayer and was inactive for the isomerization. However, the second-layers are suggested to possess the activity for dehydration of *tert*-butanol, because the activity continued to increase on  $\text{Al}_2\text{O}_3$  and was estimated to disappear at the concentration of Si above 30 nm<sup>-2</sup> on  $\text{TiO}_2$  and  $\text{ZrO}_2$ . Therefore, it is suggested that the second-layers possess the weak acidity compared to the monolayers; the dehydration proceeds even over such weak acid sites. It is assumed that the species M-O-Si-O-SiOH possesses acidity; the strength is lower than M-O-SiOH due to the longer distance between M and SiOH.

## References

- [1] C. L. Thomas, Ind. Eng. Chem., **1949**, 41, 2564
- [2] K. Tanabe, Catalysis, **1984**, 2, 231
- [3] M. Niwa, S. Kato, T. Hattori and Y. Murakami, J. Chem. Soc., Faraday Trans. 1, **1984**, 80, 3135
- [4] M. Niwa, T. Hibino, H. Murata, N. Katada and Y. Murakami, J. Chem. Soc., Chem. Commun., **1989**, 289
- [5] M. Niwa, N. Katada and Y. Murakami, J. Phys. Chem., **1990**, 94, 6441
- [6] M. Niwa, N. Katada and Y. Murakami, J. Catal., **1992**, 134, 340
- [7] T. Jin, T. Okuhara and J. M. White, J. Chem. Soc., Chem. Commun., **1987**, 1248
- [8] Y. Imizu, Y. Tada, K. Tanaka and I. Toyoshima, Shokubai, **1988**, 30, 525
- [9] S. Sato, M. Toita, Y. Yu-Qing, T. Sodesawa and F. Nozaki, Chem. Lett., **1987**, 1535
- [10] B. -Q. Xu, T. Yamaguchi and K. Tanabe, Chem. Lett., **1989**, 149
- [11] M. Niwa, S. Inagaki and Y. Murakami, J. Phys. Chem., **1985**, 89, 3869
- [12] M. Niwa, K. Suzuki, M. Kishida and Y. Murakami, Appl. Catal., **1991**, 67, 297
- [13] H. Knötinger and P. Ratnasamy, Catal. Rev. - Sci. Eng., **1978**, 17, 31
- [14] A. Corma and B. W. Wojciechowski, Catal. Rev. - Sci. Eng., **1982**, 24, 1
- [15] E. L. Mackor, A. Hofstra and J. H. Van der Waals, Trans. Faraday Soc., **1958**, 54, 186

### 3.17 Preparation of Silica-Deposited Alumina Catalyst by Utilizing Organosilicon Complexes as Building Blocks for the Synthesis of Acidic Sites

Y. Imizu,<sup>\*a</sup> K. Takahara,<sup>a</sup> N. Okazaki,<sup>b</sup> H. Itoh,<sup>a</sup> A. Tada<sup>b</sup>,  
R. Ohnishi,<sup>c</sup> and M. Ichikawa<sup>c</sup>

<sup>a</sup>Department of Materials Science, Kitami Institute of Technology, Kitami, Hokkaido 090, Japan

<sup>b</sup>Department of Applied and Environmental Chemistry, Kitami Institute of Technology, Kitami, Hokkaido 090, Japan

<sup>c</sup>Catalysis Research Center, Hokkaido University, Sapporo 060, Japan

#### Abstract

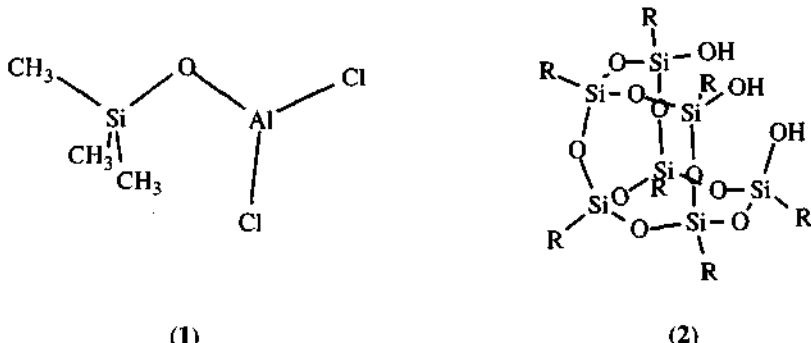
To elucidate the structural details of the interface and its catalytic properties of silica-alumina, we prepared three types of silica-alumina catalysts employing trimethylsiloxyaluminundichloride ( $(CH_3)_3SiOAlCl_2$ ) **1**, polyhedral oligosilsesquioxane ( $(c-C_5H_9)_7Si_7O_9(OH)_3$ ) **2**, and  $CH_3Si(OCH_3)_3$ . The simultaneous silica and alumina-deposited catalysts derived from **1** exhibited high activity for cyclopropane isomerization but not for 1-butene isomerization. The results of the variation of activity for ethanol dehydration on silica and alumina-deposited catalysts suggested that the deposited  $AlO_x$  is also active for ethanol dehydration. The silica cluster-deposited alumina catalysts derived from **2** exhibited high activity for 1-butene isomerization upon deposition of a small amount of silica, indicating that the active sites for the 1-butene isomerization were formed more efficiently than those formed on the silica-deposited alumina derived from  $CH_3Si(OCH_3)_3$ . The nature of active sites on the several types of silica-alumina for these reaction are discussed in terms of the structure of deposited silica.

#### 1. INTRODUCTION

Mixed oxides such as silica-alumina often exhibit stronger acidity than that of each component. Although largely because of its amorphous structure, definite picture of the acidic sites of silica-alumina has not been established, the acidic sites are believed to exist in a newly formed oxide phase or at the interface between the two component oxides.[1] Our laboratory has focused primarily upon preparation of acidic sites of mixed oxides by synthetic methods using organometallic complexes. Most recently we have reported that the deposition of silica submonolayer on alumina by CVD method using  $CH_3Si(OCH_3)_3$  resulted in the generation of Brönsted acid sites.[2] Moreover, we have found that upon deposition of proper amounts of silica, the catalyst became very active for the isomerization of olefins,[3] suggesting that Si-O-Al linkages at the interface between silica and the alumina substrate are involved in the active sites.

To elucidate the structural details of the interface and its catalytic properties, we prepared two types of silica-deposited alumina catalysts employing trimethylsiloxyaluminundichloride ( $(CH_3)_3SiOAlCl_2$ ) **1** and polyhedral oligosilsesquioxane ( $(c-C_5H_9)_7Si_7O_9(OH)_3$ ) **2**.[4] The adsorption of **1** containing Si-O-Al bond on alumina followed by thermal decomposition and oxidation with  $O_2$  results in simultaneous deposition of both silica and alumina on the substrate and homogeneous dispersion of two components into mixed oxide thin layer (denoted as  $SiO_x \cdot AlO_x/Al_2O_3$  hereinafter). Trisilanol **2** possessing the unique

coordinating ability of the sterically demanding tridentate ligand, in which three hydroxyl group are arranged with the similar manner as observed on (111) octahedral face of the cristobalite modification of  $\text{SiO}_2$ .[4] provides a model for silica aggregate formed on the silica-deposited alumina surfaces. We have found that even though deposition of a small amounts of silica, the trisilanol-derived silica-deposited alumina exhibited remarkably high catalytic activity for 1-butene isomerization.[5] In the present study, we examine the catalytic properties of three types of silica-deposited alumina to explore the nature of active sites for isomerization of olefins.



## 2. EXPERIMENTAL METHODS

### 2.1 Catalyst Preparation

All preparative procedures were performed in Schlenk-type glassware interfaced to a vacuum line under an argon atmosphere. Various types of silica-deposited alumina catalysts were prepared by adsorption of organosilicon complexes on  $\text{Al}_2\text{O}_3$  (JRC-ALO4) at 298 K, followed by thermal decomposition and oxidation with  $\text{O}_2$  at 773 K.  $(\text{CH}_3)_3\text{SiOAlCl}_2$  was obtained by a reaction of  $(\text{CH}_3)_3\text{SiOSi}(\text{CH}_3)_3$  with  $\text{AlCl}_3$  at 313 K and purified by sublimation. The adsorption of  $(\text{CH}_3)_3\text{SiOAlCl}_2$  was carried out by vaporizing solid  $(\text{CH}_3)_3\text{SiOAlCl}_2$  at 423 K. Silsesquioxane (trisilanol) 2 was prepared by the heptameric hydrolytic condensation of cyclopentyltrichlorosilane ( $c\text{-C}_5\text{H}_9\text{SiCl}_3$ ) in aqueous acetone [4b] and was deposited from  $\text{CH}_2\text{Cl}_2$  solution, followed by removing the solvent in vacuo for the subsequent pretreatment. The resulting catalyst was denoted as  $\text{Si}_7\text{O}_{19}/\text{Al}_2\text{O}_3$  hereinafter. Preparation of  $\text{CH}_3\text{Si}(\text{OCH}_3)_3$ -derived silica-deposited  $\text{Al}_2\text{O}_3$  catalysts (denoted as  $\text{SiO}_X/\text{Al}_2\text{O}_3$  hereinafter) was previously described.[2]

### 2.2 Reaction Procedure

Prior to a reaction, the catalyst (0.05–0.2 g) was outgassed at 773 K for 3 h. All reactions including dehydration of ethanol, isomerization of 1-butene and cyclopropane were carried out in a recirculation reactor with a volume of about  $580 \text{ cm}^3$ . Products were withdrawn periodically from the system for gas chromatographic analysis.

## 3. RESULTS AND DISCUSSION

### 3.1 Catalytic Activity of $\text{SiO}_X\text{-AlO}_X/\text{Al}_2\text{O}_3$

The catalytic activities of  $\text{SiO}_X\text{-AlO}_X/\text{Al}_2\text{O}_3$  were compared with that of  $\text{SiO}_X/\text{Al}_2\text{O}_3$  [3] as shown in Figure 1A and 1B. The deposition of  $\text{SiO}_X$  remarkably increased the activities of  $\text{Al}_2\text{O}_3$  for the isomerization of 1-butene and cyclopropane. The maximum activities were much higher than that of commercial silica-alumina catalysts. On the contrary, the simultaneous deposition of both  $\text{SiO}_X$  and  $\text{AlO}_X$  did not show significant effect on the activity for 1-butene isomerization and the catalysts were only active for cyclopropane isomerization. IR spectroscopic studies of adsorbed pyridine on  $\text{SiO}_X\text{-AlO}_X/\text{Al}_2\text{O}_3$

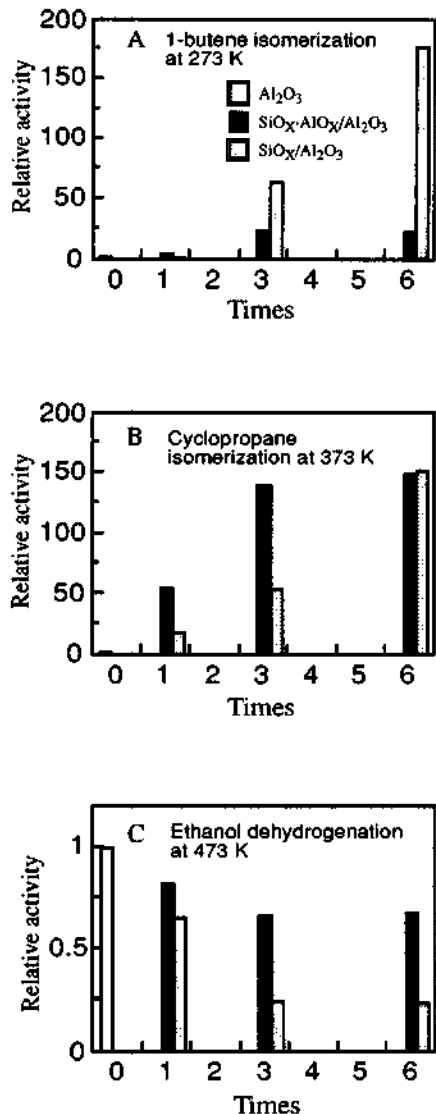


Figure 1. Catalytic activities of various silica-deposited alumina catalysts as a function of deposition times.

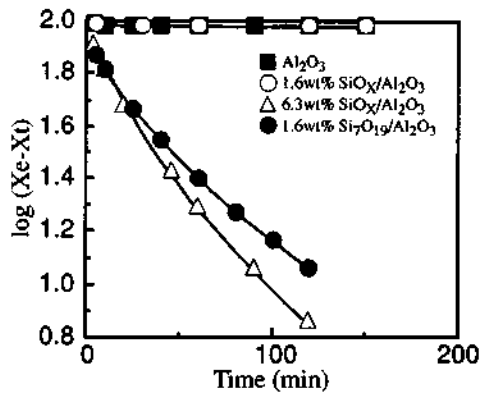


Figure 2. First-order plots for 1-butene isomerization at 273 K over  $\text{SiO}_X/\text{Al}_2\text{O}_3$ ,  $\text{Si}_7\text{O}_{19}/\text{Al}_2\text{O}_3$  and  $\text{Al}_2\text{O}_3$ .

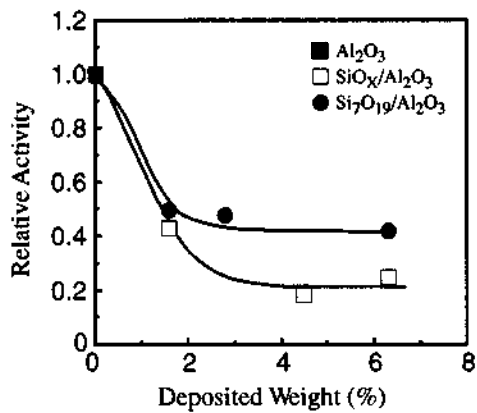


Figure 3. Ethanol dehydrogenation activity of silica-deposited alumina catalysts as a function of deposition weight.

showed the generation of Brönsted acid sites as observed on  $\text{SiO}_x/\text{Al}_2\text{O}_3$ .[2] These results indicate that Brönsted acid sites generated on  $\text{SiO}_x\text{-}\text{AlO}_x/\text{Al}_2\text{O}_3$  are effective for cyclopropane isomerization but not for 1-butene isomerization, suggesting that the exposed alumina substrate as well as the newly formed Brönsted acid sites are involved in the active sites for 1-butene isomerization. Ethanol on  $\text{Al}_2\text{O}_3$  surface undergoes dehydration to give diethylether at around 473 K. Since the diethylether is formed by the recombination of surface ethoxide on  $\text{Al}_2\text{O}_3$ , deposited  $\text{SiO}_x$  is expected to acts as a site-blocking agent. Upon deposition of  $\text{SiO}_x$ , the activities decreased about one third, indicating that the active sites for ethanol dehydration were site-blocked with  $\text{SiO}_x$ . On the other hand, simultaneous deposition of both  $\text{SiO}_x$  and  $\text{AlO}_x$  slightly decreased the activities (Figure 1C). This result suggests that the deposited  $\text{AlO}_x$  is also active for ethanol dehydration.

### 3.2 Catalytic Activity of $\text{Si}_7\text{O}_{19}/\text{Al}_2\text{O}_3$

Figure 2 shows first-order plots for 1-butene isomerization on  $\text{Si}_7\text{O}_{19}/\text{Al}_2\text{O}_3$  compared with that of  $\text{SiO}_x/\text{Al}_2\text{O}_3$ . The most remarkable feature is the increase in the activity of alumina when a small amount of silica was deposited from trisilanol **2**. Indeed, 1.6 wt% of silica increased the activity by a factor of about 200. We previously reported that the similar increase in activity for 1-butene isomerization was observed on  $\text{SiO}_x/\text{Al}_2\text{O}_3$  when 6.3 wt% of silica was deposited from  $\text{CH}_3\text{Si}(\text{OCH}_3)_3$ .[3] These results clearly indicate that the active sites for the isomerization of 1-butene were formed on  $\text{Si}_7\text{O}_{19}/\text{Al}_2\text{O}_3$  more efficiently by deposition of smaller amount of silica than that deposited on  $\text{SiO}_x/\text{Al}_2\text{O}_3$  by a factor of about 1/4.

Figure 3 shows ethanol dehydration activity of silica-deposited alumina as a function of deposition weight.  $\text{SiO}_x/\text{Al}_2\text{O}_3$  displayed more significant decrease in activity than  $\text{Si}_7\text{O}_{19}/\text{Al}_2\text{O}_3$ , suggesting that these alteration is due to the lower dispersion compared with that of  $\text{SiO}_x$  deposited using  $\text{CH}_3\text{Si}(\text{OCH}_3)_3$ . Moreover,  $\text{Si}_7\text{O}_{19}/\text{Al}_2\text{O}_3$  exhibited dehydrogenation activity to yield acetaldehyde from ethanol. Although the dehydrogenation process on  $\text{Si}_7\text{O}_{19}/\text{Al}_2\text{O}_3$  could not proceed catalytically, only one report that silica showed the activity for ethanol dehydrogenation has been described.[6] It was observed that silica dehydrated above 1000 K brought about ethanol dehydrogenation to form acetaldehyde and suggested that a distorted Si-O-Si oxygen bridge formed at high temperature was involved in the active sites. Trisilanol **2** has the similar Si-O-Si linkages in the polyhedral framework, suggesting that upon deposition the framework of **2** remains almost unchanged and active sites for the dehydrogenation are formed on  $\text{Si}_7\text{O}_{19}/\text{Al}_2\text{O}_3$ .

It is interesting to speculate on the structure of  $\text{Si}_7\text{O}_{19}/\text{Al}_2\text{O}_3$ . The precursor trisilanol **2** possesses bulky seven cyclopentyl groups attached to Si atoms at seven corners. Upon deposition, three hydroxyl groups of the trisilanol were probably adsorbed on  $\text{Al}_2\text{O}_3$  surface, since hydrophobic interaction between cyclopentyl groups and the oxide surface should not prefer at the opposite way (the face to which the hydroxyl groups are not coordinated). These unique structural characteristics of the precursor could be responsible for the generation of acidic sites on  $\text{Si}_7\text{O}_{19}/\text{Al}_2\text{O}_3$  and the formation of the active sites for 1-butene isomerization.

## 4. REFERENCES

1. K. Tanabe, M. Misono, Y. Ono, and H. Hattori, "New Solid Acid Bases", Kodansha, 1989, p. 108.
2. Y. Imizu and A. Tada, "Proc. Inter. Symp. Acid-Base Catalysis", K. Tanabe, H. Hattori, T. Yamaguchi, T. Tanaka, eds., Kodansha, 1989, p. 281.
3. Y. Imizu and A. Tada, *Chem. Lett.*, 1989, 1793.
4. a) F. J. Feher, D. A. Newman, J. F. Walzer, *J. Am. Chem. Soc.*, 1989, 111, 1741 and  
b) F. J. Feher, T. A. Budzichowski, R. L. Blanski, K. J. Weller, J. W. Ziller, *Organometallics*, 1991, 10, 2526.
5. Y. Imizu, K. Takahara, H. Itoh, and A. Tada, manuscript in preparation.
6. Y. Matsumura, K. Hashimoto, S. Yoshida, *J. Catal.*, 1989, 117, 135.

### **3.18 Activity Enhancement of $\text{Me}^{n+}/\text{SiO}_2$ Catalysts by Sulfiding with Hydrogen Sulfide for Acid-Catalyzed Reactions**

Masatoshi Sugioka, Nobuyuki Sato and Daisuke Uchida  
Department of Applied Chemistry, Muroran Institute of Technology, 27-1 Mizumoto-cho, Muroran 050, Japan

#### **Abstract**

The effect of sulfiding with hydrogen sulfide on the catalytic activity of metal ions supported on silica gel ( $\text{Me}^{n+}/\text{SiO}_2$ ) for the isomerization of 1-butene and cyclopropane was investigated. It was revealed that the catalytic activity of some kind of  $\text{Me}^{n+}/\text{SiO}_2$  was remarkably enhanced by sulfiding with hydrogen sulfide for these acid-catalyzed reactions.

#### **1. INTRODUCTION**

In the previous paper[1-3], we showed that the catalytic activities of some kind of metal ion exchanged zeolites ( $\text{MeZ}$ ) for various acid-catalyzed reactions were remarkably enhanced by sulfiding with hydrogen sulfide. In the present work, we studied the effect of sulfiding with hydrogen sulfide on the catalytic activity of various  $\text{Me}^{n+}/\text{SiO}_2$  for the isomerization of 1-butene and cyclopropane. We also discussed the mechanism of formation of the acidic sites on  $\text{Me}^{n+}/\text{SiO}_2$  surface by sulfiding.

#### **2. EXPERIMENTAL METHODS**

The isomerization of 1-butene(25°C) and cyclopropane(150°C) over  $\text{Me}^{n+}/\text{SiO}_2$  with and without sulfiding were carried out by use of a conventional closed circulating reactor system with 40 Torr of initial pressure of both reactants. Reaction products in these catalytic reactions were analyzed on a gaschromatograph. A 0.05g of  $\text{Me}^{n+}/\text{SiO}_2$  were used after evacuation at 500°C for 2hr.

$\text{Me}^{++}/\text{SiO}_2$  were prepared by ion-exchange method with metal chloride(except  $\text{Ag}^+$ ) aqueous solutions.  $\text{Me}^{++}/\text{SiO}_2$  were sulfided at various temperatures by 40 Torr of hydrogen sulfide.

### 3. RESULTS AND DISCUSSION

Fig.1 shows the isomerization of 1-butene over  $\text{Ag}^+/\text{SiO}_2$  before and after sulfiding. It was found that the catalytic activity of  $\text{Ag}^+/\text{SiO}_2$  before sulfiding for the isomerization of 1-butene was very low, but its catalytic activity was remarkably enhanced by sulfiding with hydrogen sulfide at 300°C. A cis/trans ratio in the formed 2-butenes was almost equal to one, indicating that the active site of sulfided  $\text{Me}^{++}/\text{SiO}_2$  catalysts is the Brönsted acid site.

Table 1 shows the catalytic activities of various  $\text{Me}^{++}/\text{SiO}_2$  before and after sulfiding in the isomerization of 1-butene and cyclopropane.  $\text{Me}^{++}/\text{SiO}_2$  before sulfiding showed low activities except  $\text{Ni}^{2+}/\text{SiO}_2$  in both reactions. However, the catalytic activities of some kind of  $\text{Me}^{++}/\text{SiO}_2$  such as  $\text{Ag}^+/\text{SiO}_2$ ,  $\text{Cu}^{2+}/\text{SiO}_2$ ,  $\text{Cd}^{2+}/\text{SiO}_2$  were enhanced by sulfiding at 300°C. Especially, the catalytic activity of  $\text{Ag}^+/\text{SiO}_2$  was markedly increased by sulfiding about thirteen times for the isomerization of 1-butene and about twenty six times for cyclopropane.

It can be assumed that high activity of sulfided  $\text{Me}^{++}/\text{SiO}_2$  might be attributed to the increase of the Brönsted acidity of  $\text{Me}^{++}/\text{SiO}_2$  by sulfiding with hydrogen sulfide.

Fig.2 shows the relationship between the enthalpy changes( $\Delta H^\circ$ ) of formation of various metal sulfides and the catalytic activity of sulfided  $\text{Me}^{++}/\text{SiO}_2$  in the isomerization of

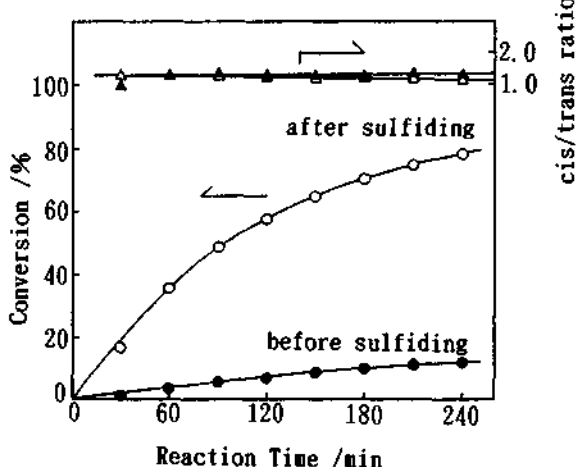


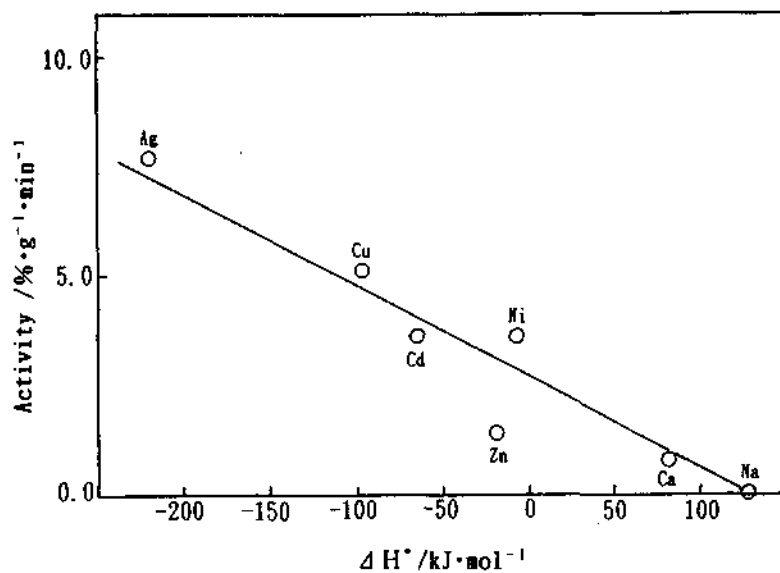
Fig.1 Isomerization of 1-butene over  $\text{Ag}^+/\text{SiO}_2$  at 25°C.  
 $\text{Ag}^+/\text{SiO}_2$  was sulfided at 300°C.  
●,▲ : before sulfiding  
○,△ : after sulfiding

**Table 1** Effect of sulfiding on the catalytic activity of various  $\text{Me}^{n+}/\text{SiO}_2$  in the isomerization of 1-butene and cyclopropane.

Catalysts supported(wt%)* $\times 10^2$	Amount of metal ion supported(wt%)* $\times 10^2$	Activity(%/g·min)				$A_1/A_0^{(1)}$	
		Before sulfiding( $A_0$ )		After sulfiding( $A_1$ ) <sup>(2)</sup>			
		1-butene	c-propane	1-butene	c-propane		
$\text{Ag}^{+}/\text{SiO}_2$	8.7	0.9	0.3	11.9	7.7	13.2	
$\text{Cu}^{2+}/\text{SiO}_2$	4.8	0.9	0.8	10.2	5.1	11.3	
$\text{Cd}^{2+}/\text{SiO}_2$	13.5	2.3	1.7	6.5	3.6	2.8	
$\text{Ni}^{2+}/\text{SiO}_2$	6.6	18.5	3.2	7.0	3.6	0.4	
$\text{Co}^{2+}/\text{SiO}_2$	5.4	4.4	2.6	7.0	3.9	1.6	
$\text{Mg}^{2+}/\text{SiO}_2$	3.7	3.0	1.8	2.7	1.6	0.9	
$\text{Zn}^{2+}/\text{SiO}_2$	1.9	2.2	1.2	2.5	1.4	1.1	
$\text{Ca}^{2+}/\text{SiO}_2$	1.6	2.0	1.1	1.7	0.8	0.9	
$\text{Na}^{+}/\text{SiO}_2$	4.8	0.0	0.0	0.0	0.0	—	
$\text{SiO}_2$	0.0	0.0	0.3	0.0	0.3	—	
HNaY	79.4 <sup>(3)</sup>	6.1	20.0	—	—	—	

1)  $\text{Me}^{n+}/\text{SiO}_2$  were sulfided at 300°C. 2) Ratio of activity increase

3) % -Ion exchange

**Fig. 2** Relationship between the enthalpy changes ( $\Delta H^\circ$ ) of formation of various metal sulfides and the catalytic activity of  $\text{Me}^{n+}/\text{SiO}_2$  in the isomerization of cyclopropane. $\text{Me}^{n+}/\text{SiO}_2$  were sulfided at 300°C.

cyclopropane. It was found that there existed a linear relationship between the enthalpy changes ( $\Delta H^\circ$ ) of formation of metal sulfides and the activity of sulfided  $M^{n+}/SiO_2$  catalysts. This indicates that the facility of the formation of metal sulfides in  $M^{n+}/SiO_2$  by sulfiding is an important factor for the enhancement of catalytic activity of  $M^{n+}/SiO_2$  by sulfiding treatment.

Fig.3 shows the effect of sulfiding temperature on the catalytic activity of  $M^{n+}/SiO_2$  in the isomerization of 1-butene and cyclopropane. It was found that the catalytic activity of sulfided  $M^{n+}/SiO_2$  depended strongly on the sulfiding temperature. In the case of the isomerization of 1-butene, the catalytic activity of  $M^{n+}/SiO_2$  attained maximum at around 300°C and decreased above 300°C.

On the other hand, in the isomerization of cyclopropane, the catalytic activity of  $M^{n+}/SiO_2$  was almost constant up to 300°C, and then decreased above 300°C. These indicate that the amount of newly formed Brönsted acid sites on  $M^{n+}/SiO_2$  by sulfiding decreased above 300°C.

In the previous papers[1-3], we proposed the mechanism for the formation of new Brönsted acid sites on  $M^{n+}/SiO_2$  by sulfiding with hydrogen sulfide, in which metal sulfide species and acidic hydroxyl groups were formed on  $M^{n+}/SiO_2$  surface by sulfiding. Thus, we assumed that the mechanism for the formation of Brönsted acid sites on sulfided  $M^{n+}/SiO_2$  is similar to the case of sulfided  $M^{n+}/ZrO_2$  as shown in scheme 1. That is to say, the surface of silica gel is supposed to be covered by neutral or very weak acidic hydroxyl groups as shown in step(I). After  $SiO_2$  is treated by metal ion salt aqueous solutions, a part of

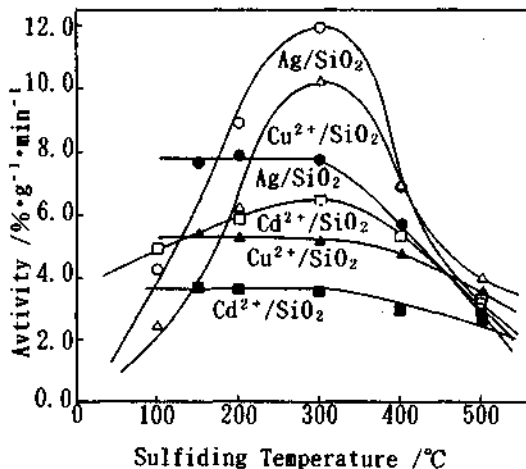
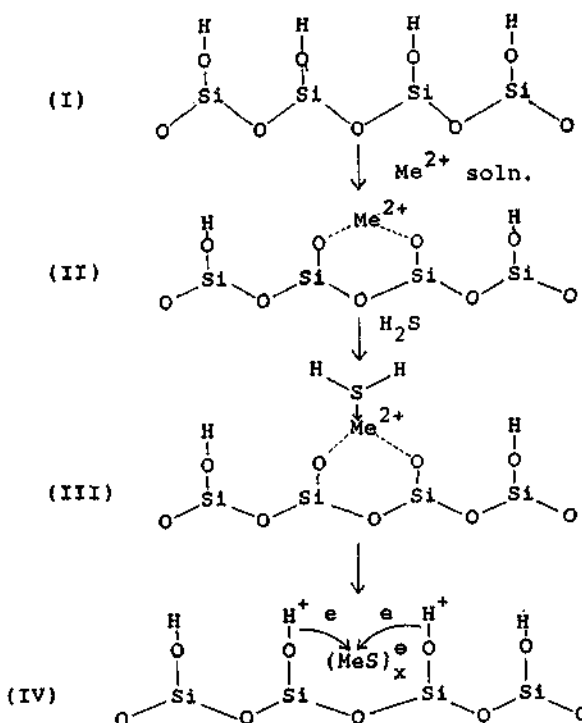


Fig.3 Effect of sulfiding temperature on the catalytic activity of various  $M^{n+}/SiO_2$  for the isomerization of 1-butene and cyclopropane.

○,△,□ : 1-butene  
●,▲,■ : cyclopropane



Scheme 1 A possible mechanism for the formation of new Brønsted acid sites on  $\text{Me}^{n+}/\text{SiO}_2$  by sulfiding with hydrogen sulfide.

surface hydroxyl groups on  $\text{SiO}_2$  are ion-exchanged with metal ions (step (II)). When hydrogen sulfide is introduced on  $\text{Me}^{n+}/\text{SiO}_2$ , metal sulfide is formed and surface hydroxyl groups is regenerated as shown in step (III) and (IV). It is assumed that the regenerated surface hydroxyl groups is strongly affected by the metal sulfide species and the hydrogen atoms of surface hydroxyl group are changed into protons by the electron attractive action of metal sulfide species as shown in step (IV).

Therefore, it is concluded that the enhancement of catalytic activities of some kind of  $\text{Me}^{n+}/\text{SiO}_2$  after sulfiding is attributed to the transformation of neutral hydroxyl groups into the

Brönsted acid site by the inductive effect of metal sulfide species as shown in scheme 1.

#### 4. CONCLUSION

The catalytic activity of some kind of  $\text{Me}^{++}/\text{SiO}_2$  were remarkably enhanced by sulfiding with hydrogen sulfide in the isomerization of 1-butene and cyclopropane. We concluded that new Brönsted acid site are formed on sulfided  $\text{Me}^{++}/\text{SiO}_2$  by the inductive effect of metal sulfide species.

It was revealed that there is a possibility to convert low acidic  $\text{Me}^{++}/\text{SiO}_2$  into high acidic catalysts by sulfiding with hydrogen sulfide.

#### 5. REFERENCES

- [1] M.Sugioka, Hyōmen(Surface), 1987, 25, 522.
- [2] M.Sugioka, S.Nakayama, T.Kanazuka, T.Hosotsubo, Proc. of Intern. Symp. on Acid-Base Catal. (Sapporo), 1988, 305.
- [3] M.Sugioka, N.Sato and D.Uchida, Proceedings of 9th International Zeolite Conference (Montreal), 1992, 493.

## 3.19 Preparation of Basic Zeolite

F. Yagi, N. Kanuka, H. Tsuji, H. Kita and H. Hattori

Graduate School of Environmental Earth Science, Hokkaido University, Sapporo 060, Japan

### Abstract

Zeolites containing cesium oxide in the cavities were prepared under different conditions to establish the preparative conditions under which the crystalline structures are retained. The types of cesium salt used as ion-exchange and impregnation solution did not affect much the crystallinities of the resulting materials. The most important factor in terms of the retention of the crystalline structure of the resulting zeolites was the presence of water vapor during calcination. In the presence of water vapor, the zeolite structures collapsed at relatively low temperatures. On the bases of  $^{29}\text{Si}$  and  $^{27}\text{Al}$  MAS NMR, it was suggested that the collapse of the zeolite structures occurs by breaking of Si-O-Si bonds rather than Al-O-Al bonds for K ion-exchanged zeolite.

### 1. INTRODUCTION

Alkali cation-exchanged zeolites exhibit basic properties and promote a number of base-catalyzed reactions[1-2]. The basic sites of the alkali cation-exchanged zeolites, however, are relatively weak, and the zeolites possessing strong basic sites are desired to be prepared. Hathaway and Davis reported that introduction of excess alkalis in the zeolite cavities resulted in an increase in the activity for base-catalyzed reactions such as dehydrogenation of 2-propanol and side chain alkylation of toluene with methanol[3-4]. They suggested that the catalytically active basic sites are alkali metal oxides encapsulated in the zeolite cavities[5]. Recently, Rodriguez et al. prepared basic zeolites by *in situ* formation of cesium oxide in the cavities[6-7]. The zeolites containing alkalis in excess of the ion-exchanged capacities show strongly basic properties. The zeolites of strongly basic properties are expected to show shape selective catalysis in base-catalyzed reactions.

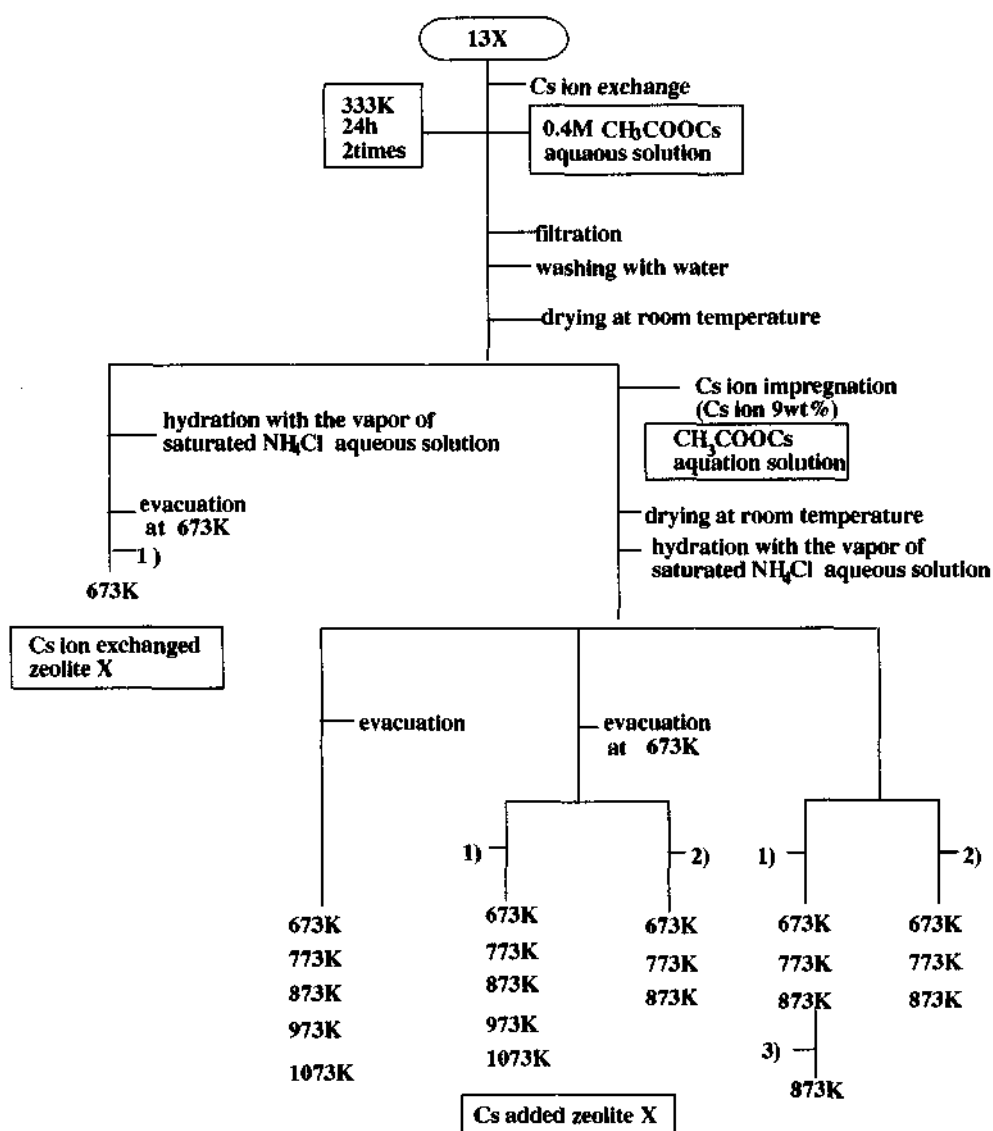
During the preparative procedures for basic zeolites, a loss of crystallinity of the zeolite framework occurs. It is not certain in which steps in the preparative procedures the zeolite frameworks collapse. The present study aims to establish the preparative methods for strongly basic zeolites. The zeolites containing excess alkali cations were prepared by changing the preparative parameters such as type of alkali salt, type of zeolite, heat-treatment temperature, pressure of water vapor in heat-treatment, etc. to clarify what factors affect the collapse of the zeolite structures during preparation. The resulting zeolites were subjected to XRD measurements and surface area measurement. For selected samples, the local structure was examined by  $^{29}\text{Si}$  and  $^{27}\text{Al}$  MAS NMR.

### 2. EXPERIMENTAL METHODS

#### 2.1. Sample Preparation

Zeolites of X, Y, and ZSM-5 containing Na ion as an exchangeable cation were used as starting materials. X type zeolite was Linde molecular sieves 13X ( $\text{Si}/\text{Al}=1.2$ ) in a powder form. Y type zeolite was supplied from the Catalyst Society of Japan (JRC-Z-1,  $\text{Si}/\text{Al}=2.4$ ). ZSM-5 was supplied from Tohsoh Co. ( $\text{Si}/\text{Al}=47.6$ ).

The preparative procedures are shown in Scheme 1. Zeolite was soaked in 0.4mol/l aqueous solution of Cs salt at 0.02g-zeolite/ml-soln and stirred for 24h at 333K. As Cs salts,  $\text{CH}_3\text{COOCs}$ ,  $\text{CsOH}$ , and  $\text{CsNO}_3$  were used. The pH's of these solutions were 6.5, 13.6, and 6.3, respectively.



Scheme 1 Preparative procedures of Cs ion exchanged and Cs added zeolite X

- 1) Calcination in dry oxygen
- 2) Calcination in air
- 3) Exposure to water vapor(12Torr) at 873K

The ion-exchange was proceeded two times. After the ion-exchange, the sample was filtered and washed with deionized water. For Cs ion-added zeolites which contain Cs ion in excess of the ion-exchange capacities, the ion-exchanged zeolite was impregnated with aqueous solutions of Cs salts. The Cs content except ion-exchanged Cs was adjusted to be 9wt% Cs ion. The sample was then dried in a vacuum dessicator at room temperature. The dried sample was rehydrated by exposure to water vapor of the saturated NH<sub>4</sub>Cl aqueous solution to keep the hydration state constant before further heat-treatment. The rehydrated sample was heat-treated at different temperatures under different conditions; evacuation, calcination in dry oxygen, evacuation at 673K followed by calcination in dry oxygen, calcination in air, and evacuation at 673K followed by calcination in air. For one case, the sample was calcined in dry oxygen at 873K followed by exposure to water vapor(12Torr) at the same temperature.

For MAS NMR measurements, K ion-exchanged and K ion-added X were prepared. Linde 13X was soaked in 0.5 mol/l aqueous solution of CH<sub>3</sub>COOK at 0.02g zeolite/ml-soln at 333K. On completion of five times exchange, the sample was divided into two parts. One part was filtered and left unwashed, and the other part filtrered and washed. The former part is K ion-added X and the latter part is K ion-exchanged X. Each part of the sample was dried in a vacuum dessicator at room temperature and calcined in dry oxygen at 773K. One ion-exchanged sample was also calcined in air at 773K to obtain the sample whose structure was collapsed.

## 2.2. Surface Area and XRD Measurements

X-Ray diffraction patterns of the samples were recorded on a RIGAKU RINT 2000 diffractometer using CuK $\alpha$  radiation. All the measurements were performed at the range of  $2\theta=5^\circ\sim65^\circ$ . The surface areas of the zeolites were calculated by applying the adsorption isotherm of nitrogen at 77K to Langmuir equation.

## 2.3. NMR

High-resolution solid-state NMR spectra were recorded at room temperature with magic angle spinning(MAS) on a Fourier transform pulsed NMR spectrometer (BRUKER MSL-200) equipped with a CP/MAS unit. <sup>27</sup>Al MAS NMR spectra were taken at 70.4MHz with high power decoupling. The typical cycle time was 1s and typical 90° pulse width was 4.0μs. <sup>27</sup>Al chemical shifts were referenced to (Al(H<sub>2</sub>O)<sub>6</sub>)<sup>3+</sup>. <sup>29</sup>Si MAS NMR spectra were taken at 39.8MHz with high power decoupling. The typical cycle time was 7.0s and the typical 90° pulse width was 4.0μs. <sup>29</sup>Si chemical shifts were referenced to Q8M8.

## 3.RESULTS AND DISCUSSION

### 3.1.Influence of Heat-treatment Atmosphere

The surface areas of the Cs added zeolite X heat-treated under different conditions are given in Fig.1. When the sample was heat-treated in a vacuum, the surface area kept constant up to 973K. Further increase in the temperature markedly decreased the surface area. For the sample pre-evacuated at 673K and calcined in dry oxygen, the surface area was constant up to 873K, and slightly decreased on calcination at 973K. Pre-evacuation at 673K did not make significant difference in the surface area. Calcination in air resulted in the surface area decrease at low temperatures. The surface area began to decrease when calcined at 773K, and decreased to about 30% original one when calcined at 873K. The sample calcined in dry oxygen at 873K possessed original surface area but the surface area decreased to about 30% original value when exposed to water vapor(12Torr) at 873K.

X-Ray diffraction patterns for Cs added zeolite X gave us the same information as the surface area measurements. The samples possessing surface areas about 390m<sup>2</sup>g<sup>-1</sup> showed intense diffraction peaks, while the sample calcined in air at 873K, or exposure to water vapor at 873K showed weak and broad peaks.

These results indicate that the crystalline structures of the Cs ion-exchanged or Cs ion-added zeolite X are retained after the heat-treatment at 973K as far as the sample is kept from contact with water vapor. Exposure to water vapor at high temperatures facilitates the collapse of the crystalline structure.

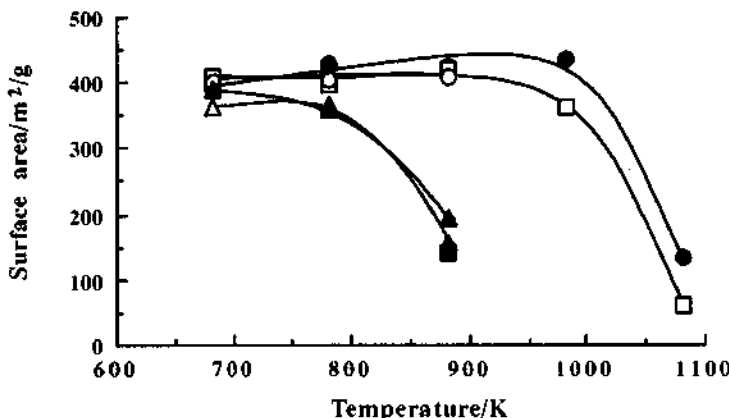


Fig. 1 Surface area of Cs added zeolite X.

- Evacuation ○ Calcination in dry oxygen ▲ Calcination in air
- Evacuation at 673K followed by calcination in dry oxygen
- △ Evacuation at 673K followed by calcination in air
- Evacuation at 673K followed by calcination in dry oxygen at 873K and exposed to water vapor(12Torr) at 873K

Table 1 Surface area of zeolites prepared with  $\text{CH}_3\text{COOCs}$ 

Zeolites	Treatment <sup>1)</sup>	Surface area / $\text{m}^2 \cdot \text{g}^{-1}$
NaX		750
Cs ion exchanged X	a)	540
Cs added X	a)	390
NaY		820
Cs ion exchanged Y	a)	630
Cs added Y	a)	460
NaZSM-5		420
Cs ion exchanged ZSM-5	a)	330
Cs added ZSM-5	a)	90

1) a) Evacuation at 673K followed by calcination in dry oxygen at 673K

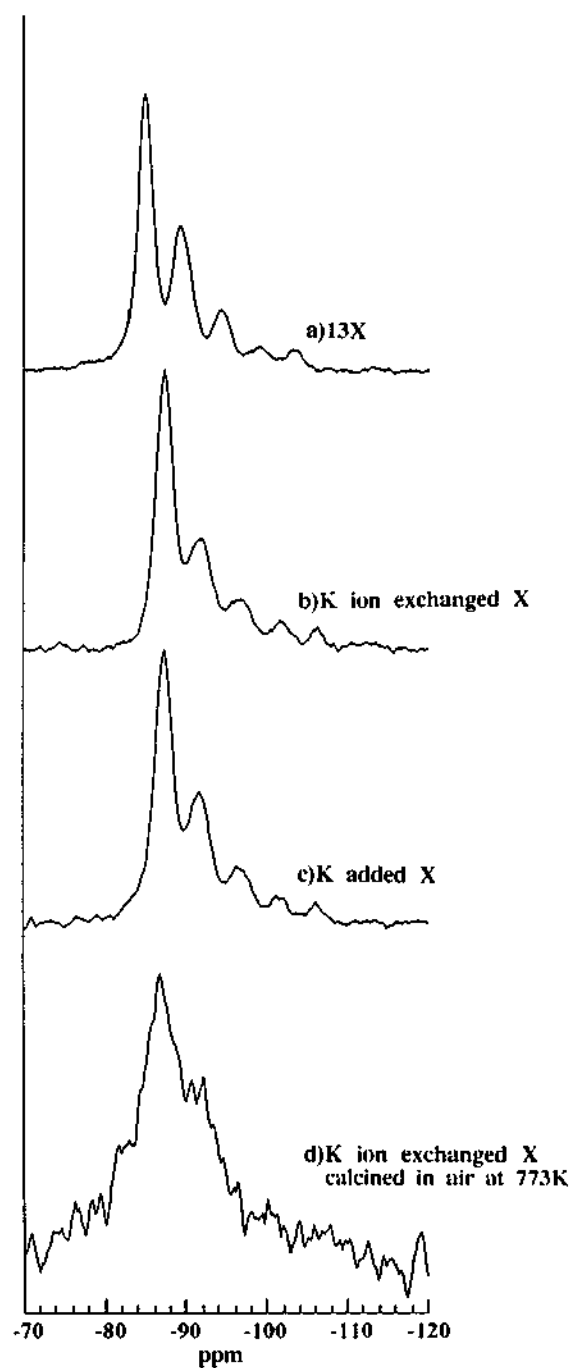


Fig. 2  $^{29}\text{Si}$  MAS NMR spectra of zeolites.

### 3.2. Influence of Type of Cs Salt

The surface areas of the samples prepared by use of aqueous solutions of different Cs salts were measured after heat-treatment in a vacuum at 673K followed by calcination in dry oxygen at 673K. The surface areas of Cs added X prepared by use of aqueous solutions of  $\text{CH}_3\text{COOCs}$ ,  $\text{CsNO}_3$ , and  $\text{CsOH}$ , were 390, 330, and  $390\text{m}^2\text{g}^{-1}$ , respectively. XRD measurements also showed that there observed no significant changes among these samples. The crystalline structures were retained for these samples. The pH of ion-exchange and impregnation solution did not affect much the crystalline structure at least for zeolite X.

### 3.3. Influence of Type of Zeolite

Zeolites X, Y, and ZSM-5 were ion-exchanged and impregnated with  $\text{CH}_3\text{COOCs}$  aqueous solution, and their surface areas and XRD patterns were measured after evacuation at 673K followed by calcination 673K in dry oxygen. The surface areas are given in Table 2. For all types of zeolites, the surface areas decreased on Cs ion-exchange by about 25%. Further decrease in the surface area was observed on Cs ion impregnation. For X and Y zeolites, the surface area decreased on Cs ion impregnation by 27% referenced to the ion-exchanged samples. For ZSM-5, the surface areas decreased by 77%. XRD measurements indicated that all the samples except Cs added ZSM-5 retained their crystalline structures. For Cs added ZSM-5, the intensities of the XRD peaks markedly weakened, showing that the crystalline structure of ZSM-5 collapsed to a considerable degree. The decreases in surface area observed for X and Y zeolites during Cs ion-exchange do not seem to result from collapse of zeolite framework. It seems to be a result of the change in available pore volume by exchange of Na cations by the larger Cs cations. For Cs added samples, the decreases in the surface area are considered to result from the formation of cesium oxide in the cavities to decrease the pore volume. Collapse of the structure of ZSM-5 may be due to a high Si/Al ratio.

### 3.4. $^{29}\text{Si}$ and $^{27}\text{Al}$ MAS NMR Measurements for Local Structure

The changes in the state of Si and Al in zeolite X during ion-exchange, ion impregnation and calcination were examined by MAS NMR. Selected  $^{29}\text{Si}$  MAS NMR spectra are shown in Fig. 2. On K ion-exchange, the five peaks shifted upfield by -2.5ppm, which is in agreement with the reported value[8]. The zeolite X to which K was added showed the same spectrum as K ion-exchanged one. The ion-exchanged K and ion-added K exert the same electronic effect on the zeolite framework. Calcination of K ion-exchanged X in air at 773K brought about a marked change in the spectrum. The five peaks became broadened to give one peak with a shoulder at about 85ppm. It is obvious that the crystalline structure collapsed during calcination. Although drastic change was observed for  $^{29}\text{Si}$  MAS NMR spectrum, essentially no changes were observed for  $^{27}\text{Al}$  MAS NMR spectrum. All the Al are in the state of four coordination number. The shoulder peak at about 85ppm in  $^{29}\text{Si}$  MAS NMR spectrum is assigned to the Si having a low degree of condensation of the Si-O-Si linkage. Taking account of the appearance of only one peak for  $^{27}\text{Al}$  MAS NMR spectrum and the shoulder at about 85ppm in  $^{29}\text{Si}$  MAS NMR spectrum, it is suggested that calcination in air at 773K results in the bond breaking at Si-O-Si, and that the Si-O-Al bonds persisted. Therefore, the crystalline structure was collapsed by breaking the Si-O-Si bonds of zeolite framework.

## 4 REFERENCES

1. W. F. Hölderich, "Acid-Base Catalysis," Kodansha Tokyo and VCH Weinheim, 1989, p.1.
2. A. Corma, V. Fornes, R. M. M-Aranda, H. Garcia and J. Primo, Appl. Catal., 1990, 59, 237.
3. P. E. Hathaway and M. E. Davis, J. Catal., 1989, 116, 263.
4. P. E. Hathaway and M. E. Davis, J. Catal., 1989, 116, 279.
5. P. E. Hathaway and M. E. Davis, J. Catal., 1989, 119, 497.
6. I. Rodrigues, H. Cambon, D. Brunel, M. Lasperas and P. Geneste, "Heterogeneous Catalysis and Fine Chemicals III," Elsevier, 1993, p.623.
7. M. Lasperas, H. Cambon, D. Brunel, I. Rodriguez and P. Geneste, Microporous Mater., 1993, 1, 343.
8. G. Engelhart and D. Michel, "High Resolution Solid-State NMR of Silicates and Zeolites," John Wiley & Sons, 1987.

## 4. Catalytic Features

### 4.1 Prominent Change in Reaction Characteristics of High Silica Zeolite Induced by Isomorphous Substitution with Transition Metals

T. Inui and K. Matsuba

Division of Energy and Hydrocarbon Chemistry, Graduate School of Engineering, Kyoto University, Sakyo-ku, Kyoto 606-01

#### Abstract

Acidic properties of 12 significant high-silica microporous crystallites having MFI and BEA structures were examined by computer simulations for ammonia adsorptions applying Monte Carlo method. Computer calculations was conducted with a graphics super computer TITAN 750V(Stardent Inc. ) and using a software CERIUS. The potential energy calculation was performed by DREIDING II force field. Amounts of NH<sub>3</sub> adsorbed was the following order; Al > Ga ≈ Fe as expressed with kind of metal and MFI > BEA as expressed with crystal structure. These results consistently coincided with the results of NH<sub>3</sub>-TPD measurements and the catalytic reactions of hydrocarbon conversions.

#### 1. INTRODUCTION

Acidic property of zeolitic catalysts is usually measured by NH<sub>3</sub> TPD method, and actually the TPD profiles of different kind of zeolites can be differentiated both in the integral area of profiles and in the shift of peak temperature. The former corresponds to the amounts of acid sites and the latter indicates the strength of acid sites. Especially, a high-temperature peak above ca 300 ~ 400°C is regarded as the desorption from the strong acid sites, which are mainly responsible for acid catalyzed reaction in hydrocarbon synthesis. However, in general, these informations persistently remain in qualitative ones, and therefore, so far, the information from the feature of a consecutive acid catalyzed reactions such as methanol-to-hydrocarbon conversion via dimethyl ether formation, for example, would be the most suggestive tool to determine more precisely the acidic property of zeolitic catalysts.

Narrow pore-size zeolites such as chabazite and ZSM-34 produce light olefins from methanol with high selectivities. However, in spite of their not so strong acidities, the pore is so narrow that the diffusivity of reactants inside the pore is very small or the interparticle residence time becomes large, the activity is rapidly deactivated owing to the coke deposit at the space of their cavity and/or blockage of the entrance of pores located at the outer surface of crystallite particles.

Wide pore-size zeolites such as H-Y and H-M have a considerably strong acidity which is enough strength to convert methanol or olefins into aromatics, and the beginning short period on stream these catalysts exhibited high activity for alkane conversion, for example, as high as H-ZSM-5, however, they are very rapidly deactivated, although H-ZSM-5 maintaining the initial activity without any change in the activity under the same reaction conditions. The cause of the deactivation is ascribed to that the diffusivity of reactants is considerably fast but the spaces consisted of large cavity and wide pores

allow to grow the bulky fused-ring aromatics and then successive coke formation on the strong acid sites [1].

Exceptionally, only H-ZSM-5 showed a very stable against the coke formation in spite of the strong acid sites. The medium pore size of H-ZSM-5, and its three-dimensionally connected pore structure without any cavity does not allow the coke deposit. Notwithstanding its excellent property, H-ZSM-5 cannot be gotten away from the intrinsic fatal property of zeolite or aluminosilicate that the hydrogen evolved during the course of aromatization shifts toward intermediate olefins and hydrogenates them into corresponding paraffins, resulting the decrease in the yield of more valuable olefins, gasoline, or aromatics. It has been emphasized that the activity of n-hexane cracking is strictly proportional to the content of Al in the ZSM-5's framework even in the range of ppm order [2]. Reflecting this nature, the quality of acidic property of H-ZSM-5 could not be changed by mere decrease in Al content.

In order to overcome the disadvantage in H-ZSM-5 and to investigate a wider extension as the microporous crystalline catalysts, we have conducted isomorphous substitution of transition elements for Al in the framework of ZSM-5 maintaining the favorable feature of its pore structure. In general, conventional zeolitic materials consume a considerably long time for nucleation and successive crystallization at a definite temperature. However, in this kind of slow-crystallization process, ununiformity in crystal size and distribution of active species in the crystal particles are involved, and furthermore, elements to be incorporated are apt to be expelled from the framework except Al and some other small number of elements.

On the other hand, the rapid crystallization method [3] increases the possibility of occlusion of the hetero compounds in the early stage of crystallization, and then they are incorporated into the framework more easily resulting that the formation of small and uniform crystals, which are generically called as metallosilicates. The incorporated elements exist much more stably in the framework of metallosilicates than those prepared by slow crystallization method.

Among the various kinds of metallosilicates, Ga- and Zn-silicates exhibited a remarkable activity and selectivity for aromatization of paraffinic hydrocarbons with evolving hydrogen into gas phase from the catalyst surface. Modification with a small amount of Pt not only enhanced the activity markedly but also moderated the coke deposit [4].

Fe-silicate exerted an extraordinary high conversion rate and selectivity in olefin oligomerization into gasoline range fraction [5], and showed a very high selectivity to ethylene and propylene in methanol conversion at lower temperature range [6]. Since the reaction advancing on Fe-silicate is not affected by hydrogen, it can be used as the second-reactor catalyst for hydrogenation of carbon oxides to synthesize high octane number gasoline with high selectivity avoiding hydrogen-related unfavorable reactions for the products [7].

The size of pentasil pore opening of ZSM-5 was delicately modified by the isomorphous substitution of other kinds of elements for Al and the amount of incorporated elements. These factors would affect on the diffusivity of reactants and shape selectivity of the reaction products. However, more evident effects of isomorphous substitution are that the change in acidic property and the exertion of intrinsic metallic and/or metal oxide catalysis. The change in effective diffusivity and different kind of catalysis caused by the metal incorporation can be observed experimentally. Through the measurements of NH<sub>3</sub>-TPD, one can recognize in general, the order of acid strength among the metallosilicates, for example, is in the order of



as expressed by the kind of metal incorporated. However, the feature of the reaction indicates much larger difference than that expected from the qualitative information of the NH<sub>3</sub>-TPD.

In order to elucidate more precise difference in acidic property among those metallosilicates, we newly studied on the computer simulation of NH<sub>3</sub> adsorption on the acidic sites of different kind of metallosilicates by applying Monte Carlo method, and estimated the precise position of adsorption sites and amount of NH<sub>3</sub> adsorbed, and the results were visualized by computer graphics [8, 9].

In this paper, sequential results of NH<sub>3</sub> adsorptions were shown for different kinds of high silica zeolites, MFI (ZSM-5)-type 10 oxygen-member ring metallosilicates and BEA(beta)-type 12 oxygen-member ring metallosilicates were calculated by computer and depicted by computer graphics. The feature of the adsorption patterns NH<sub>3</sub> is discussed comparing with the NH<sub>3</sub>-TPD profile and reaction characteristics in some hydrocarbon conversion reactions.

## 2. EXPERIMENTAL METHODS

### 2.1 Catalyst Preparation

Protonated H-ZSM-5, i. e. alumino silicate (Al-MFI), was prepared by our intrinsic rapid crystallization method [3], which enables high and uniform dispersion of aluminum in crystallites resulting high activity in acid catalyzed reactions [3, 10]. Though detailed procedures of the method of the rapid crystallization have been described in our previous papers [3], the following points should be emphasized as improvements made in the present method to rapidly prepare uniform and fine zeolitic crystals: (i) the preparation of supernatant solution was separated from that of gel, which was important for preparing uniform crystals; (ii) the precipitated gel was milled before the crystallization in the hydrothermal condition, which was essential for obtaining uniform and fine crystals and for providing the rapid crystallization; and (iii) the temperature was programmed under the hydrothermal treatment to minimize the time necessary for the crystallization. By applying this synthetic method, Ga-silicate (Ga-MFI) [4], Fe-silicate (Fe-MFI) [6], and bi-metallosilicates such as Al-Ga-silicate (Al, Ga-MFI) [11] were synthesized.  $\beta$ -type metallosilicates [Al-BEA, Ga-BEA, Fe-BEA] and their bi-metallosilicates [12, 13] were synthesized by also applying the principle of the rapid crystallization method.

### 2.1 Configuration of Metallosilicates Treated

Three kinds of MFI-type mono-metallosilicates were treated for calculation. As shown in Fig. 1, (open circulars) most probable four silicon atoms of the T12 site in the MFI-type silicate were respectively replaced by four atoms of Al, Ga, or Fe, according to the evaluation of the lowest potential energy, which fulfilled Loewenstein law. Since the number of Si atoms in the unit cell of MFI crystal is 92, Si to the substituted metal atomic ratio was 23 in each case, which is similar to those of synthesized crystals, i. e. Si to metal ratio around 20.

Another three kinds of BEA-type mono-metallosilicates were treated for calculation, and four of T5 site in BEA-type silicate structure were replaced by four atoms of Al, Ga and Fe. As the number of Si atoms in the unit cell is 64, the Si to replaced atom ratio in those metallosilicates was 15.

Besides those six kinds of mono-metallosilicates, totally six kinds of bi-metallosilicates of MFI- and BEA-type ones were also treated for calculation. In those cases, two atoms from two kinds of elements among Al, Ga, and Fe, therefore totally four atoms, were substituted for Si atoms. The positions of substituted two kinds of metals were decided to maintain symmetric positions. The Si to metals 1 and 2 atomic ratios were, therefore, 46 and 46 for MFI-type bi-metallosilicates and 30 and 30 for BEA-type bi-metallosilicates. In every case, the total metal content was the same as those of corresponding mono-metallosilicates.

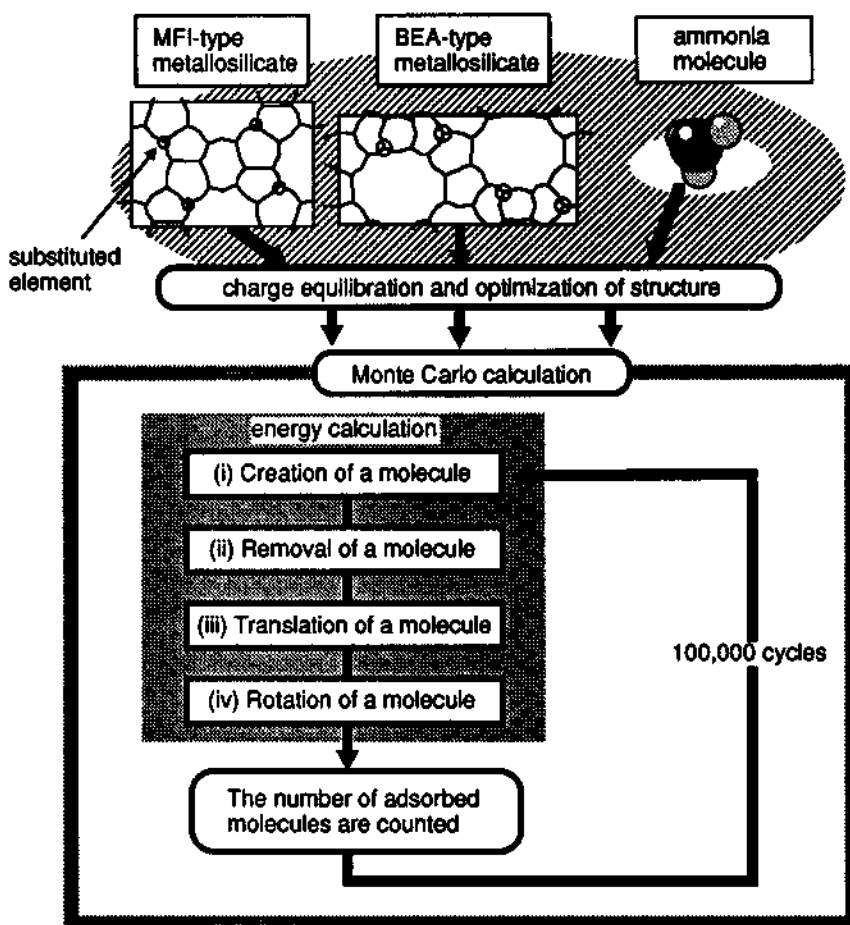


Fig. 1 Flow chart of computer calculation for ammonia adsorption on metallosilicates

Counterpart alkali metal cations for substituted elements in those metallosilicates were totally exchanged by proton. The positions of proton and configurations of  $\text{NH}_3$  molecules were optimized by energy minimization. The charge of the metallosilicates and  $\text{NH}_3$  molecule were calculated with charge equilibration method [14] before simulation of  $\text{NH}_3$  adsorption.

## 2.2 Monte Carlo Simulations for $\text{NH}_3$ Adsorption

The Monte Carlo simulations were carried out for the twelve kinds of metallosilicates mentioned above with the *CERIUS* software as illustrated in Fig. 1, which was computational instrument for material research offered by Molecular Simulations Inc.. The potential energies of  $\text{NH}_3$  molecules in the metallosilicate were calculated by using the DREIDING II force field [15] developed by Goddard III. In this force field the interactions ( $E$ ) consist of bond stretch ( $E_B$ , two-body), bond-angle bend ( $E_A$ , three-body), dihedral angle torsion ( $E_T$ , four-body), inversion ( $E_I$ , four-body), van der

Waals ( $E_{vdw}$ ), electrostatic ( $E_Q$ ), and hydrogen bond ( $E_{hb}$ ) terms, as the following equation.

$$E = E_B + E_A + E_T + E_I + E_{vdw} + E_Q + E_{hb} \quad (1)$$

The fixed pressure (grand canonical) algorithm [16] used in these simulations was as follows;

(i) Creation of a molecule : an ammonia molecule is placed at a random position in the framework domain of the metallosilicate, and whether we should accept of the configurations or not is judged according to the energy change, i. e. with the probability  $P$  expressed as the following equation.

$$P = \min [1, \exp\{-\Delta U / kT - \ln\{(N+1) kT / pV\}\}] \quad (2)$$

where  $\Delta U$  is configurational energy change,  $N$  is current number of NH<sub>3</sub> in the framework of metallosilicate,  $p$  is pressure of NH<sub>3</sub> in the gas phase, and  $V$  is cell volume.

(ii) Removal of a molecule : a random ammonia molecule located in the framework is chosen, and new configuration will be accepted with the following probability:

$$P = \min [1, \exp\{-\Delta U / kT + \ln\{NkT / pV\}\}] \quad (3)$$

(iii) Translation of a molecule : we choose a random NH<sub>3</sub> molecule in the framework and translate it by random amount within a cube of size  $2\delta$  ( $\delta = 1 \text{ \AA}$ ), and will accept new configuration with probability  $P$  :

$$P = \min [1, \exp\{-\Delta U / kT\}] \quad (4)$$

(iv) Rotation of a molecule : a random NH<sub>3</sub> molecule in the framework is chosen, and a random axis in the framework is chosen and the molecule is rotated by a random amount within the range  $-\delta$  to  $+\delta$  ( $\delta = 50$  degrees). New configuration will be accepted based on the energy change as for Eq. (4).

The amount of NH<sub>3</sub> adsorbed was counted after this cycle and these cycles were repeated 100,000 times. These calculations were carried out at 300K under 100 kPa by graphics supercomputer TITAN 750V(Stardent Inc.). The results of these calculations were investigated by visualizing with computer graphics.

### 3. RESULTS AND DISCUSSION

#### 3.1 Relationship between Al Content and Number of Acid Sites

Haag and Lago [2] reported that the hexane cracking activity in H-ZSM-5 having Si - Al ratio from 17 to 180,000 has been formed to be strictly proportional to their aluminum concentration and hence to their content of active sites. Since those active sites to contribute hydrocarbon cracking can be regarded as the acid sites, especially strong acid sites, those would reflect to the high temperature in NH<sub>3</sub>-TPD profiles.

The similar situation would be expected in case of another high-silica zeolite H-Al-BEA, however systematic experimental result still not yet reported. Here, in order to evaluate the correlation relationship between the content of Al and the number of acid sites in H-

Al-BEA, the results of the simulation for NH<sub>3</sub> adsorption are plotted in Fig. 2, as the function of Al to (Al + Si) atomic ratio. The content of Al was varied from 0 to 0.125 or from infinity to 7, respectively, as expressed with Si to Al atomic ratio. As shown in this figure, fairly good correlation, a line goes through the origin, between the average number of adsorbed NH<sub>3</sub> on unit cell of Al-BEA and content of Al was recognized. This indicates validity of the presented simulation method and the potential to prospect the amount of adsorbed NH<sub>3</sub> on H-Al-BEAs involving different Al contents.

### 3.2 Simulation of NH<sub>3</sub> Adsorption on Various Metallosilicates

Since expression like as Fig. 2 shows the amount of NH<sub>3</sub> adsorbed in a unit cell of crystals but does not show the geometric distribution of the adsorbed NH<sub>3</sub>, detail descriptions for various metallosilicates are shown in the following figures, and the differences will be discussed comparing with the NH<sub>3</sub>-TPD profiles and the catalytic performance.

Figures 3 ~ 6 show the results obtained for three kinds of MFI-type mono-metallosilicates, BEA-type mono-metallosilicates, MFI-type bi-metallosilicates and BEA-type bi-metallosilicates, respectively. The lower figure for each metallosilicate shows the geometry of NH<sub>3</sub> adsorbed on the unit cell depicted as A-C coordinate and the area composed of the dots is proportional to the number of NH<sub>3</sub> molecules. The upper figure shows number of the adsorbed NH<sub>3</sub> expressed with bar graph as the function of coordinate A, and the average number of adsorbed NH<sub>3</sub> per unit cell is indicated on the same graph.

In Table 1, amount of NH<sub>3</sub> and average potential energy of unit amount of NH<sub>3</sub> for every metallosilicate are listed. Comparing with those figures and table, the order of adsorption amount of NH<sub>3</sub> is as follows, as expressed with kind of metal,



for both MFI- and BEA-type metallosilicates, and as expressed with the kind of metallosilicate



Reflecting their pore structures, distribution of adsorption sites for NH<sub>3</sub> molecules and concentration of NH<sub>3</sub> adsorbed in MFI structure are much more localized and concentrated, respectively.

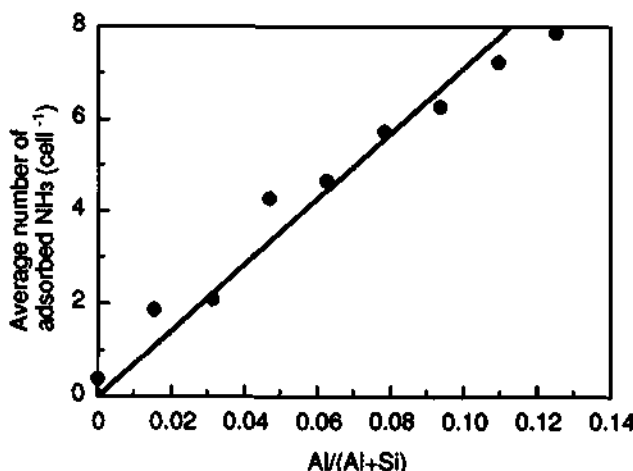
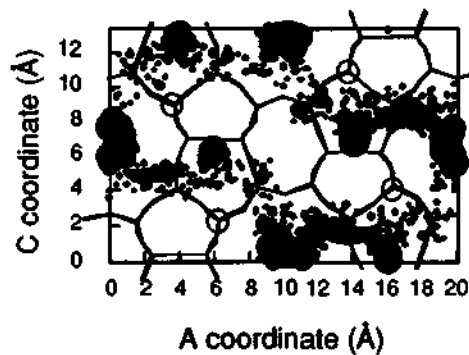
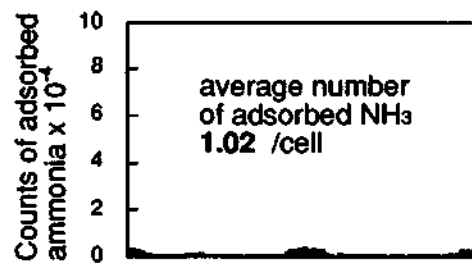
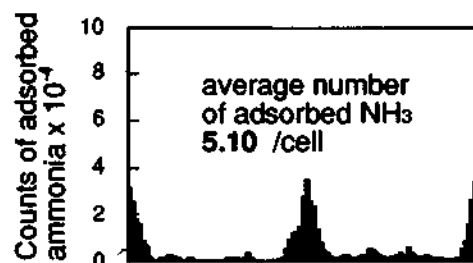
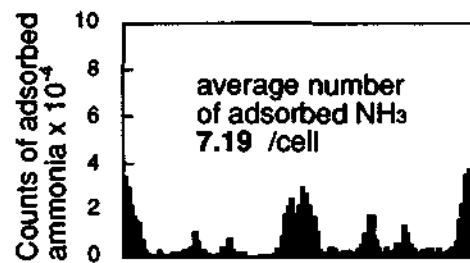
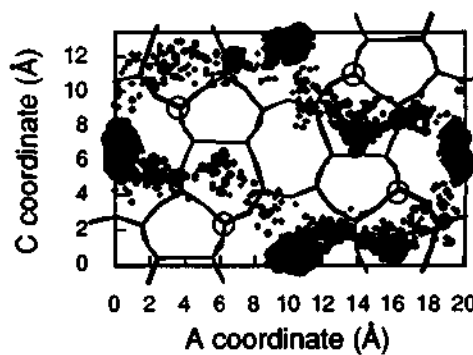


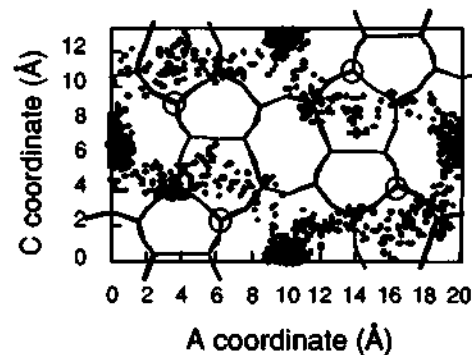
Fig. 2 Number of NH<sub>3</sub> adsorbed on H-Al-BEA versus Al content



a) H-Al-MFI



b) H-Ga-MFI



c) H-Fe-MFI

Fig. 3 Distribution of ammonia adsorbed on MFI-type mono-metallocosilicates

open circulars : T sites substituted by metal

closed circulars : positions and counts of ammonia adsorbed

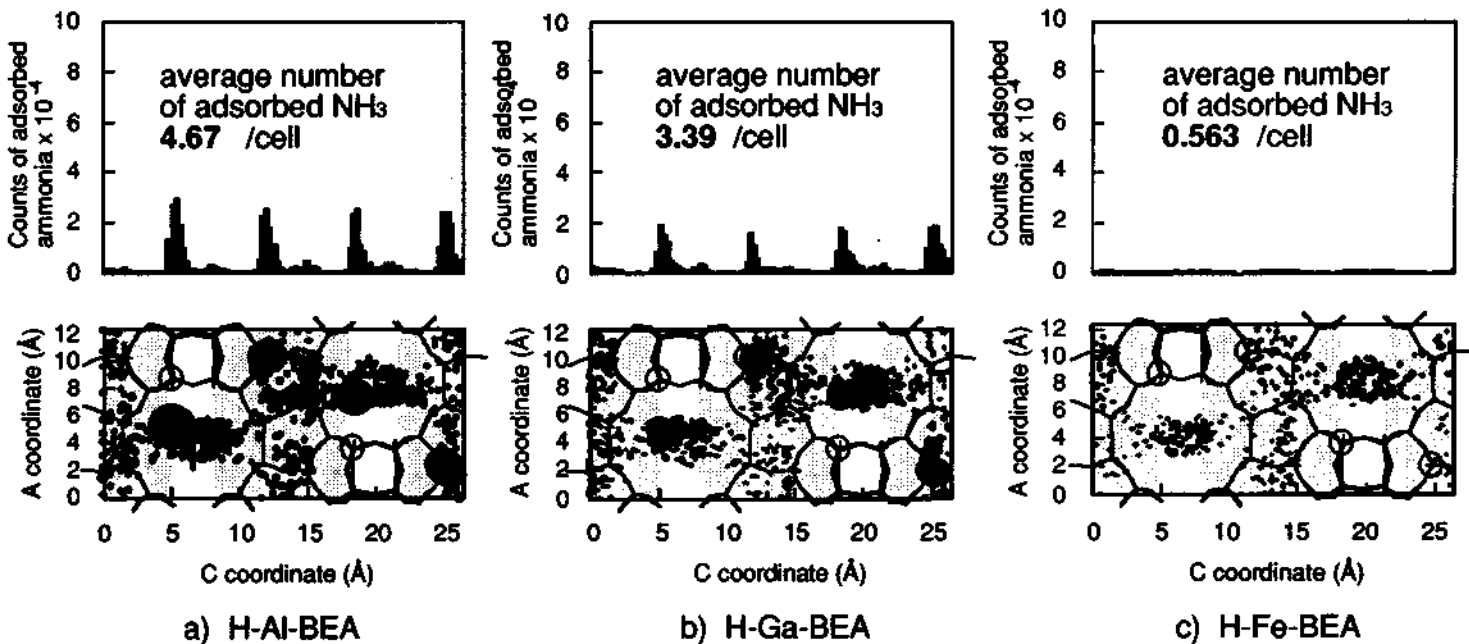


Fig. 4 Distribution of ammonia adsorbed on BEA-type mono-metallosilicates

open circulars : T sites substituted by metal  
closed circulars : positions and counts of ammonia adsorbed

Shadow parts represent domains of pores which make a right angle with pores whose 12-oxygen member ring openings are shown on this sheet.

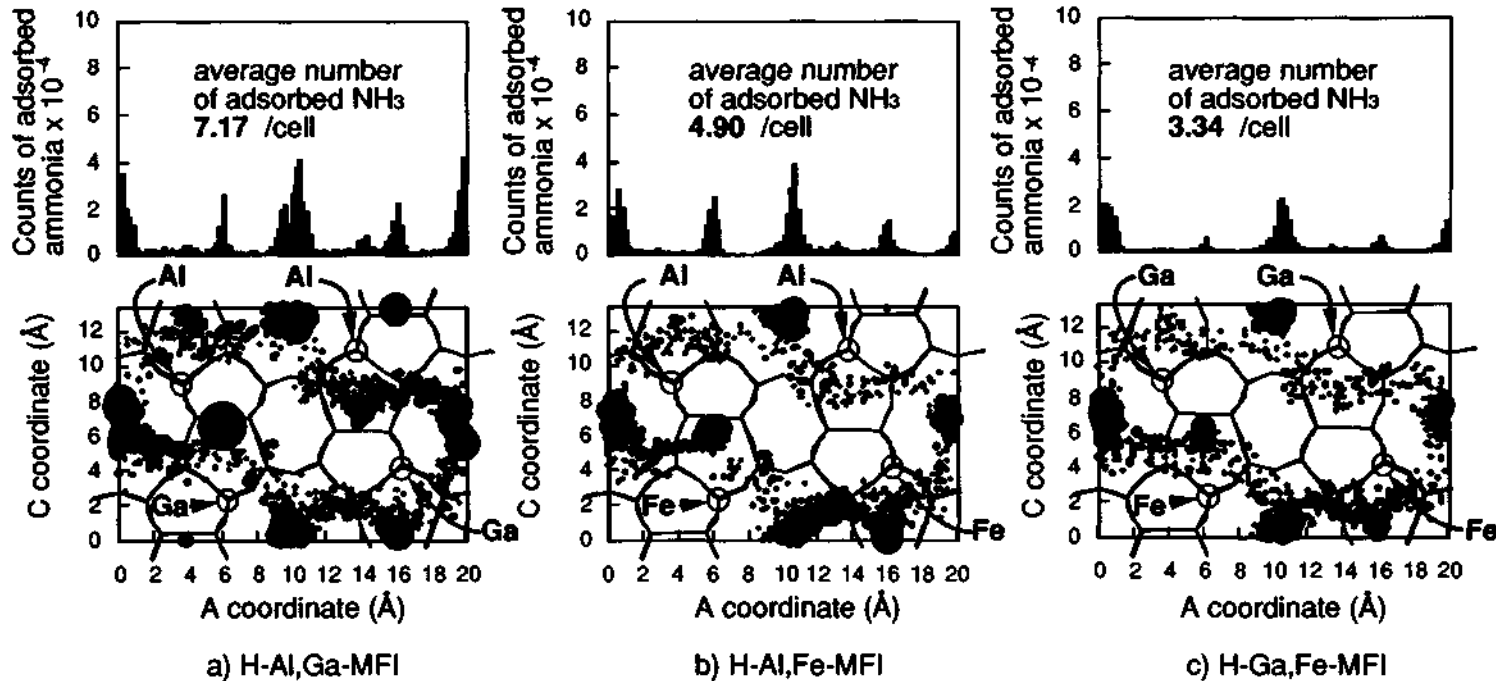


Fig. 5 Distribution of ammonia adsorbed on MFI-type bi-metallosilicates

open circulars : T sites substituted by metal  
closed circulars : positions and counts of ammonia adsorbed

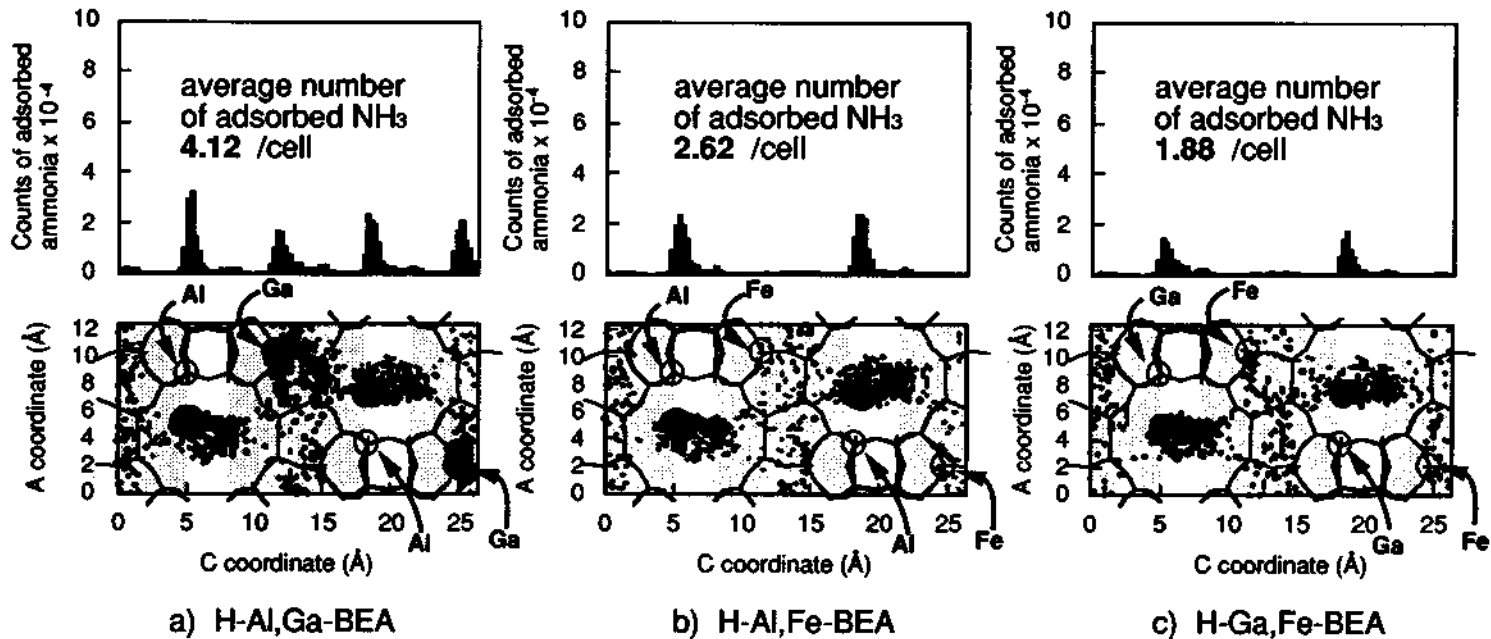


Fig. 6 Distribution of ammonia adsorbed on BEA-type bi-metallosilicates

open circulars : T sites substituted by metal

closed circulars : positions and counts of ammonia adsorbed

Shadow parts represent domains of pores which make a right angle with pores whose 12-oxygen member ring openings are shown on this sheet.

These simulation results consistently correspond to the experimental results of NH<sub>3</sub>-TPD as shown in Fig. 7 and the results of hydrocarbon conversion, for example, ethyl benzene conversion as shown in Fig. 8. Conversion of ethylbenzene on MFI-metallocsilicates were higher than those on BEA-metallocsilicates. Conversion of ethylbenzene on both H-Al-MFI and H-Ga-MFI were large enough as high as 90%, therefore, the difference between them is not clear. Catalytic functions rather than acidity also reflect in the reaction results. Ga ingredient has a function of hydrogen evolution from the reaction sites to gas phase, whereas Al ingredient has a function of hydrogen shift on the catalyst surface as a result heavier aromatics are produced much, and counterpartly light paraffinic hydrocarbons are produced less in Ga-containing metallocsilicates.

In bi-metallocsilicates, amount of NH<sub>3</sub> and average potential energy of NH<sub>3</sub> were delicately deviated from the simple average of both elements. These calculated results suggest the cause of markedly improvement in catalytic performance of bi-metallocsilicates in conversion reactions of propane [4] and n-hexane [11].

#### 4. CONCLUSION

Acidic property of high-silica zeolites MFI and BEA and their metallocsilicates, which can be synthesized by isomorphous substitution of transition elements for Al, were evaluated precisely in both number of acid sites and its strength and distribution. Very

Table 1 The amount and average energy of NH<sub>3</sub> adsorbed on various metallocsilicates

	silicate form	mono-metallo			bi-metallo		
		Al	Ga	Fe	Al/Ga	Al/Fe	Ga/Fe
amount of NH <sub>3</sub> (g/mol-metal)	MFI	30.6	21.7	4.34	30.5	20.9	14.2
	BEA	19.9	14.4	2.40	17.5	11.2	8.00
average energy (kcal/mol-NH <sub>3</sub> )	MFI	-7.66	-6.72	-3.26	-7.31	-7.17	-6.31
	BEA	-8.06	-6.42	-2.72	-7.46	-7.32	-5.64

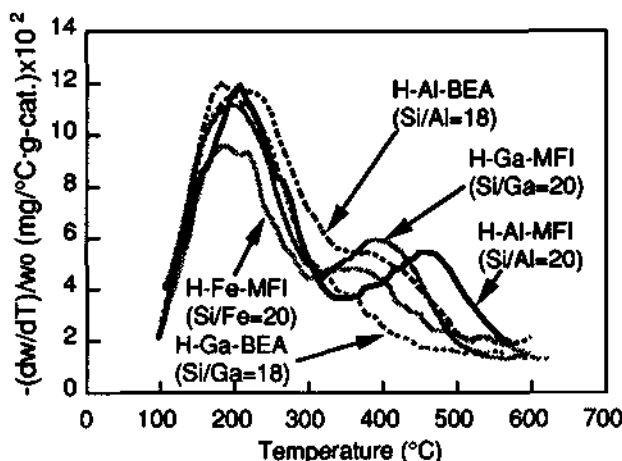


Fig. 7 NH<sub>3</sub>-TPD profiles for various metallocsilicate catalysts

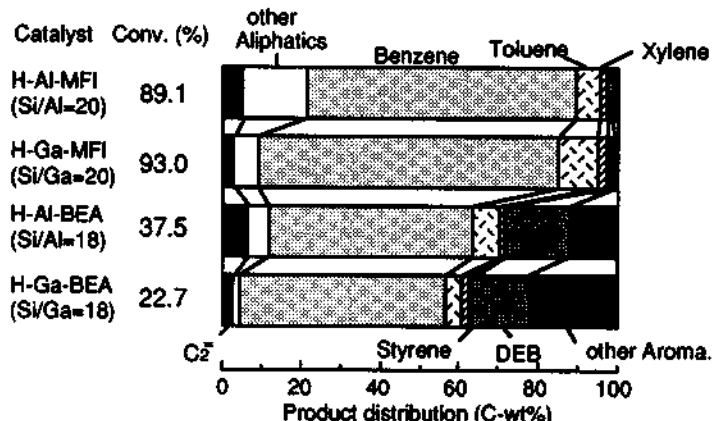


Fig. 8 Distribution of products in ethylbenzene conversion on MFI- and BEA-type metallosilicates  
(reaction temp. 450°C ; GHSV 2000 h<sup>-1</sup>)

localized distribution of NH<sub>3</sub> and the difference between every metallosilicate including one kind and two kinds substitutions were depicted by computer graphics. These results consistently coincided with the experimental results of NH<sub>3</sub> adsorption and hydrocarbon conversion reaction, although more quantitative correspondence should be elucidate in the future.

## 5. REFERENCES

- [1] T. Inui, J. Japan Petrol. Inst., 1990, 33, 198
- [2] W. O. Haag, R. M. Lago, and P. B. Weisz, Nature, 1984, 309, 590
- [3] T. Inui, ACS Symp. Series, 1989, 398, 479
- [4] T. Inui, Y. Makino, F. Okazumi, S. Nagano, and A. Miyamoto, IEC Res, 1987, 26, 647
- [5] T. Inui, React. Kinet. Catal. Lett., 1987, 35, 227
- [6] T. Inui, H. Matsuda, O. Yamase, H. Nagata, K. Fukuda, T. Ukawa, and A. Miyamoto, J. Catal., 1986, 98, 491
- [7] T. Inui, T. Takeguchi, A. Kohama, and K. Tanida, Energy Convers. Mgmt., 1992, 33, 513
- [8] T. Hattori, N. Goto, Y. Nakazaki, M. Inoue, and T. Inui, Preprints 65th Annual Meeting of Chem. Soc. Japan., 1993, I, 435
- [9] K. Matsuba, Y. Tanaka, N. Goto, Y. Nakazaki, M. Inoue and T. Inui, Preprints 9th Annual Meeting of Zeolite Association of Japan., 1993, 52
- [10] T. Inui, Proc. Inter. Confer. Zeolite and Microporous Crystals, Nagoya, 1993, in press
- [11] J. Ito and T. Inui, Sekiyu Gakkaishi, 1993, 36, 114
- [12] M. Okabe, A. Matsuoka, M. Inoue and T. Inui, Preprints 8th Annual Meeting of Zeolite Association of Japan., 1992, 153
- [13] S. Iwamoto and T. Inui, Preprints 9th Annual Meeting of Zeolite Association of Japan., 1993, 36
- [14] A. K. Rappe and W. A. Goddard III, J. Phys. Chem., 1991, 95, 3358
- [15] S. Dasgupta and W. A. Goddard III, J. Phys. Chem., 1989, 90, 7207
- [16] M. R. Stapleton, D. J. Tildesley and N. Quirke, J. Chem. Phys., 1990, 92, 4456

## 4.2 Aromatization of Short Chain Alkanes on Ga MFI Catalysts

M. Guisnet and D. Lukyanov

URA CNRS 350, Université de Poitiers, 40 avenue du Recteur Pineau, 86022 Poitiers Cedex, France

### Abstract

Propane aromatization on GaZSM5 catalysts was reexamined in order to clarify the nature and the role of gallium species. Kinetic modeling allows to conclude that gallium species play a significant role in the dehydrogenation of propane, of C<sub>6</sub>-C<sub>9</sub> alkenes and of cycloalkenes and also catalyze the formation of methane from propane and the hydrogenation of ethene. These two latter reactions are responsible for limiting aromatic selectivity. The effect of calcination of gallosilicates on their catalytic properties shows that framework gallium species are much less active for dehydrogenation than extraframework species and indeed are probably inactive. Model reactions show that hydrogen treatment at 873 K of a Ga<sub>2</sub>O<sub>3</sub>-HZSM5 mixture causes a significant increase in the dehydrogenating and hydrogenolysis activities of gallium but only a small decrease in the protonic activity of the zeolite. The great activity and selectivity to aromatics of hydrogen pretreated catalysts can be explained through the bifunctional scheme of propane aromatization.

### 1. INTRODUCTION

Naphtha feedstock currently represents about 80 % of the production cost of BTX (Benzene-Toluene-Xylenes). It is therefore tempting to substitute a less expensive material such as liquefied petroleum gas (LPG) for naphtha. A process named Cyclar using a gallium doped zeolite (probably MFI-type) has been developed by UOP and BP for converting LPG (propane-butane) into aromatics. A large scale pilot plant (1000 bbl/d capacity) was built at the British Petroleum Grangemouth Refinery in Scotland. Because of the rapid deactivation of the catalysts a continuous regeneration technology was necessary. The following yields were obtained : aromatics 65 wt %, hydrogen 6 %, fuel gas (methane + ethane) 29 % [1]. The production with aromatics of hydrogen makes this process particularly attractive provided however that the production of fuel is limited. The demonstration unit closed down at the end of 1991.

In addition to the industrial interest, the aromatization of short chain alkanes on Ga MFI catalysts represents an original complex system which consequently is particularly interesting from a fundamental point of view. That is why a great number of papers have been recently published on this subject included two review papers [2,3].

Non doped ZSM5 zeolites catalyze the aromatization of propane. The reaction scheme is indicated in Figure 1. Steps 2-6 occur through classical acid mechanisms

involving carbenium ions as intermediates while steps i and i' would occur mainly through the scission of carbonium ion intermediates formed by propane protonation.

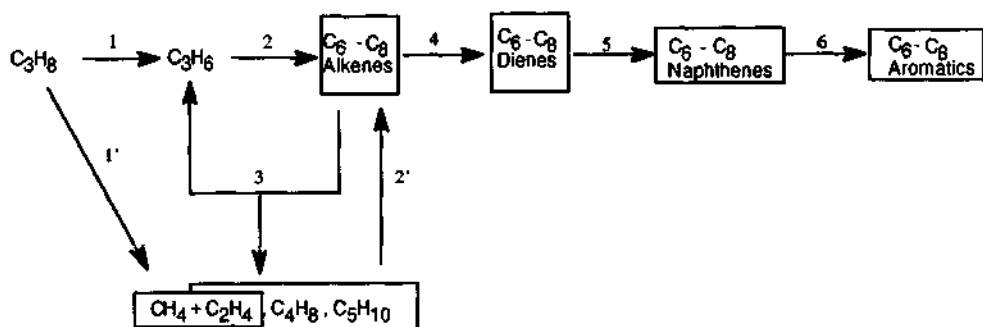


Figure 1. Reaction scheme of propane aromatization on HZSM5 and GaHZSM5 catalysts.

It has been shown that the rate of propane aromatization and the selectivity towards aromatics can be increased significantly by using various gallium containing ZSM5 catalysts : gallium exchanged or impregnated HZSM5 catalysts, physical mixtures of  $\text{Ga}_2\text{O}_3$  and HZSM5, gallosilicate or galloaluminosilicates of MFI structure. Although all the investigators agree that gallium species provide a new route for aromatics formation via dehydrogenation steps, the exact role of gallium species is not very well understood. For instance it is not clear whether gallium species are involved in step 5 (dehydrogenation of oligomers into dienes) or in step 6 (dehydrogenation of naphthenes into aromatics) or in both. Furthermore gallium species could catalyze other reactions such as hydrogenation of alkenes or hydrogenolysis. In order to discuss these points, kinetic modeling was used for a quantitative estimation of the role of Ga in the various steps involved in propane aromatization on Ga/HZSM5 [4,5].

The nature of the gallium species active for dehydrogenation is another point which needs to be clarified. From the effect of calcination under dry air of a gallosilicate sample it will be shown that framework gallium species are much less active than extraframework species, and indeed are probably inactive [6]. On gallium ZSM5 catalysts hydrogen, which is coproduced with aromatics, can provoke modifications of the gallium species hence of the activity and selectivity of these bifunctional catalysts. The effect of hydrogen pretreatment at high temperature of a physical  $\text{Ga}_2\text{O}_3$ -HZSM5 mixture will be considered, various model reactions being used to determine quantitatively the changes in the acid, dehydrogenating and bifunctional properties [7].

## 2. KINETIC MODELING OF PROPANE AROMATIZATION OVER HZSM5 AND GaHZSM5

A large amount of data on propene and propane aromatization on HZSM5 and Ga impregnated HZSM5 samples were collected in our laboratory. These reactions were carried out at 803 K in a flow reactor, the pressure of propene or propane being equal to 1 bar. Contact time was varied from about  $1.10^{-3}$  h to  $40.10^{-3}$  h for propene transformation and from  $10.10^{-3}$  to  $500.10^{-3}$  h for propane transformation so as to obtain conversions in the range of a 5-90 %. Moreover additional data existed on

transformations of C<sub>4</sub>-C<sub>8</sub> alkanes on the same catalysts. All these make kinetic modeling of propene and propane aromatization possible. The catalysts considered in this work are a HZSM5 zeolite with a Si/Al ratio equal to 40 and a Ga HZSM5 (4 wt % of gallium) prepared by impregnation of this HZSM5 zeolite with a gallium nitrate solution.

### 2.1. Kinetic model

Obviously, propane aromatization reaction is far too complex to consider in kinetic model chemical transformations of every single hydrocarbon. In the previous kinetic models for various reactions over ZSM-5 catalysts, e.g., methanol to hydrocarbon conversion [8], alkene oligomerization reaction [9], alkene aromatization reaction [10], the number of the reaction species was reduced by lumping into a single component all the isomers with the same carbon number. The same method was used in our study [4,5]. Thus, 42 components, representing all the reaction species involved in propane aromatization reaction, were considered : 9 alkenes C<sub>2</sub>-C<sub>10</sub>, 10 alkanes C<sub>1</sub>-C<sub>10</sub>, hydrogen, 7 dienes D<sub>4</sub>-D<sub>10</sub>, 5 alkylcyclohexenes X<sub>6</sub>-X<sub>10</sub>, 5 alkylcyclohexadienes Y<sub>6</sub>-Y<sub>10</sub>, and 5 alkylbenzenes A<sub>6</sub>-A<sub>10</sub> (subscript index denotes the number of carbon atoms). The following adsorption and reaction steps were considered :

1. Hydrocarbon adsorption on zeolite protonic acid sites and on gallium catalytic sites (not indicated in Figure 1).

2. Reaction steps on zeolite protonic acid sites :

- protolytic cracking of propane resulting in the formation of the primary products : hydrogen + propene and methane + ethene (steps 1 and 1' in Figure 1) ;
- protolytic cracking of C<sub>4</sub><sup>+</sup> product alkanes (not indicated in Figure 1) ; - hydrogen transfer between propane and product alkenes (not indicated in Figure 1) ; - alkene oligomerization and cracking (steps 2, 2' and 3) ; - diene formation via hydrogen transfer between two alkene molecules (steps 4) ; - interaction of alkenes and dienes with formation of higher molecular weight dienes (not indicated in Figure 1) ; - diene cyclization (steps 5) ; - aromatic formation via hydrogen transfer between alkenes and cyclic alkenes and dialkenes (steps 6 in Figure 1).

3. Reaction steps on gallium catalytic sites :

- dehydrogenation of propane and C<sub>4</sub><sup>+</sup> product alkanes (step 1) ; - transformation of propane and C<sub>4</sub><sup>+</sup> product alkanes into methane and corresponding alkene (step 1') ; - diene formation via alkene dehydrogenation (steps 4) ; - aromatics formation via dehydrogenation of cyclic alkenes and dialkenes (steps 6).

The reaction steps were considered to occur on zeolite protonic acid sites (Z) or on gallium catalytic sites (Z<sub>G</sub>), as illustrated below for the steps of propane transformation via protolytic cracking and hydrogen transfer.

Protolytic cracking of C-H and C-C bonds :



Hydrogen transfer between propane and alkenes :



The well-known effect of the molecular weight on the hydrocarbon reactivity was considered : e.g., the rate constant  $K_{HT}(n)$  depends on the number of carbon atoms in the molecule of  $C_n$ = alkene participating in the hydrogen transfer steps shown above.

For derivation of the rate equations two simplifying assumptions were introduced : (i) adsorption equilibrium was considered to be established, and (ii) adsorption constants were considered to be independent of hydrocarbon molecular weight. The equations for the rates of the reaction steps were derived on the basis of the mass action law [11], and the reactions over zeolite and gallium catalytic sites were treated independently. Steady-state concentrations of Z and  $Z_g$  were determined as :

$$[Z] = \frac{1}{1 + \sum K_{a1} P_{Cn} + \sum K_{a2} P_{Dn} + \sum K_{a3} P_{Xn} + \sum K_{a4} P_{Yn} + \sum K_{a5} P_{An}}$$

$$[Z_g] = \frac{1}{1 + \sum K_{a6} P_{Cn} + \sum K_{a7} P_{Dn} + \sum K_{a8} P_{Xn} + \sum K_{a9} P_{Yn} + \sum K_{a10} P_{An}}$$

where  $P_{Cn}$ ,  $P_{Dn}$ ,  $P_{Xn}$ ,  $P_{Yn}$ , and  $P_{An}$  are the partial pressure of  $C_n$ = alkene,  $D_n$  diene,  $X_n$  cyclic alkene,  $Y_n$  cyclic dialkene, and  $A_n$  alkylbenzene, respectively. Adsorption of alkanes and hydrogen on Z and  $Z_g$  catalytic sites was considered to be negligible.

The kinetic model can be represented as a set of 42 equations describing the rates of transformations of 42 components in 275 reaction steps :

$$R_i = \sum_{s=1}^{275} v_{is} r_s \quad (1 \leq i \leq 42)$$

where  $R_i$  is the rate of transformation of the i-th component ;  $v_{is}$  is the stoichiometric coefficient of the i-th component in the s-th reaction step ;  $r_s$  is the rate of the s-th reaction step. For the kinetic modeling the plug flow reactor model was used :

$$\frac{dC_i}{dt} = R_i M_i \quad (1 \leq i \leq 42)$$

where  $C_i$  is the weight fraction of the i-th component in the reaction mixture ;  $\tau$  the contact time (h) ;  $R_i$  the rate of transformation of the i-th component (mol/(g h)) ;  $M_i$  the molecular weight of the i-th component (g/mol). For the numerical integration of the system of differential equations, the Runge-Kutta-Gear method was applied.

Estimation of the rate constants was carried out step by step. First, the rate constants of alkene aromatization steps over zeolite protonic acid sites were determined. Then the effect of gallium species on alkene aromatization was clarified. Finally, the values of the rate constants of propane transformation steps catalyzed by zeolite and gallium catalytic sites were estimated. During the rate constant estimation

procedure, which is described in detail in references 4 and 5, the effect of different rate constants on propene and propane transformation and on product distribution was investigated.

## 2.2. Kinetic modeling of propene aromatization over HZSM5 and GaHZSM5

At the beginning the rate constants of the acid catalyzed reaction steps were estimated, and the description of propene aromatization reaction over HZSM5 was obtained. This is illustrated in Figure 2 in which simulated and experimental data on the concentrations of the main reaction products (light alkanes and aromatics) are compared. The steps of diene formation via hydrogen transfer between alkenes and carbonium ions (steps 4 in Figure 1) were found to be the slowest in the sequence of the acid catalyzed alkene aromatization steps shown in Figure 1. It has been also established that aromatic products inhibit alkene transformation over HZSM5 due to a partial blocking of the zeolite acid sites.

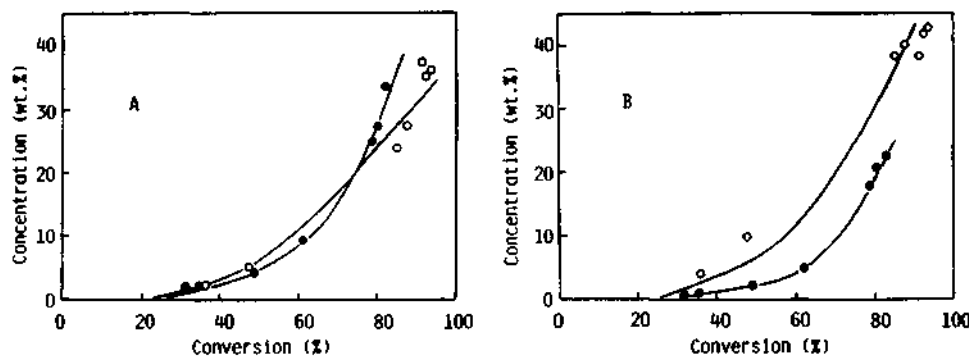


Figure 2. Final description of propene aromatization over HZSM5 (●) and GaHZSM5 (○) zeolites. Experimental data (points) and calculated curves for the concentrations of C<sub>2</sub>-C<sub>5</sub> alkanes (A) and aromatics (B) as functions of propene conversion.

Recent analysis of the literature data on aromatization reactions over Ga containing HZSM5 zeolites [2,3] has led us to the conclusion that the effect of Ga on the alkene aromatization results mainly from Ga participation in the steps of alkene dehydrogenation into dienes, as was proposed by Ono and coworkers [12,13] and Meriaudeau et al. [14], or/and in the steps of naphthene dehydrogenation, as proposed by Gnepp et al. [15,16]. In order to discuss this conclusion we investigated the effect of the rate constants of these steps on the concentrations of the main products (aromatics and C<sub>2</sub>-C<sub>5</sub> alkanes). The kinetic modeling results obtained show that Ga participation only in alkene dehydrogenation or only in naphthene dehydrogenation does not allow to describe quantitatively the experimental data on both aromatics and alkane formation on GaHZSM5. Therefore, the rate constants for alkene and naphthene dehydrogenation were introduced simultaneously in the kinetic model and a good agreement between experimental and calculated concentrations was obtained (see Figure 2). One rate constant was used for the steps of alkene dehydrogenation and another for the subsequent steps of dehydrogenation of cyclic alkenes and cyclic dialkenes into aromatics. Comparison of these rate constants show that dehydrogenation of cyclic alkenes and cyclic dialkenes proceeds 8 times faster than the dehydrogenation of alkenes.

It was interesting to compare quantitatively the contributions of Ga species and zeolite catalytic sites to the formation of dienes and aromatics on the GaHZSM5 catalyst. The results of kinetic modeling performed with this aim are shown in Figure 3. Curves 1 correspond to the formation of dienes and aromatics on the zeolite protonic acid sites via hydrogen transfer, and curves 2 correspond to the formation of these hydrocarbons on the gallium species via dehydrogenation. From the data presented it is clear that gallium plays a very significant role in propene aromatization : about 70 % of dienes and 30 % of aromatics are produced via dehydrogenation reactions catalyzed by gallium species.

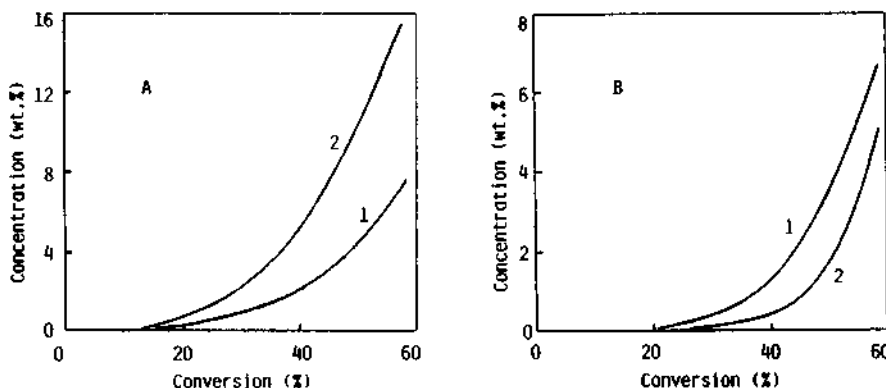


Figure 3. Calculated curves for the concentrations of dienes (A) and aromatics (B) as functions of propene conversion. Curves 1 : diene and aromatics formation is considered to occur only in zeolite catalyzed hydrogen transfer reactions ; curves 2 : diene and aromatics formation is considered to occur only in gallium catalyzed dehydrogenation reactions.

### 2.3. Kinetic modeling of propane transformation over HZSM5 and GaHZSM5

Kinetic modeling demonstrated, in agreement with the previous proposal [12], that propane transformation over HZSM5 occurs via two routes : (i) in the steps of protolytic cracking and (ii) in the steps of hydrogen transfer between propane and carbonium ions generated from the alkenes produced. The rate constants of the protolytic cracking route were estimated on the basis of the data concerning the formation of the primary products : methane + ethene, hydrogen + propene. The values obtained (Table 1) demonstrate that the cracking of a C-C bond occurs 2.7 times faster than the cracking of a C-H bond as reported by Guisnet et al. [3] for HZSM5 catalysts with different Si/Al ratio.

On the basis of the kinetic modeling results the contribution of hydrogen transfer to the overall propane conversion was established (Figure 4). At propane conversions of 20-40 % this contribution is of about 20 %. It has also been shown that hydrogen transfer plays a very important role in the formation of ethane and butanes. Thus, at high propane conversions, about 50 % of ethane and butanes are formed through this reaction.

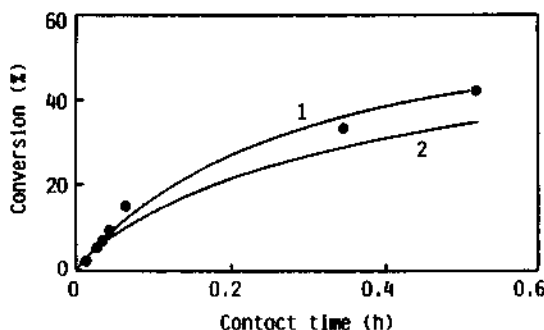


Figure 4. Experimental data (points) and calculated curves for propane conversion over HZSM5. Curve 1 : final description ; curve 2 : rate constants of hydrogen transfer route ( $k_{HT}(n)$ ) are equal to zero.

For propane transformation over GaHZSM5 catalyst we have introduced into the kinetic model, in agreement with the literature data [2,3,15-17], gallium catalyzed steps of dehydrogenation of propane and product  $C_4^+$  alkanes. We performed kinetic modeling of propane conversion and found out that kinetic model describes with good accuracy formation of hydrogen and propene. At the same time, simulated concentrations of methane (Figure 5A : curve 2) and ethane (Figure 5B : curve 2) were found to be essentially lower than experimental concentrations. Then, the reaction step of propane transformation into methane and ethene over gallium catalytic sites was introduced into the kinetic model and the description of methane formation (see Figure 5A : curve 1) was improved. We have therefore concluded that gallium active species participate not only in propane dehydrogenation but also in propane cracking into methane and ethene. Comparison between the rate constants of these reaction steps over gallium catalytic sites appears in Table 1.

Table 1 Rate constants (mol/(g bar h)) of initial steps of propane transformation over HZSM5 and GaHZSM5 catalysts.

Reaction step	HZSM5	GaHZSM5 total	$H^+$	Ga
$C_3 \rightarrow C_1 + C_2^-$	34.6	57.2	34.6	22.6
$C_3 \rightarrow H_2 + C_3^-$	12.6	100.4	12.6	87.8

The above conclusion is further supported by earlier data on propane transformation over pure  $Ga_2O_3$  [15], which demonstrate that the rate of formation of methane and ethene is about 2.5 times lower than the rate of formation of hydrogen and propene. The ability of gallium species to catalyze propane transformation into methane probably results from the strong electron acceptor properties of these species [18]. If so, the mechanism of this reaction can be the same as the one proposed recently by Ono [2] for zinc species in ZnSM5 catalysts.

On the basis of the discrepancy between experimental and calculated data on ethane formation (see Figure 5B), we have concluded that over GaHZSM5 catalyst ethane is produced not only on the zeolite acid sites but on gallium species also through ethene hydrogenation by molecular hydrogen produced during propane aromatization. We carried out kinetic modeling under this assumption and obtained

good agreement between the experimental and the calculated data (see Figure 5B : curve 1). The ability of gallium species to catalyze ethene hydrogenation has been recently confirmed [19].

Gallium species are therefore active not only in the desired dehydrogenation of hydrocarbons (propane into propene, alkenes into dienes, naphthenes into aromatics), as generally considered [2,3], but catalyze also the formation of the main undesired products, namely methane and ethane. It seems probable that these gallium catalyzed reactions are the main reasons for limiting the aromatic selectivity over GaHZSM5 catalysts.

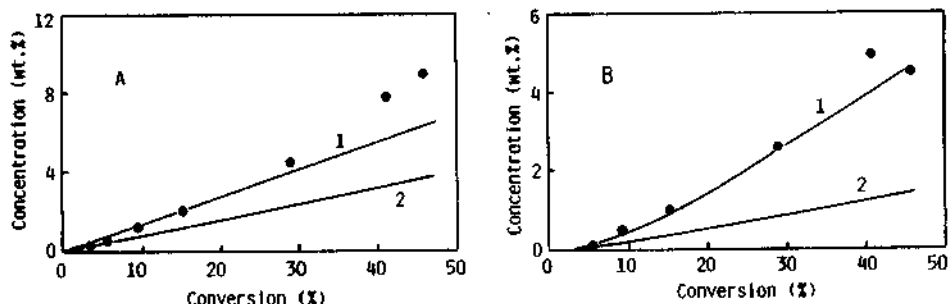


Figure 5. Experimental data (points) and calculated curves for the concentrations of methane (A) and ethane (B) as functions of propane conversion over GaHZSM5. Curves 1 : methane and ethane formation is considered to occur on both zeolite and gallium catalytic sites ; curves 2 : metane and ethane formation is considered to occur only on zeolite acid sites.

### 3. GALLIUM ACTIVE SPECIES. MODIFICATIONS INDUCED BY HYDROGEN TREATMENT

#### 3.1. Dehydrogenating activities of framework and non framework Ga species

All the formulations of Ga MFI catalysts : gallium catalysts prepared by gallium exchange of HZSM5 by the impregnation of this zeolite with gallium salts, by mixing it with  $\text{Ga}_2\text{O}_3$ , gallosilicates, galloaluminosilicates have been found more selective than HZSM5 for alkane aromatization. In principle the location of the gallium species depends on the formulation : exchange position for gallium exchanged zeolite, framework position for gallosilicates or galloaluminosilicates, extraframework position for impregnated ZSM5 samples or for physical mixtures of  $\text{Ga}_2\text{O}_3$  and HZSM5. In fact the situation is more complex. Indeed, ion exchange of high silica zeolites with trivalent ions is very difficult and after calcination treatment the gallium species in the GaZSM5 catalysts prepared by ion exchange or by impregnation are most likely  $\text{Ga}_2\text{O}_3$  deposited in the pores or on the outer surface of the zeolite crystallites [2,3]. Furthermore during the pretreatment, degallification of the framework of gallosilicates or of galloaluminosilicates can occur with formation of extraframework gallium species. Hence all the samples present extraframework gallium species while only gallosilicates and galloaluminosilicates present framework gallium species. Therefore while it can be concluded that extraframework gallium species are active in

dehydrogenation steps nothing can be said concerning the activity of framework gallium species.

To obtain information on this point, a mild treatment (under dry air flow at temperatures  $T_c$  between 803 and 1073 K) was applied to a gallosilicate sample ( $\text{Si}/\text{Ga} = 30$ ) so as to have a limited degallification of the framework. The activity and selectivity of the resulting samples were determined in a flow reactor at 803 K and with a pressure of propane equal to 1 bar. X-ray diffraction showed that, even after calcination at 1073 K the crystallinity of the samples remained high. A small decrease of the unit cell parameters (particularly of the  $a$  parameter) with increasing  $T_c$  was found, which indicates a slight degallification of the framework [20]. Indeed the  $\text{Ga}-\text{O}$  bond is longer than the  $\text{Si}-\text{O}$  bond (1.83 Å instead of 1.63 Å). Furthermore there was a slight decrease in the capacity for nitrogen and 3-methylpentane adsorption when  $T_c$  was increased (about 10 % from 803 to 1073 K), which can be related to a slight collapse of the gallosilicate or/and to a blockage of the access of adsorbates to the pore volume by extraframework gallium species.

Above 873 K,  $T_c$  had a significant positive effect on the activity for propane aromatization (Figure 6). The selectivity to aromatics increased while the one to undesired products (methane + ethane) decreased significantly. The mass aromatics/(methane + ethane) ratio was therefore much greater at 1073 K than at 803 or at 873 K (Figure 6). There was also a large increase in the production of hydrogen : at high conversion, the  $\text{H}_2/\text{aromatic}$  molar ratio was close to 4 for  $T_c = 1073$  K instead of 2 for  $T_c = 803-873$  K.

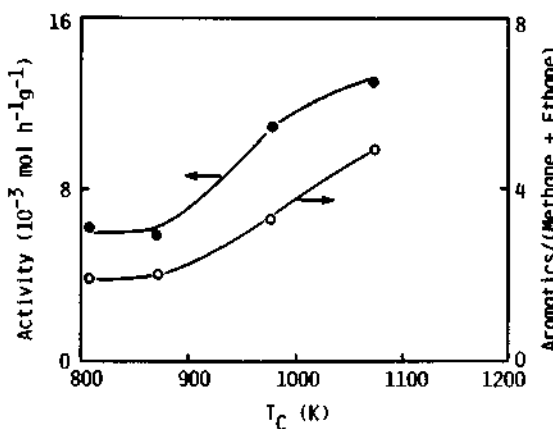


Figure 6. Influence of the temperature of calcination  $T_c$ (K) on the activity of a  $\text{Ga}_2\text{O}_3$ -HZSM5 mixture for propane transformation and on the mass aromatics/(methane + ethane) ratio for a conversion of propane into aromatics of 10%.

All these observations can be related to an increase in the dehydrogenation activity of the gallosilicate. This increase is demonstrated by the significant increase in the initial rate of propane dehydrogenation at 1073 K : this rate was at least 5 times the one found for  $T_c = 803-873$  K. On the other hand,  $T_c$  had practically no effect on the initial rate of propane cracking : thus the rate of methane formation decreased by less than 10 % when  $T_c$  increased from 803 to 1073 K. This decrease could be due to a decrease in the acidity of the gallosilicate caused by extraction of Ga from the framework. Only less than 10 % of gallium would be extracted by treatment at 1073 K.

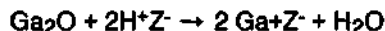
Furthermore for  $T_c = 803\text{-}873\text{ K}$  it was estimated that 20-30 % of propene was formed by dehydrogenation on gallium (and 70-80 % on the acid sites) while for  $T_c = 1073\text{ K}$  this was the case for more than 85 %. Therefore the dehydrogenation of propane on gallium species was at least 15 times faster for  $T_c = 1073\text{ K}$  than for  $T_c = 803\text{-}873\text{ K}$ .

If we suppose that for  $T_c = 803\text{-}873\text{ K}$  there were only framework gallium species and for  $T_c = 1073\text{ K}$  there were framework (90 %) and extraframework species (10 %) it means that extraframework gallium species are at least 150 times more active for propane dehydrogenation than framework species. Therefore, the activity of framework Ga can be questioned [6]. Indeed for  $T_c = 803\text{-}873\text{ K}$  the presence of a very small amount of Ga extraframework species is enough to explain the low dehydrogenating activity. These extraframework Ga species cannot be formed during the pretreatment since the dehydrogenating activity is the same for  $T_c = 803$  and 873 K. They are probably created during the synthesis of the gallosilicate [6].

### 3.2. Modifications Induced by hydrogen treatment

It has been shown that the hydrogen pretreatment of GaZSM5 catalysts has a positive effect on their activity and selectivity for aromatization. This effect could be due to an increase of the dehydrogenating activity of gallium species caused by an increase of their dispersion and/or by their reduction (as shown by various techniques: TPR, X-ray diffraction, STEM, etc [21-24]).

A thorough investigation of the reduction under hydrogen of intimate  $\text{Ga}_2\text{O}_3$ -zeolite mixtures was carried out by Price and Kanizarev [23]. The reduction of  $\text{Ga}_2\text{O}_3$  into  $\text{Ga}_2\text{O}$  occurred at 750-900 K ; however its extent depended very much on the gallium/protonic sites ratio of the catalyst and was limited to one atom of gallium per acid site. It was proposed that the reduction of  $\text{Ga}_2\text{O}_3$  was followed by a reaction between  $\text{Ga}_2\text{O}$  and the protonic sites :



This reaction would be the limiting step of the process, the reduction of  $\text{Ga}_2\text{O}_3$  ceasing when all the acid sites were neutralized. However since the protonic sites are involved in the oligomerization and cyclization steps of the bifunctional pathway, the pronounced neutralization of these sites could cause a decrease in the aromatization although the contrary has been observed. Therefore either the neutralization of the protonic sites or the bifunctional scheme can be questioned [3,7].

That is why we have investigated the effect of hydrogen treatment of a  $\text{Ga}_2\text{O}_3/\text{HZSM5}$  mixture on the protonic acidity [7]. All the conditions (873 K, 10 hours, etc) were chosen following reference 23 so as to obtain the maximum percentage of  $\text{Ga}_2\text{O}_3$  reduction hence the complete neutralization of the acid sites. Two model reactions : n-heptane cracking and metaxylene isomerization at 623 K were used for comparing the protonic activity after treatment under hydrogen or under nitrogen flow. Model reactions have various advantages compared to physicochemical methods which however are more often used for acidity characterization. In particular they can be carried out under conditions close to those of propane aromatization ; they give information specifically on the active acid sites [25]. Two other model reactions : propane and methylcyclohexane transformations at 803 and 773 K were also used to specify the effect of the hydrogen treatment on the dehydrogenating activity of the gallium species [7].

The most significant effect of hydrogen treatment was to increase the dehydrogenating activity of the catalysts. This was shown in particular for reactions carried out at high temperatures. Thus the dehydrogenation of propane into propene and that of methylcyclohexane into C<sub>6</sub>-C<sub>8</sub> aromatics were about 5 times faster after

hydrogen treatment than after nitrogen treatment. Furthermore, the alkene/alkane ratio in the products of methylcyclohexane cracking decreased from 2.1 after nitrogen treatment to 0.9 after hydrogen treatment (Table 2). This decrease can be explained by the hydrogenation of the olefinic cracking products. The hydrogen treatment created also a significant hydrogenolysis activity as shown by the large amount of methane in the cracking products (Table 2) and of benzene in the C<sub>6</sub>-C<sub>8</sub> aromatic products (45 mol % after hydrogen treatment instead of 15 % after nitrogen treatment). Hydrogenolysis was also responsible for methane formation at high propane conversion on the hydrogen treated catalyst.

Table 2 Methylcyclohexane transformation at 773 K over a Ga<sub>2</sub>O<sub>3</sub>/HZSM5 mixture pretreated under nitrogen or hydrogen flow at 873 K. Cracking product distribution (mol %) for a conversion into cracking products of 6.6 %.

Pretreatment	C <sub>1</sub>	C <sub>2</sub>	C <sub>3</sub>	C <sub>4</sub>	C <sub>5</sub>	C <sub>6</sub>	o/s*
N <sub>2</sub>	15.1	17.2	41.0	21.6	3.4	1.7	2.1
H <sub>2</sub>	45.1	14.6	26.1	13.5	0.3	0.4	0.9

\*alkene/alkane ratio

Lastly, hydrogen pretreatment affects also the acid sites. However the decrease in the activity of acid sites caused by hydrogen treatment was much smaller than the decrease of acidity expected from the model proposed by Kanazirev and Price [23]. The acid activity was not totally suppressed but only divided by 1.5 for m-xylene isomerization and by 1.15 for n-heptane cracking. Therefore the increase in the aromatization activity caused by the hydrogen treatment can be explained through the classical bifunctional scheme. This increase is related to the increase in the rate of propane dehydrogenation, which is most likely the limiting step of propane aromatization on GaZSM5 catalysts [3].

## CONCLUSIONS

Kinetic modeling of propane and propene aromatization on HZSM5 and GaHZSM5 catalysts allowed to estimate quantitatively the role of Ga species and of acid sites in the various steps of propane aromatization. Gallium species play a significant role in the dehydrogenation of propane into propene, of oligomers into dienes and of cycloalkenes into aromatics. They catalyze also propane transformation into methane and ethene hydrogenation into ethane. Both reactions appear to be responsible for limiting the aromatic selectivity over GaHZSM5 catalysts.

The effect of the temperature of calcination in dry air on the acid, dehydrogenating and bifunctional activities of a gallosilicate was determined. From this effect it can be concluded that framework gallium species are much less active for dehydrogenation than extraframework species and, indeed, are probably inactive. Model reactions were used to specify the effect of hydrogen pretreatment on the acid and redox properties of GaHZSM5 catalysts. It was thus demonstrated that hydrogen treatment at 873 K provoked a significant increase in the dehydrogenating activity of the gallium species, created a significant hydrogenolysis activity but caused only a small decrease in the protonic activity. The increase in the aromatization activity due to this treatment can be explained through the bifunctional aromatization scheme by an increase in the rate of propane dehydrogenation.

## References

- [1] R.F. Anderson, J.A. Johnson and J.R. Mowry, Paper presented at the AIChE Spring National Meeting, Houston, TX, March 1985.
- [2] Y. Ono, *Catal. Rev.-Sci. Eng.* **1992**, *34*, 179.
- [3] M. Guisnet, N.S. Gnepr and F. Alario, *Appl. Catal., A*, **1992**, *89*, 1.
- [4] D.B. Lukyanov, N.S. Gnepr, M.R. Guisnet, *Ind. Eng. Chem. Res.*, **1994**, *33*, in press.
- [5] D.B. Lukyanov, N.S. Gnepr, M.R. Guisnet, *Ind. Eng. Chem. Res.*, Submitted.
- [6] G. Giannetto, A. Montes, N.S. Gnepr, A. Florentino, P. Carraud and M. Guisnet, *J. Catal.*, **1994**, in press.
- [7] M. Barré, N.S. Gnepr, P. Magnoux, S. Sansare, V.R. Choudhary and M. Guisnet, *Catalysis Letters*, **1993**, *21*, 275.
- [8] D.B. Lukyanov, V.I. Timoshenko, M.G. Slinko, V.V. Vinogradov, *Doklady Phys. Chem. Proc. Acad. Sci., USSR.*, **1985**, *192*.
- [9] R.J. Quann, F.J. Krambeck, in "Chemical Reactions in Complex Mixtures. The Mobil Workshop", A.V. Sapre, F.J. Krambeck, Eds., Van Nostrand Rheinhod, **1991**, 143.
- [10] D.B. Lukyanov, V.I. Shtral, in "Preprints of Symposium on Alkylation, Aromatization, Oligomerization and Isomerization of Short-Chain Hydrocarbons over Heterogeneous Catalysts", ACS Division of Petroleum Chemistry : New-York, **1991**, *36*, 693.
- [11] M.I. Temkin, *Adv. Catal.* **1979**, *28*, 173.
- [12] H. Kitagawa, Y. Sendoda, Y. Ono, *J. Catal.* **1986**, *101*, 12.
- [13] M. Shibata, H. Kitagawa, Y. Sendoda, Y. Ono, in "Proc. 7th Intern. Zeolite Conf.", Y. Murakami, A. Iijima, J.W. Ward, Eds., Kodansha, Tokyo, **1986**, 717.
- [14] P. Meriaudeau, G. Sapaly, C. Naccache, in P.A. Jacobs and R.A. Van Santen (Editors), *Zeolites, Facts, Figures, Future, Studies in Surface Science and Catalysis*, Vol. 49B, Elsevier, Amsterdam, **1989**, p. 1423.
- [15] N.S. Gnepr, J.Y. Doyemet, M. Guisnet, *J. Mol. Catal.*, **1988**, *45*, 281.
- [16] N.S. Gnepr, J.Y. Doyemet, A.M. Seco, F.R. Ribeiro, M. Guisnet, *Appl. Catal.*, **1988**, *43*, 155.
- [17] T. Inui, Y. Makino, F. Okazumi, S. Nagano, A. Miyamoto, *Ind. Eng. Chem. Res.*, **1987**, *26*, 647.
- [18] V.B. Kazansky, L.M. Kustov, A. Yu. Khodakov, in P.A. Jacobs and R.A. Van Santen (Editors), *Zeolites, Facts, Figures, Future, Studies in Surface Science and Catalysis*, Vol. 49B, Elsevier, Amsterdam, **1989**, p. 1173.
- [19] M. Barré, N.S. Gnepr, M. Guisnet, unpublished data, **1993**.
- [20] G. Giannetto, A. Montes, N.S. Gnepr and M. Guisnet, Preprints Symposium on Chemically Modified Molecular Sieves, Division of Petroleum Chemistry, Inc., A.C.S., **1993**, *38(3)*, 559.
- [21] L. Petit, J.P. Bournonville and F. Raatz, in P.A. Jacobs and R.A. Van Santen (Editors), *Zeolites, Facts, Figures, Future, Studies in Surface Science and Catalysis*, Vol. 49B, Elsevier, Amsterdam, **1989**, p. 1163.
- [22] J.F. Joly, H. Ajot, E. Merlen, F. Raatz and F. Alario, *Appl. Catal. A*, **1991**, *79*, 249.
- [23] G.L. Price and V. Kanazirev, *J. Catal.*, **1990**, *126*, 267.
- [24] V. Kanazirev, G.L. Price and K.M. Dooley, in P.A. Jacobs, N.I. Jaeger, L. Kubelkova and B. Wichterlova (Editors), *Zeolite Chemistry and Catalysis, Studies in Surface Science and Catalysis*, Vol. 69, Elsevier, Amsterdam, **1991**, p. 277.
- [25] M. Guisnet, *Acc. Chem. Res.*, **1990**, *23*, 392.

## 4.3 Shape Selective Alkylation of Aromatics on Metallosilicates

T. Yashima<sup>a</sup>, J.-H. Kim<sup>b</sup>, H. Ohta<sup>a</sup>, S. Namba<sup>c</sup>, and T. Komatsu<sup>a</sup>

<sup>a</sup>Department of Chemistry, Tokyo Institute of Technology, Ookayama,  
Meguro-ku, Tokyo 152, Japan

<sup>b</sup>Department of Material Science, Tottori University, Kozan-cho, Tottori 680,  
Japan

<sup>c</sup>Department of Materials, The Nishi-Tokyo University, Uenohara-machi,  
Kitatsuru-gun, Yamanashi 409-01, Japan

### Abstract

The alkylations of toluene with methanol and of ethylbenzene with ethanol on metallosilicates having MFI structure were studied. It was found that the primary product in these alkylations was only para isomer, because the formation of ortho isomer could be depressed through the restricted transition state selectivity in the pore of MFI structure. The strength of acid sites on the metallosilicate can be controlled with the kind of trivalent ions introduced into the zeolite framework with a minor change of the effective pore dimension. The highest para selectivity was observed on arsenosilicate with the weak acid sites on which the alkylation can be accelerated but the isomerization of para isomer produced primarily is scarcely promoted. Therefore, it is concluded that the main factor to obtain the high para selectivity of MFI type zeolite catalyst is the strength of the acid sites.

### 1. INTRODUCTION

It is widely known that HZSM-5 zeolite(aluminosilicate with MFI structure) modified with some kinds of oxides, such as magnesium, boron and phosphorous oxides, exhibit a high para selectivity for alkylation[1-4] or disproportionation[5-7] of alkylbenzenes, such as toluene and ethylbenzene. It is expected that the strength of acid sites was weakened and also the effective pore dimension was narrowed by this modification. Kaeding et al. proposed that the high para selectivity of the modified HZSM-5 zeolite for the alkylation[2] and the disproportionation[5-6] was due to the product selectivity, namely the difference of intracrystalline diffusivity between para isomer and other two isomers(ortho and meta) of dialkylbenzene produced was enlarged much more by the modification. Olson and Haag

reported the evidence for diffusion control of para selectivity in the case of disproportionation of toluene on modified HZSM-5 zeolites[7].

Paparatt et al. reported that para isomer formed selectively inside the pore of MFI type zeolite in the alkylation of toluene with ethanol, while the isomerization of p-ethyltoluene was accelerated by the acid sites on the external surface of zeolite crystallite. And the improvement of para selectivity by the modification was due to the selective poisoning of the acid sites on the external surface[8].

We have proposed[1, 3-4] that a primary product in these alkylations on MFI type zeolite catalysts is only para dialkylbenzene due to the restricted transition-state selectivity, namely the transition-state to form para isomer is smaller than that to form ortho isomer. The improvement in para selectivity by the modification of HZSM-5 with oxides was due to the depression of the isomerization of para isomer produced primarily. Namely, such modification resulted in a reduction of acid strength, so on the reduced acid sites the alkylation could be promoted but the isomerization could not be accelerated. Recently, some researchers supported our proposal[9-12].

On the other hand, metallosilicates are prepared by the isomorphous substitution of other elements, such as B, Be, Cr, Fe, Ga, Ti, etc., for aluminium in the zeolite framework[13]. Several kinds of metallosilicates with MFI structure have been synthesized[14]. Since trivalent ions, such as aluminium ions, replace tetravalent silicone ions at the tetrahedral framework positions, the framework bears a net negative charge, which must be compensated for by counter cations. When the counter cations are protons, Bronsted acid sites occur in metallosilicates including trivalent ions in the framework. The strength of Bronsted acid sites on the metallosilicates with MFI structure changes with the kinds of trivalent ions introduced into the framework[14-16]. Therefore, we can get the zeolite catalysts with MFI structure having various strength of Bronsted acid sites and nearly same effective pore dimension.

In this paper, we aim to clarify the reason why the metallosilicate catalysts with MFI structure exhibit a high para selectivity for the alkylations of toluene with methanol and of ethylbenzene with ethanol.

## 2. EXPERIMENTAL METHODS

### 2.1. Preparation of catalysts

ZSM-5(aluminosilicate, Al-Sil, Si/Al=80), gallosilicate(Ga-Sil, Si/Ga=64), borosilicate(B-Sil, Si/B=70) and ferrisilicate(Fe-Sil, Si/Fe=56) were synthesized hydrothermally. Antimonosilicate(Sb-Sil, Si/Sb=120) and arsenosilicate(As-Sil, Si/As=92) were prepared by the atom-planting method[17-18]. These metallosilicates were ion-exchanged with  $\text{NH}_4^+$  and were converted to proton form by calcination at 773K for 2h. The proton type Al-Sil modified with B or P oxide were prepared by the impregnation method[3-4]. And also the modification of steaming was done with steam at 1223K for 1h[3-4].

## 2.2. Determination of strength of acid sites

The acidic properties of metallosilicates were measured by IR and NH<sub>3</sub>-TPD methods. In infrared measurements, we weighed a 20 mg of the metallosilicate powder, and then pressed into a 15 mm diameter self-supported wafer. This wafer was placed in the IR cell and evacuated at 773K for 1.5h before measurements. In observations of adsorbed pyridine on samples, a wafer evacuated at 773K for 1.5h was exposed to pyridine vapor(1.3kPa) at 423K for 1h, then the IR cell was evacuated at 423K for 1h. All IR spectra were recorded at room temperature.

Ammonia-TPD experiments were performed using a conventional static-adsorption system connected to a quadrupole mass spectrometer through a high vacuum line. Sample evacuated at 773K for 1h were exposed to ammonia(21kPa) at 423K for 0.5h, evacuated at 423K for 1h, and then cooled to room temperature. Spectra were obtained at a heating rate of 10K min<sup>-1</sup> from 323 to 823K. In general, the peak position in NH<sub>3</sub>-TPD corresponds intrinsically to the acid strength of catalysts, but sometimes shifts to higher temperatures due to the re-adsorption of ammonia desorbed. In this study, NH<sub>3</sub>-TPD measurements were performed using a same amount of the trivalent ion in the zeolite framework, that is a same amount of acid sites, by adjusting the weight of each sample to minimize the re-adsorption effects. We used the peak temperature in NH<sub>3</sub>-TPD spectrum, T<sub>max</sub>, as a parameter of the strength of acid sites on the metallosilicate.

## 2.3. Determination of effective pore dimension

The effective pore dimension of each metallosilicate was measured by a relative adsorption rate of o-xylene as follows. Gravimetric measurements of o-xylene adsorption were performed by using a highly sensitive thermal balance under 0.48kPa of o-xylene at 393K. The time to reach 30% of amount of o-xylene adsorbed at infinite time, t<sub>0.3</sub>, corresponds to the diffusivity of o-xylene[7]. We used the value of t<sub>0.3</sub> as a parameter of the effective pore dimension[4, 19-22].

## 2.4. Alkylation

The alkylations of toluene with methanol and of ethylbenzene with ethanol were carried out with a continuous flow reactor system at 673K under atmospheric pressure. The partial pressure of each reactant was same, 20kPa, and helium was used as a carrier gas.

In this study, the para selectivity of metallosilicate catalysts is defined as a fraction of para isomer in the dialkylbenzenes produced.

## 3. RESULTS AND DISCUSSION

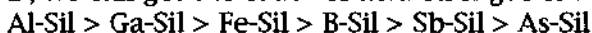
### 3.1. Characterization of metallosilicate catalyst

It is confirmed by XRD measurements that all metallosilicates prepared has MFI structure. In IR spectra of all metallosilicates we observed the absorption band attributed to the acidic silanol group between 3600 and

$3700\text{ cm}^{-1}$  which were confirmed by the adsorption of pyridine. Namely, one of the absorption bands appeared between  $3600$  and  $3700\text{ cm}^{-1}$  disappeared and a new band attributed to the pyridinium ion at  $1540\text{cm}^{-1}$  appeared when pyridine was adsorbed on each metallosilicate. From these results it is concluded that the trivalent ions, such as  $\text{Al}^{3+}$ ,  $\text{Ga}^{3+}$ ,  $\text{B}^{3+}$ ,  $\text{Fe}^{3+}$ ,  $\text{Sb}^{3+}$ , and  $\text{As}^{3+}$ , can be successfully inserted into the zeolite framework.

The absorption band attributed to the acidic silanol group appears at the higher wavenumber when the strength of Bronsted acid sites is the weaker[23]. The wavenumber of the absorption band of each metallosilicate is shown in Table 1.

The strength of acid sites on the metallosilicates were also measured by  $\text{NH}_3\text{-TPD}$  method. Each metallosilicate has a peak at a characteristic temperature in its  $\text{NH}_3\text{-TPD}$  profile. These results are shown in Table 1. When the acid strength of the metallosilicate is the weaker, the peak in spectrum appears at the lower temperature. From the results of IR and  $\text{NH}_3\text{-TPD}$ , we can get the order of acid strength of metallosilicates, as follows;



The value of  $t_{0.3}$  of metallosilicates were shown in Table 1. When this value is the larger, the effective pore dimension of metallosilicate is the narrower. The effective pore dimension of the metallosilicates prepared by hydrothermal synthesis, Al-Sil, Ga-Sil, Fe-Sil, and B-Sil, were almost the same( $t_{0.3}=1.4$  -  $3.5$  min). On the other hand, the effective pore dimension of Sb-Sil( $t_{0.3}=14.7$  min) and As-Sil( $t_{0.3}=12.1$  min) prepared by the atom-planting method were slightly narrower than those of metallosilicates prepared hydrothermally. By atom-planting method, a part of the trivalent ions was also introduced out of zeolite framework[16,24]. These trivalent ions would make narrow the effective pore dimension. In HZSM-5 modified by oxides which showed high para selectivity for the alkylation of ethylbenzene with ethanol,  $t_{0.3}$  values could not be determined too long time to obtain the amount of o-xylene adsorbed at infinite time[4].

Table 1 Characterization of various metallosilicates

Metallo-silicate	Si/Me atomic ratio	Acid strength $T_{\max}/\text{K}$	Effective pore dimension $t_{0.3}/\text{min}$
Al-	80	570	3610
Ga-	64	530	3625
Fe-	56	520	3630
B-	70	510	-----
Sb-	120	490	3655
As-	92	460	3678

### 3.2. Alkylation of toluene with methanol

In this reaction, the substitution of methyl group occurs preferentially at ortho and para position of benzene ring on the acid catalysts. It is expected that the primary products are ortho and para xylenes. Figure 1 shows the effect of contact time on the distribution of xylene isomer produced on HZSM-5 catalyst. At the shorter contact time, W/F, we can observe the higher fraction of para isomer and the lower fractions of ortho and meta isomers. Therefore, it is suggested that a primary product is only p-xylene on HZSM-5 catalyst. This result shows that the formation of o-xylene by the alkylation is depressed. However, the isomerization of p-xylene to o- and m-xylanes proceeds at the longer contact time. From these results it can be concluded that in the alkylation of toluene with methanol the formation of o-xylene is depressed through the restricted transition state selectivity, because the size of transition state to form o-xylene is larger than that to form p-xylene. On the other hand, the isomerization of p-xylene to o- and m-xylanes proceeds without any difficulties, because isomerization of xylene can proceed through the mono-molecular mechanism.

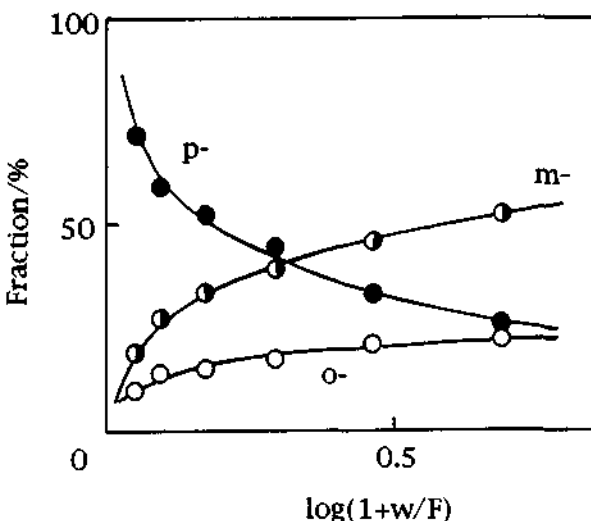


Fig. 1 Effect of W/F on the distribution of xylene isomers produced at 673K over HZSM-5 in the alkylation of toluene with methanol

The results of the alkylation of toluene with methanol on various metallosilicates are shown in Table 2. In order to compare the para selectivities of these catalysts, an almost same yield of xylene(ca. 20%) was achieved by adjusting W/F. The para selectivities of metallosilicates were higher than that of HZSM-5. Especially, As-Sil exhibited a high para

selectivity. In order to clarify what is a main factor to get such high para selectivity, the relationship between the para selectivity and the effective pore dimension or the strength of acid sites will be discussed.

Table 2 Para-selectivity of metallosilicates in the alkylation of toluene with methanol.

Metallo-silicate	W/F /g h mol <sup>-1</sup>	Xylene yield/%	Para-selectivity/%
Al-	0.59	20.9	45.0
Ga-	0.59	21.6	51.9
B-	5.88	19.1	55.0
Sb-	2.06	19.8	71.7
As-	2.06	20.7	81.1

Figure 2 shows the relationship between the para selectivity and the effective pore dimension,  $t_{0.3}$ . It could be observed to have some connection between them. Namely, the para selectivity increased with increasing  $t_{0.3}$  value, that is, decreasing the effective pore dimension.

The relationship between the para selectivity and the strength of acid

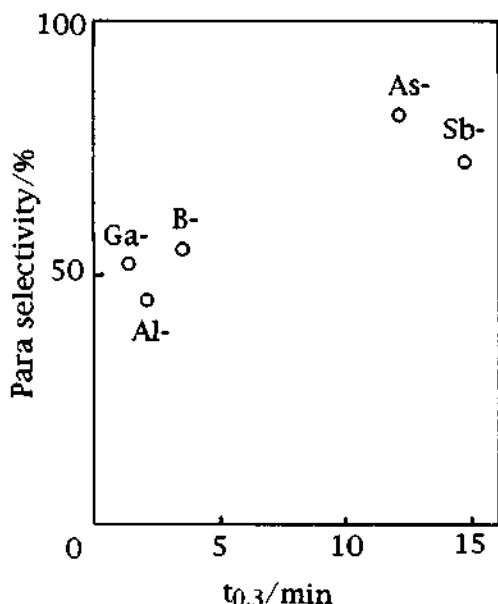


Fig. 2 Relationship between para selectivity and effective pore dimension( $t_{0.3}$ )

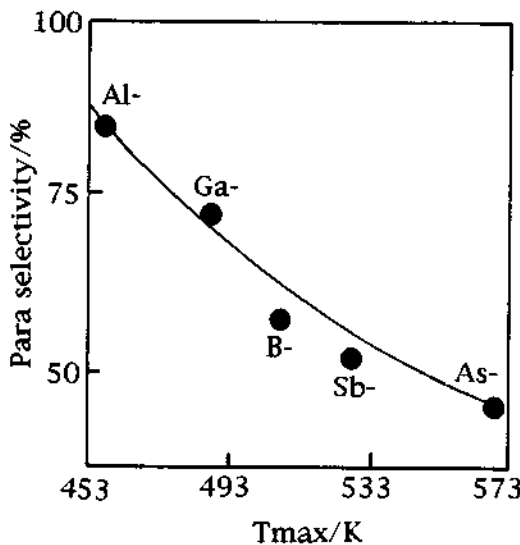


Fig. 3 Relationship between para selectivity and strength of acid sites( $T_{\text{max}}$ )

sites,  $T_{max}$ , is shown in Fig. 3. We observed good relationship between them. Namely, the para selectivity increased with weakening the strength of acid sites. From these results, it can be concluded that the strength of acid sites is concerned with the para selectivity more closely than the effective pore dimension.

On the other hand, the isomerization of o-xylene on metallosilicates is studied. When the effective pore dimension is a main factor to get high para selectivity, namely p-xylene can go out preferentially through the narrowed pore window, the activity for the xylene isomerization must be maintained at high level, because o- and m-xylenes remained in the zeolite pore must be isomerized quickly to p-xylene. Figure 4 shows the relationship between the activity or the apparent activation energy and the strength of acid sites. On the weaker acid sites, the lower activity and the higher activation energy for o-xylene isomerization were observed. Therefore, it is concluded on the weak acid site the isomerization of p-xylene produced primarily hardly occurs, so As-Sil having the weakest acid sites exhibits the highest para selectivity in our metallosilicates.

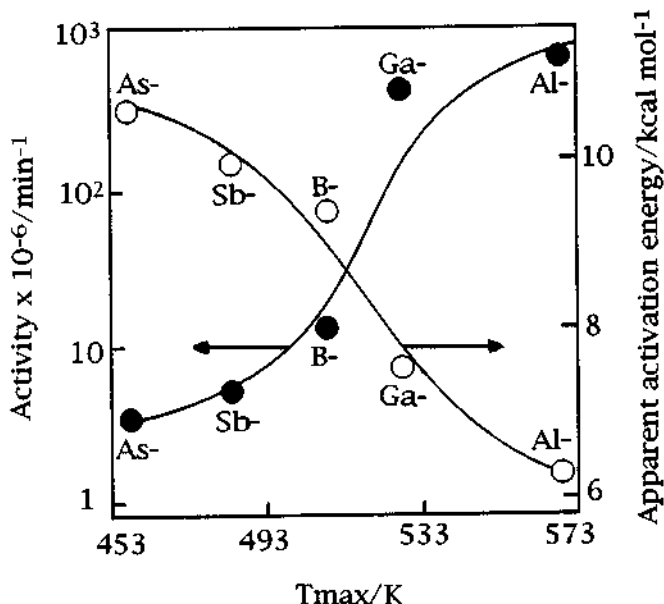


Fig. 4 Relationship between activity or apparent activation energy for isomerization of o-xylene and acid strength( $T_{max}$ )

### 3.3. Alkylation of ethylbenzene with ethanol

The alkylation of ethylbenzene with ethanol on metallosilicates is also studied. The main differences between ethylbenzene alkylation and toluene alkylation are size of substitution groups, ethyl and methyl, and the mechanism of isomerization of primary product. Namely, ethyl group is

larger than methyl group and the isomerization of diethylbenzene does not proceed through mono-molecular mechanism, but proceeds through di-molecular mechanism.

Figure 5 shows the effect of contact time on the distribution of diethylbenzene isomer produced on HZSM-5 catalyst. In this alkylation, para isomer was also a primary product and the formation of ortho isomer was depressed so much through the restricted transition state selectivity in both of alkylation and isomerization.

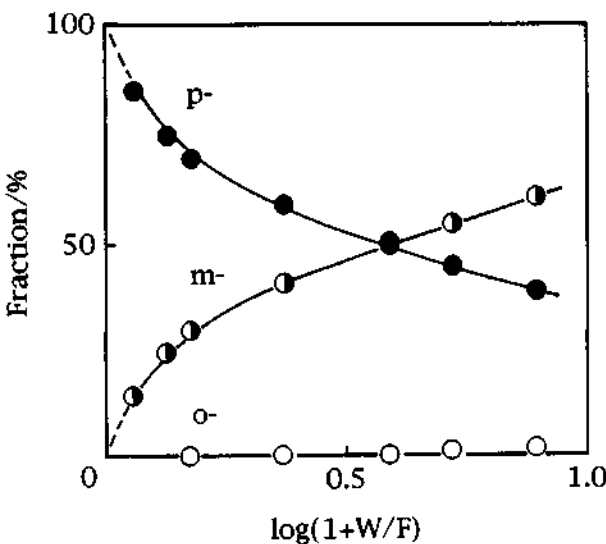


Fig. 5 Effect of W/F on the distribution of diethylbenzene isomers produced at 673K over HZSM-5 in ethylbenzene alkylation with ethanol

The results of the alkylation of ethylbenzene with ethanol on various metallosilicates and modified HZSM-5 catalysts are shown in Table 3. At an almost constant yield of diethylbenzene(15-20%), the para selectivities of metallosilicates and modified HZSM-5 catalysts were higher than that of HZSM-5. On the metallosilicates the order of the para selectivity agreed with that in the alkylation of toluene with methanol. Table 3 Para-selectivity of various catalysts with MFI structure

The relationship between the para selectivity and the effective pore dimension,  $t_{0.3}$ , is shown in Fig. 6. In this case, it could be observed to have some connection between them in the similar manner to the case of toluene alkylation.

The relationship between the para selectivity and the strength of acid sites,  $T_{\max}$ , is shown in Fig. 7. We observed a good relationship between

them including the plots on the modified HZSM-5 catalysts. From these results, it is concluded that the strength of acid sites is concerned with the

Table 3 Para-selectivity of various catalysts with MFI structure in the alkylation of ethylbenzene with ethanol.

Catalyst	W/F /g h mol <sup>-1</sup>	Diethylbenzene yield/%	Para- selectivity/%
Al-	3.57	19.8	43.2
Ga-	1.07	16.9	59.6
Fe-	7.14	16.5	61.0
B-	7.14	16.6	70.3
Sb-	7.14	15.0	90.4
As-	7.14	15.3	94.1
B-(3)Al-	3.57	18.8	55.3
P(1)Al-	3.57	20.1	49.3
Stm.Al-	21.4	15.1	84.5

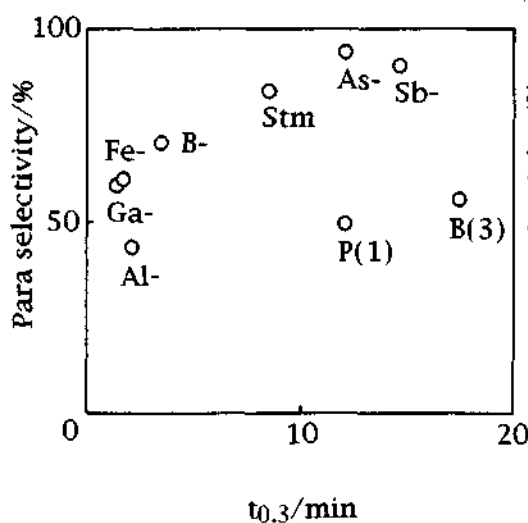


Fig. 6 Relationship between para selectivity and effective pore dimension( $t_{0.3}$ )

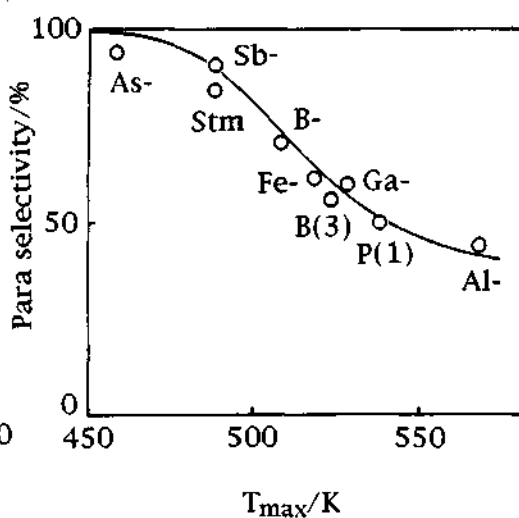


Fig. 7..Relationship between para selectivity and strength of acid sites( $T_{\text{max}}$ )

para selectivity much more closely than the effective pore dimension.

On As-Sil having the highest para selectivity in our metallosilicates, the isomerization of p-diethylbenzene primarily produced hardly proceeded even at the longer contact time as shown in Fig. 8. From these results, it is concluded that the strength of acid sites is the most important factor to obtain a high para selectivity. Namely, to prepare the high para selective catalyst, the strength of acid sites on MFI type zeolites must be controlled to be able to promote the alkylation but not to accelerate the isomerization.

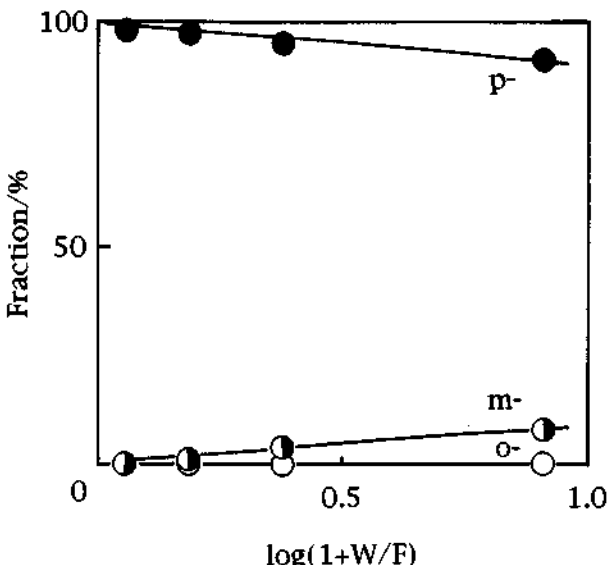


Fig. 8 Effect of W/F on the distribution of diethylbenzene isomers produced at 673K over Sb-Sil in ethylbenzene alkylation with ethanol

#### 4. CONCLUSION

The strength of acid sites on the metallosilicates can be controlled with choosing the kind of trivalent ions introduced into the zeolite framework with only a minor change of the effective pore dimension. By using these metallosilicates as a catalyst for the alkylations of toluene with methanol and of ethylbenzene with ethanol, it is found that a primary product is only para isomer and the formation of ortho isomer is depressed through the restricted transition state selectivity. It is concluded that the main factor to get the high para selective catalyst with MFI structure is the strength of acid sites. Namely, in order to prepare the high para selective catalyst with MFI structure must be controlled to be able to promote the alkylation but not to accelerate the isomerization of para isomer produced primarily,

## 5. REFERENCES

- 1 T. Yashima, Y. Sakaguchi and S. Namba, *Stud. Surf. Sci. Catal.*, **1981**, 7, 739
- 2 W.W. Kaeding, C. Chu, L.B. Young, B. Weinstein and J. Butter, *J. Catal.*, **1981**, 67 159
- 3 J.-H. Kim, S. Namba and T. Yashima, *Bull. Chem. Soc. Jpn.*, **1988**, 61, 1051
- 4 J.-H. Kim, S. Namba and T. Yashima, *Stud. Surf. Sci. Catal.*, **1989**, 46, 71
- 5 W.W. Kaeding, C. Chu, L.B. Young and S.A. Butter, *J. Catal.*, **1981**, 69, 392
- 6 W.W. Kaeding, *J. Catal.*, **1985**, 95, 512
- 7 D.H. Olson and W.O. Haag, in T.E. Whyte (ed.) *Catalytic Materials*, ACS Symp. Ser. 248, ACS Washington D.C., 1984, p.275
- 8 G. Paparatto, E. Moretti, G. Leofanti and F. Gatti, *J. Catal.*, **1987**, 105, 227
- 9 F. Lonyi, J. Engelhardt and D. Kallo, *Stud. Surf. Sci. Catal.*, **1989**, 49, 1357
- 10 F. Lonyi, J. Engelhardt and D. Kallo, *Zeolites*, **1991**, 11, 169
- 11 P.A. Parikh and N. Subrahmanyam, *Catal. Lett.*, **1992**, 14, 107
- 12 K.H. Chandevvar, S.G. Hedge, S.B. Kulkarni, P. Ratnasamy, G. Chitlangia, A. Singh and A.V. Deo, in D. Olson and A. Bisio (eds.) *Proc. 6th Int. Zeolite Conf.*, Butterworth, Guilford, UK, 1984, p.325
- 13 R.M. Barrer, in *Hydrothermal Chemistry of Zeolites*, Academic Press, London, UK, 1982, p.251
- 14 N. Tielen, M. Geelen and P.A. Jacobs, *Acta Phys. Chem.*, **1985**, 31, 1
- 15 C.T.-W. Chu and C.D. Chang, *J. Phys. Chem.*, **1985**, 89, 1569
- 16 K. Yamagishi, S. Namba and T. Yashima, *Bull. Chem. Soc. Jpn.*, **1991**, 64, 949
- 17 K. Yamagishi, S. Namba and T. Yashima, *Stud. Surf. Sci. Catal.*, **1989**, 49, 459
- 18 J.-H. Kim, K. Yamagishi, S. Namba and T. Yashima, *J. Chem. Soc., Chem. Commun.*, **1990**, 1793
- 19 J.-H. Kim, S. Namba and T. Yashima, *Appl. Catal.*, **1993**, 100, 27
- 20 J.-H. Kim, S. Namba and T. Yashima, *Appl. Catal.*, **1992**, 83, 51
- 21 J.-H. Kim, S. Namba and T. Yashima, *Zeolites*, **1991**, 11, 59
- 22 J.-H. Kim, H. Ohta, S. Namba and T. Yashima, *Stud. Surf. Sci. Catal.*, **1993**, 75, 1685
- 23 D. Barthomeuf, *Stud. Surf. Sci. Catal.*, **1980**, 5, 55
- 24 K. Yamagishi, S. Namba and T. Yashima, *J. Catal.*, **1990**, 121, 47

This Page Intentionally Left Blank

## 4.4 Alkylation of Naphthalene with Propene to 2,6-Diisopropynaphthalene on Mordenite Catalysts

E. Kikuchi\*, K. Sawada, M. Maeda, and T. Matsuda

Department of Applied Chemistry, School of Science & Engineering, Waseda University,  
3-4-1 Okubo, Shinjuku-ku, Tokyo 169, JAPAN

### ABSTRACT

Liquid phase alkylation of naphthalene with propene was investigated using silica-alumina and mordenite as catalysts. 2,6- and 2,7-diisopropynaphthalene (DIPN) were selectively and equally formed on silica-alumina catalyst, indicating that DIPN isomers with isopropyl groups at  $\beta$  positions would be thermodynamically more stable than those at  $\alpha$  positions. The selectivity of mordenite for 2,6-DIPN was higher than that for 2,7-DIPN, and it increased with increasing  $\text{SiO}_2/\text{Al}_2\text{O}_3$  ratio. The increased selectivity for 2,6-DIPN is attributed to the reduced contribution of external acid sites. The high selectivity of mordenite for the production of 2,6-DIPN seems to be caused by product molecular shape selectivity.

### 1. INTRODUCTION

Alkylation of naphthalene and/or 2-methylnaphthalene (2-MN) on various zeolite catalysts was reported by Fraenkel et al. [1] and Weitkamp et al. [2]. A high selectivity for the formation of 2,6- and 2,7-dimethylnaphthalene (DMN) was observed with ten-membered ring zeolites such as ZSM-5. We showed in our previous papers [3,4] that 2-MN was selectively disproportionated to 2,6- and 2,7-DMN on ZSM-5 catalyst, although 2,7-DMN was formed in a slightly higher proportion than 2,6-DMN. It was reported [5] that 2,6-DMN was more selectively formed on mordenite than on ZSM-5, and the selectivity for 2,6-DMN increased with increasing  $\text{SiO}_2/\text{Al}_2\text{O}_3$  ratio and with the degree of proton exchange. However, the catalytic activity of mordenite for disproportionation of 2-MN was low, and was rapidly deteriorated with time on stream. It was reported [6-8] that mordenite catalyst was active and selective to produce 4,4'-diisopropylbiphenyl by liquid phase alkylation of biphenyl with propene. Lee and co-workers [7] showed that the amount of deposited coke was reduced by an increase in  $\text{SiO}_2/\text{Al}_2\text{O}_3$  molar ratio, and catalyst deactivation could be prevented using mordenite dealuminated with HCl and subsequently with  $\text{HNO}_3$ . It was reported by Katayama et al. [8] that 2,6-diisopropynaphthalene (2,6-DIPN) was selectively produced on H-mordenite in liquid phase alkylation of naphthalene with propene.

In this paper, we describe the catalytic performance of H-mordenites with different  $\text{SiO}_2/\text{Al}_2\text{O}_3$  ratios for alkylation of naphthalene with propene to 2,6-DIPN in comparison with that of silica-alumina.

## 2. EXPERIMENTAL

### 2.1 Catalyst

H-mordenites ( $\text{SiO}_2/\text{Al}_2\text{O}_3=10, 15$ ) were supplied by the Catalysis Society of Japan. Sodium-type mordenite ( $\text{SiO}_2/\text{Al}_2\text{O}_3=20$ ) supplied by Tosoh Corp. was exchanged 5 times with 0.1N  $\text{NH}_4\text{Cl}$  solution at 70°C for 6 h. Thus obtained ammonium-type mordenite was calcined at 540°C for 4 h to form the proton-type. H-mordenites are abbreviated to HM(10), HM(15), and HM(20). The value in parenthesis represents the  $\text{SiO}_2/\text{Al}_2\text{O}_3$  molar ratio. HM(68) was obtained by dealumination of HM(20) using 5N HCl solution at 98°C for 5 h. Silica-alumina ( $\text{SiO}_2/\text{Al}_2\text{O}_3=12$ ) was purchased from Nikka Seiko Co., Ltd.

### 2.2 Apparatus and Procedures

The catalytic study was carried out at 250°C using a suspension of catalyst in n-tridecane as a liquid medium. The liquid phase reactor was a stainless steel autoclave, having an internal volume of 388ml, equipped with a stirrer. The reactor containing 1.2 g of catalyst, 45 mmol of naphthalene, and 40 ml of n-tridecane was heated to 250°C in nitrogen atmosphere and then 45 mmol of propene was admitted. Liquid products were analyzed by means of FID gas chromatography using TC-17 glass capillary separation column with temperature programmed heating from 150 to 230°C.

## 3. RESULTS AND DISCUSSION

### 3.1 Catalytic Performance of Silica-alumina

Silica-alumina catalyst was used to investigate the nonselective features of catalytic conversion of naphthalene and propene. On this catalyst, isopropyl naphthalene (IPN), diisopropyl naphthalene (DIPN), and triisopropyl naphthalene (TIPN) were formed at 250°C. The composition of IPN isomers produced is shown in Fig. 1. 1-IPN was more selectively formed at the initial stage of run than 2-IPN. The selectivity for 1-IPN decreased from 61 to 7% and that for 2-IPN increased from 39 to 93% with increasing conversion level. These results indicate that 2-IPN is thermodynamically more stable than 1-IPN.

The high selectivity of 1-IPN at low conversion level seems to be explained by taking the stability of carbocation intermediates leading to IPN into consideration. Either intermediate for 1-IPN or that for 2-IPN has five resonating structures. The resonating structure with benzene ring structure is most stable among them. The carbocation intermediate for 1-IPN gives two such resonating structures, while one resonating structure is possible for 2-IPN. Thus, the carbocation intermediate for 1-IPN seems to be more stable than that for 2-IPN.

Figure 2 shows the variation in composition of DIPN isomers produced on silica-alumina as a function of the conversion level of naphthalene. At low conversion levels, 2,6- and 2,7-DIPN were formed with low selectivity, while DIPN isomers with isopropyl groups at  $\alpha$ - $\alpha$  and  $\alpha$ - $\beta$

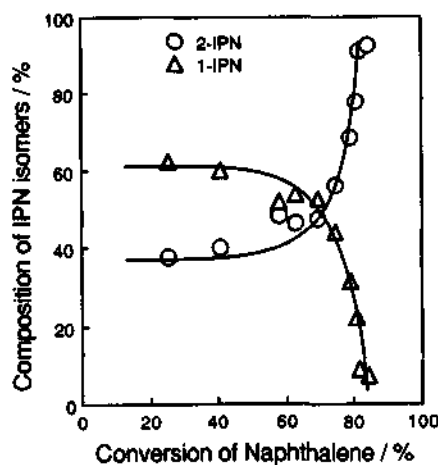


Figure 1. Composition of IPN isomers produced by alkylation of naphthalene with propene on silica-alumina catalyst

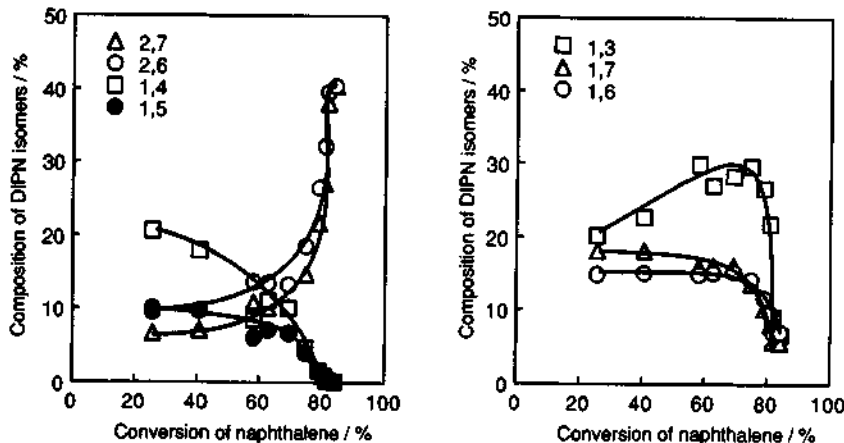


Figure 2. Composition of DIPN isomers produced by alkylation of naphthalene with propene on silica-alumina catalyst.

positions such as 1,3-, 1,4-, 1,6-, and 1,7-DIPN were selectively formed. The 2,6- and 2,7-DIPN selectivities increased with increasing level of naphthalene conversion. However, there was no appreciable difference in selectivity for 2,6- and 2,7-DIPN production on this catalyst.

Figure 3 shows the results of isomerization of DIPN. Here, we used a mixture of DIPN isomers: 18.8% 2,6-, 15.3% 2,7-, 20.6% 1,3-, 14.5% 1,6-, 17.7% 1,7-, 4.1% 1,5-DIPN, 1.4% other C<sub>16</sub> aromatics. The proportions of 2,6- and 2,7-DIPN increased and those of the DIPN isomers having isopropyl groups at  $\alpha$ - $\alpha$  and  $\alpha$ - $\beta$  positions decreased with reaction time, and reached to a definite composition. As shown in Figs. 2 and 3, alkylation of naphthalene and isomerization of DIPN mixture gave a similar composition of DIPN isomers. Thus, about 40% of 2,6- and 2,7-DIPN in DIPN isomers at 250°C are considered to be equilibrium concentrations.

### 3.2 Catalytic Activity and Selectivity of Mordenite

The catalytic activities and selectivities of HM for alkylation of naphthalene with propene were compared with those of silica-alumina. Typical results are summarized in Table 1. Silica-alumina catalyst was more active for this reaction than HM catalysts, although the acidity of silica-alumina was lower than those of HM. Thus, it is indicated that the activity of HM catalysts for this reaction is controlled by diffusion of naphthalene into the pore. The SiO<sub>2</sub>/Al<sub>2</sub>O<sub>3</sub> molar ratio hardly affected the catalytic activity of HM in the range from 10 to 20, while HM(68) showed the lowest activity among the HM, due to its less acidic property.

The selectivities for alkylated products markedly varied from one catalyst to another. The consecutive alkylation of DIPN to TIPN took place on silica-alumina, while this reaction was retarded on HM catalysts probably due to their shape selective property.

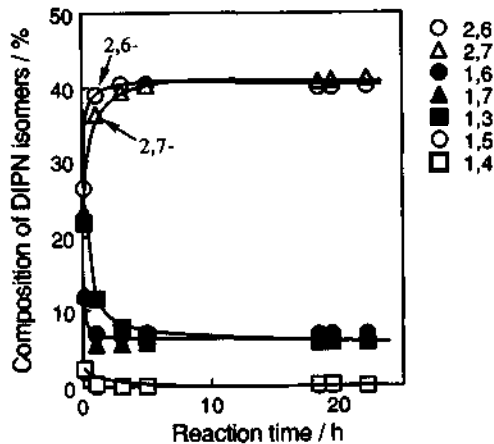


Figure 3. Composition of DIPN isomers produced by isomerization of DIPN mixture on silica-alumina at 250°C.

Table 1. Catalytic activity of  $\text{SiO}_2\text{-Al}_2\text{O}_3$  and HM for alkylation of naphthalene with propene.

Catalyst	$\text{SiO}_2\text{-Al}_2\text{O}_3$	HM10		HM15		HM20		HM68	
Reaction time / min.	60	60	240	60	180	60	240	60	240
Conversion / %	76.8	57.8	74.2	61.7	73.9	52.6	69.8	31.5	60.7
Yield / %									
IPN	38.9	41.1	46.8	42.9	45.8	40.4	46.5	25.9	41.2
DIPN	30.0	15.0	23.9	17.1	25.2	12.2	22.3	5.6	19.0
TIPN	7.9	1.7	3.5	1.7	2.9	0.0	1.0	0.0	0.5

The selectivity for TIPN decreased with increasing  $\text{SiO}_2/\text{Al}_2\text{O}_3$  molar ratio, and consequently TIPN was hardly formed on HM(68).

HM catalysts were more selective for 2-IPN production than silica-alumina. The selectivity for 2-IPN varied with  $\text{SiO}_2/\text{Al}_2\text{O}_3$  molar ratio. Figure 4 shows the variation in percentage of 2-IPN in IPN isomers produced on HM catalysts as a function of the conversion level of naphthalene. HM(68) showed high selectivity for 2-IPN production in the whole range of conversion level. The molecular dimension of 2-IPN is smaller than 1-IPN, so that HM(68) is considered to be more shape selective than HM catalysts with lower  $\text{SiO}_2/\text{Al}_2\text{O}_3$  ratios.

There are ten isomers of DIPN, and these isomers can be classified into three groups based on the position of isopropyl groups:

$\alpha-\alpha$ : 1,4-, 1,5-, and 1,8-DIPN

$\alpha-\beta$ : 1,2-, 1,3-, 1,6-, and 1,7-DIPN

$\beta-\beta$ : 2,3-, 2,6-, and 2,7-DIPN

DIPN isomers having isopropyl groups at  $\beta$ -positions are of the smallest molecular dimension, and those at  $\alpha$ -positions are of the largest. Thus, it is expected that HM(68) catalyst will show the highest selectivity for the production of  $\beta-\beta$  isomers. Figure 5 shows the variation in composition of DIPN isomers as a function of the conversion level of naphthalene. The selectivities for 2,6- and 2,7-DIPN isomers, especially for 2,6-DIPN, increased with  $\text{SiO}_2/\text{Al}_2\text{O}_3$  ratios. The high selectivity of HM(68) for 2,6-DIPN production was independent of the level of naphthalene conversion.

We showed in our previous paper [4] that the selectivity of H-ZSM-5 for the production of 2,6-dimethylnaphthalene by disproportionation of 2-methylnaphthalene was strongly influenced by the presence of external acid sites. In order to investigate the effect of external acid sites on 2,6-DIPN production, the bulk and surface  $\text{SiO}_2/\text{Al}_2\text{O}_3$  ratios were determined by means of XRF, NMR, and XPS. In the cases of HM(10), HM(15), and HM(20), no appreciable difference was observed between the surface and bulk  $\text{SiO}_2/\text{Al}_2\text{O}_3$  ratios, determined by XPS and other measurements, respectively. In contrast, there were great discrepancies in the surface and bulk  $\text{SiO}_2/\text{Al}_2\text{O}_3$  ratios of HM(68), determined as 120 and 69, respectively. These results indicate that contribution

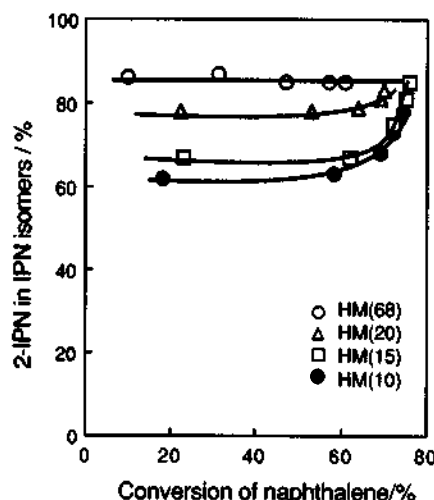


Figure 4. Percentage of 2-IPN in IPN isomers produced by alkylation of naphthalene with propene on HM catalysts.

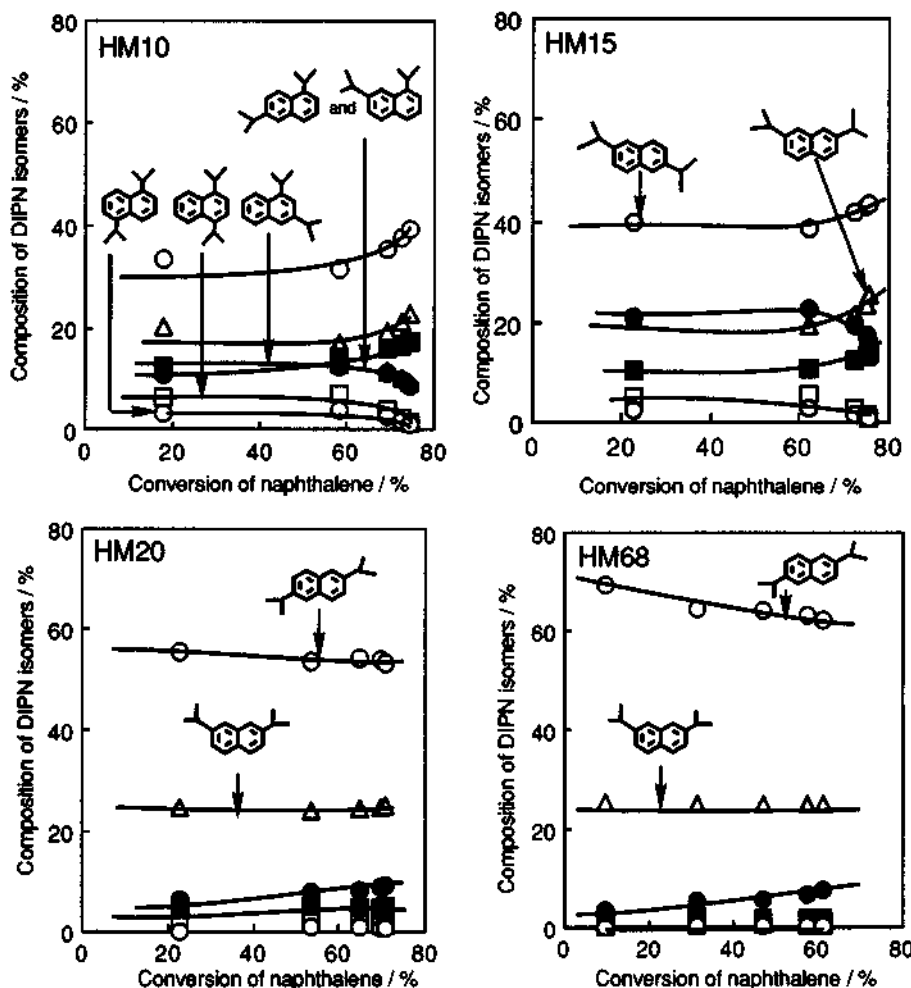


Figure 5. Composition of DIPN isomers produced by alkylation of naphthalene with propene on HM catalysts.

Table 2.  $\text{SiO}_2/\text{Al}_2\text{O}_3$  molar ratio in HM catalyst.

Catalyst	$\text{SiO}_2/\text{Al}_2\text{O}_3$ ratio determined by			
	XRF	NMR	XPS	XPS (After sputtering)
HM(10)	10	14	12	9
HM(20)	20	24	26	21
HM(68)	68	68	118	69

of external acid sites on HM(68) is small compared with other HM catalysts. Thus, 2,6-DIPN seems to be selectively produced by alkylation of naphthalene with propene in the pore of HM catalyst.

Adsorption experiments were carried out at 50°C using a mixture consisting of 2g catalyst, 0.5ml DIPN mixture, and 15ml tridecane. It was reported by Katayama and co-workers [8] that 2,6- and 2,7-DIPN are of similar molecular size. As shown in Fig. 6, however, 2,6-DIPN was selectively adsorbed on HM(20), and adsorption of 2,7- and DIPN isomers having isopropyl groups at  $\alpha$ - $\alpha$  and  $\alpha$ - $\beta$  positions was markedly suppressed. It is obvious from these results that alkylation of naphthalene with propene on HM gave 2,6-DIPN selectively, due to shape selective property of HM.

#### 4. CONCLUSION

Liquid phase alkylation of naphthalene with propene was studied using silica-alumina and mordenite as catalysts. 2,6- and 2,7-diisopropynaphthalene (DIPN) isomers are thermodynamically more stable than other isomers, and these isomers were selectively obtained even when silica-alumina was used as a catalyst. However, silica-alumina gave no appreciable difference in the selectivity between 2,6- and 2,7-DIPN. The consecutive alkylation of DIPN to TIPN took place on silica-alumina, while this reaction was retarded on HM catalysts. The selectivity for TIPN decreased with increasing  $\text{SiO}_2/\text{Al}_2\text{O}_3$  molar ratio. HM catalysts exhibited high selectivity for 2,6-DIPN production compared with that of silica-alumina. HM(68) gave 2,6-DIPN in a proportion exceeding the thermodynamically attainable level, and the selectivity was reduced by the decrease in  $\text{SiO}_2/\text{Al}_2\text{O}_3$  ratio. Adsorption of 2,7- and DIPN isomers having isopropyl groups at  $\alpha$ - $\alpha$  and  $\alpha$ - $\beta$  positions was retarded on HM, and 2,6-DIPN was selectively adsorbed. We conclude from these results that 2,6-DIPN was selectively produced by alkylation of naphthalene with propene in the pore of HM.

#### REFERENCES

- 1 D. Fraenkel, M. Cherniavsky, B. Ittash, and M. Levy, *J. Catal.*, **1986**, *101*, 273.
- 2 M. Neuber and J. Weitkamp, in J.C. Jansen, L. Moscou, M.F.M. Post (Eds.), *Zeolites for the Recent Research Reports*, Amsterdam, **1989**, p.425.
- 3 T. Matsuda, K. Yogo, T. Nagaura, and E. Kikuchi, *Sekiyu Gakkaishi*, **1990**, *33*, 214.
- 4 T. Matsuda, K. Yogo, Y. Nagaura, and E. Kikuchi, *Chem. Lett.*, **1990**, 1085.
- 5 E. Kikuchi, Y. Mogi and T. Matsuda, *Collect. Czech. Chem. Commun.*, **1992**, *57*, 909.
- 6 T. Matsuzaki, Y. Sugi, T. Hanaoka, T. Takeuchi, H. Arakawa, T. Tokoro, G. Takeuchi, *Chem. Express*, **1989**, *4*, 413.
- 7 G.S. Lee, J.J. Maj, S.C. Rocke, and J.M. Garces, *Catal. Lett.*, **1989**, *2*, 243.
- 8 A. Katayama, M. Toba, G. Takeuchi, F. Mizukami, S. Niwa, and S. Mitamura, *J. Chem. Soc. Chem. Commun.*, **1991**, 39.

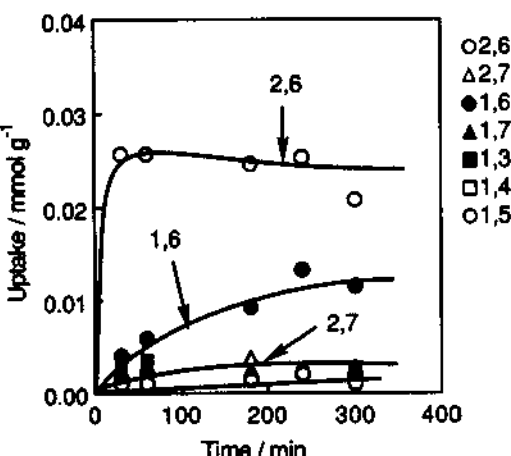


Figure 6. The amount of DIPN isomers adsorbed on HM(20).

## 4.5 Shape-selective Isopropylation of Naphthalene and Biphenyl over Dealuminated H-Mordenites

Y.Sugi<sup>\*\*</sup>, T.Matsuzaki<sup>a</sup>, T.Hanaoka<sup>a</sup>, Y.Kubota<sup>a</sup>, and J.-H.Kim<sup>a</sup>, X.Tu<sup>b</sup>, and M.Matsumoto<sup>b</sup>

<sup>a</sup> National Institute of Materials and Chemical Research, AIST, Tsukuba, Ibaraki 305, Japan

<sup>b</sup> Research & Development Center, Osaka Gas Co., Ltd., Osaka 554, Japan

### Abstract

Dealumination of H-mordenite enhanced catalyst performance in the isopropylation of naphthalene and biphenyl. The activity for naphthalene and biphenyl to diisopropynaphthalene (DIPN) and diisopropylbiphenyl (DIPB) isomers was increased by the dealumination, but further alkylation to polyisopropylated compounds was inhibited. The selectivity of 2,6-DIPN and 4,4'-DIPB increased with the increase of  $\text{SiO}_2/\text{Al}_2\text{O}_3$  ( $\text{Si}/\text{Al}_2$ ) ratio. The enhancement of catalytic activity by the dealumination is ascribed to the decrease of coke deposition because of the decrease of acid sites and strength. The increase of the selectivities of 2,6-DIPN and 4,4'-DIPB is due to the decrease of acid sites at the external surface.

The selectivity of 4,4'-DIPB was varied with the change of propylene pressure in the isopropylation of biphenyl over a highly dealuminated mordenite HM220. The selectivity of 4,4'-DIPB was achieved up to 90 % under high propylene pressures such as  $10 \text{ kg/cm}^2$ , whereas the decrease of the selectivity of 4,4'-DIPB due to the isomerization to 3,4'-DIPB was observed during the reaction under low propylene pressure such as  $0.8 \text{ kg/cm}^2$ . Propylene prevents the isomerization because of its preferential adsorption on acid sites. The yield of 4-IPBP reached maximum at 50–60 % conversion, whereas the yield of 3-IPBP increased monotonously. These results are explained by two-stage alkylation mechanism: in the first stage, biphenyl is alkylated to IPBP isomers, in which 4-IPBP is predominant. 4-IPBP only participates in the second stage alkylation, to yield 4,4'-DIPB shape-selectively.

Coke deposition occurred rapidly at the early stages in the isopropylation of biphenyl over HM220. However, the oligomerization of propylene began after the yield of DIPB isomers reached 20 %. Propylene adsorbed on acid sites is preferentially consumed by the isopropylation, especially at the early stages. Principal biphenyl derivatives encapsulated in HM pore were identified as 4-IPBP and 4,4'-DIPB.

### 1. INTRODUCTION

Zeolites are the most promising microporous crystalline compounds for achieving highly shape-selective catalysis because their pores are uniformly distributed and have dimensions allowing both the organic reactants and products to enter, to reside, and to leave. The catalytic alkylation of aromatics using zeolites has been the subject of much research [1,2] since it is essential to match the dimensions between reactants, products, and zeolite pores to achieve highly shape-selective catalysis. H-mordenites have been found to work as the most potential catalysts

for the alkylation of polynuclear aromatics such as biphenyl and naphthalene to yield the most slim isomers [2–12]. Dealumination of H-mordenite enhanced catalyst performance for the alkylation in spite of the decrease of acid density [4–6]. The dealumination not only reduces acid density, but also modifies acid properties [12]. We have reported that the isopropylation of naphthalene and biphenyl to 2,6-diisopropylnaphthalene, and 4,4'-diisopropylbiphenyl over highly dealuminated HM zeolites occurred with high activity, but further alkylation of these products occurred negligibly [2,4–9]. These phenomena are explained by steric fitness of H-mordenite pore for the substrate and the products at transition state of the alkylation. In this paper, we discuss the factors governing the catalysis of dealuminated HM in the isopropylation of naphthalene and biphenyl.

## 2. EXPERIMENTAL

### 2.1. Catalyst

H-mordenite (HM) zeolites ( $\text{SiO}_2/\text{Al}_2\text{O}_3$ ,  $\text{Si}/\text{Al}_2$ ) = 10, 15, 20, 23, 30, 73, 110, 128, and 220) were obtained from Tosoh Corporation, Tokyo, Japan. Naphthalene, biphenyl and propylene were purchased from Tokyo Kasei Co. Ltd., Tokyo, and used without further purifications.

### 2.2. Isopropylation of naphthalene (NP), 2-isopropylnaphthalene (2-IPN), and 2,6-diisopropylnaphthalene (2,6-DIPN)

The isopropylation was carried out in a 200 ml SUS-316 autoclave using propylene as alkylating reagent. The autoclave containing naphthalene and HM was purged with  $\text{N}_2$  before heating. After reaching reaction temperature, propylene was supplied to the autoclave and kept at constant pressure throughout the reaction. Standard set of the reaction included: naphthalene 400 mmol, HM 5 g, propylene pressure 10 kg/cm<sup>2</sup>, and temperature 250 °C. The product was analyzed with a Shimadzu GC-14 Gaschromatograph equipped with a 30 m TC-17 capillary column, and identified with a HP-5978 GC-MS.

### 2.3. Isopropylation of biphenyl (BP)

The isopropylation was done in similar manners as the case of naphthalene. Standard set of the reaction included: biphenyl 200 mmol, HM 2 g, propylene pressure 10 kg/cm<sup>2</sup>, and temperature 250 °C. The product was analyzed with a HP-5890 GC equipped with a 25 m Ultra-1 capillary column.

### 2.4. Isomerization of 4,4'-diisopropylbiphenyl (4,4'-DIPB)

The isomerization was examined under the condition as follows: 4,4'-DIPB 100 mmol, HM 1 g, propylene pressure 0–10 kg/cm<sup>2</sup>, reaction temperature 250 °C, and reaction period 4 h.

### 2.5. Characterization of dealuminated H-mordenites

The characterization of dealuminated HM was carried out by XRD (MAC Science, MXP 18), XRF (Seiko Instruments Inc., SEA 2010) and XPS (Perkin-Elmer PHI 5500).

Measurements of temperature-programmed desorption of adsorbed ammonia ( $\text{NH}_3$ -TPD) were carried out as follows [13]: the catalyst was used in minimized amount (10 mg) to exclude the influence of re-adsorption of ammonia. The catalyst was evacuated at 500 °C for 2 h, and exposed to 150 torr of ammonia at 150 °C for 30 min. Then, the catalyst was evacuated at 150 °C for 1 h and cooled to room temperature. The desorption of ammonia was analyzed under vacuum using a mass spectrometer with temperature raising to 600 °C at 10 °C/min.

Coke deposition on catalysts used after the reaction was determined by thermogravimetric analysis (MAC Science TG-DTA 2000). Biphenyl derivatives encapsulated in the pore was analyzed by GC after the destruction of HM using aqueous hydrofluoric acid solution.

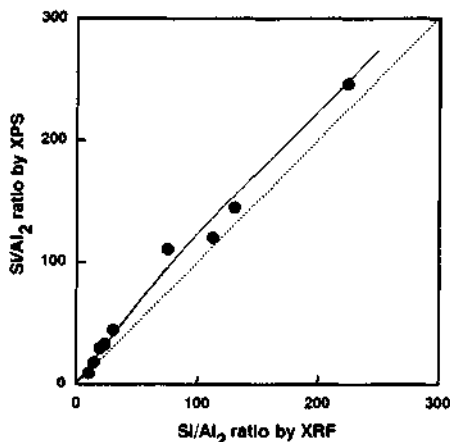


Fig. 1 Relation between  $\text{Si}/\text{Al}_2$  ratios of HM by XRF and XPS analyses

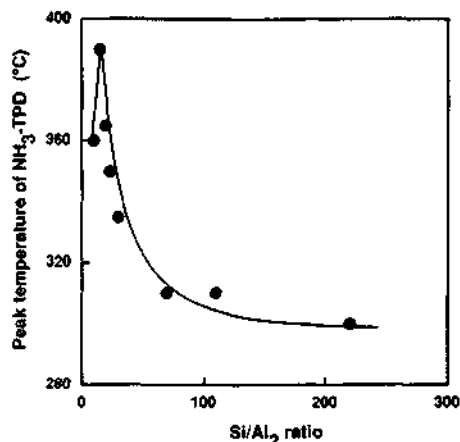


Fig. 2 Effect of  $\text{Si}/\text{Al}_2$  ratio of HM on peak position of  $\text{NH}_3\text{-TPD}$

### 3. RESULTS AND DISCUSSION

#### 3.1. Characterization of dealuminated H-mordenites

XRD patterns of HM zeolites showed no significant structural change by the dealumination. Dealumination of HM zeolites did not afford a regular shift of their surface areas and pore-volumes [8]. These results show that the dealumination did not cause significant structural destruction of HM zeolites used in this work.

There was a linear relationship between  $\text{Si}/\text{Al}_2$  ratio measured by XRF and the ratio measured by XPS as shown in Fig. 1. The former ratio is related to bulk aluminum concentration of HM zeolite, and the latter indicates aluminum concentration on external surface [9]. These results show that no preferential dealumination occurs at external surface of H-mordenites.

$\text{NH}_3\text{-TPD}$  is one of useful indication of the change of acid strength of dealuminated HM zeolites, because the temperature of peak position in the profile corresponds intrinsically to acid strength of the zeolite [13]. Figure 2 shows the relationship between  $\text{Si}/\text{Al}_2$  ratio and the temperature of peak position in  $\text{NH}_3\text{-TPD}$  profile. The increase of the temperature at peak position decreased significantly with the ratio less than 70, whereas almost constant temperature was observed at the ratio higher than 100. The dealumination of HM zeolites decreases acid strength as well as acid density, especially in the range of  $\text{Si}/\text{Al}_2$  ratio less than 70. However, no significant change of acid strength occurs by further dealumination. These results showed that strong acid sites are preferentially removed by the dealumination.

#### 3.2. Isopropylation of naphthalene

##### 3.2.1. Effect of $\text{Si}/\text{Al}_2$ of H-mordenite

Figures 3 and 4 show typical isopropylations of naphthalene over HM10 (number after HM expresses  $\text{Si}/\text{Al}_2$  ratio) and over HM220, respectively. HM220 exhibited higher catalytic activity than HM10 in spite of significant decrease of acid sites. Over both the catalysts, the formation of diisopropynaphthalene (DIPN) isomers increased with the decrease of isopropynaphthalene (IPN) isomers, and the formation of polyisopropynaphthalenes (PIPN) increased at final stage

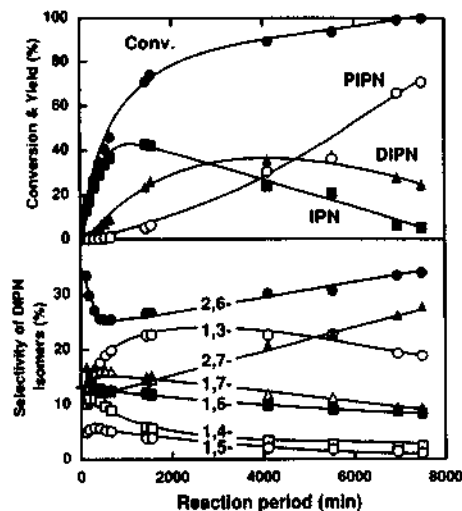


Fig. 3 The isopropylation of naphthalene over HM10

Reaction conditions: NP 400 mmol, HM10 5 g, 250 °C, propylene 10 kg/cm<sup>2</sup>.

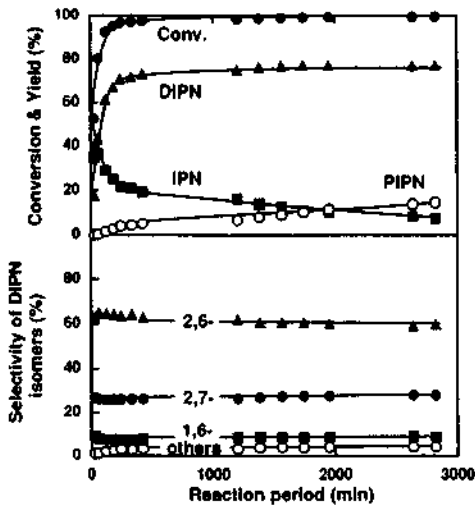


Fig. 4 The isopropylation of naphthalene over HM220

Reaction conditions: NP 400 mmol, HM220 5 g, 250 °C, propylene 10 kg/cm<sup>2</sup>.

of the reaction. The activity for the isopropylation and the distribution of PIPN and DIPN isomers are quite different between both the zeolites. Tetraisopropylnaphthalenes (TIPN) in PIPN was at a level of about 30 % at 100 % conversion over HM10, whereas only a few amounts of TIPN (less than 2 % in PIPN) were formed in the case of HM220.  $\alpha,\alpha$ - and  $\alpha,\beta$ -DIPN isomers (*i.e.*, 1,5-, 1,4-, 1,6-, 1,8- and 1,3-DIPN) were produced in considerably high amounts at early stage of the reaction over HM10. However, they were isomerized to thermodynamically more stable  $\beta,\beta$ -DIPN isomers (2,6- and 2,7-DIPN) as the reaction proceeded. These results indicate that non-selective isopropylation occurs at acid sites on external surface. On the other hand, the distributions of DIPN isomers were almost constant, and the selectivities of  $\beta,\beta$ -DIPN isomers, especially 2,6-DIPN, were as high as *ca.* 60 % during the reaction over HM220. These results suggest that the isopropylation over HM220 occurred mainly at acid sites inside the pores. Predominant formation of the least bulky 2,6-DIPN is due to its minimum steric hindrance among DIPN isomers at the transition of alkylation in HM pore.

Products distributions of the isopropylation of naphthalene at 80 % conversion on HM zeolites with various Si/Al<sub>2</sub> ratios are summarized in Table 1. Catalytic features of HM zeolites varied significantly with the ratio. The dealumination enhanced both catalytic activity and the selectivity of 2,6-DIPN. These results indicate that the alkylation is not governed by acid density, and that only small amounts of acid sites participate in the reaction. Remarkable changes in the selectivities of IPN and DIPN isomers occurred at the ratio among 23 and 30. Reaction period to reach 80 % conversion over HM with the ratio less than 23 is significantly longer than that over HM zeolites with the ratio higher than 30. Discrepancy of the selectivities of 2-IPN and 2,6-DIPN was also observed at the ratio among 23 and 30. Over HM zeolites with the ratio less than 23 gave lower selectivities for 2-IPN and for 2,6- and 2,7-DIPN as high as 70% and 30–50 %, respectively. However, the selectivities increased as high as 85–90 % for 2-IPN and 60–65 % for 2,6-DIPN over HM zeolites with the ratio higher than 30. Combined selectivity of 2,6- and 2,7-DIPN, two of the most slim isomers, increased from 40-

Table 1 Effect of Si/Al<sub>2</sub> ratio of H-mordenites on the isopropylation of naphthalene

Table 1 Effect of Si/Al<sub>2</sub> ratio of H-mordenites on the isopropylation of naphthalene

Si/Al <sub>2</sub>	Period <sup>a</sup> (min)	Yield (%) <sup>b</sup>			Isomer composition of IPN and DIPN (%)			
		IPN	DIPN	PIP <sup>c</sup>	2-	2,6-	2,7-	1,6-
10	1800	39.8	31.6	9.3	67.1	28.5	17.0	11.1
15	720	48.9	31.1	3.5	66.6	37.9	16.2	11.6
20	450	49.7	28.2	2.4	69.9	44.8	17.8	10.2
23	660	48.6	29.1	1.9	73.3	51.5	20.1	9.4
30	330	46.7	32.8	0.8	86.9	60.8	22.5	9.1
73	300	44.9	34.1	0.2	92.2	59.3	29.4	9.2
110	60	39.4	41.1	0.5	88.4	63.5	27.1	8.1
128	180	35.9	43.8	0.9	87.2	64.6	25.7	8.0
220	60	36.6	43.3	0.2	88.6	65.1	26.0	8.0

Reaction conditions: naphthalene, 400 mmol; HM, 5 g; propylene pressure, 10 kg/cm<sup>2</sup>; temperature, 250 °C.

<sup>a</sup> Reaction period to reach 80% of naphthalene conversion. <sup>b</sup> Based on amount of introduced naphthalene at 80 % conversion.

70 % to 80–90 %. These results mean that the participation of non-selective catalysis on external surface of HM zeolites with the ratio less than 23 is higher than that of zeolites with higher ratio. The dealumination caused the decrease of acid strength of the zeolite, especially for HM zeolites with the ratio higher than 70. From above discussions, it is concluded that the catalysis of dealuminated HM zeolites as HM220 occurs selectively at acid site in the pore.

Horsley and his coworkers calculated the conformation and the diffusion of 2,6- and 2,7-DIPN inside HM pore [15]. They concluded that the diffusion rate of 2,6-DIPN is higher than that of 2,7-DIPN, because the former has a more linear and slim structure than the latter. The selectivity of 2,6-DIPN should be higher than that of 2,7-DIPN if the alkylation of naphthalene occurs inside the pore. Furthermore, the formation and the diffusion of PIPN and DIPN isomers with α-isopropyl group in HM pore are strongly prevented because corresponding transition state has as bulky conformations. These results suggest that the alkylation over HM zeolites with low

Table 2 Effect of Si/Al<sub>2</sub> ratio of H-mordenites on the isopropylation of 2-isopropynaphthalene and 2,6-diisopropynaphthalene

Substrate	Si/Al <sub>2</sub>	Conv. (%)	Yield (%)				2,6-DIPN Select. (%)
			NP	IPN	DIPN	PIP <sup>c</sup>	
2-IPN	10	37.5	—	—	32.2	5.3	26.1
	23	52.4	0.2	—	45.0	6.9	42.5
	220	54.6	0.1	—	50.8	3.7	61.6
2,6-DIPN	10	77.4	0.2	0.1	1.3 <sup>d</sup>	75.7	
	23	59.3	0.4	0.9	10.3 <sup>d</sup>	48.1	
	220	32.9	1.0	3.0	9.9 <sup>d</sup>	18.9	

Reaction conditions: substrate, 400 mmol, HM, 5 g; propylene, 10 kg/cm<sup>2</sup>; temperature, 250 °C; period, 20 h.

<sup>c</sup> Amounts of DIPB isomers except 2,6-DIPN.

$\text{Si}/\text{Al}_2$  ratio such as HM10 occurs mainly at acid sites on external surface, and that the alkylation over HM zeolites with higher ratio proceeds inside the pores.

### 3.2.2. Isopropylation of 2-isopropynaphthalene and 2,6-diisopropynaphthalene

The activities for the isopropylation of 2-IPN and 2,6-DIPN over HM10, HM23 and HM220 were summarized in Table 2. Catalytic activity for 2-IPN increased in the order: HM10 > HM23 > HM220. This order coincides with the case of naphthalene. The selectivity of 2,6-DIPN has also the almost same features as that of naphthalene. The isomerization of 2-IPN did not occur under those conditions. In the case of the isopropylation of 2,6-DIPN, catalytic activity decreased in the order: HM10 > HM23 > HM220. This result shows that the isopropylation of 2,6-DIPN is suppressed over highly dealuminated HM zeolites. The high activity of the isopropylation over HM10 suggests that the catalysis occurs at acid sites on external surface. The enhancement of the selectivity of 2,6-DIPN over highly dealuminated HM zeolites in the isopropylation of naphthalene is ascribed to the decrease of external acid sites. The products of various reactions such as dealkylation, isomerization and transalkylation were found in the isopropylation of 2,6-DIPN in addition to those of alkylation. Similar tendency is observed in the reaction of 2-IPN in the absence of propylene.

### 3.2.3. Coke deposition on HM zeolites

Coke deposition takes place at acid sites, and causes catalyst deactivation [16–18]. It is known that dehydrogenation of substrates at acid sites is an initiation reaction to form carbonaceous deposits. Carbonaceous deposits in zeolite pores are usually aromatic hydrocarbons having 2–4 nuclei, which are precursors of coke. They decrease with the decrease of acid density, because cooperation between acid sites in neighborhood is essential for the dehydrogenation. The dealumination of HM zeolites modifies also acidic properties to decrease the formation of carbonaceous deposits and coke. To understand coke deposition of dealuminated HM zeolites during the reaction, TG analysis of the catalysts after the reaction was conducted in air stream (Fig. 5). Peak around 500–600 °C is due to the combustion of deposited coke, because evolved gas is identified as carbon dioxide by MS analysis. They

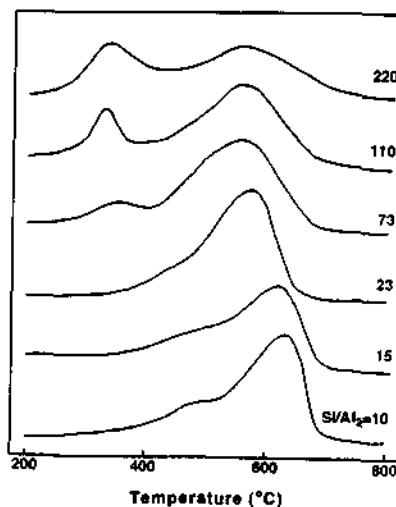


Fig. 5 TG profile of H-mordenites after the isopropylation of naphthalene

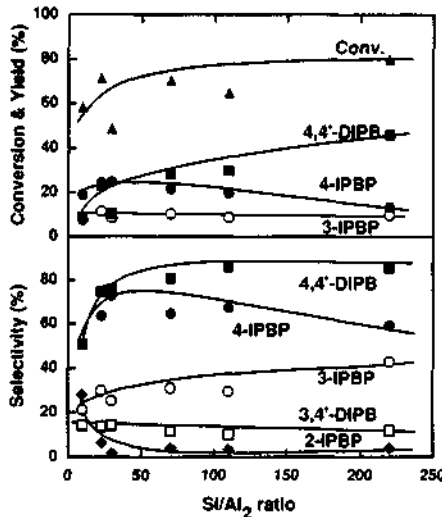


Fig. 6 Effect of  $\text{Si}/\text{Al}_2$  ratio on the isopropylation of biphenyl  
Reaction conditions: BP 200 mmol; HM 2 g; propylene 10 kg/cm<sup>2</sup>; period 4 h; temperature 250 °C.

decreased with the increase of  $\text{Si}/\text{Al}_2$  ratio. The peak at lower temperatures appeared for HM zeolites with the ratio higher than 72. These peaks are assigned as naphthalene derivatives by MS analysis. The peak area increased with the increase of the ratio. The increase of encapsulated biphenyls are ascribed to the decrease of coke deposition because of the decrease of acid sites and strength. The change of property of HM zeolites by the dealumination results in low coke deposition and high catalytic activity in the isopropylation. Highly dealuminated HM effectively catalyzes shape-selective alkylation with minimum coke deposition.

### 3.3. Isopropylation of biphenyl

#### 3.3.1. Effect of $\text{Si}/\text{Al}_2$ ratio

Figure 6 shows the effect of the dealumination of HM zeolites on the isopropylation under 10 kg/cm<sup>2</sup> of propylene pressure. Tendency of the change of both catalytic activity and selectivity of products quite resembled the case of naphthalene. The selectivity of isopropylbiphenyl (IPBP) and diisopropylbiphenyl (DIPB) isomers changed significantly at  $\text{Si}/\text{Al}_2$  ratio less than 20. The selectivities over HM10 were as low as ca. 60% for 4-IPBP and 52% for 4,4'-DIPB. The resultant low selectivities at low ratios suggest that non-shape-selective alkylation and isomerization of 4,4'-DIPB occur at acid sites on external surface as the case of naphthalene. The selectivities of 4,4'-DIPB gradually increase with increasing the ratio. Especially, the selectivity of 4,4'-DIPB was achieved up to ca. 90% with increasing the conversion over HM220. These results suggest that the isopropylation occurs inside HM pore to form 4,4'-DIPB shape-selectively, and that the dealumination decreases the isomerization of 4,4'-DIPB because of the elimination of acid sites from external surface. With the increase of the ratio, the selectivity of 4-IPBP decreased gradually, and that of 3-IPBP increased, because only 4-IPBP was consumed in further isopropylation to form DIPB isomers (see below).

#### 3.3.2. Effect of propylene pressure

Figure 7 shows dependence on reaction period of the isopropylation of biphenyl over HM220

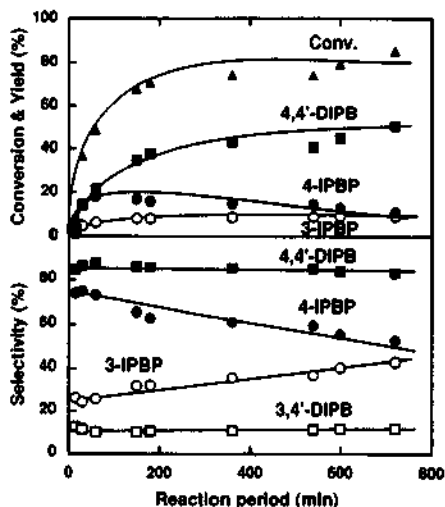


Fig. 7 The isopropylation of biphenyl over HM220  
Reaction conditions: BP 200 mmol, HM220 2 g, propylene 10 kg/cm<sup>2</sup>, temperature 250 °C

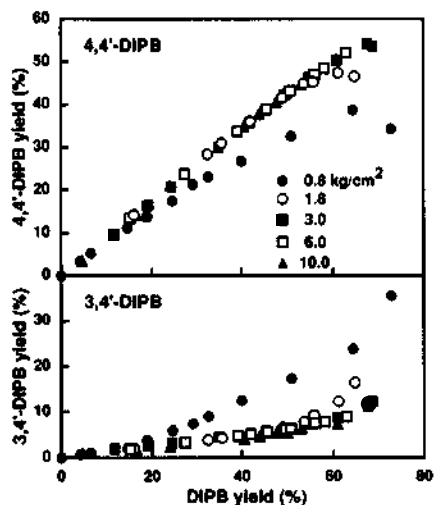


Fig. 8 Effect of propylene pressure on 4,4'- and 3,4'-DIPB yields  
Propylene 0.8–10 kg/cm<sup>2</sup>. Other conditions are the same as Fig. 7.

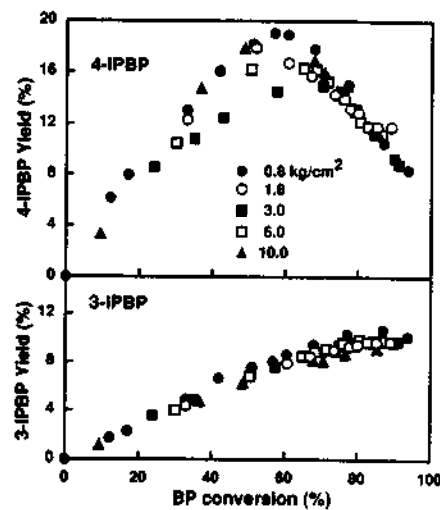


Fig. 9 Effect of propylene pressure on 3-, 4- and 3,4'-IPBP yields  
Propylene 0.8–10 kg/cm<sup>2</sup>. Other conditions are the same as Fig. 7.

under 10 kg/cm<sup>2</sup> of propylene pressure. At early stage of the reaction, biphenyl was converted to IPBP isomers, especially to 4-IPBP. DIPB isomers increased with the consumption of IPBP isomers. The formation of 4,4'-DIPB was highly selective throughout the reaction. The selectivity of 4-IPBP decreased with increasing that of 3-IPBP. The amount of higher products such as triisopropylbiphenyls (TriPB) was negligibly low because their formation was restricted by HM pores.

The product distribution varied with propylene pressure. Under high pressures as 10 kg/cm<sup>2</sup>, selective formation of 4,4'-DIPB was observed as described above. However, the selectivity of 4,4'-DIPB decreased during the reaction under the pressures less than 3.0 kg/cm<sup>2</sup>. Fig. 8 summarizes the effects of propylene pressure on 4,4'- and 3,4'-DIPB yields. Under pressures higher than 3 kg/cm<sup>2</sup>, the yields of 4,4'- and 3,4'-DIPB increased linearly with the increase of combined yield of DIPB isomers. However, downward deviation from linear relation occurred significantly under 0.8 kg/cm<sup>2</sup>. The yield of 4,4'-DIPB increased up to 40 % at the yield of DIPB isomers, and decreased after reaching the maximum value. Corresponding to the decrease of 4,4'-DIPB yield, significant increase of 3,4'-DIPB yield was observed under pressures lower than 3.0 kg/cm<sup>2</sup>.

Figure 9 shows effect of propylene pressure on 3- and 4-IPBP yields. No significant influence of propylene pressure was observed on yields of 3- and 4-IPBP. The yield of 4-IPBP increased linearly with the conversion, and reached the maximum at around 50–60 % of the conversion. It decreased linearly with the further increase of the conversion. On the other hands, the yield of 3-IPBP increased monotonously with increasing the conversion.

These results are summarized as follows: The isopropylation of biphenyl to IPBP isomers is not influenced by propylene pressure. 4-IPBP is an intermediate to form DIPB isomers, principally 4,4'-DIPB. The decrease of the yield of 4,4'-DIPB under low propylene pressure is due to its isomerization to 3,4'-DIPB. The difference of the effect of propylene pressure on the formation of IPBP and DIPB isomers suggests the pathway as follows. The first stage reaction to form IPBP isomers is governed by the shape-selectivity of HM pore to yield 4-IPBP as principal isomer. 4,4'- and 3,4'-DIPB were formed only from 4-IPBP at the second stage of the reaction. 3-IPBP does not participate in the formation of 3,4'-DIPB, because it is bulkier than 4-IPBP. Some of 4,3'-DIPB are isomerized to 3,4'-DIPB under low propylene pressures (see below).

### 3.3.3. Isomerization of 4,4'-DIPB

To understand the effect of propylene pressure on decreasing the selectivity of 4,4'-DIPB for the isopropylation, the isomerization of 4,4'-DIPB under propylene pressure over HM zeolites was examined. As summarized in Fig. 10, high extent of isomerization of 4,4'-DIPB to 3,4'-DIPB was observed under propylene pressure below 0.8 kg/cm<sup>2</sup>. However, the isomerization significantly decreased under pressures higher than 3 kg/cm<sup>2</sup>. The isomerization occurs likely on external acid sites because transition state to form of 3,4'-DIPB is restricted by steric circumstance inside HM pore. Propylene prevents the isomerization probably due to its preferential adsorption at acid sites on external surface. From above discussions, it is concluded that the decrease of the selectivity of 4,4'-DIPB in the isopropylation of biphenyl at low propylene pressure occurs by the isomerization of 4,4'-DIPB, not by the decrease of shape-selective catalysis. The low formation of TriPB supports that the isopropylation of biphenyl to 4,4'-DIPB occurs inside HM pores by shape-selective catalysis, and that TriPB hardly accommodates in them. The formation of TriPB under 0.8 kg/cm<sup>2</sup> of propylene pressure likely proceeded by the isopropylation of 3,4'-IPBP at acid sites on external surface.

### 3.3.4. Coke deposition, encapsulation of products and propylene oligomerization

Similar phenomena on coke deposition described in the case of naphthalene were also observed in the isopropylation of biphenyl. Fig. 11 shows effect of Si/Al<sub>2</sub> ratio on deposited coke and encapsulated biphenyl derivatives observed by TG analysis. Coke deposition decreased

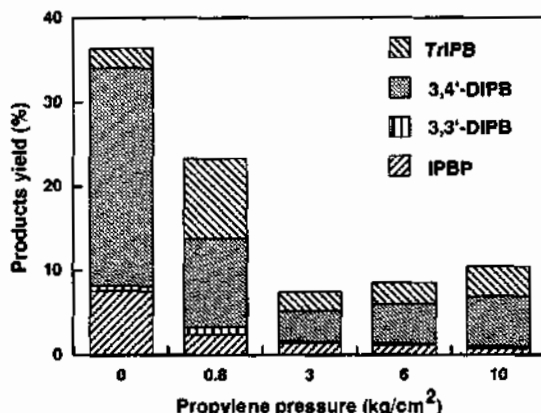


Fig. 10 The isomerization of 4,4'-DIPB over HM220  
Reaction conditions: 4,4'-DIPB 100 mmol, HM220 1 g, temperature 250 °C, period 4 h

with increasing the ratio, and volatile biphenyl derivatives were observed in the case of dealuminated HM zeolites. Biphenyl derivatives were not found for HM with the ratio less than 30, whereas they increased with the increase of the ratio. These results show that biphenyl derivatives are precursors of coke. The decrease of coke deposition and the increase of encapsulated biphenyl derivatives are related with the increase of both selectivity and yield of 4,4'-DIPB as shown in Fig. 7.

Figure 12 shows coke deposition, encapsulation of biphenyl derivatives and propylene oligomerization over HM220. Coke deposition occurred rapidly at the early stage, and amount of deposited coke increased gradually up to 5–6 % on the catalyst with prolonging reaction period. Biphenyl derivatives encapsulated inside HM pore also increased rapidly at the early stages, however, they reached constant amount at high conversion. On the other hand, the formation of propylene oligomer began after the yield of DIPB isomers reached ca. 20 % (this

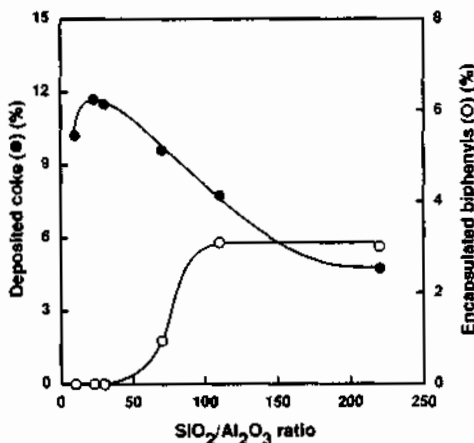


Fig. 11 Effect of Si/Al<sub>2</sub>O<sub>3</sub> ratio on coke deposition, encapsulation of biphenyl derivatives

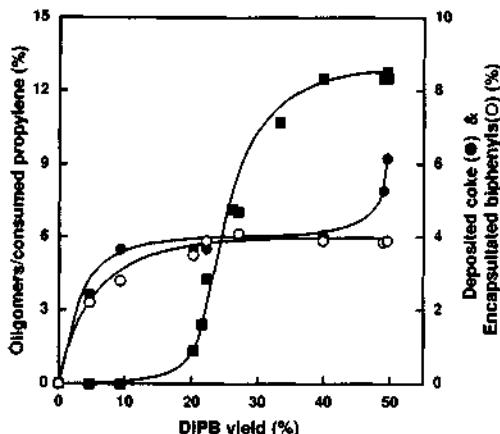


Fig. 12 Coke deposition, encapsulation of biphenyl derivatives and propylene oligomerization over HM220

yield corresponds to ca. 40 % for conversion of biphenyl). The amount of propylene oligomer in consumed propylene increased rapidly up to 10–12 %, whereas it saturated with further increase of the yield of DIPB isomers. Propylene oligomer consisted mainly of propylene dimers and trimers, however higher oligomer than tetramers contained only in small amount. These results shows that propylene is consumed preferentially by the isopropylation at the early stages, and that coke deposition on acid sites occurs rapidly, and that the coke is formed from biphenyl derivatives.

Organic compounds encapsulated in HM220 pore after the reaction were identified as 4-IPBP and 4,4'-DIPB as principal components by GC analysis after the destruction of the catalyst with aqueous hydrofluoric acid solution. This result indicates that shape-selective catalysis occurs inside HM pores.

#### 4. CONCLUSIONS

Dealuminated HM zeolites with high Si/Al<sub>2</sub> ratio (> 23) exhibited higher selectivity of 2,6-DIPN in the isopropylation of naphthalene than HM zeolites with low ratio (< 30). Moreover, the activities for the alkylation of naphthalene and 2-IPN increased by the dealumination, but the alkylation of 2,6-DIPN was suppressed. The enhancement in the formation of 2,6-DIPN by the dealumination is due to the decrease of external acid sites. Similar catalytic features of HM zeolites by the dealumination were observed in the isopropylation of biphenyl.

Highly dealuminated HM zeolite such as HM220 gave selective formation of 4,4'-DIPB in the isopropylation of biphenyl. The increase of propylene pressure suppressed the isomerization of 4,4'-DIPB to keep high selectivity for the isopropylation. However, the isomerization of 4,4'-DIPB caused the decrease of the selectivity under low pressure of propylene. The isomerization occurs likely on acid sites of external surface because isomerized products hardly accommodate inside HM pores by steric restriction. Propylene prevents the isomerization probably due to its preferential adsorption on acid sites.

Coke deposition in the isopropylation of naphthalene and biphenyl decreased by the dealumination, whereas encapsulated naphthalene and biphenyl derivatives were found in highly dealuminated HM. These results support that the dealumination enhances shape-selective

catalysis in HM pore with minimum deactivation by coke deposition.

In the isopropylation of biphenyl over HM220, coke deposition occurred rapidly at initial stages. However, the oligomerization of propylene began after the yield of DIPB isomers reached 20 %. Propylene adsorbed on acid sites is consumed preferentially by the isopropylation, especially at early stages. Principal biphenyl derivatives encapsulated in HM pore were identified as 4-IPBP and 4,4'-DIPB.

## 5. REFERENCES

1. S.Csicsery, *Zeolites*, **4**, 203 (1984).
2. Y.Sugi and M.Toba, *Catal.Today*, in press.
3. A.Katayama, M.Toba, G.Takeuchi, F.Mizukami, S.Niwa, and S.Mitamura, *J.Chem.Soc., Chem. Commun.*, **39** (1991).
4. Y.Sugi, T.Matsuzaki, T.Hanaoka, K.Takeuchi, T.Tokoro, and G.Takeuchi, *Stud.Surf.Sci.Catal.*, **60**, 303 (1991).
5. X.Tu, M.Matsumoto, T.Matsuzaki, T.Hanaoka, Y.Kubota, J.-H.Kim, Y.Sugi, *Catal.Lett.*, **21**, 71 (1993).
6. J.-H.Kim, T.Matsuzaki, K.Takeuchi, T.Hanaoka, Y.Kubota, Y.Sugi, X.Tu, and M.Matsumoto, *IUMRS 93'*, in press.
7. X.Tu, M.Matsumoto, T.Maeda, Y.Sugi, M.Matsuzaki, T.Hanaoka, Y.Kubota, and J.-H.Kim, *IUMRS 93'*, in press.
8. Y.Sugi, T.Matsuzaki, T.Tokoro, T.Hanaoka, K.Takeuchi, X.Tu, and G.Takeuchi, *Sekiyu Gakkai Shi*, in press.
9. J.-H.Kim, T.Matsuzaki, T.Hanaoka, Y.Kubota, Y.Sugi, X.Tu, and M.Matsumoto, submitted for publication.
10. G.S.Lee, J.J.Maj, S.C.Rocke, and J.M.Garces, *Catal.Lett.*, **2**, 243 (1989).
11. G.Takeuchi, H.Okazaki, M.Yamae, and K.Kito, *Appl.Catal.*, **76**, 49 (1991).
12. H.G.Karge and J.Weitkamp, *Chem.Ind.Tech.*, **58**, 946 (1986).
13. J.-H.Kim, S.Namba, and T.Yashima, *Zeolites*, **11**, 59 (1991).
14. M.Sawa, M.Niwa, and Y.Murakami, *Appl.Catal.*, **53**, 169 (1989).
15. J.A.Horsley, J.D.Fellmann, E.G.Derouane, and C.M.Freeman, Computer Aided Innovation of New Materials II, M.Doyama, J.Kihara, M.Tanaka and R.Yamamoto (editors), Elsevier, Amsterdam, 1993, pp.985-989..
16. O.Dejaive, A.Aurox, P.C.Gravelle, J.C.Vedrine, Z.Gabelica, and E.Derouane, *J.Catal.*, **70**, 123 (1981).
17. N.Neuber, H.G.Karge, and J.Weitkamp, *Catal.Today*, **3**, 11 (1988).
18. N.Neuber, S.Ernst, H.Geerts, P.J.Grobet, P.A.Jacobs, G.T.Kokotailo, and J.Weitkamp, Catalytic deactivation 1987 (*Stud.Surf.Sci.Catal.*, **34**), B.Delmon and G.F.Froment (eds.), Elsevier, Amsterdam, 1988, pp.567-577.

## 4.6 Promotion Effect of Hydrogen on Catalytic Decomposition of Nitrous Oxide ( $N_2O$ ) by H-ZSM-5 Catalyst

K. Ebitani, N. Ohshio and A. Morikawa  
Department of Chemical Engineering, Faculty of Engineering,  
Tokyo Institute of Technology,  
2-12-1 Ookayama, Meguro-ku, Tokyo 152, Japan

### Abstract

The rate of the decomposition of  $N_2O$  over hydrogen-form of ZSM-5 zeolites (H-ZSM-5) was greatly enhanced when the reaction was carried out in the presence of hydrogen( $H_2$ ). The promotion of the rate by  $H_2$  was found to be reversible in the presence or absence of  $H_2$ , and was remarkable at higher reaction temperature (563-643 K) and at higher  $H_2$  pressure (0.3-7 kPa). The degree of the promotion was proportional to the aluminium content of the zeolite. The promotion can be explained by the alteration of the surface acid properties, e.g., formation of protonic acid sites of H-ZSM-5 by hydrogen molecule.

### 1. INTRODUCTION

Much attention has been paid for the decomposition of nitrous oxide ( $N_2O$ ) concerned to its unique behavior as an oxidizing agent in benzene oxidation[1-3] and its contributions to the stratospheric ozone destruction and the green house effect[4]. While the decomposition of  $N_2O$  on metal ion-exchanged zeolites has been extensively studied[4], it has been scarcely investigated on metal-free zeolite due to its small activity at the reaction temperature lower than 723 K[5]. In the present paper, the authors wish to report the promotion effect of hydrogen upon the decomposition of  $N_2O$  on the metal-free H-ZSM-5 zeolites at the reaction temperature lower than 650 K.

### 2. EXPERIMENTAL METHODS

Na-ZSM-5 (Si:Al=44), prepared by the procedure proposed by Yoshimura et al.[6], was ion-exchanged at 343 K for 12 h in an aqueous  $NH_4NO_3$  solution of 0.05 mol l<sup>-1</sup>, dried at 383 K, followed by calcination at 773 K. The H-ZSM-5 zeolites (Si:Al = 142.2, and 420) were supplied by TOSOH Co. Ltd. The Fe content, the specific surface area and the degree of ion-exchange of the samples are summarized in Table 1. The contents of Fe in the samples were analyzed by atomic absorption spectroscopy. The specific surface areas of the samples after degassing at 723 K were determined by isothermal adsorption of  $N_2$  at 77K.

Table 1 The Si:Al ratio, Fe content, specific surface area and percent exchange of H-ZSM-5 zeolites.

Si:Al ratio	44	142.2	420
Fe content (g/g-zeolite)	$1.74 \times 10^{-4}$	$2.22 \times 10^{-4}$	$2.31 \times 10^{-4}$
Surface area (m <sup>2</sup> /g <sup>-1</sup> )	533	527	505
Degree of exchange(%)	96.9	96.5	96.7

A powdered H-ZSM-5 placed in a quartz reactor was heated in oxygen (5 kPa) at 773 K for 1 h and degassed( $<1.3 \times 10^{-5}$  kPa) at 773 K for 20 min prior to the use of the reaction. The reaction of  $\text{N}_2\text{O}$  (99.5 % purity) of 0.7 kPa diluted by He or  $\text{H}_2$  was carried out in the conventional closed gas-circulating system with an apparent volume of 188 ml at 293 K. The products were analyzed by gas chromatography. The hydrogen was purified by passing through the molecular sieves and a liquid-nitrogen trap.

### 3. RESULTS AND DISCUSSION

Figure 1 shows the change in the nitrogen ( $\text{N}_2$ ) yield for the reaction of  $\text{N}_2\text{O}$  in the absence and presence of  $\text{H}_2$  (7.1 kPa) at various reaction temperature for H-ZSM-5 (Si:Al=44) zeolite. In the absence of  $\text{H}_2$ , the  $\text{N}_2$  yield was very small even when the reaction temperature was raised to 643 K. The  $\text{N}_2$  formation was greatly enhanced, when the reaction was carried out in the presence of  $\text{H}_2$ . At any  $\text{N}_2\text{O}$  conversion level in the experiments reported here, no detectable  $\text{O}_2$  could be found in gas phase. The formation of water was detected, but the amount of water produced was not successfully determined. Without the catalyst, no  $\text{N}_2\text{O}$  decomposition, even in the presence of  $\text{H}_2$ , was observed. The rate of  $\text{N}_2$  formation in the presence of  $\text{H}_2$  was greater at higher reaction temperature. These results clearly demonstrate that  $\text{H}_2$  present in vapor

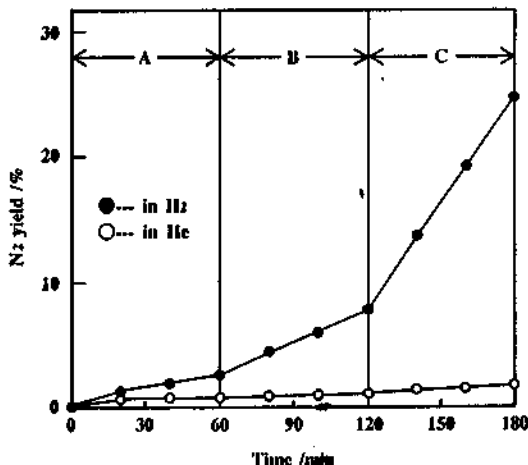


Figure 1 The change of  $\text{N}_2$  yield for the decomposition of  $\text{N}_2\text{O}$  on the H-ZSM-5 (Si:Al=44) zeolite in the absence and presence of  $\text{H}_2$  at various reaction temperatures. (A) at 563 K, (B) at 603 K, (C) at 643 K. The initial  $\text{H}_2$  pressure was 7 kPa.

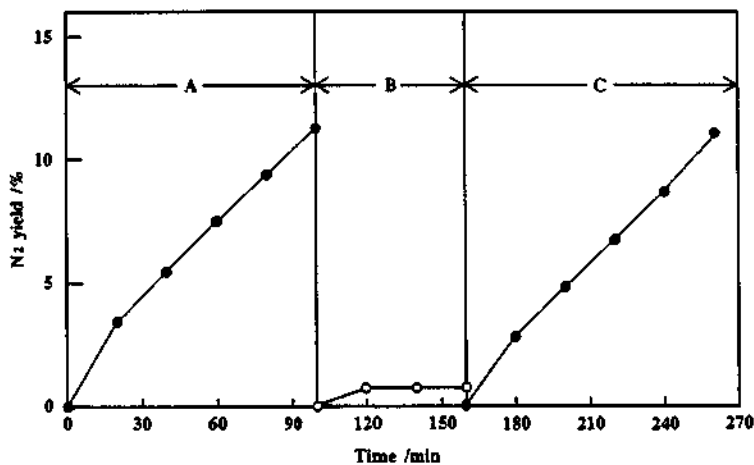


Figure 2 The responses of  $\text{N}_2\text{O}$  decomposition activity of H-ZSM-5 (Si:Al=44) to introduction and removal of  $\text{H}_2$  in the reaction mixture (The reaction temperature was 603 K). (A) in the presence of  $\text{H}_2$  (6.2 kPa), (B) in the absence of  $\text{H}_2$  (The  $\text{N}_2\text{O}$  was diluted by 6.7 kPa He), (C) in the presence of  $\text{H}_2$  (6.9 kPa).

phase enhances the catalytic activity of the zeolite in the decomposition of N<sub>2</sub>O.

The responses of the N<sub>2</sub>O decomposition activity at 603 K to the introduction and the removal of H<sub>2</sub> in the reaction mixture are shown in Fig.2. After the first reaction was carried out in the presence of H<sub>2</sub> for 100 min, the reaction mixture was evacuated and the catalyst was degassed at 603 K for 20 min. When the reaction mixture without H<sub>2</sub> was re-introduced to the reaction system, the considerable suppression of the rate of N<sub>2</sub> formation was observed. The decomposition activity was restored when H<sub>2</sub> was re-admitted to the reaction mixture. These results indicate that the promotion effect of H<sub>2</sub> upon the N<sub>2</sub>O decomposition on the zeolite was reversible.

Figure 3 shows the effect of the H<sub>2</sub> pressure on the rate of N<sub>2</sub> formation on H-ZSM-5 (Si:Al = 44) at 603 K. The H<sub>2</sub> pressure was varied under a constant total pressure adjusted with He diluent. The rate of N<sub>2</sub> formation on the H-ZSM-5, determined from the change in the N<sub>2</sub> yield between the time of 20 min and 80 min, was increased with increase in the H<sub>2</sub> partial pressure. The rate of N<sub>2</sub> formation was linearly correlated to the H<sub>2</sub> pressures greater than 1 kPa, but a remarkable and sharp enhancement of the rate at the lower pressures than 1 kPa was observed. This sharp enhancement in the rate may correspond to the increase of the catalytic activity of the zeolite by hydrogen.

When the reaction in the presence of 7 kPa H<sub>2</sub>, at 603 K was carried out with NH<sub>3</sub> of less than 0.13 kPa, almost equivalent to the amount of aluminum contained in the catalyst, the reaction rate was decreased to 40 % value of that without NH<sub>3</sub>. This suggests that the acid character of the catalyst is concerned to the reaction. Addition of water (0.37 kPa) to the reaction mixture of 7 kPa H<sub>2</sub> caused decrease of the rate of N<sub>2</sub> formation about 40 % at 603 K. The rate of N<sub>2</sub> formation in the presence of H<sub>2</sub> was not influenced by the addition of carbon monoxide of ca. 0.15 kPa into the reaction mixture.

The results obtained here stress that the activation of H<sub>2</sub> on the H-ZSM-5 is essential to promote the reaction of N<sub>2</sub>O. If the trace metallic component, e.g. Fe, in the H-ZSM-5 acts as a H<sub>2</sub> activator, the addition of CO in the reaction mixture would suppress the rate of N<sub>2</sub> formation in the presence of H<sub>2</sub>, since CO is known as a poison of the metallic sites. The suppression of the activity by CO was not observed in the present study. Therefore, the metal-catalyzed reduction of N<sub>2</sub>O by H<sub>2</sub> could be excluded.

Above results clearly demonstrated that the N<sub>2</sub>O decomposition activity of the H-ZSM-5 is controlled by the H<sub>2</sub> pressure and reaction temperature. Hattori et al.[7,8] reported that the activation of molecular hydrogen into protonic (H<sup>+</sup>) acid sites on a metal-free H-ZSM-5 catalyst

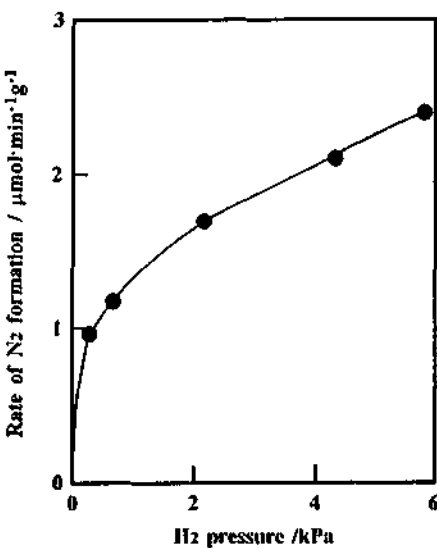


Figure 3 Dependence of the rate of N<sub>2</sub> formation on H<sub>2</sub> pressure on H-ZSM-5 (Si:Al=44) at 603 K. The H<sub>2</sub> pressure was varied under a constant total pressure (7 kPa) adjusted with He diluent.

was observed by using the infrared spectroscopy of adsorbed pyridine. The concentration of the protonic acid sites increases with increase in the temperature of the exposure of the zeolite to H<sub>2</sub> and in the H<sub>2</sub> pressure[7]. The generation and elimination of the protonic acid sites on the H-ZSM-5 are reversible for the introduction and removal of H<sub>2</sub>[7]. Thus, it is plausible that the promotion effect of H<sub>2</sub> upon the N<sub>2</sub>O decomposition on the H-ZSM-5 is due to the generation of the protonic acid sites on the H-ZSM-5 catalyst from hydrogen molecule in vapor phase, in reference to the proposal for the mechanism of the (protonic) acid-catalyzed N<sub>2</sub>O decomposition on H-ZSM-5 catalyst through hydroxyl diazonium ion (+N=N-OH)[2]. As shown in Figure 4, the activity enhanced by H<sub>2</sub> of 6.5 kPa was proportional to the content of Al in H-ZSM-5 zeolites, suggesting that the acidity related to aluminium in the zeolite lattice functions to the N<sub>2</sub>O decomposition and the activity enhancement by H<sub>2</sub> is closely related to the surface structure of Al in the zeolite.

#### 4. REFERENCE

1. M. Iwamoto, J. Hirata, K. Matsukami and S. Kagawa, *J. Phys. Chem.*, **1983**, *87*, 903
2. E. Suzuki, K. Nakashiro and Y. Ono, *Chem. Lett.*, **1988**, 953
3. G. I. Panov, A. S. Kharitonov and V. I. Sobolev, *Appl. Catal., A*, **1993**, *98*, 1
4. Y. Li and J. N. Armor, *Appl. Catal., B*, **1992**, *1*, L21
5. A. A. Slinkin, T. K. Lavrovskaya, I. V. Mishin and A. M. Rubinshtein, *Kinet. Katal.*, **1978**, *19*, 922; A. V. Kucherov, T. N. Kuchenova and A. A. Slinkin, *Kinet. Katal.*, **1992**, *33*, 877
6. A. Yoshimura, S. Namba and T. Yashima, *Shokubai(Catalyst)*, **1981**, *23*, 232
7. J. Tsuji, K. Ebitani, H. Hattori and H. Kita, *React. Kinet. Catal. Lett.*, **1992**, *48*, 17; K. Ebitani, J. Tsuji, H. Hattori and H. Kita, *J. Catal.*, **1992**, *138*, 750
8. H. Hattori, *Stud. Surf. Sci. Catal.*, (Eds., T. Inui, K. Fujimoto, T. Uchijima, M. Masai), Elsevier, Amsterdam, **1993**, *77*, 69

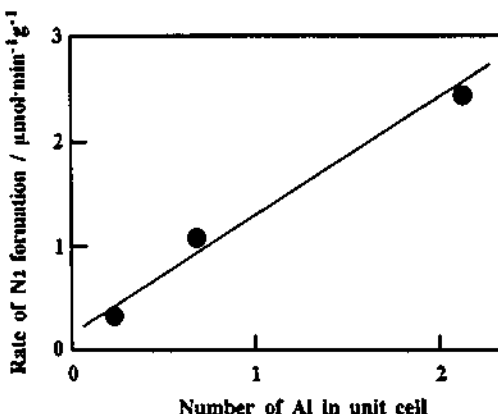


Figure 4 Dependence of the rate of N<sub>2</sub> formation in the presence of H<sub>2</sub> (6.5 kPa) on the content of aluminium in the H-ZSM-5 zeolites.

## 4.7 Acid-Base Properties of ALPO-5 Molecular Sieves Modified by Nickel and Molybdenum

Yu.Kalvachev, A.Spojakina, N.Kostova, and L.Dimitrov  
Institute of Kinetics and Catalysis, Bulgarian Academy of  
Sciences, Sofia 1113, Bulgaria

### Abstract

The decomposition of 2-propanol has been chosen as a test reaction to study the acid-base character of ALPO-5 molecular sieves modified by nickel and molybdenum. It was found that the type of the active components as well as the mode of their introduction affect acid-base properties of catalysts. Arguments for formation of heteropolymolybdate structures on the molecular sieve surface have been adduced. The role of different fragments in the structure of the modified molecular sieves has been discussed in connection with acidity and basicity of the catalysts.

### 1. INTRODUCTION

The acid and base properties of catalysts have gained growing attention for the purpose of developing specific criteria for the science of catalysis. Since alcohols are highly reactive, they can be used as probe molecules to characterize the acid-base properties of solid catalysts. This method was used for the first time with metal oxides [1-4]. The molecules of the lower monovalent alcohols, being small in size, are convenient to study the acid-base properties of catalysts. A great number of publications report the use of 2-propanol as a model compound for the study of solid catalysts. It was shown that 2-propanol conversion to propene and acetone is useful reaction for characterizing acidic, acid-base and redox properties of catalysts [2,5]. It is known that 2-propanol dehydration proceeds on acid sites whereas dehydrogenation occurs on basic sites [6]. Recently, modified and unmodified ZSM-5, ALPO, and SAPO catalysts were investigated by this technique [7-9].

ALPO-5 molecular sieves possess well defined microporous structure and adsorptive properties. Their crystalline structure involves alternating  $\text{AlO}_4^-$  and  $\text{PO}_4^+$  tetrahedra, the framework being neutral as a whole. Introduction of elements of another oxidation state presumes the appearance of active sites. ALPO-5 modified by nickel and molybdenum have received considerable attention [10-12]. High activity in n-alkane cracking was found [12] owing to the molecular sieve features, hydrogenolysis function of metal and acidity. The presence of nickel ions in the framework of SAPO [13,14] strongly enhances their catalytic

activity in methanol conversion and selectivity to ethylene.

In the present study we examined the acid-base properties of ALPO-5 modified by nickel and molybdenum in the model reaction of 2-propanol conversion. We followed the effect of the mode of introduction of the active components to the catalysts on their acid-base properties.

## 2. EXPERIMENTAL METHODS

### 2.1. Catalyst Preparation

An ALPO-5 molecular sieve (sample 1) was synthesized according to US patent [15]. NiALPO-5 (sample 2) was prepared under hydrothermal conditions for 20 h at 448 K from a gel with the following composition:

1.100 Et<sub>3</sub>N : 0.042 NiO : 0.979 Al<sub>2</sub>O<sub>3</sub> : P<sub>2</sub>O<sub>5</sub> : 50 H<sub>2</sub>O  
 X-ray analysis of the sample after removing the template at 823 K for 10 h showed good crystallinity and absence of dense phases. Chemical analysis indicated the presence of 1.3 wt. % nickel. Sample 3 (Ni + ALPO-5) was prepared by impregnation of ALPO-5 with an aqueous solution of Ni(NO<sub>3</sub>)<sub>2</sub> · 6 H<sub>2</sub>O whereas ALPO-5, NiALPO-5 and Ni + ALPO-5 were impregnated with an aqueous solution of (NH<sub>4</sub>)<sub>6</sub>Mo<sub>7</sub>O<sub>24</sub> · 4 H<sub>2</sub>O to give sample 4 (Mo + ALPO-5), sample 5 (Mo + NiALPO-5) and sample 6, respectively. Ni + ALPO-5 contains 1 wt. % nickel. Mo + ALPO-5 and Mo + NiALPO-5 contain 10 wt. % molybdenum. The sample 4 was calcined for 4 h at 773 K to give the sample MoO<sub>3</sub>/ALPO-5.

### 2.2. Catalytic tests

Measurements were performed using the flow method. 0.2 g of catalyst was charged into the reactor. The catalyst was activated under flow of air at 623 K and flushed with argon before experiment. Argon was used as a carrier gas at the rate of 150 ml/min at 273 K. The reactor was directly connected to a 2 m GC column filled with Chromosorb W (60-80 mesh) with 20 % Carbowax 400 at 313 K. All the experiments were performed at 448 and 473 K. The results are summarized in Table 1.

2-propanol conversion to propene was used as a measure of acidity and that to acetone is a measure of basicity.

### 2.3. IR and ESR measurements

IR spectroscopy in the region 400 - 1200 cm<sup>-1</sup> using pellets in KBr (sample : KBr ratio is 1 : 150) has been used for characterization of state of catalysts.

The ESR spectra have been recorded on a Bruker ER 200D spectrometer operating at 9.7 MHz (X band) at room temperature. Prior to registration of the spectra, the samples had been pretreated in a quartz reactor.

## 3. RESULTS AND DISCUSSION

As it is seen in Table 1, ALPO-5 was not active for the conversion of 2-propanol. This was evidence for the absence of active sites capable to provoke 2-propanol conversion. The degree of 2-propanol dehydration increased significantly after introducing small amounts of nickel (1.0-1.3 %) into the catalyst. It is seen that the activity was dependent on the mode of introduction of the nickel : directly during the synthesis of the zeolite (sample 2) or upon impregnation (sample 3). A higher

selectivity to propene was demonstrated by sample 2.

Table 1. Catalytic activity in 2-propanol conversion (wt %)

No	Catalyst	T, K	Propene	Acetone	2-propanol
1.	ALPO-5	448	-	-	100
		473	traces	-	100
2.	NiALPO-5	448	23	traces	77
		473	29	1	70
3.	Ni + ALPO-5	448	4	1	95
		473	10	3	87
4.	Mo + ALPO-5	448	15	7	78
		473	21	8	71
5.	Mo + NiALPO-5	448	26*	14	60
		473	37*	14	49
6.	Mo + Ni + ALPO-5	448	22	12	66
		473	27	13	60
7.	$\text{MoO}_3/\text{ALPO-5}$	448	12	-	88
		473	17	traces	83

\* mixture of  $\text{C}_1\text{-C}_3$  hydrocarbons

Reduction of sample 3 in a flow of hydrogen at 623 K gave rise to a singlet at  $g = 2.56$  in the electron spin resonance (ESR) spectrum which is due to ferromagnetic nickel. The high  $g$  value and the broad resonance line (Fig.1) can mean significant

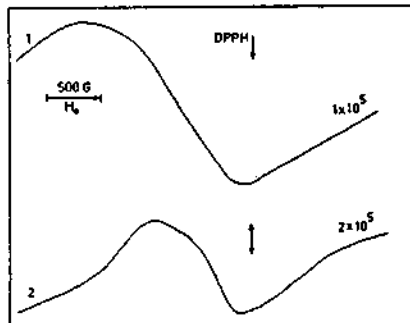


Figure 1. ESR - spectra after reduction with hydrogen of  
a) Ni + ALPO-5 at 623 K; b) NiALPO-5 at 773 K (hydrothermal treatment).

sintering of the nickel metal particles [16]. No ESR signal with sample 2 was observed under the same conditions. In this case the ESR signal of ferromagnetic nickel is appeared only at 773 K after the hydrothermal treatment. The low values of  $g$  and  $\Delta H$  for this sample show that the finely divided nickel particles are formed. These results indicate that the state of nickel in the two catalysts was different.

The higher activity of NiALPO-5 could be explained by assuming that in this case the nickel is incorporated in the zeolite lattice. Thus novel active sites are formed because the framework of the molecular sieve loses its electrical neutrality. 2-propanol dehydrogenation proceeded over these samples, however, the amounts of acetone were very small. On the sample 4 (Mo + ALPO-5) both the dehydration and dehydrogenation activities were enhanced. Sample 5 manifested the highest activity in 2-propanol conversion. Introduction of molybdenum into ALPO-5 increases significantly the role of basic sites in the 2-propanol conversion (Table 1 - acetone/propene ratio).

The infrared spectra of samples 4, 5 and 6 showed that aluminium polymolybdate structures (bands at 650, 890, 910, 950  $\text{cm}^{-1}$  - Fig.2) were formed in these catalysts as a result of specific interaction between the zeolite and the modifying components [11].

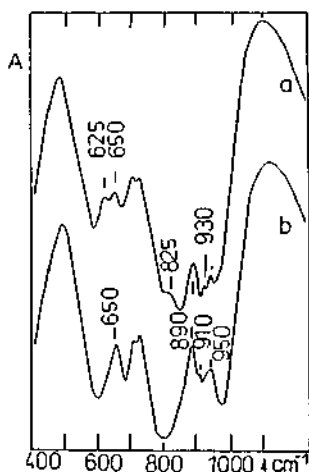


Figure 2. IR - spectra of  
a) Mo + Ni + ALPO-5  
b) Mo + NiALPO-5

Upon impregnation of ALPO-5 with nickel and molybdenum, nickel heteropolymolybdate is formed along with aluminium heteropolymolybdate.

Contrary to this, the IR spectrum of sample 5 produced bands due only to aluminium heteropolymolybdate. The absence of nickel heteropolymolybdate can be explained by limited access to the nickel which is probably incorporated in the zeolite lattice. Molybdenum reacts easily with accessible aluminium from the molecular sieve.

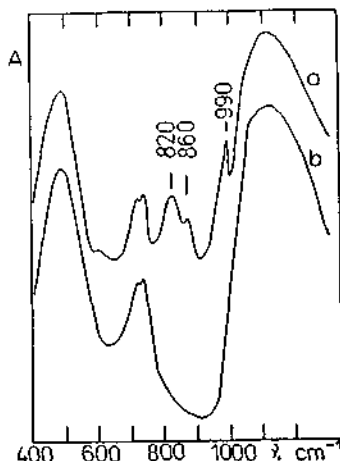


Figure 3. IR - spectra of : a)  $\text{MoO}_3/\text{ALPO-5}$   
b)  $\text{ALPO-5}$ .

In the spectrum of the sample 7, calcined at 773 K, the bands corresponding to the polymolybdate structure were not observed. The bands at 820, 860, 990  $\text{cm}^{-1}$  indicate the presence of  $\text{MoO}_3$  on the surface of ALPO-5 (Fig.3a). In contrast with Mo-ALPO-5 only 2-propanol dehydration was observed for this sample (Table 1). Our results show that the investigated catalysts containing polymolybdate structures exhibit both acid and base properties. The results obtained enabled us to suggest that the acetone formation over the molybdenum-containing molecular sieves is related to the existing aluminium(nickel)heteropolymolybdate structures. Basic sites are not revealed in the sample 7, where polymolybdates are absent.

The bifunctional properties of heteropolymolybdates (acid-base and redox) are well known. This means that different mechanisms of 2-propanol decomposition (selectivity to propene and acetone formation) could be involved [2,5,17]. Brønsted sites of Mo-Al-heteropoly complexes affect the 2-propanol dehydration. But the acetone formation can take place through participation of acid-base pair in the Al-O-Mo fragments of these compounds and their redox properties. The reaction products can affect formation of acetone too.

#### ACKNOWLEDGEMENT

The authors gratefully acknowledge financial support from the Bulgarian National Foundation for Scientific Research (Project X-91).

## 4. REFERENCES

1. H.Pines and J.Manassen, *Adv.Catal.*, 1966, 16, 49
2. M.Ai and S.Suzuki, *J.Catal.*, 1973, 30, 362 ; M.Ai and T.Ikawa,*ibid.*, 1975, 40, 203 ; M.Ai, *ibid.*, 1975, 40, 318 ; *ibid.*, 1975, 40, 327
3. A.Gervasini and A.Auroux, *J.Catal.*, 1991, 131, 190
4. C.Bezouhanova and M.Al-Zihari, *Catal.Lett.*, 1991, 11, 245
5. A.Ougour, G.Coudurier and J.C.Vedrine, *Actas XIII Simposio Iberoamericano de Catalisis*, Segovia, p.1163, 1992
6. K.Tanabe, in "Solid Acid and Bases", p.p.122, 141, Kodansha Ltd, Tokyo, 1970
7. J.Lercher, G.Warecka and M.Derewinski, *Proc. 9<sup>th</sup> Int. Congr. Catal.*, Calgary, M.Phillips and M.Ternan (Eds.), The Chemical Institute of Canada, Ottawa, p.364, 1988.
8. R.Khouzami, G.Coudurier, B.Mentzen and J.Vedrine, *Actas XI Simposio Iberoamericano de Catalisis*, Guanajuato, F.Cossio, O.Bermudez, G. del Angel, and R.Gomez (Eds.), Mexico, p.473, 1988
9. C.Bezoukhanova and Yu.Kalvachev, *Catal.Rev.- Sci.Eng.*, in press
10. I.Ming, S.Gui-Fa, S.Dekum and F.Xian-cai, *J.Catal.(China)*, 1989, 10, 282
11. A.Spojakina, N.Kostova, and L.Dimitrov, *Collect.Czech.Chem. Commun.*, 1992, 57, 836
12. P.Jia-lu, C.Zhao, and X.Qin-hua, *J.Catal.(China)*, 1989, 10, 208
13. J.Thomas, Y.Xu, C.Catlow, and I.Coves, *Chem.Mater.*, 1991, 31, 667
14. T.Inui, 199<sup>th</sup> ACS National Meeting, Part II, Boston, Division of Petroleum 56, ACS, 1990
15. US Patent 4310440 (1982)
16. S.Damyanova, A.Spojakina and D.Shopov, *Appl.Catal.*, 1989, 48, 177
17. H.Vinek, H.Noller, M.Ebel and K.Schwarz, *J.Chem.Soc. Trans. Faraday I*, 1977, N5, 734.

## 4.8 Novel Catalysis of Cesium Salt of Heteropoly Acid and its Characterization by Solid-state NMR

T. OKUHARA, T. NISHIMURA, H. WATANABE, K. NA and M. MISONO

Department of Synthetic Chemistry, Faculty of Engineering, The University of Tokyo,  
Bunkyo-ku, Tokyo 113, Japan

### ABSTRACT

Acid-catalyzed reactions by acidic cesium salts of 12-tungstophosphoric acid ( $H_3PW_{12}O_{40}$ ) have been studied in relation to the acidities and microstructure of the particles. Liquid-phase alkylation of 1,3,5-trimethylbenzene with cyclohexene, decomposition of cyclohexylacetate and gas-phase skeletal isomerization of *n*-butane were performed over heteropoly compounds and other typical solid acids such as zeolites, Nafion-H,  $SO_4^{2-}/ZrO_2$ , etc. It was found that  $Cs_{2.5}H_{0.5}PW_{12}O_{40}$  showed very high activities for these reactions and the excellent selectivity for the skeletal isomerization. XRD, TEM and  $N_2$  adsorption revealed that  $Cs_{2.5}H_{0.5}PW_{12}O_{40}$  consists of ultrafine primary particles (~8 nm) and therefore has a high surface area. High resolution solid-state NMR demonstrated that the chemical shift of  $^{31}P$  (central atom of the polyanion) is determined by the number of proton which is directly attached to the polyanion and all protons are distributed randomly through the whole bulk of the particles. Owing to this,  $Cs_{2.5}H_{0.5}PW_{12}O_{40}$  possesses a high surface protonic acidity, which is a reason for its high activity. The quantity of acid sites of  $Cs_{2.5}H_{0.5}PW_{12}O_{40}$  was less than those of zeolites and  $SO_4^{2-}/ZrO_2$  and the acid strength was lower than that of  $SO_4^{2-}/ZrO_2$ . It is presumed, therefore, that the acid-base bifunctional action together with the high surface acidity brought about the high activity of  $Cs_{2.5}H_{0.5}PW_{12}O_{40}$ .

### 1. INTRODUCTION

Heteropoly compounds are good cluster models of mixed oxide catalysts because of their well-defined structures and are thus of great interests for the fundamental study. At the same time, they have been utilized for practical processes such as hydration of olefins, oxidation of aldehydes and polymerization of tetrahydrofuran [1-3]. The use of solid acid catalysts in place of homogeneous catalysts such as  $H_2SO_4$  and  $AlCl_3\text{-HCl}$  is generally desirable for liquid-phase reactions. In only a few examples solid heteropoly compounds were applied to liquid-phase reactions [4]. Recently it was found that  $H_3PW_{12}O_{40}$  and its acidic Cs salts possess superacidities [5].

Here we wish to report the superacid catalysis of the acidic Cs salt,  $Cs_{2.5}H_{0.5}PW_{12}O_{40}$  (abbreviated as Cs2.5), for surface-type reaction [1a,6]. We already reported that Cs2.5 was more active than the parent acid-form for conversion of dimethyl ether and dehydrations of alcohols [7,8]. In addition, remarkably high activities of Cs2.5 were recently found for liquid-phase reactions [9,10]. In the present study, the acidic property, proton distribution and particle size of the Cs salts have been investigated by

TPD of NH<sub>3</sub>, solid-state NMR, N<sub>2</sub> adsorption and XRD in relation to their novel catalytic activities.

## 2. EXPERIMENTAL METHODS

### 2.1 Catalyst Preparation

The acidic Cs salts (Cs<sub>x</sub>H<sub>3-x</sub>PW<sub>12</sub>O<sub>40</sub>, abbreviated as CsX) were prepared by the titration of an aqueous solution of H<sub>3</sub>PW<sub>12</sub>O<sub>40</sub> (0.08 mol dm<sup>-3</sup>) with an aqueous solution of Cs<sub>2</sub>CO<sub>3</sub> (Cs<sup>+</sup>: 0.25 mol dm<sup>-3</sup>) [5]. The Keggin structure of all the heteropoly compounds was confirmed by IR spectroscopy. Sulfated ZrO<sub>2</sub> (SO<sub>4</sub><sup>2-</sup>/ZrO<sub>2</sub>) was prepared from Zr(OH)<sub>4</sub> and H<sub>2</sub>SO<sub>4</sub> by a method as described in the literature [11]. SO<sub>4</sub><sup>2-</sup>/ZrO<sub>2</sub> was calcined in air at 923 K for 5 h. Nafion-H (NR-50, Mitsui Toatsu Fine Chemical), HY zeolite (Reference Catalyst, HY-4.8, Catalysis Society of Japan), SiO<sub>2</sub>-Al<sub>2</sub>O<sub>3</sub> (SA-1, Catalysts and Chemical Industries; Al<sub>2</sub>O<sub>3</sub>; 13 wt%) were used. Furthermore, H<sub>2</sub>SO<sub>4</sub> (Nacalai Tesque, ultrafine grade) and AlCl<sub>3</sub>-HCl, which was prepared by the method described previously [12], were used.

### 2.2 Catalytic Reactions

Alkylation of 1,3,5-trimethylbenzene (abbreviated as TMB) with cyclohexene (without solvent) and decomposition of cyclohexylacetate (solvent: *n*-nonane) were carried out at 353 and 373 K, respectively, under the atmospheric pressure of N<sub>2</sub> in a three-neck flask (Pyrex glass) with a magnetic stirrer [5]. Skeletal isomerization of *n*-butane was performed in a flow reactor (Pyrex tube, 8 mm internal diameter) at 573 K under atmospheric pressure. The feed gas consisted of 0.05 atm (5 vol.%) of *n*-butane and N<sub>2</sub> balance [13,14]. In some cases, H<sub>2</sub> was added to the feed gas. Total flow rates were 10~20 cm<sup>3</sup> min<sup>-1</sup>. Prior to the reaction, the catalysts were pretreated at 573 K in a N<sub>2</sub> flow for 2 h. The products were analyzed by gas chromatography.

### 2.3 Characterization of Catalysts

The acidity was measured by Temperature Programmed Desorption (TPD) of NH<sub>3</sub> and the color changes of the Hammett indicators [5]. In the case of NH<sub>3</sub>-TPD, the gases that were desorbed were analyzed by an on-line mass spectrometer (Anelva NAG-110). Solid-state NMR spectra were obtained with magic-angle spinning (MAS) on a Fourier transform pulsed NMR spectrometer (JEOL JNM-GX270) as in the previous reports [15]. It was necessary to dry the samples carefully to get reproducible data.

## 3. RESULTS AND DISCUSSION

The Keggin structure (e.g., PW<sub>12</sub>O<sub>40</sub><sup>3-</sup>) is illustrated in Fig. 1a. The size of the Keggin anion is about 11 Å and this anion is thermally stable up to at least about 573 K in the solid state. XRD revealed that Cs<sub>2.5</sub> has a structure in which the Keggin anions are arranged in bcc, as in the case of Cs<sub>3</sub>. The particle size (crystallite size) of Cs<sub>2.5</sub> was determined to be 8~10 nm by the XRD-line width and the surface area (130~150 m<sup>2</sup> g<sup>-1</sup>) [5,7,10]. The model of the primary particle of Cs<sub>2.5</sub> is shown in Fig. 1b.

### 3.1 Catalysis of Cs<sub>2.5</sub>H<sub>0.5</sub>PW<sub>12</sub>O<sub>40</sub>

Figure 2 shows the catalytic activities of various acid catalysts for the two liquid-phase reactions. Cs<sub>2.5</sub> was most active among the solid acid catalysts used in the present study. The activity of Cs<sub>2.5</sub> for the alkylation was about 15 and 50 times as high as those of SO<sub>4</sub><sup>2-</sup>/ZrO<sub>2</sub> and Nafion-H, respectively, although SO<sub>4</sub><sup>2-</sup>/ZrO<sub>2</sub> and Nafion-H have superacidities [11,16]. HY and H-ZSM-5 zeolites exhibited poor activities. It is noted that Cs<sub>2.5</sub> was also superior to liquid acids such as H<sub>2</sub>SO<sub>4</sub> and AlCl<sub>3</sub>-HCl. Also in the case of

the decomposition of cyclohexylacetate, the high catalytic performance of Cs2.5 was confirmed as shown in Fig. 2.

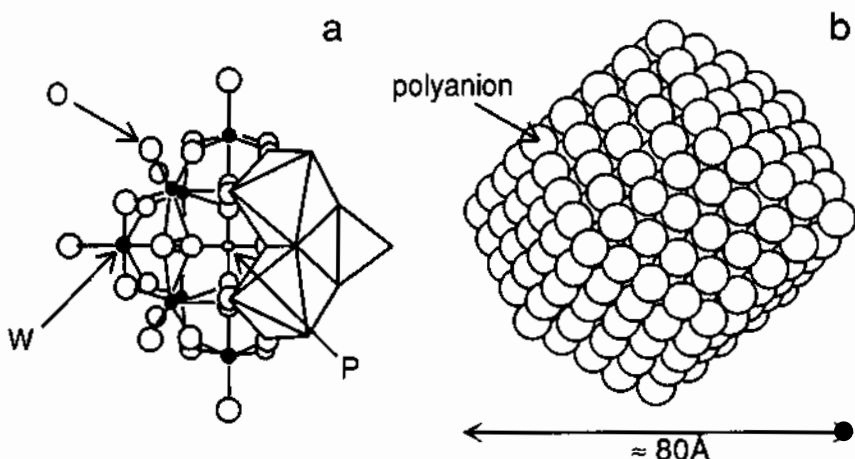


Fig. 1 (a) Keggin structure,  $\text{PW}_{12}\text{O}_{40}^{3-}$ ; (b) Model of primary particle of Cs2.5.

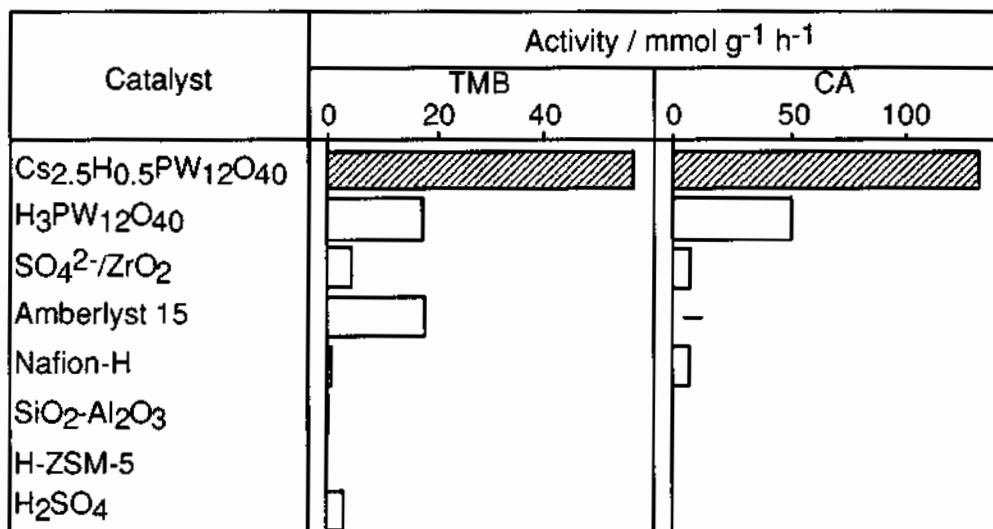


Fig. 2 Catalytic activities of various acid catalysts for liquid-phase reactions.

TMB: Alkylation of 1,3,5-trimethylbenzene with cyclohexene,

CA: Decomposition of cyclohexylacetate.

When Cs2.5 was filtered after the first run of the alkylation and reused (second and third runs), the rates were nearly equal to the steady-state value of the first run, showing that the deactivation of the catalyst was small under the reaction conditions. This indicates that the reaction did not take place in the solution, and the active component was not dissolved in the liquid.

Figure 3 shows the activities and selectivities for the gas-phase skeletal isomerization of *n*-butane over the various kinds of solid acids. The conversion at 573 K is in the order Cs2.5 > SO<sub>4</sub><sup>2-</sup>/ZrO<sub>2</sub> > H<sub>3</sub>PW<sub>12</sub>O<sub>40</sub>. The order in the selectivity to isobutane is Cs2.5 (83%) > H<sub>3</sub>PW<sub>12</sub>O<sub>40</sub> (81%) > SO<sub>4</sub><sup>2-</sup>/ZrO<sub>2</sub> (61%), where the figures in parentheses are the selectivity. H-ZSM-5 produced mainly propane (about 75%), while the conversion was high [13]. These results demonstrate that Cs2.5 was an effective catalyst for the isomerization of *n*-butane. It was further found that the activity of Cs2.5 was greatly enhanced by the addition of Pt or Pd and the coexistence of H<sub>2</sub>. Remarkably, Pt-Cs2.5 and Pd-Cs2.5 exhibited very high selectivities (94–96%) as compared with Pt-SO<sub>4</sub><sup>2-</sup>/ZrO<sub>2</sub> (47%) (see Fig. 3) and Pt-H-ZSM-5 (34%). Pt-Cs2.5 was also active and selective even at a low H<sub>2</sub> concentration (5%) [14].

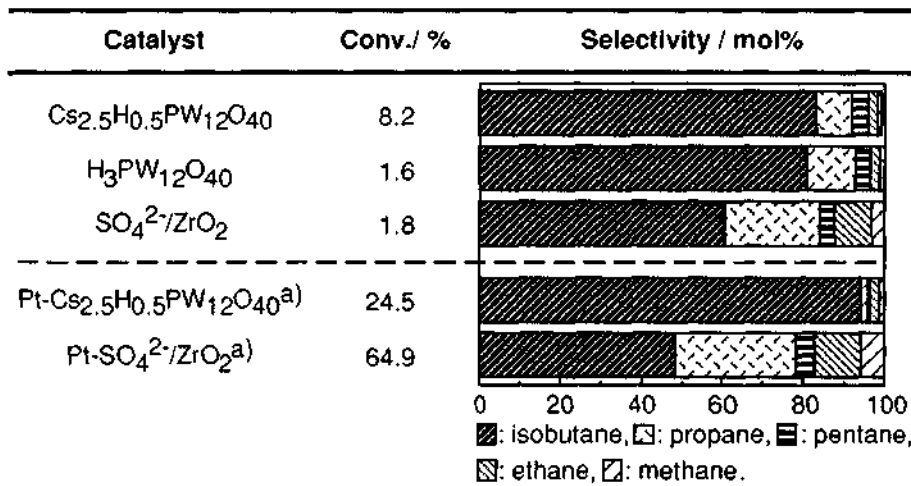


Fig. 3 Activity and selectivity for skeletal isomerization of *n*-butane at 573 K.  
 Feed gas: *n*-butane 5% and N<sub>2</sub> balance, W/F = 40 g h mol<sup>-1</sup>.  
 a) *n*-butane 5%, H<sub>2</sub> 50% and N<sub>2</sub> balance, Pt 1wt%.

In Fig. 4, the catalytic activities for these reactions are plotted against the extent of Cs substitution for three protons of H<sub>3</sub>PW<sub>12</sub>O<sub>40</sub>. As the Cs content (*x*) increases, the catalytic activity decreases at first, but greatly increases when the Cs content is 2.5. That is, there are two maxima at *x* = 0 and *x* = 2.5.

Figure 5 provides the surface area as a function of the Cs content. While the surface area of H<sub>3</sub>PW<sub>12</sub>O<sub>40</sub> is about 5 m<sup>2</sup> g<sup>-1</sup>, it increased significantly to more than 130 m<sup>2</sup> g<sup>-1</sup>, when the Cs content exceeded 2.5. As reported previously [8], the precipitates formed during the titration have the composition of Cs<sup>+</sup>:H<sup>+</sup> = 2:1 (Cs<sub>2</sub>HPW<sub>12</sub>O<sub>40</sub>) in the range of 0.5 ≤ *x* ≤ 2. The precipitates consist of large particles (about 10<sup>4</sup> Å), while the crystallite size estimated from XRD line-width was about 200 Å [17]. By the further addition of Cs<sup>+</sup> to

the solution containing the precipitates, the large particles changed into the smaller ones to have the high specific surface area. The concentration of  $H^+$  in the Cs salt decreased monotonically from 3 ( $x = 0$ ) to 0 ( $x = 3$ ) (shown by the broken line in Fig. 5). If all protons in the particles of the salts distribute randomly through the surface and the whole bulk, the surface acidity (the acid amount on the surface) can be estimated by multiplying the formal concentration of  $H^+$  on the surface by the specific surface area (the number of polyanion on the surface).

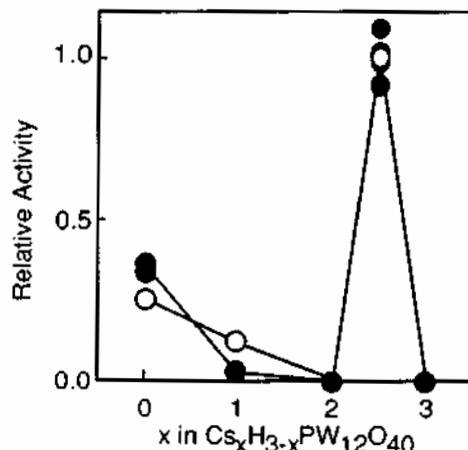


Fig. 4 Catalytic activities for (O) decomposition of cyclohexylacetate and (●) alkylation of 1,3,5-trimethylbenzene with cyclohexene as a function of Cs content.

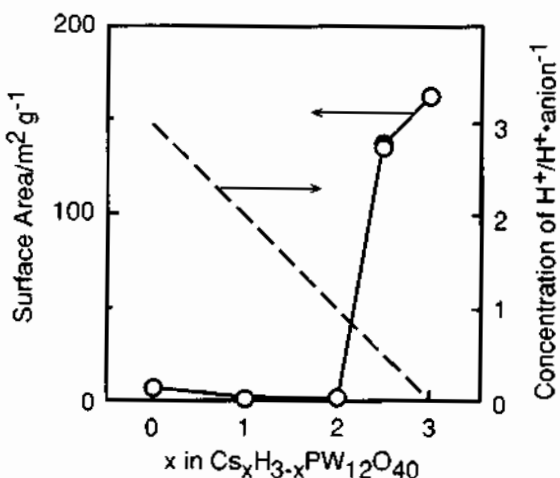


Fig. 5 Surface area and proton concentration of  $Cs_xH_{3-x}PW_{12}O_{40}$ .

The distribution of  $H^+$  will be stated on the basis of the result of solid-state NMR and the correlation between the catalytic activity and the surface acidity will be discussed below. It is difficult to measure the surface acidity by the adsorption of basic molecules, since basic molecules are readily absorbed into the bulk of  $H_3PW_{12}O_{40}$  and some of the Cs salts [1].

### 3.2 Acidic Properties and Structure of $Cs_{2.5}H_{0.5}PW_{12}O_{40}$

TPD profiles of  $NH_3$  are given in Fig. 6 [5].  $Cs_{2.5}$  gave a broad desorption peak of  $NH_3$  in the temperature range 633~923 K, together with sharp but smaller peaks of  $N_2$  and  $H_2O$  (not shown) having maxima at about 800 K.  $N_2$  was very probably formed by the reaction of  $NH_3$  with oxygen of the heteropoly anion. It may be stated that, if the decomposition to  $N_2$  had not occurred,  $NH_3$  would have desorbed at a temperature not lower than the temperature at which  $N_2$  formed. Hence, the formation of  $N_2$  is also a measure of acid strength. The peak temperature of  $NH_3$ -TPD for  $Cs_{2.5}$  was close to that for  $H_3PW_{12}O_{40}$ , indicating that the acid strength of  $Cs_{2.5}$  is similar to that of  $H_3PW_{12}O_{40}$ . In the case of  $SO_4^{2-}/ZrO_2$ , the desorption of  $NH_3$  was observed at a low temperature region (<800 K). On the other hand, the desorption as  $N_2$  took place at much higher temperatures (>973 K). The high temperature of  $N_2$  originated from  $NH_3$  indicates the high acid strength.  $NH_3$  adsorbed on  $SiO_2-Al_2O_3$  and H-ZSM-5 were mostly desorbed at temperatures lower than 800 K, which is in agreement with the previous reports [18,19], showing that their acid strengths are not high. Thus the order of acid strength is estimated as follows:  $SO_4^{2-}/ZrO_2 > H_3PW_{12}O_{40}, Cs_{2.5} > H-ZSM-5 > SiO_2-Al_2O_3$ .

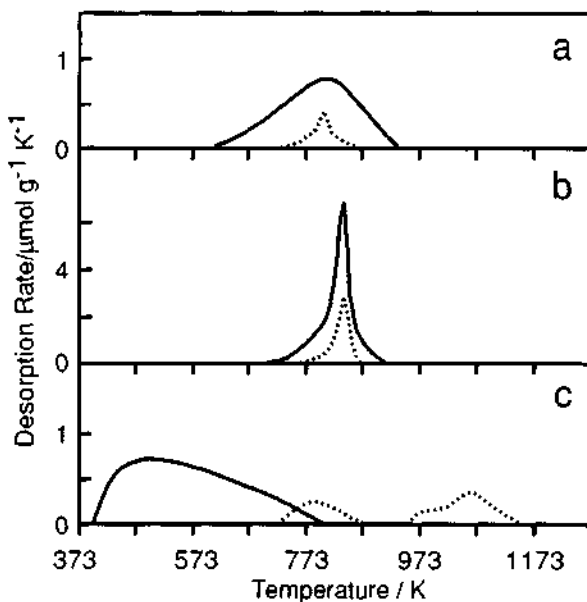


Fig. 6  $NH_3$ -TPD profiles of (a)  $Cs_{2.5}H_{0.5}PW_{12}O_{40}$ , (b)  $H_3PW_{12}O_{40}$  and (c)  $SO_4^{2-}/ZrO_2$ . Solid line;  $NH_3$ , dotted line;  $N_2$ .

Table 1 shows the acid strengths measured by the color changes in Hammett indicators. After the dryness at 573 K,  $H_3PW_{12}O_{40}$  and Cs2.5 showed acidities of  $H_0 = -13.16$ , indicating that these heteropoly compounds are superacids [5]. As reported previously [11],  $SO_4^{2-}/ZrO_2$  had much more higher superacidity ( $H_0 = -14.52$ ).

Table 1. Acid Strength Measured by Hammett Indicators

Catalyst	pKa of indicator					
	-8.2	-11.35	-12.70	-13.16	-13.75	-14.52
$Cs_{2.5}H_{0.5}PW_{12}O_{40}$	+	+	+	+	-	-
$H_3PW_{12}O_{40}$	+	+	+	+	-	-
$SO_4^{2-}/ZrO_2$	+	+	+	+	+	+

### 3.3. Proton Distribution by Solid-State NMR

We already reported the results of solid-state NMR of the heteropolyacid and alcohols activated in its pseudoliquid phase [15,20]. Protonated ethanol dimer ( $C_2H_5OH)_2H^+$  gave very clear  $^1H$  NMR peaks and the chemical shift of hydroxyl proton of the dimer (9.5 ppm) suggests that the pseudoliquid of  $H_3PW_{12}O_{40}$  is a superacid. In addition, the chemical shift of solid-state NMR of  $^{31}P$ , which is the central atom of Keggin anion, was very sensitive to the quantity of crystallization water or ethanol molecules absorbed. This suggests that  $^{31}P$  NMR chemical shift reflects sensitively the coordination state around the polyanion.

NMR spectra of  $^{31}P$  for  $CsX$  were measured after the samples were evacuated at 473 K for 2 h.  $H_3PW_{12}O_{40} \cdot 6H_2O$  (hexahydrated) showed one peak at -15.6 ppm, which is consistent with the previous data [20]. On the other hand, anhydrous  $H_3PW_{12}O_{40}$  gave one peak at -10.9 ppm. That is, the chemical shift changed depending on the number of the crystallization water. In the crystal structure of  $H_3PW_{12}O_{40} \cdot 6H_2O$ , the protonated water dimers,  $H^+(H_2O)_2$ , connect with the polyanions by hydrogen-bonding at the terminal oxygens (W=O) [21]. On the other hand, 3 protons in the anhydrous  $H_3PW_{12}O_{40}$  attach directly to the more basic bridging oxygens (W-O-W) [22]. Thus the different chemical shift between the hexahydrated and anhydrous  $H_3PW_{12}O_{40}$  is attributable to the different location of  $H^+$ . The stoichiometric salt,  $Cs_3PW_{12}O_{40}$ , which has no proton, gave the one peak at -14.9 ppm, which is close to that of  $H_3PW_{12}O_{40} \cdot 6H_2O$ . Since the polyanions of the two samples have no proton attached directly, the agreement in the chemical shift is understandable.

The salts with the composition of Cs1, Cs2 and Cs2.5 showed four peaks consisting of -10.9, -14.9 and other two, -12.1 and -13.5 ppm. If one considers the presence of additional two peaks between -14.9 and -10.9 ppm for  $CsX$  (X = 1, 2 and 2.5), the chemical shift of  $^{31}P$  is thought to be determined by the number of the proton directly bonded to the bridging oxygens; the peaks at -14.9, -13.5, -12.1, and -10.9 ppm can be assigned to the Keggin anion having 0, 1, 2 and 3 protons, respectively. When the sample absorbed water, the signal at lower field shifted reversibly to higher field. So it was necessary to dry the sample carefully.

The detailed  $^{31}P$  NMR spectrum of Cs2.5 is shown in Fig. 7. The solid line shows the experimental result and the broken one is the random distribution calculated on the basis of the compositions (Cs/H ratio). The relative intensities of these peaks for Cs2.5 were in good agreement with those expected from the random distribution of protons. This indicates that all the protons in the salts distribute nearly statistically to all the polyanions, that is, uniform acidic salts like solid solutions are formed. When the sample having Cs:anion = 2.5:1 was prepared by impregnating Cs3 with an aqueous solution of

$\text{H}_3\text{PW}_{12}\text{O}_{40}$  and was evacuated at 473 K, a  $^{31}\text{P}$  NMR spectrum same as  $\text{Cs}_2.5$  was observed. Probably homogenization proceeded by the migration of Cs ion and proton as suggested before [8].

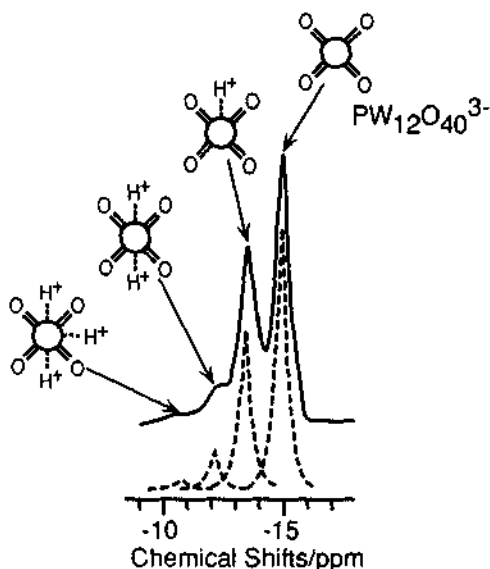


Fig. 7  $^{31}\text{P}$ -NMR spectrum of  $\text{Cs}_2.5\text{H}_0.5\text{PW}_{12}\text{O}_{40}$ .

XRD measurement supported the migration of Cs ion and proton in the  $\text{Cs}_1\text{H}_2\text{PW}_{12}\text{O}_{40}$  which was obtained by the titration. After the evaporation at 313 K, this salt gave two sets of XRD peaks due to  $\text{H}_3\text{PW}_{12}\text{O}_{40} \cdot 6\text{H}_2\text{O}$  (cubic) and those close to  $\text{Cs}_3$  and/or  $\text{Cs}_2$  (cubic). Thus the precipitate (without heat treatment) is a mixture of  $\text{H}_3\text{PW}_{12}\text{O}_{40} \cdot 6\text{H}_2\text{O}$  and probably  $\text{Cs}_2\text{HPW}_{12}\text{O}_{40}$ . The two sets of the peaks changed into one set of the peaks located between the two by the heat treatment at 473 K, suggesting the migration of Cs ion and proton to form the homogeneous salt.

Assuming the uniform distribution of protons through the surface and bulk, the surface acidity for  $\text{CsX}$  was estimated by multiplying the formal concentration of  $\text{H}^+$  on the surface by the specific surface area, and is shown in Fig. 8 as a function of the Cs content. As the Cs content increases, the surface acidity decreases at first, but greatly increases when the Cs content is 2.5. The change in Fig. 8 is very close to that of the catalytic activities as shown in Fig. 4. Therefore, the catalytic activity was well correlated with the surface acidity for  $\text{CsX}$ . The estimated surface acidity of  $\text{Cs}2.5$  ( $60 \mu\text{mol g}^{-1}$ ) is less than those of  $\text{SiO}_2\text{-Al}_2\text{O}_3$  ( $150\sim220 \mu\text{mol g}^{-1}$ ) and  $\text{SO}_4^{2-}/\text{ZrO}_2$  ( $200 \mu\text{mol g}^{-1}$ ). It is notable that the activity of the Cs salts per unit acidity is much greater than those of  $\text{SiO}_2\text{-Al}_2\text{O}_3$ ,  $\text{SO}_4^{2-}/\text{ZrO}_2$  and zeolites. K and  $\text{NH}_4$  salts also gave the same trends [23]. The much greater activities of Cs salts than  $\text{SiO}_2\text{-Al}_2\text{O}_3$  and  $\text{SO}_4^{2-}/\text{ZrO}_2$  cannot be explained simply by the surface acidity. An additional effect is necessary to explain the high activities of the heteropoly compounds.

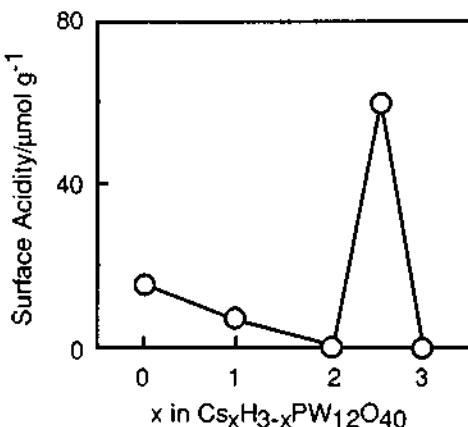


Fig. 8 Estimated surface acidities of  $\text{Cs}_x\text{H}_{3-x}\text{PW}_{12}\text{O}_{40}$ .

Take *et al.* [18] reported that only weak acid sites were present on the external surface of these zeolites, while the strong acid sites were located at the internal surface. Therefore, the low activities of these zeolites are presumably due to the difficulty of the diffusion of the reactants into the pores of the zeolites. The average pore size (between the primary particles) of Cs2.5 was determined to be about 3.5 nm from the isotherm of N<sub>2</sub> adsorption [5,24], which is wide enough for the diffusion of the molecules. Cs3 had pores of average size 8.0 nm, which is consistent with the result of Moffat *et al.* [25].

Izumi *et al.* [26] pointed out the importance of the soft basicity of the heteropoly anion in catalysis in homogeneous liquid-phase systems; the heteropoly anion stabilizes and activates reaction intermediates such as carbocation or oxonium ion. The basicity of the heteropoly anion presumably plays an important role in those reactions through acid-base bifunctional acceleration by proton (acid) and polyanion (base) and/or a special state of proton on the surface.

Another new aspect of CsX we found recently is shape selectivity [24]. Intraparticle void depends on the size of primary particle that varies with the preparation conditions and the content of Cs. The pore size for Cs2.1~2.2 was significantly smaller (less than 10 Å) than that of Cs2.5. Reflecting the difference, the activities of Cs2.1 and Cs2.2 for the alkylation were much lower than expected from the surface acidity, although they showed expected activities for the reactions of the smaller molecules such as dehydration of ethanol and 2-propanol and skeletal isomerization of *n*-butane.

In conclusion, Cs2.5 is an extraordinary efficient solid acid catalyst for several organic reactions in liquid phase. The reasons for the high activity are firstly that it has very high surface protonic acidity (ultrafine particles with nearly uniform proton distribution) with high acid strength and secondly that unique role of basic polyanion or unique proton acidity may be present.

#### 4. ACKNOWLEDGMENT

The authors would like to thank Dr. Shin-ichi Nakata (Chiyoda Corporation) for the NMR measurements and discussion.

## 5. REFERENCES

- 1 (a) M. Misono, *Catal. Rev.-Sci. Eng.*, **1987**, *29*, 269; **1988**, *30*, 339; (b) M. Misono, in L. Guczi, F. Solymosi and P. Tétényi (eds.), *Proc. 10th Intern. Congr. Catal.*, Part A, Elsevier Sci. Publ. B. V., Amsterdam and Akadémiai Kiadó, Budapest, 1993, p. 69.
- 2 Y. Izumi, K. Urabe and M. Onaka, In *Zeolite, Clay, and Heteropolyacid in Organic Reaction*, Kodansha, Tokyo-VCH, Weinheim, 1992.
- 3 Y. Ono, In *Perspectives in Catalysis*, Blackwell Sci. Publ., London, 1992, p.431.
- 4 Y. Izumi, N. Natsume, H. Tamamine, I. Tamaoki and K. Urabe, *Bull. Chem. Soc. Jpn.*, **1989**, *62*, 2159.
- 5 T. Okuhara, T. Nishimura, H. Watanabe and M. Misono, *J. Mol. Catal.*, **1992**, *74*, 247.
- 6 T. Okuhara, A. Kasai, N. Hayakawa, Y. Yoneda and M. Misono, *J. Catal.*, **1983**, *83*, 121.
- 7 T. Hibi, K. Takahashi, T. Okuhara, M. Misono and Y. Yoneda, *Appl. Catal.*, **1986**, *24*, 69.
- 8 S. Tatematsu, T. Hibi, T. Okuhara and M. Misono, *Chem. Lett.*, **1984**, 865.
- 9 T. Okuhara, T. Nishimura, K. Ohashi and M. Misono, *Chem. Lett.*, **1990**, 1201.
- 10 T. Nishimura, T. Okuhara and M. Misono, *Appl. Catal.*, **1991**, *73*, L7.
- 11 (a) K. Arata, *Adv. Catal.*, **1990**, *37*, 165; (b) M. Hino and K. Arata, *React. Kinet. Catal. Lett.*, **1982**, *19*, 101.
- 12 H. C. Brown and H. W. Pearsall, *J. Am. Chem. Soc.*, **1952**, *74*, 191.
- 13 K. Na, T. Okuhara and M. Misono, *Chem. Lett.*, **1993**, 1141.
- 14 K. Na, T. Okuhara and M. Misono, *J. Chem. Soc. Chem. Commun.*, **1993**, 1422.
- 15 (a) K. Y. Lee, T. Arai, S. Nakata, S. Asaoka, T. Okuhara and M. Misono, *J. Am. Chem. Soc.*, **1992**, *114*, 2836; (b) K. Y. Lee, Y. Kanda, N. Mizuno, T. Okuhara, M. Misono, S. Nakata and S. Asaoka, *Chem. Lett.*, **1988**, 1175.
- 16 G. K. S. Prakash and G. A. Olah, in K. Tanabe, H. Hattori, T. Yamaguchi and T. Tanaka (eds.), *Acid-Base Catalysis: Proc. Intern. Symp. on Acid-Base Catal.*, Sapporo, Japan, Nov. 28-Dec. 1, 1988, Kodansha, Tokyo and VCH, Weinheim, New York, 1989, p. 59.
- 17 To be published.
- 18 J. Take, H. Yoshioka and M. Misono, in M. J. Philips and M. Ternan (eds.), *Proc. 9th Intern. Congr. Catal.*, Vol. 1, The Chemical Institute of Canada, Ottawa, 1988, p. 372.
- 19 C. V. Hidalgo, H. Itoh, T. Hattori, M. Niwa and Y. Murakami, *J. Catal.*, **1984**, *85*, 362.
- 20 Y. Kanda, K. Y. Lee, S. Nakata, S. Asaoka and M. Misono, *Chem. Lett.*, **1988**, 139.
- 21 G. M. Brown, M.-R. Noe-Spirlet, W. R. Busing and H. A. Levy, *Acta Crystallogr.*, Sect. B, **1977**, *33*, 1038.
- 22 (a) M. Filowitz, W. G. Klemperer, L. Messerle and W. Shum, *J. Am. Chem. Soc.*, **1976**, *98*, 2345; (b) K. Y. Lee, N. Mizuno, T. Okuhara and M. Misono, *Bull. Chem. Soc. Jpn.*, **1989**, *62*, 1731.
- 23 T. Nishimura, T. Okuhara and M. Misono, The 70th Meeting of Catalysis Society of Japan, Niigata, 4F420 (1992).
- 24 T. Nishimura, T. Okuhara and M. Misono, The 65th National Meeting of the Chemical Society of Japan, Tokyo, 2F108 (1993).
- 25 J. B. McMonagle and J. B. Moffat, *J. Colloid Interface Sci.*, **1984**, *101*, 479.
- 26 Y. Izumi, K. Matsuo and K. Urabe, *J. Mol. Catal.*, **1983**, *18*, 299.

## 4.9 The Role of Acid-Base and Redox Features in the Catalytic Behavior of Vanadium-Phosphorous-Oxygen Formulations

Laura M. Cornaglia and Eduardo A. Lombardo

Instituto de Investigaciones en Catálisis y Petroquímica - INCAPe - (FIQ, UNL - CONICET)  
Santiago del Estero 2829 - 3000 - Santa Fe - Argentina

### Abstract

The role played by bulk VOPO<sub>4</sub> phases, surface V(V) centers and Lewis/Brönsted acid sites in defining the catalytic behavior of VPO formulations is discussed in terms of the information provided by a battery of spectroscopic techniques. All selective catalysts for the oxidation of n-butane to maleic anhydride only show the diffraction patterns of vanadyl pyrophosphate. Through <sup>31</sup>P MAS NMR and Raman spectroscopy it is possible though, to detect the presence of small amounts of VOPO<sub>4</sub> phases in the used solids but the best catalysts are those containing traces of V(V) phases. V(V) centers are detected through XPS on the surface of fresh and used catalysts but their concentration does not correlate with catalytic performance. The existence of Lewis and Brönsted acid sites has been documented through the adsorption of basic probe molecules whose fate was followed by FTIR spectroscopy. Very strong Lewis and Brönsted acid sites play key roles in the paraffin activation as well as in the rates of oxygen insertion/hydrogen abstraction on the furan-like intermediates. The data analyzed here also provide new insight on the structural changes occurring in the catalyst during the first few hundred hours on stream as well as the role of these modifications in the reaction mechanism and catalytic performance.

### 1. INTRODUCTION

In industrial practice n-butane is selectively oxidized to maleic anhydride (MAN) using vanadium-phosphorus-oxygen (VPO) based catalysts. This 14 electron oxidation carried out in a single step was first reported by Bergman and Frisch (1) in 1966. Almost 10 years later the first industrial process using a fixed-bed multitubular reactor went on stream.

In going from the paraffin to MAN only minor amounts (< 1%) of secondary products, other than CO<sub>x</sub> and water, are formed under steady state operation in industrial fixed bed reactors. The competitive VPO catalysts only show the presence of one crystalline phase, (VO)<sub>2</sub>P<sub>2</sub>O<sub>7</sub>, although in common practice these solids always contain excess phosphorus (P/V = 1.0-1.3). The presence of amorphous materials has been claimed (2) but no definite proof of its existence and catalytic role has been presented so far.

This may seem to indicate a straightforward relationship between catalytic performance and solid structure were it not by the fact that the molar yields obtained on vanadyl pyrophosphate vary between 30 and 55%.

This has spurred much activity in industrial and academic labs in the last ten years trying to ascertain which features distinguish the best from the good catalysts. The search

is complicated by the existence of a large number of VPO phases, containing V(V), V(IV) and even V(III) in minor proportion, which can co-exist under reaction conditions (3).

The behavior of complex solids involved in heterogeneous selective oxidation reactions has been interpreted in terms of both acid-base and redox properties (4,5). The role of acidity and redox couples has also been discussed in relationship to butane oxidation on VPO catalysts.

- A school of thought (6,7) envisages the active surface as a mosaic made of patches of  $(VO)_2P_2O_7$ , and  $\gamma$ -VOPO<sub>4</sub> [V(IV)-V(V) couple] which in close proximity are responsible for the good selectivity of catalysts. One of them (8) seems to have modified its view and now does not discard that the same couple may co-exist on the surface of the vanadyl pyrophosphate phase.

- Another important school (9) have assigned a central role in the reaction mechanism to coordinatively unsaturated V(IV) Lewis acid sites on which two hydrogens from n-butane would be abstracted to form the adsorbed olefin. However, Trifirò in a recent article (10) hesitates to define in which stage of the reaction mechanism V(IV) centers participate. They also claim in an earlier work that V(V) sites may be deleterious to selectivity for they are thought to be responsible of the total oxidation of MAN at the exit end of the fixed bed reactor (11).

- Brønsted sites, also present on the surface of these oxides (11) intervene in the reaction mechanism probably during the steps of oxygen insertion and further hydrogen abstraction from the already partially oxygenated intermediates (12,13).

The viability and interplay of these views will be discussed below, bearing in mind the effect that time on stream undoubtedly has on the redox behavior (14) and acidity strength (15) of VPO solids which in turn is reflected in the different catalytic performance of the so called non-equilibrated (fresh) catalysts and equilibrated ones (14-17) (> 400 hs on stream).

## 2. THE NON-EQUILIBRATED AND EQUILIBRATED CATALYSTS

In order to understand what follows, one has to review the differences found between the freshly activated non-equilibrated solid and the equilibrated catalyst which develops after several hundred hours on stream.

In most academic studies and in industrial practice, the solid prepared is a catalyst precursor which is characterized by the diffraction patterns (more or less distorted) of VOHPO<sub>4</sub>.1/2H<sub>2</sub>O. This precursor is then dehydrated to yield the fresh catalyst which already shows the diffraction patterns of  $(VO)_2P_2O_7$ . The best gas phase composition to carry on the dehydration is the reacting mixture (ca. 1.7% butane in air). However, in academic studies several other gases have been used.

Table 1 exemplifies the changes occurring in a set of organic preparations during equilibration. All the solids were prepared starting from V<sub>2</sub>O<sub>5</sub> which was reduced in either an alcohol mixture (organic) or in 37% HCl in water (aqueous). Orthophosphoric acid was then added in the required proportion to obtain the catalyst precursor with the desired P/V ratio. More details about the preparation procedure and chemistry have been reported elsewhere (16). The more rapidly equilibrated aqueous formulation (50 hours on stream) is included for comparison.

The key feature observed in the organic preparations reported in Table 1 is the increase in selectivity and yield during equilibration. Another relevant finding is the development of a better crystallized structure with increasing time on stream as revealed by the sharpening of the XRD pattern (fourth column of Table 1) and the identical intensity ratios of the [024]/[200] reflections (16). The lack of correlation between XRD pattern distortion and catalytic performance has been discussed in more detail elsewhere (16).

**Table 1 Catalytic behavior of non-equilibrated (ne) and equilibrated (e) catalysts**

CATALYSTS	P/V <sub>b</sub> <sup>a</sup>	FWHM		I(101) <sup>d</sup> — I(001)	SURFACE AREA (m <sup>2</sup> /g)	PERFORMANCE <sup>e</sup>		
		(001) <sup>b</sup>	(100) <sup>c</sup>			C	S	Y
(ne) ORGANIC (e)	1.16	0.90	1.4	3.0	--	72	39	28
			0.45		15.5	53	69	37
(ne) ORGANIC (e)	1.26	0.45	1.4	1.6	12.0	60	62	37
			0.45		9.0	52	83	43
(ne) ORGANIC (e)	1.25	0.45	f	1.6	--	65	60	39
			0.45		9.0	59	85	50
(ne) ORGANIC (e)	1.20	0.35	1.4	1.2	11.0	40	63	25
			0.45		12.0	44	87	38
AQUEOUS <sup>g</sup> (e)	1.25	0.35	0.35	1.0	5.0	38	65	25

a. Bulk phosphorus/vanadium ratio calculated from EPMA data.

b. V(OHPO<sub>4</sub>)<sub>0.5</sub>H<sub>2</sub>O (2θ = 15°.5). Full width at half maximum (FWHM) measured in degrees (2θ).c. (VO)<sub>2</sub>P<sub>2</sub>O<sub>7</sub> (2θ = 23°.2).d. Height ratio of [101] and [001] planes of V(OHPO<sub>4</sub>)<sub>0.5</sub>H<sub>2</sub>O.e. Reaction temperature: 688K, GHSV: 2500 h<sup>-1</sup>, 1.5% n-C4 in air; conversion (c), selectivity (s), yield (y).

f. This width was not measured because the activation procedure continued.

g. The FWHM and height ratio are the average of six aqueous preparations.

After several hundred hours on stream in contact with the reacting mixture, the following distinct features have been observed:

- The diffraction patterns show much higher crystallinity (10,16) in the equilibrated than in the fresh (non-equilibrated) catalysts.
- A decrease of about two orders of magnitude in the rate of V(IV) —> V(V) oxidation in air at 773 K (14).
- Average vanadium oxidation state of 4.00-4.03 were measured in a large number of equilibrated industrial catalysts (3).
- Detectable quantities of VOPO<sub>4</sub> phases in commercial catalysts (equilibrated) have been reported to be associated with performance loss (18).
- A greater amount of carbon residues are left on the surface of the fresh catalysts than on the equilibrated ones (19). This might explain the observed lower MAN selectivities of the non-equilibrated solids (Table 1).

The ample majority of academic studies has been done using non-equilibrated solids and this has to be kept in mind when using this information to understand the way industrial catalysts operate.

### 3. THE ROLE OF V(V) PHASES

Using  $^{31}\text{P}$  MAS NMR and Raman Spectroscopy, the presence of small amounts of V(V) phases, not seen in the XRD patterns has been detected in active catalysts. Volta and co-workers have reported NMR and Raman data obtained in both non-conventionally (7) and conventionally (20) prepared catalysts. In both cases, however, these solids have been maintained on stream for less than 30 hours (non-equilibrated).

Table 2 The presence of V(V) phases, strength of Lewis acid sites and catalytic behavior of VPO formulations

CATALYSTS*	$\text{P}/\text{V}_B$	$^{31}\text{P}$ NMR SIGNALS <sup>c</sup> (ppm)			LEWIS <sup>c,d</sup> ACIDITY		CATALYTIC PERFORMANCE		
		-13	-30	-46	MS	VS	c	s	y
OURS <sup>e</sup> AQUEOUS (e)	1.25	W	-	S	-	M	49	23	11
ORGANIC (ne)	1.26	W	S	-	-----	-----	83	10	8
ORGANIC (e)	1.26	W	-	-	-	S	65	85	55
ORGANIC (e)	1.20	W	-	-	-	S	72	67	48
ORGANIC (ne)	1.26	-	S	-	W	M	57	52	30
H.BATIS et al.(7) <sup>f</sup> VPO <sub>0.91.0</sub> (ne)	1.0	NO NARROW SIGNAL			-----	-----	97	63	61
BUSCA et al.(12) <sup>g</sup> AQUEOUS (ne)	1.0	-----			M	W	58	3	2
ORGANIC (ne)	1.0	-----			W	S	58	61	35

a. Non-equilibrated (ne). Equilibrated (e) 380 hours or more on stream.

b. Bulk phosphorus/vanadium ratio calculated from EPMA data.

c. w, m, and s indicate weak, medium, and strong intensities, respectively.

d. Medium strong (MS) and very strong (VS) sites. See Figure 5 for details.

e. Reaction temperature: 711K, GHSV = 2500 h<sup>-1</sup>, 1.5% n-butane in air.

f. Reaction temperature: 643K, GHSV = 7450 h<sup>-1</sup>, 2.8% n-butane in air.

g. Reaction temperature: AQUEOUS at 750 K and ORGANIC at 607 K, GHSV = 5840 h<sup>-1</sup>, 0.6% n-butane, 11.6% O<sub>2</sub>, 87.8% N<sub>2</sub>.

We have done similar studies obtaining  $^{31}\text{P}$  MAS NMR spectra of non-equilibrated and equilibrated catalysts prepared in alcohol mixture including for comparison an aqueous formulation. The common trend observed in Volta's spectra and ours is that the best catalysts show the weakest signals of V(V) phases. Our own NMR results are summarized in Table 2 which also includes the best catalyst of the eight reported by Volta (7).

The same holds true for the detection of V(V) phases using Raman spectroscopy. H. Batis et al. (7) show that in the best catalyst the 1016 cm<sup>-1</sup> band assigned to  $\gamma$ -VOPO<sub>4</sub> is hardly visible while the signals of this and other phases increase in the poorer catalysts.

Fig. 1 shows for comparison the  $^{31}\text{P}$  NMR spectra of the best catalyst of Volta and coworkers (7) and one of ours. The broad P signal of the Volta catalyst is due to the

presence of highly dispersed V(V) centers in the paramagnetic vanadyl pyrophosphate-V(IV)-matrix.

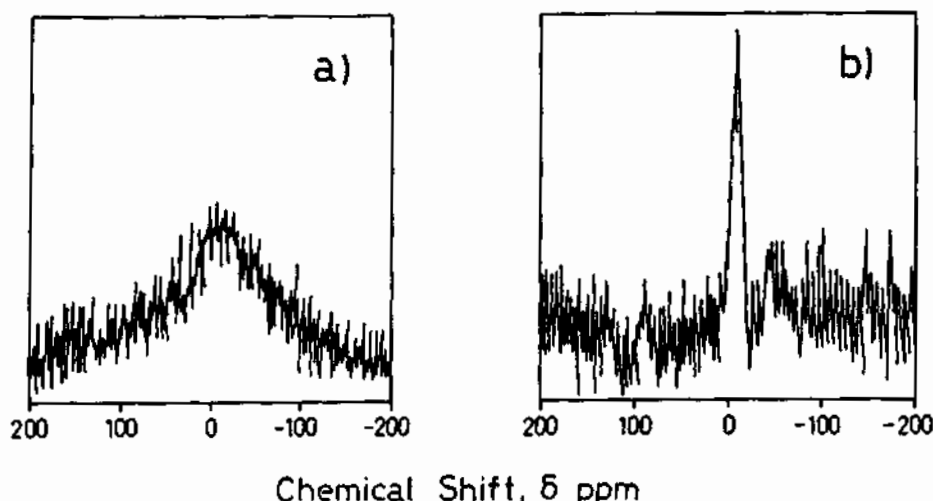


Figure 1.  $^{31}\text{P}$  MAS-NMR spectra of: a) The best catalyst of H. Batis et al. (7)  $\text{VPO}_{\text{O}_{11.0}}$ , b) Equilibrated organic catalyst, with  $\text{P}/\text{V} = 1.26$  (Table 1).

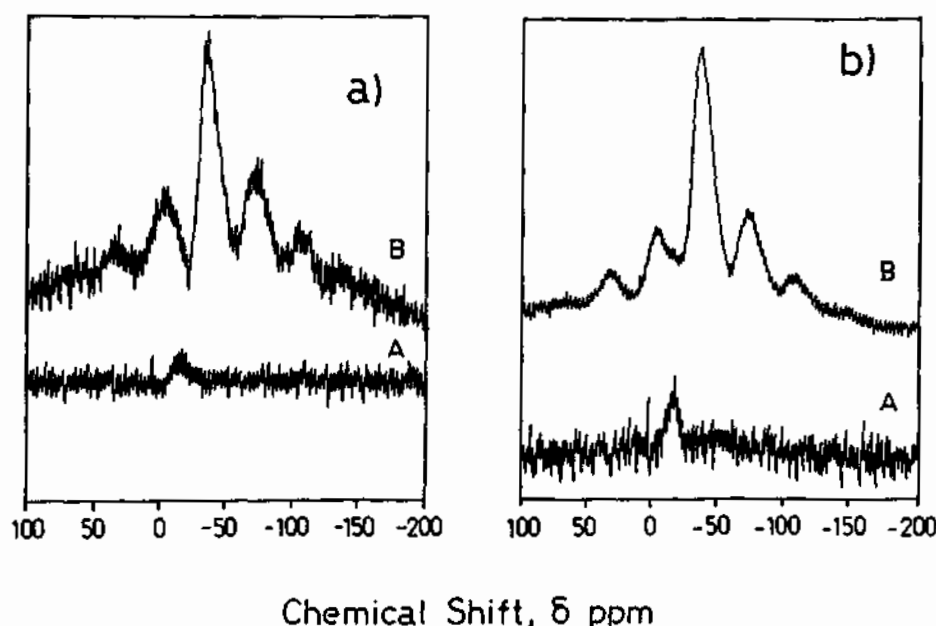


Figure 2.  $^{31}\text{P}$  MAS-NMR spectra of VPO catalysts: a)  $\text{P}/\text{V} = 1.25$  (aqueous), fresh catalyst (A), same catalyst after 2000 hours on stream (B). b)  $\text{P}/\text{V} = 1.32$  (organic), catalyst after 2000 hours on stream (A); catalyst A after heating in oxygen at 763 K for 4 hours (B).

This assignment is further substantiated by the data shown in Fig. 2. The fresh aqueous catalyst (Fig. 2a) shows an extremely noisy background on which a barely visible signal appears at -13 ppm. After equilibration the XRD patterns reveal the presence of low intensity peaks of  $\beta$ -VOPO<sub>4</sub>, while the <sup>31</sup>P NMR spectrum exhibits a peak centered at -39 ppm superimposed on a broad signal similar to the one seen in Volta's catalyst (Fig. 1a).

In the more resistant to oxidation alcohol preparation the precursor does not show any signal even after 14 hours spectra accumulation. The equilibrated catalyst (> 1000 hours on stream) shows a <sup>31</sup>P spectrum (Fig. 2b) similar to the fresh aqueous catalyst (Fig. 2.a) but after a severe oxidation treatment develops an overall spectrum similar to the equilibrated aqueous solid. However, no VOPO<sub>4</sub> phases were detected through XRD in this solid.

Confirming the above, Centi et al. (14) using TEM and EXAFS were unable to detect the presence of any VOPO<sub>4</sub> phase in an equilibrated catalyst which has been on stream for 800 hours.

The data shown here, the absence of VOPO<sub>4</sub> phases in equilibrated catalysts reported by Centi et al. (14) and the performance loss associated with the presence of VOPO<sub>4</sub> phases in commercial catalysts (18) are all consistent with the harmful effect of V(V) phases in MAN selectivity. This is particularly applicable to the conditions of operation of commercial fixed-bed reactor (oxygen-rich mixture). At the exit end of the tubes, the presence of V(V) phases would favor the combustion of MAN as suggested by Centi et al. (11).

#### 4. V(IV)-V(V) CENTERS ON THE CATALYST SURFACE

The above discussion does not discard the existence of V(V) centers on the surface of the vanadyl pyrophosphate lattice. In fact, the <sup>31</sup>P spectrum of Volta's catalyst (Fig. 1a) suggests the likelihood of finding V(V) centers on the surface. To find an answer to this question XPS techniques should be most appropriate.

More than a dozen papers report XPS data of different formulations (21). Based on limited data, most authors including us said that the catalyst exhibits V2p signals which indicate the presence of only V(IV) on the surface.

In Table 3 we have collected our own data obtained with pure V(IV) and V(V) phases as well as with precursors and catalysts. The vanadyl hydrogen phosphate hemihydrate shows the V2p signal with a binding energy of 517.5 eV which should correspond to V(IV) in this oxide matrix. However, the V2p signal of vanadyl pyrophosphate appears at 517.9 eV and in used organic catalysts at 517.8 eV. This displacement towards higher B.E. may be due to either a matrix effect or to the coexistence of V(IV) and V(V) on the surface. The latter hypothesis may be supported by the increasing width of the signal (2.0 eV vs 2.4 eV).

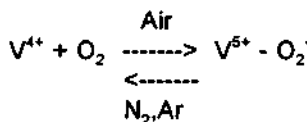
To further investigate this matter, the oxidation and reduction of (VO)<sub>2</sub>P<sub>2</sub>O<sub>7</sub> and used catalysts was carefully studied. The samples were subjected to oxidation or reduction in a pretreatment chamber directly attached to the XPS spectrometer.

Fig. 3 shows the evolution of the V2p and O1s signals during oxygen treatment at temperatures up to 823 K. One can observe that the oxidation to  $\beta$ -VOPO<sub>4</sub> becomes apparent at temperatures above 773 K.

The effect of heating the samples in inert gases (N<sub>2</sub> or Ar) at temperatures up to 723K is shown in Fig. 4a. It is now seen how the V2p signal shifts to lower B.E.s approaching the value recorded with the precursors (Table 3). A similar trend is observed in Fig. 4.b when the inert gas was replaced by hydrogen.

To verify the data obtained with our spectrometer one of us took a couple of samples to the Surface Science Center at the University of Pittsburgh. The data obtained with their instrument were essentially the same as ours (Table 3). It was also checked that the V2p<sub>3/2</sub> signal of the vanadyl pyrophosphate shifted to 517.5eV after heating the solid in Ar at 723K.

An important conclusion from these reduction studies is that the catalyst surface contains both V(IV) and V(V) species. It seems also to support the idea that the V(V) species seen by this technique may be originated by strong oxygen chemisorption.



Our data, however, do not discard the partial transfer of charge between  $\text{V}^{4+}$  and  $\text{O}_2(\text{O}_2^-)$ . In any case this strongly adsorbed oxygen might be the species denoted by  $\text{O}_2^-$  by Gleaves et al. (19). They have proposed that this chemisorbed oxygen is responsible for both the butane dehydrogenation and the oxidation of the furan like intermediate to MAN.

Table 3 XPS data of Vanadium-Phosphorus-Oxygen compounds and catalysts \*

SOLID	PREPARATION <sup>b</sup>	P/V <sub>B</sub> <sup>c</sup>	O1s s <sup>d</sup>	V2p <sub>3/2</sub> s <sup>d</sup>	P2p
VOHPO <sub>4</sub> ·½H <sub>2</sub> O	ORGANIC (1)	1.0	532.2 (3.0)	517.5 (2.0)	134.0 (2.1)
PRECURSORS VOHPO <sub>4</sub> ·½H <sub>2</sub> O'	ORGANIC (13)	1.00-1.26	532.2 0.05 (3.0)	517.5 0.05 (2.0)	134.0 (2.1)
(VO) <sub>2</sub> P <sub>2</sub> O <sub>7</sub>	AQUEOUS (2)	1.0	532.2 (2.5)	517.9 (2.4)	134.3 (2.2)
(VO) <sub>2</sub> P <sub>2</sub> O <sub>7</sub> *	AQUEOUS (1)	1.0	532.2 (2.6)	517.9 (2.3)	134.5 (2.3)
CATALYSTS (VO) <sub>2</sub> P <sub>2</sub> O <sub>7</sub> '	AQUEOUS (6)	1.25	532.3 0.16 (3.1)	517.7 0.13 (2.4)	134.3 (2.2)
	ORGANIC (13)	1.16-1.26	532.2 0.13 (2.8)	517.8 0.09 (2.4)	134.3 (2.2)
β-VOPO <sub>4</sub>	AQUEOUS (1)	1.0	531.1 (1.9)	518.2 (1.6)	133.6 (1.9)
β-VOPO <sub>4</sub> *	AQUEOUS (1)	1.0	531.3 (2.0)	518.3 (2.0)	133.3 (2.0)

- a. Binding energies and full widths at half maximum (shown between brackets) are given in electron volts.
- b. Number of samples measured shown between brackets.
- c. Bulk phosphorus/vanadium ratio calculated from EPMA data.
- d. Standard deviation.
- e. A second aliquot of each previous sample was measured in the Surface Research Center, University of Pittsburgh.
- f. Compound shown in the XRD patterns.

Another equally important conclusion is that the presence of this V(V) type species cannot be quantitatively correlated with catalytic behavior for the 19 catalysts assayed

include aqueous and alcoholic formulations, non-equilibrated as well as equilibrated solids with MAN molar yields varying between 10 and 58%.

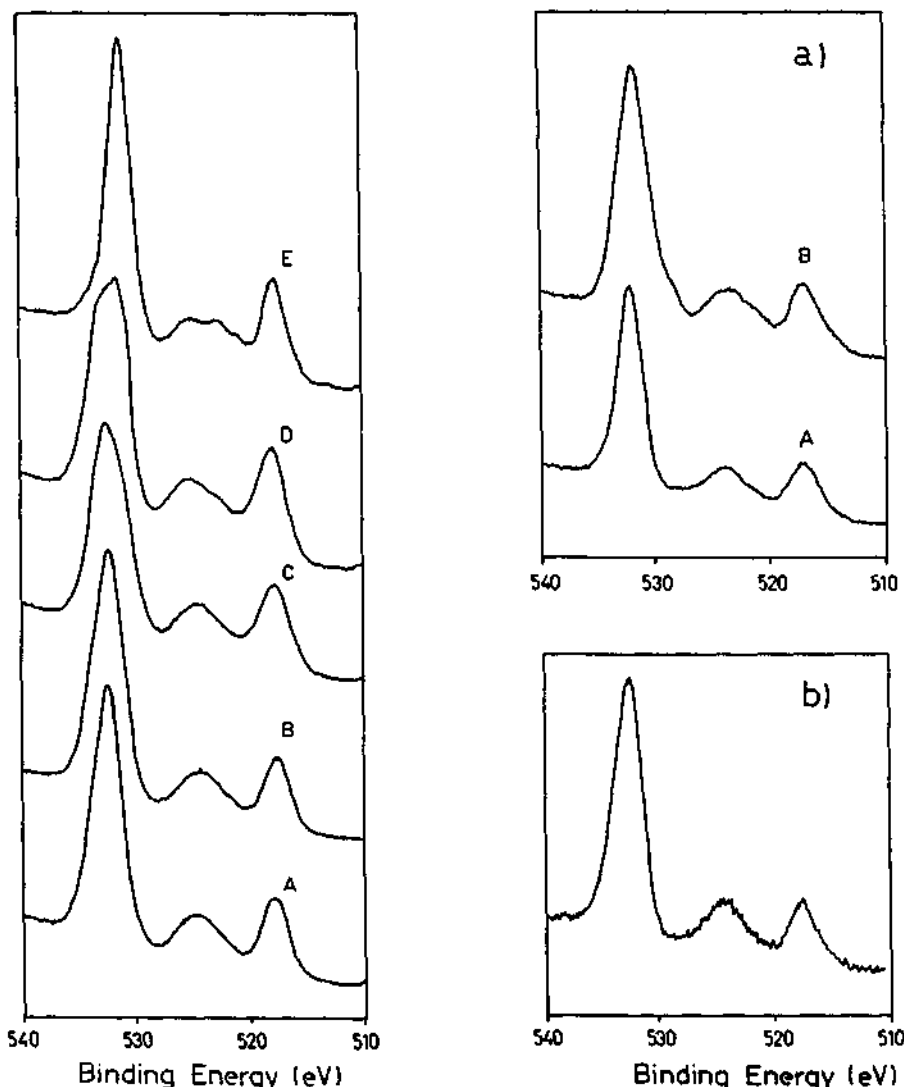


Figure 3. The oxidation of  $(VO)_2P_2O_7$ : starting solid (A), after oxygen exposure (760 Torr) at: 573 K(B), 742K(C), 770K(D), 823K(E).

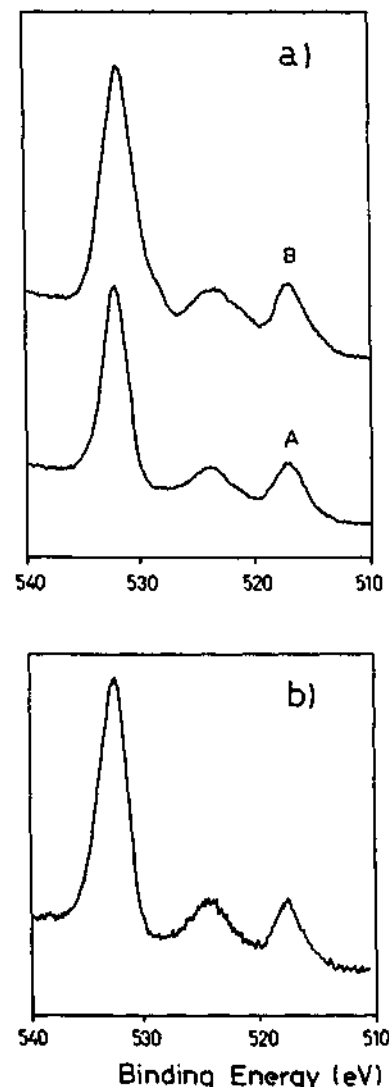


Figure 4. XPS spectra of  $(VO)_2P_2O_7$ : a) After heating at 683K in Ar (A) or  $N_2$  (B). b) After reduction at 623K in  $H_2$  during 4 hours. in all cases  $p = 760$  Torr.

Another piece of information obtained from the analysis of the XPS data is the surface phosphorus enrichment observed by most researchers including us (7,16,21). This surface enrichment ( $P/V_s \approx 2$ ) is also supported by SIMS measurements (22), zeroth order crystal

modelling (18) and FTIR results (13). The only exception to this general rule is the data obtained by Misono and co-workers (23). It may be that the way they activate their catalysts yield a surface with no or very little phosphorus enrichment.

The excess surface phosphorus is a key factor in preventing the over oxidation of the catalyst surface which deleteriously affects the MAN selectivity. The sharp decrease in the oxidation rate of V(IV) to V(V) with increasing P/V bulk ratio was demonstrated (3) several years ago.

## 5. LEWIS AND BRÖNSTED ACIDITY

The adsorption of basic probe molecules provides an interesting tool in order to find clues to explain the important difference in performance (mainly in selectivity) of the non-equilibrated and equilibrated alcohol preparations illustrated in Table 1.

Despite the key role assigned to electron acceptor (Lewis) and proton donor (Brönsted) sites in the reaction mechanism, only two groups had studied the adsorption of basic probe molecules on these catalysts and they were limited to either pure vanadyl pyrophosphate (24) or non-equilibrated catalysts (12,13).

We have now studied the adsorption of NH<sub>3</sub>, pyridine and the weaker base acetonitrile on both non-equilibrated and equilibrated catalysts (15). The adsorption of the strong bases indicates, in agreement with Busca et al (12), that the surface of all the VPO solids studied, including  $\beta$ -VOPO<sub>4</sub>, contain in varying proportions strong Lewis and Brönsted acid sites.

However, as has been discussed by Knözinger (25), strong bases are not sensitive to discriminate centers of different strength. For this purpose acetonitrile was used. In agreement with Busca et al. (12) this probe molecule indicates that very strong (VS) Lewis sites are more abundant in organic than in aqueous preparations (Fig. 5). Extending these studies to equilibrated solids, we have now found that the ratio of VS to medium strong (MS) Lewis sites (detected in non-equilibrated organic catalysts) significantly increases with time on stream (Fig. 5). Also note that the equilibrated organic catalysts retain the very strong Lewis band at temperatures up to 423 K while this band has practically disappeared in both the non-equilibrated and aqueous solids. This evidence is at variance with a previous interpretation (12) linking the presence of VS sites to the increased width and decreased height of the [100] reflection seen in most non-equilibrated catalysts (e.g. Table 1).

In any case, the increasing abundance of VS Lewis sites qualitatively correlates with higher MAN yields (Table 2). This is in agreement with the role assigned to this kind of sites in the concerted removal of two hydrogen atoms (9), which is the rate determining step in this process. Moreover, the higher concentration of very strong sites seems to correlate with the increased selectivity measured in equilibrated catalysts (Table 1).

The reason why the concentration of VS Lewis sites increases in the better crystallized structure of the equilibrated catalysts is not quite clear at this time. It may well be that the highly distorted lattice of the non-equilibrated solid could still contain a certain number of coordinatively saturated VO<sub>5</sub> centers which behave as MS Lewis sites. At longer time on stream, the lattice is healed (increased crystallinity) and the surface VO<sub>5</sub> centers with the apex oxygen towards the bulk become coordinatively unsaturated due to the effective interaction with the second vanadium layer as proposed by Ebner and Thompson (18).

The role of Brönsted sites in the reaction mechanism has been studied by Centi et al. (11,13) combining selective poisoning with catalytic tests and infrared spectroscopy. Potassium selectively blocks VPO Brönsted sites and in doing so considerably modifies the selectivity for MAN and indirectly through increased deposition of hydrocarbon residues also affects the conversion. Through these studies the authors suggest that the Brönsted sites actively participate in the transformation of furan-like intermediates to corresponding lactones

and then to anhydrides in the presence of gaseous oxygen. The dehydrated P-OH centers may provide acceptor sites for the hydrogens abstracted from the starting paraffin which condensate to yield the water product which is desorbed from the catalyst surface.

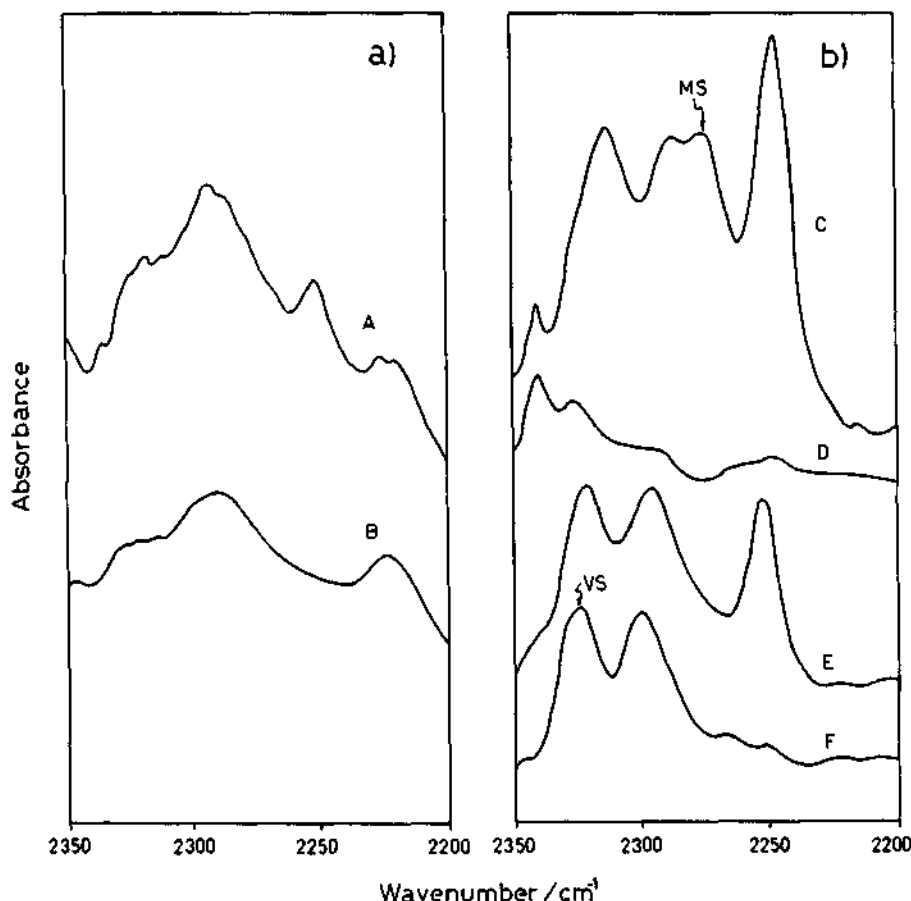


Figure 5. FTIR spectra of acetonitrile adsorption on: a) Aqueous catalyst ( $P/V = 1.25$ ) at room temperature (A), after evacuation at 423K(B). b) Non-equilibrated and equilibrated organic catalyst at room temperature (C), (E); after evacuation at 423 K (D), (F), respectively. MS medium strong and VS very strong Lewis acid sites.

## 6. REACTION MECHANISM

From the reported experimental data and the comparison of results coming from different sources, it is concluded that:

- VPO catalysts contain strong Lewis and Brönsted sites (12,13,15).
- The non-equilibrated catalysts contain both medium strong and very strong Lewis sites but the former disappear in the equilibrated solid which then becomes more selective for MAN production. (Table 1, Fig. 5).
- The Lewis acid sites are associated with coordinatively unsaturated V(IV) centers present in the [100] plane of the vanadyl pyrophosphate (12,13,15).

- The Brønsted sites are assigned to P-OH groups that terminate the vanadyl pyrophosphate lattice (11).
- Selective poisoning of Brønsted sites strongly modify the relative rates of O-insertion and H-abstraction on the furan-like intermediates (11).
- The best catalysts contain at most traces of V(V) phases detectable by  $^{31}\text{P}$  MAS NMR and Raman spectroscopy. Increasing amounts of V(V) phases decrease the catalytic performance. (Table 2 and references 11,14,18).
- Although V(V) centers at the surface have been detected through careful XPS measurements (Table 3) their concentration does not correlate with catalytic performance.
- XPS, SIMS and IR data show surface phosphorus enrichment. This is supported by zeroth order modelling of the solids which indicate that the surface is terminated by the pyrophosphate groups (18).

From these observations the complex evolution from n-butane to MAN may be tentatively pictured as follows:

The n-butane is dehydrogenated to n-butene and then to butadiene after adsorption on the coordinatively unsaturated V(IV) Lewis site which is paired to another V(IV) center with the V = O pointing to the gas phase. The H-abstraction being assisted by the pendant P-O/P-OH groups (18). The adsorbed butadiene might then insert in the neighboring V = O to yield a 2,5 dihydrofuran intermediate liberating the Lewis site for activated oxygen adsorption. This surface oxygen may also be adsorbed in  $\eta^1$ -superoxo or  $\eta^2$ -peroxy coordination mode and could react in two steps to produce MAN as pictured by Schiott and Jorgensen (26). This oxygen might be the same strongly chemisorbed  $\text{O}_2^-$  detected by Gleaves et al. (19) during transient experiments. These steps may also be assisted by Brønsted acid sites as suggested by Centi et al. (11).

The unique selectivity of the phosphorus surface enriched catalysts may be rationalized in terms of the model advanced by Ebner and Thompson (18) who pictured the lattice terminated by the pyrophosphate groups on which clefts are formed which contain up to four vanadium centers. This picture is on line with the active site isolation concept first described by Grasselli(27) which essentially requires a surface configuration which limits the number of neighboring active oxygens thereby restricting over oxidation.

Note that the mechanism sketched here is applicable to equilibrated industrial catalysts in a lean butane reacting mixture. Using fresh catalysts and/or different reactant concentrations will undoubtedly affect the relative reaction rates of the several processes occurring on the catalyst surface.

Extensive in situ dynamic experiments are needed to confirm the details of this tentative mechanism and to establish a quantitative correlation with the number and strength of acid sites on the surface of these solids.

## ACKNOWLEDGMENTS

Financial support for the work carried out in the authors' laboratory was provided by CONICET (National Research Council of Argentina) and the University of Litoral (CAI+D program). We are indebted to the Japan International Cooperation Agency - JICA - for the donation of an ESCA spectrometer extensively used in our work. We also thank Prof. George Marcellin and Mary Eberhardt for their help in obtaining the NMR and some XPS data, and Prof. Elsa Grimaldi for her assistance in the edition of the English manuscript.

**REFERENCES**

1. R.L. Bergman and N.W. Frisch, US Patent 3293268, 1966.
2. M. David, F. Lefebvre and J.C. Volta, in Proc. of the XI Simposio Iberoamericano de Catálisis, Guanajuato, México, 1988, p. 365.
3. J. Ebner, V. Franchetti, G. Centi and F. Trifiró, Chem. Rev., 1988, 88, 55.
4. J. Haber, in Proc. 8th ICC, Berlin, Dechema: Frankfurt A.M., 1984, Vol. I, p.85.
5. M. Ai, J. Catal., 1986, 100, 336.
6. E. Bordes, Catal. Today, 1987, 1, 527.
7. N. Harrouch Batis, H. Batis, A. Ghorbel, J.C. Vedrine and J.C. Volta, J. Catal., 1991, 128, 248.
8. E. Bordes, Catal. Today, 1993, 16, 27.
9. G. Busca, G. Centi, F. Trifiró, Appl. Catal., 1986, 25, 265.
10. F. Trifiró, Catal. Today, 1993, 16, 91.
11. G. Centi, G. Golinelli and F. Trifiró, Appl. Catal., 1989, 48, 13.
12. G. Busca, G. Centi, F. Trifiró and V. Lorenzelli, J. Phys. Chem., 1986, 90, 1337.
13. G. Centi, G. Golinelli and G. Busca, J. Phys. Chem., 1990, 94, 8813.
14. G. Centi, F. Trifiró, G. Busca, J.R. Ebner, J.T. Gleaves, T. Faraday Discuss. Chem. Soc., 1989, 87, 214.
15. L.M. Cornaglia, E.A. Lombardo, J.A. Anderson and J.L. García Fierro, Appl. Catal., 1993, 100, 37.
16. L.M. Cornaglia, C. Caspani and E.A. Lombardo, Appl. Catal., 1991, 74, 15. L.M. Cornaglia, C.A. Sánchez and E.A. Lombardo, Ibid, 1993, 95, 117.
17. E.A. Lombardo, C.A. Sánchez and L.M. Cornaglia, Catal. Today, 1992, 15, 407.
18. J.R. Ebner and M.R. Thompson, Catal. Today, 1993, 16, 51. M.R. Thompson and J.R. Ebner, in New Developments in Selective Oxidation by Heterogeneous Catalysis, P. Ruiz and B. Delmon (Editors), Elsevier , Amsterdam, 1992, p. 352.
19. J.T. Gleaves, J.R. Ebner, T.C. Kuechler, Catal. Rev.-Sci. Eng., 1988, 30, 49.
20. Y. Zhang, R.P.A. Sneeden and J.C. Volta, Catal. Today, 1993, 16, 39.
21. F. Garbassi, J. Bart, R. Tassinari, G. Vlaic and P. Labarde, J. Catal., 1986 98, 317.; Ph. Bastians, M. Genet, L. Daza, D. Acosta, P. Ruiz, B. Delmon, in New Developments in Selective Oxidation by Heterogeneous Catalysts, P. Ruiz and B. Delmon (Editors), Elsevier, Amsterdam, 1992, p. 267.
22. J. Hyaas, C. Plog, W. Maunz, K. Mittag, K. Goilmer and B. Kloppriess, in Proceed. 9th Int. Congress on Catalysis, M.J. Philips and M. Ternan (Editors), Chemical Institute, Ottawa, Canada, 1988, Vol. 4, p. 1632.
23. T. Okuhara and M. Misono, Catal. Today, 1993, 16, 81.
24. S.J. Puttock and C.H. Rochester, J. Chem Soc., Faraday Trans., 1986, 1, 82, 2773.
25. H. Knözinger, in Proc. Int. Symp. on Acid-Base Catalysis, K. Tanabe, H. Hattori, T. Yamaguchi and T. Tanaka (Editors), Kodansha, Tokyo, Japan, 1988, p. 147.
26. B. Schiott and K.A. Jorgensen, Catal. Today, 1993, 16, 79.
27. R.Grasselli, in Surface Properties and Catalysis by Non-Metals, J. Bonelle, B. Delmon, E. Derouane (Editors), Reidel , 1983, p. 273.

## 4.10 Role of Acidic Sites on Metal Phosphates in the Catalytic Oxidation of *iso*-Butane

Y. Takita, K. Kurosaki, T. Ito, Y. Mizuhara, and T. Ishihara

Department of Applied Chemistry, Faculty of Engineering, Oita University,  
Danno-haru, Oita 870-11, Japan

### Abstract

Catalysis by lanthanide phosphates (LnPs) were studied. Only LaPO<sub>4</sub> and CePO<sub>4</sub> are effective catalysts in various LnPs for oxidative dehydrogenation of *iso*-butane. Using a *iso*-butane rich reactant gas mixture, the selectivity of *iso*-butene showed 79–86% at 450–550°C. LnPs have no adsorbed oxygen species and the surface lattice oxygen reacted with hydrogen at >200°C. The activity of the lattice oxygen not affected the catalytic activity. A linear relationship has observed between the acid amount and the catalytic activity of the catalysts. This suggests that acidic sites of intermediate strength play a key role in the oxidative dehydrogenation of *iso*-butane.

### 1. INTRODUCTION

MTBE (Methyl-tert-butylether), which is formed from *iso*-butene and methanol, has been utilized in the many countries as a gasoline additive to improve octane number and to reduce oxidant production. Thus, it is estimated that the demand for *iso*-butene will increase. So that, the production of *iso*-butene from the corresponding alkane, will be much more important in the near future. A great many studies on the catalytic dehydrogenation of *iso*-butane have been carried out, however, many problems still remain.[1]

Authors found out that metal pyrophosphates were effective for oxidative dehydrogenation of *iso*-butane into *iso*-butene, especially Ni<sub>2</sub>P<sub>2</sub>O<sub>7</sub> showed an excellent activity and high selectivity such as more than 80%[2]. Mg<sub>2</sub>P<sub>2</sub>O<sub>7</sub> and Zn<sub>2</sub>P<sub>2</sub>O<sub>7</sub> also showed high activity but deep oxidation into CO and CO<sub>2</sub> was favored on Sn<sub>2</sub>P<sub>2</sub>O<sub>7</sub> and Cu<sub>2</sub>P<sub>2</sub>O<sub>7</sub>. Temperature-Programmed-Desorption study revealed that there are acidic sites on the pyrophosphate catalysts, and the acidity of the catalysts is a key factor in the oxidative dehydrogenation of *iso*-butane.[3]

The relation between the acid-base properties and the catalytic activity of the lanthanide phosphate catalysts is studied in this paper.

### 2. EXPERIMENTAL

**Catalysts:** Metal phosphates were prepared from aqueous solutions of sodium pyrophosphate and metal nitrates or chlorides. The precipitates were well washed and then dried at 130°C overnight.

**Procedure and Analysis:** Catalytic reaction was carried out using an ordinary flow type reaction system with a fixed catalyst bed depicted in Fig. 1. The reactant gas, effluent gas, and the aqueous solution of compounds condensed in a cold trap kept at 0°C were analyzed by gas chromatography.

Measurement of Temperature-Programmed-Reduction (TPR) spectra was carried out using 5 mol% H<sub>2</sub> and 95 mol% He mixture. A sample (0.5 g) was packed in a reactor and the temperature was raised by a rate of 10 K/min. Flow rate of the gas was 40 cm<sup>3</sup>/min.

In the measurement of NH<sub>3</sub> TPD spectra, about 100Torr of NH<sub>3</sub> was preadsorbed on the samples followed by the evacuation at ambient temperature.

### 3. RESULTS AND DISCUSSION

#### 3.1. Catalytic activity of LaPO<sub>4</sub>:

Table 1 shows the results over LaPO<sub>4</sub>. iso-butane began to react at 450°C and a small amount of iso-butene was formed. Oxidative dehydrogenation into iso-butene took place with a significant reaction rate at 500°C and its selectivity was 86.2%. Propylene, which is also a useful raw material in industrial chemistry, was also formed with 7.4% of selectivity. The sum of the selectivities of propylene and iso-butene reached to 93.6%. The formation rate of iso-butene increased with increase in reaction temperature and the high selectivity, 84.2%, was maintained at 550°C. The sum of the selectivity of CO and CO<sub>2</sub> was only 4.7%-6.2% at 500-550°C.

Only a small amount of oxygen containing compounds such as acetone, acrolein, methacrolein, methanol, and carboxylic acids, were obtained at the temperatures examined.

#### 3.2. Catalytic activity of CePO<sub>4</sub>:

Over the CePO<sub>4</sub> catalyst,

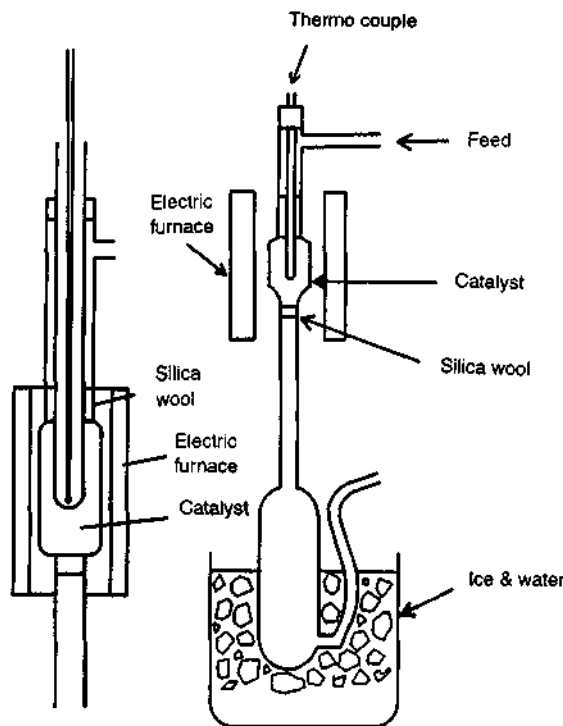


Fig. 1 Flow type reaction system.

Table 1 Oxidation of iso-butane over LaPO<sub>4</sub>

Temp. /°C	450		500		550		
	Conv. /%	i-C <sub>4</sub> H <sub>10</sub>	O <sub>2</sub>	rate	select.	rate	select.
1/4 CH <sub>4</sub>	0.01	7.1		0.11	0.5	0.69	0.9
1/2 C <sub>2</sub> H <sub>4</sub>						0.09	0.1
3/4 C <sub>3</sub> H <sub>6</sub>				1.67	7.4	5.96	7.8
i-C <sub>4</sub> H <sub>8</sub>	0.13	92.9		19.5	86.2	64.0	84.2
1/4 CO				0.90	4.0	2.34	3.1
1/4 CO <sub>2</sub>				0.16	0.7	2.33	3.1
(CH <sub>3</sub> ) <sub>2</sub> CHCHO						0.04	0.1
3/4 CH <sub>3</sub> COCH <sub>3</sub>				0.05	0.2	0.09	0.1
CH <sub>2</sub> =C(CH <sub>3</sub> )CHO				0.24	1.1	0.44	0.6
1/2 CH <sub>3</sub> COOH				0.01	trace		

Feed gas composition (mol%) : iso-butane 75.0, O<sub>2</sub> 5.0, N<sub>2</sub> 20.0 ; Catalyst 5.5 cm<sup>3</sup> (5.07 g), Feed rate : 30 cm<sup>3</sup>.min<sup>-1</sup>, rate=μmol·min<sup>-1</sup>, select.=selectivity %

*iso*-butene was formed selectively (Table 2). Almost all the oxygen molecules were consumed at 500°C and the selectivity to *iso*-butene reached 78.7%. The selectivity of deep oxidation into CO and CO<sub>2</sub>, 15.1%, was relatively high. The rate of formation of *iso*-butene at 550°C over the catalyst was the best result among all the catalysts examined so far.

Table 2 Oxidation of *iso*-butane over CePO<sub>4</sub>

Temp. /°C	450		500		550	
	Conv. /%	i-C <sub>4</sub> H <sub>10</sub>	O <sub>2</sub>	rate	select.	rate
1/4 CH <sub>4</sub>	0.04	1.9		0.14	0.4	1.32
1/2 C <sub>2</sub> H <sub>6</sub>						0.05
1/2 C <sub>2</sub> H <sub>4</sub>						0.15
3/4 C <sub>3</sub> H <sub>6</sub>	0.23	10.8		1.81	4.6	6.58
i-C <sub>4</sub> H <sub>8</sub>	1.67	78.8		31.0	78.7	85.4
1/4 CO				3.36	8.5	2.98
1/4 CO <sub>2</sub>	0.04	1.9		2.62	6.6	1.96
(CH <sub>3</sub> ) <sub>2</sub> CHCHO						0.07
3/4 CH <sub>3</sub> COCH <sub>3</sub>				0.08	0.2	0.14
CH <sub>2</sub> =C(CH <sub>3</sub> )CHO	0.14	6.6		0.37	0.9	0.15
1/4 CH <sub>3</sub> OH						0.01
1/2 CH <sub>3</sub> COOH				0.01	trace	trace

The other conditions are the same as shown in Table 1.

Table 3 Oxidative dehydrogenation of *iso*-butane over Lanthanide Phosphates

Phosphate	Temp. (°C)	i-C <sub>4</sub> H <sub>10</sub> Conv. (%)	Selectivity (%)				SSA (m <sup>2</sup> /g)
			CH <sub>4</sub> +C <sub>2</sub> H <sub>4</sub>	C <sub>3</sub> H <sub>6</sub>	i-C <sub>4</sub> H <sub>8</sub>	CO <sub>x</sub>	
Y	525	2.4	4.0	19.8	43.1	33.1	36.6
	550	3.0	5.5	27.1	41.5	25.9	
La	525	2.9	0.3	6.7	80.0	11.0	30.8
	550	6.1	0.8	6.3	84.6	5.4	
Ce	525	2.9	2.5	12.5	76.8	8.2	16.8
	550	7.4	1.8	10.2	77.1	10.9	
Pr	525	1.3	9.2	23.6	20.9	46.3	6.8
	550	1.6	10.2	26.4	21.5	42.2	
Nd	525	2.2	7.4	28.2	30.0	34.4	15.9
	550	2.9	8.7	33.2	32.3	25.9	
Gd	525	4.1	8.2	35.7	37.7	18.5	11.1
	550	4.9	8.5	36.9	36.7	17.9	
Er	525	2.6	7.5	30.7	37.1	24.6	10.5
	550	2.7	8.3	32.6	36.7	21.5	
Yb	525	4.1	7.7	33.7	36.3	22.3	8.7
	550	4.9	8.3	34.4	37.7	19.6	

Catalyst: 2.3 cm<sup>3</sup>, other reaction conditions are the same as shown in Table 1.

### 3.3. Catalytic activity of the Lanthanide Phosphates:

Table 3 shows the catalytic activity of various lanthanide phosphate catalysts. Selective oxidative dehydrogenation into *iso*-butene took place only over LaPO<sub>4</sub> and CePO<sub>4</sub>. The other catalysts showed 20–40% *iso*-butene selectivity and the formation of C<sub>3</sub>H<sub>6</sub> and CO<sub>x</sub> was promoted. Only a small amount of hydrogen was obtained in the oxidation over LaPO<sub>4</sub> and CePO<sub>4</sub>. On the contrary, hydrogen was formed at a significant rate over YPO<sub>4</sub>, GdPO<sub>4</sub>, and YbPO<sub>4</sub>. This suggests that pyrolysis of *iso*-butane also took place over these catalysts.

It is also clear that the specific surface area(SSA) of the catalysts does not correlate to the catalytic activities.

### 3.4. Catalytic activity of La<sub>2</sub>O<sub>3</sub> and CeO<sub>2</sub>:

Since LaPO<sub>4</sub> and CePO<sub>4</sub> showed a high *iso*-butene selectivity, the catalytic properties of the corresponding oxides were studied (Tables 4 and 5). Although *iso*-butene was formed over La<sub>2</sub>O<sub>3</sub>, its selectivity never exceeded 47.0%. This oxide catalyst is characterized by an outstanding selectivity to propylene. The selectivity to deep oxidation products was considerably larger than that over the LaPO<sub>4</sub> catalyst. On the contrary, the selectivity to *iso*-butene over the CeO<sub>2</sub> catalyst was comparable to that over the CePO<sub>4</sub> catalyst. Moreover, the selectivities to propylene and to CO+CO<sub>2</sub> over CeO<sub>2</sub> were only slightly higher than those over CePO<sub>4</sub>. Another feature among metal oxides emerges. It was confirmed by separate experiments that carbon deposition was dominant at 500–550°C over the CuO and Co<sub>3</sub>O<sub>4</sub> catalysts. No carbon deposition, however, became dominant over both La<sub>2</sub>O<sub>3</sub> and CeO<sub>2</sub> catalysts even at 550°C. It can be said from these results that LaPO<sub>4</sub> is more suitable for oxidative dehydrogenation of *iso*-butane than the La<sub>2</sub>O<sub>3</sub> but catalytic activity of CePO<sub>4</sub> is comparable to that of the corresponding metal oxide, CeO<sub>2</sub>, in this reaction.

Table 4 Oxidation of *iso*-butane over La<sub>2</sub>O<sub>3</sub>

Temp. /°C	450		500		525		550	
Conv. /%	1-C <sub>4</sub> H <sub>10</sub>	O <sub>2</sub>						
	rate	select.	rate	select.	rate	select.	rate	select.
1/4 CH <sub>4</sub>	0.36	2.2	0.83	3.9	1.37	5.3	2.24	6.6
1/2 C <sub>2</sub> H <sub>4</sub>	0.02	0.1	0.05	0.2	0.06	0.2	0.09	0.3
3/4 C <sub>3</sub> H <sub>6</sub>	1.41	8.6	3.79	17.9	6.18	23.8	9.74	28.5
1-C <sub>4</sub> H <sub>8</sub>	7.68	46.9	9.42	44.5	11.04	42.3	14.27	41.8
1/4 CO	2.65	16.2	3.15	14.9	3.01	11.6	2.88	8.4
1/4 CO <sub>2</sub>	4.26	26.0	3.93	18.6	4.36	16.8	4.92	14.4

Other reaction conditions are the same as shown in Table 1.

Table 5 Oxidation of *iso*-butane over CeO<sub>2</sub>

Temp. /°C	450		500		525		550	
Conv. /%	1-C <sub>4</sub> H <sub>10</sub>	O <sub>2</sub>						
	rate	select.	rate	select.	rate	select.	rate	select.
1/4 CH <sub>4</sub>	0.04	0.4	0.26	1.6	0.86	3.3	2.79	5.3
1/2 C <sub>2</sub> H <sub>4</sub>							0.04	0.1
3/4 C <sub>3</sub> H <sub>6</sub>	0.79	7.9	1.48	9.2	2.65	10.1	5.84	11.0
1-C <sub>4</sub> H <sub>8</sub>	4.43	44.5	9.97	62.1	18.21	69.0	36.89	69.8
1/4 CO	0.32	3.2	0.44	2.7	1.46	5.5	4.62	8.7
1/4 CO <sub>2</sub>	4.38	44.0	3.90	24.3	3.20	12.1	2.70	5.1

Other reaction conditions are the same as shown in Table 1.

### 3.5. TPR of the lattice oxygen of Lanthanide Phosphates:

Lanthanide phosphates have no adsorbed oxygen on the surface. Figure 2 shows the TPR spectra of lanthanide phosphates. Reduction of  $\text{NdPO}_4$  began at about 200°C and the  $\text{CePO}_4$ ,  $\text{YPO}_4$ ,  $\text{ErPO}_4$ ,  $\text{PrPO}_4$  can be reduced at about 250°C but  $\text{LaPO}_4$  was hard to reduce and the reduction by gaseous  $\text{H}_2$  started at about 500°C. As for the amount of reduced lattice oxygen, that of  $\text{CePO}_4$  was the largest, followed by  $\text{ErPO}_4$ . That of  $\text{LaPO}_4$  was the smallest.

### 3.6. Relation between the activity of lattice oxygen and catalytic activity of Lanthanide Phosphates:

Catalytic activity of the catalysts is plotted in Fig. 3 (left) against the temperatures where the  $\text{H}_2$  consumption rate reaches to a certain rate as an index of the activity of lattice oxygen, and in Fig. 3 (right) against the amount of  $\text{H}_2$  consumed up to 550°C in TPR. However, no correlations can be observed in the figures, suggesting that the activity of the lattice oxygen is not a key factor in the iso-butene formation.

### 3.7. Acidic properties of Lanthanide Phosphates:

To examine the participation of the acidic sites over the catalysts to the oxidation, TPD spectra of  $\text{NH}_3$  adsorbed on the various lanthanide phosphates are examined and

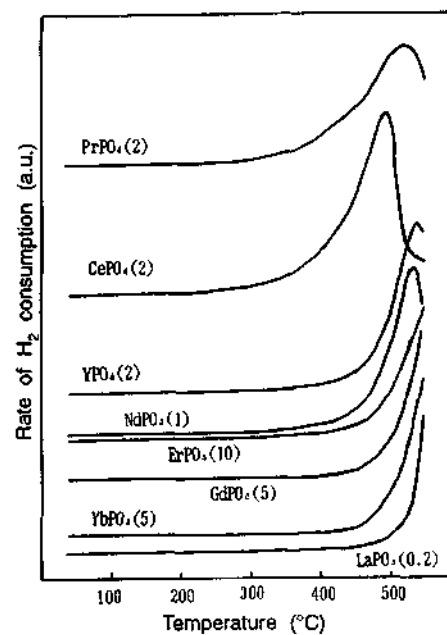


Fig. 2 TPR spectra of Lanthanide Phosphates. Figures in parentheses indicate the factor of redorder response.

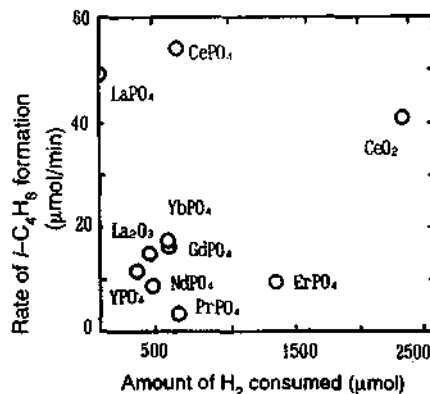
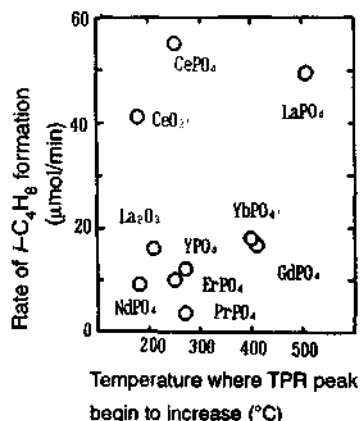


Fig. 3 Relation between the activity of lattice oxygen and catalytic activity of the catalysts.

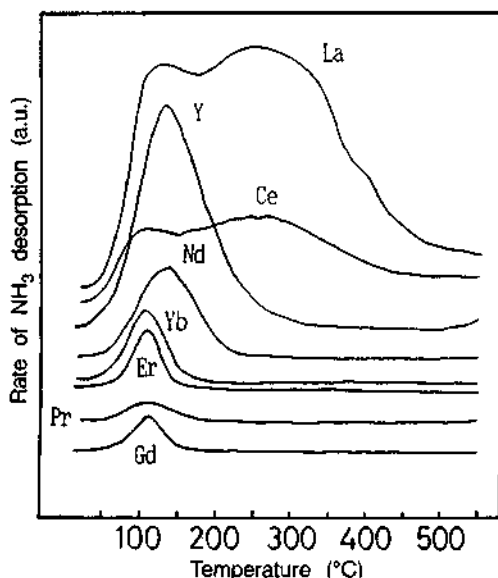


Fig. 4 TPD spectra of  $\text{NH}_3$  from Lanthanide phosphates.

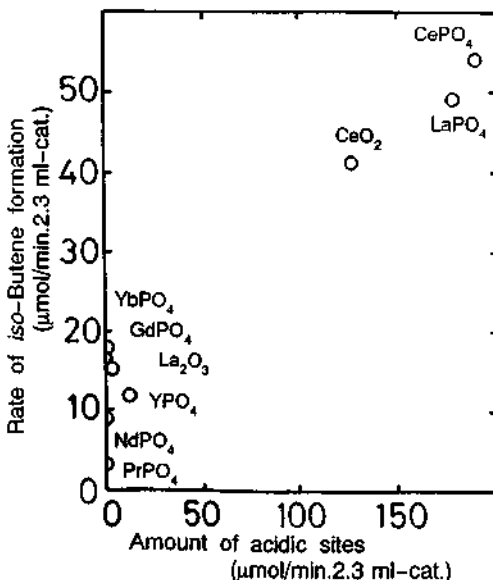


Fig. 5 Relation between acidity and activity of the catalysts.

shown in Fig. 4. Every spectrum has a desorption peak at 50–200°C. TPD spectrum from  $\text{LaPO}_4$  composed of two large desorption peaks with peak tops at around 120°C and 260°C and the desorption continued at 550°C. The TPD spectrum from  $\text{CePO}_4$  closely resembled that of  $\text{LaPO}_4$  except for peak height. The desorption of  $\text{NH}_3$  at 350–550°C was also observed in this spectrum. It is apparent that only  $\text{LaPO}_4$  and  $\text{CePO}_4$  have acidic sites of intermediate strength.

### 3.8. Relation between the acidity and the catalytic property of the catalysts:

The rates of *iso*-Butene formation are plotted against acid amounts of the intermediate strength on the catalysts (Fig. 5). The points are separated into two groups, however, they can be regarded as a straight line. This suggests that the acidic sites of intermediate strength on the catalyst surface is a key factor for the *iso*-butene formation.

### Conclusions

- (1)  $\text{LaPO}_4$  and  $\text{CePO}_4$  are the effective catalysts for oxidative dehydrogenation of *iso*-butane into *iso*-butene.
- (2)  $\text{CeO}_2$  is also an effective catalyst for oxidative dehydrogenation of *iso*-butane into *iso*-butene.
- (3) Lanthanide phosphates have no adsorbed oxygen on the surface, and the lattice oxygen can be reduced by  $\text{H}_2$  at >200°C and the reduced amounts are below mono layer oxygen.
- (4) Acidic sites of intermediate strength on the catalyst surface play a key role in the *iso*-butene formation.

### References

- (1) I. Suzuki, Y. Kaneko, *J. Catal.*, 1977 47, 239.
- (2) Y. Takita, K. Kurosaki, Y. Mizuhara, and T. Ishihara, *Chem. Lett.*, 1993, 1993, 335.
- (3) Y. Takita, K. Kurosaki, Y. Mizuhara, and T. Ishihara, Proceedings of Natural Gas Conversion Symposium, Sydney, July 4–9, 1993.

## 4.11 Production of Silane and Dialkoxysilane by the Disproportionation of Trimethoxy- and Triethoxysilanes over Solid Base Catalysts

Y. NOMOTO, E. SUZUKI, and Y. ONO

Department of Chemical Engineering, Tokyo Institute of Technology,  
Ookayama, Meguro-ku Tokyo 152, Japan

### Abstract

Alumina-supported KF catalyst showed a high catalytic activity for the silane formation by the disproportionation of trimethoxysilane at 393 K, the yield being 18% at a 72% conversion of trimethoxysilane. Disproportionation of triethoxysilane over CaO and MgO at 393 K gave diethoxysilane with 14 and 8% yields, respectively, only small amounts of silane being formed.

### 1. INTRODUCTION

Silane,  $\text{SiH}_4$ , is one of the important chemicals in the semiconductor industry, since highly pure silicon is easily obtained by thermally decomposing  $\text{SiH}_4$ . Silane can be formed by the disproportionation of chlorosilanes,  $\text{Cl}_n\text{SiH}_{4-n}$ , the distribution of the by-product falling in wide range among  $\text{Cl}_n\text{SiH}_{4-n}$  [1]. On the other hand, silane formation by the disproportionation of alkoxy silanes such as  $(\text{C}_2\text{H}_5\text{O})_3\text{SiH}$  [2] and  $(\text{CH}_3\text{O})_3\text{SiH}$  [3] is advantageous, since only tetraalkoxysilane is formed as a by-product. The aim of this work is to demonstrate the catalysis of solid bases towards the disproportionation of  $(\text{CH}_3\text{O})_3\text{SiH}$ ,



The authors have found that diethoxysilane,  $(\text{C}_2\text{H}_5\text{O})_2\text{SiH}_2$ , can be obtained by the disproportionation of  $(\text{C}_2\text{H}_5\text{O})_3\text{SiH}$  over solid base catalysts,



Diethoxysilane has a potential for the starting material for producing two-dimensional silicones upon a hydrolysis. The performance of catalysts for this disproportionation reaction will also be reported.

## 2. EXPERIMENTAL

Trimethoxy- and triethoxysilanes from Shin-Etsu Chemical Co., Ltd. were used as obtained. Alumina (Merck, 90 aktiv)-supported KF, NaF, and CsF were prepared by impregnating the catalytic component from the aqueous solutions. After the catalyst was preheated in a fixed-bed flow reactor (10 mm i.d.) at 573 K for 1 h under a helium stream, trimethoxysilane was fed into the reactor. The effluent gas from the reactor was analyzed by a gas chromatograph. Propane and heptane were fed into the reactor as internal standards. Hydrotalcite was synthesized by Miyata's method [4]. Calcium and magnesium oxides as obtained from Wako Pure Chemical Ind., Ltd. were calcined under a helium stream at given temperatures.

## 3. RESULTS AND DISCUSSION

### 3.1. Silane Formation by Disproportionation of $(\text{CH}_3\text{O})_3\text{SiH}$

Table 1 lists the conversion of trimethoxysilane in the disproportionation over several catalysts at 393 K. Among these catalysts, KF/Al<sub>2</sub>O<sub>3</sub> showed a preponderant activity. Figure 1 shows the changes in the  $(\text{CH}_3\text{O})_3\text{SiH}$  conversion and the SiH<sub>4</sub> yield based on  $(\text{CH}_3\text{O})_3\text{SiH}$  converted at 393 K with the time on stream. The catalyst was KF(2 mmol g<sup>-1</sup>)/Al<sub>2</sub>O<sub>3</sub> which had been preheated under a helium stream at 573 K for 1 h before feeding  $(\text{CH}_3\text{O})_3\text{SiH}$ . The  $(\text{CH}_3\text{O})_3\text{SiH}$  conversion slightly decreased and then attained a steady value of 72% for 2-4 h of time on stream. During the stream, the SiH<sub>4</sub> yield fell around 25%, the material balance of silicon calculated from the amount of SiH<sub>4</sub> and  $(\text{CH}_3\text{O})_4\text{Si}$  formed being 99-104%. These results indicates that the reaction pro-

Table 1 Disproportionation of trimethoxysilane<sup>1)</sup>

Catalyst	$(\text{CH}_3\text{O})_3\text{SiH}$ conversion / %
KF/Al <sub>2</sub> O <sub>3</sub> <sup>2)</sup>	72
Hydrotalcite <sup>3)</sup>	56
CaO	50
Ru/Al <sub>2</sub> O <sub>3</sub>	23
Pt/Al <sub>2</sub> O <sub>3</sub>	42
Active alumina	30
SiO <sub>2</sub> -Al <sub>2</sub> O <sub>3</sub> <sup>4)</sup>	20
Hydrotalcite <sup>5)</sup>	37

<sup>1)</sup>Reaction conditions: Catalyst= 0.5 g, T= 393 K,  $(\text{CH}_3\text{O})_3\text{SiH}= 23$  kPa, W/F= 8.6 g h mol<sup>-1</sup>.

<sup>2)</sup>10 mmol-KF / g

<sup>3)</sup>Calcined at 733 K for 1 h.

<sup>4)</sup>Preheated at 473 K for 1 h.

<sup>5)</sup>Mg<sub>6</sub>Al<sub>2</sub>(OH)<sub>16</sub>CO<sub>3</sub>·4H<sub>2</sub>O, W/F= 17 g h mol<sup>-1</sup>.

ceeds according to Eq.(1).

As shown in Fig. 2, the loading amount of KF onto  $\text{Al}_2\text{O}_3$  affected the  $(\text{CH}_3\text{O})_3\text{SiH}$  conversion: the conversion increased from 30% to 72% at 0-2 mmol g<sup>-1</sup>-loading and further increase of the loading up to 15 mmol g<sup>-1</sup> did not give a change in the conversion. A loading amount by 2 mmol-KF g<sup>-1</sup> is enough to catalyze the reaction effectively. Figure 3 shows the effect of contact

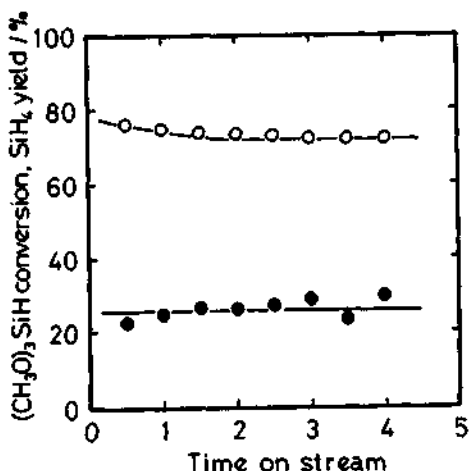


Fig. 1 Trimethoxysilane conversion and silane yield as a function of time on stream.

Catalyst:  $\text{KF}(2 \text{ mmol g}^{-1})/\text{Al}_2\text{O}_3 = 0.2 \text{ g}$ , Preheating: 573 K, 1 h, Reaction: 393 K,  $(\text{CH}_3\text{O})_3\text{SiH} = 21 \text{ kPa}$  (4.8 mmol h<sup>-1</sup>), W/F = 8.6 g h mol<sup>-1</sup>. (○)  $(\text{CH}_3\text{O})_3\text{SiH}$  conversion and (●)  $\text{SiH}_4$  yield based on  $(\text{CH}_3\text{O})_3\text{SiH}$  converted.

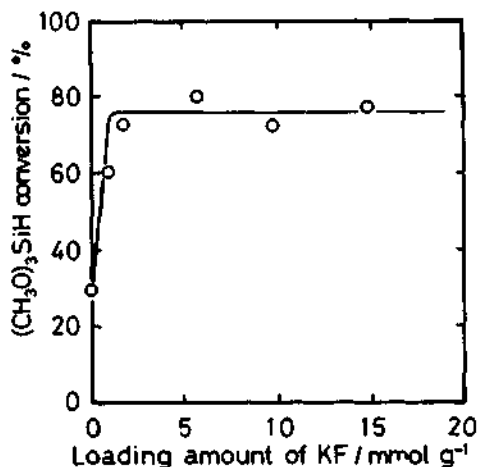


Fig. 2 Effect of loading amount of KF on the trimethoxysilane conversion.

Catalyst:  $\text{KF}/\text{Al}_2\text{O}_3 = 0.5 \text{ g}$ , Preheating: 573 K, 1 h, Reaction: 393 K,  $(\text{CH}_3\text{O})_3\text{SiH} = 21 \text{ kPa}$  (4.8 mmol h<sup>-1</sup>), W/F = 8.6 g h mol<sup>-1</sup>.

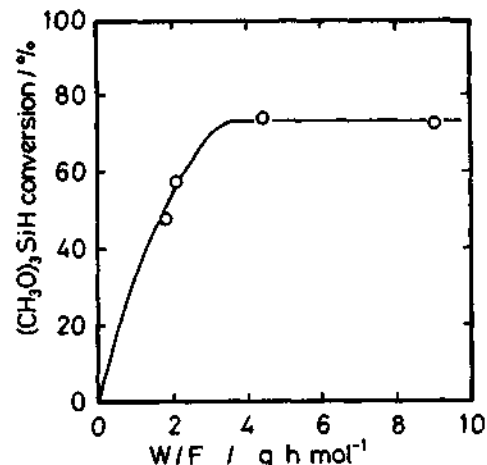


Fig. 3 Effect of contact time on the trimethoxysilane conversion.

Catalyst:  $\text{KF}(10 \text{ mmol g}^{-1})/\text{Al}_2\text{O}_3$ , Preheating: 573 K, 1 h, Reaction: 393 K,  $(\text{CH}_3\text{O})_3\text{SiH} = 21 \text{ kPa}$ .

time, W/F, on the  $(\text{CH}_3\text{O})_3\text{SiH}$  conversion. The conversion increased with W/F and was constant (72%) at 4.3–8.6 g h mol<sup>-1</sup>.

Alkaline metal fluorides other than KF was also effective as a catalyst. NaF, CsF, and KF loaded on  $\text{Al}_2\text{O}_3$  by 0.5 mmol g<sup>-1</sup> gave 34, 29, and 24% of  $(\text{CH}_3\text{O})_3\text{SiH}$  conversion at 3 h of time on stream, respectively, under the same reaction conditions as those in Fig. 1.

### 3.2. Diethoxysilane Formation by Disproportionation of $(\text{C}_2\text{H}_5\text{O})_3\text{SiH}$

Disproportionation reactions of triethoxysilane were carried out using several catalysts, and the results are summarized in Table 2. Over the KF/ $\text{Al}_2\text{O}_3$  and hydrotalcite (calcined) catalysts, which showed high activities for the silane formation by the disproportionation of trimethoxysilane, silane was formed by ca. a fourth part of triethoxysilane converted, and the tetraethoxysilane yield was close to three times of the silane yield. This shows that the reaction proceeds analogously according to Eq. (1).

Over CaO and MgO, the reaction gave  $(\text{C}_2\text{H}_5\text{O})_2\text{SiH}_2$ ,  $(\text{C}_2\text{H}_5\text{O})_4\text{Si}$ , and a small amount of  $\text{SiH}_4$ . For example, using MgO catalyst was obtained the  $(\text{C}_2\text{H}_5\text{O})_2\text{SiH}_2$  yield of 8.1% to which the  $(\text{C}_2\text{H}_5\text{O})_4\text{Si}$  yield was close, the material balance of silicon being complete. These results indicates that the reaction proceeds according to Eq.(2).

Table 2 Disproportionation of triethoxysilane<sup>1)</sup>

Catalyst	$(\text{C}_2\text{H}_5\text{O})_3\text{SiH}$ conversion/%	$\text{SiH}_4$ yield/%	$(\text{C}_2\text{H}_5\text{O})_2\text{SiH}_2$ yield/%	$(\text{C}_2\text{H}_5\text{O})_4\text{Si}$ yield/%
KF/ $\text{Al}_2\text{O}_3$	88	20	0.5	68
Hydrotalcite <sup>2)</sup>	76	18	1.6	61
MgO	18	0.1	8.1	11
CaO	39	0.6	14	25

<sup>1)</sup>Reaction conditions: Catalyst= 0.5 g, T= 393 K,  $(\text{C}_2\text{H}_5\text{O})_3\text{SiH}$ = 21 kPa, W/F= 23 g h mol<sup>-1</sup>.

<sup>2)</sup>Calcined at 733 K for 1 h.

### REFERENCES

- 1) Jpn. Tokkyo Kokai Koho, 58-217422 (1983); 63-192786 (1988) and United States Patent, 4667048 (1987)
- 2) C. Friedel and A. Ladenburg, Ann. Chem., 1867, 143, 118; United States Patent, 2530367; Jpn. Tokkyo Kokai Koho, 51-20040 (1976)
- 3) Eur. Patent Appl., 201919 (1986)
- 4) S. Miyata, Clays and Clay Miner., 1983, 31, 305; *ibid.*, 1975, 23, 369

## 4.12 Oxidative Dehydrogenation of Ethane over Modified Magnesium Oxides

Xiao-ming Zheng, Jian-xin Mao, Bing-xin Cai, Jin-hua Fei, and Song-shou Jin  
Institute of Catalysis, Hangzhou University, Hangzhou, 310028, China

### Abstract

The catalytic activities and selectivities of a crystalline MgO and MgO pretreated with water or ethanol for the oxidative dehydrogenation of ethane have been studied together with the effect of Li<sup>+</sup> addition. It has been found that MgO pretreated with water having lattice distortion showed the highest catalytic activity and that the addition of a suitable amount of Li<sup>+</sup> enhanced the catalytic activity mainly due to the acid-base bifunctional catalysis. The active sites are discussed on the basis of the results by XRD, IR, and TPD of carbon dioxide and n-butylamine.

### 1. INTRODUCTION

Different preparation methods and pretreatment conditions of MgO are expected to give different catalytic properties. The addition of Li<sup>+</sup> to MgO is known to change the catalytic properties for oxidative coupling of methane, etc. Therefore, we attempted to use three kinds of MgO as catalysts for the oxidative dehydrogenation of ethane and to examine the effect of the addition of Li<sup>+</sup> to MgO. In order to study the active sites and the reaction mechanism, the lattice constants, the surface hydroxyl groups, and the acid-base properties of MgO and Li<sup>+</sup>/MgO have been measured. The catalytic properties were also compared with those of ZrO<sub>2</sub>, Al<sub>2</sub>O<sub>3</sub>, and SiO<sub>2</sub>.

### 2. EXPERIMENTAL

Li<sup>+</sup>/MgO(EtOH) was prepared by impregnating a crystalline MgO (UBE product, diameter: 1000 Å) with an ethanol solution of LiNO<sub>3</sub> followed by drying at 293 K and calcining at 973 K for 2 h. Li<sup>+</sup>/MgO(H<sub>2</sub>O) was prepared similarly as above except that an aqueous solution of LiOH was used as an impregnating solution. MgO (EtOH) and MgO(H<sub>2</sub>O) were prepared by immersing the above crystalline MgO in ethanol and aqueous solution, respectively, followed by the same pretreatment as above.

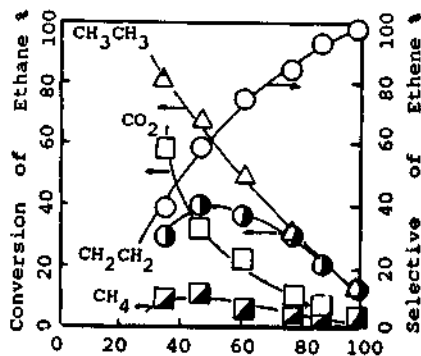
The lattice distortion of the materials was estimated by Voight Function analysis of (100) diffraction profile alone [1].

The oxidative dehydrogenation of ethane was carried out by use of a closed recirculating apparatus with a quartz reactor. The catalyst (50 mg) was evacuated at 958 K and  $10^{-2}$  Pa for 1.5 h before reaction. The ratio of ethane/oxygen was usually 4.

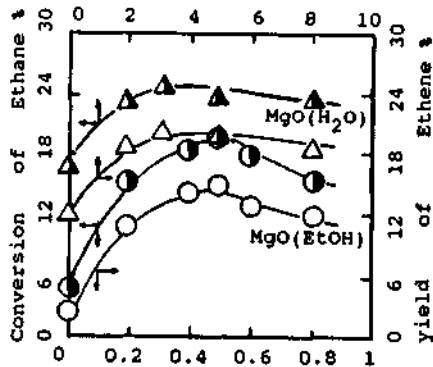
### 3. RESULTS and DISCUSSION

#### 3.1. The effects of ethane/oxygen ratio and $\text{Li}^+$ addition

The effect of ethane/oxygen ratio on the conversion of ethane and the selectivity for ethene formation is shown in Fig. 1. When the ratio is less than 1, the main product is  $\text{CO}_2$ . As the ratio increases, the conversion decreases, while the selectivity increases. The maximum yield (38.9%) of ethene was obtained when the ratio was 1.



Ethane Content      vol.-%  
Fig. 1. Effect of Ethane/oxygen



Amount of  $\text{Li}^+$  % (atom)  
Fig. 2. Effect of  $\text{Li}^+$  amount

$\text{MgO}(\text{H}_2\text{O})$  showed higher catalytic activity and selectivity than  $\text{MgO}(\text{EtOH})$ , a crystalline  $\text{MgO}$  being between them.

The effect of  $\text{Li}^+$  addition to  $\text{MgO}$  is shown in Fig. 2. The conversion of ethane and the yield of ethene increase with the increase of added amount of  $\text{Li}^+$  in both cases of  $\text{MgO}(\text{H}_2\text{O})$  and  $\text{MgO}(\text{EtOH})$ . In the case of  $\text{MgO}(\text{EtOH})$ , the maximum values of the conversion and yield which were attained with 0.5 atom% of  $\text{Li}^+$  content are 19.6 and 15.0%, respectively.  $\text{MgO}(\text{H}_2\text{O})$  showed the maximum catalytic activity at 0.3 atom% of  $\text{Li}^+$  content, which was higher than that of  $\text{MgO}(\text{EtOH})$ .

The rate of ethane conversion is expressed by the following equation.

$$r = k P_{\text{ethane}} P_{\text{oxygen}}$$

where  $P_{\text{ethane}}$  and  $P_{\text{oxygen}}$  are the partial pressures of ethane and oxygen and  $k$  is the rate constant. On the basis of the reaction rate connected with the adsorption of two reactants on  $\text{MgO}$ , the reaction mechanism is considered to be Langmuir-Hinshelwood type.

The activation energies over crystalline  $\text{MgO}$ ,  $\text{Mg}(\text{H}_2\text{O})$ ,  $\text{Li}^+(0.05\text{atom}\%)/\text{MgO}(\text{H}_2\text{O})$ , and  $\text{Li}^+(0.5\text{atom}\%)/\text{MgO}(\text{EtOH})$  were 191, 168,

161, and 134 KJ, respectively. Pretreatment with  $H_2O$  or  $C_2H_5OH$  and addition of  $Li^+$  are considered to lower the activation energy.

### 3.2. The structural variation of MgO with different preparation conditions

**Table 1. The structural effect of MgO with different preparation conditions**

Catalysts	Crystalline MgO	MgO( $H_2O$ )	MgO(EtOH)
Specific surface ( $m^2/g$ )	15.0	92.6	15.4
Distortion ( $\epsilon$ ) $\times 10^3$	$\approx 0$	7.3	$\approx 0$

Crystalline MgO is hydrolyzed when it is immersed in distilled water. The specific surface area of  $MgO(OH)_2$  was much larger than that of crystalline MgO, as shown in Table 1. The XRD pattern showed the existence of  $MgO(H_2O)$  phase, after calcination at 873K, the  $MgO(OH)_2$  phase disappeared completely. The lattice of crystalline MgO was regular, whereas the lattice of  $MgO(H_2O)$  was distorted. Thus, the crystallite form of  $MgO(H_2O)$  is different from that of crystalline MgO. On the other hand, MgO (EtOH) kept almost the same structure as crystalline MgO, as seen in Table 1.

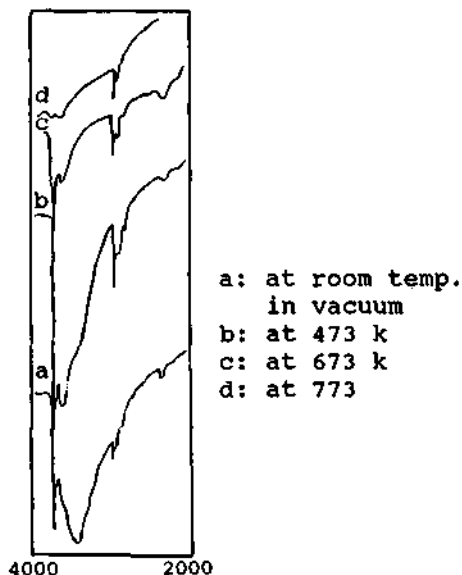


**Fig 3. IR spectra of  $MgO(H_2O)$**

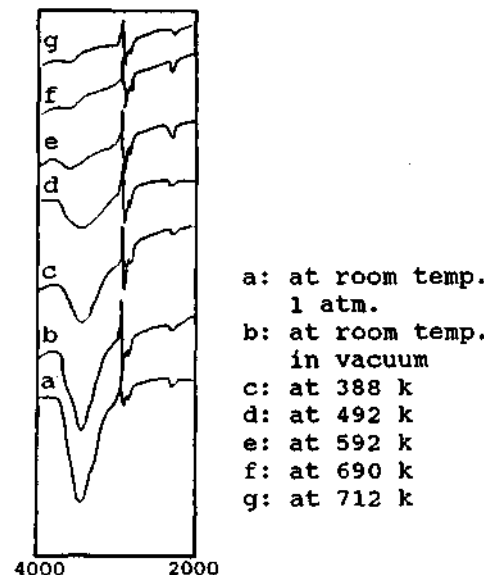
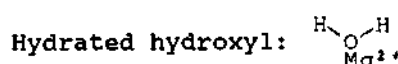
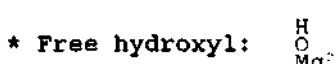


**Fig 4. IR spectra of  $MgO(EtOH)$**



The IR spectra of  $\text{MgO}(\text{H}_2\text{O})$  evacuated at different temperatures are shown in Fig. 3. Two peaks appeared at 3700 and 3400  $\text{cm}^{-1}$ , which correspond to the absorptions of free hydroxyl and hydrated hydroxyl, respectively [2]\*. In the case of  $\text{MgO}(\text{EtOH})$ , however, only one peak appeared at 3400  $\text{cm}^{-1}$  (Fig. 4), which was similar to the case of crystalline  $\text{MgO}$ . Thus, the distortion of  $\text{MgO}(\text{H}_2\text{O})$  is considered to cause the appearance free hydroxyl. Both kinds of hydroxyl peaks almost disappeared at evacuation temperatures higher than 673 K. This indicates that the main active centers on the catalysts activated at temperatures above 873 K are basic sites ( $\text{O}^{2-}$ ) formed by dehydration of hydroxyl group. The loss of free hydroxyl on evacuation may also form anion holes on the surfaces, which facilitate the transfer of oxygen during the reaction.

The higher catalytic activity of  $\text{MgO}(\text{H}_2\text{O})$  than that of crystalline  $\text{MgO}$  can be interpreted by the lattice distortion of  $\text{MgO}(\text{H}_2\text{O})$ . The lowest catalytic activity of  $\text{MgO}(\text{EtOH})$  is considered due to that a part of the surface is covered with coke formed by the decomposition of ethanol.

### 3.3. Increases of the basic and reducing properties of $\text{MgO}$ on the addition of $\text{Li}^+$

The XRD patterns of  $\text{Li}^+/\text{MgO}(\text{EtOH})$  were similar to those of  $\text{MgO}(\text{EtOH})$ , only  $\text{MgO}$  phase being found. The lattice parameters did not change on the addition of  $\text{Li}^+$ . This seems to indicate that  $\text{Li}^+$  does not enter the lattice is dispersed on the surface of  $\text{MgO}$ . The IR spectra of  $\text{Li}^+/\text{MgO}(\text{EtOH})$  containing different amounts of Li showed only one peak at 3400  $\text{cm}^{-1}$  similarly as in the case of  $\text{MgO}(\text{EtOH})$ . On evacuation at 492 K, the peak height of hydrated hydroxyl diminished and moved to higher frequency with increasing the added amount of  $\text{Li}^+$ . When 0.5 atom% of  $\text{Li}^+$  was added, the frequency attained to a maximum of 3668  $\text{cm}^{-1}$  (Table 2), which is ascribed to the characteristic peak of free hydroxyl. These facts indicate that a part of hydrated hydroxyl is removed under the above condition and changed to free hydroxyl. Thus, the addition of  $\text{Li}^+$  is considered to change the property of basic sites on  $\text{MgO}$  and, hence, to enhance the catalytic activity of  $\text{MgO}$  for the oxidative dehydrogenation of ethane. However, the addition of excess  $\text{Li}^+$  will cover the basic sites on  $\text{MgO}$ , resulting in the decrease of the catalytic activity.

Table 2. IR bands ( $\text{cm}^{-1}$ ) of  $\text{Li}^+/\text{MgO}(\text{EtOH})$

Outgas Temp. K	0	Amount of $\text{Li}^+$ added %(atom)		
		0.05	0.5	1.0
298	3440	3448	3450	3463
492	3440	3625	3668	3543

The XRD patterns of  $\text{Li}^+/\text{MgO}(\text{H}_2\text{O})$  were similar to those of  $\text{MgO}(\text{H}_2\text{O})$ . The hydrolysis of crystalline  $\text{MgO}$  as a support during the preparation caused the distortion of  $\text{MgO}$  lattice, but  $\text{MgO}$  phase was recovered by thermal decomposition of  $\text{Mg}(\text{OH})_2$ . The

hydrolysis also led  $\text{Li}^+$  ion to partly enter the lattice of  $\text{MgO}$ , resulting in the lattice distortion and the increase of basicity.

The IR spectra of  $\text{Li}^+/\text{MgO}(\text{H}_2\text{O})$  were similar to those of  $\text{MgO}(\text{H}_2\text{O})$ . On stepwise evacuation, two peaks appeared in the range of  $3000 - 4000 \text{ cm}^{-1}$ . On the addition of a small amount of  $\text{Li}^+$  (0.2 atom%), the free hydroxyl became weaker, while the hydrated hydroxyl became stable. On evacuation at higher temperature, the peak of free hydroxyl disappeared. On the other hand, the addition of a large amount of  $\text{Li}^+$  (5 atom%) made free hydroxyl stronger. In the case of the addition of a small amount of  $\text{Li}^+$ ,  $\text{Li}^+$  is considered to interact with the free hydroxyl and strengthen the interaction between the proton of a hydrated hydroxyl and the neighboring hydroxyl [3]. The  $\text{Li}^+$  ion also increased negative charge of oxygen atom of the hydroxyl and enhanced the basicity  $\text{MgO}$ . In the case of the addition of a large amount of  $\text{Li}^+$ ,  $\text{Li}^+$  covered the  $\text{MgO}$  surface and formed new basic sites which is different from free hydroxyl.

**Table 3.  $\text{CO}_2$ -TPD peak temperature on  $\text{Li}^+/\text{MgO}(\text{H}_2\text{O})$**

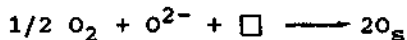
Amount of $\text{Li}^+$ added %(atom)	0	0.05	0.2	1.0	2.5	7.5
$T_m$ K	403	433	457	487	504	550

Table 3 shows the TPD results of  $\text{CO}_2$  adsorbed on  $\text{Li}^+/\text{MgO}(\text{H}_2\text{O})$ . As the amount of  $\text{Li}^+$  increases, the desorption temperature of  $\text{CO}_2$  becomes higher, indicating the increase of basicity. The TPD results of n-butylamine adsorbed on  $\text{Li}^+/\text{MgO}(\text{H}_2\text{O})$  are shown in Table 4. The results indicate that the amount of acid sites increases when a small amount of  $\text{Li}^+$  is added and decreases on the addition of a large amount of  $\text{Li}^+$ . Therefore, the cooperation of basic sites with acidic sites seems to be necessary for the oxidative dehydrogenation of ethane in the ion type mechanism. the acid-base bifunctional catalysis explains the appearance of maximum values of activity and selectivity of  $\text{Li}^+/\text{MgO}$  with suitable amount of  $\text{Li}^+$ .

**Table 4. n-Butylamine-TPD results on  $\text{Li}^+/\text{MgO}(\text{H}_2\text{O})$**

$\text{Li}^+$ %(atom)	0	0.1	0.2	1.0	2.5	7.5
Peak	I	II	I	II	I	II
Temp. (K)	397	776	405	777	397	770
Area	63	12	75	16	75	18

It was reported that the addition of  $\text{Li}^+$  to  $\text{MgO}$  improves the catalytic activity for oxidative coupling of methane due to the increase of reducing property (single electron donating property) of  $\text{MgO}$  [4], which is different from basic property (electron pair donating property). It seems possible that the oxidative dehydrogenation of ethane proceeds not only over acid-base sites by the ionic bifunctional mechanism [5], but also over reducing sites formed by adding  $\text{Li}^+$  to  $\text{MgO}$  by a radical mechanism.



### 3.4. The comparison of activities of different kinds of oxide catalysts

In order to discuss the mechanism of the oxidative dehydrogenation of ethane, the catalytic activities and selectivities of several kinds of oxides were compared. Table 5 shows that the order of ethane conversion is  $\text{MgO}(\text{H}_2\text{O}) >$  crystalline  $\text{MgO} > \text{SiO}_2 > \text{Al}_2\text{O}_3$ , while the order of ethene selectivity is crystalline  $\text{MgO} > \text{ZrO}_2 > \text{MgO}(\text{H}_2\text{O}) > \text{Al}_2\text{O}_3 > \text{SiO}_2$ .

**Table 5. The oxidative dehydrogenation of ethane on the various oxides**

Catalyst	no Catal.	$\text{MgO}(\text{H}_2\text{O})$	$\text{ZrO}_2$	Cryst. $\text{MgO}$	$\text{Al}_2\text{O}_3$	$\text{SiO}_2$
Cov. Ethane %	1.2	33.3	26.2	19.4	13.5	16.5
Yield Ethene %	1.2	28.9	23.0	17.9	10.0	10.9
Select. Ethene %	100	86.8	87.7	92.6	74.4	66.0
Cov. Oxygen %	2.2	88.8	69.0	57.1	62.8	72.5
Yield $\text{CO}_2$ %	0	3.3	3.2	1.4	3.4	5.6
Yield $\text{CH}_4$ %	0	1.1	0	0	0	0

Two kinds of  $\text{MgO}$ ,  $\text{ZrO}_2$ , and  $\text{Al}_2\text{O}_3$  are known to have acidic, basic, and reducing sites. However, the catalytic activities and selectivities are different. The difference is considered due to the differences in relative acid-base strength, the orientation of acid-base pair sites, and the strength of reducing sites. In the case of  $\text{SiO}_2$  which has weak acid-base pair sites and no reducing sites, the reaction seems to proceed by the acid-base bifunctional mechanism, and the activity depends on the relative acid-base strength and the orientation of acid-base pair sites.

**Acknowledgement:** We gratefully acknowledge the support of the National Science foundation of China and the National Science foundation of Zhejiang. We also thank Prof. K. TANABE for assistance with this paper.

### 4. REFERENCES

- [1] Ph. h. De keijser, J.I.Langford, J. Appre. cryst., 1982, 15, 308
- [2] L. wang., Moden Chemical Industry (china), 1988, 8, 14
- [3] J. Fei, X. Zheng, et al., Chem. J. Chin. Univ., 1993, 14, 248
- [4] Kenneth J. Klabunde, Hiromi Matsuhashi, J. Am. Soc., 1987, 109, 1111
- [5] Z. G. Szabo, et al., J. Catal., 1975, 39, 225

## 4.13 Hydrogenation of 1,3-Dienes over Tetramethyltin-Promoted Zinc Oxide Catalyst

Y. Imizu,<sup>\*a</sup> M. Toyofuku,<sup>a</sup> N. Okazaki,<sup>b</sup> H. Itoh,<sup>a</sup> and A. Tada<sup>b</sup>

<sup>a</sup>Department of Material Science, Kitami Institute of Technology, Kitami, Hokkaido 090, Japan

<sup>b</sup>Department of Applied and Environmental Chemistry, Kitami Institute of Technology, Kitami, Hokkaido 090, Japan

### Abstract

The catalytic properties of  $\text{Sn}(\text{CH}_3)_4$ -modified  $\text{ZnO}$  for the hydrogenation of 1, 3-dienes were examined as a function of pretreatment temperature. Upon deposition of  $\text{Sn}(\text{CH}_3)_4$  on  $\text{ZnO}$ , the activities for the hydrogenation of 1, 3-dienes increased by a factor of more than 10 at optimum pretreatment temperature, especially, acceleration factor was observed to be 30 for 1, 3-pentadiene hydrogenation. The product for hydrogenation of 1, 3-butadiene was exclusively 1-butene, however, regioselectivity for 1, 2-hydrogen addition to the methyl substituted 1, 3-dienes were altered by variation of pretreatment temperature of  $\text{Sn}(\text{CH}_3)_4$ . In sharp contrast to  $\text{ZnO}$ ,  $\text{Sn}(\text{CH}_3)_4$  failed to improve the activities of other basic oxides including  $\text{MgO}$ ,  $\text{La}_2\text{O}_3$ ,  $\text{CdO}$ ,  $\text{ZrO}_2$ , indicating  $\text{Sn}(\text{CH}_3)_4$  acts as a sites blocking agent on these oxides. Moreover, no promoting effect was observed for ethylene, propylene, and 1-butene hydrogenation. It was suggested that the partially demethylated Sn complexes are effective for improving the catalytic properties of  $\text{ZnO}$  for the 1, 3-dienes hydrogenation and the interaction between the conjugated dienes and Sn complexes is responsible for promoting the activity. The methyl moieties attached to Sn complexes may also serve as a template to orient or align the reactant and the intermediate.

### 1. INTRODUCTION

Tin alkyl complexes were well known as a promoter for several type of reactions, especially for olefin metathesis. Recently it was reported that when rhodium metal particles were covered with  $\text{Sn}(\text{C}_4\text{H}_9)_x$  fragments, the catalyst was found to be very active and selective in the hydrogenation of citral to the corresponding unsaturated alcohols. [1] The study of such surface metal-hydrocarbyl (alkyl, aryl, etc.) as a new catalytic material provides us an attractive approach to improve catalytic activity and selectivity since unique surface coordination environments derived from hydrocarbyl ligand may give rise to enhancements in chemical reactivity. To extend this strategy to metal oxide systems, we conducted a general survey the reactivity of  $\text{Sn}(\text{CH}_3)_4$ -modified basic oxides toward hydrogenation of simple 1, 3-dienes. Among basic oxides including  $\text{MgO}$ ,  $\text{La}_2\text{O}_3$ ,  $\text{CdO}$ ,  $\text{ZrO}_2$ , and  $\text{ZnO}$ , we have found that  $\text{ZnO}$  was effectively promoted by the modification of  $\text{Sn}(\text{CH}_3)_4$  for the hydrogenation. [2] In the present paper, to understand the origin of promoting effects as well as the nature of the catalytically active sites, we examined the catalytic behavior of  $\text{Sn}(\text{CH}_3)_4$ -promoted  $\text{ZnO}$  for the hydrogenation of olefins and 1, 3-dienes, comparing with other modified basic oxides.

## 2. EXPERIMENTAL METHODS

### 2.1 Preparation of Tetramethyltin-Modified Catalysts

Zinc oxide (Kadox-25 from New Jersey Zinc Co.),  $ZrO_2$  and  $CdO$  were outgassed at 723 K, 773 K, and 723 K, respectively. Magnesium oxide and  $La_2O_3$  were obtained by outgassing the corresponding hydroxides at 1273 and 873 K, respectively. The modification of catalysts was carried out by exposing the outgassed sample (1g) to about 3ml of gaseous  $Sn(CH_3)_4$  (from Janssen) at 77K followed by decomposition of adsorbed  $Sn(CH_3)_4$  by outgassing for 30 min at the temperature elevated to the desired temperatures at a linear heating rate of 4 K/min. The amount of  $Sn(CH_3)_4$  deposited was weighed by using quartz spring balance and was controlled by the repetitive deposition-decomposition cycle.

### 2.2 Reaction Procedures

Hydrogenation was carried out at 300 K in a recirculation reactor with a volume of ca.582 cm<sup>3</sup>. Reactants consisted of 8 kN m<sup>-2</sup>(1 Torr = 133.3 kN m<sup>-2</sup>) of dihydrogen and 8 kN m<sup>-2</sup> of hydrocarbon. Products were withdrawn periodically from the system for GC analysis.

## 3. RESULTS AND DISCUSSION

### 3.1 Catalytic Activity of $Sn(CH_3)_4$ -Modified ZnO

The catalytic activities of  $Sn(CH_3)_4$ -modified ZnO for the hydrogenation of 1, 3-dienes were examined as a function of decomposition temperature. The results are shown in Figure 1. Upon deposition of only 0.75 wt% of  $Sn(CH_3)_4$  on ZnO, the activities for the hydrogenation of 1, 3-butadiene increased remarkably with increasing decomposition temperature and reached a maximum at around 523 K. The maximum activity ( $2.6 \times 10^{-6}$  mol/g·s) was 16 times higher than that of ZnO itself. Similar promoting effects were observed for the hydrogenation of 2-methyl-1, 3-butadiene and 1, 3-pentadiene, respectively. Further increasing decomposition temperature caused in the complete decomposition of  $Sn(CH_3)_4$  to produce metallic Sn deposited on the surface which did not participate in any promoting effects. These results indicate that the partially demethylated Sn complexes (hereafter referred to as  $Sn(CH_4)_x$ ) are effective for improving the activity of ZnO for the 1, 3-dienes hydrogenation. Indeed, further deposition of  $Sn(CH_3)_x$  increased the hydrogenation activities. At 2.2wt% loading the acceleration factors were observed to be 22 for 1, 3-butadiene hydrogenation and 30 for 1, 3-pentadiene hydrogenation. However, at this loading level  $Sn(CH_4)_x$  was rather detrimental for 2-methyl-1, 3-butadiene hydrogenation (acceleration factor observed to be 7). Furthermore, no promoting effect was observed in the monoene hydrogenation, suggesting that the interaction between the conjugated dienes and  $Sn(CH_4)_x$  is responsible for enhancement of activity of  $Sn(CH_3)_4$ -modified ZnO.

### 3.2 Regio and Stereoselectivity for Hydrogenation of 1, 3-Dienes

The selectivity features for the hydrogenation of 1, 3-butadiene, 2-methyl-1, 3-butadiene, and 1, 3-pentadiene are summarized in Table 1. It was known that the hydrogenation over ZnO occurred selectively by the process of 3, 4-addition of hydrogen atoms to 1, 3-dienes. [3] Note that the process of 3, 4-addition giving 1-pentene can be classified into the process of 1, 2-addition in nature. When ZnO was modified with  $Sn(CH_3)_4$ , the selectivity of 1, 2-hydrogen addition to 1, 4-hydrogen addition were slightly improved in the hydrogenation of 2-methyl-1, 3-butadiene and 1, 3-butadiene, respectively. In the case of hydrogenation of 1, 3-pentadiene, the relative contribution of 1, 2-and 1, 4-addition could not discriminate since both process yield 2-pentene. Regioselectivities of 1, 2-hydrogen addition to the methyl substituted 1, 3-dienes were observed to be altered by variation of decomposition temperature of  $Sn(CH_3)_4$ . When the catalyst modified at 523 K, the formation of 3-methyl-1-butene is comparable to that of 2-methyl-1-butene, which is predominated in the hydrogenation of 2-methyl-1, 3-butadiene over ZnO. Also, in the hydrogenation of 1, 3-pentadiene, the catalyst modified at 623 K gave surprisingly high selectivity for the formation of 1-pentene (97%) compared with that over ZnO itself. [3] These alteration in the regioselectivity of 1, 2-hydrogen addition to methyl substituted 1, 3-dienes suggest that the regioselectivity can be controlled by the nature of  $Sn(CH_3)_x$  on ZnO surface.

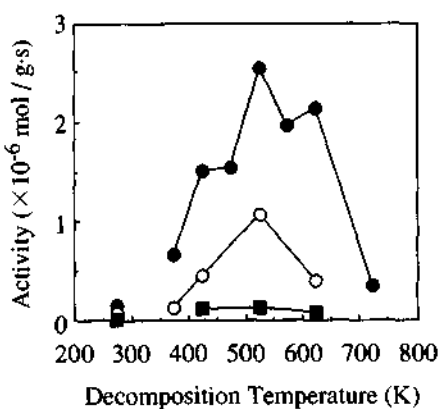


Figure 1. Variation in activities of  $\text{Sn}(\text{CH}_3)_4$ -modified  $\text{ZnO}$  for hydrogenation of 1, 3-butadiene (●), 2-methyl-1, 3-butadiene (○), and *cis*-1, 3-pentadiene (■) as a function of decomposition temperature. The activity data for  $\text{ZnO}$  are plotted at the position of 273 K for comparison.

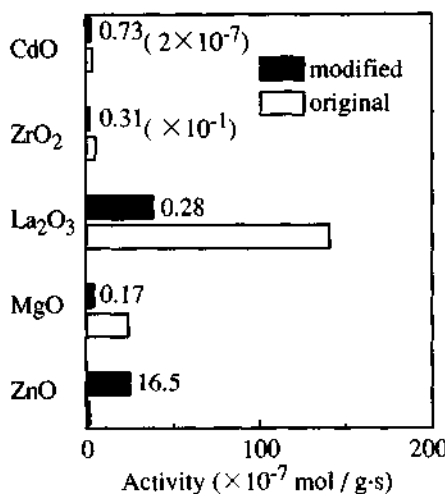


Figure 2. Catalytic activity in the hydrogenation of 1, 3-butadiene over  $\text{Sn}(\text{CH}_3)_4$ -modified  $\text{ZnO}$  and original basic oxides. The value shown in figure is the relative activity compared with each original oxide.

Table 1. Distribution of Products for 1, 3-dienes hydrogenation over  $\text{ZnO}$  and  $\text{Sn}(\text{CH}_3)_4$ -promoted  $\text{ZnO}$ <sup>a)</sup>

Catalyst	Conversion %	Hydrogenation of 1, 3-butadiene		
		1-butene	<i>trans</i> -2-butene	<i>cis</i> -2-butene
$\text{ZnO}$	7.0	92.2	3.0	4.8
$\text{Sn}(\text{CH}_3)_4/\text{ZnO}$ <sup>b)</sup>	72.7	97.7	0.5	1.8

Catalyst	Conversion %	Hydrogenation of 2-methyl-1, 3-butadiene		
		3-methyl-1-butene	2-methyl-1-butene	2-methyl-2-butene
$\text{ZnO}$	5.8	17.7	77.0	5.3
$\text{Sn}(\text{CH}_3)_4/\text{ZnO}$ <sup>c)</sup>	8.9	23.1	74.2	2.8
$\text{Sn}(\text{CH}_3)_4/\text{ZnO}$ <sup>d)</sup>	30.7	50.5	46.9	2.6

Catalyst	Conversion %	Hydrogenation of <i>cis</i> -1, 3-pentadiene		
		1-pentene	<i>trans</i> -2-pentene	<i>cis</i> -2-pentene
$\text{ZnO}$	4.9	81.2	5.7	13.2
$\text{Sn}(\text{CH}_3)_4/\text{ZnO}$ <sup>e)</sup>	19.0	51.7	5.0	43.3
$\text{Sn}(\text{CH}_3)_4/\text{ZnO}$ <sup>d)</sup>	28.6	96.7	0.5	2.8

<sup>a)</sup> 0.75wt% loading.  
Prepared by heating at b) 523K; c) 373K; d) 623K; e) 423K.

### 3.3 Catalytic Activities of $\text{Sn}(\text{CH}_3)_4$ -modified $\text{MgO}$ , $\text{La}_2\text{O}_3$ , $\text{ZrO}_2$ , and $\text{CdO}$

The effect of  $\text{Sn}(\text{CH}_3)_4$  on the catalytic activities of  $\text{MgO}$ ,  $\text{La}_2\text{O}_3$ ,  $\text{ZrO}_2$ , and  $\text{CdO}$  in the hydrogenation of 1, 3-butadiene are shown in Figure 2, compared with that of  $\text{ZnO}$ . In sharp contrast to  $\text{ZnO}$ ,  $\text{Sn}(\text{CH}_3)_4$  failed to improve the activities of these basic oxides although the product distributions tended to remain unchanged. Interestingly, all of these oxides brought about hydrogenation of 1, 3-dienes mainly by 1, 4-addition[5-6] except for  $\text{CdO}$ , indicating that  $\text{Sn}(\text{CH}_3)_4$  acts as a site blocking agent over these oxides, probably by bonding to the basic oxygen atoms. Although  $\text{ZnO}$  [3],  $\text{MgO}$  [4], and  $\text{CdO}$  [5] catalyze the 1, 3-diene hydrogenation by different hydrogen addition process, the same  $\pi$ -allyl anion intermediate was proposed independently over these catalysts. Tanaka et al. rationalized the relative contribution of 1, 2-and 1, 4-hydrogen addition via the same intermediate by considering the kinetic facility caused by surfaces. However, the present results indicate that the promoting effect of  $\text{Sn}(\text{CH}_3)_4$  over  $\text{ZnO}$  could be related to the mechanistic aspects. Therefore, it is difficult to rationalize why  $\text{Sn}(\text{CH}_3)_4$  acts as a promoter over  $\text{ZnO}$ , on the other hand as an inhibitor over  $\text{MgO}$ . Clearly further study is needed to clarify this inconsistency.

### 3.4 Role of $\text{Sn}(\text{CH}_3)_4$ on $\text{ZnO}$

One decade ago, the surface science study of Pt catalyzed hydrogenation revealed that ethylene hydrogenation occurred over platinum surface partially covered by the irreversibly deposited organic layer containing  $\text{CH}$  and  $\text{CH}_2$  fragments. [7] Somorjai et al. proposed the following molecular model. The hydrogenation must occur on bare Pt metal islands. However, intermediates or products may not readily desorb from the bare metal sites and these species diffuse over onto the carbonaceous overlayer from which desorption commences. They also pointed out the role of the organic overlayer that may serve as a template to orient or align the reactant. The role of the carbonaceous overlayer formed on Pt single crystal surface can not directly applied to our system of  $\text{Sn}(\text{CH}_3)_4$  on  $\text{ZnO}$  since the alkylidyne group hardly forms on oxide surfaces during the hydrogenation at relatively low reaction temperature. However the concept of the role of the carbonaceous overlayer seem to be general for both metals and oxide surface. When organic group is introduced by surface modification technique instead of the catalytic reaction, such organic group is expected to provide the beneficial effects for the reaction.

We found that the  $\text{Sn}(\text{CH}_3)_4$  displays several effects for the hydrogenation of 1, 3-diene over  $\text{ZnO}$ . First  $\text{Sn}(\text{CH}_3)_4$  promotes the hydrogenation activity. Secondly,  $\text{Sn}(\text{CH}_3)_4$  controls the regioselectivity of 1, 2-hydrogen addition to the unsymmetrically methyl substituted 1, 3-dienes. Thirdly, a large amount of  $\text{Sn}(\text{CH}_3)_4$  shows a small promoting effect for the hydrogenation of 2-methyl-1, 3-butadiene. This is probably due to steric hindrance since 2-methyl-1, 3-butadiene, which exhibits an inside methyl substituent, is a bulky reactant compared with 1, 3-butadiene and 1, 3-pentadiene. Although the metal part of  $\text{Sn}(\text{CH}_3)_4$  also may provide electronic effects for hydrogenation, we considered that the methyl moieties of  $\text{Sn}(\text{CH}_3)_4$  acts as a template to orient or align the reactant and the intermediate.

## 4. REFERENCES

1. B. Didillon, J. P. Candy, A. El Mansour, C. Houtman, and J.-M. Basset, *J. Mol. Catal.*, **1992**, 74, 43.
2. Y. Imizu, M. Toyofuku, H. Itoh, and Akio Tada, manuscript in preparation.
3. (a) T. Okuhara and K. Tanaka, *J. Chem. Soc., Chem. Comm.*, **1978**, 53 and (b) K. Tanaka, K. Aomura, T. Okuhara, and K. Miyahara, *J. Chem. Soc., Faraday Trans. 1*, **1981**, 77, 1697 and references cited therein.
4. H. Hattori, Y. Tanaka, and K. Tanabe, *J. Am. Chem. Soc.*, **1976**, 98, 4652.
5. K. Tanabe, M. Misra, Y. Ono, H. Hattori, "New Solid Acids and Bases", **1989**, Kodansha, Tokyo, p.308.
6. T. Okuhara and K. Tanaka, *J. Catal.*, **1980**, 61, 135.
7. (a) S. M. Davis, F. Zaera, and G. A. Somorjai, *J. Catal.*, **1982**, 77, 439 and (b) G. A. Somorjai and S. M. Davis, *CHEMTECH*, **1983**, 502.

## 4.14 Dehydrogenation of Ethylbenzene over KFeO<sub>2</sub> —Catalyst Structure and Reaction Intermediate

Hiroshi Miura, Hiroki Kawai and Tomohiro Taguchi

*Department of Applied Chemistry, Saitama University, Shimo-Okubo 255,  
Urawa-shi, Saitama 338 Japan*

### Abstract

The structure of Fe<sub>2</sub>O<sub>3</sub>-K<sub>2</sub>CO<sub>3</sub> dehydrogenation catalyst and the reaction route of ethylbenzene dehydrogenation were studied. Formation of double oxides, KFeO<sub>2</sub> and K<sub>2</sub>Fe<sub>22</sub>O<sub>34</sub>, was found by solid state reaction of Fe<sub>2</sub>O<sub>3</sub> and K<sub>2</sub>CO<sub>3</sub>, but only KFeO<sub>2</sub> was stable in the condition of dehydrogenation reaction. The equilibrium pressure of CO<sub>2</sub> in the solid state reaction was measured and the stability of KFeO<sub>2</sub> in the dehydrogenation condition was suggested. By means of hydrogen-deuterium exchange of ethylbenzene, the participation of the hydrogen attached to  $\alpha$ -position of ethyl group was found. It was suggested that ethylbenzene adsorbed on the catalyst by reversible dissociation of  $\alpha$ -hydrogen. The rate of exchange was compared for different alkylbenzene and the following order was observed; toluene>ethylbenzene>cumene. This order suggests that the exchange proceeds by heterolytic abstraction of  $\alpha$ -hydrogen as H<sup>+</sup> on basic sites of the catalyst surface.

### 1. INTRODUCTION

Dehydrogenation of ethylbenzene has been performed industrially using mixed oxide catalysts containing iron oxide and potassium carbonate as major components [1]. We reported that the mixture of Fe<sub>2</sub>O<sub>3</sub> and K<sub>2</sub>CO<sub>3</sub> easily form KFeO<sub>2</sub> by solid state reaction at elevated temperatures[2]. The double oxide KFeO<sub>2</sub>, however, is reported[3] to decompose when it is in contact with steam or CO<sub>2</sub>. Because steam is usually introduced into the reaction system to remove carbonaceous deposition as CO<sub>2</sub>, the catalyst is used in steam and CO<sub>2</sub>, and there remains room for discussion on the active phase of the catalyst[4-7]. Here we studied the catalyst structure in the reaction condition.

We also examined isotopic exchange reaction of ethylbenzene to study the structure of the intermediate of surface reaction. Basic oxides such as KFeO<sub>2</sub> may

posses one electron donor centers as well as basic sites, and both homolytic and heterolytic splitting of C-H have been supposed as the initial step of dehydrogenation [8-10]. We tried H-D exchange reaction between deuterated alkylbenzene and H<sub>2</sub>O and found that the reaction proceeds by base-catalyzed proton abstraction.

## 2.EXPERIMENTAL

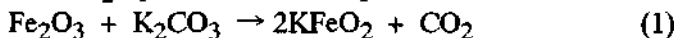
Characterization; X-ray diffraction of Fe<sub>2</sub>O<sub>3</sub>-K<sub>2</sub>CO<sub>3</sub> mixtures was measured using X-ray diffractometer(Rigaku Rad-B, CuK $\alpha$ , 40kV 30mA). After heat treatment, samples were attached to sample holder in N<sub>2</sub> atmosphere and were covered by mylar film. The composition of each phase was calculated based on the relative intensities of (104) plane ( $\alpha$ -Fe<sub>2</sub>O<sub>3</sub>), (200) plane (KFeO<sub>2</sub>) and (001) plane (K<sub>2</sub>Fe<sub>22</sub>O<sub>34</sub>). XPS was measured using ULVAC-PHY ESCA 558UP.

Equilibrium Pressure of CO<sub>2</sub>; The mixture of Fe<sub>2</sub>O<sub>3</sub> and K<sub>2</sub>CO<sub>3</sub> was packed in a quartz tube reactor attached to a closed recirculation system and evacuated at 300° C to remove moisture. The sample was then heated up and kept at constant temperature until the pressure of CO<sub>2</sub> attained equilibrium.

Isotope Exchange Reaction; The exchange reaction was carried out in a stainless steel reactor of 10mm diameter attached to a flow reaction system. A commercial Fe<sub>2</sub>O<sub>3</sub>-K<sub>2</sub>CO<sub>3</sub>-Cr<sub>2</sub>O<sub>3</sub> catalyst was packed in the reactor and a mixture of H<sub>2</sub>O(or D<sub>2</sub>O), H<sub>2</sub> and ethylbenzene(or toluene, cumene, styrene), H<sub>2</sub>O/H<sub>2</sub>/C<sub>8</sub>H<sub>10</sub>=8/8/1, was passed through at 500-600° C. The products were trapped by ice bath and analyzed by GC-mass spectrometer(Shimazu QP-1000) and <sup>1</sup>H-NMR(JEOL JNM-PMX 60si) for the determination of number and position of exchanged atoms.

## 3. RESULTS AND DISCUSSION

3.1. Structure of the catalyst Figure 1 shows the XRD of Fe<sub>2</sub>O<sub>3</sub> and K<sub>2</sub>CO<sub>3</sub> calcined at 750 and 900° C with different values of K/Fe atomic ratio. When the mixture was heated at 900° C, formation of both KFeO<sub>2</sub> and K<sub>2</sub>Fe<sub>22</sub>O<sub>34</sub> was observed, but only KFeO<sub>2</sub> was found when it was heated at 750° C. The solid state reaction to form KFeO<sub>2</sub> proceeds following the eq.(1), and the equilibrium constant K<sub>p</sub> is expressed as (1'). Because activities of solid phases are unity, K<sub>p</sub> is proportional to P<sub>CO<sub>2</sub></sub>. We tried to measure the equilibrium pressure of CO<sub>2</sub> and found that the CO<sub>2</sub> pressure was independent of K/Fe molar ratio and changed



$$K_p = [\text{KFeO}_2]^2[\text{CO}_2]/[\text{Fe}_2\text{O}_3][\text{K}_2\text{CO}_3] = kP_{\text{CO}_2} \quad (1')$$

with temperature as shown in Fig.2. At temperatures of dehydrogenation reaction, i.e. about 600° C, the CO<sub>2</sub> pressure was 7 Torr. If the catalyst is in contact with

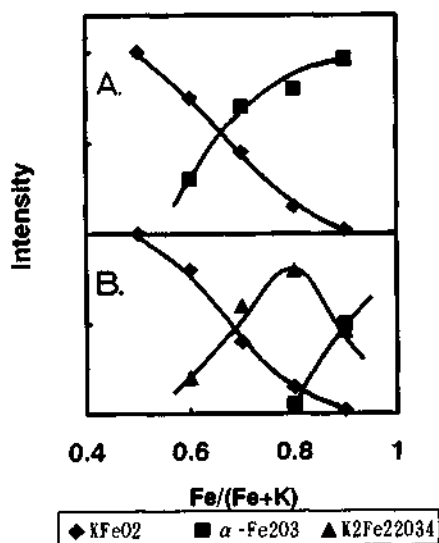


Fig.1. X-ray Diffraction of  $\text{Fe}_2\text{O}_3\text{-K}_2\text{CO}_3$ .  
A. at 700°C, B. at 950°C.

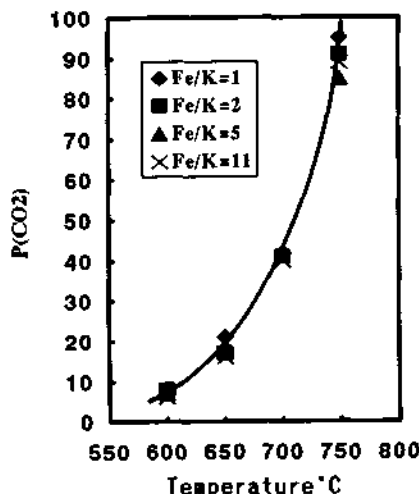


Fig.2. Equilibrium Pressure of  $\text{CO}_2$  in the solid state reaction (1).

$\text{CO}_2$  pressure higher than equilibrium, the reversal reaction of eq.(1) results in the decomposition of KFeO<sub>2</sub>. However, typical reaction products contain less than 2 Torr of  $\text{CO}_2$ , and the pressure is less than equilibrium and the reaction (1) proceeds completely to the right side. Thus it is clear that KFeO<sub>2</sub> exists stably in the reaction condition although it is in contact with  $\text{CO}_2$ . Indeed, we examined XRD of the catalysts after dehydrogenation reaction and found that KFeO<sub>2</sub> stayed stable, while K<sub>2</sub>Fe<sub>22</sub>O<sub>34</sub> decomposed to  $\text{Fe}_3\text{O}_4$  and KFeO<sub>2</sub>.

We tried dehydrogenation of ethylbenzene adding  $\text{CO}_2$  in the reactor. When the  $\text{CO}_2$  pressure was less than 7 Torr, the catalyst activity and selectivity was stable and kept high yield of styrene. When the  $\text{CO}_2$  pressure was higher than 7 Torr, both activity

and selectivity decreased rapidly within 3 hours. Decomposition of KFeO<sub>2</sub> by  $\text{CO}_2$  caused the catalyst deactivation.

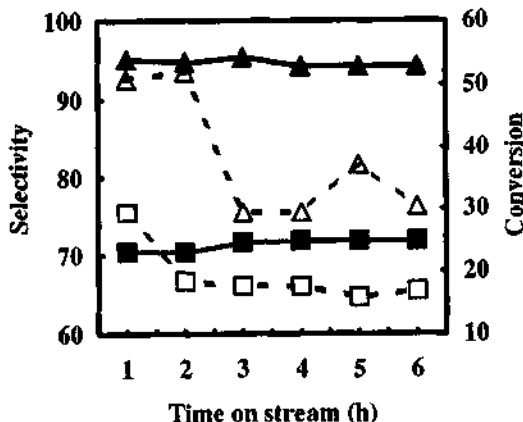


Fig.3. Effect of  $\text{P}_{\text{CO}_2}$  on catalytic activity and selectivity.  
 △▲; selectivity,      □■; conversion,  
 △□;  $\text{P}_{\text{CO}_2} = 30 \text{ Torr}$ ,      ▲■;  $\text{P}_{\text{CO}_2} = 2 \text{ Torr}$ .

**2. Deuterium exchange reaction of ethylbenzene** Because the activation of C-H bond in ethylbenzene seems the essential step of dehydrogenation, we examined hydrogen-deuterium exchange reaction of ethylbenzene over industrial  $\text{Fe}_2\text{O}_3$ - $\text{K}_2\text{CO}_3$ - $\text{Cr}_2\text{O}_3$  catalyst. We tried  $\text{C}_8\text{D}_{10}$ - $\text{H}_2\text{O}$  reaction as well as  $\text{C}_8\text{H}_{10}$ - $\text{D}_2\text{O}$  reaction.

Exchange reaction of  $\text{H}_2$  with  $\text{D}_2\text{O}$  proceeded rapidly at temperatures of dehydrogenation, and so  $\text{C}_8\text{D}_{10}$ - $\text{H}_2\text{O}$  exchange reaction gave similar result as  $\text{C}_8\text{D}_{10}$ - $\text{H}_2$  exchange. The products of  $\text{C}_8\text{H}_{10}$ - $\text{D}_2\text{O}$  exchange reaction were analyzed by GC-MS. The distribution of deuterium exchange for each fragment is shown in Fig.4. Phenyl( $\text{C}_6\text{H}_5-$ ) group itself contained deuterium by exchange.

Because the number of deuterium exchange of benzyl( $\text{C}_6\text{H}_5\text{CH}_2-$ ) group was larger than that of phenyl group, hydrogen atoms attached to the  $\alpha$ -carbon also exchanged with deuterium. In contrast,  $\text{C}_6\text{H}_5\text{CH}_2\text{CH}_3$  group suggested similar distribution to  $\text{C}_6\text{H}_5\text{CH}_2-$  group, indicating that hydrogen atoms attached to  $\beta$ -carbon did not exchange with deuterium.

Similar result was observed also by NMR analysis of the reaction products of ethylbenzene- $d_{10}$  and  $\text{H}_2\text{O}$  (Fig.5.). We found that deuterium atoms attached to benzene ring and  $\alpha$ -position exchanged with H atoms of water, but deuterium atoms attached to  $\beta$  position did not exchange. These results clearly suggest that ethylbenzene adsorbed on the catalyst by the dissociation of C-H bond at the  $\alpha$ -position. This process is reversible and occurs in advance to the rate

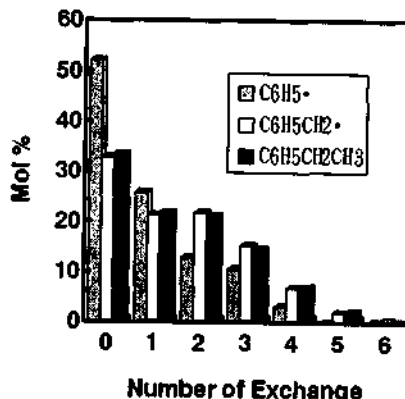


Fig.4. Distribution of the number of D for different fragment of ethylbenzene after H-D exchange reaction at 600°C.

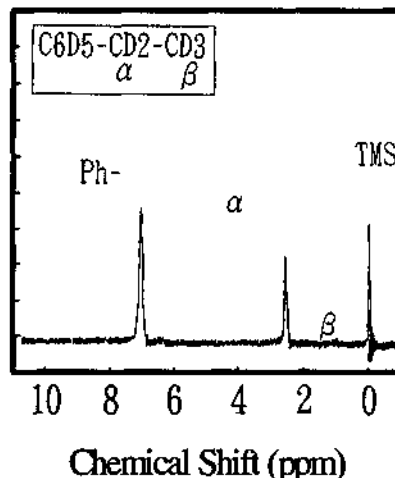
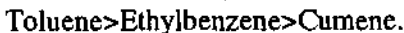


Fig.5.  $^1\text{H-NMR}$  of ethylbenzene- $d_{10}$  after exchange reaction with  $\text{H}_2\text{O}$ .

determining step of the dehydrogenation reaction.

In addition to ethylbenzene, we tried the exchange reaction of D<sub>2</sub>O using toluene and cumene. The rate of exchange measured by GC-MS is shown in Fig.6. Toluene exchanged its hydrogen more easily than ethylbenzene. By NMR analysis, most of hydrogen atoms were introduced at the  $\alpha$ -position of toluene by the exchange reaction. Cumene did not exchange its hydrogen at any temperature. Thus we concluded the order of exchange reaction as follows;



These results suggest that the dissociation of  $\alpha$ -hydrogen occurs by hetero-lytic splitting of C-H bond to form H<sup>+</sup> and R<sup>-</sup>, because the stability of the R<sup>-</sup> intermediate follows the same order. If C-H bond dissociates heterolytically, the opposite order should result. Thus we concluded that dehydrogenation of ethylbenzene proceeds by abstraction of  $\alpha$ -hydrogen catalyzed by the basic sites of KFeO<sub>2</sub> surface.

#### 4. CONCLUSIONS

1. Two double oxides, KFeO<sub>2</sub> and K<sub>2</sub>Fe<sub>22</sub>O<sub>34</sub>, formed by solid state reaction of Fe<sub>2</sub>O<sub>3</sub> with K<sub>2</sub>CO<sub>3</sub>, but only KFeO<sub>2</sub> stayed stable in the reaction condition.
2. The solid state reaction of KFeO<sub>2</sub> formation was reversible and the equilibrium was controlled by the pressure of CO<sub>2</sub> (P<sub>CO<sub>2</sub></sub>). Activity and selectivity of the catalyst was also controlled by P<sub>CO<sub>2</sub></sub>. If P<sub>CO<sub>2</sub></sub> was less than the equilibrium pressure, activity and selectivity stayed stable and the catalyst contained KFeO<sub>2</sub> after reaction. If P<sub>CO<sub>2</sub></sub> was higher than equilibrium, activity and selectivity dropped down and decomposition of KFeO<sub>2</sub> was observed after reaction.
3. H-D exchange reaction proceeded between ethylbenzene-H<sub>2</sub>O and ethylbenzene-H<sub>2</sub>. Because the  $\alpha$ -hydrogen of ethylbenzene exchanged, ethylbenzene adsorbed on the catalyst by reversible dissociation of C-H bond at the  $\alpha$ -position, and this process takes place in advance to the rate determining step.
4. The rate of exchange reaction followed the order, toluene>ethylbenzene>cumene. This order suggests that the C-H bond dissociates heterolytically to form H<sup>+</sup> and benzyl anion.

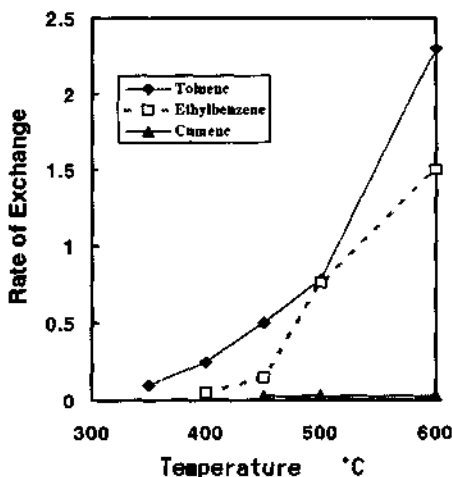


Fig.6. Rate of H-D exchange reaction for toluene, ethylbenzene and cumene.

5. The dehydrogenation of ethylbenzene proceeds on the basic centers of the surface of  $\text{KFeO}_2$  in  $\text{Fe}_2\text{O}_3-\text{K}_2\text{CO}_3$  catalyst.

## REFERENCES

1. H.Un-ei, *Shokubai(Catalyst)*,33,9(1991).
2. H.Miura, R.Ansei, Y.Mizushima, A.Kurita, T.Matsuda, *J.Jpn.Petrol.Inst.*,33, 397 (1990).
3. M.Muhler, J.Schutze, M.Wesemann, T.Rayment, A.Dent, R.Sehiogl, G.Ertl, *J.Catal.*, 126,339(1990).
4. K.Shibata, T.Kiyoura, *Bull.Chem.Soc.Jpn.*,42,871(1969).
5. J.Koppe, I.Rapthel, P.Kraak, *Chem. Tech.*, 40,81(1988).
6. T.Hirano, *Appl. Catal.*, 26,65(1986).
7. D.E.Stobbe, F.R.van Buren, A.J. van Dillen, J.W. Geus, *J.Catal.*, 135,533(1992).
8. T.Hirano, *Shokubai(Catalyst)*,29,641(1987).
9. C.Jianping, H.Danyun, C.Shoujin, *Gaodeng Xuexia Zuebao*, 7,1020(1986); CA 107:21689x.
10. K.Miyata, S.Ozawa, Y.Yamamoto, Y.Ogino, *J.Jpn.Petrol.Inst.*,31,210(1988).

## 4.15 Acid-Base Nature of Antimony Oxides

S. Tsuchiya, T. Yamada, K. Ishikawa, Y. Sakata, and H. Imamura

Department of Advanced Materials Science and Engineering, Faculty of Engineering, Yamaguchi University, Ube 755, Japan

### Abstract

The dehydrogenation and the dehydration of 2-propanol have been investigated over several types of antimony oxides. The amounts and strength of acid and base were measured by the n-butylamine and the benzoic acid titration method. The values of  $H_{0\max}$  obtained were good measure of the product selectivity of 2-propanol reaction.

### 1. INTRODUCTION

Since antimony oxides are amphoteric oxides, they would show some interesting acid-base catalytic properties. However, relatively little information has been so far reported on their catalytic property. In this study, we measured the reaction of 2-propanol over some antimony oxides samples, and correlated with the both acid and basic properties of these oxide.

### 2. EXPERIMENTALS

#### 2.1. Catalysts

The catalysts used were  $Sb_2O_3$ ,  $Sb_2O_3-S$ ,  $Sb_6O_{13}$ ,  $Sb_2O_4$ , and  $Sb_2O_5$ , which were supplied from Nihon Seiko Co. Ltd. The  $Sb_2O_3$ -750,  $Sb_2O_3$ -800 and  $Sb_2O_3$ -1000 samples were obtained by the oxidation of antimony at 1023, 1073 and 1273 K, respectively. The  $Sb_2O_3-S$  sample was produced from  $Sb_2S_3$  by oxidation. The  $Sb_6O_{13}$  sample was obtained from  $Sb_2O_5$  by heat treatment at 1073 K.  $Sb_2O_3$  was oxidized at 723 K to form the  $Sb_2O_4$  sample.  $Sb_2O_5$  was obtained from  $Sb_2O_5 \cdot nH_2O$ , which was decomposed from  $NaSb(OH)_6$  at 673 K.  $Sb_2O_3-R$  was obtained by hydrolysis from  $SbCl_3$  via antimony oxychloride.

#### 2.2. Measurement of acid and basic nature

The n-butylamine titration method and the benzoic acid titration method were employed to measure the amount and the strength of the acid and of the base,

respectively [1]. Since  $Sb_2O_5$  is yellowish and the color change of indicators cannot be visually observed, we mixed the  $Sb_2O_3$ -R sample with the  $Sb_2O_5$  sample. Since the color of  $Sb_2O_3$ -R is white, the color change of indicator is visible on its surface. By the titration method the summation of the amounts of acid and of base on the surface of  $Sb_2O_5$  and that of  $Sb_2O_3$ -R. We could therefore estimate the amounts and strength of acid and base on the surface of  $Sb_2O_5$  alone by subtracting the contribution of the  $Sb_2O_3$ -R. We had measured the amount and the strength of acid and base on the surface of the  $Sb_2O_3$  beforehand.

### 2.3. Procedure

The apparatus used was a closed circulating system having a U-shaped reactor with a conventional vacuum line and a gas-chromatograph. By the gas-chromatograph, we analyzed the reaction mixtures at suitable time to follow the reaction. The volume of the closed circulating system corresponds to about 300  $\text{cm}^3$  at the reaction temperature at 573 K. The catalysts were evacuated for 2 h at 573 K before the reaction.

## 3. RESULTS AND DISCUSSION

Figure 1 and 2 show the results of the reaction of 2-propanol over the  $Sb_2O_3$ -800 and the  $Sb_2O_3$ -S, respectively. The formation of propylene and acetone was observed in both cases, the dehydration and the dehydrogenation of 2-propanol taking place. These results were reasonably explained on the basis that the propylene formed on the acid sites, and that the acetone formed on the basic sites. The formation of acetone was predominant over the  $Sb_2O_3$ -800. Over the  $Sb_2O_3$ -S, on the other hands, propylene predominantly formed. These results are very important, and suggest that the difference in the reaction selectivity was due to that of the surface acid-base nature.

Figure 3 shows the amount and strength of acid and base on the surface of the  $Sb_2O_3$ -800, and the  $Sb_2O_3$ -S. Both acid and basic sites were observed on the surface. In both cases, acid and basic sites observed were not very much strong. The value of  $H_0\text{max}$  of the  $Sb_2O_3$ -800, 3.9, was larger than that of the  $Sb_2O_3$ -S, 3.6. The definition of

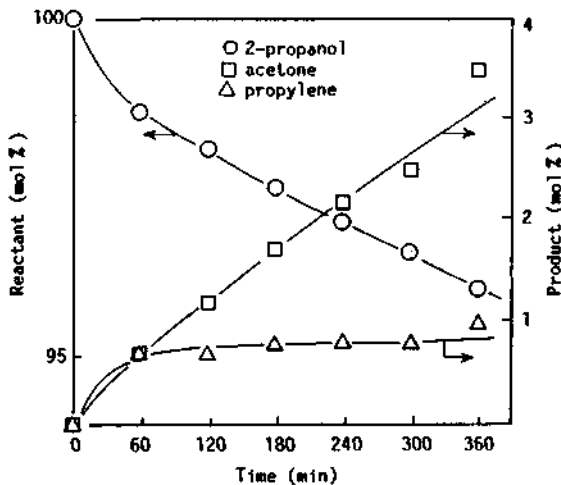


Fig. 1 Reaction of 2-propanol over  $Sb_2O_3$ -800 at 573 K.

$H_0\text{max}$  is described in Ref.[2]. This result suggests that the predominance of reaction products is dependent on the value of  $H_0\text{max}$ .

Figure 4 shows the amounts and strength of acid and base on the surface of the  $\text{Sb}_2\text{O}_5$  and the  $\text{Sb}_2\text{O}_4$ . Both acid and basic sites were also observed on the surface. Since the value of  $H_0\text{max}$  of the  $\text{Sb}_2\text{O}_5$ , 2.9, was less than 3.6, it was reasonably predicted beforehand that the main product from 2-propanol would be propylene. Since the value of  $H_0\text{max}$  of  $\text{Sb}_2\text{O}_4$  and  $\text{Sb}_2\text{O}_3\text{-}800$  was same, main product from 2-propanol would be acetone.

Figures 5 and 6 shows the results of the reaction of 2-propanol over the  $\text{Sb}_2\text{O}_4$  and the  $\text{Sb}_2\text{O}_5$ , respectively. The formation of propylene and acetone was also observed, and acetone predominantly formed over the  $\text{Sb}_2\text{O}_4$ . Over the  $\text{Sb}_2\text{O}_5$  propylene predominantly formed. These results confirmed the prediction mentioned above.

Figure 7 show the amounts and strength of acid and base on the surface of the  $\text{Sb}_6\text{O}_{13}$  and the  $\text{Sb}_2\text{O}_3\text{-R}$ . Since the value of  $H_0\text{max}$  of the  $\text{Sb}_6\text{O}_{13}$ , 1.0, was less than that of the  $\text{Sb}_2\text{O}_3\text{-S}$ , 3.6, and that of the  $\text{Sb}_2\text{O}_3\text{-R}$  was much larger than that of the  $\text{Sb}_2\text{O}_3\text{-800}$ . From there results the main product from 2-propanol would be predicted.

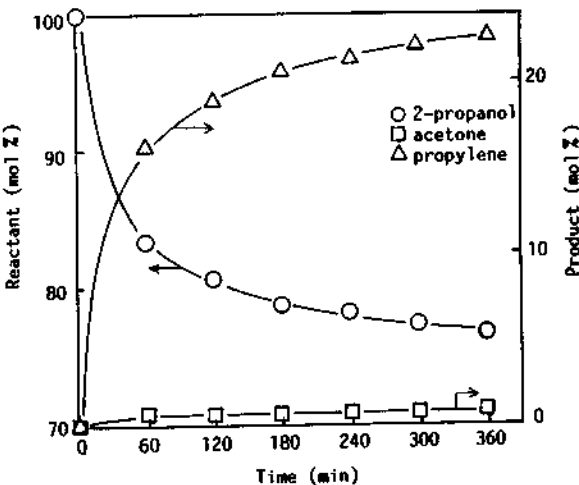


Fig. 2 Reaction of 2-propanol over  $\text{Sb}_2\text{O}_3\text{-S}$  at 573 K.

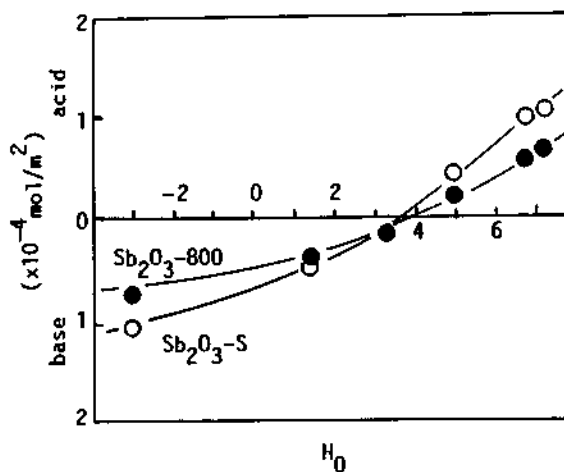


Fig. 3 The amounts and strength of acid and base on  $\text{Sb}_2\text{O}_3\text{-800}$  and  $\text{Sb}_2\text{O}_3\text{-S}$ .

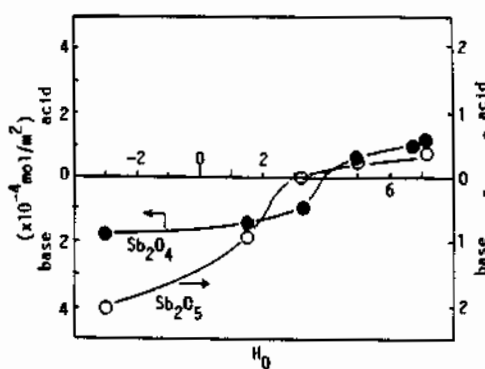


Fig. 4 The amounts and strength of acid and base on  $Sb_2O_5$  and  $Sb_2O_4$ .

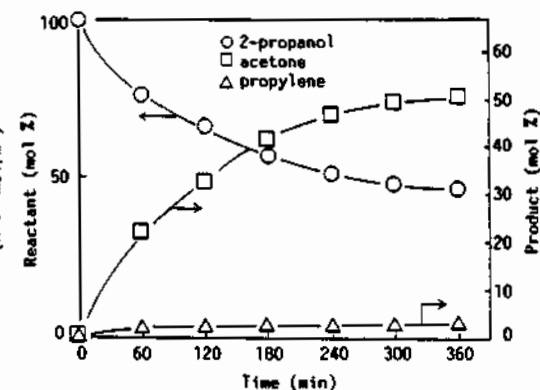


Fig. 5 Reaction of 2-propanol over  $Sb_2O_4$  at 573 K.

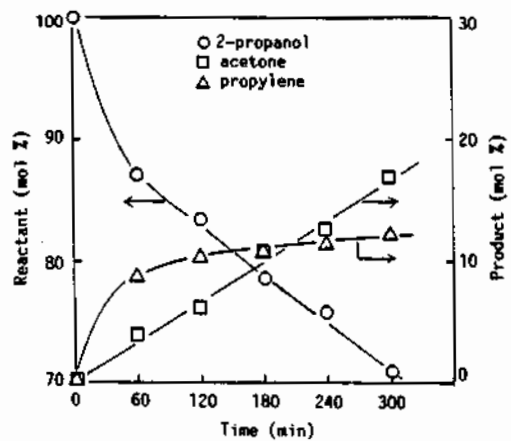


Fig. 6 Reaction of 2-propanol over  $Sb_2O_5$  at 573 K.

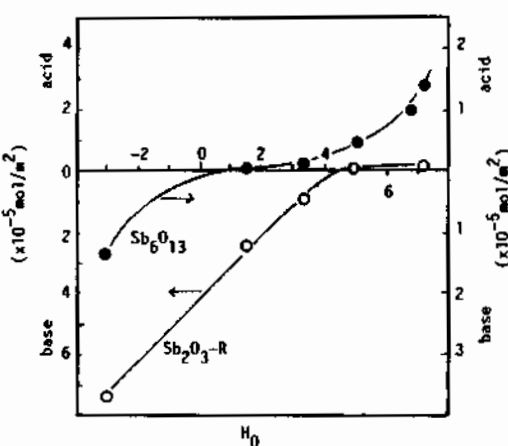


Fig. 7 The amounts and strength of acid and base on  $Sb_6O_{13}$  and  $Sb_2O_3-R$ .

Figure 8 and 9 shows the results of the reaction of 2-propanol over the  $Sb_6O_{13}$  and the  $Sb_2O_3\text{-R}$ , respectively. The main product could be again predicted from the value of  $H_0\text{max}$ .

As for eight kinds of antimony oxides catalysts, the  $H_0\text{max}$  and the BET surface area and the main product of the reaction of 2-propanol were summarized in Table 1. When  $H_0\text{max} \geq 3.9$ , acetone was the main product. Propylene was the main product, when  $H_0\text{max} \leq 3.6$ .

Although the amounts and strength of acid and base on the surface are very important informations, the values of  $H_0\text{max}$  are very much important and are very sufficient to predict the selectivity of the reaction of 2-propanol over the antimony oxides. The n-butenes isomerization is one of the typical model reactions of acid-base catalysis. The reaction profile of n-butenes isomerization is useful to classify the type of acid-base catalysts[3]. However, the catalytic activity of the antimony oxides used were too small to isomerization n-butenes, except  $Sb_2O_5$ .

It was accordingly concluded that the hydration and dehydrogenation of 2-propanol were better than n-butenes isomerization for the antimony oxides.

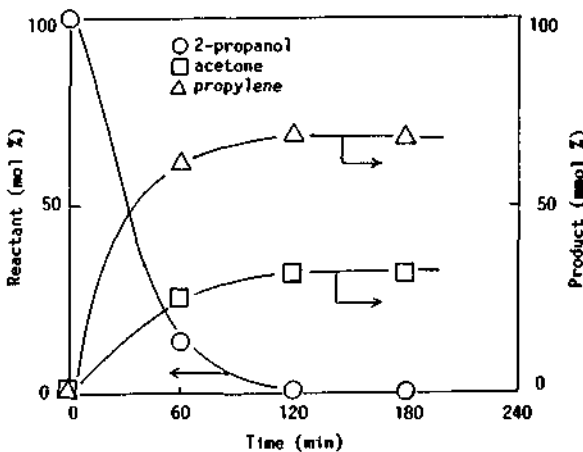


Fig. 8 Reaction of 2-propanol over  $Sb_6O_{13}$  at 573 K.

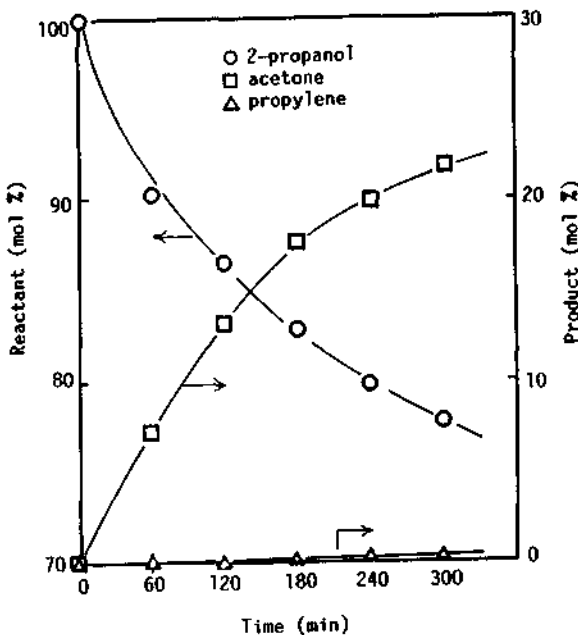


Fig. 9 Reaction of 2-propanol over  $Sb_2O_3\text{-R}$  at 573 K.

**Table 1** BET surface area,  $H_{0\max}$ , and main reaction product.

Catalyst	S.A. A/(m <sup>2</sup> /g)	$H_{0\max}$	Main product
Sb <sub>2</sub> O <sub>3</sub> -800	4.97	3.9	acetone
Sb <sub>2</sub> O <sub>3</sub> -1000	1.27	4.1	acetone
Sb <sub>2</sub> O <sub>3</sub> -750	2.85	3.6	propylene
Sb <sub>2</sub> O <sub>3</sub> -S	2.07	3.6	propylene
Sb <sub>6</sub> O <sub>13</sub>	5.25	1.0	propylene
Sb <sub>2</sub> O <sub>4</sub>	0.53	3.9	acetone
Sb <sub>2</sub> O <sub>5</sub>	5.95	2.9	propylene
Sb <sub>2</sub> O <sub>3</sub> -R	1.17	4.5	acetone

#### 4. CONCLUSION

Both acid and basic sites were observed on the surface of antimony oxides. Both dehydrogenation and dehydration of 2-propanol took place over antimony oxides, and the formation of both propylene and acetone were observed. The value of  $H_{0\max}$  is the good measure of the product selectivity of 2-propanol reaction and the acid-base nature of the surface of the antimony oxides.

#### Reference.

- [1] K. Tanabe, "Solid Acids and Bases: their catalytic properties", Kodansha, Tokyo, 1970, p. 17, p.38.
- [2] K. Tanabe, M. Misono, Y. Ono and H. Hattori, "New Solid Acids and Bases Their Catalytic Properties", Kodansha Tokyo, 1989, p.20.
- [3] S. Tsuchiya and H. Imamura, Shokubai (Catalyst) Tokyo, 1983, 25, 133.

## 4.16 Base Sites of Magnesium Oxide Dispersed on Silica as Active Sites for CO Photooxidation

Hisao Yoshida, Tsunehiro Tanaka, Kazuhiro Nakatsuka, Takuzo Funabiki and Satohiro Yoshida  
Department of Molecular Engineering, Kyoto University, Kyoto 606-01, Japan

### Abstract

Base sites and photoactive sites of fine particles of MgO dispersed on silica have been studied. In order to control the population of the coordinatively unsaturated surface Mg and O ions ( $Mg_{CUS}$  and  $O_{CUS}$ ), some samples including magnesium oxide fine particles were prepared. These samples are well defined and have each specific amount of CUS ions by changing amount of loading on silica. Thus prepared samples were free from  $F^*$  center trapping an electron which have been proposed to be photoactive sites. From the correlation between the population of CUS ion pairs and the rate of photooxidation, we have concluded that the catalytic active sites for CO photooxidation are ( $Mg_{CUS}$ - $O_{CUS}$ ) pairs. Since a good relationship between the amount of base sites where  $CO_2$  molecules are chemisorbed and the rate of photooxidation of CO is observed, base sites and photoactive sites are considered to be identical.

### 1. INTRODUCTION

MgO is a typical solid base catalyst [1]. Its active sites are thought to be associated to coordinatively unsaturated surface (CUS) O ions [2]. To elucidate surface structure of MgO, phosphorescent emission from UV-excited MgO is often used [3,4]. Excitation and emission wavelengths are closely related to the coordination circumstance of surface Mg and O ions [4], because the process of excitation and emission involves the charge transfer between  $Mg_{CUS}$  and  $O_{CUS}$ . These ions are also admitted to play an important role in photocatalysis by MgO [5].

Some researchers [6] insist that photoemission sites are not  $Mg_{CUS}$  or  $O_{CUS}$  but  $F^*$  centers trapping an electron. It is difficult to identify photocatalytic active sites to one of them because bulk MgO usually includes both CUS ions and  $F^*$  centers on the surface.

We have prepared the MgO/SiO<sub>2</sub> samples free from  $F^*$  centers in the present work, and thus we have examined the role of CUS ions. On these samples, photocatalytic active sites would be restricted to CUS ions. The specific population of such surface ions would be controlled by changing the size of MgO particle dispersed on silica support. Furthermore, we have discussed a relation between the active sites for CO photooxidation and base sites.

## 2. EXPERIMENTAL

Samples ( $\text{MgO}/\text{SiO}_2$ , MS) were prepared in the manner described elsewhere [7]. A series of samples of different  $\text{Mg}^{+}$  loading were prepared; 1MS (1 wt.% as  $\text{MgO}$ ) to 20MS (20 wt.% as  $\text{MgO}$ ). The loading amounts of  $\text{MgO}$  were determined by X-ray fluorescence analysis.

Chemisorbed amounts of  $\text{CO}_2$  on the base site at 273 K were estimated by extrapolation of adsorption isotherms to the zero pressure. X-band electron spin resonance (ESR) spectra were recorded at 77 K using a JEOL JES-PE ESR-spectrometer, and X-ray photoelectron spectra (XPS) were recorded with a Perkin Elmer Phi model 5500 spectrometer.

X-ray absorption spectra were recorded in a total electron yield mode at room temperature with the facility of the BL-7A station at UVSOR in Institute for Molecular Science for Mg K-edge with a beryl tow-crystal monochromator [8]. Energy calibration was made by using K-edge absorption of Al in beryl. Samples were mixed with active carbon in dry hexane and were pasted on the first photocathode made of CuI of the electron multiplier.

Photooxidation of CO was carried out at room temperature in a closed circulating reaction system ( $250 \text{ cm}^3$ ). The initial amounts of CO and  $\text{O}_2$  as reactants were respectively 200  $\mu\text{mol}$ . Produced  $\text{CO}_2$  was immediately frozen out in a liquid  $\text{N}_2$  trap and the amount was evaluated by the decrease in pressure of the reaction system. A super high pressure 250 W Hg lamp was used as a light source.

## 3. RESULTS AND DISCUSSION

### 3.1. $\text{F}^+$ centers

ESR study was carried out to detect  $\text{F}^+$  centers on the sample.  $\text{F}^+$  centers and Mn ions as impurity were detected for a commercial  $\text{MgO}$  bulk sample evacuated at 673 K. Figure 1-a) shows ESR signals due to  $\text{F}^+$  centers of  $\text{MgO}$  bulk.

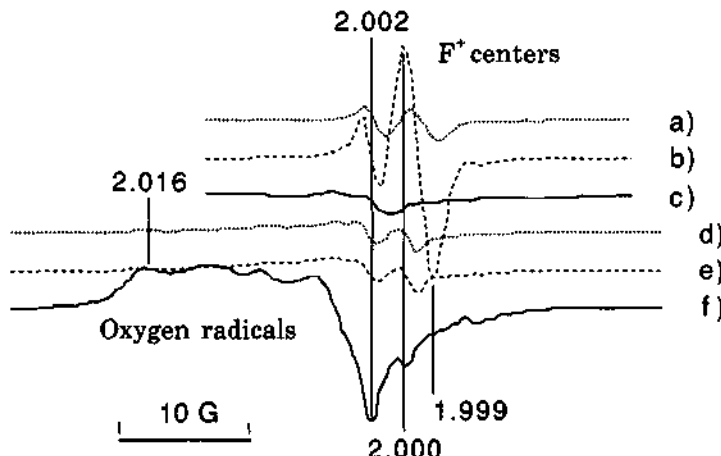


Fig. 1 ESR spectra of bulk  $\text{MgO}$  sample a) in *vacuo*, b) in *vacuo* under irradiation, c) in the presence of  $\text{O}_2$  under irradiation, and 17MS sample d) in *vacuo*, e) in *vacuo* under irradiation, f) in the presence of  $\text{O}_2$  under irradiation. Spectra were recorded at 77 K.

With UV-irradiation *in vacuo*, the signal intensity due to F\* centers increased (fig. 1-b), but in the presence of O<sub>2</sub> the signal decreased significantly (fig. 1-c), indicating that the F\* centers exist on the surface of bulk MgO.

On the contrary, 17MS sample did not exhibit such a signal. Only small unidentified signals were observed on the broad back ground due to the silica support. Back ground subtracted ESR spectra of 17MS sample are shown in fig. 1-d) to f). Since these small signals are characterized by different g values from those of F\* centers mentioned above and were not affected by UV-irradiation (fig. 1-e) and were not quenched by O<sub>2</sub> molecules (fig. 1-f), these signals are different from that due to the F\* centers. From these results, we have concluded that MS samples are free from F\* centers. Even if they were other kinds of F\* centers, these F\* centers are not related to photooxidation because that they are not excited by irradiation (fig. 1-e).

In the presence of O<sub>2</sub> under UV-irradiation (fig. 1-f), some undefined signals by presumable oxygen radicals were obviously detected. It strongly suggests that these oxygen radicals would bring about the photooxidation on the MS samples.

### 3.2. Local Structure and Dispersion

In order to obtain fine particles of MgO, we prepared MS samples in which the loading amount of magnesium oxide were less than 20 wt.% as MgO. These samples exhibited no appreciable peaks in the XRD pattern. Therefore, XANES and XPS analyses were carried out to obtain information about the local structure and dispersion of magnesium oxide on silica.

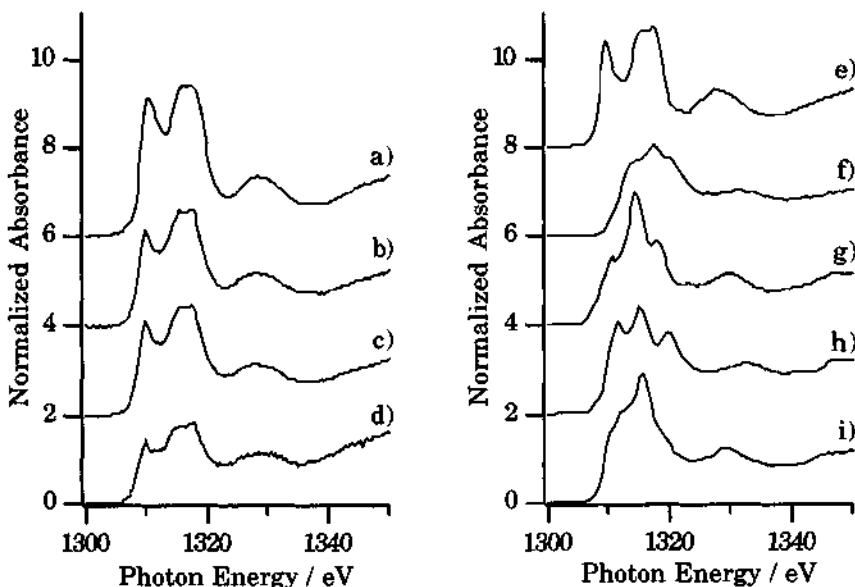


Fig. 2 Mg K-edge XANES of MS samples and references; a) MgO prepared by calcination of Mg(OCH<sub>3</sub>)<sub>2</sub>, b) 20MS, c) 5MS, d) 1MS, e) pulverized MgO single crystal, f) Mg(OCH<sub>3</sub>)<sub>2</sub> extracted from methanol solution, g) Mg(OH)<sub>2</sub> evacuated at 473 K, h) MgSiO<sub>3</sub>, i) Mg<sub>2</sub>SiO<sub>4</sub>.

XANES spectra are sensitive to coordination symmetry around the target atoms. Figure 2 shows XANES spectra of MS samples (b,c,d) together with that of bulk MgO and several compounds as references (a, e-i). All MS samples gave approximately the same spectra regardless of the loadings. They are identical with that of MgO of a typical rock salt structure but different from that of other reference compounds. It indicates that Mg ions in MS samples are located at a center of a regular octahedron of oxygen ions.

It was possible that a compound such as  $\text{MgSiO}_3$  or  $\text{Mg}_2\text{SiO}_4$  were produced in MS samples. However, the XANES spectra of these compounds (fig. 2-h,i) are quite different from that of MS samples, suggesting that there are no such compounds but magnesium oxide of rock salt structure in MS samples. Therefore, magnesium oxide particles in MS samples would possess the same characters as those of bulk MgO.

The surface concentration of MgO in MS samples estimated by XPS is shown in fig. 3. The surface concentration increases linearly with the loading of magnesium oxide up to 5 wt.%, but the linearity did not hold above 5 wt.%. It suggests that MgO is highly dispersed as crystallite of raft-like structure in the samples up to 5 wt.% loading, and the crystallites have grown to large particles in the samples of loading above 5 wt.% [9].

The results mentioned above indicate that MgO crystallites sizes were controlled by changing amount of loading of MS samples, so that specific population of CUS ions could be controlled.

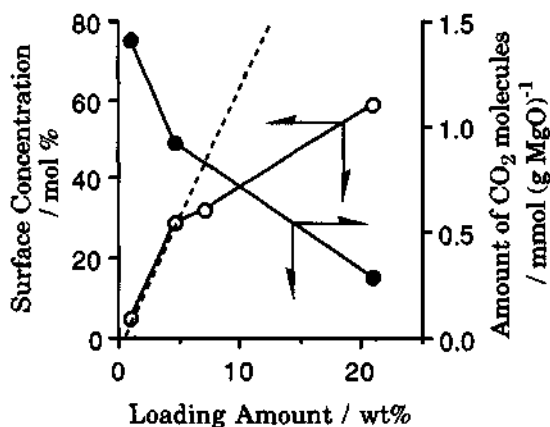


Fig. 3 Surface concentration of MgO in MS samples estimated by XPS (○), and amount of  $\text{CO}_2$  molecules adsorbed on the base sites of MgO (●).

### 3.3. Amount of base sites

We estimated specific population of base sites on MgO surface using the characteristic property of  $\text{CO}_2$  molecules which are adsorbed selectively on the base sites [1]. As shown in fig. 3, the smaller loading amount of MgO is, the larger amount of chemisorption normalized to one gram of MgO is. This shows that normalized amount of base sites on the surface of magnesium oxide in these samples decreases with an increase in loading amount of MgO, even in the case of that MgO crystallites present as the raft-like structure. Since specific population of

CUS ions on magnesium oxide is larger in MS samples of low loading, it suggests that base sites relate to CUS ions.

### 3.4. Photooxidation of CO

The amount of catalysts for CO photooxidation was adjusted as that the equal amount of MgO crystallites (5 mg, 125 μmol) is contained, therefore, the conversion of CO is proportional to the specific activity of the MgO crystallites. The time course of photooxidation is shown in fig. 4. Each sample exhibited an induction period about for 40 minutes. After the induction period, the conversion increased with time linearly. The reaction did not proceed in the dark, indicating it was photocatalytic oxidation. The photooxidation took place very slowly on silica without magnesium oxide loading, suggesting that photocatalytic active sites exist on the MgO crystallites.

Obviously in fig. 4, a lower loading MS sample exhibits higher activity. Since the lower loading sample is supposed to have higher specific population of CUS ion pairs, it is indicated that the photoactive sites are the CUS ions on magnesium oxide fine particle.

Figure 5 shows a relationship between reaction rate of CO photooxidation and the amount of chemisorbed CO<sub>2</sub> on MS samples. The reaction rate was evaluated from the region of the last 20 minutes. This good correlation between amount of chemisorbed CO<sub>2</sub> and reaction rate indicates that base site and photoactive site are identical. Since the photoactive sites are (Mg<sub>CUS</sub>-O<sub>CUS</sub>) pairs, we have concluded that base sites are the O<sub>CUS</sub> ions in the pairs, as suggested in the section 3.3.

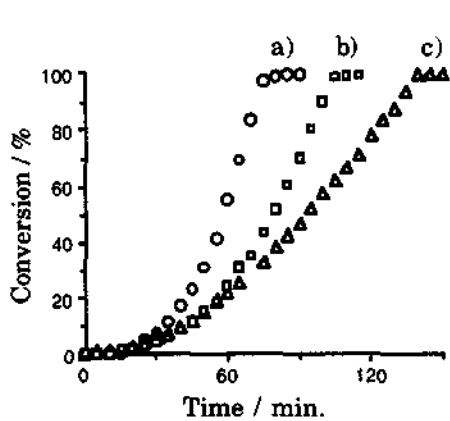


Fig. 4 Time course of CO photooxidation on MS samples; a) 1MS, b) 5MS and c) 20MS.

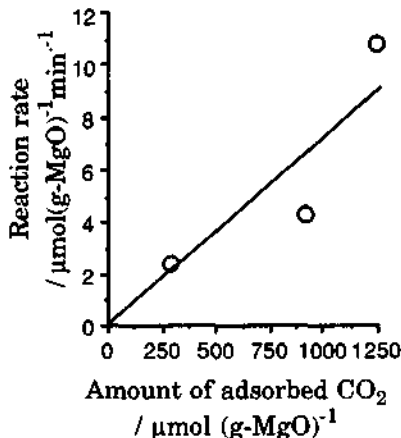


Fig. 5 Relation between reaction rate of CO photooxidation and the amount of chemisorbed CO<sub>2</sub> on MS samples.

## 4. CONCLUSION

As a conclusion, the coordinatively unsaturated surface Mg and O ion pairs on the magnesium oxide fine particle in the MgO/SiO<sub>2</sub> samples function as catalytic active sites in the photooxidation of CO. The base sites on the magnesium oxide detected as adsorption sites of CO<sub>2</sub> coincide with such CUS ion pairs.

**ACKNOWLEDGEMENT**

X-ray absorption experiments were approved by the Joint Studies Program (1991 - 92) of UVSOR of the Institute for Molecular Science. The authors would like to thank Professor Masao Kitamura (Kyoto Univ.) and Professor Sadao Hasegawa (Tokyo Gakugei Univ.) for their kindness to offer some reference samples. HY is supported by a grant in aid from the Japan Society for the Promotion of Science for Japanese Junior Scientists.

**REFERENCES**

- [1] K. Tanabe, M. Misono, Y. Ono, H. Hattori, *New Solid Acids and Bases* (Kodansha, Tokyo, 1989).
- [2] H. Kawakami and S. Yoshida, *J. Chem. Soc., Faraday Trans. 2*, **1984**, 80, 921.
- [3] A. J. Tench and G. T. Pott, *Chem. Phys. Lett.*, **1974**, 26, 590.
- [4] S. Coluccia, A. M. Deane and A. J. Tench, *J. Chem. Soc., Faraday Trans. 1*, **1978**, 74, 2913; S. Coluccia and A. J. Tench, *J. Chem. Soc., Faraday Trans. 1*, **1979**, 75, 1769; S. Coluccia and A. J. Tench, *Proc. 7th Int. Congr. Catal.* (Kodansha, Tokyo, 1981) 1154; S. Coluccia, A. Barton and A. J. Tench, *J. Chem. Soc., Faraday Trans. 1*, **1981**, 77, 2203; M. Anpo, Y. Yamada, S. Coluccia, A. Zecchina and M. Che, *J. Chem. Soc., Faraday Trans. 1*, **1989**, 85, 609.
- [5] M. Anpo, Y. Yamada, S. Coluccia, A. Zecchina and M. Che, *J. Chem. Soc., Faraday Trans. 1*, **1989**, 85, 609.
- [6] V. A. Shvets, A. V. Kuznetsov, V. A. Fenin and V. B. Kazansky, *J. Chem. Soc., Faraday Trans. 1*, **1985**, 81, 2913.
- [7] T. Tanaka, H. Yoshida, K. Nakatsuka, T. Funabiki and S. Yoshida, *J. Chem. Soc., Faraday Trans.*, **1992**, 88, 2297.
- [8] T. Murata, T. Matsukata, M. Mori, M. Obashi, S. Naoe, H. Terauchi, Y. Nishihata, O. Matsudo and J. Yamazaki, *J. de Phys.*, **1986**, C8, 135; T. Murata, T. Matsukawa, S. Naoe, T. Horigome, O. Matsudo and M. Watanabe, *Rev. Sci. Instrum.*, **1992**, 63, 1309.
- [9] F. P. J. M. Kerkhof and J. A. Moulijn, *J. Phys. Chem.*, **1979**, 83, 1612.

## 4.17 Dynamics of the Adsorption and Hydrogenation of CO on Active ZrO<sub>2</sub> Catalyst —*In Situ* Photoluminescence, FT-IR, and ESR Investigations—

Sang-Chul Moon, Hiromi Yamashita and Masakazu Anpo\*

Department of Applied Chemistry, University of Osaka Prefecture, Gakuen-Cho,  
Sakai, Osaka 593, Japan

### Abstract

The role of coordinatively unsaturated surface sites (CUS) onto the activation of CO adsorbed on the ZrO<sub>2</sub> catalyst was studied, the results indicating that the various types of adsorbed CO species involving polymeric radical anion species of CO were formed on the CUS of the ZrO<sub>2</sub> catalyst. It was also found that these CO adsorption species easily react with hydrogen to form CH<sub>4</sub> and CH<sub>3</sub>OH, showing the different reactivity with the kinds of CO adsorption species.

### 1. INTRODUCTION

Dynamic studies on the adsorption and the activation of CO and H<sub>2</sub> on catalyst surfaces are vital in gaining a comprehensive understanding of the hydrogenation reaction of CO. It is known that zirconium oxide is an active catalyst for CO hydrogenation with hydrogen to produce alcohol and isobutene. The reaction mechanism for the synthesis of alcohol and isobutene on the zirconium oxide has been studied by the Onishi and Ekerdt groups.<sup>1-4)</sup> On the other hand, we have recently reported that coordinatively unsaturated surface sites (CUS) are formed on the same ZrO<sub>2</sub> catalyst by evacuation at high temperatures.<sup>5,6)</sup> Furthermore, it is well known that such CUS play a significant role in the catalytic reactions on MgO powders.<sup>7)</sup>

However, the role of CUS in the activation of CO and H<sub>2</sub> on the ZrO<sub>2</sub> catalyst as well as details of the hydrogenation of CO on the catalyst has not yet been clarified. In the present work, we studied the role of CUS in the adsorption of CO and the activation of CO adsorption species by *in situ* photoluminescence (PL), FT-IR, UV-reflectance, and ESR measurements as well as an analysis of the reaction products.

### 2. EXPERIMENTAL METHODS

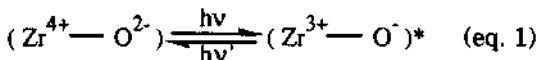
Zirconium oxide was prepared by the precipitation of a ZrO(NO<sub>3</sub>)<sub>2</sub> solution with NH<sub>4</sub>, as has been previously reported,<sup>5)</sup> and by the calcination of the precipitate in air at 773 K. Before recording the spectra and measuring the reactivity, the ZrO<sub>2</sub> catalyst was degassed for 1 - 9 h at the desired temperatures (from 300 to 1173 K). Photoluminescence (PL) and the ESR spectra were recorded at 77 and 298 K. The

FTIR and UV-reflectance spectra were measured at 298 K. Details of the experiment and procedure have already been described in previous papers.<sup>5,6)</sup>

### 3. RESULTS AND DISCUSSION

#### 3. 1. Identification of the CUS on the well-degassed ZrO<sub>2</sub> Catalyst and Adsorption of H<sub>2</sub>

Figure 1 shows the PL spectrum and UV-reflectance spectrum of the pretreated ZrO<sub>2</sub> catalyst. After the catalyst was evacuated, a new absorption band at around 33000 cm<sup>-1</sup>, which was different from that of the ZrO<sub>2</sub> bulk (band gap: 4.96 eV = 250 nm), appeared. This ZrO<sub>2</sub> catalyst exhibited the PL spectrum at around 420 - 550 nm when excited with a 280 - 330 nm light that was of a lower energy than the band gap of the ZrO<sub>2</sub> bulk (250 nm). The PL-excitation spectrum coincided with the UV-reflectance spectrum. It was also found that the PL spectrum was observed at a detectable intensity only when the sample was exhaustively degassed at temperatures higher than 600 K. The observed PL spectrum was efficiently and completely quenched by the addition of O<sub>2</sub> or air, indicating that PL is not a bulk but a surface phenomenon. These results suggest that the appearance of a new absorption band and the PL spectrum of the well-evacuated ZrO<sub>2</sub> catalyst may be attributed to the charge-transfer processes (in eq. 1) associated with coordinatively unsaturated surface sites (CUS) in a manner similar to those for MgO and SrO powders.<sup>8,9)</sup>



The effect of the addition of H<sub>2</sub> on the PL spectrum of the active ZrO<sub>2</sub> catalyst is shown in Fig. 2. The addition of H<sub>2</sub> leads to the efficient and irreversible quenching of the PL [Fig. 2- (b, c)], its extent depending on the pressure of the added H<sub>2</sub> and on the types of emitting moieties on the surface. From these distinctions, the PL spectrum is well deconvoluted into four different emitting moieties, i. e., sites A, B, C, D. Table 1 shows the characteristics of these four emitting sites on the active ZrO<sub>2</sub> catalyst.

Figure 3 shows the FT-IR spectrum recorded for the adsorption of H<sub>2</sub> on the sample that had been evacuated at 750 K. As has been described previously,<sup>5,6)</sup> the addition of H<sub>2</sub> onto the catalyst leads to the formation of different types of H<sub>2</sub> adsorption species, namely, (1) the homolytic dissociative adsorption species which are observed at around 1560 cm<sup>-1</sup>; (2) the heterolytic dissociative adsorption species at around 1562 and 3668 cm<sup>-1</sup>; and (3) the adsorption species which produce -OH groups are observed at around 3668 and 3782 cm<sup>-1</sup>. Of special interest is the determination of which emitting site among sites A, B, C, and D directly corresponds to one of the three adsorption species observed by FT-IR absorption. Our present results obtained on the ZrO<sub>2</sub> catalyst are shown in Table 1.

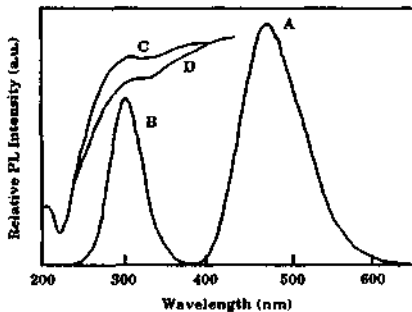
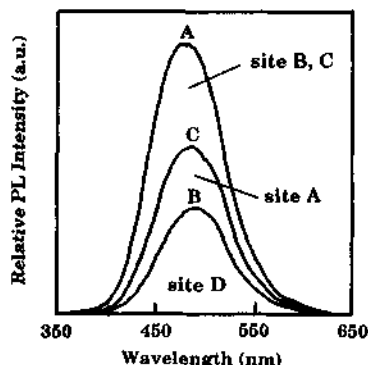
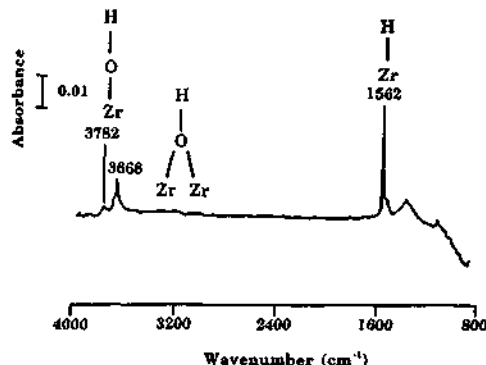


Fig. 1. PL spectra and diffuse reflectance spectra of the active ZrO<sub>2</sub> catalyst; A: PL spectrum after pretreatment at 973 K, B: excitation spectrum after pretreatment at 973 K, C: diffuse reflectance spectrum before pretreatment, D: diffuse reflectance spectrum after pretreatment at 973 K.



**Fig. 2.** PL spectrum of the active ZrO<sub>2</sub> and the effect of the addition of H<sub>2</sub> on the spectrum; A: PL spectrum of the active ZrO<sub>2</sub>, B: after the addition of H<sub>2</sub>, C: after the evacuation of H<sub>2</sub>.



**Fig. 3.** FT-IR spectrum of H<sub>2</sub> adsorbed on the active ZrO<sub>2</sub>.

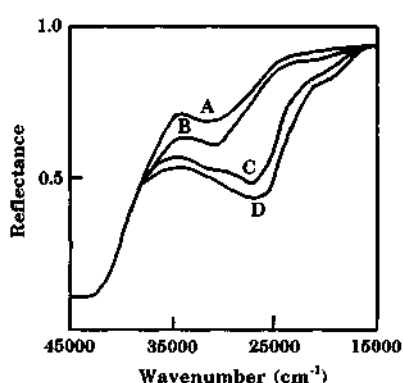
**Table 1.** Characterization of four emitting sites on the active ZrO<sub>2</sub> catalyst

	Site A	Site B	Site C	Site D
Excitation	310 nm	310 nm	300 nm	310 nm
Emission	490 nm	490 nm	460 nm	495 nm
Lifetime	$1.2 \times 10^{-3}$ s	$1.2 \times 10^{-3}$ s	$1.1 \times 10^{-2}$ s	$6.0 \times 10^{-5}$ s
Adsorption of H <sub>2</sub>	heterolytic reversible	homolytic irreversible	homolytic irreversible	no adsorption
	1562, 3668 cm <sup>-1</sup>	3668 cm <sup>-1</sup>	3782 cm <sup>-1</sup>	

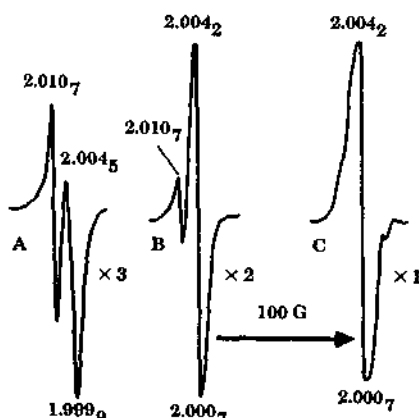
### 3. 2. Adsorption and Activation of CO on the Activated ZrO<sub>2</sub> Catalyst

Figure 4 shows the UV-reflectance spectra obtained after the addition of CO onto the ZrO<sub>2</sub> catalyst which had been evacuated at 1073 K. The three absorption bands at around 33000, 26000, and 20000 cm<sup>-1</sup> developed immediately upon the addition of CO onto the catalyst, and markedly increased in their intensities with the increase in contact time with CO. According to reports by Zecchina et. al.,<sup>10,11</sup> the addition of H<sub>2</sub> onto the well-evacuated MgO catalyst generated absorption bands attributed to the formation of oxocarbonates. The results which were obtained by UV-reflectance (Fig. 4) with the present ZrO<sub>2</sub> catalyst are similar to the results obtained by Zecchina et. al. On the basis of both findings, these absorption bands can be assigned to oxocarbonates, in other words, the absorption band of 33000 cm<sup>-1</sup> was attributed to (CO)<sub>2</sub>; 26000 and 20000 cm<sup>-1</sup> to polymeric CO species. The formation of C=C bonds attributed to polymeric CO species was also observed by FT-IR measurement.

Klabunde et. al., have reported that radical anionic species are formed on the well-degassed MgO by the addition of CO and these radical anionic species are assigned to oxocarbonates.<sup>12</sup> The ESR signals observed after the addition of CO onto the active ZrO<sub>2</sub> catalyst is shown in Fig. 5. The signal with g values of 2.0107



**Fig. 4.** UV-reflectance spectra of CO adsorbed on the active  $\text{ZrO}_2$  catalyst; A: spectrum of the active  $\text{ZrO}_2$  degassed at 973 K, B: just after the addition of CO onto the spectrum (A), C: 1 h after the addition of CO onto the spectrum (A), D: 24 h after the addition of CO onto the spectrum (A).



**Fig. 5.** ESR spectra of CO on the active  $\text{ZrO}_2$  catalyst degassed at 973 K; A: 5 h after the addition of CO on the active  $\text{ZrO}_2$  catalyst, B: 24 h after the addition of CO on the active  $\text{ZrO}_2$  catalyst, C: after the UV-irradiation of the previous spectrum (A) for 2 h ( $\lambda$ : 300 nm).

and 2.0042 appeared after the contact of CO with the  $\text{ZrO}_2$  catalyst for 24 h, and the signal increased gradually with the contact time. The maximum intensity of the signal was observed after 7 days of the contact of CO with the catalyst. Together with the data obtained by UV-reflectance measurements, the signal with *g* values of 2.0107 and 2.0042 were assigned to the  $(\text{CO})_2^{2-}$  species and the polymeric radical anion species of CO, respectively. It was also found that UV-irradiation of the catalyst in the presence of CO led to the selective formation of the polymeric radical anion species of CO. These results obtained by UV-reflectance, FT-IR, and ESR measurements on the CO adsorption species on the active  $\text{ZrO}_2$  catalyst clearly suggest that initially the  $(\text{CO})_2^{2-}$  species was produced and with increasing the contact time of CO with the catalyst, the polymeric radical anion species of CO were gradually formed on the CUS. The identification of these CO adsorption species on the  $\text{ZrO}_2$  catalyst is summarized in Table 2.

**Table 2.** Identification of the CO species adsorbed on the active  $\text{ZrO}_2$  catalyst

Contact time	Analysis	$(\text{CO})_2^{2-}$	polymeric CO species
Just	UV ( $\text{cm}^{-1}$ )	33000	
	FTIR ( $\text{cm}^{-1}$ )	1176, 1344	
	ESR (g-value)	2.0107	
24 h	UV ( $\text{cm}^{-1}$ )	33000	26000, 20000
	FTIR ( $\text{cm}^{-1}$ )	1176, 1344	1251, 1500
	ESR (g-value)	2.0107	2.0042
Irradiation onto Just	UV ( $\text{cm}^{-1}$ )		20000
	FTIR ( $\text{cm}^{-1}$ )		1251, 1500
	ESR (g-value)		2.0042

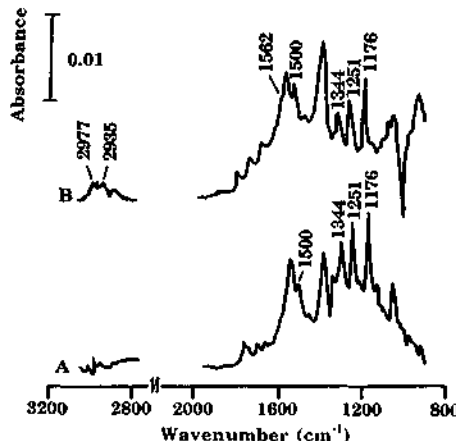


**Fig. 6.** FT-IR spectra of the active ZrO<sub>2</sub> catalyst having CO adsorption species and of the addition of H<sub>2</sub> onto the active ZrO<sub>2</sub> catalyst having CO adsorption species; A: 24 h after the addition of CO on the active ZrO<sub>2</sub> catalyst, B: after the addition of H<sub>2</sub> onto the spectrum (A).

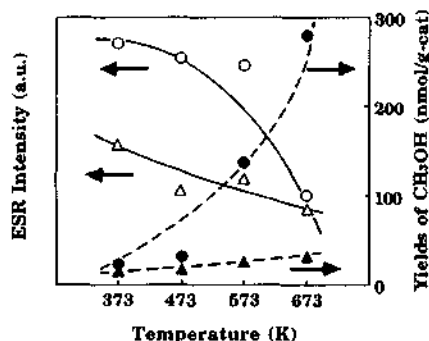


**Fig. 7.** The relationship between the intensity of ESR signal due to CO adsorption species and the yield of CH<sub>3</sub>OH in the reaction of H<sub>2</sub> with CO adsorption species on the ZrO<sub>2</sub> catalyst; △,▲: CO adsorption species formed after 24 h of the addition of CO on the active ZrO<sub>2</sub> catalyst, ○,●: CO adsorption species formed by UV-irradiation for the active ZrO<sub>2</sub> catalyst preadsorbed CO.

### 3. 3. Hydrogenation of CO Adsorption Species with H<sub>2</sub>

Figure 6 shows the FT-IR spectra recorded after the addition of H<sub>2</sub> onto the ZrO<sub>2</sub> catalyst having preadsorbed CO species. Spectrum A is obtained after a 24 h contact of CO with the active ZrO<sub>2</sub> catalyst. The absorption bands were observed at around 1251 and 1500 cm<sup>-1</sup> and these bands were attributed to the C=C and the C=O vibrations, respectively. Spectrum B is obtained after the addition of H<sub>2</sub> onto the ZrO<sub>2</sub> catalyst having preadsorbed CO species. As spectrum B shows, the intensity of the absorption bands at around 1251 and 1500 cm<sup>-1</sup> decreased, and simultaneously, bands at around 2977 and 2935 cm<sup>-1</sup>, attributed to the C-H vibration, were newly formed. ESR investigations have indicated that the same reactions occur by the addition of H<sub>2</sub> onto the ZrO<sub>2</sub> catalyst having preadsorbed CO species. In fact, CH<sub>4</sub> and CH<sub>3</sub>OH were observed as the major products in these systems. As mentioned above (Table 2), the concentration of the CO adsorption species varies with the contact time of CO with the catalyst, as well as with the pretreatment conditions on the sample.

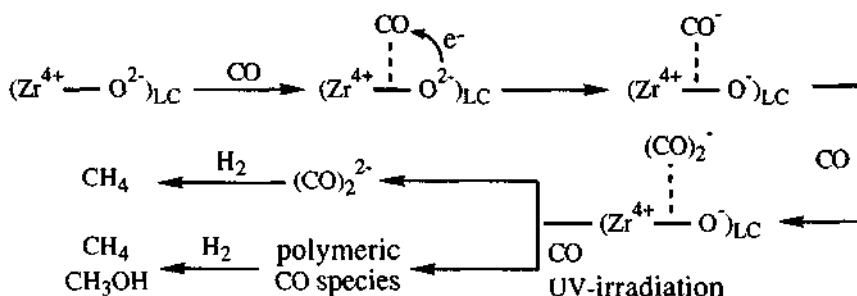
The reactivity of various CO adsorption species with H<sub>2</sub> has been investigated. Fig. 7 shows the relationship between the intensity of the ESR signal assigned to the CO adsorption species and the yield of CH<sub>3</sub>OH formation in the reaction of preadsorbed CO species with H<sub>2</sub> on the ZrO<sub>2</sub> catalyst. With increasing the reaction temperature, the yield of CH<sub>3</sub>OH formation gradually increased, accompanied by a decrease in the intensity of the ESR signal. The yield of CH<sub>3</sub>OH formation was greater in the system which had been irradiated by UV-light after the addition of CO onto the catalyst than for those which had been in contact with CO for 24 h. On the other hand, CH<sub>3</sub>OH was not observed in the system which had not involved the polymeric radical anion species of CO on the catalyst. These results clearly suggest that the reactivity of CO adsorption species with H<sub>2</sub> is different with the type of CO adsorption species, and that the formation of CH<sub>3</sub>OH is associated with the presence of the polymeric radical anion species of CO.

From these results, the following reaction mechanism (scheme I) is proposed for the hydrogenation of CO species adsorbed on the CUS of the ZrO<sub>2</sub> catalyst: CO molecules are adsorbed on the active surface sites, namely, CUS, and then an electron transfers from the oxygen which is constituted in the CUS to the CO molecule adsorbed on the site. The adsorbed CO species then reacts with CO molecules which is supplied from the gas phase to form the dimeric species, (CO)<sub>2</sub><sup>·</sup>. This dimeric species further reacts with the CO molecule in a step by step process to form the relatively stable polymeric radical anion species of CO. These CO species easily react with activated H<sub>2</sub> species which are also formed through the dissociative adsorption of H<sub>2</sub> on the CUS of the ZrO<sub>2</sub> catalyst, resulting in the formation of CH<sub>4</sub> and CH<sub>3</sub>OH as the major products in these systems. It is worth emphasizing that the formation of CH<sub>3</sub>OH is only observed by the addition of H<sub>2</sub> onto the ZrO<sub>2</sub> catalyst having the polymeric radical anion species of CO.

### 3. 4. Conclusions

Investigations of the surface active sites on the ZrO<sub>2</sub> catalyst and the adsorption and activation of CO and H<sub>2</sub> on the catalyst as well as the hydrogenation of the CO adsorption species with H<sub>2</sub> were carried out by in situ PL, FT-IR, and ESR techniques. It was found that the four different types of CUS were formed on the ZrO<sub>2</sub> catalyst by the evacuation of the sample at high temperatures. The number of these CUS on the ZrO<sub>2</sub> catalyst was about 100 pair/10<sup>5</sup> (Zr<sup>4+</sup>—O<sup>2-</sup>) pair sites. The adsorption of CO onto the CUS led to the formation of various types of CO adsorption species having different reactivities to hydrogen. These species also play a significant role in the hydrogenation of CO to form CH<sub>4</sub> and CH<sub>3</sub>OH on the ZrO<sub>2</sub> catalyst.

Scheme I



1. N. B. Jackson and J. G. Ekerdt, *J. Catal.*, **1986**, *101*, 90
2. R. G. Silver, C. J. Hou, and J. G. Ekerdt, *J. Catal.*, **1989**, *118*, 400
3. T. Onishi et al., *Bull. Chem. Soc. Jpn.*, **1988**, *61*, 667
4. T. Onishi et al., *Chem. Lett.*, **1984**, 747
5. M. Anpo et al., *Res. Chem. Intermedi.*, **1990**, *13*, 195
6. M. Anpo et al., *Shokubai*, **1990**, *32*, 376
7. M. Anpo, S. C. Moon, and K. Chiba, *Res. Chem. Intermedi.*, **1993**, *19*(6), 495
8. M. Anpo et al., *J. Chem. Soc., Faraday Trans. 1*, **1988**, *84*(3), 751
9. A. J. Tench et al., *J. Chem. Soc., Faraday Trans. 1*, **1978**, *74*, 2763
10. A. Zecchina et al., *J. Chem. Soc., Faraday Trans. 1*, **1975**, *71*, 1476
11. A. Zecchina et al., *J. Chem. Soc., Chem. Comm.*, **1974**, 582
12. J. Klabunde et al., *J. Am. Chem. Soc.*, **1983**, *105*(9), 2633

## 4.18 Photocatalytic Oxidation of Ethanol over Tantalum Oxide Supported on Silica

Tsunehiro Tanaka, Sakae Takenaka, Takuzo Funabiki and Satohiro Yoshida  
Department of Molecular Engineering, Kyoto University, Kyoto 606-01, Japan

### Abstract

Silica-supported tantalum oxide can catalyze the photooxidation of ethanol to form diethyl acetal selectively. Turnover number is more than 40 in the present system. In the dark, the reaction hardly takes place and the addition of pyridine suppress the reaction as well as the formation of diethyl acetal, showing that the photoactive sites are closely related to the acid site. The reaction with ethanol and ethanal to produce diethyl acetal showed that acetal formation is not a photoprocess but an acid-catalyzed process. It is concluded that on Ta=O site, ethanol is photo-oxidized to ethanal and subsequently acetal formation occurs on the same site.

### 1. INTRODUCTION

Photoenergy conversion using heterogeneous catalysts is of current interest. From the view of chemical synthesis, the reactions on photocatalysts are promising because photocatalytic reactions usually take place under mild conditions and the reaction can be controlled easily by light irradiation.

V-group metal oxides supported on silica like vanadium oxide [1] and niobium oxide [2] promote photoassisted oxidation of olefins to produce aldehydes and ketones selectively in a marked contrast to semiconductor photocatalysts like TiO<sub>2</sub>, on which olefins are photo-oxidized to result in total oxidation even at a low level of conversion [3]. Tantalum oxide, belonging to the same group as vanadium and niobium, is expected to have the capability of the photocatalytic and selective oxidations although only a few reports have been published so far [4,5]. We describe the photocatalysis by silica-supported tantalum oxide in the present paper. The photoactive sites of silica-supported niobium oxide and vanadium oxide have been concluded to be Nb=O and V=O bonds in surface species [1,2] and Ta=O bonds are presumably the active site for photooxidation by silica-supported tantalum oxide [6]. When metal oxide is highly dispersed on another oxide, generation of acid sites are well known and very often the dispersed metal ions are Lewis acid sites [7]. Silica-supported tantalum oxide may be this case that photoactive sites and Lewis acid sites are identical as pointed out in the case of silica-supported vanadium oxide [8]. If the reaction product is affected by acid sites easily, the photocatalytic reaction is accompanied by acid-induced reaction. In the present paper, we report that silica-supported tantalum oxide (Ta<sub>2</sub>O<sub>5</sub>/SiO<sub>2</sub>) promotes photocatalytic oxidation of ethanol accompanied by acid-catalyzed reaction.

oxidation of ethanol accompanied by acid-catalyzed reaction.

## 2. EXPERIMENTAL

The catalyst samples  $Ta_2O_5/SiO_2$  were prepared by impregnation of silica [9] with an aqueous solution of tantalum oxalate, followed by calcination in a dried air stream for 5 h. Prior to the reactions, the catalysts were evacuated for 1 h at 673 K and treated with 60 Torr of oxygen at 673 K for 2 h. Ethanol ( $1\text{ cm}^3$ ) and the catalyst (0.2 g) were put in a quartz test tube of 16 mm diameter filled with atmospheric oxygen. The reaction was carried out with stirring the reaction liquid to suspend the catalysts. A 500 W super high pressure Hg lamp was used as a light source. The products were analyzed by *g. l. c.*

Table 1 Photoassisted reaction of ethanol under atmospheric  $O_2$  over  $Ta_2O_5/SiO_2$ <sup>a)</sup>

Entry	$Ta_2O_5$ loading / wt% <sup>b)</sup>	UV irradiation	Temp. / K	Conv. / % <sup>c)</sup>	Selectivity <sup>d)</sup> / mol%		
					$CH_3CHO$	$CH_3CH(OC_2H_5)_2$	$CH_3CO_2H$
1	100	UV	320	0.3	64.1	23.5	12.5
2	1	UV	320	2.0	2.7	91.1	6.2
3	5	UV	320	3.6	1.2	96.5	2.3
4	10	UV	320	6.6	2.2	93.4	4.4
5	15	UV	320	6.9	2.2	94.4	3.9
6	20	UV	320	5.0	1.7	94.4	3.5
7	5	Filter <sup>e)</sup>	320	tr	-	-	-
8	5	Dark	343	0.0	-	-	-
9 <sup>f)</sup>	15	UV	320	0.5	tr	100	tr
10 <sup>g)</sup>	5	UV	320	1.3	31.1	52.8	16.2
11 <sup>h)</sup>	5	UV	320	1.0	45.6	35.9	18.5

a)Catalyst 0.2 g ; neat ethanol  $1\text{ cm}^3$  ; reaction time 7 h. b) Weight % as  $Ta_2O_5$ . c)Based on ethanol. d)Products selectivity based on converted ethanol. Trace of ethene was found in gas phase for entries 2-6 e)UV-irradiated through a glass filter permitting the light of wavelength  $\lambda > 320$  nm. f)Without  $O_2$ . g)  $17.3\text{ }\mu\text{mol}$  of pyridine was added. h) $52.2\text{ }\mu\text{mol}$  of pyridine was added.

## 3. RESULTS AND DISCUSSION

### 3.1. PHOTO-ASSISTED REACTION AND ACTIVE SPECIES

Table 1 lists the product distribution after 7 h reaction. Ethene of less than  $1\text{ }\mu\text{mol}$  was detected in gas phase for each run. The formation of diethyl ether was not observed for any runs. The results show that dehydration of ethanol proceeds quite slow. Tantalum oxide of a single phase is almost inactive referring the result of entry 1. On the other hand, in the case of silica-supported tantalum oxide (entries 2-6), diethylacetal (1,1-diethoxyethane) was produced with a quite high selectivity accompanied by the formation of ethanal and acetic acid.

Reaction hardly takes place under irradiation by UV light of wavelength  $\lambda > 320$  nm (entry 7), in the dark (entry 8) and in the absence of oxygen (entry 9). In particular, in the absence of oxygen, the catalyst is almost inactive although slight evolution of hydrogen was found in gas phase, indicating that dehydrogenation occurs in some extent on irradiated catalyst. These results clearly show that UV-irradiation of the silica-supported

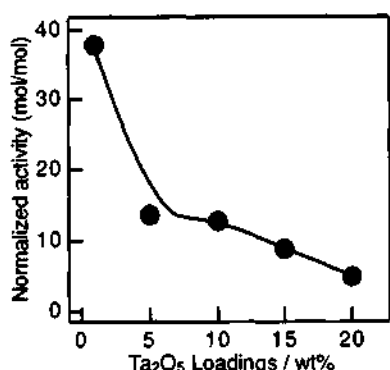


Fig. 1 Normalized activity of the photooxidation of ethanol to the number of loaded Ta ions.

niobium oxides [1,2]. When loading amount of such metal oxides becomes larger, polymetalates form to result in sluggish reaction rates. For the present catalyst system, this must be also the case. This reasoning is supported by the activity normalized to the number of Ta ions as shown in Fig. 1. The normalized activity, which would correspond to turnover number if all of Ta ions participated in the reaction, is the highest at 1 wt% of loading. We conclude that active species in the reaction is the highly dispersed tantalate.

### 3.2. REACTION PATHS

To examine the reaction path, we investigated the time course of the reaction. Fig. 2 (a) and (b) show time courses of ethanol conversion and product selectivities, respectively. Catalyst (0.5 g) was suspended in 4 cm<sup>3</sup> of ethanol and irradiated. Small portion of the reaction solution (less than 0.05 ml) was filtered and analyzed by *g. l. c.* The reaction proceeds almost linearly and no induction period was observed. Diethyl acetal

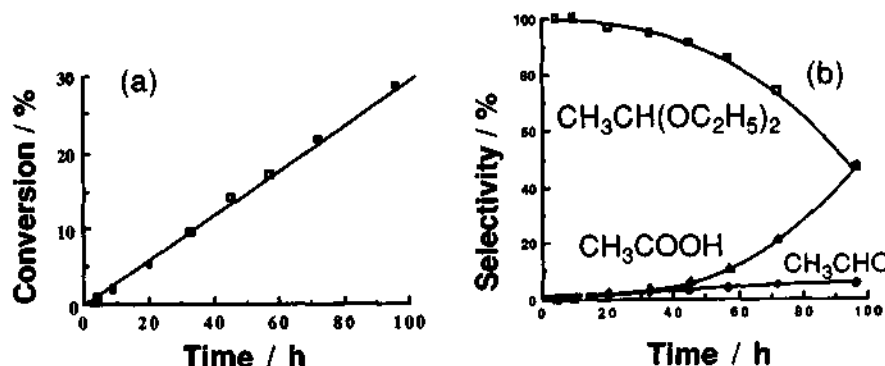


Fig. 2 Time course of the reaction. a) conversion, b) selectivities to the products. Catalyst, 500 mg; Ethanol, 4 cm<sup>3</sup>; light source, 250 W super high pressure lamp.

tantalum oxide with the light of wavelength  $\lambda < 320$  nm promotes the oxidation of ethanol to produce diethylacetal. As found in Table 1, entries 2-6, the conversion increases with an increase in loading amount to a maximum at 15 wt% and then falls at higher loadings. At 20 wt% of loading, tantalum ions should be aggregated to form polytantalate and bulk tantalum oxide on the surface, which is almost inactive for the reaction. Provided that tantalum ions are dispersed atomically, loadings of Ta ions in all the supported samples are much less than that of full coverage of silica. However, the conversion does not increase linearly, suggesting that Ta ions are supported inhomogeneously. We have drawn a conclusion that surface monatomic metal oxides are the most active species in alkene photo-oxidation in the case of vanadium and

Table 2 Reactions of ethanolic solution of ethanal over 15 wt% Ta<sub>2</sub>O<sub>5</sub>/SiO<sub>2</sub>.<sup>a)</sup>

Entry	condition	Conversion <sup>b)</sup>	CH <sub>3</sub> CH(OC <sub>2</sub> H <sub>5</sub> ) <sub>2</sub>	Selectivity / %
			CH <sub>3</sub> COOH	
1	UV	75.4	99.9	tr.
2	dark	72.8	99.9	tr.
3	dark, pyridine <sup>c)</sup>	0.1	100	0.0

a) Catalyst 0.2 g, ethanolic solution (14.7 mol% CH<sub>3</sub>CHO) 1.2 g, reaction time 1 h, reaction temperature 310 K. b) Based on CH<sub>3</sub>CHO. c) pyridine 263 μmol.

was selectively formed at the initial stage, showing that diethyl acetal is a primary product or the step of the formation of diethyl acetal is very fast. After 40 h, a decrease in selectivity to diethylacetal is found corresponding to an increase in selectivity to acetic acid while formation rate of ethanol is constant. This is an indication that acetic acid formation as the last step of oxidation is closely related to decomposition of diethylacetal.

As for the reaction to form diethylacetal, the following path is very likely.

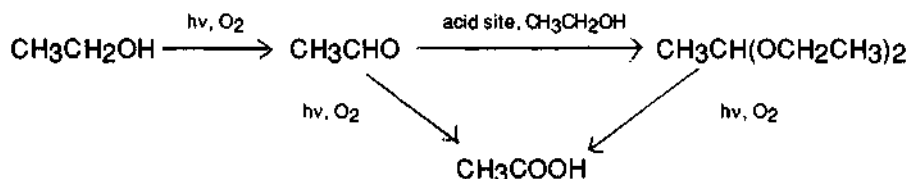


To find out which step involves the photoactivation, we have carried out the reaction between ethanol and ethanal. Catalyst samples were suspended in the ethanolic solution including 9 mol% ethanol under atmospheric oxygen. The results are given in Table 2. After 1 h reaction, ca. 75 % of ethanol is converted to diethylacetal even in the dark. UV-irradiation does not have any effect upon step 2. This strongly suggests that step 2 does not require UV-irradiation but the oxidative dehydrogenation of ethanol (step 1) is a photoprocess. This is acceptable taking into account that silica-supported vanadium oxide can catalyze photo-oxidative dehydrogenation of alcohols to form corresponding ketones and aldehydes.

It is well known that dispersion of metal cations on inorganic carrier causes the generation of acid sites [4]. Tantalum ions are naturally thought to be Lewis acid sites [10-14]. Simultaneously, as well as the case of V<sub>2</sub>O<sub>5</sub>/SiO<sub>2</sub> [5,15], Ta=O bonds are thought to be active sites for photooxidation. The formation of ethene, a product resulting from dehydration (Table 1, entry 2-6), should be noted. Dehydration is promoted ordinarily on the acid sites. Therefore, the result may suggest that acid sites also participate in the reaction or induce parallel reactions. The thermal desorption profiles of pyridine from the catalyst sample have shown that acid sites are present on the catalyst sample although its strength is not high. To examine the role of acid sites, the reaction was carried out in the presence of pyridine. The color of the catalyst changed from white to yellow by immersing them into a pyridine-ethanol solution due to the adsorption of pyridine molecules on Ta ions. In Table 1, the results are given in entries 10 and 11. The activity was reduced and also the products distribution significantly changed in comparison with the reactions without pyridine. Ethene formation was much suppressed. This presumably results from

poisoning both acid sites and photoactive sites. By increasing the amount of pyridine, the selectivity to diethylacetal decreased much more. These results strongly appeal that the formation of diethylacetal, step 2, is promoted on the acid sites on the catalyst surface. Actually, when pyridine is added to the ethanolic solution of 9 mol% ethanal and the solution mixture is stirred, diethylacetal is seldom formed as shown in entry 3 of Table 2. Now, we can conclude that the first step of the reaction is photooxidation of ethanol to form ethanal taking place on  $Ta=O$  sites and subsequently the formation of diethyl acetal occurs on the same site. Consecutive oxidation to form acetic acid is closely related to the decomposition of diethylacetal.

We summarize the reaction scheme as follows:



Scheme 1

Since the site for photoassisted formation of  $\text{CH}_3\text{CHO}$  or its precursor is identical with the acid site, the subsequent formation of diethylacetal is faster than desorption of  $\text{CH}_3\text{CHO}$ .

Suggestion that acid sites may play a role in heterogeneous photocatalysis has been already postulated by Djeghri and Teichner [16], Pichat *et al.* [17] and us [5], in which acid-catalyzed reactions always take place accompanied by photoreactions and the role of acid sites can not be discussed apart from photo-induced reaction. The present paper reports the different type of the reaction, in which the role of acid sites is definitely analyzed apart from the photoreaction.

#### 4. REFERENCES

1. S. Yoshida, Y. Nishimura, T. Tanaka and T. Funabiki, *Catal. Today*, **1990**, *8*, 67; T. Tanaka, H. Nojima, H. Yoshida, H. Nakagawa, T. Funabiki and S. Yoshida, *Catal. Today*, **1993**, *16*, 297.
2. S. Yoshida, T. Tanaka, M. Okada and T. Funabiki, *J. Chem. Soc., Faraday Trans. 1*, **1984**, *80*, 119; T. Tanaka, M. Ooe, T. Funabiki and S. Yoshida, *J. Chem. Soc., Faraday Trans. 1*, **1986**, *82*, 35; T. Tanaka, Y. Nishimura, S. Kawasaki, T. Funabiki and S. Yoshida, *J. Chem. Soc., Chem. Commun.*, **1987**, 506.
3. P. Pichat, J.-M. Herrman, J. Disdier and M.-N. Mozzanega, *J. Phys. Chem.*, **1979**, *83*, 3122.
4. D. L. Nguyen, P. C. Roberge and S. Kalliaguine, *Canad. J. Chem. Eng.*, **1979**, *57*, 288.
5. S. Kalliaguine, M. Gnakoury and P. C. Roberge, *iCanad. J. Chem. Eng.*, **1981**, *59*, 710.
6. T. Tanaka, H. Nojima, T. Funabiki and S. Yoshida, unpublished.
7. K. Tanabe, M. Misono, Y. Ono and H. Hattori, *New Solid Acids and Bases*, Kodansha, Tokyo and Elsevier, Amsterdam Oxford New York Tokyo, 1989.

8. T. Tanaka, Y.Nishimura, S.Kawasaki, M.Ooe, T. Funabiki and S.Yoshida, *J. Catal.*, **1989**, 118, 327.
9. S. Yoshida, T. Matsuzaki, T. Kashiwazaki, K. Mori and K. Tarama, *Bull. Chem. Soc. Jpn.*, **1974**, 47, 1564.
10. S.Yoshida, T.Hanada, T.Hiraiwa, T.Tanaka, H. Kanai and T. Funabiki, *Catal. Lett.*, **1992**, 12, 277.
11. M. Nishimura, K. Asakura and Y. Iwasawa, *J. Chem. Soc., Chem. Commun.*, **1991**, 112.
12. J.-M. Jehng and I. E. Wachs, *Catal. Today*, **1993**, 16, 471.
13. S. Yoshida and H. Kawakami, in *Acid-Base Catalysis*, ed. by K. Tanabe, H. Hattori, T. Yamaguchi, and T. Tanaka, p. 123, Kodansha, Tokyo and VCH, Weinheim New York, 1989.
14. K. Tanabe, *Solid Acids and Bases*, Kodansha, Tokyo and Academic Press, New York London, 1970.
15. H.Kobayashi, M.Yamaguchi, T. Tanaka, Y.Nishimura, H. Kawakami and S. Yoshida, *J. Phys. Chem.*, **1988**, 92, 2516.
16. N. Djeghri and S. J. Teichner, *J. Catal.*, **1980**, 62, 99 (1980).
17. P.Pichat., M.-N.Mozzanega and H. Courbon, *J. Chem. Soc., Faraday Trans. 1.*, **1987**, 83, 697.

## 4.19 The Relationship between the Absolute Acidities of Monoatomic Cations and their Catalytic Activities in a Few Heterogeneous Systems

R.Notoya<sup>a</sup> and A.Matsuda<sup>b</sup>

<sup>a</sup>Catalysis Research Center, Hokkaido University, Sapporo 060 Japan

<sup>b</sup>Late Emeritus Professor, Hokkaido University, Sapporo 060 Japan

### Abstract

The absolute acidity  $\epsilon_i$  of a monoatomic cation  $i$  which had been expressed numerically in terms of the ionization energy of  $I_i$  of cation  $i$  on the basis of the empirical rules for solvation of monoatomic ions, was found to give a measure of the catalytic activity for many catalysis systems in both cases of acid and base catalysts. The present paper is concerned with the elucidation of the selectivity of catalyst in terms of this acidity in a few cases of heterogeneous systems.

### 1. Introduction

Since the absolute acidity  $\epsilon_i$  of a monoatomic cation  $i$  was determined on the basis of the electron donor-acceptor concept for solvation[1],  $\epsilon_i$  proved to be a measure of catalytic activity of various catalysis[2-3]. It was revealed that catalytic reactions were divided into two groups, one of which was accelerated with increasing  $\epsilon_i$  and on the contrary the other, retarded with increasing  $\epsilon_i$ . In both groups, the relationships between  $\epsilon_i$  and the catalytic activity in the cases of the homogeneous catalysis, catalysis of metallo-porphyrines and zeolites showed more quantitative than that in the case of heterogeneous one.

The present paper aims for revealing such relationships as described above concerning not overall reaction but elementary acts or partially grouped elementary steps even in a few cases of heterogeneous catalysis[4-5]. We shall start by the basic concept for

the evaluation of the absolute acidity  $\varepsilon_i$  of cation i.

## 2. The Empirical Rules for Solvation of Monoatomic Cation

Two empirical rules were found to be present for the relationships, between chemical free energy  $\Delta G^{\circ}_{i,g\leftarrow s}$  of solvation of ion i for solvent s and that  $\Delta G^{\circ}_{i,g\leftarrow w}$  for water w, and between chemical free energy  $\Delta G^{\circ}_{i,g\leftarrow s}$  of solvation of ion i for solvent s and the total ionization energy for ion i  $I_i$ , i.e.:

$$\text{the rule I; } \Delta G^{\circ}_{i,g\leftarrow w} = \beta \Delta G^{\circ}_{i,g\leftarrow s} \quad (1)$$

$$\text{and the rule II; } \Delta G^{\circ}_{i,g\leftarrow s} = \rho_s^a \cdot \varepsilon_i. \quad (2)$$

where  $\beta$  equal to the ration  $\rho_s^a/\rho_w^a$  and  $\rho_s^a$  denote the proportional constant and the absolute basicity of solvent s. All monoatomic cations on the periodic table are divided by the electronic configuration of ion i into three groups which are characterized by the electronic configuration of ion i, i.e. a-, b- and c-groups' ions which configurations can be specified by the rare gas type X,  $X+d^310$  and  $X+5d^{10}$ , respectively. Each  $\varepsilon_i$  is given by the total ionization energy  $I_i$  and the valence  $z_i$  of ion i, as follows:

$$\text{for a-group's ion; } \varepsilon_i = I_i/z_i, \text{ eV} \quad (3a)$$

$$\text{for b-group's ion; } \varepsilon_i = 0.936[(I_i/z_i) - 0.94], \text{ eV} \quad (3b)$$

$$\text{and for c-group's ion; } \varepsilon_i = 0.862[(I_i/z_i) - 1.43], \text{ eV.} \quad (3c)$$

## 3. The Selectivities of Some Metal Pyrophosphates for Oxidation of Iso-butane

The oxidation of iso-butane was studied by use of various metal pyrophosphates[4]. As the products of this reaction, iso-butene ('C<sub>4</sub>), propylene('C<sub>3</sub>), CO and CO<sub>2</sub>(CO<sub>x</sub>) were observed. The relations between the selectivities for the formations of 'C<sub>4</sub>+ 'C<sub>3</sub> and for that of CO+CO<sub>2</sub>, and  $\varepsilon_i$  are shown in Figure 1. It is found that the oxidation reaction of iso-butane is including the two types of catalytic reactions, one of which is accelerated with increasing  $\varepsilon_i$  ('C<sub>4</sub> and 'C<sub>3</sub> formation) and another is retarded with increasing  $\varepsilon_i$  (CO<sub>x</sub> formation). The correlation coefficients of these linear relations were found to be 0.985 for the former reaction and 0.981

for the latter, respectively, if the valencies of copper and chromium ions were assumed to be +1 and +2. Such assumption may be reasonable because some kinds of cations often can be reduced in the conditions of lack of oxygen and excess of hydrocarbon.

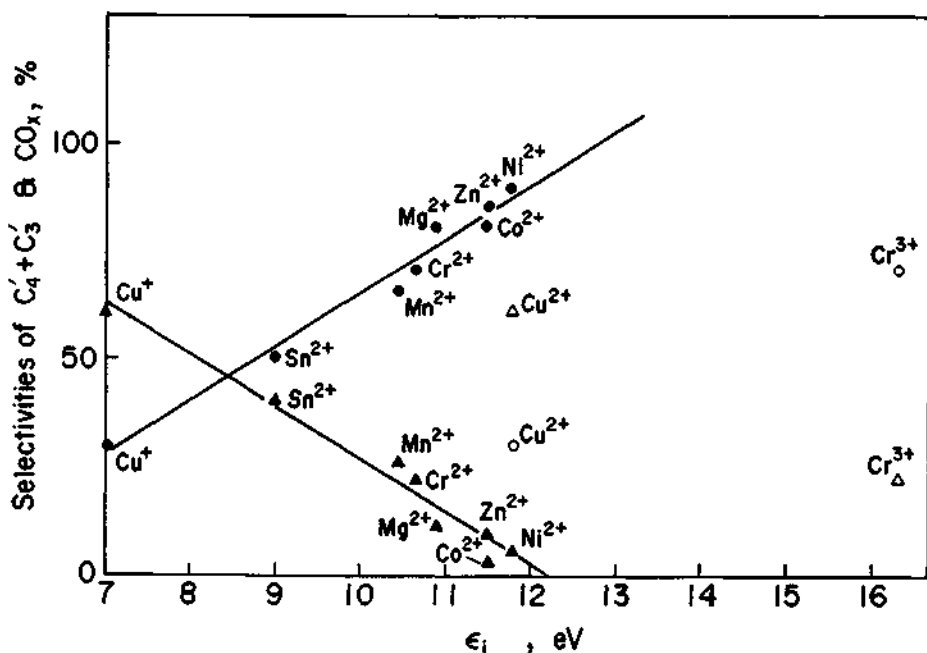


Fig.1 Relations between selectivities and the absolute acidity  $\epsilon_i$  of cation  $i$  of catalyst, for formations of ' $C_4' + C_3'$ (●) and of  $CO_x$  (▲) in iso-buthane oxidation on metal-pyrophosphates; (○) and (△) if  $Cr^{3+}$  and  $Cu^{2+}$  remain to be not reduced.

#### 4. The Effect of Component in Mixed Metallo-Cation Catalyst on Oxygen Coverage of Cu Surface in Methanol Synthesis

Methanol synthesis from  $CO_2$  and  $H_2$  was investigated on the mixed catalysts of  $Cu$ ,  $ZnO$  and  $Al_2O_3$ , or  $Cu$ ,  $ZnO$  and  $Ga_2O_3$  with the variety of the component ratio[5]. The absolute acidity  $\Sigma \epsilon_i$  of a mixed cation catalyst was given by the mean value of  $\epsilon_i$  taking account of the molar ratios and the valencies of the component cations. The relation between oxygen coverage of Cu surface on the various catalysts and  $\Sigma \epsilon_i$  is shown in Figure 2. The correlation coefficient of this line was found to be 0.979.

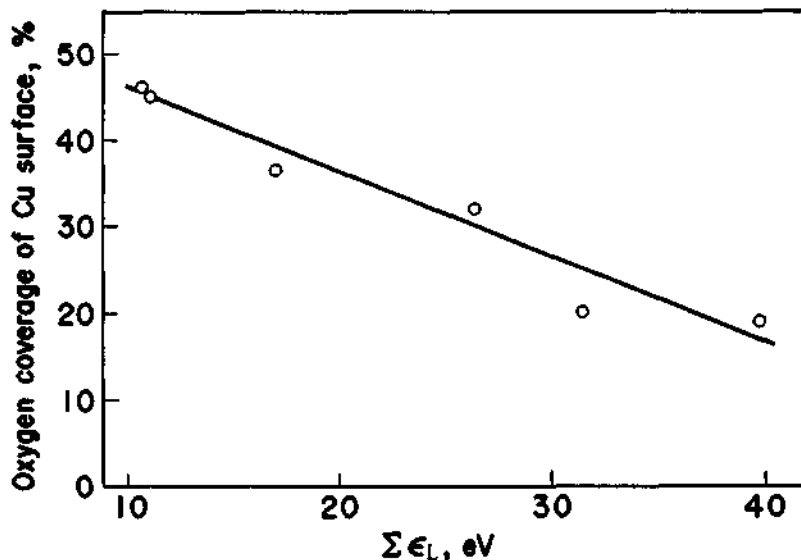


Fig.2 Relation between oxygen coverage of Cu surface and mean value of the absolute acidities  $\Sigma \epsilon_i$  of cations of oxides, on mixed oxide catalysts(Cu-ZnO-Al<sub>2</sub>O<sub>3</sub> and Cu-ZnO-Ga<sub>2</sub>O<sub>3</sub>) in methanol synthesis.

The slope of the line is understandable by reason that a catalyst having larger  $\Sigma \epsilon_i$  can induce a negatively charged particle more strongly from Cu to himself.

#### Conclusion

It is proved that catalysis actions in considerably complicated systems as like as heterogeneous one can be clarified by means of the absolute acidity as the measure of the catalytic activity.

- [1] R.Notoya and A.Matsuda, J.Phys.Chem., 1985, 89, 3922.
- [2] R.Notoya and A.Matsuda, Fundamental Problems of Interface Structure and Electrochemical Kinetics, Ed. A.Matsuda, S.Haruyama and R.Notoya, Hokkaido University Press, 1988, p.41.
- [3] R.Notoya and A.Matsuda, Acid-Base Catalysis, Ed. K.Tanabe, H.Hattori, T.Yamaguchi and T.Tanaka, Kodansha Ltd., 1989, p.505.
- [4] Y.Takita, K.Kurosaki, S.Ichimaru, Y.Mizuhara and T.Ishihara, 71th CATSJ Meeting Abstracts:NolA2, Shokubai(Catalyst), 1993, 35, 62.
- [5] T.Fujiya, M.Saito, Y.Kanai, M.Takeuchi, K.Moriya and T.Watanabe, 71th CATSJ Meeting Abstracts:No2A2, Shokubai(Catalyst), 1993, 35, 92.

## 4.20 The Role of Support in Methane Reforming with CO<sub>2</sub> over Rhodium Catalysts

Junji NAKAMURA, Keita AIKAWA, Koichi SATO, and Toshio UCHIJIMA  
Institute of Materials Science, University of Tsukuba, Tsukuba, Ibaraki 305, Japan

### Abstract

The catalytic activity of Rh/SiO<sub>2</sub> for reforming of CH<sub>4</sub> with CO<sub>2</sub> was promoted by mixing physically with Al<sub>2</sub>O<sub>3</sub>, MgO, TiO<sub>2</sub>, K/SiO<sub>2</sub>. The order in PCO<sub>2</sub> and PCH<sub>4</sub> for CH<sub>4</sub> + CO<sub>2</sub> reaction over Rh/SiO<sub>2</sub> were unity and - 0.6, respectively, indicating that CO<sub>2</sub> dissociation was the rate-limiting step which was promoted by the mixing of metal oxides. In-situ FT-IR studies showed that dominant species formed by exposing Rh/SiO<sub>2</sub> + Al<sub>2</sub>O<sub>3</sub> to CO<sub>2</sub> + H<sub>2</sub> was formate at high temperatures above 400 K. The promotion in the activity of Rh/SiO<sub>2</sub> by mixing with the metal oxides is ascribed to the rise of CO<sub>2</sub> concentration in the vicinity of Rh particles, where CO<sub>2</sub> is trapped as carbonate and/or formate on the surface of the metal oxides. The basic property of metal oxide surface may be responsible for the activity of CO<sub>2</sub> dissociation.

### 1. INTRODUCTION

Methane can be converted to synthesis gas by reactions with H<sub>2</sub>O (CH<sub>4</sub> + H<sub>2</sub>O → CO + 3H<sub>2</sub>) and CO<sub>2</sub> [1-8] (CH<sub>4</sub> + CO<sub>2</sub> → 2CO + 2H<sub>2</sub>) using VIII group metal catalysts. Although the former, steam reforming, is an established process, the latter is relatively new process as an alternative route to synthesis gas. The industrial interest on the CH<sub>4</sub> + CO<sub>2</sub> reaction is related to the CO/H<sub>2</sub> ratio of unity which is less than that obtained by steam reforming of CH<sub>4</sub>. Most of the group VIII metals except Os are known to catalyze more or less CH<sub>4</sub> + CO<sub>2</sub> reaction. The serious problem is deactivation of catalyst by carbon deposition on the surface of catalyst. Rh is a superior component in respect of the high activity and the coking-free nature. The combination of metal and support significantly influence the catalytic activity as well as the extent of carbon deposition. In this paper, we report the role of metal oxides in CH<sub>4</sub> + CO<sub>2</sub> reaction over Rh catalysts.

### 2. EXPERIMENTAL

The supports used here were Al<sub>2</sub>O<sub>3</sub> (JRC - ALO4), SiO<sub>2</sub> (JRC - SIO7), and TiO<sub>2</sub> (JRC - TiO4) supplied by the Catalyst Society of Japan and MgO manufactured by Wako pure chemical industries, LTD, and calcined at 1073 - 1173 K before preparation of catalysts. The supported catalysts with 0.5 wt% loading of Rh were prepared by an impregnation method using rhodium chlorides. The catalysts were dried at 383 K for c.a. 2 hr, calcined at 723 K for 3 hr in air. Prior to the reaction, the catalysts were reduced with H<sub>2</sub> at 773 K for 1 hr in a flow reactor. The reforming of CH<sub>4</sub> with CO<sub>2</sub> was conducted using mixtures of CH<sub>4</sub> : CO<sub>2</sub> : N<sub>2</sub> = 3.4 : 3.4 : 93.2 at total flow rates of 50

ml / min. The total pressure is 1 atm. Reaction products were analyzed by an on-line gas chromatograph. Dispersion of Rh was determined by static measurement of H<sub>2</sub> chemisorption. In situ FT-IR measurement was made using a JEOL JIR 6000 connected to a flow reactor. Measurements of TPD (thermal programmed desorption) were done using an apparatus manufactured by Bell Japan.

### 3. RESULTS AND DISCUSSION

The results of CH<sub>4</sub> + CO<sub>2</sub> reaction at 893 K for Rh/Al<sub>2</sub>O<sub>3</sub>, Rh/SiO<sub>2</sub>, and Rh/TiO<sub>2</sub> catalysts and the dispersions of Rh are summarized in Table 1. The conversion of CH<sub>4</sub> and CO<sub>2</sub> and the reaction rate on the basis of the unit 10<sup>-4</sup> mol / sec g clearly indicated a significant effect of support on the catalytic activity where its order of supports was Al<sub>2</sub>O<sub>3</sub>>TiO<sub>2</sub>>SiO<sub>2</sub> and Rh/Al<sub>2</sub>O<sub>3</sub> was 18 times more active than Rh/SiO<sub>2</sub> at 893 K. The activities were also compared by turnover frequency (TOF) considering the dispersion of Rh particle, and the order of activity was found to be TiO<sub>2</sub> > Al<sub>2</sub>O<sub>3</sub> > SiO<sub>2</sub>, where Rh/TiO<sub>2</sub> was 6 times more active than Rh/SiO<sub>2</sub> at 893 K. The significant effect of support was also observed for Pd catalyst where Pd/Al<sub>2</sub>O<sub>3</sub> was above 100 times more active than Pd/SiO<sub>2</sub> for methane reforming with CO<sub>2</sub>. The dispersion of Rh and Pd could not account for the marked effect of supports on the activity.

Table 1 Catalytic activity at 893 K and dispersion of Rh

	Dispersion	Conversion		Yield			Reaction rate	
		CH <sub>4</sub> (%)	CO <sub>2</sub> (%)	H <sub>2</sub> (%)	CO (%)	H <sub>2</sub> /CO ratio	10 <sup>-4</sup> mol / sec g	TOF /sec site
Rh/Al <sub>2</sub> O <sub>3</sub>	0.514	83.8	85.7	66.2	78.3	0.85	632	25.5
Rh/TiO <sub>2</sub>	0.068	88.7	88.2	80.7	82.4	0.98	123	37.5
Rh/SiO <sub>2</sub>	0.121	5.8	5.1	4.4	5.4	0.81	35.7	6.1

The catalytic activity of Rh/SiO<sub>2</sub> was also enhanced by mixing physically with various metal oxides. Fig. 1 shows conversions of CH<sub>4</sub> as a function of the amount of Al<sub>2</sub>O<sub>3</sub>, TiO<sub>2</sub>, MgO, K/SiO<sub>2</sub> mixed with Rh/SiO<sub>2</sub>. It is clear that these metal oxides promote the catalytic activity of Rh/SiO<sub>2</sub> significantly. No activity of Al<sub>2</sub>O<sub>3</sub> alone was observed for methane reforming with CO<sub>2</sub>. This indicates that the metal oxides directly activate either CO<sub>2</sub> or CH<sub>4</sub>.

To clarify which molecule, CH<sub>4</sub> or CO<sub>2</sub>, is activated by the mixing of metal oxides, dependences of reaction rate on CO<sub>2</sub> and CH<sub>4</sub> pressure were measured on Rh/SiO<sub>2</sub> as shown in Fig.2 and 3, respectively, where the constant pressure was 26 Torr. The order in PCO<sub>2</sub> and PCH<sub>4</sub> for methane reforming with CO<sub>2</sub> over Rh/SiO<sub>2</sub> were unity and -0.6. Taking into account the fact that dissociation of CO<sub>2</sub> on the surface of Rh is known to be slower than dissociation of CH<sub>4</sub> [9,10], the rate determining step for CH<sub>4</sub> + CO<sub>2</sub> reaction over Rh/SiO<sub>2</sub> can be attributed to dissociation of CO<sub>2</sub> on Rh surface. It is therefore concluded that the role of the metal oxides in the promotion of activity for CH<sub>4</sub> + CO<sub>2</sub> reaction is due to the acceleration of CO<sub>2</sub> dissociation.

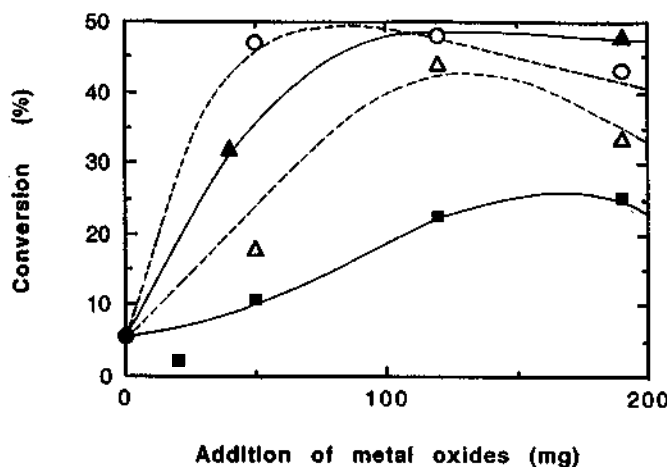


Fig.1 Effect of metal oxides mixed with Rh/SiO<sub>2</sub> on the conversion of CH<sub>4</sub>. Reaction temperature is 893 K. Rh/SiO<sub>2</sub> (10 mg) + metal oxide (x mg) + SiO<sub>2</sub> (190 - x mg). Total amount of the mixtures is 200 mg. (○) Al<sub>2</sub>O<sub>3</sub>, (Δ) TiO<sub>2</sub>, (□) MgO, (▲) K/SiO<sub>2</sub>, (●) none.

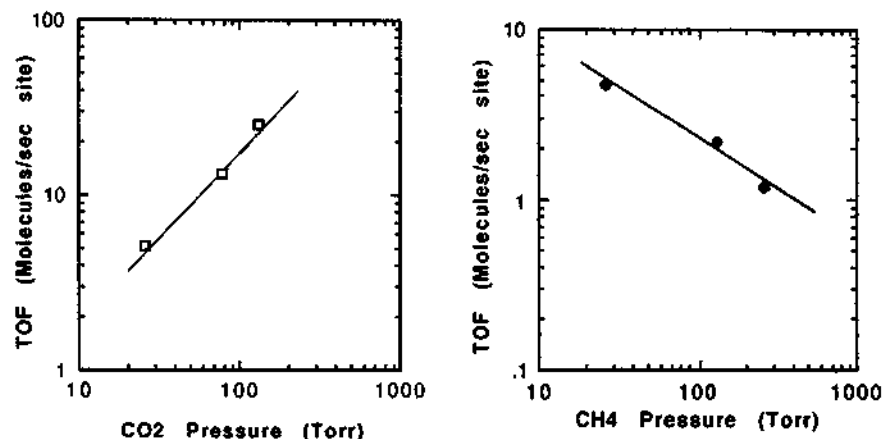


Fig.2 Dependence of TOF for CH<sub>4</sub> conversion on the partial pressure of CO<sub>2</sub> in the CH<sub>4</sub> + CO<sub>2</sub> reaction over Rh/SiO<sub>2</sub> at 963 K. The pressure of CH<sub>4</sub> is 26 Torr.

Fig.3 Dependence of TOF for CH<sub>4</sub> conversion on the partial pressure of CH<sub>4</sub> in the CH<sub>4</sub> + CO<sub>2</sub> reaction over Rh/SiO<sub>2</sub> at 963 K. The pressure of CO<sub>2</sub> is 26 Torr.

In the dissociation of CO<sub>2</sub> on Rh surface, the precursor of the CO<sub>2</sub> dissociation may be adsorbed CO<sub>2</sub> which coverage is very small under the CH<sub>4</sub> + CO<sub>2</sub> reaction at high temperatures as 800 - 1000 K because of small adsorption energy (~ 5 kcal/mol) of CO<sub>2</sub> on Rh surface [11]. It is known that CO<sub>2</sub> over Rh surface desorb at low temperatures as 130 - 200 K. On the other hand, CO<sub>2</sub> can adsorb as carbonate form or formate in the presence of hydrogen on the surface of Al<sub>2</sub>O<sub>3</sub>, TiO<sub>2</sub>, and MgO above room temperature. The carbonates on TiO<sub>2</sub> [12] and MgO [13] decomposes in vacuum at 350, 420, and 580 K, respectively. As for formate [14] on Al<sub>2</sub>O<sub>3</sub>, TiO<sub>2</sub>, and MgO, the peak tops of temperature programmed desorption for CO<sub>2</sub> are 650, 540, 730 K, respectively, which are higher than the decomposition temperature of carbonate. No carbonate or formate, however, was observed on SiO<sub>2</sub> [15]. In this study, the formation of carbonate and formate and their decomposition were examined by in situ FT-IR and TPD. Fig. 4 shows the results of FT-IR for the surface of Rh/Al<sub>2</sub>O<sub>3</sub> exposing to a mixture of 190 Torr : 570 Torr CO<sub>2</sub> + H<sub>2</sub> at various temperatures. At 300 K, the peaks attributable to formate and carbonate as well as CO which was formed by dissociation of CO<sub>2</sub> were observed. Above 433 K, the carbonate peak disappeared, while the formate peak remained.

Fig.5 shows TPD for adspecies on Rh/Al<sub>2</sub>O<sub>3</sub> formed by exposing to CO<sub>2</sub> + H<sub>2</sub> at 433 K, where CO<sub>2</sub> desorbs from the catalyst at 355 and 588 K and the latter peak accompanies desorption of H<sub>2</sub>, indicating that the former and latter peaks are due to decomposition of carbonate and formate species, respectively. The TPD results are in good agreement with the results of FT-IR with respect to the relative amount of carbonate and formate existing at various temperatures. That is, the formation of formate is predominant at high temperatures above 400 K.

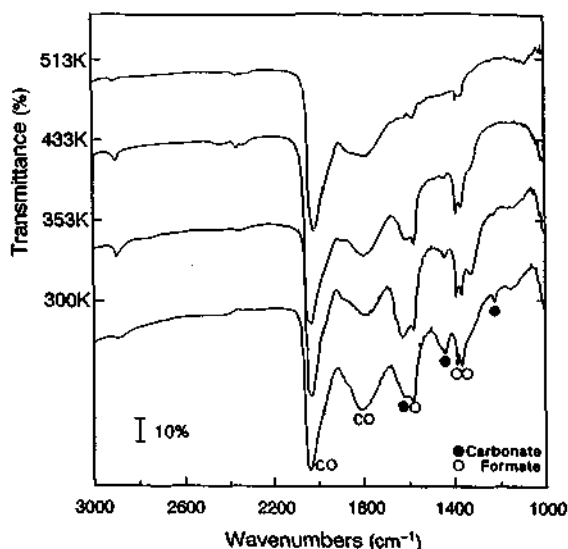


Fig.4 In-situ FT-IR spectra of adspecies on 5wt% Rh/Al<sub>2</sub>O<sub>3</sub> after exposing to 1 : 3 CO<sub>2</sub> + H<sub>2</sub> (1atm) at various temperatures.

The species over Rh/Al<sub>2</sub>O<sub>3</sub>, Rh/SiO<sub>2</sub>, Al<sub>2</sub>O<sub>3</sub>, and Rh/SiO<sub>2</sub> + Al<sub>2</sub>O<sub>3</sub> (physical mixture) observed in FT-IR spectra are summarized in Table 2. On the surface of Rh/SiO<sub>2</sub>, neither carbonate nor formate was observed by exposing to CO<sub>2</sub> or CO<sub>2</sub> + H<sub>2</sub>, whereas both species were formed over Rh/SiO<sub>2</sub> + Al<sub>2</sub>O<sub>3</sub> (physical mixture). The formate species may be formed on the surface of Al<sub>2</sub>O<sub>3</sub> by reaction of CO<sub>2</sub> with spillover atomic hydrogen from Rh to Al<sub>2</sub>O<sub>3</sub>. It was also confirmed that formate species was more stable than carbonate on the surface of Al<sub>2</sub>O<sub>3</sub> as shown in Table 3. Note that the difference in the catalyst systems between Rh/SiO<sub>2</sub> and Rh/SiO<sub>2</sub> + Al<sub>2</sub>O<sub>3</sub> on the state of catalyst surface observed in FT-IR is the formation of formate on the Al<sub>2</sub>O<sub>3</sub>.

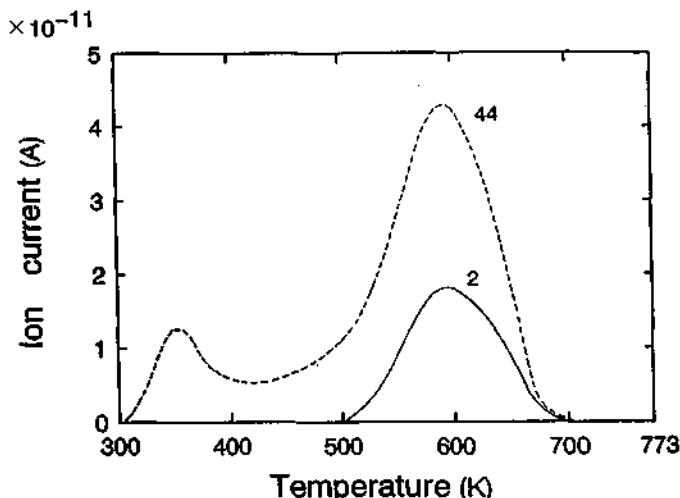


Fig.5 TPD for adspecies on 5wt% Rh/Al<sub>2</sub>O<sub>3</sub> formed by exposing to CO<sub>2</sub> + H<sub>2</sub> at 433 K. Heating rate; 10 K/min. Helium carrier gas.

Table 2 Observed species in FT-IR spectra over Rh/Al<sub>2</sub>O<sub>3</sub>, Rh/SiO<sub>2</sub>, Al<sub>2</sub>O<sub>3</sub>, and Rh/SiO<sub>2</sub> + Al<sub>2</sub>O<sub>3</sub> (physical mixture)

		adsorbed species		
		CO	carbonate	formate
CO <sub>2</sub>	Rh/Al <sub>2</sub> O <sub>3</sub>	○	○	×
	Rh/SiO <sub>2</sub>	○	×	×
CO <sub>2</sub> +H <sub>2</sub> (1:3)	Rh/Al <sub>2</sub> O <sub>3</sub>	○	○	○
	Rh/SiO <sub>2</sub>	○	×	×
	Al <sub>2</sub> O <sub>3</sub>	×	○	×
	Rh/SiO <sub>2</sub> +Al <sub>2</sub> O <sub>3</sub>	○	○	○

**Table 3** Decomposition temperature of carbonate and formate on Rh/Al<sub>2</sub>O<sub>3</sub> and Al<sub>2</sub>O<sub>3</sub>.

		Peak temperature (K)	
		carbonate	formate
CO <sub>2</sub> +H <sub>2</sub> (1:3)	Rh/Al <sub>2</sub> O <sub>3</sub>	353	588
	Al <sub>2</sub> O <sub>3</sub>	353	-
HCOOH	Rh/Al <sub>2</sub> O <sub>3</sub>	-	443, 588
	Al <sub>2</sub> O <sub>3</sub>	-	573

Accordingly, the formate on Al<sub>2</sub>O<sub>3</sub> may be responsible for the promotion of activity of Rh/SiO<sub>2</sub> for CH<sub>4</sub> + CO<sub>2</sub>, where Al<sub>2</sub>O<sub>3</sub> plays a role in raising CO<sub>2</sub> concentration in the vicinity of Rh particles by trapping CO<sub>2</sub> as formate on the surface. In the other cases such as K/SiO<sub>2</sub> mixed with Rh/SiO<sub>2</sub>, the promotion of activity may be ascribed to formation of carbonate. The basic property of the metal oxides and alkali may be important to react with CO<sub>2</sub> to form carbonate and/or formate.

#### Acknowledgement

The authors wish to acknowledge Mr. Y.Kanai and Dr. T.Fujitani for their help in taking the FT-IR and TPD spectra.

#### REFERENCE

- [1] T.Sodesawa, A.Dobashi and F.Nozaki, React.Kinet.Catal.Lett., 1979, 12, 107.
- [2] Y.Sakai, H.Saito, T.Sodesawa and F.Nozaki, React.Kinet.Catal.Lett., 1984, 24, 253.
- [3] A.M.Gadalla and B.Bower, Chem.Eng.Sci., 1988, 43, 3049.
- [4] A.M.Gadalla and Sommer, Chem.Eng.Sci., 1988, 44, 2825 ; J.Am.Ceram.Soc. , 1989, 72, 683.
- [5] F.Solymosi and Gy.Kutsán and A.Erdőhelyi, Catal.Lett., 1991, 11, 149.
- [6] A.Erdőhelyi, J.Cserenyi and F.Solymosi, J.Catal., 1993, 141, 287.
- [7] M.Masai, H.Kado, A.Miyake, S.Nishiyama and S.Tsuruya, Stud.Surf.Sci.Catal., 1988, 36, 67.
- [8] J.Nakamura, S.Umeda, K.Kubushiro, K.Kunimori, Sekiyu Gakkaishi, 1993, 36, 97.
- [9] A.Frennet, Catal.Rev.-Sci. Eng., 1974, 10, 37 ; S.G.Brass, G.Ehrlich, Surf.Sci. 1987, 187, 21.
- [10] D.W.Goodman, D.E.Peebles, J.M.White, Surf.Sci., 1984, 140, L239.
- [11] W.H.Weinberg, Surf. Sci., 1983, 128, L224.
- [12] F.Solymosi, A.Erdőhelyi, T.Bánsági, J.Chem.Soc. Faraday Trans. 1, 1981, 77, 2645.
- [13] T.Kanno, S.Matoba, F.Yamazaki, M.Kobayashi, Shokubai, 1992, 34, 395.
- [14] F.Solymosi and A.Erdőhelyi, J.Catal., 1985, 91, 327.
- [15] F.Solymosi, H.Knözinger, J.Catal., 1990, 122, 166.

## 4.21 Laser Stimulated CO + H<sub>2</sub> to Form C<sub>2</sub>H<sub>4</sub> on the Surface of Nickel Sulfate

Wen Li and Shunhe Zhong

(Dept. of Chem. Eng., Tianjin Univ., Tianjin 300072, P.R.China)

### Abstract

The title reaction was studied using the techniques of LSSR, XRD, TGA and TPD. Under the conditions of ordinary pressure and 200°C with 1047cm<sup>-1</sup> laser exciting the surface of nickel sulfate 1000 times, CO conversion of 30.7% and C<sub>2</sub>H<sub>4</sub> selectivity of 100% are obtained. The reactive horizontal-adsorbed CO takes part in the reaction of CO hydrogenation. The surface of nickel sulfate supplies B-acid and L-acid sites for the reaction.

### 1. INTRODUCTION

Recently, we obtained an interesting result, i.e. the formation of C<sub>2</sub>H<sub>4</sub> by CO<sub>2</sub> laser stimulating adsorbed CO and H<sub>2</sub> on the surface of nickel sulfate, a known solid acid [1], that is widely used in many chemical reactions. The reaction of CO + H<sub>2</sub> to form C<sub>2</sub>H<sub>4</sub> is very important in the chemical industry. Many scientists are working to enhance the selectivity for it by thermal catalytic surface reaction, but no one has yet obtained ideal results [2]. The technique of Laser Stimulated Surface Reaction (LSSR) is also used extensively in many scientific fields [3], and many chemical reactions have obtained ideal results by taking advantage of the features of monochromaticity and high energy density of laser[4].

### 2. EXPERIMENTS

The sample of nickel sulfate was prepared by desiccating and calcining to remove as much free and combined water as possible. After comparison, we selected the basic carrier MgO and prepared a sample, NiSO<sub>4</sub>/MgO, by macerating. In the technique of LSSR, CO<sub>2</sub> laser (wave range 9 — 11 μm) was used as the light source, and a controllable temperature transmissible-reflectible mini-reactor was also used. The solid sample was made into a round piece (Φ 20 — 2mm) and put into the sample case of the reactor. Before the reaction began, the reactor was exhausted to 10<sup>-3</sup> torr with vacuum-pump, and maintaining the state for 2 hours. Then the mixed gases, N<sub>2</sub>, H<sub>2</sub>, CO (volume ratio is 85:10:5), were put into it, adsorbing for 1 hour under the conditions of static state

and ordinary pressure. The surface of the sample was stimulated 1000 times by CO<sub>2</sub> laser under selected frequency and temperature. Finally, the gas in the reactor was analyzed by gas chromatograph.

The structure and the combined water's distribution of nickel sulfate were studied using XRD and TGA.

The technique of Temperature Programmed Desorption-Mass Spectrum (TPD-MS) was used for studying the adsorbed species of CO and C<sub>2</sub>H<sub>4</sub> on the surface of samples. We weighed each sample to about 500mg, put it into a quartz tube, raising its temperature to 200°C and exhausting the tube to 10<sup>-6</sup> torr with a vacuum-pump, maintaining it for 2 hours, in this way, a clear surface was obtained. After that, we reduced the temperature of the tube to room temperature, put the adsorbed gas (CO or C<sub>2</sub>H<sub>4</sub>) into it, controlling the tube pressure at 300 torr, keeping it for 2 hours under the condition of static state, then exhausting the tube to 10<sup>-6</sup> torr, finally raising the temperature of the tube in a program-controlled state, at the same time, inspecting the desorbed species by quadpole mass spectrometry.

### 3. RESULTS and DISCUSSION

Table 1 displays the results of CO<sub>2</sub> laser stimulated CO + H<sub>2</sub> surface reaction at 25°C with different frequencies. Because the frequency of the C=O band does not belong to the range of CO<sub>2</sub> laser frequencies, it can not be stimulated to activate by CO<sub>2</sub> laser. So, the solid stimulated model<sup>[4]</sup> is the only way to activate the adsorbed C=O band in this system. In general, the laser photons at 944 cm<sup>-1</sup> can not be absorbed by all the solid surface bands of NiSO<sub>4</sub>, NiSO<sub>4</sub>/MgO or MgO, but those at 1047cm<sup>-1</sup> can be absorbed effectively by the S=O band, and those at 1079 cm<sup>-1</sup> can be absorbed effectively by the S=O band<sup>[5]</sup>. After comparison, we selected the three frequencies. This table shows that CO<sub>2</sub> laser at any selected frequency can not stimulate the C=O band to activate on the surface of MgO. The laser photons of 1047 cm<sup>-1</sup> and 1079cm<sup>-1</sup> can effectively stimulate adsorbed CO and H<sub>2</sub> to form C<sub>2</sub>H<sub>4</sub>. Like the reaction on the surface of MgO, on the surface of NiSO<sub>4</sub> and NiSO<sub>4</sub>/ MgO, the laser photons of 944cm<sup>-1</sup> are ineffective for the reaction. As a result, the laser photon-stimulated solid surface S=O band is much more effective than the S=O band. Another result is that the reaction of forming C<sub>2</sub>H<sub>4</sub> is much more effective on the surface of NiSO<sub>4</sub> than on the surface of NiSO<sub>4</sub>/MgO.

Table 1. Results of Laser Stimulated CO+H<sub>2</sub> Surface Reaction

Sample	at 25°C with Different Waves									
	MgO			NiSO <sub>4</sub>			NiSO <sub>4</sub> /MgO			
Laser waves cm <sup>-1</sup>	944	1047	1079	944	1047	1079	944	1047	1079	
CO conversion %	0.0	0.0	0.0	0.0	0.48	0.06	0.0	0.16	trace	
C <sub>2</sub> H <sub>4</sub> selectivity%	0	0	0	0	100	100	0	100	100	

For this reason, the frequency of 1047 cm<sup>-1</sup> was selected to stimulate the adsorbed CO and H<sub>2</sub> on the surface of the samples to form C<sub>2</sub>H<sub>4</sub> at different temperatures. In this way, the effects of temperature in the reaction are obtained. Table 2 shows the results.

**Table 2. Results of Laser Stimulated CO+H<sub>2</sub> Surface Reaction**

by 1047cm<sup>-1</sup> Laser at Different Temperatures

Sample	MgO			NiSO <sub>4</sub>			NiSO <sub>4</sub> /MgO		
	25	100	200	25	100	200	25	100	200
Reaction temperature °C	25	100	200	25	100	200	25	100	200
CO conversion %	0.0	0.0	0.0	0.48	6.79	30.7	0.16	0.49	0.69
C <sub>2</sub> H <sub>4</sub> selectivity%	0	0	0	0	100	100	100	100	100

With raising temperature on the surface of MgO, there were no products even C<sub>2</sub>H<sub>4</sub>. But, on the surface of NiSO<sub>4</sub> or NiSO<sub>4</sub>/MgO, the conversion of CO rises with the temperature. The difference is, when the temperature rises from 25°C to 200°C on the surface of NiSO<sub>4</sub>, the conversion of CO increases from 0.48% to 30.7%, but on the surface of NiSO<sub>4</sub>/MgO, it only increases from 0.16% to 0.69%. So, the laser photons are more effective in activating adsorbed CO and H<sub>2</sub> to form C<sub>2</sub>H<sub>4</sub> on the surface of NiSO<sub>4</sub> than on the surface of NiSO<sub>4</sub>/MgO.

XRD was used to investigate the crystalline forms of samples so that the processes of gas adsorption and laser stimulating surface reaction could be analyzed exactly. The structure of nickel sulfate consists of NiSO<sub>4</sub> belonging to the orthorhombic system and NiSO<sub>4</sub>·H<sub>2</sub>O belonging to the monoclinic system. From the literature<sup>[6]</sup>, we noted that NiSO<sub>4</sub>·7H<sub>2</sub>O belongs to the orthorhombic system, that NiSO<sub>4</sub>·6H<sub>2</sub>O, which is complicated, belongs to the orthorhombic, tetragonal, and monoclinic systems, that NiSO<sub>4</sub>·4H<sub>2</sub>O belongs to the monoclinic system, and that NiSO<sub>4</sub>·2H<sub>2</sub>O belongs to the monoclinic system. So, the process of losing water from crystal nickel sulfate reflects the transition from the orthorhombic to the monoclinic system. When it loses all the combined water, the structure of NiSO<sub>4</sub> is restored to the orthorhombic system. This process can be compared with that of acid change when the sample is calcined. By losing the combined water during the calcination process, the acid of this solid increases. But, when the crystal water is less than 0.5 mol, the acid begins to decrease until all the combined water is lost, and the solid becomes a non-acid solid. During the process, L-acid sites gradually increase. When the crystal is restored to the orthorhombic system, all acid disappears.

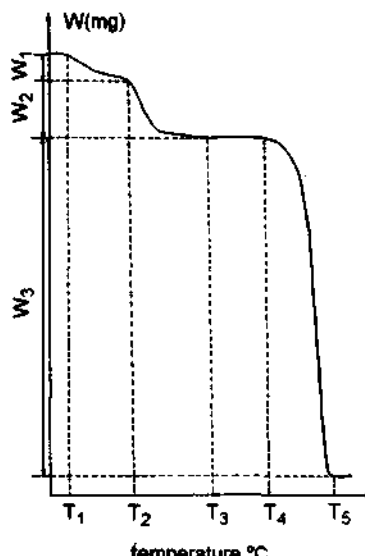


Fig.1 TGA Results on Solid Nickel Sulfate

But the L-acid sites' increasing or decreasing is not as same as the B-acid sites'. The structure of  $\text{NiSO}_4/\text{MgO}$  includes  $\text{MgO}$ ,  $\text{MgNiO}_2$ ,  $\text{Ni}_3\text{O}_2(\text{OH})_4$  and  $\text{NiSO}_4 \cdot \text{H}_2\text{O}$ . The last one is very little. So, we can affirm that  $\text{MgO}$  destroys the crystalline form of  $\text{Ni}^{2+}$  of nickel sulfate.

Figure 1 is the TGA curve of nickel sulfate (10.9mg). Table 3 shows the results. Through analysis, we believe that the free water and part of the combined water are lost during the first stage. The remaining combined water is lost during the second stage, and  $\text{NiSO}_4$  decomposes into  $\text{NiO}$  and  $\text{SO}_3$  gas during the last stage. For the whole process of LSSR, 200°C is an ideal reactive temperature, because at this temperature some B-acid and L-acid sites can be supplied for the reaction. If the sample calcining temperature is too high, the solid acid decreases, and even the solid  $\text{NiSO}_4$  decomposes.

**Table 3. Thermal Gravity Analysis Results of Nickel Sulfate**

Stage Temperature °C	first		second		third	
	T <sub>1</sub> 25	T <sub>2</sub> 200	T <sub>2</sub> 200	T <sub>3</sub> 412	T <sub>4</sub> 604	T <sub>5</sub> 820
Weightlessness mg	W <sub>1</sub> 0.38		W <sub>2</sub> 0.86		W <sub>3</sub> 4.96	

Figure 2 shows the results of TPD-MS of CO chemical adsorption on the surface of samples. The results show strong interaction between  $\text{MgO}$  and  $\text{NiSO}_4$ . For this reason, the desorption peak of CO at 329°C on the surface of  $\text{NiSO}_4$  disappears. Because  $\text{NiSO}_4$  can not cover the entire surface of  $\text{MgO}$  during the macerating, the desorption peak of CO at 340°C still exists on the surface of  $\text{NiSO}_4/\text{MgO}$ . Our study indicates that the desorbed species at 376°C (Fig.2-b) and at 373°C (Fig.2-c) are the same, that is, line-adsorbed CO on  $\text{Ni}^{2+}$ :  $\text{O}=\text{C}-\text{Ni}^{2+}$ . Also the desorbed species at 343°C (Fig. 2-a) and at 340°C (Fig.2-b) are the same, that is, line-adsorbed CO on  $\text{Mg}^{2+}$ :  $\text{O}=\text{C}-\text{Mg}^{2+}$ . The desorbed peak at 329°C (Fig.2-b) is an activated adsorbed species in the laser-stimulated  $\text{CO} + \text{H}_2$  surface reaction. We believe that it is horizontal-adsorption  $\text{CO}$ [2]:

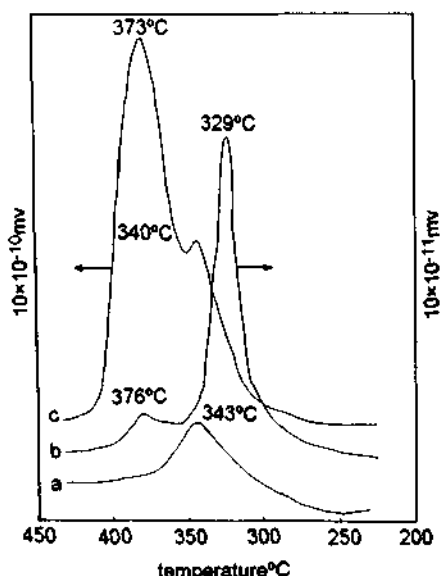
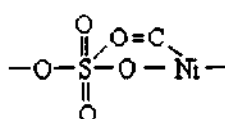


Fig.2 Adsorbed CO TPD-MS Spectra on The Solid Surface

a: on  $\text{MgO}$  b: on  $\text{NiSO}_4$  c: on  $\text{NiSO}_4/\text{MgO}$



To investigate the adsorbing behavior of the product C<sub>2</sub>H<sub>4</sub> during LSSR of CO + H<sub>2</sub>, we conducted TPD-MS of C<sub>2</sub>H<sub>4</sub> chemical adsorbing on the surface of samples.

Figure 3 shows the results. During the process, we found that basic C<sub>2</sub>H<sub>4</sub> did not adsorb on the surface of the basic carrier MgO. The low temperature desorption peaks of C<sub>2</sub>H<sub>4</sub> at 93°C (Fig.3-a) and 91°C (Fig.3-b) are the result of forming s-p complex bonds between C<sub>2</sub>H<sub>4</sub> and Ni<sup>2+</sup>:

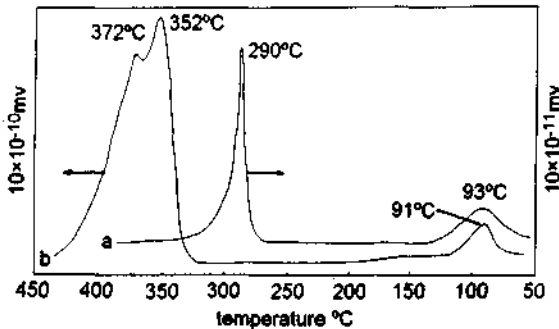
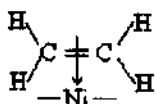
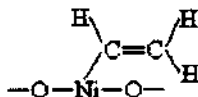


Fig.3 Adsorbed C<sub>2</sub>H<sub>4</sub> TPD Spectra on The Solid Surface  
a: on NiSO<sub>4</sub> b: on NiSO<sub>4</sub>/MgO

The high temperature desorption peaks of C<sub>2</sub>H<sub>4</sub> at 290°C (Fig.3-a), at 352°C, and 372°C (Fig.3-b) are the result of the formation of an s-s complex bond between C<sub>2</sub>H<sub>4</sub> and Ni<sup>2+</sup>. In this complex bond, C<sub>2</sub>H<sub>4</sub> dissociates and the dissociative H<sup>+</sup> complexes with nearby surface oxygen sites:



Because the basic carrier MgO promotes the d-electron feedback of Ni<sup>2+</sup>, the s-s complex bond between -CHCH<sub>2</sub> and Ni<sup>2+</sup> on the surface of NiSO<sub>4</sub>/MgO is stronger than that on the surface of NiSO<sub>4</sub>, and the amount of adsorbed C<sub>2</sub>H<sub>4</sub> on the surface of NiSO<sub>4</sub>/MgO is larger than that on the surface of NiSO<sub>4</sub>. In Fig. 3-b, the production of two high temperature desorption peaks may be the result of MgO, making Ni<sup>2+</sup> in different crystal environments. For this reason, we believe that the C<sub>2</sub>H<sub>4</sub> product of LSSR of CO + H<sub>2</sub> will first adsorb in the s-p complex band on Ni<sup>2+</sup>. As we know, this band is weak and easy to desorb by heating. In this way, the active sites will be obtained again on the surface, so the LSSR of CO + H<sub>2</sub> can continue.

#### 4. CONCLUSIONS

Under the conditions of ordinary pressure and 200°C, laser of 1047cm<sup>-1</sup> stimulated the surface of nickel sulfate 1000 times, resulting in the CO conversion of 30.7% and C<sub>2</sub>H<sub>4</sub> selectivity of 100% are obtained.

Nickel sulfate supplies L-acid and B-acid sites for the reaction.

During the reaction, horizontal-adsorbed CO is a reactive species that can be activated by CO<sub>2</sub> laser. The temperature can be controlled to promote desorption of the products C<sub>2</sub>H<sub>4</sub> and H<sub>2</sub>O.

## REFERENCES

- [1] Kozo Tanabe Solid Acid and Bases Their Catalytic Properties, Kodansha, 1970
- [2] Wen Li, Shun-he Zhong, The 6th China Conference on Catalysis, Shanghai, China, 1992, 140-141
- [3] T.J.Chuang, Conf. Solid State Devices and Mater., Tokyo, Japan, 1986, 193-199
- [4] T.J.Chuang, Surface Science Reports 3, 1983
- [5] Richard O.Kagel, Infared Spectra of Inorganic Compounds, 1971
- [6] Powder Diffraction File Inorganic Phases, Published by the JCPDS, 1983

## 4.22 Characterization of Solid Superacidity by *n*-Alkane Isomerization Reactions at Low Temperature

Gao Zi Chen Jian-min Hua Wei-ming Tang Yi

Department of Chemistry, Fudan University, Shanghai 200433, China

### Abstract

Butane and pentane reactions on solid acids such as  $\text{SO}_4^{2-}/\text{M}_x\text{O}_y$  and zeolites were studied. At low temperatures the isomerization selectivities of the reactions reach 90-100%, and the reaction kinetics follow the rate law of a first-order reversible reaction. As the acid strength of the solid acids increases, the conversions and rate constants of the butane and pentane reactions increase as well, but the activation energies of the reactions are diminished. *n*-Butane isomerization is a good probe reaction for the testing of the superacidity of solids with  $\text{H}_0 < -13$ , and *n*-pentane isomerization is more sensitive for samples whose acid strengths are in the range of  $-12 > \text{H}_0 > -16$ .

### 1. INTRODUCTION

Solid superacid is a new type of catalytic materials which has been found to exhibit extremely high activities for the reactions such as dehydration, isomerization, esterification, acylation and polymerization. The superacidity of solids is commonly characterized by Hammett indicators or IR spectroscopy[1]. However, it is impossible to detect the color change of an indicator on colored samples. And moreover Umansky and Hall[2] have pointed out that conclusions reached by observing color changes of the indicators sometimes can be misleading due to the red shifts of the absorption bands of the adsorbed indicators on the samples. On the other hand, IR spectroscopic studies of ammonia or pyridine adsorbed on solid surface are reliable to distinguish Bronsted and Lewis acid sites, but the acid amounts measured are more or less semiquantitative and the results of acid strength are relative and rough. Therefore improved methods are needed for the assay of superacidity of solid samples.

In the present work, isomerization reactions of *n*-butane and *n*-pentane on various solid superacids at low temperatures were investigated for the purpose of finding good

probe reactions for evaluating the superacidity of a variety of solid samples in ordinary laboratories.

## 2.EXPERIMENTAL METHODS

### 2.1 Sample Preparation

$\text{SO}_4^{2-}/\text{ZrO}_2$ ,  $\text{SO}_4^{2-}/\text{TiO}_2$  and  $\text{SO}_4^{2-}/\text{Fe}_2\text{O}_3$  samples were prepared by impregnating amorphous hydroxide precipitate predried at 110°C with 1 M  $\text{H}_2\text{SO}_4$  and then drying at 110°C and calcining in air at the desired temperatures.

HM, HY, HB and HZSM-5 zeolites were prepared by ion-exchanging the respective zeolite powders with  $\text{NH}_4\text{Cl}$  or dilute HCl solution. The dealuminated HM zeolites were prepared by treating HM with 6 N HCl repeatedly. The isomorphous substituted zeolite HSY was obtained by reacting  $\text{NH}_4\text{Y}$  with a controlled amount of  $(\text{NH}_4)_2\text{SiF}_6$  solution at pH 6 and 70°C.

### 2.2 Activity Measurement

Isomerization of n-butane or n-pentane was carried out at 20°-35°C and 35°-75°C respectively in a closed reacting system. The catalyst loading was 0.5 g, and before measurement the catalysts were activated in situ via evacuation at elevated temperature. The amount of n-butane or n-pentane injected for each test is 5 mL of gas(S.T.P.) or 25  $\mu\text{L}$  of liquid respectively. The reaction products were sampled and analyzed by using a gas chromatograph equipped with FID.

## 3. RESULTS

### 3.1 Butane Isomerization

#### 3.1.1 Reaction on $\text{SO}_4^{2-}/\text{ZrO}_2$ catalysts

Butane isomerization reaction was carried out on  $\text{SO}_4^{2-}/\text{ZrO}_2$  catalysts precalcined at different temperatures. As shown in Table 1, at 20°C the reaction proceeded with high selectivity on all the catalysts. Only very small amounts of propane and isopentane were found in the reaction products of some of the catalysts.

The reaction data in Table 1 have been fitted on computer using the least square method. Calculation results show that they obey the rate law of a first-order reversible reaction,

$$-\ln[1-(1+1/K)x] = k_1(1+1/K)t,$$

where x,  $k_1$  and K are the concentration of i-C<sub>4</sub> in the product, the rate constant of the forward reaction and the equilibrium constant respectively. The calculated kinetic data for the samples at 20°C are listed in Table 2.

Table 1 Reaction data for butane isomerization at 20°C

Sample*	Time (h)	Product(mol%)			Conversion (%)	Isomerization selectivity (%)	
		C <sub>3</sub>	i-C <sub>4</sub>	n-C <sub>4</sub>	i-C <sub>5</sub>		
$\text{SO}_4^{2-}/\text{ZrO}_2$ (500)	90	-	3.5	96.5	-	3.5	100
	115	0.1	4.7	95.3	-	4.8	98
	140	-	5.9	94.1	-	5.9	100
	165	-	6.6	93.4	-	6.6	100
	190	-	8.5	91.6	-	8.5	100
	215	-	9.8	90.2	-	9.8	100
	240	-	10.7	89.3	-	10.7	100
$\text{SO}_4^{2-}/\text{ZrO}_2$ (600)	65	-	8.7	91.3	-	8.7	100
	90	0.2	14.3	85.5	-	14.5	99
	115	-	19.3	81.7	-	19.3	100
	140	-	23.0	77.0	-	23.0	100
	165	-	28.4	71.6	-	28.4	100
	190	-	34.8	66.2	-	34.8	100
	215	-	38.9	61.1	-	38.9	100
$\text{SO}_4^{2-}/\text{ZrO}_2$ (650)	240	-	41.4	58.6	-	41.4	100
	65	0.1	8.5	91.4	-	8.6	99
	90	0.4	14.7	84.9	-	15.1	97
	115	0.6	23.6	75.8	-	24.2	98
	140	0.7	29.5	69.8	-	30.2	98
	165	1.0	38.9	59.8	0.3	40.3	97
	190	1.2	44.8	53.7	0.3	46.4	97
$\text{SO}_4^{2-}/\text{ZrO}_2$ (700)	215	1.1	50.2	48.2	0.5	51.9	93
	240	1.2	54.6	43.7	0.5	56.6	96
	65	0.2	7.3	92.5	-	7.5	97
	90	0.1	8.5	91.4	-	8.6	99
	115	0.2	11.2	88.6	-	11.4	98
	140	0.2	14.1	85.7	-	14.3	99
	165	0.1	16.5	83.4	-	16.6	99
$\text{SO}_4^{2-}/\text{ZrO}_2$ (800)	190	0.2	20.8	79.0	-	21.0	99
	215	0.2	23.8	76.0	-	24.0	99
	240	-	25.6	74.4	-	25.6	100

\* Figures in parenthesis are the calcination temperatures of the samples.

Table 2 Kinetic data for butane isomerization at 20°C

Sample	$k_1$ ( $10^{-3}\text{h}^{-1}$ )	$k_{-1}$ ( $10^{-3}\text{h}^{-1}$ )	r
$\text{SO}_4^{2-}/\text{ZrO}_2(500)$	1.40	0.350	0.998
$\text{SO}_4^{2-}/\text{ZrO}_2(600)$	3.00	0.750	0.995
$\text{SO}_4^{2-}/\text{ZrO}_2(650)$	5.14	1.29	0.998
$\text{SO}_4^{2-}/\text{ZrO}_2(700)$	1.53	0.383	0.996
$\text{SO}_4^{2-}/\text{ZrO}_2(800)$	0.104	0.026	0.974

The effect of temperature on the activity and selectivity of  $\text{SO}_4^{2-}/\text{ZrO}_2$  catalysts was investigated in the range of 20°-35°C. Table 3 gives the experimental results of one of the catalysts,  $\text{SO}_4^{2-}/\text{ZrO}_2(650)$ , which are representative of the results of all the other samples. As the reaction temperature is raised, the rates of the isomerization reaction increase evidently. In the meantime the isomerization selectivities remain higher than 90%, so long as the total conversions are lower than 70%. The measuring time for each sample at 35°C can be shortened to less than 2 days.

Table 4 Kinetic data for butane isomerization on  $\text{SO}_4^{2-}/\text{ZrO}_2$  catalysts

Sample	$k_1(10^{-3}\text{h}^{-1})$				$k_{-1}(10^{-3}\text{h}^{-1})$				$E(\text{kJmol}^{-1})$
	20°C	25°C	30°C	35°C	20°C	25°C	30°C	35°C	
$\text{SO}_4^{2-}/\text{ZrO}_2(500)$	1.40	3.47	6.76	16.4	0.350	0.937	2.03	5.25	118±3
$\text{SO}_4^{2-}/\text{ZrO}_2(600)$	3.00	6.15	9.88	21.7	0.750	1.66	2.96	6.72	95±5
$\text{SO}_4^{2-}/\text{ZrO}_2(650)$	5.14	10.8	16.0	40.1	1.29	29.2	48.0	12.8	97±8
$\text{SO}_4^{2-}/\text{ZrO}_2(700)$	1.53	3.69	8.38	21.0	0.383	0.996	2.66	6.72	129±2
$\text{SO}_4^{2-}/\text{ZrO}_2(800)$	0.104	0.874	4.16	8.98	0.026	0.236	1.25	2.87	221±24

Table 3 Reaction data for butane isomerization on  $\text{SO}_4^{2-}/\text{ZrO}_2(650)$  at various temperatures

Temprature (°C)	Time (h)	Product(mol%)				Conversion (%)	Isomerization selectivity (%)
		C3	n-C4	i-C4	i-C5		
20	65	0.1	8.5	91.4	-	8.6	99
	90	0.4	14.7	84.9	-	15.1	97
	115	0.6	23.6	75.8	-	24.2	98
	140	0.7	29.5	69.8	-	30.2	98
	165	1.0	38.9	59.8	0.3	40.3	97
	190	1.2	44.8	53.7	0.3	46.4	97
	215	1.1	50.2	48.2	0.5	51.9	93
	240	1.2	54.6	43.7	0.5	56.6	96
25	20	0.1	8.1	91.8	-	8.2	99
	30	0.1	16.5	93.4	-	16.6	99
	40	0.3	22.6	77.1	-	22.9	99
	50	0.3	30.0	69.7	-	30.3	99
	60	0.4	36.7	62.9	-	37.1	99
	75	0.6	46.0	53.3	-	46.8	98
	90	0.8	51.6	47.4	0.2	52.7	98
30	20	0.2	17.7	82.2	-	17.8	99
	30	0.3	28.7	71.0	-	29.0	99
	40	0.4	38.5	61.1	0.1	39.0	99
	50	0.7	47.2	52.1	0.2	47.9	99
	60	1.0	54.3	44.7	0.2	55.4	98
	70	4.0	67.3	28.1	0.6	72.5	93
	80	18.7	58.0	22.4	0.9	81.2	71
35	10	0.1	14.4	85.5	-	14.5	99
	15	0.3	27.0	72.8	-	27.2	99
	20	0.4	36.7	62.9	-	37.2	99
	25	0.6	46.3	53.0	0.1	47.1	98
	30	0.7	54.0	45.1	0.2	55.0	98
	40	1.3	69.3	29.0	0.4	71.2	97
	50	4.1	71.1	23.9	0.9	76.7	93
	60	13.6	63.7	22.1	0.6	80.6	79

The rate constants of the  $\text{SO}_4^{2-}/\text{ZrO}_2$  catalysts at different temperatures and their activation energies are listed in Table 4. The rate constants were calculated according to the rate equation of a first-order reversible reaction. The temperature dependence of them was found to fit the Arrhenius expression, and the activation energies were determined from plots of  $\ln k_1$  against  $1/T$  by least square method.

### 3.1.2. Correlation between superacidity and reaction data

It has been reported that the acid strength of  $\text{SO}_4^{2-}/\text{ZrO}_2$  catalysts depends on the calcination temperature of the catalysts after exposing to dilute  $\text{H}_2\text{SO}_4$ [3,4]. The acid strengths of the samples prepared in this work were tested by using Hammett indicator method, and the results were given in Table 5.

Table 5 Acid strengths of the  $\text{SO}_4^{2-}/\text{ZrO}_2$  catalysts

Sample	$\text{SO}_4^{2-}/\text{ZrO}_2$ (500)	$\text{SO}_4^{2-}/\text{ZrO}_2$ (600)	$\text{SO}_4^{2-}/\text{ZrO}_2$ (650)	$\text{SO}_4^{2-}/\text{ZrO}_2$ (700)	$\text{SO}_4^{2-}/\text{ZrO}_2$ (800)
H <sub>0</sub>	12.7	-14.5	-16.0	-13.8	-12.7

Figure 1 illustrates how the conversions, rate constants and activation energies for butane isomerization reaction and the acid strengths of the  $\text{SO}_4^{2-}/\text{ZrO}_2$  samples change with the calcination temperature. Obviously the conversion and rate constant for the isomerization reaction change concurrently with the acid strength, but the activation energy changes in an opposite way. It has been reported that in acid catalyzed isomerization of saturated hydrocarbons the reaction is initiated by the formation of carbonium ion via protonation[5]. Solid superacid catalysts with  $H_0 \leq -12.7$  are capable of initiating the reaction at room temperature, and the initial carbocation is enhanced as the superacidity of the catalysts is increased.

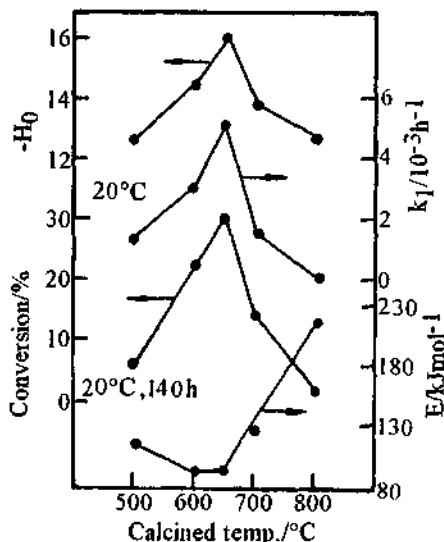


Fig. 1 Effect of calcination temperature on  $H_0$  and kinetic data for butane isomerization

This may explain the good correlation found between the acid strengths measured by indicator method and the kinetic data for butane isomerization.

It has been noted that the reaction conversion and rate constant of  $\text{SO}_4^{2-}/\text{ZrO}_2(800)$  are much smaller than that of  $\text{SO}_4^{2-}/\text{ZrO}_2(500)$ , and the activation energy of the former is much higher than that of the latter, although they have nearly the same acid strength. Results of chemical analysis tell that  $\text{SO}_4^{2-}/\text{ZrO}_2(800)$  contains only 0.2 wt%  $\text{SO}_3$  after calcination while the amount of  $\text{SO}_3$  in  $\text{SO}_4^{2-}/\text{ZrO}_2(500)$  is 16 times greater, i.e.  $\text{SO}_4^{2-}/\text{ZrO}_2(500)$  may have more acid sites than  $\text{SO}_4^{2-}/\text{ZrO}_2(800)$ . This suggests that the activity for butane isomerization might have been influenced by the acid amount of the catalysts as well, so like all the other probe reactions butane isomerization has the same disadvantage of being not possible to distinguish between the acid strength and acid amount of the samples exactly.

### 3.1.3. Measurement on other solid acid samples

Butane isomerization reaction was used to check the superacidity of other solid acids such as  $\text{SO}_4^{2-}/\text{TiO}_2(500)$ ,  $\text{SO}_4^{2-}/\text{Fe}_2\text{O}_3(500)$ , HM, HSY and HZSM-5. It was found that the isomerization of *n*-butane to isobutane is only catalyzed by  $\text{SO}_4^{2-}/\text{TiO}_2(500)$  below 35°C, demonstrating that the other samples probably have milder acidity, e.g.  $H_0 > 12.7$ . Experimental results on  $\text{SO}_4^{2-}/\text{TiO}_2(500)$  are listed in Table 6 together with some of the results on  $\text{SO}_4^{2-}/\text{ZrO}_2$  for comparison.

Table 6 Kinetic data for butane isomerization on  $\text{SO}_4^{2-}/\text{TiO}_2$  and  $\text{SO}_4^{2-}/\text{ZrO}_2$

Sample	$k_1(10^{-3}\text{h}^{-1})$			E (kJ mol <sup>-1</sup> )	$H_0$
	25°C	30°C	35°C		
$\text{SO}_4^{2-}/\text{TiO}_2(500)$	0.0827	0.254	0.706	165±6	-13.2[6]
$\text{SO}_4^{2-}/\text{ZrO}_2(700)$	3.69	8.88	21.0	129±2	-13.8
$\text{SO}_4^{2-}/\text{ZrO}_2(650)$	10.8	16.0	40.1	97±8	-16.0

## 3.2 Pentane Isomerization

### 3.2.1. Reaction on solid acids

Since butane isomerization reaction below 35°C cannot be utilized to measure the superacidity of catalysts with  $H_0 > 12.7$ , pentane isomerization was studied to see whether this limitation can be overcome. Table 7 gives some examples of the reaction data for pentane isomerization on solid superacids at 35°C. As was expected the rates

of isomerization have increased a great deal in comparison with that of butane isomerization, while the isomerization selectivities remain higher than 90% on all the catalysts except the  $\text{SO}_4^{2-}/\text{Fe}_2\text{O}_3$  samples.

Table 7 Reaction data for pentane isomerization at 35°C

Sample	Time (min)	Product(mol%)				conversion (%)	Isomerization selectivity (%)
		i-C <sub>4</sub>	i-C <sub>5</sub>	n-C <sub>5</sub>	C <sub>6</sub>		
$\text{SO}_4^{2-}/\text{ZrO}_2$ (600)	70	0.7	37.6	61.7	-	38.3	98
	90	1.3	47.6	51.1	-	48.9	97
	110	2.2	55.0	42.8	-	57.2	96
	120	2.1	58.6	39.2	0.1	60.8	96
	130	2.8	61.8	35.3	0.1	66.6	96
$\text{SO}_4^{2-}/\text{ZrO}_2$ (650)	60	-	25.2	74.8	-	25.2	100
	80	0.1	40.7	59.2	-	40.8	100
	100	0.1	50.9	49.0	-	51.0	100
	120	0.2	59.6	40.2	-	59.8	100
	140	0.5	66.1	33.4	-	66.9	99
$\text{SO}_4^{2-}/\text{TiO}_2$ (500)	120	-	5.2	94.8	-	5.2	100
	150	0.1	7.4	92.5	-	7.5	99
	180	0.2	10.9	88.9	-	11.5	98
	210	0.5	15.2	84.3	-	15.7	97
	240	0.8	18.9	80.3	-	19.7	96
$\text{SO}_4^{2-}/\text{TiO}_2$ (550)	315	-	4.9	95.1	-	4.9	100
	345	-	7.0	93.0	-	7.0	100
	360	0.1	8.1	91.8	-	8.2	99
	375	0.1	9.1	90.8	-	9.2	99
	420	0.3	11.7	88.0	-	12.0	98
	480	0.6	13.5	85.9	-	14.1	96

	60	0.2	1.5	98.3	-	1.7	88
	75	0.2	1.7	98.1	-	1.9	90
SO <sub>4</sub> <sup>2-</sup> /Fe <sub>2</sub> O <sub>3</sub>	90	0.2	1.8	98.0	-	2.0	90
(450)	120	0.4	1.9	97.7	-	2.2	86
	150	0.4	2.1	97.5	-	2.4	88
	15	0.2	1.0	98.8	-	1.2	83
	30	1.0	2.4	96.6	-	3.2	75
SO <sub>4</sub> <sup>2-</sup> /Fe <sub>2</sub> O <sub>3</sub>	45	1.5	3.4	95.1	-	4.6	74
(500)	60	1.7	4.1	94.2	-	5.5	75
	90	1.6	4.5	93.9	-	5.8	78
	3960	-	4.7	95.3	-	4.7	100
HM(6.9)*	5040	-	6.7	93.3	-	6.7	100
	6510	-	8.7	91.3	-	8.7	100
	7950	-	12.2	88.8	-	11.2	100
	9720	-	14.1	85.9	-	14.1	100
	11340	-	16.8	83.2	-	16.8	100

\* The Si/Al ratio of HM is 6.9.

Computational results show that the rates of all the solid acid catalysts for pentane isomerization also obey the rate law of a first-order reversible reaction. The calculated kinetic data of the catalysts at 35°C are listed in Table 8.

The rate constants of all the solid acid catalysts for pentane isomerization correlate fairly well with the acid strengths in the range of  $-16 < -H_0 < -12$ , as shown in figure 2. Therefore, similar to butane isomerization this reaction can also be used as a probe reaction for the estimation of superacidity of solids, in particular for colored samples with lower acid strengths such as SO<sub>4</sub><sup>2-</sup>/Fe<sub>2</sub>O<sub>3</sub> and SO<sub>4</sub><sup>2-</sup>/TiO<sub>2</sub>.

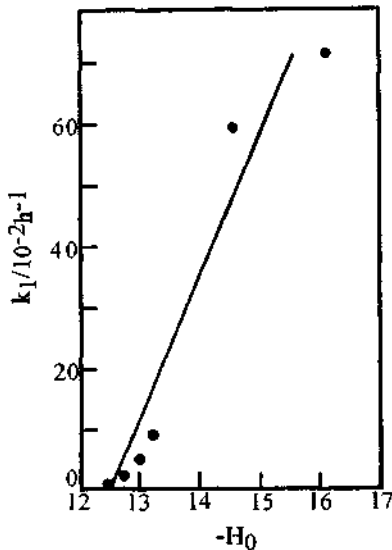


Fig. 2 Relationship between the rate constants for pentane isomerization and the acid strengths

Table 8 Kinetic data for pentane isomerization at 35°C

Sample	$k_1$ ( $10^{-2} \text{h}^{-1}$ )	$k_{-1}$ ( $10^{-2} \text{h}^{-1}$ )	r	$H_0$
$\text{SO}_4^{2-}/\text{ZrO}_2(500)$	1.78	0.297	0.999	-12.7
$\text{SO}_4^{2-}/\text{ZrO}_2(600)$	59.4	9.92	0.999	-14.5
$\text{SO}_4^{2-}/\text{ZrO}_2(650)$	72.0	12.0	0.999	-16.0
$\text{SO}_4^{2-}/\text{TiO}_2(450)$	0.489	0.0816	0.998	-
$\text{SO}_4^{2-}/\text{TiO}_2(500)$	8.18	1.37	0.992	-13.2[6]
$\text{SO}_4^{2-}/\text{TiO}_2(550)$	4.37	0.730	0.999	-
$\text{SO}_4^{2-}/\text{Fe}_2\text{O}_3(450)$	0.368	0.0614	0.977	-
$\text{SO}_4^{2-}/\text{Fe}_2\text{O}_3(500)$	4.25	0.710	0.989	-13.0[7]
$\text{SO}_4^{2-}/\text{Fe}_2\text{O}_3(550)$	0.504	0.0842	0.977	-
HM(6.9)	0.112	0.0187	0.999	-12.4[2]

### 3.2.2. Measurement on zeolites

It has been reported that the acid strengths  $H_0$  of some of the high silica zeolites are around -12[2]. Pentane isomerization reactions on various types of zeolites have been investigated at 75°C. The reaction data are given in Table 9. The isomerization selectivities of HM and HZSM-5 zeolites are higher than 90%. However, on H $\beta$ , HSY and HY zeolites cracking reaction predominates, and the isomerization selectivity approaches zero.

Table 9 Reaction data for pentane isomerization at 75°C on zeolites.

Sample*	Time (h)	C <sub>3</sub>	Product(mol%)	conversion (%)	Isomerization selectivity (%)
			i-C <sub>4</sub> i-C <sub>5</sub> n-C <sub>5</sub>		
HM(6.9)	10	0.2	0.1 10.6 89.0	11.0	96
	12	0.2	0.3 15.7 83.8	16.2	97
	14	0.3	0.5 20.1 79.1	20.9	96
	18	0.4	1.1 29.1 69.4	30.6	95
	23	0.5	2.7 38.0 58.8	40.7	93
	30	0.3	5.2 45.9 48.6	50.7	91

HM(10.2)	30	-	0.1	10.7	89.2	10.8	99
	38	-	0.2	16.3	83.5	16.5	99
	45	-	0.4	21.7	77.9	22.1	98
	62	-	1.4	32.5	66.1	33.9	96
	70	-	1.8	36.8	61.4	38.6	95
	73	-	2.5	38.2	59.3	40.4	95
HM(12.5)	30	-	-	5.7	94.3	5.7	100
	48	0.1	0.2	14.9	84.8	15.2	98
	53	0.1	0.3	18.0	81.6	18.4	98
	67	0.2	0.6	25.6	73.6	26.4	97
	69	0.2	0.8	26.5	72.7	27.5	96
	76	0.2	1.3	30.4	68.1	31.9	95
ZSM-5(25.7)	13	-	-	0.4	99.6	0.4	100
	23	-	-	0.8	99.2	0.8	100
	30	-	-	0.9	99.1	0.9	100
	42	-	-	1.1	98.9	1.1	100
	48	-	-	1.2	98.8	1.2	100
	65	-	-	1.5	98.5	1.5	100
HB(10.3)	23	0.2	1.4	0.3	98.2	1.5	20
	120	1.2	0.9	-	98.0	1.4	0
HSY(9.8)	42	1.7	-	-	98.3	1.0	0
	120	1.7	-	-	98.3	1.0	0
HY(2.6)	42	0.3	-	-	99.7	0.2	0
	120	0.5	-	-	99.5	0.3	0

\* Figures in parenthesis are the Si/Al ratios of the samples.

The reaction data of HM and HZSM-5 zeolites were fitted according to the rate law of the first-order reversible reaction and given in Table 10.

The above experimental results suggested that the HM zeolites are mild superacids with acid strengths higher than 100%  $H_2SO_4$ , so they can catalyze alkane isomerization at the temperature of 75°C or below with very high selectivity. The

order of acid strengths for the zeolites with different framework structures measured by pentane isomerization reaction is probably HM>HZSM-5>H $\beta$ >HSY>HY, which is consistent with the results of Umansky[2] obtained by using UV spectroscopic method.

Table 10 Kinetic data for pentane isomerization at 75°C on zeolites.

Sample	$k_1$ (10 <sup>-3</sup> h <sup>-1</sup> )	$k_{-1}$ (10 <sup>-3</sup> h <sup>-1</sup> )	r
HM96.9)	31.9	10.2	0.999
HM(10.2)	9.98	3.20	0.999
HM(12.5)	7.38	2.51	0.999
HZSM-5(25.7)	0.201	0.0645	0.982

## REFERENCES

1. K. Tanabe, M. Misono, Y. Ono, H. Hattori, New Solid Acids and Bases, Kodansha, Japan, 1989, p.5
2. B. S. Umansky, W. K. Hall, J. Catal., 1990, 124, 97
3. M. Hino, K. Arata, J. C. S., Chem. Comm., 1980, 851
4. Z. Gao, J. M. Chen, Y. Tang, J. Chem. Chinese Univ., 1992, 13, 1498
5. G. A. Olah, G. K. S. Prakash, J. Sommer, "Superacids", John Wiley & Sons, N. Y., 1985, p.254
6. K. Arata, Advances in Catalysis, 1990, 37, 165
7. M. Honi, K. Arata, Chem. Lett., 1979, 1259

## 4.23 Sulfated Zirconia for *n*-Butane Isomerization Experimental and Theoretical Approaches

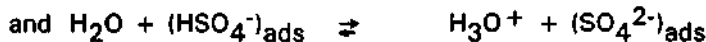
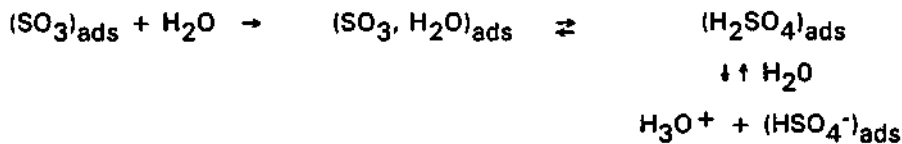
F. Babou <sup>a</sup>, B. Bigot <sup>a,b</sup>, G. Coudurier <sup>a</sup>, P. Sautet <sup>a,b</sup> and J.C. Védrine <sup>a\*</sup>

<sup>a</sup> Institut de Recherches sur la Catalyse, UPR 5401 CNRS, 2 avenue A Einstein, F. Villeurbanne 69626, France

<sup>b</sup> Ecole Normale Supérieure de Lyon, 46 allée d'Italie, Lyon 69007, France

### Abstract

Sulfated zirconia was prepared in conditions of optimal acidic properties, namely calcination at 600 °C and with 2 wt % sulfur content. Infrared studies allowed us to identify SO<sub>3</sub> species by absorption bands at 1390 and 1027 cm<sup>-1</sup>. Such a species was found to be very sensitive to water giving rise with increasing water adsorption to IR bands first at 1368 and 1200 cm<sup>-1</sup> (assigned to adsorbed H<sub>2</sub>SO<sub>4</sub><sup>+</sup>), then at 1320 and 1138 cm<sup>-1</sup> (attributed to HSO<sub>4</sub><sup>-</sup> ions) and at last for H<sub>2</sub>O saturation at 1207, 1136, 1053 and 997 cm<sup>-1</sup> (attributed to bidentate SO<sub>4</sub><sup>2-</sup> species). The 1390 cm<sup>-1</sup> band disappeared for a H<sub>2</sub>O/S atomic ratio close to 1. This phenomenon was observed to be reversible according to the equilibria



The use of incremental amounts of D<sub>2</sub>O allowed us to identify D<sub>3</sub>O<sup>+</sup> at 1250 cm<sup>-1</sup> (i.e. H<sub>3</sub>O<sup>+</sup> at 1680 cm<sup>-1</sup>).

Lewis sites associated to SO<sub>3</sub> and Brönsted sites associated to H<sub>2</sub>SO<sub>4</sub> were identified by pyridine adsorption on the 200°C outgassed sample. They corresponded to pyridine species at 1459 cm<sup>-1</sup> for pyridine/Lewis site and at 1542 cm<sup>-1</sup> for pyridinium ions. Lewis sites associated to Zr cation corresponded to pyridine species at 1444 cm<sup>-1</sup>.

The samples exhibited strong acidic properties in n-butane isomerization to isobutane in the 150 to 250°C range. Such properties were shown to strongly depend on H<sub>2</sub>O content of the solid and of the butane feed as usually observed for Friedel Crafts catalysts.

Quantum chemistry calculations using ab initio methods allowed us to suggest that the acidity of sulfated zirconia corresponds to roughly that of pure H<sub>2</sub>SO<sub>4</sub> i.e. that the material is not really superacidic but only strongly acidic.

\* to whom correspondence should be sent.

## 1. INTRODUCTION

Great interest has been focused to the synthesis of strong solid acids in order to substitute unfriendly liquid acids for important catalytic reactions as isomerization of low molecular weight alkanes C<sub>4</sub> to C<sub>8</sub>, alkylation of isobutane by butene, esterification of acids by alcohols, etc. The grafting of anions such as sulfates, tungstates or molybdates on simple oxides as ZrO<sub>2</sub>, TiO<sub>2</sub>, Fe<sub>2</sub>O<sub>3</sub>,...has been shown to lead to strong solid acids [1] particularly due to the pioneer works by Arata, Tanabe, Yamaguchi and coworkers. [1-6]

Although large efforts have been devoted to such studies, there is still disagreement between different authors concerning the acid strength (is sulfated zirconia really superacidic ?) and more importantly concerning the exact nature of such acidity. Some authors claim that protonic acidity of Brönsted type is present and responsible of catalytic properties whereas other authors report only the existence of strong aprotic acidity of Lewis type.

In order to try to bring some insight to this controversial system we have performed detailed analysis by infrared spectroscopy and we have tried to substantiate our conclusion by theoretical quantum chemistry calculations of sulfated zirconia.

In a previous work [7] we have shown how the preparation conditions of sulfated zirconia sample are critical for obtaining highly acidic materials. In particular we have shown that the calcination of the samples at 600-650°C and a sulfur content after calcination of about 2 wt % sulfur, corresponding to a theoretical monolayer coverage of the zirconia surface by sulfate anions, are two important parameters. In the present work we have studied in more details the role of water content of the catalyst after its activation at 600 °C on acidic properties.

## 2. EXPERIMENTAL

Zirconium hydroxide was prepared in a classical way as described in ref 7 starting from ZrOCl<sub>2</sub>. 8H<sub>2</sub>O 0.4 M aqueous solution and precipitated by NH<sub>4</sub>OH solution at a pH of 10. After washing with water and drying at 120°C the gel was immersed in a 0.2 N H<sub>2</sub>SO<sub>4</sub> aqueous solution for 15 minutes and filtered. The sample was then dried at 120°C for 24 h and calcined under air flow at 600 °C for 3 hours. The sulfur content was determined by atomic absorption in the Central

Analysis Laboratory of CNRS in Solaise and the surface area by BET method of N<sub>2</sub> adsorption. Sulfur content of the activated sample was found to equal 2 % in weight and its surface area equalled 80 m<sup>2</sup>.g<sup>-1</sup>.

Infrared spectroscopy study was performed on self supported wafers of 30 mg (12 mg.cm<sup>-2</sup>) using a FTIR spectrometer from Brücker (IFS 48).

Catalytic properties were determined for *n*-butane isomerization using a differential flow microreactor ( $\approx$  200 mg of catalyst) and gas chromatographic detection on line. The flow rate was 2.2 dm<sup>3</sup>. h<sup>-1</sup>, P<sub>butane</sub> = 9 kPa and H<sub>2</sub> or N<sub>2</sub> as carrier gases.

Theoretical calculations were performed by a molecular approach of the material and of the sulfated species. Acidity features were determined by calculating the energy variations involved in elementary steps which could occur during the acid-base reactions between weakly basic probe molecules as CO and H<sub>2</sub>O and a pure and a sulfated zirconia surfaces. The structure of the corresponding intermediates was calculated by SCF-LCAO-MO Hartree Fock ab-initio method using a modified version of the 86 Monster Gauss program. All geometrics were optimised with the gradient method. Details of the calculations are given in ref 8.

### 3. RESULTS AND DISCUSSION

#### 3.1 Infrared study

After impregnation and drying at 120°C, characteristic peaks were observed at 1207, 1136, 1053 and 997 cm<sup>-1</sup> and are assigned to bidentate SO<sub>4</sub><sup>2-</sup> anion in C<sub>2v</sub> symmetry. The former three bands correspond to the degenerate  $\nu_3$  vibrations and the latter one to  $\nu_1$  vibration of the free anion SO<sub>4</sub><sup>2-</sup> in Td symmetry. Infrared spectra of the sample calcined at 600°C equilibrated at room temperature in air resulted in a shift of these four bands to 1229, 1153, 1043 and 1000 cm<sup>-1</sup> respectively. Two new bands appeared as shoulders at 1067 and 937 cm<sup>-1</sup> (figure 1.a).

Outgassing at room temperature and 180°C lead to IR spectra shown in fig 1.b and 1.c where appeared progressively a band near 1380 cm<sup>-1</sup>, as usually described [4, 9-12].

Outgassing at 200°C (figure 2a) shifted this band to 1390 cm<sup>-1</sup> and lead to a decrease of the band intensity at 1320 cm<sup>-1</sup>.

The addition of incremental amounts of water was observed to displace this band from 1390 to 1350 cm<sup>-1</sup> while new bands progressively appeared at 1320, 1200 and 1055 cm<sup>-1</sup> as shown in figure 2.

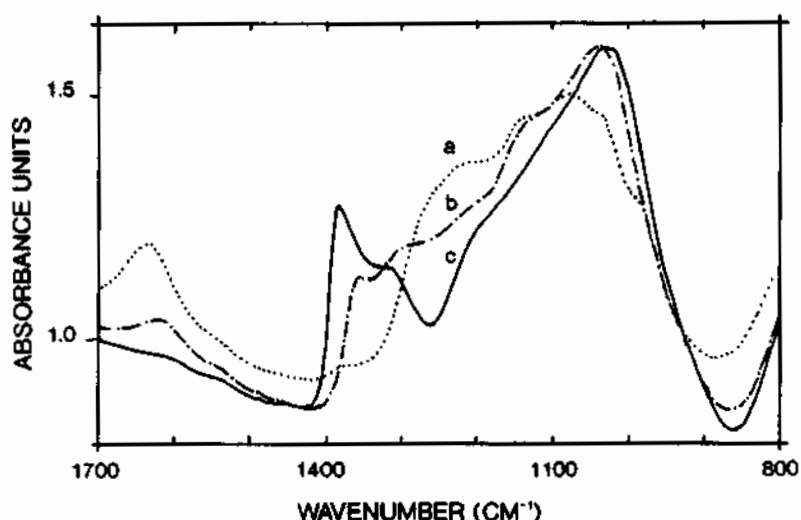


Figure 1 : Infrared spectra of sulfated zirconia a) calcined at 600°C in air and equilibrated in air at room temperature, b) outgassed at room temperature for one hour, c) outgassed at 180°C for one hour.

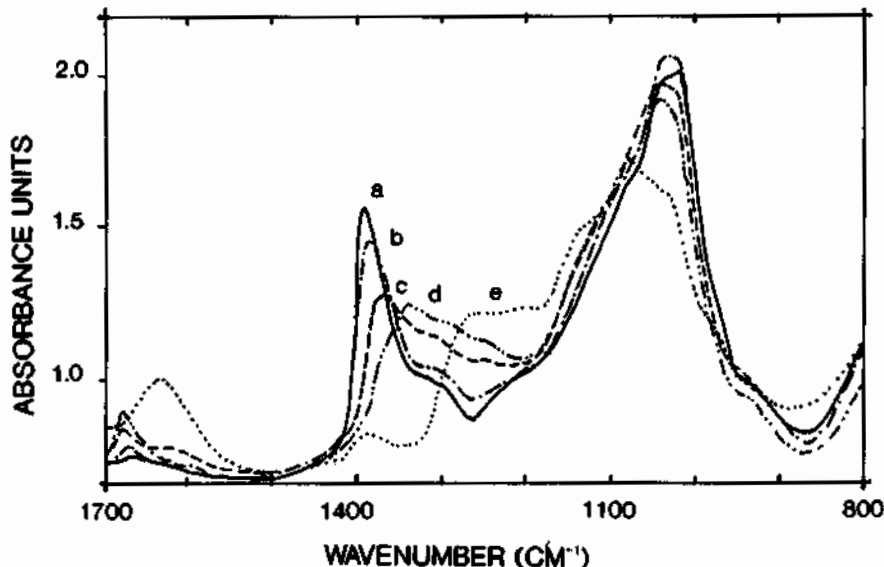


Figure 2 : Adsorption of  $\text{H}_2\text{O}$  on sulfated zirconia a) sulfated zirconia, calcined at 600°C and outgassed at 200°C, b) molar ratio  $\text{H}_2\text{O}/\text{S} = 0.17$ , e) molar ratio  $\text{H}_2\text{O}/\text{S} = 0.41$ , d) molar ratio  $\text{H}_2\text{O}/\text{S} = 0.54$ , e) equilibration under 0.65 kPa of  $\text{H}_2\text{O}$

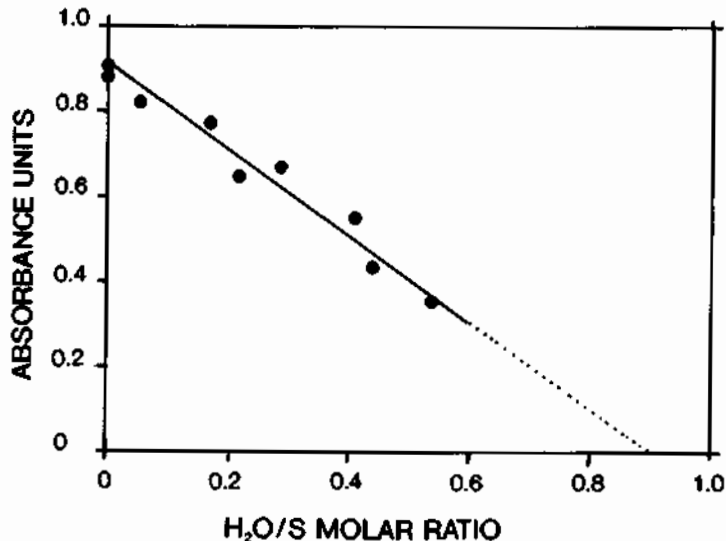


Figure 3 : Variations of intensity of the  $1390\text{ cm}^{-1}$  infrared band versus  $\text{H}_2\text{O}/\text{S}$  molar ratio.

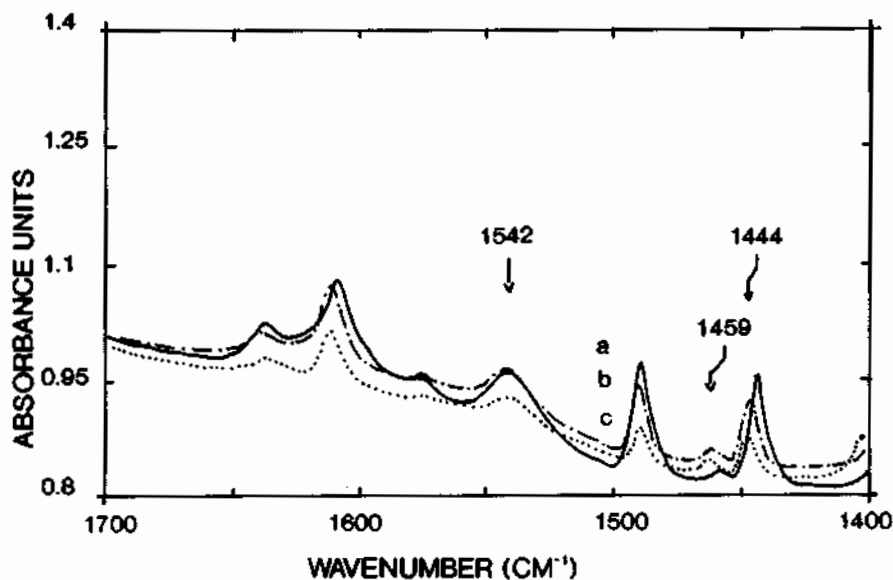


Figure 4 : Adsorption of pyridine at room temperature on sulfated zirconia calcined at  $600^\circ\text{C}$  and outgassed at  $180^\circ\text{C}$  a) desorption of pyridine at  $150^\circ\text{C}$  for 2 hours, b) at  $250^\circ\text{C}$  for 2 hours, c) at  $450^\circ\text{C}$  for 2 hours.

The changes in intensity of the former band at ca  $1390\text{ cm}^{-1}$  as a function of the amount of  $\text{H}_2\text{O}$  added and referred to S content are displayed on Figure 3 for the sample previously outgassed at  $200\text{ }^{\circ}\text{C}$ .

It can be observed a linear decrease of the  $1390/1380\text{ cm}^{-1}$  band versus  $\text{H}_2\text{O}/\text{S}$  molar ratio. Extrapolation to zero corresponds to a molar ratio  $\approx 0.90$ . At saturation of  $\text{H}_2\text{O}$  the band still existed but with a very low intensity (fig 2). In the  $\delta(\text{H}_2\text{O})$  region, it was observed a weak band at  $1600\text{ cm}^{-1}$  for the first  $\text{H}_2\text{O}$  increments, then a band at  $1680\text{ cm}^{-1}$  and for higher  $\text{H}_2\text{O}$  amounts the classical  $1638\text{ cm}^{-1}$  one. If  $\text{D}_2\text{O}$  was used, the same sulfate bands were observed and intermediately a band at  $1250\text{ cm}^{-1}$  ( $1680/1250 = 1.34$ ) which can be assigned to  $\text{D}_3\text{O}^+$  ion suggesting the presence of  $\text{H}_3\text{O}^+$  species.

These data clearly indicate that the sulfate species are strongly influenced by water addition and thus are on the surface with a molar ratio  $\text{H}_2\text{O}/\text{S}$  close to 1. This ratio obviously depends on the starting state i.e. on the more or less completely dehydrated state.

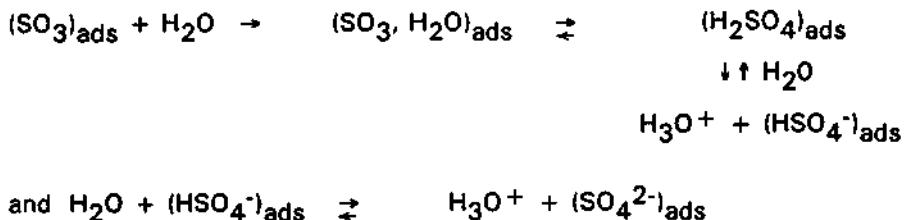
Pyridine adsorption was performed on more or less dehydrated samples. The IR spectra are shown on fig 4 for the sample outgassed at  $180\text{ }^{\circ}\text{C}$ . Brönsted site ( $\nu = 1542\text{ cm}^{-1}$ ) is clearly identified while two Lewis sites are seen at  $1459-1464$  and  $1450-1444\text{ cm}^{-1}$  respectively the frequency depending on the amount of pyridine adsorbed. The former Lewis site is assigned to  $\text{ZrO}_2$  surface since it was observed for pure zirconia. On the contrary the new site at  $1459-1464\text{ cm}^{-1}$  is assigned to Lewis site associated to adsorbed  $\text{SO}_3$  species.

We can then suggest from the IR study that on zirconia surface activated at  $600\text{ }^{\circ}\text{C}$  one has  $\text{SO}_3$  species associated to  $1390$  and  $1027\text{ cm}^{-1}$  band corresponding to a Lewis site with a band at  $1459-1464\text{ cm}^{-1}$  for adsorbed pyridine.

This  $\text{SO}_3$  species was reversibly transformed upon increasing water adsorption into :

- (i) adsorbed  $\text{H}_2\text{SO}_4$  species associated to  $1368$  and  $1200\text{ cm}^{-1}$  bands and to pyridinium species at  $1542\text{ cm}^{-1}$ ,
- (ii) then into  $\text{H}_3\text{O}^+$  (associated to the  $1680\text{ cm}^{-1}$  band) and  $\text{HSO}_4^-$  ( $1320$  and  $1138\text{ cm}^{-1}$  bands),
- (iii) and at last into bidentate  $\text{SO}_4^{2-}$  anion associated to  $1207$ ,  $1136$ ,  $1053$  and  $997\text{ cm}^{-1}$  bands.

The following equilibria are thus suggested :



### 3.2 Catalytic properties for *n*-butane isomerization

The sample calcined at 600°C was rehydrated under air at room temperature and then activated in the microreactor before reaction by flowing nitrogen at 600°C. *n*-butane isomerization reaction was performed in the 150°C-250°C range and was observed to yield high selectivity ( $\approx 97\%$ ) in isobutane which decreased at higher temperature. However as indicated in ref 7 the activity was observed to sharply decrease with time on stream. At variance when hydrogen was used as carrier gas the catalytic activation was observed to be much more stable with time on stream.

The presence of water in the feed was shown to be of particular importance. With excess water (e.g. 0.6 kPa partial pressure) introduced in the feed, the activity was shown to drop to zero. Moreover if butane was dehydrated by passing through a molecular sieve column, the activity was also shown to decrease by 20% to 30% ; if the normal feed (neither dried nor humidified) was used again catalytic activity was recovered. This reversible effect of water is very important and is to be compared with Friedel Crafts-type reactions which are also sensitive to water and are efficient in the presence of low moisture content.

### 3.3 Theoretical approach

The surface of sulfated zirconia was modelled by a coordination complex, built by comparison with a peridiodic calculation of bulk tetragonal zirconia. The neighbouring of Zr-atom in the bulk was modelled by a  $\text{Zr(OH)}_4(\text{H}_2\text{O})_4$  complex, giving correct O environment and formal oxidation number. The surface of zirconia was then represented by the  $\text{Zr(OH)}_4(\text{H}_2\text{O})_2$  molecule where two water fragments have been removed compared to the previous complex, which creates a Lewis acid unsaturation on Zr similar to the one present on the (001) surface. Starting from this surface site, many complexes have been used and compared to describe the sulfated zirconia surface, among which the three more important ones will be described here : a Lewis type adduct  $\text{Zr(OH)}_4(\text{H}_2\text{O})_2\text{SO}_3$  (model S<sub>3</sub>), a Brönsted type adduct  $\text{Zr}(\text{OH})_4(\text{H}_2\text{O})_2\text{H}_2\text{SO}_4$  (model S<sub>4</sub>) and Tanabe's model, a sulfated inserted compound,

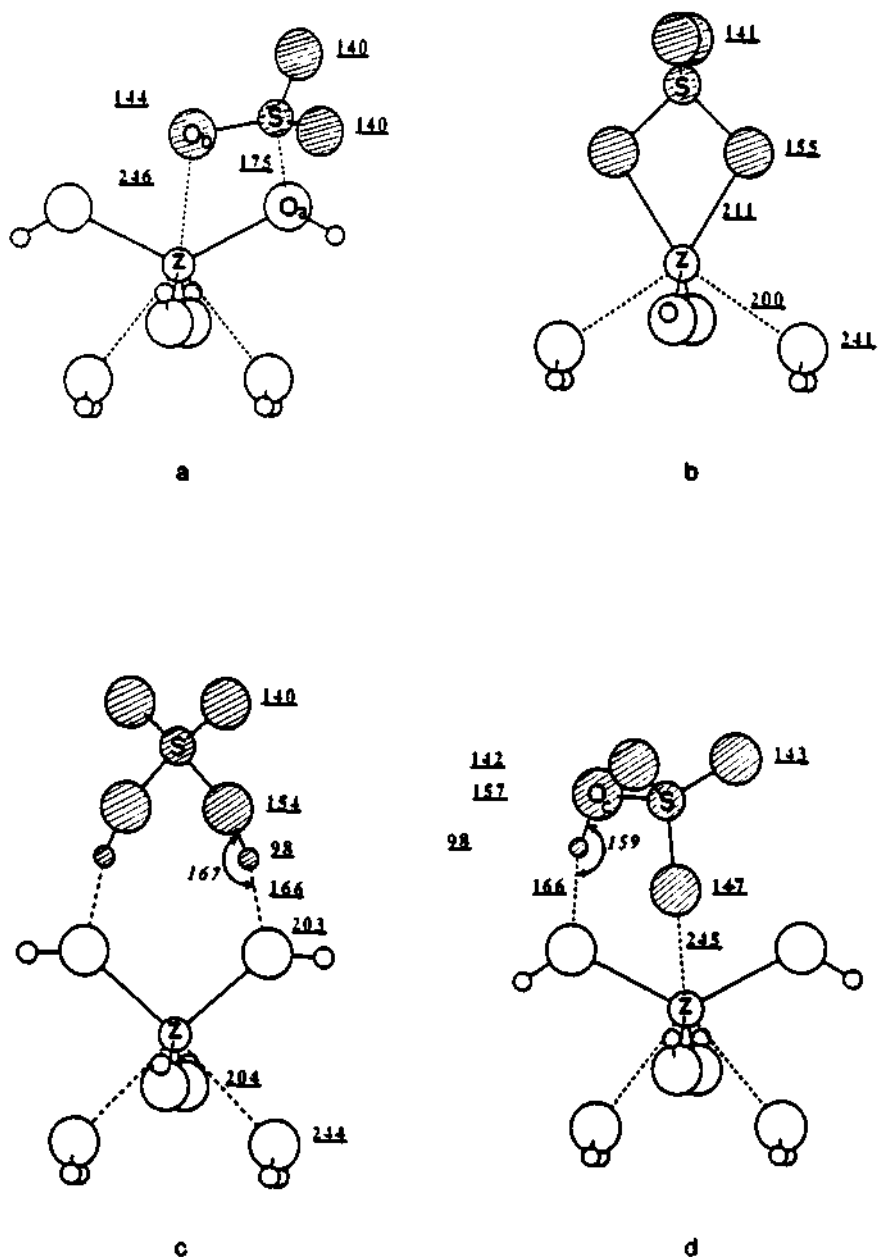


Figure 5 : Structure of the molecular complexes : a) model  $S_3$ , b) model  $S_5$ , c) model  $S_4$ , d)  $Zr(OH)_4(H_2O)_2(HSO_4^-)$ .

$\text{Zr(OH)}_4(\text{H}_2\text{O})\text{SO}_4$  (model S<sub>5</sub>) schematized in figure 5 where underlined numbers give the bond lengths in pm. The relative energies of these systems, with additional gas phase molecules to keep the total formula constant, are given in table 1 where the  $\text{Zr(OH)}_4(\text{H}_2\text{O})_2 + \text{SO}_3 + \text{H}_2\text{O}$  is taken as reference. The complex of sulfuric acid (model S<sub>4</sub>) was found to be the most stable situation. However the  $\text{SO}_3$  Lewis complex can be present in anhydric conditions. Notice that the formation energy of  $\text{H}_2\text{SO}_4$  from  $\text{SO}_3$  and  $\text{H}_2\text{O}$  is reduced from 155 kJ.mol<sup>-1</sup> in the gas phase to 84 kJ.mol<sup>-1</sup> on the zirconia surface, which makes easier the presence of  $\text{SO}_3$  species.

Table 1 Molecular models of zirconia surface and sulfated species adsorbed

Model	Molecular complexes	Relative stabilization energies (kJ.mol <sup>-1</sup> )
S <sub>1</sub>	$\text{Zr(OH)}_4(\text{H}_2\text{O})_2 + \text{SO}_3 + \text{H}_2\text{O}$	0
S <sub>2</sub>	$\text{Zr(OH)}_4(\text{H}_2\text{O})_2(\text{H}_2\text{O}) + \text{SO}_3$	-54
S <sub>5</sub>	$\text{Zr(OH)}_2(\text{H}_2\text{O})_2\text{SO}_4 + 2\text{H}_2\text{O}$	-117
S <sub>6</sub>	$\text{Zr(OH)}_4(\text{H}_2\text{O})_2 + \text{H}_2\text{SO}_4$	-155
S <sub>3</sub>	$\text{Zr(OH)}_4(\text{H}_2\text{O})_2\text{SO}_3 + \text{H}_2\text{O}$	-184
S <sub>4</sub>	$\text{Zr(OH)}_4(\text{H}_2\text{O})_2\text{H}_2\text{SO}_4$	-268

The acidity of these model species was studied by the interaction of CO as a Lewis acid probe and  $\text{H}_2\text{O}$  as a Brönsted acid probe.

A weak adsorption was found for CO on the zirconia surface. For the sulfated surface models only the complex involving  $\text{SO}_3$  can yield a Lewis acidity. The adsorption of CO on these complexes is comparable to the case of isolated  $\text{SO}_3$ , showing no enhancement of the Lewis acidity due to the interaction of  $\text{SO}_3$  with the surface. Thus it can be concluded that the Lewis acidity of sulfated zirconia is of similar strength to that of  $\text{SO}_3$ .

On the other hand only model S<sub>4</sub> can lead to a Brönsted acidity which was tested by a proton transfer reaction from the  $\text{H}_2\text{SO}_4$  fragment towards a water molecule (figure 5d)



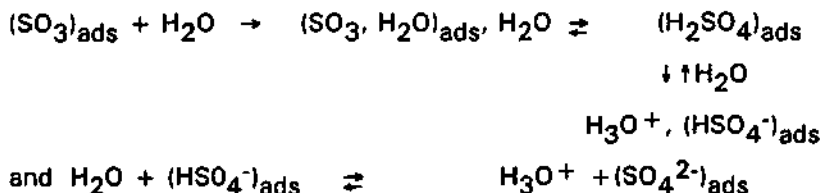
In the case of the gas phase  $\text{H}_2\text{SO}_4$  the large endothermic value (+573 kJ.mol<sup>-1</sup>) is comparable to previous calculations. This reaction is indeed only feasible in the case

of much larger solvation of the produced cation and anion than it is considered here. It is however interesting to notice that the reaction energy for the sulfated zirconia site ( $594 \text{ kJ.mol}^{-1}$ ) is very close to that of isolated  $\text{H}_2\text{SO}_4$ , within the uncertainty of calculations. It allows us to conclude that the sulfated surface is as acidic as liquid  $\text{H}_2\text{SO}_4$ .

#### 4. CONCLUSION

It was shown in a previous paper [7] how critical was the activation temperature of sulfated zirconia to get a very acidic material. The  $600\text{-}650^\circ\text{C}$  domain of activation temperature and a ca 2 wt % S content were found to be the optimum conditions. Moreover after outgassing the samples at  $400^\circ\text{C}$  very strong electron acceptor properties were identified by ESR of benzene adsorption. This could be correlated to strong Lewis type acidity only observed for strongly acidic zeolites as H-ZSM5 and H-MOR. [13, 14].

In the present work we have shown using IR spectroscopy that the  $600^\circ\text{C}$  activated sulfated species correspond to  $\text{SO}_3$  species which is reversibly very sensitive to water. This reversibility may be described by the following equilibria.



These different species were identified by IR spectroscopy and correspond to Lewis site associated to  $\text{SO}_3$  and Brönsted site associated to  $\text{H}_2\text{SO}_4$ .

Catalytic activity for n-butane isomerization in the  $150\text{-}250^\circ\text{C}$  range was shown to be sensitive to water content of the material, i.e. to the presence of Brönsted sites and also to the presence of some moisture in the butane feed. Such a conclusion is to be compared to Friedel Crafts reactions which also necessitate some moisture present in the feed.

Quantum chemistry calculations taking a surface zirconia cluster as model allowed us to represent the sulfated zirconia as similar to sulfuric acid deposited on the zirconia surface. The study of the adsorption of CO as Lewis acid probe and of  $\text{H}_2\text{O}$  as Brönsted acid probe allowed us to conclude that Lewis acidity is not stronger than that of  $\text{SO}_3$  and that Brönsted acidity is similar to that of sulfuric acid. This

leads to the conclusion that sulfated zirconia is not really a superacid material but rather as strong acid as  $H_2SO_4$ . It then follows that zirconia does not enhance strongly the acidity of  $H_2SO_4$ . It only stabilizes sulfuric acid in a form which is reversibly sensitive to water.

## 5. REFERENCES

1. V.C.F. Holm and G.C. Bailey, US patent 3, 032, 599, 1962
2. a) M. Hino and K. Arata, J. Chem. Soc., Chem. Comm., 1979, 1148  
b) M. Hino and K. Arata, J. Chem. Soc., Chem. Comm., 1980, 851  
c) M. Hino and K. Arata, J. Chem. Soc., Chem. Comm., 1980, 963  
d) M. Hino and K. Arata, Chem. Lett., 1979, 1259
3. T. Jin, M. Machida, T. Yamaguchi and K. Tanabe, Inorg. Chem., 1984, 23, 4396.
4. T. Jin, T. Yamaguchi and K. Tanabe, J. Phys. Chem., 1986, 90, 4794
5. T. Yamaguchi, T. Jin and K. Tanabe, J. Phys. Chem., 1986, 90, 3148
6. K. Arata and M. Hino, Mater. Chem. and Phys., 1990, 26, 213
7. F.R. Chen, G. Coudurier, J.F. Joly and J.C. Védrine, J. Catal., 1993, 148, 616
8. F. Babou, B. Bigot and P. Sautet, J. Phys. Chem., 1993, 97, 11501
9. a) M. Bensitel, O. Saur, J.C. Lavalley and G. Mabilon, Mater. Chem. and Phys., 1987, 17, 249  
b) M. Bensitel, O. Saur, J.C. Lavalley and B. Morrow, Mater. Chem. and Phys., 1988, 19, 147
10. T. Yamaguchi, Appl. Catal., 1990, 61, 1
11. V.S. Komarov and M. F. Siniol, Kinet. Catal., 1988, 29, 605
12. C. Morterra, G. Cerrato, C. Emanuel and V. Bolis, J. Catal., 1993, 142, 349
13. J.C. Védrine, A. Auroux, V. Bolis, P. de Dejaifve, C. Naccache, P. Wierzchowski, E.G. Derouane, J.B. B-Nagy, J.P. Gilson, J.H.C. Van Hoff, J.P. Van der Berg and J. Wolthuizen, J. Catal., 1979, 59, 248
14. P.Wierzchowski, E. Garbowksi and J.C. Védrine, J. Chim. Phys., 1982, 78, 41

This Page Intentionally Left Blank

## 4.24 Modification of Isomerization Activity and Selectivity over Sulfated Zirconia Catalysts

S. L. Soled<sup>a</sup>, E. Iglesia<sup>b</sup>, and G. M. Kramer<sup>a</sup>

<sup>a</sup>Corporate Research, Exxon Research and Engineering Co., Rt. 22 East, Annandale, NJ. 08801

<sup>b</sup>Department of Chemical Engineering, University of California, Berkeley, California 94720

### Abstract

Alkane isomerization over Pt/ZrO<sub>2</sub>/SO<sub>4</sub><sup>=</sup> shows a positive hydrogen kinetic order, suggesting the reaction proceeds via chain transfer pathways, rather than by conventional bifunctional (metal-acid) sequences. Adamantane, a molecular hydride transfer agent, when added in small quantities to n-heptane feeds increases isomerization rates while inhibiting cracking reactions. The faster hydride transfer rates and accompanying shorter carbocation surface residence times decrease secondary cracking. This effect differs significantly from acid site poisoning by aromatic molecules, which decreases both isomerization and cracking rates.

### 1. INTRODUCTION

Branched C<sub>6</sub>-C<sub>10</sub> paraffins are important components in motor fuels; they are produced by processes such as alkylation, isomerization, and oligomerization, all of which require strong acid catalysts. Environmental concerns about halide-containing solids and about strong liquid acids continue to drive the search for new oxide-based solid acids.

Holm and Bailey in 1962 discovered the unusual strong acidity of a sulfate-modified zirconia gel<sup>1</sup>, but this class of anion modified oxides was not examined in detail until the 1980's<sup>2,3,4,5,6,7,8,9,10</sup>. Hammett indicators suggested that sites with H<sub>0</sub> < -16 exist<sup>2</sup>. These sites are much stronger than 100% sulfuric acid (H<sub>0</sub> ~ -12) or acidic zeolites. Jin et al. proposed that the strong acidity of these materials arises from the electron donation to the SO<sub>4</sub><sup>=</sup> ligand, which creates a coordinatively unsaturated and electron deficient metal center acting as a strong Lewis acid<sup>3</sup>. Ebitani and coworkers suggested the interaction of H<sub>2</sub> with Pt forms hydride ions that titrate Lewis acid sites, and protons that form OH groups acting as new Bronsted acid sites<sup>11,12</sup>. Hall et al. have recently questioned Hammett acidity measurements on ZrO<sub>2</sub>/SO<sub>4</sub><sup>=</sup><sup>13</sup>, but these acids catalyze n-hexane isomerization at room temperature for several turnovers; in the presence of hydrogen and with supported platinum, they isomerize light alkanes (C<sub>4</sub>-C<sub>9</sub>) for long periods of time at 200°C<sup>14</sup>.

Here, we show that the addition of adamantane increases isomerization rate and decreases cracking selectivity during n-C<sub>7</sub>+ paraffin isomerization over Pt/ZrO<sub>2</sub>/SO<sub>4</sub><sup>=</sup><sup>15</sup>. Isomerization proceeds through a hydride transfer chain mechanism and adamantane, because of its unique ability to easily form tertiary carbocations at bridgehead carbon atoms, increases the intermolecular hydride transfer rate. In effect, the lifetime of carbocation intermediates decreases because of faster hydride transfer rates. Isomerized surface chains desorb more rapidly, and sites for ionizing new reactant molecules turnover more frequently. The lower surface residence times of carbocation intermediates leads to fewer opportunities for cracking side reactions.

## 2. EXPERIMENTAL METHODS

$\text{Pt/ZrO}_2/\text{SO}_4^=$  was prepared by precipitating zirconium hydroxide from the nitrate salt using a 28% ammonium hydroxide solution. Ten grams of  $\text{Zr}(\text{OH})_4$  dried at 110°C were slurried into 20 cm<sup>3</sup> of an aqueous chloroplatinic acid solution containing 0.05 g Pt. After stirring for 5 min, the solids were filtered and dried overnight at 110°C. They were then placed into 22 cm<sup>3</sup> of the 1N sulfuric acid solution, stirred for 5 min, filtered, dried overnight at 110°C, and calcined at 600°C for 3 h in air. Chemical analysis of the resulting solids showed that about 75% of the platinum in the solution exchanges onto the support (i.e. ~0.4% Pt content and 4.5 wt%  $\text{SO}_4^{=}$ ).

The catalyst was pressed into a wafer, crushed and sieved to retain the 0.25 to 0.50 mm fraction and then recalcined at 600°C in air for 1 hour immediately prior to being loaded into the reactor. The catalyst was reduced in flowing hydrogen at 200°C for 1 h. n-Pentane, n-hexane, n-heptane, n-octane and n-decane (Fluka, puriss grade, >99% purity) were introduced into the H<sub>2</sub> stream and the flow rates were adjusted to obtain the desired space velocity and H<sub>2</sub>/hydrocarbon ratio. Catalytic tests were carried out between 180 and 240°C at total pressures between 300 and 2500 kPa. Reaction products were analyzed by on-line capillary chromatography using flame ionization and mass spectrometric detection.

## 3. RESULTS AND DISCUSSION

### 3.1. Catalytic Reactions of n-Hexane

At 200°C, isomerization rates resemble those on Pt/mordenite catalysts reported at 250-270°C. n-Hexane isomerization selectivities exceed 98% and depend weakly on conversion. The cracking products consist primarily of isobutane, isopentane, and propane. From the observed selectivities, cracked products must arise predominantly from polymerization/cracking cycles rather than from direct hexane cracking.

Both thermodynamic and kinetic barriers limit isomerization to multibranched alkanes. Thermodynamic constraints require low temperatures to favor multibranched isomers, which in turn necessitates strong acidity to obtain the desired activity. The approach to thermodynamic isomer concentrations is usually kinetically limited. In practice, this translates into extensive recycle of unconverted reactants and monobranched products. Our isomerized products contain a dibranched/monobranched ratio of 0.23 (at 200°C, 780 kPa, and 17% conversion), much lower than the equilibrium value (1.10). The 2,2 dimethylbutane isomer, which contains a quaternary carbon atom, forms substantially below equilibrium level. This quaternary isomer requires the strongest acidity and the longest surface residence time; its formation apparently requires transformation from the stable tert-2,3 dimethylbutyl cation to the less stable and sterically hindered sec-2,2 dimethyl-3 butyl cation. Hence, kinetic factors limit the approach to equilibrium on all but the strongest acids because of the slow carbocation rearrangements required to produce these quaternary isomers. Therefore, although  $\text{Pt/ZrO}_2/\text{SO}_4^=$  shows isomerization activity at lower temperatures than other oxide catalysts, multibranched isomer formation remains kinetically limited.

### 3.2 Catalytic Reactions of n-Heptane and C<sub>7</sub><sup>+</sup>

C<sub>7</sub><sup>+</sup> paraffin isomerization presents additional challenges. The presence of stable leaving groups containing tertiary carbons (e.g. isobutane) promotes cracking; thus, commercial isomerization practice is limited to C<sub>4</sub>-C<sub>6</sub> feeds. Both desired (isomerization) and undesired (cracking) reactions occur on strong acid sites; thus control of cracking during C<sub>7</sub><sup>+</sup> paraffin isomerization remains a difficult challenge. Table 1 shows how cracking/isomerization ratios on a platinum/sulfated zirconia catalyst increase markedly with increasing size of paraffin reactants.

Cracking selectivities increase from a few percent for n-hexane reactants to nearly 50% for

**n-heptane.** This abrupt change reflects the availability of stable (non-primary carbon) decomposition products, isobutane and propane, formed by  $\beta$ -scission of 2-methylhexyl carbocations (Table 2).

**Table 1. Cracking/Isomerization Ratio For Different n-Paraffins over Pt/ZrO<sub>2</sub>/SO<sub>4</sub><sup>2-</sup>**

<b>n-paraffin</b>	<b>cracking/isomerization (wt ratio)</b>
<b>n-pentane</b>	<b>0.05</b>
<b>n-hexane</b>	<b>0.02</b>
<b>n-heptane</b>	<b>0.71</b>
<b>n-octane</b>	<b>2.01</b>

conditions: 200°C, 780 kPa, conv <30%, 6.2/1 H<sub>2</sub>/n-paraffin

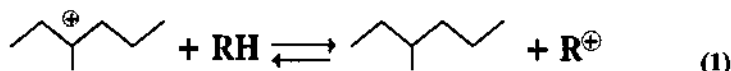
**Table 2.** Cracked Products Formed During n-Heptane Isomerization over Pt/ZrO<sub>2</sub>/SO<sub>4</sub><sup>2-</sup>

<u>Product</u>	<u>Mole (%) in C<sub>5</sub> Fraction</u>
methane	2.0
ethane	0.1
propane	43.6
n-butane	1.1
i-butane	48.1
n-pentane	0.7
i-pentane	4.0

conditions: 200°C, 6.2/1 H<sub>2</sub>/n-C<sub>7</sub>, 780kPa, 10.1% conversion

Therefore, in contrast with the oligomerization/cracking sequence required for cracking of n-hexane and iso hexanes, n-heptane feeds easily form C<sub>3</sub> and C<sub>4</sub> leaving groups by direct β-scission and hydride transfer steps. Consequently, the isomerized reaction products crack more easily than the linear feed molecules and cracking selectivity increases with increasing conversion (Fig. 1). In analogy with n-C<sub>6</sub>, the quaternary isomers 2,2 and 3,3 dimethylpentane form below equilibrium values during n-C<sub>7</sub> isomerization.

A plot of n-heptane reaction rate divided by H<sub>2</sub> partial pressures over a range of hydrogen (0.8-2.9 MPa) and n-heptane (0.033-0.2 MPa) partial pressures is nearly horizontal (Fig. 2); thus the total reaction rate is approximately first order in hydrogen and zero order in heptane. Ebitani et al.<sup>11</sup> also found a positive H<sub>2</sub> rate order and suggested that it was not consistent with a conventional bifunctional isomerization mechanism. In the latter case, negative H<sub>2</sub> rate order normally reflects rate-limiting nature of the acid-catalyzed rearrangement of olefin intermediates (with the metal catalyzed dehydrogenation/hydrogenation at equilibrium). However, a bimolecular chain mechanism involving hydride transfer can account for the positive order kinetics of the isomerization reaction. If the chain isomerization mechanism is operating here, we might expect addition of hydride transfer agents to promote the isomerization rate.



### 3.3 Adamantane Addition to C<sub>7</sub><sup>+</sup> Feeds

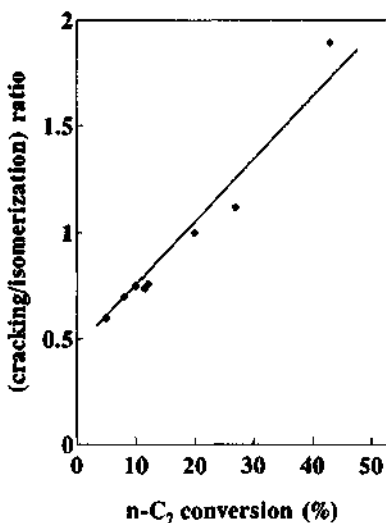
Adamantane was previously reported to act as a hydride transfer agent and to inhibit cracking during paraffin isomerization on Friedel-Craft acids<sup>16</sup>. On Pt/SO<sub>4</sub>/ZrO<sub>2</sub>, adamantane also decreases cracking selectivity during isomerization of n-heptane and n-octane. Other cracking inhibitors, such as toluene, also decrease cracking selectivity, but concurrently decrease paraffin isomerization rates.

Table 3. Selectivity Ratio (cracking/isomerization) for n-paraffins with adamantane addition

n-paraffin	no additive	0.8% adamantane	1% toluene
n-heptane	0.73	0.14	0.53
n-octane	2.1	0.28	

200°C, 6.2/1 H<sub>2</sub>/n-C<sub>7</sub>, 780 kPa, 12-22% conversion

Fig. 1. Cracking/Isomerization Ratio as a Function of Conversion



200°C, 780kPa, H<sub>2</sub>/n-C<sub>7</sub> = 6.2

Isomerization rate enhancements by adamantane can occur only if catalytic reactions on Pt/ZrO<sub>2</sub>SO<sub>4</sub><sup>-</sup> proceed by carbocation chain reactions. With 0.8 wt% adamantane addition, we observe a substantial increase in n-heptane conversion rate. Figure 3 compares the rate of n-C<sub>7</sub> conversion (moles C<sub>7</sub>/sulfur atom/sec) with either 0.8% adamantane or 1% toluene added to n-heptane reactants. Addition of toluene decreases C<sub>7</sub> reaction rate. Both toluene and adamantane decrease the average lifetimes of carbocation intermediates. However, toluene titrates the strongest acid sites, thereby decreasing both the cracking/isomerization ratio and the C<sub>7</sub> conversion rate. In contrast, adamantane decreases carbocation surface lifetimes by enhancing the hydride transfer rate, so that reaction turnovers occur faster, and the cracking/isomerization ratio decreases.

These kinetic data and the effects of adamantane addition on isomerization rate and selectivity suggest that acid sites on Pt/ZrO<sub>2</sub>/SO<sub>4</sub><sup>-</sup> are sufficiently strong and metal sites sufficiently poisoned by sulfate that the isomerization of n-alkanes occurs by carbocation chain mechanisms rather than by bifunctional metal/acid sequences.

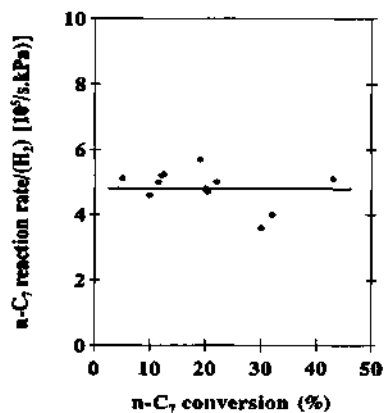
It has also been shown that n-heptane isomerizes first to methyl hexanes; rapid methyl shifts equilibrate methyl positions before subsequent conversion to dimethylpentanes<sup>17</sup>. The path to dibranched quaternary ions (2,2 and 3,3 dimethylpentanes) involves initial formation of 2,3 dimethylpentyl cations. Adamantane decreases the lifetime of all cations (including methyl hexyl and 2,3 dimethylpentyl), so that the yield of multibranched-isomers (Table 4) decreases.

**Table 4. Percent of Monobranching in Isomerate During n-Heptane Isomerization over Pt/ZrO<sub>2</sub>/SO<sub>4</sub>\* with Added Adamantane**

wt % adamantane added	% dibranched isomers
0	28
0.1	26
0.4	25
0.8	24

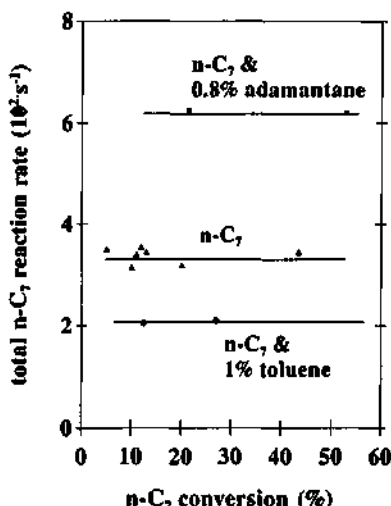
conditions: 200°C, 6.2/1 H<sub>2</sub>/n-C<sub>7</sub>, 780kPa, 20-25% conversion

**Fig. 2. H<sub>2</sub> Rate Order for C<sub>7</sub> Isomerization**



200°C, 0.8-3 MPa H<sub>2</sub>, 0.1-0.2 MPa n-C<sub>7</sub>,

**Fig. 3. Adamantane and Toluene Addition Effect C<sub>7</sub> Conversion Rate**



200°C, 780kPa, H<sub>2</sub>/n-C<sub>7</sub> = 6.2

These results suggest that quaternary isomers and cracked products probably share a common intermediate and both require longer surface lifetimes than monobranched isomers. The decrease in carbocation lifetimes caused by adamantane addition and resulting in higher isomerization turnover rates also limits the selectivity to multibranched isomers.

#### ACKNOWLEDGMENTS

The authors would like to thank William E. Gates, Sal Miseo and Richard Ernst for their experimental assistance, and Gary McVicker for discussions on solid acid chemistry.

REFERENCES

- 1 V. C. F. Holm and G. C. Bailey, U.S. Patent 3,032,599(1962)
- 2 M. Hino and K. Arata, Chem Comm., 1980, 851.
- 3 T. Jin, M. Machida, K. Tanabe, Inorg. Chem., 1984, 23, 4396.
- 4 T. Yamaguchi, T. Jin, and K. Tanabe, J. Phys. Chem., 1986, 90, 3148.
- 5 T. Jin, T. Yamaguchi, and K. Tanabe, J. Phys. Chem., 1986, 90, 4794.
- 6 T. Yamaguchi, T. Jin, T. Ishida, and K. Tanabe, Mat. Chem. Phys., 1987, 17, 3.
- 7 H. Matsuhashi, M. Hino, and K. Arata, Chem. Lett., 1988, 1027.
- 8 M. Hino and K. Arata, J. Chem. Soc. Chem. Commun., 1987, 1259.
- 9 T. Ishida, T. Yamaguchi, and K. Tanabe, Chem Lett., 1988, 1869.
- 10 K. Tanabe, Crit. Rev. Surf. Chem., 1990, 1(1),1.
- 11 K. Ebitani, J. Konishi, and H. Hattori, J. Cat. 1991, 130, 257.
- 12 K. Ebitani, J. Tsuji, H. Hattori, and H. Kita, J. Cat. 1992, 135, 609.
- 13 B. Umansky, J. Engelhardt, and W. K. Hall, J. Cat. 1991, 127, 128.
- 14 T. Hosoi, T. Shimidzu, S. Itoh, S. Baba, H. Takaoka, T. Imai, and N. Yokoyama, Prepr. -Am. Chem. Soc., Div. Pet. Chem., 1988, 33(4), 562.
- 15 E. Iglesia, S. L. Soled, and G. M. Kramer, J. Cat. 1993, 144,238.
- 16 G. M. Kramer, U.S. Patent 4,357,484(1984); U.S. Patent 4, 424, 387(1984).
- 17 G. M. Kramer and A. Schriesheim, J. Phys. Chem., 1961, 65, 1283.

## 4.25 Butene Dimerization over Sulfate and Tungstate Modified Solid Acids

S. Soled<sup>a</sup>, N. Dispensiere<sup>b</sup>, and R. Saleh<sup>b</sup>

<sup>a</sup>Exxon Research and Engineering Company, Corporate Research Laboratories, Clinton Township, Route 22 East, Annandale, N.J. 08801

<sup>b</sup>Exxon Chemical Company, Intermediates Technology Division, Clinton Township, Route 22 East, Annandale, N.J. 08801

### Abstract

Butene dimerization was studied over a series of bulk and supported sulfate and tungstate-modified zirconia and titania catalysts. Homogeneous precipitation and precipitation-deposition techniques were used to prepare multicomponent catalysts, some containing dispersed NiO on the acid. The NiO tempers the acidity, favoring trimers at the expense of cracked (C<sub>5</sub>-C<sub>7</sub>) products, and also decreases branching of the octenes.

### 1. INTRODUCTION

Propylene and butylene dimerize on supported acids (such as phosphoric acid on kieselguhr) or dispersed nickel oxide phases supported on silica or silica-alumina [1-5]. The latter catalysts display good dimer selectivity, without producing high yields of cracked or oligomerized products; however, substantial amounts of C<sub>8</sub> paraffins can form at high conversions.

Recently, an interesting class of new solid acids, consisting of anion-treated oxides, has been described [6-14]. Typically, oxides of zirconium, titanium, tin or iron are treated with such anions as sulfate or tungstate to produce solid acids. The strongest acids are reported to contain sites with Hammett acid values ( $H_o$ ) < -16, four orders of magnitude stronger than 100% sulfuric acid ( $H_o$  ~ -12). Paraffin isomerization, a reaction requiring strong acidity, occurs over some of these acids [13,14] at low temperatures. Sohn et al. have reported that precipitated nickel oxide-zirconia or nickel oxide titania catalysts which were sulfate-modified, effectively catalyze ethylene dimerization [15,16]. Nickel oxide was essential to obtain dimerization activity.

The present work examines several anion-modified catalysts for butene dimerization. We tested bulk and silica-supported versions; in some cases dispersed nickel oxide was precipitated on the acidic surfaces. Short term batch runs measured overall activity. We compared dimer versus higher oligomer selectivity, as well as monitored cracked (C<sub>5</sub>-C<sub>7</sub>) product selectivity, isomer branching and C<sub>8</sub> paraffin content.

### 2. EXPERIMENTAL

We examined the catalysts listed in table 1 by thermal gravimetry (TG), x-ray diffraction, and reaction tests. ZrO<sub>2</sub>/SO<sub>4</sub> and TiO<sub>2</sub>/SO<sub>4</sub> were prepared by precipitating zirconyl nitrate or titanium

chloride solutions with concentrated aqueous ammonium hydroxide. The titanium chloride solution was carefully prepared by slowly adding ice water to neat  $TiCl_4$  keeping the solution near 0°C. After washing and slurring with warm (60°C) dilute  $NH_4OH$  (at pH 10) to remove any residual chloride, the precipitated hydroxides were dried at 110°C. They were then slurried in 1N sulfuric acid (1 gm hydroxide/2cc acid solution) for 5 minutes, filtered, dried at 110°C, and calcined in air at 600°C for 3 hours.  $ZrO_2/WO_3$  was prepared by slurring zirconium hydroxide in a 0.5 molar ammonium metatungstate solution, drying and calcining at 800°C for three hours. NiO supported on  $ZrO_2/SO_4$  was prepared by slurring  $ZrO_2/SO_4$  in a 1M nickel nitrate solution at 35°C, and adding 1 molar ammonium carbonate dropwise to the slurry until the pH reached 6.8 to 7. After drying at 110°C, the catalysts were calcined in air at 600°C for three hours.  $ZrO_2/SO_4$  supported on silica was prepared by slurring Davison #62 silica gel with zirconyl nitrate and urea (1:4 molar ratio), and stirring at 90°C for six hours. During this period, the slurry pH rises from ~2 to above 6, as  $Zr(OH)_4$  precipitates onto silica during the homogeneous decomposition of urea. After drying at 110°C, the precipitated  $Zr(OH)_4/SiO_2$  is slurried with 1N  $H_2SO_4$  as described above, dried and calcined at 600°C. A portion of this catalyst is treated with nickel nitrate and ammonium carbonate and calcined as described above to form the NiO on  $ZrO_2/SiO_2/SO_4$  catalyst. The 28% NiO on silica-alumina catalyst is prepared by slurring a 75/25 wt% amorphous  $SiO_2-Al_2O_3$  support obtained from Davison with nickel nitrate and treating with ammonium carbonate analogous to the procedure already described with the final calcination at 500°C.

For the thermal analysis experiments, approximately 50 to 200 mg of catalyst were loaded into a Mettler TA-2000C to measure weight changes at a heating rate of 5 deg C/min in either oxidizing or reducing atmospheres. Wide angle powder x-ray scans were obtained on a Philips wide angle x-ray diffractometer operating with  $Cu K\alpha$  radiation.

Activity and selectivity parameters were measured in a batch 300 ml Parr autoclave. All catalysts were recalcined at 550°C, 0.5-1 hr in air, immediately prior to charging, and then loaded into the autoclave along with a known amount of decane (internal standard) and trans-butene-2 (feed). The reactor was purged with  $N_2$  prior to start-up. The reaction conditions were varied between: weight butene/weight catalyst: 0.8 to 4.0, reaction time: 5 hours, temperature: 95-220°C. Aliquots were withdrawn during the five hours to obtain data at shorter residence times. Residence times were defined as the product of catalyst weight times reaction time divided by the weight of butene feed. At the end of run, the autoclave was cooled to 5°C, vented and the recovered liquid analyzed by GC. An HP 5880 gas chromatograph, equipped with a 30 m SPB-1/SE-30 capillary column, measured the  $C_4$  consumption and oligomer formation. A second column (50 m HP-Pena capillary) analyzed the products following hydrogenation over a  $Pt/Al_2O_3$  catalyst to determine isomer distribution and  $C_8$  branching. GC/MS analysis was performed on a limited number of samples to determine paraffin content.

### 3. RESULTS AND DISCUSSION

**Fig. 1. Homogeneous Urea-Precipitation of Zirconium Hydroxide onto  $SiO_2$  at 90°C**

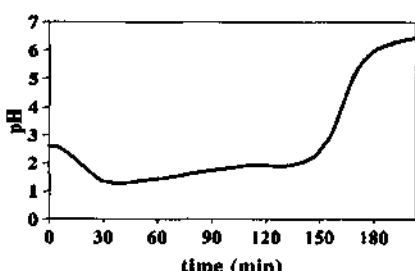
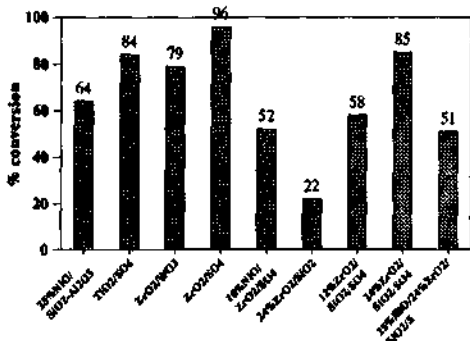
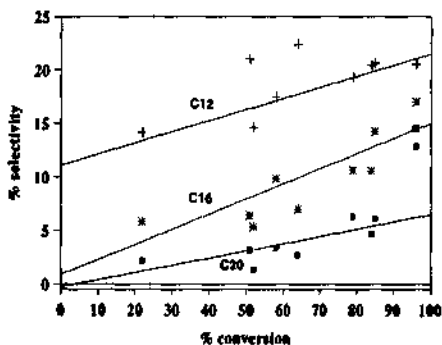


Figure 1 shows the homogeneous precipitation of zirconium hydroxide onto the silica support; after an initial induction period the pH rapidly increases as the urea hydrolyses. The x-ray spectra in figures 2-4 follow the genesis of the supported dispersed nickel oxide on sulfated zirconia. A dispersed x-ray amorphous zirconium hydroxide precipitates onto silica (fig. 2), no crystalline

**Fig. 5. Activity Comparison at 125°C, 0.34 hr Residence Time, t-butene-2 feed**



**Fig. 7. C<sub>12</sub>, C<sub>16</sub> & C<sub>20</sub><sup>+</sup> Selectivity as a Function of Conversion at 125°C, 0.34 hr Residence Time**



**Fig. 6. C<sub>8</sub> Selectivity as a Function of Conversion at 125°C, 0.34 hr Residence Time**

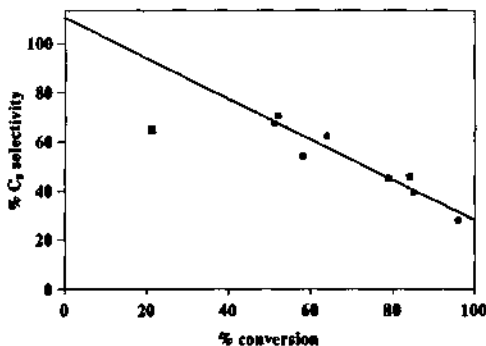
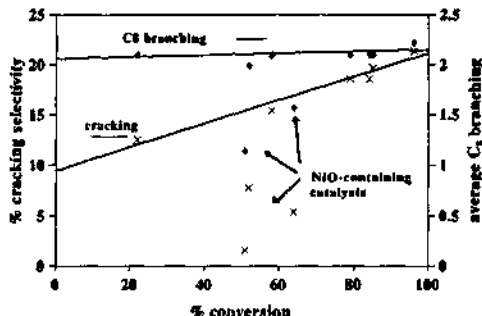


**Fig. 8. Cracking Selectivity and Average C<sub>4</sub> Branching as a Function of Conversion at 125°C and 0.34 hr Residence Time**



#### 4. CONCLUSION

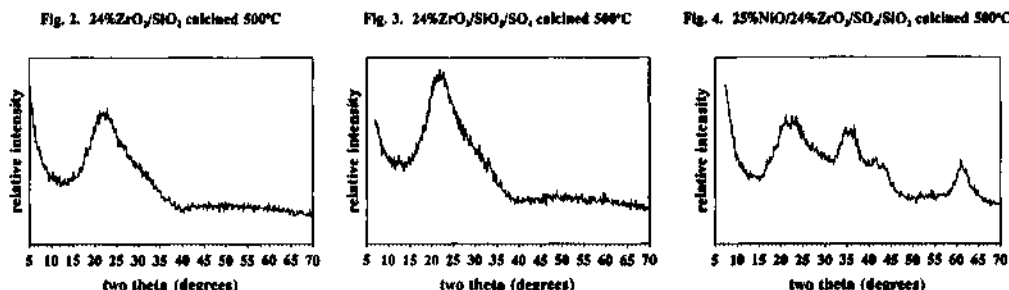
The anion modified oxides dimerize butene efficiently. Sulfated ZrO<sub>2</sub> and TiO<sub>2</sub> catalysts have the strongest acidity followed by tungstated zirconia. The silica supported catalysts show lower acidity than their bulk analogs, with the acidity depending on the loading level of the oxide. Nickel oxide can be formed as a dispersed phase by an ascending pH precipitation preparation. NiO tempers the acidity and appears to provide an independent reaction pathway that favors C<sub>12</sub> trimers at the expense of cracked products (C<sub>5</sub>-C<sub>7</sub>). In addition, less C<sub>8</sub> branching is observed on the nickel oxide-containing catalysts.

#### ACKNOWLEDGEMENTS

The authors wish to thank Sal Miseo and Joe Scanlon for their assistance.

#### REFERENCES

1. G. Wendt, E. Fritsch, R. Schollner, and H. Siegel, *Z. Anorg. Allg. Chem.*, 1980, 167, 51-60.
2. G. Wendt, J. Finster, D. Hentschel, R. Schollner, S. Hanafi, R. Shmikhail, *J. Chem. Soc. Faraday Trans. I*, 1983, 79, 2013.
3. D. Hentschel, G. Wendt, W. Engerwald, and R. Schollner, *Chem. Techn.*, 1982, 346, 313.



changes occur on addition of sulfate (fig. 3), and the precipitated nickel oxide forms a dispersed phase with broad x-ray diffraction peaks (fig. 4). Surface area measures about  $110 \text{ m}^2/\text{gm}$  for the  $\text{ZrO}_2/\text{SO}_4$  catalyst calcined in air to  $600^\circ\text{C}$ , significantly higher than for a non-sulfated zirconia calcined at the same temperature ( $30 \text{ m}^2/\text{gm}$ ). For tungsten oxide on zirconia, the catalyst remains stable at elevated temperatures under both oxidizing ( $T_{\text{decomp}} > 800^\circ\text{C}$ ) and reducing ( $T_{\text{decomp}} > 600^\circ\text{C}$ ) conditions.  $\text{ZrO}_2/\text{SO}_4$  decomposed near  $650^\circ\text{C}$ , whereas  $\text{TiO}_2/\text{SO}_4$  begins to decompose at lower temperatures in air, losing some sulfate during the  $600^\circ\text{C}$  calcination.

Table 1 lists all the catalysts compared in this study. These include bulk as well as supported versions of anion-modified solid acids (with and without NiO). Butene dimerization was measured at  $125^\circ\text{C}$  and 0.34 hr residence time, and the results are summarized in figures 5-8, showing the final conversions. The conversions should parallel relative acid strengths, with the caveat that acidity differences are underestimated for high conversion catalysts. The activity of the supported sulfated zirconia catalyst increases with increased zirconia loading, as might be expected since at both loadings, the catalysts contain dispersed zirconia phases on silica.

**Table 1. Catalysts**

Catalyst Description	Calcination Temperature (°C)
<b>Bulk Anion-Modified Solid Oxides</b>	
$\text{ZrO}_2/\text{SO}_4$	600
$10\%\text{NiO}/\text{ZrO}_2/\text{SO}_4$	600
$\text{TiO}_2/\text{SO}_4$	600
$\text{ZrO}_2/\text{WO}_3$	800
<b>Supported Catalysts</b>	
$24\%\text{ZrO}_2/\text{SiO}_2$	600
$12\%\text{ZrO}_2/\text{SiO}_2/\text{SO}_4$	600
$24\%\text{ZrO}_2/\text{SiO}_2/\text{SO}_4$	600
$25\%\text{NiO}/24\%\text{ZrO}_2/\text{SiO}_2/\text{SO}_4$	600
$28\%\text{NiO}/\text{SiO}_2-\text{Al}_2\text{O}_3$	500

Figures 5 and 6 show that a strong correlation between conversion and  $\text{C}_8$  selectivity occurs across the entire catalyst series (with  $\text{ZrO}_2/\text{SiO}_2$  an outlier). Selectivities are affected by secondary reactions, particularly by formation of higher oligomers and cracked products. Figure 7 shows that higher oligomer selectivity increases as the  $\text{C}_8$  selectivity decreases. The two high loaded nickel oxide catalysts are more selective to  $\text{C}_{12}$  than the non nickel-containing catalysts. For  $\text{ZrO}_2/\text{SO}_4$ , the apparent rapid conversion and resulting long residence time favors dimer or trimer

coupling to make  $\text{C}_{20}^+$  oligomers. As Figure 8 illustrates, the cracking selectivity ( $\text{C}_5-\text{C}_7$ ) also increases with increasing conversion. All three nickel-containing catalysts show lower amounts of cracking than the nickel-free catalysts. Branching is independent of conversion, but the nickel-containing catalysts produce less branched products than the acid catalysts without nickel. In summary, the nickel-containing catalysts display lower  $\text{C}_8$  branching, lower cracking and higher  $\text{C}_{12}$  selectivity.

4. R.L. Espinosa, R. Snel, C.J. Korf, and C.P. Nicolaides, *Appl. Catal.*, **1987**, *29*, 295.
5. Y. Chauvin, D. Commereuc, F. Hughes, and J. Thivolle-Cazat, *Appl. Catal.*, **1988**, *42*, 205.
6. V. C. F. Holm and G. C. Bailey, U.S. patent 3,032,599 (1962).
7. M. Hino & K. Arata, *Chem Comm*, **1980**, 851.
8. T. Jin, M. Machida, T. Yamaguchi, and K. Tanabe, *Inorg. Chem.*, **1984**, *23*, 4396.
9. T. Yamaguchi, T. Jin, and K. Tanabe, *J. Phys. Chem.*, **1986**, *90*, 3148.
10. T. Jin, T. Yamaguchi, and K. Tanabe, *J. Phys. Chem.*, **1986**, *90*, 4794.
11. T. Yamaguchi, T. Jin, T. Ishida, and K. Tanabe, *Mat. Chem. Phys.*, **1987**, *17*, 3.
12. H. Matsuhashi, M. Hino and K. Arata, *Chem Lett*, **1988**, 1027.
13. M. Hino & K. Arata, *J. Chem. Soc. Chem. Commun.*, **1987**, 1259.
14. K. Tanabe, *Crit. Rev. Surf. Chem.*, **1990**, *1*(1), 1.
15. B. Umansky, J. Engelhardt, and W.K. Hall, *J. Cat.*, **1991**, *127*, 128-40.
16. J. R. Sohn, H. W. Kim and J.T. Kim, *J. Mol. Catalysis*, **1987**, *41*, 375.
17. J. R. Sohn and H. J. Kim, *J. Catal.* **1986**, *101*, 428.

This Page Intentionally Left Blank

## 4.26 Alkylation of Isobutane with Butenes over Silica-supported $\text{SO}_4^{2-}-\text{ZrO}_2$

Canyiong Guo<sup>a</sup>, Zhongwei Yu<sup>a</sup>, Zaihu Qian<sup>a</sup>, Jiasheng Huang<sup>b</sup> and Yide Xu<sup>b</sup>

<sup>a</sup>Department of Chemistry, Jilin University, Changchun 130023, China

<sup>b</sup>State Key Laboratory of Catalysis, Dalian Institute of Chemical physics, Chinese Academy of Sciences, Dalian 116023, China

### Abstract

Solid superacids  $\text{SO}_4^{2-}-\text{ZrO}_2$  were supported on porous silica gel, and applied to the liquid phase alkylation of isobutane with butenes at 100 °C in a fixed bed flow reactor. The catalyst showed a high catalytic activity, selectivity, and stability for the alkylation. The optimum temperature for the reaction is 100 °C. An increase of isobutane/butene ratio and a decrease of feeding rate of the reactant improved the alkylation selectivity. TPD studies showed that the silica-supported  $\text{SO}_4^{2-}-\text{ZrO}_2$  can activate butene as well as isobutane at a low temperature. The high ability in alkylation may relate to the generation of isobutyl cation from isobutane by strong surface acidity of catalyst.

### 1. INTRODUCTION

Alkylation of isobutane with butenes is an important route to obtain a high octane number gasoline [1,2]. For the purpose of the solving the problems such as corrosion of reactor, environmental pollution, separation difficulties, etc.. caused by the use of concentrated sulfuric acid or hydrofluoric acid catalyst in industrial processes of alkylation, many works using solid acid catalysts have been done [3-5]. However, there has been no significant advance.

In previous works, we have reported that  $\text{H}_3\text{PO}_4-\text{BF}_3-\text{H}_2\text{SO}_4$  supported on silica gel and  $\text{ZrO}_2$  showed the efficient catalytic properties for the gas phase alkylation of isobutane with butenes [6]. The high activity and selectivity of  $\text{H}_3\text{PO}_4-\text{BF}_3-\text{H}_2\text{SO}_4$  supported on silica gel and  $\text{ZrO}_2$  are considered to be due to strong acidic properties. The solid superacids,  $\text{SO}_4^{2-}-\text{ZrO}_2$  in particular, were found to show noticeable catalytic properties for the gas phase alkylation reaction [7]. As for the liquid phase alkylation of isobutane with butenes, it was reported that the solid superacid catalysts  $\text{SO}_4^{2-}-\text{ZrO}_2$  and  $\text{SO}_4^{2-}-\text{ZrO}_2\cdot\text{TiO}_2$  showed considerably high selectivities at low temperatures of -5 °C [8] and 0 °C [9], in batch and flow reaction systems, respectively. Unfortunately, the superacid catalysts deactivated very quickly under the conditions. In the present work, we wish to report that solid superacid  $\text{SO}_4^{2-}-\text{ZrO}_2$  supported on the porous silica gel shows high activity in

liquid phase alkylation at the reaction temperature of about 100 °C.

## 2. EXPERIMENTAL METHODS

### 2.1. Catalyst Preparation

Silica-supported  $\text{SO}_4^{2-}\text{-ZrO}_2$  catalyst was prepared by suspending the porous silica gel into an aqueous solution of  $\text{ZrOCl}_2\cdot 8\text{H}_2\text{O}$  (10 wt%). An aqueous ammonia was added to hydrolyze  $\text{ZrOCl}_2$  at  $\text{pH} \geq 8$  to form  $\text{Zr(OH)}_4$  on silica gel. The supernatant was removed by decantation. After drying at 110 °C, the  $\text{Zr(OH)}_4$  supported on silica gel was soaked in 0.5 M  $\text{H}_2\text{SO}_4$ , followed by drying at 110 °C and calcining at 600 °C in air for 5 h. The content of  $\text{SO}_4^{2-}\text{-ZrO}_2$  was 8.7 wt%. Non-supported  $\text{SO}_4^{2-}\text{-ZrO}_2$  catalyst was prepared by hydrolyzing an aqueous solution of  $\text{ZrOCl}_2$  with aqueous ammonia at  $\text{pH} \geq 8$  to form  $\text{Zr(OH)}_4$  as a precipitate. The precipitate was washed with water several times and then dried at 110 °C. Followed by the same procedures as above.

### 2.2. Alkylation Reaction

As a source of isobutane, a mixture containing 20 wt% of n-butane and 5 wt% of pentane and 2 wt% of propane was used. As a source of butene, a mixture containing 28 wt% of 1-butene, 2 wt% of isobutene and 1 wt% of trans-2-butene was used. The other components in the butene mixture are 30 wt% of n-butane and 35 wt% of isobutane as well as about 5 wt% of propane and pentane. These two mixtures were mixed in the proper ratio to adjust the  $i\text{-C}_4^0/\text{C}_4^-$  ratio.

A fixed bed flow reactor was employed for carrying out alkylation under the pressure of 20-40 atm. In the reactor (10 mm diameter stainless steel), 2 ml of catalyst was placed and pretreated at 350 °C in a stream of nitrogen for 1 h prior to the reaction. For the analysis of gaseous and liquid products, a column packed with squalane and a capillary column of OV-101 were operated, respectively.

### 2.3. Measurements of Acidic Properties

Acid strength of superacid catalyst was determined using Hammett indicator method in sulfonyl chloride solvent [10].

IR spectra of pyridine adsorbed on the catalyst were recorded on JASCO FT/IR-5300 spectrometer at room temperature. A self supported wafer was outgassed at 450 °C and exposed to 2 Torr of pyridine vapor at 150 °C. Then the catalyst was evacuated at different temperatures.

### 2.4. TPD of Adsorbed Reactants

Temperature-programmed desorption (TPD) of the adsorbed isobutane or 1-butene was carried out in He flow (20 ml/min) as follows. The catalyst (150 mg) was pretreated at 450 °C for 1 h and cooled to room temperature, followed by introducing isobutane or 1-butene (99.99 %) for 5 min, and degassing under 450 Torr until the base line was kept steady. The desorbed products were detected by mass spectrometry (MS). The temperature raising rate was 10 °C/min.

## 3. RESULTS AND DISCUSSION

### 3.1. The Comparison of Catalytic Properties of Supported and Non-supported $\text{SO}_4^{2-}\text{-ZrO}_2$ Catalyst

Table 1 shows the results of alkylation over different catalysts. Non-supported  $\text{SO}_4^{2-}\text{-ZrO}_2$  catalyst showed a higher butene conversion than the supported  $\text{SO}_4^{2-}\text{-ZrO}_2$  catalyst. The results were obtained with the same volume of the catalyst, and the content of  $\text{SO}_4^{2-}\text{-ZrO}_2$  in supported catalyst was 8.7 wt%. When a comparation is made on the same amount of  $\text{SO}_4^{2-}\text{-ZrO}_2$ , the supported catalyst shows higher butene conversion.

In addition, the supported  $\text{SO}_4^{2-}\text{-ZrO}_2$  gave high  $C_8$  hydrocarbon selectivity and low  $C_9^+$  ( $C_9$  and heavier hydrocarbons) content in  $C_5^+$  ( $C_5$  and heavier hydrocarbons) products. Over non-supported  $\text{SO}_4^{2-}\text{-ZrO}_2$ , the butene conversion decreased with time on stream from 98.9 % at the initial stage of the reaction to 95 % in 4 h, while over the supported  $\text{SO}_4^{2-}\text{-ZrO}_2$ , the butene conversion kept steady value of 87.5 % for 4 h. A low  $C_9^+$  selectivity and small deactivation with time on stream for the supported  $\text{SO}_4^{2-}\text{-ZrO}_2$  catalyst suggest that the polymerization is suppressed on the supported  $\text{SO}_4^{2-}\text{-ZrO}_2$  catalyst.

Table 1 Comparison of catalytic properties of supported  $\text{SO}_4^{2-}\text{-ZrO}_2$  with non-supported one for the alkylation

Catalyst	$\text{SO}_4^{2-}\text{-ZrO}_2/\text{SiO}_2$	$\text{SO}_4^{2-}\text{-ZrO}_2$
Conversion of $C_4^=$ (%)	87.5	95
$C_8^o$ in $C_5^+$ product (wt%)	62.5	53.6
$C_8^o$ in $C_8$ product (%)	63.7	65.9
$C_9^+$ in $C_5^+$ product (wt%)	26.5	36.8

Reaction condition: 100 °C, 20 atm,  $i\text{-C}_4^o/C_4^=$  = 11.5, LHSV of reactant was 7.5 h<sup>-1</sup>, LHSV of  $C_4^=$  was 0.337 h<sup>-1</sup>.

### 3.2. Effect of Reaction Temperature on the Catalytic Performance of Silica-supported $\text{SO}_4^{2-}\text{-ZrO}_2$ in the Alkylation

The butene conversion and the alkylate selectivity varied with reaction temperature. At reaction temperature of 100 °C, the highest butene conversion and the least deactivation were observed. The butene conversion became decreased and the deactivation also became severe when the reaction was carried out at temperature higher or lower than 100 °C, as shown in Fig. 1.

The product distribution also varied with reaction temperature (see Table 2). In addition to the highest butene conversion, the  $C_8$  selectivity in  $C_5^+$  products and  $C_8^o$  selectivity in  $C_8$  products also showed high values at 100 °C. At low temperature, the  $C_9^+$  content became high while the  $C_8$  content in  $C_5^+$  products became low. Octenes produced by dimerization of butenes tend to polymerize to heavier hydrocarbons. The  $C_9^+$  products consisted mainly of  $C_{12}$  and  $C_{16}$  alkenes.

At high temperatures, the  $C_8$  content in reaction temperature: o 100 °C, ■ 125 °C, ▲ 150 °C, ● 75 °C, ▲ 50 °C, □ 27 °C.

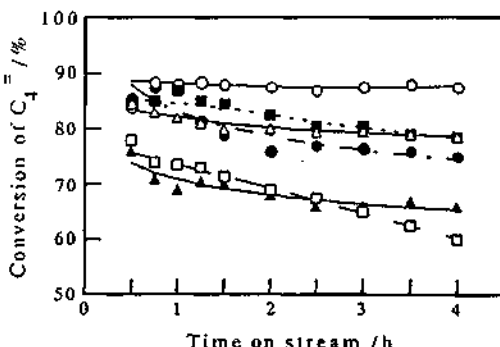


Fig. 1 Catalytic activity of  $\text{SO}_4^{2-}\text{-ZrO}_2/\text{SiO}_2$  catalyst at different temperatures; temperatures, the  $C_8$  content in reaction temperature: o 100 °C, ■ 125 °C, ▲ 150 °C, ● 75 °C, ▲ 50 °C, □ 27 °C.

the  $C_8^0$  content in  $C_8$  products and  $C_9^+$  content in  $C_5^+$  products were small. Dimerization of butenes took place to a considerable extent as compared to alkylation.

Table 2 Effect of reaction temperature on alkylation products

Reaction temperature ( $^{\circ}$ C)	27	50	75	100	125	150
$C_8^0$ in $C_5^+$ product (wt%)	52.8	50.5	57.2	62.5	65.3	70.4
$C_8^0$ in $C_8$ product (%)	73.5	69.8	66.0	63.7	63.8	59.3
$C_9^+$ in $C_5^+$ product (wt%)	35.4	40.0	32.4	26.5	25.1	16.7

Reaction conditions were the same as those in Table 1.

### 3.3. Effect of Ratio of i-Butane/Butene of Reactant on the Catalytic Alkylation

The selectivity for the  $C_8^0$  products resulting from alkylation could be improved by changing the isobutane/butene ratio. At a low isobutane/butene ratio, the amount of  $C_9^+$  products was large and the  $C_8^0$  content in  $C_8$  products was low. The polymerization proceeded to a considerable extent under a low  $i-C_4^0/C_4^=$  ratio condition as shown in Table 3.

When the ratio was increased to 6, the  $C_9^+$  content in  $C_5^+$  products was decreased and  $C_8^0$  content in  $C_5^+$  products was slightly increased. However, the  $C_8^0$  content in  $C_8$  products did not change much.

Further increase of the ratio to 12 improved the selectivity for  $C_8^0$  products remarkably. At this ratio, the  $C_9^+$  content in  $C_5^+$  products decreased considerably and the  $C_8^0$  selectivity in  $C_5^+$  products increased.

The  $C_4^=$  conversion became large with the increase of the ratio from 2 to 6 while the further increase of the ratio to 12 did not result in an obvious change of  $C_4^=$  conversion. These results indicate that a relatively high value of  $i-C_4^0/C_4^=$  is necessary for effective alkylation over the silica-supported  $SO_4^{2-}-ZrO_2$ .

Table 3 Effect of i-butane/butene ratio of reactant on the alkylation

Ratio of $i-C_4^0/C_4^=$	2	6	12
LHSV of reactant ( $h^{-1}$ )	2	4	10
Conversion of $C_4^=$ (%)	72	91	90
$C_8^0$ in $C_5^+$ product (wt%)	41.1	47.8	53.4
$C_8^0$ in $C_8$ product (%)	25.8	26.2	70.7
$C_9^+$ in $C_5^+$ product (wt%)	53.9	46.6	39.7

Reaction condition: 100  $^{\circ}$ C, 25 atm, LHSV of butenes was 0.4  $h^{-1}$ .

### 3.4. Effect of Space Velocity on the Catalytic Alkylation

Increase in the contact time could improve the alkylation selectivity. With a decrease in the space velocity, the  $C_8^0$  content in  $C_5^+$  products increased remarkably from 58.6 to 75.6 wt% corresponding to the change of LHSV of  $C_4^=$  from 0.449  $h^{-1}$  to 0.168  $h^{-1}$ . The  $C_9^+$  content in  $C_5^+$  products, on the other hand, decreased with a decrease of space velocity while the  $C_8^0$  content in  $C_8$  products did not change significantly. The  $C_4^=$  conversions did not decrease with reaction time at all space velocities.

The polymerization of olefin is the main side reaction competing with alkylation. The polymerized byproducts adsorbed on catalyst deactivate catalyst. In the alkylation system, the reaction of alkenes can easily take place as compared to the alkanes. The hydride transfer step by the reaction of alkyl cation with isobutane is often the rate controlling step in overall reaction scheme [11]. The present system showed that the increase of contact time is beneficial for the formation of alkylate.

### 3.5. Acidic and Adsorption Properties of Catalyst

Silica-supported  $\text{SO}_4^{2-}\text{-ZrO}_2$  exhibited the same acid strength as that of non-supported  $\text{SO}_4^{2-}\text{-ZrO}_2$ . The strength was in the range of  $-16.12 < \text{H}_\text{o} < -13.75$ . IR spectra of pyridine adsorbed on the silica-supported  $\text{SO}_4^{2-}\text{-ZrO}_2$  showed that Lewis acid sites predominate on the catalyst after the pretreatment at  $450^\circ\text{C}$ . With the increase of degassing temperature, the acid amount decreased.

TPD profiles of 1-butene adsorbed on catalyst showed the desorption peaks of butene and isomers of octene. It indicates that the isomerization of 1-butene and polymerization of butenes took place. TPD profiles of isobutane adsorbed on catalyst, as seen in Fig. 2, showed the desorption peaks of isobutane, n-butane at temperature of about  $38^\circ\text{C}$ . The desorption of considerably large amount of octanes is noticeable. The desorption suggests that the silica-supported  $\text{SO}_4^{2-}\text{-ZrO}_2$  can activate isobutane and convert it to octane.

Isobutane is inert even to the  $\text{BF}_3$  promoted HF catalyst in the absence of alkene [12]. Isoalkanes undergo reaction only when initiated by an alkylfluoride. Generation of tert-butyl cation by activation of isobutane may be one of the most important reasons of the high catalytic activity and selectivity of silica-supported  $\text{SO}_4^{2-}\text{-ZrO}_2$  catalyst. At temperature of  $105^\circ\text{C}$ , the desorption of octanes showed the maximum. An agreement in temperature of the optimum reaction and the maximum desorption of octanes suggests that the diffusion of products may also be one of the most important factors affecting selectivity of alkylation in present case.

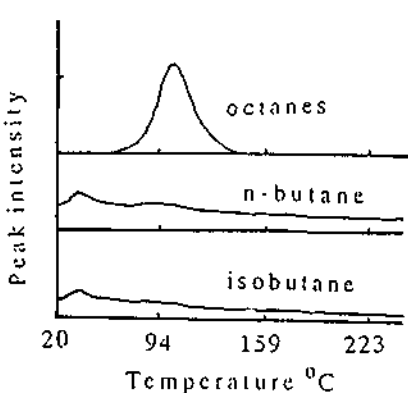


Fig. 2 TPD profiles of isobutane adsorbed  $\text{SO}_4^{2-}\text{-ZrO}_2/\text{SiO}_2$  catalyst

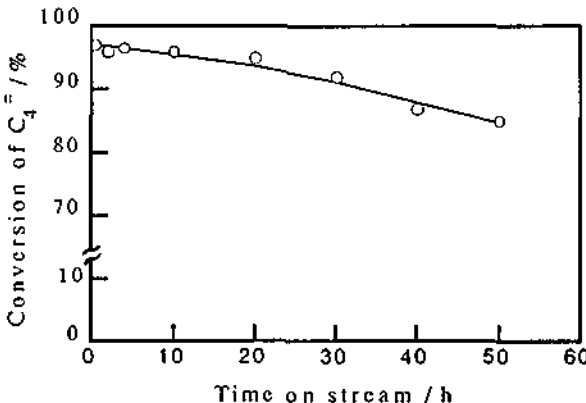


Fig. 3 Stability of activity of  $\text{SO}_4^{2-}\text{-ZrO}_2/\text{SiO}_2$

### 3.6. Stability of Activity of Silica-supported $\text{SO}_4^{2-}\text{-ZrO}_2$ Catalyst

The silica-supported  $\text{SO}_4^{2-}$ - $\text{ZrO}_2$  catalyst has been tested for alkylation reaction for 50 h time on stream. The variation of the  $\text{C}_4^-$  conversion with time on steam is shown in Fig. 3. The catalyst showed a considerable stability during the test.

Among the catalysts that had been tested for the alkylation, rare earth cation-exchanged Y-type zeolites are the most noticeable. The comparison of catalytic properties of the present catalyst with those of the catalysts reported in literatures is made in Table 4. Silica-supported  $\text{SO}_4^{2-}$ - $\text{ZrO}_2$  showed higher activity and stability than others.

Table 4 Comparison of alkylation ability of supported  $\text{SO}_4^{2-}$ - $\text{ZrO}_2$  with other catalysts

Catalyst	$\text{SO}_4^{2-}$ - $\text{ZrO}_2/\text{SiO}_2$	CaREHY <sup>[2]</sup>	REHY <sup>[13]</sup>	$\text{SO}_4^{2-}$ - $\text{ZrO}_2$ <sup>[8]</sup>
Temperature ( $^{\circ}\text{C}$ )	100	100	90	-5
Pressure (atm)	40	20	22	1.7
$i\text{-C}_4^-/\text{C}_4^-$	11.5	20	9	74
WHSV of $\text{C}_4^-$ ( $\text{h}^{-1}$ )	0.302	0.087	0.5	0.08
Type of reactor	flow	flow	batch	batch
Time on stream (h)	4	4	4	0.5
Conversion of $\text{C}_4^-$ (%)	88.5	<70	77	
$\text{C}_{5-7}$ in $\text{C}_5^+$ product (wt%)	9.2	9.3	26.3	30.6
$\text{C}_8$ in $\text{C}_5^+$ product (wt%)	75.6	77.7	70.2	54.5
$\text{C}_9^+$ in $\text{C}_5^+$ product (wt%)	15.2	13.0	3.5	14.8

## References

- 1 M. R. Kennedy, Catalysis, VI, ed. P. H. Emmett, Chapman & Hall LTd., London, 1958, p. 1.
- 2 KH. M. Minachev, E. S. Mortikov, S. M. Zenkovsky, N. V. Mostovoy and N. F. Kononov, Prepr. ACS Div. Petr. Chem., 1977, 22, 1020.
- 3 W. E. Garwood and O. B. Venuto, J. Catal., 1968, 11, 175.
- 4 J. Weitkamp, Catalysis by Zeolites, Elsevier Sientific Publishing Company, Amsterdam, 1980, p. 65.
- 5 T. J. Huang and S. Yurchak, ACS. Symp. Ser., 1977, 55, 75.
- 6 C. Guo, S. Liao, Z. Qian and K. Tanabe, to be published.
- 7 C. Guo, S. Yao, J. Cao, and Z. Qian, to be published.
- 8 K. Hatakeyama, T. Suzuka and M. Yamane, Sekiyu Gakkaishi, 1991, 34, 267.
- 9 S. Nojima, T. Imai, T. Hosoi, and S. Kitada, Prepr. 63rd Chem. Soc. Jpn. Spring Meeting, 1992, 66.
- 10 M. Hino, S. Kobayashi, and K. Arata, J. Am. Chem. Soc., 1979, 101, 6439.
- 11 L. F. Albright, Preprints of Symposium on Recent Advaces in Alkylation, Div. Petr. Chem. Inc., Am. Chem. Soc., 1977, 22, 378.
- 12 E. C. Hughes and S. M. Darling, Ind. Eng. Chem., 1951, 43, 746.
- 13 W. E. Chu and A. W. Chester, Zeolites, 1986, 6, 195.

## 4.27 Acid Property and Metathesis Activity of $\text{WO}_3\text{-ZrO}_2$ Catalysts

Masataka Kudo\*, Yusuke Yoshinaga and Sadao Hasegawa

*Department of Chemistry, Tokyo Gakugei University,  
Koganei-shi, Tokyo 184, Japan*

### ABSTRACT

Acidity and acid strength of  $\text{ZrO}_2$  were enhanced by addition of  $\text{WO}_3$ . Surface OH group as Brønsted acid was divided into two groups by  $\text{WO}_3$  content. One of them is a group of acid sites which are able to convert to metathesis active sites while the other is not. The metathesis activity was produced by evacuation at over 300°C. It is assumed that the low valent tungsten ions are generated by dehydration of surface tungsten hydroxide as precursors of metathesis active sites. The spectra shapes of  $\text{O}_2^-$  formed on the catalysts were different from low content catalysts ( $\text{W/Zr} \leq 0.1$ ) and high content catalysts ( $\text{W/Zr} \geq 0.2$ ). There appeared to be two kinds of  $\text{O}_2^-$  on the high content catalysts. The metathesis active sites, which act as formation sites of  $\text{O}_2^-$ , were only produced on high content catalysts.

### 1. INTRODUCTION

Some binary metal oxides containing  $\text{WO}_3$  are used as catalysts for the isomerization, metathesis, oxidation and hydrogenation of olefin hydrocarbons. Hattori et al. reported the relation between the acidity of  $\text{WO}_3$  catalysts and the activity for isomerization of n-butene or dehydration of 2-propanol [1]. On  $\text{WO}_3/\text{ZrO}_2$ , superacid sites ( $\text{H}_0 < -14.52$ ) were generated by calcination of impregnated sample at around 800~850°C. These superacid sites were created by interaction of amorphous  $\text{WO}_3$  with tetragonal  $\text{ZrO}_2$  [2]. On the other hand, supported  $\text{WO}_3$ ,  $\text{MoO}_3$  or  $\text{Re}_2\text{O}_7$  catalysts have high activity for metathesis. From an XPS study, it was obvious that reduction level of tungsten oxide varied depending upon its support [3]. The mechanism of metathesis was

---

\*Address : Criminal Investigation Laboratory, Metropolitan Police Department, Kasumigaseki, Tokyo 100

discussed from deuterium distributions of products [4]. Metathesis and isomerization of n-butene on non-reduced  $\text{MoO}_3/\text{Al}_2\text{O}_3$  catalysts was also reported [5].

In a previous paper, we discussed surface OH group of hydrogen treated  $\text{MoO}_3/\text{TiO}_2$  catalysts, and found that the formation of basic sites on  $\text{TiO}_2$  was suppressed by  $\text{MoO}_3$  doping [6]. In the present work, from the view of the nature of the surface OH group, the relationship between catalytic activity for metathesis or double bond isomerization of 1-butene and the acidity on amorphous  $\text{WO}_3\text{-ZrO}_2$  catalysts was examined.

## 2. EXPERIMENTAL METHODS

### 2.1. Preparation of catalysts

Zirconium oxychloride [ $\text{ZrOCl}_2 \cdot 8\text{H}_2\text{O}$ ] and ammonium paratungstate [ $(\text{NH}_4)_{10}\text{W}_{12}\text{O}_4 \cdot 5\text{H}_2\text{O}$ ] corresponding to 0~0.5 W/Zr atomic ratio were dissolved in water. Tungstate ion was coprecipitated with zirconium hydroxide by hydrolysis with aqueous ammonia. The precipitate was calcined in air at 500°C for 3h. From the result of XRF analysis, the tungsten content of each  $\text{WO}_3\text{-ZrO}_2$  catalyst agreed with the atomic ratio of W/Zr in starting solution before coprecipitation. Therefore the tungstate ion was completely incorporated into zirconium hydroxide in this preparation method. From the result of XRD measurement, the crystal form of  $\text{ZrO}_2$  powder is a mixture of comparatively imperfect monoclinic and tetragonal forms. Sharp XRD lines due to  $\text{WO}_3$  were recognized on the tungsten oxide which was prepared by calcination of ammonium paratungstate at 500°C in air for 3h. No clear diffraction lines were observed on  $\text{WO}_3\text{-ZrO}_2$  catalysts (W/Zr=0.2~0.5) as shown in Fig.1. It was indicated that each oxide inhibited the crystallization and tungsten ion was well dispersed in the bulk of  $\text{ZrO}_2$ .

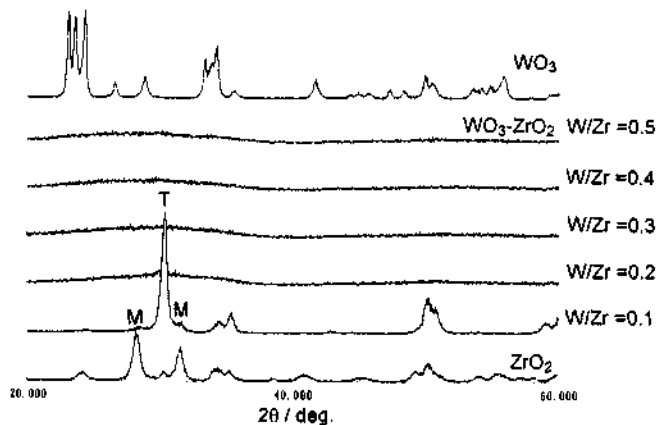


Fig. 1 XRD patterns of prepared samples.

T:  $\text{ZrO}_2$  tetragonal

M:  $\text{ZrO}_2$  monoclinic

### 2.2. Measurements of acid sites and hydrogen radical donor sites (HRD)

Acidity and acid strength were measured by Benesi method. The indicators employed were methyl red ( $\text{pK}_a=+4.8$ ), benzeneazodiphenylamine (+1.5), Dicinnamalacetone (-3.0) and benzalacetophenone (-5.6).

The number of HRD sites on the surface of catalysts was determined by DPPH method [6, 7], i.e.,  $\text{DPPH}_2$  (1,1-di-phenyl-2-picrylhydrazine) is formed from the reaction between DPPH (1,1-di-phenyl-2-picrylhydrazil) and hydrogen radical donor site, which is a nonbasic OH species in dry benzene. The amount of produced  $\text{DPPH}_2$  was determined by UV/VIS spectroscopy, and the value corresponded to the number of HRD sites.

### 2.3. ESR measurement of adsorbed oxygen

100mg of catalyst was pretreated at 500°C *in vacuo* for 1h before  $\text{O}_2$  adsorption. ESR measurement was carried out at room temperature by X-band, and *g*-values were determined by  $\text{Mn}^{2+}$  marker as a reference.

### 2.4. Gas phase reaction

The gas phase reactions were carried out at 150°C in a circulation system of ca.170cm<sup>3</sup>. The catalysts were pretreated at 500°C *in vacuo* for 1h before reaction. The weight of catalyst was 100mg and the pressure of 1-butene was 150torr. Products were analyzed by gas chromatograph with a 10m column of VZ-7 at 0°C.

## 3. RESULTS AND DISCUSSION

### 3.1. Acid sites and HRD sites

On  $\text{ZrO}_2$  catalyst, most of acid sites were weak ( $H_0=4.8\sim1.5$ ), while both acid amount and strength increased by the addition of  $\text{WO}_3$ , as shown in Fig.2. The distribution of HRD amount

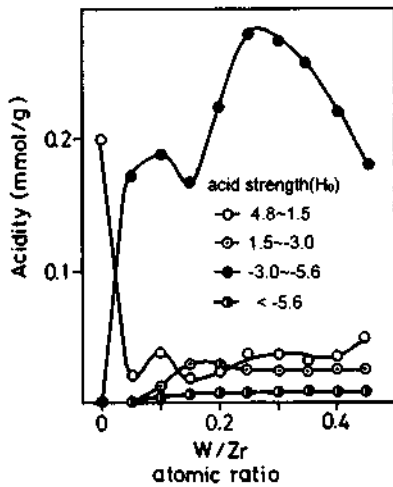


Fig. 2 Acidity of  $\text{ZrO}_2$  and  $\text{WO}_3\text{-ZrO}_2$  catalysts against W/Zr atomic ratio.

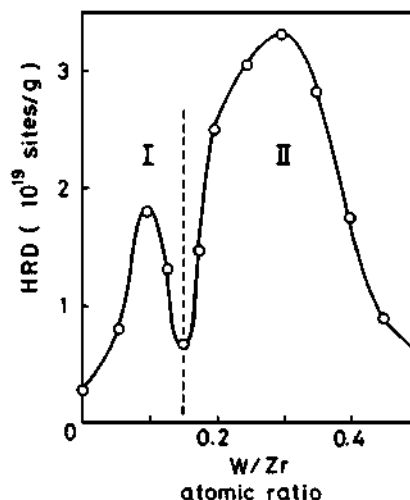


Fig. 3 Distribution of HRD amount of  $\text{ZrO}_2$  and  $\text{WO}_3\text{-ZrO}_2$  catalysts.

of  $\text{ZrO}_2$  and  $\text{WO}_3\text{-ZrO}_2$  is very similar to that of acid sites ( $H_0=-3.0\sim-5.6$ ) as shown in Fig.3. The distribution of HRD amount can be divided into two regions (I, II) which have peaks at  $\text{W/Zr}=0.1$  and 0.3, respectively. A similar division is recognized in  $\text{MoO}_3\text{-MgO}$  [8]. In the case of  $\text{MoO}_3\text{-MgO}$ , there were peaks in the distribution of HRD amount bordering  $\text{Mo/Mg}=0.3$ . From the change in coordination number of  $\text{Mo}^{5+}$  measured by ESR,  $\text{Mo}^{5+}$  existed in the bulk for  $\text{Mo/Mg}<0.3$  and appeared on the surface for  $\text{Mo/Mg}>0.3$  catalysts. It is impossible to estimate the valence deviation or coordination number of tungsten ion by ESR measurement. On the low content catalysts ( $\text{W/Zr}\leq 0.1$ ), we assumed that tungsten ions exist in the bulk of  $\text{ZrO}_2$  as in the case of  $\text{MoO}_3\text{-MgO}$  catalyst. The acid sites on the low content catalysts were generated by interaction between surface  $\text{Zr-OH}$  and bulk tungsten ion, while tungsten ions appeared on the surface of high content catalysts ( $\text{W/Zr}\geq 0.2$ ). Thus surface W-OH also acted as acid sites in high content catalysts. The curve of dehydration from samples is shown in Fig.4. The maximum quantity of dehydrated  $\text{H}_2\text{O}$  was observed on  $\text{W/Zr}=0.3$ . It was assumed that most of these  $\text{H}_2\text{O}$  were due to dissociation of  $\text{Zr-OH}$  or W-OH. As mentioned above, a large amount of HRD was recognized around  $\text{W/Zr}=0.3$  catalyst in region-II. These results support the idea that surface OH acts as an HRD and/or acid site.

### 3.2. ESR spectra of adsorbed oxygen

As a result of ESR measurement for adsorbed oxygen species, signals given at  $g_i=2.028_3$ ,  $g_i=2.010_3$  and  $g_i=2.004_0$  due to  $\text{O}_2^-$  were observed on low content catalysts. On the high content catalysts, another kind of  $\text{O}_2^-$  overlapped

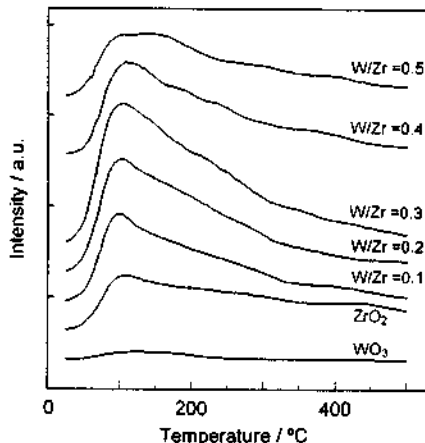


Fig. 4 Dehydration curve on  $\text{WO}_3$ ,  $\text{ZrO}_2$  and  $\text{WO}_3\text{-ZrO}_2$  ( $\text{W/Zr} = 0.1\sim 0.5$ ). The intensity of mass spectra ( $m/e=18$ ) was measured when the samples were evacuated at programmed temperature.

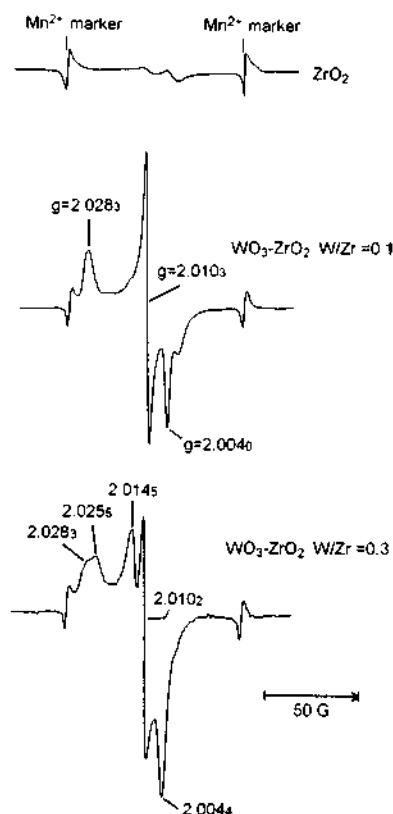
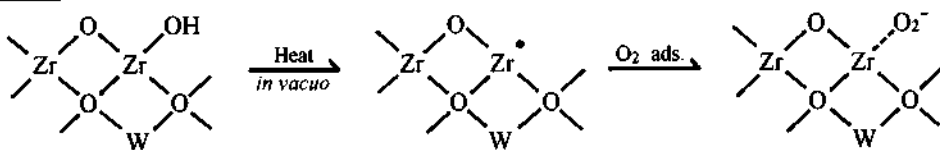


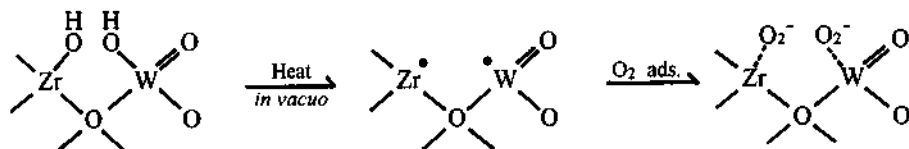
Fig. 5 ESR spectra of  $\text{O}_2^-$  observed on respective catalysts by exposure to oxygen.

(Fig. 5). The signal of another kind of  $\text{O}_2^-$  disappeared by heating at over  $180^\circ\text{C}$ , and became a simple  $\text{O}_2^-$  spectrum as observed for the low content catalyst. By TPD technique, no desorbed gas was observed from oxygen exposed high content catalysts. The result indicates that surface  $\text{O}_2^-$  was consumed for lattice oxygen. It was assumed that  $\text{O}_2^-$  was produced by coordination to  $\text{Zr}^{3+}$  on low content catalysts, and by coordination to low valent tungsten ion or  $\text{Zr}^{3+}$  on high content catalysts. From the above results, the surface OH and the electron-donating site of  $\text{O}_2$  coordination are assumed to be as shown in the following scheme.

W/Zr=0.1



W/Zr $\geq$ 0.2



### 3.3. Activity of metathesis and/or isomerization

$\text{ZrO}_2$  catalyst indicated rather basic on isomerization of 1-butene as written in a past report [9]. Only double bond isomerization of 1-butene proceeded on  $\text{WO}_3\text{-ZrO}_2$  catalysts pretreated at  $500^\circ\text{C}$  in air. On the other hand, metathesis activity appeared by evacuation pretreatment at over  $300^\circ\text{C}$ . The surface of  $\text{WO}_3\text{-ZrO}_2$  easily changed to the reduced state even by evacuation without treatment with reducing gas. As shown in Fig. 6, isomerization was the principal reaction on low content catalyst, and metathesis activity was higher at around  $\text{W/Zr}=0.3$ . The result suggested there hardly was tungsten oxide on the surface of low content catalyst. Alternatively, tungsten oxide could not be reduced even when tungsten oxide was present on the surface of the low content catalyst. There was agreement between the

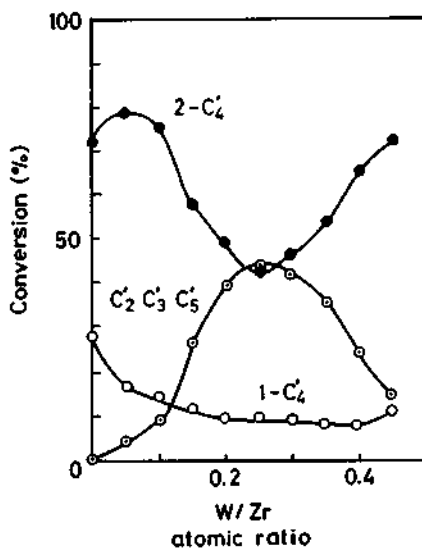


Fig. 6 Conversion of isomerization and metathesis products from 1-butene over  $\text{ZrO}_2$  and  $\text{WO}_3\text{-ZrO}_2$  pretreated by evacuation at  $500^\circ\text{C}$ .

metathesis activity and the HRD amount in region II. Consequently, the surface W-OH can be a precursor of metathesis active site, and the site is generated by dissociation of W-OH bond.

#### 4. CONCLUSION

Acidity and acid strength of  $ZrO_2$  were enhanced by addition of  $WO_3$ . This is caused that the bulk tungsten cation attracts electrons from surface Zr-OH. Surface OH acting as HRD were classified into two groups. One group was attributable to Zr-OH which was enhanced acid character by interaction with bulk tungsten ion in  $W/Zr=0.1$  catalyst, and the other was attributable to W-OH dispersed on the surface of  $W/Zr\geq 0.2$  catalysts. ESR measurement of  $O_2^-$  suggested that there were two kinds of oxygen adsorption sites existing as electron-donating sites on the surface. These sites were assumed to be low valent zirconium and tungsten. As a result of agreement between the activity of metathesis and the latter OH group, the low valent tungsten which was effective for metathesis or  $O_2^-$  production was concluded to be created by the dissociation of surface W-OH bond.

#### ACKNOWLEDGMENT

The authors gratefully acknowledge the cooperation of Mr. M. Todayama.

#### REFERENCES

- [1] H. Hattori, N. Asada, K. Tanabe, *Bull. Chem. Soc. Jpn.*, 1978, 51, 1704
- [2] K. Arata, M. Hino, Proc. 9th Intern. Congr. Catal., 1988 Calgary, p1727
- [3] P. Biloen, G. T. Pott, *J. Catal.*, 1973, 30, 169
- [4] Ka. Tanaka, K. Tanaka, K. Miyahara, *J. Chem. Soc., Chem. Commun.*, 1980, 666  
Ka. Tanaka, K. Tanaka, K. Miyahara, *J. Mol. Catal.*, 1982, 15, 133  
Ka. Tanaka, K. Tanaka, K. Miyahara, *J. Chem. Soc., Chem. Commun.*, 1984, 1626  
C. P. Casey, H. E. Tuinstra, *J. Am. Chem. Soc.*, 1978, 100, 2270
- [5] J. Goldwasser, J. Engelhardt, W. K. Hall, *J. Catal.* 1981, 70, 275
- [6] S. Hasegawa, M. Kudo, T. Tanaka, in "Acid-Base Catalysis: Proc. Intern. Symp. on Acid-Base Catalysis, Sapporo, 1988" Kodansha-VCH, pp183-190
- [7] S. Hasegawa, K. Yasuda, T. Mase, T. Kawaguchi, *J. Catal.*, 1977, 36, 125
- [8] S. Hasegawa, T. Tanaka, M. Kudo, H. Mamada, H. Hattori, S. Yoshida, *Catalysis Letter*, 1992, 12, 255
- [9] Y. Nakano, T. Iizuka, H. Hattori, K. Tanabe, *J. Catal.*, 1979, 57, 1

# Key Words Index

absolute acidity	491	condensation of alcohol with methanol	35
acetic acid, esterification of	303	coordination number of MgO	233
acidic clay K10, intrinsic nanospaces of	85	cracking	531
acrylonitrile	35	Cs <sub>2.5</sub> Ho <sub>3</sub> PW <sub>12</sub> O <sub>40</sub>	419
adamantane, a molecular hydride transfer agent	531	Cu(II)(OTf) <sub>2</sub>	97
Ag <sub>3</sub> PW <sub>12</sub> O <sub>40</sub>	117	CVD	333
aldehyde, polymerization-cyclization of	85	cyclohexane, aromatization of	257
aldolic condensation	183	cyclohexanone oxime	67
n-alkane conversion	147	cyclohexylacetate, decomposition of	419
— isomerization	507, 531	cyclopropane, isomerization of	263
alkylation	9, 147, 379, 391, 419	dealuminated mordenite	397
alkylsilane, disproportionation of	263	decomposition of N <sub>2</sub> O	409
ALPO-5	413	dehydration	273, 333
aluminosilicate	129	denOX	217
amination of alkene	71	dienedione	89
antimonation	295	disformylation of polynuclear aromatic compound	93
antimony oxide	467	ESR	479
aromatic aldehyde	47	ester	35
atom-planting	295	ethane, oxidative dehydrogenation of	451
BEA structure	355	etherification of diethylene glycol	77
Beckmann rearrangement	67	ethylbenzene	461
benzaldehyde	59	extra framework site	129
benzene adsorption	163	Fe <sub>2</sub> O <sub>3</sub> -K <sub>2</sub> CO <sub>3</sub>	461
— alkylation	257	Friedel-Crafts polyalkylation of mesitylene	97
BF <sub>3</sub>	89	— reaction	1
biphenyl, isopropylation of	397	FT-IR	157, 273, 429, 479, 495
B <sub>2</sub> O <sub>3</sub> /ZrO <sub>2</sub> , superacidity of	251	fine chemical synthesis	21
Brønsted acid (and basic) site, role of	147	formylation of aromatic compound	93
butane	419, 429, 507, 519	gallosilicate	129
1-butene, isomerizations of	263, 311, 317, 321, 333, 339, 343	Ga <sub>2</sub> O <sub>3</sub> -HZSMS	367
butene dimerization	537	GaZSMS	367
CaO	447	grinding effect	311
ε-caprolactam	67	H <sub>max</sub>	467
Cannizzaro disproportionation	183	H-mordenite	157, 397
cation-exchanged synthetic taeniolite	273	H-X/H-Y	105, 157
CH <sub>4</sub>	233	H <sub>y</sub> BiNb <sub>2</sub> O <sub>7</sub>	285
CO	233, 473, 479	H/D exchange	141
— monomers adsorbed on MgO	177	heteropolyacid	1, 21, 77, 117, 135, 419
— photooxidation	473	HF-SbF <sub>5</sub>	93
CO <sub>2</sub>	201, 207	high-silicious pentasil zeolite	67
computer graphics	217	HSO <sub>3</sub> F-SbF <sub>5</sub>	93
— simulation	355	hydrogen	233, 409

- hydrogenation of 1, 3-diene 47, 101, 457  
 hydrolysis of ethyl acetate 1  
 hydrotalcite 183  
 H-ZSM-5 105, 157, 409  
 IR 147, 163, 169, 207, 213, 295, 519  
 interaction of NH<sub>3</sub> with O<sub>2</sub> 169  
 interlayer acid site 273  
 irradiation of ultrasound 9  
 isobutane 279, 441, 543  
 isomerization 117, 147, 263, 311, 317, 321, 333, 343, 339, 531  
 isomorphous substitution with transition metal 355  
 KF catalyst 9, 447  
 KFeO<sub>2</sub> 461  
 KH<sub>β</sub> zeolite 163  
 ketone 35  
 kinetic modeling 367  
 lanthanide phosphate 441  
 laser stimulated CO + H<sub>2</sub> 501  
 MFI 355, 379  
 MgO 169, 177, 183, 201, 207, 447, 451, 473  
 MTG process 105  
 magnesia-silicate 245  
 magnesium oxide 35, 473  
 metal ions supported on silica gel 343  
 — phosphate 441  
 — substituted aluminum phosphate 317  
 metathesis 549  
 methane reforming 495  
 methanol 35, 147  
 mixed oxide, acid strength of 229  
 modified magnesium oxide 451  
 molecular dynamics 217  
 — orbital calculation 89  
 molten state 59  
 molybdenum, modified by 413  
 mordenite 217, 295, 317, 327  
 N<sub>2</sub>O 195  
 NH<sub>3</sub>-TPD measurement 355  
 NMR 105, 117, 129, 135, 273, 295, 303, 349, 419, 429  
 naphthalene, isopropylation of 397  
 neural network 229  
 nickel, modified by 413  
 — sulfate 501  
 niobic acid, layered 285  
 nitrile 35  
 nitrogen adsorption 157  
 O<sub>2</sub>-formation 195  
 organosilicon complex 339  
 oxidation of toluene 59  
 oxygen isotope exchange 201  
 pentacyclic mesylketone 89  
 pentane isomerization 507  
 photoluminescence 479  
 photooxidation of ethanol 485  
 pillared heteropolyoxometalate 279  
 platinum-supported alumina 257  
 porphyrin 85  
 potassium fluoride on alumina 9  
 preparation of basic zeolite 349  
 propane aromatization 367  
 2-propanol 413, 467  
 Pt/ZrO<sub>2</sub>/SO<sub>4</sub><sup>=</sup> 531  
 pyrrole 85, 213  
 quantum chemical study 233  
 — chemistry calculation 519  
 Raman spectroscopy 429  
 redox feature 429  
 reforming of CH<sub>4</sub> with CO<sub>2</sub> 495  
 Rh/SiO<sub>2</sub> 495  
 sepiolite, acidity of 245  
 short chain alkane, aromatization of 367  
 silica-alumina 391, 339  
 — included heteropolyacid 1  
 — monolayer on metal oxide 333  
 — supported SO<sub>4</sub><sup>2-</sup>ZrO<sub>2</sub> 543  
 silver-substituted heteropolyacid 135  
 SO<sub>4</sub><sup>2-</sup>/M<sub>2</sub>O<sub>7</sub> 507  
 stabilisation of ZrO<sub>2</sub> by sulphate 269  
 sulfate ion-promoted Zr-pillared clay 263  
 sulphated zirconia 269, 519, 531  
 sulfiding with hydrogen sulfide 343  
 superacid 251, 257, 507  
 superconducting oxide 321  
 surface lattice oxygen 441  
 taeniolite 273  
 tantalum oxide, silica-supported 485  
 TPD 273  
 triethoxysilane, disproportionation of 447  
 trimethoxysilane, disproportionation of 447  
 trisilver dodecatungstophosphate 135  
 α,β-unsaturated compound 35  
 UV-Vis diffuse-reflectance spectroscopy 183  
 vanadium-phosphorous-oxygen(VPO) 429  
 V<sub>2</sub>O<sub>5</sub>-base metal oxide 59  
 VOPO<sub>4</sub> 429  
 VPI-5, controlled pore opening of 291  
 WO<sub>3</sub>-ZrO<sub>2</sub> 549  
 XRD 273

- ZnO, Sn(CH<sub>3</sub>)<sub>4</sub>-modified 457  
Zn(II)(OTf)<sub>2</sub> 97  
ZrO<sub>2</sub> 195, 251, 263, 269, 479, 507, 519, 531,  
537, 543, 549  
Zr-Pd/C catalyst 101  
ZSM-48 299  
ZSM-5 71, 217, 409
- zeolite 105, 129, 147, 157, 163, 217, 295, 299,  
327, 355, 379, 391, 397, 507  
zirconia 47, 537  
zirconium phosphonate 303  
— polycation-exchange montmorillonite 263  
— pyrophosphate 311

This Page Intentionally Left Blank

## **STUDIES IN SURFACE SCIENCE AND CATALYSIS**

### **Advisory Editors:**

**B. Delmon, Université Catholique de Louvain, Louvain-la-Neuve, Belgium  
J.T. Yates, University of Pittsburgh, Pittsburgh, PA, U.S.A.**

---

- Volume 1** **Preparation of Catalysts I.** Scientific Bases for the Preparation of Heterogeneous Catalysts. Proceedings of the First International Symposium, Brussels, October 14–17, 1975  
edited by **B. Delmon, P.A. Jacobs and G. Poncelet**
- Volume 2** **The Control of the Reactivity of Solids.** A Critical Survey of the Factors that Influence the Reactivity of Solids, with Special Emphasis on the Control of the Chemical Processes in Relation to Practical Applications  
by **V.V. Boldyrev, M. Bulens and B. Delmon**
- Volume 3** **Preparation of Catalysts II.** Scientific Bases for the Preparation of Heterogeneous Catalysts. Proceedings of the Second International Symposium, Louvain-la-Neuve, September 4–7, 1978  
edited by **B. Delmon, P. Grange, P. Jacobs and G. Poncelet**
- Volume 4** **Growth and Properties of Metal Clusters.** Applications to Catalysis and the Photographic Process. Proceedings of the 32nd International Meeting of the Société de Chimie Physique, Villeurbanne, September 24–28, 1979  
edited by **J. Bourdon**
- Volume 5** **Catalysis by Zeolites.** Proceedings of an International Symposium, Ecully (Lyon), September 9–11, 1980  
edited by **B. Imelik, C. Naccache, Y. Ben Taarit, J.C. Vedrine, G. Coudurier and H. Praliaud**
- Volume 6** **Catalyst Deactivation.** Proceedings of an International Symposium, Antwerp, October 13–15, 1980  
edited by **B. Delmon and G.F. Froment**
- Volume 7** **New Horizons in Catalysis.** Proceedings of the 7th International Congress on Catalysis, Tokyo, June 30–July 4, 1980. Parts A and B  
edited by **T. Seiyama and K. Tanabe**
- Volume 8** **Catalysis by Supported Complexes**  
by **Yu.I. Yermakov, B.N. Kuznetsov and V.A. Zakharov**
- Volume 9** **Physics of Solid Surfaces.** Proceedings of a Symposium, Bechyňe, September 29–October 3, 1980  
edited by **M. Láznička**
- Volume 10** **Adsorption at the Gas–Solid and Liquid–Solid Interface.** Proceedings of an International Symposium, Aix-en-Provence, September 21–23, 1981  
edited by **J. Rouquerol and K.S.W. Sing**
- Volume 11** **Metal-Support and Metal-Additive Effects in Catalysis.** Proceedings of an International Symposium, Ecully (Lyon), September 14–16, 1982  
edited by **B. Imelik, C. Naccache, G. Coudurier, H. Praliaud, P. Merlaudeau, P. Gallezot, G.A. Martin and J.C. Vedrine**
- Volume 12** **Metal Microstructures in Zeolites.** Preparation – Properties – Applications.  
Proceedings of a Workshop, Bremen, September 22–24, 1982  
edited by **P.A. Jacobs, N.I. Jaeger, P. Jiru and G. Schulz-Ekloff**
- Volume 13** **Adsorption on Metal Surfaces. An Integrated Approach**  
edited by **J. Bénard**
- Volume 14** **Vibrations at Surfaces.** Proceedings of the Third International Conference, Asilomar, CA, September 1–4, 1982  
edited by **C.R. Brundle and H. Morawitz**

- Volume 15 **Heterogeneous Catalytic Reactions Involving Molecular Oxygen**  
by G.I. Golodets
- Volume 16 **Preparation of Catalysts III. Scientific Bases for the Preparation of Heterogeneous Catalysts.** Proceedings of the Third International Symposium, Louvain-la-Neuve, September 6-9, 1982  
edited by G. Poncelet, P. Grange and P.A. Jacobs
- Volume 17 **Spillover of Adsorbed Species.** Proceedings of an International Symposium, Lyon-Villeurbanne, September 12-16, 1983  
edited by G.M. Pajonk, S.J. Teichner and J.E. Germain
- Volume 18 **Structure and Reactivity of Modified Zeolites.** Proceedings of an International Conference, Prague, July 9-13, 1984  
edited by P.A. Jacobs, N.I. Jaeger, P. Jiří, V.B. Kazansky and G. Schulz-Eckloff
- Volume 19 **Catalysis on the Energy Scene.** Proceedings of the 9th Canadian Symposium on Catalysis, Quebec, P.Q., September 30-October 3, 1984  
edited by S. Kaliaguine and A. Mahay
- Volume 20 **Catalysis by Acids and Bases.** Proceedings of an International Symposium, Villeurbanne (Lyon), September 25-27, 1984  
edited by B. Imelik, C. Naccache, G. Coudurier, Y. Ben Taarit and J.C. Vedrine
- Volume 21 **Adsorption and Catalysis on Oxide Surfaces.** Proceedings of a Symposium, Uxbridge, June 28-29, 1984  
edited by M. Che and G.C. Bond
- Volume 22 **Unsteady Processes in Catalytic Reactors**  
by Yu.Sh. Matros
- Volume 23 **Physics of Solid Surfaces 1984**  
edited by J. Koukal
- Volume 24 **Zeolites: Synthesis, Structure, Technology and Application.** Proceedings of an International Symposium, Portorož-Portorose, September 3-8, 1984  
edited by B. Držaj, S. Hočevar and S. Pejovnik
- Volume 25 **Catalytic Polymerization of Olefins.** Proceedings of the International Symposium on Future Aspects of Olefin Polymerization, Tokyo, July 4-6, 1985  
edited by T. Keii and K. Soga
- Volume 26 **Vibrations at Surfaces 1985.** Proceedings of the Fourth International Conference, Bowness-on-Windermere, September 15-19, 1985  
edited by D.A. King, N.V. Richardson and S. Holloway
- Volume 27 **Catalytic Hydrogenation**  
edited by L. Cerveny
- Volume 28 **New Developments in Zeolite Science and Technology.** Proceedings of the 7th International Zeolite Conference, Tokyo, August 17-22, 1986  
edited by Y. Murakami, A. Iijima and J.W. Ward
- Volume 29 **Metal Clusters in Catalysis**  
edited by B.C. Gates, L. Guczi and H. Knözinger
- Volume 30 **Catalysis and Automotive Pollution Control.** Proceedings of the First International Symposium, Brussels, September 8-11, 1986  
edited by A. Crucq and A. Frennet
- Volume 31 **Preparation of Catalysts IV. Scientific Bases for the Preparation of Heterogeneous Catalysts.** Proceedings of the Fourth International Symposium, Louvain-la-Neuve, September 1-4, 1986  
edited by B. Delmon, P. Grange, P.A. Jacobs and G. Poncelet
- Volume 32 **Thin Metal Films and Gas Chemisorption**  
edited by P. Wissmann
- Volume 33 **Synthesis of High-silica Aluminosilicate Zeolites**  
edited by P.A. Jacobs and J.A. Martens
- Volume 34 **Catalyst Deactivation 1987.** Proceedings of the 4th International Symposium, Antwerp, September 29-October 1, 1987  
edited by B. Delmon and G.F. Froment

- Volume 35 **Keynotes in Energy-Related Catalysis**  
edited by S. Kaliaguine
- Volume 36 **Methane Conversion. Proceedings of a Symposium on the Production of Fuels and Chemicals from Natural Gas**, Auckland, April 27–30, 1987  
edited by D.M. Bibby, C.D. Chang, R.F. Howe and S. Yurchak
- Volume 37 **Innovation in Zeolite Materials Science. Proceedings of an International Symposium**, Nieuwpoort, September 13–17, 1987  
edited by P.J. Grobet, W.J. Mortier, E.F. Vansant and G. Schulz-Ekloff
- Volume 38 **Catalysis 1987. Proceedings of the 10th North American Meeting of the Catalysis Society**, San Diego, CA, May 17–22, 1987  
edited by J.W. Ward
- Volume 39 **Characterization of Porous Solids. Proceedings of the IUPAC Symposium (COPS I)**, Bad Soden a. Ts., April 26–29, 1987  
edited by K.K. Unger, J. Rouquerol, K.S.W. Sing and H. Kral
- Volume 40 **Physics of Solid Surfaces 1987. Proceedings of the Fourth Symposium on Surface Physics**, Bechyné Castle, September 7–11, 1987  
edited by J. Koukal
- Volume 41 **Heterogeneous Catalysis and Fine Chemicals. Proceedings of an International Symposium**, Poitiers, March 15–17, 1988  
edited by M. Guisnet, J. Barrault, C. Bouchoule, D. Duprez, C. Montassier and G. Pérot
- Volume 42 **Laboratory Studies of Heterogeneous Catalytic Processes**  
by E.G. Christoffel, revised and edited by Z. Paál
- Volume 43 **Catalytic Processes under Unsteady-State Conditions**  
by Yu. Sh. Matros
- Volume 44 **Successful Design of Catalysts. Future Requirements and Development.**  
Proceedings of the Worldwide Catalysis Seminars, July, 1988, on the Occasion of the 30th Anniversary of the Catalysis Society of Japan  
edited by T. Inui
- Volume 45 **Transition Metal Oxides. Surface Chemistry and Catalysis**  
by H.H. Kung
- Volume 46 **Zeolites as Catalysts, Sorbents and Detergent Builders. Applications and Innovations. Proceedings of an International Symposium**, Würzburg, September 4–8, 1988  
edited by H.G. Karge and J. Weitkamp
- Volume 47 **Photochemistry on Solid Surfaces**  
edited by M. Anpo and T. Matsuura
- Volume 48 **Structure and Reactivity of Surfaces. Proceedings of a European Conference**, Trieste, September 13–16, 1988  
edited by C. Morterra, A. Zecchina and G. Costa
- Volume 49 **Zeolites: Facts, Figures, Future. Proceedings of the 8th International Zeolite Conference**, Amsterdam, July 10–14, 1989. Parts A and B  
edited by P.A. Jacobs and R.A. van Santen
- Volume 50 **Hydrotreating Catalysts. Preparation, Characterization and Performance. Proceedings of the Annual International AIChE Meeting**, Washington, DC, November 27–December 2, 1988  
edited by M.L. Occelli and R.G. Anthony
- Volume 51 **New Solid Acids and Bases. Their Catalytic Properties**  
by K. Tanabe, M. Misono, Y. Ono and H. Hattori
- Volume 52 **Recent Advances in Zeolite Science. Proceedings of the 1989 Meeting of the British Zeolite Association**, Cambridge, April 17–19, 1989  
edited by J. Klinowsky and P.J. Barrie
- Volume 53 **Catalyst in Petroleum Refining 1989. Proceedings of the First International Conference on Catalysts in Petroleum Refining**, Kuwait, March 5–8, 1989  
edited by D.L. Trimm, S. Akashah, M. Absi-Halabi and A. Bishara

- Volume 54** **Future Opportunities in Catalytic and Separation Technology**  
edited by M. Misuno, Y. Moro-oka and S. Kimura
- Volume 55** **New Developments in Selective Oxidation. Proceedings of an International Symposium, Rimini, Italy, September 18–22, 1989**  
edited by G. Conti and F. Trifiro
- Volume 56** **Olefin Polymerization Catalysts. Proceedings of the International Symposium on Recent Developments in Olefin Polymerization Catalysts, Tokyo, October 23–25, 1989**  
edited by T. Keii and K. Soga
- Volume 57A** **Spectroscopic Analysis of Heterogeneous Catalysts. Part A: Methods of Surface Analysis**  
edited by J.L.G. Fierro
- Volume 57B** **Spectroscopic Analysis of Heterogeneous Catalysts. Part B: Chemisorption of Probe Molecules**  
edited by J.L.G. Fierro
- Volume 58** **Introduction to Zeolite Science and Practice**  
edited by H. van Bekkum, E.M. Flanigen and J.C. Jansen
- Volume 59** **Heterogeneous Catalysis and Fine Chemicals II. Proceedings of the 2nd International Symposium, Poitiers, October 2–6, 1990**  
edited by M. Guisnet, J. Barrault, C. Bouchoule, D. Duprez, G. Pérot, R. Maurel and C. Montassier
- Volume 60** **Chemistry of Microporous Crystals. Proceedings of the International Symposium on Chemistry of Microporous Crystals, Tokyo, June 26–29, 1990**  
edited by T. Inui, S. Namba and T. Tatsumi
- Volume 61** **Natural Gas Conversion. Proceedings of the Symposium on Natural Gas Conversion, Oslo, August 12–17, 1990**  
edited by A. Holmen, K.-J. Jens and S. Kolbos
- Volume 62** **Characterization of Porous Solids II. Proceedings of the IUPAC Symposium (COPS II), Alicante, May 6–9, 1990**  
edited by F. Rodríguez-Reinoso, J. Rouquerol, K.S.W. Sing and K.K. Unger
- Volume 63** **Preparation of Catalysts V. Proceedings of the Fifth International Symposium on the Scientific Bases for the Preparation of Heterogeneous Catalysts, Louvain-la-Neuve, September 3–6, 1990**  
edited by G. Poncelet, P.A. Jacobs, P. Grange and B. Delmon
- Volume 64** **New Trends in CO Activation**  
edited by L. Guczi
- Volume 65** **Catalysis and Adsorption by Zeolites. Proceedings of ZEOCAT 90, Leipzig, August 20–23, 1990**  
edited by G. Öhlmann, H. Pfeifer and R. Fricke
- Volume 66** **Dioxygen Activation and Homogeneous Catalytic Oxidation. Proceedings of the Fourth International Symposium on Dioxygen Activation and Homogeneous Catalytic Oxidation, Balatonfüred, September 10–14, 1990**  
edited by L.I. Simándi
- Volume 67** **Structure-Activity and Selectivity Relationships in Heterogeneous Catalysis. Proceedings of the ACS Symposium on Structure-Activity Relationships in Heterogeneous Catalysis, Boston, MA, April 22–27, 1990**  
edited by R.K. Grasselli and A.W. Sleight
- Volume 68** **Catalyst Deactivation 1991. Proceedings of the Fifth International Symposium, Evanston, IL, June 24–26, 1991**  
edited by C.H. Bartholomew and J.B. Butt
- Volume 69** **Zeolite Chemistry and Catalysis. Proceedings of an International Symposium, Prague, Czechoslovakia, September 8–13, 1991**  
edited by P.A. Jacobs, N.I. Jaeger, L. Kubelková and B. Wichterlová

- Volume 70 **Poisoning and Promotion in Catalysis based on Surface Science Concepts and Experiments**  
by M. Kisekinova
- Volume 71 **Catalysis and Automotive Pollution Control II. Proceedings of the 2nd International Symposium (CAPoC 2), Brussels, Belgium, September 10–13, 1990**  
edited by A. Crueg
- Volume 72 **New Developments in Selective Oxidation by Heterogeneous Catalysis.**  
Proceedings of the 3rd European Workshop Meeting on New Developments in Selective Oxidation by Heterogeneous Catalysis, Louvain-la-Neuve, Belgium, April 8–10, 1991  
edited by P. Ruiz and B. Delmon
- Volume 73 **Progress in Catalysis. Proceedings of the 12th Canadian Symposium on Catalysis, Banff, Alberta, Canada, May 25–28, 1992**  
edited by K.J. Smith and E.C. Sanford
- Volume 74 **Angle-Resolved Photoemission. Theory and Current Applications**  
edited by S.D. Kevan
- Volume 75 **New Frontiers in Catalysis, Parts A-C. Proceedings of the 10th International Congress on Catalysis, Budapest, Hungary, 19–24 July, 1992**  
edited by L. Guczi, F. Solymosi and P. Tétányi
- Volume 76 **Fluid Catalytic Cracking: Science and Technology**  
edited by J.S. Magee and M.M. Mitchell, Jr.
- Volume 77 **New Aspects of Spillover Effect in Catalysis. For Development of Highly Active Catalysts. Proceedings of the Third International Conference on Spillover, Kyoto, Japan, August 17–20, 1993**  
edited by T. Inui, K. Fujimoto, T. Uchijima and M. Masai
- Volume 78 **Heterogeneous Catalysis and Fine Chemicals III,**  
Proceedings of the 3rd International Symposium, Poitiers, April 5–8, 1993  
edited by M. Guisnet, J. Barbier, J. Barrault, C. Bouchoule, D. Duprez, G. Pérot and C. Montassier
- Volume 79 **Catalysis: An Integrated Approach to Homogeneous, Heterogeneous and Industrial Catalysis**  
edited by J.A. Moulijn, P.W.N.M. van Leeuwen and R.A. van Santen
- Volume 80 **Fundamentals of Adsorption. Proceedings of the 4th International Conference on Fundamentals of Adsorption, Kyoto, Japan, May 17–22, 1992**  
edited by M. Suzuki
- Volume 81 **Natural Gas Conversion II. Proceedings of the Third Natural Gas Conversion Symposium, Sydney, Australia, July 4–9, 1993**  
edited by H.E. Curry-Hyde and R.F. Howe
- Volume 82 **New Developments in Selective Oxidation II. Proceedings of the Second World Congress and Fourth European Workshop Meeting, Benalmádena, Spain, September 20–24, 1993**  
edited by V. Cortés Corberán and S. Vic Bellón
- Volume 83 **Zeolites and Microporous Crystals. Proceedings of the International Symposium on Zeolites and Microporous Crystals, Nagoya, Japan, August 22–25, 1993**  
edited by T. Hattori and T. Yashima
- Volume 84 **Zeolites and Related Microporous Materials: State of the Art 1994. Proceedings of the 10th International Zeolite Conference, Garmisch-Partenkirchen, Germany, July 17–22, 1994**  
edited by J. Weitkamp, H.G. Karge, H. Pfeifer and W. Hölderich

- Volume 85 **Advanced Zeolite Science and Applications**  
edited by J.C. Jansen, M. Stöcker, H.G. Karge and J. Weltkamp
- Volume 86 **Oscillating Heterogeneous Catalytic Systems**  
by M.M. Slin'ko and N.I. Jaeger
- Volume 87 **Characterization of Porous Solids III. Proceedings of the IUPAC Symposium (COPS III), Marseille, France, May 9-12, 1993**  
edited by J. Rouquerol, F. Rodriguez-Reinoso, K.S.W. Sing and K.K. Unger
- Volume 88 **Catalyst Deactivation 1994. Proceedings of the 6th International Symposium, Ostend, Belgium, October 3-5, 1994**  
edited by B. Delmon and G.F. Froment
- Volume 89 **Catalyst Design for Tailor-made Polyolefins. Proceedings of the International Symposium on Catalyst Design for Tailor-made Polyolefins, Kanazawa, Japan, March 10-12, 1994**  
edited by K. Soga and M. Terano
- Volume 90 **Acid-Base Catalysis II. Proceedings of the International Symposium on Acid-Base Catalysis II, Sapporo, Japan, December 2-4, 1993**  
edited by H. Hattori, M. Misuno and Y. Ono